Lecture Notes in Civil Engineering

Riccardo Zanon
Elide Nastri
Marco Simoncelli
Fabrizio Paolacci *Editors*

Proceedings of the XXX Congress CTA 2026

Springer

Lecture Notes in Civil Engineering 942

Series Editors

Marco di Prisco, *Politecnico di Milano, Milano, Italy*
Sheng-Hong Chen, *School of Water Resources and Hydropower Engineering, Wuhan University, Wuhan, China*
Ioannis Vayas, *Institute of Steel Structures, National Technical University of Athens, Athens, Greece*
Sanjay Kumar Shukla, *School of Engineering, Edith Cowan University, Joondalup, Australia*
Anuj Sharma, *Iowa State University, Ames, USA*
Nagesh Kumar, *Department of Civil Engineering, Indian Institute of Science Bangalore, Bengaluru, India*
Chien Ming Wang, *School of Civil Engineering, The University of Queensland, Brisbane, Australia*
Zhen-Dong Cui, *China University of Mining and Technology, Xuzhou, China*
Xinzheng Lu, *Department of Civil Engineering, Tsinghua University, Beijing, China*

Lecture Notes in Civil Engineering (LNCE) publishes the latest developments in Civil Engineering—quickly, informally and in top quality. Though original research reported in proceedings and post-proceedings represents the core of LNCE, edited volumes of exceptionally high quality and interest may also be considered for publication. Volumes published in LNCE embrace all aspects and subfields of, as well as new challenges in, Civil Engineering. Topics in the series include:

- Construction and Structural Mechanics
- Building Materials
- Concrete, Steel and Timber Structures
- Geotechnical Engineering
- Earthquake Engineering
- Coastal Engineering
- Ocean and Offshore Engineering; Ships and Floating Structures
- Hydraulics, Hydrology and Water Resources Engineering
- Environmental Engineering and Sustainability
- Structural Health and Monitoring
- Surveying and Geographical Information Systems
- Indoor Environments
- Transportation and Traffic
- Risk Analysis
- Safety and Security

To submit a proposal or request further information, please contact the appropriate Springer Editor:

– Pierpaolo Riva at pierpaolo.riva@springer.com (Europe and Americas);
– Swati Meherishi at swati.meherishi@springer.com (Asia—except China, Australia, and New Zealand);
– Wayne Hu at wayne.hu@springer.com (China).

All books in the series now indexed by Scopus and EI Compendex database!

Riccardo Zanon · Elide Nastri ·
Marco Simoncelli · Fabrizio Paolacci
Editors

Proceedings of the XXX Congress CTA 2026

Springer

Editors
Riccardo Zanon
ArcelorMittal
Esch-sur-Alzette, Luxembourg

Marco Simoncelli
Department ABC
Politecnico di Milano
Milano, Italy

Elide Nastri
Laboratory L2
University of Salerno
Fisciano, Italy

Fabrizio Paolacci
Department of Civil, Computer Science
and Aeronautical Technologies Engineering
Roma Tre University
Rome, Italy

ISSN 2366-2557 ISSN 2366-2565 (electronic)
Lecture Notes in Civil Engineering
ISBN 978-3-032-39504-7 ISBN 978-3-032-39505-4 (eBook)
https://doi.org/10.1007/978-3-032-39505-4

© The Editor(s) (if applicable) and The Author(s), under exclusive license
to Springer Nature Switzerland AG 2026

This work is subject to copyright. All rights are solely and exclusively licensed by the Publisher, whether the whole or part of the material is concerned, specifically the rights of translation, reprinting, reuse of illustrations, recitation, broadcasting, reproduction on microfilms or in any other physical way, and transmission or information storage and retrieval, electronic adaptation, computer software, or by similar or dissimilar methodology now known or hereafter developed. Unless otherwise expressly agreed by the Publisher in writing, the Publisher does not authorize use or reproduction of all or any part of this work in any manner for the purpose of training, fine-tuning, evaluating, or developing artificial intelligence models, technologies, or systems. In accordance with Article 4(3) of the EU Directive 2019/790 on copyright and related rights in the Digital Single Market, the Publisher expressly reserves all rights with respect to this work under the text and data mining exception of the directive.
The use of general descriptive names, registered names, trademarks, service marks, etc. in this publication does not imply, even in the absence of a specific statement, that such names are exempt from the relevant protective laws and regulations and therefore free for general use.
The publisher, the authors and the editors are safe to assume that the advice and information in this book are believed to be true and accurate at the date of publication. Neither the publisher nor the authors or the editors give a warranty, expressed or implied, with respect to the material contained herein or for any errors or omissions that may have been made. The publisher remains neutral with regard to jurisdictional claims in published maps and institutional affiliations.

This Springer imprint is published by the registered company Springer Nature Switzerland AG
The registered company address is: Gewerbestrasse 11, 6330 Cham, Switzerland

If disposing of this product, please recycle the paper.

Preface

For six decades, the Congress of the *Collegio dei Tecnici dell'Acciaio* (CTA) has represented one of the principal opportunities for exchange and discussion within the Italian steel construction community. Since the first Congress, held in Pisa in 1967, the event has travelled across Italy with the aim of promoting the culture of steel construction and fostering cooperation among researchers, engineers, architects, contractors, manufacturers and institutions. Over the years, the Congress has become the main meeting point for the three complementary actors which fosters the development of steel construction: academia, professional practice and industry.

The 30th edition of the CTA Congress marks an important milestone in this long-standing tradition. For the first time in its history, the Congress is being held in Rome, from 30 September to 2 October 2026, at the Centro Congressi Fontana di Trevi, in the heart of the Italian capital. The choice of Rome reflects the strategic role of steel structures in contemporary infrastructure, buildings, industrial facilities and special engineering works. It will also the contribution that steel construction can make to the transformation and renewal of the built environment and the infrastructure of tomorrow.

The theme selected for this edition, *Innovation, Reliability and Sustainable Development: All Roads Lead to Steel*, expresses the central challenges facing structural engineering today. Safety, sustainability and technological innovation can no longer be addressed as separate objectives. They are closely interconnected requirements that must be considered throughout the entire life cycle of a structure, from conception and design to fabrication, erection, operation, maintenance, adaptation, reuse and eventual disassembly.

Steel is particularly well suited to meeting these challenges. Its high structural efficiency, flexibility of use, industrialised production, suitability for prefabrication and rapid erection, together with its potential for reuse and recycling, provide engineers and architects with a broad range of opportunities. At the same time, the continuous development of materials, structural systems, fabrication processes, computational methods and monitoring technologies is expanding the boundaries of steel construction and renewing its role within the broader construction sector.

The scientific programme of the 30th CTA Congress reflects this breadth of perspectives. The contributions collected in these proceedings address steel and aluminium structures, major infrastructure and bridges, geotechnical works, tall buildings, industrial facilities, energy plants and special structures. Particular attention is devoted to seismic design, including isolation and energy dissipation, as well as to structural fire engineering and other accidental actions. Composite steel–concrete and steel–timber systems, together with structural systems made of cold-formed profiles, are also prominently represented.

The programme also encompasses advanced structural analysis and computational methods, fatigue assessment and welding technologies, erection procedures and bolted connections, and the assessment, maintenance and monitoring of existing bridges and

buildings. Corrosion, durability, reuse, structural circularity, innovative production technologies, additive manufacturing and digitalisation complete a framework that brings together established areas of steel engineering and emerging fields of research and application.

The Congress maintains the CTA tradition of linking scientific advancement with the experience of design and construction. General lectures focusing on research advances and recent steelwork project offer complementary perspective on the current state of the field. Invited contributions on the innovative design of major works and on the safety of industrial facilities further illustrate the importance of integrating scientific knowledge, engineering judgement, construction expertise and technological innovation.

A distinctive feature of the 2026 edition is the attention devoted to the transformations brought about by artificial intelligence and digital technologies. The international workshop *Artificial Intelligence and Steelwork Structural Design… Let's Get Started!* brings together fundamental concepts, optimisation methods, large language models and applications to the design of tall buildings and gridshell structures. Its organisation in collaboration with ARtISTE—Artificial Intelligence in Structural Engineering—highlights the growing role of data-driven and AI-informed approaches within structural design.

In parallel, the professional course on the fire resistance of steel structures addresses the regulatory framework, calculation methods, advanced numerical analyses and practical applications. Collaboration with the *Associazione Nazionale per l'Ingegneria del Vento*, the *Commissione per la Sicurezza delle Costruzioni di Acciaio in caso di Incendio* and ARtISTE demonstrates the Congress's commitment to creating connections among specialised scientific and professional communities.

The special session devoted to the Marangara suspension bridge in Rwanda has particular meaning for the Collegio. The bridge, co-funded by CTA and developed in collaboration with Bridges to Prosperity, shows how engineering expertise and collective commitment can generate a tangible social impact. It reminds us that structural engineering is not concerned only with technical performance, but also with accessibility, territorial development and the improvement of people's living conditions.

The papers included in this volume document the vitality and diversity of contemporary research and professional practice in steel construction. They present theoretical developments, experimental investigations, numerical methods, design procedures, innovative technologies and relevant case studies. Taken together, they provide a broad overview of the current state of knowledge while also identifying directions for future research, standardisation and practical implementation.

These proceedings are intended not merely as a record of the Congress, but as a resource for researchers, designers, manufacturers, contractors, students and all those involved in the development of steel construction. The interaction among these communities remains essential. Research contributes new knowledge and methods; industry transforms innovation into materials, products and construction technologies; professional practice integrates these resources into creative, safe and efficient engineering solutions. Their continuous dialogue is one of the defining principles of CTA and the foundation on which the future of steel construction must be built.

We wish to express our sincere gratitude to the authors for the quality of their contributions, to the invited speakers for sharing their knowledge and experience, and to the members of the Scientific Committee for their valuable work in reviewing and selecting the papers. Our appreciation also goes to the Organising Committee, the CTA Board, the scientific and professional partner associations, the institutional patrons, the sponsors and all those whose commitment has made the Congress possible.

Special thanks are due to Springer Nature for publishing these proceedings and for contributing to the international dissemination of the scientific and technical work presented at the Congress. The publication of this volume strengthens the connection between the long-standing Italian tradition of steel construction and the broader international scientific and professional community.

We warmly welcome all participants to Rome and to the thirtieth CTA Congress. We trust that the presentations, discussions and encounters generated by these days will encourage new collaborations, new research questions and new engineering solutions. Above all, we hope that this Congress will confirm the capacity of steel construction to unite innovation, safety, architectural ambition and environmental responsibility in the creation of a more sustainable built environment.

Riccardo Zanon
Fabrizio Paolacci
Marco Simoncelli
Elide Nastri

Organization

C.T.A. Board of Directors

Riccardo Zanon (Presidente)
Riccardo De Col (Vice Presidente)
Elena Mele (Vice Presidente)
Leonardo Bandini
Simone Caffe'
Alessandro Desimoni
Elisa Faretina
Elide Nastri
Vincenzo Piluso
Paolo Sattamino
Marco Simoncelli
Riccardo Tognaccini

Organizing Committee

Fabrizio Paolacci (Presidente)
Tommaso Albanesi
Attilio De Martino
Cristoforo De Martino
Gianluca Quinci

Administrative Secretariat

Valeria Pasina

Scientific Secretariat

Elide Nastri
Maria Maglio
Alessandro Pisapia
Marco Simoncelli
Paolo Todisco

Scientific Committee

Giulio Ballio
Chiara Bedon
Andrea Belleri
Federico Baiardo
Claudio Bernuzzi
Melina Bosco
Giuseppe Brando
Oreste S. Bursi
Paolo Castaldo
Carlo Andrea Castiglioni
Benedetto Cordova
Andrea Dall'Asta
Marina D'Antimo
Mario D'Aniello
Gaetano Della Corte
Antonello De Luca
Gianfranco De Matteis
Mario de Miranda
Luigino Dezi
Massimiliano Ferraioli
Bruno Finzi
Luigi Fiorino
Antonio Formisano
Fabio Freddi
Fabrizio Gara
Aurelio Ghersi
Lidia La Mendola
Raffaele Landolfo
Massimo Latour
Emanuele Maiorana
Massimo Majowiecki
Alberto Mandara
Edoardo Marino
Federico M. Mazzolani
Salvatore Giacomo Morano
Rosario Montuori
Renato Morganti
Paolo Napoli
Emidio Nigro
Maria Rosaria Pecce
Carlo Pellegrino
Vincenzo Piluso
Pierangelo Pistoletti
Raffaele Pucinotti
Francesco Ricciardelli
Gianvittorio Rizzano
Pier Paolo Rossi
Walter Salvatore
Alessandra Tosone
Nicola Tondini
Carlo Urbano
Riccardo Zandonini
Alessandro Zona

Contents

Sustainability and Reuse

Learning from Covre: Mid-century Steel Construction and New Paths for Structural Reuse 3
Riccardo Maria Polidoro and Elena Mele

Experimental Evaluation of Reused Structural Steel Elements 14
Vittoria Laghi, Elisabetta Savino, Neira Babovic, and Giada Gasparini

Steel Structures for the Adaptive Reuse of Historic Railway Buildings: Large-Span Roofs, Aerial Walkways and Wind-Induced Dynamic Effects in the Campo Marzio Station in Trieste 24
Gerardo Masiello, Chiara Bedon, and Sabato Gargiulo

AI-Driven Structural Reuse for Steel Re-manufacturing: An Integrated Methodology for Circular Steel Design 36
Vittoria Laghi, Antonio D'Anna, Emma Ghini, Stefano Silvestri, Giada Gasparini, and Pierluigi D'Acunto

Rediscovering Structural Steel Reuse: Practice and Perception in Italy 46
Giulio Basileo, Viorel Ungureanu, Renato Morganti, Alessandra Tosone, Matteo Abita, and Danilo Di Donato

Design and LCA Assessment of a Hospital Building with a CFST (Concrete-Filled Steel Tubes) Structural System 58
Marco Dal Ben, Edoardo Runcio, and Giuliana Somma

A Comparative Life Cycle Assessment of Load-Bearing Structural Systems for Multi-Storey Buildings: Steel vs. Reinforced Concrete 67
Marta Maria Sesana, Paolo Dell'Oro, Marianna Sgarbanti, and Simona Martelli

Re_Grid: A Reuse-Based Optimization Approach for the Design of Environmentally Efficient Steel Gridshell Structures 79
Valentina Tomei, Ernesto Grande, Marina Serpe, and Maura Imbimbo

From Demolition to Reuse: A Decision-Oriented Perspective on Reclaimed Structural Steel 91
Fabrizio Ascione, Carmine Galasso, and Elena Mele

Reuse Based Design of Steel Gridshells Through Multi-Objective Optimization 103
Fabrizio Ascione, Francesco Esposito, Diana Faiella, and Elena Mele

Non-linear Assessment of Gridshells Designed with Reuse-Based Structural Optimization Strategies 115
Marina Serpe, Valentina Tomei, Ernesto Grande, and Maura Imbimbo

Metallic Spans Replacement for 150-Year-Old Viaduct 128
Riccardo Stroscio, Rebekah Kovacs, Mark Scrivener, and Douglas Blogg

Steel Connections

Optimized Numerical Model for TTI Connectors 143
Paulo H. R. Moura, Ramon Silva, Jerfson M. Lima, Luciano M. Bezerra, and Jorge Bonilla

Influence Of Laser-Cutting Technology on The High-Cycle Fatigue Response of Bolted Steel Joints 156
Hasan N. Olmez, Gabriele Zanon, Marco Brugnolli, Mattia Vanin, and Oreste S. Bursi

Numerical Analysis and Design of a Telescopic Joint for Rapid Assembly of Steel Frames 165
Emanuele Maiorana and Mattia Sperandio

Firmly Bolted – Functional Levels of Bolt Tightening 174
Frank Götz

Ultimate Response of Bolted Gusset Plate Connections in Concentrically Braced Frames: Design Predictions Versus Finite Element Simulations 188
Massimo Cicia, Mario D'Aniello, and Raffaele Landolfo

Structural Performance of Orthogonal Joints in Tube-and-Joint Scaffolding Systems: Advanced Numerical Analyses and EN1993-1-8-Compliant Classification 200
Aldo Milone, Raffaele Landolfo, Gemma Bozzacco, and Luigi Rama

Seismic Response of New Extended Bracket-Shaped Beam-to-Column Joint for SMF 208
Bahram Mirzaie Abar, Mario D'Aniello, Arsalan Sadeghi Shaghaghi, and Raffaele Landolfo

Experimental and Numerical Behavior of Steel L-Stub Under Monotonic Loading 217
Emanuela Luisi, Francesco Monte, Roberto Tartaglia, Gaia Berruti, Marco Consales, Andrea Cusano, and Giuseppe Maddaloni

Comparative FEM Investigation into the Interaction Between RC Slabs and Removable Bolted Links in Eccentrically Braced Frames 226
Francesco Plaitano, Elide Nastri, and Aurel Stratan

Acoustic Emission Monitoring for Damage Diagnosis in Welded Steel Components 245
Roberto Andreotti, Gabriele Zanon, Rocco Di Filippo, Alessio Bonelli, and Oreste S. Bursi

Structural Performance and Design Assessment of Balustrade Connection Systems 256
Muhammad T. Naqash and Antonio Formisano

Cold-Formed and Lightweight Structures

Determination of the Effective Properties of Composite Perforated Cold-Formed Beams 269
Claudio Bernuzzi, Alice Lucidi, and Marco Simoncelli

Torsional Response of Cold-Formed Members Under Shear and Axial Forces: Experimental Evidence 283
Nadia Baldassino, Claudio Bernuzzi, Marco Simoncelli, Stefano Girardi, and Davide Melis

Shear Behaviour of Screwed Connections in LSF Systems: An Experimental Study 296
Nadia Baldassino, Stefano Girardi, Arianna Serraiotto, and Riccardo Zandonini

AI-Based Design: Prediction of Load-Carrying Capacity in Cold-Formed Members 310
Marco Simoncelli and Alice Lucidi

Monotonic and Cyclic Response of Strengthened Dry Joints in Steel Pallet Racks 322
Alessandro Mei, Giovanni Lavacchini, Sandro Chiostrini, Mario Fagone, Giovanna Ranocchiai, and Maurizio Orlando

Preliminary Results from Pushover Tests on Pallet Racks with Strengthened Beam-to-Upright Connections 334
Alessandro Mei, Giovanni Lavacchini, Francesca Matteini, and Maurizio Orlando

Lattice Infill Strategies for Lightweight and Stiffened Steel Structural Joints Enabled by Additive Manufacturing 346
Daniele Mattoccia, Agnese Natali, and Francesco Morelli

Structural Assessment of Steel Racking Systems: Gaps in Current European Standards and Perspectives 357
Alessia Campiche, Roberto Tartaglia, Giuseppe Maddaloni, and Antonio Occhiuzzi

M-N Interaction in Steel Storage Pallet Rack Base Joints 369
Nadia Baldassino, Arianna Serraiotto, Martina Bernardi, and Riccardo Zandonini

Buckling and Strength Performance of CFS Back-to-Back Folded-Flange Beams: A Numerical Study 381
Ward Alarab Safarani, Francesco Tondolo, and Donato Sabia

Influence of Inherent Damping in Modelling Steel Storage Racks 389
Jorge Ruiz-Oronia, Bryan Chalarca, and Giammaria Gabbianelli

Stub-Column Tests on Pallet Racks Uprights with and Without Reinforcements 401
Marina Pastore, Francesco Pisciottano, Rosario Montuori, and Elide Nastri

Experimental Tests and Fem Simulations of Pallet Racks Beam-to-Column Joints 410
Marina Pastore, Tahir Ahmad, Francesco Pisciottano, Roberto Tartaglia, Massimiliano Ferraioli, Rosario Montuori, and Elide Nastri

Shear Behaviour of Gypsum Board-to-CFS Profile Screw Connections 419
Vito D'Addesa, Alessandro Prota, Luigi Fiorino, and Raffaele Landolfo

On the Seismic Performance of Large-Area Lightweight Steel Suspended Ceilings: Experimental Set-Up 432
Alessandro Prota, Vito D'Addesa, Luigi Fiorino, and Raffaele Landolfo

Aluminium H-Sections under Uniform Compression: Initial Imperfection Modelling 444
Ida Pia Parzanese, Alessandro Pisapia, Francesco Fabbrocino, Vincenzo Piluso, Elide Nastri, and Francesco Pisciottano

Modular System in Lightweight Alloy for the Restoration of the Leaning Tower of Pisa: Design Innovations for Monument Preservation 456
Giuseppe Carluccio and Guido Maccone

Fire Protection and Thermal Effects

Optimisation of Fire Passive Protection for Steel Buildings Based on Vulnerability and Cost-Benefit Analysis 471
Antonio Cibelli, Paola De Santis, Donatella de Silva, Andrea Miano, and Emidio Nigro

Fire Protection of Steel Structures in High Corrosive Environments 482
Riccardo Tognaccini, Erik van Schaijk, and Roger Soler

Strengthening of RC Structures with Steel Plates: Fire Behaviour Analysis Between State-of-the-Art and Practical Applications 494
Nunzia Gargiulo, Antonio Cibelli, Donatella de Silva, and Emidio Nigro

Effects of Temperature on the Dynamic Characterization of Composite Steel-Concrete Highway Decks 502
Giuseppe Mugnos

Fire Assessment of Steel–Concrete Composite Bridges: Fragility and Life-Cycle Cost Evaluation of Alternative Passive Fire Protection System 512
Donatella de Silva, Andrea Miano, Gabriella De Rosa, and Emidio Nigro

Steel and Composite Structures

Structural Robustness of Steel-Timber Composite Frames Under Column Loss Scenarios 527
Nikolaos Anagnostou, Cristiano Loss, and Dan V. Bompa

Classification of Shear Connection Systems for Composite Action in Steel-Timber Floor Systems 540
Dan V. Bompa and Cristiano Loss

A Novel Concept of Steel Timber Concrete Composite Slim Floor Beams: Experimental and Analytical Investigations 554
Adil Ahmad, Teodora Bogdan, Jie Yang, Riccardo Zanon, Edoardo Benvenuti, Micael Bello, Francesco Profico, and Christoph Odenbreit

Types of Hybrid Steel-Timber Structural Systems for Sustainable Constructions 567
Giacomo Iovane, Raffaele Landolfo, and Beatrice Faggiano

Structural Performance of Steel–Concrete Composite Slabs Incorporating Recycled Concrete Aggregates 576
Flavio Stochino, Marta Saccone, Alireza Alibeigibeni, Marco Zucca, Monica Valdes, Giovanna Concu, Marco Simoncelli, Marco Andrea Pisani, and Claudio Bernuzzi

Experimental Analysis of a Novel Hybrid Timber-Concrete-Steel Flooring System 586
Carmen Amaddeo, Raffaele Pucinotti, and Wit Derkowski

Integrated Experimental Procedures for the Static Load Testing of Steel-Concrete Composite Highway Decks 598
Giuseppe Mugnos

Sagging Bending Moment Resistance of Steel-Concrete Composite Beams with Hot-Rolled Stock Sections: Extension of the Simplified Analytical Method to High-Strength Steel and Steel Fiber Reinforced Concrete 611
Francesco Profico, Riccardo Zanon, and Markus Schäfer

Analysis of Steel-Concrete Composite Spiral-Confined Slabs According to the Second-Generation Eurocodes 621
Irene Polesel, Marco Fasan, and Chiara Bedon

Seismic Design and Retrofitting

Design of Steel Moment Resisting Frames with Predetermined Collapse Mechanism 635
Bruna Barbieri, Maria Maglio, Rosario Montuori, Elide Nastri, and Vincenzo Piluso

Dissipative Elliptic-Braced Steel Frames for Seismic Retrofit of RC Buildings 646
Anna Carmela Ansalone, Salvatore Mottola, Osvaldo Pecorari, and Massimiliano Ferraioli

Steel Exoskeleton System for Strengthening Infilled RC Frames: Experimental Evidence and Numerical Modelling Under Monotonic and Cyclic Loading 659
Emilia Meglio and Antonio Formisano

Experimental and Numerical Evaluation of an Aluminium Alloy Exoskeleton for the Seismic and Energy Retrofit of Masonry Buildings 669
Giovanna Longobardi and Antonio Formisano

A Simplified Method for the Preliminary Assessment of the Optimal Damping Ratio of Dissipative Exoskeletons 681
Jana Olivo, Raffaele Cucuzza, Goffredo Orsi, Gabriele Bertagnoli, and Giuseppe Carlo Marano

Seismic Retrofit of RC Buildings Using Self-centering Friction-Damped Steel Exoskeletons Based on P-Spectra Design Methodology 690
Salvatore Mottola, Annarosa Lettieri, Massimiliano Ferraioli, and Atsushi Sato

Seismic Improvement of an Existing School Building Through Supplemental Energy Dissipation, Local Strengthening and Continuous Structural Monitoring the Case Study of the "G. Galilei" Science High School in Ancona 702
Matteo Giuseppe Blasi

Nonlinear Response of EC8-Compliant Dissipative Steel Concentrically Braced Frames Under Seismic Loading 712
Massimino Gnazzo, Mario D'Aniello, and Raffaele Landolfo

Towards Smart Steel Structures: Active Mass Dampers for Wind Comfort and Torsional Control in the Genoa Port Control Tower 723
Fabio Menardo, Leonardo Bandini, Barbara Zulian, Valentina Bellotti, and Stefani Cii

Behaviour Factors for the Seismic Design of Steel Frames Equipped with Pinching-Free Devices 735
Rio Saito, Annarosa Lettieri, Atsushi Sato, and Massimo Latour

Influence of Connection Design on the Seismic Response of School Building Retrofitted with Steel Orthogonal Exoskeletons 747
Alessandro Prota, Roberto Tartaglia, and Raffaele Landolfo

Seismic Retrofit of Pre-code RC Structures Using a Hybrid Timber-Aluminium Exoskeleton: Numerical Definition of the Earthquake-Resisting System and Reduced-Scale Testing 758
Emilia Meglio, Marco Domaneschi, and Antonio Formisano

Visual Scripting-Based Design Methodology for Lattice-Structured Metallic Dampers Produced via Additive Manufacturing 770
Francesca Romana Andreacola, Marco Di Cristofano, Valentino Sangiorgio, and Giuseppe Brando

Seismic Design in Greece and Italy: A Comparative Study of a Steel Frame 782
Maria Liapopoulou and Maria Maglio

Comparative Analysis and TPMC (θ) Design Approach for a Moment-Resisting Frame Structure 793
Rosario Montuori, Elide Nastri, Vincenzo Piluso, and Chiara Scafuri

Robustness

Nonlinear Response of Steel Storage Racks Under Progressive Collapse Scenarios 809
Tahir Ahmad, Massimiliano Ferraioli, Angelo Lavino, and Alberto Mandara

A Hybrid SDOF Model for Thin Steel Plates Under Dust-Explosion Loading: Dynamic Response and Preliminary Collapse Assessment 820
Francesco Pinna, Marco Zucca, Marco Simoncelli, and Flavio Stochino

Bridges and Large-Span Structures

Design, Fabrication and Erection of a Large-Span Steel Vierendeel Girder: The New SCC Railway Control Centre in Turin 835
Andrea Imbrenda and Giuseppe Vigoriti

Environmental Assessment of a Suspended Pedestrian Bridge Built with Mostly Recovered Materials: The Marangara School Bridge, Rwanda 845
Edoardo Benvenuti, Riccardo Zanon, Nicola Turrini, Godfrey Uwiringiyimana, and Tina Gunnarsson

Steel Roof for the "PALARICCIARDI SPORTS HALL": Design and Construction Process 858
Marco Stizzo, Vito Elia, and Aldo Giordano

New Termini Bridge: Design and Construction of a Steel Deck Integrated Within a Historic Structure 870
Giorgio Rizzo, Salvatore Condurso, Federico Panighel, and Enrico Parcianello

AI-Driven Composite Bridge Design Using Machine Learning and Genetic Algorithms 878
Ali Yousefi, Valentina Boretti, Umberto Folco, Pietro Palumbo, Rodolfo Epicoco, Daniele Cantelmi, Gabriele Bertagnoli, and Davide Masera

Analytical and Empirical Fragility Assessment of Italian Single-Storey Steel Industrial Structures 890
Antonio Davino, Emilia Meglio, Iolanda Cerbone, Gianmaria Di Lorenzo, Antonio Formisano, and Raffaele Landolfo

The Braila Suspension Bridge, Erection and Commissioning 901
Massimo Averardi Ripari, Fabio Brancaleoni, Andrea Del Vecchio, and Giovanni Massimo Aluffi

Level-4 Safety Evaluation and Subsequent Interventions for the Retrofit of the "Ponte Blu" in Rome 914
Mario Paolo Petrangeli, Luigi Fieno, Andrea Polastri, and Simone Trentacarlini

Geotechnical Steel Works for the Repair of Damage Caused by Landslides and for Infrastructures Protection 925
Michelangelo Micheloni, Domenico Paldino, and Erica Antonuccio

Structural Retrofit of Steel Truss Girders Using Prestressing Strands: The Roof of the Nelson Mandela Forum in Florence 936
Paolo Cioni, Claudia Chioatero, and Alexandra Szokalska

Residual Stresses and Corrosion

Assessment of the Influence of Corrosion on the Structural Performance of a Steel Truss Railway Bridge 947
Giuseppe Mugnos

Enhanced Durability for Corrosion Protection of Steel Structures 960
Riccardo Tognaccini and José Fernandes

Stress Concentrations in Steel Structural Details: A Linear Strain-Based Approach for Cyclic Plasticity 971
Marco Gastaldello, Alessandro Catanzano, Filippo Berto, Anna Saetta, and Roberto Scotta

Residual Stress Distribution in Cold Bent Hot Rolled Shapes: Analytical Model and Numerical Simulation 982
Francesco Pisciottano and Riccardo Zanon

Structural Optimisation

Identification of Optimal Parameters for Lateral Impact-Resilient Friction Pendulum Isolators 991
Diego Gino, Elena Miceli, Gabriele Neri, Gaspar Andrés Auad, and Paolo Castaldo

Optimal Seismic Isolation Properties of Multi-Span Bridges Under Asynchronous Earthquakes 1001
Elena Miceli, Diego Gino, Gabriele Neri, Luca Giordano, and Paolo Castaldo

Nonlinear Response Prediction for Stock-Constrained Optimized Steel Gridshells 1012
Farzin Kazemi, Elena Mele, Neda Asgarkhani, Francesco Esposito, and Fabrizio Ascione

Pre-sizing and Optimal Cross-Section Selection of Steel Gravity-Load Columns in Multi-story Concentrically Braced Frames 1024
Gianmaria Di Lorenzo, Giusy Terracciano, and Raffaele Landolfo

Vibrations

Human-Induced Vibrations on Steel-Glass Floors: Guidelines, Experiments and Modelling of a Case-Study 1039
Chiara Bedon and Marco Fasan

Wind-Induced Fragility and Vulnerability of Industrial Steel Buildings: Preliminary Considerations 1052
M. Eteme Minkada, A. Belleri, M. Gualdi, G. Della Corte, G. Cantisani, J. Žužul, L. Pagnini, and A. Ricci

Emerging Technologies for Steel Structures

Integrated Approach to the Structural Assessment of the Rai Tower of Caltanissetta 1063
Giuseppe Mugnos

Steel and BIM for Digital Twins. Information Modelling of the Buildings in the Hall B of LNGS 1075
Matteo Abita, Renato Morganti, Alessandra Tosone, Daniele Castri, Umberto Di Sabatino, and Danilo Di Donato

A Tool for Informed Choices of Post-production Protocols: The Pre-deconstruction Audit Model 1087
Renato Morganti, Laura Ciammitti, Alessandra Tosone, Alessandra Bellicoso, Danilo Di Donato, Matteo Abita, Alessia Panepucci, and Simone Rea

InSAR-Based Monitoring of the Diego Armando Maradona Stadium 1097
Pier Francesco Giordano, Riccardo Liuzzo, and Maria Pina Limongelli

Strengthening of Metal Thin Plates Through Wire-Arc Additive Manufacturing 1109
Vittoria Laghi, Elisabetta Savino, Neira Babovic, Giada Gasparini, and Tomaso Trombetti

Robotic Repair of Steel Structural Elements by Wire Arc Additive Manufacturing 1116
Alessandro Menghini, Alper Kanyilmaz, Saad Waqar, Barbara Previtali, and Ilchat Sabirov

Structural Engineering Insights from Darkside-20k: Steel Design for Underground and Cryogenic Environments 1128
Michele Angiolilli, Andrea Zani, Marco Carlini, Roberto Tartaglia, Marta Galuppi, Filippo Grande, Andrea Ianni, Mario D'Aniello, and Marzio Nessi

Author Index 1139

Sustainability and Reuse

Learning from Covre: Mid-century Steel Construction and New Paths for Structural Reuse

Riccardo Maria Polidoro[1(✉)] and Elena Mele[2]

[1] University of Bari Aldo Moro; CIRICE - University of Naples Federico II, Bari, Naples, Italy
riccardomaria.polidoro@unina.it
[2] University of Naples Federico II, Naples, Italy
elenmele@unina.it

Abstract. This paper re-examines the work of Gino Covre through the lens of contemporary structural reuse and circular construction. Combining archival-based historical analysis with an applied, design-oriented hypothesis, the study identifies recurring constructive principles in Covre's metalwork and translates those principles into a conceptual proposal for a reconfigurable steel grid intended to host salvaged members from selective demolition. Emphasis is placed on historically grounded documentation (project records, fabrication marks, and typical member geometries) as a necessary precondition for safe, economical reuse. The proposed grid relies on a limited family of node-adaptors and bolted interfaces that accommodate variability in recovered sections while preserving structural clarity and reversibility. By situating Covre's practice as a technical resource rather than only a historical subject, the paper builds a pragmatic bridge between heritage knowledge and present sustainability targets: mapping archives and material typologies informs design rules; these rules enable pilot prototyping, FEM assessment, and a preliminary life-cycle assessment (LCA) to quantify embodied-carbon savings. The contribution is aimed at historians, conservation practitioners, and structural engineers interested in operational, low-tech pathways to steel reuse, showing how mid-century industrial vocabularies can be reactivated to serve circular building strategies today.

Keywords: Structural Steel · Mid-Century Construction · Circular Economy · Structural Reuse · Bolted Connections · Modularity.

1 Introduction

The ambition of this paper is to recover a largely overlooked figure of postwar Italian engineering and to demonstrate that his constructive logic carries immediate operative value for the circular building economy of the present. Gino Covre – structural steel designer, patent-holder, and consistent collaborator of Pier Luigi Nervi on the most demanding projects of the early 1960s – has remained on the margins of architectural historiography despite his central technical role in works that are now studied as canonical megastructures, such as the *Palazzo del Lavoro* in Turin (1959–1961), the *Cartiera*

© The Author(s), under exclusive license to Springer Nature Switzerland AG 2026
R. Zanon et al. (Eds.): CTA 2026, LNCE 942, pp. 3–13, 2026.
https://doi.org/10.1007/978-3-032-39505-4_1

Burgo in Mantova (1961–1964), and the *Padiglione dell'Automobile* at the *Fiera del Levante* in Bari (1960).

The selective invisibility of Covre in the historical literature is partly structural: collaborators of Nervi were routinely absorbed into the maestro's larger narrative, and Covre's domain left fewer traces. Sergio Poretti's foundational essay on the *Cartiera Burgo* [1] is the principal published account that names and contextualizes Covre directly, describing him as «well-known as the creator of various solutions for a monumental metal arch at EUR» and as the engineer to whom Nervi entrusted the executive design of the metalwork at Mantova. This characterization, though compact, establishes Covre as a named specialist with a pre-existing relationship with Nervi; his contribution was specifically executive and therefore constructive, and the *Cartiera Burgo* project represented, in Poretti's reading, an exceptionality within Nervi's output precisely because the iron structure took on as a protagonist [1].

Covre's contributions are also recoverable through archival documents, fabrication drawings, and the structural surveys that have been conducted on these buildings in recent decades [2, 3]. Foraboschi places Covre in the lineage of structural engineers who constitute an Italian tradition distinct from its European counterparts – alongside Krall, Musmeci, Morandi, and Nervi – noting specifically his combination of mathematical rigour with constructive intuition [4].

The paper's argument proceeds in three steps. Section 2 reconstructs the core characteristics of what might be called the *Covre system*: the design principles that recur across his documented projects and that distinguish his approach. Section 3 translates these principles into a conceptual framework for structural reuse, proposing a reconfigurable grid system in which salvaged mid-century steel members can be reassembled under controllable conditions. Section 4 sketches the assessment methodology that would validate this framework in practice, including FEM verification protocols and a preliminary LCA. Section 5 discusses limitations and directions for further research.

This contribution does not aim to assert that Covre anticipated circular economy thinking, which would be anachronistic and misleading. The claim is more modest and more useful: the constructive principles he applied for reasons of economy, speed, and constructability happen to align closely with the criteria that contemporary guidance on structural steel reuse identifies as enabling conditions, and this alignment warrants systematic investigation.

2 Gino Covre: Constructive Principles and Historical Recovery

2.1 The Collaborative Context

Gino Covre enters the historical record through Pier Luigi Nervi. The two engineers first encountered each other in 1940, during a competition for a monumental arch at the EUR district in Rome, where they designed different structural solutions for the arch [1, 3]. The professional relationship crystallized twenty years later, when Nervi – pressed by the impossibility of building the roof of the *Palazzo del Lavoro* (Fig. 1) in reinforced concrete within the deadline – turned to steel for the mushroom capitals and called Covre to manage the design [3]. Covre then moved to the *Cartiera Burgo* with the same team

(Nervi, Covre, the fabricator Antonio Badoni of Lecco), working through 1961–1964 on the suspended steel roof that spans 164 m between external pylons [1, 3, 5, 6].

A third documented project predates both: the *Padiglione dell'Automobile* at the *Fiera del Levante* in Bari, completed in 1960 [7]. Here Covre signs as sole author of the structural concept – a groin vault in steel, 60 by 60 m, supported on chamfered RC perimeter columns – a construction method he had patented: welded workshop elements assembled on-site by bolted connections, defined «Covre structure» [7]. The Bari pavilion thus provides a self-authored baseline against which the later collaborative works can be read as elaborations.

The broader Italian context matters. Poretti [1] argues that the great structural works of the 1950s and 1960s are the culmination of an uninterrupted experimentation through the entire century, from the patents of the early reinforced concrete era through the autarchy years, when the need to economize on steel stimulated intense research into thin membrane construction, to the postwar international recognition of Italian structural engineering. Covre belongs to this lineage, contributing specifically at the steel end of a practice that Nervi had anchored almost exclusively in experimentation on reinforced concrete.



Fig. 1. The mushroom pillars with radial roof structure of the Palazzo del Lavoro. Photo by Riccardo Maria Polidoro (July 2023).

2.2 Modular Decomposition as Structural Strategy

The most consistent principle across Covre's documented work is the decomposition of large-span structures into families of repeated elements fabricated off-site and assembled with dry connections. This "prefabrication" can be read as a specific discipline, in which element families are sized to be transported without special permits, connection details are standardized across the family so that the same tools serve multiple joints, and the assembly sequence exploits the repetition to compress construction time.

In the *Palazzo del Lavoro*, the steel roof of each of the sixteen 40 × 40 m mushroom panels consists of twenty radial cantilever beams – welded I-sections with variable cross-section, ranging from 2800 mm at the fixed-end drum connection to 700 mm at the edge beam – joined to the circular drum of each capital by bolted fixed-end connections [2]. The circular steel drum serves as the organizing node to which all radial beams connect through triangular bearing plates, seated in a groove at the column top, concentrating the complexity of the capital into one precisely fabricated component and converting field assembly into a sequence of repetitive bolting operations [2, 3].

In the Bari pavilion, the structure is similarly organized: four diagonal lattice arches, each composed of pentagonal-section elements of varying length and solidarized by bracing, cross at a central ring that carries the spherical dome lantern [7]. The construction report notes that the central ring was assembled first using a provisional tower, after which the ribs and secondary trusses were mounted in sequence in thirty days, with an equal period for workshop preparation [7]. The use of tubular profiles alongside mild-steel rolled sections was calibrated to the required stiffness-to-weight ratio, with working stresses maintained below 140 MPa [6, 7].

At the *Cartiera Burgo*, Covre's role regarded the suspended steel roof: four main lattice beams, 164 m long, suspended from parabolic catenary chains of rigid bolted bars at 10 m intervals, with vertical hangers of 45 mm diameter supporting the roof structure at the same spacing [1, 3]. The 10 m module governs the geometry from the catenary chain through the hanger spacing to the secondary beam grid – a scalar discipline that ensures every member in the assembly is dimensioned to the same load case. Poretti notes that the entire suspended structure weighs no more than 700 tons and describes its composition as a grid of reticular beams disposed orthogonally and diagonally, with a combined depth of approximately two meters [1]. While a material incidence of roughly 90 to 140 kg per square meter aligns with standard 1960s parameters for space grids, achieving this metric over a 164 m clear span constitutes a striking economy of material. This structural efficiency derives directly from the suspension system, which permits a two-meter-thick grid to bridge a distance that would otherwise require unfeasible structural depths and prohibitive steel tonnages using a conventional framework.

2.3 Bolted Assembly and Accessible Joints

Across all three projects, connections between primary elements are bolted rather than field welded. This was dictated by tight construction schedules, but the consistency of the preference across projects operating under very different constraints suggests that bolted assembly was a design choice as much as a logistical accommodation [3, 6, 7].

We infer that the significance of this choice for structural reuse is direct, as bolted connections can be disassembled without cutting; furthermore, these elements retain their full section, with known geometry and without heat-affected zones introduced by field welding. Poretti [1] describes the suspension chains at the *Cartiera Burgo* as rigid jointed bars formed from assembled steel plates (a structural typology reminiscent of 19th-century chain suspension bridges) at 10 m intervals: a detail that is simultaneously a structural choice, a solution for fabrication economy and – without any contemporary intention – a design for disassembly. The surveys conducted on the *Palazzo del Lavoro* decades after construction confirm that the bolted interfaces at the column-drum and drum-beam connections remain functionally effective and accessible for inspection [2, 3]. Cresciani and Forth observe that Nervi's modular approach explicitly allowed regular maintenance [3], including the provision of internal access staircases within the hollow columns; this design attitude contributed directly to the building's resilience over fifty years of use. The same logic applies at the steel-element level: connections designed to be made and inspected can, in principle, be unmade.

2.4 Section Typology and Material Consistency

Covre's work exhibits a consistent discipline of limiting the assortment of section types within each project. In the *Palazzo del Lavoro*, the three radial beam variants share the same steel specification – yielding stress fy = 235 MPa, equivalent to current S235JR – the same web thickness range (5–7 mm), and the same flange proportioning logic [2]; the Bari pavilion mixes different sections but specifies them by a single material grade and a single allowable stress limit [7]. This discipline reflects the supply conditions of the Italian steel market in the early 1960s, where section variety was limited and delivery times for special profiles could disrupt construction schedules; it also reflects a preference for modular assemblies with uniform structural capacity across member families, since this minimizes both the engineering calculation effort and the range of special fabrication required.

From a reuse perspective, homogeneity of the donor stock reduces uncertainty in condition assessment and simplifies the structural verification of recovered elements. A project in which every primary beam shares a section family and a material grade is a significantly more compliant donor than one in which section types vary continuously; a historical coincidence with contemporary practical value.

3 A Conceptual Framework for Structural Reuse

3.1 Premises and Scope

The conceptual framework proposed here rests on a specific claim: the constructive logic of the *Covre system* constitutes a set of enabling conditions for structural steel reuse that can be articulated as design rules and applied to recovered members in new configurations.

This claim operates within the broader context of circular economy frameworks for the built environment, where structural steel reuse has been identified as one of the

highest-value strategies for embodied-carbon reduction. Steel production accounts for approximately 7–9% of global CO_2 emissions [8]; the marginal embodied carbon of reuse operations (transport, surface treatment renewal, connection preparation) is a fraction of the carbon cost of equivalent new production, an advantage that the LCA methodology of EN 15978:2011 [9] can quantify systematically by assigning new-production impact only to material that crosses the system boundary for the first time. Under this framework, a recovered structural member that has borne its production-stage burden enters the reuse system with marginal impacts limited to transport, any refurbishment needed for re-incorporation, and end-of-life treatment at the close of the reuse cycle [9].

The bottleneck for structural steel reuse is not material performance but information: safe reuse requires knowledge of original section geometry, material specification, connection and loading history [11, 12]. Where these are documented, the path to safe structural reuse is technically straightforward; where they are not, conservative assumptions (that may reduce economic feasibility) are required. Archival documentation of the kind available for Covre's projects provides exactly the information base that makes responsible reuse achievable.

3.2 Archival Mapping as Design Input

The first step of the proposed framework is a systematic archival mapping of Covre's documented projects, producing a catalogue of member types with their geometrical and material characteristics.

For the *Cartiera Burgo*, Poretti [1] bases his study primarily on «400 executive drawings made by the Nervi & Bartoli company» and on photos of the construction site, conserved at the CSAC at Parma (Fondo Nervi) and in the *Archivio delle Cartiere Burgo* at Mantova. These two archives provide detailed drawings and material certifications, a documentary basis for any reuse-oriented member catalogue [1, 6]. The Bari pavilion is presented in an autographic 1960 article [7] with sufficient geometric specificity to reconstruct the member catalogue with reasonable confidence.

The output of archival mapping is a matrix of donor member types (a design basis for the grid): for each type, the matrix records nominal section, material grade, original span and load condition, connection geometry and condition notes from available surveys.

3.3 The Reconfigurable Grid: Concept

The proposed grid is intended as a structural logic: a node-and member system whose geometry can be adjusted to accommodate variability in the recovered members while maintaining predictable structural behavior and reversible assembly.

The organizing principle borrows directly from Covre's practice: a primary grid of standardized nodes, connected by members whose section varies within a predefined family. In the proposed reuse grid, a family of node-adaptors – steel castings or fabricated plates in three to five standard geometries – provides the interface between the grid and the variable geometry of recovered beams. The node-adaptor family is designed to accommodate the range of section heights, flange widths and web thicknesses documented in the Covre catalogue, using slotted holes and packing plates to absorb variability without requiring specific fabrication at each joint. The possible stiffness reduction due

to slotted holes is considered in a simplified manner, through coefficients calibrated on the basis of detailed FEM analyses.

The grid geometry is a square arrangement at primary spacing S (typical range 6–10 m), with secondary members at S/2 or S/3 depending on the load condition and the available donor spans. The primary grid is carried by standard steel columns at grid intersections; secondary members span between primary beams. All connections are bolted, using 8.8-grade bolts in standard sizes, installed finger-tight during assembly and torqued to specification as a final operation, permitting alignment adjustments.

The grid is reversible by design: no field welding is required, connection plates are reusable and the node-adaptors are recoverable. This reversibility is the expression of the circularity principle: the grid functions for multiple cycles of use and disassembly, where individual elements are replaceable. EN 15978:2011 [9] defines reuse as «any operation through which products or components that are not waste are used again for the same purpose for which they were conceived or used for other purposes without reprocessing»; this reversible grid assembly satisfies the definition, allowing recovered members to re-enter construction without reprocessing.

3.4 Member Selection and Section Substitution

The critical structural design problem in a reuse grid is section substitution: when a nominally identical recovered member is not available, a substitute must be found that maintains the structural performance of the assembly without requiring redesign of the node-adaptor family. This problem is well-posed when the donor catalogue is sufficiently rich – an argument for archival completeness – and tractable when the grid design is organized around families of structurally equivalent sections rather than nominal identity.

The concept of structural equivalence used here draws on the verified finding of Sorace and Terenzi that the three drafts for the radial beam types in the *Palazzo del Lavoro* roof were deliberately designed to equivalent bending and shear resistance and equivalent local buckling performance [2]. Applied to the reuse grid, considering an uniform steel grade (equivalent to S235), member acceptance is governed by minimum moment of inertia about both axes, minimum plastic section modulus, and minimum web slenderness ratio, rather than by nominal profile identity. Recovered members satisfying these threshold values are interchangeable within the family, regardless of dimensional differences arising from original fabrication tolerances or minor section loss (addressed through conservative capacity reduction factors).

Structural verification of individual recovered members follows standard non-destructive testing protocols: visual inspection for surface defects, measurement of section dimensions at multiple locations, hardness testing for material grade confirmation and, where loading history is uncertain, magnetic particle or dye penetrant inspection of critical weld zones and connection areas. Members satisfying all requirements without excessive section loss can be incorporated at full characteristic strength; members with quantified reduction are downgraded to their verified reduced capacity and assigned to positions in the grid where said capacity is structurally adequate.

Corrosion-induced thickness loss is the dominant time-dependent variable behind these reduction factors and warrants explicit treatment, since it directly affects cross-section classification. Plate thickness reduction as a function of elapsed exposure time

can be estimated through standard atmospheric corrosion curves, giving a predicted thickness for each member prior to physical survey. Because classification under EN 1993-1-1 Table 5.2 [10] depends on the width-to-thickness ratio of flange and web, a reduction in t at constant c can shift a member from Class 3 to Class 4 or increase the effective slenderness of a section already Class 4 as-built. The redefined, corrosion-adjusted thickness is therefore used to re-verify classification and to compute effective cross-section properties.

4 Proposed Assessment Methodology

4.1 FEM Verification of the Reuse Grid

Full FEM assessment of the proposed grid under governing load combinations may follow the methodology established by Sorace and Terenzi for the *Palazzo del Lavoro*, adapted to the specific geometry and loading conditions of the reuse application. The analysis employs shell-element mesh resolution calibrated to the section slenderness of the members being verified, consistent with EN 1993-1-1 [10].

For the primary grid members – typically welded I-sections recovered from mid-century frames – the critical verification is lateral-torsional buckling (LTB) under major-axis bending. The verification follows EN 1993-1-1 Clause 6.3.2 [10], using imperfection factor $\alpha LT = 0.76$ for welded I-sections with $h/b > 2$. The design buckling resistance moment is computed accounting for the effective cross-section properties of Class 4 sections, where web slenderness governs classification; a member that cannot satisfy normative LTB at its original span under its original loading can satisfy it at a shorter span or under a lower load: the reuse grid provides both options through its modular geometry and load configuration, converting a normative non-conformity into an engineering problem rather than a barrier to recovery.

For the node-adaptors, the governing failure modes are bearing at bolted interfaces and block shear at plate perimeters, verified analytically and, for critical configurations, numerically with mesh refinement at the bolt-hole periphery. The parametric study covers the range of section depths and flange widths in the donor catalogue, confirming the adequacy of the node-adaptor family across the documented variability.

4.2 Life-Cycle Assessment

The LCA is structured according to EN 15978:2011 [9], covering life-cycle stages A1-A3 (product stage: raw material extraction, transport, and manufacturing), A4 (transport to site), B5 (refurbishment, covering any surface treatment or connection preparation required for re-incorporation), C1-C4 (end of life: deconstruction, transport, waste processing, disposal), and D (benefits and loads beyond the system boundary, covering the second cycle of material flow). The functional unit is one ton of structural steel in service for fifty years.

The system boundary for the reuse scenario excludes the production-stage embodied carbon of the original manufacture, which was expended in the first cycle. The marginal impact assigned to reuse in the new assembly is restricted to transport from donor building

to refurbishment facility; surface treatment and corrosion protection renewal; connection preparation including drilling or reaming. These marginal impacts are substantially lower than the production-stage carbon of equivalent new steel, whose magnitude depends on production route and national grid intensity and is available from Environmental Product Declarations (EPDs) per EN 15804 as referenced by EN 15978 [9]. Module D captures the benefit of avoided primary production, accounted for as a credit outside the system boundary following EN 15978:2011 [9], and the prospect of a further reuse or high-efficiency EAF recycling (assumed scrap recovery 98%) at end of service life.

The comparator scenario is new S235 structural steel from a current European EAF producer, whose EPD-based production-stage carbon is available from published data sources [8]. Sensitivity analysis should cover transport distance, surface treatment intensity, and the number of reuse cycles achievable before the member reaches end of structural life, parameters that collectively determine the total system-level carbon savings. This multi-cycle modelling is consistent with the EN 15978 framework's treatment of replaceable components across a reference study period [9].

5 Discussion and Limitations

5.1 The Archival Precondition

The proposed framework depends on adequate archival documentation of donor buildings. For the three principal Covre projects, the archival situation is favourable but incomplete: the available sources do not always provide fabrication-level documentation, the workshop drawings that would confirm actual as-built dimensions and connection details at the bolt-hole level. The gap between design drawings and as-built condition is relevant: for example, Cresciani and Forth note that the original roof covering designed by Covre for the Palazzo del Lavoro was replaced by Nervi in 1963 with a new one in ferrocement [3], a modification whose full structural implications for the retained steel components were analysed only in the 2011 structural survey [2, 3]. This history underlines the importance of condition surveys as a complement to design archives.

The broader implication for the reuse framework is that archival mapping and physical survey are complementary, not alternative, information sources. A systematic program of non-destructive testing on buildings identified as donor candidates would significantly reduce uncertainty in the donor catalogue and improve the reliability of section equivalence assessments.

5.2 Covre's Legacy and the Limits of the Analogy

The alignment between Covre's constructive principles and contemporary reuse criteria is genuine but partial. Covre designed for speed and economy under mid-century production conditions; he did not design for disassembly in the contemporary sense, and there is no evidence that reversibility of assembly was an explicit design objective. What he achieved was a set of structural conditions that happen to be favorable for reuse, as a consequence of the practical logic of his time rather than any anticipatory sustainability intent.

This distinction matters because it limits the degree to which Covre's practice can serve as a direct model for contemporary design; the lesson is to extract the organizing principles and apply them to current conditions, rather than mimicking his designs. The structural logic of the modular node-and member system, the discipline of limited section families, the preference for bolted interfaces: these are principles, which can be transferred across contexts in ways that specific details cannot.

5.3 The Broader Research Program

The extension of this argument points toward a broader research agenda: systematic and multidisciplinary documentation and study of mid-century steel buildings across Italy and Europe with a view to identifying the buildings that carry the most recoverable structural steel, cataloguing the section types and quantities available and developing region-specific design guides for reuse applications. The Covre buildings, precisely because they are well-documented and structurally assessed, provided the initial, provocatory case study for this contribution.

Covre's practice is also, as Foraboschi argues in a broader context, part of an Italian engineering tradition that deserves more rigorous historiographical attention precisely because it operated at the intersection of structural intelligence and constructive craft [4], a combination that produced buildings difficult to categorize under either purely architectural or purely engineering rubrics. The reuse lens proposed here is one method of recovering that tradition: it asks what these buildings can contribute now and how their constructive principles stood the test of time.

6 Conclusions

This paper has argued, based on archival and structural evidence, that Gino Covre's mid-century steel practice embodies a set of constructive principles that align with the operational requirements of contemporary structural steel reuse. The alignment is not coincidental, as both the mid-century practice and the contemporary reuse imperative are responses to constraints on resources, time, and technical complexity; the difference is that today the constraint is planetary rather than contractual.

The proposed conceptual framework translates this alignment into a design protocol: archival mapping of donor buildings produces a member catalogue; the catalogue informs a reconfigurable grid system organized around node-adaptors that accommodate section variability; the grid is assembled and disassembled using bolted connections compatible with the documented joint geometry of the donor stock. FEM assessment and LCA quantify structural adequacy and carbon savings respectively, with the LCA structured within the EN 15978:2011 framework to ensure methodological rigour and comparability.

The following findings warrant emphasis. First, Poretti's account of the *Cartiera Burgo* establishes Covre as the named author of the executive metalwork design, a fact that justifies treating his approach as a coherent engineering program rather than a series of project-specific accommodations. Second, the archival record for Covre's

major projects is sufficient to support a first-iteration donor catalogue, though it requires supplementation by physical survey to bridge the design-to-as-built gap.

Covre's work offers history of engineering as a technical resource. The task now is to extend this methodology to broader cases, complete the archival documentation, develop the physical survey program and advance the grid concept through prototype testing and pilot application. The constructive knowledge embedded in these buildings has not expired, it has simply been waiting for a new set of questions.

References

1. Poretti S (1997) La Cartiera Burgo, Mantova 1960-1964. Casabella 651-652:96–107
2. Sorace S, Terenzi G (2011) Non-linear finite element assessment analysis of a modern heritage structure. In: Oñate E, DRJ O, Peric D, Suárez B (eds) Proceedings of the XI international conference on computational plasticity: fundamentals and applications (COMPLAS XI). CIMNE, Barcelona, pp 1446–1457
3. Cresciani M, Forth J (2014) Three resilient megastructures by pier Luigi Nervi. Int. J. Archit. Herit. 8(1):49–73
4. Foraboschi P (2023) Appunti per una inedita epistemologia dell'ingegneria strutturale / suggestions for a new epistemology of structural engineering. Vesper J. Archit. Arts Theory 8:154–168
5. Nervi Project Association, Il Giornale dell Ingegnere (2018) Pier Luigi Nervi: Arte e Scienza del Costruire. Quine S.r.l, Milan
6. Giovannardi F (2021) Gino covre vita & opere. https://www.academia.edu/45656606/Gino_Covre_vita_e_opere. Accessed 18 May 2026
7. Covre G (1960) Pabellón del automóvil, Bari. Inf Constr 12(120):15–22
8. World Steel Association (2022) Steel's contribution to a low carbon future and climate resilient societies: world steel position paper. World Steel Association, Brussels
9. CEN (2011) EN 15978: 2011: sustainability of construction works - assessment of environmental performance of buildings - calculation method. CEN, Brussels
10. CEN (2005) EN 1993-1-1: Eurocode 3: Design of Steel Structures - part 1–1: general rules and rules for buildings. CEN, Brussels
11. Dunant CF, Drewniok MP, Sansom M, Corbey S, Allwood JM, Cullen JM (2017) Real and perceived barriers to steel reuse across the UK construction value chain. Resour Conserv Recycl 126:118–131
12. Tingley DD, Cooper S, Cullen J (2017) Understanding and overcoming the barriers to structural steel reuse: a UK perspective. J Clean Prod 148:642–652

Experimental Evaluation of Reused Structural Steel Elements

Vittoria Laghi(✉), Elisabetta Savino, Neira Babovic, and Giada Gasparini

University of Bologna, Viale del Risorgimento, Bologna, Italy
vittoria.laghi2@unibo.it

Abstract. One of the major challenges faced by structural engineers is the increase in carbon dioxide emissions associated with the construction sector and the use of energy-intensive materials. In response, European policies promote decarbonization strategies, which must also include extending the service life of existing structures. In this context, the reuse of structural elements represents an effective solution to reduce resource consumption and embodied carbon, supporting circular economy principles. Steel structures are particularly suitable for reuse due to their mechanical properties, durability, and ease of disassembly. This study investigates the feasibility of reusing steel beams recovered from a controlled dismantling process and classified as potentially reusable elements. An experimental campaign combining full-scale bending tests and tensile tests on extracted specimens was conducted to assess both global structural behavior and local material properties, with particular attention to possible degradation phenomena such as aging, residual stresses, and long-term loading effects. Results show that, when properly characterized, these elements can be safely reused in new structures. The study contributes to defining reliable criteria for reuse, supporting sustainability and circularity in the construction sector.

Keywords: Structural Steel Reuse · Sustainability · Circular Construction · Experimental Assessment

1 Introduction

The building sector is today recognized as one of the main drivers of global environmental impact, due to its high energy consumption, intensive use of raw materials and significant contribution to greenhouse gas emissions over the entire life cycle of buildings [1, 2]. In Europe, buildings account for a substantial share of final energy consumption and are responsible for a significant portion of total CO_2 emissions, while also generating large quantities of construction and demolition waste that put pressure on natural resources and waste management systems [3, 4]. In this context, the choice of construction materials and building techniques plays a central role in reducing the ecological footprint of the sector and in steering the transition towards a more sustainable built environment [5].

Among structural materials, steel occupies a strategic yet ambivalent position: on the one hand, its production, especially when based on traditional processes with high fossil energy demand, entails significant environmental impacts in terms of greenhouse gas

© The Author(s), under exclusive license to Springer Nature Switzerland AG 2026
R. Zanon et al. (Eds.): CTA 2026, LNCE 942, pp. 14–23, 2026.
https://doi.org/10.1007/978-3-032-39505-4_2

emissions and resource use, contributing notably to the carbon footprint of buildings [6]. On the other hand, the mechanical properties and modular nature of steel elements make this material particularly suited to a circular economy approach, in which structures can be dismantled, recovered and reused in new projects without necessarily resorting to energy-intensive recycling processes, with considerable environmental and performance benefits [7].

Aware of the weight of the building sector on climate and sustainability targets, the European Union has defined, within the framework of the Green Deal and the strategies for climate neutrality by 2050, a set of policies and instruments aimed at reducing the environmental impacts of the built environment, promoting energy efficiency, material decarbonization and the adoption of circular mod-els throughout the entire life cycle of buildings [8].In particular, European initiatives increasingly focus on design for disassembly, on durability and extension of component service life, on the re-duction of demolition waste and on the systematic integration of Life Cycle Assessment (LCA) into decision-making processes, with the goal of shifting from a "build and demolish" logic to a "pre-serve, adapt and reuse" [9]. In this framework, recent work has been done by both academia and industry towards more conscious reuse of structural elements, with specific focus on steel (see e.g [10–12].). In this context, several second-hand use projects have already been developed for ware-house construction, as demonstrated by the NTS Building project [13]. Furthermore, storey extensions have been successfully implemented on top of existing structures as part of broader refurbishment strategies. An example of this approach is the Sloane Square House project, where an additional floor extension was added to the existing structure as part of the wider office refurbishment [13].

Within the context of structural steel reuse, this study aims to provide a novel investigation into the physical and mechanical properties of reused steel components. Specifically, the present work ex-amines the behavior of a beam disassembled from a building through a four-point bending test, as well as its tensile properties, determined by extracting dog-bone specimens from sections of the beam not involved in the bending tests.

2 Methodologies

Two reclaimed Universal Beam (UB) sections were supplied by Cleveland Steel in Fig. 1, a UK-based company specializing in the reuse of structural steel elements. The members were transported in their original full lengths via dedicated haulage to the DICAM laboratory facilities in Bologna, Italy, where all experimental investigations were carried out. Hereafter, the specimens are designated as Beam 1 (UB305 × 102 × 25) and Beam 2 (UB203 × 133 × 30).

Beam 1, characterized by a UB305 × 102 × 25 cross-section and an overall length of 649 cm (6487 mm), was previously employed as part of a façade retention system in London. The system was installed in 2017 and remained in service for approximately five years. As shown in Fig. 1, the beam exhibited a symmetric arrangement of 6 mm-thick transverse stiffeners: one positioned 14 cm from each end and three located in the central region, with a clear spacing of 24 cm between adjacent stiffeners. For experimental

purposes, the member was segmented into five portions, denoted as 1A, 1B, 1C, 1D, and 1E; specifically, sects. 1 B and 1D were subjected to bending tests.

Beam 2, with a UB203 × 133 × 30 cross-section and an overall length of 568 cm (5767 mm), was previously utilized in a temporary structure at Gatwick Airport, with a service duration comparable to that of Beam 1. The member is equipped with substantial end plates and gusset plates welded to the flanges on both sides at each end, indicating its likely application within a braced frame system.

Unfortunately, the exact steel grade of the beams is unknown, as the precise traceability of the individual members was lost during the dismantling process. However, the experimental tests described below make it possible to obtain more detailed information regarding the material properties and, consequently, to identify the steel grade with greater confidence.

For testing purposes, this member was likewise divided into five segments, labeled 2A, 2B, 2C, 2D, and 2E; however, only sect. 2 C was subjected to bending tests due to the presence of numerous flange connections along the beam, which significantly increased the geometric and structural complexity of the remaining segments.

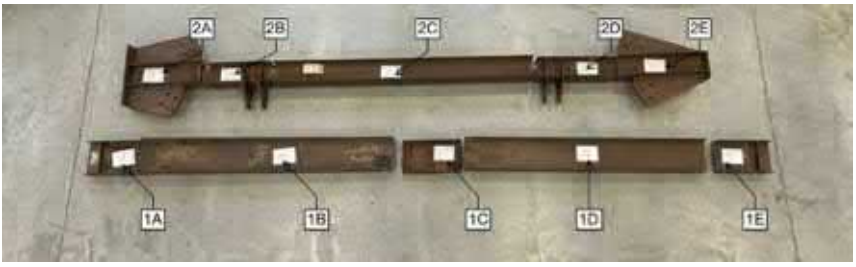


Fig. 1. Beams 1 (bottom) and 2 (top) divided into segments.

The tensile tests were carried out on specimens extracted from the beam elements 2D, 2B, 1C, and 1A. For each beam, dog-bone specimens were water-jet cut from three distinct positions across the height of the web: the upper region, the central region, and the lower region. This sampling strategy was adopted to investigate possible material heterogeneity and to evaluate the influence of the extraction location on the mechanical response.

Accordingly, each group of specimens is identified by a three-character code. The first two characters refer to the source beam (2D, 2B, 1C, or 1A), while the third letter specifies the extraction position within the web: L (lower), C (central), and U (upper). This classification allows for a systematic comparison of the results obtained from different regions of the same structural element, ensuring traceability of the experimental data.

3 Tensile Tests

3.1 Test Set-up

All tensile tests were performed using the Metrocom testing machine, operating in displacement-controlled mode, up to the complete failure of the specimens. The experimental campaign was conducted in the structural laboratory of the DICAM Department in Bologna. The testing procedure ensured consistent boundary conditions and loading application, allowing for the acquisition of reliable stress–strain data for each specimen.

3.2 Test Results

The results of the tensile tests carried out on steel dog-bone specimens show a mechanical behavior overall consistent with that typically observed in structural steels. The stress–strain curves exhibit a well-defined initial linear region, from which an elastic modulus compatible with expected values for steel can be derived. The yield strength lies in the range of approximately 420–450 MPa, which is higher than that of conventional structural steels but can be attributed to high-strength steels or to materials subjected to processing routes that enhance their mechanical performance (see Figs. 2 and 3). Following yielding, a clear strain hardening behavior is observed, with stress increasing up to the ultimate tensile strength, ranging between approximately 540 and 570 MPa. Beyond this point, the curves display a gradual decrease in stress, associated with the onset of necking and even-tual specimen failure, indicating a ductile behavior.

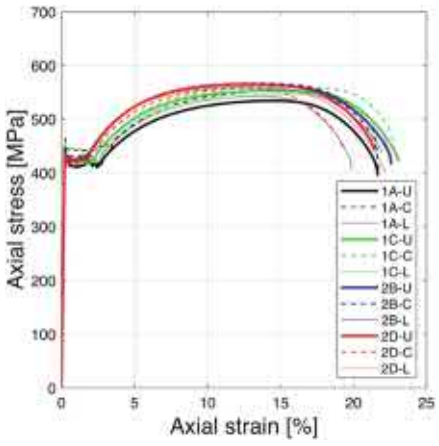


Fig. 2. Stress and Strain diagram.

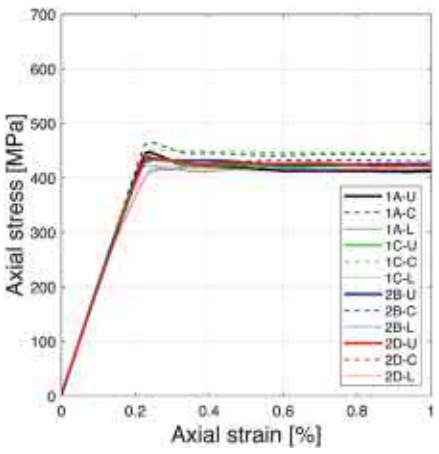


Fig. 3. Zoomed-in stress–strain diagram.

The scatter among different samples is limited in the elastic region and becomes more pronounced in the advanced plastic regime, particularly near the peak stress and at failure strain, which is consistent with the typical variability of metallic materials. Overall, the results confirm good repeatability of the tests and the absence of significant anomalies in the material behavior.

Table 1 summarizes the mechanical properties obtained from the tensile tests. The reported parameters include the 0.2% proof strength (Rp0.2), defined as the conventional yield strength corresponding to a permanent plastic strain of 0.2%; the upper (ReH) and lower (ReL) yield strengths, representing the onset of yielding and the subsequent yield plateau, respectively; the ultimate tensile strength (Rm), corresponding to the maximum engineering stress reached during the test; and the elastic modulus (E5–25), evaluated from the slope of the stress–strain curve between 5% and 25% of the maximum load to minimize the influence of initial seating effects and non-linearities.

Table 1. Table captions should be placed above the tables.

	Rp02 (MPa)	ReH (MPa)	ReL (MPa)	Rm (MPa)	E-5-25 (MPa)
1A_U	421,38	447,15	410,11	534,28	201083
1A_C	444,42	463,93	438,91	552,34	204735
1A_L	412,78	428,31	417,64	542,24	194579
1C_U	422,64	435,72	415,82	552,61	204858
1C_C	447,83	451,82	437,46	560,22	204213
1C_L	417,61	422,06	414,52	546,61	196093
2B_U	430,99	435,37	422,43	565,26	202041
2B_C	430,76	433,98	429,40	566,95	200834
2B_L	420,80	421,04	415,00	560,51	202535
2D_U	426,83	438,18	420,92	565,17	197913
2D_C	421,04	439,58	424,70	557,28	200718
2D_L	416,56	417,09	411,54	557,85	204410

4 Four-Point Bending Tests

4.1 Test Set-up

As previously stated, the experimental campaign focused on three specimens: 1B, 1D, and 2C. The structural response of these elements was investigated through four-point bending tests conducted under simply supported conditions.

Each specimen was tested using a statically determinate setup consisting of two supports and two symmetrically applied concentrated loads. The loads were introduced through hydraulic actuators (pistons), generating a constant bending moment region between the two loading points and zero shear in this central span. This configuration allows for an accurate assessment of the flexural behavior of the member, minimizing the influence of shear effects.

The beams were instrumented with Linear Variable Differential Transformers (LVDTs) positioned along the span to capture vertical displacements, particularly at midspan and in proximity to the loading points. Additionally, the load introduction points

and support locations were carefully de-fined to ensure symmetry and repeatability of the boundary conditions.

The geometric configuration, including the distances between supports and loading points, was selected to create a well-defined constant moment region in the central portion of the beam, where the flexural response and potential plastic hinge development could be observed. This setup is consistent with standard procedures for the characterization of bending behavior in structural steel elements.

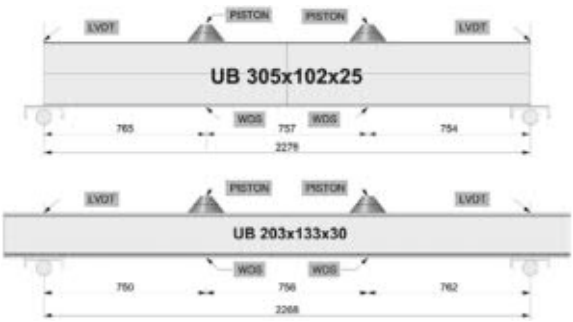


Fig. 4. Set-up model for the bending tests.

4.2 Test Results

Segment 1B was subjected to a monotonic four-point bending test to failure, whereas segments 1D and 2C were tested under cyclic loading protocols with increasing load levels, followed by mono-tonic loading to collapse. DIC results confirmed that, prior to failure, the structural response adhered to the theoretical assumptions of four-point bending, with pure flexural behavior in the central region of the beam and shear deformations confined to the zones between the load application points and the supports (see Fig. 4).

Segments 1B and 1D exhibited predominantly linear-elastic behavior up to failure, which occurred at load levels exceeding theoretical predictions and was governed by lateral–torsional buckling, likely initiated by local web buckling near the load application points. Segment 2C showed the onset of plasticity prior to collapse, followed by lateral–torsional buckling (see Fig. 5). Force–displacement curves derived from DIC data enabled the calculation of the elastic modulus through linear regression of the elastic response, yielding high coefficients of determination (see Fig. 6).

The parameters used for the analysis of the reference section were obtained from a dedicated catalog [14]. As shown in Table 2, although all specimens reached significant load-carrying capacities, the experimental lateral–torsional buckling loads were consistently lower than the corresponding theoretical predictions. The discrepancy, ranging from approximately 20% to 38%, appears to be primarily associated with the reduced elastic modulus measured for the reclaimed members (130–168 GPa), together with the influence of initial geometric imperfections and degradation accumulated during their

service life. The relatively large displacements recorded at peak load further indicate a reduction in global stiffness. These findings highlight that the structural assessment of reclaimed steel members should be based on the actual measured mechanical and geometric properties of the elements, rather than solely on nominal material values, in order to achieve a more accurate representation of their structural behavior and improve the reliability of performance predictions.

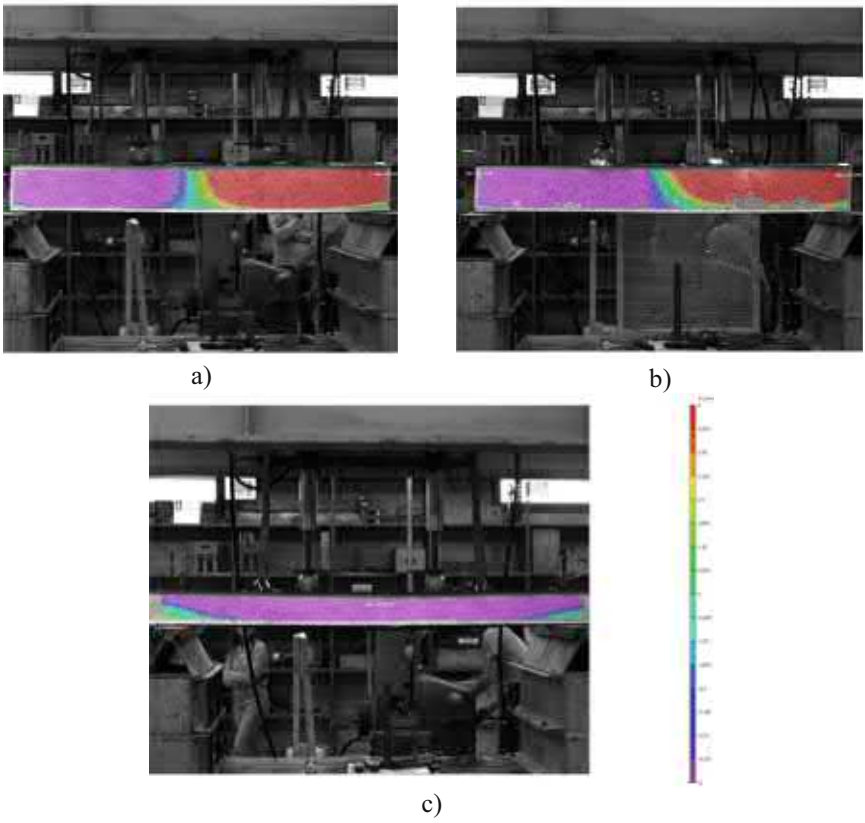


Fig. 5. Failure modes of beams (a) 1B, (b) 1D and (c) 2C.

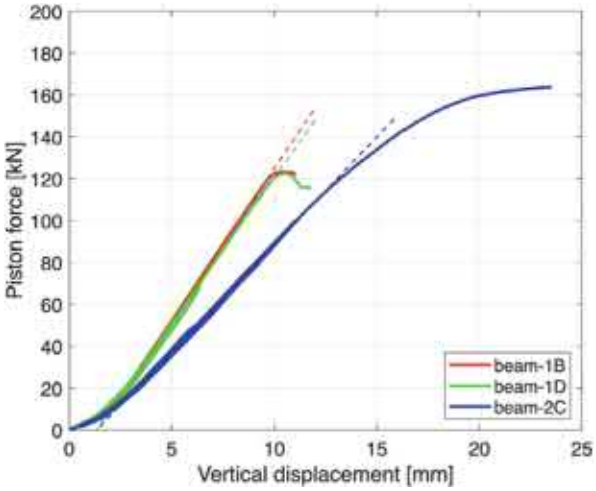


Fig. 6. Force-Displacement curves during 4-point load tests with displacement taken at mid-span.

Table 2. Four-point bending test results summary.

Specimen	E (GPa)	R^2	P _max (kN)	U (mm)	M_cr,exp. (kNm)	P_cr,exp. (kN)	E_theo (GPa)	P_cr,theo (kN)
Beam_1B	130.2	0.9997	122.7	10.55	52.84	139.1	210	224.6
Beam_1D	136.3	0.9999	128.5	12.41	55.33	145.7	210	224.6
Beam_2C	168.4	0.9994	163.8	23.52	152.64	403.8	210	503.9

5 Conclusions

The experimental campaign provided a comprehensive assessment of the structural and material behavior of reclaimed steel elements through combined four-point bending and tensile testing.

The bending tests demonstrated that all beam segments exhibited structural capacities exceeding theoretical predictions for lateral–torsional buckling, confirming the conservative nature of current de-sign approaches for reused steel members. Despite this enhanced load-bearing capacity, the measured displacements were consistently higher than expected, indicating a reduction in global stiffness. This discrepancy suggests that stiffness-related parameters, such as the effective elastic modulus, geometric imperfections, and potential section degradation, play a critical role in the structural response and should not be neglected in assessment procedures.

Failure was consistently governed by lateral–torsional buckling, in some cases preceded by local phenomena such as web instability or the onset of plasticity, as observed in segment 2C.

The tensile tests on dog-bone specimens extracted from the same beams revealed mechanical properties fully consistent with structural steel, with yield strength in the range of 420–450 MPa and ultimate tensile strength between 540 and 570 MPa. These values indicate that the material retains high mechanical performance, with no significant degradation at the material scale. The observed ductile behavior and limited scatter in the elastic range further confirm the homogeneity and reliability of the steel.

The comparison between structural-scale and material-scale results highlights a key outcome: while the intrinsic material properties remain largely unaffected, the global structural response is influenced by factors such as geometry, imperfections, and prior service conditions. This finding underscores the necessity of integrated assessment methodologies that combine material characterization with detailed geometric and structural evaluation.

Overall, the study supports the feasibility of reusing structural steel elements, while emphasizing the need to refine current guidelines by incorporating stiffness-related effects and real structural conditions, rather than relying solely on conservative strength-based approaches.

Acknowledgment. The authors would like to acknowledge Roy Fishwick from Cleveland Steel and Tubes for providing the tested beams. The authors would also like to acknowledge Ms. Elizabeth Berenice Kingsley for her help during her Master's thesis in preparing the tested samples.

References

1. European Environment Agency (2020) Report on the environmental performance of buildings in Europe. European Environment Agency
2. Intergovernmental Panel on Climate Change (2021) Climate change 2021: mitigation of climate change. Intergovernmental Panel on Climate Change
3. European Commission (2019) The European green Deal. COM(2019) 640 final. European Commission, Brussels
4. European Environment Agency (2019) Resource efficiency and the circular economy in Europ e. European Environment Agency
5. Pomponi F, Moncaster A (2017) Circular economy for the built environment: a research framework. J Clean Prod 143:710–718
6. World Steel Association (2021) Steel's contribution to a low carbon future. World Steel Association, Brussels
7. Rehborn A et al. (2020) Reuse of structural steel elements in building construction
8. European Commission (2020) A Renovation Wave for Europe – Greening Our Buildings, Creating Jobs, Improving Lives. COM (2020) 662 final. European Commission, Brussels
9. Guy B, Ciarimboli N (2008) Design for Disassembly in the built environment. The Green Building Council
10. Ascione F, Esposito F, Faiella D, Mele E (2025) Steel reuse for sustainable design of large-span structures: the case of gridshells. J Constr Steel Res 234:109743
11. Laghi V, Babovic N, Laccone F, Malomo L, Savino E, Gasparini G (2026) Automated design and fabrication framework to enhance steel reuse through structural optimization and metal 3D printing. Structure 88:111942
12. Bartsch H (2025) Reuse of reclaimed steel components in construction: a systematic review of potential, challenges and future directions. Structure 80:110057

13. Kanyilmaz A, Birhane M, Fishwick R, del Castillo C (2023) Reuse of steel in the construction industry: challenges and opportunities. Int J Steel Struct 23(5):1399–1416. https://doi.org/10.1007/s13296-023-00778-4
14. ArcelorMittal Europe – Long Products (2026) Sections and merchant bars: sales programme. https://sections.arcelormittal.com. Accessed 10 July 2026

Steel Structures for the Adaptive Reuse of Historic Railway Buildings: Large-Span Roofs, Aerial Walkways and Wind-Induced Dynamic Effects in the Campo Marzio Station in Trieste

Gerardo Masiello[1(✉)], Chiara Bedon[2], and Sabato Gargiulo[3]

[1] SMStrutture Srl, 56124 Pisa, Italy
gerardo@smstrutture.it
[2] University of Trieste, 34127 Trieste, Italy
[3] Fondazione FS Italiane - Gruppo FS, 00161 Rome, Italy

Abstract. The adaptive reuse of the former Campo Marzio railway station in Trieste required the integration of new long-span and multi-storey structures with a protected masonry complex. The project introduces a three-storey steel-framed hotel extension above the western wing, reconstructs the historic vaulted roof over the central hall, provides a new glazed facade, and suspends an elevated restaurant walkway across the hall, at ≈15 m from ground. Steel is selected to limit additional mass, enable dry and reversible construction, and control the transfer of forces to the existing masonry. The roof is formed by fifteen lattice arches supporting a steel-glass envelope, over an area of ≈94 × 36 m. A pinned-sliding support arrangement, combined with tension ties and displacement limiters, accommodates thermal movements and provides a controlled response under seismic action. The restaurant walkway behaves as a lower-deck tied-arch bridge, spanning ≈36 m, with dedicated checks for deformations and human-induced vibrations. To this aim, a hierarchical numerical strategy combined equivalent-frame and 3D FE models of the masonry-steel system with local FE models of the principal steel components. The global seismic analyses included the masses and asymmetric constraints of the roof and walkway, confirming the intended transfer of inertial forces to the strengthened western extension and selected masonry bearings. Wind actions were further investigated through CFD simulations and dynamic analyses, based on spatially and temporally variable pressure fields. Overall, this case-study efficiently demonstrates how steel structures can support heritage conservation, architectural transparency, and performance-based design within a single adaptive-reuse intervention.

Keywords: Steel structures · Heritage rehabilitation · Steel-glass envelopes · Wind-induced dynamic response · Adaptive reuse · Aerial walkway

© The Author(s), under exclusive license to Springer Nature Switzerland AG 2026
R. Zanon et al. (Eds.): CTA 2026, LNCE 942, pp. 24–35, 2026.
https://doi.org/10.1007/978-3-032-39505-4_3

1 Introduction

Historic railway buildings frequently combine monumental masonry envelopes with large internal volumes, originally shaped by iron and steel roofs. Their adaptive reuse necessarily requires two apparently conflicting objectives: the preservation of the existing fabric and the introduction of structural systems capable of supporting new functions, contemporary environmental envelopes and current safety requirements [1, 2].

Steel is particularly suited to this task because it provides high strength-to-weight ratios, dry assembly, dimensional control and the possibility of differentiating the behaviour of new structures from that of the historic construction.

The former Campo Marzio railway station in Trieste is a representative example of adaptive reuse. The station was conceived as a major terminal building, with two longitudinal masonry wings enclosing a central railway hall that was originally covered by a large metal roof. The historic roof was dismantled during the Second World War, leaving the internal tracks and the opposing facades exposed. The reuse project restores the spatial unity of the hall while transforming the complex into a multifunctional destination that combines railway heritage, public space and hospitality functions.

The structural intervention includes four closely related steel systems: a three-storey extension above the western wing for hotel use; a new cylindrical glazed roof over the central hall; a glazed entrance facade; and an elevated restaurant walkway crossing the hall. The design problem is not limited to sizing new steel members. It requires the definition of selective load paths, the control of actions introduced into the existing masonry, the management of thermal and seismic movements, and the assessment of serviceability phenomena associated with slender, transparent structures.

This paper presents the integrated structural concept and focuses on the roof and the aerial walkway, which are the most distinctive components. It also summarises the modelling hierarchy adopted for the global masonry-steel system and the site-specific investigations for wind-induced effects on the glazed roof [3, 4], in the city of Bora wind.

2 Heritage Context and Integrated Design Strategy

2.1 Existing Building and Adaptive-Reuse Programme

The existing station consists of a monumental northern head building and two elongated masonry wings, arranged around the former track hall. The historic drawings in Fig. 1 show that the original metal roof was an essential component of the architectural composition. Its reconstruction was consequently treated as both an architectural restoration objective and a contemporary structural design task (Fig. 2).

The new programme assigns different functions to the two sides of the hall. The western wing is vertically extended and converted into a hotel, while the central hall becomes a covered public space capable of accommodating preserved rolling stock and cultural activities. At the upper level, the hotel restaurant occupies an aerial volume that spans transversely across the hall and visually connects the two wings. The new roof and facades restore the perception of a unified interior, without reproducing the original construction technology literally (Fig. 2).

Such an intervention was developed under heritage constraints that required the new systems to remain recognisable, lightweight and compatible with the existing masonry. Consequently, the new structural components are mostly made of steel, whereas reinforced concrete is limited to local strengthening, foundations, bearing zones and composite slabs. This approach reduces the permanent load added to the historic walls and facilitates fabrication and erection within a constrained existing building.

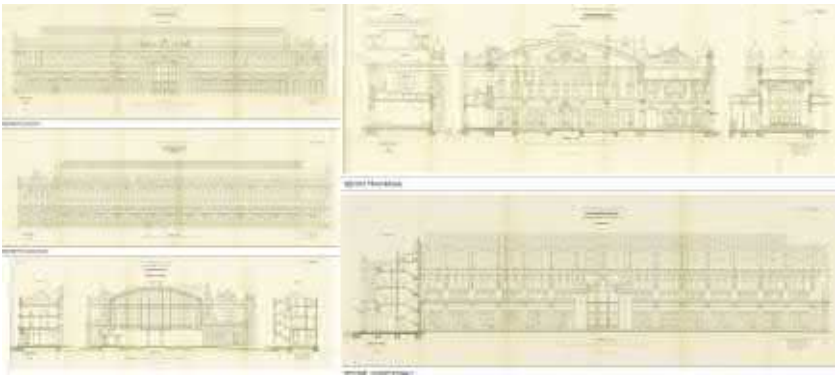


Fig. 1. Original elevations and sections of the station, showing the historic metal roof over the railway hall.



Fig. 2. Views of the proposed adaptive-reuse intervention and reconstructed glazed roof.

2.2 Structural Criteria and Modelling Hierarchy

The governing design principle was to separate, as far as practicable, the vertical and horizontal load paths (Table 1). Gravity loads generated by the new roof and the aerial walkway are mainly transferred to selected existing masonry walls and piers, after specific local verification and – where required – strengthening of the bearing zones. Conversely, the seismic actions are mainly resisted by the newly introduced steel structures, and in particular by the three braced towers of the western hotel extension. These systems collect and transfer the horizontal forces to the new foundations, thereby limiting the additional seismic demand imposed on the historic masonry. The new steel structures therefore provide a controlled horizontal-resisting system, while the existing masonry construction is mainly involved in carrying vertical actions.

Table 1. Main steel systems and structural functions.

System	Geometry and primary elements	Main structural function
Hotel extension	Three floors, 94 × 5.6 m; HEB 280 primary beams, HEB 220 secondary beams, composite slabs; three braced towers	New accommodation and braced support zone for horizontal actions
Vaulted roof	≈94 × 36 m; fifteen lattice arches spaced 6.3 m; purlins, glazing and longitudinal bracing	Reconstruction of historic hall volume with controlled reactions on masonry
Aerial walkway	≈36 m span and 12.6 m deck width; two tied lattice arches; HEB 500 deck members and in-plane bracing	Restaurant space and transverse connection between the two wings

In support of the project detailing, a hierarchical numerical strategy was adopted (Fig. 3). An equivalent-frame model of the masonry walls was first used to assess the change in static demand produced by the new structures and to verify local bearing conditions under concentrated vertical reactions. A global 3D FE model, comprising approximately 12,000 nodes, 6,600 beam elements and 10,000 plate elements, subsequently included both the existing masonry and the new steel systems. Linear and non-linear static analyses were performed to examine their global interaction under gravity and seismic actions, in accordance with [1, 2].

Additional local FE models were then developed for the typical roof arch, the full roof, the aerial walkway, the facades, the vertical circulation systems and the principal connections. This modelling hierarchy allowed each physical problem to be treated at the appropriate scale. The global FE model demonstrated the compatibility of the differentiated load paths and the controlled force transfer between the historic masonry and the new steel structures, while the local models captured member instability, connection behaviour, non-linearity, deck vibrations and local wind responses.

Unless otherwise stated, forces, stresses, reactions and stability results refer to the governing fundamental ULS combinations, while displacements refer to the SLS rare

combination and vibration checks [7–9]. Moreover, Sect. 6 reports the peak transient responses for the site-specific wind histories, rather than conventional static-combination results. The global seismic model included the hotel, roof and walkway masses and stiffnesses, verifying inertial force transfer through diaphragms and braced towers, roof-support compatibility and reactions at the selected masonry bearings.

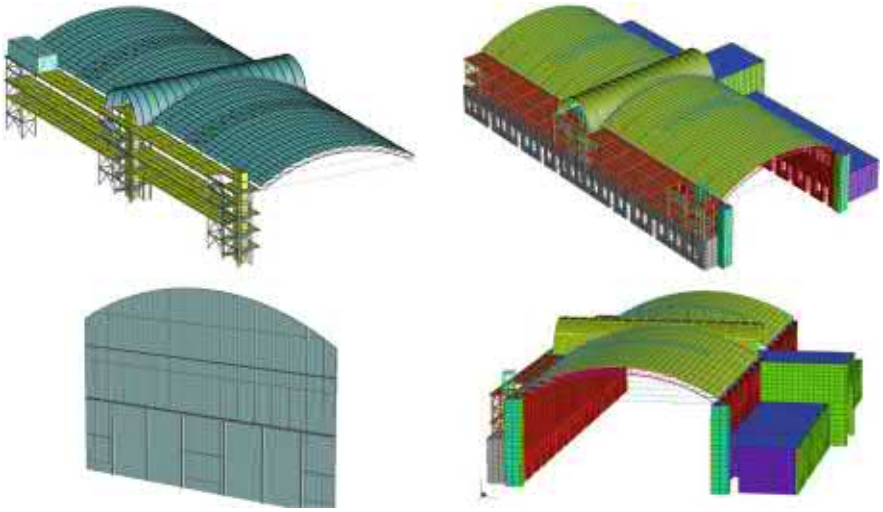


Fig. 3. Global and local FE models used to study the interaction between the existing masonry and the new steel systems.

3 Steel-Framed Hotel Extension

The hotel extension is positioned above the western masonry wing and consists of three steel-framed floors, each ≈94 m long and 5.6 m wide. The primary beams are HEB 280 sections arranged at a 6.3 m longitudinal module (the same adopted for the roof arches). Secondary HEB 220 beams, with a maximum spacing of ≈1.8 m, support profiled steel sheeting and a reinforced concrete topping. The resulting composite floor has an overall depth of ≈110 mm.

The extension is stabilised by three braced towers distributed along its length. The towers use HEB 280 columns and circular hollow-section diagonals, with the bracing system collecting longitudinal and transverse horizontal actions. External circular hollow-section columns and the regular beam grid provide a lightweight and geometrically controlled frame, that can be assembled above the existing building with limited wet construction.

The steel extension has also a broader structural role. It provides a robust support and restraint zone for the western ends of the roof and the restaurant walkway, allowing horizontal reactions to be introduced into a new, explicitly designed system, rather than on the unreinforced historic masonry. The floor diaphragms and braced towers distribute these actions and transfer them to the foundations.

4 Large-Span Glazed Roof

4.1 Structural Form and Load Path

The reconstructed roof covers an area of ≈94 × 36 m and rises ≈6 m. The principal system consists of fifteen transverse lattice arches spaced 6.3 m. The curved geometry recalls the historic roof profile, while the member arrangement and glazing technology are contemporary. Rectangular hollow-section purlins and square hollow-section secondary members support the glass panels and stabilise the upper chord. Two longitudinal bracing bays provide global stability and distribute actions along the roof.

Each typical arch spans ≈39 m and incorporates a lower tension tie (Fig. 4). The tie closes the horizontal thrust generated by gravity, so that the existing masonry mostly receives vertical reactions. The upper and lower chords, diagonals and verticals are fabricated from welded steel sects. (S355 grade). The arch located at the restaurant walkway differs from the typical units because it interacts with the larger transverse aerial structure and with the local geometry of the intersecting roof volumes.

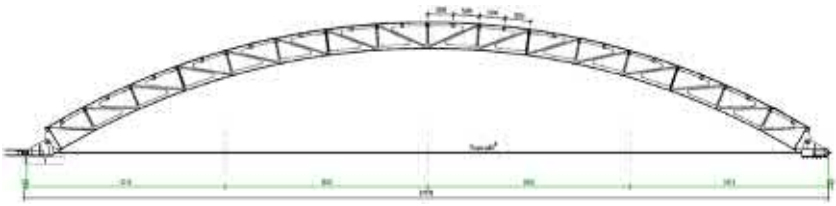


Fig. 4. Typical lattice arch geometry.

The glass envelope contributes to architectural transparency and affects the overall stiffness of the roof. Nevertheless, the principal steel system was designed to remain stable and verifiable without relying on an uncontrolled composite contribution from the glazing. The substructure, fixings and panel joints accommodate fabrication tolerances and differential movements, while maintaining the continuity of the envelope.

4.2 Supports, Movements and Verification

One end of each principal arch is arranged as a hinge, while the opposite end is supported by a sliding device. The sliding support prevents the development of excessive thermal restraint and allows the roof to move relative to the existing construction. Mechanical displacement limiters, or end-stops, become active only after a predefined travel and provide a controlled load path under exceptional uplift or horizontal actions. The design travel adopted for the detailed dynamic model was ±50 mm.

This support concept was analysed with non-linear load increments, because uplift can modify the active constraints and the force in the tie. Local checks considered the pin connections, anchorage under tension, contact and shear transfer at the sliding support, and concentrated compression in the masonry or local concrete bearing zones. The maximum design tie force for the typical arch under the governing fundamental

ULS combination was ≈621 kN, compared with a calculated resistance of 849 kN, with member and stability checks developed according to [1, 2, 5]. The first elastic buckling multiplier of the representative lattice arch was ≈23. This is above the $\alpha_{cr} = 10$ threshold specified in [5] for neglecting global second-order effects in the elastic analysis, confirming that such effects are limited for the governing static combination.

Serviceability was controlled because the glazing and its joints are sensitive to differential deformations. Under the SLS rare combination, the maximum calculated vertical displacement was ≈176 mm, over an arch length of 39 m, corresponding to ≈*L*/222 and satisfying the adopted *L*/200 criterion. The verification was complemented by local checks of purlins, secondary framing and glass-supporting members.

5 Aerial Restaurant Walkway

5.1 Structural System

The restaurant walkway is located ≈15 m above ground level and spans ≈36 m across the central hall. Its structural concept resembles a lower-deck tied-arch bridge (Fig. 5). Two longitudinal lattice arches form the primary load-bearing system, while HEB 500 members at the deck level act as lower chords and support the floor framing. Transverse HEB 500 beams are spaced ≈3.65 m; HEA 240 and HEA 220 secondary beams, together with in-plane SHS bracing, complete the deck.

The lightweight floor build-up comprises profiled steel sheeting and timber-based boards below the architectural finishes, minimizing the mass of a conventional concrete slab. The plan bracing provides diaphragm action and distributes concentrated restaurant loads to the two arch lines. The deck is ≈12.6 m wide, allowing the structure to act as a panoramic room, rather than as a narrow pedestrian bridge.

The support conditions reflect the asymmetric capacity of the existing building. Vertical reactions are transferred to the eastern masonry wing, at verified bearing locations, whereas the strengthened western extension receives both vertical and horizontal actions. This arrangement prevents the tied-arch system from imposing significant horizontal thrust on the weaker existing side. Large pinned connections, locally modelled and verified, ensure a clear transfer mechanism.

The asymmetric support scheme was also verified under seismic action. The walkway mass was included in the global model; inertial forces were transferred mainly to the strengthened western extension, while the eastern masonry bearings were checked for the associated seismic reactions. The intended load path and local bearing capacity were hence satisfied.

As the resulting reactions are elevated, dedicated checks were carried out for the existing masonry under concentrated loading [6]. The design calculations considered concentrated vertical actions up to ≈2,000 kN at the principal walkway bearings under the governing ULS combinations, with local strengthening and load-spreading details introduced where required.

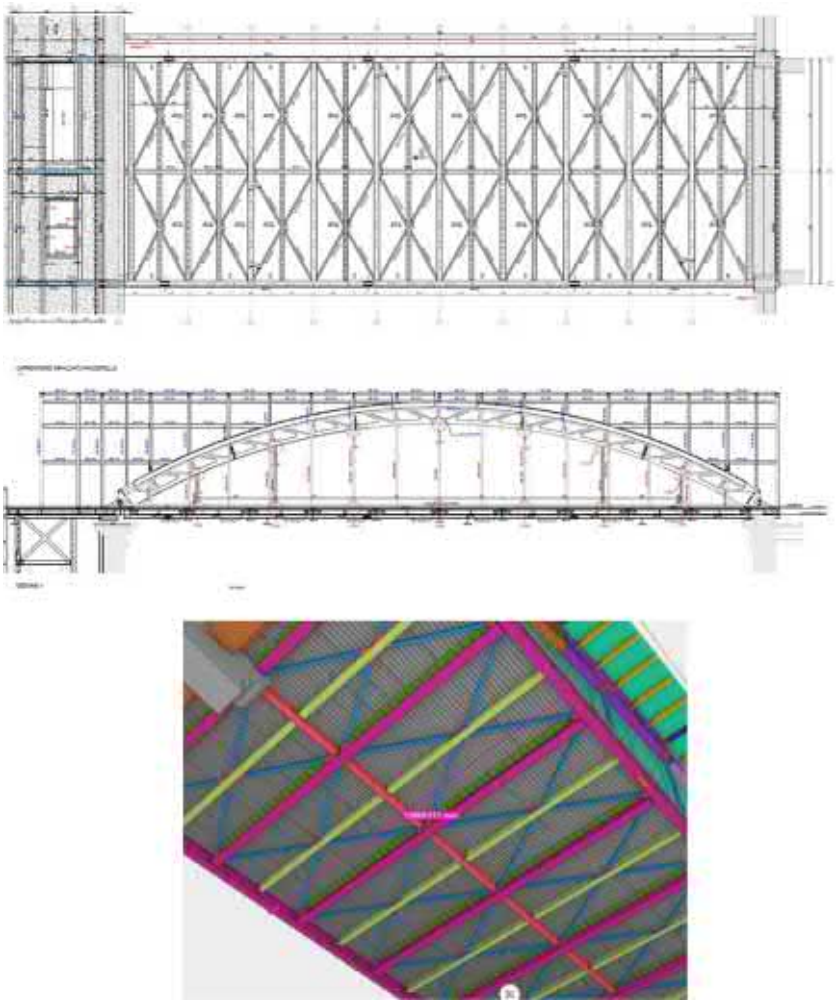


Fig. 5. Plan, transverse elevation and FE model of the aerial restaurant walkway.

5.2 Deformations and Vibrations Control

The walkway was checked not only for strength and stability, but also for deformations and human-induced vibrations. Under the rare combination, the calculated deflection ratios of 36 m lower chords, principal and secondary deck beams remained within the reference limits. The most demanding deck-beam ratio was close $\approx L/300$, and therefore required explicit control of connection stiffness and floor participation.

Two modal models were used for the occupied floor. In the first one, a 50 mm membrane represented the contribution of the floor layers; in the second, beam-to-beam connections (nominally detailed for ULS design) were modelled as rigid for vibration assessment, consistently with floor-vibration guidelines.

The first relevant vertical frequencies were ≈2.5–2.6 Hz, and the response was therefore evaluated in the resonant range. The response-factor method was applied [7–9], with separate acceptance limits for the circulation zone and the restaurant area ($R < 24$ and $R < 8$ respectively). Both modelling assumptions produced consistent results and satisfied the limits. The lowest horizontal frequencies also exceeded the 1.3 Hz threshold commonly used for human-induced lateral vibration, so no lateral synchronisation problem was detected.

6 Wind-Induced Actions and Dynamic Response

6.1 Site-Specific CFD Assessment

The dimensions, curvature and exposure of the glazed roof, together with Trieste's severe wind climate, required a site-specific assessment [10]. The building axis is rotated by ≈30° from North. Initial wind profiles were derived from CNR-DT 207/2008 and the general wind-action framework [3, 4], using reference velocity of 30 m/s, terrain factor 0.19, roughness length 0.05 m and minimum height 4 m. Additional scenarios were defined from measurements based on the ARPA FVG station at Molo Fratelli Bandiera [11], resulting in reference velocities of 34 m/s for the critical sectors.

The CFD assessment of six wind directions was first carried out with RWIND 2. The geometry of the station and a simplified representation of the surrounding buildings were included to capture shielding, channelling and local separation. The most significant cases were winds from 210°, 222° and 257° N, approximately parallel to the longitudinal development of the hall (Fig. 6).

A key result was the simultaneous occurrence of external suction and internal positive pressure. The two large openings formerly used by trains allow wind to enter the hall; the resulting internal pressure is nearly uniform and adds to the external uplift on the roof. For the three critical directions, the maximum internal pressures were ≈670 Pa, ≈969 Pa and ≈750 Pa, while the corresponding peak external suctions reached ≈1,856 Pa, ≈2,955 Pa and ≈2,620 Pa. The analysis therefore demonstrated that a closed-building assumption would not adequately represent the design condition.

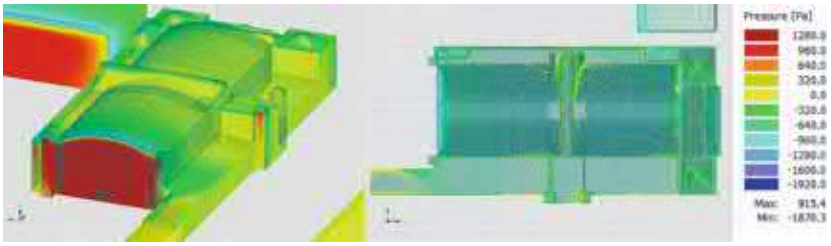


Fig. 6. Example of CFD pressure fields (RWIND 2).

6.2 Dynamic FE Model

The dynamic assessment focused on the two end bays of the roof, where the CFD study of Sect. 6.1 indicated the largest pressure gradients. A detailed ABAQUS model included two arches, purlins and transverse substructure, laminated glass panels, tension ties, pinned and sliding supports, and the displacement limiter (Fig. 7). Steel, glass and PVB were represented with linear elastic properties referred to the short duration of a wind gust. The final mesh contained ≈285,000 elements and 1.84 million DOFs.

The wind action was reproduced as a field, varying both in time and space. A normalised pressure history derived from a wind-tunnel test on a geometrically comparable roof was used to represent the temporal evolution of a gust [12]. The spatial distribution was obtained by extracting CFD pressures on a regular grid and fitting an analytical surface through the data. A uniform constant pressure was applied to the internal face of the roof. This procedure preserved the strong non-uniformity identified near the end arches, instead of replacing the CFD field with a single equivalent pressure.

Connector elements reproduced the hinge, the sliding support, the tie interaction and the ±50 mm end-stop. A sensitivity analysis also reduced the elastic modulus assigned to the glass, from the nominal 70 GPa to 1 GPa. This deliberately conservative approach was used to assess how strongly the global response depended on composite action between the glazing and the supporting steel frame [10].

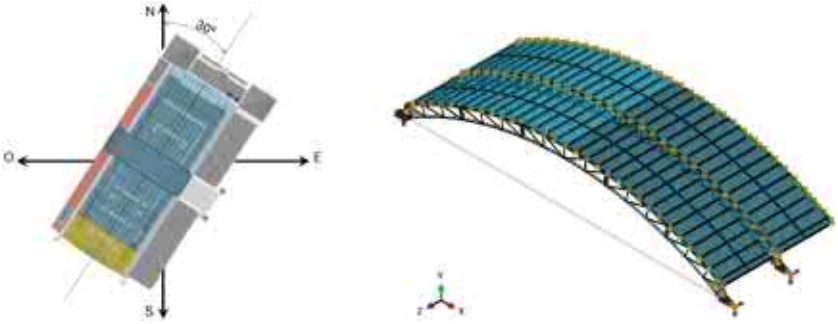


Fig. 7. Structural model for the detailed wind analysis (ABAQUS).

6.3 Results and Design Implications

For the three critical design-wind scenarios, the standard-stiffness model produced peak transient vertical displacements of 5.6–9.4 mm and maximum Von Mises stresses of 132–221 MPa (Table 2). The displacement of the monitored arch crown was 4.0–6.9 mm, while the sliding support moved only 3.4–5.0 mm. The end arch was more highly excited than the adjacent arch, despite its smaller tributary area, confirming the importance of the use of non-uniform pressure fields.

The acceleration and displacement histories did not show resonance or progressive dynamic amplification (Fig. 8). The principal contribution of the advanced analysis

was therefore not the identification of an unsafe dynamic instability, but the explicit quantification of spatial pressure effects, internal pressurisation and support travel. In the reduced-glass-stiffness sensitivity model, the monitored crown displacement increased from 4.0 to 38.3 mm and the sliding-support movement increased from 3.4 to 28.4 mm for the 210° case. Even this conservative scenario remained below the 50 mm end-stop travel.

The results confirmed that the steel roof possesses adequate stiffness and strength while retaining the movement capacity required by the heritage interface. They also show that the glazing and its connections can influence global deformation and should be represented with appropriate bounds when transparent envelopes are analysed under rapidly varying wind pressure.

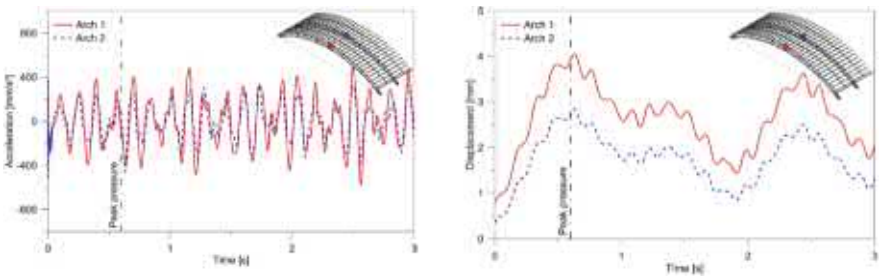


Fig. 8. Dynamic response for the 210° wind case: acceleration and displacement histories (ABAQUS).

Table 2. Summary of the peak transient dynamic wind-analysis results.

Case	Dir. [°N]	Int. press. [Pa]	Ext. suction [Pa]	Max. vert. disp. [mm]	Max. stress [MPa]
#3	210	670	1,856	5.6	132
#5	222	969	2,955	9.4	221
#6	257	750	2,620	9.0	196

7 Conclusions

The adaptive reuse project for the Campo Marzio station in Trieste demonstrates that steel can be used as an efficient and organising structural material for complex historic masonry systems. Its value lies not only in reducing weight, but also in enabling differentiated load paths, reversible assembly solutions, long spans and transparent envelopes. The three principal new systems described in this paper properly satisfy complementary functions. The hotel extension provides new usable space and a braced support zone for horizontal actions. The lattice-arch roof reconstructs the lost volume of the railway

hall, using ties, sliding bearings and displacement limiters to minimise adverse interactions with the masonry. The aerial walkway combines architectural occupation with bridge-type structural behaviour, and efficiently satisfies demanding deformations and vibration criteria.

The FE modelling strategy was essential to the design. Global masonry-steel models included the roof and walkway masses and asymmetric constraints, confirming the intended seismic load path towards the braced western extension and the compatibility of selected masonry bearings. Local models addressed instability, connections, vibrations and wind responses. The coupled CFD and dynamic analyses, in particular, showed that internal pressure and aerodynamic non-uniformity govern the roof loading, but that detrimental dynamic amplification is limited in the final configuration.

More generally, the project indicates that successful heritage interventions require new steelwork to be conceived as a controlled interface, rather than as an independent object. When geometry, supports, stiffness and construction sequence are optimally coordinated, steel structures can preserve the historic fabric while enabling substantial functional and architectural transformations.

References

1. Ministero delle Infrastrutture e dei Trasporti (2018) D.M. 17 January 2018, Aggiornamento delle Norme tecniche per le costruzioni. Gazzetta Ufficiale della Repubblica Italiana
2. Consiglio Superiore dei Lavori Pubblici (2019) Circolare 21 January 2019, n. 7 C.S.LL.PP, Istruzioni per l'applicazione dell'Aggiornamento delle Norme tecniche per le costruzioni
3. Consiglio Nazionale delle Ricerche (2008) CNR-DT 207/2008, Istruzioni per la valutazione delle azioni e degli effetti del vento sulle costruzioni, Rome, I
4. CEN (2010) En 1991–1-4:2005+A1:2010, Eurocode 1: Actions On Structures - Part 1–4: General Actions - Wind Actions, Brussels. BE
5. CEN (2014) En 1993-1-1:2005+A1:2014, Eurocode 3: Design Of Steel Structures - Part 1–1: General Rules And Rules For Buildings, Brussels, BE
6. CEN (2012) EN 1996-1-1:2005+A1:2012, Eurocode 6: Design Of Masonry Structures - Part 1–1: General Rules For Reinforced And Unreinforced Masonry Structures, Brussels, BE
7. ISO (2007) Bases for design of structures - Serviceability of buildings and walkways against vibrations, 10137:2007. ISO, Geneva, CH
8. Smith AL, Hicks SJ, Devine PJ (2007) Design of Floors for vibration, P354. SCI, Ascot
9. Willford MR, Young P (2006) Footfall-induced vibration of structures. The Concrete Centre
10. Bedon C, Ciocca M, Masiello G, Gargiulo S, Cella N (2026) Structural design and wind dynamic analysis of the new glass envelope for campo Marzio Railway Station in Trieste. In: Louter C, Bos F, Belis J (eds) challenging glass conference proceedings June 2026, vol 10. https://doi.org/10.47982/cgc.10
11. Regione Friuli Venezia Giulia: ARPA FVG - OSMER e GRN http://www.meteo.fvg.it/
12. Rizzo F, Bedon C (2023) Performance of cable-supported glass façades under time-depending wind action. Glass Struct Eng 8:81–98. https://doi.org/10.1007/s40940-022-00180-2

AI-Driven Structural Reuse for Steel Re-manufacturing: An Integrated Methodology for Circular Steel Design

Vittoria Laghi[1(✉)], Antonio D'Anna[1], Emma Ghini[1], Stefano Silvestri[1], Giada Gasparini[1], and Pierluigi D'Acunto[2]

[1] Department of Civil, Chemical, Environmental and Materials Engineering, University of Bologna, Bologna, Italy
vittoria.laghi2@unibo.it

[2] Technical University of Munich, School of Engineering and Design, Munich, Germany

Abstract. The construction sector is under increasing pressure to reduce material consumption, embodied carbon, and demolition waste while addressing a large and poorly documented existing built environment. Structural steel reuse is a promising circular strategy because reclaimed members often retain significant mechanical capacity and geometric value. Its implementation, however, remains limited by fragmented workflows, incomplete stock information, and the difficulty of adapting heterogeneous members to new structural layouts. This paper presents an integrated methodological framework for AI-assisted circular steel design and reuse. The approach combines machine-readable structural knowledge, stock-informed conceptual generation, reuse-oriented multi-objective optimization, structural verification, and adaptive remanufacturing enabled by wire arc additive manufacturing (WAAM) connections. Reclaimed members are treated as active design inputs whose availability, geometry, residual capacity, and uncertainty influence the structural configuration from the conceptual stage. The framework also incorporates fabrication constraints and iterative feedback between generation, member allocation, verification, and connection design. The proposed methodology establishes a coherent basis for future computational implementation and identifies the principal challenges related to stock characterization, data interoperability, structural reliability, and validation of non-standard WAAM components.

Keywords: Structural steel reuse · reclaimed steel · stock-informed design · AI-assisted structural design · multi-objective optimization · machine-readable structural knowledge · wire arc additive manufacturing · adaptive connections

1 Introduction

The construction sector faces increasing pressure to reduce material consumption, embodied carbon, and demolition waste while maintaining structural safety, reliability, and construction efficiency. Steel structures are particularly relevant in this transition because many steel members retain significant residual mechanical capacity and material

© The Author(s), under exclusive license to Springer Nature Switzerland AG 2026
R. Zanon et al. (Eds.): CTA 2026, LNCE 942, pp. 36–45, 2026.
https://doi.org/10.1007/978-3-032-39505-4_4

value at the end of their first service life and can, in principle, be reused in new structural systems instead of being recycled as raw material. Despite this potential, structural steel reuse is still constrained by technical and methodological barriers. Reclaimed members are usually available as heterogeneous stocks, with different geometries, section types, connection details, material properties, degradation states and documentation levels. Their use in new structures therefore requires not only mechanical assessment but also a design process capable of incorporating availability, uncertainty, and compatibility from the earliest conceptual stages.

Conventional structural design generally follows a source-after-design logic: the structural scheme is first defined, and members are then selected from standardized catalogues or newly manufactured products. This sequence is poorly suited to reuse. When reclaimed steel is the intended material resource, the available stock should influence the structural configuration itself. A reuse-oriented design strategy therefore requires a different logic, in which reclaimed members are treated as active design inputs rather than residual outputs of demolition.

Recent developments in computational design, artificial intelligence and digital fabrication provide the technical basis for this shift. Generative design can support the exploration of alternative structural configurations; optimization methods can combine structural, geometric and environmental criteria; and additive manufacturing can enable customized components for connecting non-standard reclaimed members. However, these approaches are often developed separately. As a result, structural generation, reuse-oriented member allocation, embodied-carbon assessment and connection fabrication are rarely integrated from the conceptual phase.

This paper presents the methodological basis of an integrated circular steel design framework that addresses this gap by combining: (i) the formalization of structural knowledge into machine-readable representations; (ii) AI-assisted conceptual generation; (iii) reuse-oriented multi-objective optimization; and (iv) adaptive reconfiguration through wire arc additive manufacturing connections.

2 State of the Art and Research Gap

The development of circular steel structures requires the convergence of three research areas that have mostly evolved along separate paths: generative structural design, reuse-oriented optimization, and large-scale steel additive manufacturing. Each area provides useful tools for a reuse-first design process, but none is sufficient on its own. Generative design can explore alternative structural configurations; reuse-oriented optimization can support the allocation of reclaimed members; and additive manufacturing can provide customized components for non-standard connections. The unresolved issue is their integration into a single workflow in which reclaimed stock, structural knowledge, environmental criteria, manufacturing constraints, and structural verification operate together from the conceptual phase. The three research domains and the unresolved integration gap are summarized in Fig. 1.

Generative methods in structural design were introduced well before the recent diffusion of generative artificial intelligence. Early approaches were based on parametric models, structural grammar, form-finding procedures, topology optimization and layout

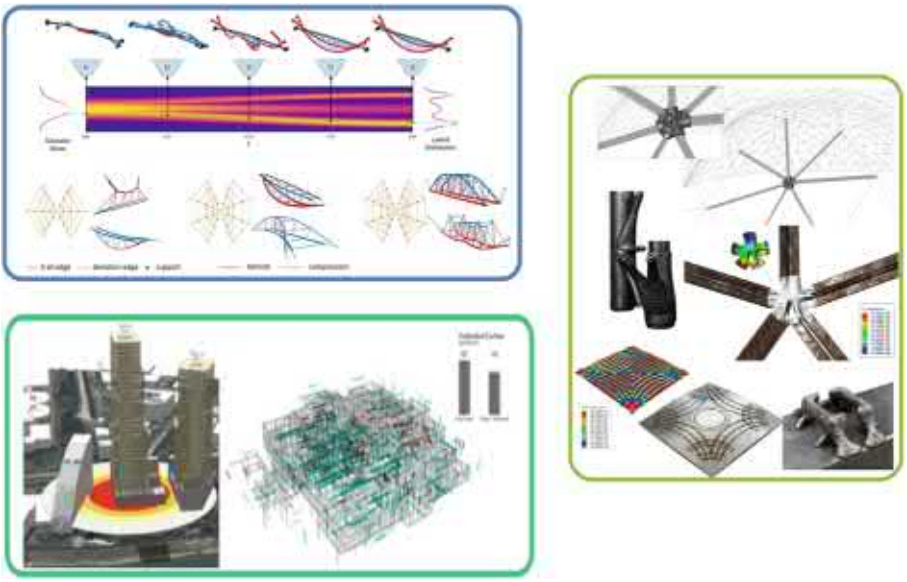


Fig. 1. Research domains and integration gap addressed by the proposed methodology. Generative structural design, reuse-oriented optimization, and WAAM-enabled adaptive connections provide complementary capabilities but are not commonly integrated within a reuse-first design-to-fabrication workflow.

optimization, allowing designers to explore structural configurations according to predefined objectives and constraints [1–3]. More recently, machine-learning methods have expanded this field by supporting performance-based design exploration and the generation of non-standard structural forms. Graph-based representations are particularly relevant for discrete structural systems because they can describe members, nodes and connectivity more directly than purely vector-based parameterizations [4–6].

However, most generative approaches still operate within idealized design spaces. Structural members are generally assumed to be newly manufactured, geometrically regular, and available from standardized catalogs. This assumption is coherent with conventional design practice, but it becomes restrictive when the objective is to reuse reclaimed steel members. In reuse-first design, the design space is defined not only by geometry, loads, and boundary conditions but also by the availability, variability, residual capacity, and uncertainty of existing components. For this reason, generative design cannot be limited to form exploration; it must become stock-informed and mechanically constrained.

Structural steel reuse has been recognized as a promising strategy for reducing the environmental impact of construction, particularly when compared with recycling alone. Reuse preserves not only the material but also part of the geometric and manufacturing value embedded in existing members. Nevertheless, practical implementation remains limited by incomplete documentation, uncertain material properties, residual defects, non-standard geometries, previous connection details, logistical constraints, and the absence of consolidated design procedures [7, 8]. As a result, reuse often requires

extensive survey, classification, assessment, and matching operations before reclaimed members can be accepted in a new structural system.

Computational design tools can support this process by treating reclaimed members as stock-constrained design inputs. Optimization algorithms can, in principle, search for structural configurations that satisfy mechanical requirements while maximizing reuse and reducing embodied carbon. In practice, however, reuse-oriented workflows are still frequently fragmented and case-specific. The matching between available elements and structural demand is often performed after the main structural scheme has already been defined, with limited feedback between conceptual design, structural verification, environmental assessment and fabrication constraints [9]. This limits scalability and keeps reuse dependent on ad hoc procedures.

A further limitation concerns the physical reconfiguration of reclaimed members. Even when a reuse-oriented layout is structurally efficient, connections between heterogeneous elements may require non-standard details. Existing members may differ in section size, orientation, end cuts, residual holes, tolerances, and connection history. Standard connection systems cannot always accommodate this variability without excessive additional fabrication or loss of structural efficiency. The feasibility of reuse is therefore directly linked to the availability of adaptive connection strategies. Large-scale metal additive manufacturing, particularly wire arc additive manufacturing (WAAM), offers a possible route for addressing this problem [10]. Previous studies have investigated WAAM-based strengthening of existing steel profiles [11] and topology-optimized custom joints for assembling reused members [12]. Nevertheless, the integration of WAAM into structural reuse workflows remains at an early stage. In many cases, additive manufacturing is still treated as a fabrication technology applied after the structural design has been defined, rather than as a design variable influencing the generation and selection of structural solutions.

Therefore, the research gap lies in the absence of an integrated methodology connecting these technologies. Generative design rarely starts from heterogeneous reclaimed stock; reuse-oriented optimization is often separated from early-stage conceptual generation and adaptive fabrication; and WAAM-based components are not yet systematically embedded in reuse-first structural design. The main challenge is to connect these domains within a coherent design-to-fabrication workflow. In such a workflow, structural knowledge is translated into machine-readable descriptors, reclaimed members become active design inputs, AI-assisted generation remains constrained by structural mechanics, optimization includes reuse and embodied-carbon criteria, and adaptive WAAM connections enable compatibility between non-standard elements.

3 The Proposed Methodological Framework

The proposed methodology is conceived as an integrated design-to-fabrication framework for circular steel structures. It connects reclaimed-steel stock, structural knowledge, AI-assisted generation, reuse-oriented optimization, and adaptive manufacturing within a single workflow. Rather than relying on a single autonomous algorithmic step, the framework consists of interdependent operations in which each phase provides information, constraints, and feedback to the others. Operationally, the workflow maps

reclaimed-stock data and machine-readable structural representations to candidate layouts, member assignments, and connection geometries that are subsequently evaluated and verified (Fig. 2).

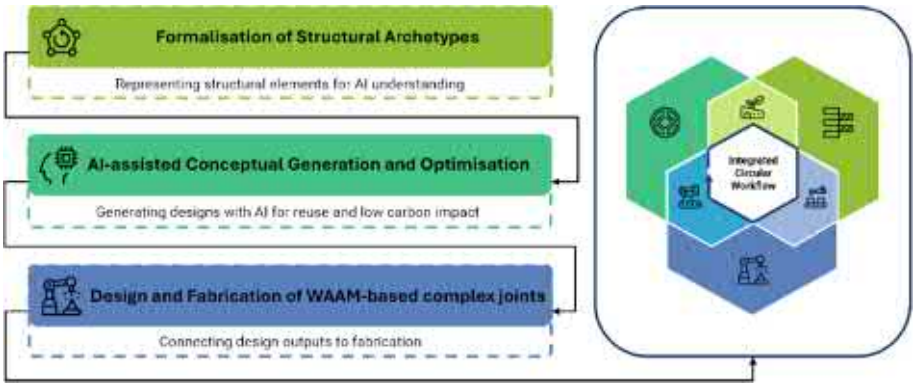


Fig. 2. Integrated methodology workflow: structural knowledge formalization, AI-assisted generation, reuse-oriented optimization, structural verification and WAAM-based adaptive connections within a circular design-to-fabrication process.

The first operation is the formalization of structural knowledge. Existing and historical steel structures are interpreted not only as physical reservoirs of reusable material but also as sources of structural information. Typologies, load-transfer schemes, member functions, connection principles, boundary conditions, and mechanical behaviors are translated into machine-readable descriptors. This step is necessary because AI-assisted design cannot rely solely on geometric data. It also requires structured information on how a structural system works, how loads are transferred, which members are critical, and which constraints define admissible configurations.

The structural catalog therefore has a dual function. It classifies recurring systems, such as frames, trusses, braced systems, and hybrid configurations, and defines the descriptors required to connect structural knowledge with computational generation. These descriptors may include geometry, section properties, member hierarchy, connectivity, load-path role, reuse constraints, and uncertainty levels associated with reclaimed members. The catalog is not intended as a passive archive but as a computational knowledge base that can be queried during design. The structural knowledge formalization process is illustrated in Fig. 3.

The second operation is AI-assisted conceptual generation. Starting from the structural catalog and the available reclaimed stock, the generative module produces alternative structural configurations. In this phase, artificial intelligence is used as a design-support tool to explore combinations that would be difficult to evaluate manually. The generated alternatives, however, must remain mechanically admissible. For this reason, the generation process is constrained by structural rules, load-path consistency, connectivity requirements, and preliminary checks on member suitability. The role of AI is not to produce arbitrary forms but to expand the range of feasible design options within a controlled structural domain.

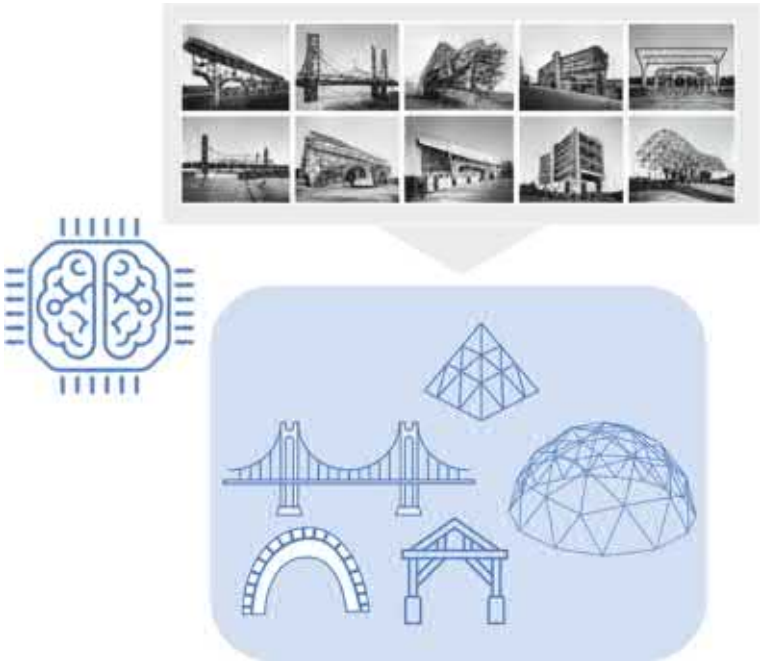


Fig. 3. Formalization of structural knowledge: representative steel structural typologies are translated into machine-readable geometric, topological, and mechanical descriptors.

The third operation is reuse-oriented multi-objective optimization. The alternatives generated during the conceptual phase are evaluated according to structural performance, compatibility with the available stock, reuse rate, embodied-carbon reduction, and geometric adaptability. This broadens the optimization objective relative to conventional design. The preferred solution is not necessarily the lightest or stiffest configuration under idealized assumptions but the one that achieves a balanced trade-off between mechanical efficiency, reclaimed-member utilization, environmental benefit, and implementation feasibility. In this sense, the available stock becomes part of the design problem and directly influences the resulting structural configuration. The stock-informed redesign process is illustrated in Fig. 4.

The fourth operation concerns WAAM-based adaptive connections. Reclaimed members are rarely compatible with new structural layouts without local adaptation. Differences in section size, end geometry, residual holes, tolerances, and previous connection details can prevent the direct use of standard joints. The methodology therefore introduces adaptive nodes and local transition components fabricated using WAAM. These components are intended to reconcile the geometric variability of reclaimed members with the load-transfer requirements of the new structural system. The adaptive reconfiguration process is illustrated in Fig. 5.

The use of WAAM is deliberately local and strategic. It is not proposed as a replacement for conventional steel construction or as a method for producing entire structures. Its role is to enable localized connection, strengthening, or geometric adaptation where



Fig. 4. Stock-informed structural redesign: reclaimed members are selected and assigned to a new structural layout under structural, geometric, and environmental constraints.



Fig. 5. WAAM-enabled adaptive reconfiguration: locally fabricated nodes and transition components connect heterogeneous reclaimed members within a new structural assembly.

standard solutions would be inefficient, impractical, or unable to accommodate the variability of reclaimed elements. For this reason, WAAM-related constraints, including manufacturability, deposition strategy, geometric tolerances, and mechanical validation, are incorporated into the design process rather than checked only after the structural solution has been selected.

The final operation integrates the previous phases into a circular workflow. The structural catalog provides structured knowledge; the AI module generates candidate configurations; the optimization framework selects and refines solutions according to structural and circularity criteria; and the WAAM connection logic assesses whether the proposed assemblies can be fabricated and assembled. Structural verification remains active throughout the process, both as a constraint during generation and as a validation layer for the final design alternatives.

4 Implementation Challenges

The proposed methodology changes the role of structural steel reuse within the design process. In conventional practice, reuse is often treated as a verification problem: reclaimed members are surveyed, classified, and checked against a structural scheme that has already been defined. This approach is technically valid for specific cases, but it limits scalability because the design process remains based on standardized new products. The proposed methodology instead treats reclaimed-steel stock as an active design input that can influence topology, member assignment, connection strategy, and fabrication feasibility.

This shift has direct methodological consequences. Stock-driven design expands the design space because different inventories can lead to different structural configurations. At the same time, it increases complexity: member geometry, residual capacity, connection history, and uncertainty levels become explicit design parameters. For this reason, AI-assisted generation cannot be used as an unconstrained form generator. It must operate within a domain defined by structural typologies, load-path logic, member functions, and admissibility rules. Without this mechanically grounded knowledge base, the generated alternatives would not be sufficiently reliable for load-bearing structures.

Optimization is also redefined in a reuse-first workflow. The preferred solution is not necessarily the one that minimizes weight or material quantity under idealized assumptions. Instead, it is the solution that achieves a balanced trade-off between structural performance, reuse efficiency, embodied-carbon reduction, geometric adaptability, and fabrication feasibility. Optimization therefore changes from a purely mechanical or material-minimization task into a multi-objective design process driven by both structural and circularity requirements.

WAAM-based adaptive connections address one of the most critical barriers to reuse: the incompatibility between heterogeneous reclaimed members and new structural layouts. However, additive manufacturing should not be interpreted as a replacement for conventional steel fabrication. Its role is local and strategic. It can enable customized transition components where standard connection solutions would be inefficient, impractical, or unable to accommodate reclaimed-member variability. This distinction is essential for keeping the methodology technically realistic.

Several implementation challenges remain open. The first concerns data quality. Reclaimed steel members may have incomplete documentation, uncertain steel grades, unknown loading histories, defects, corrosion, or limited information on previous connections. A computational reuse workflow must therefore include uncertainty descriptors and cannot treat reclaimed elements as equivalent to new catalog products unless adequate inspection and verification procedures are available. Structural validation is another critical issue: generated solutions require global checks of load paths, stiffness, strength, and stability, as well as local checks of member capacity, connection behavior, and WAAM-node performance.

A further challenge is interoperability. The workflow requires communication among structural catalogs, stock inventories, AI models, optimization procedures, environmental indicators, fabrication constraints, and verification tools. If these components remain separated by incompatible data formats or software environments, the method risks

becoming a sequence of isolated operations rather than an integrated design process. Professional and regulatory acceptance is equally important. Black-box outputs are unsuitable for structural applications, particularly when uncertain reclaimed materials and non-standard additively manufactured joints are involved. The workflow must therefore remain human-in-the-loop, auditable, and supported by explicit decision records.

The proposed methodology should consequently be interpreted as a conceptual framework rather than as a mature design procedure or standard. Further work is needed to consolidate data-acquisition protocols, reliability models for reclaimed members, structural validation procedures, mechanical testing of adaptive WAAM nodes, benchmark case studies, and alignment with future standardization processes. Despite these open challenges, the approach provides a coherent route for embedding circularity within the generation, evaluation, and realization of steel structures rather than adding it after the main design decisions have already been made.

5 Conclusions

This paper presents the methodological basis of an integrated framework for the AI-assisted circular design of steel structures using reclaimed members and adaptive remanufacturing. The framework combines four components: machine-readable structural knowledge, AI-assisted conceptual generation, reuse-oriented multi-objective optimization, and WAAM-based adaptive connections. Structural knowledge provides the mechanical and typological rules that constrain generation; AI-assisted design expands the set of feasible alternatives; optimization compares solutions in terms of structural performance, reuse efficiency, embodied-carbon reduction, and geometric adaptability; and adaptive WAAM components enable the connection of heterogeneous reclaimed members within new structural systems.

The main contribution of the proposed methodology lies in reframing structural steel reuse from an assessment-driven task into a reuse-first design workflow. In this workflow, circularity is not treated as an additional criterion applied after conventional design decisions but as a design condition that influences topology, member assignment, connection strategy, and fabrication feasibility. This shift is necessary if structural steel reuse is to move beyond isolated demonstrators and become a systematic design strategy.

The work also highlights the main challenges that must be addressed before practical implementation. These include the quality and completeness of reclaimed-stock data, uncertainty in material and geometric properties, structural verification at global and local scales, mechanical validation of adaptive WAAM nodes, interoperability among computational tools, and the need for transparent and auditable workflows suitable for professional engineering practice.

Overall, the proposed methodology defines a possible path toward circular steel construction in which structural mechanics, artificial intelligence, reuse-oriented optimization, and additive manufacturing are combined within a coherent design-to-fabrication process. Future work should validate the workflow through benchmark case studies and experimental assessment of adaptive connection strategies, clarifying the conditions under which the proposed approach provides structural, environmental, and manufacturing advantages over conventional steel design.

References

1. Shea K, Aish R, Gourtovaia M (2005) Towards integrated performance-driven generative design tools. Autom Constr 14(2):253–264. https://doi.org/10.1016/j.autcon.2004.07.002
2. Shea K, Cagan J (1999) Languages and semantics of grammatical discrete structures. Artif. Intell. Eng. Des. Anal. Manuf. 13(4):241–251. https://doi.org/10.1017/S0890060499134012
3. Brown NC, Mueller CT (2019) Design variable analysis and generation for performance-based parametric modeling in architecture. Int J Archit Comput 17(1):36–52. https://doi.org/10.1177/1478077118799491
4. Saldana Ochoa K, Ohlbrock PO, D'Acunto P, Moosavi V (2021) Beyond typologies, beyond optimization: exploring novel structural forms at the interface of human and machine intelligence. Int J Archit Comput 19(3):466–490. https://doi.org/10.1177/1478077120943062
5. Hayashi K, Ohsaki M (2020) Reinforcement learning and graph embedding for binary truss topology optimization under stress and displacement constraints. Front. Built Environ. 6:59. https://doi.org/10.3389/fbuil.2020.00059
6. Bleker L, Tam KMM, D'Acunto P (2024) Logic-informed graph neural networks for structural form-finding. Adv Eng Inform 61:102510. https://doi.org/10.1016/j.aei.2024.102510
7. Bartsch H (2025) Reuse of reclaimed steel components in construction: a systematic review of potential, challenges and future directions. Structure 80:110057. https://doi.org/10.1016/j.istruc.2025.110057
8. Kanyilmaz A, Birhane M, Fishwick R, del Castillo C (2023) Reuse of steel in the construction industry: challenges and opportunities. Int J Steel Struct 23(5):1399–1416. https://doi.org/10.1007/s13296-023-00778-4
9. Mei L, Wang Q (2021) Structural optimization in civil engineering: a literature review. Buildings 11(2):66. https://doi.org/10.3390/buildings11020066
10. Ngo TD, Kashani A, Imbalzano G, Nguyen KTQ, Hui D (2018) Additive manufacturing (3D printing): a review of materials, methods, applications and challenges. Compos Part B 143:172–196. https://doi.org/10.1016/j.compositesb.2018.02.012
11. Kloft H, Schmitz LP, Müller C, Laghi V, Babovic N, Baghdadi A (2023) Experimental application of robotic wire-and-arc additive manufacturing technique for strengthening the I-beam profiles. Buildings 13(2):366. https://doi.org/10.3390/buildings13020366
12. Laghi V, Babovic N, Laccone F, Malomo L, Savino E, Gasparini G (2026) Automated design and fabrication framework to enhance steel reuse through structural optimization and metal 3D printing. Structure 88:111942. https://doi.org/10.1016/j.istruc.2026.111942

Rediscovering Structural Steel Reuse: Practice and Perception in Italy

Giulio Basileo[1](✉), Viorel Ungureanu[2,3], Renato Morganti[1], Alessandra Tosone[1], Matteo Abita[1], and Danilo Di Donato[1]

[1] University of L'Aquila, L'Aquila, Italy
giulio.basileo@graduate.univaq.it
[2] Universitatea Politehnica Timișoara, Timișoara, Romania
[3] Romanian Academy, Timișoara Branch, Timișoara, Romania

Abstract. The publication of CEN/TS 1090-201:2024 represents a step towards the formal recognition of structural steel reuse within the European regulatory framework. By providing a formal technical reference, the specification contributes to achieving the decarbonisation objectives of the European construction industry. Nevertheless, the implementation of structural steel reuse depends not only on technical provisions but also on the practices and perceptions of the actors involved. Building on this background, this research explores stakeholder perspectives on structural steel reuse in the Italian construction sector, with particular attention to direct experiences and perceived barriers to its adoption. Among the actors of the construction supply chain, steel fabrication workshops were selected as the survey target, since they represent the technical node where reclaimed steel is reprocessed and adapted for reuse. To investigate these aspects, an exploratory survey was administered to companies operating in the Italian construction sector. The questionnaire distinguishes between respondents with and without direct experience of structural steel reuse and, where applicable, investigates how reuse practices were implemented and which difficulties were encountered. For respondents without direct experience, the survey focuses on perceived obstacles to the adoption of structural steel reuse. Barriers are examined across technical, regulatory, economic and practical dimensions. The collected data are intended to inform future research and support policymakers and standardisation bodies by assessing whether established but undocumented practices of structural steel reuse exist within the construction sector.

Keywords: Structural Steel Reuse · Circular Economy · Construction Sector · Reuse Stakeholders · Stakeholder Survey

1 Introduction

Steel is one of the most widely used and resource-intensive materials in the construction sector. At the end of a building's life cycle, structural steel elements are typically recycled, producing high-quality secondary material that is significantly less polluting

© The Author(s), under exclusive license to Springer Nature Switzerland AG 2026
R. Zanon et al. (Eds.): CTA 2026, LNCE 942, pp. 46–57, 2026.
https://doi.org/10.1007/978-3-032-39505-4_5

than the corresponding primary raw material [1]. In recent years, driven by the European Green Deal [2] and by the broader objective of improving the sustainability of the construction sector, the possibility of reusing structural steel components has been widely investigated, and several European countries have developed protocols or regulatory frameworks to support this practice [3]. Recently, in 2024, the CEN/TS 1090–201 specification was published [4], introducing provisions for structural steel reuse across Europe.

In Italy, however, structural steel reuse does not yet appear to be an established practice. The starting point of this research was the identification of a steel fabrication workshop in Abruzzo with direct experience in the reuse of structural steel elements. This case raised a broader research question: whether similar experiences exist elsewhere in Italy, and to what extent they are known, repeated, or structured within the national construction sector. Based on this observation, the study aims to document the existence and operational characteristics of structural steel reuse practices in Italy, distinguishing isolated experiences from more recurrent company-level practices.

Drawing on similar studies conducted in the United Kingdom [5], the research therefore focuses on the development of an exploratory survey addressed to companies involved in the construction, transformation, demolition, and reuse of steel structures. The questionnaire investigates previous experiences of reuse, the types of projects in which reused elements were employed, the perceived economic outcomes, the main technical, organisational, regulatory, and documentary barriers, and the conditions that could support a wider adoption of this practice in the Italian context.

2 Reuse Practices in Abruzzo

An interview with a steel fabrication workshop in Abruzzo provided the initial evidence that structural steel reuse was already being practised in Italy. The case concerned a large stock of steel originally intended for the Montalto di Castro nuclear power plant. The material had already been cut to length but had never been assembled or coated. Since it had remained stored indoors, it was still in good condition and showed no significant corrosion.

The stock was subsequently acquired from ENEL by a steel producer and section manufacturer, which decided to use it for the construction of an industrial building of approximately 14,000 m^2 in Abruzzo. To implement the project, the company supplied the material to a local steel fabrication workshop. The workshop carried out the required fabrication and adaptation work and then supplied the finished structural components back to the client. Completed around 2013–2014, the building therefore represents a client-driven reuse process: the owner of the existing stock initiated the operation, while the workshop provided the technical capacity required to adapt the material to its new structural application.

The feasibility of the operation was supported by the availability of technical documentation. The interview nevertheless suggested that the available records may have included both original production documents and reports resulting from subsequent laboratory testing. Building on this case and on experience acquired over the years, the interviewee described a case-specific approach for steel lacking complete documentary

traceability. Where neither an adequate technical file nor an EN 10204 3.1 inspection certificate is available, representative samples may be submitted to an authorised laboratory for mechanical characterisation. On the basis of the test results, the structural designer may then assign the material to an appropriate strength class, adopting conservative assumptions where necessary, for example by treating material compatible with S355 as S275.

Such a procedure, however, is economically justified only for sufficiently large and homogeneous lots. According to the workshop, quantities of approximately 20–30 t or more are generally required, since the costs of testing, documentation, and adaptation may otherwise offset the economic advantage of reuse. Moreover, documentary evidence and sample testing do not entirely eliminate uncertainties concerning traceability. The implementation of reuse therefore also depends on coordination and trust among the material owner, the fabricator, the laboratory, and the structural designer.

This case provided the empirical basis for extending the investigation beyond Abruzzo. A questionnaire was therefore developed, in collaboration with the Universitatea Politehnica Timișoara, to determine whether comparable and potentially undocumented practices existed elsewhere in Italy and to identify the principal technical, economic, regulatory, and documentary barriers to their wider adoption.

3 Methodology

The study is exploratory in nature. In Italy, the reuse of structural steel has not been systematically documented, and no national data on its prevalence were identified. The aim of this study is therefore not to measure how widespread the practice is, but to document that it exists and how it works, based on the direct experience of the companies involved.

The study focuses on steel fabrication workshops for two reasons. First, these companies possess the expertise and equipment required to reprocess and adapt reclaimed structural components and represent a key technical node within Italy's fragmented, SME-dominated supply chain. Second, the preliminary evidence of structural steel reuse emerged from an interview with a workshop reporting direct, although limited, experience of the practice.

The analysis combines descriptive statistics for closed-ended questions with thematic analysis of open-ended responses. The main analytical approach consists of comparing the responses provided by the two branches of the questionnaire, respondents with direct experience of reuse and respondents without such experience, across three key dimensions: the assessment of the economic implications of reuse compared with new material, the role of CE marking as a barrier, and awareness of the relevant technical standards. Figure 1 presents the questionnaire structure and branching logic.

This comparison, inspired by the "perceived versus real" approach proposed by Dunant et al. [5], makes it possible to isolate the role of perception from that of direct experience. Open-ended responses concerning motivations for reuse, conditions required for wider adoption, and the main barriers were analysed in full and grouped according to recurring themes, without imposing rigid classification criteria.

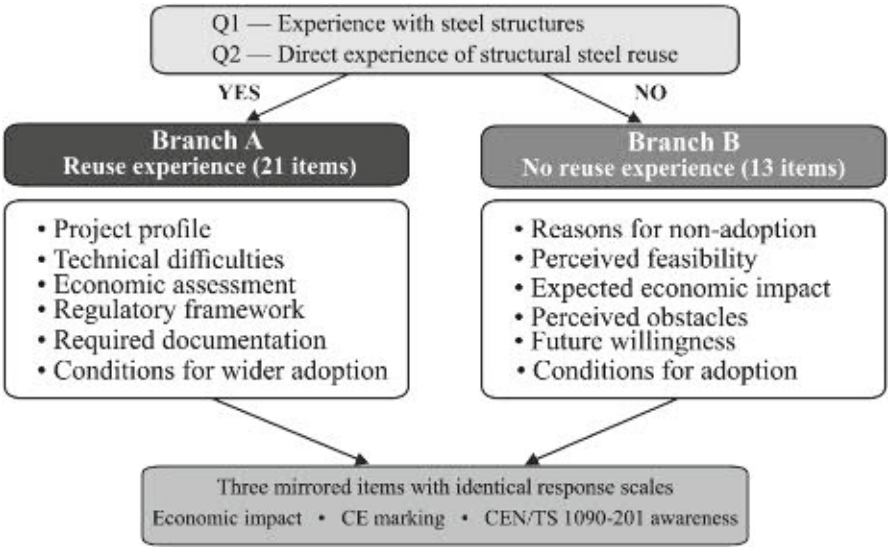


Fig. 1. Structure of the questionnaire

To operationalise this analytical framework, the questionnaire was administered online through Microsoft Forms between February and June 2026. The median completion time for valid responses was 4.5 min.

The questionnaire used conditional branching based on a key filtering question [Q2: direct experience of reusing structural steel elements in at least one completed project], which directed respondents towards one of two branches. Branch A included 21 questions concerning completed projects, technical difficulties, economic implications, regulatory issues, and the potential for wider application. Branch B included 13 thematically equivalent questions formulated conditionally to capture perceptions rather than direct experience.

Three mirrored pairs of questions [Q13/Q31 on economic impact; Q16/Q32 on CE marking; Q20/Q33 on awareness of UNI CEN/TS 1090–201] used identical response options in both branches, enabling direct comparison between experience and perception. Most questions were single- or multiple-choice, while ten open-ended questions addressed motivations, barriers, and conditions for wider adoption that could not be categorised a priori.

The sampling strategy was designed to achieve broad geographical coverage. Companies were identified province by province through LLM-assisted searches, search engines, and professional directories, and all entries were manually verified before contact. Of the 672 companies contacted, 26 completed the questionnaire, corresponding to a response rate of approximately 3.9%. The sample comprised 22 steel fabrication workshops and 4 construction companies. Overall, 11 respondents reported direct experience of structural steel reuse, while 15 reported no direct experience.

Personal and company information was optional and collected only for possible follow-up. Questions were worded neutrally, and conditional branching was used to separate direct experience from hypothetical perception. Three mirrored questions retained identical response scales across the two branches. Motivations, barriers, and enabling conditions were investigated through open-ended questions to avoid directing respondents towards predefined explanations, particularly environmental motivations, whose explicit inclusion could have increased their salience or encouraged socially desirable responses.

Nevertheless, the low response rate creates a risk of self-selection and non-response bias, potentially overrepresenting companies already interested in or familiar with reuse. Since no information was available on non-respondents, the magnitude of this bias could not be assessed. The findings should therefore be interpreted as exploratory evidence rather than as estimates of the prevalence of structural steel reuse in Italy.

4 Results

4.1 Geographical Distribution and Profile of Reuse Experiences

The analytical sample comprised 26 cases. Of these, 11 (42%) reported direct experience of structural steel reuse, while 15 (58%) reported no such experience. The analysis presented in the following sections is structured around this distinction, which constitutes the analytical basis of the study.

The sample covers 11 of the 20 Italian regions (Fig. 2), although companies in all Italian regions were contacted; the regions not represented therefore reflect the absence of responses rather than the absence of contact. Documented reuse experiences are distributed across the country: Lombardy (3), Abruzzo (2), Lazio (2), Sicily (2), Tuscany, Marche, and Apulia (1 each).

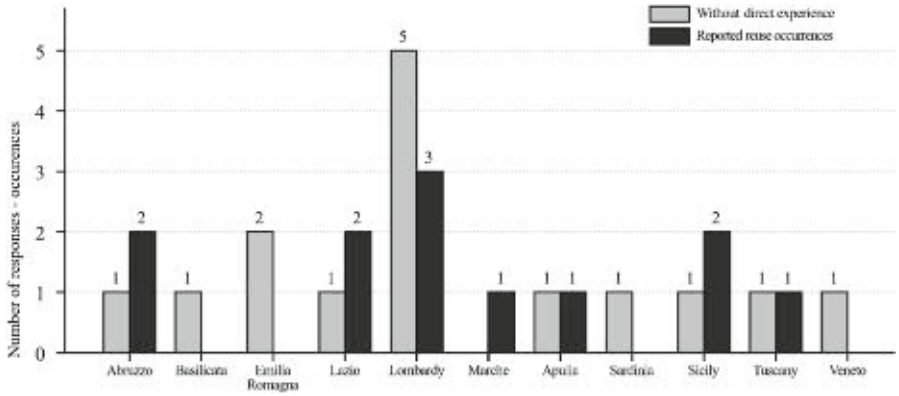


Fig. 2. Distribution and numbers of respondents and experiences

With the exception of the initial Abruzzo case, all reported reuse experiences involved material originating from and reused within the same region.

It is important to note that the only respondent from Marche also operates in Sicily and reported reuse experiences in both regions. For this reason, the respondent was counted twice. Although exploratory, the geographical distribution indicates that the documented reuse experiences were not confined to a specific area of the country. However, in some regions from which responses were received, namely Veneto, Emilia-Romagna, Basilicata, and Sardinia, no respondent reported direct reuse experience. This absence concerns only the available data and does not allow the conclusion that no reuse practices exist within those regions. Likewise, no conclusions can be drawn regarding the presence or absence of reuse experiences in regions from which no responses were obtained.

Beyond their geographical distribution, the documented cases were examined in terms of recurrence, intended use, and types of components reused. The 11 respondents with direct experience reported several common characteristics. All respondents described their reuse projects as "sporadic cases": no workshop reported practising reuse systematically.

The number of projects per company was distributed as follows: one project (1; 9%); between two and five projects (8; 73%); more than five projects (2; 18%).

The fact that 10 of the 11 companies reported more than one reuse experience suggests that firms engaging in reuse tend to repeat the practice rather than treating it as an isolated event. Reuse therefore appears to constitute a recurring activity at company level, although still sporadic when compared with the firms' overall production volume. It should nevertheless be noted that some companies, such as the workshop from which the survey originated, reported having discontinued reuse practices over time. The destination structures were predominantly permanent buildings (7/10), with a smaller number involving temporary structures (2/10) or both types (1/10).

The elements most commonly reused were IPE, HEA and HEB rolled sections, large tubular profiles, plates, and accessories such as parapets and fall-protection systems.

4.2 Economic Implications and Documentation Requirements

Among the ten respondents with direct experience who answered this question, 4/10 (40%) reported cost savings, 4/10 (40%) considered the costs comparable to those of new steel, and 2/10 (20%) were unable to provide an assessment; none reported higher costs. Among respondents without direct experience, only 1/15 (7%) expected savings, while 4/15 (27%) anticipated costs comparable to new steel, 6/15 (40%) expected higher costs, and 4/15 (27%) were unable to assess the economic implications (Fig. 3). The comparison therefore indicates a clear divergence between experience and perception: respondents without direct experience predominantly anticipated additional costs, whereas 8/10 (80%) of experienced respondents reported either savings or costs comparable to new steel.

This pattern is consistent with the findings of Dunant et al. [5], who also identified a gap between actual and perceived reuse costs in the United Kingdom, although their sample was more heterogeneous. Among Italian respondents with direct experience, additional costs were attributed mainly to processing and adaptation (8/10; 80%) and less frequently to characterisation testing (2/10; 20%).

Economic feasibility was also closely linked to the availability of adequate technical documentation. Experienced respondents identified original material certificates,

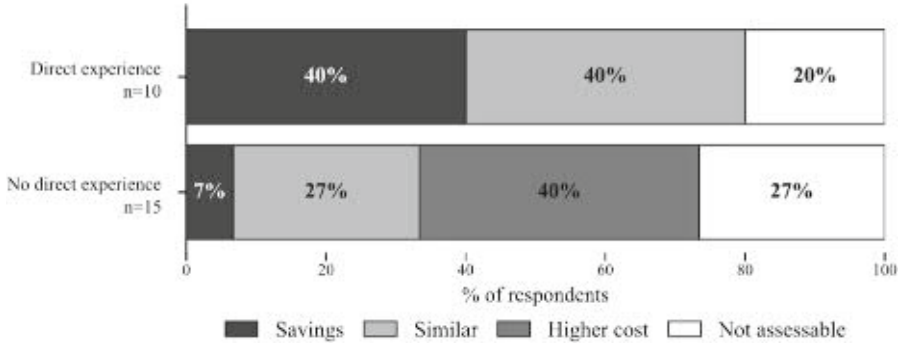


Fig. 3. Economic impact of reuse. Percentage may not total 100% because of rounding.

fabrication drawings, inspection and testing records, and detailed design documentation as the main information required to assess reclaimed steel. Where these records were incomplete, laboratory testing and material characterisation were considered the principal alternatives. One respondent also reported that a dedicated structural calculation had been prepared for beams reused as temporary lifting spreaders, confirming that verification requirements depend on the intended application.

The preliminary workshop interview provided further insight into documentary traceability, showing that a technical dossier may collect material identification, certificates, and test reports, although its contents are not standardised and may not reconstruct the complete production history. Original certificates describe the declared properties of a production lot, whereas later laboratory reports establish the measured properties of the tested samples.

Incomplete documentation therefore does not necessarily prevent reuse. Representative samples may be mechanically characterised and the steel subsequently assigned to an appropriate strength class, using conservative assumptions where required. According to the interviewee, this procedure is generally economical only for homogeneous lots of approximately 20–30 t or more. Overall, original documentation remains preferable, while experimental testing provides a more costly alternative when traceability is incomplete.

4.3 CE Marking and Awareness of CEN/TS 1090–201

CE marking showed the sharpest contrast between experience and perception (Fig. 4). Among respondents without direct experience, 14/15 (93%) considered the absence of CE marking a significant obstacle.

Among the ten respondents with direct experience who provided a response, only 1/10 (10%) identified the absence of CE marking as a concrete problem, while 9/10 (90%) did not report it as such. These findings do not imply that CE marking is irrelevant; they indicate only that its absence was rarely experienced as a concrete obstacle in the projects reported. Since the questionnaire did not establish project dates, no chronological interpretation can be made.

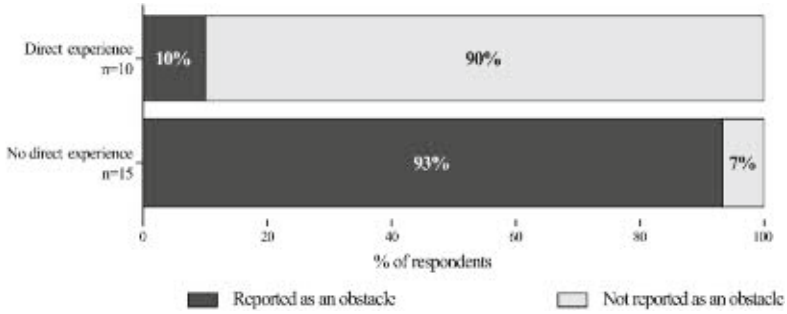


Fig. 4. CE marking as a perceived or experienced obstacle to structural steel reuse

Alongside CE marking, the survey examined respondents' awareness of the recently published CEN/TS 1090–201. Awareness remained limited in both groups. Among respondents with direct experience, 4/11 (36%) were aware of the specification but had not applied it, 6/11 (55%) were unaware of it, and 1/11 (9%) did not answer. Among respondents without direct experience, 3/15 (20%) were aware, 11/15 (73%) were unaware, and 1/15 (7%) did not answer. None of the respondents with direct reuse experience reported having applied the specification (Fig. 5).

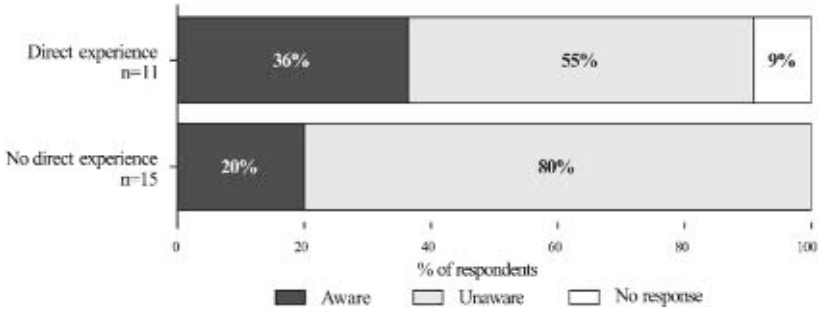


Fig. 5. Awareness of CEN/TS 1090–201 among respondents

4.4 Drivers and Prospects for Wider Adoption

Because the questions were open-ended and optional, responses were analysed thematically rather than as mutually exclusive quantitative categories. Among experienced respondents, the reported motivations were predominantly pragmatic: the availability of unused or stored material, client requests, expected cost savings, and the perceived durability of properly preserved steel. In some cases, reuse arose from components left unused after the abandonment of the original project; in others, clients already controlled stocks of beams or dismantled structures and requested their adaptation. None of the valid responses from experienced respondents identified environmental or sustainability concerns as the principal driver.

A different pattern emerged among respondents without direct experience. Their answers associated possible future adoption mainly with reduced environmental impact, lower energy consumption, resource conservation, and demand from clients seeking more sustainable materials. Environmental considerations therefore dominated the anticipated motivations for reuse, whereas they were absent from the accounts of completed projects.

The documented cases also indicate that reuse was generally initiated by the client, particularly when the client already owned the available material. Steel fabrication workshops mainly acted as technical executors, adapting the components to the requirements of the new project rather than actively promoting their reuse. The comparison thus reveals a clear motivational gap: reuse is commonly imagined as an environmentally driven practice, but the documented processes were initiated primarily by material availability and economic opportunity.

Beyond the motivations underlying individual projects, respondents were asked whether reuse could be extended beyond isolated or project-specific cases. Among respondents with direct experience, 4/11 (36%) considered wider application feasible under certain conditions, 3/11 (27%) excluded this possibility, 2/11 (18%) were uncertain, and 2/11 (18%) did not answer. The conditions identified by experienced respondents were pragmatic and operational in nature: reuse of structural elements without additional processing; greater standardisation of adopted profiles and element dimensions; availability of original documentation, certificates, and testing records; "understanding whether adaptation to the new project is actually worthwhile"; avoiding the need to reprocess the component; greater awareness of the possibility of reuse.

Among respondents without direct experience, 7/15 (47%) considered reuse applicable only in specific cases and 8/15 (53%) regarded it as difficult to apply. None considered the practice easily generalisable; nevertheless, 9/15 (60%) stated that they would consider reuse in the future (Fig. 6).

To complement this assessment of future applicability, respondents without direct experience were also asked whether reuse had previously entered their company's decision-making process. Of the 15 respondents, 5/15 (33%) had considered reuse at least preliminarily, whereas 10/15 (67%) had not. Seven of the ten respondents who answered negatively provided an explanation. Of these, 2/7 (29%) referred to their limited involvement in project decision-making, since they worked on client commissions or followed designs prepared by external engineers; 2/7 (29%) referred to certification and documentation issues; and 3/7 (43%) stated that reuse had never been considered, evaluated, or known as a possible option.

These responses suggest that steel fabrication workshops generally react to decisions made by clients and designers rather than initiating reuse processes themselves. Particularly relevant is that, in three cases, reuse had not entered the company's decision-making process at all, including one respondent who was unaware that structural steel reuse was possible.

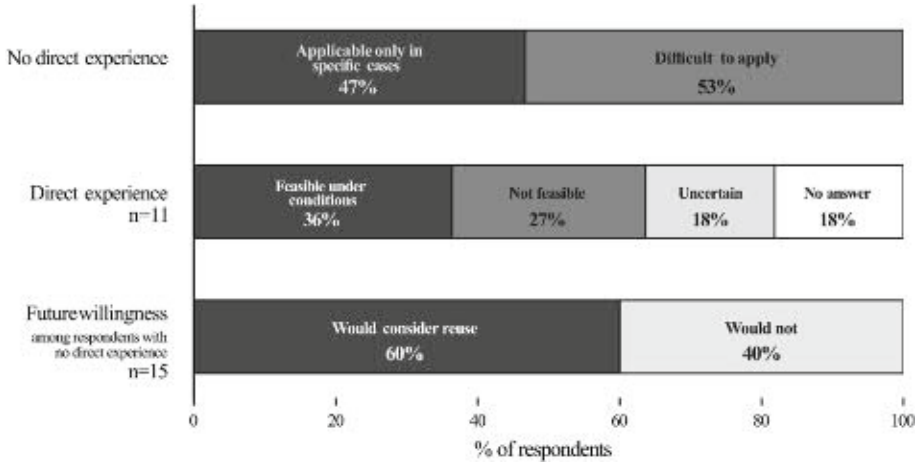


Fig. 6. Prospects for wider adoption of structural steel reuse and willingness to consider reuse among respondents without direct experience. Percentages may not total 100% due to rounding.

5 Discussion

The principal finding of this study is the documentation of structural steel reuse practices in Italy. Among the 26 respondents, 10 steel fabrication workshops and 1 construction company reported direct reuse experience. These practices appear sporadic, local, and largely dependent on contingent opportunities rather than on a structured market. Their geographical distribution suggests that reuse is not confined to a specific area of the country, although material flows were predominantly regional.

The results also indicate, within the Italian context, a discrepancy similar to that identified by Dunant et al. [5] between perceived barriers and those reported through direct experience. Respondents without direct experience more frequently anticipated higher costs and regarded the absence of CE marking as a significant obstacle, whereas respondents with experience rarely reported either issue as decisive. This suggests that some barriers may arise from professional perceptions before being encountered in practice.

The documented cases generally identify the material owner or client as the main initiator of reuse. Projects typically originated from the availability of existing steel stocks combined with a request for their adaptation, while fabrication workshops mainly acted as technical executors rather than promoters. This configuration partially aligns with observations from the United Kingdom [6], although the Italian context appears less mature and more dependent on the prior availability of material.

A further divergence concerns motivations. Respondents without direct experience associated reuse mainly with environmental sustainability, whereas experienced respondents referred primarily to material availability, client requests, and economic opportunity. This misalignment has practical implications: environmental arguments alone may

be insufficient to engage the actors directly involved in implementation. Measures supporting material availability, local circulation, documentation, and technical verification may therefore be more effective.

The UNI CEN/TS 1090–201 specification remains largely absent from current practice. None of the respondents with direct reuse experience reported having applied it, while only 7/26 respondents (27%) declared any awareness of its existence. Its limited diffusion may partly reflect its recent publication in 2024. The reported projects instead relied on case-specific combinations of laboratory testing, structural calculations, inspection certificates, and available original documentation. Wider dissemination through professional associations, technical guidance, and training could support its future application.

The study nevertheless presents several limitations. The sample is small and not statistically representative, geographical coverage is incomplete, and the analysis focuses mainly on fabrication workshops rather than on the entire supply chain. The low response rate also creates a risk of self-selection and non-response bias, potentially overrepresenting companies already interested in or familiar with reuse. The findings should therefore be interpreted as exploratory: they document the existence and operational characteristics of structural steel reuse practices in Italy rather than their national prevalence.

6 Conclusions

This study documents contemporary structural steel reuse practices in Italy and provides exploratory evidence of how they are currently implemented and perceived. Three main findings emerge: (i) structural steel reuse exists as a sporadic but recurrent practice, geographically distributed across the country and characterised by predominantly local material flows; (ii) respondents without direct experience generally expressed more negative expectations than those with experience, particularly regarding economic implications and the absence of CE marking; and (iii) the documented processes were generally initiated by clients or material owners, while the main drivers were material availability and economic opportunity rather than environmental considerations.

Future research should extend the investigation to other actors within the supply chain, including designers, demolition contractors, stockholders, and public and private clients, through semi-structured qualitative interviews. Replication of the study in other European contexts would also help establish a comparative framework.

A further element likely to influence this development is the increasing regulatory emphasis on life-cycle-based sustainability assessment. The new Italian Minimum Environmental Criteria for buildings include specific provisions for Life Cycle Assessment studies within the design documentation of public works [7]. Within this framework, structural steel reuse may contribute to reducing the embodied environmental impacts of new construction and could therefore acquire growing relevance. Nevertheless, wider adoption will also depend on material availability, adequate documentation, reliable verification procedures, and clearer allocation of responsibilities. The practices documented in this study may thus find a more favourable regulatory context, provided that the gap between perceived and experienced barriers is progressively reduced.

Acknowledgments. This publication is part of the PNRR-NGEU project, funded by the Italian Ministry of University and Research (MUR) through Ministerial Decree 118/2023.

References

1. Gorgolewski M (2018) Resource salvation: The architecture of reuse. Wiley, Hoboken. https://doi.org/10.1002/9781118928806
2. European Commission (2019) The European Green Deal. COM(2019) 640 final, Brussels
3. Bartsch H et al (2025) Guidance on establishing European rules for the design of reclaimed steel components for reuse. Publications Office of the European Union, Luxembourg
4. CEN (2024) CEN/TS 1090–201:2024, execution of steel structures and aluminium structures—reuse of structural steel. European Committee for Standardization, Brussels
5. Dunant CF, Drewniok MP, Sansom M, Corbey S, Allwood JM, Cullen JM (2017) Real and perceived barriers to steel reuse across the UK construction value chain. Resour Conserv Recycl 126:118–131. https://doi.org/10.1016/j.resconrec.2017.07.036
6. The Alliance for Sustainable Building Products DISRUPT 2 Steel Reuse Project—Toolkit. https://asbp.org.uk/toolkit/disrupt-2-steel-reuse-project-toolkit. last accessed 26 February 2026
7. Ministero dell'Ambiente e della Sicurezza Energetica (2025) Decreto 24 novembre 2025: Adozione dei criteri ambientali minimi per l'affidamento di servizi di progettazione e affidamento di lavori per interventi edilizi Serie Generale 281, 3 dicembre 2025. Gazzetta Ufficiale della Repubblica Italiana

Design and LCA Assessment of a Hospital Building with a CFST (Concrete-Filled Steel Tubes) Structural System

Marco Dal Ben, Edoardo Runcio(✉), and Giuliana Somma

University of Udine, Udine, UD 33100, Italy
edoardo.runcio@uniud.it

Abstract. The construction industry is one of the most environmentally impactful, with carbon dioxide emissions accounting for nearly 39% of global emissions and extremely high consumption of natural resources, including water and aggregates. It is crucial to identify solutions not only for finishing products but also for structural solutions, initiating a transition from legacy techniques to new, more environmentally friendly construction methods. Three main strategies are available to reduce concrete-related emissions: reducing the clinker content in cement, reducing the cement content in concrete, and reducing the size of structural elements and consequently limiting the volume of material used. This study explores the last of these three strategies in particular, evaluating the possibility of replacing simple reinforced concrete with CFST jacketed column technology, composed of an external metal jacket and a concrete core. This solution offers advantages not only in terms of mechanical performance, ensuring greater resistance for the same cross-section size, but also in terms of the CO2 released into the atmosphere. An LCA analysis compares the emissions of two equal size buildings, one constructed with reinforced concrete walls and the other with a CFST frame. The aim of this research is to demonstrate the effectiveness and potential of this construction method, which is often neglected by designers, proposing it as a valid alternative to traditional solutions for reducing the CO2 global emissions.

Keywords: CFST · LCA · Design · Concrete · Steel

1 Introduction

The construction sector is a major contributor to global environmental impact, accounting for approximately 39% of global CO_2 emissions and requiring substantial consumption of natural resources. In this context, the development of more sustainable structural solutions has be-come essential. These solutions should comply with circular economy principles and reduce the environmental footprint of buildings throughout their entire life cycle [1].

Traditional reinforced concrete construction presents significant limitations, mainly related to the high cement content and the often considerable dimensions of structural members. The principal mitigation strategies include reducing the clinker-to-cement

© The Author(s), under exclusive license to Springer Nature Switzerland AG 2026
R. Zanon et al. (Eds.): CTA 2026, LNCE 942, pp. 58–66, 2026.
https://doi.org/10.1007/978-3-032-39505-4_6

ratio, lowering the cement content in concrete mixtures, and optimizing structural cross-sections. Among the emerging alternatives, the Concrete-Filled Steel Tube (CFST) system represents a promising solution due to the synergistic interaction between the external steel tube and the concrete core. Although widely adopted in several countries, this technology remains relatively underexplored within the Italian construction sector.

This study investigates the third of the aforementioned mitigation strategies by evaluating the replacement of reinforced concrete elements with CFST columns. A Life Cycle Assessment (LCA) is performed to compare the CO_2 emissions of two structurally equivalent buildings: one incorporating reinforced concrete walls and the other adopting a CFST frame. Both structures are designed with identical dimensions and performance requirements in accordance with European technical standards. The study aims to demonstrate the potential of CFST technology as a viable low-emission alternative, with particular emphasis on the contribution of material recovery at end-of-life.

The LCA boundary includes the vertical structural elements of the ground floor, the intermediate slab, and the beams of the corresponding floor system. Foundations, the ground-floor slab, and the roof are excluded from the analysis, as these components are identical in both configurations and therefore do not affect the comparative assessment.

2 Methodology

2.1 Case Study

The case study concerns a pavilion of a hospital building located in Azzano Decimo, Pordenone, Italy. This occupancy category is characterized by high variable loads ($qk = 5{,}0\ kN/m^2$) and stringent serviceability requirements to ensure adequate user comfort, in accordance with NTC 2018. The structural block under investigation has a rectangular plan approximately 40 m × 14 m in size and a total height of 8.30 m.

Numerical modelling and Structural Verification

A three-dimensional finite element model (FEM) was developed using SAP2000. For conservative purposes, only the superstructure above ground level was modelled, assuming fully fixed base conditions. This assumption neglects soil–structure interaction, thereby reducing the fundamental period of the structure and maximizing the design seismic actions (Fig. 1).

The CFST columns and composite steel–concrete beams were modelled as frame elements. Composite cross-sections were defined using the Section Designer tool, assuming full shear interaction between the constituent materials (Figs. 2 and 3).

For the beams, the effective section includes the steel profile and the collaborating concrete slab (55 mm thickness), while the contribution of the corrugated steel deck was conservatively neglected. The modelling approach was validated analytically. Column behaviour was verified by comparing the free-end displacement obtained from the numerical model with the exact cantilever solution. Beam behaviour was assessed by verifying the consistency of the flexural moments of inertia with those derived from the transformed-section method.

To simulate cracked-section behaviour under seismic conditions (NTC 2018, §7.2.6) [2], the flexural and shear stiffnesses of the concrete component were reduced by 30% for

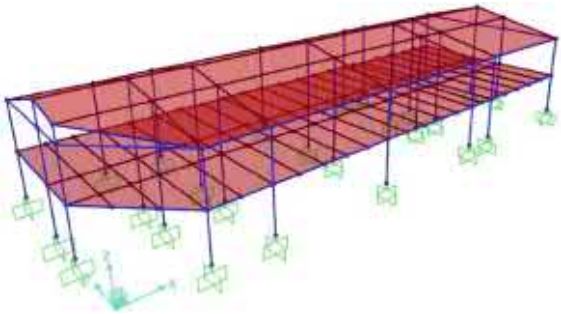


Fig. 1 FEM Model of the above-ground structure developed in SAP2000

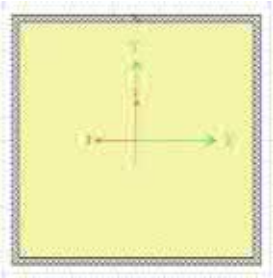


Fig. 2. CFST column cross-section modelled using SAP2000 Section Designer

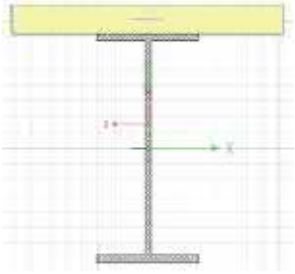


Fig. 3. Composite beam cross-section modelled using SAP2000 Section Designer

the columns and by 50% for the composite beams. Seismic actions at the Life Safety Limit State (SLV) were evaluated through linear dynamic analysis using a response spectrum, adopting the Complete Quadratic Combination (CQC) rule and four simplified seismic load combinations along the principal X and Y directions.

Design and safety verifications were performed in accordance with NTC 2018 and Eurocode 3 [3] and Eurocode 4 [4]. Within the scope of this comparative study, the governing design mechanisms are identified as follows: for the CFST columns, the governing verification is bi-axial bending under seismic combinations (SLV); for the main composite beams, lateral–torsional buckling governs at the Ultimate Limit State (SLU); for the secondary framing, de-flection checks govern at the Serviceability Limit State (SLE), owing to the more restrictive limits associated with hospital occupancy. The design of structural connections is governed by the tensile resistance of the bolted assemblies [2–4].

2.2 Reinforced Concrete Shear Wall Building

The second structural solution consists of a load-bearing system composed of 25 cm thick reinforced concrete shear walls (Fig. 4), with a structural layout identical to that of the previous-ly described building. In this configuration, the floor slabs were constructed

using prefabricated trussed slabs of the "Predalles" type, with a total thickness of 25 cm. The foundations and roof slab are identical to those adopted in the reference building.

The numerical model was developed using Sismicad (Concrete S.r.l.). The walls were mod-elled as shell elements with a maximum mesh size of 30 cm and assumed to be fully fixed at the base, consistent with wall-type structural systems. The intermediate and roof slabs were modelled as surface loads with rigid and membrane in-plane behaviour, respectively, in accordance with NTC 2018 [11]. An in-plane stiffness equivalent to that of OSB sheathing was adopted.

To account for cracking effects in reinforced concrete elements under seismic combinations, a reduced elastic modulus equal to 70% of the uncracked value was adopted for the concrete walls.

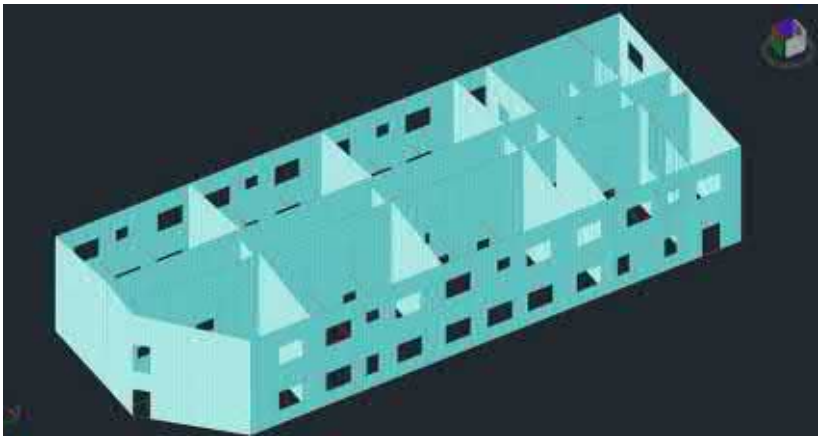


Fig. 4 View of the numerical model developed in Sismicad

Structural verifications were performed in accordance with the current Italian building code, following the design provisions of Chapters 4 and 7 of D.M. 17/01/2018.

2.3 Life Cycle Assessment (LCA) and GWP Calculation

The environmental impact assessment follows the guidelines of the Royal Institution of Chartered Surveyors (RICS) and the principles of Life Cycle Assessment (LCA) methodology [5–7]. The functional unit is defined as 1 m^2 of gross floor area of the intermediate slab, ensuring comparability between the two structural configurations, which have identical geometry and intended use.

Embodied carbon, quantified through the Global Warming Potential (GWP) indicator and expressed in $kgCO_2e$, was calculated for each life-cycle module: product and construction stages (A1–A5), component replacement (B4), end-of-life (C1–C4), and benefits beyond the system boundary (D). The embodied carbon (EC) associated with each module was calculated according to Eq. (1):

$$EC = \sum_i (Q_i \cdot ECF_i) \tag{1}$$

where Qi is the quantity of the i-th material (kg) and ECFi is the corresponding carbon emission factor ($kgCO_2e/kg$), derived from established databases reported in the scientific literature [8]. The contribution of each module was normalised with respect to the gross floor area of the intermediate slab ($kgCO_2e/m^2$), enabling a detailed stage-by-stage comparison of environmental performance. The normalised values associated with all modules were subsequently summed to determine the total emissions for each investigated scenario.

To provide a comprehensive assessment covering the entire life cycle — from material production to end-of-life, including potential recycling benefits and emissions associated with major maintenance interventions — the system boundary was divided into three progressive scenarios:

(i) Cradle-to-Grave (A + C): a 50-year assessment including production, construction, and end-of-life stages, excluding extraordinary maintenance.
(ii) Circular Economy (A + C + D): includes material recycling credits (Module D) within the same 50-year assessment period.
(iii) Extended Time Horizon (A + B4 + C + D): a 100-year assessment that additionally includes component replacement (B4), enabling evaluation of the long-term environmental impact associated with extraordinary maintenance.

3 Results and Discussion

3.1 Comparative Analysis of Material Quantities

To enable an objective comparison, Table 1 reports the total quantities Q (in tonnes, t) of concrete and steel for each structural element type. This quantitative assessment provides the basis for interpreting the LCA results, as it highlights the significant difference in material intensity between the two structural systems. For brevity, the item "Steel" includes structural steel profiles, reinforcing bars, corrugated steel decking, shear studs, and connection steel elements at structural joints. The table also reports the percentage variation ΔQ in material usage for the CFST solution relative to the shear wall solution.

The adoption of the CFST solution results in an approximately 80% reduction in concrete volume relative to the shear wall building. This decrease is almost entirely attributable to the vertical structural elements. Conversely, total steel usage increases by approximately 57% in the CFST configuration, owing to the steel composition of the beam elements.

When the vertical elements are considered independently, the CFST column solution achieves a 45% reduction in steel quantity compared with the reinforced concrete wall system.

3.2 LCA Results

Table 2 reports the normalized embodied carbon values, expressed in $kgCO_2e/m^2$, for each life-cycle module.

These values were subsequently summed to obtain the results for the three scenarios considered (Fig. 5). A progressive reduction in environmental impact, expressed in CO_2-equivalent terms, is observed for the structural configuration with CFST columns when moving from scenario (i) to scenario (iii).

Table 1. Total material quantities by structural element type

Structural element	Material	CFST solution Q [t]	Shear wall solution Q [t]	ΔQ [%]
Vertical elements	Concrete	15,42	343,47	−95,5
	Steel	9,55	17,42	−45,2
Beams	Concrete	/	71,14	/
	Steel	34,85	5,73	+508,2
Slab	Concrete	108,86	185,95	−41,5
	Steel	8,84	10,82	−18,3
Total	Concrete	125,28	600,56	−79,1
	Steel	53,24	33,97	+56,7

Table 2. Normalized embodied carbon by LCA module [$kgCO_2e/m^2$]

LCA module	Description	CFST solution	Shear wall solution
A1-A3	Material production	201,2	181,5
A4-A5	Transport and construction	5,0	17,1
C1-C4	End-of-life	5,1	11,0
D	Beyond system boundary benefits/loads	−45,2	−3,8
B4	Replacement of building components	0,8	31,0

3.3 Discussion of the Results

The bill of quantities (Table 1) highlights a marked divergence between the two structural con-figurations. Although still relatively uncommon in the Italian construction sector, the CFST solution offers significant technological advantages: passive confinement of the concrete core enhances strength and ductility, enables spatial rationalization, and eliminates the need for conventional formwork [9, 10]. These advantages result in a substantial reduction in material quantities, corresponding to an 80% decrease in concrete volume relative to the reinforced-concrete shear-wall solution.

This reduction is accompanied by a 56% increase in total steel mass, predominantly concentrated in the beam system. These quantitative differences form the basis for interpreting the environmental results across the three scenarios examined.

Scenario (i) – "Cradle-to-Grave" (Stages A + C)
Under Scenario (i), the overall impacts of the two solutions are nearly equivalent (211,4 vs. 209,6 $kgCO_2e/m^2$). The material production stage (Modules A1–A3) dominates total emissions, accounting for 95% of the impact in the CFST solution and 87% in the reinforced-concrete shear-wall system. The construction stages (A4–A5) and end-of-life stages (C1–C4) contribute only marginally to the overall balance (Table 2).

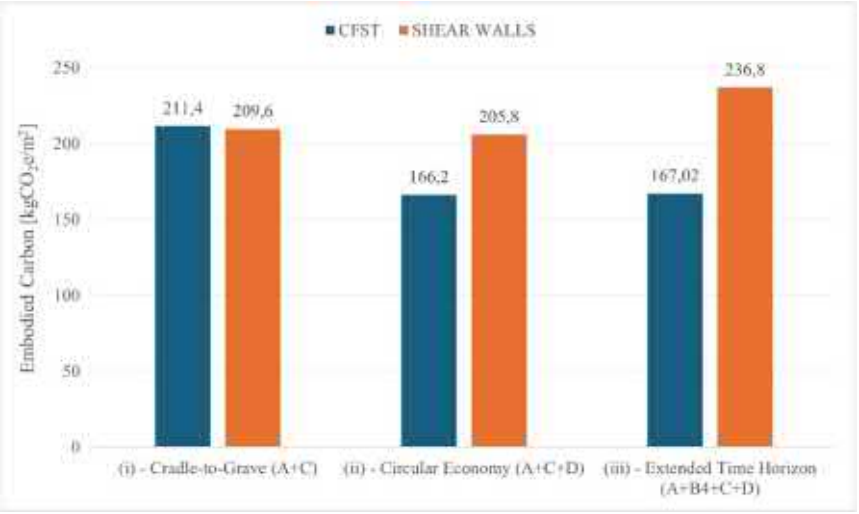


Fig. 5 Comparison of Embodied Carbon [kgCO2/m2] between the CFST solution and the reinforced concrete wall solution across the three analysis scenarios: (i) Cradle-to-grave, (ii) Circular Economy, (iii) Extended Time Horizon

The high emission intensity associated with structural steel production (Modules A1–A3), an energy-intensive industrial process, offsets the benefits associated with the reduced concrete quantities. Consequently, the greater steel content of the CFST configuration neutralizes the expected emission reductions during the early life-cycle stages, resulting in an overall environmental performance comparable to that of the alternative solution.

Scenario (ii) – "Circular Economy" (Stages A + C + D)

When benefits and loads beyond the system boundary are included (Scenario (ii), Stages A + C + D), the CFST solution demonstrates superior environmental performance, reducing embodied carbon by 19% relative to the reinforced-concrete shear-wall system (166,2 vs. 205,8 $kgCO_2e/m^2$). The environmental credit associated with the end-of-life stage amounts to 45,2 $kgCO_2e/m^2$ for the CFST system and 3,8 $kgCO_2e/m^2$ for the conventional solution.

The high recyclability of the metallic components — namely the steel tube of the columns and the steel profiles of the beams — generates a substantial end-of-life environmental credit, sufficient to offset the high emission burden associated with the production stage. By contrast, the reinforced-concrete shear-wall solution is limited to crushing and downcycling processes, which provide only marginal benefits to the overall balance. In this scenario, the greater steel mass of the CFST configuration translates into a net environmental advantage.

Scenario (iii) – "Extended Time Horizon" (Stages A + B4 + C + D)

In Scenario (iii), the extension of the reference service life to 100 years and the inclusion of replacement interventions (Module B4) further amplify the divergence between the

two alter-natives. The CFST system maintains a substantially unchanged emission level (167,0 $kgCO_2e/m^2$), whereas the reinforced-concrete shear-wall solution exhibits a significant in-crease due to extraordinary maintenance requirements (236,8 $kgCO_2e/m^2$). The resulting difference in embodied carbon between the two structural systems reaches 29%.

Extraordinary maintenance of the composite system is limited to renewal of the intumescent coating, which represents a low emission burden (0,8 $kgCO_2e/m^2$). Conversely, the reinforced-concrete solution requires a considerably more impactful intervention — namely the removal and reinstatement of the deteriorated concrete cover — to address degradation phenomena such as carbonation-induced corrosion. The associated emission burden (31,0 $kgCO_2e/m^2$) becomes dominant over the long term, establishing the CFST solution as the most sustainable option within an extended life-cycle framework.

4 Conclusions

This study demonstrates that the adoption of alternative structural technologies, particularly CFST columns, represents an effective strategy for reducing the environmental impact of the construction sector and overcoming the limitations associated with conventional reinforced-concrete shear-wall systems.

The life-cycle analysis indicates that the environmental performance of a building cannot be assessed solely on the basis of the construction phase. In the short term, the two solutions ex-hibit comparable emission levels, as the reduction in concrete volume is offset by the higher emission intensity associated with structural steel production. The environmental advantage of the composite steel-concrete solution becomes evident only over an extended time horizon.

Within a circular-economy framework, the high recyclability of metallic components shifts the overall balance in favour of the composite solution. Furthermore, the comparatively low emission burden associated with the extraordinary maintenance of CFST columns — substantially lower than that required for reinforced-concrete structures affected by carbonation-induced degradation — further consolidates its long-term environmental advantage.

Overall, the composite steel-concrete configuration combines high mechanical performance, spatial efficiency, and rapid construction with a reduced overall environmental impact. These findings support a reassessment of current structural design paradigms: the selection of a structural system should move beyond established practice and adopt a holistic approach focused on durability, deconstruction, and material-cycle closure, which are essential conditions for achieving a meaningful and measurable reduction in environmental impact within the construction sector.

References

1. Runcio E, Somma G (2025) Comparison in terms of CO2 footprint between RC and CLT buildings. In: Proceedings of SEMC 2025 the ninth international conference on structural engineering, mechanics and computation. ISBN: 978-1-041-15001-5, 1-3 September, 2025, Cape Town (South Africa)

2. Ministero delle Infrastrutture e dei Trasporti (2018) Norme Tecniche per le Costruzioni (NTC 2018). Consiglio Superiore dei Lavori Pubblici
3. Comitato Europeo di Normazione (CEN) (2005) Eurocodice 3: progettazione delle strutture di acciaio – EN 1993. CEN Publications
4. Comitato Europeo di Normazione (CEN) (2004) Eurocodice 4: progettazione di strutture com-poste acciaio-calcestruzzo – EN 1994. CEN Publications
5. UNI (2006) EN ISO 14040: Gestione ambientale – Valutazione del ciclo di vita – Principi e quadro di riferimento. UNI, Ginevra
6. UNI (2006) EN ISO 14044: Gestione ambientale – Valutazione del ciclo di vita – Principi e quadro di riferimento. UNI, Ginevra
7. UNI (2011) EN ISO 15978: Sostenibilità delle costruzioni – Valutazione della prestazione ambientale degli edifici – Metodo di calcolo. UNI
8. Gibbons OP, Orr JJ, Archer-Jones C, Arnold W, Green D (2020) A brief guide to Calculat-ing embodied carbon. The institution of structural engineers
9. Somma G, Vit M (2023) Evaluation of the bond stress transfer mechanism in CFSTs. Int J Civ Eng 21:363–378
10. Tommaso D, Giuliana S, Van Engelen N (2025) Investigation of bond-slip behavior in concrete-filled steel tubes. In: Proceedings of SEMC 2025 the ninth inter-national conference on structural engineering, mechanics and computation, ISBN: 978–1–041-15001-5, 1–3 September, 2025, Cape Town (South Africa)
11. Nuove norme tecniche per le costruzioni D.M. 17 Jan. 2018

A Comparative Life Cycle Assessment of Load-Bearing Structural Systems for Multi-Storey Buildings: Steel vs. Reinforced Concrete

Marta Maria Sesana[1(✉)], Paolo Dell'Oro[1], Marianna Sgarbanti[2], and Simona Martelli[3]

[1] Department of Civil, Environmental, Architectural Engineering and Mathematics, Università degli Studi di Brescia, Brescia 25123, Italy
marta.sesana@unibs.it
[2] ATI Project, Pisa 56124, Italy
[3] Fondazione Promozione Acciaio, Milan 20122, Italy

Abstract. The construction sector plays a pivotal role in global decarbonization efforts, requiring robust methodologies to assess and reduce environmental impacts across the building life cycle. In this context, this study presents a comparative Life Cycle Assessment (LCA) of load-bearing structural systems for multi-storey buildings, focusing on steel and reinforced concrete solutions. The analysis is based on a real case study: a 14-storey building located in Pisa, Italy, ensuring identical boundary conditions in terms of geometry, function, and location. Adopting a cradle-to-grave approach in accordance with EN 15978 and ISO 14040–44 standards, the study evaluates embodied carbon and Global Warming Potential (GWP) over a 50-year reference period. The methodology analysis focuses on the preliminary parametric assessments to testify the critical role of early-stage LCA in guiding design decisions and identifying environmental hotspots. Results show that the steel structural solution achieves a significantly lower carbon footprint compared to reinforced concrete, with reductions in CO_2 emissions, mainly due to lower material intensity and higher recyclability. The findings highlight the importance of material selection and circularity strategies in achieving low-carbon buildings. This research provides practical insights for designers, stakeholders, and policymakers aiming to support sustainable construction and accelerate the transition toward a decarbonized built environment.

Keywords: Life Cycle Assessment · comparative analysis · environmental impacts · steel building · recyclable material

1 Introduction

The construction sector plays a central role in the transition towards a decarbonized built environment. Buildings are responsible for a significant share of global energy consumption, greenhouse gas emissions, and resource use, not only during the operational phase but also through the production, transport, construction, maintenance, and

© The Author(s), under exclusive license to Springer Nature Switzerland AG 2026
R. Zanon et al. (Eds.): CTA 2026, LNCE 942, pp. 67–78, 2026.
https://doi.org/10.1007/978-3-032-39505-4_7

end-of-life management of construction materials and systems [1, 2]. While energy efficiency strategies have traditionally focused on reducing operational carbon, the growing relevance of embodied carbon is shifting attention towards the environmental impact of materials and construction technologies across the whole building life cycle [3–5].

In this context, Life Cycle Assessment (LCA) has become one of the most established methodologies for quantifying and comparing the environmental performance of buildings, construction products, and technical solutions [6]. Regulated by the ISO 14040–44 standards [7, 8], LCA allows the systematic evaluation of environmental impacts from raw material extraction to end-of-life scenarios. At the building scale, EN 15978 [9] provides a structured framework for assessing environmental performance across life-cycle modules, supporting the comparison of design alternatives.

Among the different environmental indicators considered in LCA studies, Global Warming Potential (GWP) has gained particular relevance due to its direct connection with climate change mitigation policies and whole-life carbon assessment [10–12]. GWP expresses the contribution of greenhouse gas emissions in terms of carbon dioxide equivalent and is increasingly adopted as a key metric for evaluating the carbon footprint of buildings [13–15]. Its relevance has been further strengthened by the revised Energy Performance of Buildings Directive, Directive (EU) 2024/1275 [16], which introduced the requirement for Member States to ensure that the life-cycle GWP of new buildings is calculated and disclosed in the Energy Performance Certificate (EPC) [17]. To implement this requirement, Commission Delegated Regulation (EU) 2026/52 [18] established the Union framework for the national calculation of life-cycle GWP, defining a harmonized methodological basis for the assessment, reporting, data hierarchy, life-cycle stages, and building elements to be considered. Within this regulatory framework, GWP is reported in $kgCO_2eq/m^2$ over a 50-year reference study period, supporting the comparability of results and reinforcing the role of LCA as a design-support tool from the early project stages.

Load-bearing structural systems are among the most influential components in determining embodied carbon, particularly in multi-storey buildings [19]. The choice between different structural materials, such as steel and reinforced concrete, can significantly affect the quantity of products used, the construction process, the design of foundations, and the potential for reuse, recycling, and recovery at the end of life [20]. For this reason, structural design should not be evaluated only in terms of mechanical performance, cost, and construction feasibility, but also through quantified environmental indicators able to support informed and evidence-based decisions.

Steel and reinforced concrete represent two of the most widely adopted structural solutions for multi-storey buildings [21, 22]. Reinforced concrete is traditionally associated with high material availability, massiveness, and consolidated construction practices. Steel structures, on the other hand, are characterized by high strength-to-weight ratio, industrialized production, dry and off-site construction processes, adaptability, and high recyclability. These characteristics make steel particularly relevant in the context of circular construction, where material efficiency, design for disassembly, reuse, and recycling are key strategies for reducing environmental impacts throughout the building life cycle.

Despite the growing number of studies applying LCA to building structures [23–26], comparisons between alternative structural systems are often affected by different assumptions, geometries, locations, functions, or data sources. This limits the possibility of deriving robust and project-specific conclusions. Therefore, comparative assessments based on real case studies and equivalent boundary conditions are needed to better understand how structural choices influence embodied carbon and to provide practical guidance for designers and stakeholders.

This paper presents a comparative LCA of two alternative load-bearing structural systems applied to the same multi-storey building case study located in Pisa, Italy. The analysis compares a steel structural solution with a reinforced concrete alternative, maintaining the same architectural configuration, location, function, and non-structural elements. The study focuses specifically on GWP as the main impact indicator, with the aim of assessing the influence of the structural system on the embodied carbon of the building.

The objective of the paper is twofold. First, it aims to quantify and compare the GWP of steel and reinforced concrete load-bearing structural systems under equivalent design conditions. Second, it aims to demonstrate the potential of LCA as an early-stage and detailed design-support methodology for guiding structural material selection in multi-storey buildings. The results are intended to support designers, engineers, construction stakeholders, and policymakers in the transition towards low-carbon and circular building practices.

2 Case Study

The case study selected for the comparative Life Cycle Assessment is the Torre Nord building, located within the wider Parco delle Torri development in the Cisanello district of Pisa, Italy. The building is a 14-storey tower with an overall height of approximately 50 m and a gross floor area of 5,365 m^2. The project concerns the refurbishment and completion of an existing unfinished building, originally designed with a steel load-bearing structure. The refurbished building is mainly intended for office use, while the ground floor includes commercial and food-service areas. From an architectural perspective, the tower is characterized by a compact and vertically organized layout. The office floors are designed around the central reinforced concrete core, which presents stairs, elevators, and the main vertical service spaces. The core also forms part of the lateral load-resisting system.

The present study compares two hypothetical new-construction scenarios applied to the same building configuration, in order to assess the environmental implications of different structural choices under equivalent design conditions. The two scenarios considered in the study are: Scenario A, based on a steel load-bearing structure, and Scenario B, based on a reinforced concrete load-bearing structure. Both scenarios are designed to provide functionally equivalent structural solutions for the same multi-storey building. The comparison is focused on the load-bearing system and related structural components, while all non-structural elements are kept identical. The same building plan, floor-to-floor organization, usable areas, façade configuration, and functional layout were adopted in both alternatives, so that the comparison focuses on the environmental effects associated with the load-bearing structural system.

2.1 Structural Scenarios

Scenario A considers the new construction of a steel load-bearing structure that replicates the structural configuration of the existing building. The vertical structural system consists of CHS columns in S355 steel, with variable sections according to the building height. The horizontal structural system is composed of steel beams, including HE, IPE and UPN profiles, and composite floor slabs. The slabs are made of galvanized corrugated steel sheets with a concrete topping and electrowelded reinforcement mesh.

The steel structural system is combined with a reinforced concrete core, with stairs and elevators, and reinforced concrete foundation elements. The foundation system includes a reinforced concrete raft and 37 foundation piles. This scenario represents a lightweight and industrialized structural solution, characterized by dry construction processes, high prefabrication potential, and high recyclability of steel components.

Scenario B considers the new construction of an equivalent reinforced concrete load-bearing structure. In this scenario, the steel columns, steel beams, and composite slabs of Scenario A are replaced by cast-in-place reinforced concrete elements. The vertical structural system consists of reinforced concrete columns with variable diameters. The horizontal structural system consists of 240 mm thick solid reinforced concrete slabs, also designed to ensure continuity in the balcony areas.

Table 1. Main characteristics of the two structural scenarios considered in the comparative LCA.

Component	Scenario A	Scenario B
Vertical structure	CHS S355 steel columns	Circular reinforced concrete columns
Column dimensions	From 406.4 x 20 mm to 273 x 6.3 mm	From Ø500 mm to Ø350 mm
Horizontal structure	Steel beams and composite slabs	Reinforced concrete beams/slabs
Slabs	Corrugated steel sheets with concrete topping and electrowelded mesh	240 mm solid reinforced concrete slabs
Core	Reinforced concrete core	Reinforced concrete core
Foundations	Reinforced concrete raft and 37 piles	Reinforced concrete raft and 46 piles
Main material	Structural steel and concrete topping	Reinforced concrete

Compared with Scenario A, the reinforced concrete solution requires a different foundation configuration due to the higher structural mass. The foundation system includes 46 piles, corresponding to 9 additional piles compared with the steel scenario, and an increased reinforcement ratio in the foundation raft. The average reinforcement ratio is assumed to be 300 kg/m^3 for columns and 125 kg/m^3 for slabs.

The two structural scenarios are summarized in Table 1.

3 LCA Methodology

The comparative assessment was developed according to the Life Cycle Assessment framework defined by ISO 14040–44. The methodological structure follows the main LCA phases: goal and scope definition, Life Cycle Inventory, Life Cycle Impact Assessment, and interpretation. In this study, the interpretation phase is presented together with the results in Sect. 4, in order to directly discuss the environmental meaning of the outcomes obtained for the two structural scenarios. The analysis focuses on Global Warming Potential (GWP), expressed in $kgCO_2eq$ and $kgCO_2eq/m^2$ of gross floor area, as the main indicator for climate-change mitigation and structural decision-making.

The workflow includes two levels of analysis: first, a preliminary assessment was performed with Carbon Designer 3D, integrated within One Click LCA, to compare the two alternatives during the early design stage; second, a detailed design-stage assessment was performed in One Click LCA using project-specific quantities derived from design documentation and BIM-based modelling. This combined workflow allows rapid early feedback and following refinement through more accurate data.

3.1 Goal and Scope

The goal of the study is to quantify and compare the GWP of two functionally equivalent load-bearing systems for the same multi-storey building. The functional unit is 1 m^2 of gross floor area (GFA), and results are expressed in $kgCO_2eq/m^2$ GFA. The reference study period is 50 years.

The system boundaries include the main embodied-carbon modules related to the structural systems: A1-A3 production, A4 transport to site, A5 construction and installation, and C1-C4 end of life. Operational energy and water use are excluded because the objective is to compare structural alternatives rather than operational performance. Building services, furniture, and external works are also excluded. Since both scenarios share the same architectural and functional conditions, the assessment isolates the contribution of the load-bearing structure and related components.

3.2 Life Cycle Inventory

The Life Cycle Inventory was developed using a combination of primary project data and environmental datasets available within the LCA software platform. Primary data were derived from the design documentation and project information of the Torre Nord case study, including structural configuration, material specifications, element dimensions, and quantities.

The preliminary inventory was developed through Carbon Designer 3D, using standardized input parameters related to the building geometry, location, number of storeys, function, and main construction systems. This phase allowed the two structural alternatives to be compared during the early design stage, when detailed quantities are not always fully available but design decisions can still significantly influence the final environmental performance.

The detailed inventory was developed using project-specific quantities obtained from the design-stage documentation and BIM-based modelling. The building model was

developed in Autodesk Revit and the relevant material quantities were transferred to One Click LCA through the dedicated workflow. The modelling process enabled the association of building elements and material quantities with environmental datasets, including Environmental Product Declarations and generic datasets available in the One Click LCA database.

For Module A4, transport impacts were calculated using the default transport scenarios available in One Click LCA for the selected material datasets. These scenarios consider road transportation by heavy-duty trucks over representative average distances between the production facility and the construction site. The same modelling criteria were applied to both structural alternatives; therefore, the differences in A4 impacts mainly reflect the different quantities and total masses of the transported materials.

The end-of-life stage was modelled through Modules C1–C4, including demolition or deconstruction activities, transport of waste materials, waste processing, and final disposal. The adopted end-of-life scenarios were based on the datasets and default assumptions associated with the selected materials in One Click LCA. Structural and reinforcement steel were assumed to be recycled and reused as materials, while concrete was assumed to be processed and used as energy source.

3.3 Impact Assessment

The Life Cycle Impact Assessment focuses on Global Warming Potential as the only impact category considered in the paper. GWP was selected because it represents the main indicator for evaluating the contribution of buildings and construction systems to climate change. It is expressed in kilograms of carbon dioxide equivalent and allows the different greenhouse gases emitted throughout the life cycle to be converted into a common metric.

The impact results are analyzed according to three complementary perspectives: total GWP of each structural scenario; GWP distribution across life-cycle modules; GWP contribution by structural element and material category.

This structure makes it possible to identify the main environmental hotspots of each scenario and to understand the drivers behind the differences between the steel and reinforced concrete solutions. The interpretation of the results also supports the discussion of material efficiency, structural configuration, and circularity potential as key aspects for reducing embodied carbon in multi-storey buildings.

4 Results and Interpretation

This section presents and interprets the results of the comparative Life Cycle Assessment conducted on the two structural scenarios. The interpretation follows the two levels of assessment described in the methodology: the preliminary early-stage assessment and the detailed design-stage assessment. The results are then discussed according to life-cycle modules, structural elements, and material categories, with the aim of identifying the main environmental hotspots and the drivers behind the differences between the two scenarios.

4.1 Preliminary Early-Stage Assessment

The preliminary assessment shows that Scenario A, corresponding to the steel structure, achieves a GWP of 453 $kgCO_2eq/m^2$ GFA, while Scenario B, corre-sponding to the reinforced concrete structure, reaches 555 $kgCO_2eq/m^2$ GFA. The reinforced concrete scenario therefore presents an increase of approximately 23% compared with the steel scenario (Fig. 1).

This result highlights the value of early-stage LCA for structural decision-making. Even when the design is not yet fully detailed, a preliminary assessment can identify the lower-carbon option and indicate the elements that most affect embodied carbon. In this case, the advantage of the steel scenario is mainly related to its lighter structural configuration, composite slabs, and reduced material intensity compared with the reinforced concrete alternative.

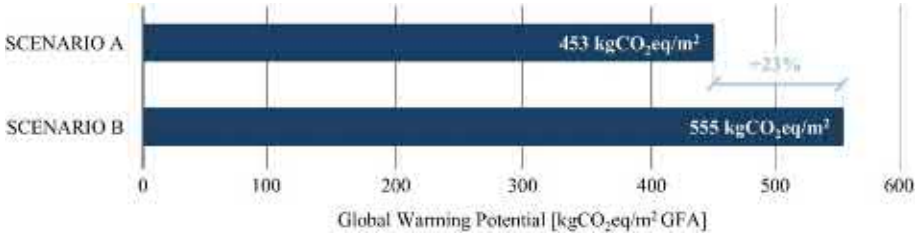


Fig. 1. GWP comparison of the preliminary early-stage assessment.

4.2 Detailed Design-Stage Assessment

The detailed design-stage assessment was performed using project-specific material quantities derived from the design documentation and BIM-based modelling. The quantities were implemented in One Click LCA in order to refine the results obtained during the preliminary phase and to quantify the GWP of the two scenarios with a higher level of detail.

The results of the detailed design-stage assessment are presented in Fig. 2 and confirm the trend observed in the preliminary assessment. Scenario A achieves a total GWP of 550 $kgCO_2eq/m^2$ GFA. Scenario B achieves a total GWP of 603 $kgCO_2eq/m^2$ GFA. The reinforced concrete scenario therefore remains more impactful than the steel scenario, although the relative difference is reduced compared with the preliminary assessment.

The reduction in the percentage difference between the two stages can be attributed to the refinement of material quantities and the inclusion of more specific design-stage information. Nevertheless, the results confirm that the structural system has a measurable influence on building-scale GWP and that the environmental advantage of the steel scenario is maintained when project-specific data are used.

4.3 Contribution by Life-Cycle Module and Structural Elements

The analysis by life-cycle module shows that the highest contribution to total GWP is associated with the production stage (A1-A3) for both scenarios (Fig. 3). This result is

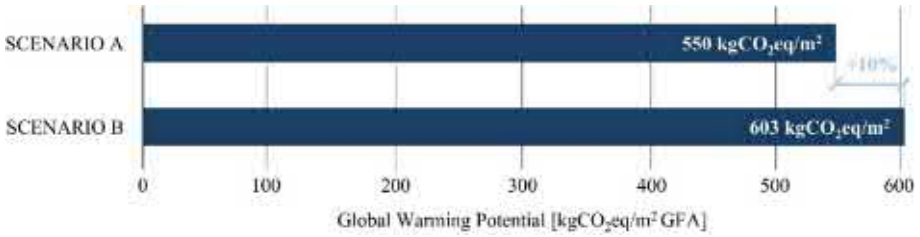


Fig. 2. GWP comparison of the detailed design-stage assessment.

consistent with the focus on embodied carbon and structural materials. In the steel scenario, relevant contributions are associated with structural steel profiles, reinforcement steel, corrugated sheets, and concrete components. In the reinforced concrete scenario, ready-mix concrete and reinforcement steel dominate the production-stage impact.

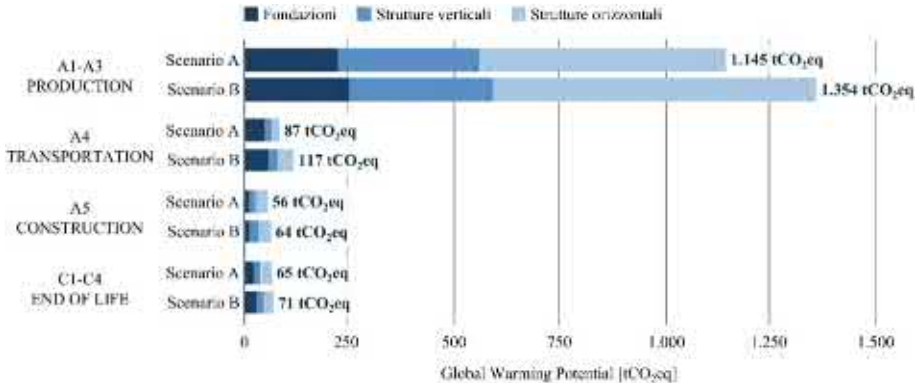


Fig. 3. GWP comparison by life-cycle module for Scenario A and Scenario B [tCO_2eq].

Transport (A4), construction and installation (A5), and end-of-life modules (C1-C4) contribute less than A1-A3 but remain relevant for the comparison because the two systems imply different material quantities, logistics, and construction processes. The steel scenario is associated with a higher level of prefabrication and dry assembly, while the reinforced concrete scenario requires larger quantities of cast-in-place materials.

The interpretation by structural element highlights foundations, vertical structures, and horizontal structures as the components most affected by the choice of structural system. Horizontal structures are particularly relevant: in Scenario B, 240 mm solid reinforced concrete slabs require significant concrete and reinforcement quantities, whereas Scenario A uses lighter composite slabs based on corrugated steel sheets and concrete topping.

Vertical structures also contribute to the difference. Scenario A uses CHS steel columns with variable sections, while Scenario B requires circular reinforced concrete columns with diameters from 500 mm to 350 mm. Foundations further increase the difference because the higher mass of the reinforced concrete scenario requires 46 piles

instead of 37 and a higher reinforcement ratio in the foundation raft. Overall, the lower GWP of the steel scenario is mainly linked to its lighter load-bearing configuration and reduced material requirements.

4.4 Contribution by Material Category

The material-category analysis explains the differences between the two scenarios (Fig. 4). In Scenario A, structural steel represents a major contribution to GWP; however, the overall impact remains lower because the steel structure requires lower total material quantities. In Scenario B, ready-mix concrete and reinforcement steel are the dominant contributors due to the larger volumes needed for slabs, columns, and foundations.

The results confirm that structural environmental performance cannot be assessed only through the impact factor of individual materials. Building-scale GWP depends on the interaction between material intensity, structural efficiency, construction technology, and design assumptions. In this case study, the higher specific impact of some steel components is compensated by lower quantities, lower structural mass, and reduced foundation requirements.

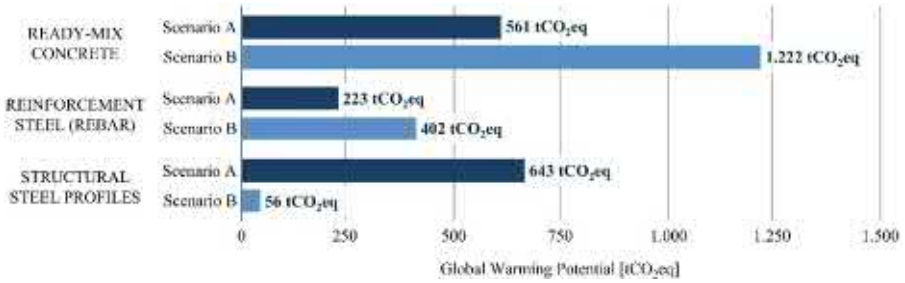


Fig. 4. GWP comparison by material category for Scenario A and Scenario B [tCO_2eq].

5 Discussion and Conclusions

The comparative LCA confirms that the selection of the load-bearing structural system can significantly influence the GWP of multi-storey buildings. In the analyzed case study, the steel scenario shows lower GWP values than the reinforced concrete alternative in both the preliminary and detailed assessments. The preliminary comparison indicates a 23% increase for the reinforced concrete scenario, while the detailed assessment confirms the same trend with 550 kgCO2eq/m2 GFA for steel and 603 kgCO2eq/m2 GFA for reinforced concrete.

The main drivers are material intensity and structural configuration. The reinforced concrete solution requires larger quantities of concrete and reinforcement for slabs, columns, and foundations, and its higher mass leads to additional foundation requirements. Conversely, the steel scenario benefits from a lighter structural configuration,

composite slabs, and reduced foundation needs. The study therefore confirms that comparative assessments should be conducted at the building or structural-system scale under equivalent boundary conditions, rather than through direct comparison of individual material impact factors.

The real refurbishment project also underlines the relevance of circularity strategies. The existing steel structure is recovered and reused for the completion of the building, demonstrating the potential of structural reuse to reduce demand for new materials and avoid production-related impacts. Although this benefit is not quantified in the two new-construction scenarios, it indicates an important future development for LCA-based structural design. Steel structures are particularly suitable for circular approaches because of their recyclability, potential for disassembly, and possible reuse after inspection and verification.

From a methodological perspective, the two-step workflow proved useful. The early-stage assessment provides rapid feedback when design decisions are still flexible, while the detailed assessment refines the results through project-specific quantities and more accurate modelling. This confirms the role of LCA as a design-support tool rather than only as a final verification procedure.

The study has some limitations. Results are case-study-specific and should not be generalized without considering geometry, spans, foundation conditions, datasets, transport distances, construction processes, and end-of-life assumptions. Moreover, the paper focuses only on GWP, which is central for climate-change mitigation but does not represent the complete environmental profile of the two structural systems. Finally, benefits and loads beyond the system boundary are not quantified; therefore, reuse, recovery, and recycling are discussed qualitatively rather than through Module D.

Future research should include Module D to quantify reuse and recycling benefits, as well as sensitivity analyses on EPD selection, transport scenarios, recycled content, and end-of-life pathways. Additional studies could compare hybrid systems and investigate how structural optimization and circular design strategies can further reduce whole-life carbon.

In conclusion, the paper demonstrates that LCA can effectively support the selection of low-carbon structural systems for multi-storey buildings. For the analyzed case study, the steel load-bearing structure achieves lower GWP values than the reinforced concrete alternative, mainly due to lower material intensity, structural efficiency, and reduced foundation requirements. In a context increasingly oriented towards whole-life carbon assessment, the systematic use of LCA represents a strategic opportunity to guide more informed and climate-conscious structural design choices.

References

1. United Nations Environment Programme (UNEP) (2024) Global status report for buildings and construction - as climate risks rise and cities grow, we must rethink how we build to create better lives for all. UNEP publications, Nairobi
2. Ghazwani K, Beach T, Rezgui Y (2025) Energy retrofitting using advanced building envelope materials for sustainable housing: a review. Build Environ 267:112243
3. Santos AK, Ferreira VM, Dias AC (2025) Promoting decarbonisation in the construction of new buildings: a strategy to calculate the embodied carbon footprint. J Build Eng 103:112037

4. Torabi M, Evins R (2025) Towards net-zero carbon buildings: investigating the impact of early-stage structure design on building embodied carbon. Int J Life Cycle Assess 30:2374–2389
5. Greer F, Horvath A (2025) Exploring the significance of transportation emissions in upfront embodied carbon in buildings. Build Environ 269:112457
6. Sesana MM, Dell Oro P, Salvalai G, Gervasio H (2025) Building life cycle assessment and digital technologies: a bibliometric and systematic literature review and recent advances on their integration to boost the decarbonization of the construction sector. Energ Buildings 352:116833
7. ISO (2006) Environmental management — life cycle assessment — principles and framework, ISO 14040:2006. International Organization for Standardization
8. ISO (2006) Environmental management — Life cycle assessment — Requirements and guidelines, ISO 14044:2006. International Organization for Standardization
9. CEN (2026) Sustainability of construction works - assessment of environmental performance of buildings - requirements and guidance, EN 15978:2026. European Committee for Standardization
10. Pajek L, Božiček D, Potočnik J, Košir M (2026) Impact of passive energy efficiency measures on embodied and operational GWP: a parametric study of detached houses under evolving grid and climate conditions. Energ Buildings 359:117308
11. Kumar V, Ricco ML, Bergman RD, Nepal P, Poudyal NC (2024) Environmental impact assessment of mass timber, structural steel, and reinforced concrete buildings based on the 2021 international building code provisions. Build Environ 251:111195
12. Palomar-Torres A, Rey-Hernández JM, Rey-Hernández A, Rey-Martínez FJ (2025) Decarbonizing near-zero-energy buildings to zero-emission buildings: a holistic life cycle approach to minimize embodied and operational emissions through circular economy strategies. Appl Sci 15(5):2670
13. Trabucco D, Perrucci G (2025) Steel–timber hybrid buildings: a comparative life cycle assessment study of global warning potential impacts. Sustainability 17(2):718
14. Arbulu M, Oregi X, Etxepare L (2025) Optimisation of passive energy renovation strategies in residential buildings for life cycle global warming potential reduction and cost-effectiveness. Circ Econ Sustain 5:6803–6823
15. Ferrari S, Zoghi M, Blazquez T, Dall O G (2022) New level(s) framework: assessing the affinity between the main international green building rating systems and the european scheme. Renew Sust Energ Rev 155:111924. https://doi.org/10.1016/j.rser.2021.111924
16. Directive (EU) 2024/1275 of the European Parliament and of the Council of 24 April 2024 on the energy performance of buildings (recast) (Text with EEA relevance)
17. Sesana MM, Salvalai G, Della Valle N, Melica G, Bertoldi P (2024) Towards harmonising energy performance certificate indicators in Europe. J Build Eng 95:110323. https://doi.org/10.1016/j.jobe.2024.110323
18. Commission Delegated Regulation (EU) 2026/52 of 16 December 2025 amending Annex III to Directive (EU) 2024/1275 of the European Parliament and of the Council as regards the Union framework for the national calculation of life-cycle global warming potential
19. Sesana MM, Dell Oro P, Sgarbanti M (2025) Assessing environmental impacts of buildings: an LCA comparison of technological construction solutions for a building refurbishment in Italy. In: Albatici R, Dalprà M, Gatti MP, Maracchini G, Torresin S (eds) Envisioning the futures designing and building for people and the environment. Colloqui.AT.e 2025, Lecture notes in civil engineering, vol 766. Springer, Cham
20. Yakimchuk T, Linhares P, Hermo V (2023) Evaluation of a modular construction system in accordance with the Passivhaus standard for components. J Build Eng 76:107234. https://doi.org/10.1016/j.jobe.2023.107234

21. Lavagna M (2022) LCA in Edilizia: Ambiti applicativi e orientamenti futuri della metodologia Life Cycle Assessment nel settore delle costruzioni, ISBN: 9788891655806, 1st edn. Maggioli Editore, Santarcangelo di Romagna
22. Torres J et al (2021) Plug and play modular façade construction system for renovation for residential buildings. Buildings 11(9):419. https://doi.org/10.3390/buildings11090419
23. Fnais A et al (2022) The application of life cycle assessment in buildings: challenges and directions for future research. Int J Life Cycle Assess 27(3):627–654. https://doi.org/10.1007/s11367-022-02058-5
24. Abouhamad M, Abu-Hamd M (2021) Life cycle assessment framework for embodied environmental impacts of building construction systems. Sustainability 13(2):461. https://doi.org/10.3390/su13020461
25. Alshamrani OS (2021) Integrated LCA-LCC assessment model of offsite, onsite, and conventional construction systems. J. Asian Archit. Build. Eng. 21(5):2058–2080. https://doi.org/10.1080/13467581.2021.1942001
26. Pakdel A, Ayatollahi H, Sattary S (2021) Embodied energy and CO2 emissions of life cycle assessment (LCA) in the traditional and contemporary Iranian construction systems. J Build Eng 39:102310. https://doi.org/10.1016/j.jobe.2021.102310

Re_Grid: A Reuse-Based Optimization Approach for the Design of Environmentally Efficient Steel Gridshell Structures

Valentina Tomei[1,2](✉), Ernesto Grande[1,2], Marina Serpe[1,2], and Maura Imbimbo[1,2]

[1] Department of Civil and Mechanical Engineering, University of Cassino and Southern Lazio, via G. Di Biasio, 23 Cassino, FR, Italy
v.tomei@unicas.it

[2] European University of Technology EUT+ European Union, Cassino, Italy

Abstract. The paper presents the main results conducted within the PRIN project: *Re_Grid – Reuse-based optimization approach for environmentally efficient steel grid structures*, related to the design of environmentally friendly gridshells using reusable components. An innovative design workflow for gridshells based on structural optimization is presented. The proposed approach strategically combines both reused and new components with the aim of reducing the weight of newly manufactured elements. More in detail, the optimization algorithms start from a regular mesh and strategically vary the position of the joints with the dual objective of identifying a minimum-weight solution and an optimal geometric configuration capable of accommodating reused components along their entire length, also reducing material waste. To demonstrate the applicability of the proposed algorithm, it is applied to gridshells with different geometrical configurations, referring to the Freegrid Benchmark, considering different spans and both fully constrained and partially constrained boundary conditions. The solutions are further explored by varying the characteristics of theoretical stocks of reusable elements in terms of length, quantity, and cross-section. The results are presented in terms of structural weight, structural response (buckling factors and utilization ratios for stresses and displacements), and greenhouse gas (GHG) emissions. The results validates the proposed approach and its ability to identify environmentally friendly design solutions, while also providing valuable considerations into the use of reused elements in the sustainable design of gridshell structures.

Keywords: Reuse-Based Design · Gridshells; Steel · Optimization · Freegrid

1 Introduction

The building sector is one of the main consumers of resources, due to the necessity of energy-intensive processes. Based on the consciousness of its impact growth, the industry has an increasing interest in design principles that reduce the environmental impact through effective and innovative solutions. Among these, recycling has been employed

© The Author(s), under exclusive license to Springer Nature Switzerland AG 2026
R. Zanon et al. (Eds.): CTA 2026, LNCE 942, pp. 79–90, 2026.
https://doi.org/10.1007/978-3-032-39505-4_8

for decades, but it requires a great amount of energy for to recover and process material, so may limit the reduction of environmental impact [1]. In this framework, less impactful solutions can be based on the idea of reuse, offering the possibility to reduce environmental impact by reusing structural parts derived from dismantled buildings into new structures [1, 2]. This approach has been recently applied to various structural typologies, like timber [3, 4], concrete [5], and steel structures [1, 6, 7]. Steel members are particularly well-suited for reuse, considering their preservation of mechanical properties. In this framework, the paper shows the main results carried out within the PRIN project *Re_Grid – Reuse-based optimization approach for environmentally efficient steel grid structures*, about the design of environmentally friendly gridshells with reused elements. In particular, an innovative design workflow for gridshells based on structural optimization is proposed, which strategically combines new and reused members with the aim of reducing the weight of newly manufactured elements. The results highlight the environmental benefit of the proposed solutions, together with their structural efficacy.

2 Geometry-Sizing Optimization Approach

Figure 1 describes the steps of the proposed geometry-sizing (GEO-SI) optimization approach:

- Geometry generation: it begins with the definition of an elementary sector mirrored in order to generate the full geometry, so the gridshells are characterized by a double symmetry. The geometry of the elementary sector is generated by modifying the arrangement of the nodes over a predefined surface, starting from an initial regular gridshell with a square mesh. The geometric parameters of the algorithm are the controlled movements of the nodes employed to modify the grid.
- Disposition of new and reused members: a subroutine has been developed to identify the lines of the modified grid whose lengths fit those of the elements of the available stock of reusable elements. The position of the corresponding end joints is slightly modified to match the lengths of the selected reusable members.
- Structural model: to reused beams the corresponding material properties and cross-section from the stock are assigned. The cross-section of new beams is as a variable of the optimization problem. All structural members are modeled as beams, with fixed connections at all joints. Loads are applied as concentrated forces at the joints. About support conditions both fully constrained gridshell (with hinges at the base) and partially constrained gridshell (with a free-edge at the base) have been analyzed.
- Structural analyses: the gridshells are analyzed thought linear static analyses and linear buckling analyses, in order to provide information on the structural weight of the new members (W_{new}) and on structural metrics like the buckling factor (BF), the maximum displacement ratio (Δ), and the maximum utilization ratio (U_{max}), necessary to evaluate the objective function to minimize. The linear buckling factor (BF) is the ratio between the critical buckling load and the applied load, imposed greater than 1; the displacement ratio (Δ) is the ratio between the maximum displacement (D_{max}) and the limit one ($D_{lim} = B/250$), and it should be less than 1; U_{max} represents the maximum utilization ratio among all beams, i.e. the demand-to-capacity ratio [8], which also have to be smaller that 1.

– Optimization: the optimization design process is governed by Genetic Algorithms, which aim is to identify the gridshell configuration that minimizes the weight of the new beams, considering a solution that includes both reused members and new ones.

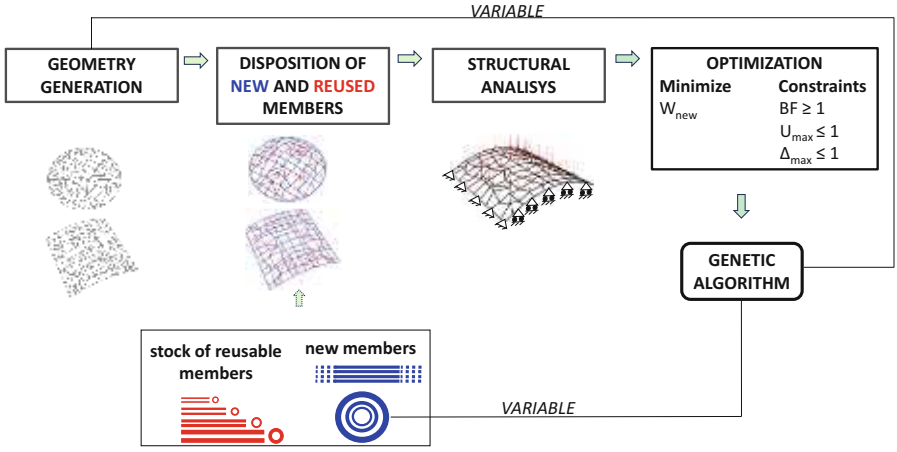


Fig. 1. Geometry-sizing optimization approach (GEO-SI).

3 Case Studies

3.1 Gridshells

The design optimization process has been applied to two gridshells described by the Free-grid benchmark [9, 10], and shown in Fig. 2. The Dome and the Barrel Vault geometries have been selected, which are both derived from a parabolic generatrix - in blue - and a parabolic directrix - in red – defined by the following Equations:

$$z = -\frac{x^2}{2B} + f \tag{1}$$

$$-\frac{B}{2} \leq x \leq \frac{B}{2} \tag{2}$$

$$A = B\left[\frac{\sqrt{5}}{4} + \ln\left(\frac{1+\sqrt{5}}{2}\right)\right] \tag{3}$$

where B represents the generatrix span (equal to 30 m); $f = B/8$ is the rise of the generatrix span. The gridshells are subjected to a vertical uniform distributed load of 1800 N/m^2 at Ultimate Limit State (ULS), de-amplified of 2/3 at Service Limit State (SLS), applied in terms of concentrated forces to the nodes of the gridshells. About the support conditions, the following cases are considered:

– fully-constrained gridshells: all the circular base boundary is constrained by hinges (in gray in Fig. 2b, e);
– partially-constrained gridshells: a part of the external boundary is free by constraints (the boundary in gray in Fig. 2c, f is constrained by hinges).

About the span, different values of B are considered: B = 20 m; B = 30 m; B = 40 m. The mesh discretization was assumed to consist of 10x10 bays (Fig. 2b, c, e, f). About the mesh pattern, a quadrilateral mesh pattern is considered, where all members are rigidly connected to the joint. Pipe cross-sections with a ratio between the diameter and the thickness of 10 are considered for new beams, while to reused members pipe cross-section are assigned when derived by theoretical stocks, while different shapes are considered when derived by real case studies. Steel S355 is assigned to both new and reused beams.

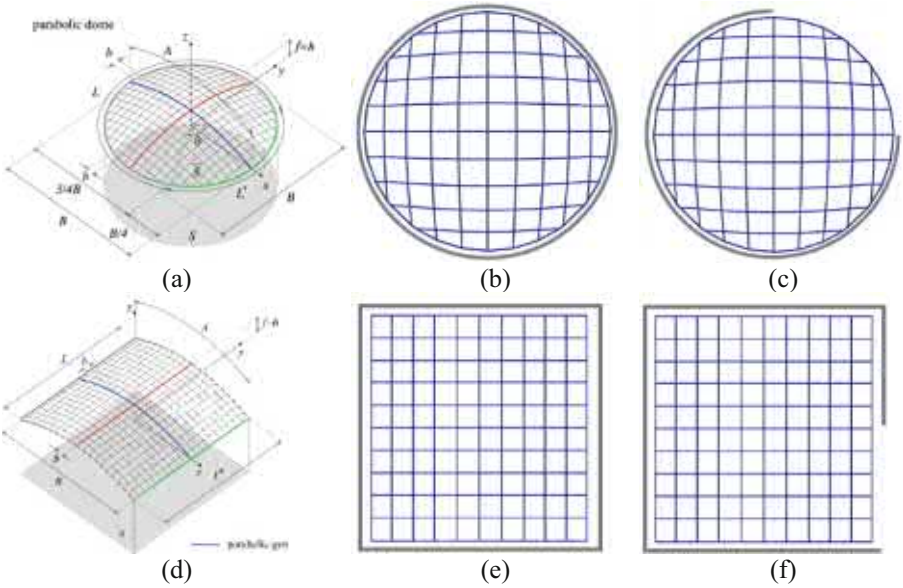


Fig. 2. Plan and axonometric view: a) 20x20 Dome gridshell proposed by [9, 10]; 10x10 Dome gridshell considered in the present work: b) fully-constrained gridshell; c) partially-constrained gridshell; d) 20x20 Barrel Vault proposed by [9, 10]; 10x10 Barrel Vault gridshell considered in the present work: e) fully-constrained gridshell; f) partially-constrained gridshell.

3.2 Stock of Reusable Members

Several theoretical stocks of reusable members have been defined by varying their number *N*, length *L* and cross section *CS*, to be inserted in the elementary sector of the gridshell (the position of reused beams is double mirrored to define the whole gridshells). The stocks considered are characterized by: different numbers of members; members

of the same length; members of different lengths. For the stocks, pipe cross-sections of different dimensions are considered:

– CS1: cross-section of the dimensions proposed within the Freegrid benchmark [9, 10];
– CS2: cross-sections with twice the diameter and thickness of *CS1*.

These cross-sects. *CS1* and *CS2* are different for the Barrel Vault and for the Dome (Table 1), according to the Freegrid benchmark [9, 10]. Table 2 shows the stocks considered in the different gridshell geometries.

Table 1. Cross-sections of reusable members.

	CS1		CS2	
	Φ1 (mm)	t1 (mm)	Φ2 (mm)	t2 (mm)
Dome	101.6	10	2 Φ1	2 t1
Barrel Vault	139.7	14.2	2 Φ1	2 t1

Table 2. Case studies and characteristics of theoretical stocks of reusable members.

Stock characteristics	B = 20 m	B = 30 m	B = 40 m
N = 8 – L = 4 m	–	CS1, CS2	–
N = 12 – L = 4 m	–	CS1, CS2	–
N = 8 – L = 5 m	–	CS1, CS2	–
N = 12 – L = 5 m	–	CS1, CS2	–
N = 12 – L = 2 m; L = 2.5 m; L = 3 m	CS1	CS1	CS1
N = 12 – L = 4 m; L = 4.5 m; L = 5 m	CS1	CS1, CS2	CS1
N = 12 – L = 5 m; L = 5.5 m; L = 6 m	CS1	CS1	CS1

3.3 Assessment of the Solutions

The solutions have been evaluated according to both structural performance and environmental impact. These were assessed and compared in terms of weight of reused (W_{reused}) and new (W_{new}) beams, total weight (W_{tot}), percentage of reused weight (% Reused), and structural performance evaluated through the linear static analyses performed during the optimization phase, like the buckling factor BF, the maximum utilization ratio U_{max} and the displacement ratio Δ. Furthermore, an environmental assessment was also developed to evaluate the ecological benefits of integrating reused members into new structural designs. Greenhouse Gas (GHG) emissions have been quantified considering the formula derived by the work of Brütting et al. [11], obtained by combining their data with inputs from the Swiss Federal LCA database [12] and other literature sources [13,

14]. The emissions are calculated using a simplified relationship that connect the GHG emissions to the mass of reused components (M_{reused}) and the mass of new-factored elements (M_{new}), both expressed in kilograms:

$$GHG = \frac{0.447\ kgCO_2}{kg} \bullet M_{reused} + \frac{0.844\ kgCO_2}{kg} \bullet M_{new} \quad (4)$$

4 Results

The results of the GEO-SI optimization approach are presented with the aim of analyzing: the effect of partial constraints, the effect of the span, the effect of the stock characteristics in terms of number, length of element and cross-sectional dimension. Each solution is compared with the solution of the base case, which is a regular gridshell designed with a classic sizing optimization approach. To improve readability, different effects have been included in the same plot, indeed, for both fully and partially constrained gridshell, the results are grouped to highlight: the effect of the span and of the stock (number and length of reusable beams); the effect of the stock in terms of cross-section.

For each group, four graphs are presented (see for example Fig. 5). On the left there are two plots referring to fully constrained gridshells, while on the right there are the ones referring to partially constrained gridshells. The labels of the bottom graph indicate the base case solutions and the stock used to find the solutions with reused beams. The vertical axes show the results in terms of weight per base area of new beams W_{new} (in blue) and reused beams W_{reused} (in red) - on the primary vertical axis- while the results in terms of Buckling Factor BF (circle indicator), maximum Utilization U_{max} (square indicator), displacement ratio Δ (triangular indicator), and percentage of reused weight (rhomboidal indicator) are indicated on the secondary vertical axis. The upper graph presents the greenhouse gas emissions GHG, distinguishing the contribution of new beams (in dark grey) and reused beams (light gray). At title of example, for some solution, also the obtained geometries and disposition of new and reused members are presented.

4.1 The Effect of the Span and of the Stock (Number and Length of Reusable Beams) for both Fully Constrained and Partial Constrained Gridshells

Figures 3, 4, 5 and 6 shows the results obtained for the Dome and the Barrel Vault gridshells, respectively, characterized by the span of 20 m, 30 m and 40 m, and obtained with stocks composed by 12 elements in the elementary sector, each divided into 3 equal groups of the same length, which entity is indicated in the labels of the graphs. By analyzing the solutions of the fully constrained gridshells (Figs. 3 and 5a), looking at the total weight, in some the solution with reused members is heavier than the base case: this results is expected, since it derives from a design process constrained on the available characteristics of the stock elements, that limit the problem exploration. In any case, most solutions with reused members show a reduction in terms of weight of new members than the base case, leading to advantages in terms of both cost and environmental impacts. By considering the solutions L = 2/2.5/3 and L = 5/5.5/6 for

B = 30 m and L = 2/2.5/3 for B = 40 m obtained for the Dome, the one with reused members shows a reduction of total weight than the base case, showing the ability of the GEO-SI approach to dispose the elements in order to obtain the minimum- weight solutions constrained to the stock characteristics. The same consideration can be made for the Barrel Vault with B = 40 m.

By considering the GHG emissions, in most cases, the solution with reused members shows lower values than the base case, but not always, meaning that it is not convenient a priori to design with reused elements. By observing the results in terms of BF and U_{max} of both fully constrained (Figs. 3a and 5a) and partially constrained (Figs. 3b and 5b) gridshells, the BF is ever almost similar to the limit value of 1, leading to the conclusion that the solutions are governed by buckling phenomena; for partially constrained gridshells, U_{max} is ever close to the limit value, leading to the conclusion that the solution is governed by the strength of the elements. These results highlight that the proposed design process can take into account of the different structural demands. Figures 4 and 6 show the variability of the solutions in terms of geometry and reused elements disposition.

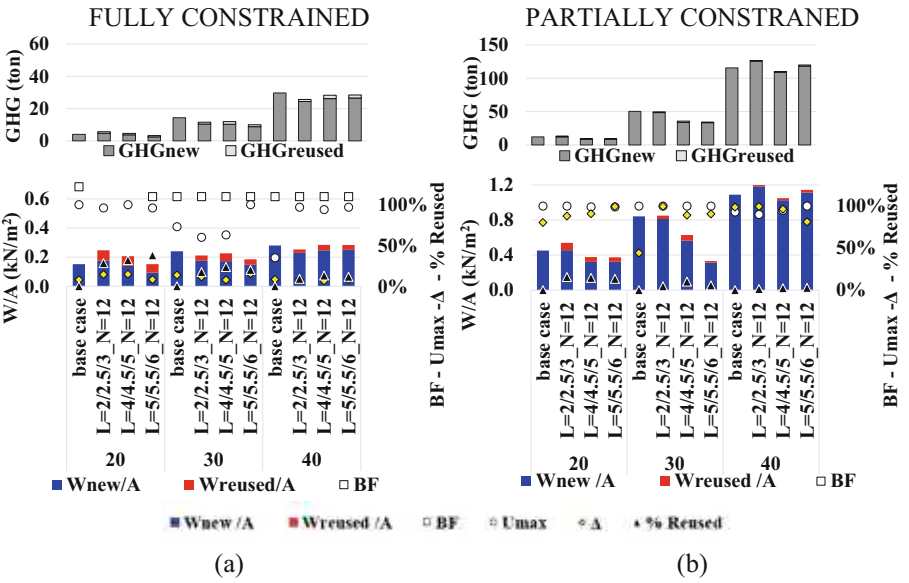


Fig. 3. Dome - the effect of the span and of the stock: (a) fully constrained solutions; (b) partially constrained solutions.

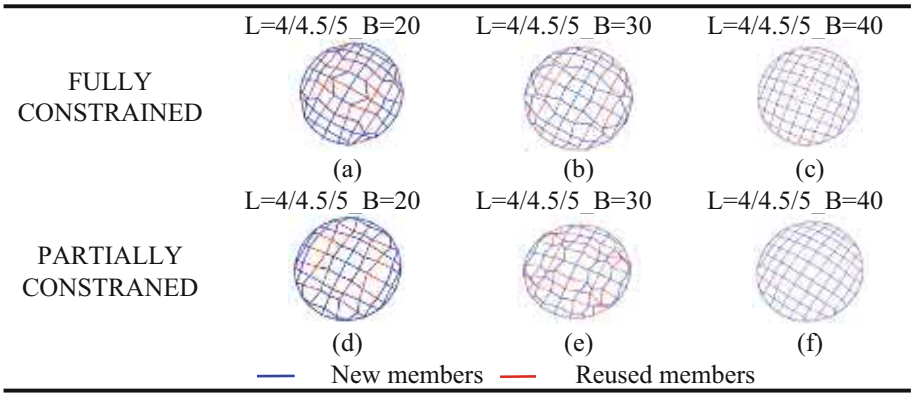


Fig. 4. Dome - the effect of the span and of the stock: obtained geometries and arrangement of reused (red) and new members (blue).

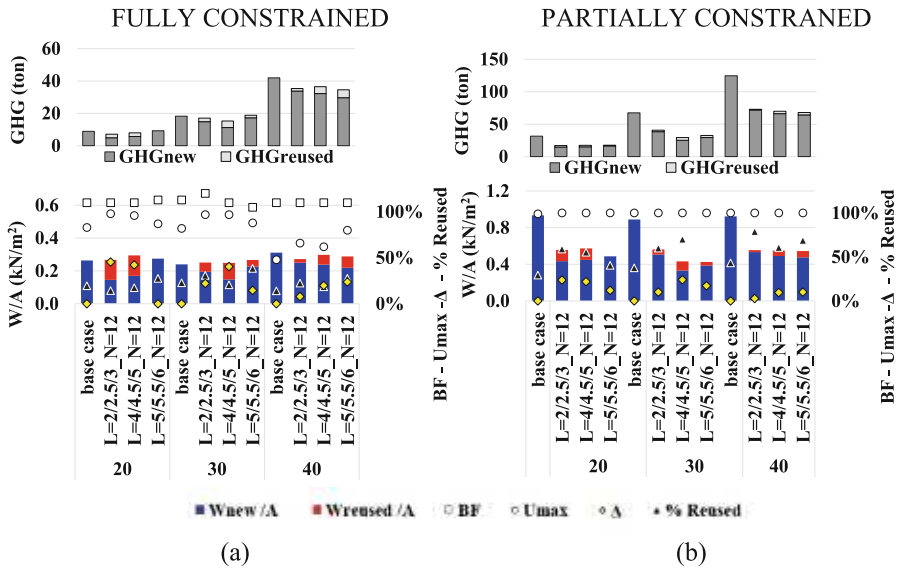


Fig. 5. Barrel Vault - the effect of the span and of the stock: (a) fully constrained solutions; (b) partially constrained solutions.

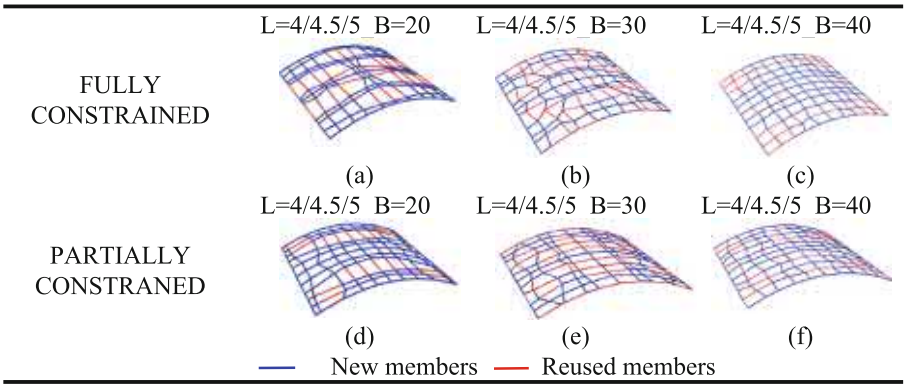


Fig. 6. Barrel Vault - the effect of the span and of the stock: obtained geometries and arrangement of reused (red) and new members (blue).

4.2 The Effect of the Cross-Section for both Fully Constrained and Partial Constrained Gridshells

Figures 7 and 8 show the results obtained for the Dome and the Barrel vault gridshells, respectively, characterized by a span of 30 m and obtained with stocks composed of 8 or 12 elements, in the elementary sector, of lengths equal to 4 m or 5 m, or with mixed lengths of 4, 4.5, 5 m (4 elements for each length). The stocks named CS1 have pipe cross-section of diameter $\Phi_1 = 101.6$ mm and thickness $t = 10$ mm, while the stocks named CS2 have a pipe cross-section of diameter $2\Phi_1$ and thickness $2t_1$. It is evident that, in fully constrained solutions, an increase of the cross-section in reused beams corresponds to an increase of the total weight, due to the fact the reused members have a higher cross-section with respect to the minimum required one. Further, in most cases, it is also observed that there is an increase in GHG emissions in solutions CS2 with respect solutions CS1. On the other hand, in partially constrained gridshells, an increase in the cross-section of reused beams lead to a decrease of both total weight and GHG emissions with respect the solutions CS1, or with respect to the base case. These results are due to the higher demand in terms of strength of the partially constrained gridshells compared to the fully constrained ones, due to the presence of the free edge.

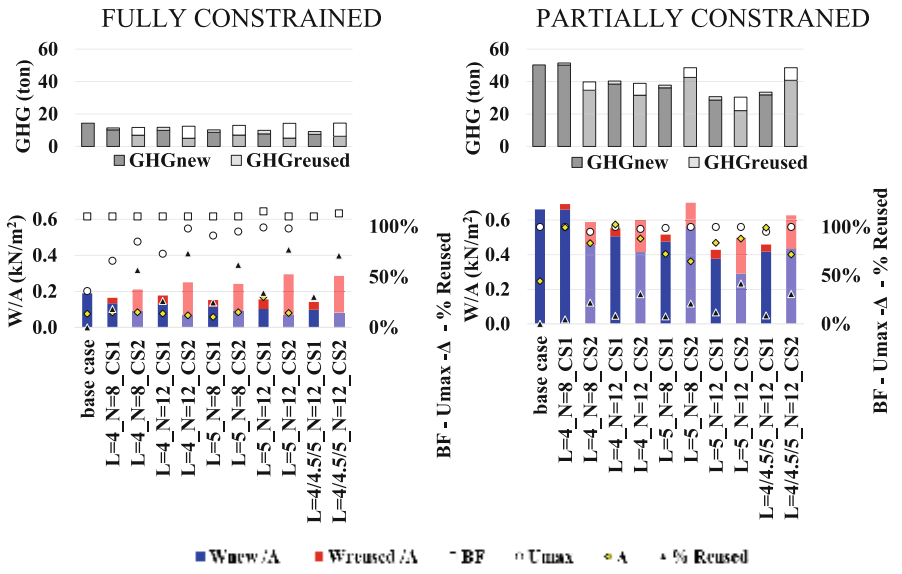


Fig. 7. Dome - the effect of the cross-section: (a) fully constrained solutions; (b) partially constrained solutions.

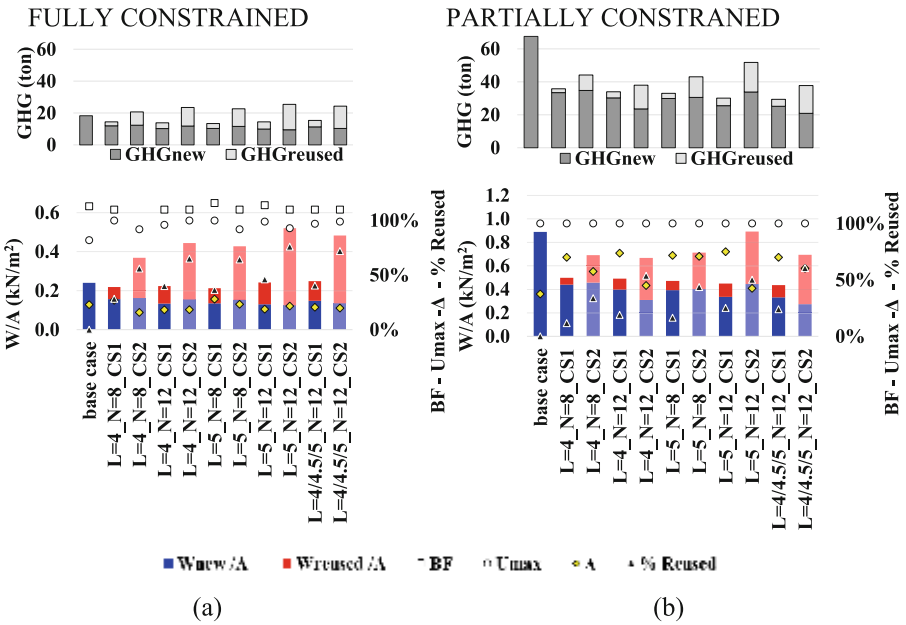


Fig. 8. Barrel Vault - the effect of the cross-section: (a) fully constrained solutions; (b) partially constrained solutions.

5 Conclusions

The paper presents a design framework for the design of gridshells, with a reuse-based approach, though a combination of new and reused members. Several scenarios have been considered in terms of case studies and stocks of reusable members. Regarding the case studies, gridshells with a dome shape and a barrel vault shape have been considered, varying their span and the boundary conditions. In particular, both fully constrained and partially constrained external conditions have been considered. Theoretical stocks of reusable members have been analyzed to study the effect of their characteristics, in terms of number, length and cross-section, on the obtained solutions. The solutions have been evaluated in terms of strength and stiffness constraints, with particular attention to the linear buckling factor, and in terms of greenhouse gas (GHG) emissions. From a structural point of view, the results show a different structural behavior between fully and partially constrained solutions; the former are mainly governed by buckling phenomena, whereas the latter are governed by the strength of the material.

The results in terms of both weight and environmental impact highlight that, for both dome and barrel vault gridshells, the use of reused members generally allows a reduction of GHG emissions then the reference solutions composed of new elements only. Nevertheless, when the geometrical and mechanical characteristics of the stock are not compatible with the gridshell geometry, an increase in the total structural weight is observed. Overall, the study demonstrates that reuse-based design can reduce environmental effects while maintaining structural performance, provided that the characteristics of the available stock are aligned with the geometrical and mechanical requirements of the gridshell.

Acknowledgements. The research leading to these results has received funding from Project" Re_Grid – Reuse-based optimization approach for environmentally efficient steel Grid structures" CUP H53D23008610001 funded by EU in NextGenerationEU plan through the Italian "Bando Prin 2022 - D.D. 1409 del 14–09–2022″ by MUR.

References

1. Brütting J, Desruelle J, Senatore G, Fivet C (2019) Design of Truss Structures through Reuse. Structure 18:128–137
2. Brütting J, Senatore G, Schevenels M, Fivet C (2020) Optimum Design of Frame Structures from a stock of reclaimed elements. Front Built Environ 6:57
3. Brütting J, Senatore G, Fivet C (2021) Design and fabrication of a reusable kit of parts for diverse structures. Autom Constr 125:103614
4. Ottenhaus LM, Yan Z, Brandner R, Leardini P, Fink G, Jockwer R (2023) Design for adaptability, disassembly and reuse – a review of reversible timber connection systems. Constr Build Mater 400:132823
5. Xia B, Jiao J, Li S (2022) Sustainability-based reliability design for reuse of concrete components. Struct Saf 98:102241
6. Van Marcke A, Laghi V, Carstensen JV (2024) Automated planar truss design with reclaimed partially disassembled steel truss components. J Build Eng 84:108458

7. Tomei V, Grande E, Imbimbo M (2025) A novel optimization approach for the design of environmentally efficient gridshells with reclaimed steel members. Adv Eng Softw 200:103825
8. Tomei V, Grande E, Imbimbo M (2025) A combined topology-sizing optimization approach for the sustainable design of steel gridshells with reclaimed bars. Structure 77:109114
9. Bruno L et al (2023) Exploring new frontiers in gridshell design: the FreeGrid benchmark. Structure 58:105678
10. Raffaele L, Bruno L, Laccone F, Venuti F, Tomei V (2024) Holistic performance assessment of gridshells: methodological framework and applications to steel gridshells. J Build Eng 90:109406
11. Brütting J, Senatore G, Schevenels M, Fivet C (2020) Optimum Design of Frame Structures from a stock of reclaimed elements. Front. Built Environ. 6:57
12. KBOB (2016) Ökobilanzdaten im Baubereich 2009/1:2016
13. Warmuth J, Brütting J, Fivet C (2022) Computational tool for stock-constrained design of structures. In: Conference proceedings of IASS/APCS 2022. https://www.ingentaconnect.com. Last Accessed 22 May 2024
14. Engineering G (1977) Demolition energy analysis of office building structural systems. Athena Sustainable Materials Institute, Ottawa

From Demolition to Reuse: A Decision-Oriented Perspective on Reclaimed Structural Steel

Fabrizio Ascione[1], Carmine Galasso[2], and Elena Mele[1](✉)

[1] Department of Structures for Engineering and Architecture, University of Naples Federico II, Umberto I street, 40, 80138 Naples, Italy
elena.mele@unina.it

[2] Department of Civil, Environmental and Geomatic Engineering, University College London, Gower Street, London WC1E 6BT, UK

Abstract. The reuse of structural steel offers an opportunity to reduce the environmental impact of the construction sector. In current practice, however, steel elements recovered from decommissioned buildings are still predominantly directed toward recycling rather than direct reuse. While steel production technologies are progressively moving toward lower-carbon routes, the direct reuse of structural components can already provide significant environmental benefits. Nevertheless, structural steel reuse is still limited by technical, regulatory, and logistical barriers. This paper discusses the main information needs and decision-making challenges associated with the transition from conventional demolition to decommissioning-informed steel reuse. Attention is given to Italian industrial steel buildings, where large quantities of potentially reusable members may become available at the end of service life. Reuse-oriented approaches require the integration of several phases, including preliminary survey of the donor structure, member identification, assessment of residual geometric and mechanical properties, evaluation of degradation mechanisms, selection of deconstruction strategies, and consideration of stock variability, economic feasibility, and environmental implications. A conceptual decision pathway is proposed to support the assessment of whether recovered steel should be reused, recycled, or managed through hybrid strategies. The paper frames the key requirements for future circular structural design tools.

Keywords: Steel Reuse · Industrial Buildings · Circular Economy · Sustainability

1 Introduction

Reducing resource consumption and embodied carbon emissions is one of the main challenges for the building and construction sector, which is responsible for a substantial share of global environmental impacts and accounts for around 37% of global CO_2 emissions [1]. Within this framework, circular economy strategies have gained increasing attention, as they aim to retain the value of materials and components already embedded in the built environment [2]. Existing buildings reaching the end of their service life, or already decommissioned, should therefore be regarded as potential urban

© The Author(s), under exclusive license to Springer Nature Switzerland AG 2026
R. Zanon et al. (Eds.): CTA 2026, LNCE 942, pp. 91–102, 2026.
https://doi.org/10.1007/978-3-032-39505-4_9

mines. However, this perspective should not be limited to the extraction of materials to be reprocessed into new products through recycling. In many cases, existing buildings may also contain components that could be directly reused, provided that their geometry, conditions, and structural reliability are properly assessed. This opportunity is particularly relevant for steel structures. Structural steel buildings are generally composed of members assembled through mechanical connections, often bolted, which may facilitate dismantling and recovery. Recent studies on material stock analysis have shown that large quantities of construction materials are already stored in existing buildings and infrastructure [3]. Bottom-up, GIS-based, archetype-based, and data-driven approaches are increasingly used to estimate the amount, location, age, and composition of these stocks at different scales [4]. Nevertheless, the availability of material in the built environment does not automatically translate into actual reuse potential: it is necessary to assess the state of conservation of the elements, the residual mechanical properties of the material, the degree of corrosion and the corresponding residual cross-section, the possible presence of fatigue damage, the connection systems adopted in the original structure, and the expected losses associated with dismantling operations. Economic aspects are also relevant, including the costs of selective deconstruction, transport, inspection, possible cutting or reconditioning, and protective treatments required before reinstallation. These factors strongly influence whether a reclaimed steel member can be considered suitable, convenient, and reliable for future structural applications. This paper presents a decision-oriented perspective on reclaimed structural steel, focusing on the upstream phase of the reuse chain: the moment in which an existing steel structure is assessed before demolition. The objective is to frame structural steel reuse as a decommissioning problem, where the decision between conventional demolition, selective deconstruction, direct reuse, recycling, or hybrid strategies should be supported by component-level and condition-aware information. In this perspective, a pre-demolition audit can become a key decision-support step, enabling the evaluation of reuse convenience under different damage, deconstruction, and future-use scenarios. Such an approach can support designers, owners, and stakeholders in the early stages of decision-making.

2 Structural Steel Reuse

2.1 Advantages and Barriers of Direct Steel Reuse

The potential benefits of reusing construction components are well established. The reuse of building materials is not a new practice: throughout history, elements from existing structures have often been incorporated into new constructions, as shown by the widespread use of architectural spolia in Roman, medieval, and Renaissance buildings. In the contemporary context, this long-standing practice has acquired renewed relevance due to the urgent need to reduce resource consumption and embodied carbon emissions. For structural steel, direct reuse is particularly attractive because it preserves not only the material itself, but also the component-level value associated with fabrication, rolling, cutting, drilling, and previous assembly. Compared with recycling, which requires reprocessing the material, direct reuse can therefore provide substantial environmental benefits, with studies reporting significant reductions in greenhouse gas

emissions [5]. Despite these advantages, the direct reuse of structural steel still faces several barriers. As highlighted in previous studies, major limitations are related to the lack of harmonised design rules for reused components, the limited availability of practical tools for designers, the uncertainty surrounding the mechanical properties of reclaimed members, and the difficulty of assessing residual geometric and structural characteristics after years of service [6]. Additional barriers concern traceability, certification, liability, inspection procedures, economic feasibility, and the absence of a consolidated supply chain connecting donor structures, deconstruction companies, reuse platforms, and new design projects [6]. In response to these issues, several countries have started to develop guidelines, protocols, and pre-normative documents to support the assessment and reuse of structural steel components, thereby providing an important basis for wider implementation [7, 8]. A further limitation is related to the design process itself. Designing with reclaimed steel is inherently stock-constrained: the structural layout must adapt to the available members, rather than selecting new profiles directly from a catalogue. This often requires advanced design and optimisation tools capable of matching existing elements with new structural demands [9–11]. Although several research contributions have addressed this topic, most approaches focus on the downstream phase of reuse, namely the design of a new structure using an already available stock. Less attention is given to the upstream phase, where the key decision is whether an existing donor structure should be selectively deconstructed for reuse or simply demolished and recycled. For this reason, the advantages and barriers of direct structural steel reuse should be considered before demolition. At this stage, it is necessary to assess whether the expected reclaimed stock is sufficiently valuable in terms of quantity, member typology, residual length, condition, economic feasibility, environmental benefit, and possible compatibility with future applications. The objective is therefore not only to promote reuse in principle, but to support a decision-making process capable of identifying when reuse is preferable to recycling.

2.2 From Recycling-Oriented Demolition to Reuse Oriented Decommission

Steel is one of the most widely used construction materials worldwide. Global crude steel production was approximately 1.9 billion tonnes in 2024, with around 70% produced through the blast furnace–basic oxygen furnace (BF-BOF) route and about 30% through electric arc furnaces (EAF) [12]. In the BF–BOF route, iron ore is reduced in the blast furnace using coke and coal-based reductants, producing hot metal that is subsequently refined into steel in a basic oxygen furnace. By contrast, the EAF route mainly relies on electricity to melt recycled steel scrap, often in combination with direct reduced iron [12]. The EAF route can substantially reduce carbon intensity compared with conventional BF–BOF production when a high share of scrap and low-carbon electricity is used. At the same time, broader decarbonisation pathways include hydrogen-based direct reduced iron, renewable electricity, and carbon capture, utilisation and storage [13]. At first sight, this transition may suggest that recycling should remain the preferred route for end-of-life structural steel, since scrap represents a valuable input for lower-carbon steelmaking. However, recycling preserves only the base material and still requires collection, sorting, transport, melting, refining, and manufacturing into new products. Direct reuse, when technically feasible, avoids these additional processes and

preserves the component-level value of structural products. This distinction is particularly important in the current climate context. The year 2024 was the warmest on record, with the global mean temperature reaching about 1.55 °C above the 1850–1900 baseline [14]. Immediate reductions in material-related emissions are therefore needed while low-carbon steelmaking technologies continue to scale up.

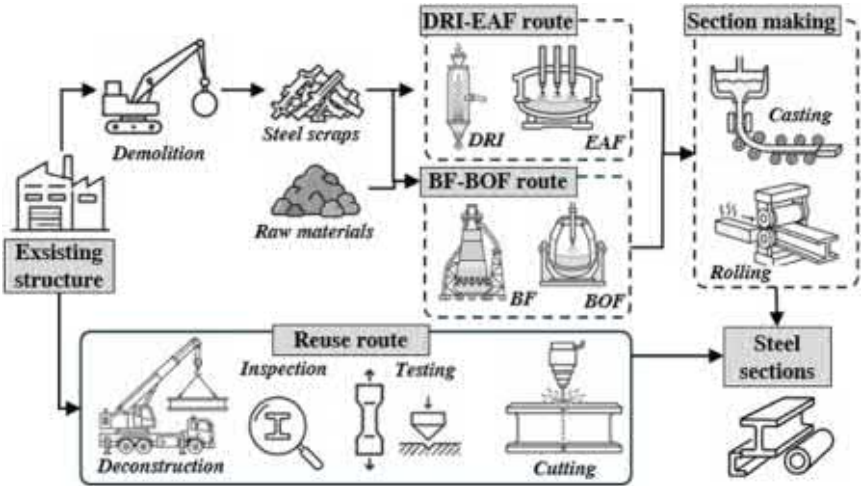


Fig. 1. Schematic representation of alternative end-of-life pathways for industrial steel structures.

Moving from recycling-oriented demolition to reuse-oriented decommissioning requires a change in perspective. Conventional demolition generally aims to remove the structure quickly and economically, with steel recovered as scrap. Reuse-oriented decommissioning, instead, requires the structure to be assessed before dismantling, so that recoverable members can be identified, selectively removed, documented, and preserved. The decommissioning strategy should therefore be consistent with the expected reuse potential of the donor structure, the economic cost of recovery, and the environmental benefit that may be achieved. In this sense, the decision to reuse, recycle, or adopt a hybrid strategy should be made before demolition.

2.3 From Reuse Potential to Reusability Evaluation

As illustrated in Fig. 1, direct reuse is not a zero-impact or zero-operation strategy. Although it avoids the complete reprocessing of steel through conventional recycling routes, it requires a set of additional operations that are not usually considered in demolition-oriented practices. Each of these operations may involve additional costs, time, energy consumption, and environmental impacts. A reclaimed stock may appear promising in terms of quantity or member typology, but its actual reuse convenience depends on several factors. In this perspective, reuse potential can be understood as the theoretical propensity of a donor structure, or of the resulting member database, to provide reusable components. Reusability evaluation, instead, should assess whether this

potential can be effectively translated into a technically feasible, economically convenient, and environmentally beneficial reuse strategy. Simulation-informed and scenario-based assessments can provide a practical way to address this uncertainty before any irreversible operation is carried out on the structure. By considering alternative assumptions on degradation level, residual cross-section, member cutting losses, dismantling strategy, testing requirements, reconditioning needs, transport distance, resale value, and future design demand, decision-makers can compare different end-of-life routes at an early stage. A decision-support tool for structural steel reuse should move from identifying reuse potential to evaluating actual reusability. Required inputs include the surveyed or simulated geometry, structural layout, member cross-sections, and material properties. When direct measurements are unavailable, simplified corrosion and fatigue models can estimate residual section properties, accumulated damage, and fatigue resistance. This supports the pre-demolition decision between component reuse and recycling.

3 Strategic Urban Mines

3.1 Italian Industrial Steel Buildings

Industrial buildings represent one of the most promising archetypes for urban mining strategies aimed at the direct reuse of structural components. Compared with other building typologies, industrial facilities are often characterised by large spans, repetitive layouts and relatively standardised structural members. In the Italian context, this perspective is particularly relevant because the national territory includes a significant number of former industrial areas, contaminated sites, orphan sites, and underused productive assets. The Italian National System for Environmental Protection identifies 42 Sites of National Interest for remediation, covering about 148,594 ha, many of which are associated with former or existing industrial activities [15]. In addition, the Italian Recovery and Resilience Plan include specific actions for the remediation and redevelopment of orphan sites, further highlighting the national relevance of abandoned or contaminated areas [16]. The transformation of Italian productive territories is also reflected in national statistical data. ISTAT identified 141 industrial districts in 2011, 40 fewer than in 2001 [17]. These indicators do not directly quantify abandoned industrial buildings or reusable steel structures. However, they highlight an ongoing spatial reorganisation and concentration of productive areas, supporting the need to investigate decommissioned and underused industrial assets as potential urban mines. In addition to their potential material availability, industrial steel buildings are also relevant because of the relative repetitiveness of their structural configurations. This repetitiveness can facilitate the development of simplified and parametric modelling strategies capable of reconstructing representative geometries with limited input information. Such models may support the preliminary assessment of donor structures before demolition. Starting from survey data, including digital surveys using aerial imagery, satellite data (e.g., Google Earth), street-level imagery (e.g., Google Street View), drone photogrammetry, and LiDAR, a digital representation of the existing structure can be generated and used to organize component-level information such as member layout, section types, spans, connections, and accessible structural elements. Such datasets are especially valuable for industrial buildings because of their large spans, repetitive geometries, and façades

that can be readily observed in imagery and point-cloud data. A simulation-informed representation of the existing building can support the evaluation of environmental exposure conditions, degradation scenarios, dismantling strategies, and expected recoverable stock. The aim is not to replace detailed inspection or certification procedures, but to provide an early-stage decision-support layer capable of linking the observed condition of the structure with the potential quantity, quality, and usability of reclaimed steel members.

3.2 Simulation-Informed Stock Characterisation

To evaluate the feasibility and convenience of reuse before the actual stock from an existing structure is available, decision-support tools are required to simulate scenarios, assumptions, and decommissioning actions. Figure 2 presents a possible workflow, outlining the main phases needed to support a preliminary reuse-oriented assessment.

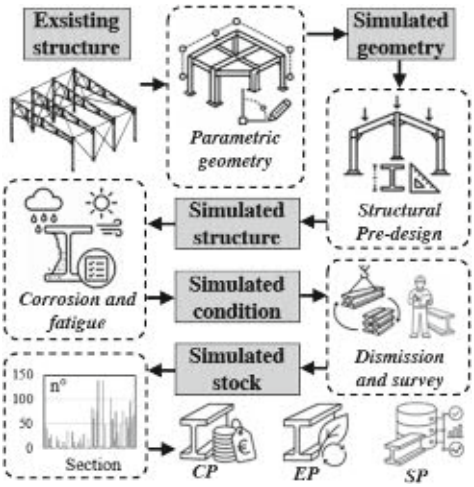


Fig. 2. Simulation-informed workflow for the preliminary characterisation of reclaimed steel stock from an existing industrial structure. CP, EP, and SP denote cost performance, environmental performance, and stock performance, respectively. Stock performance accounts for the characteristics and usability of the recovered database, including the variability of section profiles, the number and residual length of the members, and their condition and potential for reuse.

The process starts from the donor structure, namely the existing building to be assessed before demolition. At this stage, the available information may include original drawings, visual inspections, survey data, photographs, and field measurements, as discussed above. The first step is the generation of a simulated geometry, aimed at reconstructing the main geometric features of the existing structure through parametric geometry tools, providing a simplified but consistent representation of the donor structure for preliminary assessment. Once the geometry has been defined, a simulated structural model can be generated. The simulated model should be consistent with the design rules

and common construction practices that were in use at the time when the building was originally designed. At this stage, simplified structural checks or pre-design assumptions can be used to assign representative cross-sections to the main members and to obtain a first component-level description of the building. At this stage, simplified structural checks or pre-design assumptions can be used to assign representative cross-sections to the main members. The model may adopt idealised schemes, such as trusses, cantilever columns, or simple portal frames, consistent with the design practices of the relevant construction period. If detailed survey data are available, the actual member sections can instead be directly implemented in the model. Therefore, the tool should allow different levels of input detail, ranging from simplified pre-design procedures to the direct use of measured or documented structural information. This flexibility is particularly relevant for two different purposes. On the one hand, the workflow can support the modelling of realistic existing structures, for which drawings, surveys, or partial information are available. On the other hand, it can be used to generate multiple non-real but realistic structural configurations, representative of specific construction periods, industrial typologies, or design practices. These simulated structures can provide useful datasets for stock-constrained optimisation tools or probabilistic analyses aimed at evaluating the potential benefits of structural steel reuse under different scenarios. The same approach can be adopted to simulate or represent the condition of structural elements at the time of decommissioning, with reference to corrosion and fatigue phenomena, which are among the main degradation mechanisms affecting steel structures. Since the actual state of conservation may be uncertain before detailed inspection, different assumptions can be introduced to represent possible environmental exposure, corrosion, fatigue, local damage, maintenance history, or degradation levels. The final output of the workflow is a simulated stock of reclaimed steel members. This stock can be described in terms of the number of elements, section types, lengths, conditions, expected cutting losses, and possible classification for reuse.

3.3 Corrosion and Fatigue Scenarios

The simulation of the stock resulting from a decommissioning process should also account for damage and degradation accumulated during the service life of the structure, with particular attention to corrosion and fatigue. Corrosion generally leads to a reduction in the effective cross-sectional area of steel members and may affect their mechanical behaviour [18]. At a preliminary stage, this effect can be represented through simplified assumptions, for instance by idealising corrosion as a uniform thickness loss over the member surface, while neglecting localised phenomena such as pitting corrosion. Corrosion progression depends on several factors, including environmental exposure, industrial activity, protective systems, and maintenance history. Alternatively, standard-based approaches can be adopted to assign atmospheric corrosivity classes and estimate corrosion development over time [19, 20]. In this framework, different corrosion classes may be assigned during the service life of the structure to account for changes in use, exposure conditions, or damage to envelope components (Fig. 3). This allows a simplified reconstruction of the expected corrosion level at decommissioning and the definition of residual cross-sectional properties for the simulated reclaimed stock.

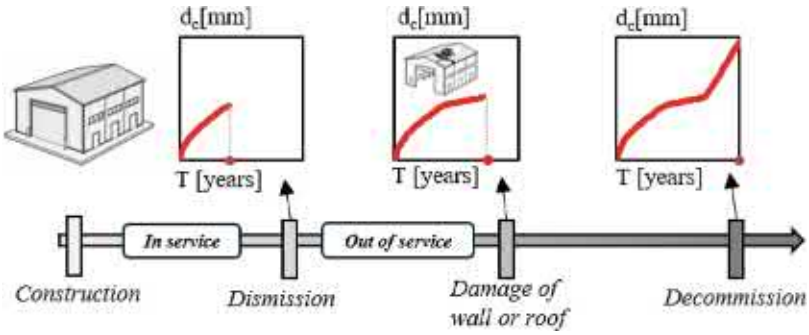


Fig. 3. Corrosion scenario used to simulate changes in corrosion classes over the structure's service life for structural elements, where d_c is the corrosion degree in millimeters.

Fatigue may also be relevant, especially for structures subjected to cyclic actions during their service life, such as wind-induced effects, machinery vibrations, or recurrent operational loads. Conventional fatigue assessment is generally based on S–N curves and cumulative damage concepts, as provided by Eurocode 3 [21]. However, when corrosion and cyclic loading occur simultaneously, the two phenomena interact. For this reason, simplified corrosion–fatigue scenarios can be introduced by adapting the reference fatigue curves to the expected degradation level [22] (Fig. 4).

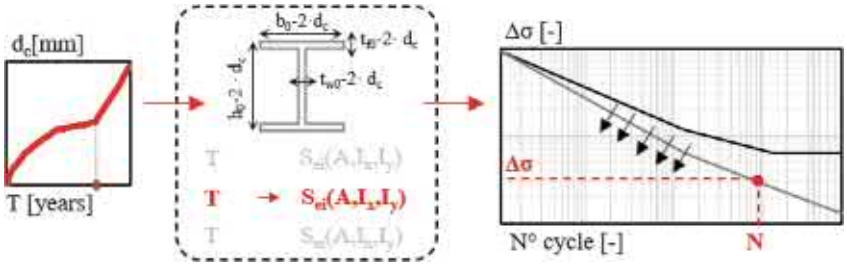


Fig. 4. Corrosion–fatigue interaction scenario evaluated throughout the structure's service life, accounting for the evolution of corrosion-induced section loss and the resulting variation in the section dimensions b_0, h_0, t_{w0}, and t_{f0}, denoting the flange width, overall section depth, web thickness, and flange thickness, respectively, as well as in the cross-sectional area A and second moments of area I_x and I_y about the two principal axes. The corresponding reduction in fatigue resistance is expressed in terms of stress range $\Delta\sigma$ and number of load cycles N.

When sufficient information is available, code-based approaches or cumulative damage concepts may be adopted to estimate the residual fatigue life of structural details. However, in the absence of detailed information on the actual loading history or connection details, simplified preliminary evaluations can still be used to obtain a first indication of the possible fatigue damage affecting structural members. Such evaluations may support the classification of elements according to their expected residual reliability, distinguishing between members that can be potentially reused and members that should be excluded from structural reuse.

3.4 Simulated Deconstruction and Reclaimed Stock Definition

Different decommissioning strategies may produce different residual member lengths, cutting losses, local damage, recovery costs, and environmental impacts. In conventional demolition, steel members are generally removed rapidly and directed to scrap. By contrast, reuse-oriented decommissioning requires selective dismantling, controlled handling, and, when necessary, trimming or removal of connection zones. These operations usually require more time, labour, equipment, and cost. Faster strategies, such as crane-assisted dismantling, may reduce operational complexity but can also decrease the quality and usability of the recovered stock by increasing local damage or cutting losses. Moreover, a detailed survey is needed to correctly identify member dimensions, section profiles, connection details, and possible defects. Depending on the accuracy of the survey, a certain degree of uncertainty may be introduced to simulate the resulting database. A simulated deconstruction process can therefore generate alternative reclaimed-stock databases under different assumptions. Each database may include section profiles, residual lengths, estimated condition, cutting losses, testing or reconditioning needs, and possible reuse classification. This allows the influence of decommissioning strategy and survey accuracy on the final stock to be evaluated before dismantling.

3.5 Uncertainty Characterisation and Sampling Methods

To account for epistemic and aleatory uncertainty in the simulated stock and deconstruction scenarios, probabilistic sampling and inference methods can be integrated into the workflow. Monte Carlo sampling provides a straightforward way to propagate uncertainty in input variables (e.g., section loss, residual lengths, cutting losses, and corrosion rates) to outputs such as expected recoverable stock and reuse classification. Multilevel Monte Carlo or variance-reduction variants can reduce computational cost when coupled with finite-element or high-fidelity checks. Bayesian hierarchical models allow separation and joint quantification of epistemic and aleatory uncertainty, enabling posterior updates when field inspections or test results become available. When high-fidelity simulations are expensive, surrogate models (e.g., Gaussian process or neural-network surrogates) can approximate responses and accelerate sampling. For strategic decisions under deep uncertainty (unknown models, non-stationary exposure), robust decision-making approaches and ensemble scenario analysis can identify reuse strategies across a wide range of plausible futures.

4 Scenario-Based Reusability Evaluation

4.1 Multi-Function Evaluation Criteria for Reclaimed Steel Stocks

Once the simulated reclaimed-stock database has been generated, its characteristics must be evaluated in order to understand whether it can effectively support future reuse applications. A comprehensive assessment should not be limited to the total amount of recovered steel, but should consider the overall quality and usability of the stock. In this sense, the evaluation should account for the variability of available section profiles, the number of members within each section group, the residual lengths after deconstruction,

and the condition of the elements in terms of corrosion, fatigue damage, and expected need for testing or reconditioning. A database containing many elements with similar short lengths, limited section variability, or severe degradation may be less adaptable than a smaller but more diverse and better-preserved stock. Therefore, the performance of a reclaimed-stock database should be interpreted as its general propensity to be reused in future applications. In addition to stock-related criteria, economic and environmental aspects should be included in the evaluation. From an economic perspective, the convenience of reuse depends on the balance between the potential value of the recovered members and the costs associated with selective deconstruction, survey, cutting, transport, testing, reconditioning, and protective treatments. From an environmental perspective, the benefits of avoiding new steel production must be compared with the additional impacts generated by the recovery and preparation processes. Scenario-based evaluation is particularly useful when the future reuse project is not yet known. By comparing alternative degradation, survey, deconstruction, and processing scenarios, together with different reuse fractions — namely, the proportion of database elements reused in a new project — it is possible to assess the sensitivity of the resulting stock performance to uncertain assumptions. This allows decision-makers to identify whether a donor structure is generally promising for reuse, whether only selected member groups should be recovered, or whether recycling remains the most appropriate route. A possible multi-criteria evaluation framework is illustrated in Fig. 5. The simulated stock is assessed through three complementary dimensions: stock performance, environmental performance and economic performance. The combined interpretation of these criteria can support preliminary decisions between direct reuse, recycling, or hybrid end-of-life strategies.

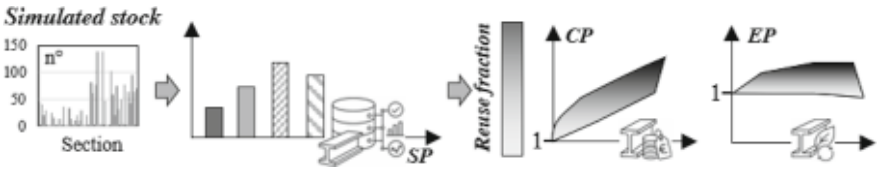


Fig. 5. Database performance assessment in terms of reusability (SP), cost (CP), and sustainability (EP), considering different reuse fraction scenarios.

5 Conclusions

The direct reuse of structural steel from industrial buildings represents a relevant opportunity to reduce the environmental impact of the steel construction sector. However, the transition from conventional recycling-oriented demolition to reuse-oriented decommissioning requires more than the simple recognition that large quantities of steel are embedded in the built environment. This paper discussed structural steel reuse from an upstream decision-making perspective, focusing on the phase in which an existing donor structure is assessed before demolition. The effective reuse potential of an existing structure depends on several uncertain factors, including member geometry, connection

details, degradation state, dismantling strategy, survey accuracy, and compatibility with future applications. A simulation-informed workflow is therefore outlined as a possible decision-support approach for preliminary reuse assessment. Starting from the donor structure, the workflow links geometric reconstruction, structural interpretation, condition and degradation scenarios, simulated deconstruction, and reclaimed-stock definition. In this framework, corrosion, fatigue, cutting losses, survey uncertainty, and deconstruction strategies can be considered through alternative scenarios before irreversible demolition operations are carried out. The resulting reclaimed stock should then be evaluated through multiple criteria, including stock performance, environmental performance, and economic performance. Such an assessment can support the comparison between direct reuse, recycling, selective recovery, and hybrid strategies. Overall, the proposed perspective highlights the need to move from material stock quantification toward component-level, condition-aware, and scenario-based reusability evaluation.

References

1. UNEP, GlobalABC (2024) Global status report for buildings and construction: beyond foundations – mainstreaming sustainable solutions to cut emissions from the buildings sector. United Nations Environment Programme, Nairobi
2. Ellen MacArthur Foundation (2013) Towards the circular economy, vol. 1 an economic and business rationale for an accelerated transition. Ellen MacArthur Foundation, Cowes
3. Ajayebi A, Hopkinson P, Zhou K, Lam D, Chen HM, Wang Y (2021) Estimation of structural steel and concrete stocks and flows at urban scale – towards a prospective circular economy. Resour Conserv Recycl 174:105821. https://doi.org/10.1016/j.resconrec.2021.105821
4. Gillott C, Lanau M, Mitchell Reid E, Sharmin F, Densley Tingley D (2025) Material stocks and embodied carbon in UK buildings: an archetype-based, bottom-up, GIS approach. J Ind Ecol 29(5):1748–1762. https://doi.org/10.1111/jiec.70066
5. Iacovidou E, Purnell P (2016) Mining the physical infrastructure: opportunities, barriers and interventions in promoting structural components reuse. Sci Total Environ 557–558:791–807. https://doi.org/10.1016/j.scitotenv.2016.03.098
6. Kanyilmaz A, Birhane M, Fishwick R et al (2023) Reuse of steel in the construction industry: challenges and opportunities. Int J Steel Struct 23:1399–1416. https://doi.org/10.1007/s13296-023-00778-4
7. Royal Netherlands Standardization Institute (2023) NTA 8713: Hergebruik van constructiestaal [Reuse of structural steelwork]. Royal Netherlands Standardization Institute, Delft
8. Brown DG, Pimentel RJ, Sansom MR (2019) Structural steel reuse: assessment, testing and design principles. Steel Construction Institute, Berkshire
9. Brütting J, Desruelle J, Senatore G, Fivet C (2019) Design of truss structures through reuse. Structure 18:128–137. https://doi.org/10.1016/j.istruc.2018.11.006
10. Tomei V, Grande E, Imbimbo M (2025) A novel optimisation approach for the design of environmentally efficient gridshells with reclaimed steel members. Adv Eng Softw 200:103825. https://doi.org/10.1016/j.advengsoft.2024.103825
11. Esposito F, Ascione F, Faiella D, Mele E (2026) Stock-constrained optimisation of diagrid exoskeletons using reclaimed steel for seismic retrofit of RC buildings. Structure 86:111304. https://doi.org/10.1016/j.istruc.2026.111304
12. World Steel Association (2025) World steel in figures 2025. World Steel Association, Brussels. https://worldsteel.org/data/world-steel-in-figures/world-steel-in-figures-2025/. Accessed 27 July 2026

13. International Energy Agency (2025) Iron and steel. International Energy Agency, Paris. https://www.iea.org/energy-system/industry/steel. Accessed 27 July 2026
14. World Meteorological Organization (2025) State of the global climate 2024 WMO-no 1368. World Meteorological Organization, Geneva. https://wmo.int/publication-series/state-of-global-climate/state-of-global-climate-2024. Accessed 27 July 2026
15. ISPRA (2026) Siti contaminati di interesse nazionale. Istituto Superiore per la Protezione e la Ricerca Ambientale, Rome. https://indicatoriambientali.isprambiente.it/it/siti-contaminati/siti-contaminati-di-interesse-nazionale. Accessed 27 July 2026
16. Ministero dell'Ambiente e della Sicurezza Energetica (2026) Elenco dei siti orfani. MASE, Rome. https://www.mase.gov.it/portale/elenco-dei-siti-orfani. Accessed 27 July 2026
17. ISTAT (2015) I distretti industriali. Anno 2011. Istituto Nazionale di Statistica, Rome. https://www.istat.it/it/archivio/150320. Accessed 27 July 2026
18. Landolfo R, Cascini L, Portioli F (2010) Modeling of metal structure corrosion damage: a state-of-the-art report. Sustainability 2(7):2163–2175. https://doi.org/10.3390/su2072163
19. International Organization for Standardization (2012) ISO 9223:2012, corrosion of metals and alloys – corrosivity of atmospheres – classification, determination and estimation. ISO, Geneva
20. International Organization for Standardization (2012) ISO 9224:2012, corrosion of metals and alloys – corrosivity of atmospheres – guiding values for the corrosivity categories. ISO, Geneva
21. European Committee for Standardization (2005) EN 1993-1-9:2005, Eurocode 3: design of steel structures – part 1–9: fatigue. CEN, Brussels
22. Milone A, Landolfo R (2022) A simplified approach for the corrosion fatigue assessment of steel structures in aggressive environments. Materials 15(6):2210. https://doi.org/10.3390/ma15062210

Reuse Based Design of Steel Gridshells Through Multi-Objective Optimization

Fabrizio Ascione, Francesco Esposito, Diana Faiella, and Elena Mele(✉)

University of Naples Federico II, Department of Structures for Engineering and Architecture, Umberto I street, 40, 80138 Naples, Italy
elena.mele@unina.it

Abstract. Gridshells are particularly suitable for the reuse of structural steel members, as their lattice-based configuration and geometric flexibility enable the integration of elements with varying lengths and cross-sectional properties within the structural grid. However, their structural response is highly sensitive to geometric and material nonlinearities, making reuse-oriented stock-constrained optimization complex and computationally demanding, in fact performing full nonlinear analyses for every candidate solution is impractical. In addition, most studies rely on idealized stock databases, often neglecting degradation and variability of reclaimed members caused by the service history of the original structures. This study addresses these limitations through a simplified framework based on stock databases generated from the simulated decommissioning of steel transmission towers, explicitly accounting for corrosion during service life. A multi-objective optimization procedure is developed for gridshells incorporating reclaimed steel members and applied to two benchmark geometries: a barrel vault and a dome. The grid layout is geometrically controlled, while simplified response parameters are adopted during optimization to approximate nonlinear structural behaviour and reduce computational cost. Optimal solutions are identified by comparing reuse-based steel gridshells with benchmark solutions, made of new steel, in terms of structural performance, cost, and sustainability. Full nonlinear analyses are performed only at the verification stage to assess the reliability of the simplified parameters. The study provides a tool for integrating structural, economic, and environmental criteria in reuse-based design.

Keywords: Steel reuse · Gridshells · Sustainability · Corrosion · Multi-objective Optimization

1 Introduction

Sustainability is currently one of the main challenges in the construction sector, which is responsible for a significant share of global greenhouse gasses (GHG) emissions and raw material consumption [1]. In this context, structural systems play a crucial role, since their embodied impact represents a substantial portion of the total environmental burden of buildings [2]. Steel structures are particularly relevant, as steel production contributes significantly to global greenhouse gas emissions, and a large share of the

© The Author(s), under exclusive license to Springer Nature Switzerland AG 2026
R. Zanon et al. (Eds.): CTA 2026, LNCE 942, pp. 103–114, 2026.
https://doi.org/10.1007/978-3-032-39505-4_10

steel produced worldwide is used in the construction sector [2–4]. Although steel recycling is a well-established strategy to reduce environmental impacts, the direct reuse of structural components represents an even more effective circular approach [5]. However, the reuse of structural steel elements introduces additional complexity into the design process [6, 7]. Unlike conventional design, where members can be selected from standardized catalogues according to structural efficiency, reuse-oriented design introduces a stock-constrained problem. In this case, the structural layout and member assignment depend on the geometry, length, cross-section, mechanical properties, and availability of reclaimed elements. Several studies have investigated stock-constrained design strategies for different structural typologies developing optimization algorithms aimed at efficiently assigning reclaimed members to new structures [8–12]. Nevertheless, multi-objective approaches remain relatively unexplored in this field. Another critical aspect concerns the actual condition of the reclaimed stock. Structural steel elements recovered from existing structures may be affected by corrosion, which reduces the effective cross-sectional area and consequently modifies the associated geometric and mechanical properties. Despite this, many studies in the literature still rely on idealized or theoretical stock databases, often neglecting degradation effects [8–12]. This study aims to address these limitations by adopting a realistic stock database generated through the simulated decommissioning of steel transmission towers from the Italian electricity network. A simplified corrosion scenario is considered in order to estimate the residual cross-sectional of the reclaimed members. The resulting database is then used within a multi-objective optimization framework for the design of steel gridshells, in which structural performance, economic cost, and environmental impact are considered simultaneously. The objective is to obtain a set of feasible design alternatives, allowing the designer to select the most suitable solution according to the desired balance between structural performance, sustainability, and cost. Steel gridshells are particularly suitable for the reuse of structural members because of their lattice-based configuration. However, their structural behavior is strongly influenced by global instability phenomena and requires nonlinear analyses accounting for both geometric and material nonlinearities [13]. Since performing full nonlinear analyses for each candidate solution during multi-objective optimization process would be impractical, a simplified performance indicator, previously adopted in [11], is used during the optimization stage. Full nonlinear analyses are then carried out only at the final verification stage to assess the reliability of the selected solutions. Although the adopted indicator exhibits a high level of variability and does not accurately predict the nonlinear load multiplier, it generally provides conservative estimates.

2 Case Study

2.1 Barrel Vault and Dome Case Study

The FreeGrid benchmark [14, 15] includes a set of reference gridshells case studies, namely a barrel vault, a dome, and a hyperbolic paraboloid, developed for optimization problems involving partially constrained boundary conditions. In this study, the barrel vault and dome configurations are selected as reference geometries; however, fully restrained boundary edges are considered, and a reduced 10×10 mesh instead of the

original 20 × 20 discretization is used. The corresponding geometries, shown in Fig. 1a and b, are defined through the generatrix equation z_G, given in Eq. (1) and the directrix equation z_D, given in Eq. (3) for the barrel vault and Eq. (4) for the dome. The generatrix arc length A is defined in Eq. (2).

$$z_G = -\frac{x^2}{2B} + f \quad -\frac{B}{2} \le x \le \frac{B}{2} \tag{1}$$

$$A = B\left[\frac{\sqrt{5}}{4} + \ln\left(\frac{1+\sqrt{5}}{2}\right)\right] \quad -\frac{B}{2} \le x \le \frac{B}{2} \tag{2}$$

$$z_D = f \quad -\frac{B}{2} \le y \le \frac{B}{2}, x = 0 \tag{3}$$

$$z_D = -\frac{y^2}{2B} + f \quad -\frac{B}{2} \le y \le \frac{B}{2}, x = 0 \tag{4}$$

In both case studies, the span B is set equal to 30 m, while the rise f is equal to *B/8*. The length L is taken equal to A for the barrel vault and to *2/3πB* for the dome. All internal joints are modelled as rigid connections. For the barrel vault, pinned supports are assigned along the external edges parallel to L. Along the edges parallel to B, the translational degrees of freedom δ_x and δ_z are restrained, whereas δ_y is released. For the dome configuration, pinned supports are assigned along all external boundary edges.

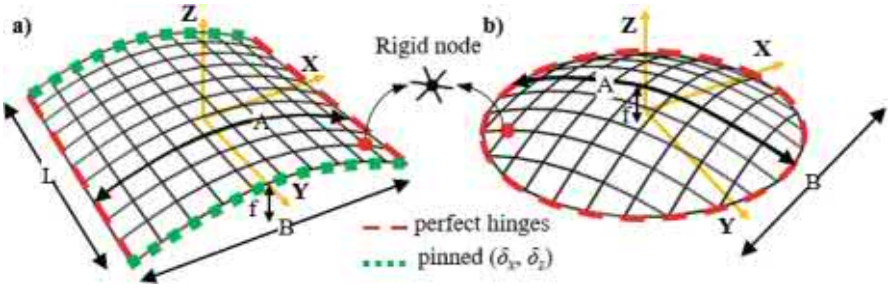


Fig. 1. reference geometry and constraints conditions for the barrel vault case study (a) and for the dome case study (b).

Among the two loading configurations proposed in the benchmark, namely LC_1, corresponding to a uniform load distribution, and LC_2, corresponding to an asymmetric load distribution, the present study adopts LC_2, as it represents a more severe loading condition for the structure. Both Ultimate Limit State (ULS) and Serviceability Limit State (SLS) load combinations are considered. The applied actions include the self-weight of the structural members, the permanent load associated with the glass cladding, equal to $q_{1,ULS} = 0.60$ kN/m^2 and $q_{1,SLS} = 0.40$ kN/m^2, and the snow load, equal to $q_{2,ULS} = 1.20$ kN/m^2 and $q_{2,SLS} = 0.80$ kN/m^2 [14]. The corresponding ULS load distributions are shown in Fig. 2a and b for the barrel vault and the dome, respectively.

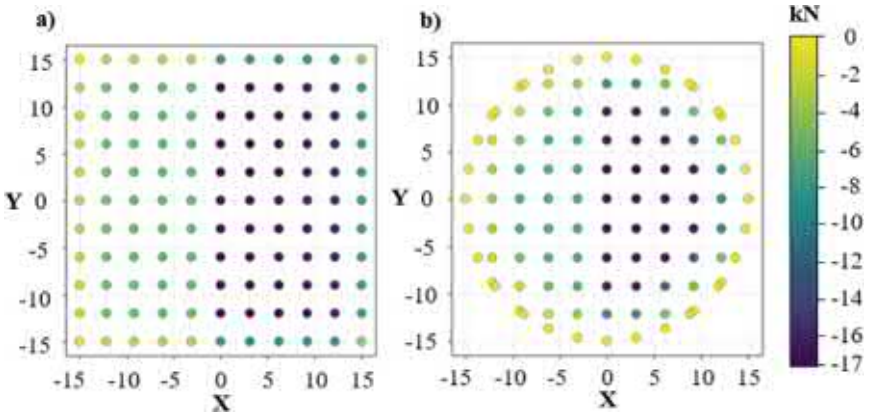


Fig. 2. Load distribution for the barrel vault case study (a) and for the dome case study (b).

2.2 Benchmark Solution with New Steel Elements

Reuse-based structures may often be significantly heavier than equivalent solutions designed with new steel, due to the oversizing frequently required to adapt the available stock sections to the target geometry [10, 11]. For this reason, in the present research work, benchmark solutions made of new steel are defined and used as references for comparison with the reused-steel solutions. These benchmark solutions are mechanically optimized without modifying the structural grid. The mechanical optimization is carried out by minimizing the structural mass while satisfying the following constraints:

$$\frac{DCR_{max}}{DCR_{lim}} - 1 \leq 0 \tag{5}$$

$$\frac{u_{max}}{u_{lim}} - 1 \leq 0 \tag{6}$$

$$\frac{\lambda_{lim}}{\lambda_B} - 1 \leq 0 \tag{7}$$

$$\frac{MR_{lim}}{MR} - 1 \leq 0 \tag{8}$$

where

- DCR_{max} is the maximum demand-to-capacity ratio of the grid members, including instability effects, calculated according to Eurocode 3 (EC3) [16];
- DCR_{lim} is set equal to 1;
- u_{max} is the maximum vertical displacement along the z-direction of the grid nodes;
- u_{lim} is set equal to 15 cm, corresponding to B/200 [14, 15];
- λ_B is the minimum load multiplier obtained from linear elastic buckling analysis;
- λ_B is set equal to 1;
- MR is a simplified Merchant–Rankine parameter (Eq. (9)), defined in [11], which aims to combine the effects of sectional yielding and global instability of the grid. In this formulation, λ_P is defined as $1/DCR_{max}$;

– MR_{lim} is set equal to 1.

$$MR = \frac{1}{\frac{1}{\lambda_P} + \frac{1}{\lambda_B}} \tag{9}$$

Figure 3 shows the DCR distribution for the dome ($DCR_{max} = 0.36$) and barrel vault ($DCR_{max} = 0.64$). Circular hollow sections made of S355 steel are considered.

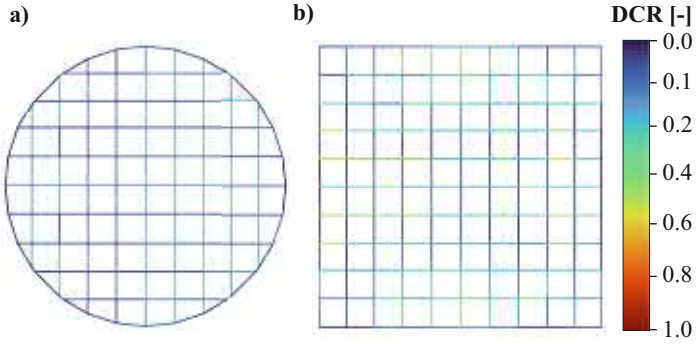


Fig. 3. DCR distributions **(a)** and displacement **(b)** for the benchmark solutions.

3 Database of Reclaimed Steel Elements

3.1 Simulated Dismission of Electric Transmission Towers

A database of reclaimed steel elements is generated following the approach proposed in [12], by simulating the decommissioning of two steel transmission towers. The database is reported in Fig. 4, where the reclaimed elements are classified according to their L-shaped cross-section type and described in terms of both number of available members and total cumulative length. The stock comprises 3,404 L-shaped steel members, with an overall length of 10,055 m. All members are made of S355 steel.

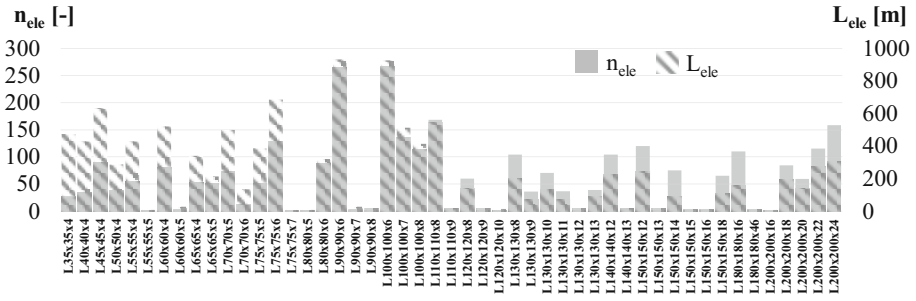


Fig. 4. Database of reused elements considered

3.2 Corrosion Scenario

Steel members may often be affected by corrosion phenomena. Corrosion occurs in the presence of oxygen and moisture and leads to a reduction in the effective resistant sect [17]. An accurate modelling of this phenomenon would require in-situ inspections and direct measurements of the members. However, in this study, in order to simulate the effects of corrosion in a simplified manner, the modelling approach proposed in [18–20] is adopted, assuming uniform corrosion. The resulting corrosion curve, obtained for an exposure period of 50 years is shown in Fig. 5a. Figure 5b illustrates the adopted thickness-reduction model for the cross-section, where d_{max} denotes the maximum corrosion depth after 50 years of exposure.

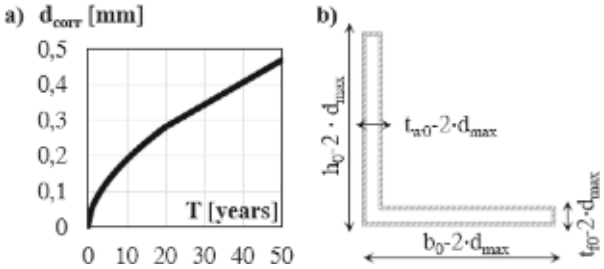


Fig. 5. Corrosion evolution over the service life **(a)** and thickness-reduction model adopted **(b)**.

4 Optimization Problem Formulation

4.1 Multi-Objective Optimization

In the context of steel reuse, a multi-objective approach enables the designer to explore a set of optimal solutions and select the most suitable alternative according to the desired performance priorities. Accordingly, this research adopts a multi-objective optimization algorithm to account not only for the environmental performance of the solution, but also for its economic impact and structural performance. The entire optimization workflow, illustrated in Fig. 6, is developed in Python, using OpenSees [21] and the NSGA-II algorithm [22].

For each candidate generated by the genetic algorithm, a mechanical optimization is performed according to the procedure described in Sect. 2.2, assuming all members to be made of new steel. The optimized solution is then processed by a matching algorithm, which replaces the newly designed elements with reused elements from the stock database. The matching process selects the most suitable associations by considering both the reduction of generated steel waste and the compatibility between the geometric properties of the sections. The resulting solution, incorporating reused members, is subsequently re-checked to verify compliance with all structural constraints. If these constraints are satisfied, the solution is considered feasible and included among the candidates used to construct the Pareto front. The analyses are carried out on a desktop computer equipped with an Intel(R) Core (TM) i7-14700F CPU @ 2.10 GHz, a 954 GB SSD, and 32 GB RAM, using parallel processing.

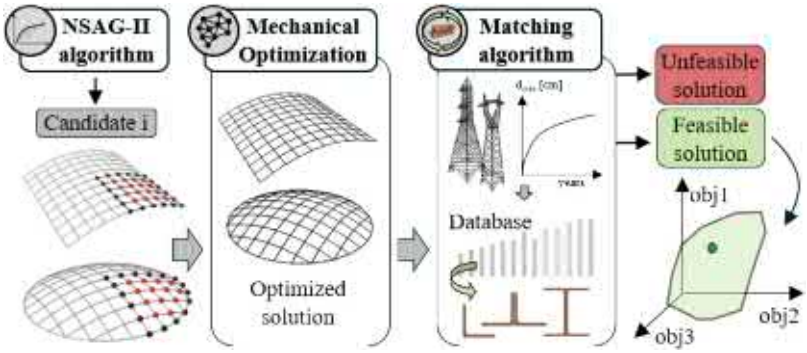


Fig. 6. Optimization workflow adopted.

4.2 Objective Functions

To identify the best-performing solutions with respect to the benchmark designs, the objective functions are defined as relative performance indicators to be maximized. Specifically, P_M accounts for mass-related performance, P_S for sustainability-related performance, and P_C for cost-related performance, as defined in (Eqs. 10–12) where M_B, EC_B and C_B are respectively the mass, the embodied carbon and the cost of the benchmark solutions while M_R, EC_R and C_R are the corresponding values for the reuse-based candidate. Higher values of P_M, P_S, and P_C indicate an improved performance of the reuse-based solution compared with the benchmark.

$$P_M = \frac{M_B - M_R}{M_B} \tag{10}$$

$$P_S = \frac{EC_B - EC_R}{EC_B} \tag{11}$$

$$P_C = \frac{C_B - C_R}{C_B} \tag{12}$$

The values of EC_B and EC_R are evaluated by accounting exclusively for the impacts related to material production. For newly produced steel members, an embodied carbon coefficient equal to 2.5 $kgCO_2e/kg$ is adopted [23], whereas to reused steel members a coefficient equal to 0.27 $kgCO_2e/kg$ is assigned [24]. Consistently, C_B and C_R are estimated by considering only the material acquisition cost. The unit cost of new steel is assumed to be 1250 €/t, which represents an intermediate value within the 1000–1500 €/t range. For reused steel, a unit cost of 550 €/t is adopted, corresponding to the average value of the 500–600 €/t range. The economic assessment also includes the scrap generated during the matching procedure, which is assumed to be sold at a unit price of 250 €/t. Accordingly, the proposed cost model should be interpreted as a preliminary simplified scenario based on average unit costs. The same framework can accommodate more detailed economic assumptions when project-specific data are available.

4.3 Constraints

The constraints adopted in the multi-objective optimization are consistent with those used for the benchmark design solutions described in Sect. 2.2. Each candidate is initially generated as a mechanically optimized solution composed entirely of new members. However, the subsequent replacement of some members with reused members may alter the stiffness distribution of the structure, resulting in changes in the internal force distribution. Therefore, all mechanical constraints are re-evaluated after the reuse-matching stage.

4.4 Variables

To increase the possibility of reusing available members and to minimize the generation of offcuts during the matching procedure, the optimization framework is allowed to adjust the nodal layout of the gridshell. Only one quarter of the grid is directly modified, while the remaining portions are obtained by mirroring the optimized quarter. Within the selected quarter, the internal nodes can move in the horizontal plane through variations of their x and y coordinates. The corresponding z coordinate is then updated according to Eqs. (1), (3) and (4) In this study, the maximum admissible variation of the horizontal coordinates is limited to ± 0.50 m. A further group of design variables is introduced by means of a gate-based mechanism. These variables control whether each member is included in the reuse-matching procedure. Members selected by the gate variables are assigned through the matching algorithm, whereas the remaining members keep the new steel sections previously defined by the optimizer.

4.5 Matching Algorithm

The matching algorithm, developed by the authors in [12], replaces new steel members with reused elements by matching the geometric and mechanical requirements of each target member with the properties of the available reclaimed stock, while allowing stock elements to be cut up to a maximum length $L_{CUT,max}$. A reused member can replace a new one only if its relevant cross-sectional properties, such as area A, moments of inertia I_y and I_z, and elastic section moduli $W_{el,y}$ and $W_{el,z}$, are greater than or equal to the required values. For each structural member, the database is sorted by length and grouped by cross-section. Additional fictitious databases with 2 L- and 4 L-shaped sections are generated to increase the number of possible matching combinations. Among the compatible elements, the algorithm selects the member that minimizes both the difference in cross-sectional performance and the cutting waste. After assignment, the resulting offcut is either reintegrated into the database, if longer than $L_{CUT,min}$, or counted as steel waste. In this study, $L_{CUT,max}$ is set equal to 10 m, while $L_{CUT,min}$ is defined as the minimum length of the structural members.

5 Results

5.1 Reuse-Based Solutions

The results obtained from the multi-objective optimization analyses are shown in Figs. 7 and 8. For both the dome and barrel-vault case studies, the plots highlight that increasing structural performance P_S leads to a reduction in mass performance P_M. This behavior reflects the overdesign typically associated with steel reuse, where available members often exceed the minimum required properties. Cost performance P_C increases with P_M at first, but decreases as P_M approaches unity, i.e., near the benchmark solution. In contrast, P_C remains almost constant with respect to P_S, with a slight decrease at high P_S values, caused by the higher mass of these solutions.

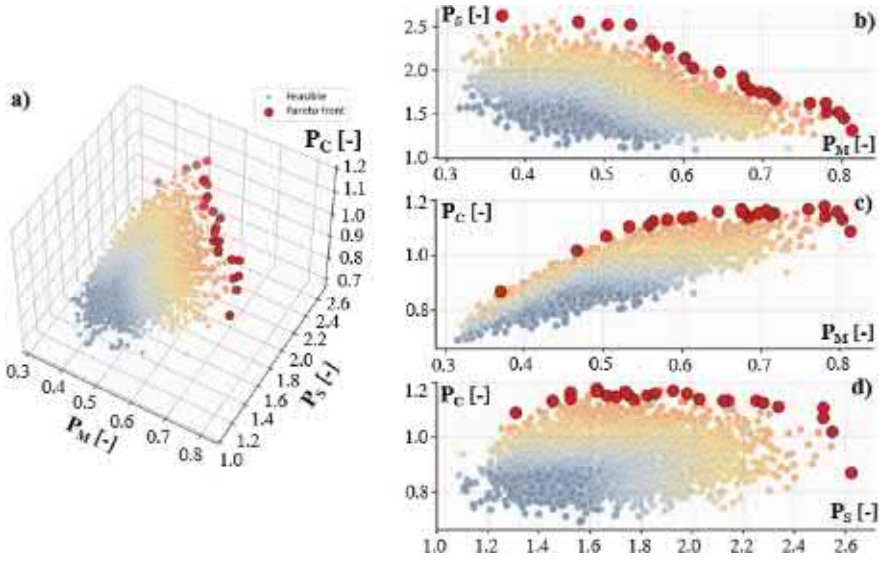


Fig. 7. Pareto front (red) and feasible solutions obtained from the multi-objective optimization of the barrel vault case study. A total of 25 Pareto-optimal solutions are identified.

Figure 9 compares the different Pareto-optimal solutions, highlighting a significant variability in the reuse percentage, generated scrap length (L_{scrap}), and number of required cuts (N_{CUT}). Since these parameters directly influence constructability, fabrication effort, and the number of processing operations, they play a key role in the selection of the most suitable design solution.

5.2 Non-linear Analysis

To validate the M_R parameter nonlinear analyses are carried out in OpenSees [21] on both the Pareto-optimal solutions and the benchmark designs. The nonlinear analyses are set up according to the procedure described in [14, 15]. Figure 10 presents the comparison

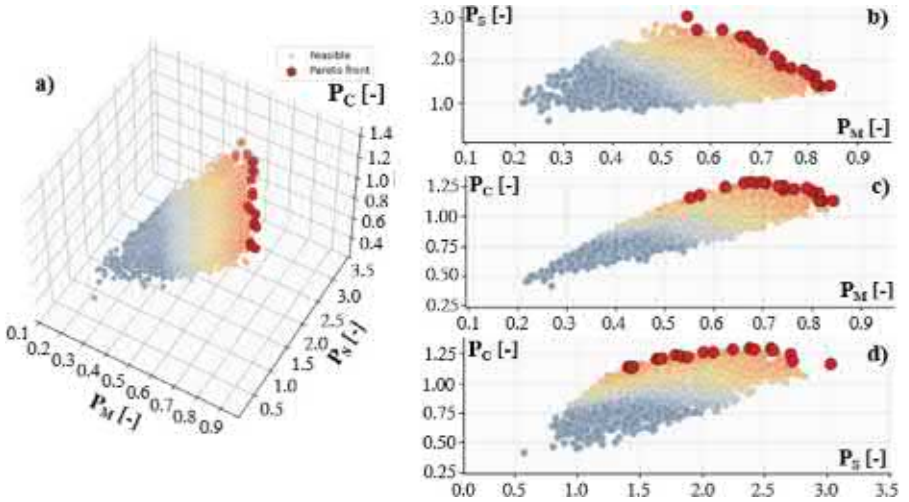


Fig. 8. Pareto front (red) and feasible solutions obtained from the multi-objective optimization of the dome case study. A total of 20 Pareto-optimal solutions are identified.

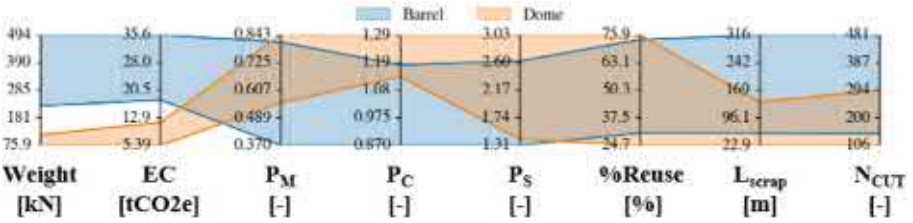


Fig. 9. Comparison of barrel and dome Pareto solutions in terms of performance and reuse metrics.

between the load factor obtained from the nonlinear analyses, LF_{NL}, the corresponding Merchant–Rankine parameter, MR, the linear buckling load factor, λ_B and λ_P.

The results show significant variability between the two case studies. For the dome, the *MR* parameter is particularly conservative, with an average deviation from the LF_{NL} values equal to 35%. Conversely, the linear buckling load factor, λ_B, provides a closer approximation to the LF_{NL} values, with an average deviation of 14%. For the barrel vault, instead, the collapse mechanism is strongly influenced by material nonlinearity. As a result, the *MR* parameter is much closer to LF_{NL}, with an average deviation of 24%, compared with the average deviation of 150% observed between λ_B and LF_{NL}. Overall, the *MR* is on the safe side with values always lower than the corresponding LF_{NL} values. However, further investigations are needed to assess the reliability of the *MR* parameter across different structural typologies and collapse mechanisms, and to identify possible modifications aimed at improving its predictive capability.

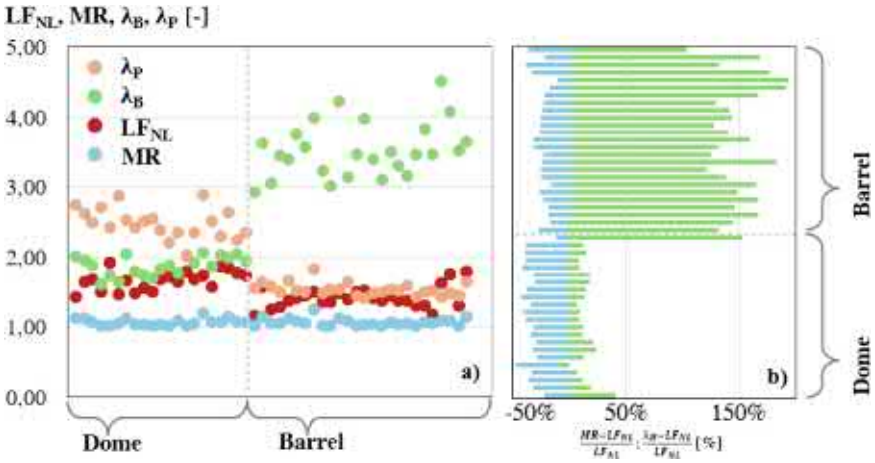


Fig. 10. Comparison of **(a)** LF_{NL}, MR, λ_B, λ_B values and **(b)** percentage difference with respect to LF_{NL} and MR for the dome and barrel vault case studies.

6 Conclusion

This work presents an optimization framework for the design of gridshells integrating reused steel members. The proposed approach enables the identification of a broad set of Pareto-optimal solutions, allowing different trade-offs among structural performance, environmental impact, and cost to be explored by comparing reuse-based alternatives with mechanically optimized new-steel benchmark designs. The results show significant variability among the Pareto-optimal solutions in terms of reuse-related parameters, such as the cutting length and the number of cuts required. This highlights the importance of explicitly including reuse-specific indicators in the optimization process. Overall, the framework proves particularly suitable for reuse-oriented design, as it allows multiple optimal alternatives to be identified and selected according to the performance criterion to be prioritized, while keeping the other objectives under control. The simplified MR parameter adopted to account for nonlinear response does not appear fully reliable, especially for the dome case study, whereas it provides more acceptable predictions for the barrel vault. In all cases, however, MR remains on the safe side, suggesting that further investigations are required to improve its predictive capability.

Acknowledgements. Study funded by the European Union – Next-GenerationEU - National Recovery and Resilience Plan (PNRR) – MISSIONE 4 COMPONENTE 2, INVESTIMENTO N. 1.1, BANDO PRIN 2022 PNRR D.D. 1409 del 14-09-2022 (Re_Grid: Reuse-based optimization approach for environmentally efficient steel Grid structures) CUP N. E53D23017270001."

References

1. United Nations Environment Programme, Global Alliance for Buildings and Construction (2025) Global status report for buildings and construction 2024/2025: not just another brick in the wall. United Nations Environment Programme, Nairobi

2. British Constructional Steelwork Association (2021) UK structural steelwork: 2050 decarbonisation roadmap. British Constructional Steelwork Association, London
3. Berglund-Brown J, Ochsendorf J (2025) Reusing heavy-section steel in buildings: carbon reduction potential and material availability. J Archit Eng 31(2):04025020
4. World Steel Association (2025) World steel in figures 2025. World Steel Association, Brussels
5. Iacovidou E, Purnell P (2016) Mining the physical infrastructure: opportunities, barriers and interventions in promoting structural components reuse. Sci Total Environ 557–558:791–807
6. Kanyilmaz A, Birhane M, Fishwick R, del Castillo C (2023) Reuse of steel in the construction industry: challenges and opportunities. Int J Steel Struct 23(5):1399–1416
7. Bartsch H (2025) Reuse of reclaimed steel components in construction: a systematic review of potential, challenges and future directions. Structure 80:110057
8. Brütting J, Desruelle J, Senatore G, Fivet C (2019) Design of truss structures through reuse. Structure 18:128–137
9. Brütting J, Senatore G, Schevenels M, Fivet C (2020) Optimum design of frame structures from a stock of reclaimed elements. Front Built Environ 6:57
10. Tomei V, Grande E, Imbimbo M (2025) A novel optimization approach for the design of environmentally efficient gridshells with reclaimed steel members. Adv Eng Softw 200:103825
11. Ascione F, Esposito F, Faiella D, Mele E (2025) Steel reuse for sustainable design of large-span structures: the case of gridshells. J Constr Steel Res 234:109743
12. Esposito F, Ascione F, Faiella D, Mele E (2026) Stock-constrained optimization of diagrid exoskeletons using reclaimed steel for seismic retrofit of RC buildings. Structure 86:111304
13. Gioncu V (1995) Buckling of reticulated shells: state-of-the-art. Int J Space Struct 10(1):1–46
14. FreeGrid Benchmark. https://sites.google.com/view/freegrid/home. Accessed 17 Apr. 2024
15. Bruno L et al (2023) Exploring new frontiers in gridshell design: the FreeGrid benchmark. Structure 58:105678
16. European Committee for Standardization (CEN) (2005) EN 1993-1-1:2005, Eurocode 3: design of steel structures—part 1–1: general rules and rules for buildings. CEN, Brussels
17. Landolfo R, Cascini L, Portioli F (2010) Modeling of metal structure corrosion damage: a state of the art report. Sustainability 2(7):2163–2175
18. International Organization for Standardization (ISO) (2012) ISO 9223:2012, corrosion of metals and alloys—corrosivity of atmospheres—classification, determination and estimation. ISO, Geneva
19. International Organization for Standardization (ISO) (2012) ISO 9224:2012, corrosion of metals and alloys—corrosivity of atmospheres—guiding values for the corrosivity categories. ISO, Geneva
20. International Organization for Standardization (ISO) (2012) ISO 9226:2012, corrosion of metals and alloys—corrosivity of atmospheres—determination of corrosion rate of standard specimens for the evaluation of corrosivity. ISO, Geneva
21. Zhu M, McKenna F, Scott MH (2018) OpenSeesPy: python library for the OpenSees finite element framework. SoftwareX 7:6–11
22. Blank J, Deb K (2020) Pymoo: multi-objective optimization in python. IEEE Access 8:89497–89509
23. Gibbons OP, Orr JJ (2022) How to calculate embodied carbon, 2nd edn. The Institution of Structural Engineers, London
24. Brütting J, Senatore G, Fivet C (2018) Optimization formulations for the design of low embodied energy structures made from reused elements. In: Smith IFC, Domer B (eds) Advanced computing strategies for engineering. EG-ICE 2018, Lecture notes in computer science, vol 10863. Springer, Cham, pp 139–163

Non-linear Assessment of Gridshells Designed with Reuse-Based Structural Optimization Strategies

Marina Serpe[1,2], Valentina Tomei[1,2(✉)], Ernesto Grande[1,2], and Maura Imbimbo[1,2]

[1] Department of Civil and Mechanical Engineering, University of Cassino and Southern Lazio, via G. Di Biasio, 23 Cassino, FR, Italy
v.tomei@unicas.it

[2] European University of Technology EUT+, European Union, Cassino, Italy

Abstract. Recently, optimization-based design approaches have explored the feasibility of integrating reclaimed elements into efficient gridshell configurations. The structural design of gridshells, and with optimization frameworks, is typically carried out through linear analyses. Furthermore, considering that gridshells are particularly prone to buckling phenomena, the governing design criterion is often the buckling factor, which is usually evaluated during the design phase through linear buckling analyses. However, due to the intrinsic slenderness and geometric characteristics of gridshells, the linear buckling factor provides only a simplified estimate of their sensitivity to buckling phenomena based on a linearized model that does not capture the actual load path or deformation pattern. This modelling approach may not offer a realistic assessment of the actual buckling behaviour. In this context, nonlinear analyses become crucial to simulate the progressive application of loads while continuously updating the structural geometry. This paper investigates the structural performance of gridshells designed using reuse-based optimization strategies that incorporate reclaimed steel members, employing nonlinear analysis procedures. Applications to representative case studies based on benchmark Freegrid configurations highlight conditions under which linear analyses may underestimate critical effects. The results demonstrate the importance of nonlinear assessment to ensure reliable and safe designs and provide insights into appropriate buckling factor thresholds to be adopted in linear analyses, with the aim of achieving solutions consistent with the nonlinear structural response. The results support the integration of nonlinear analyses within optimization-based design frameworks for reuse-oriented gridshells, enhancing confidence in structural performance while preserving the environmental benefits associated with structural reuse.

Keywords: reuse-based design · gridshells · steel · nonlinear buckling · Freegrid

© The Author(s), under exclusive license to Springer Nature Switzerland AG 2026
R. Zanon et al. (Eds.): CTA 2026, LNCE 942, pp. 115–127, 2026.
https://doi.org/10.1007/978-3-032-39505-4_11

1 Introduction

The construction sector represents one of the main consumers of resources worldwide, owing to its significant dependence on energy-intensive production processes and materials. Driven by growing concerns regarding environmental degradation, the building industry has focused increasing attention on design criteria developed to lower its ecological footprint by means of effective and innovative solutions. Within these approaches, recycling has constituted a standard practice for several decades; nevertheless, since the material recovery and reprocessing phases are inherently energy-intensive, the overall environmental benefits can be restricted. In this context, lower-impact solutions based on structural reuse strategies emerge as a competitive alternative, capable of mitigating environmental impacts through the direct reincorporation of structural members derived from decommissioned structures into new constructions [1].

Specifically, steel elements are exceptionally suitable for reuse applications due to their intrinsic capacity to maintain their structural and mechanical properties over time. Among different structural typologies, gridshells appear highly compatible with the use of reclaimed components; indeed, they consist of a mesh layout arranged along a curved surface, where the joints can be positioned in a flexible manner to facilitate the allocation of structural members with varied lengths and cross-sectional properties. Under these circumstances, automated structural optimization workflows can provide a valuable contribution to identifying the optimal mesh configuration for the assignment of such reused elements. In this framework, structural optimization strategies routinely generate a vast number of alternative solutions via parametric modeling; consequently, to maintain computational efficiency, they are generally combined with linear static and/or linear buckling analyses to account for global instability phenomena [2].

Nevertheless, because single-layer gridshell structures are highly sensitive to global instability, geometric nonlinear analysis (GNA) procedures become necessary for an accurate assessment. In fact, while the linear buckling factor evaluated through conventional eigenvalue analysis serves as a useful benchmark for preliminary design stages, it operates strictly on a linearized model. As a consequence, it does not account for progressive load-path trends, pre-buckling deformations, and the continuously evolving geometry of the structure under load, frequently leading to a significant overestimation of the actual buckling resistance. Conversely, GNA applies external actions incrementally and updates the structural response at each computational step, thereby capturing a more realistic mechanical behavior. This methodological approach complies with the recommendations of international design codes such as EN 1993-1-6 [3], which mandate nonlinear verification for thin-walled or stability-governed structures, and aligns with established literature emphasizing the intricate structural mechanics that dictate gridshell buckling susceptibility [4].

Downstream of this discussion, the present paper investigates the geometric nonlinear behavior of gridshell configurations obtained by combining new and reclaimed structural members via advanced structural optimization algorithms. The corresponding results provide useful insights for selecting the target linear buckling factor threshold to be met during the preliminary optimization phase.

2 Optimization Approach for Reuse-Based Design

The steps of the reuse-based optimization framework utilized for the gridshell design are illustrated in the workflow of Fig. 1. The initial phase involves geometry generation, which is performed by modifying the position of nodal coordinates along a predefined surface, starting from a regular grid with a square mesh. The geometric variables within the optimization algorithm are these controlled nodal displacements, which modify the global grid configuration. To maintain the original footprint of the structure, specific geometrical constraints are prescribed for the boundary and corner nodes of the elementary sector. Specifically, boundary joints are restricted to movement along their relevant boundary curves, whereas corner joints remain fully fixed. Furthermore, the maximum admissible displacement of each node is bounded within pre-established limits to prevent spatial overlap with neighboring joints. Upon completion of this stage, the main configuration of the gridshell is defined. Subsequently, an ad hoc subroutine identifies the grid lines whose lengths are closest to those of the components available in the stock of reclaimed elements. The dimensions of these lines are then adjusted to match the exact lengths of the selected reused members. Following the geometry generation and the mapping of both new and reclaimed members, the structural model of the gridshell should be defined. Material properties and cross-sections derived from the available stocks are assigned to the reused components, whereas the cross-sectional dimensions of the new elements are a design variable in the optimization problem. All structural members are modeled as beam elements rigidly connected at the nodes. The design loading conditions are represented by nodal concentrated forces, derived from an equivalent uniformly distributed load. Depending on the case study under consideration, the boundary conditions simulate either a fully-constrained gridshell (with pinned supports along the entire base) or a partially-constrained configuration (with a free edge at the base).The structural response is evaluated during the design phase through linear static and linear buckling analyses. The numerical outcomes provide the necessary inputs to evaluate the objective function, which aims to minimize the structural weight of the new components (W_{new}) subject to specific performance criteria: the global linear buckling factor, the maximum displacement ratio, and the maximum utilization ratio (i.e., the demand-to-capacity ratio of each member). The linear buckling factor—defined as the ratio of the critical buckling load to the applied load—must exceed 1.0 to ensure global stability. The maximum displacement ratio, calculated as the peak displacement divided by the allowable threshold (span/250), must be below 1.0, while the maximum utilization ratio - the demand-to-capacity ratio of each member - must not exceed 1.0. Within this framework, the optimization process, executed via Genetic Algorithms, aims to determine the optimal gridshell layout that minimizes the weight of the new members within a mixed solution combining new and reclaimed structural components.

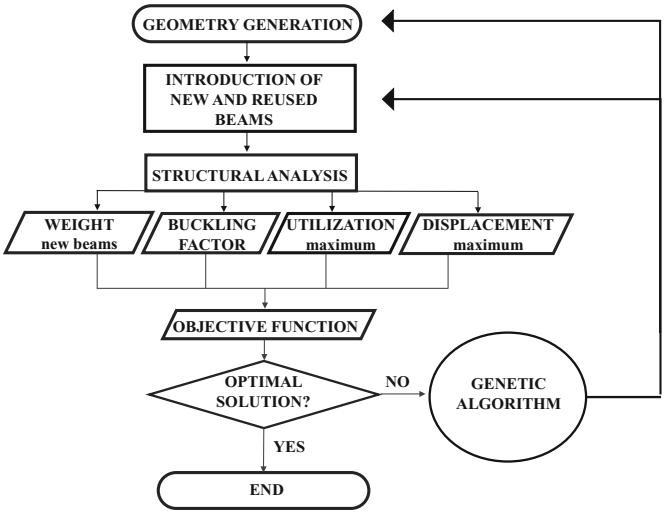


Fig. 1. Proposed optimization approach for reuse-based design.

3 Case Studies

3.1 Gridshells

The proposed design optimization process was applied to two of the gridshell geometries from the Freegrid benchmark [5], which are graphically illustrated in Fig. 2. Specifically, the selected geometries include the Barrel Vault ([5]) a single-curvature gridshell, and the Dome (Fig. 2c, d), a double-curvature gridshell. Both shapes are defined by a parabolic generatrix and a parabolic directrix according to the following equations:

$$z = -\frac{x^2}{2B} + f \tag{1}$$

$$-\frac{B}{2} \leq x \leq \frac{B}{2} \tag{2}$$

$$A = B\left[\frac{\sqrt{5}}{4} + \ln\left(\frac{1+\sqrt{5}}{2}\right)\right] \tag{3}$$

where B represents the generatrix span (equal to 30 m according to Freegrid [1]) and $f = B/8$ is the rise of the generatrix.

The gridshells are subjected to a uniform vertically distributed load of 1800 N/m^2 at the Ultimate Limit State (ULS) and 1200 N/m^2 at the Serviceability Limit State (SLS). These loads are applied as concentrated forces at the grid joints to replicate Load Condition LC1 described [5].

Regarding the support conditions, two scenarios are considered: fully-constrained gridshells: the entire external boundary is constrained by hinges (shown in gray in Fig. 2a,

c); partially-constrained gridshells: a portion of the external boundary is free, while the remaining part is constrained by hinges (shown in gray in Fig. 2b, d).

To evaluate different configurations, three span lengths are considered: $B = 20$ m, $B = 30$ m, and $B = 40$ m. The mesh discretization consists of 10×10 bays (Fig. 2) arranged in a quadrilateral pattern where all members are rigidly connected to the joints. Regarding the structural profiles, circular hollow cross-sections with a diameter-to-thickness ratio of 10 are specified for the new members. For the reused elements, circular hollow cross-sections are assigned. S355 steel is adopted as the material for both new and reused components.

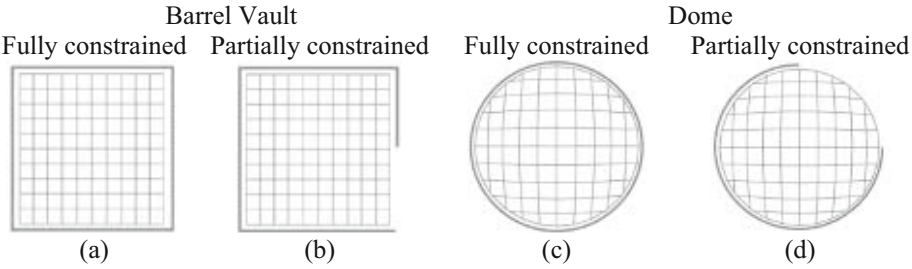


Fig. 2. Plan view of the accounted case: a) fully constrained and b) partially constrained Barrel Vault gridshells; c) fully constrained and d) partially constrained Dome gridshells.

3.2 Stock of Reusable Members

Several theoretical stocks of reusable elements are defined by varying the total number of members N and their individual lengths L. Regarding the structural profiles, circular hollow sections have been selected based on the Freegrid benchmark [5]. Due to the distinct structural demands of each geometry, these cross-sections vary between the Dome and the Barrel Vault. For the Dome, the profile has an outer diameter of 101.6 mm and thickness of 10 mm; for the Barrel Vault, the profile has an outer diameter of 139.7 mm and thickness of 14.2 mm.

The correlation between these reusable stocks and the gridshell span lengths B = 20 m, 30 m and 40 m defines the investigated case studies. Multi-length stocks composed of N = 12 members with variable dimensions are deployed across all three span lengths (B = 20 m, 30 m and 40 m): the short-member stock, composed of three groups of four members of length 2 m, 2.5 m and 3 m, respectively; the intermediate-member stock, composed of three groups of four members of length 4 m, 4.5 m and 5 m, respectively; the long-member stock, composed of three groups of four members of length 5 m, 5.5 m and 6 m, respectively.

4 Results

The case studies described in Sect. 3 have all been designed following the flowchart described in Fig. 1 while respecting conditions on linear buckling factor, utilization ratio and maximum displacement, obtained through linear static analyses, which results are

presented in [6]. Figures 3 and 4 show geometries and disposition of new and reused members obtained for some configuration of the Barrel Vault and the Dome, respectively. Due to the potential limitation of linear buckling analyses, all the solutions obtained are here analyzed through Geometric Nonlinear Analyses (GNA). To handle the complexity of this analysis, Abaqus v.2025 [7] was employed. A custom Python v3.14 interface was developed to seamlessly integrate the optimized geometrical layouts into the numerical model. This script automated the entire modeling workflow, directly transforming the data from the optimization phase into the Abaqus input format. Specifically, the routine read the geometrical, structural, loading, and boundary data to generate the corresponding input files, ensuring consistent implementation across all case studies. The gridshells were discretized using 3D Timoshenko beam elements (specifically, the B31 element type in Abaqus) [7], which are two-node linear elements capable of capturing both bending and shear deformations. All members were modeled as fully fixed beams. Support conditions and load applications were consistent with the descriptions provided in Sect. 3. The nonlinear analyses utilized a load-controlled incremental scheme, applying the total load across 1000 incremental steps. The Newton–Raphson method was used to iteratively solve the equilibrium equations, with convergence verified against a weighted residual norm tolerance of 5×10^{-3}. The results are presented as load factor–vertical displacement (Δz) curves, where the load factor represents the ratio between the current load step and the total nominal load applied to the gridshell. The buckling factor (BF) was assumed to correspond to the load factor at either a limit point (zero tangent stiffness) or an inflection point; the latter indicates the entry into a post-buckling regime characterized by an alternative deformation mode [8]. The point of the curves corresponding to the nonlinear buckling factor are identified with diamond indicators in Figs. 5 and 6, while in the same graphs the dotted linear correspond to the linear buckling factor obtained downstream of the design workflow (Fig. 1). The results show that the fully-constrained gridshells (Fig. 5a, Fig. 6a), which are almost characterized by a linear buckling factor of about 1, also show a nonlinear buckling factor similar to this value or ever larger, meaning that the solutions are admissible also if designed-based on a linear buckling analysis. An exception is for three Barrel Vault gridshells (Fig. 5a) that show a nonlinear buckling factor slightly smaller than one, suggesting the necessity to design by imposing a linear buckling factor larger than one, in order to guarantee safe solution also under nonlinear effects. By observing the results of the Dome configurations, two gridshells characterized by the smallest span (B = 20 m), show both a linear and a nonlinear buckling factor larger than 1, suggesting that in this case the solution is not governed by the buckling susceptibility of the structures, but by the strength of the elements [6]: indeed, the smaller span provide to the gridshell a higher global stiffness. The partially-constrained gridshells (Fig. 5b, Fig. 6b) show that the linear buckling factor is often overestimated with respect to the non-linear one. Despite this, the reaching of a linear buckling factor is very larger than one, assures that also the nonlinear buckling factor is greater than the limit values, so the proposed solutions are feasible. The reason why the buckling factor systematically remains well above the threshold limit lies in the structural behavior of partially-constrained gridshells. In these cases, the beams adjacent to the free-edge are subjected to high concentrations of stress. Consequently, structural design and member sizing are predominantly governed by the cross-sectional strength

requirements of these boundary beams rather than global stability criteria, as also highlighted in [6]. Table 1 supports this discussion showing the values of both linear and non-linear buckling factors, and their differences. The differences between the results in terms of buckling factor obtained by the linear buckling analyses and the GNA, are also testified by the qualitative differences, in terms of shape, between the first buckling modes and the deformed shape obtained by the GNA in correspondence of the reaching of the buckling factor (Fig. 7 and 8).

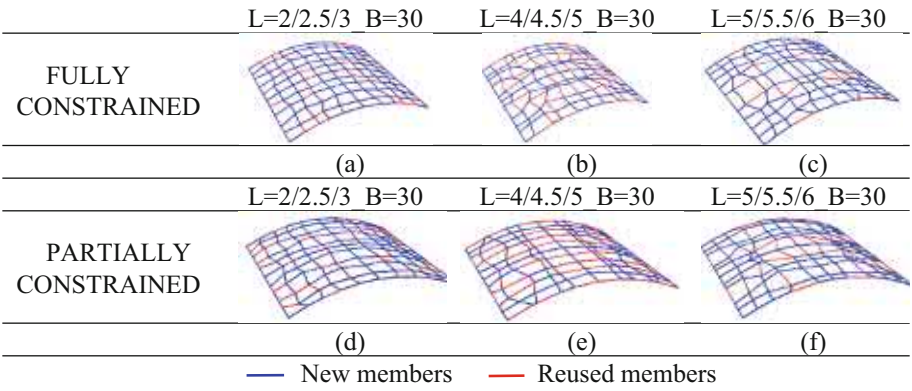


Fig. 3. Barrel Vault: obtained geometries and disposition of new (blue) and reused members (red) for B = 30 m.

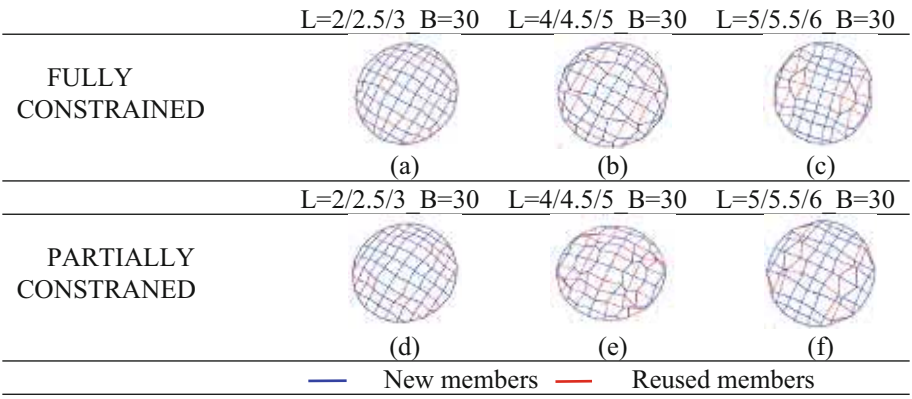
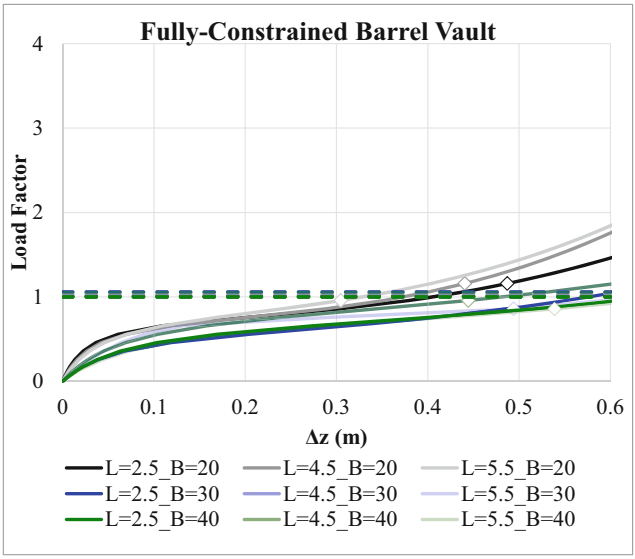
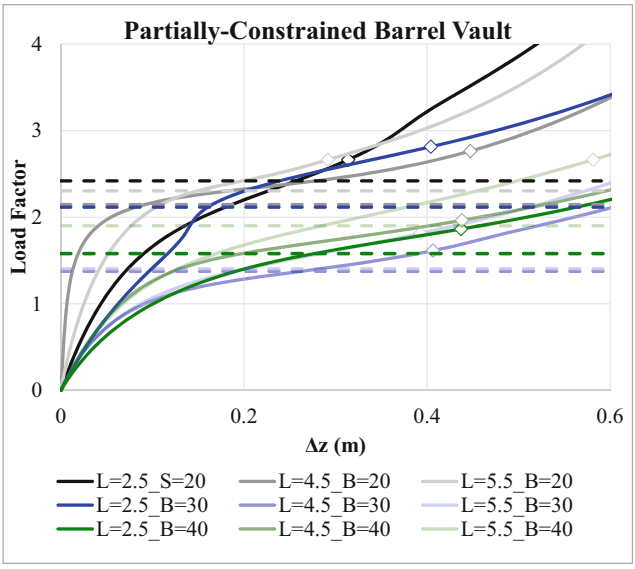


Fig. 4. Dome: obtained geometries and disposition of new (blue) and reused members (red) for B = 30 m.

By comparing the Barrel Vault configuration and the Dome configuration in terms of deformability, it is evident from the pushdown curves (Figs. 5 and 6) and also from the deformed shapes obtained by the GNA in correspondence of the nonlinear buckling factor (Figs. 7 and 8), the Barrel Vault shows higher deformations than the Dome. Indeed, the Dome is characterized by a doble curvature, which provides a higher global stiffness to the structures.

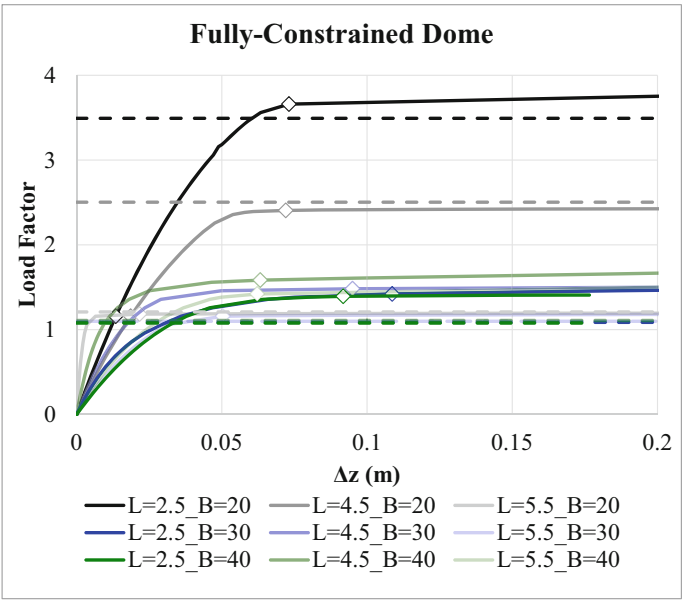


(a)

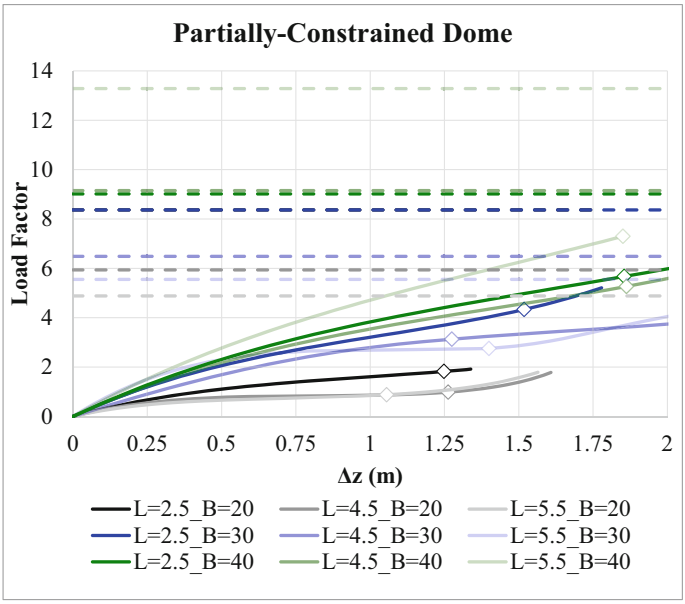


(b)

Fig. 5. Barrel Vault - Geometric Nonlinear Analyses curves: (a) fully constrained solutions; (b) partially constrained solutions.



(a)



(b)

Fig. 6. Dome – Geometric Nonlinear Analyses curves: (a) fully constrained solutions; (b) partially constrained solutions.

As noted in a previous work by the authors [4], the structural response of grid-shells is significantly influenced by imperfections. Nevertheless, they were omitted here to facilitate a preliminary assessment of the solutions. Consequently, incorporating imperfections represents a crucial next step to complete the evaluation in future research.

Table 1. Barrel Vault and Dome: comparison between linear and non-linear buckling factors.

	FULLY CONSTRAINED			PARTIALLY CONSTRAINED		
BARREL VAULT	BF (LIN)	BF (NLIN)	%	BF (LIN)	BF (NLIN)	%
L = 2.5_B = 20	1,1	1,2	8%	2,4	2,7	11%
L = 4.5_B = 20	1,1	1,2	8%	2,1	2,7	22%
L = 5.5_B = 20	1,1	1	10%	2,3	2,7	15%
L = 2.5_B = 30	1,2	0,9	33%	3,1	2,8	11%
L = 4.5_B = 30	1,1	1,2	8%	1,4	1,6	13%
L = 5.5_B = 30	1,1	0,9	22%	1,4	1,8	22%
L = 2.5_B = 40	1,1	1	10%	1,6	1,9	16%
L = 4.5_B = 40	1,1	1,2	8%	1,6	2	20%
L = 5.5_B = 40	1,1	0,9	22%	1,9	2,6	27%
DOME						
L = 2.5_B = 20	3,5	3,7	5%	8,2	1,2	583%
L = 4.5_B = 20	2,5	2,4	4%	5,9	1	556%
L = 5.5_B = 20	1,2	1,2	0%	4,9	1	444%
L = 2.5_B = 30	1,1	1,4	21%	8,4	4,3	95%
L = 4.5_B = 30	1,1	1,5	27%	6,5	3,1	110%
L = 5.5_B = 30	1,1	1,2	8%	5,6	2,8	100%
L = 2.5_B = 40	1,1	1,4	21%	9,1	5,7	60%
L = 4.5_B = 40	1,1	1,6	31%	9,1	5,3	72%
L = 5.5_B = 40	1,1	1,4	21%	13,2	7,3	81%

L=5.5_B=40	1,1	1,4	21%	13,2	7,3	81%

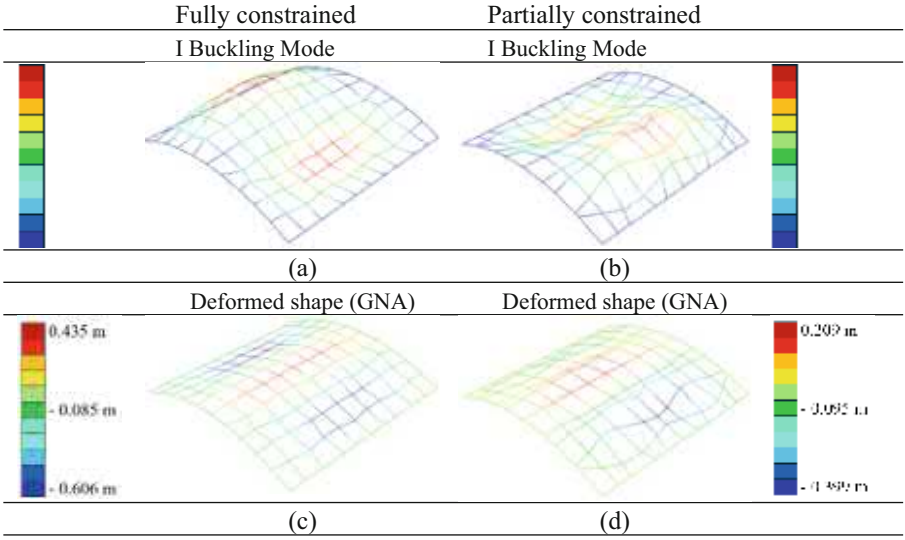


Fig. 7. Barrel Vault: I buckling mode (a,b); Deformed shape from GNA for the (c,d).

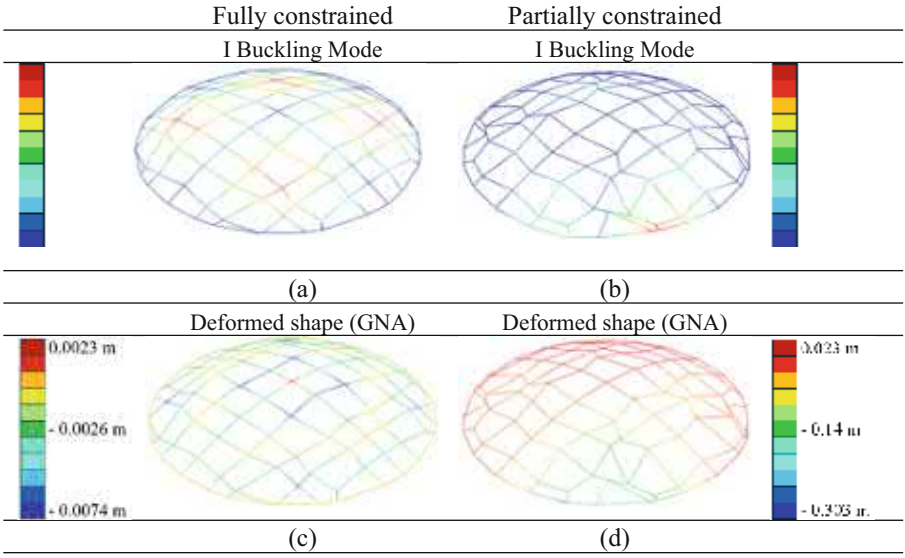


Fig. 8. Dome - I buckling mode (a, b); Deformed shape from GNA for the (c, d).

5 Conclusions

This study evaluated the geometric nonlinear behavior of steel gridshells designed using a workflow, based on structural optimization, that integrates new and reclaimed structural members. By performing Geometric Nonlinear Analyses (GNA) on both single and double curvature gridshells fully- and partially-constrained at the base, the aim of the work was to assess the accuracy and limits of design methods based on linear analyses. The structural assessments show that for fully-constrained configurations, optimization strategies based on linear buckling benchmarks generally yield valid and reliable solutions. However, a slight overestimation of actual structural capacity was observed in some single-curvature cases. This difference suggests that the target linear buckling factor within early-stage design should be set above the limit value to guarantee an adequate safety margin. For partially-constrained configurations characterized by a free edge, the linear buckling factor is systematically higher than the nonlinear one. Despite this overestimation, the final optimized designs remain safe and structurally feasible. This result was obtained because the high stress concentrations close the free-edge force the optimization algorithm to size elements based on cross-sectional capacity rather than global stability, providing an adequate safety margin against global buckling phenomena. These results offer insights on how to calibrate linear buckling thresholds during early-stage design. From these preliminary results, some specific suggestion could be made:

- Fully-constrained double-curvature gridshells (Domes): A threshold of BF = 1.1–1.2 is sufficient for preliminary design. The high global stiffness provided by the double curvature ensures that geometric non-linearities do not significantly reduce stability,
- Fully-constrained single-curvature gridshells (Barrel Vaults): A higher threshold of BF = 1.3, 1.5 should be adopted during the optimization phase. Due to greater deformability, single-curvature layouts exhibit capacity reductions of up to 33% under GNA, which can cause the non-linear buckling factor to drop below unity if designed with a tight target
- Partially-constrained gridshells (with free edges): The design is not governed by buckling phenomena, so the solution is not affected by the limit buckling factor value imposed during the optimization phase.

Future developments will focus on integrating initial geometric imperfections, joint flexibility, increasing the number of case studies, to refine the threshold recommendations.

Acknowledgement. The research leading to these results has received funding from the project ECS 0000024 “Ecosistema dell’innovazione—Rome Technopole” was financed by the EU through the NextGenerationEU plan and MUR Decree No. 1051 23.06.2022 PNRR Missione 4 Componente 2 Investimento 1.5—CUP H33C22000420001.

References

1. Brütting J, Desruelle J, Senatore G, Fivet C (2019) Design of Truss Structures through Reuse. Structure 18:128–137

2. Tomei V (2023) The effect of joint stiffness on optimization design strategies for gridshells: the role of rigid, semi-rigid and hinged joints. Structure 48:147–158
3. European Committee for Standardization (2005) EN 1993–1-1: Eurocode 3: Design of Steel Structures—Part 1–1: General Rules and Rules for Buildings. Brussels, Belgium.
4. Kato S (2014) Guide to buckling load evaluation of metal reticulated roof structures
5. Raffaele L, Bruno L, Laccone F, Venuti F, Tomei V (2024) Holistic performance assessment of gridshells: methodological framework and applications to steel gridshells. J Build Eng 90:109406
6. Tomei V, Grande E, Serpe M, Imbimbo M (2026) A reuse-based optimization approach for the Design of Sustainable Steel Gridshell: Re_Grid project submitted
7. Dassault Systèmes Simulia Corp (2023) Abaqus
8. Bažant ZP, Cedolin L (2010) Stability of structures: elastic, inelastic, fracture and damage theories. World Scientific Publishing, pp 1–1012

Metallic Spans Replacement for 150-Year-Old Viaduct

Riccardo Stroscio[1(✉)], Rebekah Kovacs[1], Mark Scrivener[1], and Douglas Blogg[2]

[1] Tony Gee and Partners LLP, Esher KT10 9QJ, UK
Riccardo.Stroscio@tonygee.com
[2] Tony Gee and Partners LLP, Stonehouse GL10 3UT, UK

Abstract. Barmouth Viaduct is a 150-year-old listed structure and a significant landmark on the north-west coast of Wales in the UK. The bridge is carrying a single-track railway, and a public footpath with cycleway over an estuary. The 820 m long structure consists of the longest timber railway bridge in Great Britain and five metallic spans over the navigation channel.

In 2020 it was recognised that the metallic spans were life expired and a design and build contract was awarded for their replacement. An innovative method for reconstruction of the structure was needed as traditional methods using jack-up barges and cranes introduced additional risk to the project. This paper covers the technical aspects related to the detailed design of the steel superstructure including the main truss members, the steel deck comprising cross girders, rail bearers and direct track fastening. It will also present the main temporary works and the construction methodology adopted for the successful delivery of the heritage structure.

Keywords: Steel Bridge · Truss Structure · Construction Method · Temporary Works

1 Introduction

1.1 The Original Structure

Barmouth Viaduct is a Grade II* listed structure in North Wales that carries a single bi-directional railway track and a public footpath/cyclepath over the tidal River Mawddach Estuary (see Fig. 1). Originally constructed in 1867, the 820 m long viaduct is formed of three different structures: Underbridge 40 is a 113-span timber trestle viaduct forming the southern approach to the five metallic spans over the navigation channel, that is Underbridges 41 (UB-41) and 42 (UB-42).

The original construction of UB-41 and UB-42 included a wooden deck supported on iron piers. A drawbridge was created near its northern end allowing tall ships to pass upstream. The drawbridge was never regularly used as the unveiling of the new railway effectively eliminated the need for traditional boat traffic.

© The Author(s), under exclusive license to Springer Nature Switzerland AG 2026
R. Zanon et al. (Eds.): CTA 2026, LNCE 942, pp. 128–140, 2026.
https://doi.org/10.1007/978-3-032-39505-4_12



Fig. 1. Barmouth Viaduct: from left to right: UB-42, UB-41 and UB-40 (photo courtesy Dominic Vacher)

In 1899, an underwater inspection was undertaken to check the integrity of the drawbridge span's ironwork. It discovered that the supports were severely corroded, undermining its structural integrity and requiring the replacement of the ironwork except for the northernmost piers (Piers P1 and P2).

As part of the repair works in 1902, the wooden drawbridge was replaced with a swing bridge with a 41.5-m-long steel swing span, which rotated around a central pivot, followed by a 36-m-long fixed span. Both these spans comprise the UB-41 spans and are hogback-shaped lattice trusses, supported by pairs of cylindrical iron caissons (Pier P4 and P5), and the turntable was supported on a cluster of four caissons (Pier P3). The UB-42 spans are respectively 11.7 m and 12.2 m simply supported early-steel lattice half-through trusses (see Fig. 2). The single track was connected on longitudinal wheel timbers running along rail bearer troughs supported on cross girders. Infill steel plates spanning between cross girders formed the deck.

A previous structural assessment of the viaduct in 2009 identified the crossbeams and connections were over-utilised due to the limited capacity of the rivets in tension, requiring short term remediation and urgent strengthening to temporarily extend the life of the structure until replacement was possible.

Routine inspections identified ageing and corrosion in the viaduct's timber and metallic elements, consistent with long-term marine exposure. To secure its continued service, Network Rail initiated a £30 m (complete restoration programme of this historical structure under design and build contracts split into phases, starting in 2020. The timber Underbridge 40 was refurbished under a separate contract by Griffiths and is not discussed in this paper.

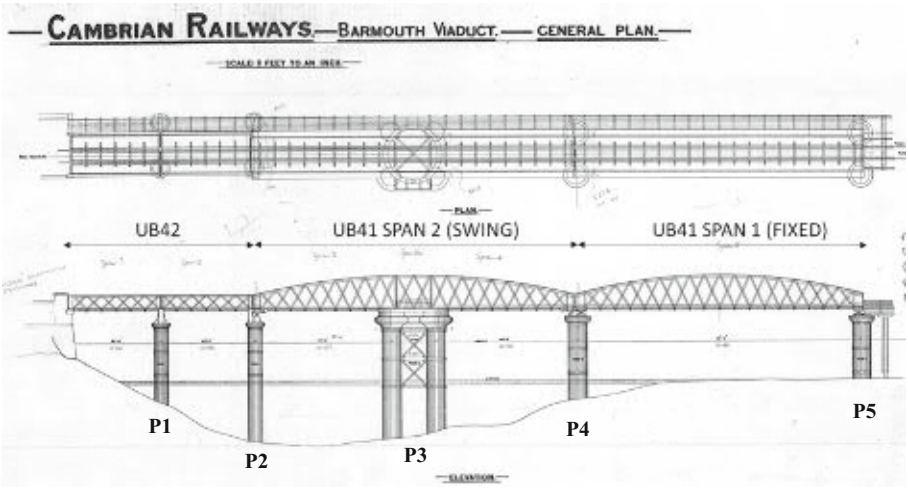


Fig. 2. Barmouth Metallic Spans definition (annotated from 1900 archive drawing)

Previous structural assessments indicated generally a traffic rating capacity of RA-5 to Network Rail CIV/025 [1], except for some connections between the underslung cross girders and the bottom chord of the main truss beams that had rivets acting in tension where the assessed capacity was found to be more critical (RA-3 and less). Several steel sections were identified with loss that was beyond repair (see Fig. 3), and the bridge was found to have a limited residual fatigue life.



Fig. 3. Barmouth Metallic Spans conditions before the replacement with detail of bottom chord

1.2 The Design and Build Tender for Metallic Spans Replacement

In 2020 Network Rail instigated a tender process to choose a design and build team to replace the metallic trusses.

The main challenges of the scheme can be summarized as follows [2]:

Historic Heritage Aspects – Grade II* Listed: The new superstructure had to match the appearance of the existing Grade II* listed structure. At UB-41, the bottom chord was made with double UK T rolled sections while the hogback top chord was formed using a fabricated double T section. Truss diagonals included castellated webs with a geometry that matched the existing braces and bolted to the chord members with splices. Imitation rivet heads were welded along the top face of the top chord to reinstate the historical look of the bridge. Elsewhere, tension control bolts with domed heads were adopted as a rivet lookalike connection. The half-through trusses at UB-42 included single UK T rolled sections matching the existing structure. The lower swing elements were retained, although as agreed with the client, the new structure would not require any opening span. The swing control elements needed to be reinstated but not functioning.

Re-using Substructure and Existing Structure Interfaces: To re-use the existing substructure, the new bridge articulation had to replicate as far as possible the existing arrangement that had performed adequately for over 100 years. Under horizontal rail loading induced by braking and traction forces, it was found that the jointed track is stiffer than the four-column support at Pier P3. As the timber viaduct (UB-40) comprises a series of trestle supports without any longitudinal bracing, the overall longitudinal stability of the whole viaduct (UB-40, UB-41 and UB-42), under the theoretical traction and braking forces, is thus relying on approximately 100 m length of track beyond each abutment. Within UB-42 spans, a pin connection was introduced to connect the rail bearers directly at pier P1. Between span 1 and span 2 of UB-42, a half-joint detail was introduced such that the vertical loads remain centered onto the existing pier. Bespoke steel rocker bearings have been adopted for UB-42 half-through deck while the UB-41 structure is supported on proprietary pot bearings.

Designed to Facilitate Temporary Works Methodology: The above were the challenges for permanent design, but more importantly were the challenges faced in trying to implement the design. The key challenge was how to rebuild these spans working above the tidal estuary. Access was difficult from all directions, north abutment on rocky outcrop, south via the timber viaduct, below has the estuary.

Water depth varies considerably with fast flowing water up to 9knot currents over a 5 m tidal range with sections almost drying out, and in other places depths up to 13 m.

Some options that were considered for the proposed construction were a causeway but dismissed due to SSSI requirements (Site of Special Scientific Interest, which is a designation in UK identifying land or water of high importance for rare wildlife, habitats or geological features). Large pontoons for crane and bridge decks were also considered, dismissed due to requirement to sail over 80 miles by sea from Holyhead in winter, and tidal range in the estuary. Spud leg pontoons could have been used to counter the tidal range, however the presence of the 33Kv cable beneath the seabed adjacent to the structure would have been an issue for the location of spud legs. To add to all this there were concerns regarding the stability of the piers without the stabilising influence of the bridge decks.

Limited Construction Period: The structure and those using it significantly contribute to the heritage, commerce and tourism of the area. As well as being a listed structure

and the importance of conserving the original heritage with the necessary listed building consent, the construction needed to minimise disruption to the nearby town, railway and pedestrian traffic, particularly during the tourist season, by utilising a 12-week track blockade.

The successful tender was awarded to Griffiths Contractors who employed Tony Gee and Partners as permanent and temporary works designers. The team developed a unique methodology to meet the site-specific constraints. The solution involved constructing the new girders offline and driving the 200 t arrangement of temporary and permanent steelwork along the railway track to position each hogback span of UB-41 inside its predecessor before dismantling the old superstructure around it.

2 Detail Design of Permanent Works

2.1 Design and Assessment Criteria

The new decks have been designed to sustain RA10 railway traffic at a speed of 20mph (32 km/h) to UK railway standard [1] including dynamic factor and load classification factor of 1.21. Due to the track having a direct fastening arrangement, at ultimate limit state only, the RA10 load model was modified to include one of the railway axles as 600kN. Deformation criteria are as per Eurocodes and UK railway standard NR/L3/CIV/020 [3]. The fatigue criteria were set as 5 million tonnes per annum based on LM-71 load model to BS EN 1991–2 [4] as the single track is mainly used by passenger trains.

A 5.0 kPa uniformly distributed load was considered on the 1.8 m wide pedestrian/cycle footpath. Finally, the superstructure was also verified for accidental vessel impact from the mast of a sailing boat.

The assessment criteria for the reused substructure were RA5 at 20mph (32 km/h) to UK railway standard [1]. The stability of the caissons was verified with effects from traction and braking loads from the railway as well as the hydrodynamic actions arising from a peak tidal flow of 9 knots (4.51 m/s). The existing pier bracings within the caissons were redesigned and repaired as part of the scope.

2.2 Deck Details

The single-track runs between the main truss girders spaced at 5.334 m center to center and was originally connected on longitudinal wheel timbers running along rail bearer troughs supported on cross girders with infill steel deck plates. In the new configuration, each rail is supported by direct fastening using the proprietary Pandrol VIPA system at typically 600 mm centers and directly above the steel rail bearers (UKC 254x254x89). The interface between rail bearers and the cross girders includes a welded connection with end plates.

The 12 mm thick steel deck plate is also welded to the top flanges of the rail bearers and the cross girders. The cross girders are underslung to the main trusses as per existing arrangement. They are made of UKC 356x368x202 at typically 2 m centers and bolted

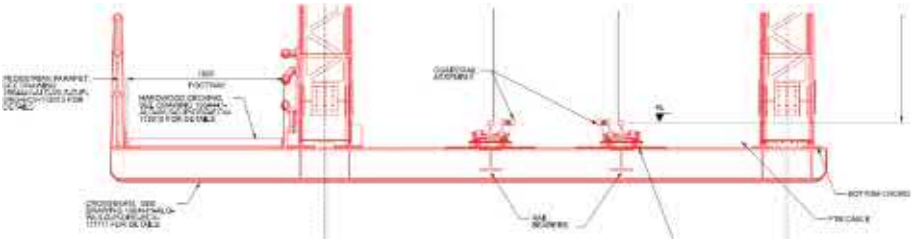


Fig. 4. Typical deck cross section



Fig. 5. Track with direct fastening details on bridge deck (photo courtesy Dominic Vacher)

to the bottom chords of the trusses with a cantilever portion to support the footway that includes a timber decking (see Figs. 4 and 5).

To enable the segmental assembly of the new deck from below the trusses, the steel deck panels were split based on the erection methodology and works sequence. Bolted splices were introduced within the steel deck plate and longitudinal bearers at typically 2 m centers for UB-42 (i.e. one cross girder per panel) and 4 m for UB-41 (including two cross girders per panel). Typical details of deck splices are shown in Figs. 6 and 7.

Due to their connection to the bottom chord of the truss, the deck plate and the longitudinal rail bearers form an integral part of the global system. The bottom chords were designed and verified at ultimate limit state without reliance on the contribution from the deck plate system. However, a global analysis was also undertaken considering the composite contribution of the plate/bearers as to extract the longitudinal stresses induced for the design of these elements (including the connections) and verification of the structural deformations.

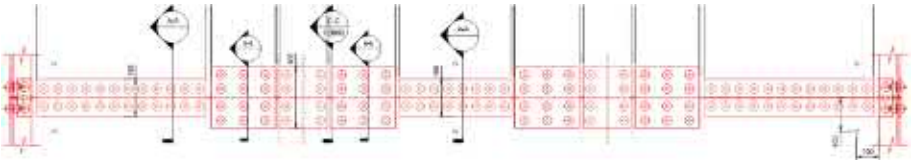


Fig. 6. Typical deck splice: plan view showing deck plate and rail bearers

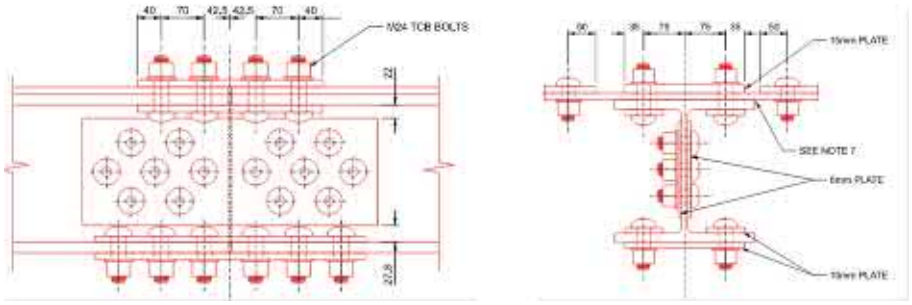


Fig. 7. Typical Rail bearer splices: elevation (left) and cross section (right)

2.3 Bridge Articulation Details

To maintain the vertical load distribution onto the existing supports, the structural articulation was reinstated. Due to the geometrical constraints at Pier P1, it required the introduction of a steel half-joint allowing spans 1 and 2 to be kept in a simply supported configuration for UB-42. The half-joint is created within the end of the trusses using rocker bearings set within stiffened webs as shown in Fig. 8. As the half-joint is aligned with the pier-caisson centerline, it mitigates any eccentricity effects onto the existing caisson foundation that would be caused by the effect from traffic loading over one adjacent span only.

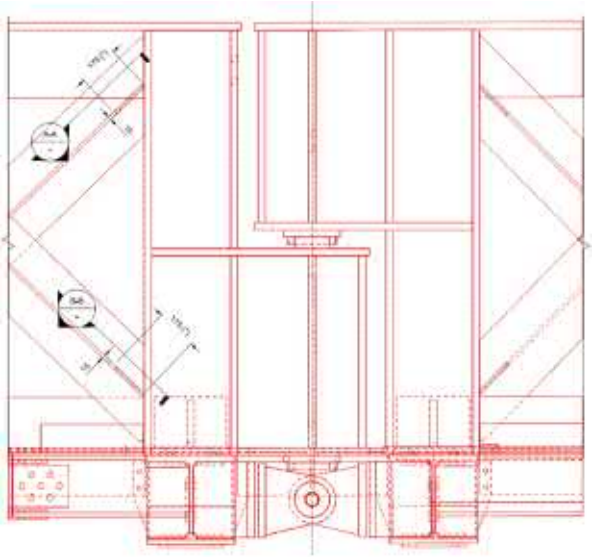


Fig. 8. UB-42 half-joint detail at Pier P1

The railway track includes traditional system with joints (i.e. not continuously welded rails). For direct transfer of longitudinal forces to the bridge abutment, in addition to the steel rocker bearings articulation, span 1 and span 2 are coupled at rail bearer level with a pin connection as shown in Fig. 9.

2.4 Design Life and Maintenance

The new superstructure has been designed to modern standards with 120-year design life in line with UK Network Rail standard approach. The new steel bracings of the caissons and the new anchors for of masonry abutment have a minimum of 60-years design life while the parts of the existing pier caissons that have been repaired have 30-years design working life as agreed with Network Rail.

To mitigate the risk of future corrosion, the new superstructure has been detailed to prevent water traps where possible. For example, drainage points were introduced within the steel deck plates to allow water to freely discharge into the estuary. Most parts of the new superstructure are accessible for future inspection and maintenance. The new superstructure has been protected with N4 coating to Network Rail Specifications (18 to 22 years of expected service life prior maintenance). The existing caissons have been protected using a certified three-layer moisture-cure polyurethane coating suitable for marine environment and approved by Network Rail UK (XM92-MCU-174 by Steelpaint), which has an average service life of 15 to 25 years before the first major maintenance is required.

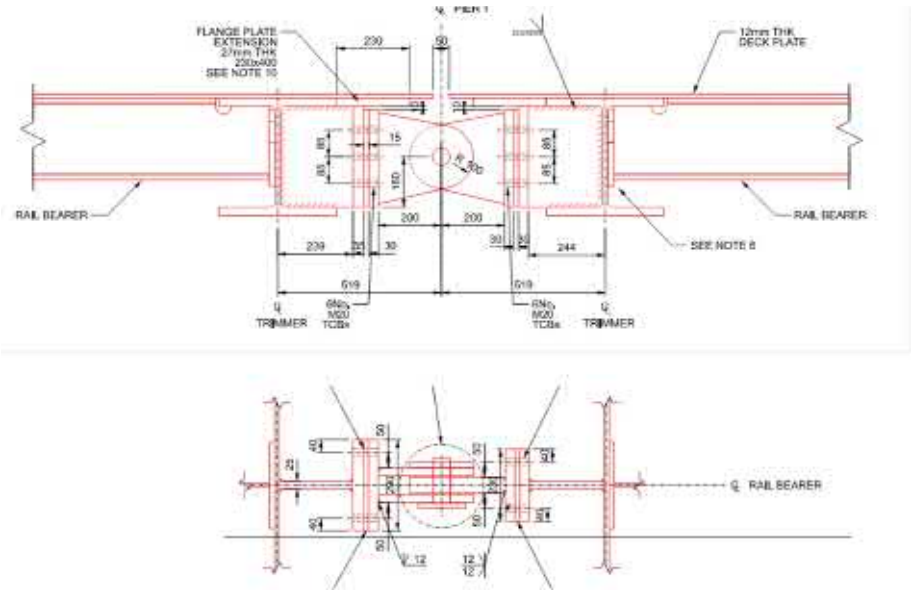


Fig. 9. UB-42 rail bearers' connections at Pier P1: elevation (top) and plan (bottom)

3 Demolition and Replacement Method

3.1 Overall Methodology

A unique solution that was employed by the design and build team for UB-41 spans: it used the Permanent works girders for temporary support throughout construction phases, which removed the requirements for craneage within the estuary, as the new main beams created a 85 m long runway to allow two bespoke gantries to operate – these were used for both the demolition of the existing and the installation of the new cross girder/deck panels (Fig. 10).

This solution ensured that continuous longitudinal support was provided between the piers. At UB-42, the work was more conventional and mainly completed with a TXM rail mounted monster crane [5].

3.2 Preparatory Work, Pre-Assembly and Transportation

The new truss girders were constructed offline and transported to the site. For the installation of new UB-41 trusses, it was decided to drive them along the track 800 m from the contractor's site compound to the East, which included crossing the recently refurbished UB-40 timber viaduct.

To ensure that there were no issues with driving 200 T of beams and temporary works, a 90 m long trial track was created within the site compound. The existing track was fully surveyed at 3 m intervals to mitigate risk of derailment during the works. The trial track replicated the track defects to be representative of expected geometry during



Fig. 10. UB-41 gantries after demolition of existing superstructure (photo courtesy Dominic Vacher)



Fig. 11. UB-41 transportation: crossing timber viaduct UB-40

transportation. The beams were transported onto the existing structure using rail Unimog tractor and 6 rail trailers (Fig. 11).

With the new truss girders fitted inside the existing structure, it could be jacked onto temporary supports at the piers to release the rail trailers.

3.3 Dismantling Existing Superstructure

With the gantries in position, the demolition of UB-41 could start. The existing spans were split into seven sections longitudinally with each section supported off the new truss girders and temporary works using four high strength bars. Once fully supported, each section of the existing superstructure (comprising steel truss and deck with cross girders and deck plate) was cut away in a specific sequence so that it would be supported by the new truss girders.

The gantry cranes were then used to hold of a 23 t section lift and lowered it to an awaiting pontoon below. The sections were transported to the beach where shears would cut them up for recycling (Fig. 12).



Fig. 12. UB-41 dismantling existing superstructure from new truss girders and gantries

3.4 Lateral Slide, Jacking and Deck Installation

As the new truss girders were transported inside the existing structure, they required sliding transversally to their final lateral position. This was achieved using eight 20 t push pull jacks and each truss was moved by approximately 960 mm. To achieve this, all the connection elements from the temporary work to the main truss girders were designed to either be removed prior to the slide or extend during the slide.

The completion of this stage allowed the jacking down of the truss girders onto their correct bearing levels and the start of installation for the new deck panels. Prior to transportation of the deck segments, an access platform was suspended from each deck panel. The deck details included a vertical gusset plate to the top of each cross girder that was bolted to the main girder stiffener from above so the gantry crane could be released prior to connecting all the permanent works bolts from below (Fig. 13).



Fig. 13. UB-41 New deck panel installation

4 Conclusions

Barmouth viaduct metallic spans required replacement after over 100 years in the marine estuary. The five trusses to be replaced were in an environmentally sensitive coastline and located at the end of the longest timber railway viaduct still operational in the UK. The unique de-construction and re-construction method adopted by the Design and Build team proved to be the right solution to meet the site-specific constraints.

The reconstruction was completed in November 2023 and successfully handed back on time much to the delight of the Barmouth residents and admirers of the old bridge who had been following the construction works closely throughout the blockade (Fig. 14).



Fig. 14. Completed works (photo courtesy Dominic Vacher)

5 Acknowledgements

The authors would like to thank Jon Powell, project director, for Tony Gee and Partners LLP during tender design, preliminary design and detail design of Barmouth Metallic Span replacement. The authors wish also to thank the design and build contractor Alun Griffiths Contractors, and the end client Network Rail for permission to publish this paper.

References

1. Network Rail (2006) NR/GN/CIV/025 ISSUE 3. The structural assessment of underbridges, NR, London, UK
2. Ashworth T, Scrivener M, Blogg D, Richardson S, Tod J, Cheah R (2026) The replacement of Barmouth viaduct metallics from concept to construction. Emerald Publishing Limited, Proceedings of the Institution of Civil Engineering
3. Network Rail (2011) NR/L3/CIV/020 issue 1, Design of Bridges, NR, London, UK
4. BSI (2010) BS EN 1991–2:2003 Eurocode 1: actions on structures — part 2: traffic loads on bridges. BSI, London, UK
5. Scrivener M, Blogg D, Cheah R, Stroscio R, Ashworth T (2026) Ensuring stability for all stages of Barmouth viaduct metallic spans replacement. In: Structural engineering international. International Association for Bridge and Structural Engineering manuscript in press

Steel Connections

Optimized Numerical Model for TTI Connectors

Paulo H. R. Moura[1(✉)], Ramon Silva[1], Jerfson M. Lima[2], Luciano M. Bezerra[1], and Jorge Bonilla[1]

[1] Department of Civil and Environmental Engineering, University of Brasília, Brasília, Brazil
phrmoura035@gmail.com

[2] Campus Russas, University of Ceará, Brasília, Brazil

Abstract. Shear connectors ensure the transfer of forces at the interface of composite steel–concrete structures. Although the headed stud is the conventional solution, the Truss Type Isosceles (TTI) shear connector has emerged as a promising alternative due to its ease of fabrication, ductile behavior, and economic feasibility. Because experimental push-out tests are costly, finite element models (FEMs) are widely employed, although they often require significant computational resources owing to material and contact nonlinearities. In this context, this study developed a three-dimensional nonlinear finite element model (FEM) in ABAQUS with the objective of reducing the computational cost associated with the analysis of the TTI connector. The proposed strategy consisted of discretizing the connector using beam elements instead of the solid elements commonly adopted in the literature, thereby drastically reducing the number of nodes and mesh elements. The model was validated against experimental and numerical results available in the literature by comparing the load–slip curves, failure modes, and shear resistance. The results demonstrated that the proposed discretization strategy did not compromise the accuracy or efficiency of the numerical model, providing a satisfactory representation of the connector behavior. Furthermore, the proposed approach achieved a substantial reduction in computational cost and processing time, establishing it as a highly efficient and computationally inexpensive methodology for the analysis of composite steel–concrete structures.

Keywords: Truss shear connector · Push-out test · Numerical model · FEM

1 Introduction

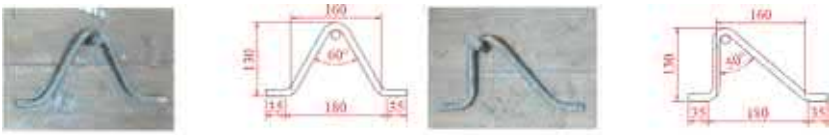
Composite steel–concrete structures optimize structural performance by combining the high tensile strength of steel sections with the compressive strength

Supported by University of Brasília.

© The Author(s), under exclusive license to Springer Nature Switzerland AG 2026
R. Zanon et al. (Eds.): CTA 2026, LNCE 942, pp. 143–155, 2026.
https://doi.org/10.1007/978-3-032-39505-4_13

of concrete slabs. The efficiency of these systems depends directly on the transfer of longitudinal shear forces at the steel–concrete interface. Although this transfer involves adhesion and friction, current design standards [1,2,8,12] consider only mechanical shear connectors to perform this function. The headed stud is the most widely used shear connector worldwide due to its high installation productivity. However, its application presents limitations, such as the need for high-power welding equipment (≈ 225 kW), susceptibility to fatigue under cyclic loading, and high import costs, which can compromise project economic feasibility [4–6,19,24].

To overcome these limitations, several alternative shear connectors have been investigated [9–11], including Perfobond [16], Crestbond [25], V-shaped [5,7], V-angle [24], Y-type [14], top-hat [15], rolled-steel [23], and hybrid welded–bolted connectors [13]. These studies aimed to increase shear resistance, improve ductility, and enhance fatigue performance through experimental tests and numerical analyses.



(a) TTI shear connector (b) TTR shear connector

Fig. 1. Truss type shear connector geometries in mm [4].

Among these alternatives, Bezerra et al. [4] developed the Truss-Type Shear Connector (Fig. 1) in two configurations registered with the INPI: isosceles triangular (TTI connector, Fig. 1(a)) and right triangular (TTR connector, Fig. 1(b)). Manufactured from widely available CA-50 steel bars, this connector eliminates specialized welding equipment and exhibits a geometry fully compatible with precast slabs. The TTI model consists of legs inclined at 60°, horizontal bases for conventional welding, and a 40-mm-long upper bar (⌀ 16 mm) to prevent vertical separation (uplift).

Bezerra et al. [4] conducted 24 push-out tests according to Eurocode 4 [12], demonstrating that the 12.5-mm-diameter TTI connector achieved a shear resistance of 104.50 kN, outperforming the TTR connector (87.50 kN) and the reference 19.0-mm headed stud (62.45 kN). Furthermore, these truss-type connectors were classified as ductile due to their excellent plastic deformation capacity prior to failure.

These results motivated subsequent studies. Lima et al. [20] developed three-dimensional nonlinear finite element models (FEMs) in ABAQUS to investigate geometric and material parameters, proposing a mathematical equation to predict nominal shear resistance. However, this equation was derived from a non-linear regression based on a dataset of only 9 samples, owing to the high

computational cost of the numerical models (19 h of processing time). Subsequently, Lima et al. [18] evaluated geometric variations and the reorientation of the TTR connector, which increased shear resistance by 17.86% compared to its original orientation. More recently, Lima et al. [19] confirmed the effectiveness of truss-type connectors in full-scale composite beams, while Moura et al. [21] simplified the connector discretization. However, applying this simplified strategy to the isosceles truss-type connector (TTI) remains unexplored in the literature. Despite these advances, existing 3D finite element models require substantial computational resources and long processing times due to the detailed discretization of the TTI connector, limiting their efficiency in complex simulations involving material and contact nonlinearities.

Literature review highlights the structural viability of the TTI connector due to its high load capacity in push-out tests and sound global performance in composite beams [19]. However, existing 3D numerical models for the TTI connector rely exclusively on solid elements for connector discretization [17]. Although accurate, these models incur high computational costs (19 h/analysis), hindering the large-scale parametric studies required to propose comprehensive analytical equations and enable the technical implementation of the TTI connector in practical designs. Although beam-element discretization was recently tested for the right-angle connector (TTR) [21], its feasibility, geometric adaptation, and calibration had not yet been investigated for the isosceles connector (TTI). Therefore, the main contribution and originality of this work lie in the development and validation of an ultrafast numerical model applied specifically to the TTI connector, establishing a geometric idealization strategy that replaces solid elements with 3D beam elements (B31) in ABAQUS software.

Therefore, this study develops a computationally efficient three-dimensional nonlinear finite element model (FEM) in ABAQUS for the TTI connector. The novelty lies in a discretization strategy using beam elements for the TTI connector, significantly reducing computational cost and processing time without compromising accuracy. The proposed model accounts for constitutive and contact nonlinearities, is validated against experimental data from Bezerra et al. [4], and is compared with the solid-element numerical model by Lima et al. [20], enabling a direct evaluation of accuracy and computational efficiency for both approaches.

2 Finite Element Model

This section describes the three-dimensional nonlinear finite element model (FEM) developed in ABAQUS, which accounts for material and contact nonlinearities. Individual components were modeled separately using extrusion and wire features.

2.1 Idealization of the TTI Shear Connector Using 3D Beam Elements

To reduce computational cost, the TTI connector was discretized using three-dimensional beam elements following Moura et al. [21]. This strategy minimizes the number of elements and structural complexity since truss-type connectors are predominantly subjected to axial forces (Sect. 1). The idealization process is illustrated in Fig. 2.

Based on the experimental specimen tested by Bezerra et al. [4] (Figs. 2a–b), a simplified geometry was established along the centerline (Fig. 2c). The upper pin and horizontal base portions welded to the steel section were removed (Fig. 2d), and the curved base segments were straightened to achieve the final idealized geometry for numerical discretization (Fig. 2e).

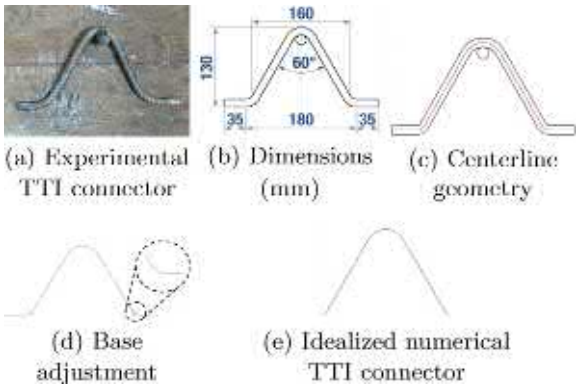
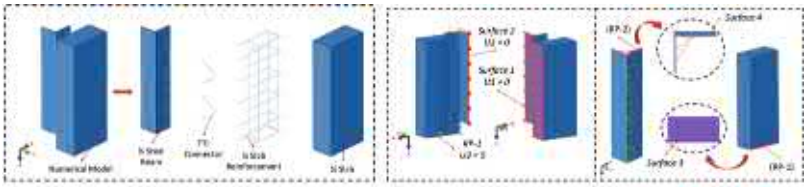


Fig. 2. Idealization process of the TTI shear connector using 3D beam elements.

2.2 Geometry, Assembly, and Boundary Conditions

Taking advantage of symmetry conditions, only one-quarter of the experimental specimen was modeled [6,18,20]. The concrete slab ($300 \times 150 \times 750$ mm) and the steel section (W250×73, 700 mm length) were created using extrusion techniques, while the TTI connector and slab reinforcement were modeled using wire features in ABAQUS. The complete assembly is shown in Fig. 3(a).

To reproduce the experimental push-out test, appropriate boundary and loading conditions were applied (Fig. 3b). Nodal displacements on Surfaces 1 and 2 were restrained in the $U1$ (X-axis) and $U2$ (Y-axis) directions, respectively, to satisfy symmetry. Reference points RP-1 and RP-2 were coupled to Surfaces 3 and 4, respectively, using coupling constraints [20,21]. Displacement at RP-1 was restrained in the $U3$ (Z-axis) direction to simulate the support condition, while a displacement-controlled loading rate of 1 mm/s was applied at RP-2 on Surface 4.



(a) Developed finite element model (b) Boundary conditions and loading

Fig. 3. Numerical model setup: geometry, assembly, and boundary conditions.

Due to material, contact, and geometric nonlinearities, a dynamic explicit analysis procedure was adopted. This procedure is suitable for quasi-static analyses if inertial effects are controlled. According to the ABAQUS User Manual (2021), an analysis is considered quasi-static when the kinetic energy remains below 10% of the internal energy throughout the simulation, a methodology validated by several researchers [14,18,20–22].

2.3 Constitutive Models

The Concrete Damage Plasticity (CDP) model was adopted in ABAQUS 2021 with a non-associated flow rule and a Drucker–Prager hyperbolic plastic potential. Following Nguyen and Kim [22], the plasticity parameters were set to: dilation angle $\psi = 20°$, eccentricity $\varepsilon = 0.1$, and biaxial-to-uniaxial compressive strength ratio $f_{b0}/f_{c0} = 1.16$.

The uniaxial compressive stress–strain curve of concrete is divided into three regions (Fig. 4a). The first region corresponds to the linear elastic regime up to $0.4f_{ck}$, being defined by the mean elasticity modulus calculated by Eq. 1 according to Eurocode 2 [8].

$$E_{cm} = 9.5\sqrt[3]{f_{ck} + 8} \tag{1}$$

The second region, corresponding to the hardening regime, comprises the interval between $0.4f_{ck}$ and f_{ck} and is represented by a nonlinear parabolic curve calculated by Eq. 2 [8], where the strain at peak stress is $\varepsilon_{c1} = 0.0022$. Finally, the third region corresponds to the softening regime and is represented by a descending linear branch down to rf_{ck} at a strain of $\alpha\varepsilon_{c1}$. The parameters n and k are calculated by Eqs. 3 and 4, respectively.

$$\sigma_c = \left(\frac{kn - n^2}{1 + (k-2)n}\right) f_{ck} \tag{2}$$

where:

$$n = \frac{\varepsilon_c}{\varepsilon_{c1}} \tag{3}$$

$$k = 1.1E_{cm}\frac{\varepsilon_{c1}}{f_{ck}} \tag{4}$$

Concrete tensile behavior comprises two regions (Fig. 4a). The first region corresponds to the linear elastic regime defined by the tensile strength f_t (Eq. 5) [12] combined with E_{cm}. The second region corresponds to the softening regime, represented by a descending linear branch dropping to zero stress at a final strain of $\beta\varepsilon_{ck}$.

$$f_t = 0.3 f_{ck}^{2/3} \tag{5}$$

The parameters r, α, and β are used to adjust the constitutive curve of the concrete and are directly related to its mechanical behavior. Based on the formulations by Ellobody et al. [11] and following a procedure analogous to that adopted by Nguyen and Kim [22], a parametric calibration step was performed to determine the set of values that best represented the mechanical behavior of the concrete in the *push-out* test. During this process, the parameters r, α, and β were systematically and iteratively varied, with the numerical load–slip curve being plotted and superimposed on the corresponding experimental response for each trial. The final calibration values selected were those that provided the best match between the numerical and experimental curves [[3]]. This procedure was carried out individually for each analyzed TTI connector diameter (8.0 mm, 10.0 mm, and 12.5 mm). The final values obtained in this calibration phase are presented in Table 1. Concrete properties include $f_{ck} = 34$ MPa, $E_{cm} = 33022.25$ MPa [4], Poisson's ratio $\nu = 0.2$, and density 2.5×10^{-6} kg/mm^3.

Table 1. Parameters of the concrete constitutive model.

Diameter	r	α	β
8.0 mm	0.65	11	50
10.0 mm	0.54	5	30
12.5 mm	0.54	2	60

A trilinear elastoplastic model was adopted for the Brazilian CA-50 steel used in the TTI connectors and reinforcement bars (Fig. 4b). It comprises a linear elastic range up to the yield stress σ_{ys}, a linear hardening branch up to the ultimate stress σ_{us}, and a perfectly plastic plateau. This model employs the Von Mises yield criterion and an associated flow rule. Mechanical properties from Bezerra et al. [4] are summarized in Table 2, using $\nu = 0.3$ and density 7.85×10^{-6} kg/mm^3.

Table 2. Mechanical properties of CA-50 Brazilian steel.

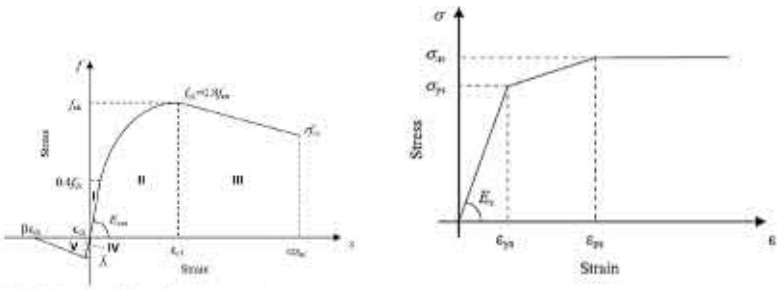
Part	E_s (MPa)	σ_y (MPa)	σ_u (MPa)	ε_u (%)
TTI 8.0 mm	198400	561.2	663.2	0.6
TTI 10.0 mm	194500	591.6	722.4	0.6
TTI 12.5 mm	195300	595.3	716.6	0.6

Note: Slab reinforcement bars share the 10.0 mm connector properties.

For the MR250 steel beam, which experiences low stress levels [4,18], a linear elastic model was used, defined by $E = 210000$ MPa, $\nu = 0.3$, and density 7.85×10^{-6} kg/mm^3.

2.4 Interactions and Mesh Discretization

The TTI shear connector and the reinforcement were embedded into the concrete slab using the *Embedded Region* constraint, while a *Tie* constraint was applied between the connector base and the steel section to simulate the weld connection (Fig. 5a). To replicate the lubricant applied during standardized push-out tests [12], a surface-to-surface contact interaction was defined at the steel–concrete interface (Surfaces 1 and 2 in Fig. 5a). This interaction combined a *frictionless* tangential behavior to allow free sliding with a *hard contact* normal behavior to prevent components interpenetration.



(a) Uniaxial behavior of concrete (adapted from [22])

(b) Trilinear elastoplastic model for CA-50 steel

Fig. 4. Constitutive material models utilized in the finite element formulation.

Independent meshes were generated for each part of the model (Fig. 5b). The concrete slab and the steel beam were discretized using eight-node three-dimensional brick elements with reduced integration (C3D8R), which yielded the best balance between accurate load–slip curves and computational cost during model calibration. Slab element sizes varied by connector diameter–15 mm (for 8.0 mm TTI), 25 mm (for 10.0 mm TTI), and 35 mm (for 12.5 mm TTI)–while the steel beam mesh was kept constant at 17.5 mm.

The connector was discretized using two-node three-dimensional Timoshenko beam elements (B31) with a mesh density of 3.25 mm. This simplification was a key strategy to reduce computational cost (Sect. 2.1), resulting in models with only 92 finite elements and 134 nodes. This layout is significantly more efficient than the 2105 elements and 2080 nodes employed in the reference model by Lima et al. [20], which was validated against experimental data from Bezerra et al. [4]. Finally, the reinforcement bars were discretized using two-node three-dimensional truss elements (T3D2) with a mesh size of 28 mm.

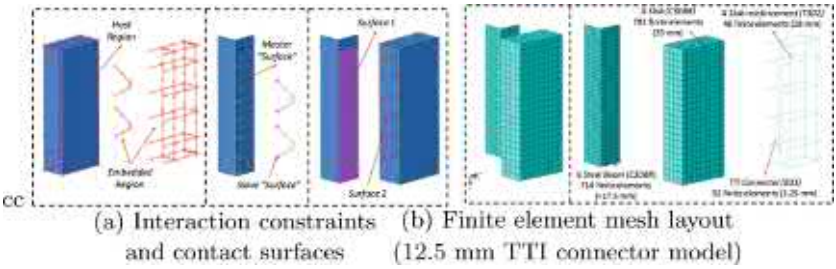


Fig. 5. Numerical model setup: interaction properties and finite element mesh.

A systematic mesh sensitivity study was conducted for both the concrete slab and the TTI connector. For the concrete slab, element sizes ranging from 15 mm to 40 mm (in increments of 5 mm) were evaluated, alongside different element formulations (C3D8R, C3D8, and C3D4). The numerical model exhibited low sensitivity to both the slab element formulation and the connector element size (tested at 1.0 mm, 2.0 mm, 3.25 mm, and 6.5 mm—the latter suggested by ABAQUS). The connector mesh size primarily influenced the computational processing time, with larger element sizes leading to increased processing times. Regarding the concrete mesh size, the model demonstrated higher sensitivity; however, this did not compromise the accuracy of the results. Ultimately, the mesh size was selected to achieve the lowest computational effort while maintaining overall precision.

3 Validation of the Numerical Model

The numerical model calibration (See 2.3) consisted of determining parameters r, α, and β based exclusively on fitting the load–slip curve. Subsequently, during the validation phase, a comprehensive verification of the proposed numerical model was conducted. This validation evaluated the load–slip behavior, the accuracy of the predicted shear resistance, and the computational efficiency gains.

The numerical model was validated using the experimental data from Bezerra et al. [4] and the numerical results from Lima et al. [20]. The experimental study [4] provided the required parameters for the model development, including specimen geometry, material properties, loading, and boundary conditions, serving as the baseline for calibration and validation.

The numerical work of Lima et al. [20] was adopted as a reference to evaluate the accuracy of the proposed simplified model and quantify the reduction in computational cost. This comparison is highly advantageous since both numerical models were calibrated against the same experimental program [4]. The novelty of this study lies in discretizing the TTI connector using three-dimensional beam elements, whereas Lima et al. [20] employed three-dimensional solid elements. This allows a direct assessment of computational cost reduction and its impacts on accuracy.

3.1 Load–Slip Curves

Figure 6 presents the numerical and experimental load–slip curves. Figures 6(a)–(c) show the comparison for the 8.0, 10.0, and 12.5 mm TTI connectors against experimental data [4], while Fig. 6(d) compares the proposed model with the numerical results from Lima et al. [20] for all diameters.

A good agreement is observed between the numerical and experimental curves, particularly for the 12.5 mm connector (Fig. 6c), where the experimental curves exhibit low dispersion. Conversely, for the 10.0 mm connector (Fig. 6b), a significant divergence exists among the experimental results. Consequently, the numerical curve captures the mean response of the test data, confirming the efficiency of the simplified model.

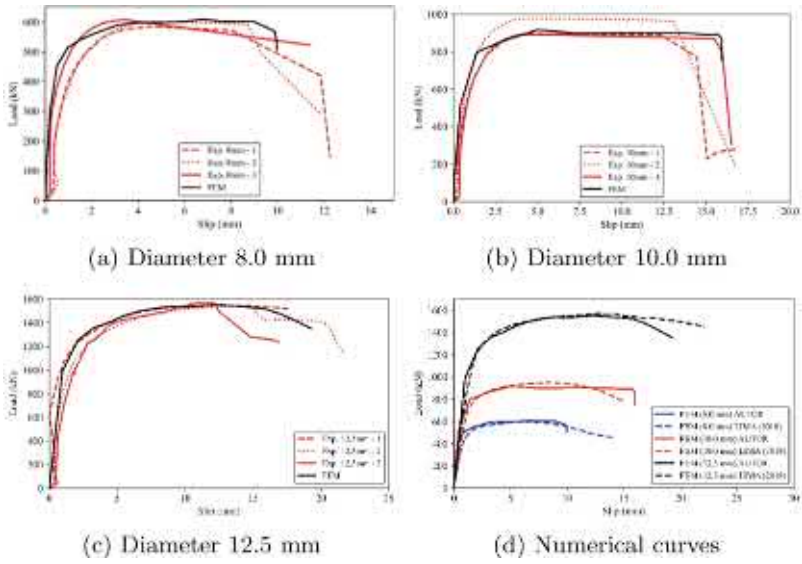


Fig. 6. Comparison of load–slip curves.

Figure 6(d) reveals an excellent agreement between the proposed model and the reference model [20], proving that the simplified connector discretization reproduces the push-out test behavior accurately. However, a subtle difference occurs after the peak load: the beam elements in this study cause a more abrupt stiffness reduction, whereas the three-dimensional solid elements used by Lima et al. [20] exhibit a more gradual degradation.

This behavior is associated with the element formulations. Due to their simplified kinematic representation, beam elements drop stiffness suddenly under high strain levels. In contrast, solid elements represent the internal stress redistribution along the connector cross-section in a more refined manner, resulting in a smoother transition along the descending branch of the load–slip curve.

Although the primary scope of this study focuses on the macroscopic load–slip response and ultimate capacity, the evolution of von Mises stresses highlighted critical stress concentrations at the base of the connector legs and in the adjacent concrete, consistent with the localized crushing failure trends reported in the literature. Furthermore, the stability of the quasi-static explicit analysis was confirmed through internal energy monitoring, maintaining kinetic energy strictly below 10% of the internal energy throughout the simulation. Future investigations focusing on microstructural damage evolution and detailed energy dissipation tracking could provide further insights into local failure mechanisms.

3.2 Shear Resistance

Table 3 presents the comparison of the shear resistance (Q_{TTI}), corresponding to the ultimate load capacities obtained experimentally and numerically. Column 1 identifies the experimental specimens from Bezerra et al. [4]. Column 2 lists the experimental values ($Q_{\mathrm{TTI,E}}$). Columns 3 and 4 report the numerical peak loads obtained in the present study ($Q_{\mathrm{TTI,FEM}}$) and by Lima et al. [20] ($Q_{\mathrm{TTI,Lima}}$), respectively. Columns 5 and 6 display the ratios comparing the proposed numerical model to the experimental data ($R_{\mathrm{E}} = Q_{\mathrm{TTI,FEM}}/Q_{\mathrm{TTI,E}}$) and to the numerical literature ($R_{\mathrm{Lima}} = Q_{\mathrm{TTI,FEM}}/Q_{\mathrm{TTI,Lima}}$). Additionally, relative percentage errors ($\mathrm{Error} = |Q_{\mathrm{TTI,FEM}} - Q_{\mathrm{TTI,E}}|/Q_{\mathrm{TTI,E}} \times 100$) are provided. At the bottom of the table, the mean values (μ) and Coefficients of Variation ($\mathrm{CoV} = \sigma/\mu \times 100$, where σ is the standard deviation) are summarized for the calculated ratios and errors.

Table 3. Experimental and numerical shear resistance.

Experimental specimen	$Q_{\mathrm{TTI,exp}}$ (kN)	$Q_{\mathrm{TTI,FEM}}$ (kN)	$Q_{\mathrm{TTI,Lima}}$ (kN)	$\frac{Q_{\mathrm{TTI,FEM}}}{Q_{\mathrm{TTI,exp}}}$	$\frac{Q_{\mathrm{TTI,FEM}}}{Q_{\mathrm{TTI,Lima}}}$
TTI connector – 8.0 mm					
EXP. 8.0 mm–1	73.10			4.04%	
EXP. 8.0 mm–2	75.13	76.05	74.51	1.22%	2.07%
EXP. 8.0 mm–3	75.93			0.16%	
TTI connector – 10.0 mm					
EXP. 10.0 mm–1	112.13			2.18%	
EXP. 10.0 mm–2	122.10	114.58	115.27	6.16%	0.60%
EXP. 10.0 mm–3	111.35			2.90%	
TTI connector – 12.5 mm					
EXP. 12.5 mm–1	193.69			0.25%	
EXP. 12.5 mm–2	192.60	194.08	195.96	0.77%	0.96%
EXP. 12.5 mm–3	196.25			1.11%	
Statistics			Mean	2.09%	1.21%
			CoV	0.05	0.37

Note: Reported shear resistance values are given on a per-connector basis.

The differences between the proposed numerical model and experimental results ranged from 0.16% to 6.16%. The 12.5 mm TTI connector yielded the lowest discrepancies (maximum error of 1.11%), corroborating the close agreement observed in the load–slip curves (Sect. 3.1). The 10.0 mm TTI connector exhibited the largest differences, ranging between 2.18% and 6.16%, due to a high experimental dispersion among its samples ($Q_{\mathrm{TTI,exp}}$ values of 112.13, 122.10, and 111.35 kN).

The maximum nominal divergence between tests for the 10.0 mm diameter was 10.75 kN, whereas for the 8.0 and 12.5 mm connectors, it was only 2.83 and 3.65 kN, respectively. This trend is confirmed by the experimental standard deviations: 1.46 (8.0 mm), 5.94 (10.0 mm), and 1.88 (12.5 mm). Despite this test scatter, the overall $Q_{\mathrm{TTI,FEM}}/Q_{\mathrm{TTI,exp}}$ ratio presented a mean error of only 2.09% and a CoV of 0.05, demonstrating the accuracy and predictive capacity of the proposed model.

When compared with the solid-element model by Lima et al. [20] ($Q_{\mathrm{TTI,Lima}}$), the differences ranged between 0.60% and 2.07%, with a mean of 1.21% and a CoV of 0.37. These metrics prove that the proposed discretization using B31 beam elements does not compromise ultimate shear capacity predictions while achieving high computational efficiency.

3.3 Computational Cost

The numerical model proposed in this study discretizes the TTI connector using three-dimensional beam elements (B31), in contrast to the 3D solid element discretization employed by Lima et al. [20]. To ensure a direct and unbiased comparison independent of hardware specifications, the model proposed by Lima et al. [20] was re-executed on the exact same workstation used for the present study (equipped with an Intel(R) Xeon(R) W-2255 CPU @ 3.70 GHz and 128 GB of RAM). Under identical hardware conditions, the solid-element model required approximately 57 min of processing time, whereas the model proposed in this work was completed in just 70 s. This corresponds to a computational time reduction of approximately 98%. This drastic improvement is directly attributed to the simplified connector discretization (substantial reduction in degrees of freedom), proving that the proposed approach achieves high computational efficiency without sacrificing precision.

4 Conclusion

The objective of this study was to develop a three-dimensional nonlinear numerical model via the Finite Element Method (FEM) to simulate the push-out test with the TTI connector using the ABAQUS 2021 software, aiming to significantly reduce the computational cost compared to models available in the literature. The obtained load–slip curves presented good agreement with both the experimental and numerical results reported in the literature, adequately reproducing the elastic and plastic regimes and satisfactorily representing the post-peak strength degradation, particularly for the 8.0 and 10.0 mm TTI connectors.

Regarding shear resistance, the model demonstrated high accuracy. Except for specimen EXP. 10.0 mm–2, which had an error of 6.16%, all other results presented differences below 5.00% compared to experimental values. Across all specimens, the mean error was 2.09% with a CoV of 0.05. When compared to the reference numerical model from the literature, the differences were 2.07%, 0.60%, and 0.96% (averaging 1.21%) for the 8.0, 10.0, and 12.5 mm connectors, respectively. Compared directly to the average experimental results, the errors were 1.75%, 0.53%, and 0.04% for the same diameters. Additionally, the kinetic energy remained below 10% of the internal energy throughout the analysis, validating the use of the Dynamic, Explicit procedure.

Finally, the discretization of the TTI connector using beam elements (B31), replacing the 3D solid elements used in previous studies, resulted in a processing time of just 70 s, representing a direct computational time reduction of approximately 98% compared to the 3D solid model re-executed on the same workstation (57 min). These results demonstrate that the proposed modeling strategy drastically reduces computational cost without compromising accuracy. Consequently, the developed model constitutes an efficient and robust tool. Its practical application is twofold: first, it enables comprehensive, large-scale parametric studies by allowing the simultaneous variation of geometric characteristics and material strengths; second, it paves the way for generating extensive numerical databases, which are essential for the development of future analytical equations to calculate the shear capacity of the truss-type connector.

References

1. (2024). ABNT: NBR 8800 - Projeto de Estruturas de Aço e Estruturas Mistas de Aço e Concreto de Edifícios. Associação Brasileira de Normas Técnicas
2. AISC: 360-16 - Load and Resistance Factor Design Specification for Structural Steel Buildings (2016)
3. Barbosa WC S (2016) Estudo de conectores de cisalhamento em barras de aço para vigas mistas de aço-concreto. Universidade de Brasília,Ph.D. thesis
4. Bezerra LM, Barbosa WCS, Bonilla J, Cavalcante ORO (2018) Truss-type shear connector for composite steel-concrete beams. Constr Build Mater 167:757–767. https://doi.org/10.1016/J.CONBUILDMAT.2018.01.183
5. Bezerra LM, Cavalcante OO, Chater L, Bonilla J (2018) V-shaped shear connector for composite steel-concrete beam. J Constr Steel Res 150:162–174. https://doi.org/10.1016/J.JCSR.2018.07.016
6. Bonilla J, Bezerra LM, Mirambell E (2019) Resistance of stud shear connectors in composite beams using profiled steel sheeting. Engineering Structures 187:478–489. https://doi.org/10.1016/J.ENGSTRUCT.2019.03.004
7. Cavalcante O (2010) Estudo de Conectores de Cisalhamento do Tipo V em Vigas Mistas. Universidade de Brasília,Ph.D. thesis
8. (1992) CEN: Eurocode-2: Design of Concrete Structures, Part 1: General Rules and Rules for Building
9. Ellobody E, Young B (2006) Performance of shear connection in composite beams with profiled steel sheeting. J Constr Steel Res 62:682–694. https://doi.org/10.1016/J.JCSR.2005.11.004

10. Ellobody E, Young B (2015) Nonlinear analysis of composite castellated beams with profiled steel sheeting exposed to different fire conditions. J Constr Steel Res 113:247–260. https://doi.org/10.1016/J.JCSR.2015.02.012
11. Ellobody E, Young B, Lam D (2006) Behaviour of normal and high strength concrete-filled compact steel tube circular stub columns. J Constr Steel Res 62:706–715. https://doi.org/10.1016/J.JCSR.2005.11.002
12. European Committee for Standardization: Eurocode 4 - Design of Composite Steel and Concrete Structures - Part 1-1: General Rules and Rules for Buildings (2004)
13. He, J., Wang, Z., Vasdravellis, G., Wang, L., Xin, H., Correia, J.: Fatigue tests and fatigue-life prediction models for hybrid welded-bolted demountable shear connectors. Int J Fatigue **175** (2023). https://doi.org/10.1016/J.IJFATIGUE.2023.107826
14. Kim SH, Park S, Kim KS, Jung CY (2017) Generalized formulation for shear resistance on y-type perfobond rib shear connectors. J Constr Steel Res 128:245–260. https://doi.org/10.1016/J.JCSR.2016.08.016
15. Lacki P, Nawrot J, Derlatka A, Winowiecka J (2019) Numerical and experimental tests of steel-concrete composite beam with the connector made of top-hat profile. Composite Struct. 211:244–253. https://doi.org/10.1016/J.COMPSTRUCT.2018.12.035
16. Leonhardt F, Andrä W, Andrä HP, Harre W (1987) New improved shear connector with high fatigue strength for composite structures. Beton und Stahlbetonbau 12:325–331
17. Lima JM (2018) Estudo da capacidade resistente do conector de cisalhamento treliçado via Método dos Elementos Finitos. Master's thesis. Universidade de Brasília,
18. Lima JM, Bezerra LM, Bonilla J, Barbosa WCS (2022) Study of the behavior and resistance of right-angle truss shear connector for composite steel concrete beams. Eng Struct **253**. https://doi.org/10.1016/J.ENGSTRUCT.2021.113778
19. Lima JM, Bezerra LM, Bonilla J, Mirambell E (2024) Experimental study on full scale steel-concrete composite beams using truss-type shear connectors. Eng Struct **303** (2024). https://doi.org/10.1016/j.engstruct.2024.117490
20. Lima JM, Bezerra LM, Bonilla J, Silva RS Y R C, Barbosa WC S (2020) Behavior and resistance of truss-type shear connector for composite steel-concrete beams. Steel Composite Struct 36:569–586
21. Moura, P.H.R., Silva, R., Lima, J.M., Bezerra, L.M., Rodrigues, G.H.S., Bezerra, E.M.F.: Investigation of the resistance capacity of the right-angle truss-type shear connector using finite element method. Latin Am J Solids Struct **21** (2024). https://doi.org/10.1590/1679-78258266
22. Nguyen HT, Kim SE (2009) Finite element modeling of push-out tests for large stud shear connectors. J Constr Steel Res 65:1909–1920. https://doi.org/10.1016/j.jcsr.2009.06.010
23. Qiu, S.Y., Guo, Y.T., Nie, X., Fan, J.S., Tao, M.X.: Experimental study on shaped steel shear connectors used in large-scale composite structures. J Constr Steel Res **172** (2020). https://doi.org/10.1016/J.JCSR.2020.106201
24. Shariati M, Ramli Sulong NH, Shariati A, Khanouki MA (2016) Behavior of v-shaped angle shear connectors: experimental and parametric study. Mater Struct 49:3909–3926. https://doi.org/10.1617/s11527-015-0762-8
25. Veríssimo OS (2007) Desenvolvimento de um conector de cisalhamento em chapa dentada para estruturas mistas de aço e concreto e estudo do seu comportamento. Universidade Federal de Minas Gerais,Ph.D. thesis



Influence Of Laser-Cutting Technology on The High-Cycle Fatigue Response of Bolted Steel Joints

Hasan N. Olmez[1(✉)], Gabriele Zanon[1], Marco Brugnolli[2], Mattia Vanin[2], and Oreste S. Bursi[1]

[1] University of Trento, Trento, Italy
hasannuman.olmez@unitn.it
[2] Adige-sys, BLM Group, Trento, Italy

Abstract. Laser cutting is extensively employed in the fabrication of structural steel components; however, its influence on the fatigue performance of bolt-hole edges–particularly in terms of process-induced variability–remains insufficiently quantified. This study presents a comparative high-cycle fatigue investigation of S355 steel bolted joints incorporating laser-cut holes produced using five fiber-laser cutting configurations: standard oxygen-assisted, high-pressure oxygen-assisted, high-quality oxygen-assisted, nitrogen-assisted, and compressed-air cuttings. For each cutting configuration, multiple nominally identical specimens were manufactured and tested to explicitly assess the inherent variability of the laser-cutting process and its impact on fatigue life. Load-controlled tension–tension fatigue tests were carried out. The results show that high-quality oxygen-assisted cutting exhibits the highest and most consistent fatigue resistance, with characteristic strengths exceeding those associated with FAT 71. In contrast, nitrogen- and air-assisted cutting display comparatively lower fatigue strength and reduced number of cycles; however, their performance still satisfies the median curve threshold defined by the Eurocode, indicating their suitability for structural applications within the prescribed design framework. These findings demonstrate that laser-cut bolt-hole edges exhibit process-dependent fatigue behavior with non-negligible variability. The results highlight the importance of considering the influence of cutting technology and its associated variability within the fatigue design framework, to ensure reliable and consistent performance of structural details in safety-critical applications.

Keywords: Laser Cutting · High-cycle Fatigue · Structural Steel · Eurocode 3

1 Introduction

Laser cutting has become a key manufacturing technology for structural steel components due to its high geometric accuracy, flexibility in producing complex

© The Author(s), under exclusive license to Springer Nature Switzerland AG 2026
R. Zanon et al. (Eds.): CTA 2026, LNCE 942, pp. 156–164, 2026.
https://doi.org/10.1007/978-3-032-39505-4_14

shapes, and suitability for automated fabrication lines. The increasing availability of high-power fiber laser systems has further expanded its application in civil and mechanical engineering, particularly for plate components incorporating bolt holes and connection details [1,2]. Despite these advantages, fatigue performance remains a governing design criterion for many steel structures subjected to cyclic loading.

Fatigue behavior is strongly influenced by local stress concentrations and surface conditions, making bolt-hole regions especially sensitive to manufacturing-induced imperfections. Experimental studies have shown that fatigue cracks in thermally cut components often initiate at the cut edge, where surface roughness, kerf morphology, and microstructural gradients introduced by the heat-affected zone (HAZ) reduce fatigue resistance when compared to mechanically drilled holes [3,4]. This sensitivity is particularly critical for bolted joints, in which the hole boundary represents a well-known fatigue hotspot.

The characteristics of the HAZ produced during laser cutting depend strongly on process parameters such as laser power, cutting speed, focus position, and assist-gas selection. Oxygen-assisted cutting promotes exothermic reactions that enhance cutting efficiency but may increase oxidation and hardness gradients, whereas nitrogen-assisted cutting limits oxidation but can lead to rougher cut-edge morphologies and altered residual stress states [5]. These process-dependent variations have been shown to significantly affect high-cycle fatigue performance.

A systematic comparison of industrially relevant laser cutting configurations is therefore required to clarify the relationship between assist-gas selection, cut-edge quality, and fatigue performance in bolted steel joints. Such understanding is essential to support reliable fatigue design and informed process selection for structural steel applications.

2 Experimental Campaign

2.1 Material Characterization

The experimental program was conducted on structural steel grade S355, supplied in plate thicknesses of 10 mm and 12 mm. The material was selected due to its widespread use in fatigue-critical structural applications. The chemical composition of the investigated steel, determined from material certification is summarized in Table 1.

Table 1. Chemical composition of the S355 steel (wt.%).

C	Mn	Si	P	S
0.039	0.456	0.025	0.005	0.001
Al	Cu	Cr	Mo	Ni
0.032	0.144	0.025	0.008	0.049

Mechanical properties were determined at room temperature through uniaxial tensile tests performed on 3 dog-bone specimens. The geometry of the tensile specimens is shown in Fig. 1. The measured means values of yield strength, ultimate tensile strength, and elastic modulus are reported in Table 2. These properties form the basis for the fatigue assessment and interpretation of the manufacturing effects discussed in the following sections.

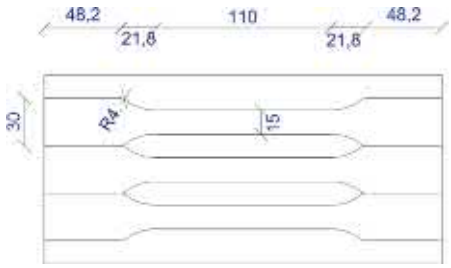


Fig. 1. Dog-bone coupon samples for tensile test (units in mm).

Table 2. Mechanical properties of the S355 steel.

Yield strength (MPa)	Ultimate strength (MPa)	Elastic modulus (GPa)
333	457	206

2.2 Geometry of the Bolted Joint

The fatigue specimens were designed as double-strap bolted joints, as illustrated in Fig. 2. Each specimen consists of a 12 mm thick central S355 plate connected to two 10 mm thick S355 cover plates using M14 bolts. To minimize the influence of thermal effects outside the investigated region, the holes in the cover plates were produced by mechanical drilling, resulting in smooth, thermally unaffected edges. In contrast, the bolt holes in the central plate were manufactured by laser cutting and represent the focus of the present investigation.

The total thickness of the cover plates (20 mm) exceeds that of the central plate, leading to reduced nominal stresses in the straps under cyclic loading. This configuration ensures that fatigue crack initiation consistently occurs in the central plate, thereby isolating the influence of the laser cutting process on fatigue performance.

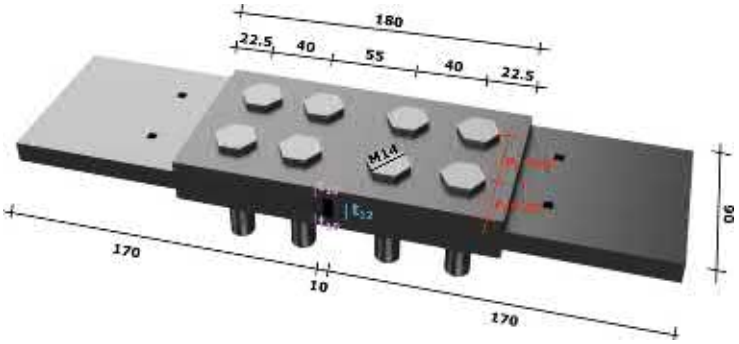


Fig. 2. Geometry of the bolted joint specimen (units: mm).

2.3 Laser Cutting and Drilling Procedures

All specimens were fabricated using a BLM Group LS7 fiber-laser cutting system with a maximum available power of 20 kW. Five laser cutting configurations were considered to investigate the effect of assist-gas selection and process parameter variation on fatigue behavior. These included standard oxygen-assisted, high-pressure oxygen-assisted, high-quality oxygen-assisted configuration, nitrogen-assisted, and air-assisted cutting. Together, these configurations represent commonly adopted industrial cutting strategies spanning different thermal inputs, oxidation conditions, and melt-ejection mechanisms.

The selection of cutting parameters was guided by previous experimental findings reported by Olmez et al. [6] and by the surface-quality requirements specified in EN ISO 9013:2017 [7]. Drilling parameters applied to the cover plates are summarized in Table 3, while the laser cutting parameters for the central plates are listed in Table 4.

Table 3. Drilling parameters for the cover plates.

Parameter	Value
Cutter diameter (mm)	15
Rotational speed (rev/min)	510
Cutting speed (mm/rev)	0.07

2.4 High-Cycle Fatigue Testing and Data Evaluation

High-cycle fatigue tests were carried out using a servo-hydraulic MTS Landmark testing system, as shown in Fig. 3. All tests were performed under load-controlled tension–tension conditions with a sinusoidal waveform and a frequency of 18 Hz.

Table 4. Laser cutting parameter sets adopted for the investigated configurations.

Set ID	SC1	SC2	SC3	SC4	SC5
Power (kW)	6.0	3.7	12.0	12.0	12.0
Assist gas	O_2	O_2	O_2	N_2	Air
Mode	CW	CW	CW	CW	CW
Velocity (mm/min)	1800	1600	900	4300	4400
Nozzle diameter (mm)	1.2	1.2	1.5	7.0	4.0
Stand-off (mm)	1.0	1.0	0.5	0.3	0.3
Focus (mm)	6.0	5.0	10.0	−1.0	−4.5
Gas pressure (bar)	0.8	2.0	0.5	6.0	8.0



Fig. 3. Test setup used for the high-cycle fatigue experiments.

The maximum nominal stress was set to 165 MPa, and a stress ratio of $R = 0.01$ was used.

To comply with the updated Eurocode 3 requirements in EN 1993-1-9:2023 for detail category FAT 71, the applied net section stress, σ_{net}, was converted into an equivalent nominal stress range, $\Delta\sigma$ [8]. This calculation accounts for the nominal stress conversion factor according to

$$\Delta\sigma = \sigma_{\text{net}} \left[1 + \left(1.6 - 2.7 \frac{d_0}{w} \right)^3 \right], \tag{1}$$

where d_0 is the hole diameter and w is the parameter that is taken as the maximum of p_2 or $2e_2$ (see Fig. 2). Although the applied net stress of 165 MPa

provides a conservative baseline, the corresponding nominal stress for the tested geometry is approximately 260 MPa, which is more consistent with the current Eurocode [9].

To facilitate comparison with design-code fatigue classifications, the experimental results were evaluated using a probabilistic S–N framework. Survival probabilities of 5%, 50%, and 95% (P_s) were considered to account for the statistical scatter inherent in fatigue data and to enable benchmarking against the FAT71 reference curve proposed in the next-generation Eurocode 3 [9].

The S–N relationship was expressed in logarithmic form as

$$\log N = \log A_{\text{test}} - m_{\text{test}} \log \Delta\sigma, \tag{2}$$

where m_{test} denotes the slope of the S–N curve, adopted as $m = 3$ in accordance with Eurocode 3 recommendations for laser-cut edges [9], and $\log A_{\text{test}}$ is the fatigue strength parameter. Survival-dependent fatigue strengths were obtained by adjusting the mean value $\log A_{m,\text{test}}$ using the logarithmic standard deviation Stv:

$$\log A_{(P_s=95\%)} = \log A_{m,\text{test}} - k \cdot Stv, \tag{3}$$

$$\log A_{(P_s=50\%)} = \log A_{m,\text{test}}, \tag{4}$$

$$\log A_{(P_s=5\%)} = \log A_{m,\text{test}} + k \cdot Stv, \tag{5}$$

where $k = 2$ corresponds to the 5% and 95% survival levels assuming a normal distribution, and $Stv = 0.2095$ was adopted in line with BS 7608 guidance for thermally affected regions [10]. The fatigue strength at 2×10^6 cycles, denoted as $\text{FAT}_{P_s\%}$, was then calculated as

$$\text{FAT}_{P_s\%} = 10^{\left(\log A_{P_s\%} - m_{\text{test}} \log(2\times10^6)\right)/m_{\text{test}}}. \tag{6}$$

3 Results

The fatigue test results offer a comprehensive assessment of the HCF behavior of the laser-cut bolted joints, revealing distinct differences in performance across the five manufacturing configurations. Table 5 presents the number of cycles to failure for all specimens, illustrating the considerable scatter associated with the thermally affected edges of the holes. This variability indicates that crack initiation is highly sensitive to local edge conditions, which are influenced by the specific cutting strategies employed. Consequently, these results highlight the importance of interpreting the data within a probabilistic framework rather than relying solely on deterministic S–N curves.

A preliminary analysis of the measured fatigue lives reveals clear groupings associated with the assist-gas regime and specific cutting parameters. These trends are illustrated in Fig. 4, which presents the experimental S–N results together with the corresponding fatigue-assessment thresholds. Specimens fabricated with oxygen-assisted cutting generally exhibit higher fatigue lives, with the

Table 5. Fatigue test results expressed in number of cycles to failure for each specimen set.

Set ID	Test 1	Test 2	Test 3	Test 4	Test 5	Test 6
SC1	180221	363264	245348	346115	313621	270345
SC2	551966	917606	578429	586769	–	–
SC3	1035253	1260370	–	–	–	–
SC4	179014	123018	–	–	–	–
SC5	201566	237600	238738	–	–	–

high-quality oxygen-assisted configuration (SC3) showing the most pronounced improvement. These samples cluster in the upper range of tested cycles, surpassing the upper bound of the survival curve and reflecting enhanced cut-edge quality. In addition, the standard oxygen-assisted and high-pressure oxygen-assisted configuration (SC1 and SC2) demonstrate intermediate fatigue performance, generally positioned between SC3 and the nitrogen- and air-assisted cases, while still reaching and in several instances exceeding the upper bound of the reference fatigue design curve. Conversely, specimens produced with nitrogen-assisted (SC4) and air-assisted (SC5) cutting display comparatively shorter fatigue lives, indicating that these strategies induce surface or microstructural characteristics that accelerate crack initiation, although their performance remains within the acceptable range defined by the design framework.

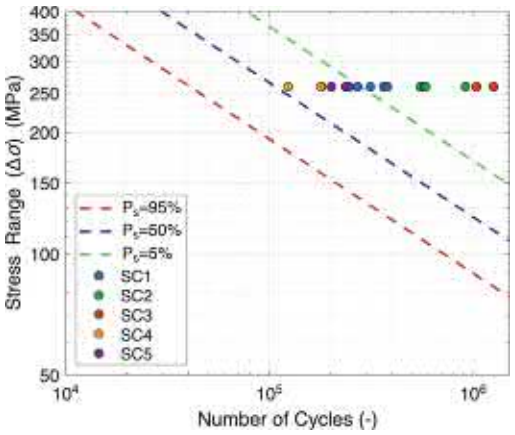


Fig. 4. Experimental S–N data for the investigated laser cutting configurations (SC1–SC5). Symbols represent experimental results, while the dashed curves include the reference fatigue design curve FAT 71 and the associated survival probability curves and the associated survival probability curves (P_s).

Overall, these findings confirm that the fatigue behavior of laser-cut bolt holes is highly sensitive to the cutting strategy employed. Nevertheless, all investigated cutting configurations demonstrate performance within acceptable design limits, indicating their suitability for structural applications, while emphasizing the importance of accounting for process-specific characteristics in fatigue-critical assessments.

4 Conclusions

This work presents a comparative high-cycle fatigue investigation of bolted S355 steel joints fabricated using five distinct fiber-laser cutting configurations: standard oxygen-assisted (SC1), high-pressure oxygen-assisted (SC2), high-quality oxygen-assisted (SC3), nitrogen-assisted (SC4), and air-assisted cutting (SC5). The study aims to evaluate the effects of assist-gas type and cutting parameters on fatigue performance, while assessing their alignment with conventional design classifications.

Experimental results reveal a pronounced impact of the selected laser-cutting approach on fatigue life. Specimens produced under the SC3 configuration consistently exhibited the highest fatigue resistance, with their life distributions shifted toward the high-cycle range and exceeding the upper bound of the FAT71 reference curve. The standard and high-pressure oxygen-assisted configurations (SC1 and SC2) demonstrate intermediate performance, often reaching or exceeding the upper bound of the reference fatigue design curve. In contrast, nitrogen- and air-assisted (SC4 and SC5) configurations exhibit comparatively lower fatigue lives; however, they remain above the median curve threshold, indicating acceptable performance within the Eurocode framework.

Overall, the findings demonstrate that fatigue performance of laser-cut bolt holes is strongly influenced by the chosen cutting strategy. Nevertheless, all investigated configurations satisfy the relevant design criteria, confirming their suitability for structural applications, while highlighting the importance of incorporating process-specific effects when evaluating fatigue-critical components.

Acknowledgments. The authors gratefully acknowledge the BLM-Group support for the realisation of laser-cut elements. Additionally, we would like to acknowledge the laboratory staff at the University of Trento for their assistance. The corresponding author acknowledges the Italian Ministry of Education, Universities, and Research (MUR) in the framework of the project DICAM-EXC (Departments of Excellence 2023–2027, grant L232/2016) and the National Project MUR PNRR M4C2-CN1-SPOKE 9.

References

1. Steen WM, Mazumder J, Watkins KG (2010) Laser Material Processing, vol. 4. Springer
2. Powell J (2017) CO_2 Laser Cutting, 3rd edn. Springer, Berlin
3. Garcia T, Cicero S, Ibáñez FT, Álvarez JA (2015) Fatigue performance of thermally cut bolt holes in structural steel S460M. Procedia Eng 114:442–449

4. Bursi OS, D'Incau M, Zanon G, Raso S, Scardi P (2017) Laser and mechanical cutting effects on the cut-edge properties of steel S355N. J Constr Steel Res 133:181–191
5. Zanon G, Bursi OS, Scardi P, D'incau M, Raso S (2017) 09.02: effects of laser cutting on the cut-edge properties of structural steel s355n subjected to high-cycle fatigue. ce/papers, 1(2-3):2359–2367
6. Olmez, HN, Shamlooei M, Zanon G, Brugnolli M, Bursi OS (2024) Study of the effect of laser cutting technologies in manufacturing of structural steel components. In: International Conference on Flexible Automation and Intelligent Manufacturing, pp. 66–73. Springer Nature Switzerland, Cham
7. (2017) EN ISO 9013:2017 – Thermal cutting – Classification of thermal cuts – Geometrical product specification and quality tolerances product specification and quality tolerances
8. Maljaars J, Euler M (2021) Fatigue SN curves of bolts and bolted connections for application in civil engineering structures. Int J Fatigue 151:106355
9. (2023) CEN. EN1993-1-9:2023 Eurocode 3: Design of Steel Structures – Part 1-9: Fatigue. Final Draft European Standard, European Committee for Standardization, Brussels, Belgium
10. (2015) BS 7608:2014+A1:2015–Guide to fatigue design and assessment of steel products

Numerical Analysis and Design of a Telescopic Joint for Rapid Assembly of Steel Frames

Emanuele Maiorana(✉) and Mattia Sperandio

Department of Economics, Science, Engineering and Design, University of the Republic of San Marino, San Marino, San Marino
e.maiorana@unirsm.sm

Abstract. Steel modular construction is increasingly adopted due to its high level of prefabrication and rapid on-site assembly; however, its widespread application remains constrained by the tolerance sensitivity of structural connections. Conventional bolted joints require precise geometric alignment, often resulting in time-consuming assembly procedures and increased construction complexity.

This study introduces a novel telescopic beam-to-column joint for rectangular hollow section (RHS) steel frames, explicitly conceived to accommodate geometric tolerances through a geometry-driven assembly mechanism. The proposed system enables vertical insertion of beams into pre-welded column supports, where gravity-assisted positioning ensures initial alignment, while bolted fastening provides structural continuity and load transfer. A nonlinear finite element framework, calibrated against experimental data available in the literature, is employed to investigate four joint configurations characterized by increasing levels of geometric confinement and stiffness. The findings highlight that connection systems explicitly designed to accommodate geometric tolerances can simultaneously improve constructability and structural performance, providing a viable design strategy for modular steel buildings and industrialized construction.

Keywords: Steel frame · Joints · Bolts · Erection · Buildings · Assembly

1 Introduction

The increasing demand for rapid, cost-effective and industrialized construction processes has led to the growing adoption of modular steel buildings (MSBs), in which prefabricated volumetric units are manufactured off-site and assembled on-site through mechanical connections. This construction paradigm offers significant advantages in terms of quality control, construction speed and reduction of environmental impact; however, its structural performance is strongly governed by the behaviour of inter-module connections [1–3]. Among the various connection typologies, bolted beam-to-column joints remain the most widely adopted solution due to their simplicity, reliability and ease of disassembly. Extensive experimental and numerical investigations have demonstrated that their structural response depends on a complex interaction between geometric configuration, bolt arrangement, plate thickness and local stiffening details, which collectively control stiffness, strength and energy dissipation capacity [4, 5–8]. In particular,

© The Author(s), under exclusive license to Springer Nature Switzerland AG 2026
R. Zanon et al. (Eds.): CTA 2026, LNCE 942, pp. 165–173, 2026.
https://doi.org/10.1007/978-3-032-39505-4_15

recent studies have shown that properly designed bolted connections can achieve stable hysteretic behaviour and satisfactory seismic performance in modular steel systems [7, 9].

Despite these advances, conventional bolted connections inherently rely on strict geometric tolerances. The need for precise alignment of bolt holes and contact surfaces often results in time-consuming assembly procedures, increased labour effort and a higher probability of installation errors. This issue becomes particularly critical in modular construction, where cumulative tolerances across prefabricated units can significantly affect the feasibility and efficiency of on-site assembly. As a result, current design approaches tend to treat geometric tolerances as constraints to be minimized, rather than as parameters to be explicitly incorporated into the connection design. To address these limitations, recent research has explored alternative connection strategies based on post-tensioning systems, friction-based interfaces and rocking mechanisms, aiming to improve structural performance and robustness under cyclic loading [9, 10]. While these solutions provide enhanced mechanical behaviour, they often introduce additional complexity in design and construction, requiring careful control of preload forces, contact conditions and interface behaviour. Consequently, the challenge of achieving both high structural performance and simplified assembly remains largely unresolved.

In this context, the development of connection systems explicitly designed to accommodate geometric tolerances—rather than minimize them—represents a promising but still underexplored research direction. Such an approach implies a shift in the design paradigm, where assembly robustness is treated as a primary design objective and is integrated with structural performance requirements. The present study introduces a novel telescopic beam-to-column joint for steel frames made of rectangular hollow sections (RHS), in which the assembly process is governed by a geometry-driven mechanism. The proposed solution allows beams to be installed through vertical insertion into pre-positioned supports welded to the column, eliminating the need for precise alignment during assembly. Gravity-assisted positioning ensures initial geometric compatibility, while bolted connections provide shear transfer and rotational restraint, enabling the joint to develop a structural response consistent with capacity design principles.

The main objective of this work is to investigate the influence of geometric configuration on the mechanical performance of the proposed joint, with particular reference to stiffness, load-bearing capacity and failure mechanisms. To this end, a nonlinear finite element model is developed and validated against experimental results available in the literature. Four joint configurations, characterized by progressively increasing geometric confinement and stiffening, are analysed to quantify the role of local detailing in controlling stress distribution and plastic hinge development. The results aim to demonstrate that a geometry-driven approach to connection design can effectively reconcile constructability and structural performance, offering a viable alternative to conventional tolerance-sensitive solutions.

This contribution is particularly relevant for modular and industrialized construction, where the efficiency of assembly operations plays a key role in the overall feasibility and competitiveness of the structural system.

2 Calibration of the Numerical Model

As a preliminary step, the numerical modelling strategy was validated against an experimental–numerical benchmark available in the literature [7]. The selected reference case involves bolted beam-to-column connections representative of modular steel building systems, for which experimental moment–rotation curves and failure modes are available. The Finite Element Model was developed to replicate the geometry, material properties and boundary conditions of the reference configuration. Particular attention was devoted to the modelling of contact interfaces and bolt representation, in order to capture the nonlinear response of the joint.

The comparison between numerical predictions and experimental results shows a close agreement in terms of initial rotational stiffness, ultimate moment capacity, global shape of the moment–rotation response and failure mode and localization of plastic deformation. In particular, the numerical model accurately reproduces the transition from elastic behaviour to plastic hinge development, as well as the distribution of stresses in the connection region. The discrepancy between numerical and experimental results remains within an acceptable range (2%), confirming the reliability of the modelling approach. This validation provides confidence in the ability of the adopted numerical framework to simulate the structural behaviour of steel joints and justifies its application to the analysis of the proposed telescopic connection (Fig. 1).

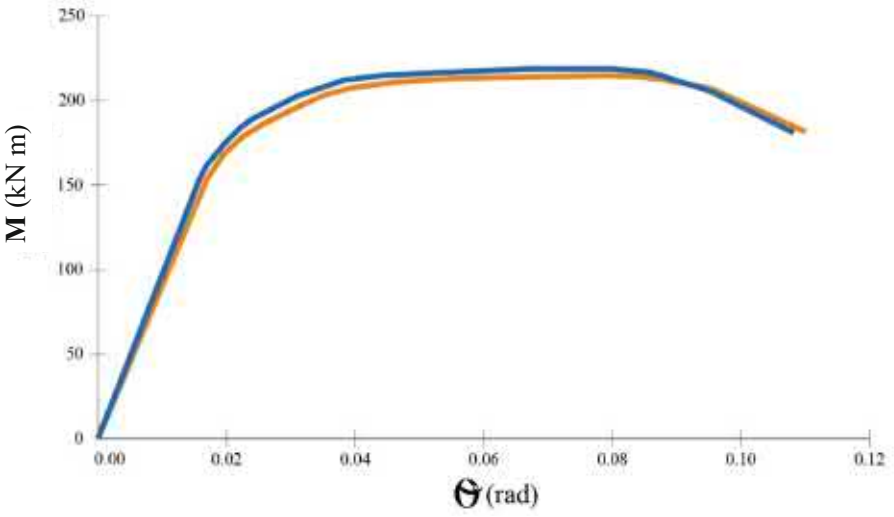
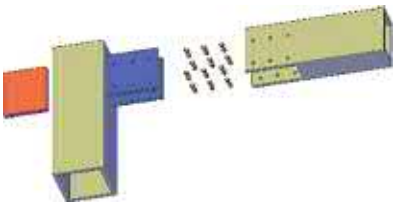
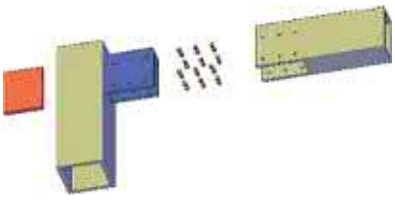
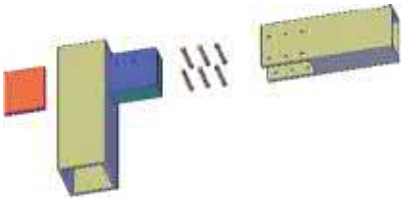
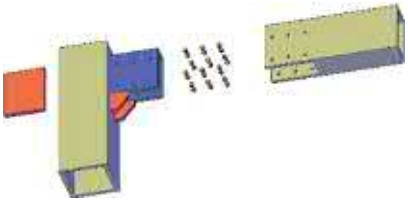


Fig. 1. Moment–rotation curves comparison: numerical ( ) and experimental ( ) results

3 Description of the Telescopic Joint

Based on the validated numerical framework, a novel telescopic beam-to-column joint was developed for steel frames composed of rectangular hollow section (RHS) profiles. The key feature of the proposed system lies in its geometry-driven assembly mechanism, which enables the beam to be installed through vertical insertion into pre-welded supports attached to the column. Unlike conventional bolted connections, which require precise alignment of bolt holes, the proposed joint allows for geometric accommodation during assembly, thereby reducing sensitivity to fabrication and erection tolerances. Initial positioning is achieved through gravity-assisted insertion, while structural continuity is ensured by bolted fastening. Four joint configurations (A01–A04) were investigated, characterized by progressively increasing geometric confinement and stiffness (Table 1).

Table 1. Joint configurations investigated

n.	Configuration	Description
A01		basic configuration with two vertical flanges acting as lateral supports; an internal plate is added within the column
A02		U-shaped support formed by two vertical flanges connected by a horizontal element, improving load transfer continuity
A03		closed rectangular support, providing increased confinement and stiffness
A04		enhanced configuration based on A02, with the addition of triangular stiffening plates connecting the flanges to the column

This parametric variation allows the systematic evaluation of the influence of geometric detailing on load transfer mechanisms, stress distribution and plastic hinge development.

4 Finite Element Modelling and Loading Conditions

The numerical analyses were performed using the software Strand7. The structural system consists of RHS columns (200 × 200 × 16 mm), primary beams (120 × 200 × 16 mm) and secondary beams (100 × 120 × 8 mm), made of S275 structural steel. Connection plates were modelled using S355 steel. To optimize computational efficiency, symmetry conditions were exploited by modelling half of the structural assembly. A refined mesh was adopted in the joint region to accurately capture stress gradients, with element sizes ranging from 10 mm in the connection region, 15 mm in transition zones and 50 mm in remote regions. Bolts were modelled using beam elements with a nominal diameter of 20 mm (class 8.8), providing an equivalent representation of axial and shear stiffness. Plate components were discretized using higher-order quadrilateral elements (Quad8).

Material behaviour was assumed to be elastic–perfectly plastic. Contact interactions between connected components were implicitly considered through compatible nodal constraints (or, if implemented, specify friction/contact model). The loading scheme includes self-weight, constant axial load applied to the column (145 kN) and horizontal displacement-controlled loading applied at the beam level, simulating lateral (seismic-type) actions. Nonlinear analyses were carried out by maintaining the vertical load constant while incrementally increasing the horizontal displacement until failure. This approach allows the full characterization of the joint response, including stiffness degradation, plasticization and failure mechanisms (Fig. 2).

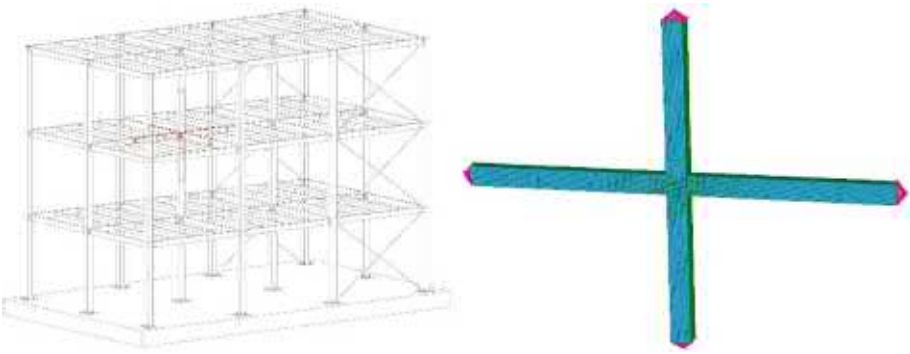


Fig. 2. Analysed frame using the software Strand7

5 Results and Discussion

The structural response of the investigated joint configurations was assessed in terms of stress distribution, stiffness and failure mechanisms, with particular attention to compliance with capacity design principles. The Von Mises equivalent stress criterion was adopted to evaluate yielding in the steel components.

A preliminary comparison between RHS profiles and equivalent open sections (HE/IPE) indicates a potential reduction in material usage of approximately 25% for beams and 28% for columns. While this comparison is indicative, it suggests that the proposed solution may provide additional economic benefits due to reduced material consumption and simplified construction procedures.

The design objective was to promote a "strong column – weak beam" mechanism, ensuring that plastic hinges develop in the beams while maintaining the integrity of the columns (Fig. 3).

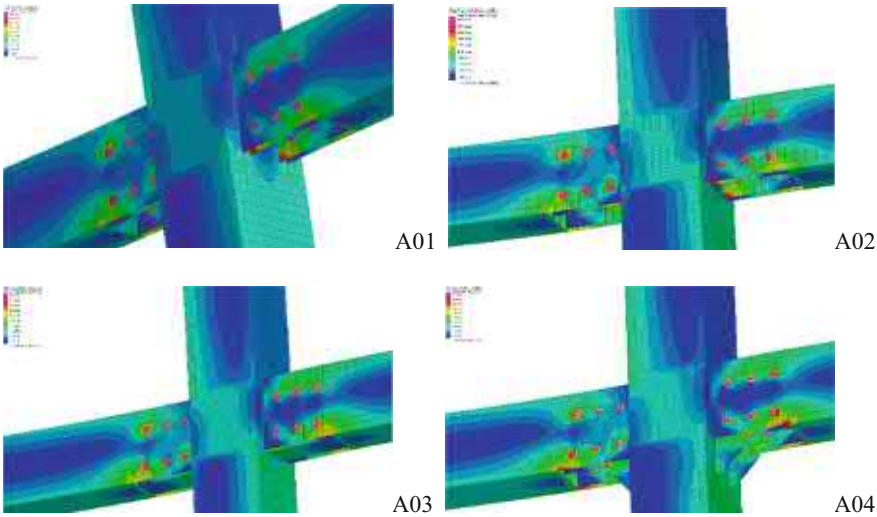


Fig. 3. Numerical models

The results highlight a clear influence of geometric configuration on the structural response. A01 and A02 exhibit inefficient load transfer, with significant stress concentration in the connection region and early plasticization of the support elements. A03 provides improved stress distribution due to increased geometric confinement, although its closed configuration may introduce practical difficulties during assembly. A04 demonstrates the most favourable behaviour, with a pronounced redistribution of stresses away from the joint and a clear localization of plastic deformation in the beam. In configuration A04, the introduction of triangular stiffening elements modifies the internal load path, reducing stress concentration in the connection and increasing global stiffness.

The first three configurations (A01–A03) show similar failure modes, primarily governed by beam bending, local instability of flanges and partial plasticization of the connection region. In contrast, configuration A04 exhibits a more controlled failure mechanism, characterized by localized plastic hinge formation at the beam end, limited plastic deformation in the connection and preservation of column integrity. This behaviour is fully consistent with capacity design requirements. No significant plastic deformation was observed in the columns for any configuration, confirming that the design objective of hierarchy of strength is achieved. Bolt slippage phenomena were limited, and the use of slotted holes proved beneficial in accommodating geometric tolerances during assembly without compromising structural response.

The graph of Fig. 4 also re-ports the results of the B models, considering the bolting present asymmetrically on one side only.

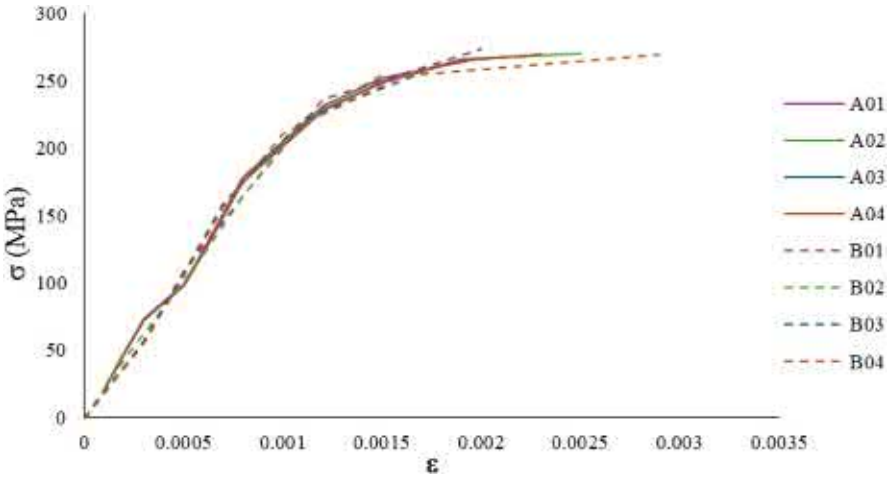


Fig. 4. Stress vs. Strain

6 Conclusions

This study has investigated the structural behaviour of a novel telescopic beam-to-column joint for RHS steel frames, explicitly designed to accommodate geometric tolerances through a geometry-driven assembly mechanism. The numerical results demonstrate that the proposed connection concept is capable of ensuring both structural performance and constructability. In particular the telescopic configuration enables rapid and tolerance-insensitive assembly through vertical insertion, the introduction of stiffening elements significantly improves stress redistribution and global stiffness and the optimized configuration (A04) promotes plastic hinge formation in the beam, ensuring compliance with capacity design principles and enhancing ductility.

The findings highlight that connection systems explicitly conceived to accommodate geometric tolerances can represent a viable alternative to conventional bolted joints, particularly in modular and industrialized construction, where assembly efficiency is a key design driver. From a broader perspective, the proposed approach introduces a shift in connection design philosophy, from tolerance-sensitive to tolerance-accommodating systems, in which constructability is integrated into the structural design process. Future research should focus on experimental validation of the proposed joint, cyclic loading tests to assess seismic performance and refinement of numerical models including detailed bolt and contact behaviour.

Acknowledgements. The University of the Republic of San Marino is gratefully acknowledged for the support in the framework of the Research Project PRIU2024: "*Progettazione Sostenibile e Tecnologie Avanzate per il Settore delle Costruzioni: Caratterizzazione e Analisi di Materiali e Sistemi Strutturali Innovativi ed Ecocompatibili*".

References

1. Wu H, Tu T, Sui L, Yan F, Zhou T (2024) A novel modular CFS composite frame-wall structure: experimental investigation and numerical analysis. J Constr Steel Res 218:108702
2. Li T, Liu M, Mushi W, Huang Z, Wang X (2024) Hysteretic performance of novel grouted steel beam-column corner-connections for modular integrated construction. J Constr Steel Res 220:108828
3. Wang W, Guo L, Hu Z, Liu Y (2024) Numerical and analytical behavior of UHPC encased CFST column blind bolted modular joints. J Constr Steel Res 222:108924
4. Liu X, Li B, Chen X, Zhang Y, Zhang A (2024) Seismic performance of bolted middle joint for modular steel structure. J Constr Steel Res 220:108861
5. Deng E, Zong L, Ding Y, Luo Y (2018) Seismic behavior and design of cruciform bolted module-to-module connection with various reinforcing details. Thin-Walled Struct 133:106–119
6. Liu X, Liu Y, Chen X, Zhang A (2024) Analysis of bolted connection for H-section beam and square steel tube column. Structure 60:105945
7. Zhai S, Lyu Y, Cao K, Li G, Wang W, Chen C (2023) Experimental-numerical investigation and design of bolted-cover plate connections under bending for modular steel buildings. J Build Eng 75:107057
8. Yang C, Wang X, Wang Q, Ou J (2023) Seismic performance of cruciform bolted joints with various reinforcing details in modular steel construction. Eng Struct 285:116069

9. Atashfaraz B, Sharafi P, Shadan P, Goudarzi A (2025) Rocking interconnection for moment resisting modular buildings: experimental and numerical investigation. J Constr Steel Res 224:109193
10. Lee K, Rasmussen K, Cho B (2024) Bolt-free post-tensioned connection for steel-framed modular buildings and design for optimal preloading. J Constr Steel Res 218:108703

Firmly Bolted – Functional Levels of Bolt Tightening

Frank Götz(✉)

Nord-Lock GmbH, Lauchheim 73466, Germany
frank.goetz@nord-lock.com

Abstract. This paper provides a functional framework for bolted connections in steel construction by distinguishing non-preloaded, serviceability-oriented preloaded, and structurally relevant preloaded connections. It maps these functional levels to the preload force levels $F_{p,C}$ and $F_{p,C}{}^{*}$ used in European practice, and relates them to tightening methods, bolt assembly classes, execution requirements, and inspection practice. The paper also discusses the newly published ISO 18954 as a qualification route for non-standard pretensioning situations and evaluates practical issues such as preload loss, self-loosening, and wedge-locking washers. The main contribution is a practice-oriented but systematically structured interpretation of bolt preload that improves the link between design intent, execution, and qualification.

Keywords: Bolted Connections · Structural bolting · Preload · Pretension · Tightening parameters · Bolting Assemblies · Wedge-Locking washers

1 Introduction

Bolted connections are among the most widely used and at the same time most frequently misunderstood details in steel construction. In practice, project stakeholders often face a fundamental question: is preload structurally necessary, or is it merely applied for quality assurance, tradition, or to "make the joint feel right" on site? This distinction is not academic. It directly affects design intent, execution method, inspection effort, documentation, and the long-term performance of the connection.

Under EN 1993-1-8 [13], preload becomes structurally relevant whenever the designer deliberately relies on slip resistance or fatigue performance. This is the case, for example, in Category B and C shear connections, where slip resistance must be ensured at serviceability or ultimate limit state, as well as in preloaded tension connections where the preload contributes to the resistance of fatigue-critical joints. In contrast, many connections are preloaded for practical reasons only, such as gap closure, increased stiffness, improved serviceability, or noise reduction [3]. Although these joints do not rely on preload for load-bearing safety, they still require careful detailing and controlled execution.

This ambiguity creates different technical requirements for fabrication, installation, and inspection. EN 1090–2 [12] therefore plays a decisive role by defining

© The Author(s), under exclusive license to Springer Nature Switzerland AG 2026
R. Zanon et al. (Eds.): CTA 2026, LNCE 942, pp. 174–187, 2026.
https://doi.org/10.1007/978-3-032-39505-4_16

approved tightening methods, site execution requirements, and inspection procedures for preloaded bolting assemblies.

The present paper focuses on torque-controlled and angle-controlled tightening procedures used in continental European steel construction practice; tightening by direct tension indicators (DTI) in accordance with EN 14399–9 [17] or the use of HRC bolting assemblies in accordance with EN 14399–10 [18] are explicitly not part of the scope of this article. Its scientific contribution is not an experimental validation of a new fastener system, but a functional and normative synthesis: the paper develops a classification of bolted connection according to the role of preload and links this classification to preload levels, bolt assembly concepts, tightening methods, execution requirements, and qualification procedures. In this way, it aims to provide a more systematic basis for engineering decisions and to clarify where practical tightening concepts coincide with, or diverge from, the structural logic of the connection.

2 Functional Levels of Bolt Tightening and Preloading

From a structural engineering perspective, EN 1993-1-8 [13] distinguishes only between preloaded and non-preloaded bolted connections. EN 1090–2 [12] further specifies preloading as a quality measure (e.g. for durability). To facilitate distinction, [3] classifies three functional levels for bolted connection

- Non-preloaded
- Target level II (preloading as a quality measure)
- Target level I (preloading for structural reasons)

This is especially useful for engineering practice because many familiar details look similar on site, although the functional significance of the tightening force differs fundamentally. The distinction also provides the conceptual bridge to the later discussion of preload force levels, HV assemblies and tightening procedures. It also follows the approach used in North America. The RCSC boltcouncil distinguishes in its specification for structural joints [9] snug-tightening (comparable with non-preloaded), pretensioned joints (comparable with target level II) and slip-critical joints (comparable with target level I).

2.1 Non-preloaded Connections

Non-preloaded connections are designed without taking any defined preload force into account. In Eurocode terminology, this mainly concerns category A shear-bearing connections and category D tension connections (Fig. 1), provided that no deliberate preload is specified for serviceability or robustness reasons. Even in these cases the bolts are, of course, tightened during erection, but only to the snug-tight condition; the resulting clamping force is undefined and is not used as a design parameter.

From the load-transfer perspective, these joints rely on bearing, shear and direct tensile resistance of the fasteners rather than on frictional resistance or on the beneficial effects of a verified preload. In category A shear connections, slip is generally accepted once the hole clearance is exhausted and the bolt starts to act in bearing. In category D

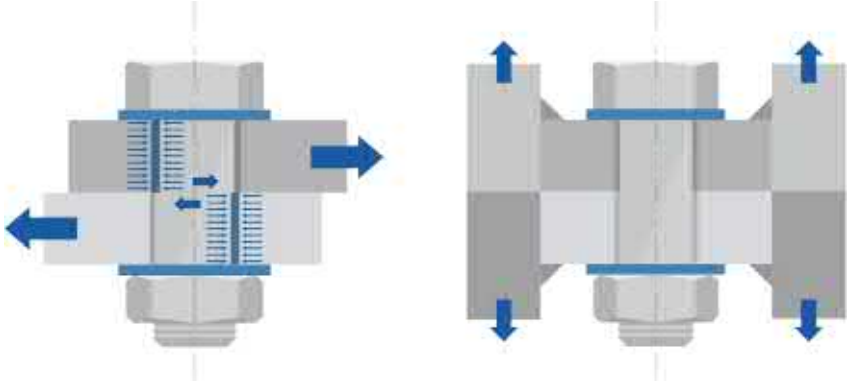


Fig. 1. Shear connection category A (left) and tension connection category D (right)

tension connections, the tensile force is carried directly by the bolt, without relying on a pre-existing compressive state in the clamped package.

Typical practical examples are simple shear connections in secondary members, bracing details, cover plates and ordinary site joints where a limited initial slip is structurally acceptable. Similar considerations apply to many simple tension details that are checked as non-preloaded category D connections, as long as no fatigue-sensitive behaviour, no slip-free force transfer and no specific serviceability requirements are imposed. In everyday steel building practice, these non-preloaded joints remain important because they are economical, robust in ordinary static applications and comparatively simple to execute and inspect.

At the same time, the apparent simplicity of non-preloaded joints must not be misunderstood as a universal solution. Where repeated transverse movement, vibration or impact loading occurs, a nominally admissible category A or D detail may become sensitive to slip, local movement and eventually self-loosening. For the practising engineer, this is the first important practical message of the present chapter: a connection may be formally "non-preloaded" in the design sense and still require more than mere snug-tight assembly if the real service conditions are demanding.

2.2 Target Level II: Preloading for Serviceability and Quality Assurance

Target level II comprises connections that are deliberately preloaded although the preload is not directly used in the structural resistance check. Here, preloading serves the improvement of serviceability, robustness, fit-up quality or durability rather than the formal proof of load-bearing capacity. In other words, the connection is still designed as a category A or D joint in the Eurocode sense, but a defined preload is intentionally introduced because this improves the practical behaviour of the connection in service (Fig. 2). In detail this could mean:

- Minimisation of slip in service
- Higher deformation stiffness
- Reliable closing of gaps
- Better behaviour against loosening

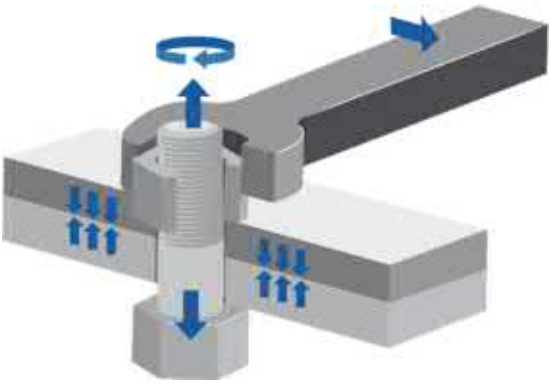


Fig. 2. Preload force and clamping force in a bolted connection

This level is especially important for engineering practice because it explains why many joints are executed with high-strength preloaded bolting assemblies even though they are not formally slip-resistant or fatigue-designed joints.

The decisive point is that the preload is beneficial and often highly desirable, but small deviations in the achieved preload force do not invalidate the structural design, because the resistance model itself does not depend on a verified minimum preload.

In central Europe, this often leads to the use of HV bolting assemblies according to EN 14399–4 [16] with a reduced preload level that is sufficient to improve service behaviour and erection quality without imposing the same strict requirements that apply to structurally relevant preloading. This is precisely the field in which the distinction between the preload force levels $F_{p,C}$ and $F_{p,C}{}^{*}$ becomes practically relevant and will therefore be developed in the next chapter.

Execution and inspection consequences follow directly from this classification (see chapter 3.4). For target level II, it is essential that the connection is not damaged by tightening and that a meaningful preload is actually introduced; however, it is less critical to prove that every individual joint has achieved the exact same minimum preload level as would be required for target level I. Even so, Stranghöner and Jungbluth [6] explicitly recommend determining tightening parameters for target-level-II connections in a manner analogous to target level I wherever possible, because this yields a technically sound and reproducible basis for site application, while acceptance criteria on site may be somewhat less stringent.

A further practical aspect should already be noted here. If target-level-II preloading is combined with special details such as head-side tightening, tapped holes, repeated use of components or non-standard component combinations, the standard rules of EN 1090–2 [12] may no longer be sufficient. In such situations, the engineer must already think ahead to the need for a procedure qualification as described in chapter 4, even though the connection itself may still only belong to target level II.

2.3 Target Level I: Structurally Relevant Preloading

Target level I refers to preloading that is directly relevant to structural resistance. Here the preload is not merely beneficial; it is an integral part of the load-bearing concept and must therefore be introduced with sufficient reliability. According to the established classification, this concerns category B and C slip-resistant connections and category E preloaded tension connections (Fig. 3). In all of these cases, the design assumptions are valid only if the required preload level is actually achieved in the structure.

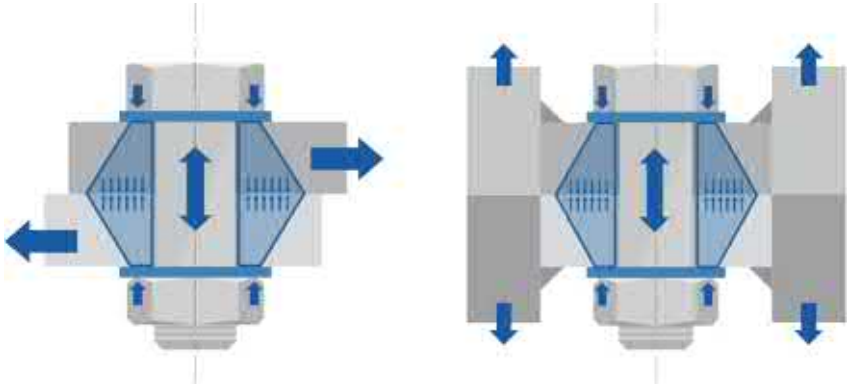


Fig. 3. Slip-resistant connection category B/C (left) and preloaded tension connection category E (right)

In slip-resistant connections of categories B and C, preload generates the clamping force that creates friction between the faying surfaces. This friction is then used to prevent relative movement between the connected parts, either in the serviceability limit state or in the ultimate limit state. If the required preload is not present, the connection no longer behaves as intended and may effectively revert to a bearing-type connection with slip, with all associated consequences for deformation, fatigue and robustness.

In category E tension connections, the role of preload is different but equally important. The preload reduces the stress range in the bolt under fluctuating tensile actions because part of the external action first relieves the clamping force before it increases the bolt force. This mechanism is decisive for fatigue-sensitive details, which is why dynamically tension-loaded joints, such as certain flange splices or heavily cyclic structural details, belong to target level I. Once the joint opens, the full external action is carried directly by the bolt, and the beneficial effect of preloading is lost.

Classical applications of target level I therefore include slip-resistant splice connections, joints in which slip would impair structural performance, and fatigue-relevant tension splices in cyclically loaded structures. In the broader steelwork practice described in the literature, this also includes crane runway details, selected bridge details, and other heavily used joints where load reversal, repeated movement or fatigue sensitivity make a defined preload indispensable rather than optional. The common denominator is always the same: preload is part of the resistance model, not just part of good workmanship.

Because of this, target level I imposes the highest demands on bolting assemblies, tightening procedures and inspection. The tightening parameters must be linked to a defined preload level, the suitability of the assembly for preloading must be ensured, and the execution must prevent both under-tightening and damage by over-tightening. Where the standard rules do not apply, for example in head-side tightening, tapped holes, multiple use or special component combinations, a procedure qualification as described in chapter 4 becomes necessary precisely because the structural safety of the connection depends on the reliability of the preloading process.

Once the functional level has been established, the next question is which preload level and tightening method are appropriate for the intended application.

3 Preload Levels, Tightening Methods and Bolt Assemblies

Once the functional level of tightening has been established, the next practical question is which preload force level is required and by which tightening method it can be introduced reliably and economically on site. For engineering practice, this question is decisive because the selected preload level governs not only structural behaviour, but also the choice of the bolting assembly, the admissible tightening method, the inspection effort and the robustness of the erection process. In this context, the distinction between $F_{p,C}$ and $F_{p,C}{}^{*}$ is of central importance.

3.1 Preload Levels and National Adoption

The full preload level is defined as

$$F_{p,C} = 0,7\, f_u\, A_s \tag{1}$$

With f_u as tensile strength of the bolt and A_s the stress area of the bolt. In EN 1090–2 [12], this is the minimum preload level that is to be used for preloaded connections unless a lower level is explicitly specified, and it is the natural reference value for slip-resistant and otherwise structurally relevant preloaded connections (target level I). A lower level that is specified in different national frameworks [10, 20] is the so-called reduced preload level

$$F_{p,C}{}^{*} = 0,7\, f_y\, A_s \tag{2}$$

for HV assemblies of property class 10.9, using the yield strength f_y instead of the ultimate tensile strength f_u of the bolt. $F_{p,C}{}^{*}$ is typically about 7–15% lower than $F_{p,C}$, depending on diameter and the tabulated values used in practice (see Table 1). In practical terms, this means that the reduced preload level is mechanically close enough to remain effective for serviceability-oriented tightening (target level II), but sufficiently lower to simplify execution and avoid an overtightening. More about the backgrounds of this different preload level will be provided in the next chapter. This numerical reduction is one of the main reasons why $F_{p,C}{}^{*}$ has become so attractive in erection practice.

From a practical perspective, the engineering interpretation is straightforward. The reduced preload level $F_{p,C}{}^{*}$ is often entirely sufficient for target level II, where the

Table 1. Preload force $F_{p,C}^{*}$ and $F_{p,C}$ in kN for HV 10.9 and different bolt diameter

	M12	M16	M20	M24	M27	M30	M36
Fp,C*	50 kN	100 kN	160 kN	220 kN	290 kN	350 kN	510 kN
Fp,C	59 kN	110 kN	172 kN	247 kN	321 kN	393 kN	572 kN
Difference	15%	9%	7%	11%	10%	11%	11%

preload improves stiffness, fit-up, gap closure, slip minimisation or general execution quality, but where the design model does not rely on a verified full preload. For target level I, however, the technically cleaner solution remains the use of $F_{p,C}$, because the preload then contributes directly to the intended structural behaviour and should therefore be introduced with the reliability envisaged by the European execution logic. This distinction is for instance handled differently for German and Austrian practice.

In Austria, the preload $F_{p,C}^{*}$ is used only for the serviceability-oriented field, that is, effectively for target level II, while the full preload $F_{p,C}$ is assigned to target level I where slip resistance or structural resistance must be ensured [20]. Austria therefore maintains a clear separation between the reduced preload concept and structurally relevant preloading.

Germany adopts a broader approach. Through national application documents and the long-standing technical framework around DASt-Guideline 024 [10], the lower preload level $F_{p,C}^{*}$ may also be used for cases extending into target level I. This is one of the characteristic features of German practice and should be stated explicitly, because it differs from the stricter Austrian allocation of $F_{p,C}^{*}$ to target level II only.

For the purposes of the present article, however, a clear practical recommendation remains useful. Even though Germany permits the use of $F_{p,C}^{*}$ more broadly, $F_{p,C}^{*}$ is particularly well suited to target level II, while $F_{p,C}$ should generally be preferred for target level I. This recommendation aligns better with the structural logic of the joint and provides a clearer basis for execution, inspection and later discussion of procedure qualification.

3.2 HV and HR Assemblies, K-Classes and Practical Focus

The preload concept cannot be separated from the type of preloaded bolting assembly used in execution. In European structural bolting, the two most relevant standardised assembly systems are HR assemblies according to EN 14399–3 [15] and HV assemblies according to EN 14399–4 [16]. In practical market availability, HV assemblies are very often supplied in k-class K1, while HR assemblies are commonly encountered in k-class K2.

The k-class describes the tightening behaviour of a bolting assembly in relation to friction and therefore the relationship between applied torque M and achieved preload F. The corresponding k-value is defined as

$$K = M/F/d \tag{3}$$

where d is the nominal bolt diameter. In practical terms, the k-value expresses how much torque is required to generate a certain preload and is therefore an indirect measure of the friction conditions within the assembly, especially in the threads and under the nut bearing surface.

For k-class K1, the k-value of individual test assemblies may vary between 0.10 and 0.16. K1 therefore permits a comparatively broad scatter of the torque-preload relationship, but within a defined range that is suitable for a standardized tightening procedures called the modified torque method [10] with tabulated parameters. For k-class K2, by contrast, the mean k-value of the test lot may range from 0.10 to 0.23, while the scatter within the lot is limited to a coefficient of variation of not more than 6%. Thus, K2 does not primarily require a narrow absolute k-range, but a well-controlled and reproducible friction behaviour within the tested lot.

These differences are directly relevant for execution. K1 strongly supports standardized site procedures with predefined tightening parameters (modified torque method), whereas K2 is associated with a more calibration-sensitive torque concept and therefore requires a closer link between the tested lot and the tightening parameters used on site (torque method). The torque for the latter varies from bolt assembly lot to bolt assembly lot. Consequently, practical handling, inspection logic, and site logistics can differ substantially between the two systems.

HV assemblies are especially attractive in the context of the present article because they are closely linked to the differentiated use of target level II and target level I in practice. In particular, HV assemblies in k-class K1 allow execution and inspection simplifications that become highly relevant when reduced preload concepts such as $F_{p,C}^{*}$ are used. This is one of the central reasons why the present paper focuses primarily on HV assemblies and k-class K1.

A further practical advantage of HV/K1 assemblies is the extended assembly-lot concept that is associated with the modified torque method in everyday use. Components of the assembly, namely bolt, nut, and washers, can be exchanged across production lots as long as they come from the same manufacturer, and the same tightening torques continue to apply. This makes HV assemblies with K1 and the modified torque method particularly user-friendly and robust in site logistics and replacement practice.

3.3 Tightening Methods and Practical Consequences

From the perspective of the practicing engineer, the decisive question is which tightening method matches the intended preload force level and the chosen assembly system. If the objective is to achieve the full preload level $F_{p,C}$, the preferred route for k-class K1 assemblies is the combined method, while for k-class K2 assemblies the torque method or the combined method is the appropriate normative route [12]. Both methods are geared towards achieving the full structurally relevant preload with the reliability required when preload enters the mechanical model of the joint.

The modified torque method, by contrast, is closely associated with the reduced preload level $F_{p,C}^{*}$. Its major attraction lies in its practical simplicity: the erection crew can work with fixed torque values for the standard HV dimensions (see Table 2), benefiting from the user-friendly K1 concept and the extended assembly-lot handling.

Compared to this, the torque values for the torque method according EN 1090–2 [12] vary from lot to lot, depending on the k_m-value specified for the bolting assembly lot.

Table 2. Reduced preload force $F_{p,C}^*$ and torque values for the modified torque method for HV 10.9 K1

	M12	M16	M20	M22	M24	M27	M30	M36
Preload $F_{p,C}^*$ [kN]	50	100	160	190	220	290	350	510
1st tightening step [Nm]	75	190	340	490	600	940	1.240	2.100
Final tightening step [Nm]	100	250	450	650	800	1.250	1.650	2.800

This is exactly what has made the HV/K1/modified-torque combination so successful in practice. The limitation must nevertheless be stated clearly. The modified torque method reaches only the reduced preload level $F_{p,C}^*$, not the full preload level $F_{p,C}$ and does not provide such high preload reserves [5, 8]. For target level II this is often entirely sufficient, and in many cases economically very attractive, but for target level I the engineer should in principle prefer $F_{p,C}$, either by the combined method for k-class K1 or by the torque method for k-class K2.

This practical recommendation also offers a clean narrative for the article. It explains why the reduced preload concept is so widespread and useful without overstating its field of preferred application. At the same time, it preserves a clear engineering distinction between serviceability-oriented preloading and structurally relevant preloading, which is exactly the distinction on which the entire article is built.

3.4 Consequences for Execution and Inspection

For target level I, the execution requirements extend beyond tightening itself. If torque or modified torque procedures are used, verification is carried out with a test torque; if the combined method is used, the additional rotation must be visually checked and the rotation marks must be verified. In all target level I cases, the maximum coating thickness on all surfaces in the clamped interface must be limited to 0.100 mm, including the surfaces under the washers. Otherwise, settlement-related preload losses have to be taken into account. For this purpose EN 1090–2 [12], Annex I gives some recommendations.

For target level II, the same care is required during tightening as for target level I, but the inspection concept is less stringent because the connection is treated for verification purposes as a non-preloaded connection [10]. In practice, a visual inspection is sufficient, focusing on closed gaps, correct assembly, and the presence of all required components. Although coating thickness is not a controlling criterion in the same way as for target level I, keeping it low remains desirable in order to support durable and robust bolted connections (Fig. 4).

Non-preloaded connections are only brought to the snug-tight condition and then subjected to visual inspection. This distinction is important because it shows that the



Fig. 4. Target level II with coated component (left) and Target level I with a masked or merely primed component (right)

functional level of preloading affects not only the design model, but also the quality-assurance route on site.

4 Procedure Qualification for Non-standard Tightening Situations: Introduction to ISO 18954 [19]

For pretensioned structural bolting, standard tightening rules do not cover all practical applications. This is particularly relevant where tightening is carried out by turning the bolt head instead of the nut, where bolts are installed in tapped holes, where stainless steel bolting assemblies are used, or where special lubrication conditions apply [7]. In such cases, a procedure qualification is required to determine suitable tightening parameters for the specific application.

The newly published ISO 18954 [19] provides an international framework for this purpose. The document is intended for pretensioned bolted connections in structural steelwork for which no approved tightening parameters are available in national or international standards, and it sets out a Bolt Tightening Qualification Procedure (BTQP) to establish secure tightening parameters for one defined configuration. In this respect, the standard does not replace established rules for conventional bolting, but complements them wherever the usual normative provisions no longer apply.

A key strength of ISO 18954 [19] is that it does not rely primarily on empirical pre-installation verification practice, such as the Tension calibrator testing [9] (aka Skidmore) widely used in North American structural bolting practice, but on a structured qualification process combining testing, evaluation, and documentation. The procedure is explicitly configuration-specific, meaning that the determined tightening parameters are valid only for the tested combination of assembly, lubrication, tightening method, and target pretension level. This is fully consistent with the established principle that the result from procedure tests cannot simply be transferred to other bolting situations without renewed verification.

From the perspective of the present article, the statistical basis of the procedure is particularly important. ISO 18954 [19] determines tightening parameters by evaluating minimum and maximum values, mean values, and 5% and 95% fractiles of the achieved pretension forces, assuming a normal distribution of the test results. This reflects the use of EN 1990-conforming statistical methods [13] for the evaluation of test data and supports a safety format that is familiar from structural reliability verification in steel construction.

Thus, ISO 18954 [19] can be understood as a systematic route for qualifying tightening procedures in non-standard applications while maintaining a safety-oriented and statistically founded basis for execution. For the purposes of this paper, its significance lies less in the detailed test mechanics than in the fact that it provides a transparent and internationally understandable framework for deriving project-specific tightening parameters where standard rules are unavailable.

Even a correctly qualified tightening procedure does not eliminate the risk of preload loss in service. This leads directly to the question of how joints can be secured in the long term and which additional measures are compatible with the functional classification developed above.

5 Loosening and Wedge-Locking Washers

Preloaded bolted connections may lose preload in service due to settlement, relaxation, or cyclic loading, and under unfavourable conditions this can develop into self-loosening or complete unscrewing [1]. In the context of dynamically loaded structural connections, wedge-locking washers have proven to be an effective solution for maintaining preload and preventing self-loosening [2, 4].

One such system is the Nord-Lock SC washer, which is covered by ETA-20/0010 [11] for high-strength structural bolting assemblies for preloading and is intended to prevent self-loosening under static, quasi-static, fatigue-relevant, dynamic, or shock loading. The ETA further states that these washers replace the conventional flat washers in preloaded structural bolting assemblies and may be used for bolting categories A to E according to EN 1993-1-8 [14], provided that the specified execution requirements are observed.

With Nord-Lock SC washers, the modified torque method, the torque-controlled method, and the combined method are in principle all possible, but with tightening parameters that differ from those of conventional washer arrangements. These parameters may be taken from ETA-20/0010 [11] where applicable, may be determined by a Bolt Tightening Qualification Procedure according to ISO 18954 [19], or may be derived from suitability testing according to EN 14399-2 [16] including the determination and evaluation of the relevant tightening parameters and k-factor-related behaviour. For the modified torque method a comparison is made in Table 3.

Table 3. Comparison of torque values to achieve $F_{p,C}{}^{*}$ with HV 10.9 K1

	M12	M16	M20	M22	M24	M27	M30	M36
Preload $F_{p,C}{}^{*}$ [kN]	50	100	160	190	220	290	350	510
M_T with flat washers [Nm]	100	250	450	650	800	1.250	1.650	2.800
M_T with NLSC [Nm]	165	400	800	1.100	1.300	1.900	2.300	4.050

The required tightening torques with Nord-Lock washer are visibly higher. This is due to the higher bearing friction between the Nord-Lock washer and the rotating element. Even though the torque is significantly higher, the preload in the bolt remains unchanged. Therefore, bolt overload is excluded despite the higher torque values. The additional torque is used solely to overcome friction and does not result in any additional torsional stress. The latter depends exclusively on the friction in the bolt or nut threads.

The use of wedge-locking washers is therefore best understood not as a substitute for proper design and execution, but as an additional measure within a coherent bolting concept.

6 Conclusion

The key issue in bolted steel connections is not whether preload is present, but what structural role it is intended to play. This functional distinction determines design assumptions, tightening method, execution quality, and inspection strategy. The proposed classification helps distinguish between joints where preload is beneficial and joints where preload is structurally required. A corresponding flowchart is shown in Fig. 5. To avoid ambiguity, the intended connection type should therefore be defined explicitly as target level I, target level II, or non-preloaded, and this information should be stated clearly in drawings, specifications, and execution documents.

ISO 18954 is relevant when the pretensioning situation is not covered by conventional normative tightening parameters. It complements the existing preload concepts by providing a structured route for special configurations, without replacing the basic distinction between target level I, target level II, and non-preloaded connections.

Finally, preload retention in service remains an issue, because settlement, relaxation, vibration, and cyclic effects may reduce the initial clamping force. Where such effects are expected, wedge-locking washers can be considered as a supplementary measure to improve resistance against self-loosening, but they do not alter the functional classification of the joint and do not replace correct design, qualified tightening, or proper execution.

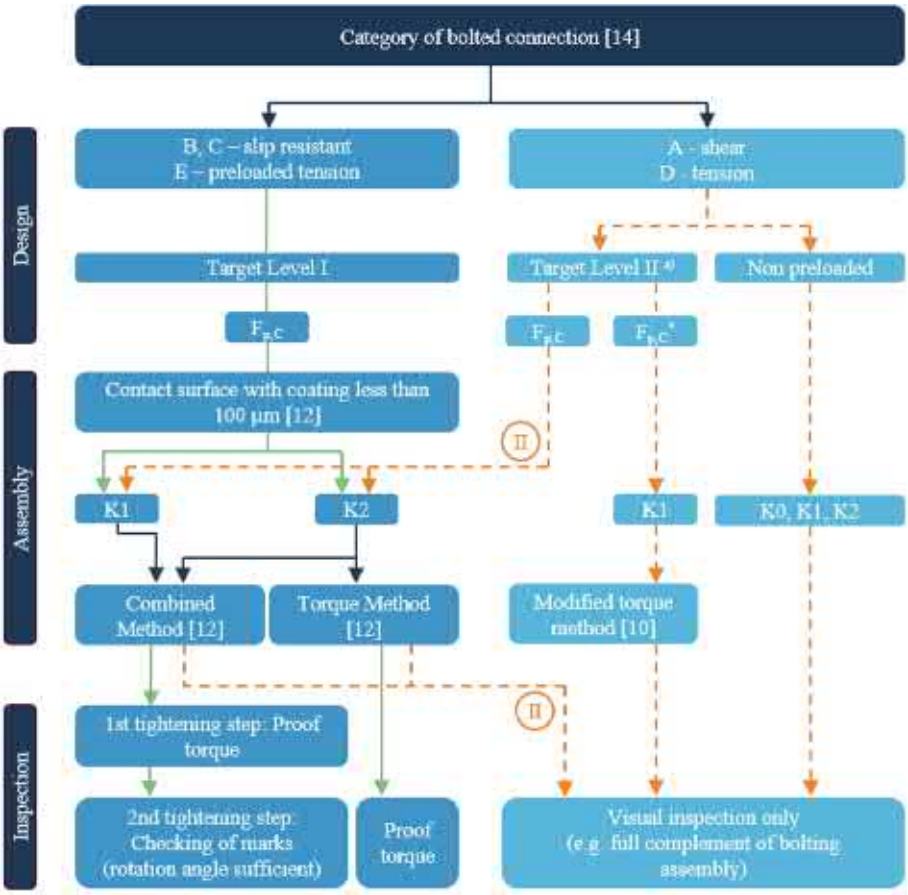


Fig. 5. Flowchart for selecting the correct Preload Level (HRC - and DTI-tightening method are explicitly not mentioned)

References

1. Götz F (2023) Durable bolted joints for steel structures. ce/papers 6:1399–1405
2. Misiek T, Götz F, Volz M (2021) Dauerhaftigkeit und Robustheit von Schraubenverbindungen bei Kranbahnträgern. Stahlbau 90(S1):36–53
3. Schmidt H, Korth J-D, Machura G, Podleschny R, Kammel C, Volz M (2019) Ausführung von Stahlbauten, Kommentare zu DIN EN 1090–2 und DIN EN 1090–4, 2nd edn. DIN Deutsches Institut für Normung e.V, Berlin
4. Seeßelberg C (2020) Kranbahnen, 6th edn. Beuth Verlag, Berlin
5. Stranghöner N, Makevicius L, Henkel K-M, Glienke R, Dörre M (2018) Vorspannkraftverluste geschraubter Verbindungen infolge beschichteter Kontaktflächen. Stahlbau 87(10):991–1009

6. Stranghöner N, Jungbluth D (2017) Verfahrensprüfung zur Bestimmung von Anziehparametern für vorgespannte geschraubte Verbindungen. Stahlbau 86(12):1079–1088
7. Stranghöner N, Jungbluth D, Hüller V, Machura G (2016) Anziehen von geschraubten Verbindungen nach Eurocode 3 und DIN EN 1090-2. Stahlbau 85(5):327–335
8. European Commission research Programm of the research Fund for Coal and Steel, technical group 8 (2018) Execution and reliability of slip resistant connections for steel structures using CS and SS SIROCO. Final Report
9. Research Council on Structural Connections (RCSC) (2020) Specification for Structural Joints Using High-Strength Bolts. Research Council on Structural Connections, Chicago
10. DASt-Richtlinie 024 (2024) Anziehen von geschraubten Verbindungen der Abmessungen M8 bis M39. Deutscher Ausschuss für Stahlbau (DASt). Stahlbau Verlags- und Service GmbH, Düsseldorf
11. ETA-20/0010 (2025) Nord-lock SC-washers for high-strength structural bolting assemblies for preloading. Deutsches Institut für Bautechnik, Berlin
12. EN 1090–2:2024–09 (2024) Execution of steel structures and aluminium structures — Part 2: Technical requirements for steel structures
13. EN 1990:2021–10 (2021) Eurocode: Basis of structural design
14. EN 1993-1-8:2025–04 (2025) Eurocode 3: Design of steel structures — Part 1–8: Joints
15. EN 14399–3:2015–04 (2015) High-strength structural bolting assemblies for preloading — Part 3: System HR — Hexagon bolt and nut assemblies
16. EN 14399–4:2015–04 (2015) High-strength structural bolting assemblies for preloading — Part 4: System HV — Hexagon bolt and nut assemblies
17. EN 14399–9:2019–06 (2019) High-strength structural bolting assemblies for preloading — Part 9: System HR or HV — Direct tension indicators for bolt and nut assemblies
18. EN 14399–10:2019–06 (2019) High-strength structural bolting assemblies for preloading - Part 10: System HRC - Bolt and nut assemblies with calibrated preload
19. ISO 18954:2026–05 (2026) Steel structures — Structural bolting — Test method to determine parameters of bolt tightening procedures
20. ÖNORM B 1993-1-8:2015–11 (2015) Eurocode 3: Bemessung und Konstruktion von Stahlbauten - Teil 1–8: Bemessung von Anschlüssen - Nationale Festlegungen zu ÖNORM EN 1993-1-8, nationale Erläuterungen und nationale Ergänzungen

Ultimate Response of Bolted Gusset Plate Connections in Concentrically Braced Frames: Design Predictions Versus Finite Element Simulations

Massimo Cicia(✉), Mario D'Aniello, and Raffaele Landolfo

Department of Structures for Engineering and Architecture, University of Naples Federico II, Naples, Italy
massimo.cicia@unina.it

Abstract. Design provisions for gusset plate connections of concentrically braced frames are commonly based on simplified analytical approaches to estimate the force distribution within the connection components. According to EN 1993-1-8, bolted gusset plate connections require the verification of several potential failure mechanisms involving plates, bolts and connecting angles. However, the actual stress distribution, nonlinear response and governing failure modes may differ from those predicted by simplified design models. In this study, bolted gusset plate connections to beams and columns through angles are designed in accordance with the second generation of EN 1998-1-2, while the resistance checks are carried out according to EN 1993-1-8. Four configurations with different brace inclinations are considered. For each case, the governing design checks are identified in terms of demand-to-capacity ratios. Detailed finite element models are then developed to investigate the connection response. The numerical results are used to evaluate the strength reserve beyond the design force and to assess whether the critical mechanisms observed in the simulations are consistent with the governing analytical checks.

Keywords: Bolted connections · gusset plates · concentrically braced frames · finite element modelling · EN 1993-1-8 · EN 1998-1-2

1 Introduction

Steel concentrically braced frames are widely used as seismic-resistant systems because of their high lateral stiffness and efficient force-transfer mechanism. In these systems, the axial force developed in the brace has to be safely transferred to the surrounding beam-column assemblage through the gusset plate connection. As a consequence, the design of the connection plays a key role in ensuring the intended seismic response of the bracing system and in avoiding premature local failures that could compromise the global structural performance. Previous experimental and analytical studies have shown that gusset plate detailing and deformation capacity can significantly influence

© The Author(s), under exclusive license to Springer Nature Switzerland AG 2026
R. Zanon et al. (Eds.): CTA 2026, LNCE 942, pp. 188–199, 2026.
https://doi.org/10.1007/978-3-032-39505-4_17

the seismic response of concentrically braced frames, especially when local yielding, brace buckling and connection flexibility interact [1–3]. Bolted gusset plate connections may involve several components, including the gusset plate, connecting angles, bolts, welds and the connected beam and column elements. Their design is therefore governed by multiple resistance checks, such as bolt shear and tension, bearing resistance, net-section resistance, block tearing, local yielding and combined shear-bending interaction of the connected components. According to EN 1993-1-8 [4], these checks are generally carried out by evaluating the demand acting on each component and comparing it with the corresponding design resistance. However, the estimation of the internal force distribution is usually based on simplified analytical assumptions, which may not fully reproduce the actual nonlinear behaviour of the connection. These assumptions are rooted in classical effective-width concepts and force-based approaches for bracing connections, which remain widely used for preliminary design and component-level verification [5, 6]. In particular, the response of bolted gusset plate connections may be strongly affected by local stress concentrations around bolt holes, non-uniform bearing pressure, progressive yielding of plates and angles, contact interaction among connected parts and possible bolt damage. These phenomena may lead to force redistributions that are difficult to capture through simplified design models. Therefore, the analytical check associated with the largest demand-to-capacity ratio does not necessarily coincide with the critical mechanism that develops in the actual nonlinear response of the connection. Within this framework, finite element simulations represent a useful tool to investigate the stress distribution, yielding patterns and local mechanisms developing in gusset plate connections and steel braced systems [7]. In addition, nonlinear numerical analyses can provide an estimate of the strength reserve available beyond the design force, which is particularly relevant when capacity design principles are adopted for seismic applications. This paper investigates bolted gusset plate connections of concentrically braced frames designed according to the second generation of EN 1998-1-2 [8], within the broader context of recent studies on updated Eurocode-oriented seismic design rules for steel and lightweight steel structural systems [9–18]. Four configurations with different brace inclinations are considered. For each configuration, the governing analytical design checks are first identified in terms of demand-to-capacity ratios. Detailed finite element models are then developed to evaluate the numerical force-displacement response, the stress distribution and the local critical mechanisms. The main objectives of the study are: (i) to quantify the reserve of strength between the design force and the numerical capacity of the connection, and (ii) to assess whether the failure modes or critical mechanisms observed in the finite element simulations are consistent with those predicted by the governing analytical checks.

2 Design of Investigated Connections

2.1 Reference Structural System

The investigated bolted gusset plate connections are derived from a reference steel concentrically braced frame designed according to European seismic design provisions. The reference structure consists of a six-storey steel building in which the lateral resistance is provided by concentrically braced frames arranged along the main plan directions.

The bracing system is characterised by X-shaped diagonal members connected to the surrounding beam-column assemblage through gusset plate connections. The seismic design of the reference structure was carried out for ductility class DC2. Structural members are made of S355 steel. Beams are realised using IPE profiles, columns using HE profiles, and braces using circular hollow sections. From the global structure, the fourth storey was selected as representative for the detailed investigation of the gusset plate connection response. At this level, the structural members consist of an IPE 360 beam, an HE 220 B column and a CHS 88.9/6 diagonal brace, all made of S355 steel. These profiles were kept unchanged in all the investigated configurations, so that the influence of the brace inclination could be assessed without introducing additional variations related to member sizing. The corresponding corner beam-column-brace joint was therefore adopted as the reference configuration for the design and numerical assessment of the bolted gusset plate connections.

2.2 Reference Gusset Plate Connection

The selected joint consists of a corner gusset plate connection between the diagonal brace and the surrounding beam-column assemblage. The diagonal member is connected to the gusset plate through a welded slotted connection, while the gusset plate is connected to the beam and column by means of double angle components and preloaded bolts. The slotted brace end is reinforced by additional plates in order to avoid premature net-section failure of the brace. The design of the gusset plate was carried out according to the provisions of the second generation of EN 1998-1-2. In particular, the geometry of the plate was defined to allow the development of a linear yielding mechanism, providing the rotational capacity required during brace buckling while avoiding premature failure of the connection components. The gusset plate connection was therefore proportioned to transfer the expected brace force to the beam and column, while maintaining adequate strength and stability of the gusset plate, bolts, angles and connected components. The connection design followed a sequential procedure. First, the brace-to-gusset welded connection was defined on the basis of the expected tensile resistance of the brace. Then, the gusset plate geometry was selected to satisfy the geometrical requirements associated with the intended yielding mechanism. Finally, the bolted angle connections to the beam and column were proportioned and verified according to EN 1993-1-8. The resistance checks considered in the design included the main potential failure mechanisms involving the brace, gusset plate, bolts and connecting angles. In particular, the checks included brace net-section fracture and block shear, weld resistance, gusset plate yielding and fracture, gusset plate buckling under compression, bolt shear and tension, bearing resistance, block tearing, net-area resistance, and combined shear-bending interaction of the connected components.

2.3 Investigated Configurations and Design Checks

Starting from the reference configuration, four connection layouts with different brace inclinations were considered. The beam, column and brace cross-sections were kept unchanged, whereas the brace inclination was varied. For each inclination, the gusset plate and the associated bolted angle connections were redesigned in order to obtain

a mechanically consistent connection configuration. This modelling choice allows the influence of the brace inclination on the design outcome and on the subsequent nonlinear response of the connection to be isolated. In fact, by keeping the brace, beam and column profiles constant, the observed differences among the investigated configurations can be mainly attributed to the change in connection geometry and force-transfer mechanism induced by the brace angle. For each configuration, the design checks were expressed in terms of demand-to-capacity ratios, according to Eq. (1):

$$D/C = E_d/R_d \tag{1}$$

where E_d is the design demand acting on the considered component and R_d is the corresponding design resistance. The governing design check was identified as the check associated with the maximum demand-to-capacity ratio. These analytical results provide the reference basis for the subsequent comparison with the finite element simulations, where the observed critical mechanisms are assessed against the checks that governed the design procedure. The main geometrical properties of the investigated connections and the corresponding governing analytical checks are summarised in Table 1. For each brace inclination, the gusset plate thickness and the profiles of the GP-to-column and GP-to-beam connecting angles were selected as a result of the design procedure. The governing design check was identified as the verification associated with the maximum demand-to-capacity ratio among all the considered resistance checks. As shown in Table 1, the governing analytical checks are mainly associated with the connecting angles. In particular, the 30° and 60° configurations are governed by bearing checks of the GP-to-beam and GP-to-column angles, respectively, whereas the 40° and 50° configurations are governed by yielding of the corresponding connecting angles. This confirms that the brace inclination affects not only the geometry of the gusset plate, but also the most demanding component-level verification within the bolted connection.

Table 1. Main connection details and governing analytical design checks

Brace Inclination [°]	GP thickness [mm]	Column-side angle [mm]	Beam-side angle [mm]	Governing check [−]	$(D/C)_{max}$ [−]
30	10	L 65x65x6	L 65x65x6	Angle Bearing (Beam side)	1.00
40	15	L 65x65x6	L 65x65x8	Angle Yielding (Beam side)	0.97
50	25	L 65x65x8	L 70x70x9	Angle Yielding (Column side)	0.99
60	15	L 65x65x7	L 65x65x6	Angle Bearing (Column side)	0.85

3 Finite Element Modelling

3.1 Model Layout and General Assumptions

The numerical assessment of the investigated connections was carried out through three-dimensional finite element models developed in ABAQUS [19]. The model includes the gusset plate, the diagonal brace, the double angle connections, and deformable plates

representing the beam and column flanges. This modelling strategy allows both sides of the bolted connections to be explicitly represented, while accounting for the local flexibility of the connecting angles and supporting plates. The finite element model adopted in this study is shown in Fig. 1. As illustrated, the supporting plates on the beam and column sides are constrained through reference points (RPs) located at the centroids of the connected regions, whereas an additional RP is defined at the brace end. This latter RP is used to apply the imposed displacement along the brace axis and to evaluate the corresponding axial reaction force. In order to focus the analysis on the ultimate response of the connection, the diagonal brace was modelled as an elastic member. This assumption prevents brace yielding or fracture from governing the response and allows the nonlinear behaviour of the bolted gusset plate connection to be investigated up to the development of local failure mechanisms in the connection components. The same modelling strategy was adopted for all the investigated brace inclinations. Therefore, the differences observed in the numerical response can be mainly attributed to the variation of the connection geometry and to the associated changes in the force-transfer mechanism.

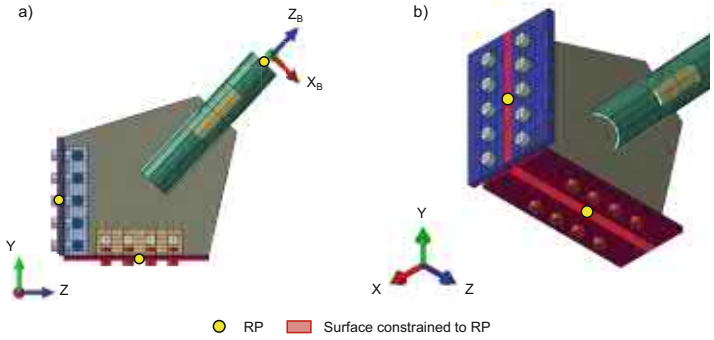


Fig. 1. Finite element model adopted in the study: (a) front view and (b) axonometric view

3.2 Material Modelling, Contacts and Damage

Unlike the analytical design checks, the finite element models were defined using mean material properties. As a consequence, the numerical simulations are intended to reproduce the expected nonlinear response of the connection, rather than a code-based design resistance. This distinction should be considered when interpreting the strength reserve with respect to the design force. Gusset plates, connecting angles and supporting plates were modelled using an elasto-plastic constitutive law for structural steel. Mean values of yield and ultimate strength were adopted for these components. Bolts were modelled explicitly using three-dimensional solid elements and a ductile damage formulation calibrated consistently with available experimental evidence and finite element modelling criteria for European preloadable grade 10.9 bolt assemblies [20, 21]. Conversely, ductile damage was not introduced for gusset plates, connecting angles and supporting plates. For these components, the critical mechanisms were therefore interpreted in terms of

stress distribution, local yielding and plastic strain localisation. This distinction is relevant for the interpretation of the results, since bolt failure can be directly assessed from the damage variables, whereas mechanisms involving plates and angles are identified from the evolution of stresses and plastic strains. Contact interactions were explicitly defined between the connected parts. A surface-to-surface contact formulation was adopted, with hard contact in the normal direction and frictional behaviour in the tangential direction. Contact was defined between the bolt shanks and the corresponding holes, as well as between bolt heads, nuts and the external surfaces of the connected plates and angles. Welded connections were modelled by enforcing displacement compatibility between the connected components.

3.3 Boundary Conditions and Loading Protocol

The analyses were performed under monotonic quasi-static loading conditions using a displacement-controlled procedure. Only tensile loading of the diagonal brace was considered. As shown in Fig. 1, the imposed displacement was applied at the brace-end reference point along the longitudinal axis of the brace, so that the resulting response could be directly interpreted in terms of axial force versus axial displacement. The beam-side and column-side supporting plates were restrained through the corresponding reference points, reproducing the kinematic conditions adopted for the numerical idealisation of the connection. The axial force was evaluated from the reaction force associated with the imposed displacement, while the axial displacement was taken as the displacement imposed at the brace end along the brace axis. The numerical response of each configuration was therefore described through force-displacement curves, where F_{axial} is the axial force transferred by the brace to the connection and u_{axial} is the imposed axial displacement along the brace axis. These curves were used to evaluate the maximum numerical resistance of the connection and to quantify the strength reserve with respect to the design axial force. In addition, stress distributions, plastic strain fields and bolt damage were examined to identify the critical mechanisms developing in the numerical models.

4 Numerical Results and Discussion

4.1 Force-Displacement Response and Strength Reserve

The numerical response of the investigated connections was first evaluated in terms of normalised axial force versus axial displacement. The axial force was normalised with respect to the design force of the brace (F_d), equal to 700 kN. The design condition, hereinafter referred to as CD, corresponds to the attainment of $F/F_d = 1$, whereas the ultimate condition, hereinafter referred to as CU, is defined as the condition associated with the maximum axial force reached in the numerical force-displacement curve. The normalised force-displacement curves are reported in Fig. 2. All the investigated configurations exhibit a significant strength reserve with respect to the design force, as summarised in Table 2. It should be emphasised that the design force and analytical checks are based on design values, whereas the finite element capacities are obtained

using mean material properties. Therefore, $F_{(u,FEM)}/F_d$ should be interpreted as a numerical strength reserve within the adopted modelling assumptions. The 30° configuration shows the lowest strength reserve and develops a more evident plateau in the force-displacement response. Conversely, the 40° and 50° configurations exhibit the largest numerical capacities, with strength ratios close to 2.5 and 2.4, respectively. The 60° configuration reaches a strength ratio of about 2.3. Overall, the results indicate that, within the adopted modelling assumptions, the investigated connections provide a considerable reserve of strength beyond the design axial force.

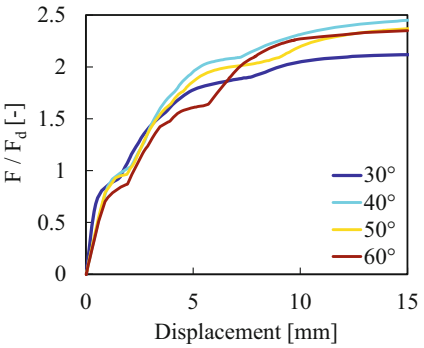


Fig. 2. Normalised axial force-displacement response of the investigated connections

Table 2. Numerical strength reserve of the investigated connections

Brace inclination [°]	F_d [kN]	$F_{u,FEM}$ [kN]	$F_{u,FEM}$ / F_d [−]
30	700	1483	2.12
40		1733	2.48
50		1664	2.38
60		1581	2.26

4.2 Stress Distribution and Local Damage Evolution

The local response of the connections was investigated by monitoring bolt damage, equivalent plastic strain and von Mises stress distributions. The scalar damage variable SDEG was used for bolts, for which ductile damage was explicitly included in the numerical model. Conversely, for gusset plates and connecting angles, where no damage formulation was introduced, the response was interpreted in terms of PEEQ, stress distribution and hole ovalization. The comparison was carried out at two relevant stages: the design condition CD, corresponding to $F/F_d = 1$, and the ultimate condition CU, corresponding to the maximum axial force reached in the numerical response. The von Mises stress distributions at CD and CU are shown in Fig. 3. The stress scale is limited to the yield stress of the material; therefore, grey regions indicate areas where the yield threshold is exceeded.

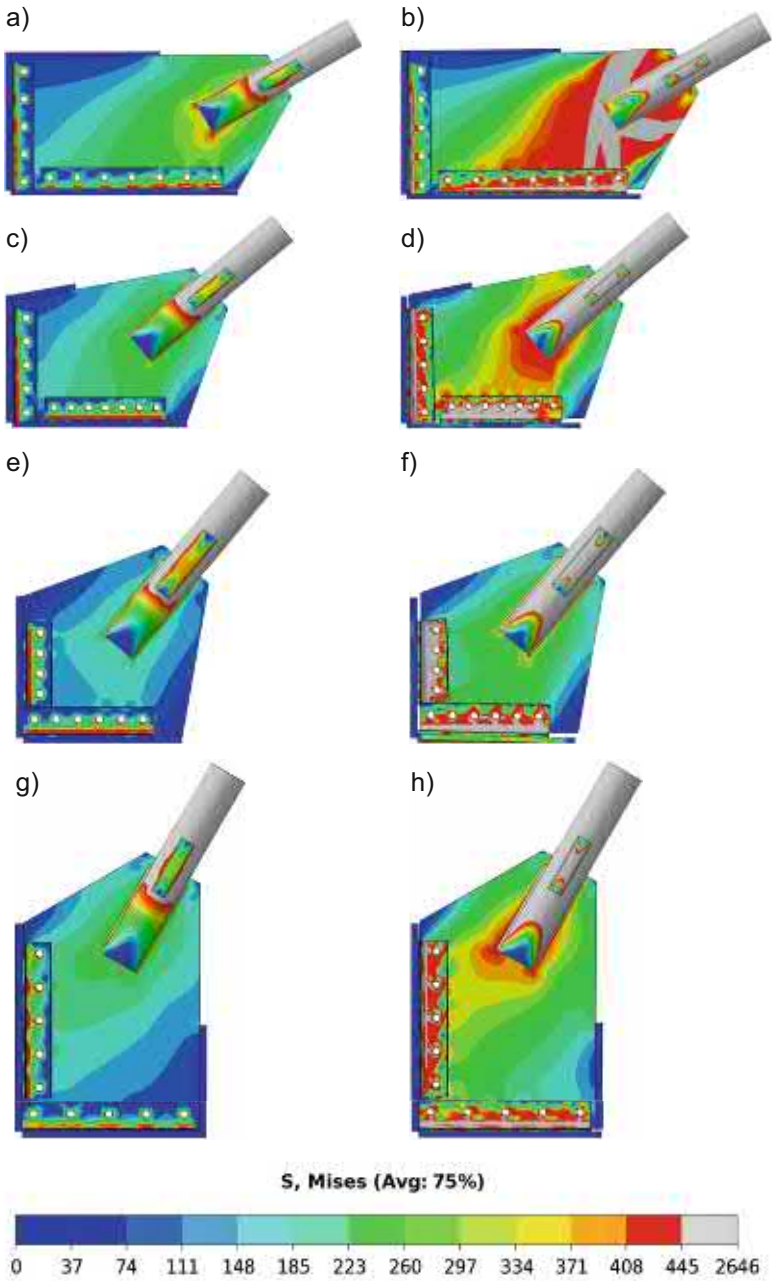


Fig. 3. Von Mises stress distributions for the investigated configurations at the design condition CD and ultimate condition CU: (a, b) 30°, (c, d) 40°, (e, f) 50° and (g, h) 60°. The first column, namely (a, c, e, g), refers to CD, whereas the second column, namely (b, d, f, h), refers to CU. The stress scale is capped at the yield stress; grey regions denote zones where the von Mises stress exceeds the yielding threshold

These regions should be interpreted as zones of inelastic stress redistribution rather than as direct evidence of fracture. At the design condition, no bolt damage is observed in any of the investigated configurations, with $SDEG_{max} = 0$. Moreover, the gusset plate remains essentially elastic in terms of PEEQ, while only limited local yielding is observed in the connecting angles, mainly around fillets or local discontinuities. This confirms that, at the design force, the connection is far from the development of the critical mechanisms observed at larger deformation levels. For the 30° configuration, the ultimate condition is characterised by a bearing-dominated response in the beam-side region. Bolt damage remains limited, with $SDEG_{max} = 0.1$ in the outer bolt of the GP-to-beam connection. The connecting angles exhibit plastic strain concentration mainly in the GP-to-beam angle, with $PEEQ_{max} = 0.25$, accompanied by slight hole ovalization. The observed bearing-dominated ovalization around bolt holes is consistent with previous studies on bearing stress distribution and bearing resistance in bolted steel connections [22, 23]. The most severe localisation occurs in the gusset plate, where PEEQ values larger than 1 are reached near the outer hole of the GP-to-beam connection, together with pronounced yielding and severe hole ovalization. For the 40° configuration, the ultimate response is governed by a stronger involvement of the beam-side bolted connection. At CU, the maximum bolt damage reaches $SDEG_{max} = 1.0$, located in the outer bolt on the gusset side of the GP-to-beam connection. The connecting angles exhibit diffuse yielding, with $PEEQ_{max} = 0.41$, and visible ovalization mainly in the beam-side angle. The gusset plate also shows plastic strain concentration near the outer beam-side hole, with $PEEQ_{max} = 0.40$, together with diffuse yielding in the GP-to-beam region. For the 50° configuration, the numerical response shifts towards the column-side connection. At CU, bolt damage reaches $SDEG_{max} = 0.5$, mainly in the outer bolt on the column side, with some damage also affecting the outer beam-side bolt. The connecting angles show the largest plastic strain in the GP-to-column angle, with $PEEQ_{max} = 0.34$, accompanied by diffuse yielding and hole ovalization in the column-side angle. The gusset plate remains less severely plasticised than in the previous cases, with $PEEQ_{max} = 0.20$, localised near the outer column-side bolt, and only limited ovalization. For the 60° configuration, the ultimate response is less severe in terms of bolt damage, with $SDEG_{max} = 0.16$. The connecting angles exhibit $PEEQ_{max} = 0.23$, mainly on the beam side, while limited ovalization is observed on the column side. In the gusset plate, plastic strain remains moderate, with $PEEQ_{max} = 0.16$, localised in the column-side region. The stress distribution shows yielding concentrated around the column-side holes, consistently with a bearing-related mechanism in this area.

4.3 Comparison with Analytical Design Checks

The numerical results were finally compared with the analytical governing checks identified in the design phase. The comparison, summarised in Table 3, aims to assess whether the regions and mechanisms identified as critical by the finite element analyses are consistent with the component-level checks governing the analytical design. For the 30° configuration, the analytical design is governed by bearing of the beam-side angle. The finite element results confirm that the beam-side region is critical and that the ultimate response is governed by a bearing-related mechanism. However, the most severe localisation is observed in the gusset plate, with pronounced ovalization of the outer GP-to-beam

hole. Therefore, the agreement is satisfactory in terms of critical region and mechanism type, although the numerical model highlights a more complex interaction between angle bearing, bolt force transfer and gusset plate deformation. For the 40° configuration, the analytical design is governed by yielding of the beam-side angle. This prediction is consistent with the numerical response, which shows diffuse yielding and ovalization in the beam-side angle, together with damage in the outer bolt of the GP-to-beam connection. The critical region predicted by the analytical design is therefore confirmed by the finite element simulation. For the 50° configuration, the governing analytical check is yielding of the column-side angle. The finite element results show localisation of plastic strains and ovalization in the column-side angle, accompanied by damage in the outer column-side bolt. In this case, the numerical evidence is consistent with the analytical prediction in terms of both critical side and involved component. For the 60° configuration, the analytical design is governed by bearing of the column-side angle. The numerical results confirm the relevance of the column-side region, where stress concentration and local ovalization are observed. Nevertheless, the response appears more distributed than in the previous cases, with plastic demand also developing in the beam-side angle. The agreement is therefore only partial, since the finite element model indicates a broader stress-transfer mechanism involving both sides of the connection.

Table 3. Comparison between governing analytical checks and numerical critical mechanisms

Brace inclination	Governing check	Main FE evidence at CU	Comment
30°	Angle Bearing (Beam side)	Beam-side bearing; severe gusset ovalization	Partly consistent
40°	Angle Yielding (Beam side)	Beam-side angle yielding; bolt damage	Consistent
50°	Angle Yielding (Column side)	Column-side angle yielding; bolt damage	Consistent
60°	Angle Bearing (Column side)	Column-side bearing; distributed yielding	Partly consistent

5 Conclusions

This paper compared analytical design predictions and nonlinear finite element simulations for four bolted gusset plate connections in concentrically braced frames, designed according to the second-generation provisions of EN 1998-1-2 and checked according to EN 1993-1-8. The main outcomes can be summarised as follows:

- All configurations showed a significant numerical strength reserve, with $F_{u,FEM}/F_d$ ranging between 2.12 and 2.48. At the design condition, no bolt damage was observed, the gusset plate remained almost elastic, and only limited local yielding developed in the connecting angles.

- Brace inclination strongly affected the force-transfer mechanism. Lower inclinations mainly activated the beam-side connection region, whereas larger inclinations progressively shifted the demand towards the column-side region.
- The finite element results were generally consistent with the governing analytical checks. Angle-yielding cases showed local deformation in the corresponding connection region, while bearing-governed cases confirmed bearing-related mechanisms, although the local response involved interaction among angles, bolts and gusset plate.

The study is limited to monotonic tensile loading and to models in which ductile damage was explicitly assigned only to bolts. Future developments should include fracture models for plates and angles, additional geometrical configurations and cyclic loading histories, in order to address seismic degradation, local fracture and low-cycle fatigue effects.

References

1. Astaneh-Asl A, Cochran ML, Sabelli R (2006) Seismic detailing of gusset plates for special concentrically braced frames. Steel TIPS, Structural Steel Educational Council, Moraga
2. Lehman DE, Roeder CW, Herman D, Johnson S, Kotulka B (2008) Improved seismic performance of gusset plate connections. J Struct Eng 134(6):890–901. https://doi.org/10.1061/(ASCE)0733-9445(2008)134:6(890)
3. Roeder CW, Lumpkin EJ, Lehman DE (2011) A balanced design procedure for special concentrically braced frame connections. J Constr Steel Res 67(11):1760–1772. https://doi.org/10.1016/j.jcsr.2011.04.016
4. CEN (2024) EN 1993-1-8: Eurocode 3: design of steel structures — part 1–8: joints. European Committee for Standardization, Brussels
5. Whitmore RE (1952) Experimental investigation of stresses in gusset plates. Bulletin no. 16, Engineering Experiment Station. University of Tennessee, Knoxville
6. Muir LS, Thornton WA (2014) Vertical bracing connectio000ns — analysis and design. Steel Design Guide 29. American Institute of Steel Construction, Chicago
7. Freddi F et al (2025) Seismic retrofitting of existing steel frames with external BRBs: pseudo-dynamic hybrid testing and numerical parametric analysis. Earthq Eng Struct Dyn 54(3):1064–1083. https://doi.org/10.1002/eqe.4292
8. CEN: EN 1998-1-2: Eurocode 8: design of structures for earthquake resistance — part 1–2: buildings. European Committee for Standardization, Brussels (2026)
9. Cicia M, D'Aniello R, Landolfo R (2024) Behaviour of gusset plate connections designed according to prEN 1998-1-2:2022. In: Mazzolani FM, Piluso V, Nastri E, Formisano A (eds) Proceedings of the 11th International Conference on Behaviour of Steel Structures in Seismic Areas, STESSA 2024, Lecture notes in civil engineering, vol 520. Springer, Cham, pp 688–698. https://doi.org/10.1007/978-3-031-62888-7_60
10. Cicia M, D'Aniello M, Landolfo R (2024) Brace-to-beam connections of chevron-concentrically braced frames in the framework of prEN 1998-1-2:2022. In: Mazzolani FM, Piluso V, Nastri E, Formisano A (eds) Proceedings of the 11th International Conference on Behaviour of Steel Structures in Seismic Areas, STESSA 2024, Lecture notes in civil engineering, vol 520. Springer, Cham, pp 711–720. https://doi.org/10.1007/978-3-031-62888-7_62
11. Cicia M (2025) Concentrically braced frames connections according to the second generation of Eurocode 8. In: Papadrakakis M, Fragiadakis M (eds) COMPDYN 2025: 10th international

conference on computational methods in structural dynamics and earthquake engineering, Rhodes Island, Greece, 15–18 June 2025. ECCOMAS Proceedia, pp 4211–4219. https://doi.org/10.7712/120125.12729.25244
12. Gnazzo M, Mahmoudi B, D'Aniello M, Imanpour A, Landolfo R (2026) Seismic design and response of inverted-V CBFs compliant with European and Canadian standards. Eng Struct 363:123071. https://doi.org/10.1016/j.engstruct.2026.123071
13. Milone A, Prota A, Landolfo R (2026) Ultimate and repairability performance of steel eccentrically braced frames designed according to the 2nd generation of Eurocode 8: a parametric study for medium-rise buildings. Eng Struct 365:123283. https://doi.org/10.1016/j.engstruct.2026.123283
14. Fiorino L, D'Addesa V, Landolfo R (2024) Seismic design rules for lightweight steel shear walls with wood panel sheathing within the Eurocode format. Thin-Walled Struct 204:112293. https://doi.org/10.1016/j.tws.2024.112293
15. Prota A, Fiorino L, Landolfo R (2026) Quantification of seismic performance factors according to FEMA P695 for Eurocode DC2-compliant lightweight steel shear walls with gypsum board sheathing. Thin-Walled Struct 230:115297. https://doi.org/10.1016/j.tws.2026.115297
16. Tartaglia R, Monte F, Demonceau J-F, Maddaloni G (2026) Monotonic behaviour of 4-bolt row connections: analytical and numerical analyses. J Constr Steel Res 236:110048. https://doi.org/10.1016/j.jcsr.2025.110048
17. Ascione F, D'Aniello M, Leonardi A (2026) Numerical and analytical modelling of a novel hybrid ductile connection between FRP composite elements. Thin-Walled Struct 227:115008. https://doi.org/10.1016/j.tws.2026.115008
18. Fiorino L, Campiche A, Grzesik P, Landolfo R (2024) Experimental evaluation of in-plane seismic demand on power actuated fasteners (PAF) connecting CFS drywall partitions and concrete surrounding elements. Bull Earthq Eng 22:2025–2057. https://doi.org/10.1007/s10518-023-01838-0
19. Dassault Systèmes (n.d.) Abaqus analysis user's manual. Dassault Systèmes Simulia Corp, Providence
20. D'Aniello M, Cassiano D, Landolfo R (2016) Monotonic and cyclic inelastic tensile response of European preloadable Gr10.9 bolt assemblies. J Constr Steel Res 124:77–90. https://doi.org/10.1016/j.jcsr.2016.05.017
21. D'Aniello M, Cassiano D, Landolfo R (2017) Simplified criteria for finite element modelling of European preloadable bolts. Steel Compos Struct 24(6):643–658. https://doi.org/10.12989/scs.2017.24.6.643
22. Može P, Beg D (2014) A complete study of bearing stress in single bolt connections. J Constr Steel Res 95:126–140. https://doi.org/10.1016/j.jcsr.2013.12.002
23. Može P (2018) Bearing strength at bolt holes in connections with large end distance and bolt pitch. J Constr Steel Res 147:132–144. https://doi.org/10.1016/j.jcsr.2018.04.006

Structural Performance of Orthogonal Joints in Tube-and-Joint Scaffolding Systems: Advanced Numerical Analyses and EN1993-1-8-Compliant Classification

Aldo Milone[1](✉), Raffaele Landolfo[1], Gemma Bozzacco[2], and Luigi Rama[3]

[1] Department of Structures for Engineering and Architecture, Via Forno Vecchio 36, 80134 Naples, Italy
aldo.milone@unina.it
[2] Zona Industriale, Condor Research S.r.l., 83040 Conza della Campania, Italy
[3] Zona Industriale, Condor S.p.A., 83040 Conza della Campania, Italy

Abstract. Tube-and-Joint scaffolding systems (TJSSs) are widely used as temporary structures in the construction industry due to their strong versatility deriving from *i*) the possibility of arranging even complex geometric patterns by properly assembling the components and *ii*) the intrinsic ease of dismantling and reusing of constituent elements. The overall behaviour of TJSSs is strongly influenced by the local response of cruciform joints, which connect horizontal chords and vertical studs using pressed steel elements ("caps" and "cores") and hammer-shaped bolts. In compliance with current standards, the structural performance of such joints – which must be explicitly considered during the design phase – must be determined on an experimental basis, i.e., also due to the absence of established theoretical formulations capable of adequately describing their mechanical behaviour. To this end, in this work, the performance of cruciform nodes in TJSSs is hence assessed through an extensive parametric study based on advanced local finite element models. The study accounts for the influence of *i*) material parameters, *ii*) components' thickness, and *iii*) bolts' diameter. Obtained results allow for an initial identification of most influent factors for the local and system-level structural response, as well as the definition of preliminary EN1993-1-8 compliant classification criteria in terms of strength and stiffness.

Keywords: Tube-and-joint Scaffolding Systems (TJSSs) · Cruciform Joints · EN1993-1-8 · Advanced Finite Element Models

1 Introduction

Scaffoldings are temporary (pseudo)reticular structures with both functional and workers' safety purpose. Although movable scaffolding systems are also available on the market (e.g., self-lifting structures), fixed scaffoldings still represent the most common option to support construction stages when realizing a new manufact or maintaining an existing one [1].

© The Author(s), under exclusive license to Springer Nature Switzerland AG 2026
R. Zanon et al. (Eds.): CTA 2026, LNCE 942, pp. 200–207, 2026.
https://doi.org/10.1007/978-3-032-39505-4_18

Three main typologies of fixed scaffoldings are typically adopted for construction works, i.e., prefabricated frame ("multi-directional") scaffolding systems (MDSSs), prefabricated stud & chords scaffolding systems (PSCSSs) and tube-and-joint scaffolding systems (TJSSs). While the former solutions find large applications for complex and/or large constructions, TJSSs are typically the preferred solution when realizing buildings.

TJSSs are made of hollow steel tubes (CHS), with standardized dimensions and grade (typically Ø48.3 × 3.2 mm, S235), i.e., joined together using cast components with variable steel grade (from S235 up to S355). The key component of TJSSs is the so-called cruciform joint (see Fig. 1), which orthogonally connects a vertical stud and an horizontal chord via three curved, thin components (outer "caps" and central core) fastened via hammer-shaped bolts.

In compliance with current European standards (e.g., EN 12810–2:2004 [2] and EN 74–1:2022 [3]), the structural performance of cruciform joints shall be explicitly considered during the design phase and determined on an experimental basis. This is due to *i*) the recognized influence of local joint response on the overall behaviour of steel structures [4–6] and *ii*) more critically, the absence of established theoretical formulations capable of adequately describing the mechanical behaviour of cruciform couplers.

In this regard, in the present work the structural performance of TJSS' cruciform joints is thoroughly investigated trough advanced numerical analyses. To identify key governing parameters, this study parametrically investigates the influence of *i*) material properties, *ii*) components' thickness, and *iii*) bolts' diameter.

In light of the above, this manuscript is mainly divided in three parts. In §2, key features of considered configurations and assumptions for finite element (FE) modelling are summarized. Subsequently, the local response of joints is discussed in §3, with

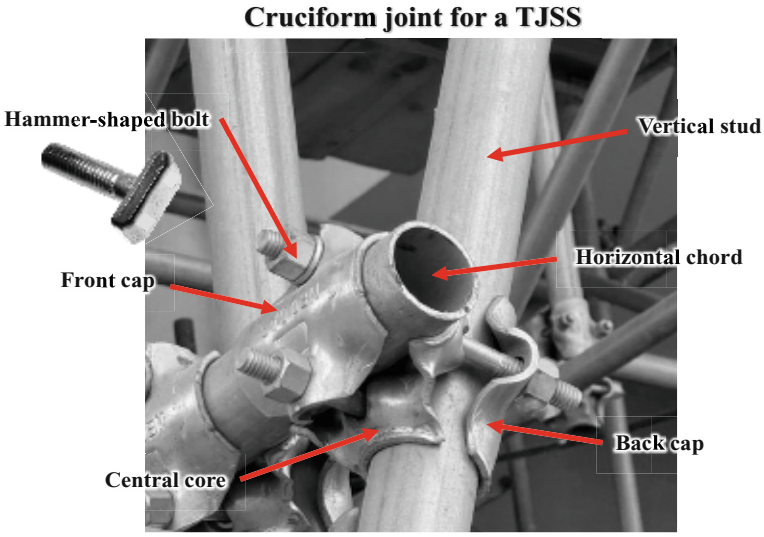


Fig. 1. Key components of a cruciform joints for a TJSS

peculiar reference to classification methods encoded in EN1993-1-8 [7]. Finally, the impact of joints' response on the overall behaviour of TJSSs is preliminarily addressed in §4.

2 Assumptions for Parametric Investigations

2.1 Extent of the Study

The most common configuration of cruciform joint for TJSSs involves Ø48.3 × 3.2 mm steel tubes connected through 4.5 mm thick caps + core and M12 hammer-shaped bolts, with all components being made of S235 European steel. Bolts are arranged in couples to connect core/front cap and core/back cap by passing through Ø17 slotted holes. To infer the contribution of each component to the local joint response, the following variation of parameters was assumed:

- Steel grade of caps/core: S235 – S275 – S355;
- Tubes' thickness: 3.2 mm – 4 mm – 5 mm;
- Bolts' diameter: M12 – M14 – M16.

A variation of the tubes' steel grade was not considered as they were expected to always remain within their elastic range. Similarly, the range of possible diameters was selected to avoid modifications in the geometry of complex cast components.

2.2 Modelling Assumptions for Local FE Analyses

Each joint configuration was modelled in ABAQUS 2017 environment [8] (see Fig. 2). Developed models reproduce test conditions for the derivation of cruciform joints' bending strength and stiffness as per INAIL QdR 12/2017 [9]. Namely, assemblies' response was assessed by imposing monotonic displacements on one end of the horizontal tube, i.e., up to a chord rotation of ≈ 0.15 rad.

All parts were discretized using 3D brick elements (C3D8R). The average mesh size (2 mm for bolts, caps and core, 10 mm for tubes) was selected based on previous sensitivity studies referred to bolted steel joints [10]. The contact among the parts was accounted for through suitable surface interactions ("hard contact" normal behaviour, "penalty" tangential behaviour with $\mu = 0.3$). Friction resistance of the joint was ensured by simulating pre-tightening of fasteners, i.e., via the "bolt-load" command.

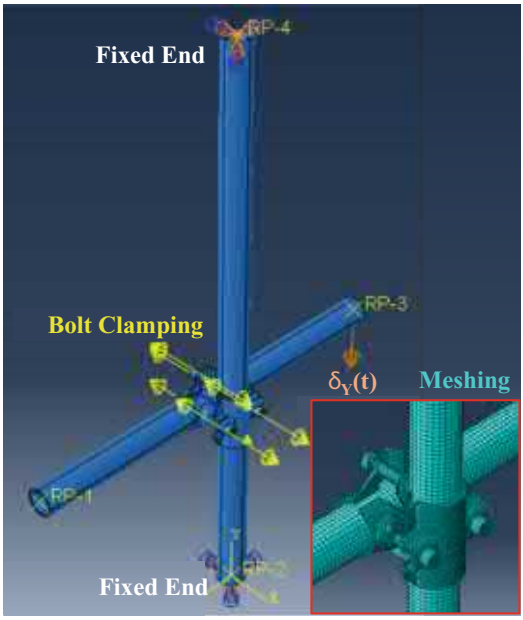


Fig. 2. Main modelling assumptions and boundary conditions for FE analyses

3 Local Response of TJSS Cruciform Joints

Local response of TSJJ cruciform joints was investigated in terms of *i*) moment-rotation curves, *ii*) distribution of Von Mises stresses (S_MISES) at peak chord rotation and *iii*) distribution of equivalent plastic strains (PEEQ).

For the sake of brevity, Fig. 3 only depicts numerical results referred to the most typical (i.e., "base") configuration (CHS Ø48.3 × 3.2 used for tubes, M12 bolts, all components made of S235 steel).

It can be easily noticed how *i*) the joint response is highly non-linear even for very low chord rotation values – i.e., due to the initial mobilization of friction being followed by fasteners' adjustments in slotted holes, *ii*) plasticization only occurs in caps and core, while bolts and tubes remain in their elastic range, *iii*) although a non-negligible resistance is developed within the joint, the bending stiffness is very low.

Although with some differences – mainly caused by changes in the steel grade of caps/core – the above evidences are shared by each considered configuration.

In order to better understand these results, stiffness and resistance classification was carried out for all configuration based on EN1993-1-8 [7] recommendations for conventional steel joints. Due to the observed nonlinearities, some choices had to be made to uniquely identify the equivalent, initial joints' stiffness $S_{j,ini}$.

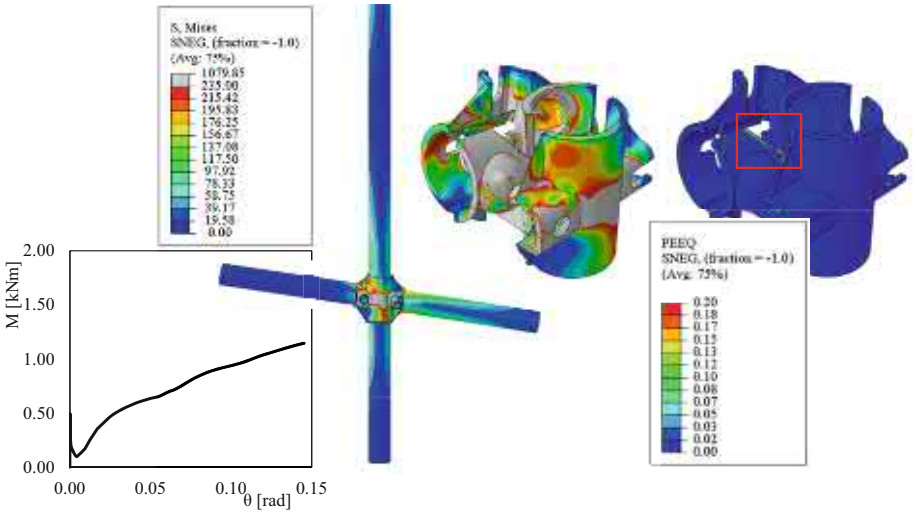


Fig. 3. FE analyses results for cruciform joints: S_MISES, PEEQ and moment-rotation curve referred to the base configuration

Namely – in line with typical assumptions made for lightweight steel systems, in which connections' performance is also highly nonlinear from the very start of load-displacement curves [11, 12] – $S_{j,ini}$ was conventionally calculated as the secant stiffness for an endured moment equal to 0.4 M_u, with M_u being the ultimate bending resistance of the assembly. The mechanical classification of all configurations is summarized in Fig. 4.

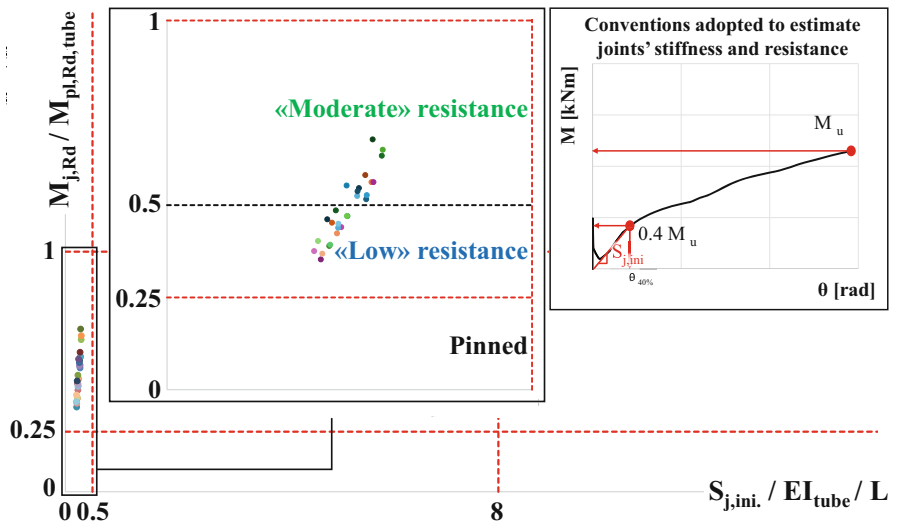


Fig. 4. EN1993-1-8-based classification for each considered cruciform joint

Remarkably all joints can be deemed as nominally pinned in terms of stiffness (i.e., due to $S_{j,ini}$ being always smaller than 50% of the corresponding chord bending stiffness), while a partial resistance restoration is instead always achieved (30–70% of the chord plastic resistance in bending $M_{pl,Rd,tube}$ – being 0.25 $M_{pl,Rd,tube}$ the strength limit for pinned connections as per EN1993-1-8 [7]).

Although further studies are needed, a preliminary distinction can be hence made among "low" resistance cruciform joints ($M_u < 0.5\ M_{pl,Rd,tube}$ – low-grade steel joints connecting thicker tubes) and "moderate resistance cruciform joints ($M_u > 0.5\ M_{pl,Rd,tube}$ – high-grade steel joints connecting thinner tubes).

4 Influence of Joints Response on the Global Scaffolds Behaviour

After assessing the local performance of joints, their influence on the global TJSSs behaviour was preliminarily investigated through non-linear static ("pushdown") analyses on 2-storey simple assemblies, i.e., performed in SAP2000 environment [13]. The nonlinear performance of joints was accounted for through properly calibrated link elements, i.e., as e.g. suggested in [14, 15].

Results in terms of total vertical load-top displacement curves are depicted in Fig. 5, i.e., compared with limit cases referred to ideally pinned and ideally fixed chord-stud joints. It can be easily noticed how cruciform joints decisively influence the system-level

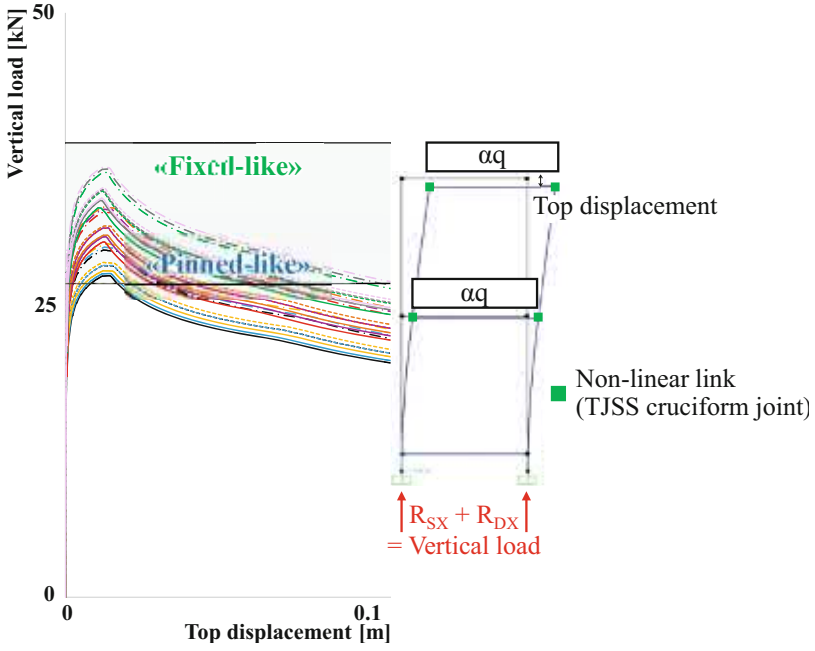


Fig. 5. Influence of joints' behaviour on the global response of a simple TJSS: load-displacement curves derived through pushdown analyses

response, with load multipliers being either close to the strongest assembly ("fixed-like" schemes) or to the weakest one ("pinned-like" schemes).

It is however worth to highlight that no biunivocal correspondence could be found between the joints' and the system strength. This outcome – which is mainly due to *i*) the concurring influence of the elastic response of profiles and *ii*) the occurrence of P-Delta effects – clearly denotes the need for further investigations on the coupled local-global behaviour of TJSSs.

5 Conclusions

In the present work, the structural performance of cruciform joints belonging to tube-and-joint scaffolding systems was investigated through FE analyses. Based on derived outcomes, the following concluding remarks can be pointed out:

- Cruciform joints are surely the key component of TJSSs. Currently, experimental characterization is mandatory for these couplers due to absence of reliable predictive models. The present study attempted at addressing this gap through a parametric study;
- When framed within EN1993-1-8 provisions, cruciform joints can be regarded as partial strength nodes with no stiffness restoration, although their bending capacity is highly sensitive to design parameters – i.e., especially the steel grade adopted for caps and core;
- As expected, the local joints' response strongly influences the system-level performance, although no biunivocal correspondence was found between local and global results due to the concurring impact of other factors (e.g., elastic members' response, second order effects);
- Further studies will be carried out to more clearly emphasize the influence of design parameters for cruciform joints at both node - and scaffold-level.

References

1. Thatcher AGH (2023) Scaffolding: design, erection, and legal aspects for contractors and builders. Sothis Press, London
2. CEN (2004) EN 12810–2: Façade scaffolds made of prefabricated elements – part 2: particular methods of structural design. CEN, Brussels
3. CEN (2022) EN 74–1: couplers, spigot pins and baseplates for use in falsework and scaffolds. CEN, Brussels
4. Tartaglia R, Monte F, Demonceau JF, Maddaloni G (2025) Monotonic behaviour of 4-bolt row connections: analytical and numerical analyses. J. Constr. Steel Res. 236B:110048
5. Tartaglia R, D'Aniello M, Demonceau JF, Landolfo R (2025) Seismic design and testing of EC8-1-2-compliant unstiffened end-plate beam-to-column joints. J. Constr. Steel Res. 235B:109916
6. Fiorino L, Campiche A, Grzesik P, Landolfo R (2024) Experimental evaluation of in-plane seismic demand on power actuated fasteners (PAF) connecting CFS drywall partitions and concrete surrounding elements. Bull. Earthq. Eng. 22(4):1–33
7. CEN (2024) EN1993-1-8: Eurocode 3 – Design of steel structures – part 1–8: design of joints

8. Simulia (2017) ABAQUS 2017 User's manual. Dassault Systemes, Vélizy-Villacoublay
9. INAIL (2017) QdR n.12: Metodologia per prove di rigidezza e resistenza per i dispositivi di collegamento montante-traverso nei ponteggi metallici fissi di facciata. INAIL, Rome (in Italian)
10. Freddi F et al (2025) Seismic retrofitting of existing steel frames with external BRBs: pseudo-dynamic hybrid testing and numerical parametric analysis. Earthq. Eng. Struct. Dyn. 54:1064–1083
11. Prota A, Fiorino L, Landolfo R (2026) Quantification of seismic performance factors according to FEMA P695 for Eurocode DC2-compliant lightweight steel shear walls with gypsum board sheathing. Thin-Walled Struct. 230A:115297
12. Fiorino L, D'Addesa V, Landolfo R (2024) Seismic design rules for lightweight steel shear walls with wood panel sheathing within the Eurocode format. Thin-Walled Struct. 204:112293
13. CSI (2021) SAP2000 v23 User's manual. CSI, Walnut Creek
14. Gnazzo M, Mahmoudi B, D'Aniello M, Imanpour A, Landolfo R (2026) Seismic design and response of inverted-V CBFs compliant with European and Canadian standards. Eng Struct 363:123071
15. Milone A, Prota A, Landolfo R (2026) Ultimate and repairability performance of steel eccentrically braced frames designed according to the 2nd generation of Eurocode 8: a parametric study for medium-rise buildings. Eng Struct 365:123283

Seismic Response of New Extended Bracket-Shaped Beam-to-Column Joint for SMF

Bahram Mirzaie Abar[1](✉), Mario D'Aniello[1], Arsalan Sadeghi Shaghaghi[2], and Raffaele Landolfo[1]

[1] Department of Structures for Engineering and Architecture, University of Naples "Federico II", Via Forno Vecchio 36, 80134 Naples, Italy
Bahram.mirzaieabar@unina.it

[2] School of Civil Engineering, Iran University of Science and Technology, Tehran, Iran

Abstract. The damage mechanisms of the newly developed stiffened extended bracket joints were systematically investigated and compared with those of the prequalified Cast Bolted Bracket (CBB) connections. A comprehensive set of performance indicators-including initial stiffness, cyclic response, skeleton curves, strength degradation patterns, bracket deformation response, bolt force evolution, bolt rotation demand, and observed failure modes-was employed to evaluate and contrast the seismic behavior of the two connection types. The results demonstrate that the proposed stiffened extended bracket joints exhibit superior structural performance relative to conventional CBB connections. In particular, they show enhanced stiffness retention, improved cyclic stability, reduced strength deterioration, and more favorable damage distribution, confirming their potential as an efficient and reliable alternative for seismic-resistant steel structures.

Keywords: Cast Bolted Bracket · Steel connection · Prequalified connection, cyclic response, connection failure mode

1 Introduction

Many studies have investigated the behavior of the components used in moment connections, including reduced beam sects [1]., bolted brackets [2, 3], T-stiffeners [4], and retrofitting elements [5]. Since moment connections are essential elements in structural systems, their influence on stiffness and strength requirements, as well as their role in shifting failure behavior from brittle to ductile, has always been a key concern.

Undesirable early failures in moment connections may occur due to factors such as stress concentration, accumulation of plastic strain in the connection region, or excessive deformation and buckling, which can delay or prevent the formation of a ductile plastic hinge in the beam [6, 7].

Alongside experimental approaches, high-fidelity finite element (FE) modeling has proven to be an effective tool for accurately predicting connection behavior and evaluating the efficiency of different design strategies. The FE method also allows for an economical assessment of load transfer mechanisms within the connection.

© The Author(s), under exclusive license to Springer Nature Switzerland AG 2026
R. Zanon et al. (Eds.): CTA 2026, LNCE 942, pp. 208–216, 2026.
https://doi.org/10.1007/978-3-032-39505-4_19

To interpret FE results, several damage indices have been introduced, including the plastic equivalent strain index [8], the triaxiality ratio [8], and the rupture index [8]. These indices are used to evaluate the likelihood of fracture under three-dimensional stress conditions and to quantify inelastic strain demand in steel materials.

Similar damage indicators have been successfully applied in previous studies to assess fracture and failure behavior in moment connections [8]. The Cast Bolted Bracket (CBB) connection is a bolted bracket connection that has been prequalified by design codes was originally introduced by Adan and Gibb through experimental testing of four successful specimens. Based on their test results, the CBB connection was recognized by AISC provisions [10] as a fully restrained moment connection.

Unlike the CBB system, the SSBB connection benefits from using thinner plate thicknesses and offering more flexible bolt configurations, providing more convenient options for various beam types and effectively addressing the initial stiffness problem reported in previous studies for the CBB system. In this study, a parametric investigation is performed by modeling SSBB connections with eight-bolt configuration. Through this analysis, the effectiveness of the proposed connection and the suitability of the bracket geometry are examined and compare with its counterpart CBB joint.

The hysteretic behavior of all parametric models is assessed by examining strength degradation and reduction in initial stiffness. In addition, the local stress–strain response is investigated using damage indicators applied to the bracket components.

2 Numerical Investigation

2.1 FE Modeling and Validation of Reference Stainless Steel Connections

A full-scale reference CBB connection consisting of KBB four-bolt configuration tested by [11] was modeled by means of ABAQUS [9]. Correspondingly, the benchmark failure modes and values were extracted for the connection components based on the equivalent plastic strain (PEEQ) and rupture index [8]. The detailed verification presented in [8].

2.2 Definition and Design Result of Specimens

The geometry of the beam–column assemblies and the material properties of the SSBB and CBB specimens are summarized in Fig. 1. The beam and column sect. W760*270*161 and W14*223, respectively.

The beam length and column height were considered as 4500 mm and 3800 mm [11], respectively. The yield stress, tensile strength, and ultimate strain were considered respectively as 366 MPa, 462 MPa, and 25% for the beam, 321 MPa, 453 MPa, and 24% for the column, and 423 MPa, 607 MPa, and 24% for the bracket components.

The ASTM A490 bolts were used to connect the connection components. The demand to capacity ratio for all the connection components were considered equal to 1 for comparison purposes.

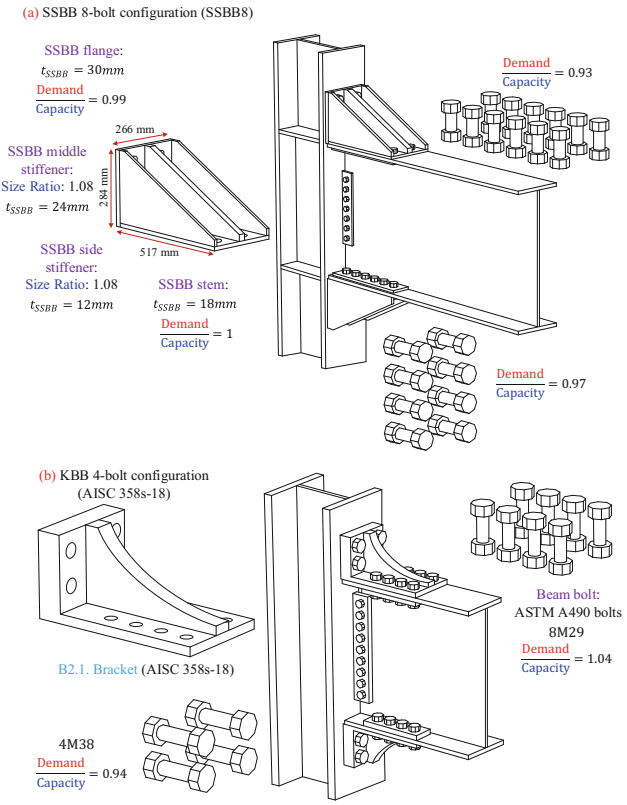


Fig. 1. SSBB and CBB specifications

2.3 FE Modeling Detail

The von-Mises yield criterion was used for modeling the stainless steel materials according to the bilinear isotropic-hardening constitutive law [9]. The moduli of elas-ticity of the steel materials were regarded as the values defined in [9] and Poisson's ratio was taken as 0.3 [8]. In order to define material properties, true stress-strain relations were used instead of the engineering stress-strain from the tests [8, 11].

The full Newton-Raphson solution technique [9] was regarded as a direct equation solver in static general analysis. General contact (standard) with selected surface pairs were used to define the contact between connection components. Likewise, in the field of initial overclosures, contact initialization should be defined as resolve with strain-free adjustment. In addition, the surface-to-surface contact was considered between connection components to simulate near-real behavior of thin-plates' buckling deformations in the analysis. Tangential behavior with isotropic directionality was chosen as well as the normal behavior with hard contact in the field of pressure-overclosure. The normal behavior used the classic Lagrange multiplier method of constraint enforcement. In order to simulate the real behavior of endplate connections, tie contact was not used between the bolts and corresponding surfaces [9]. The friction coefficient between the

contact pairs was considered as 0.3 based on the recommendations of [8, 9]. While the connection components were allowed to separate, they prevented penetration [8]. The pre-buckling analysis and mesh sensitivity analysis were also performed to ensure a more accurate and reliable numerical assessment.

3 Response Evaluation of Partial-Strength Connections

As shown in Fig. 2(a), SSBB had more stable cyclic response without meeting pinching effect than the CBB specimen. SSBB had greater initial stiffness (23.72) than the CBB specimen (16.26) as can be observed in Fig. 2(b) and Fig. 2(c). As can be seen in Fig. 2(d), SSBB had greater peak normalized moment but lower in the last cycle, which shows a sooner and proper beam hinge occurrence. SSBB had twice total energy dissipation of the joint with almost zero energy dissipation in the beam, which shows a well performance of the connection (see Fig. 2(e) and Fig. 2(f)). As shown in Fig. 2(a), SSBB had more stable cyclic response without meeting pinching effect than the CBB specimen. SSBB had greater initial stiffness (23.72) than the CBB specimen (16.26) as can be observed in Fig. 2(b) and Fig. 2(c). As can be seen in Fig. 2(d), SSBB had greater peak normalized moment but lower in the last cycle, which shows a sooner and proper beam hinge occurrence. SSBB had twice total energy dissipation of the joint with almost zero energy dissipation in the beam, which shows a well performance of the connection (see Fig. 2(e) and Fig. 2(f)).

As presented in Table 1, both joint has an acceptable minimum required strength of the joint, which shall be 0.8 beam plastic moment at 4% story rotation. CBB joint may not be considered as fully restrained joint based on the initial rotational stiffness analysis.

According to the secant stiffness analysis, CBB had 22% less secant stiffness than SSBB, which shows a more resilient performance of the SSBB joints. Regarding the strength degradation and deterioration analysis, CBB had 10% strength deterioration than the SSBB, but SSBB had about 20% strength degradation than the CBB, thus confirming more rigidity of the SSBB joints.

The beam share of the energy dissipation was almost equal to the total energy dissipation in SSBB but 80% in CBB, which shows the proper performance of the SSBB joint due to complete beam hinge formation that is the main source of dissipated energy in a joint. The SSBB joint had twice potential of dissipating energy than the CBB, thus confirming the proper performance of the SSBB joints.

Figure 3 shows Beam hinge deformation, von Mises stress and PEEQ distribution of SSBB and CBB joints. As presented in Table 2, SSBB component experienced 424 MPa unlike the CBB component, which experienced 607 MPa of von Mises stress shows that the CBB met a high range of plastic stresses. However, SSBB remained elastic.

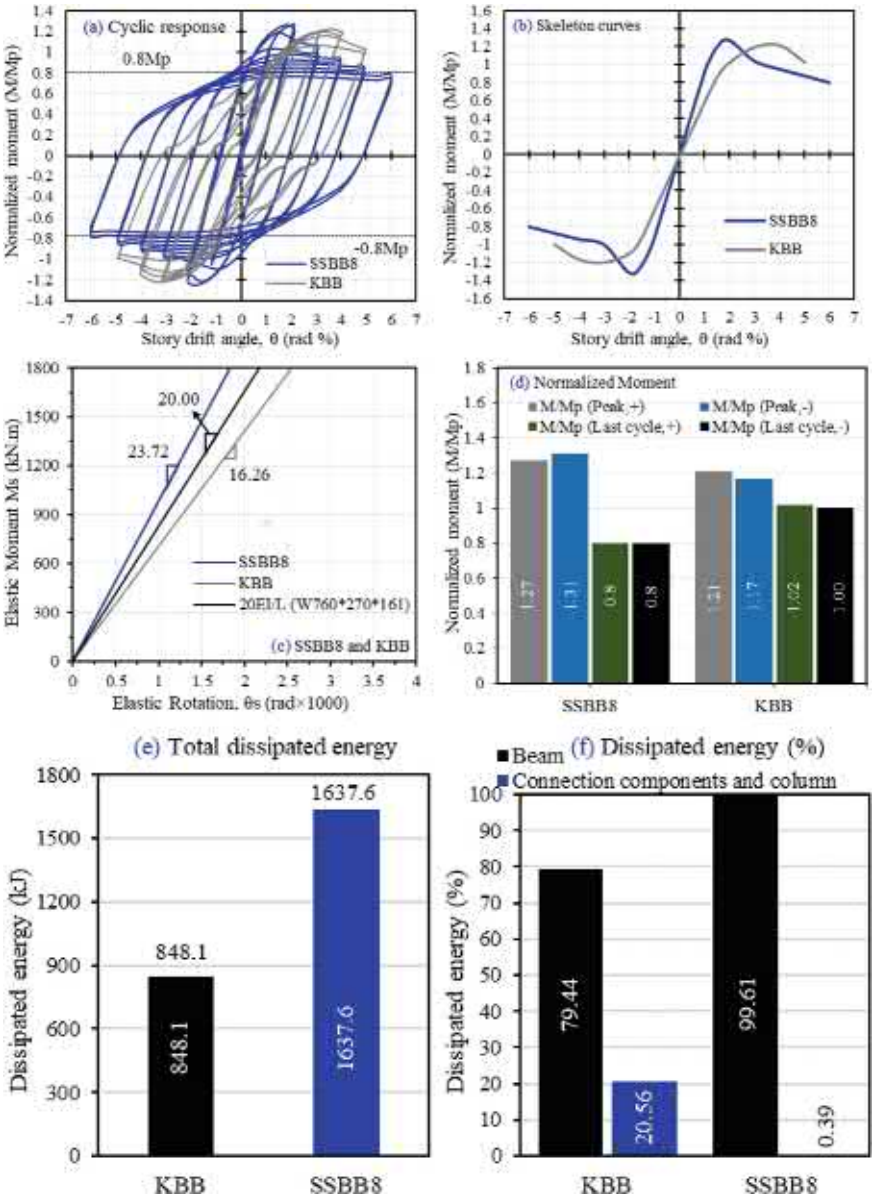


Fig. 2. (a) Cyclic response (b) skeleton curve (c) initial stiffness (d) normalized moment (e) and (f) dissipated energy

Table 1. Cyclic response comparison of the SSBB and CBB joints

Comparison item	Maximum value (SSBB)	Maximum value (CBB)	Result
Normalized connection strength at 4% drift (joint strength over beam plastic moment)	0.98	1.2	Acceptable [10]
Initial rotational stiffness of the joints	23.72	16.26	CBB lack of stiffness [10]
Secant stiffness degradation of the cyclic response	27.8°	35.6°	CBB, 21.9%
Strength deterioration of the cyclic response levels	1.31	1.17	CBB, 10.7%
Strength degradation of the cyclic response loops	0.8	1.02	SSBB, 21.6%
Energy Dissipation in the connected beam	99.61%	79.44%	CBB, 20.2%
Total energy dissipation of the joint	1637.6 kJ	848.1 kJ	CBB, 48.2%

The plastic strain analysis shows that the SSBB met almost zero plastic strain unlike CBB, which experienced 30% plastic strain confirming a proper performance of SSBB without meeting damages or failure. As can be seen in this Figure, beam hinge in SSBB experienced more buckling deformation with concentrated plastic stress than CBB but lower PEEQ and plastic stress distribution in connection components, which confirms the proper performance of the SSBB joint.

Table 2. Cyclic response comparison of the SSBB and CBB joints

Damage indictor	Maximum value (SSBB)	Maximum value (CBB)	Result
Von Mises stress distribution in the joint components	424.1 MPa	607 MPa	SSBB, 99.4%
Strain distribution, maximum principal	0.37	7.21	CBB 29.45% damaged

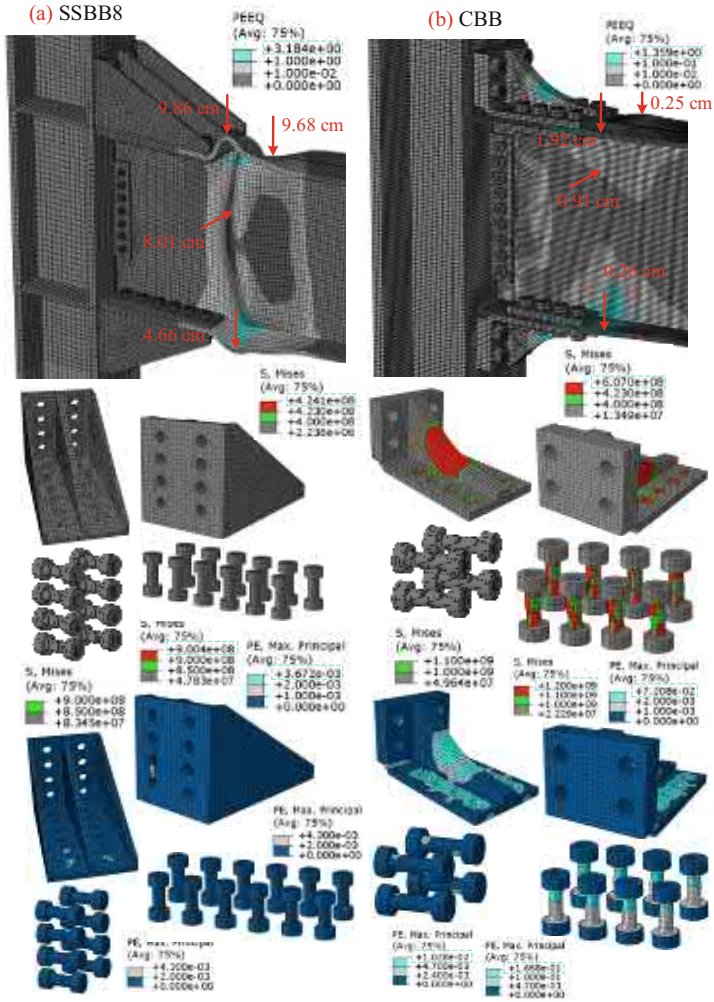


Fig. 3 Beam hinge deformation, von Mises stress and PEEQ distribution of SSBB and CBB joints

Figure 4 shows CBB Rupture index of beam bolts and stiffener. The beam bolts of the CBB were rather close to meet failure and the CBB stiffener met a large amount of rupture strain reduction unlike the SSBB joint, which shows a proper load-carrying mechanism along the SSBB connection components.

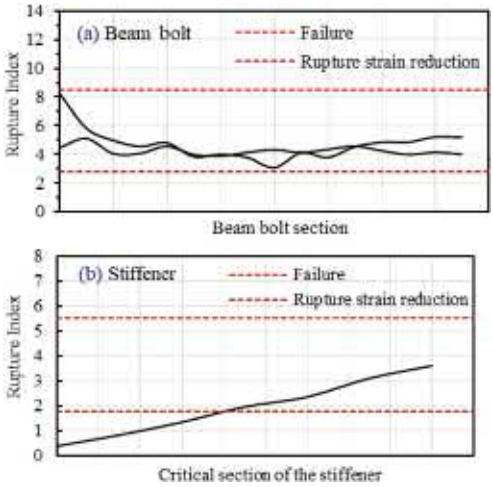


Fig. 4. Rupture index of beam bolts and stiffener

4 Concluding remarks

1. SSBB experience less plastic stress and PEEQ in connection components but more buckling deformation and stress concentration in beam hinge unlike the CBB joint.
2. SSBB met more stable cyclic response with acceptable initial stiffness (23) of the joint unlike the CBB joint (16).
3. CBB experience a high range of rupture strain reduction in stiffener (five on average) and a failure mode in the beam bolts unlike the SSBB (almost zero).
4. SSBB joint can dissipate twice energy than the CBB joint.

References

1. Abar BM, Bakhshayesh Y, Garcia R, Hajirasouliha I (2023) A new energy-dissipating RBS connection with double-nut-bolts: seismic performance assessment and design methodology. Eng Struct 293:116596
2. Abar BM, Ghobadi MS (2020) Double shear bolted bracket moment connections, part 1: four-bolt configuration design methodology. J Constr Steel Res 174:106280
3. Abar BM, Ghobadi MS, Jazany RA (2020) Double shear bolted bracket moment connections, part 2: four-bolt configuration response evaluation. J Constr Steel Res 174:106281
4. Garfamy HM, Abar BM, D'Aniello M (2023) Seismic response of CFST double-tee moment connections: design criteria and experimental tests. Eng Struct 293:116670
5. Ghobadi MS, Mirzaie Abar B (2021) Development of new fully restrained bolted bracket moment connections for strong joints. Arch. Civ. Mech. Eng. 21(4):1459
6. Abar BM, D'Aniello M, Landolfo R (2025) An extension of EC8 concepts to AISC-like design criteria for ductile stainless steel end-plate moment connections. Eng Struct 332:120035
7. Jalal S, Bakhshayesh Y, Abar BM, Garcia R, Hajirasouliha I (2025) Seismic performance of concentrically braced frames with a new double-stiffened-slit damper: a numerical investigation. J Build Eng 114:114288

8. Abar BM, Ghobadi MS (2022) New generation of bolted bracket connections: safe load-carrying capacity and structural damage assessment. Eng Struct 252:113662
9. Dassault Systèmes Simulia Corp (2011) Abaqus analysis user's manual, version 6.14. Dassault Systèmes Simulia Corp, Providence
10. American Institute of Steel Construction (AISC) (2016) ANSI/AISC 360–16, Specification for structural steel buildings. AISC, Chicago
11. Adan SM, Gibb W (2009) Experimental evaluation of kaiser bolted bracket steel moment-resisting connections. Eng. J. 46(3):181–196

Experimental and Numerical Behavior of Steel L-Stub Under Monotonic Loading

Emanuela Luisi, Francesco Monte, Roberto Tartaglia(✉), Gaia Berruti, Marco Consales, Andrea Cusano, and Giuseppe Maddaloni

University of Sannio, Piazza Roma 21, Benevento 82100, Italy
rotartaglia@unisannio.it

Abstract. The present work investigates the experimental and numerical performance of steel L-stubs subjected to monotonic loading. The aim of the study is to investigate the behavior of L-stub sub-assemblies as a function of their geometrical features, such as plate thickness and number of the bolts. All the tested specimens were equipped with sensorised bolts capable of measuring the tensile force within the bolts, strain gauges installed on each plate, and optical fiber sensors placed in parallel with the strain gauges. The experimental results show that the L-stub behavior is strictly dependent on both plate thickness and bolt capacity. In general, increasing the plate thickness produces an increase in L-stub stiffness and capacity, while reducing its ductility. An advanced three-dimensional numerical model was developed and validated against the experimental results. The adopted numerical model was able to accurately reproduce the experimental L-stub behavior in terms of elastic stiffness, yielding, and maximum capacity.

Keywords: L-stub · Optical fibers · Numerical analysis · Monotonic loading · Failure modes

1 Introduction

In recent years, scientific research in the field of steel structures has paid particular attention to optimizing the global response of structural systems, analyzing seismic-resistant braced frames [1, 2], lightweight structural systems [3–6], ductile hybrid connections [6]. However, to ensure the safety of these structures, it is fundamental to understand the local mechanical behavior of the individual joints. In this regard, the EN 1993-1-8 standard introduced the equivalent T-stub model to represent the tension zones of a bolted connection. The L-stub is a variant of the classic T-stub connection, utilized in cases where the geometry is not symmetric with respect to the bolt plane, as for instance in annular flange joints between tubular elements. This is also the case of the steel tubular towers, where the joint was represented as a flange segment, as introduced by Siedel [7].

© The Author(s), under exclusive license to Springer Nature Switzerland AG 2026
R. Zanon et al. (Eds.): CTA 2026, LNCE 942, pp. 217–225, 2026.
https://doi.org/10.1007/978-3-032-39505-4_20

A significant effect on the elastic and plastic behavior of these tension joints is due to the contact between the opposite flanges. Couchaux et al. [8] performed experimental tests and numerical analyses on L-stubs in tension and proposed an analytical model to evaluate their resistance, considering four different failure modes similar to those described by the EN 1993-1-8 standard for T-stub connections. Furthermore, Couchaux et al. [9] analyzed how contact modifies the position of the prying force. As confirmed by Kombate et al. [10], the deformation of the flange generates prying effects that increase the axial load and introduce bending stresses in the bolts. Recent studies have investigated the fatigue behavior of M20 Grade 10.9 bolts [11], as bolted connections of L-shaped components are subjected to tension-compression cycles induced by vibrations.

The present article aims to investigate the behavior of L-stubs as a function of plate thickness and the number of bolts, in order to monitor the local deformations of the connection with the purpose of designing an optical fiber monitoring system.

2 Investigated L-Stub

The experimental program was designed to investigate the non-linear behavior of these components and to systematically evaluate the influence of the flange thickness and the number of bolts on the overall structural response. All the specimens were made adopting S355 structural steel for the plates and assembled using M20 Grade 10.9 high-strength bolts. One experimental test was performed at the LINC laboratory of the University of Sannio, while a total of six L-stub configurations were numerically investigated.

The experimental monotonic tensile test was conducted using an MTS universal testing machine with a maximum tensile load capacity of 300 kN. In accordance with the objectives of the study, an advanced monitoring system was implemented to observe both global and local deformations. As illustrated in Fig. 3a, the specimens was carefully instrumented prior to testing. Strain gauges were installed on the plates, coupled with optical fiber sensors to accurately record the local strain distribution. Furthermore, sensors with Tokbo technology were employed, as shown in Fig. 3b, to obtain a direct measurement and continuous recording of the tensile force developed within the bolt shank.

Contrariwise, the numerical configurations were divided into two series based on the bolt layout. The first series comprises three specimens featuring a single M20 bolt (1-bolt L-stubs), each characterized by a different flange thickness. The second series includes three specimens equipped with two M20 bolts (2-bolt L-stubs), adopting the same flange thicknesses investigated in the first series. The 3D views of the L-stubs are illustrated in Fig. 1.

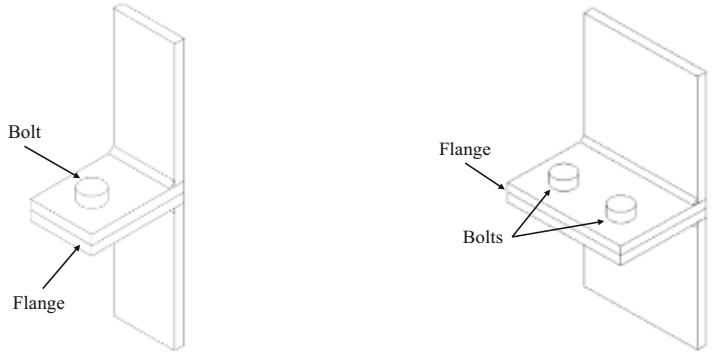
The geometrical features of all the specimens are summarized in Table 1 and illustrated in Fig. 3.

For sake of clarity, the specimens are identified with a specific labelling system. The labels start with the number of the bolts ("1b" for 1-bolt and "2b" for 2-bolts layouts), followed by the numerical value of the L-stub flange thickness. The final number indicates the web thickness (Fig. 2).



(a) (b)

Fig. 1. Experimental setup and instrumentation for the 1b_t15–15 specimen: a) detail of the strain gauges and optical fibers installation; b) overview of the specimen mounted in the testing machine with the sensorised bolt



(a) (b)

Fig. 2. Specimen configuration: a) 1 bolt L-stub; b) 2 bolts L-stub

Table 1. Geometrical features of investigated L-stub

Specimen	L	t_f	t_w	m	e	p	Bolt
	[mm]	[mm]	[mm]	[mm]	[mm]	[mm]	[−]
1b_t10–15	100	10	15	85	50	–	M20
1b_t15–15	100	15	15	85	50	–	M20
1b_t25–15	100	25	15	85	50	–	M20
2b_t10–15	200	10	15	85	50	100	M20
2b_t15–15	200	15	15	85	50	100	M20
2b_t25–15	200	25	15	85	50	100	M20

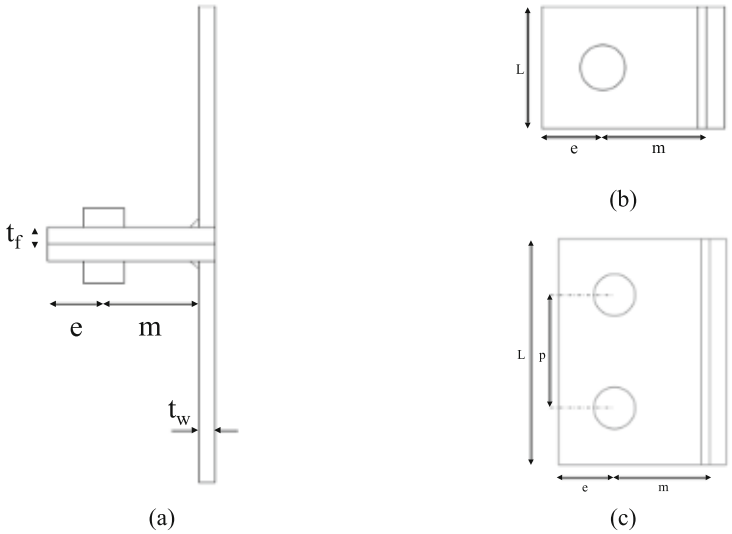


Fig. 3. Geometrical features: a) front view; b) top view 1 bolt; c) top view 2 bolts

3 Numerical Modelling

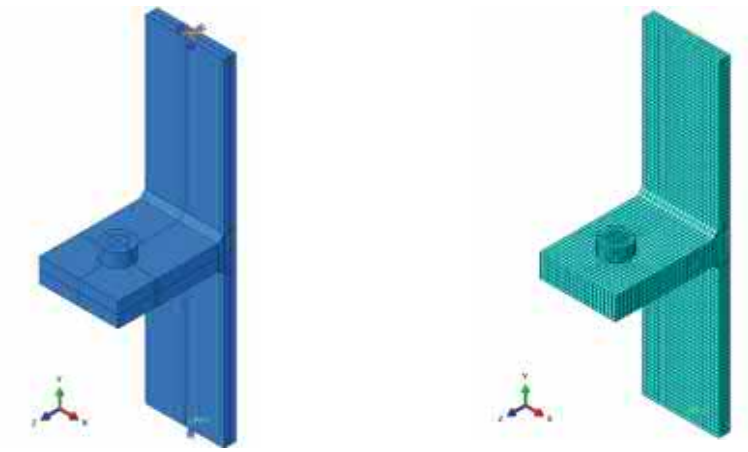
The numerical analyses were performed by means of an advanced finite element (FE) analysis using the software ABAQUS.

For the L-stub plates, an S355 structural steel was utilized, adopting the Von Mises yield criterion and the combined isotropic-kinematic hardening model available in ABAQUS. The M20 Grade 10.9 bolts were modelled as dumbbell-shaped elements, adopting the nominal bolt diameter along the entire shank. To account for the presence of the threaded portion, a reduction of the bolt cross-sectional area was performed. The normal behavior of the contact surfaces was modelled assuming a "Hard" contact, which prevents interpenetration between the parts. For the tangential behavior, the "Penalty"

formulation was adopted with a friction coefficient equal to 0.4. To model the interactions between the welded components, "Tie" constraints were used. The boundary conditions, as shown in Fig. 3a, were imposed through Reference Points (RPs) coupled to the element surfaces through "Rigid Body" constraints. Specifically, the RP associated with the bottom extremity was fully fixed, while the RP associated with the top extremity was allowed to translate freely in the vertical direction, simulating the application of the monotonic load.

All the model components were discretized using C3D8R solid elements. The elements feature an average size of 5 mm, deduced from an appropriate mesh sensitivity analysis, as shown in Fig. 3b.

A double-step dynamic implicit analysis was conducted: the clamping was applied in the first step and, subsequently, the monotonic load was simulated by imposing an increasing vertical displacement (Fig. 4).



(a) (b)

Fig. 4. FE modelling: a) Boundary conditions; b) Mesh

4 Experimental Results

The investigated specimen show a failure mode 1 with the plastic deformation within the L-stub plate and a ductile performance reaching a very large gap opening; the failure is governed by the fracture between the welds of the L-stub plates. Moreover the results pointed out by both the strain gauge and the optical fiber, placed as it can be observed in Fig. 5b, are reported in Fig. 5c. As it can be observed it is possible to correlate the bolts internal force with the deformation evaluated by means of optical fiber. In all the investigated cases and up the specimens behave in elastic range, an almost linear correlation between the bolts internal action and the deformation on both the horizontal and vertical plate can be observed.

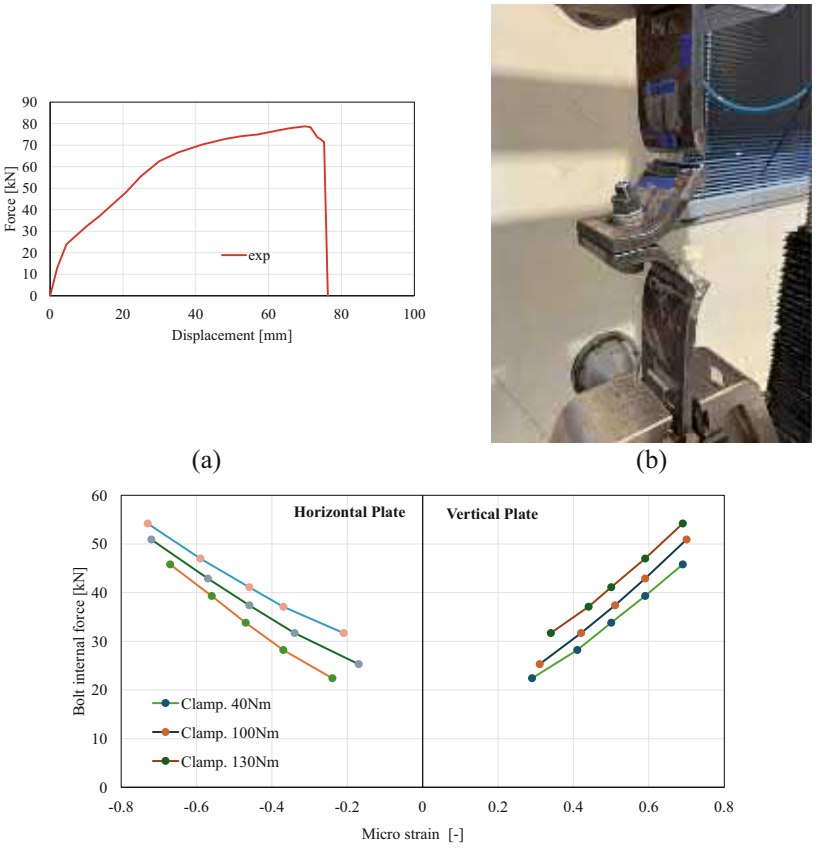
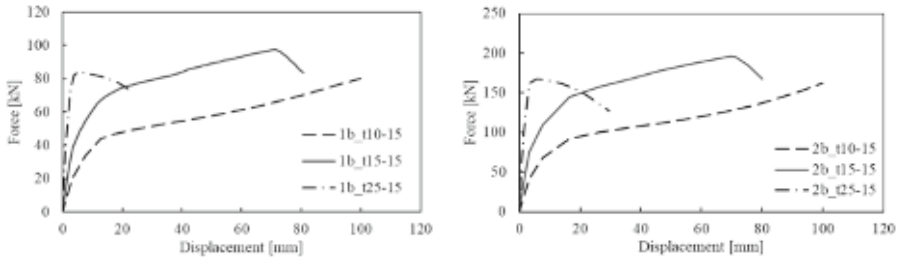


Fig. 5. Experimental results in term of: a) force displacement curve, b) failure mode and c) correlation between the bolt internal force with micro strain

5 Numerical Results

The response of all investigated specimens are reported in Fig. 5 where the two investigated L-stub configurations (i.e., 1-bolt and 2-bolts L-stub), in terms of force-displacement curves. The force represents the tensile action detected at the loaded extremity of the L-stub, while the displacement is recorded at the same location (i.e., the Reference Point, RP, introduced in Sect. 3).

As can be observed by comparing the curves, an increase in thickness leads to a higher initial elastic stiffness and yield capacity, at which correspond a reduction of ductility. The configurations with a smaller flange thickness exhibit high ductility without showing sudden failures, which is typical of Failure Mode 1. As the thickness increases, the achievement of the maximum bearing capacity and a transition from Failure Mode 1 to Failure Mode 2 are observed. The thickest flanges show high initial stiffness but reduced ductility, a condition typical of Failure Mode 3, which is characterized by the brittle failure of the bolt. Observing the graphs, the presence of a second bolt leaves the collapse trends unaltered as the thickness varies, highlighting a doubling of the bearing capacity for all the investigated L-stubs.



(a) (b)

Fig. 6. Comparison between the force-displacement curve: a) 1 bolt: b) 2 bolts

The Von Mises and PEEQ distributions obtained in Abaqus for the specimens investigated were depicted in Figs. 6, 7.

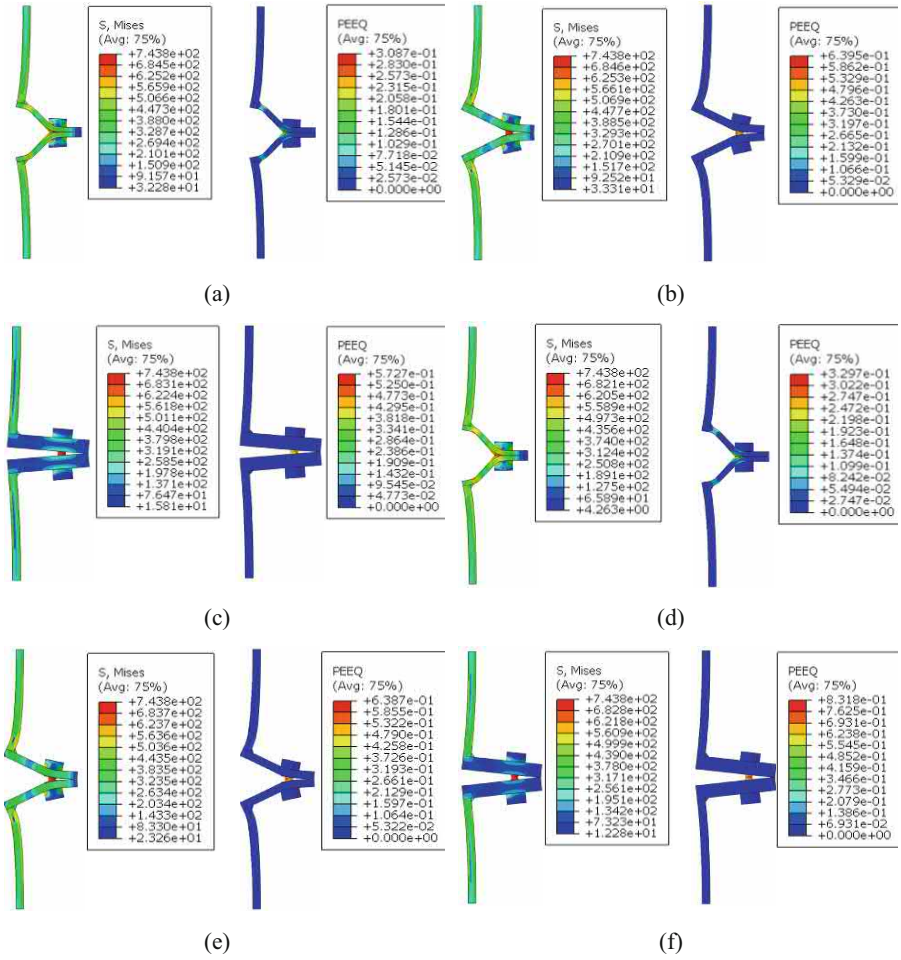


Fig. 7. Von Mises and PEEQ distributions: a) 1b_t10–15; b) 1b_t15–15; c) 1b_t25–15; d) 2b_t10–15; e) 2b_t15–15; f) 2b_t25–15

6 Conclusions

The present study investigates the experimental and numerical performance of steel L-stubs subjected to monotonic loading. The following conclusions were drawn:

- An increase in the flange thickness leads to a higher initial elastic stiffness and yield limit, at the expense of overall ductility.
- Configurations with a smaller flange thickness exhibit high ductility without showing sudden failures, a behavior typical of Failure Mode 1. For these thinner configurations, the formation of plastic hinges is observed at the bolt holes and the L-stub corner.

- The investigated specimens show an almost linear correlation between the bolts internal action and the deformation derived by the optical fiber on both the horizontal and vertical plate can be observed.

However, these findings are limited to the specific joint configurations investigated. Further numerical and experimental validations are required to generalize these conclusions to a wider range of structural scenarios.

References

1. Freddi F et al (2025) Seismic retrofitting of existing steel frames with external BRBs: pseudo-dynamic hybrid testing and numerical parametric analysis. Earthq Eng Struct Dyn 54:1064–1083
2. Gnazzo M, Mahmoudi B, D'Aniello M, Imanpour A, Landolfo R (2026) Seismic design and response of inverted-V CBFs compliant with European and Canadian standards. Eng Struct 363:123071
3. Prota A, Fiorino L, Landolfo R (2026) Quantification of seismic performance factors according to FEMA P695 for Eurocode DC2-compliant lightweight steel shear walls with gypsum board sheathing. Thin-Walled Struct 230:115297
4. Fiorino L, Prota A, Nikpour A, Landolfo R (2025) Seismic performance of lightweight steel shear walls with gypsum sheathing: experimental investigation. Earthq Eng Struct Dyn 54(11):2900–2926
5. Prota A, Fiorino L, Nikpour A, Landolfo R (2024) Test-based assessment of the seismic response of bracing systems for concealed grid suspended ceilings. J Earthq Eng 29(2):339–367
6. Ascione F, D'Aniello M, Leonardi A (2026) Numerical and analytical modelling of a novel hybrid ductile connection between FRP composite elements. Thin-Walled Struct 227:115008
7. Seidel M (2001) Zur Bemessung geschraubter Ringflanschverbindungen von Windenergieanlangen. Dissertation, heft 20. Institut fur Stahlbau, Universität Hannover, Hannover
8. Couchaux M, Hjiaj M, Ryan I, Bureau A (2017) Tensile resistances of L-stubs. J Constr Steel Res 138:131–149
9. Couchaux M, Hjiaj M, Ryan I, Bureau A (2017) Effect of contact on the elastic behaviour of tensile bolted connections. J Constr Steel Res 133:459–474
10. Kombate TJDLC, Taşkın K (2022) State-of-the-art review on the behaviour of T-stubs and prying action. J Constr Steel Res 191:107203
11. Feng XZ, Liu XC, Chen X, Zhou W, Tao YL, Zhang AL (2026) Fatigue performance of grade 10.9 M20 high-strength bolts in L-shaped component connections. Eng Fail Anal 187:110583

Comparative FEM Investigation into the Interaction Between RC Slabs and Removable Bolted Links in Eccentrically Braced Frames

Francesco Plaitano[1](✉), Elide Nastri[1], and Aurel Stratan[2]

[1] Department of Civil Engineering, University of Salerno, Via Giovanni Paolo II, 84084 Fisciano, (SA), Italy
fplaitano@unisa.it

[2] Department of Steel Structures and Structural Mechanics, Politehnica University Timisoara, Ioan Curea nr. 1, 300006 Timisoara, Romania

Abstract. Removable links are increasingly adopted in eccentrically braced frames (EBFs) as a strategy to enhance seismic performance and facilitate the post-earthquake replacement of damaged components. While the behaviour of removable links in bare-steel configurations has been extensively investigated, the interaction between these links and reinforced concrete (RC) slabs introduces additional structural complexities that require further numerical assessment.

This paper presents a detailed numerical investigation into the structural performance of removable bolted shear links interacting with RC slabs, focusing on different link-to-beam connection configurations. Drawing on modelling strategies validated in previous research, three-dimensional finite element models are developed in Abaqus to simulate the response of the link–beam–slab system under both monotonic and cyclic loading conditions. The numerical investigation is organised as a systematic comparative analysis, examining the influence of link length—specifically short (500 mm) and long (1000 mm) links—and connection detailing, such as flush and extended end-plate configurations.

The scope of the assessment covers performance parameters including initial stiffness, shear resistance, and rotation capacity. Particular attention is directed towards the redistribution of axial forces and the modification of hysteretic behaviour induced by the slab's constraint. This study aims to identify the technical trade-offs between strength, stiffness, and ductility across different assembly designs, supporting the development of resilient composite structural systems.

Keywords: Eccentrically braced frames · removable links · composite action · reinforced concrete slabs · finite element modelling · seismic resilience

1 Introduction

In steel buildings designed for seismic action, eccentrically braced frames (EBFs) occupy a well-established position. They combine the lateral stiffness typically offered by concentrically braced frames with the ductility and energy dissipation capacity associated with moment-resisting systems, an attractive compromise that has motivated their

© The Author(s), under exclusive license to Springer Nature Switzerland AG 2026
R. Zanon et al. (Eds.): CTA 2026, LNCE 942, pp. 226–244, 2026.
https://doi.org/10.1007/978-3-032-39505-4_21

widespread use in seismically active regions since the late 1970s [1–5]. The distinguishing feature of an EBF is the link element, a short segment of beam that is intentionally designed to act as a structural fuse. Under severe earthquake loading, inelastic deformations are expected to develop primarily within the link, while the surrounding members—beam segments outside the link, braces, columns, and connections—are capacity-designed to remain essentially elastic [1, 2, 6]. This deliberate separation between dissipative and non-dissipative zones is what gives EBFs their characteristic balance between stiffness and ductility, and it is also the reason why links have attracted so much research attention over the past four decades.

In parallel with this consolidation of EBF design principles, a separate line of investigation has developed around the idea of making the link itself removable. The motivation is essentially operational rather than purely structural: if damage is concentrated within a sacrificial component, then that component can in principle be unbolted and replaced after a major earthquake, avoiding the costly and time-consuming interventions that welded links typically require. Several experimental programmes have explored this concept over the last fifteen years, using bolted end-plate connections of various types [7–13]. These studies confirmed, broadly speaking, that removable bolted links can deliver seismic performance comparable to that of conventional welded links, while offering the practical advantages of easier fabrication, inspection, and post-earthquake replacement. Complementary numerical investigations, including FEM analyses of composite replaceable links [14], have further extended the understanding of the behaviour of these systems.

Most of the experimental and numerical evidence collected so far, however, refers to bare-steel assemblies. In actual buildings, EBF links are typically embedded in a composite floor system, where the steel beams that frame into the link support a reinforced concrete slab connected through shear studs. The presence of this slab is known to affect link behaviour. Early experimental work by Mansour et al. showed that composite action tends to increase both the elastic stiffness and the peak shear strength of short replaceable links, with peak shear forces about 14% higher than in the corresponding bare-steel specimens, without necessarily compromising their rotation capacity [12]. Similar conclusions were drawn by Ciutina and Danku et al. in a series of tests on single-storey EBF sub-assemblages, where the slab contribution was quantified both experimentally and numerically [15, 16]. More recently, Chesoan, Stratan and Ciutina examined the same combination for flush end-plate links and discussed the implications for repair after a seismic event [17]. The general picture that emerges from these studies is fairly consistent: the slab does help, but it also redistributes forces in ways that the original capacity-design assumptions do not always capture cleanly.

When one moves from conventional welded links to bolted removable links, the question becomes more complicated. The connection itself introduces an additional compliance into the system, and the way in which the slab interacts with this compliance is not obvious. Earlier FEM study on bare-steel removable links showed that the type of end-plate connection (flush versus extended) has a significant influence on stiffness, resistance, and the distribution of inelastic demand, even before the slab is introduced into the model [18, 19, 20]. What is still missing is a systematic numerical study that brings these two strands together: the influence of connection detailing on the one hand,

and the influence of the RC slab on the other, considered simultaneously and on the same modelling platform.

The present paper attempts to fill this gap. Three-dimensional finite element models of composite link–beam–slab assemblies subjected to both monotonic and cyclic loading were developed using Abaqus. Six configurations were considered, combining two link lengths (500 mm and 1000 mm) with three connection arrangements (continuous, flush end-plate, and extended end-plate). The models were first validated against available experimental evidence on bare-steel removable links [17, 19, 20] and then to the full parametric study. The objective is twofold. One aim is to quantify how the slab changes stiffness, resistance, and energy dissipation of removable-link systems. The other is to assess whether composite action compromises the fundamental assumption behind removable-link design, namely that damage remains localised within the replaceable element and can therefore be exploited for rapid post-earthquake recovery.

2 Numerical Modelling Strategy

2.1 Investigated Configurations

The numerical investigation was built on a series of composite link–beam–slab assemblies representative of removable-link EBFs. The geometry of the bare-steel sub-assemblies had already been validated in [18, 20], and the present study extends that framework to include the RC slab.

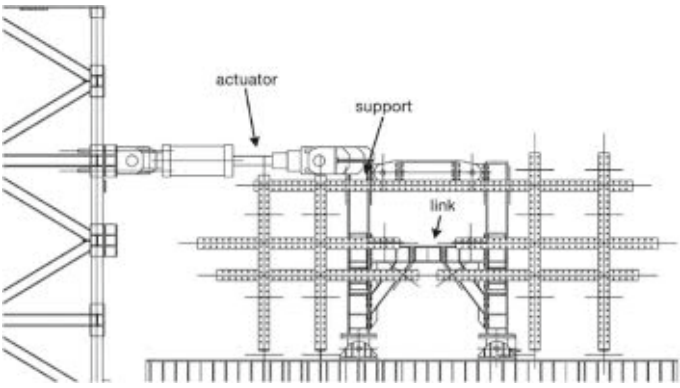


Fig. 1. Experimental setup [20]

The reference experimental setup, used as the geometric basis for all numerical models, is shown in Fig. 1. The sub-assemblage consists of a central link framed by two beam stubs and lateral bracing on both sides. The actuator applies the displacement history at one stub while the opposite stub is fixed. Two link lengths were considered. The shorter (500 mm) link develops a predominantly shear-controlled response, while the longer (1000 mm) link exhibits mixed shear–flexural behaviour. For each link length, three connection arrangements were modelled:

- a continuous, non-removable link (used as reference benchmark);
- a removable link with flush end-plate connections;
- a removable link with extended end-plate connections.

This produces six composite configurations, summarised in Table 1. The matrix allows the individual and combined effects of link length, connection rigidity, and slab interaction to be assessed systematically. The naming convention follows L*X*-C-B for continuous, LF*X*-C-B for flush end-plate, and LE*X*-C-B for extended end-plate links (where *X* denotes the link length in mm).

Table 1. Specimen matrix and notation adopted in the numerical study

Specimen	Loading	Connection	RC slab
L500-M-B	Monotonic	Continuous	Solid
LF500-M-B	Monotonic	Flush end-plate	Solid
LE500-M-B	Monotonic	Extended end-plate	Solid
L1000-M-B	Monotonic	Continuous	Solid
LF1000-M-B	Monotonic	Flush end-plate	Solid
LE1000-M-B	Monotonic	Extended end-plate	Solid
L500-C-B	Cyclic	Continuous	Solid
LF500-C-B	Cyclic	Flush end-plate	Solid
LE500-C-B	Cyclic	Extended end-plate	Solid
L1000-C-B	Cyclic	Continuous	Solid
LF1000-C-B	Cyclic	Flush end-plate	Solid
LE1000-C-B	Cyclic	Extended end-plate	Solid

2.2 Finite Element Model

Three-dimensional finite element models replicating the experimental geometry [20] were developed in Abaqus. All steel components and the concrete slab were discretised with C3D8R eight-node reduced-integration solid elements; the only exception was the top IPE360 beam, modelled with T3D2 wire truss elements—a simplification previously validated for bolted removable links [18, 20]. Reinforcement bars and shear studs were represented as T3D2 truss elements and coupled to the concrete matrix through an embedded region constraint. A refined mesh (element size ≈5 mm) was adopted in the link and connection zones, where plastic strain and contact gradients are most severe, while coarser discretisation was used in the surrounding beam segments and slab. The supporting frame was assigned linear elastic properties, consistent with its capacity design. Figure 2 shows the composite link–beam–slab assembly.

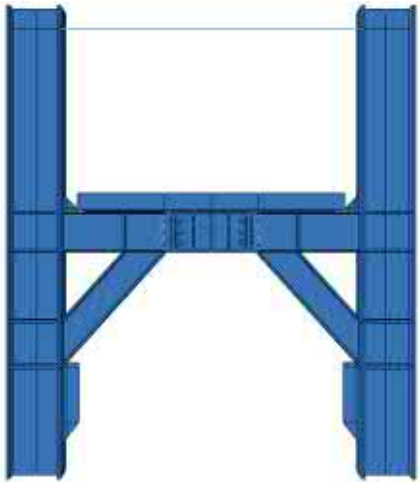


Fig. 2. Three-dimensional finite element model of the composite link–beam–slab assembly [21]

2.3 Material Models

Elastic constants were assigned as follows: for steel, $E = 210{,}000$ MPa, $\nu = 0.3$ and $\rho = 7.85$ g/cm^3; for concrete, $E = 28{,}480$ MPa, $\nu = 0.3$ and $\rho = 2.40$ g/cm^3. Under monotonic loading, steel plasticity was described by a true stress–strain curve calibrated on coupon tensile tests [20]. Under cyclic loading, the combined isotropic–kinematic hardening model of Zub et al. [22] was adopted, with five backstresses and isotropic parameters $Q\infty = 145$ MPa and $b = 10$; the kinematic hardening parameters (C^k, γ^k) were identified by iterative matching of experimental and numerical curves.

Grade 10.9 bolts were assigned $\sigma_\gamma = 940$ MPa, $\sigma^u = 1040$ MPa and the same elastic constants as structural steel; damage initiation was set at an equivalent plastic strain of 0.058 with stress triaxiality $\eta = 0.33$ [23, 22, 25].

The RC slab was modelled with the Concrete Damaged Plasticity (CDP) model [26], calibrated on the uniaxial compression law of Guo [27] for C16/20 concrete and supported by [28, 29]. The CDP parameters were $\psi = 30°$, $\varepsilon = 0.1$, fb0/fc = 1.16 and K = 0.667. Reinforcement (B450C) was modelled as elastic–plastic with combined isotropic–kinematic hardening and fully bonded to the concrete through the embedded-element formulation.

2.4 Connections and Boundary Conditions

Bolted connections were modelled explicitly using the simplified bolt representation of [23–30]. Surface-to-surface contact was defined as follows: shank-to-plate and shank-to-washer interfaces were frictionless tangentially with hard contact normally; head-to-washer, nut-to-washer and link-plate-to-beam-plate interfaces used a penalty friction coefficient of 0.3 with hard contact normally. Remaining interfaces were tied, as relative slip was negligible [20].

Analyses were run in two sequential dynamic-implicit quasi-static steps with Nlgeom activated: first, a bolt pretension of 392.7 kN was applied; then the monotonic or cyclic displacement history of each link was imposed. Boundary conditions reproduced the experimental layout, with pinned beam stubs and displacement applied through a rigid reference point. Monotonic loading increased up to ≈0.15–0.25 rad; cyclic loading followed the AISC protocol [31].

2.5 Validation

Before running the parametric investigation, the modelling strategy was validated against the LF-C-B and LE-C-B tests reported in previous works [17, 21]. Figure 3 compares numerical and experimental force–rotation curves for both configurations: (a) the flush end-plate link LF-C-B and (b) the extended end-plate link LE-C-B. The numerical analysis of the LE-C-B link exhibited behaviour closely aligned with the corresponding experimental test, with high stress concentrations and progressive degradation of the slab's integrity consistently reflected in the simulation. The LF-C-B numerical model exhibited behaviour closely matching that of the experimental test, including the V–γ hysteretic response, although the concrete slab in the numerical model remained undamaged, diverging slightly from the experimental observations due to minor construction-related imperfections (such as insufficient vibration during casting or local air pockets) that the idealised numerical model does not capture.

The validation confirmed the capability of the FEM to reproduce the principal response mechanisms of the composite removable-link systems and supports the extension of the same modelling framework to the full parametric study, noting that minor discrepancies in local behaviour are expected and acceptable given the inherent idealisations of FEM simulations.

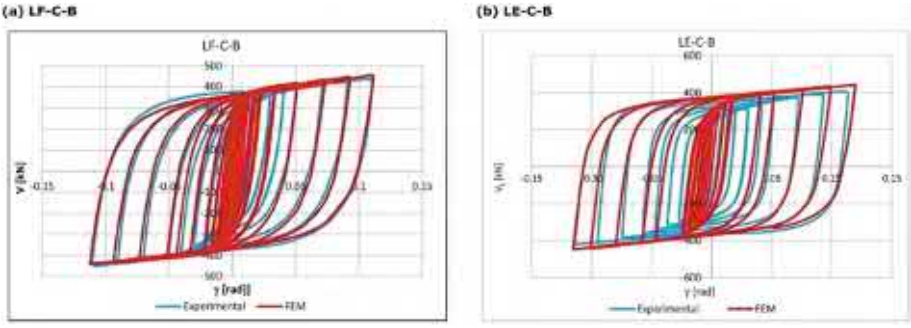


Fig. 3. Comparison between experimental and numerical force–rotation response for (a) the flush end-plate link LF-C-B and (b) the extended end-plate link LE-C-B [21]

3 Parametric Investigation

3.1 Scope and Parameters

The parametric study was designed to address a specific question: how does the RC slab change the response of removable bolted links, and does this change depend on link length and connection detailing? All other parameters were held constant—beam section, slab thickness, reinforcement ratio, stud spacing, material properties—while link length (500 vs. 1000 mm) and connection type (continuous, flush, extended) were varied. The slab was either present or absent, giving the bare-steel and composite variants for each configuration.

3.2 Performance Indicators

A consistent set of indicators was extracted from each analysis. At the global level: initial stiffness, peak shear resistance, rotation capacity, and post-yield shape. At the local level: Von Mises stress distributions and equivalent plastic strain (PEEQ) fields within the removable link and adjacent beam segments. Under cyclic loading: total hysteretic energy dissipation, stiffness degradation across cycles, peak-to-peak resistance variation, and pinching development. These indicators speak directly to two performance dimensions—structural (strength, stiffness, ductility) and functional (damage localisation, reparability)—which composite action affects in different ways, as discussed in Sects. 4, 5 and 6.

4 Influence of RC Slab Interaction Under Monotonic Loading

4.1 Strength and Stiffness

The first set of results concerns the global force–rotation response under monotonic loading, reported in Table 2. A direct bare-steel vs. composite comparison for the L500 case is provided in Fig. 4, and the complete quantitative variation of the slab influence on stiffness and peak shear resistance under cyclic loading is reported in Table 5. The general observation for monotonic loading is that the slab enhance stiffness of the assembly and produces a visible upward shift of the initial elastic–inelastic branch in all configurations, as confirmed by the direct curves comparison in Fig. 4. The most pronounced stiffening is observed in the continuous (L) and extended end-plate (LE) connections, where the composite section formed by the steel beam and the slab in compression is mobilised efficiently. For the flush end-plate (LF) connections, the slab contribution to initial stiffness is less evident, consistent with the inherent flexibility of the connection that limits the effectiveness of composite action.

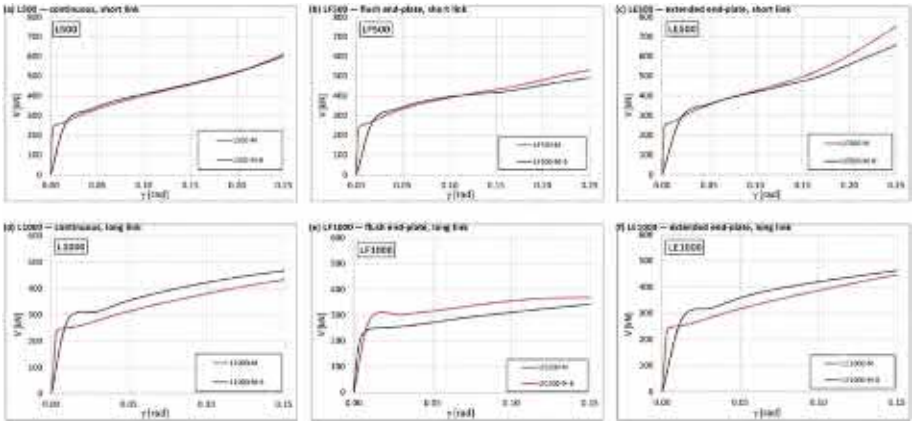


Fig. 4. Direct comparison between the bare-steel and composite configurations for all six cases under monotonic loading [21]

Table 2. Summary of monotonic response parameters: peak shear force (V) and corresponding link shear deformation (γ) for the composite configurations

Specimen	γ [rad]	V [kN]
L500-M-B	0.25	601
LF500-M-B	0.25	490
LE500-M-B	0.25	657
L1000-M-B	0.15	472
LF1000-M-B	0.15	370
LE1000-M-B	0.15	470

The dependence on link length is consistent and worth noting. For the 500 mm links, where shear yielding dominates, the upward shift of the initial branch induced by the slab is clearly visible in the continuous and extended end-plate configurations and more contained in the flush end-plate one. For the 1000 mm links, where flexural mechanisms contribute more substantially, the same qualitative trend is observed, but the gap between bare-steel and composite curves narrows. This is consistent with the idea that composite action is mobilised most efficiently when the link web is the principal dissipative region: in short links, the slab and the steel web are activated in parallel over a wide range of rotations, whereas in long links a substantial part of the deformation is absorbed by flexural mechanisms that involve the slab in a less direct way.

The direct comparison between the bare-steel L500-M and the composite L500-M-B confirms that the slab affects primarily the initial elastic–inelastic transition, while the post-yield branch remains comparable in shape between the two configurations.

Extended end-plate solutions develop the steepest initial branches and the highest peak shear forces, while flush end-plate solutions exhibit a more gradual post-yield response, indicating that the additional compliance of the connection allows a more progressive redistribution of stresses between the link and the surrounding assembly.

4.2 Stress Redistribution

To investigate what happens inside the assembly, the maximum Von Mises stress experienced by the web and the flanges of each link at the maximum monotonic link rotation were extracted from the numerical results. Figure 5 compares the bare-steel and composite configurations side by side for the 500 mm and 1000 mm links.

For the 500 mm configurations, the Von Mises stress in the bare-steel models reaches approximately 520–540 MPa in the web and 570–660 MPa in the flange across the three connection types, with the extended end-plate configuration (LE500) showing the highest flange value (around 660 MPa) because of the larger effective length occupied by the connection. With the slab, the flange Von Mises stress is reduced to 560–600 MPa across the three configurations, while the web values remain essentially unchanged (510–530 MPa).

For the 1000 mm configurations, the bare-steel flange values are around 570–620 MPa, with the continuous configuration (L1000) reaching the highest value (around 620 MPa). The composite counterparts show a markedly different pattern: the flange values drop to 430–500 MPa (a reduction of about 20–30%), while the web values increase slightly to 500–570 MPa for the extended configuration. This indicates that, for the longer links, the slab redistributes the force transfer away from the flanges towards the web, where the composite section is more efficient.

Overall, the slab contribution to the Von Mises stress indicates that the slab redistributes part of the inelastic demand away from the flanges in the longer links [21].

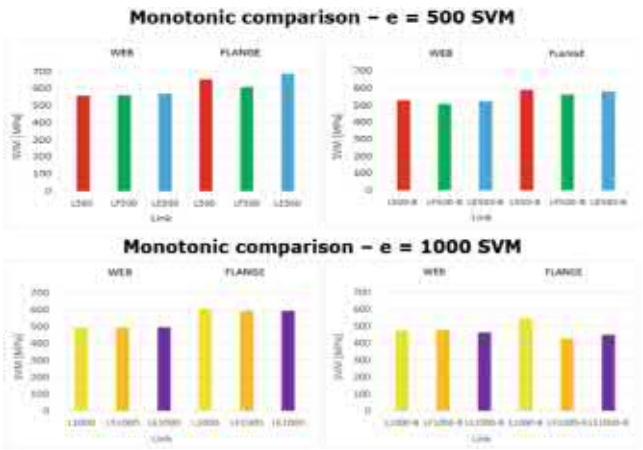


Fig. 5. Monotonic comparison of SVM in the web and flanges of the 500 mm (top) and 1000 mm (bottom) links [21]

4.3 Plastic Strain Demand and Damage Localisation

The most consequential effect of composite action, from the point of view of removable-link design, is what it does to plastic strain distribution. Figure 6 summarises the maximum equivalent plastic strain (PEEQ) experienced by the web and the flanges of each composite configuration at the maximum monotonic link rotation.

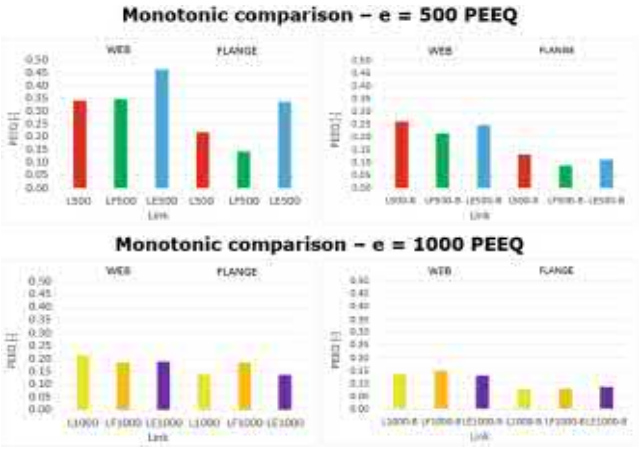


Fig. 6. Monotonic comparison of maximum equivalent plastic strain (PEEQ) in the web and flanges of the 500 mm (top) and 1000 mm (bottom) links [21]

Figure 6 presents the monotonic PEEQ comparison directly between the bare-steel and the composite configurations, organised by link length.

For the 500 mm links (top panel), the bare-steel web PEEQ values cluster around 0.30–0.45, with the extended end-plate connection (LE500) reaching the highest value (about 0.45) due to the larger effective length occupied by the connection and the associated stress concentration. In the composite counterparts (L500-B, LF500-B, LE500-B), the web PEEQ is reduced to about 0.21–0.25 and the flange PEEQ is also reduced from about 0.13–0.30 to about 0.085–0.13. This confirms that the slab redistributes part of the inelastic demand away from the link web.

For the 1000 mm links (bottom panel), the bare-steel web PEEQ values are around 0.18–0.22, while the composite counterparts are around 0.12–0.13, again indicating a slab-induced reduction. The flange PEEQ in the 1000 mm links is relatively similar between bare-steel (0.13–0.18) and composite (0.08–0.09) configurations, suggesting that in the longer links the slab contribution to plastic strain redistribution is more modest than in the shorter links.

In the short links, the slab contributes most strongly to the redistribution of inelastic demand away from the link web; in the long links, the redistribution is more modest, with a non-negligible part of the plastic activity shifted to the flanges and beam segments immediately outside the link [21].

5 Influence of RC Slab Interaction Under Cyclic Loading

5.1 Hysteretic Behaviour

Under cyclic loading, the picture becomes more complex because composite action interacts with the progressive damage that develops in both the steel and the concrete. Figure 7 shows the cyclic force–rotation curves for the 500 mm and 1000 mm configurations of the bare-steel links compared with their corresponding composite counterparts. Table 3 summarises the principal cyclic indicators.

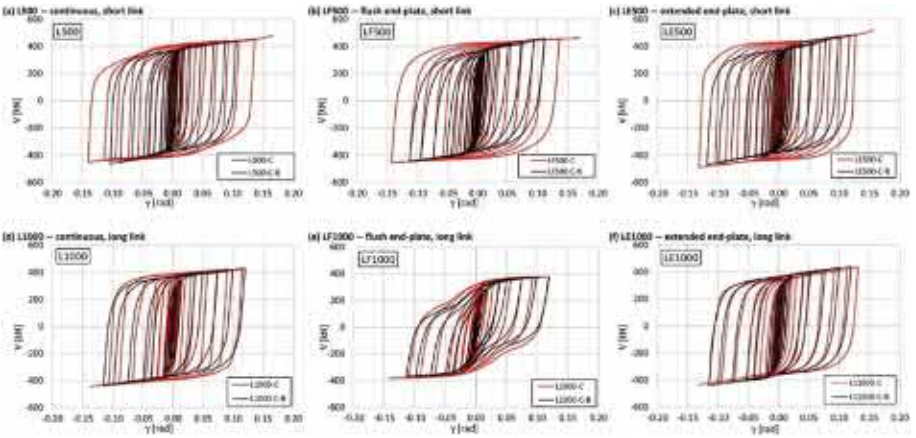


Fig. 7. Direct comparison between the bare-steel and composite configurations for all six cases under cyclic loading [21]

Table 3. Summary of cyclic performance indicators for the bare-steel and composite configurations: peak positive and negative shear forces and initial stiffness. Bare-steel values from [19]; composite values from [21]

Specimen	Bare-steel V_{max}^{+} [kN]	Composite V_{max}^{+} [kN]	Bare-steel V_{max}^{-} [kN]	Composite V_{max}^{-} [kN]	Bare-steel Initial stiffness [kN/rad]	Composite Initial stiffness [kN/rad]
L500	475	441	−451	–464	93912	112256
LF500	461	458	−454	−445	71039	86612
LE500	518	483	−489	−467	77937	90837
L1000	431	426	−443	−436	54013	62394
LF1000	380	378	−383	−369	43640	51015
LE1000	437	440	−436	−438	49234	55800

For the 500 mm configurations, the hysteresis loops are generally stable over the deformation range explored. Peak shear resistances are approximately 441 kN, 458 kN, and 483 kN for the continuous, flush, and extended end-plate composite configurations, respectively, which are consistent with the values obtained from the monotonic simulations when the comparison is performed at the same link rotation—i.e. at approximately 0.10–0.12 rad, the maximum rotation achieved in the cyclic analyses, rather than at the larger monotonic peak rotations (0.25 and 0.15 rad for the 500 mm and 1000 mm links respectively). At the cyclic maximum rotation, the monotonic and cyclic shear values are in close agreement. Corresponding initial stiffness values are approximately 112256 kN/rad, 86612 kN/rad, and 90837 kN/rad. In all three cases, the composite specimens dissipate more energy per cycle than their bare-steel counterparts at moderate rotation amplitudes—the enclosed hysteretic area is larger and the loops remain reasonably full—consistent with the monotonic observations.

For the 1000 mm configurations, the behaviour is qualitatively similar but quantitatively less favourable: the loops are somewhat narrower at large amplitudes and pinching is more visible. The increase in hysteretic energy dissipation associated with composite action may contribute to improved seismic robustness, but this benefit must be interpreted together with the accompanying redistribution of inelastic demand, which is itself one of the key parameters to be considered in the design process.

5.2 Influence of Connection Rigidity

The comparison between flush and extended end-plate configurations confirms the trends observed under monotonic loading, with additional features under cyclic conditions. Extended end-plate configurations develop larger hysteresis envelopes and higher peak resistances, and maintain their loops reasonably well at large amplitudes, suggesting that the rigid connection helps preserve the integrity of the load-transfer mechanism under repeated inelastic excursions. Flush end-plate configurations, on the other hand, exhibit more pronounced pinching in the hysteresis loops—associated with slip at the end-plate interface and bearing deformations around the bolt holes—which the slab tends to amplify, particularly in the long-link case. For the 500 mm links, these differences are not dramatic and both configurations are likely to perform adequately under design-level seismic action; for the 1000 mm links, the choice between the two connection types becomes more consequential, with extended end-plates offering better resistance and energy dissipation at the cost of higher local stress concentrations, and flush end-plates maintaining a more flexible response with a greater tendency to localise damage within the removable component, but with more pronounced pinching.

Pinching and stiffness degradation are the two phenomena that most directly capture the progressive damage of a link under cyclic loading. Pinching is most pronounced in the LF1000-C-B configuration, where the combination of long link, flexible connection, and slab-induced redistribution creates conditions for significant slip at the end-plate interface and for non-uniform contact between the slab and the steel beam top flange. The effect is more contained in the LF500-C-B configuration and much less pronounced in the extended end-plate cases, where the rigid connection maintains contact across the interface even under reversed loading. Stiffness degradation, quantified as the secant stiffness at successive cycles normalised by the initial stiffness, follows a similar pattern:

the 1000 mm configurations degrade faster than the 500 mm ones, and flush end-plates degrade faster than extended end-plates. Composite specimens degrade slightly less than bare-steel ones at moderate amplitudes, but the difference tends to disappear at large amplitudes, where concrete damage in the slab starts to dominate the response.

5.3 Damage Localisation

Crucially, the results from the cyclic campaign reinforce the main message of the monotonic study: composite action redistributes part of the inelastic demand away from the removable link and towards adjacent components—beam segments, connection regions, and the slab itself. This redistribution is documented in [21] as a consequence of the additional constraints introduced by the slab on the deformation of the steel link. In the cyclic results, the bare-steel specimens exhibit slightly less stiffness degradation over successive cycles compared to the composite specimens, indicating that the slab introduces additional constraint effects that modify the distribution of plastic strain during cyclic loading. The cyclic behaviour is otherwise consistent with the monotonic observations discussed in Sect. 4, supporting the same overall picture: the slab increases stiffness and energy dissipation capacity, while introducing additional constraints on local deformation that must be considered in the design.

6 Discussion

The numerical evidence presented in Sects. 4 and 5 supports a number of observations that are worth discussing from a design-oriented perspective.

A first important observation concerns the role of the slab in enhancing global performance. The cyclic analyses showed stiffness increases ranging from +13.3% to + 21.9%, with the largest improvements occurring in the short-link configurations; a qualitatively similar stiffening effect was observed under monotonic loading, as visible in the upward shift of the initial elastic–inelastic branch in all six configurations of Fig. 4. The cyclic analyses confirmed this behaviour, revealing larger hysteresis envelopes and increased energy dissipation capacity in the composite systems.

A second observation concerns the modification of local response mechanisms. The Von Mises stress and PEEQ distributions demonstrated that composite interaction redistributes part of the inelastic demand away from the removable link and towards adjacent structural components. From a purely strength-based perspective, this behaviour is advantageous because it reduces peak stress concentrations and delays the accumulation of severe plastic strains within the dissipative element. A distinction should be made between structural performance and functional performance.

Structural performance is primarily associated with stiffness, strength, and energy dissipation capacity, whereas functional performance is associated with damage localisation, replaceability, and downtime reduction. The numerical evidence indicates that the configuration providing the highest structural performance is not necessarily the configuration providing the highest functional performance.

The redistribution of inelastic demand induced by the slab is particularly evident when comparing flush and extended end-plate configurations. The extended end-plate

solutions generally achieved the highest strength and stiffness values because their greater rigidity promoted a more efficient mobilisation of composite action. The same rigidity, however, also encourages a stronger interaction between the removable link and the surrounding structural components, with a corresponding redistribution of inelastic demand away from the sacrificial element. Flush end-plate configurations exhibited a complementary tendency: although characterised by lower resistance levels, they generally maintained a more flexible response, greater deformation capacity, and a stronger tendency to localise damage within the removable component. These contrasting behaviours are a direct consequence of the trade-off between structural performance and damage localisation observed throughout this study.

Another important finding concerns the influence of link length. The short 500 mm links benefited most significantly from slab interaction, whereas the improvements observed in the 1000 mm links were more limited and were accompanied by a greater susceptibility to pinching and cyclic degradation. This observation suggests that the advantages associated with RC slab interaction cannot be generalised across all removable-link geometries and should be evaluated in relation to the governing deformation mechanism of the link.

The study therefore highlights a broader design implication: the optimal removable-link configuration is not necessarily the one that maximises structural resistance. In resilient seismic design, strength, ductility, damage concentration, and reparability are competing objectives rather than independent quantities. Table 4 summarises these trade-offs for the investigated configurations.

Table 4. Comparative assessment of the investigated configurations in terms of structural performance and damage concentration under cyclic loading

Configuration	Strength	Stiffness	Ductility	Damage concentration
L500-C-B (continuous, short)	Moderate	High	High	Moderate
LF500-C-B (flush, short)	Moderate	Moderate-High	High	High
LE500-C-B (extended, short)	Very high	Very high	Moderate	Low-Moderate
L1000-C-B (continuous, long)	Moderate	Moderate	Moderate	Moderate
LF1000-C-B (flush, long)	Low-Moderate	Low-Moderate	Moderate	High
LE1000-C-B (extended, long)	Moderate-High	Moderate	Low-Moderate	Low

To facilitate a direct quantitative comparison of the slab influence, Table 5 reports the percentage variation of initial stiffness (under cyclic loading) and cyclic peak shear resistance between bare-steel and composite configurations. The synthesis confirms that,

under cyclic loading, the slab induces a consistent and substantial increase in initial stiffness across all configurations, while its effect on peak shear resistance is much smaller and slightly negative in most cases—a consequence of the additional axial force demand that the slab restraint introduces in the link.

This trade-off between stiffness enhancement and modest peak resistance reduction, together with the damage redistribution discussed above, supports the design-oriented recommendations summarised in Table 4.

Table 5. Percentage variation of initial stiffness and peak shear resistance induced by the RC slab (bare-steel vs. composite) under cyclic loading

Configuration	ΔK_{cyclic} [%]	ΔV_{max}^{+} [%]	ΔV_{max}^{-} [%]
L500 (continuous, short)	+19.5	−7.2	+2.9
LF500 (flush, short)	+21.9	−0.7	−2.0
LE500 (extended, short)	+16.6	−6.8	−4.5
L1000 (continuous, long)	+15.5	−1.2	−1.6
LF1000 (flush, long)	+16.9	−0.5	−3.7
LE1000 (extended, long)	+13.3	+0.7	+0.5

The slight reduction in peak shear resistance observed under cyclic loading (Table 5) can be mechanically explained by examining the internal axial force distribution. Unlike bare-steel sub-assemblies where longitudinal deformations accommodate web distortion and connection rotation relatively freely, the reinforced concrete floor slab acts as an axial restraint across the framing beams.

Table 6 directly compares the axial stresses (σax) developed across bare-steel and composite removable links at $\gamma = 0.10$ rad under cyclic loading.

Table 6. Direct comparison of restraint-induced axial stresses (σax) between bare-steel and composite link assemblies under cyclic loading at $\gamma = 0.10$ rad

Specimen Pair (Bare vs. Composite)	Bare-Steel Axial Stress $\sigma ax_{bare\text{-}steel}$ [MPa]	Composite Axial Stress $\sigma ax_{composite}$ [MPa]	Net Axial Increase Δσax [MPa/Factor]	Dominant Mechanical Effect
L500-C vs. L500-C-B	20–35	85–110	+75 MPa (3.1x)	Moderate shear-axial (V - N) web coupling
LF500-C vs. LF500-C-B	30–45	120–145	+95 MPa (3.5x)	Bolt prying & moderate prying-axial interaction
LE500-C vs. LE500-C-B	25–40	110–130	+88 MPa (3.3x)	Rigid end-plate rotation constraint

(*continued*)

Table 6. (*continued*)

Specimen Pair (Bare vs. Composite)	Bare-Steel Axial Stress $\sigma ax_{bare\text{-}steel}$ [MPa]	Composite Axial Stress $\sigma ax_{composite}$ [MPa]	Net Axial Increase $\Delta\sigma ax$ [MPa/Factor]	Dominant Mechanical Effect
L1000-C vs. L1000-C-B	15–30	65–85	+53 MPa (2.8x)	Flexural-axial yielding redistribution
LF1000-C vs. LF1000-C-B	35–55	140–175	+115 MPa (3.6x)	Severe gap opening & high prying axial tension
LE1000-C vs. LE1000-C-B	20–35	90–115	+75 MPa (3.4x)	Balanced flexural-composite mobilization

As reported in Table 6, composite interaction induces a non-negligible amplification in longitudinal stresses along the link profile. The coexistence of substantial shear stress and restraint-induced longitudinal tension/compression (σax) consumes a significant fraction of the yield surface. This mechanical coupling accelerates web yielding and explains why, under cyclic conditions, composite action systematically enhances initial stiffness and cumulative energy dissipation, but slightly bounds the maximum attainable shear resistance, particularly in shorter shear-dominated links.

From a design perspective, these results suggest that the influence of RC slab interaction when selecting removable-link geometries and connection details should be explicitly considered. Design choices aimed solely at increasing strength may inadvertently shift the inelastic demand away from the removable component.

Overall, the numerical evidence indicates that reinforced concrete slabs should be regarded as active participants in the seismic response of removable-link EBF systems. Their influence extends beyond conventional composite strengthening effects and directly affects the balance between structural performance and damage localisation across the assembly.

7 Conclusions

This paper presented a detailed finite element investigation into the influence of reinforced concrete slab interaction on removable bolted shear links employed in eccentrically braced frame systems. Three-dimensional Abaqus models were developed and validated against available experimental evidence before being used to examine the behaviour of composite link–beam–slab assemblies subjected to monotonic and cyclic loading conditions. The investigation considered different removable-link connection typologies, including flush and extended end-plate solutions, together with two representative link lengths of 500 mm and 1000 mm. Based on the numerical results obtained, the following conclusions can be drawn:

The RC slab significantly modifies the global response of removable-link systems. Under cyclic loading, composite action systematically increased the initial stiffness of all investigated configurations, with the increase ranging between +13.3% and + 21.9% and the most pronounced effect in the 500 mm links, where the response is primarily governed by shear mechanisms and a qualitatively consistent stiffening effect was observed under monotonic loading across all investigated link geometries and connection typologies.

Peak shear resistance under cyclic loading was only marginally affected, with most configurations showing a slight reduction (between −7.2% and + 0.7%, as documented in Table 5).

Connection detailing strongly affects the interaction between the removable link and the composite floor system. Extended end-plate configurations generally developed the highest strength and stiffness levels, whereas flush end-plate solutions exhibited a more flexible response and a greater tendency to concentrate damage within the removable component.

The slab alters stress redistribution and plastic strain development. Composite interaction modifies the force-transfer mechanisms within the assembly and promotes a redistribution of inelastic demand away from highly concentrated regions, generally reducing local stress concentrations and PEEQ values within the link—particularly in short links, as visible in the comparison of Fig. 6.

Under cyclic loading, composite action enhances energy dissipation but also modifies degradation mechanisms. The investigated configurations exhibited stable hysteretic behaviour and satisfactory resistance under repeated inelastic loading, but the presence of the slab influenced pinching behaviour, stiffness degradation, and the distribution of cyclic damage, particularly in the longer-link configurations.

The benefits of composite action are accompanied by a redistribution of inelastic demand away from the removable link and towards the surrounding structural components. The configuration that maximises strength and stiffness is not necessarily the configuration that maximises damage concentration within the sacrificial element.

The observed behaviour depends on both link length and connection type. Extended end-plate configurations generally provide superior strength and stiffness, while flush end-plate configurations more effectively preserve damage localisation within the sacrificial component. Future research should focus on the experimental validation of composite removable-link systems and on the development of design-oriented procedures that explicitly account for composite action and its effect on the distribution of inelastic demand across the assembly.

References

1. Roeder CW, Popov EP (1978) Eccentrically braced steel frames for earthquakes. J Struct Div 104(3):391–412
2. Hjelmstad KD, Popov EP (1983) Cyclic behavior and design of link beams. J Struct Eng 109(10):2387–2403
3. Nastri E, Plaitano F (2022) A review on the removable link in eccentrically braced frames: benefits and performances. AIP Conf Proc 2425:120008
4. EN 1993-1-1 (2005) Eurocode 3: design of steel structures – part 1–1: general rules and rules for buildings. CEN, Brussels

5. EN 1994-1-1 (2004) Eurocode 4: design of composite steel and concrete structures – part 1–1: general rules and rules for buildings. CEN, Brussels
6. EN 1998–1 (2004) Eurocode 8: design of structures for earthquake resistance – part 1: general rules, seismic actions and rules for buildings. CEN, Brussels
7. Stratan A, Dubina D (2004) Bolted links for eccentrically braced steel frames. In: Connections in steel structures V – behaviour. Strength and Design. ECCS/AISC, Amsterdam, pp 223–232
8. Dubina D, Stratan A, Dinu F (2008) Dual high-strength steel eccentrically braced frames with removable links. Earthq Eng Struct Dyn 37(15):1703–1720
9. Ioan A et al (2016) Experimental validation of re-centring capability of eccentrically braced frames with removable links. Eng Struct 113:335–346
10. Chesoan A, Stratan A, Neagu C, Dubina D (2020) Experimental investigation of the length influence on removable links. In: Proceedings IRF2020: 7th international conference integrity-reliability-failure. INEGI-FEUP, pp 977–986
11. Mansour N (2010) Development of the design of eccentrically braced frames with replaceable shear links. PhD Thesis, University of Toronto
12. Mansour N, Christopoulos C, Tremblay R (2011) Experimental validation of replaceable shear links for eccentrically braced frames. J Struct Eng 137(10):1101–1113
13. Bozkurt MB, Topkaya C (2017) Replaceable links with direct brace attachments for eccentrically braced frames. Earthq Eng Struct Dyn 46(13):2121–2139
14. Zimbru M, D'Aniello M, Stratan A, Landolfo R, Dubina D (2018) Finite element analysis of composite replaceable short links. Key Eng Mater 763:576–583
15. Ciutina A, Dubina D, Danku G (2013) Influence of steel-concrete interaction in dissipative zones of frames: I – Experimental study. Steel Compos Struct 15(3):299–322
16. Danku G, Dubina D, Ciutina A (2013) Influence of steel-concrete interaction in dissipative zones of frames: II – numerical study. Steel Compos Struct 15(3):323–340
17. Chesoan A, Stratan A, Ciutina A (2023) Influence of reinforced concrete slab on the cyclic response of bolted shear links. ce/papers 6:2371–2376
18. Plaitano F, Stratan A, Chesoan A, Nastri E (2023) Performance of short links with flush and extended end plate connections using FEM analysis. ce/papers 6:2350–2355
19. Plaitano F, Stratan A, Nastri E (2024) Performance evaluation of short links with flush and extended end plate connections through FEM analysis under cyclic loading. In: Mazzolani FM, Piluso V, Nastri E, Formisano A (eds) Proceedings of the 11th International Conference on Behaviour of Steel Structures in Seismic Areas (STESSA 2024), Lecture notes in civil engineering, vol 520. Springer, Cham
20. Plaitano F (2020) Experimental tests and FEM simulations of bolted links with flush and extended end plates connections under monotonic and cyclic loads. Master's Thesis, University of Salerno, Fisciano
21. Plaitano F (2025) Effect of concrete slab and connection on performance of bolted links in re-centring eccentrically braced frames. PhD Thesis, University of Timisoara
22. Zub CI, Stratan A, Dubina D (2019) Modelling the cyclic response of structural steel for FEM analyses. ITM Web Conf 29:02011
23. Plaitano F, Stratan A, Nastri E (2022) Simplified modelling of failure in high strength bolts under combined tension and bending. J Compos Sci 6(10):302
24. D'Aniello M, Cassiano D, Landolfo R (2016) Monotonic and cyclic inelastic tensile response of European preloadable gr10.9 bolt assemblies. J Constr Steel Res 124:77–90
25. ISO 898-1 (2013) Mechanical properties of fasteners made of carbon steel and alloy steel – Part 1: Bolts, screws, and studs with specified property classes. International Organization for Standardization, Geneva
26. ABAQUS (2014) ABAQUS standard user's manual, version 6.14. Dassault Systèmes, Providence

27. Guo Z (2014) Principles of reinforced concrete. 1st edn. Elsevier, Oxford
28. Montuori R, Nastri E, Piluso V, Todisco P (2024) Finite element analysis of concrete filled steel tubes subjected to cyclic bending. Eng Struct 314:118364
29. Nastri E, Todisco P (2022) Macromechanical failure criteria: elasticity, plasticity and numerical applications for the non-linear masonry modelling. Buildings 12(8):1245
30. D'Aniello M, Cassiano D, Landolfo R (2017) Simplified criteria for finite element modelling of European preloadable bolts. Steel Compos Struct 24(5):643–658
31. AISC 341–16 (2016) Seismic provisions for structural steel buildings. American Institute of Steel Construction, Chicago

Acoustic Emission Monitoring for Damage Diagnosis in Welded Steel Components

Roberto Andreotti(✉), Gabriele Zanon, Rocco Di Filippo, Alessio Bonelli, and Oreste S. Bursi

University of Trento, Trento, Italy
roberto.andreotti@unitn.it

Abstract. Acoustic Emission (AE) monitoring represents a promising non-destructive technique for the identification of damage in steel structures, thanks to its high sensitivity to microcrack initiation and defect evolution. Being exposed to fatigue and cyclic loading effects, welded joints constitute critical details in steel constructions, which might develop damage difficult to detect through conventional inspection methods. AE sensors, installed close to welded regions, can capture elastic waves generated by microstructural events occurring within the material. In engineering practice, AE data is often interpreted through simple signal descriptors, such as amplitude or duration. However, such approaches may be insufficient when the objective is to characterize damage progression or to support structural diagnosis. In this contribution, experimental tests carried out on scaled full-penetration welded steel specimens are presented. The specimens reproduce the transverse weld of the lower flange of a steel bridge deck and were subjected to both low-cycle and high-cycle loading conditions to induce yielding and fatigue damage, respectively. The collected AE signals were analyzed using a data-driven approach based on transfer learning and convolutional neural networks, exploiting Mel spectrograms as time–frequency features. The results show that the proposed framework is effective in distinguishing AE signals associated with yielding-related damage, while preliminary but meaningful trends also emerge for high-cycle fatigue conditions. The study highlights the potential of combining AE monitoring and machine learning techniques to support the diagnosis of welded steel details moving toward advanced damage assessment tools for real steel structures.

Keywords: welded steel details · structural damage assessment · acoustic emissions · convolutional neural networks · transfer learning · early-stage damage

1 Introduction

Acoustic emission (AE) techniques are widely adopted for structural damage assessment. In metallic materials, AE activity is typically associated with defects, crack initiation and propagation, and plastic deformation near crack tips [1]. Compared with conventional structural health monitoring (SHM) methods, such as modal-based identification

© The Author(s), under exclusive license to Springer Nature Switzerland AG 2026
R. Zanon et al. (Eds.): CTA 2026, LNCE 942, pp. 245–255, 2026.
https://doi.org/10.1007/978-3-032-39505-4_22

or visual inspections, AE monitoring provides higher sensitivity to localized and internal damage mechanisms. Welded joints are particularly suitable for AE investigations because the microscopic defects in the heat affected zone strongly affect elastic wave generation and propagation [2]. Previous studies demonstrated the capability of AE sensors to detect microcrack opening and defect movement at the crystal lattice scale, as well as wire failures in prestressed and post-tensioned concrete structures. However, in steel structures, AE applications have mainly focused on severe damage conditions or ultimate failure, while early-stage damage detection remains less investigated despite its relevance for fatigue-critical details. Literature reviews on AE-based monitoring [3] highlighted several advantages of the methodology, including continuous and remote monitoring capabilities without interfering with bridge traffic. Modern acquisition systems also enable high-frequency measurements and real-time data transmission, while recent advances in computational power facilitate the processing of large AE datasets. Several experimental investigations proposed threshold-based approaches for fracture detection [4]. Nevertheless, such methods may not fully exploit the complexity of AE signals. To address this limitation, machine learning techniques have recently attracted increasing attention. Xin et al. [5], for example, employed convolutional neural networks (CNNs) on frequency-domain representations of AE signals for fatigue fracture detection in bridge stay cables. In this context, transfer learning allows pretrained neural networks to be reused, reducing both training data requirements and computational costs while maintaining classification performance. Building on these developments, the present study investigates AE monitoring of full-penetration welded steel specimens representative of structural details commonly adopted in steel bridges. Experimental tests under both low-cycle and high-cycle loading conditions were performed. The recorded AE signals were analyzed in the frequency domain and used to develop a CNN-based classification framework for yielding and fatigue damage detection.

2 Experimental Setup

Steel structures extensively employ welded joints to guarantee structural continuity and efficient load transfer. In particular, full-penetration welds are commonly adopted in bridge decks, where critical details such as the lower flange at midspan are permanently subjected to tensile stresses. The experimental setup shown in Fig. 1a) and b) was developed to reproduce such type of details when subjected to transversal stress. The specimen geometry was designed to allow both low-cycle fatigue (LCF) and high-cycle fatigue (HCF) investigations. The adopted weld configuration, detailed in Fig. 1a), corresponds to Ref. n. 1.3 according to EN ISO 9692-1:2013 [6], although a thickness of 15 mm was considered for testing purposes. Specimens were welded using the GMAW process (Reference Number 135). In all tests, failure was forced to occur within the reduced central cross-section, having dimensions equal to 40 mm $\times$ 15 mm. Two LCF and two HCF tests were performed. Figure 1c) and d) show, as representative examples, the specimen and the collapsed section for LCF Test #1 and HCF Test #2, respectively. Failure occurred in the base material during the LCF tests, whereas fracture developed within the welded section under HCF loading conditions. All specimens were fabricated using S355 steel, corresponding to a characteristic yielding force $F_{y,k} = 213$ kN. AE monitoring was carried out using piezoelectric sensors arranged according to the configuration

reported in Fig. 1a). The data acquisition system, provided by Vallen Systeme GmbH, comprised an AMSY-6 unit equipped with a dual-channel ASIP-2/A board, connected to six AE sensors with a resonance frequency of 150 kHz and operating within a nominal frequency range of 100–450 kHz. In particular, Channel 5 and Channel 6 were connected to a VS150-RI and VS150-RSC sensor, respectively, whose differences are negligible for the purposes of this work. Sensors were connected through 20 m coaxial cables, while data acquisition was managed using an external laptop. All measurements were performed using identical acquisition parameters. The sampling frequency was set to 10 MHz with a fixed threshold of 40 dB. A band-pass filter with cutoff frequencies of 50 kHz and 300 kHz was adopted, while both the Duration Discrimination Time (DDT) and Rearm Time (RAT) were set equal to 4000 μs.

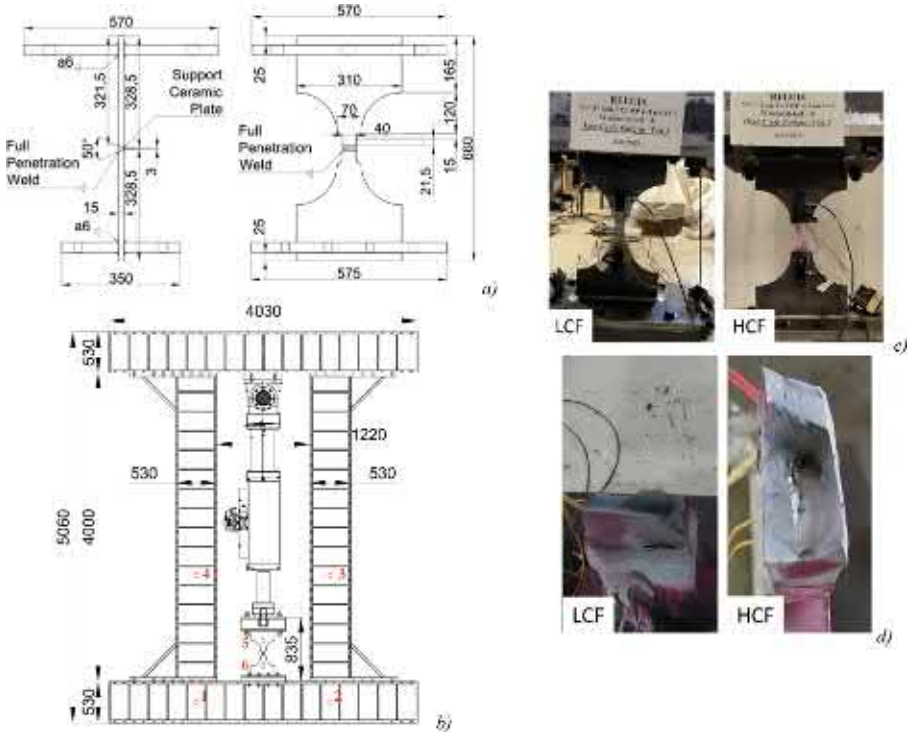


Fig. 1. *a)* Experimental specimen (dimensions in mm); *b)* Experimental test setup including acoustic emission sensors; *c)* Picture of the experimental specimen for LCF and HCF tests; *d)* Collapsed section at specimens failure for LCF and HCF tests

3 Loading Protocols

For the LCF tests, the loading protocol followed the recommendations of ASTM 2020 [7] and Chisari et al. [8]. Incremental loading steps of 0.25 $F_{y,k}$ were applied up to yielding, followed by increments of 0.1 $F_{y,k}$ until failure. Each load level was repeated twice, fully

unloading the specimen to 0 kN between consecutive steps. During the tests, the load was maintained constant for 180 s at each level, while loading and unloading phases were performed at a constant rate equal to $F_{y,k}/120$ s = 1.775 kN/s. In the HCF tests, specimens were driven to fatigue collapse under elastic loading conditions. The applied load cycles were characterized by maximum and minimum tensile forces equal to 197.3 kN and 1.97 kN, respectively, corresponding to a stress range $\Delta\sigma = 317.1$ MPa. These values were calibrated to induce fatigue failure while maintaining elastic behaviour. Consequently, failure occurred after $n_{TOT} = 118568$ cycles for HCF Test #1 and $n_{TOT} = 108138$ cycles for HCF Test #2. The large number of required cycles introduced two main experimental challenges. First, the long duration of the tests required the loading history to be subdivided into several loading blocks. Second, to protect the electrohydraulic actuator while minimizing the overall testing duration, the loading frequency had to be initially kept low when the actuator oil was cold and progressively increased as the oil temperature rose. As a result, the loading-frequency histories of the two HCF tests did not coincide. Table 1 and Table 2 summarize the loading block specifications adopted for HCF Test #1 and Test #2, respectively, including number of cycles n, loading frequency, time range and the fatigue damage index, which is defined as

$$D = \sum_i \frac{n_i}{N_i} \tag{1}$$

where n_i is the number of cycles associated with the i-th loading block and N_i represents the number of cycles to failure corresponding to the applied stress range $\Delta\sigma$. Since a constant stress range was adopted throughout the tests, N_i remained unchanged for all loading blocks.

Table 1. HCF Test #1 specifications ($n_{TOT} = 118568$ – $t_{TOT} = 8.5$ h)

n	Load Freq.	Time	D
1000	2.5	400	0.008
100	3.3	30.3	0.009
900	3.3	272.7	0.017
1000	4	250	0.025
1000	4.5	222.2	0.034
1000	5	200	0.042
45000	4	11250	0.422
3000	4	750	0.447
22000	4	5500	0.633
1000	2.5	400	0.641
4000	2.5	1600	0.675
2000	4	500	0.692
2000	4	500	0.708
23000	4	5750	0.902
11568	4	2892	1.000

Table 2. HCF Test #2 specifications ($n_{TOT} = 108138 - t_{TOT} = 7.7$ h)

n	Load Freq.	Time	*D*
501	4.0	125	0.005
2000	4.0	500	0.023
47499	4.0	11875	0.462
4000	2.5	1600	0.499
46000	4.0	11500	0.925
8138	4.0	2035	1.000

Figure 2 reports the superposition of the load history and the AE peak amplitudes and durations recorded during LCF Test #1, while Fig. 3 shows the AE peak amplitudes and durations measured during HCF Test #1.

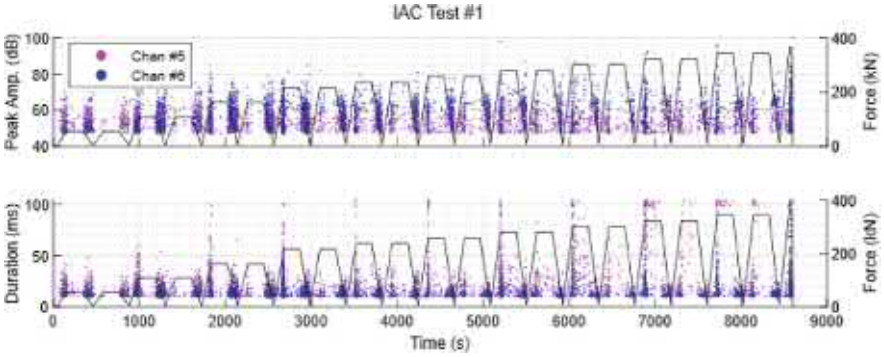


Fig. 2. Low cycle fatigue Test #1: load history superposed with peak amplitude and duration AE data features

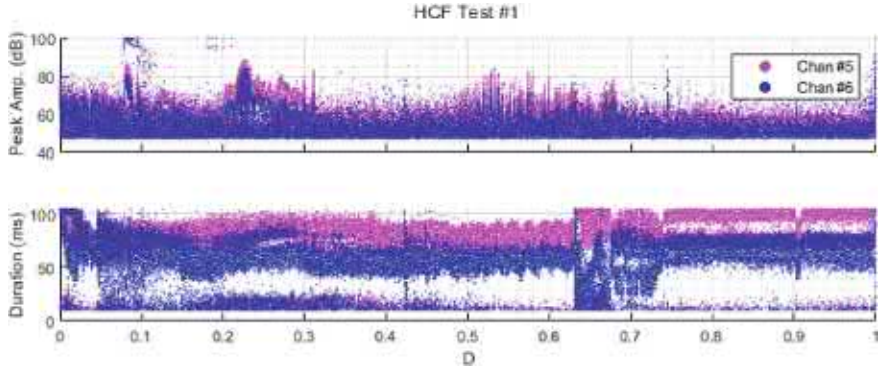


Fig. 3. High cycle fatigue Test #1: histories of peak amplitude and duration AE data features

4 Data Processing

From Figs. 2 and 3, it can be observed that damage evolution cannot be clearly identified by considering only AE peak amplitudes and durations. For this reason, the acquired dataset was further processed using more informative signal representations, namely Mel spectrograms, for supervised classification purposes. For each damage class, a balanced dataset was created by randomly selecting the same number of AE signals. A transfer learning strategy was then adopted using pretrained deep-learning architectures originally developed for audio classification. Specifically, the YAMNet convolutional neural network for audio recognition, provided by MathWorks (2024) [9], was selected as the base model. The pretrained network was subsequently retrained using the experimentally acquired AE signals. Since AE signals exhibit dominant frequencies around 150 kHz, well above the human audible range, the signals were time-stretched by reducing the sampling frequency by two orders of magnitude ($f_s^* = f_s/100$). The resulting signals were then converted into time–frequency representations through Mel spectrograms. First, the nonstationary AE signals were divided into short frames using a Hamming window defined as

$$w(k) = 0.54 - 0.46 \cdot \cos\left(\frac{2\pi k}{K-1}\right) \tag{2}$$

where $w(k)$ is the window value at sample k and K is the total number of samples within the window. The Discrete Fourier Transform (DFT) was subsequently computed for each frame as

$$X(k) = \sum_{n=0}^{N-1} x(n) e^{-j2\pi nk} \quad 0 < k < N-1 \tag{3}$$

where N denotes the number of points adopted for the DFT computation. The obtained spectrum was then mapped from the linear frequency scale to the Mel scale, which is approximately linear below 1000 Hz and logarithmic above this threshold. The Mel frequency f_{mel} can be approximated as

$$f_{mel} = \frac{1000}{\log(2)} \log\left(1 + \frac{f}{1000}\right) \tag{4}$$

The Mel spectrum was finally computed by applying a bank of triangular band-pass filters distributed along the Mel scale. The corresponding Mel spectral coefficients are given by

$$S(m) = \sum_{k=0}^{N-1} \left[|X(k)|^2 H_m(k) \right] \quad 0 < m < M-1 \tag{5}$$

where M denotes the total number of Mel filters and $H_m(k)$ is the m-th triangular filter. The adopted preprocessing generated spectrograms of size 96 × 64, corresponding to 96 time frames and 64 frequency bands. Due to differences in signal duration, each

AE signal generated a variable number of Mel spectrograms, each treated as an independent training or testing sample. The dataset was subsequently divided into training, validation, and testing subsets. Different optimization algorithms were investigated for CNN training, including stochastic gradient descent with momentum (*sgdm*), Adaptive Moment Estimation (*adam*), and Root Mean Square Propagation (*RMSProp*), observing no substantial differences in performance. The initial learning rate was set equal to 1e−3. Since classification was performed at the Mel spectrogram level rather than at the signal level, the final label assigned to each AE signal corresponded to the mode of the predicted labels associated with its spectrograms. To further improve robustness, two additional criteria were introduced: i) only AE signals for which all Mel spectrograms were classified into the same category were retained, excluding ambiguous cases; ii) only signals associated with at least four Mel spectrograms, corresponding to durations $\geq$24.16 ms, were considered for training and testing purposes.

5 Results

5.1 Low-Cycle Fatigue Tests

For the LCF tests, AE signals were divided into two damage classes according to the experimentally identified yielding force $F_y = 239.7$ kN, namely *"Before Fy"* and *"After Fy"*. To assess the robustness of the proposed framework, a cross-validation strategy based on independent experimental datasets was adopted. In the first configuration, data from Test #1 were used for training and data from Test #2 for testing, while the opposite arrangement was considered in the second configuration. The classification performance for both cases is summarized by the confusion matrices reported in Figs. 4 and 5, comparing true and predicted class labels. The obtained results show that the proposed framework can effectively distinguish between undamaged and damaged conditions of the specimen, achieving prediction accuracies higher than 85%.



Fig. 4. Confusion matrix obtained by training the network with LCF Test#1 and testing with LCF Test#2



Fig. 5. Confusion matrix obtained by training the network with LCF Test#2 and testing with LCF Test#1

5.2 High-Cycle Fatigue Tests

For the HCF tests, AE signals were grouped into four damage classes according to the fatigue damage index D, defined in Eq. 1. The four damage classes corresponded to the four quarters of the specimen fatigue life, namely *Q1* ($0 < D < 1/4$), *Q2* ($1/4 < D < 1/2$), *Q3* ($1/2 < D < 3/4$) and *Q4* ($3/4 < D < 1$). A preliminary inspection of the acquired HCF signals revealed the presence of several noisy records characterized by a steady-state behaviour rather than by the peak followed by exponential decay typically observed in damped oscillator systems, see [10]. This behaviour was mainly attributed to the relatively high loading frequencies adopted to complete the tests within a reasonable time interval. To reduce the influence of such signals, an additional filtering criterion was introduced by limiting the maximum signal duration to 80 ms. Unlike the LCF case, the cross-validation strategy based on different experimental datasets did not provide satisfactory results for the HCF tests. Networks trained using data from HCF Test #1 (#2) were unable to correctly classify signals from HCF Test #2 (#1). This limitation is mainly attributed to the different loading-frequency histories adopted in the two tests, summarized in Table 1 and Table 2. Since AE activity is sensitive to loading rate, variations in loading frequency significantly affect both the AE signals and the corresponding Mel spectrograms. Consequently, a network trained on one HCF dataset may fail to generalize to data acquired under different loading-rate conditions. Despite this limitation, meaningful results were obtained when training and testing were performed using data from the same experimental test. In this case, each HCF dataset was randomly divided into training, validation, and testing subsets corresponding to 70%, 10%, and 20% of the available signals, respectively, ensuring that different AE signals were used for training and evaluation. These results suggest that fatigue damage information is effectively embedded within the AE signals, although further investigations are required to decouple loading-rate effects and enable reliable cross-validation between different HCF datasets (Figs. 6 and 7).

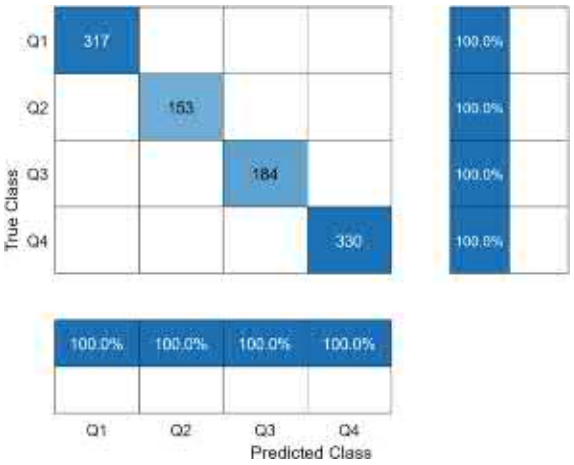


Fig. 6. Confusion matrix obtained by splitting the HCF Test #1 dataset into training and testing data

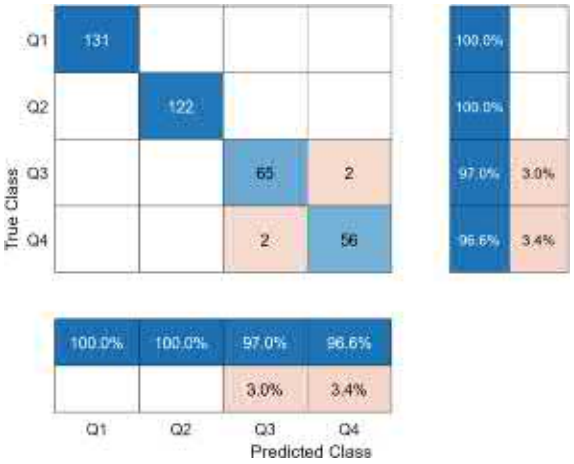


Fig. 7. Confusion matrix obtained by splitting the HCF Test #2 dataset into training and testing data

6 Conclusions

This study proposed a damage-classification framework for welded steel joints based on Acoustic Emission (AE) monitoring and transfer learning techniques. Experimental investigations were carried out on four welded steel specimens instrumented with AE sensors. Two specimens were subjected to loading up to yielding and tensile failure, while the remaining two were tested under high-cycle fatigue (HCF) conditions until collapse. The acquired AE signals were grouped into damage-related classes and transformed into Mel spectrograms, which were used as input features for training and testing the convolutional neural network at the core of the proposed framework. The results

demonstrated the capability of the framework to reliably detect yielding-related damage, correctly distinguishing between undamaged and damaged conditions with accuracies higher than 85%. Regarding HCF damage, promising results were obtained when training and testing were performed using data from the same experimental dataset. However, satisfactory performance was not achieved under cross-validation conditions between different HCF tests. This limitation suggests that the loading rate significantly influences AE signal characteristics and should therefore be further investigated to enable reliable classification of HCF damage stages based on fatigue damage indices. Several future developments are envisaged. Additional experimental campaigns are required to systematically evaluate the influence of loading frequency on AE features and to further validate the proposed framework. Further tests should also investigate different welded configurations, which may introduce variations in heat-affected zones, residual stresses, porosity, inclusion distributions, and grain morphology. Such aspects may affect both the generation and propagation of AE waves, potentially altering attenuation mechanisms and frequency content. Moreover, the present data-driven methodology should be complemented by more deterministic approaches capable of supporting the interpretation of neural-network predictions. As a final objective, the proposed framework is intended for in situ applications on real steel structures. In this perspective, CNNs trained using labelled laboratory data could support the classification of unlabeled AE signals acquired on existing structures, enabling the identification of damaged and undamaged conditions in critical steel components.

Acknowledgements. The research leading to these results has received funding from the ReLUIS-CSLLPP consortium in the framework of the DPC-ReLUIS 2022-2024 project, and by the Italian Ministry of Education, Universities and Research (MUR), in the framework of the project DICAM-EXC (Departments of Excellence 2023-2027, grant L232/2016).

References

1. Volodin TV, Khasanov OL, Konovalov SV, Volodin VL, Zuev LB (2010) Acoustic emission in steel failure. Steel Transl 40:1041–1046
2. Droubi MG, Faisal NH, Orr F, Steel JA, El-Shaib M (2017) Acoustic emission method for defect detection and identification in carbon steel welded joints. J Constr Steel Res 134:28–37. ISSN 0143-974X
3. Nair A, Cai CS (2010) Acoustic emission monitoring of bridges: review and case studies. Eng Struct 32(6):1704–1714
4. Schultz AE, Morton DL, Tillmann AS et al (2014) Acoustic emission monitoring of a fracture-critical bridge. Minnesota Department of Transportation, St. Paul
5. Xin H, Cheng L, Diender R, Veljkovic M (2020) Fracture acoustic emission signals identification of stay cables in bridge engineering application using deep transfer learning and wavelet analysis. Adv Bridge Eng 1:6
6. EN ISO 9692-1:2013 (2013) Welding and allied processes—types of joint preparation—part 1: manual metal arc welding, gas-shielded metal arc welding, gas welding, TIG welding and beam welding of steels
7. ASTM (2020) Standard practice for acoustic emission examination of reinforced thermosetting resin pipe (RTRP). Designation: E1118/E1118M – 16

8. Chisari C, Guarnaccia C, Rizzano G (2019) Numerical simulation of acoustic emission activity in reinforced concrete structures by means of finite element modelling at the macroscale. Struct Health Monit:1–15
9. MathWorks (2024) YAMNet – audio event classification using deep neural networks. MathWorks, Inc., Natick. https://it.mathworks.com/help/audio/ref/yamnet.html. Accessed 15 Jan 2026
10. Yu J, Ziehl P, Zárate B, Caicedo J (2011) Prediction of fatigue crack growth in steel bridge components using acoustic emission. J Constr Steel Res 67:1254

Structural Performance and Design Assessment of Balustrade Connection Systems

Muhammad T. Naqash[1,2] and Antonio Formisano[1,2](✉)

[1] Department of Civil Engineering, Islamic University of Madinah, Madinah, Saudi Arabia
antoform@unina.it

[2] Department of Structures for Engineering and Architecture, Polytechnic and Basic Sciences School, University of Naples Federico II, Naples, Italy

Abstract. Balustrade systems are critical safety components designed to resist prescribed lateral crowd and impact loads at slab edges, balconies, and staircases. Although design attention is often focused on the railing elements, the overall performance is frequently governed by the structural adequacy of the connection to the supporting concrete substrate. This paper investigates the structural behaviour of two widely used balustrade connection systems: embedded U-channel glass balustrades cast into concrete and bracketed steel baseplate systems anchored with chemical anchors.

The study outlines the design methodology for lateral line loads and the resulting bending stresses in accordance with relevant code provisions. Connection configurations incorporating steel brackets, welded joints, and anchor embedment are examined. Finite element analysis (FEA) models were developed to evaluate the bracketed support system under both Ultimate and Serviceability Limit State conditions, considering distributed vertical loads and applied bending moments representative of pedestrian and handrail actions.

The results show that peak stresses remain below the yield strength of the selected structural steel, confirming the adequacy of the proposed configurations. Key aspects related to anchor design, weld detailing and load transfer mechanisms are also discussed.

Keywords: Structural Glass · Anchorage systems · Cantilever behaviour · Bracket stiffness · Wind-induced loading · ULS and SLS assessment

1 Introduction

Balustrade systems are essential life-safety components installed along balconies, staircases, terraces, and slab edges to prevent accidental falls while maintaining architectural functionality. In modern construction, glass balustrades have become increasingly prevalent due to their transparency, aesthetic appeal, and support for minimalist architectural concepts. Structurally, these systems typically behave as vertical cantilever elements subjected to lateral line loads, concentrated loads, and, in exposed conditions, wind pressures.

© The Author(s), under exclusive license to Springer Nature Switzerland AG 2026
R. Zanon et al. (Eds.): CTA 2026, LNCE 942, pp. 256–265, 2026.
https://doi.org/10.1007/978-3-032-39505-4_23

Despite their architectural simplicity, glass balustrades pose complex structural challenges. Glass is a brittle material that lacks ductility and can fail without significant warning. Consequently, design approaches must address not only Ultimate Limit State (ULS) strength requirements but also Serviceability Limit State (SLS) deflection control and Post-Fracture Limit State (PFLS) residual stability. Recent developments in European guidance, particularly CEN/TS 19100 [1, 2] and EN 16612 [3], emphasize the importance of post-breakage capacity and interlayer performance in laminated systems. Earlier analytical and experimental studies have also highlighted the influence of restraint conditions and boundary stiffness on the structural response of cantilevered glass balustrades under static and impact loading [4, 5].

International standards prescribe varying load intensities depending on occupancy and risk category. Residential applications typically require horizontal line loads of approximately 0.5 kN/m. In contrast, public balconies and stadium installations may require 1.5–3.0 kN/m in accordance with EN 1991 [6, 7], BS 6399–1 [8], and AS/NZS 1170.1 [9]. Deflection limits also vary significantly among codes, ranging from Span/60 in AS 1288 [10] to L/240 (IBC 2018) and L/250 under Eurocode provisions. While these prescriptions ensure adequate panel performance, they do not always explicitly address the structural behaviour of the connection system that transfers loads to the supporting concrete substrate.

Field observations and forensic assessments indicate that balustrade failures are frequently driven not by glass rupture but by deficiencies in anchorage systems, bracket stiffness, weld detailing, or load-transfer mechanisms at the base. Anchorage pull-out, concrete edge failure, bracket yielding, and excessive rotational flexibility can compromise overall system performance even when glass stresses remain within allowable limits. The structural behaviour of the connection, therefore, plays a decisive role in ensuring robustness, particularly in high-rise or wind-exposed applications where overturning moments are amplified. Two principal connection typologies are commonly adopted in practice: (i) embedded U-channel or base-shoe systems providing continuous support along the glass edge, and (ii) discrete bracketed base plate systems anchored using mechanical or chemical fasteners. Although both systems are widely used, their structural performance differs substantially in terms of load distribution, anchor demand, and rotational restraint. Previous case studies on laminated glass balustrades in high-rise environments have demonstrated that wind-induced bending moments can exceed those generated by prescribed occupancy line loads, thereby shifting the governing design action from imposed loading to environmental loading.

In this context, the present study focuses specifically on the structural performance of balustrade connection systems. Using analytical derivations and finite element modelling supported by real project case studies, the research evaluates anchor tension forces, bracket bending stresses, weld adequacy, and global deflection behavior under both ULS and SLS conditions. By isolating the connection mechanics from the panel verification process, the study aims to clarify the load-transfer mechanisms governing system reliability and to provide design-oriented insight into the comparative performance of embedded and bracketed support configurations [11–15].

2 Methodology

The adopted methodology integrates code-based load determination, analytical verification of connection components, and finite-element modelling of representative balustrade assemblies.

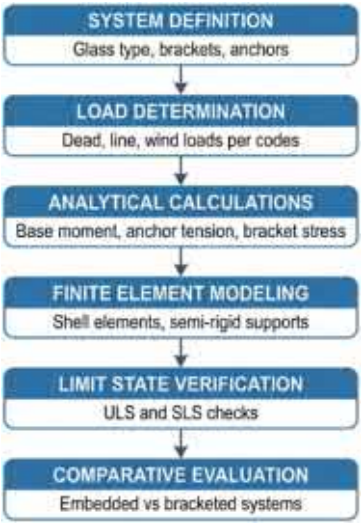


Fig. 1. Methodological framework adopted for the structural evaluation of glass balustrade connection systems

Particular emphasis is placed on the structural behaviour of the connection interface, including steel brackets, welded joints, and anchor systems that transfer loads into reinforced concrete substrates. The procedure follows a semi-probabilistic limit-state framework consistent with international standards. The adopted methodology, illustrated in Fig. 1, integrates code-based load determination, analytical verification, and finite element modeling within a unified limit-state design framework. The structured workflow ensures a systematic assessment of glass panel behaviour, connection forces, and the comparative performance of embedded and bracketed systems.

2.1 Material Modelling

The glass panels considered in this study consist primarily of laminated tempered configurations representative of typical balcony installations. A reference configuration of 8 + 1.52 PVB + 8 mm laminated glass was adopted for wind-governed high-rise cases, while monolithic tempered panels up to 19 mm thickness were considered in other case studies. The modulus of elasticity for Glass was taken as 70 GPa, with a Poisson's ratio of 0.22 and a unit weight of 27 kN/m^3. The allowable bending stress was assumed as 50 MPa in accordance with AS 1288, while a short-duration design strength of 72.3 MPa was adopted for comparison with ASTM E1300 [16] provisions.

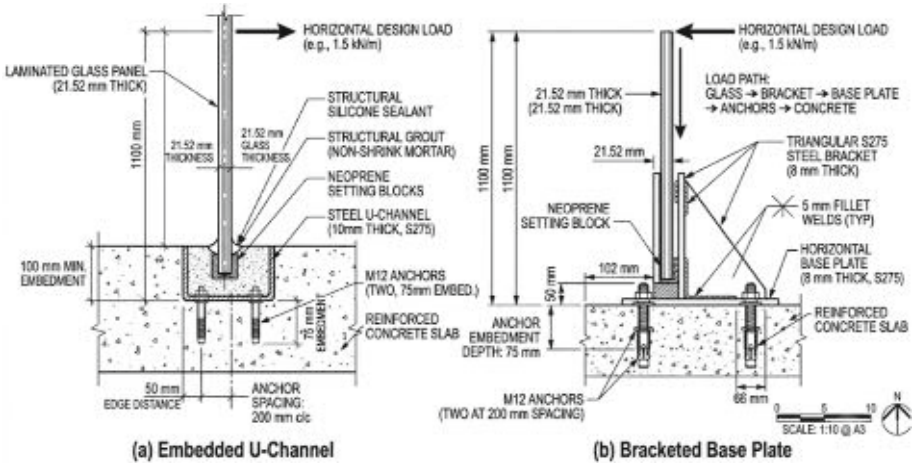


Fig. 2. Structural section details of the investigated glass balustrade base connection systems: (a) embedded U-channel system with 100 mm minimum embedment and M12 anchors; (b) bracketed base plate system with 102 mm lever arm and discrete anchor fixation

The two investigated base connection configurations are illustrated in Fig. 2, comprising (a) a continuous embedded U-channel system and (b) a discrete bracketed base plate system. Both details show the full structural load path from the laminated glass panel to the reinforced concrete slab through steel support elements and M12 anchor fixings. In contrast, the embedded U-channel system provides continuous edge restraint, resulting in a more uniform distribution of anchor forces along the base.

Steel brackets and base plates were modelled using S275 structural steel with a nominal yield strength of 275 MPa and an elastic modulus of 205–210 GPa. Stainless steel elements in stair and stadium case studies were verified against allowable stresses consistent with grade-specific limits.

Structural silicone used at the Glass-to-steel interface had a tensile modulus of approximately 0.8 MPa and a design bite of 40 mm. Although silicone does not contribute significantly to global stiffness, its tensile capacity and deformation characteristics influence local stress transfer and edge restraint behavior.

Figure 2 illustrates the geometric and structural detailing of the bracketed support assembly, including plate thickness, weld configuration, and M12 chemical anchor embedment into the concrete substrate. The elevation, section, and plan views clarify the load-transfer mechanism and the anchor spacing governing moment resistance and rotational restraint at the base.

Anchor systems were represented using manufacturer-certified mechanical or chemical anchors (Hilti HST M12 and HIT HY 200 R with HIS RN inserts) [17]. The characteristic tensile resistance of each anchor was taken as 12 kN, with a design tensile resistance of 8 kN after application of the appropriate partial safety factor ($\gamma M = 1.5$).

2.2 Load Determination

Loading conditions were derived from applicable national and international standards, depending on project typology. For residential applications, imposed horizontal line loads of 0.5 kN/m were considered, while public and high-occupancy cases adopted values of 1.5 kN/m or higher in accordance with EN 1991–1-1 and BS 6399–1.

For high-rise balcony systems exposed to environmental actions, wind loading governed the design. Using BS 6399 procedures, a basic wind speed of 25 m/s and a terrain amplification factor of 2.12 yielded an effective wind speed of 58.3 m/s. The corresponding dynamic pressure was calculated by Eq. (1):

$$q_s = 0.613 V_e^2 = 2083.5 \text{ Pa} \tag{1}$$

Applying an external pressure coefficient of −1.3 and an area reduction factor of 0.87 produced a net design pressure of approximately −2358 Pa. For a panel height of 1.1 m, this resulted in an unfactored bending moment of approximately 1.51 kNm per metre width. Ultimate limit state combinations were taken as ULS = 1.4 DL + 1.6 LL, while for wind-governed cases ULS = 1.4 WL was adopted, leading to a factored design moment of approximately 2.1 kNm at the base of the glass panel. Serviceability checks were conducted under unfactored load combinations.

2.3 Analytical Connection Design

The structural response of bracketed systems was evaluated by modelling the glass panel as a cantilever subjected to lateral loading. The overturning moment at the base generates a tension–compression couple within the anchor group. The axial tensile force in the most critical anchor was determined using Eq. (2):

$$T = \frac{M}{e} \tag{2}$$

where M is the factored bending moment and e is the lever arm between compression and tension zones. For a lever arm of 102 mm and a factored moment of 2.1 kNm, the resulting tensile force was approximately 19.6 kN.

Anchor demand was compared against design tensile resistance to determine the required number of fasteners per metre. Four anchors per metre were adopted in representative configurations to ensure adequate redundancy and load sharing. Bracket bending stresses were verified using classical flexural theory. For example, a U-channel bracket subjected to a factored moment of 0.96 kNm/m produced a maximum bending stress which remains below the yield strength of S275 steel. Welded connections between vertical bracket plates and base plates were designed in accordance with Eurocode 3 provisions. A 5 mm fillet weld with a design shear strength of approximately 1.24 kN/mm was verified against calculated force demands, ensuring adequate resistance and stiffness for moment transfer.

2.4 Finite Element Modelling

Finite element analyses were performed using SAP2000 and Autodesk Robot Structural Analysis to capture the global and local responses of the balustrade assemblies. Glass panels were modelled using four-node shell elements, with mesh refinement near fixed edges to capture stress concentrations. Mesh sensitivity analyses were conducted to ensure numerical convergence.

Boundary conditions were represented as semi-rigid supports to account for bracket flexibility and anchor deformation. Rotational springs were introduced at the base nodes to simulate realistic restraint conditions derived from bracket geometry and anchor layout. In selected models, the laminated glass interlayer was represented using effective thickness approaches consistent with EN 16612 guidance.

The analyses evaluated stress distributions, deflection profiles, support reactions, and connection forces under both ULS and SLS combinations. Demand-to-capacity ratios were computed for glass panels, steel components, anchors, and welds to verify compliance with design criteria.

3 Results and Discussion

3.1 Global Structural Response

The structural response of the investigated balustrade systems was evaluated under both Ultimate Limit State (ULS) and Serviceability Limit State (SLS) loading combinations. Across all case studies, the glass panels exhibited bending stresses ranging from 7.3 MPa to 37.8 MPa under ULS conditions. These values remain below the allowable bending stress of 50 MPa prescribed by AS 1288 and well within short-duration resistance values referenced by ASTM E1300.

In wind-governed high-rise applications, where a net pressure of approximately 2358 Pa was applied to a 1.1 m high panel, the maximum stress of 37.8 MPa occurred at the fixed base of the cantilevered glass panel. The stress distribution followed classical cantilever behavior, with tensile concentration along the restrained edge and gradual reduction toward the free top edge. No local overstress was observed at mid-height, confirming that bending demand was properly transferred to the support interface.

Deflection values under SLS conditions ranged between 3.59 mm and 15 mm, remaining below span/60 limits (approximately 19.8–25 mm depending on panel height). In all cases, serviceability deflection rather than glass strength governed panel sizing. This confirms that stiffness requirements control design in most cantilevered balustrade systems.

However, while panel behaviour remained well within acceptable limits, connection forces approached critical design thresholds in several scenarios, indicating that global safety margins are primarily governed by the support mechanism rather than by the Glass itself.

3.2 Connection Performance

The overturning moment generated by lateral loads induces a tension–compression couple within the bracket and anchor system. For the wind-governed balcony case, a factored

bending moment of approximately 2.1 kNm produced a calculated anchor tensile force of 19.6 kN, assuming a 102 mm lever arm. When compared with the design tensile resistance of 8 kN per M12 anchor (after application of $\gamma M = 1.5$), it becomes evident that multiple anchors are required to distribute the tensile demand safely. The adopted configuration of four anchors per metre provided adequate redundancy and ensured demand-to-capacity ratios below unity. Finite element reaction outputs confirmed these analytical calculations, with maximum recorded axial forces remaining within certified anchor capacities. Steel bracket stresses were also verified under ULS combinations. Representative U-channel brackets subjected to factored moments exhibited induced stresses of approximately 115 MPa, well below the yield strength of S275 steel (275 MPa). Stainless steel handrail assemblies reached maximum stresses of 190 MPa, remaining below allowable limits (Yield Strength (0.2% offset) of 205 MPa). In all examined configurations, steel components behaved elastically under design loads.



Fig. 3. Von Mises stress distribution in the bracketed support system under ULS loading

Figure 3 presents the von Mises stress distribution obtained from finite element analysis of the bracketed balustrade support system under Ultimate Limit State (ULS) loading. Stress concentrations are primarily localized at the base of the vertical brackets and near the anchor connection zones, where moment transfer is concentrated. The maximum computed stress of approximately 262 MPa (left) and 242 MPa (right) remains below the yield strength of S275 steel (275 MPa), confirming elastic structural behavior and adequacy of the bracket configuration under factored loading.

Although strength verification was satisfactory, bracket stiffness significantly influenced overall performance. Semi-rigid modeling demonstrated that excessive rotational flexibility at the base increases top-edge displacement even when glass stiffness remains unchanged. This interaction highlights the importance of accurately representing bracket geometry, weld continuity, and anchor deformation in numerical analysis. Welded joints between bracket plates and base plates were designed with 5 mm fillet welds, providing a shear resistance of approximately 1.24 kN/mm. The distributed weld layout ensured adequate moment transfer and contributed to rotational restraint. No weld configuration exceeded allowable stress or shear limits.

Table 1 summarises the structural response of several representative balustrade configurations analyzed in this study. The selected case studies cover different occupancy categories and loading conditions, including residential, public, and stadium installations

subjected to prescribed horizontal line loads, as well as a high-rise balcony governed by wind pressure. The investigated panel thicknesses and laminate compositions reflect practical design solutions commonly adopted in contemporary construction. The comparison allows evaluation of stress and deflection trends as loading intensity and panel stiffness vary.

Table 1. Glass Panel Response under Design Loading

Case Study	Panel Configuration	Governing Load	Max Stress (MPa)	Allowable Stress (MPa)	Max Deflection (mm)	Limit (Span/60) (mm)	Height (mm)
Residential Balcony	8 + 1.52PVB + 8 mm	Line Load 0.5 kN/m	7.3	50	3.59	19.8	1180
Public Balcony	10 + 1.52PVB + 10 mm	Line Load 1.5 kN/m	18.4	50	8.7	21.7	1300
Stadium Installation	12 + 1.52PVB + 12 mm	Line Load 3.0 kN/m	26.9	50	12.4	23.3	1400
High-Rise Balcony	8 + 1.52PVB + 8 mm	Wind 2358 Pa	37.8	50	15.0	18.3	1100

Table 1 confirms that all glass configurations satisfy both strength and serviceability requirements. Maximum bending stresses range from 7.3 MPa to 37.8 MPa, remaining below the allowable limit of 50 MPa. Serviceability deflections range from 3.59 mm to 15.0 mm and remain within span/60 limits. In all cases, deflection rather than strength governs panel sizing, confirming that stiffness requirements control the design of cantilevered glass balustrades.

4 Conclusions

This study evaluated the structural performance of two widely adopted balustrade connection systems: embedded U-channel supports and bracketed base plate assemblies, anchored with mechanical or chemical fasteners, under Ultimate and Serviceability Limit State conditions. The investigation combined code-based analytical calculations with finite element modeling and project-based case studies. The results demonstrate that, for properly proportioned laminated or tempered glass panels, global glass strength is generally not the governing design parameter. Maximum bending stresses across all examined configurations remained below allowable limits, and serviceability deflections satisfied span-based criteria prescribed by international standards. In contrast, connection behavior governs structural reliability. Wind-induced overturning moments generated anchor tensile demands approaching design resistance thresholds in exposed, high-rise applications. Bracket stiffness and rotational restraint were shown to significantly influence global deflection, even when glass panel stiffness remained unchanged. Analytical

and numerical results confirmed that adequate anchor spacing, verified weld detailing, and proper lever-arm assessment are essential to maintaining demand-to-capacity ratios below unity. Embedded channel systems provided more uniform load distribution and reduced peak anchor forces, whereas discrete bracketed systems concentrated tensile demand at anchor locations and were more sensitive to rotational flexibility. Nevertheless, both systems achieved full compliance with ULS and SLS requirements when designed in accordance with relevant standards and validated through finite element analysis.

The findings emphasize that balustrade systems must be treated as integrated structural assemblies in which load transfer at the connection interface dictates overall performance. Accurate modelling of boundary conditions, anchor behaviour, and bracket stiffness is therefore critical for safe and serviceable design, particularly in wind-exposed or high-occupancy environments.

Future research should extend the investigation to post-fracture behaviour and cyclic wind-loading effects, particularly in high-rise applications where connection fatigue and long-term anchor performance may govern durability.

References

1. European Committee for Standardization (CEN) (2021) CEN/TS 19100–1:2021. Design of glass structures – part 1: basis of design and materials. CEN, Brussels
2. European Committee for Standardization (CEN) (2021) CEN/TS 19100–2:2021. Design of glass structures – part 2: design of out-of-plane loaded glass components. CEN, Brussels
3. European Committee for Standardization (CEN) (2019) EN 16612:2019. Glass in building – determination of the load resistance of glass panes by calculation and testing. CEN, Brussels
4. Rizzo F, Bedon C (2022) Performance of cable-supported glass façades under time-dependent wind action. Glass Struct Eng. https://doi.org/10.1007/s40940-022-00180-2
5. Bedon C, Louter C (2018) Structural performance of glass balustrades: a review and outlook. J Build Eng. (volume and page range/article number to be added)
6. European Committee for Standardization (CEN) (2002) EN 1991–1-1. Eurocode 1: actions on structures – part 1–1: general actions – densities, self-weight and imposed loads for buildings. CEN, Brussels
7. European Committee for Standardization (CEN) (2005) EN 1991–1-4. Eurocode 1: actions on structures – part 1–4: general actions – wind actions. CEN, Brussels
8. British Standards Institution (1996) BS 6399–1:1996. Loading for buildings – part 1: code of practice for dead and imposed loads. British Standards Institution, London
9. Standards Australia, Standards New Zealand (2002) AS/NZS 1170.0:2002. Structural design actions – general principles. Building CodeHub. https://codehub.building.govt.nz/resources/1170-02002asnzs. Accessed 3 Mar 2026
10. Standards Australia (2006) AS 1288:2006. Glass in buildings. https://www.agwa.com.au/AGWA/Media/Articles/20210629-TFS-RevisionAS1288.aspx. Accessed 4 June 2023
11. Naqash MT, Formisano A (2024) Assessment of cantilevered curtain wall system supported by tension rods for an enclosed circular building. Structure 68:107133. https://doi.org/10.1016/j.istruc.2024.107133
12. Formisano A, Naqash MT (2025) Glass panels supported by spider fittings: advantages, challenges, and applications in modern masonry facades. Int J Masonry Res Innov 10(6):584–601. https://doi.org/10.1504/IJMRI.2024.10063211

13. Formisano A, Naqash MT (2024) Numerical studies on innovative prestressed aluminium alloy profiles for curtain wall systems. In: Lecture notes in civil engineering, vol 520. Springer, Cham, pp 863–871. https://doi.org/10.1007/978-3-031-62888-7_75
14. Formisano A, Naqash MT (2026) Innovative reinforced aluminium alloy curtain walls: numerical analysis and experimental validation. J Build Eng 117:114554. https://doi.org/10.1016/j.jobe.2025.114554
15. Naqash MT, Bedon C, Formisano A (2026) Structural design of balustrades: code compliance, cross-section requirements and case studies. Structure 87:111763. https://doi.org/10.1016/j.istruc.2026.111763
16. ASTM International (2012) ASTM E1300-12a. Standard practice for determining load resistance of glass in buildings, ASTM International, West Conshohocken
17. Hilti (2023) PROFIS Engineering Suite structural design software – software for fastening systems. https://www.hilti.sa/c/CLS_CUSTOMER_SOFTWARE/CLS__SOFTWARE_FASTENING_SYSTEMS/r6502279. Accessed 4 June 2023

Cold-Formed and Lightweight Structures

Determination of the Effective Properties of Composite Perforated Cold-Formed Beams

Claudio Bernuzzi, Alice Lucidi, and Marco Simoncelli(✉)

Department of Architecture, Built environment and Construction engineering, Politecnico di Milano, Piazza Leonardo da Vinci 32, 20133 Milano, Italy
marco.simoncelli@polimi.it

Abstract. The use of cold-formed steel (CFS) profiles in industrial and non-industrial buildings has significantly increased over the last decades, mainly due to their high load-carrying capacity-to-self-weight ratio. In many applications, these profiles are combined with wood-based panels to form composite flooring systems, in which the interaction between the two components can significantly influence the global behavior of the CFS joists.

A crucial aspect in this context is the evaluation of the effective properties of the composite cross-section, as the ultimate bending resistance and the flexural stiffness. These aspects are investigated in the present paper with reference to an experimental campaign carried out on nine full-scale CFS flooring specimens, characterized by different joist cross-section dimensions. In order to define the effective properties of the thin-walled profiles and to establish a reference baseline, additional tests were performed on joists without any sheathing.

The experimental results highlight the ability of the sheathing to mitigate some typical buckling phenomena associated with Class 4 elements and demonstrate that the degree of connection, and thus the level of interaction between the components, plays a key role in the system response.

Finally, theoretical formulations for the prediction of the effective bending resistance of the composite sections are proposed and validated against the experimental results.

Keywords: CFS · composite section · flooring systems · bending resistance · flexural stiffness

1 Introduction

For hot-rolled steel profiles, the benefits deriving from composite action with concrete decks are well established. In contrast, the advantages of coupling cold-formed steel profiles with top sheathing systems, such as wood-based panels, are not yet fully captured by current theoretical approaches, despite the widespread use of these systems worldwide and their significant advantages in terms of transport and installation. These benefits are mainly related to their low self-weight, dry construction process, and ease of dismantling [1, 2]. At the same time, the presence of the sheathing appears to improve beam behavior not only in terms of ultimate load-carrying capacity, but also by mitigating buckling phenomena typically associated with thin-walled profiles (Fig. 1).

© The Author(s), under exclusive license to Springer Nature Switzerland AG 2026
R. Zanon et al. (Eds.): CTA 2026, LNCE 942, pp. 269–282, 2026.
https://doi.org/10.1007/978-3-032-39505-4_24



Fig. 1. Example of a cold-formed steel-wood floor

Several studies have addressed this topic over the last decades, including both experimental and numerical investigations [3–6], highlighting a significant positive effect of flooring systems on the mechanical properties when the connection design between the two components, namely the beam and the board, is accurate. In particular, it has been shown that the influence of self-drilling screw spacing on the load-carrying capacity plays a crucial role, as it governs the applicable design approach, i.e. partial or full interaction methods, in analogy with steel–concrete composite beams [7].

The aim of the present paper is to further investigate these aspects based on the results of an experimental campaign carried out on nine full-scale CFS flooring systems with different joist cross-section dimensions. Wood-based panels were tested together with unrestrained joists in order to determine the effective properties of the bare steel members and to quantify the contribution of the panel to the global response of the system.

Finally, a theoretical formulation for the evaluation of the mechanical properties of the composite section is proposed and validated against the experimental results.

2 Experimental Campaign

2.1 Test Setup

The experimental tests were carried out using a four-point bending setup, as illustrated in Fig. 2. Each specimen was made of two C-shaped cold-formed steel joists, acting as secondary beams, with an overall length of approximately L = 5.0 m and spaced 1.0 m transversely. The joists were connected to two short transverse members, representing the primary beams, by means of four L-shaped plates. It should also be noted that the joists used in the flexural tests had a regular perforation layout along their entire length. A 40 mm diameter circular opening was located at the center of the cross-section and repeated every 200 mm along the member. In addition, four 15 mm diameter holes were positioned above and below the central opening, with a longitudinal spacing of

50 mm. Vertical loading was introduced at the quarter-span points, namely at L/4 and 3 L/4, by means of a hydraulic actuator. The actuator transferred the load to the specimens through a steel loading beam, which in turn rested on two spreader beams, as represented in Fig. 2. Each of these spreader beams had a mass of approximately 110 kg. The test was performed under displacement control, adopting a loading rate of 0.05 mm/s

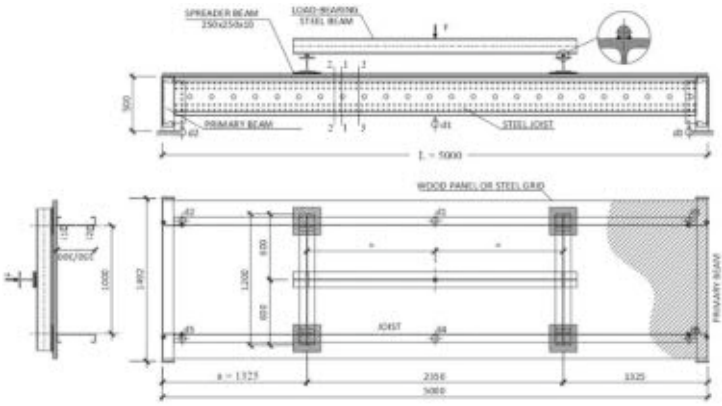


Fig. 2. Lateral view, plan view and transversal section of the test setup (measure in mm)

The flexural response of the specimens was monitored with different class 0.1 linear variable displacement transducers (identified as di, with i varying from 1 to 6). In addition, two inclinometers were used to evaluate the torsion of the cross-section at the middle span (identified as i1 and i2). A load cell of 1000 kN was used to measure the applied load. All the measuring device output have been stored with a frequency of 2 Hz. The tested specimens can be divided in the following 2 categories:

- A type. In this series the specimens presented no floor-sheathing system. To allow the application of the loads, the secondary beams were equipped with two steel plates located at L/4 and 3/4 L.
- E type. In this series the specimens were characterized by the presence of 38 mm particleboard (wood) panel (class P6, used for internal dry environments) on the top, used to connect the secondary beams. The wood panels were fixed with specific self-tapping screws spaced 1 m apart. Three nominally equal specimens have been tested for this typology.

For each category, three different joists with different height and thickness have been used. In particular, 300 mm and 350 mm of total height was considered with a thickness of 2 mm or 3 mm. More details of the specimens are depicted in Fig. 3. It can be noted the details of the load transfer plate used in case of no sheathing (A specimens) which is bolted directly on the web of the joists.

Prior to the experimental campaign, tensile coupon tests were performed on dog-bone specimens obtained from the virgin steel coils used for the production of joists and connection elements. Overall, 15 coupons were tested, with five specimens taken

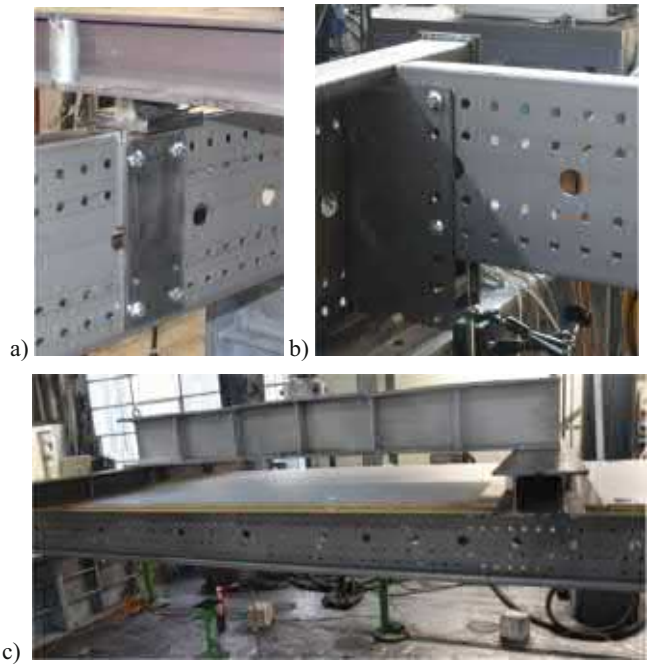


Fig. 3. Details of the specimens: a) load transfer plate for A series; b) connection between primary and secondary beams; c) wood panel sheathing detail

from each coil thickness. All components were made of S420GD steel grade, although the measured mechanical properties varied according to the thickness of the original coil. For the 3.0 mm thick coil, the average yield strength was equal to 470 MPa, with values ranging between 458 MPa and 484 MPa. The 2.0 mm thick coil exhibited a mean yield strength of 437 MPa, with a minimum value of 430 MPa and a maximum value of 447 MPa. In the case of the 4.0 mm thick coil, which was used for the connection plates, the average yield strength was 420 MPa, while the measured values varied from 405 MPa to 430 MPa. The Young's modulus obtained from the tensile coupon tests, Es, ranged from 179 GPa to 230 GPa, with an average value of 198.8 GPa. Regarding the timber panels, their mechanical properties were derived from the manufacturer's product datasheet. In particular, the bending modulus of elasticity along the strong direction was $E_w = 4000$ MPa, while the mean bending strength was equal to $f_w = 11.5$ MPa.

2.2 Evaluation of the Effective Properties of Joists

As previously discussed for Class 4 elements, and thus for cold-formed profiles, the attainment of plastic or fully elastic capacity is prevented by their susceptibility to buckling phenomena. For this reason, the evaluation of their ultimate capacity is based on the effective properties of the cross-section, which can be derived using two alternative approaches: the Direct Strength Method (DSM) or the Effective Width Method (EWM) [8]. In this study, the EWM is adopted, with specific refinements required to account

for the presence of perforations along the members. Indeed, such discontinuities are not explicitly considered in the design procedures currently prescribed by the European standard EN 1993 [9, 10]. Therefore, the provisions and recommendations of the AISI S100 specification [11] are followed.

Referring to Fig. 2, three main cross-sections can be identified: i) sect. 1–1 with a central hole of 40 mm diameter and ii) sect. 2–2 with 4 small holes; iii) sect. 3–3 with no holes. According to the procedure described in the AISI specification, the presence of a hole at the center of the web leads to treating the web as composed of two external elements (as if they were two separate flanges) rather than a single internal element, resulting in a significantly reduced effective area.

The main mechanical properties are summarized in Table 1. Specifically, the gross second moment of area about the strong, $I_{y,g}$, and the weak axis, $I_{z,g}$, and the gross cross-sectional area, A_g, are reported alongside the minimum net (perforated) area, A_f. The design bending resistance moment about the strong axis, $M_{y,Rd,eff}$, is evaluated as the product of the section modulus and the mean value of the yield strength of the corresponding coil.

Table 1. Principal properties of the joists

	350x3	300x2	300x3
A_g [mm2]	$16.80 \bullet 10^2$	$10.30 \bullet 10^2$	$15.40 \bullet 10^2$
A_f [mm2]	$15.04 \bullet 10^2$	$9.10 \bullet 10^2$	$13.54 \bullet 10^2$
$I_{y,g}$ [mm4]	$28.32 \bullet 10^6$	$13.20 \bullet 10^6$	$19.52 \bullet 10^6$
$I_{z,g}$ [mm4]	$1.28 \bullet 10^6$	$0.85 \bullet 10^6$	$1.24 \bullet 10^6$

3 Experimental Campaign

The maximum loads and the related maximum bending moments, recorded during the tests, are reported in Table 2. It can be noted that the addition of the wood panels always results in a positive effect for the ultimate capacity of the specimen, since an increase in F_{man} of approximately 20–30% compared to the case without the sheathing is observable for all the tested samples.

Table 2. Maximum forces and ratios

Profile	ID	Fmax	Mmax	ratio over config. A
		kN	kNm	
350x3	A1	95.44	30.30	–
	E11	125.57	39.87	1.32
	E12	125.56	39.87	1.32

(*continued*)

Table 2. (*continued*)

Profile	ID	Fmax	Mmax	ratio over config. A
		kN	kNm	
	E13	125.68	39.90	1.32
300x2	A2	48.46	15.39	–
	E21	62.59	19.87	1.29
	E22	60.97	19.36	1.26
	E23	61.29	19.46	1.26
300x3	A3	90.22	28.64	–
	E31	107.29	34.06	1.19
	E32	108.91	34.58	1.21
	E33	109.03	34.62	1.21

The collapse of series A specimens, as shown in Fig. 4a, corresponded to a significant lateral-torsional buckling deformation and, in case of specimen A2, also to a local buckling of the com-pressed flange. On the other hand, the collapse of series E specimens was caused by the shear failure of the wood self-tapping screws, as illustrated in Fig. 4b, while no significative damage occurred in the wood panels.


a)


b)

Fig 4. a) typical collapse in the A series; b) screws shear failure in E series

Finally, in Fig. 5 the typical deformation of a series E specimen is shown; after the failure of the screws, the coupling effect between the two materials is completely lost and the torsion is not restrained.



Fig. 5. Typical deformation for a specimen of E series, after the ultimate load is reached

4 Composite Section Properties

The ultimate bending capacity of a composite section is usually derived assuming a plastic stress distribution in the two materials. Although, when dealing with a class 4 profile this approach may not seem appropriate due to their susceptibility to local and distortional buckling phenomena. For this reason, in the following two alternative methods are proposed: one for plastic and one for elastic distributions.

Plastic Stress Distribution

According to plastic method the ultimate bending capacity is strictly related to the maximum shear force that can be transferred at the interface between the steel joist and the wood panel by the self-drilling screws. This shear action defines the degree of interaction for the composite section, which is expressed through index η, which ranges from 0 (no interaction) to 1.0 (full interaction), and it is computed as:

$$\eta = \frac{n_r}{n_f} = \frac{N_c}{N_{c,f}}\eta = \frac{\mathrm{n_r}}{\mathrm{n_f}} = \eta = \frac{\mathrm{n_r}}{\mathrm{n_f}} = \frac{\mathrm{N_c}}{\mathrm{N_{c,f}}} \tag{1}$$

In other terms, the degree of interaction is equal to the number of screws present on the beam, n_r, over the needed screws, n_f, to transfer the whole shear force $N_{c,f}$. The maximum shear load transmitted from the timber panel to the beam through the self-drilling screws is indicated as N_c. This value is defined as the lower value between the shear resistance of the screws and the bearing resistance of the weakest component involved, namely either the timber board or the steel plate. For the specimens considered in the tests, Nc was always controlled by shear failure of the screws. The corresponding resistance was equal to 8.53 kN per screw. The term $N_{c,f}$ identifies the compressive force developed in the timber board and transferable through the steel–timber interface.

The position of the neutral axis position can be obtained by imposing force equilibrium [3], as schematically represented in Fig. 6.

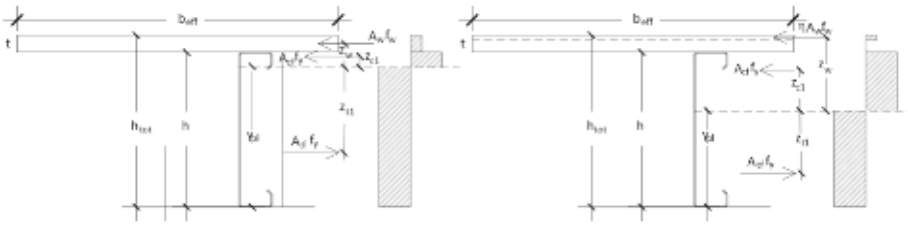


Fig. 6. Definition of the composite action: a) full interaction; b) partial interaction

With reference to Fig. 6 the composite bending moment can be computed according to the following formula, derived from the equilibrium equation:

$$M_{Rd,c} = A_{tf} f_y z_{t1} + A_{cf} f_y z_{c1} + \eta A_w f_w z_w 0.0 \leq \eta \leq 1.0 \tag{2}$$

For a cross-section which belongs to class 4, like the ones herein considered, the local and distortional buckling must be also properly considered in the definition of the equilibrium forces. As shown in Fig. 7, when full composite interaction is attained (d), the steel profile may be subjected either to tensile stresses over the entire cross-section or to a stress state in which compression is limited to the upper flange. In the latter case, distortional buckling may be reasonably disregarded owing to the continuous distribution of mechanical fasteners along the member length. Conversely, local buckling in the flange, if governing, must be explicitly considered in the resistance evaluation. As the degree of interaction decreases, the neutral axis progressively shifts downwards from the flange region towards the web of the cross-section (c). This variation is required to satisfy internal force equilibrium, due to the lower compressive force transferred by the timber panel. In this configuration, the compressed flange may become increasingly prone to local buckling, and also to distortional buckling when intermediate stiffeners are present, particularly at low levels of composite interaction. Moreover, a reduction in the degree of interaction is generally associated with an increase in the longitudinal spacing of the mechanical fasteners. As a consequence, below a given interaction threshold, the contribution of distortional buckling of the flange can no longer be neglected. The evaluation of the internal force equilibrium between the compressive and tensile resultants therefore requires an iterative procedure, in which the reduction of the cross-sectional resistance due to local and distortional buckling in the compressed regions is properly accounted for. The onset of flange distortional buckling significantly modifies the shape of the interaction domain, producing a marked variation in its slope (b). For negligible levels of composite interaction, the load-bearing capacity of the system tends to that of the cold-formed steel profile alone (a), evaluated on the basis of its effective cross-sectional properties.

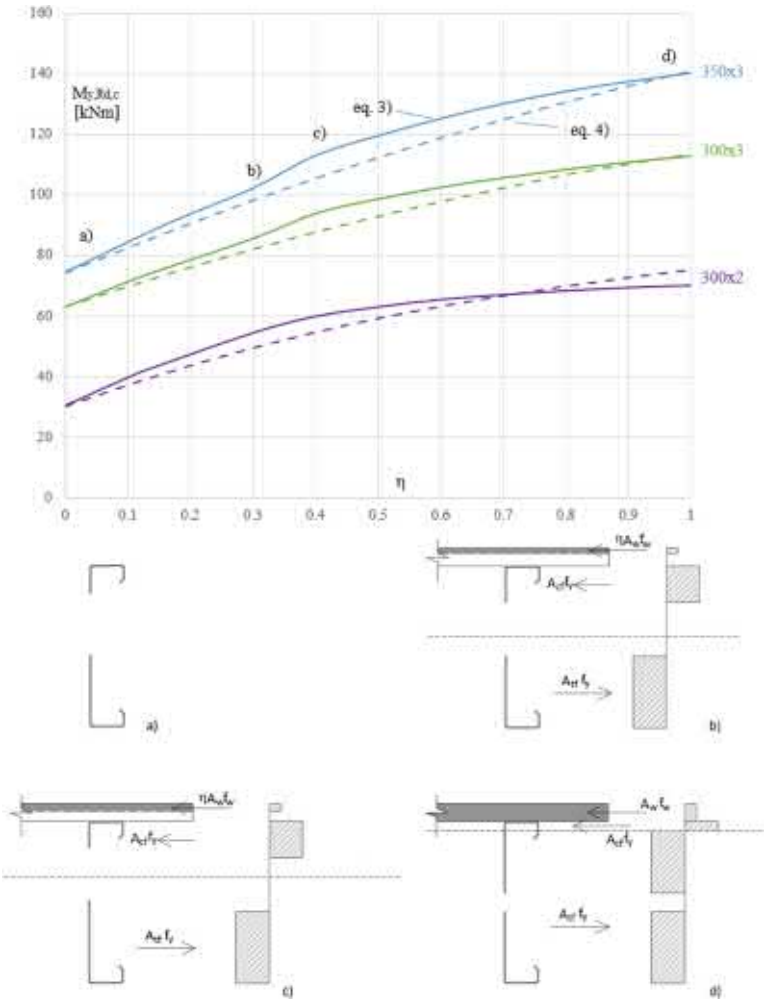


Fig. 7. Resistance domain for a class 4 cross-section, plastic distribution

The procedure discussed may appear quite complex, as it requires a great number of iterations, therefore an alternative simplified equation, presented in [3] can be used:

$$M_{y,Rd,c} = M_{y,Rd,pl} + (1-\eta)\left(M_{y,pl,bare} + M_{y,Rd,eff}\right) 0.0 \leq \eta \leq 1.0 \tag{3}$$

where $M_{Rd,\,c}$ is the resistance of the composite section considering the effective properties of the beam, $M_{Rd,\,pl}$ and $M_{pl,\,bare}$ are the plastic resistance of the composite section and the plastic resistance of the bare steel section respectively, both evaluated without considering the instability phenomena. In Fig. 7, the resistance domains, defined as the relationship between the bending resistance moment and the degree of interaction, are presented according to both the exact procedure and the simplified equation (Eq. 4). It can be observed that the most significant differences between the two curves occur in

the central region of the domain, starting from $\eta = 0.3$, where distortional buckling of the compressed flange is assumed to be no longer governing. At the same time, it is evident that the simplified equation is generally more conservative, i.e. on the safe side, with the exception of profiles in which local buckling is the governing failure mode, as in the case of the 300 × 2 specimens.

For the considered cases the neutral axis is never located inside the wood panel, hence the maximum value of $N_{c,f}$ is exactly the compressive force on the wood panel itself $A_w f_w = 327$ kN. Therefore, it is possible to evaluate the degree of interaction for the specimens considered:

$$\eta_E = \frac{5 \bullet 8.53}{327} = 0.130 \tag{4}$$

Elastic Stress Distribution

Under the assumption of an elastic stress distribution, the position of the neutral axis is obtained, for the full interaction scenario, by imposing the same deformations for the two materials at their interface, while, in case of no interaction, the neutral axis is the one derived for the steel beam. As already mentioned for the plastic method, the susceptibility to local and distortional buckling phenomena of the steel beam must be taken into account in the calculations by iteratively penalizing the steel plates. In Fig. 8 the simplified linear elastic domains for the investigated configurations are shown alongside an illustration of the stress distribution for the two extreme conditions ($\eta = 0$ and $\eta = 1$)

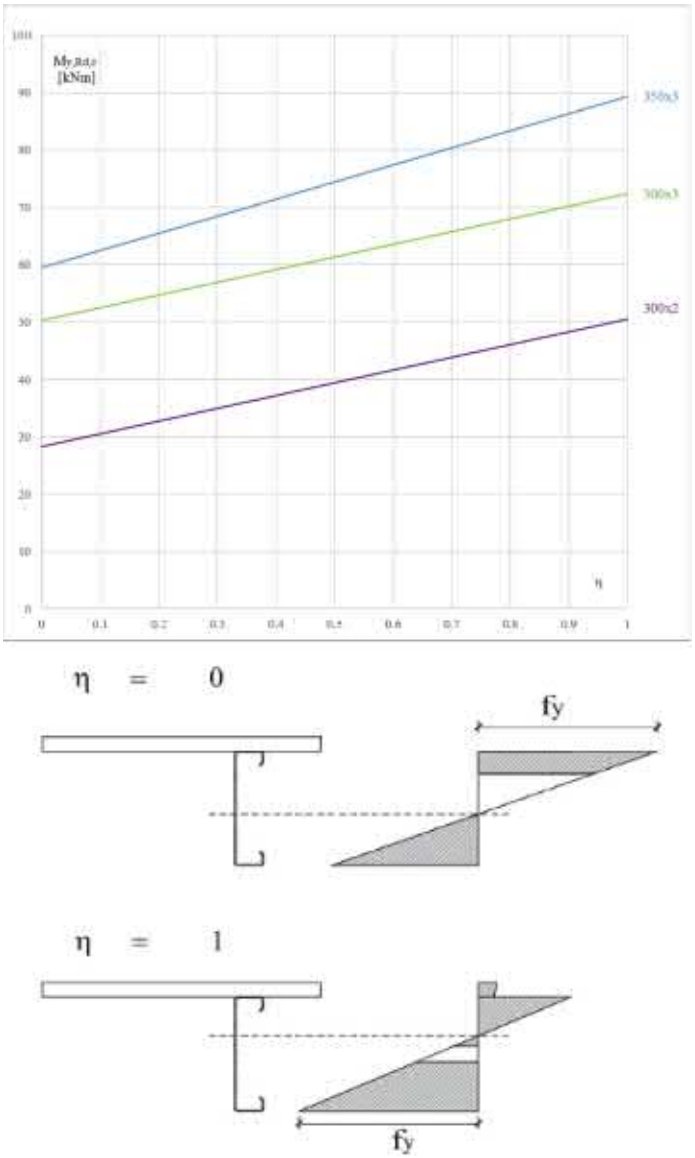


Fig. 8. Resistance domains for a class 4 cross-section according to elastic stress distribution

5 Comparison with Experimental Results

For the validation of the proposed procedure the numerical results must be compared with the experimental ones. At this point it is important to highlight that the ultimate bending moment reached during the tests is not the characteristic ultimate bending capacity of

the composite section but a reduced value that takes into account the lateral-torsional buckling susceptibility of the joists.

Plastic Stress Distribution
When a plastic distribution is assumed, the interaction level and the corresponding ultimate bending capacity of the composite section are directly derivable. It has to be noted that even though the sheathing provides a restraint for the compressed steel flange, in this phase of the analysis this effect is neglected, and the buckling reduction factor is evaluated by considering the critical moment M_{cr} resulting for A specimens and computed through LTBeam software. In the software the beam was modeled as a simply supported beam subjected to 2-point loads, presenting: free warping along all its length, restrained torsion and lateral displacement at both its ends. In particular, the susceptibility of the beam to the global lateral-buckling directly depends on its slenderness $\bar{\lambda}_{LT}$, expressed as:

$$\bar{\lambda}_{LT} = \sqrt{\frac{M_{y,Rd,\text{eff}}}{M_{cr}}} \tag{5}$$

The slenderness is connected to the reduction factor via the equations:

$$\phi_{LT} = 0.5\left[1 + \alpha_{LT}\left(\bar{\lambda}_{LT} - 0.2\right) + \bar{\lambda}_{LT}^{2}\right]\chi_{LT} = \frac{1}{\phi_{LT} + \sqrt{\phi_{LT}^{2} - \bar{\lambda}_{LT}^{2}}} \tag{6a, b}$$

In Table 3 the comparison between the experimental outcomes and the analytical ones obtained through the plastic method is presented.

Table 3. Numerical vs. experimental results

Profile	ID	M_{cr}	$M_{y,Rd,b}$	M_{exp}	%
		kNm	kNm	kNm	
350x3	A1	38.11	27.65	29.23	−5.40%
	E1_m	38.11	36.67	38.47	−4.66%
300x2	A2	21.27	14.37	14.84	−3.16%
	E2_m	21.27	20.98	18.87	11.17%
300x3	A3	32.24	23.31	27.63	−15.63%
	E3_m	32.24	31.18	33.20	−6.10%

Elastic Stress Distribution Different is the case of partial interaction when assuming an elastic distribution, since the interaction level is no more directly correlated to the shear force transferred to the panel but depends on the slip deformation recorded at the two-material interface. Assuming the same lateral-torsional buckling reduction factor mentioned above, for the condition $\eta = 0$, and a reduction factor equal to 1 for the case $\eta = 1$, the corresponding level of interaction for the beam is determined graphically, as shown in Fig. 9, and it ranges from 0.13 to 0.24.

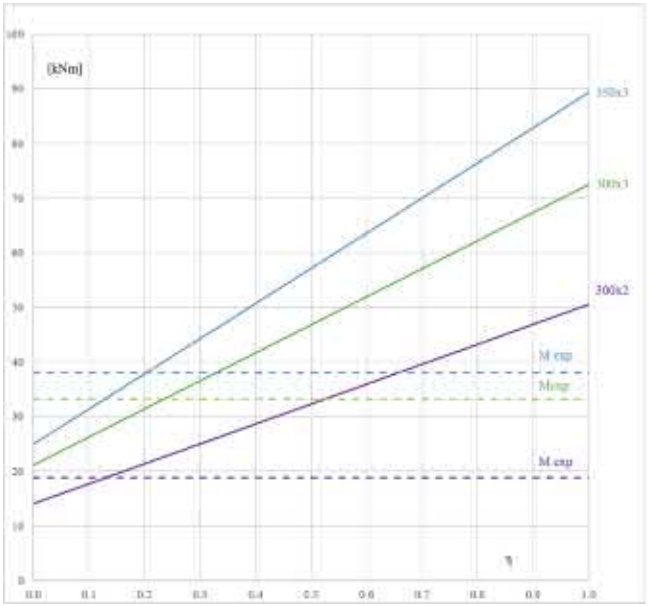


Fig. 9. Determination of the interaction level when applying the elastic method

6 Conclusion

The present study introduces two possible procedures for the evaluation of the effective properties of a composite perforated cold-formed beam, one assuming a plastic stress distribution on the beam cross section and the other assuming an elastic distribution. In the plastic procedure the main aspect highlighted by the analysis is the influence of the degree of connection between the sheathing and the joist in preventing distortional buckling phenomena of the cold-formed profile. Indeed, it was found that reducing the screw spacing down to a certain value allows the distortional buckling of the flange to be neglected. With reference to the tested specimens, this limit value of screw spacing corresponds to an interaction level equal to 0.3.

The direct effect of this behavior is also clearly observable in the correspondent plastic resistance domain of the composite section, where a change in the slope of the interaction curve is recorded when $\eta = 0.3$. By comparing this procedure with the one proposed in [3], which is much more expedient, it was observed that the latter is generally more conservative, except for profiles for which flange local buckling occurs at any level of interaction.

When comparing the experimental results with the analytical ones derived from the plastic procedure a good approximation of the real behavior of the specimens through the theoretical formulation is observed, with errors in the range of 3–12%.

On the other hand, when the elastic distribution is adopted, the ultimate bending capacity obtained for the full interaction condition is almost half of the value resulting

from the plastic procedure and to match the experimental data generally a higher interaction level is needed. At this point further investigations into the partial interaction for the elastic scenario and more precise evaluation of the sheathing effect on lateral-torsional buckling restraint are required.

References

1. Navaratnam S et al (2021) Development of cross laminated timber-cold-formed steel composite beam for floor system to sustainable modular building construction. Structure 32:681–690
2. Kitayama S, Iuorio O (2023) Disassembly and reuse of structural members in steel-framed buildings: state-of-the-art review of connection systems and future research trends. J Archit Eng 29(4):03123006
3. Kyvelou P, Gardner L, Nethercot DA (2017) Design of Composite Cold-Formed Steel Flooring Systems. Structure 12:242–252
4. Kyvelou P, Gardner L, Nethercot DA (2015) Design of Composite Action between cold-formed steel beams and wood-based floorboards. Int J Struct Stab Dyn 15(08):1540029
5. Vella N, Kyvelou P, Buhagiar S et al (2024) Experimental study of composite cold-formed steel and timber flooring systems with innovative shear connectors. Thin-Walled Struct 205:112460
6. Kyvelou P, Gardner L, Nethercot DA (2018) Finite element modelling of composite cold-formed steel flooring systems. Eng Struct 158:28–42
7. Bernuzzi C, Pisani MA, Simoncelli M (2023) Debonding strain for steel-concrete composite slabs with trapezoidal deck. Steel Compos Struct 49(1):19–30
8. Baldassino N, Bernuzzi C, Simoncelli M (2019) Evaluation of European approaches applied to TWCF steel members. Thin-Walled Struct 143:106186
9. European Committee for Standardization (CEN) (2005) EN 1993-1-3. Eurocode 3: design of steel structures – part 1-3: general rules – supplementary rules for cold-formed members and sheeting. CEN, Brussels
10. European Committee for Standardization (CEN) (2006) EN 1993-1-5. Eurocode 3: design of steel structures – part 1-5: plated structural elements. CEN, Brussels
11. American Iron and Steel Institute (AISI) (2020) North American specification for the design of cold-formed steel structural members, AISI S100-16. AISI, Washington, DC

Torsional Response of Cold-Formed Members Under Shear and Axial Forces: Experimental Evidence

Nadia Baldassino[1], Claudio Bernuzzi[2], Marco Simoncelli[2(✉)], Stefano Girardi[1], and Davide Melis[2]

[1] Università di Trento, Department of Civil, Environmental and Mechanical Engineering, Trento, Italy

[2] Politecnico di Milano, Department of Architecture Built environment and Construction engineering, Milan, Italy

marco.simoncelli@polimi.it

Abstract. It is well-known that torsional effects play a crucial role in the structural response of cold-formed steel members when subjected to eccentric transverse loads. However, torsion is often neglected in design practice when members are loaded axially, especially. This paper presents an experimental investigation on the torsional response of cold-formed members subjected separately to shear forces and to concentrated axial forces. An experimental campaign was carried out on full-scale specimens using dedicated test setups that allowed the isolated application of each loading condition. Displacements and internal stresses were monitored throughout the tests. To investigate the experimental outcomes and further exploit the topic, finite element models were also developed. As expected, the tests under shear loading confirmed the significant and detrimental influence of torsion on the global response. More importantly, the experimental results revealed that pronounced torsional deformations can also develop under eccentric axial loading, highlighting critical behavior that is commonly overlooked. The observed torsional response under axial forces was found to be strongly dependent on load eccentricity and cross-sectional geometry. The experimental evidence demonstrates that torsion represents a detrimental mechanism not only under shear forces but also under eccentric axial loading, emphasizing the need for its explicit consideration in the analysis and design of cold-formed steel members.

Keywords: CFS sections · Primary torsion · Secondary torsion · Loading conditions · Shear loading · Axial loading

1 The Vlasov Theory

The theoretical framework developed by Vlasov has its origins in the work first published in 1936, later refined and presented in a revised form in 1959. Following its translation into several languages, the theory became widely available to the international research community [1]. Compared with the classical de Saint Venant formulation, Vlasov's approach provides a more general tool for describing the mechanical response of members

© The Author(s), under exclusive license to Springer Nature Switzerland AG 2026
R. Zanon et al. (Eds.): CTA 2026, LNCE 942, pp. 283–295, 2026.
https://doi.org/10.1007/978-3-032-39505-4_25

with complex or unconventional cross-sectional geometries. Although it is most commonly applied to thin-walled structural elements, its field of application is not limited to these members; the formulation may also be employed for conventional profiles, independently of the material adopted and of the degree of cross-section symmetry [2–4]. A distinctive feature of this theory is the introduction of an additional self-equilibrated internal action, commonly referred to as the bimoment. Since the publication of the 1959 formulation, Vlasov's theory has found broad use in a wide range of engineering applications [5]. In order to provide the necessary background for the following discussion, the main concepts of Vlasov's thin-walled beam formulation are briefly recalled in this section.

In the analysis of thin-walled members, the cross-sectional geometry is commonly described through the sectorial coordinate ω(s). This quantity is associated with the area generated by a radius vector ρ as it progresses along the midline of the section, starting from the reference point s = 0 and reaching the location considered. More specifically, ω(s) is defined as twice the area enclosed during this motion, as illustrated by the shaded region in Fig. 1. According to the adopted sign convention, the sectorial area is taken as positive when the radius vector rotates clockwise

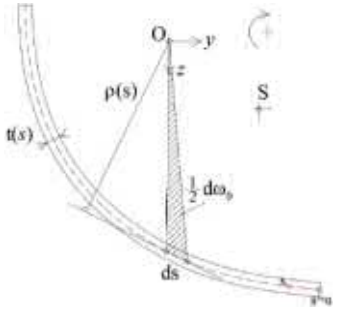


Fig. 1. Definition of sectorial area

When evaluating ω(s) with respect to the cross-section centroid (O), it can be defined as $\omega_0(s)$:

$$\omega_0 = \int_0^s \mathrm{d}\omega_0(s) = \int_0^s \rho(s)\, ds \tag{1}$$

For design and analytical purposes, it is convenient to introduce the normalized sectorial area, $\omega_s(y, z)$, defined with respect to the shear centre of the cross-section. This geometrical quantity is obtained by applying the following relationship:

$$\omega_s(y, z) = \omega_0(y, z) + z_s(y - y_0) - y_s(z - z_0) - \omega_{mean} \tag{2}$$

within this framework, the locations of the cross-sectional centroid O and shear centre S are specified by the coordinate pairs (y_0, z_0) and (y_s, z_s), respectively. The quantity ω_{mean} is introduced as a constant term corresponding to the average value of ω_0 evaluated over its effective distribution along the whole cross-section. On this basis, the longitudinal

normal strain induced by warping is directly governed by the spatial distribution of the normalized sectorial area:

$$\varepsilon_{x,\omega} = \omega_s \frac{d^2\varphi_{(x)}}{dx^2} \tag{3}$$

The response of a thin-walled member subjected to a torsional force must be evaluated by using the complete elastic torsional theory, which considers the contribution of primary (T_t) and secondary (T_w) torsion:

$$T = T_t + T_w = GI_t \frac{d\varphi_{(x)}}{dx} - EI_w \frac{d^3\varphi_{(x)}}{dx^3} \tag{4}$$

where the tangential modulus (G) is multiplied by the Saint Venant Inertia (I_t) and the Young modulus (E) is related to I_w, which is the second moment of area of the sectorial area (or warping constant) defined as:

$$I_w = \int \omega_s^2 \, dA \tag{5}$$

where *A* is the gross cross-section area. A key feature of Vlasov's theory is represented by the presence of an additional generalised internal force that is the bimoment, *B(x)*, obtained as:

$$B(x) = \int_0^x T_w ds = -E\, I_w \frac{d^2\varphi(x)}{dx^2} \tag{6}$$

which is directly related to the normal stresses on the cross-section:

$$\sigma_w(x, y, z) = \frac{B(x)}{I_w} \omega_s(y, z) \tag{7}$$

Two very important theorems can be extrapolated from the Vlasov theory.

The first theorem investigates the correlation between an external applied force and the bimoment. The axial force, *P,* applied at a point *k* (y_k, z_k), Fig. 2a, can be expressed in terms of resulting axial force (*N*), bending moments (M_y and M_z) and bimoment (B):

$$\begin{cases} N = P \\ M_y = Pz_k \\ M_z = -Py_k \\ B = P\omega_s(y_k, z_k) \end{cases} \tag{8a–d}$$

The second theorem, investigates the dependence between bending moments and bimoment. The action of the moment M at point k can be reformulated by considering an equivalent system of two longitudinal ideal forces. When these forces, each denoted by P, act with a lever arm Δs, they generate the same bending effect in the tangential plane of the cross-section, as represented in Fig. 2b. Therefore:

$$M = P\Delta s \tag{9}$$

Starting from Eq. (8d), it is in fact possible to evaluate B as:

$$B = -P\omega_{s,k} + P\left(\omega_{s,k} + \Delta\omega_{s,k}\right) = P\Delta\omega_{s,k} \tag{10a}$$

$$B = P\Delta\omega_{s,k} = M\left(\frac{\Delta\omega_{s,k}}{\Delta s}\right)_{\Delta s \to 0} = M\left(\frac{d\omega_s}{ds}\right) \tag{10b}$$

The bimoment is hence proportional to the value of the first derivate of the sectorial coordinate with respect to the abscissa s and to the applied bending moment.

These two theorems are very often neglected, especially from the finite element software standpoint, despite their importance have been deeply discussed in literature [6].

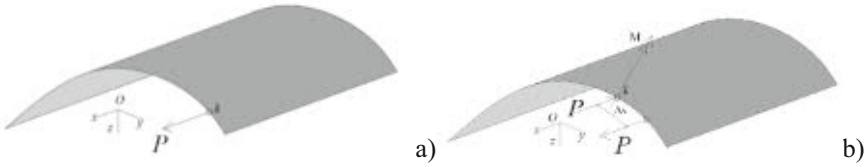


Fig. 2. Member end loaded by: a) axial force P; b) moment on the plane of the membrane

2 The Experimental Study

2.1 Considered Specimens

The study investigated the response of two different mono-symmetric cross-sections (Fig. 3): a channel with rear flanges conventionally named RFC (Fig. 3a) and a lipped channel, named LC (Fig. 3b). The thickness of both profiles was 3.0 mm.



a) RFC cross-section profile b) LC cross-section profile

Fig. 3. Geometry of the profiles investigated

The main geometrical data of these cross-sections are reported in Table 1, which presents the values of the area (A), along with the torsion and warping constants (I_t and I_w, respectively). Furthermore, the eccentricity between the cross-section centroid and

the shear centre (y_s and z_s), together with the torsional slenderness (λ_T), are reported, too. The specimens were manufactured from the same coil. Tensile tests were performed in accordance with EN ISO 6892-1 [7], on three different samples. The mean value of the yield strength (f_y) and ultimate strength (f_u) were 295.4 MPa and 376.4 MPa, respectively. Finally, the mean value of Young's modulus (E) was equal to 177.1 GPa; it should be remarked that this value is quite far from the standard value of E = 210GPa prescribed by the European design standards, i.e. EC3 [8], but however, in accordance with the research outcomes already presented in [9, 10].

Table 1. Geometrical properties of the profiles

Geometrical property	RFC profile	LC profile
A [mm^2]	814	629
I_t [mm^4]	2441	1886
I_w [mm^6]	$1.16 \cdot 10^9$	$3.12 \cdot 10^8$
y_s [mm]	34.77	24.58
λ_T	0.00091	0.00151

2.2 Testing Set-up and Load History

Tests were carried out on 1.2 m long specimens, which were restrained with hydraulic jaws to a column of a counter-frame at one end to recreate cantilevered conditions (Fig. 4). During the tests, stress distribution was monitored by strain-gauges. Two cross-sections were considered along the length of each profile, named A and B in Fig. 4. The positions of the cross-sections were selected in order to capture the deformation of the profiles in areas far from the ends, thereby ensuring that the sections were not affected by local effects associated with the fixed restraint or the applied load. Each section was equipped with ten Micro-Measurements (model CEA-06-250UW-120) self-temperature-compensated strain gauges, with a length of 6.35 mm.

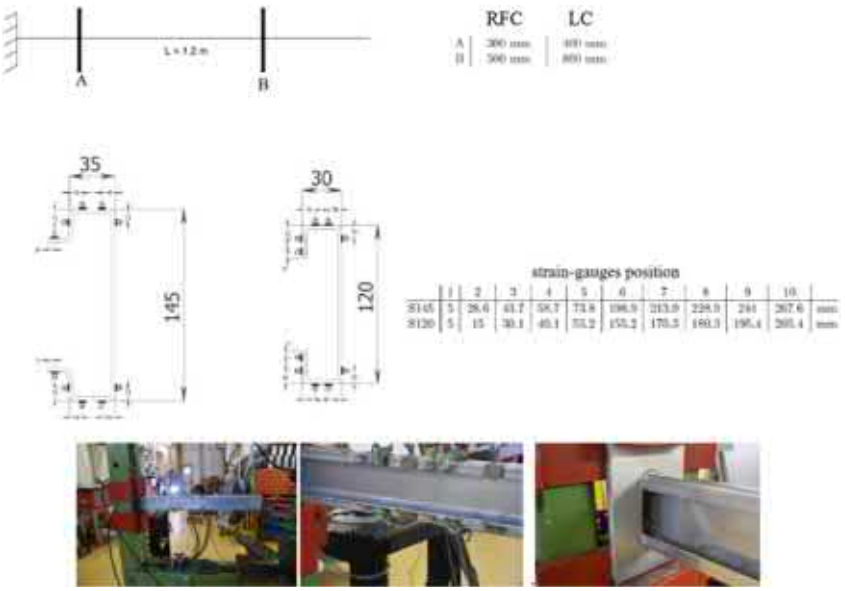


Fig. 4. Boundary conditions and deformation measurement system

The load was applied to the free end of the specimens. Two loading conditions were considered:

- Vertical shear force applied to the cross-section centroid. This loading condition was investigated for both profiles, with one test performed for each;
- Axial force applied in an eccentric position. This configuration was adopted for the RFC profile only, under an eccentric loading condition.

Therefore, a total of three tests were performed—two on the RFC profile and one on the LC profile—as specified below:

- Test S-RFC: Test on the RFC profile loaded by a shear action applied at the free end;
- Test S-LC: Test on the LC profile loaded by a shear action applied at the free end;
- Test N-RFC: Test on the RFC profile loaded by an axial force applied to the bottom rear flange.

In the S-tests, the shear force was applied via a dead-mass loading system. To this end, the free end of the specimens was equipped with a mass suspension system bolted to the profile's web (Fig. 5). The mass was applied by means of thick steel plates, each with a mass of approximately 25 kg. The total mass was increased in five steps from 0 to 250 kg, in increments of approximately 50 kg.



a) Section RFC b) Section LC

Fig. 5. Dead weight loading system for shear tests

In tests N-RFC, the load was applied via a MOOG hydraulic actuator, whose piston rod was equipped with an adapter to allow for the application of a concentrated force (Fig. 6). In both tests, the load was applied in two steps. In the first step, the load was increased from 0 to 15 kN, followed by a 40-s pause. The load was then increased up to 30 kN, followed by a 50-s pause. Finally, the load was removed completely back to zero. The actuator was coupled to a load cell with a maximum capacity of 600 kN (Class 05).

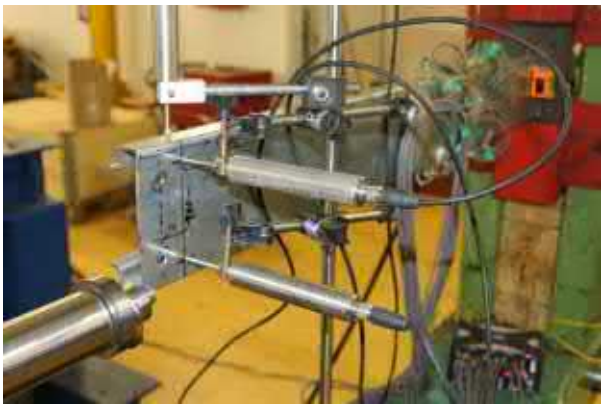


Fig. 6. Axial force loading condition

Finally, tests have been simulated by means a simple numerical finite element (FE) model using the commercial software Abaqus [11]. The cantilever beams were reproduced by means of the use of quadrangular shell elements, having dimensions 1 by 1 mm. Linear elastic analyses were performed and stress distribution along the beam was extracted. Figure 7 depicted the two models.

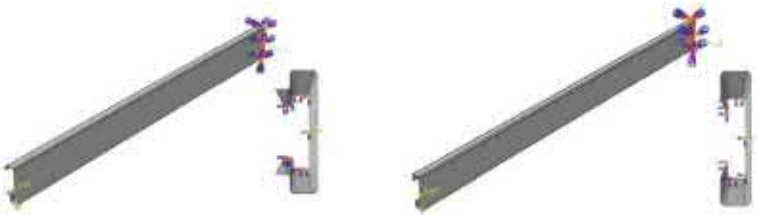


Fig. 7. Numerical 3D shell model for the two cantilever beams

3 Response to Transversal Force

Bimoment action generated by eccentric shear forces has been studied, comparing the results from the Vlasov theory, with experimental results. For a cantilever beam having length L with a torsional moment applied on the free edge, the bimoment distribution along the length by using Eq. 4 is equal to:

$$B = -\frac{F\ e}{\lambda_T} \frac{\sin[\lambda_T (L - x)]}{\cos(\lambda_T L)} \tag{11}$$

where F is the applied load and e is the load eccentricity from the cross-section shear center. As previously discussed, the load was applied on the web, in correspondence of the symmetry axis by means of a suitable steel plate; the load intensity has increased during the test, step by step, from 50 kg to 250 kg. Each load increase was maintained at least 200 s. As the load increased, strains were continuously monitored. Both the beams considered remained elastic for the whole loading process, i.e. once the loads were removed, the deformations ε return to zero. In Fig. 8 the typical output, in terms of strain distribution along the A section has been reported. It can be noted that the strains are plotted against the time, t, and the steps identify exactly the load increasing. After about 1400 s the load was removed completely and the strains returned exactly to zero, as previously discussed.

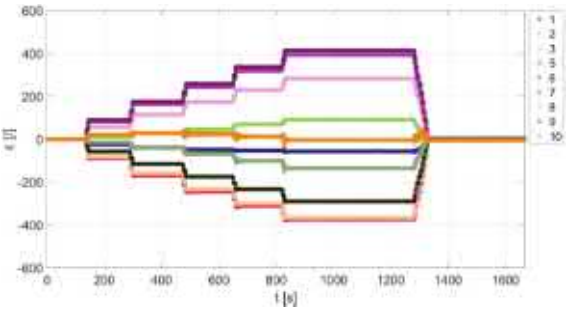


Fig. 8. Strain gauge output for S-LC section A

Finally in Fig. 9, for the RFC cross-section, the total normal stresses evaluated from the experimental results (dotted points) are compared with the numerical (solid line) and the theoretical ones (dashed lines). It can be noted that there is a perfect superimposition between the numerical and the theoretical results, while the experimental points show a little difference. To appreciate these differences also the relative numerical-experimental error is reported the figure. Considering all the cases, differences were generally below 20%. Notably, the largest errors were found for very low stress values

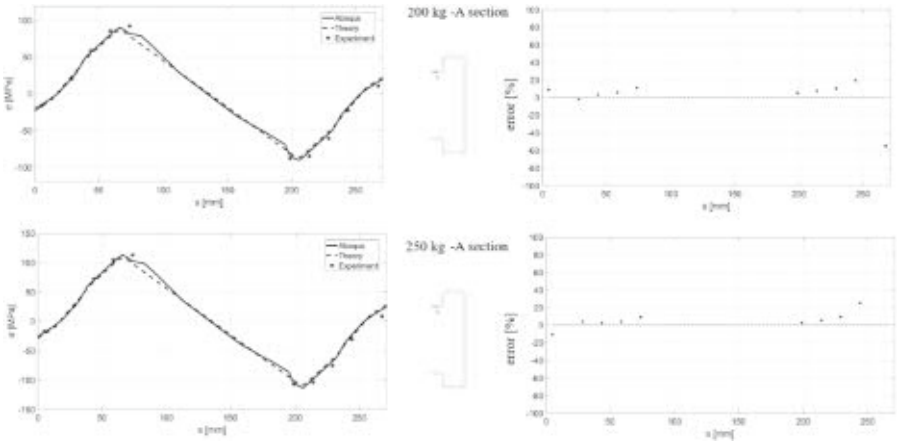


Fig. 9. Comparison between numerical, theoretical and experimental results section-A

By using the least squares method [12], it is possible to isolate the contribution of each internal force starting from the total normal stress graph. This operation can be used to appreciate the bimoment influence on the beam torsional response, In Fig. 10 the ratio between each contribution and the bimoment in terms of normal stresses, is reported against the beam length.

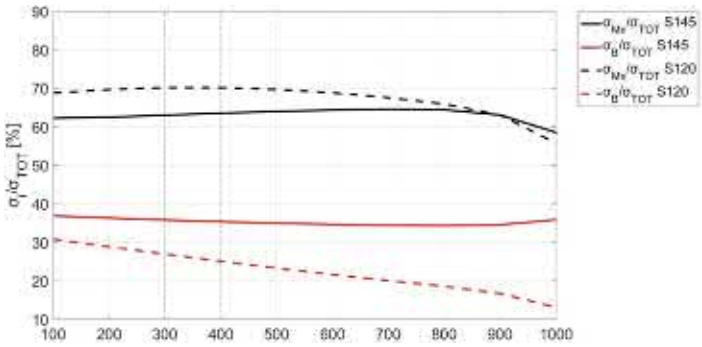


Fig. 10. Percentage of each stress component along the length of the cantilever beams

For both beams, the percentage of total stress due to the bimoment response only lays between the 30% and the 40%, showing that, when dealing with the problem of mono-symmetric beams under torsion, it cannot never be neglected its contribution.

4 Response to Axial Force

To demonstrate the Vlasov theorems, Bimoment action from a punctual axial load is considered in this section. As shown in Fig. 6, the hydraulic jack gives an eccentric punctual force on the cross-section, generating axial force, bending moments and bimoment, but creating also a local restraint to the torsion. In Fig. 11 an example of the typical output for two different cross-section and load value is depicted, by comparing the numerical result (continuous line) with the experimental ones (points).

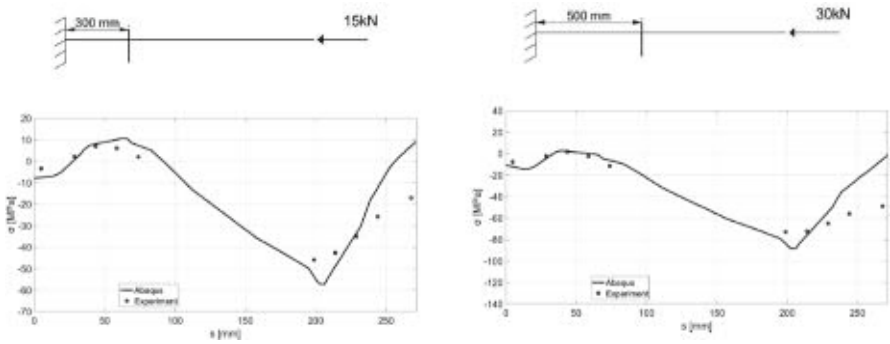


Fig. 11. Numerical vs. experimental stresses for two different load conditions

It should be noted that the numerical model overestimates the real stresses, especially close to the loaded point two to the presence of the load jack itself which creates a local support, that is not easy to calibrate numerically. The maximum difference is about 50%.

As previously discussed, by using the least squares method, it is possible to isolate the contribution of each internal force starting from the total normal stress values. As depicted in Fig. 12 the value of the bimoment is comparable to that of the other internal forces.

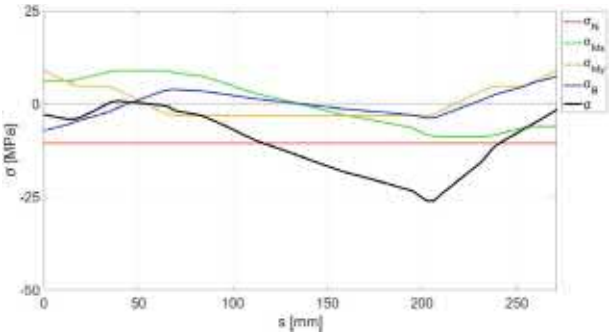


Fig. 12. Derivation of internal forces from 10kN load, section A case

Finally, the importance of the bimoment can be highlighted by considering the dimensionless quantities in Fig. 13. As can be noticed, the contribution of the bimoment reaches 40% of the total stress in many points. For this reason, neglecting its contribution when dealing with thin-walled open sections would lead to significant inaccuracies, especially for sections with a relatively small warping constant Iω or non-zero sectorial area across all points. Moreover, even though this contribution must be taken into account, current commercial software packages fail to capture this behavior. Consequently, codes must implement appropriate countermeasures to mitigate the associated risks

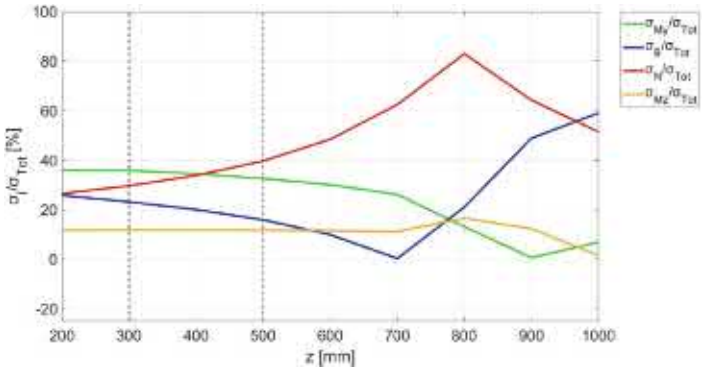


Fig. 13. Ratio between normal stresses, 30 kN axial force

5 Concluding Remarks

The paper has provided an insight into the structural response of thin-walled beams, with particular attention to the role of the bimoment. Through experimental, theoretical, and numerical analyses, the relevance of the bimoment has been investigated for two different mono-symmetric cantilever beams subjected to two loading configurations: eccentric transverse loads and eccentric axial loads.

The case of eccentric transverse loading represents a well-known and relatively common condition in the design of thin-walled members. As expected, the results confirmed that the bimoment can provide a significant contribution to the overall stress, accounting for approximately 40% of the total stress in the cases investigated. This confirms that, even for a loading condition that is already recognized as critical in literature, the bimoment contribution is far from negligible. However, it is still not always adequately considered in practical design, mainly because many widely used commercial software packages are not able to directly evaluate the bimoment response.

An even more critical outcome emerged from the analysis of beams subjected to eccentric axial loading. Unlike the transverse load case, the generation of a significant bimoment due to an axial force is rarely considered in ordinary design practice. This aspect is particularly important because axial forces are often treated as mainly producing uniform normal stresses, while their possible contribution to warping-related stresses is commonly overlooked. The theoretical evaluation of this response is more complex, due to its strong dependence on boundary conditions, cross-section geometry, and the exact point of application of the load. Nevertheless, the comparison between experimental and numerical results showed that, for the investigated case, the bimoment contribution reached up to 50% of the total stress. This result highlights a potentially dangerous design issue: neglecting the bimoment induced by eccentric axial loads may lead to a severe underestimation of the state of stress and, consequently, to an increased risk of failure in thin-walled members. Commercial software tools are generally unable to capture this response accurately. Therefore, the findings of this study suggest that the effects of eccentric axial forces on warping and bimoment generation should receive much greater attention in both research and practical design.

It should also be noted that the numerical results for the experimental case involving axial force were less accurate than those obtained for the transverse force case. This discrepancy is mainly due to the difficulty of modelling the unavoidable local constraint introduced by the hydraulic jack at the point of application of the longitudinal load during the test. Future research could further investigate similar configurations by also measuring the displacements at the point of load application. This would allow the local constraint generated during the test to be modelled more accurately, for example through equivalent springs or imposed displacements, leading to a more precise numerical representation of the experimental setup.

References

1. Vlasov VZ (1961) Thin-walled elastic beams, 2nd edn. Israel Program for Scientific Transactions, Jerusalem
2. Bernuzzi C, Bertinotti E, Simoncelli M (2020) Structural analysis of built-up members with angles. J Appl Eng Sci 18(3):443–457
3. Timoshenko SP, Gere JM (1961) Theory of elastic stability, 2nd edn. McGraw Hill, New York
4. Chen WF, Atzuta T (1977) Theory of beam-columns, vol 2. Space behaviour and design. McGraw-Hill, New York
5. Hsiao KM, Lin WY (2000) A co-rotational formulation for thin-walled beams with monosymmetric open sections. Comput Methods Appl Mech Eng 190(8):1163–1185
6. Bernuzzi C, Simoncelli M (2023) The transformation matrix in the 7DOFs beam formulation. Thin-Walled Struct 190:110951

7. International Organization for Standardization (ISO) (2020) ISO 6892-1:2020. Metallic materials — tensile testing — part 1: method of test at room temperature. ISO, Geneva
8. European Committee for Standardization (CEN) (2005) EN 1993-1-3. Eurocode 3: design of steel structures – part 1-3: general rules – supplementary rules for cold-formed members and sheeting. CEN, Brussels
9. Baldassino N, Bernuzzi C, di Gioia A, Simoncelli M (2019) An experimental investigation on solid and perforated steel storage racks uprights. J Constr Steel Res 155:409–425
10. Bernuzzi C, Simoncelli M (2023) On the variability of elastic modulus for structural steel. Struct Mag 244(3):1–10
11. Dassault Systèmes (2026) Abaqus FE software. https://www.3ds.com/it/. Accessed 2 Sept 2026
12. Simoncelli M, Zucca M, Ghilardi M (2024) Structural health monitoring of an onshore steel wind turbine. J Civ Struct Heal Monit 14:1423–1437

Shear Behaviour of Screwed Connections in LSF Systems: An Experimental Study

Nadia Baldassino(✉), Stefano Girardi, Arianna Serraiotto, and Riccardo Zandonini

University of Trento, Trento, Italy
nadia.baldassino@unitn.it

Abstract. In response to modern sustainability and seismic safety requirements, the use of Light Steel Framing (LSF) systems has increased significantly in recent years. These semi-prefabricated composite solutions combine a cold-formed steel (CFS) skeleton with sheathing panels, establishing a structural mechanism where global performance depends heavily on component-level interactions. The non-linear performance of the sheathing-to-framing connections, typically realised by self-drilling or self-tapping screws, primarily governs the overall lateral stiffness, energy dissipation, and failure modes of structural components and of the entire building. Given their critical role in ensuring system efficiency, the mechanical performance of connections has been the subject of extensive research. However, studies have prevalently relied on experimental investigations, employing diverse testing methodologies. Since different test configurations can lead to different outcomes in terms of capacity, stiffness, and failure modes, the experimental setup is a crucial variable. As part of an ongoing study on LSF systems at the University of Trento, shear tests on screwed connections between a CFS profile and two sheathing types were carried out. Two different testing setups were adopted, differing in the number of tested fasteners: six screws in one configuration and two in the other. This experimental campaign allowed for an extensive investigation of the collapse modes, resistance, stiffness, and deformation capacity of the connections. Furthermore, comparing the outcomes of the two configurations enabled the appraisal of a possible group effect associated with the distinct testing conditions. In this paper, the experimental study and its main findings are presented and discussed.

Keywords: LSF systems · Screwed connections · Testing set-ups · Monotonic tests · Group effect

1 Introduction

In recent years, worldwide attention to Light Steel Framing (LSF) construction systems has gradually increased due to their numerous advantages, including lightweight nature, cost-efficiency, optimal structural performance, high compatibility with industrial prefabrication, and the use of recyclable materials [1–2]. These systems are semi-prefabricated composite solutions made of a cold-formed steel (CFS) skeleton sheathed with panels of different materials, such as steel plates, cement-based materials, gypsum, and wood-based products. Mechanical connections, typically self-drilling or self-tapping screws, enable the interaction between the two basic components.

© The Author(s), under exclusive license to Springer Nature Switzerland AG 2026
R. Zanon et al. (Eds.): CTA 2026, LNCE 942, pp. 296–309, 2026.
https://doi.org/10.1007/978-3-032-39505-4_26

The structural behavior of LSF systems is inherently complex because the global response is governed by the interaction between framing members, sheathing materials, and mechanical connections. Since load transfer between the steel framing and the sheathing occurs through mechanical fasteners, the overall performance of LSF systems is strongly influenced by the local behavior of these connections [3–6]. Under seismic loading, energy dissipation is primarily concentrated in the fastener regions. This mechanism may enable significant deformation capacity and stable hysteretic behavior while preserving the overall integrity of the system, even under severe inter-story drift demands [6]. Given their critical role in ensuring system efficiency, the mechanical performance of connections has been the subject of extensive research**.** Numerous experimental studies have investigated the in-plane shear response of connections. In contrast, only a few numerical studies have focused on this subject, mainly due to the modeling complexity associated with CFS profiles, sheathing, screws, and their interactions. Experimental research explored both the monotonic and cyclic response, focusing on the main phenomena affecting the shear behaviour of the connections. Studies have thoroughly explored the influence of sheathing type, orientation, thickness, and the number of layers, focusing specifically on their effects on the connection's stiffness, resistance, failure modes, and energy dissipation capacity. Extensive research has been conducted on traditional sheathing options, including single or double-layer gypsum board (GB) [4, 7–10], wood-based panels such as oriented strand boards (OSB) [7–9] or plywood [11], calcium silicate boards (CSB) [9, 12], and fibre cement boards (FCB) [13]. More recently, attention has shifted toward eco-friendly alternatives such as bamboo plywood panels [14] and composite sheathing solutions, including steel-gypsum (SG) panels [13] and sandwich panels [15], further expanding the options for LSF systems. Other critical variables investigated include screw type and diameter, screw edge and end distances, screw spacing, CFS thickness, loading protocols, and environmental conditions [7–15].

The literature review reveals that past studies have mainly adopted five distinct testing methodologies to reproduce simplified screw loading conditions (Fig. 1) [16]. These include the single-lap shear test (Fig. 1a)), featuring a single fastener connecting a steel sheet to a sheathing panel, as well as multiple fastener configurations designed to recreate symmetric loading conditions (Figs. 1b), 1e)). Depending on the orientation of the screw shear force relative to the sheathing's free edge, the test setups can be divided into two categories: parallel, which includes configurations 1a), 1b), and 1c), and perpendicular, comprising configurations 1d) and 1e). While both categories aim to reproduce simplified screw loading conditions, their experimental outcomes can differ significantly, particularly in terms of ultimate capacity, stiffness, and failure modes. A few studies [17–18] have investigated the influence of parallel and perpendicular loading conditions. By combining experimental and numerical results from the setups illustrated in Fig. 1c) and Fig. 1d), the authors in [17] concluded that strength results from the perpendicular configuration are more conservative than those from the parallel setup. Conversely, the parallel configuration exhibits both lower connection stiffness and greater ductility.

To better understand the influence of test configuration on the shear performance of CFS profile-to-sheathing connections, an experimental campaign was conducted at the University of Trento. Shear tests on screwed connections between a CFS profile and two

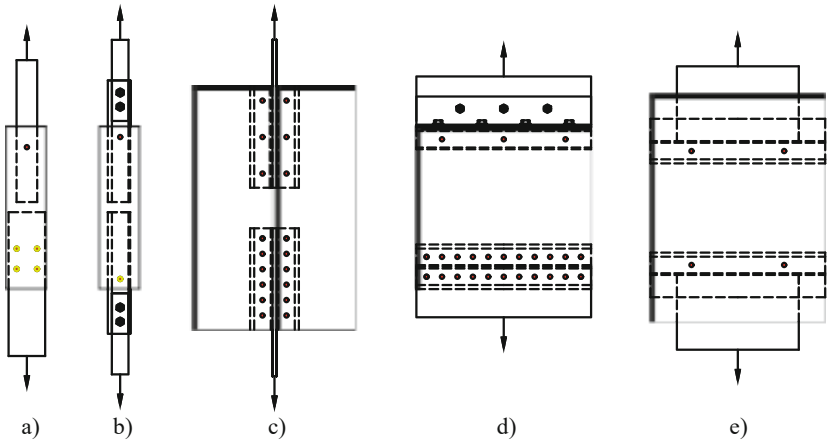


Fig. 1. Testing configurations for shear tests on connections

sheathing types were carried out. Two different testing setups were adopted, differing in the number of tested fasteners: six screws in one configuration and two in the other. This campaign allowed for a comprehensive investigation of the collapse modes, resistance, stiffness, and deformation capacity of the connections. Furthermore, comparison of the outcomes of both setups enabled the evaluation of a possible group effect associated with the six-screw configuration, resulting from the interaction of stress fields that can induce premature or group-tailored failure mechanisms. In this paper, the experimental study and its main findings are presented and discussed.

2 Experimental Program

2.1 Characteristics of the Study

The study evaluated the shear performance of self-drilling screw connecting two different sheathing types to a CFS profile. The sheathings, labelled as Gr and HF, were gypsum-based materials with the following characteristics:

- Sheathing Type Gr: 12.5 mm thick gypsum board featuring a mould- and moisture-resistant core lined with reinforced glass tissue, designed for external applications. According to the manufacturer's documentation, the sheathing has a nominal density of 885 kg/m^3. Its mechanical behaviour exhibits orthotropic properties across directions. In compression, the material achieves a strength of 6.6 MPa in the longitudinal direction (LD) and 6.3 MPa in the cross direction (CD). The tensile strength is 2.0 MPa (LD) and 1.3 MPa (CD), while the nominal shear strength reaches 2.3 MPa (LD) and 2.8 MPa (CD). In-plane compression moduli are 4700 MPa (LD) and 4100 MPa (CD), whereas tensile moduli are higher, standing at 6300 MPa (LD) and 5500 MPa (CD). Finally, the shear moduli are 1400 MPa (LD) and 1900 MPa in the cross direction (CD);

- Sheathing Type HF: 12.5 mm thick plasterboard featuring a glass-fibre-reinforced core encased in paper lining, optimized for internal load-bearing applications. Based on the technical data sheet, the material exhibits a nominal density of 985 kg/m^3. It presents in the longitudinal direction (LD) compressive and tensile strength of 9.15 MPa and 3.91 MPa, compared to 7.49 MPa and 1.93 MPa in the cross direction (CD). The corresponding nominal shear strengths are 3.25 MPa (LD) and 3.55 MPa (CD). As for the in-plane elastic moduli, compression values are 2282 MPa (LD) and 1852 MPa (CD), while in tension values reach 4701 MPa (LD) and 3758 MPa (CD). Finally, the shear moduli are 1775 MPa (LD) and 1421 MPa (CD).

The CFS profile had a C-shaped cross section with a height of 100 mm, a width of 55 mm, and a thickness of 1.2 mm made of a steel grade S280GD + Z275. Self-drilling screws (4.2 mm in diameter and 25 mm long), featuring a ribbed, double-countersunk wafer head, a cross-type H recess, and a drill point, were used to connect the sheathing to the CFS profile.

2.2 Testing Set-Up

Tests were carried out using the two different testing setups shown in Fig. 2, in the following TA and TB, respectively.

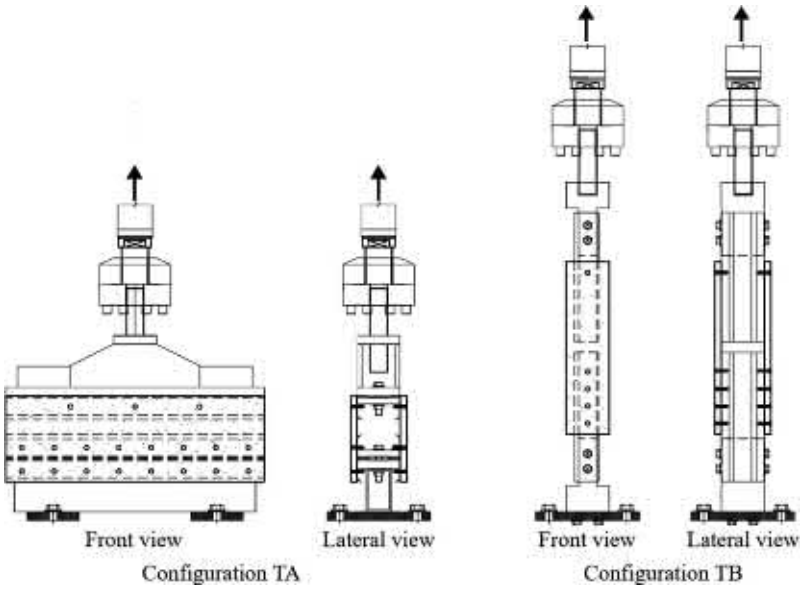


Fig. 2. Testing set-ups adopted for the study

Test configuration TA, originally proposed by Serrette et al. [19] and subsequently modified by Fiorino et al. [7], aligns with the configuration depicted in Fig. 1d). Conversely, test configuration TB is a variant of the setup illustrated in Fig. 1b). Both setups

ensure a symmetric loading condition and feature an over-strength bottom assembly designed to make deformations develop solely at the top screws of the specimens.

Specimens in test configuration TA were made of two sheathing panels, each 600 mm long and 200 mm high. At the top end, i.e., the region to be tested, the sheathing panels were screwed to the flanges of a CFS profile via six screws (three on each panel), located 25 mm from the top free edge and spaced 150 mm apart. These distances were intentionally selected to match those adopted in shear wall specimens previously tested by the authors [20]. Conversely, the bottom, over-strength end was assembled by symmetrically connecting the panels to two back-to-back CFS profiles. A total of thirty-two screws were used, sixteen on each panel.

Specimens in test configuration TB featured two sheathing panels, each 400 mm long, with widths of either 100 mm or 150 mm. Specifically, the 150 mm width was selected to replicate the screw spacing adopted in configuration TA. Regarding the fastening details, the sheathing panels were symmetrically connected to the opposite flanges of a CFS profile. At the bottom over-strength end, eight screws (four on each panel) were used, while the top end featured two screws (one on each panel). The distance of the top screws from the top free edge was set to 25 mm, in accordance with configuration TA.

For both configurations, the specimens were sampled along the longitudinal direction (LD) of the gypsum board. As to the tested screws, they were installed flush with the sheathing panels, according to the standard wall sheathing installation practice.

In the tests, a closed-loop reaction frame equipped with a servo-hydraulic actuator was used. The over-strength end of each specimen was connected to the bottom beam of the reaction frame, while the top end was connected to the actuator. The specimens were subjected to monotonically increasing tensile loading until connection failure. During the tests, the top connection deformation was monitored using displacement transducers. Specifically, four transducers (two per side) were utilized for configuration TA (Fig. 3a)), whereas only two instruments (one per side) were employed for configuration TB (Fig. 3b)).



Fig. 3. Detail of the experimental setup and instrumentation

Tests were carried out in displacement control with a rate of 5 mm/min, recording loads and displacements at a frequency of 5 Hz.

3 Test Results

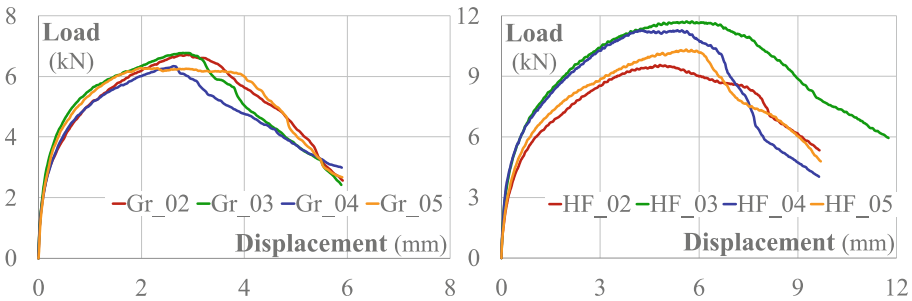
Table 1 summarizes the experimental program and the nomenclature adopted for the specimens. In nomenclature, "XX" stands for the sequential number of the test. As can be noted specimens tested in configuration TB are identified by the letter 'S' after the sheathing type notation. Furthermore, specimens with a width of 150 mm are identified by a final letter 'b'. A total of 30 monotonic tests were carried out.

Table 1. Summary of the experimental program

Sheathing type	ID	Test configuration	N tests	Spec. dimensions
Gr	Gr_XX	TA	4	600x200 mm
Gr	Gr_S_XX	TB	6	100x400 mm
Gr	Gr_S_XXb	TB	5	150x400 mm
HF	HF_XX	TA	4	600x200 mm
HF	HF_S_XX	TB	5	100x400 mm
HF	HF_S_XXb	TB	6	150x400 mm

3.1 Main Results for Test Configuration TA

The results in terms of load-displacement curves are shown for the two sheathing types in Fig. 4. The curves refer to the mean top displacement and to the total load applied to the specimens, i.e. the load associated with the six top screws.



a) Sheathing type Gr b) Sheathing type HF

Fig. 4. Test results: total load-mean deformation curves for test setup TA

The different performance of the two sheathing types is apparent: sheathing Gr is characterized by a stiffer response, but lower strength and deformation capacity than sheathing HF. Collapse in specimens Gr was mainly associated with screw tilting, delamination (Fig. 5a)) and screw pull-through (Fig. 5b)). One case of edge shear failure was observed (Fig. 5b)).

In specimens HF, collapses were associated with a combination of tilting, bearing of the sheathing, edge shear failure (Fig. 6a)) and screw pull-through (Fig. 6b)).



a) b)

Fig. 5. Typical collapse modes for test setup TA and sheathing Gr



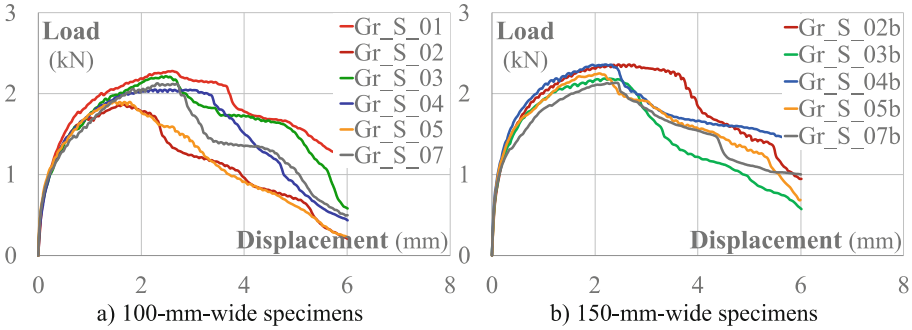
a) b)

Fig. 6. Typical collapse modes for test setup TA and sheathing HF

3.2 Main Results for Test Configuration TB

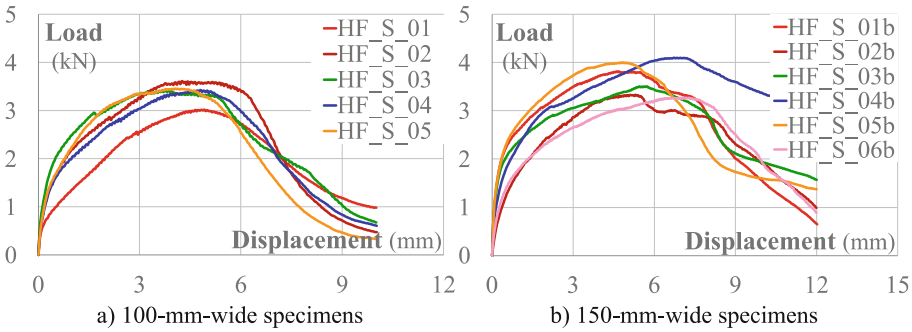
Load-displacement curves for sheathings Gr and HF are presented in Fig. 7 and Fig. 8, respectively. The graphs on the left (Fig. 7a)) and (Fig. 8a)) refer to the specimens 100 mm wide, while the ones on the right are related to specimens 150 mm wide. The curves plot the total applied load versus the relative displacement between the CFS profiles and the sheathing, measured at the top. The comparison between the curves reveals a stiffer and stronger response for the 150-mm-wide specimens compared to the 100-mm-wide ones, with this effect being more pronounced for the HF sheathing.

Regarding the collapse mode, the primary causes of failure for the 100-mm-wide specimens were tilting combined with screw pull-through and edge shear failure (Fig. 9b) and Fig. 10b)). Additionally, sheathing delamination (Fig. 9a)) was observed in two cases for the Gr sheathing. The tearing failure phenomenon, predominant in the HF sheathing, was noted in only two cases for the Gr sheathing. In the 150-mm-wide specimens, tilting, pull-through, and edge shear failure phenomena were likewise observed (Figs. 9c), 10c), 10d)). However, bearing failure occurred in both sheathing types (Fig. 9c), Fig. 10d)), whereas delamination was recorded for the Gr sheathing only (Fig. 9d)) and tearing failure was confined to the HF sheathing.



a) 100-mm-wide specimens b) 150-mm-wide specimens

Fig. 7. Test results: total load-mean deformation curves for sheathing Gr for test setup TB



a) 100-mm-wide specimens b) 150-mm-wide specimens

Fig. 8. Test results: total load-mean deformation curves for sheathing HF for test setup TB



Fig. 9. Failure mode for test setup TB and sheathing Gr (100 mm and 150 mm wide specimens)



Fig. 10. Failure mode for test setup TB and sheathing HF (100 mm and 150 mm wide specimens)

3.3 Analyses and Comparison Between Results

To compare the test outcomes, the experimental results were appraised by considering the load-mean deformation curves up to a post-peak threshold of $0.8F_{peak}$ on the descending branch. For each curve, the following parameters were evaluated:

- Peak force (F_{peak}): maximum recorded force and the associated displacement (d_{peak});
- Yield force (F_y): conventional yielding force evaluated via an energy-based approach; i.e., by equating the complementary areas, represented by the blue and red regions, in Fig. 11;
- Ultimate displacement (d_u): the conventional ultimate displacement, associated with a load drop to $0.8F_{peak}$ on the softening branch of the curve;
- Initial secant stiffness ($k_{40\%}$): the secant stiffness calculated as the ratio of $0.4F_{peak}$ to its corresponding displacement.

In order to facilitate a direct comparison between configurations TA and TB data were subsequently normalised per single screw. To this aim, the force and initial secant stiffness values were divided by the total number of tested screws in the respective connection (i.e., divided by six for configuration TA and by two for configuration TB, respectively). For each homogeneous test group, the mean values and the coefficients of variation (CoV%) of the evaluated parameters were also calculated. The results of these analyses are summarized in Table 2 and Table 3 for sheathing Gr and HF, respectively. In tables, the final column reports the specific failure mode observed for each test. In this regard, the following notation is used: T for tilting, B for bearing of the sheathing, D for delamination, ESF for edge shear failure, PT for screw pull-through, and TF for tearing failure.

A first overview of the experimental data makes apparent that, regardless of the test setup adopted, the results for both sheathings exhibit limited scatter in terms of strength parameters. Conversely, higher variability affects the deformation parameters and, consequently, the initial stiffness ($k_{40\%}$).

A further comparison between the two materials leads to the following observations:

- The superior performance of HF sheathing in terms of load-bearing capacity (F_{peak} and F_y) is consistently observed, regardless of the test setup adopted. On average, the HF sheathing resistance is approximately 60% higher than that of Gr sheathing. This enhanced strength directly reflects the superior material properties of the HF

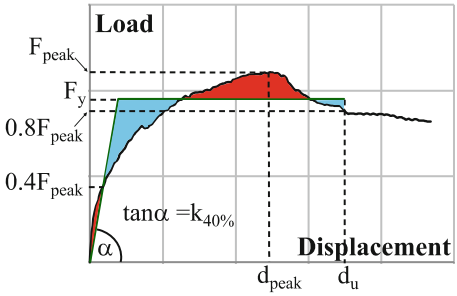


Fig. 11. Evaluation of notional strength and secant stiffness

Table 2. Summary of test results for sheathing Gr

ID Spec.	Test conf.	F_{peak}	d_{peak}	d_u	F_y	$k_{40\%}$	Collapse mode
Gr_02	TA	1.12	2.89	4.24	0.97	2.69	D + PT + T
Gr_03		1.13	2.82	3.85	0.99	3.44	ESF + PT + T
Gr_04		1.06	2.62	3.63	0.91	2.82	D + PT + T
Gr_05		1.04	1.95	4.58	0.96	3.70	D + PT + T
Mean value		1.09	2.57	4.07	0.96	3.16	
CoV%		3.93	16.62	10.32	3.44	15.32	
Gr_S_01	TB	1.14	2.61	3.86	1.02	2.54	ESF + T + TF
Gr_S_02		0.93	1.65	2.40	0.83	3.40	ESF + PT + T
Gr_S_03		1.11	2.47	3.49	0.95	2.47	ESF + PT + T
Gr_S_04		1.03	2.54	3.82	0.93	2.76	D + ESF + PT + T
Gr_S_05		0.95	1.47	2.73	0.83	4.00	ESF + T + TF
Gr_S_07		1.06	2.32	3.08	0.90	3.06	D + ESF + PT + T
Mean value		1.04	2.18	3.23	0.91	3.04	
CoV%		8.03	22.59	18.40	8.19	19.30	
Gr_S_02b	TB	1.18	2.67	3.97	1.07	3.66	D + ESF + PT + T
Gr_S_03b		1.09	2.19	3.03	0.98	4.21	B + ESF + PT + T
Gr_S_04b		1.18	2.21	3.03	1.04	4.85	ESF + PT + T
Gr_S_05b		1.13	2.09	3.25	0.97	4.77	D + PT + T
Gr_S_07b		1.07	2.42	3.25	0.92	4.70	D + ESF + PT + T
Mean value		1.13	2.32	3.31	1.00	4.44	
CoV%		4.47	9.96	11.76	5.98	11.34	

sheathing, which features a higher density (985 kg/m^3 vs. 885 kg/m^3) and higher resistance values in both LD and CD directions. Furthermore, both sheathings exhibited remarkably low scatter in peak resistance, with a coefficient of variation ranging between 4–8% for Gr and 6–10% for HF proving high experimental reliability;

- This superior strength is associated with a higher deformation capacity, as shown both from the displacement at peak load (d_{peak}) and the conventional ultimate deformation capacity (d_u). HF connections achieved average ultimate displacements up to nearly double those of Gr connections, highlighting a significantly greater energy dissipation potential;
- Conversely, Gr sheathing exhibits higher stiffness, being on average 45% stiffer than its HF counterpart. This response aligns with the intrinsic material stiffness, as Gr sheathing features substantially higher elastic moduli in both LD and CD directions. Notably, while Gr maintained low-to-moderate scatter in stiffness (CoV 11–19%), HF sheathing shows higher variability in initial stiffness (CoV 20–46%), which can be attributed to localised micro-crushing and progressive fiber engagement under initial shear force;
- Despite the different mechanical responses and material properties, both sheathings exhibited substantially similar failure modes. Failure was associated with a combination of screw pull-through, sheathing-edge bearing, and edge shear or tearing. Delamination was uniquely observed in Gr sheathing. It is worth noting that the observed failure modes are fully consistent with collapse modes reported in literature [7, 9, 16], confirming the characteristic failure behaviour typical of cold-formed steel-to-sheathing screw connections.

Regarding the influence of the different test setups on the experimental outcomes, the following observations can be made:

- The strength parameters (F_{peak} and F_y) are only slightly affected by the test configuration and specimen geometry. In particular, both materials exhibit a minor drop in mean peak resistance in the 100-mm-wide TB specimens compared to TA, whereas the highest mean values are consistently achieved in the 150-mm-wide TB configuration. However, these variations remain well within a 10% range across all configurations, confirming that connection resistance is primarily governed by intrinsic material shear strength rather than fastener arrangement;
- Unlike ultimate strength, initial stiffness ($k_{40\%}$) and deformation metrics are noticeably configuration dependent. In particular, the 150-mm-wide TB setup leads to a marked increase in stiffness for both sheathings reaching on average 4.44 kN/mm (+40.5% over TA) for Gr and 3.12 kN/mm for HF (+36.8% over TA). Furthermore, a significant increase in peak displacement (d_{peak}) is observed for the HF cases under the TB-b configuration. However, this setup entails higher scatter in initial stiffness particularly for HF specimens (CoV up to 46%) reflecting a complex fiber engagement and micro-crushing prior to reaching peak load;
- The failure modes are only marginally influenced by the test configuration. While the primary failure mechanisms (T and PT) occur consistently in all setups, shearing and tearing failures (ESF/TF) become slightly more pronounced in both TB configurations.

Table 3. Summary of test results for sheathing HF

ID Spec.	Test conf.	F_{peak}	d_{peak}	d_u	F_y	$k_{40\%}$	Collapse mode
HF_02	TA	1.59	4.82	7.97	1.39	1.82	B + ESF + PT + T
HF_03		1.95	5.79	8.71	1.73	2.54	B + ESF + PT + T
HF_04		1.88	5.35	6.93	1.65	2.79	B + ESF + PT + T
HF_05		1.72	5.61	6.94	1.48	1.97	B + ESF + PT + T
Mean value		1.79	5.39	7.64	1.56	2.28	
CoV%		9.01	7.82	11.33	9.78	20.14	
HF_S_01	TB	1.51	4.90	6.57	1.31	0.78	T + TF
HF_S_02		1.81	4.26	6.57	1.58	1.89	T + TF
HF_S_03		1.71	3.75	5.95	1.53	3.21	ESF + PT + T + TF
HF_S_04		1.72	4.79	6.34	1.46	1.98	ESF + T
HF_S_05		1.73	4.05	5.78	1.53	2.24	ESF + T + TF
Mean value		1.69	4.35	6.24	1.48	2.02	
CoV%		6.46	11.22	5.80	7.00	43.11	
HF_S_01b	TB	1.91	7.82	4.59	1.67	4.23	B + ESF + T
HF_S_02b		1.66	8.49	5.31	1.44	1.14	B + ESF + T
HF_S_03b		1.75	8.11	5.73	1.52	4.15	ESF + PT + T + TF
HF_S_04b		2.05	10.46	6.95	1.72	3.76	ESF + PT + T
HF_S_05b		2.00	6.83	4.84	1.76	3.97	ESF + PT + T + TF
HF_S_06b		1.63	8.80	7.17	1.41	1.45	ESF + PT + T + TF
Mean value		1.83	8.42	5.77	1.59	3.12	
CoV%		9.55	14.34	18.72	9.39	45.64	

The experimental results prove that while the choice of the test setup negligibly affects the connection strength, it has a significant influence on the stiffness. Specifically, the adoption of the 100-mm-wide TB setup represents a more conservative approach for design purposes, as it yields a lower initial stiffness.

It is worth noting, however, that these findings are limited to the specific cases investigated herein, and further research is necessary to validate these outcomes. To expand upon these preliminary results, a complementary series of cyclic tests has been already planned to investigate seismic performance

4 Concluding Remarks

This paper presents the results of an experimental campaign investigating the shear performance of two CFS profile-to-sheathing screwed connections, evaluating the influence of sheathing materials and of test configurations. Two different testing configurations

were adopted, and for one of them, two different specimen dimensions were considered. The tests successfully characterized the structural response of the connections, highlighting the different mechanical behaviours in terms of stiffness, resistance, and deformation capacity. Regarding the test set-up, the experimental outcomes showed that the choice of the test configuration is practically uninfluential on the connection strength. Conversely, the setup has a moderate influence on both the deformation capacity and the initial stiffness.

Acknowledgments. The study has been carried out within the framework of the project DPC-ReLUIS, funded by the Department of Civil Protection (DPC) and the Network of University Laboratories for Seismic and Structural Engineering (ReLUIS).

References

1. Mona AH, Metwally AH (2019) Framework for construction system selection based on life cycle cost and sustainability assessment. J Clean Prod 241:118397
2. Landolfo R (2109) Lightweight steel framed systems in seismic areas: current achievements and future challenges. Thin-Walled Struct 140:114–131
3. Viera LCM, Schafer BW (2012) Lateral stiffness and strength of sheathing braced cold-formed steel stud walls. Eng Struct 37:205–213
4. Selvaraj S, Madhavan M (2022) Application of direct stiffness-strength method for Design of Gypsum and Plywood sheathed CFS wall panels subjected to bending. Thin-Walled Struct 180:109874
5. Chatterjee A, Rogers CA, Moen CD (2017) High fidelity monotonic and cyclic simulation of a wood-sheathed cold-formed steel framed floor diaphragm. In: Proceedings of the 16th world conference on earthquake engineering (16WCEE), Santiago, January 2017, p 12
6. Dubina D (2008) Behavior and performance of cold-formed steel-framed houses under seismic action. J Constr Steel Res 64(7–8):896–913
7. Fiorino L, Della Corte G, Landolfo R (2007) Experimental tests on typical screw connections for cold-formed steel housing. Eng Struct 29(8):1761–1773
8. Peterman KD, Nakata N, Schafer BW (2014) Hysteretic characterization of cold-formed steel stud-to-sheathing connections. J Constr Steel Res 101:254–264
9. Ye J, Wang X, Zhao M (2016) Experimental study on shear behavior of screw connections in CFS sheathing. J Constr Steel Res 121:1–12
10. Chen W, Ye J, Chen T (2016) Design of Cold-Formed Steel Screw Connections with gypsum sheathing at ambient and elevated temperatures. Appl Sci 6(9):1–23
11. Selvaraj S, Madhavan M (2019) Sheathing braced design of cold-formed steel structural members subjected to torsional buckling. Structure 20:489–509
12. Nithyadharan M, Kalyanaraman V (2011) Experimental study of screw connections in CFS-calcium silicate board wall panels. Thin-Walled Struct 49:724–731
13. Derveni F, Gerasimidis S, Peterman KD (2020) Behavior of cold-formed steel shear walls sheathed with high-capacity sheathing. Eng Struct 225:111280
14. Zheng W et al (2020) Experimental investigation on the behavior of plybamboo sheathing-to-framing screwed connections. Constr Build Mater 262:120856
15. Jammi S, Jayachandran SA (2021) Experimental studies on screw connections between cold-formed steel framing and sandwich sheathing. Structure 32:2048–2059
16. Abeysiriwardena T, Mithum P, Mahendran M (2021) Local in-plane strength and stiffness of stud-to-sheathing fastener connections in LSF wall panels. Thin-Walled Struct 160:107383

17. Tawfik NM, Abu-Hamd M (2024) Numerical modeling of sheathed screw connections in CFS shear walls. Structure 63:106311
18. Feng R, Cai Q, Ma Y, Yan G (2020) Shear analysis of self-drilling screw connections of CFS walls with steel sheathing. J Constr Steel Res 167:105842
19. Serrette RL, Encalada J, Juadines M, Nguyen H (1973) Static racking behavior of plywood, OSB, gypsum, and FiberBond walls with metal framing. J Struct Eng 123:1079–1086
20. Baldassino N, Girardi S, Zandonini R, Cassese P (2025) Shear performance of sheathed LSF walls. In: Real E, Mirambell E (eds.) Proceedings of SDSS 2025 - The International Colloquium of Stability and Ductility of Steel Structures. ce/papers 8(6), pp. 1115–1120. Ernst & Sohn GmbH, Berlin.

AI-Based Design: Prediction of Load-Carrying Capacity in Cold-Formed Members

Marco Simoncelli(✉) and Alice Lucidi

Department of Architecture, Built environment and Construction engineering, Politecnico di Milano, Piazza Leonardo da Vinci 32, 20133 Milano, Italy
marco.simoncelli@polimi.it

Abstract. Cold-formed steel Class 4 profiles are extensively used in modern structural engineering because of their low self-weight and high load-carrying capacity. Despite these advantages, thin-walled elements are highly susceptible to local and distortional buckling, which curtails their ultimate yielding strength. Consequently, structural design requires computing effective section properties. Eurocode 3 Part 1–5 addresses this through the Effective Width Method, an iterative procedure that penalizes plate dimensions according to slenderness and stress profiles. However, this method is computationally inefficient and time-consuming, especially when dealing with complex configurations like perforated plates. This study proposes a Machine-Learning alternative to bypass these iterative calculations. An Artificial Neural Network (ANN) was developed as a high-speed surrogate model to predict effective area and section modulus ratios. The optimized network proved reliable performance, with errors below 10% for over 98% of the analyzed cases, thereby offering an efficient tool for practical structural design.

Keywords: Cold-formed profiles · Class 4 · EWM · Machine-Learning · Artificial Neural Network

1 Introduction

1.1 Machine-Learning

In recent decades, Machine-Learning (ML) has been extensively applied across various engineering domains. In structural engineering ([1–3]), ML methodologies have emerged as powerful tools to address complex tasks, such as members' load-carrying capacity prediction and structural health monitoring.

In detail, ML is a branch of artificial intelligence dedicated to teaching computers how to extract underlying patterns from available datasets to perform predictions or make decisions without being explicitly programmed for the task. Based on the learning paradigm adopted, ML algorithms are generally categorized into three main frameworks:

– Supervised learning: The algorithm is trained on a labeled dataset where each training exemplar pairs an input vector with a known target output. Classification and regression tasks are typically addressed using this approach.

© The Author(s), under exclusive license to Springer Nature Switzerland AG 2026
R. Zanon et al. (Eds.): CTA 2026, LNCE 942, pp. 310–321, 2026.
https://doi.org/10.1007/978-3-032-39505-4_27

– Unsupervised learning: The algorithm processes unlabeled data to discover intrinsic structures, clusters, or distributions without explicit target guidance.
– Reinforcement learning: The model learns optimal decision-making policies through an iterative trial-and-error interaction with a dynamic environment, guided by a reward-penalty system.

The creation of a supervised ML model systematically involves three sequential phases:

– Database preparation. This stage entails gathering and structuring the data, typically organized into features (independent input variables) and labels (dependent target variables). In structural engineering, features generally encompass geometric configurations and mechanical material properties, whereas labels correspond to structural responses such as ultimate strength or deflection. To rigorously evaluate the model's performance, the initial dataset is randomly partitioned into distinct training and testing subsets, with the larger portion allocated for training purposes.
– Model Training: A suitable ML algorithm is selected and fitted to the training dataset, optimizing its internal parameters.
– Model Evaluation: The generalization capability of the trained model is verified using the independent testing dataset. Specifically, a loss function is computed to quantitatively evaluate how far a predicted value deviates from its actual value.

In structural engineering applications, predictive models predominantly leverage supervised learning, utilizing either classification or regression techniques. Classification aims to map input vectors into discrete categorical classes within a limited group of possibilities, such as damage detection problems. Conversely, regression techniques are deployed when the expected target output is a continuous variable capable of assuming any value within a defined interval. In general, member resistance predictions are developed using regression algorithms.

A highly effective model capable of executing both classification and regression tasks is the Artificial Neural Network (ANN). An ANN consists of interconnected processing units, known as neurons, which are arranged in layers and linked by weighted connections, as shown in Fig. 1. During the training process, initial weights are assigned randomly and iteratively adjusted by minimizing the difference between predicted outputs and experimentally measured or analytically computed values. Several parameters have a major impact on the model performance, some related to the ANN architecture, such as the number of hidden layers, the number of neurons in each hidden layer and the type of activation function, and some related to the training choices, such as the learning rate and the number of epochs.

1.2 Scope of the Study

This study introduces an optimized ML framework developed for a highly specific structural task: predicting the effective cross-sectional properties of Class 4 cold-formed steel (CFS) profiles. Due to their high strength-to-weight ratio, CFS profiles are widely utilized in modern construction to optimize transportation and installation efficiency. However, owing to their thin-walled nature and cold-rolling manufacturing process,

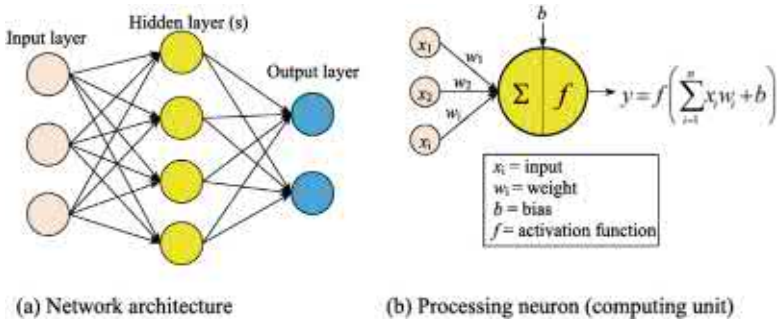


Fig. 1. Architecture of a neural network [2]

these components are highly susceptible to local and distortional buckling phenomena. These instability modes prevent the cross-section from attaining its full yielding capacity.

In this sense, for their design, two main approaches can be applied: the effective width method (EWM), presented in the Eurocode 3 part 1–5 ([4, 5]), and the direct strength method, introduced for the first time by the American standards ([6]). At European level the EWM is the most widely applied method and consists in the derivation of the effective cross-section properties through the penalization of the steel plates (web, flanges, stiffeners) composing the section according to their slenderness and tension distribution. A main distinction is made between the internal elements and the external ones, for which the formulation for penalization changes. The procedure is iterative and can appear more complex under certain conditions, as in presence of a monosymmetric section for which there is an iterative shift of the effective centroid or in presence of perforations ([7, 8]).

In this perspective, the aim of the study presented herein is the development of an accurate surrogate model capable of predicting the effective cross-sectional properties of Class 4 profiles by training a feed-forward Artificial Neural Network.

2 Dataset and Design Scenarios

The structural database established for this investigation focuses on cold-formed steel C-profiles characterized by varying thicknesses and cross-sectional dimensions. The input parameter space was populated using the following discrete values:

- Thickness (t): 7 values (1.0, 1.5, 2.0, 2.5, 3.0, 3.5, 4.0 mm).
- Steel Yield Strength (f_y): 4 grades (235, 275, 355, 420 MPa).
- Web Height (h): 6 values (50, 100, 150, 200, 250, 300 mm).
- Flange Width (b): 6 values (50, 100, 150, 200, 250, 300 mm).
- Lip Length (c): 10 values (10, 20, 30, 40, 50, 60, 70, 80, 90, 100 mm).

The full factorial combination of these parameters yields an initial database of 10080 geometric configurations. However, this raw collection includes non-physical or geometrically non-viable configurations, such as profiles where the web height is smaller than or equal to the lip length. Therefore, a data-filtering and cleaning process was enforced,

resulting in a finalized master dataset. From this filtered database, only the profiles classified as effective Class 4 sections according to Eurocode 3 standards under the respective loading conditions were isolated for the Machine-Learning pipeline (Fig. 2).

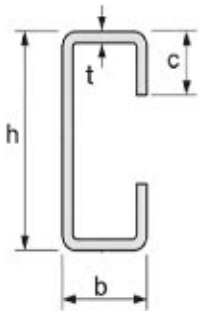


Fig. 2. Definition of the input variables

To evaluate the generalization and out-of-domain predictive capabilities of the surrogate model, the dataset was split by material grade: three steel grades (S235, S275, S355) were allocated exclusively to the training and validation phases, whereas the highest steel grade (S420) was completely isolated to serve as an independent, out-of-domain prediction set.

The structural response was investigated under three distinct loading scenarios, defining three separate study cases (Fig. 3):

- Case 1 (Fig. 3a) - Area penalization in pure axial compression: The model was trained on S235, S275, and S355 profiles (2877 configurations) and evaluated on S420 profiles (1260 configurations).
- Case 2 (Fig. 3b) - Elastic section modulus penalization in bending about the axis of symmetry (y-axis): The model was trained on S235, S275, and S355 profiles (2877 configurations) and evaluated on S420 profiles (959 configurations).
- Case 3 (Fig. 3c) - Elastic section modulus penalization in bending about the non-symmetry axis (z-axis): The model was trained on S235, S275, and S355 profiles (2877 configurations) and evaluated on S420 profiles (959 configurations).

The formulation of this out-of-domain validation task is physically justified by the quasi-linear and monotonic dependency of the cross-sectional penalization ratio on the steel yield strength, as explicitly demonstrated by the parametric analytical curves illustrated in Figs. 4, 5 and 6.

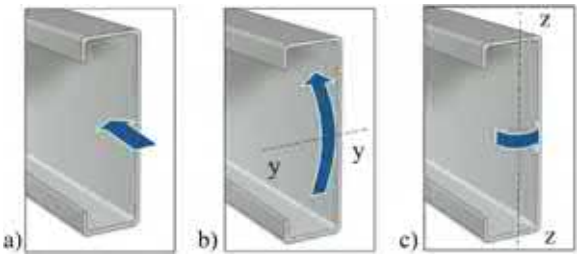
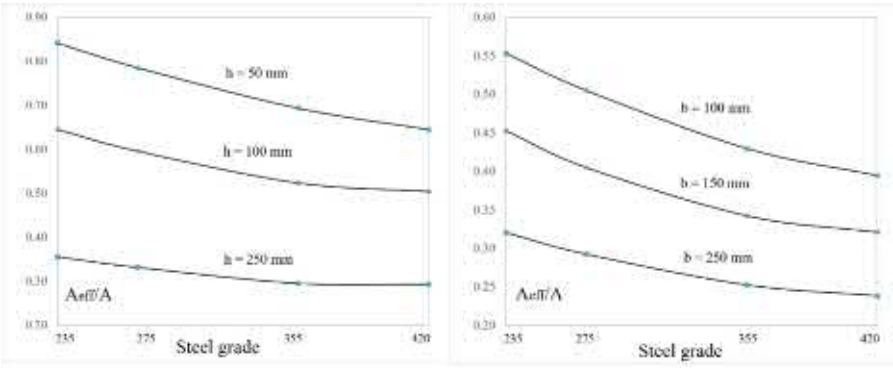


Fig. 3. Investigated loading conditions: a) pure compression; b) bending about the y-axis; c) bending about the z-axis



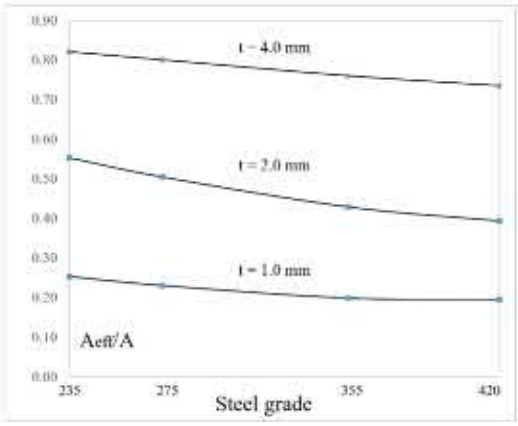


Fig. 4. Variability in the A_{eff}/A ratio for different steel grades

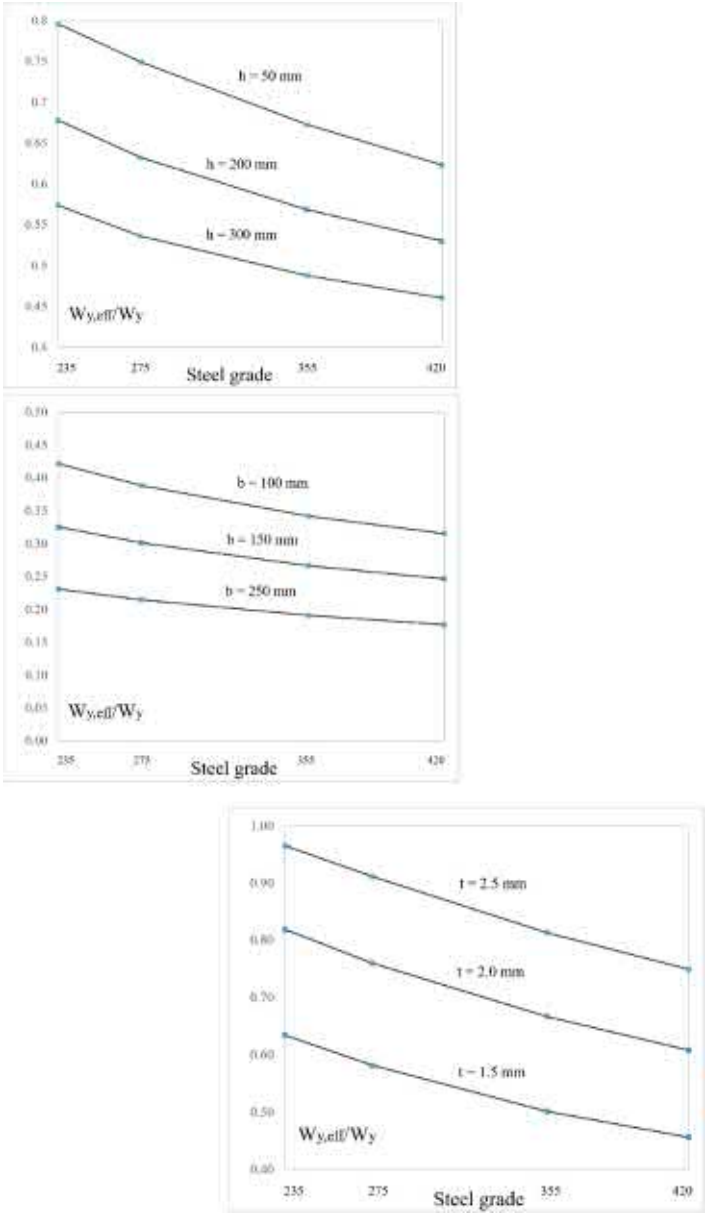


Fig. 5. Variability in the $W_{y,eff}/W_y$ ratio for different steel grades

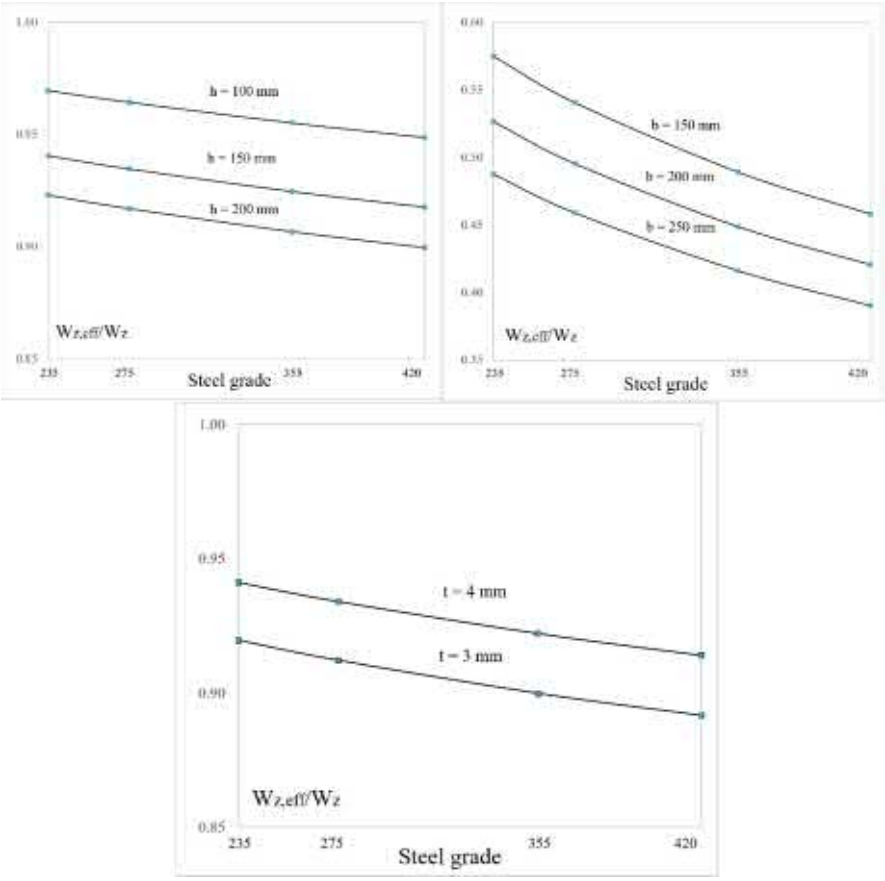


Fig. 6. Variability in the $W_{z,eff}/W_z$ ratio for different steel grades

3 Neural Network Architecture

The predictive model was implemented within the MATLAB computational environment through the supervised "fitnet" paradigm. The model belongs to the Multi-Layer Perceptron (MLP) feed-forward family, meaning that information flows strictly unidirectionally from the input layer through the hidden layer to the output layer. Mathematically, the structural network topology is structured as follows:

– Input Layer: 4 neurons representing the following structural features: f_y, h/t, b/t and c/t.
– Hidden Layer: A single hidden layer with a variable neuron density, determined dynamically via parametric optimization.
– Output Layer: 1 neuron representing the continuous penalization ratio (A_{eff} /A for Case 1; W_{eff}/W for Cases 2 and 3).

To determine the optimal network topology, a parametric sensitivity study was conducted by varying the hidden layer density within a discrete range from 4 to 20 neurons, evaluating its direct impact on predictive accuracy. To ensure strict scientific rigor and eliminate stochastic bias, the training environment was stabilized by resetting a constant random seed at the beginning of each algorithmic iteration. Crucially, this fixed seed ensures that the subsequent partitioning of the dataset—allocated as 70% for training, 15% for validation, and 15% for testing—remains identical across all iterations. This protocol guaranteed that every architectural configuration was fitted, validated, and tested on the exact same data subsets, isolating the number of hidden neurons as the sole independent variable and preventing any performance distortion from a fortunate or unfortunate data split.

Concurrently, the training epoch threshold—representing the number of complete passes through the dataset—was carefully calibrated to balance generalization capabilities. Insufficient training epochs typically result in underfitting, where the model fails to capture the underlying structural patterns. Conversely, excessive epochs trigger overfitting, causing the network to memorize local training noise rather than learning the physics of the problem, which severely compromises predictions on unseen samples. To mitigate this risk, an automated Early Stopping mechanism was implemented within the MATLAB environment by monitoring the training and validation loss curves. This regularized termination is governed by the max_fail parameter, which serves as a checkpoint tolerance threshold. When the validation loss ceases to improve, the algorithm initializes a counter; if no improvement is recorded for a consecutive number of epochs equal to max_fail, the training is definitively halted.

4 Results

To quantitatively validate the predictive accuracy of the regression models, three standard statistical metrics were adopted: Mean Squared Error (MSE), Root Mean Squared Error (RMSE), and the Coefficient of Determination (R^2).

- Mean Squared Error (MSE): It measures the average of the squared residuals between the predicted values and the actual analytical targets. By squaring the errors, it penalizes larger outliers more heavily, making it an excellent indicator of overall model stability.
- Root Mean Squared Error (RMSE): Computed as the square root of the MSE, this metric brings the error back to the same physical scale and unit of measurement as the output variables (the cross-sectional penalization ratios), representing the typical deviation of a prediction.
- Coefficient of Determination (R^2): This metric evaluates the proportion of variance in the dependent variable that is predictable from the input features. It ranges from 0 to 1, where a value close to 1 indicates an almost perfect correlation between the surrogate network's predictions and the analytical target values.

All metrics are computed exclusively on the test split of the dataset, which accounts for 15% of the original data and was never seen by the model during training.

In addition to quantitative evaluation, the model performance can also be assessed qualitatively by graphically comparing the predicted output with the corresponding normative values, as shown in Fig. 7, which illustrates a typical scenario observed after training all three models.

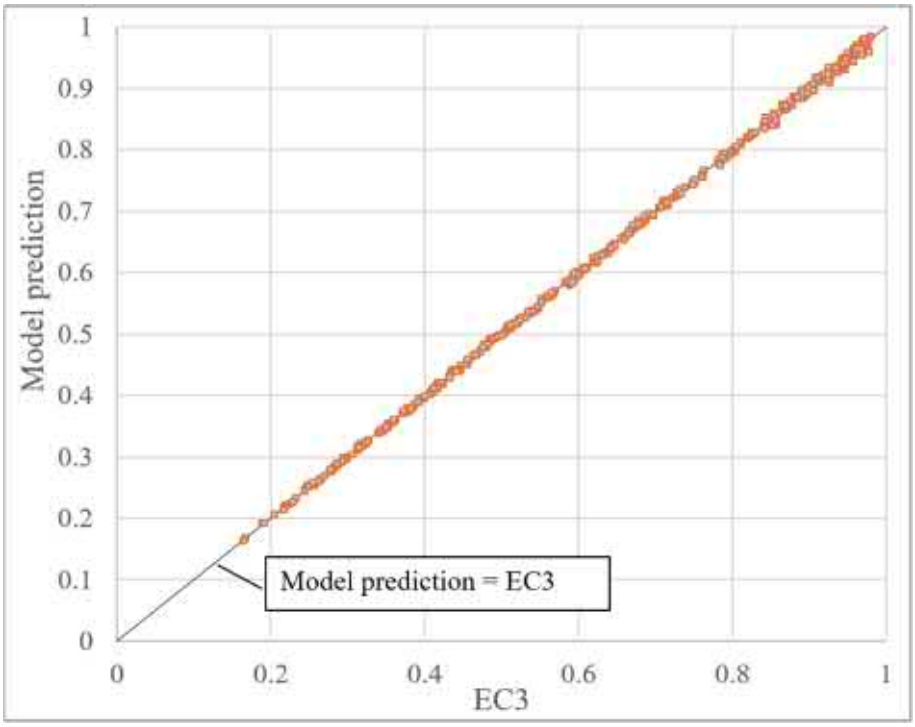


Fig. 7. Typical distribution of the model predictions on the test set after training phase

4.1 Case 1 – Pure Compression

For the pure compression scenario, the parametric optimization selected an architecture comprising 15 hidden neurons, coupled with a max_fail threshold of 10. The training dataset encompassed 2,877 profiles (S235–S355), while the out-of-domain testing set comprised 1260 profiles (S420).

The network's predictions were systematically benchmarked against the analytical targets derived from the EWM procedure of Eurocode 3. The surrogate model demonstrated adequate predictive accuracy, achieving a MSE of 0.000046, a RMSE of 0.0067, and a R^2 of 0.999. In terms of relative error distribution, only 19.44% of the out-of-domain predictions exhibited a relative error exceeding 5%, and a mere 1.19% of the profiles exceeded a 10% error threshold (Fig. 8).

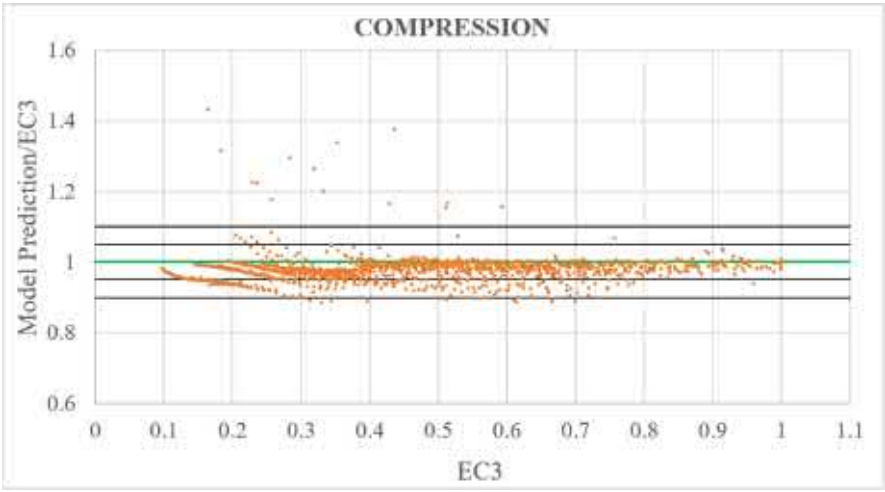


Fig. 8. Distribution of the ratio of predicted A_{eff}/A to EC3 A_{eff}/A A_{eff}/A targets for pure compression

4.2 Case 2 – Bending About the Y-Axis

The optimal topology for bending about the axis of symmetry similarly utilized 15 hidden neurons, with the max_fail parameter set to 10. The training dataset contained 2877 profiles, whereas the independent prediction dataset comprised 959 profiles characterized by $f_y = 420$ MPa.

The comparative analysis revealed outstanding alignment with the analytical standard, achieving an MSE of 0.000017, an RMSE of 0.0041, and an R^2 of 0.999. Remarkably, 100% of the surrogate model predictions fell safely below a strict 5% relative error threshold (Fig. 9).

4.3 Case 3 – Bending About the Z-Axis

In contrast to the previous scenarios, the parametric sensitivity analysis for bending about the non-symmetry axis converged toward a significantly simpler architecture featuring only 5 hidden neurons.

When tested on the 959 unseen S420 profiles, the model proved highly robust, yielding an MSE of 0.00012, an RMSE of 0.011, and an R^2 of 0.995. Regarding the error thresholds, only 6.46% of the predictions presented an error higher than 5%, and a negligible 0.52% exceeded the 10% threshold (Fig. 10)

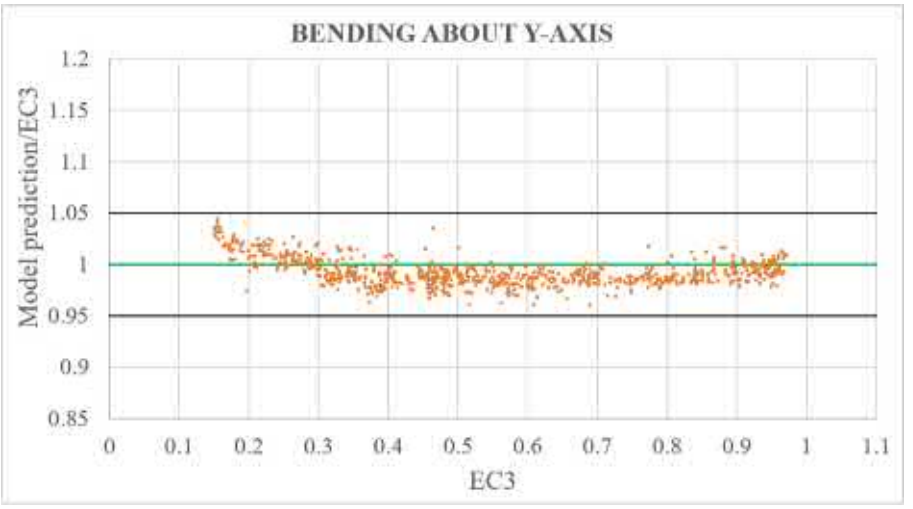


Fig. 9. Distribution of the ratio of predicted $W_{y,eff}/ W_y$ to EC3 $W_{y,eff}/ W_y$ A_{eff}/A targets for bending about the y-axis

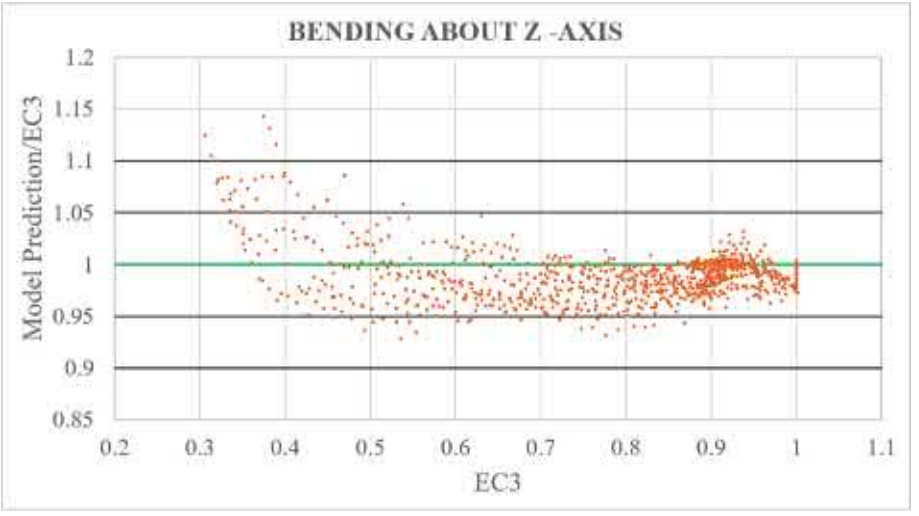


Fig. 10. Distribution of the ratio of predicted $W_{z,eff}/ W_z$ to EC3 $W_{z,eff}/ W_z$ A_{eff}/A targets for bending about the z-axis

5 Discussion and Conclusion

The developed Artificial Neural Network (ANN) proved to be a robust surrogate model for predicting the effective properties of Class 4 cold-formed steel profiles, evaluated herein through the ratio of the effective (penalized) section properties—namely area and elastic section modulus—to their gross counterparts. The model exhibited high predictive

accuracy, with fewer than 2% of the predictions exceeding a 10% error threshold across all investigated loading conditions. Furthermore, hyperparameter optimization ensured stable generalization and controlled extrapolation behaviors. Despite these positive outcomes, the training database was built upon simplified C-profile configurations, whereas commercial profiles frequently feature multiple stiffening lips and web perforations. Consequently, future developments will aim to extend this framework to accommodate advanced geometric complexities by expanding the input layer. In addition, incorporating experimental datasets alongside analytical formulations for network training will allow the model to better capture the real structural behavior of these elements.

References

1. Etim B, Al-Ghosoun A, Renno J et al (2024) Machine learning-based Modeling for structural engineering: a comprehensive survey and applications overview. Buildings 14:3515
2. Thai H (2022) Machine learning for structural engineering: a state-of-the-art review. Structure 38:448–491
3. Sun H, Burton HV, Huang H (2021) Machine learning applications for building structural design and performance assessment: state - of - the - art review. J Build Eng 33:101816
4. European Committee for Standardization (2006) "Eurocode 3: Design of Steel Structures – part 1–5: plated structural elements", EN 1993-1-5:2006. CEN, Brussels
5. Baldassino N, Bernuzzi C, Simoncelli M (2019) Evaluation of European approaches applied to TWCF steel members. Thin-Walled Struct 143:106186
6. Iron A, Steel Institute (2020) North American specification for the Design of Cold-Formed Steel Structural Members. AISI S100-16
7. Moen CD, Schafer BW (2008) Experiments on cold-formed steel columns with holes. Thin-Walled Struct 46:1164–1182
8. Smith FH, Moen CD (2014) Finite strip elastic buckling solutions for thin-walled metal columns with perforation patterns. Thin-Walled Struct 79:187–201

Monotonic and Cyclic Response of Strengthened Dry Joints in Steel Pallet Racks

Alessandro Mei[1](✉), Giovanni Lavacchini[2], Sandro Chiostrini[1], Mario Fagone[1], Giovanna Ranocchiai[1], and Maurizio Orlando[1]

[1] Department of Civil and Environmental Engineering, University of Florence, Florence, Italy
alessandro.mei@unifi.it

[2] Studio Lavacchini, Borgo san Lorenzo, Italy

Abstract. This contribution reports an experimental study on strengthening measures for dry-joint connections in cold-formed steel storage racks, focusing on their down-aisle seismic response. Conventional rack joints often represent a critical vulnerability under earthquake loading; this work therefore investigates practical, industry-feasible retrofit options intended to improve robustness and structural reliability. A test programme on full-scale specimens was carried out under both monotonic and cyclic loading, comparing the unreinforced joint with four bracket-based strengthening configurations (R1–R4), differing in bracket thickness (3 or 5 mm) and fastening system (M12 bolts or M6 self-drilling screws). Relative to the unreinforced joint, all four solutions increased the secant rotational stiffness (by 37–56%) and the peak moment (by 32–41%). Under cyclic loading, the bolted configurations (R2, R4) proved markedly more effective at dissipating energy, with increases of 212% and 205% respectively, against 82% and 148% for the screw-fastened ones (R1, R3). The discussion addresses the governing deformation mechanisms and failure modes, showing that the brackets provide a redundant load path that activates once the beam-to-connector weld fails. Overall, the findings provide actionable, quantitative insight for the seismic design and retrofit of cold-formed steel rack systems, supporting safer and more reliable storage installations in seismic regions.

Keywords: pallet racks · cold-formed steel · beam-to-upright connections · structural retrofit · dry joints

1 Introduction

Cold-formed steel (CFS) pallet racks are modular, low-mass storage structures whose speed of erection has made them ubiquitous in warehousing. Each rack is built from vertical uprights and horizontal pallet beams held together by boltless connectors. Bracing is present only in the cross-aisle plane, where paired uprights form a braced assembly (the "frame"); the down-aisle plane is intentionally left unbraced so that aisles stay clear for handling [1]. The two planes therefore react to horizontal actions differently: the cross-aisle as a truss, the down-aisle as a moment-resisting frame whose lateral stability

© The Author(s), under exclusive license to Springer Nature Switzerland AG 2026
R. Zanon et al. (Eds.): CTA 2026, LNCE 942, pp. 322–333, 2026.
https://doi.org/10.1007/978-3-032-39505-4_28

rests entirely on the rotational stiffness and strength of the beam-to-upright connectors [2, 3]. While seismic strengthening of historic and industrial buildings has progressed quickly, storage racks have attracted far less study. Most of the literature has instead examined the single members - uprights, beams and connectors - and the complete rack frame, using both laboratory tests and numerical models. Upright stability has been examined by several authors in the last decade [4–6]; upright-to-beam joint behaviour by Bernuzzi and Castiglioni [7], Zhao et al. [8, 9], Gusella et al. [10, 11], Mei et al. [12], and Bové et al. [13]; overall rack response has been assessed by fewer authors in the literature, e.g. Bernuzzi et al. [14], Kanyilmaz, Castiglioni et al. with the SEISRACK project [15–18], and Sena Cardoso & Rasmussen [19]; and advanced seismic protection systems by Kilar et al. [20] and Mei et al. [21]. Only recently has a shift in perspective begun to emerge, driven by updated regulations and increasing awareness among end users. The Italian guideline document on the design, verification and safety of racking [22] now makes vulnerability checks under seismic action - and, where they are not met, strengthening of racks already in service - a mandatory step. In parallel, the academic community has started to address this topic: Galeotti et al. [23] studied the influence of locally reinforcing down-aisle rack joints, Donà et al. [24] and Mucedero et al. [25] investigated rack vulnerability and developed fragility curves.

1.1 Aim of the Work

The aim of the present work is to investigate, at the joint scale, a set of local strengthening solutions for the upright-to-beam connections of existing cold-formed steel storage racks. The proposed strengthening configurations were conceived to simultaneously increase the rotational stiffness, ultimate moment capacity, and energy dissipation capacity under cyclic loading of the joints, while remaining simple to manufacture, easy to install on in-service racks, and cost-effective. To this end, four bracket-based configurations - differing in the bracket thickness (3 and 5 mm) and in the fastening system (M12 bolts or M6 self-drilling screws) - were tested under both monotonic and cyclic protocols, in accordance with EN 15512 and ANSI-RMI, and systematically compared with the unreinforced joints in terms of rotational stiffness, moment capacity, hysteretic behaviour, and dissipated energy. The study thus provides an experimental basis for selecting effective and practically feasible retrofit details for the joints of existing storage racks. It represents the first phase of the broader “SAVE-RackS” project, whose subsequent phases extend the investigation to full rack assemblies and to finite element modelling.

2 Experimental Campaign

2.1 Upright-to-Beam Joint Involved

The upright-to-beam joint examined in this study is a semi-rigid connection consisting of two main components: a pallet beam with a closed built-up CFS tubular section (designated A1345M, with 130 mm height, 45 mm base width, and 1.2 mm thickness) and a cold-formed perforated upright with a U-shaped cross-section (“130 U”) and a wall thickness of 2.5 mm. A five-tab connector, 3 mm thick, is welded to the beam end along

three sides. Despite its tubular appearance, the beam is a closed built-up member: two open C-sections lock into one another and are welded, at each end, to the connectors. This typology was adopted precisely because it recurs frequently in racks already installed nowadays. The geometry of the joint is illustrated in Fig. 1. When the joint carries a bending couple, tension is taken up by the connector tabs and compression is reacted by bearing of the beam-end connector against the upright flange. A safety clip is fitted on every specimen to keep the connector engaged with the upright in the event of an accidental impact.

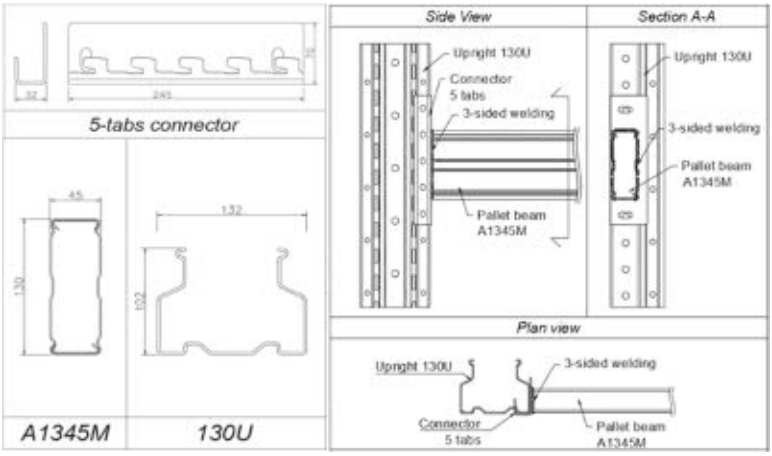


Fig. 1. Cross-sections of investigated joints

2.2 Strengthening Types

The strengthening strategies were designed with three main objectives: increasing the rotational stiffness of the connection to reduce sway sensitivity in the down-aisle direction, raising the collapse moment capacity, and improving the energy dissipation capacity under cyclic loading. In addition, all solutions were required to be simple to apply, easy to install on existing systems, and cost-effective. Several strengthening configurations were investigated during the research project; however, some of them did not yield satisfactory results and were therefore discarded (see [26]). The configurations presented here represent the most effective solutions identified, and are illustrated in Fig. 2:

- R1: 90° brackets (5 mm) fitted top and bottom of the beam and fastened with M6 self-drillers,
- R2: 90° brackets (5 mm) as R1 but secured by a single M12 bolt,
- R3: 90° brackets (3 mm) fitted top and bottom of the beam and fastened with M6 self-drillers,
- R4: 90° brackets (3 mm) as R3 but secured by a single M12 bolt,

The inclusion of the 3 mm bracket variants (R3 and R4), alongside the 5 mm ones (R1 and R2), allows the influence of bracket stiffness on the joint hierarchy to be assessed and enables the evaluation of how a more flexible bracket affects the distribution of internal forces and failure modes within the connection.

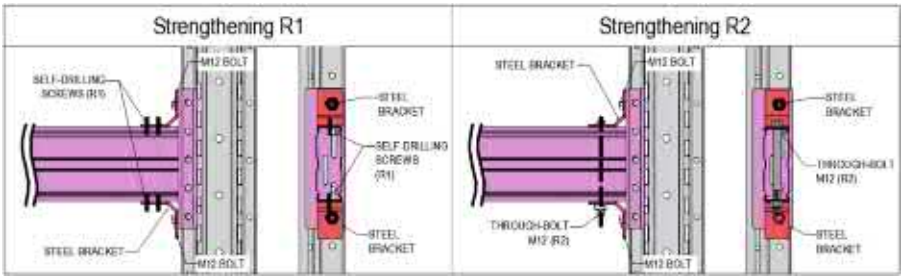


Fig. 2. Strengthening types

2.3 Testing Protocol and Instrumentation

The tests were run on a rig conforming to EN 15512 [27] (Fig. 3), using full-scale beam-to-upright sub-assemblies. Each specimen combined an upright of 750 mm with a pallet beam of 650 mm, the vertical load P being introduced 400 mm (distance d) from the upright face. Under the monotonic protocol P was driven up to collapse; under the cyclic protocol the ANSI-RMI [28] displacement sequence was reproduced. To allow for a statistically meaningful characterization of each joint configuration, the test campaign was extended to include three replicate specimens per configuration, tested under both monotonic and cyclic protocols. This approach makes it possible to account for the variability inherent in cold-formed steel components and boltless connections, and to derive more reliable estimates of stiffness, strength, and energy dissipation capacity for each strengthening type. Load P and the vertical displacement at the loading point were taken directly from the load cell and LVDT built into the machine. A supplementary set of LVDTs (m_i) and draw-wire encoders (s_i, f_i), arranged as in Fig. 4A, was logged to a PC-based acquisition unit together with the load-cell channel. Transducers m_5 and m_6 were installed on the unreinforced joint only, since no reinforcement layout leaves a repeatable position for them.

The total measured deformation is decomposed into three parts (Fig. 4B): the connector rotation Φ (Eq. (1)), the upright rotation Φ_c (Eq. (2)), and the beam rotation Φ_b. From the horizontal LVDT readings, the connector rotation follows as:

$$\Phi = \frac{\delta_1 - \delta_2}{d_{\overline{12}}}, \tag{1}$$

in which $d_{\overline{12}}$ is the gauge spacing; the upright rotation is obtained in the same way as:

$$\Phi_c = \frac{\delta_3 - \delta_5}{d_{\overline{35}}}, \tag{2}$$

with $d_{\overline{35}}$ is the spacing of the corresponding pair.

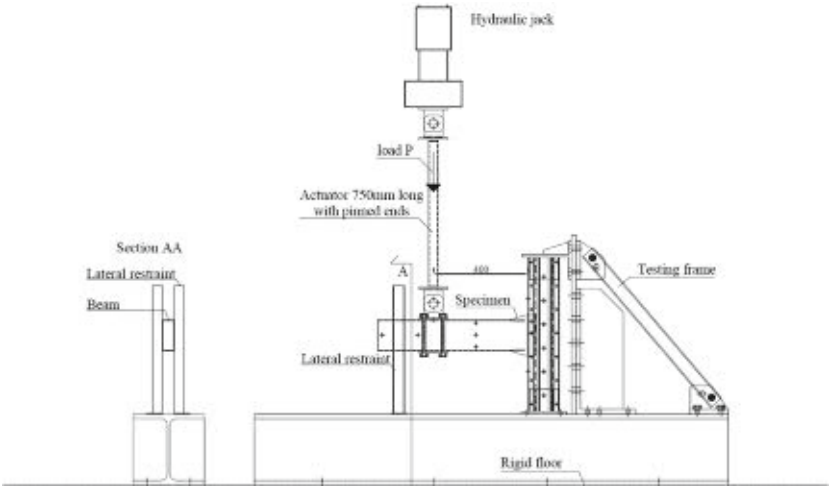


Fig. 3. Testing rig

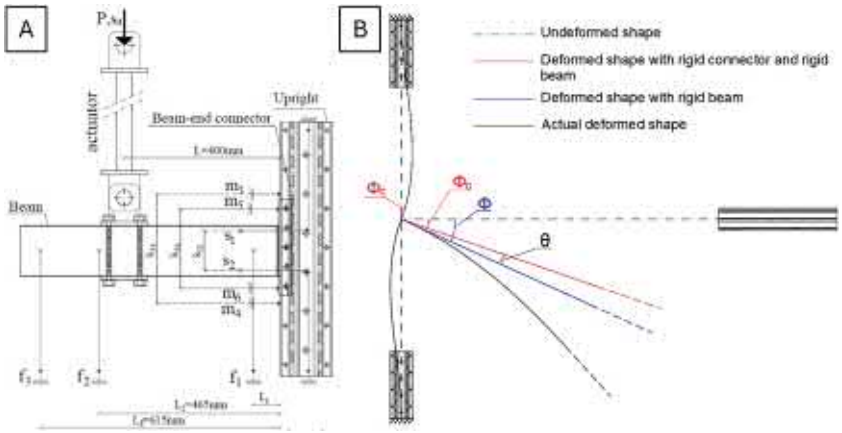


Fig. 4. (A) LVDT layout and instrumentation. (B) Component rotations at the beam-to-upright joint

3 Experimental Results

3.1 Monotonic Tests

Figure 5 reports moment–rotation curves expressed in terms of connector rotation. For each node typology, the individual experimental curves of the three repeated tests are plotted in grey, while the corresponding mean curve, obtained by interpolating the tests on a common rotation grid and averaging point by point, is overlaid in colour. Each typology is assigned a fixed colour, kept consistent throughout the paper, so that the four reinforced configurations and the unreinforced one can be compared directly. Figure 6 reports, for each node typology, the secant rotational stiffness and the ultimate (peak)

moment, both normalised with respect to the unreinforced configuration. For every test the stiffness is derived from the equivalent bilinearization according to EN 15512, while the peak moment is taken directly from the same curve. The value plotted for each typology is the mean of its three repeated tests, divided by the corresponding mean of the unreinforced configuration, taken as unity; the dashed line marks this unreinforced reference, and the error bars represent the test-to-test scatter (standard deviation) of the three repetitions. Relative to the unreinforced joint, the secant rotational stiffness increases by 54% (R1), 37% (R2), 56% (R3) and 37% (R4), and the peak moment by 41% (R1), 40% (R2), 32% (R3) and 38% (R4). All four solutions thus increase both stiffness and capacity, with the increase in peak moment being essentially independent of the configuration (32–41%), whereas the stiffness increase is slightly greater for the screw-fastened brackets (R1, R3) than for the bolted ones (R2, R4).

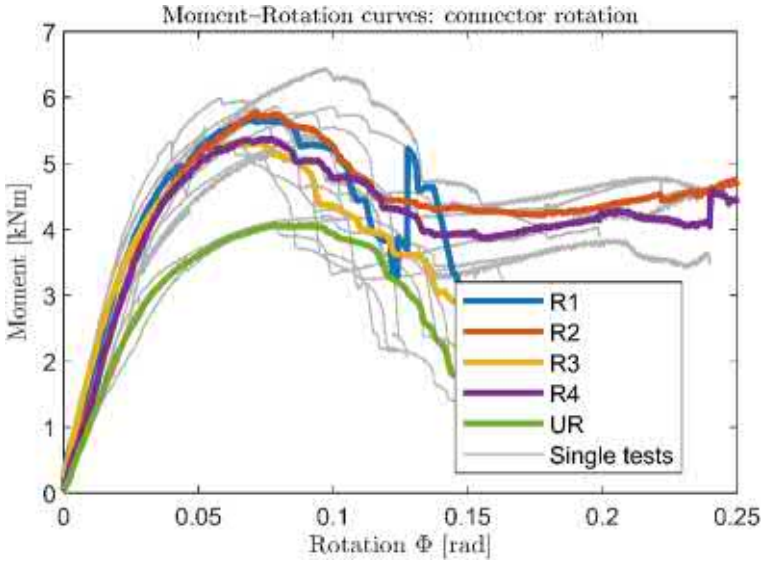


Fig. 5. Moment-rotation curves for each test and mean curve

3.2 Cyclic Tests

Full moment–rotation hysteresis of one representative test per node typology, overlaid for qualitative comparison of loop shape, stiffness degradation, and pinching across configurations is reported in Fig. 7. In terms of energy dissipation, Fig. 8 shows the evolution of the dissipated energy along the loading protocol: dissipated energy per cycle (top) and cumulative dissipated energy (bottom) as functions of cycle number. Individual tests are shown in grey, and the typology means in colour; ordinate values are normalised with respect to the total energy of the unreinforced configuration. The test results show that R2 and R4 increase energy dissipation more (+212% and + 205%) than R1 and R3 do (+82% and + 148%), confirming that M12-bolted brackets (R2, R4) sustain the additional load path more consistently under cyclic reversals than screw-fastened ones (R1, R3).

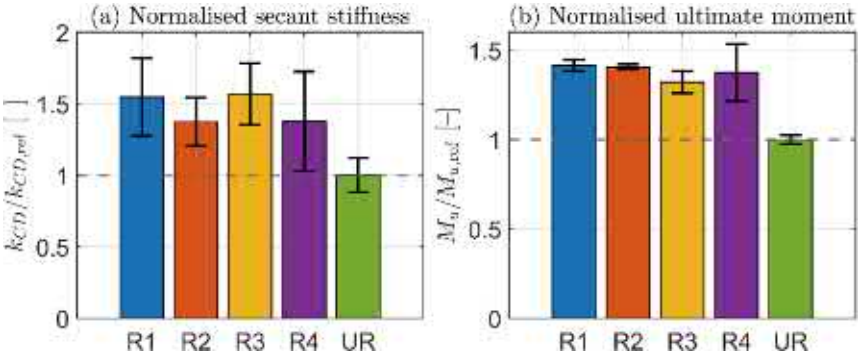


Fig. 6. (a), normalised secant stiffness. (b), normalised peak moment

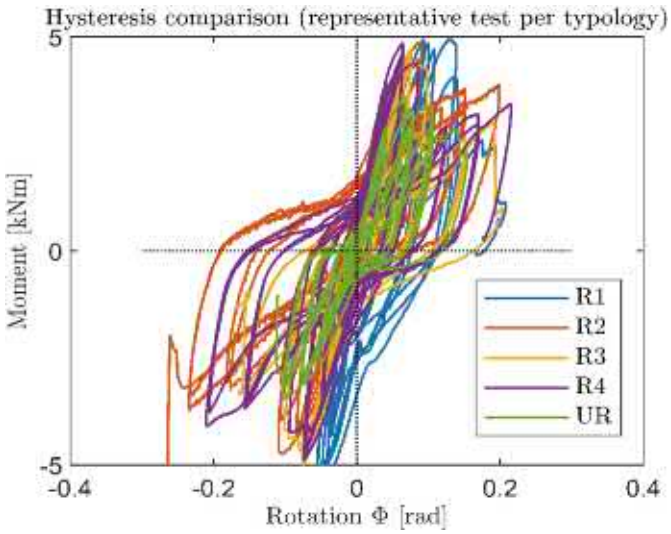


Fig. 7. Moment-rotation plot for one test per typology

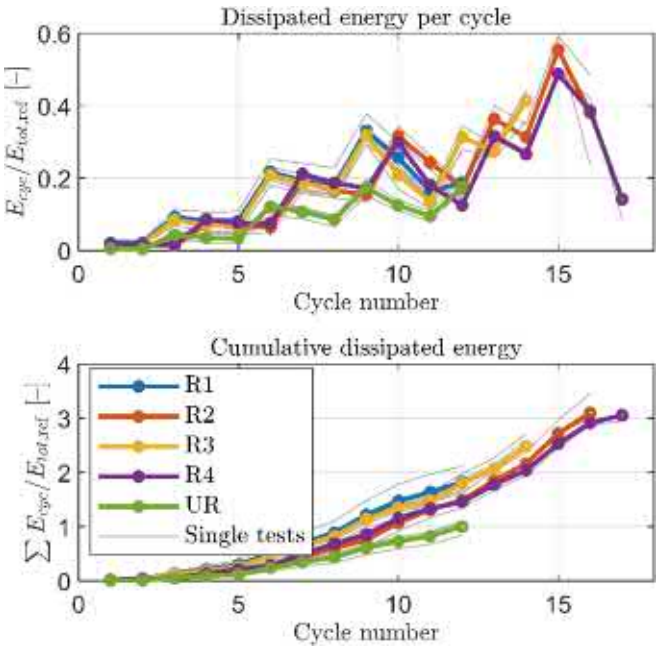


Fig. 8. Top, dissipated energy per cycle (mean). Bottom, cumulative dissipated energy (mean)

4 Discussion

All four strengthening solutions act on the down-aisle response as intended, raising both the secant rotational stiffness (by 37–56% relative to the unreinforced joint) and the peak moment (by 32–41%) (Fig. 6). This is significant because down-aisle stability relies on the flexural behaviour of the connections: a stiffer joint shortens the period and reduces drift demand, while a higher capacity delays the onset of strongly non-linear response. The decisive contribution of the brackets, however, lies in the post-weld phase. Placed above and below the beam, they form a second load path in parallel with the five-tab connector: in every specimen the beam-to-connector weld was the first element to fail, at small displacements, but the brackets then engaged and the joint kept transferring moment and shear. This redundant load path, which is absent in the unreinforced connection, is the primary reason for the observed improvements in structural performance. The capacity of this secondary load path depends on the type of fasteners used and the bracket thickness (Table 1). With M6 screws (R1, R3) collapse proceeds by tensile/pull-out failure of the fasteners, i.e. within the reinforcement itself; with M12 bolts (R2, R4) the bracket-to-beam connection holds, the demand migrates to the upper bolt and triggers punching shear of the 2.5 mm perforated upright (Fig. 9). Thickness plays a parallel role: the stiffer 5 mm brackets (R1, R2) attract more force and shift the demand toward the connector and the upright, whereas the more flexible 3 mm brackets (R3, R4) deform appreciably and spread it more evenly between bracket and connector, acting as a partly deformable, energy-absorbing element rather than a rigid link.



Fig. 9. Left and centre: punching shear failure for the R2 specimen. Right: M6 screws failure in the R1 test

Under cyclic loading all joints exhibited the pinched loops typical of boltless tab connections, with a low-stiffness reloading branch produced by gap opening and closing. By restraining these relative movements, the brackets promote fuller hysteresis loops, slower degradation and greater energy dissipation, both per cycle and cumulatively: the bolted configurations (R2, R4) increased total dissipated energy by 212% and 205% relative to the unreinforced joint, against 82% and 148% for the screw-fastened ones (R1, R3) (Fig. 8), confirming that bolted brackets retain this benefit more consistently, being less susceptible to the loosening that affects screw connections under reversed cyclic loading. Overall, the brackets appreciably improve the seismic behaviour of the joint - increasing stiffness, capacity and dissipated energy simultaneously - but their thickness together with the type of fasteners should be chosen according to capacity-design principles rather than seeking maximum stiffness alone. A few limitations should be acknowledged. All specimens came from a single manufacturer and covered a single upright-to-beam joint, so the absolute values reflect that specific product, while the relative gains between reinforced and unreinforced joints (37–56% in stiffness, 32–41% in moment, 82–212% in dissipated energy) are expected to be more transferable. Moreover, the results are established at the joint scale; their effect at the structural level was assessed in a companion study [29], where the experimental moment–rotation laws of the reinforced joints were used in pushover analyses of full racks.

Table 1. Failure modes

	UR	R1	R2	R3	R4
First element to collapse	Welding between beam and connector				
Ultimate failure (monotonic test)	Welding between beam and connector	Axial capacity of M6 screws	No failure: test halted at actuator stroke limit	Axial capacity of M6 screws	No failure: test halted at actuator stroke limit

(*continued*)

Table 1. (*continued*)

	UR	R1	R2	R3	R4
Ultimate failure (cyclic test)	Welding between beam and connector	Axial capacity of M6 screws	Punching shear failure of upright	Axial capacity of M6 screws	Punching shear failure of upright

5 Conclusions

This paper presented the preliminary experimental results of the SAVE-RackS project on the strengthening of dry beam-to-upright joints in cold-formed steel pallet racks, with reference to their down-aisle seismic response. Four local strengthening solutions, based on 90° brackets installed above and below the beam and fixed either with M12 bolts or with M6 self-drilling screws, were tested under monotonic and cyclic loading and compared with the unreinforced connection. The main findings can be summarised as follows.

1. All four strengthening configurations increased the secant rotational stiffness and the peak bending moment of the connection with respect to the unreinforced joint, confirming the effectiveness of local bracket reinforcement for improving the down-aisle behaviour of existing racks.
2. The fastening system controls the stiffness and the stability of the response: the bolted variants (R2, R4) provide a firmer anchorage of the bracket to the upright and a more regular response than the screwed variants (R1, R3), whose behaviour is more affected by the bearing capacity of the screws.
3. The bracket thickness governs the internal resistance hierarchy: the 5 mm brackets are stiffer but tend to shift the demand toward the perforated upright, whereas the 3 mm brackets deform more and distribute the demand more evenly. The latter behaviour is preferable when a ductile and repairable failure mechanism is sought.
4. Under cyclic loading the strengthened joints exhibited fuller hysteresis loops, reduced pinching and stiffness degradation, and higher per-cycle and cumulative energy dissipation than the unreinforced reference, indicating an improved capacity to withstand earthquake-type demands.

References

1. Dai L, Zhao X, Rasmussen KJR (2018) Flexural behaviour of steel storage rack beam-to-upright bolted connections. Thin-Walled Struct 124:202–217
2. Bajoria KM, Sangle KK, Talicotti RS (2010) Modal analysis of cold-formed pallet rack structures with semi-rigid connections. J Constr Steel Res 66:428–441
3. Mei A, Orlando M, Salvatori L, Spinelli P (2021) Nonlinear static and incremental dynamic analyses for seismic down-aisle behavior of rack structures. Ing. Sismica 38:21–45
4. Bernuzzi C, Pieri A, Squadrito V (2014) Warping influence on the static design of unbraced steel storage pallet racks. Thin-Walled Struct 79:71–82

5. Bertocci L, Comparini D, Lavacchini G, Orlando M, Salvatori L, Spinelli P (2017) Experimental, numerical, and regulatory P-mx-my domains for cold-formed perforated steel uprights of pallet-racks. Thin-Walled Struct 119:151–165
6. Orlando M, Lavacchini G, Ortolani B, Spinelli P (2017) Experimental capacity of perforated cold-formed steel open sections under compression and bending. Steel Compos Struct 24:201–211
7. Bernuzzi C, Castiglioni CA (2001) Experimental analysis on the cyclic behaviour of beam-to-column joints in steel storage pallet racks. Thin-Walled Struct 39:841–859
8. Zhao X, Wang T, Chen Y, Sivakumaran KS (2014) Flexural behavior of steel storage rack beam-to-upright connections. J Constr Steel Res 99:161–175
9. Zhao X, Dai L, Wang T, Sivakumaran KS, Chen Y (2017) A theoretical model for the rotational stiffness of storage rack beam-to-upright connections. J Constr Steel Res 133:269–280
10. Gusella F, Lavacchini G, Orlando M (2018) Monotonic and cyclic tests on beam-column joints of industrial pallet racks. J Constr Steel Res 140:92–107
11. Gusella F, Arwade SR, Orlando M, Peterman KD (2019) Influence of mechanical and geometric uncertainty on rack connection structural response. J Constr Steel Res 153:343–355
12. Mei A, Orlando M, Salvatori L (2023) On the seismic response of rack structures affected by pinching. Procedia Struct. Integr. 44:2318–2325
13. Bové O, López-Almansa F, Ferrer M, Roure F (2022) Ductility improvement of adjustable pallet rack speed-lock connections: experimental study. J Constr Steel Res 188:107015
14. Bernuzzi C, di Gioia A, Gabbianelli G, Simoncelli M (2017) Pushover analyses of hand-loaded steel storage shelving racks. J Earthq Eng 21:1256–1282
15. Gabbianelli G, Kanyilmaz A, Bernuzzi C, Castiglioni CA (2017) A combined experimental-numerical study on unbraced pallet rack under pushover loads. Ing Sismica 34:18–38
16. Kanyilmaz A, Castiglioni CA, Brambilla G, Chiarelli GP (2016) Experimental assessment of the seismic behavior of unbraced steel storage pallet racks. Thin-Walled Struct 108:391–405
17. Kanyilmaz A, Brambilla G, Chiarelli GP, Castiglioni CA (2016) Assessment of the seismic behaviour of braced steel storage racking systems by means of full scale pushover tests. Thin-Walled Struct 107:138–155
18. Castiglioni CA (2016) Seismic behavior of steel storage pallet racking systems, 1st edn. Springer International Publishing, Cham
19. Sena Cardoso F, Rasmussen KJR (2016) Finite element (FE) modelling of storage rack frames. J Constr Steel Res 126:1–14
20. Kilar V, Petrovčič S, Koren D, Šilih S (2011) Seismic analysis of an asymmetric fixed base and base-isolated high-rack steel structure. Eng Struct 33:3471–3482
21. Mei A, Gusella F, Orlando M (2023) A steel bracing system dissipating energy through moment-rotation hysteresis loops. Eng Struct 280:115640
22. Consiglio Superiore dei Lavori Pubblici (2023) Linee guida per la progettazione, esecuzione, verifica e messa in sicurezza delle scaffalature metalliche
23. Galeotti C, Gusella F, Orlando M, Spinelli P (2021) On the seismic response of steel storage pallet racks with selective addition of bolted joints. Structure 34:3806–3817
24. Donà M, Piredda G, Zonta A, Bernardi E, da Porto F (2024) Seismic fragility of unbraced industrial steel pallet racks. Struct Saf 110:102497
25. Mucedero G, Gabbianelli G, Rapone A, Monteiro R (2025) A practice-oriented methodology for seismic loss assessment of steel storage pallet racks. Eng Struct 333:120187
26. Mei A, Lavacchini G, Chiostrini S, Fagone M, Ranocchiai G, Orlando M (2026) Experimental study on strengthening CFS dry joints in existing racking systems. Procedia Struct Integr 78:120–127
27. CEN European Committee for Standardization (2009) EN 15512, steel static storage systems - adjustable pallet racking systems - principles for structural design. CEN, Brussels

28. ANSI-RMI (2023) ANSI MH16.1–2023: specification for the design, testing and utilization of industrial steel storage racks. RMI, Charlotte NC
29. Mei A, Lavacchini G, Matteini F, Orlando M (2026) Preliminary results from nonlinear static tests on pallet racks with strengthened beam-to-upright connections. In: XXX congress CTA 2026

Preliminary Results from Pushover Tests on Pallet Racks with Strengthened Beam-to-Upright Connections

Alessandro Mei[1(✉)], Giovanni Lavacchini[2], Francesca Matteini[2], and Maurizio Orlando[1]

[1] Department of Civil and Environmental Engineering, University of Florence, Florence, Italy
alessandro.mei@unifi.it
[2] Studio Lavacchini, Borgo san Lorenzo, Italy

Abstract. Pallet racking systems are a peculiar construction system within structural engineering. They are made of cold-formed thin-walled steel profiles and are characterized by a high ratio of live loads to self-weight. The global behaviour of these structures is complex, governed by the nonlinearity of their semi-rigid connections, by their sensitivity to second-order effects and to local and distortional buckling phenomena. Within this framework, the experimental assessment of structural capacity and collapse mechanisms plays a key role both for safety verification and for structural design. This contribution presents the preliminary results of an experimental campaign carried out on representative pallet rack configurations subjected to nonlinear static pushover tests. The research focuses on the evaluation of the seismic capacity and structural response in the longitudinal (down-aisle) direction, where global stability relies primarily on the behaviour of moment-resisting frames formed by uprights and beams connected through dry connections. The aim of the research is to identify the system response through the analysis of experimental capacity curves and the identification of ductility and behaviour (q-factor) parameters. In addition to tests on the unstrengthened configuration (reference configuration), the experimental program also investigates the effectiveness of local strengthening details applied to the beam-to-upright connections, with the goal of increasing frame stiffness and displacement capacity. The experimental results provide a basis for a qualitative and comparative discussion of the influence of the strengthening solutions on global capacity, ductility, and system stability, highlighting critical aspects related to connection response and second-order effects.

Keywords: pallet racks · seismic behaviour · pushover test · cold-formed steel · beam-to-upright connections · structural retrofit

1 Introduction

Steel storage pallet racks are peculiar construction system within structural engineering. Although they are conceived as logistics equipment rather than as conventional buildings, they are load-bearing structures, often reaching considerable heights and supporting payloads that exceed their self-weight by one to two orders of magnitude. They

© The Author(s), under exclusive license to Springer Nature Switzerland AG 2026
R. Zanon et al. (Eds.): CTA 2026, LNCE 942, pp. 334–345, 2026.
https://doi.org/10.1007/978-3-032-39505-4_29

are made from cold-formed thin-walled open profiles, systematically perforated along the uprights to allow the adjustable connection of beams, and this combination of slenderness, perforations and high live-load-to-self-weight ratio makes their structural response markedly different from that of ordinary steel frames. Their global behaviour is governed by the pronounced nonlinearity of their semi-rigid connections, by their high sensitivity to second-order (P-Δ) effects - a direct consequence of the unfavourable ratio between gravity loads and lateral stiffness - and by the susceptibility of their thin-walled members to local and distortional buckling phenomena, which may interact with global instability modes. These features are particularly critical under seismic actions, since most of the structural mass coincides with the stored goods, located at the load levels, while the sources of lateral stiffness and energy dissipation are few and concentrated in the joints. In the down-aisle direction, which is the focus of the present work, unbraced pallet racks behave as moment-resisting frames composed of uprights and pallet beams connected by means of boltless beam-end connectors ("dry connections"), in which tabs engage the perforations of the upright without welding or bolting. Lateral stability in this direction relies almost exclusively on the rotational stiffness of these connections and of the base-plate joints, both of which are semi-rigid. As a result, the down-aisle response of the system is essentially connection-driven, and the mechanical characterization of joints plays a key role. The peculiarities of rack connections have motivated an extensive experimental research effort over the past decades [1–3], showing that their hysteretic behaviour is characterized by pinching, limited energy dissipation, and degrading response. Further experimental studies on stiffness, strength and rotational capacity of beam-to-upright connections were carried out, among others, by Gusella et al. [4], who tested four families of industrial rack joints under monotonic and cyclic loading, and by Mei et al., who investigates the role of pinching in the global behaviour of the structure [5, 6]. More recently, preliminary results of monotonic and cyclic tests on dry joints strengthened with steel angles details have been presented [7], showing that suitably designed strengthening devices - particularly steel angles - can substantially increase the stiffness, moment capacity and energy dissipation of the connection.

Global seismic behaviour of racks has been investigated through full-scale testing campaigns of increasing complexity. SEISRACKS and SEISRACKS2 projects provided a comprehensive set of component tests, pallet-beam sliding tests, full-scale pushover, pseudo-dynamic and shaking-table tests on pallet racks [8]. Kanyilmaz et al. performed full-scale pushover tests on unbraced [9] and braced [10] pallet rack configurations, deriving experimental capacity curves, behaviour factor, and showing that the down-aisle seismic response of unbraced racks is governed by the behaviour of the beam-to-upright connections, by pinching-induced loss of dissipation, and by second-order effects. Within this framework, the present paper reports the preliminary results of an experimental campaign of nonlinear static (pushover) tests performed on full-scale pallet rack specimens loaded in the down-aisle direction. The research has a twofold objective. First, the global response of a reference rack configuration with dry beam-to-upright connections is characterized in terms of experimental capacity curves, from which lateral stiffness, displacement capacity, ductility and behaviour-factor estimates are derived. Second, the campaign investigates the effectiveness of local strengthening details applied to the beam-to-upright connections, conceived to increase the rotational stiffness and

the displacement capacity of the joints, and hence the global stiffness and stability of the frame; the influence of the strengthening solutions on global capacity, ductility and second-order sensitivity is discussed in qualitative and comparative terms. While numerous studies have addressed the cyclic characterization of rack joints and full-scale pushover testing of standard rack configurations, experimental evidence on the system-level effectiveness of local strengthening devices applied to existing dry beam-to-upright connections is still very limited: the present work intends to contribute to filling this gap.

The paper is organized as follows. Section 2 describes the tested rack configurations, the strengthening details and the experimental setup and instrumentation; Sect. 3 presents the test protocol and the experimental results in terms of capacity curves and observed damage mechanisms; Sect. 4 discusses the comparative performance of the reference and strengthened configurations, with reference to ductility and behaviour-factor estimates; finally, conclusions and perspectives for the further development of the experimental campaign are drawn in Sect. 5.

2 Experimental Campaign

2.1 Specimen and Investigated Configurations

The experimental campaign investigated the horizontal behaviour of a single rack geometry, representative of a typical steel storage pallet rack layout. The tested specimens consisted of a two-bay, three-level rack system. The first beam level was placed at a height of 1500 mm from the base, while the upper levels were arranged with a constant vertical spacing of 2000 mm. The transverse width of each upright frame was equal to 1000 mm.

All specimens were assembled using the same structural components, to allow a direct comparison between the unstrengthened and strengthened configurations. The upright frames were made of perforated cold-formed steel uprights named M130U, while the pallet beams were A1345 members. The beam-to-upright connections were made through a standard rack connection system consisting in a series of tabs on the beam that goes inside holes in the upright. Figure 1 shows the specimens layout and detail of a typical, unstrengthened, upright-to-beam joint.

Since one structural configuration was investigated in terms of global geometry, member typology and loading arrangement, the differences among the tested specimens were exclusively related to the presence and type of strengthening system. In total, three full-scale specimens were tested: one standard (unstrengthened) rack, used as reference configuration, and two strengthened racks, each equipped with a different strengthening layout [7]. The unstrengthened specimen allowed the baseline lateral response of the rack system to be assessed, while the strengthened specimens were used to evaluate the effectiveness of the proposed retrofit solutions in modifying the global pushover behaviour.

Materials used are S350GD for uprights and S355 for beams and angle brackets, grade 8.8 steel bolts for bolted connections. Nominal and tested properties for each steel are reported in Table 1.

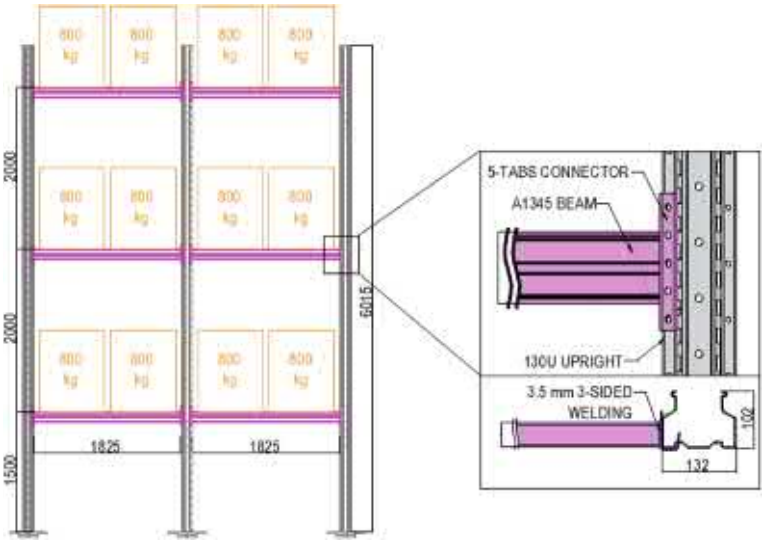


Fig. 1. On the left, the reference specimen; on the right, the upright-to-beam joint

Table 1. Nominal and experimental values of steel properties

	$f_{y,nom}$ [MPa]	$f_{u,nom}$ [MPa]	f_y [MPa]	f_u [MPa]
Uprights	350	420	368	497
Pallet beams	355	510	398	466
Steel angles	355	510	395	570

2.2 Strengthening Layouts

The configurations investigated in this study are summarized in Table 2 and displayed in Fig. 2. The reference specimen is denoted as **NR**, while the two strengthened configurations are denoted as **R1** and **R2**. This nomenclature is adopted throughout the paper to compare lateral stiffness, maximum resistance, deformation capacity and observed failure mechanisms.

Table 2. Test matrix

ID	Geometry	Uprights	Beams	Strengthening layout
NR	2 bays, 3 levels	M130U	A1345	None
R1				Steel angles + SDS
R2				Steel angles + M12

Both R1 and R2 are local retrofit measures that bolt the angle brackets to the upright and differ in the bracket-to-beam connection, aimed at improving the rotational stiffness of the beam-to-upright joint, its moment capacity, and its cyclic response (pinching reduction and energy dissipation), while remaining simple to install on existing racks:

- R1 adopts two steel angles, one above and one below the beam, each bolted to the upright and fastened to the beam by M6 self-drilling screws. The angles couple the beam end directly to the upright, activating a supplementary force-transfer path in parallel with the standard connector. This is intended to bypass the connector-to-beam welding, increase moment transfer and improve cyclic stability.
- R2 uses the same arrangement but fastens the angles to the beam with an M12 grade 8.8 through-bolt. The aim is a more robust bracket-to-member coupling than with smaller fasteners, promoting stable force transfer and a greater contribution of the angles to moment and shear transmission at large deformations.

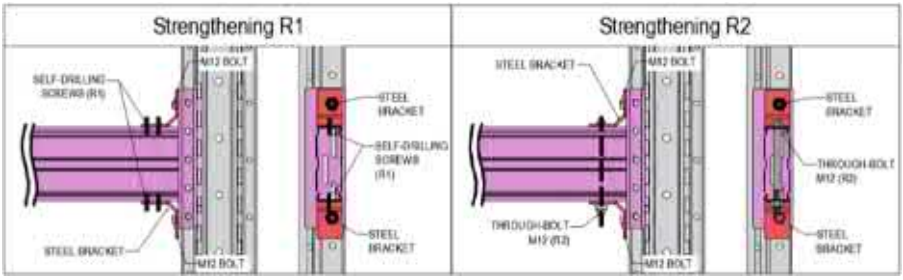


Fig. 2. Details of the two strengthening typologies

2.3 Test Protocol

Tests were carried out by means of a dedicated reaction steel frame made of HE300B columns and beams, capable of effectively reacting the lateral forces developed during testing and, at the same time, of supporting the weight of the pallets in case these fell following the collapse of the rack (Fig. 3). The rack was anchored to the test frame through bolted base plates, assuming the connections to the concrete industrial floor (or concrete foundation) to be overstrength and therefore not governing the structural response. Vertical loads were applied using reinforced concrete masses weighing approximately 8000 N each. Horizontal loads were applied through a dedicated load-distribution system, designed to produce a triangular force distribution, connected to an electro-mechanical actuator with a capacity of up to 100 kN.

A pair of encoders were used at each load level to measure the displacements and any torsional response of the system, while $4 + 4$ biaxial inclinometers were employed to measure the rotations of the upright-to-beam joints at the first load level. A close-up view of the inclinometers and encoders is reported in Fig. 4.

The load was applied in tension until collapse occurred or until the lateral load dropped by more than 15% from its peak value.



Fig. 3. Overall view of the specimen and reaction frame, showing the load distribution system used to reproduce a triangular load pattern and the load actuator (on the right), and the empty rack supporting the encoders (on the left)



Fig. 4. Details of inclinometers (left) and encoders (right). Inclinometers on beams on the other side are named 5 and 6

2.4 Performance Indices

For each test, the following performance indices were evaluated:

1. Ultimate displacement and maximum base shear. They bound the experimental capacity curve: the maximum base shear is the peak of the force–displacement response, the ultimate displacement is taken at a conventional strength-degradation threshold or at the last reliable step before collapse. Together they characterise the global lateral capacity in the down-aisle direction.
2. Beam-to-upright joint rotations. Measured by the biaxial inclinometers at the first load level, they quantify the local demand on the dry connections and allow comparison with the rotational capacity from component tests, verifying whether the connection governs the global mechanism and identifying the onset of joint nonlinearity.
3. Conventional yield point and behaviour factor (q-factor) per ECCS No. 45. The capacity curve is idealised through a bilinear approximation, from which the conventional yield displacement and force are derived following the ECCS-45 procedure.
4. Second-order sensitivity index. The ratio between the destabilising gravity action on the deformed configuration and the storey shear resistance, quantifying P–Δ effects. As the tests use physical masses, these effects are already embedded in the capacity curves, so θ measures their relative weight rather than adding a contribution. Tracking the maximum θ over the storeys versus top displacement identifies where stability becomes critical, providing a basis to discuss the influence of the strengthening details.

3 Experimental Results

3.1 Assess of Performance Indices

Figure 5 reports capacity curves of each tested rack: the horizontal load P was evaluated from a load cell placed in front of the actuator, while the displacement reported refers to the average value of the two top encoders.

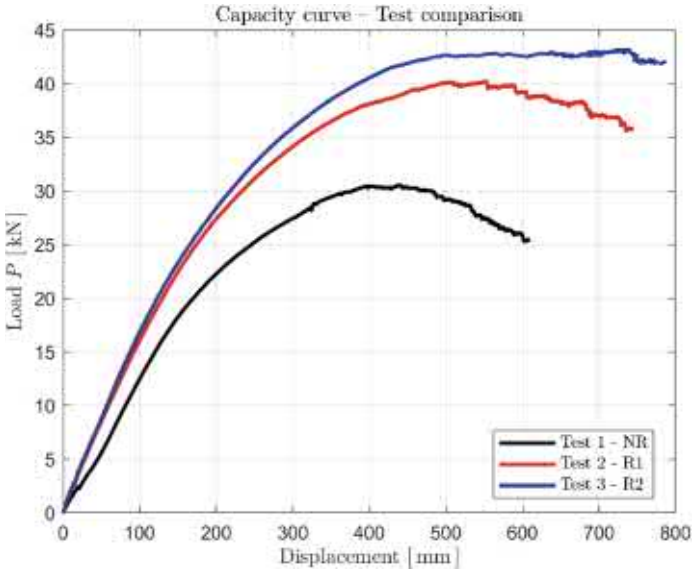


Fig. 5. Comparison of the experimental capacity curves from the three pushover tests

Figure 6 shows upright-to-beam rotation curves evaluated as the relative rotation between beam and upright, i.e. by subtracting the upright rotation from the beam rotation.

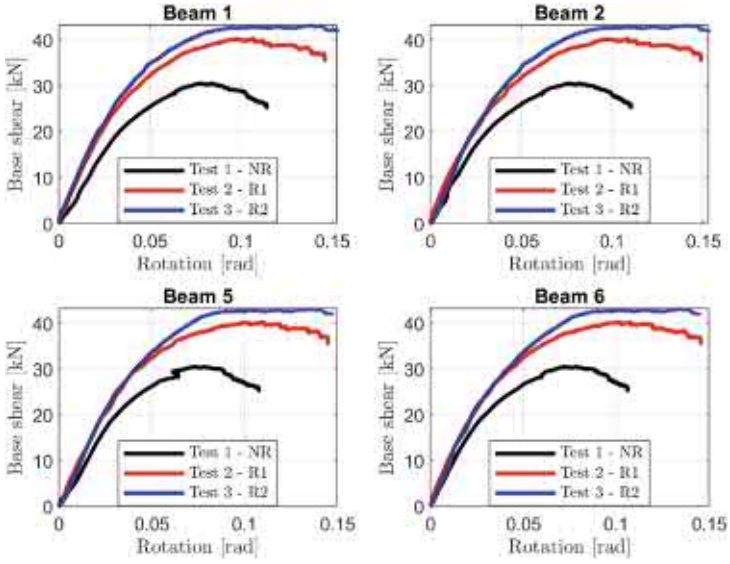


Fig. 6. Upright-to-beam rotations

Table 3 reports peak displacements and base shears for all specimens; tests marked "*" were stopped at a base-shear reduction exceeding 15%, others for safety reasons.

Table 3. Maximum displacements and base shears for all the specimens

Specimen	Maximum displ. [mm]	Maximum base shear [kN]
NR*	609.0	30.55
R1	743.8	40.23
R2	787.2	43.14

Second-order (P–Δ) effects were quantified through the interstorey stability coefficient θ (Eq. (1)), evaluated at each load level i according to EN 16681 [11]:

$$\theta_i = \left(P_{tot,i} \cdot d_{r,i}\right) / \left(V_{tot,i} \cdot h_i\right) \tag{1}$$

where $P_{tot,i}$ is the gravity load at level i and above, $d_{r,i}$ the interstorey drift, $V_{tot,i}$ the storey shear, and h_i the interstorey height. Gravity loads were obtained from the known applied masses, drifts from the encoder readings, and storey shears from the actuator force under the imposed triangular distribution. Since the tests were carried out with physical masses, P–Δ effects are inherently embedded in the measured capacity curves; θ therefore quantifies their relative weight rather than adding a further contribution. For each configuration, the envelope of the maximum θ over the stories is reported in Fig. 7 against the top displacement, with the thresholds θ = 0.10, 0.20 and 0.30 shown for reference. Lastly, Fig. 8 reports behaviour factors, maximum base shears and displacements normalised with respect to the standard rack ("NR") to clearly shows improvements in terms of seismic capacity. The behaviour factor has been evaluated according to [10] and it is derived from the experimental pushover curve following the ECCS procedure. The initial stiffness k_1 is estimated by least-squares regression through the origin over the 0–40% F_u range. The conventional yield point (d_y, F_y) is taken at the intersection of the k_1 line with a secondary line of slope $k_1/10$ passing through the peak load point (d_u, F_u). The idealised displacement $d' = F_u / k_1$ defines the elastic limit on the capacity curve. The behaviour factor is then computed as $q = \Omega \cdot q_0$, where $\Omega = F_u / F_\gamma$ is the overstrength factor and $q_0 = d_u / d'$ the idealised ductility ratio.

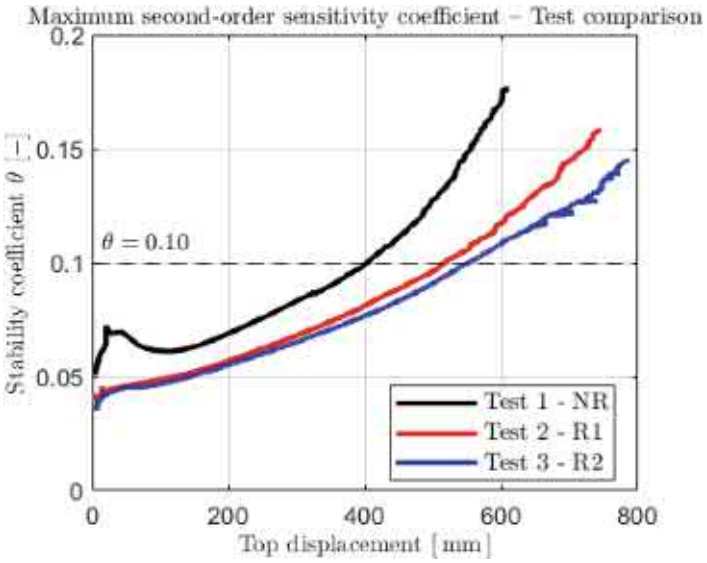


Fig. 7. Second-order sensitivity coefficient

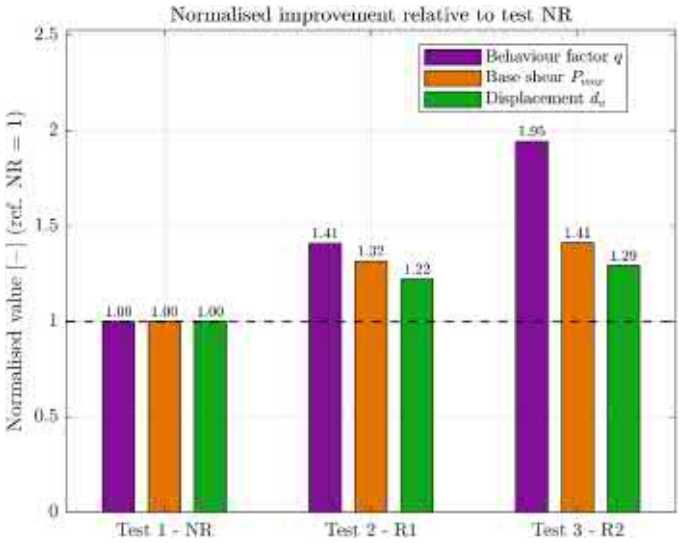


Fig. 8. Behaviour factor, maximum base shear and displacement normalised to unstrengthened specimen

4 Discussion

The three configurations share a comparable elastic branch but diverge beyond it: both retrofits improve every performance index over the reference rack, with R2 (M12 bolt) consistently outperforming R1 (self-drilling screws). The capacity curves in Fig. 5 quantify the gain in lateral capacity. The unstrengthened rack peaks at about 30 kN at roughly 400 mm, then softens to about 25 kN at the ultimate displacement (610 mm). The reinforced specimens develop a stiffer ascending branch and higher resistance, with peak base shears of approximately 40 kN (R1) and 43 kN (R2). Their post-peak response also differs: R2 sustains a nearly flat plateau up to about 785 mm with minimal degradation, whereas R1 shows a progressive, stepwise loss of resistance related to localised damage at the screwed brackets. The M12 bolt therefore delivers both the highest resistance and the most stable post-peak response, consistent with its role at large deformations. The rotation curves (Fig. 6) clarify the local origin of this behaviour and are almost identical for the four monitored joints (1, 2, 5 and 6). The brackets increase the rotational stiffness while extending the available rotation capacity, the mechanism underlying the global gains in Fig. 5. The synthetic parameters in Fig. 8 rank these improvements, R2 being the most effective: the behaviour factor increases by 1.41 (R1) and 1.95 (R2), the maximum base shear by 1.32 and 1.41, and the ultimate displacement by 1.22 and 1.29. The stability assessment in Fig. 7 shows that second-order effects, though significant given the high vertical-load-to-self-weight ratio, remain moderate, with the maximum θ below 0.20 throughout (about 0.175 for NR, 0.16 for R1, 0.145 for R2). At any given displacement NR shows the highest θ and R2 the lowest, and $\theta = 0.10$ is reached at about 430 mm for NR against roughly 560 mm (R1) and 600 mm (R2). The reinforced frames thus postpone second-order sensitivity and attain a lower θ at collapse despite their larger displacement capacity. The small early θ peak in NR ($\approx$30 mm) reflects the initial slip of the dry connection. Overall, local strengthening of the beam-to-upright connections is an effective down-aisle retrofit strategy, improving stiffness, resistance, ductility and stability margin simultaneously, with R2 best across all indices.

5 Concluding Remarks

This contribution presented the preliminary results of a pushover testing campaign on full-scale, two-bay three-level pallet racks in the down-aisle direction, comparing an unstrengthened configuration (NR) with two strengthened configuration types of local strengthening of the beam-to-upright connections: steel angles with self-drilling screws (R1) or an M12 bolt (R2). Both retrofits improve every performance index with respect to the unstrengthened rack, the bolted solution (R2) being consistently the most effective: it nearly doubles the behaviour factor (+95%) while raising base shear by 41% and ultimate displacement by 29%. The down-aisle response is governed by the beam-to-upright connection: in NR the dry tabs-in-holes joint yields and deforms first while uprights and beams stay essentially elastic, so the global nonlinearity derives almost entirely from the flexible joint; the steel angles instead increase joint stiffness and transferred moment and extend the available rotation, with R2 also providing the most stable post-peak plateau. Second-order effects remain moderate, with the maximum θ below 0.20

for all configurations and the reinforced frames attaining a lower θ at collapse despite their larger displacement capacity.

Overall, simple locally applied connection retrofits can meaningfully improve the seismic performance of existing racks, with a favourable effect on the behaviour factor beyond the mere increase in resistance. These findings rely on monotonic pushover tests, which represent the first stage of the research and are therefore preliminary and qualitative; they will be consolidated through correlation with component-level joint tests and through the cyclic pushover tests that the authors will carry out in the next stage to characterise the dissipative response of the strengthened connections.

References

1. Markazi FD, Beale RG, Godley MHR (1997) Experimental analysis of semi-rigid boltless connectors. Thin-Walled Struct 28:57–87
2. Bernuzzi C, Castiglioni CA (2001) Experimental analysis on the cyclic behaviour of beam-to-column joints in steel storage pallet racks. Thin-Walled Struct 39:841–859
3. Aguirre C (2005) Seismic behavior of rack structures. J Constr Steel Res 61:607–624
4. Gusella F, Lavacchini G, Orlando M (2018) Monotonic and cyclic tests on beam-column joints of industrial pallet racks. J Constr Steel Res 140:92–107
5. Mei A, Orlando M, Salvatori L, Spinelli P (2021) Nonlinear static and incremental dynamic analyses for seismic down-aisle behavior of rack structures. Ing Sismica 38:21–45
6. Mei A, Orlando M, Salvatori L (2022) On the seismic response of rack structures affected by pinching. Procedia Struct Integr 44:2318–2325
7. Mei A, Lavacchini G, Chiostrini S, Fagone M, Ranocchiai G, Orlando M (2026) Experimental study on strengthening CFS dry joints in existing racking systems. Procedia Struct. Integr. 78:120–127
8. Castiglioni CA (2016) Seismic behavior of steel storage pallet racking systems, 1st edn. Springer, Milan
9. Kanyilmaz A, Castiglioni CA, Brambilla G, Chiarelli GP (2016) Experimental assessment of the seismic behavior of unbraced steel storage pallet racks. Thin-Walled Struct 108:391–405
10. Kanyilmaz A, Brambilla G, Chiarelli GP, Castiglioni CA (2016) Assessment of the seismic behaviour of braced steel storage racking systems by means of full scale push over tests. Thin-Walled Struct 107:138–155
11. CEN European Committee for Standardization (2016) EN 16681: steel static storage systems — adjustable pallet racking systems — principles for seismic design. CEN, Bruxelles

Lattice Infill Strategies for Lightweight and Stiffened Steel Structural Joints Enabled by Additive Manufacturing

Daniele Mattoccia(✉), Agnese Natali, and Francesco Morelli

Department of Civil and Industrial Engineering, University of Pisa, Pisa, Italy
daniele.mattoccia@phd.unipi.it

Abstract. Additive Manufacturing (AM) introduces new possibilities for the design and fabrication of steel structural joints, where geometric complexity, stress concentrations and fabrication constraints often limit the effectiveness of traditional welded stiffeners. Among AM-enabled solutions, architected lattice materials offer a compelling opportunity to reduce weight while enhancing stiffness and improving load redistribution. Their periodic or graded cellular topology enables a highly tunable mechanical response, making them suitable for replacing solid steel regions that are typically oversized to satisfy stiffness demands. Despite the growing use of lattices in aerospace and mechanical engineering, their structural application in steel construction—particularly their integration into real joints—remains rarely explored, and a systematic framework for lattice design and application to full-scale steel joints is still lacking.

This work proposes a comprehensive framework for the design, modelling and validation of lattice-infilled steel joints. The study analyses the mechanical behaviour of BCC lattice materials, distinguishing between stretch- and bending-dominated topologies and discussing the role of unit-cell size, strut thickness and nodal blend radius. The methodology is applied to the redesign of a real steel joint, demonstrating gains of approximately 54% in stiffness and 76% in mass reduction compared to the original welded configuration.

Keywords: Additive Manufacturing · Lattice Architected Materials · Steel Structural Joints · Lightweight Design · Body-Centered Cubic · Laser Powder Bed Fusion

1 Introduction

Steel joints play a decisive role in the structural behaviour of complex systems, governing stiffness, load redistribution and overall stability. In free-form and architecturally demanding structures—such as grid-shells and spatial frames—joints become highly intricate regions where multiple members converge, often under multi-axial stress states. These zones are typically characterised by pronounced stress concentrations, geometric irregularities and strict fabrication tolerances. Traditional stiffening strategies, based on welded plates, ribs or solid steel blocks, are generally effective in ensuring structural safety, but they often result in excessive material usage, limited geometric adaptability and labour-intensive fabrication processes.

© The Author(s), under exclusive license to Springer Nature Switzerland AG 2026
R. Zanon et al. (Eds.): CTA 2026, LNCE 942, pp. 346–356, 2026.
https://doi.org/10.1007/978-3-032-39505-4_30

The increasing architectural demand for geometrically complex and non-repetitive structures has further exposed the limitations of conventional fabrication paradigms. In free-form grid-shells, joints frequently emerge as the critical bottleneck in terms of cost, constructability and structural optimisation, requiring extensive machining procedures.

In this context, metal Additive Manufacturing (AM) offers a paradigm shift in the design and production of steel structural joints. By enabling the fabrication of highly complex geometries directly from digital models, AM removes many of the constraints associated with subtractive or assembly-based manufacturing. Technologies such as Laser Powder Bed Fusion (LPBF) allow the integration of intricate internal features, smooth geometric transitions and functionally optimised material distributions within a single component.

Among the design strategies enabled by AM, lattice architected materials represent a particularly promising approach for the lightweight stiffening of structural components. Their mechanical behaviour is governed by topology, relative density and unit-cell geometry, as discussed by Gibson & Ashby [1]. Bending-dominated configurations such as Body-Centered Cubic (BCC) structures exhibit progressive deformation mechanisms characterised by strut bending, local buckling and stress redistribution (Maconachie et al. [2]; Miao et al. [3]; Liu et al. [4]).

The influence of geometric parameters — such as unit-cell size, strut thickness and nodal blending radius — on stiffness, strength and local stress distribution has been extensively documented in recent studies on lattice optimisation and AM design (Meyer et al. [5]; Pan et al. [6]).

Despite their widespread adoption in aerospace and mechanical engineering, the application of lattice architected materials to structural steel joints remains limited.

Existing research has focused on material characterisation and small-scale specimens (Köhnen et al. [7]; Alwattar & Mian [8]), and only limited work has addressed their integration within real structural scale components.

Recent investigations have also explored functionally graded lattice strategies in metallic AM components, demonstrating substantial improvements in both strength and energy absorption [Waqar et al. [9], yet such approaches have not been extended to structural steel joints in construction

This work proposes a comprehensive framework for the design, modelling and validation of lattice-infilled steel joints, positioning lattice materials as effective structural stiffening strategies for next-generation joints.

2 Methodological Framework

The methodology follows a multi-scale approach. At the mesoscale, BCC lattice configurations are investigated numerically, focusing on the influence of unit cell size, strut radius and nodal blending radius on stress distribution and peak stress sensitivity. This phase identifies a representative topology balancing mechanical performance and LPBF manufacturability constraints.

The selected configuration is then characterized through compression analyses on downscaled specimens. An equivalent continuum material model is derived through

homogenization, enabling efficient representation of the lattice in structural-scale finite element analyses.

Finally, the methodology is applied to the redesign of a real steel joint from the Fuksas Rhike Park grid-shell. The performance requirements of the original configuration define the design targets. A parametric sensitivity analysis—varying lattice thickness and unit cell size—identifies a configuration satisfying both structural and manufacturing requirements, which is then evaluated and compared against the reference solution.

3 Mesoscale Mechanical Behaviour and Stress Sensitivity of BCC Lattice Infills

A dedicated mesoscale investigation is carried out to assess the mechanical behaviour of lattice infills and support the selection of a suitable configuration. The study focuses on Body-Centered Cubic (BCC) lattices, selected for their favourable manufacturability under LPBF, including limited unsupported horizontal members, good powder removal capability and smooth load transfer at nodes.



Fig. 1. BCC unit cell: total volume (left), strut skeleton (centre), Void part (right)

A fundamental distinction is made between stretch-dominated and bending-dominated architectures (Fig. 2). In stretch-dominated lattices, loads are primarily transferred through axial forces in the struts, resulting in high stiffness and strength. Bending-dominated lattices deform through flexural mechanisms, leading to lower initial stiffness but enhanced ductility and energy absorption. This distinction directly influences stiffness, failure modes and load redistribution mechanisms.

The analysis investigates the influence of key geometric parameters—unit cell size, strut thickness and nodal blending radius—on stress distribution and peak stress development. These parameters directly control the relative density of the lattice, defined as:

$$\rho* = Vsolid/Vcell \tag{1}$$

where V_{solid} is the volume of the struts and V_{cell} is the total volume of the unit cell (Fig. 1).

A series of finite element compression simulations is performed on lattice blocks with varying geometric configurations. Three representative cases are considered: BCC $10 \times 10 \times 10$ with $t = 1.25$ mm, BCC $25 \times 25 \times 25$ with $t = 2.5$ mm, and BCC $15 \times 15 \times 15$ with $t = 2.5$ mm, and BCC $12.5 \times 12.5 \times 12.5$ with $t = 2.5$ mm.

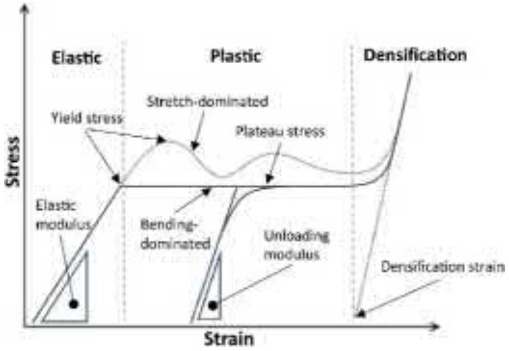


Fig. 2. Typical stress–strain behaviour of stretch-dominated (dotted) and bending-dominated (solid) lattice structures (after Maconachie et al. [2])



Fig. 3. BCC 25 × 25 × 25, t = 2.5 mm ($\rho^* \approx 4.9\%$)

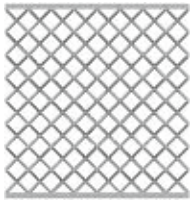


Fig. 4. BCC 10 × 10 × 10, t = 1.25 mm ($\rho^* \approx 7.1\%$)

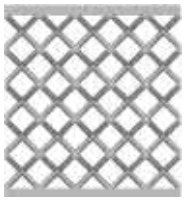


Fig. 5. BCC 15 × 15 × 15, t = 2.5 mm ($\rho^* \approx 12.7\%$)

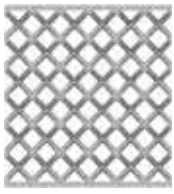


Fig. 6. BCC 12.5 × 12.5 × 12.5, t = 2.5 mm ($\rho^* \approx 17.7\%$)

The BCC 25 × 25 × 25 configuration in Fig. 3 exhibits typical bending-dominated behaviour (Figs.8,14), with low initial stiffness, a clear peak load followed by softening, and a pronounced plateau associated with progressive strut buckling. The BCC 15 × 15 × 15 configuration in Fig. 5 shows a significantly stiffer response, indicating a transition towards mixed bending–stretching behaviour (Figs.10,13). Compression simulations provide force–displacement curves capturing the full mechanical response and enabling the identification of stress hotspots at strut junctions.

The BCC 12.5 × 12.5 × 12.5 in Fig. 6 configuration, sharing the same strut thickness (t = 2.5 mm) as the 15 × 15 × 15 but with a smaller cell size, exhibits a further increase in relative density (approximately 17–18% solid), resulting in a stiffer and stronger response shown in Figs.9,12. The shorter effective strut length enhances nodal constraint

and reduces the tendency towards strut buckling, producing a more pronounced elastic regime and a higher peak load, though the post-peak behaviour retains some softening associated with residual bending-dominated mechanisms.

The BCC 10 × 10 × 10 configuration in Fig. 4, characterised by a reduced strut thickness (t = 1.25 mm) relative to the cell size, presents a distinctly different behaviour (Figs.7,11). Despite the small cell size — which would geometrically favour higher stiffness — the thinner struts limit load-bearing capacity and promote earlier stress localisation at nodal junctions. The resulting response is governed by bending mechanisms, with moderate initial stiffness, a well-defined peak followed by softening, and stress concentrations more sensitive to the nodal geometry than in the thicker-strut configurations.

The equivalent Young's moduli derived from the compression simulations for all four configurations are summarised in Table 1. The results confirm that relative density — governed by the interplay between cell size and strut thickness — is the primary driver of stiffness. The BCC 12.5 × 12.5 × 12.5 (t = 2.5 mm) configuration achieves the highest equivalent modulus (2.72 GPa), as the combination of small cell size and relatively thick struts maximises nodal constraint and axial load transfer. The BCC 15 × 15 × 15 (t = 2.5 mm) follows with 1.36 GPa, consistently with its intermediate relative density. Notably, the BCC 10 × 10 × 10 (t = 1.25 mm) yields a comparatively low modulus (0.411 GPa) despite its small cell size, demonstrating that strut thickness has a dominant influence over cell size alone. The BCC 25 × 25 × 25 (t = 2.5 mm) exhibits the lowest stiffness (0.32 GPa), reflecting its predominantly bending-dominated response at low relative density.

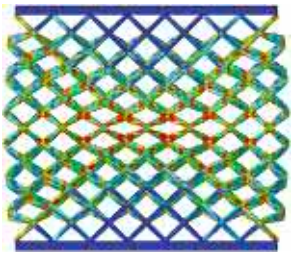


Fig. 7. Von Mises stress distribution – BCC 10 × 10 × 10, t = 1.25 mm

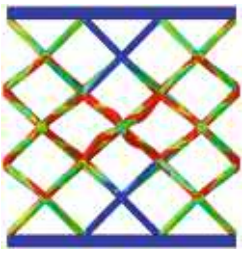


Fig. 8. Von Mises stress distribution - BCC 25x25x25, t = 2.5 mm

A sensitivity analysis on the nodal blending radius (Fig. 15) shows that increasing the radius progressively reduces peak stresses at nodes. However, this improvement is accompanied by an increase in local solid volume, reducing lightweight efficiency, and by potential overhang features that may compromise LPBF printability. Based on this trade-off, a blend radius of 1 mm was identified as the most suitable configuration. A physical demonstrator (BCC 25 × 25 × 25, t = 2.5 mm) shown in Fig. 16 has been produced via LPBF and exhibits good correspondence with the CAD model; experimental characterisation is in progress.

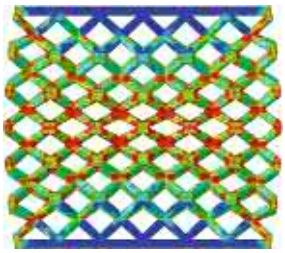


Fig. 9. Von Mises stress distribution - BCC 12.5x12.5x12.5, t = 2.5 mm

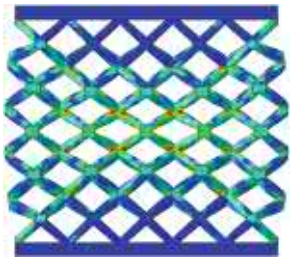


Fig. 10. Von Mises stress distribution - BCC 15x15x15, t = 2.5 mm

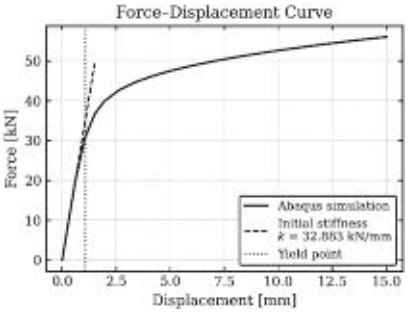


Fig. 11. Force-displacement - BCC 10x10x10, t = 1.25 mm

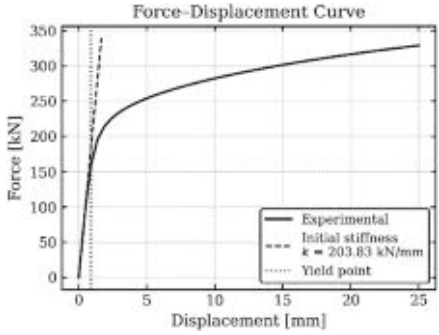


Fig. 12. Force-displacement - BCC 12.5x12.5x12.5, t = 2.5 mm

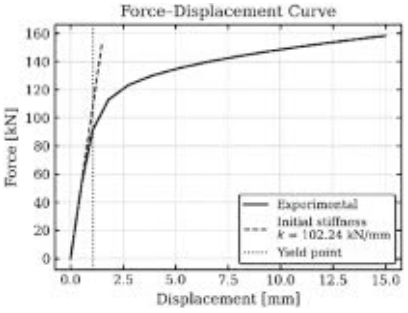


Fig. 13. Force-displacement - BCC 15x15x15, t = 2.5 mm

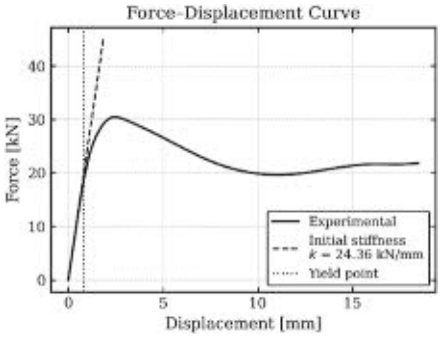


Fig. 14. Force-displacement - BCC 25x25x25, t = 2.5 mm

Table 1. Equivalent young modulus for different patterns of BCC

Lattice pattern equivalent young modulus	
10x10x10 T 1.25	0.411 GPa
12.5x12.5x12.5 T 2.5	2.72 GPa
15x15x15 T 2.5	1.36 GPa
25x25x25 T2.5	0.32 GPa

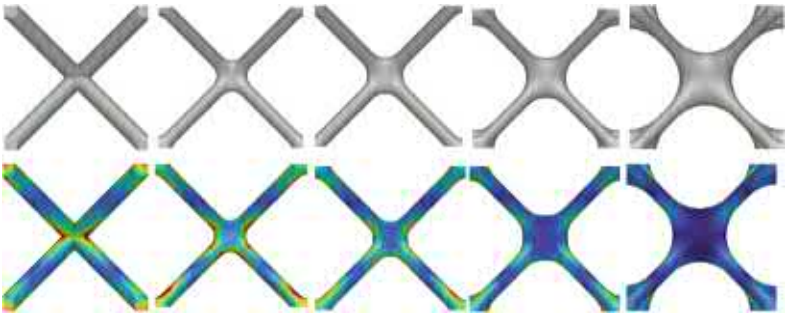


Fig. 15. Nodal blend radius sensitivity on peak stresses of lattice BCC 25x25x25mm T2.5mm from r = 0.5 mm to r = 2.5 mm



Fig. 16. LPBF produced demonstrator of BCC 25x25x25 T2.5 pattern

4 Application to a Representative Steel Joint – Fuksas Rhike Park, Tbilisi

The case study is a representative node from the free-form, double-curved grid-shell of the Fuksas Rhike Park in Tbilisi (Fig. 17), characterised by a highly irregular quadrangular mesh and non-uniform member orientations. In the original design, geometric variability was accommodated through a node-by-node approach based on welded plate assemblies and locally machined components as shown in Fig. 18. While structurally effective, this solution resulted in significant fabrication complexity, high material usage

and difficulties in achieving consistent structural verification due to variability between nodes.

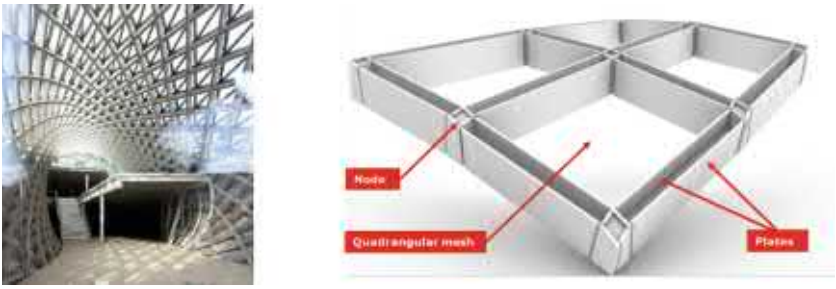


Fig. 17. Fuksas Rhike Park structure and aesthetics

The joints were required to provide high stiffness to transfer combined bending and torsional actions, leading to thick plates and heavily reinforced solid regions. Additive manufacturing offers a paradigm shift: fully customised nodes can be produced directly from digital models, without extensive machining or weld-based adjustments, and with the integration of architected lattice infills within the joint volume.

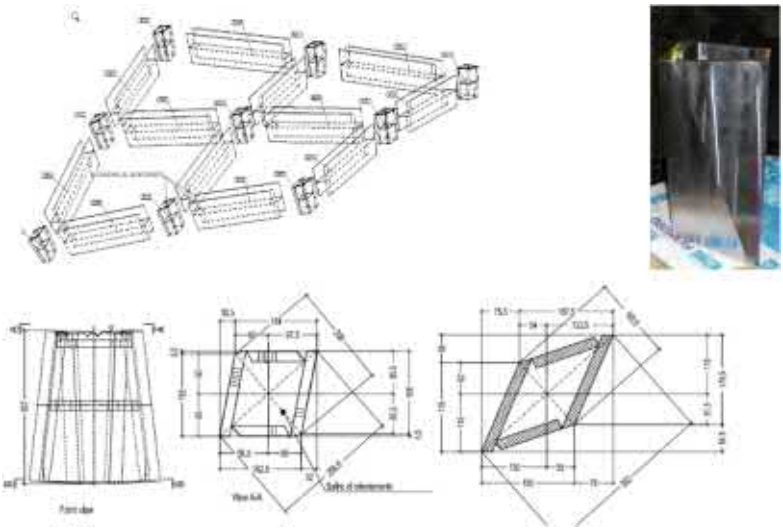


Fig. 18. Design and realization of the original nodes

4.1 Lattice-Infill Redesign and Parametric Selection

The redesign replaces solid internal regions with a BCC lattice infill, preserving solid external interfaces required for connections and load transfer. This results in a hybrid

solution combining a thin external shell with an internal architected infill. A parametric study varying unit cell size (20–40 mm) and strut thickness (1.0–4.5 mm) shows that increasing the unit cell size raises stress levels due to reduced relative density, while increasing strut thickness reduces peak stresses (Figs. 18,19). The optimal configuration has a unit cell size of 25 mm, strut thickness of 2.5 mm and a nodal blending radius of 0.5 mm, as illustrated in Fig. 21, which shows the transition from the original welded-plate joint to the lattice-infilled redesign (Fig. 20).

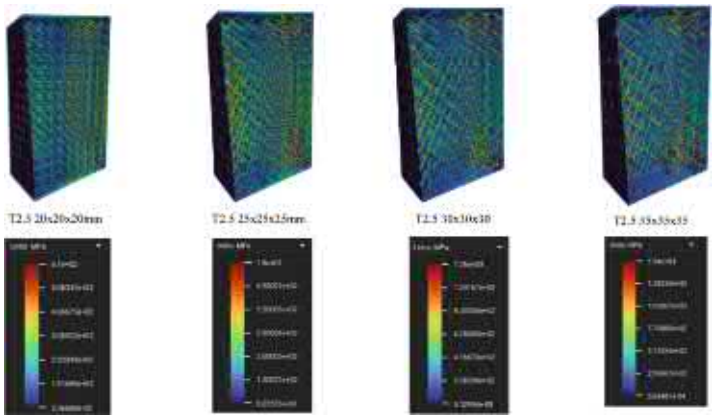


Fig. 19. Von Mises stress distribution examples under compressive loading for various BCC lattice configurations

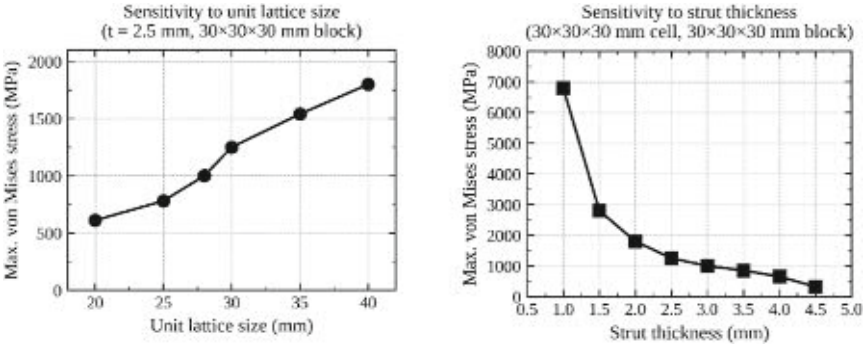


Fig. 20. Parametric sensitivity of peak von Mises stress in BCC lattice configurations: (left) effect of unit cell size at constant strut thickness (t = 2.5 mm), showing increasing nodal stress with decreasing relative density; (right) effect of strut thickness at constant cell size (30 mm)

4.2 Structural Performance and Comparison with Original Design

The structural performance of the lattice-infilled joint is evaluated through finite element analyses (Fig. 22) and compared with the original welded-plate configuration under

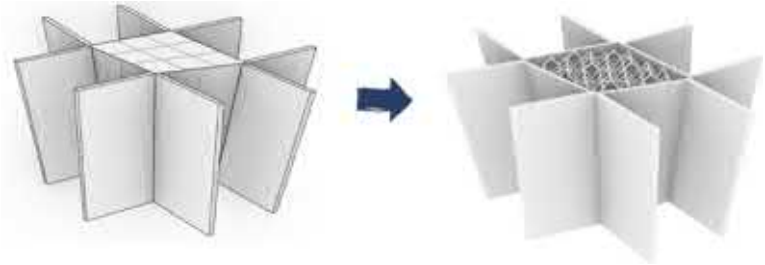


Fig. 21. Original welded-plate joint (left) and optimised BCC lattice-infilled redesign (right)

identical loading conditions. The results show a more uniform stress distribution and reduce peak stress concentrations. The redesigned configuration achieves a reduction of approximately 54% in global deformation while maintaining comparable stress levels within material limits. Mass is reduced by approximately 76% compared to the original design.

These results demonstrate that the lattice-based approach transforms the joint from a mass-driven solution into a performance-driven system where stiffness and load transfer are achieved through geometric optimisation. The negligible difference between isotropic and anisotropic material modelling confirms that the structural response is primarily governed by geometry rather than material anisotropy.

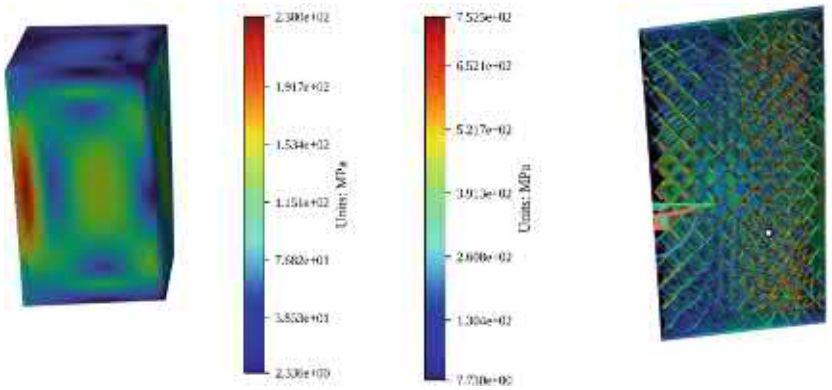


Fig. 22. Von Mises stress distribution under identical loading conditions: (left) original S355 welded-plate joint (utilization factor 64%, peak stress ~230 MPa); (right) lattice-infilled redesigned joint modelled with anisotropic material (utilization factor 69%, peak stress ~752 MPa)

5 Conclusions

This study presented a framework for the design and analysis of lattice-infilled steel structural joints enabled by additive manufacturing, combining mesoscale investigations with structural-scale application. Mesoscale numerical analyses identified unit cell

size, strut thickness and nodal blending radius as the key geometric parameters governing stiffness and stress distribution in BCC lattice configurations, with the ratio between strut thickness and blending radius playing a critical role in controlling peak nodal stress concentrations. Among the configurations investigated, the BCC 25 × 25 × 25 (t = 2.5 mm) was selected despite its bending-dominated behaviour and low equivalent stiffness (0.32 GPa), as its low relative density proved decisive in achieving the targeted mass reduction while still providing adequate load redistribution within the joint volume. The integration of this lattice infill provides a structurally efficient alternative to conventional solid stiffening solutions, achieving approximately 54% reduction in global deformation and 76% decrease in mass compared to the original welded-plate configuration, while maintaining structural adequacy.

These findings demonstrate that lattice architected materials enable a transition from conventional mass-driven design to performance-driven solutions based on geometric optimisation. Future research will focus on experimental validation, fatigue behaviour and long-term structural performance, as well as functionally graded lattice configurations and optimisation strategies coupled with global structural models.

Acknowledgments. The authors gratefully acknowledge funding provided by the EU Research Fund for Coal and Steel through the project "ConstructAdd: Resource-efficient steel CONSTRUCTion using ADDitive manufacturing," Grant Agreement No. 101057957.

References

1. Gibson LJ, Ashby MF (1997) Cellular solids: structure and properties, edition 2. Cambridge University Press
2. Maconachie T et al (2019) SLM lattice structures: properties, performance, applications and challenges. Mater Des 183:108137
3. Miao X et al (2024) Review on mechanical properties of metal lattice structures. Compos Struct 342:118267
4. Liu R, Chen W, Zhao J (2024) A review on factors affecting the mechanical properties of additively-manufactured lattice structures. J Mater Eng Perform 33(10):4685–4711
5. Meyer G, Wang H, Mittelstedt C (2022) Influence of geometrical notches and form optimization on the mechanical properties of additively manufactured lattice structures. Mater Des 222:111082
6. Pan C, Han Y, Lu J (2020) Design and optimization of lattice structures: a review. Appl Sci 10(18):6374
7. Köhnen P et al (2018) Mechanical properties and deformation behavior of additively manufactured lattice structures of stainless steel. Mater Des 145:205–217
8. Alwattar TA, Mian A (2019) Development of an elastic material model for BCC lattice cell structures using FEA and neural networks. J Compos Sci 3(2):33
9. Waqar S et al (2024) Superior strength and energy absorption capability of LPBF metallic functionally graded lattice structures. Thin-Walled Struct 205:112471

Structural Assessment of Steel Racking Systems: Gaps in Current European Standards and Perspectives

Alessia Campiche[1,2(✉)], Roberto Tartaglia[3], Giuseppe Maddaloni[3], and Antonio Occhiuzzi[1,2]

[1] Università degli Studi di Napoli Parthenope, Naples, Italy
alessia.campiche@uniparthenope.it
[2] Istituto per le Tecnologie della Costruzione (ITC) del Consiglio Nazionale delle Ricerche (CNR), San Giuliano Milanese (MI), Italy
[3] Università degli Studi del Sannio, Benevento, Italy

Abstract. Pallet racking systems are vital for logistics, and their safety relies on the mechanical performance of their steel components. While EN 15512 provides a European framework for their design and testing, limitations emerge during component-based assessments. For CE marking, EAD 200059–00-0302 supports European Technical Assessments (ETA) based on EN 15512. However, practical application reveals discrepancies between EN 15512 design parameters and ETA-declared characteristics, specifically regarding the distortional buckling of uprights and the cyclic behavior of beam-to-upright connections. This paper analyzes these inconsistencies and proposes targeted EAD revisions. These revisions aim to harmonize essential characteristic definitions, increase the transparency of experimentally derived parameters, and strengthen the correlation between physical testing and structural verification models. Ultimately, the proposed clarifications enhance the reliability and comparability of pallet-racking component assessments without imposing additional experimental burdens.

Keywords: Pallet racking systems · EN 15512 · EAD 200059–00-0302 · uprights · beam-end connectors

1 Introduction

Pallet racking systems constitute a cornerstone of contemporary logistics infrastructure, with their structural safety and long-term reliability intrinsically dependent upon the mechanical performance of their steel constituents. Structurally, these assemblies are generally composed of perforated, thin-walled uprights (1), which are stabilized at discrete intervals by horizontal (2) and diagonal bracing members (3). The longitudinal pallet beams (4) are integrated into the uprights via semi-rigid, hook-in beam-end connectors (BEC) (5), while the entire frame is securely anchored to the foundation employing base plate joints (6). A schematic overview of a typical pallet racking configuration is illustrated in Fig. 1.

© The Author(s), under exclusive license to Springer Nature Switzerland AG 2026
R. Zanon et al. (Eds.): CTA 2026, LNCE 942, pp. 357–368, 2026.
https://doi.org/10.1007/978-3-032-39505-4_31

Although these systems are categorized within the broader classification of steel structures, largely employed and investigated [1–4], and in particular cold-formed steel (CFS), which are extensively favoured in engineering applications for their optimal strength-to-weight ratios and manufacturing expediency [5–10], their structural mechanics are uniquely complex. Specifically, the presence of geometric perforations, the existence of short compression segments delineated by the bracing nodes, and the susceptibility of beam-to-upright connections to cyclic degradation cause the global structural response of pallet racks to deviate substantially from that of conventional cold-formed steel (CFS) frames [9].

The European standard EN 15512 [11] establishes the foundational framework governing both the structural design and the experimental evaluation of adjustable pallet racking systems, encompassing critical components such as uprights and beam-end connectors. In the context of CE marking, the essential characteristics evaluated within the European Technical Assessment (ETA) documentation are delineated by EAD 200059–00-0302 [12], which explicitly adopts the testing protocols outlined in EN 15512 [11]. Despite this regulatory structure, practical applications reveal a significant discrepancy: the parameters mandated for structural verification under EN 15512 [11] do not fully align with those assessed in the ETA and subsequently reported in the Declaration of Performance and Conformity (DoPC), pursuant to the Construction Product Regulation (EU) 2024/3110 (CPR). This misalignment is particularly pronounced concerning the distortional buckling behaviour of the uprights and the cyclic stiffness of beam-to-upright connections. Consequently, this study critically examines these procedural inconsistencies and proposes a targeted revision of EAD 200059–00-0302. This revision aims to foster greater transparency and ensure strict methodological consistency between the design prerequisites of EN 15512 [11] and the ETA-assessed component characteristics required for CE marking.

2 Upright and BEC Performances

2.1 Upright Characteristics According to EN 15512 [11] and EAD 200059–00-0302 [12]

The EAD mandates that the mechanical characteristics of pallet-racking uprights, as evaluated within the ETA framework, must be determined in strict accordance with EN 15512 [11]. These essential parameters encompass the effective cross-sectional properties and the buckling reduction factors that dictate the axial and bending resistance of the perforated members. Specifically, the effective cross-sectional area, A_{eff}, of a perforated upright is derived experimentally via the stub-column test, as detailed in Annex A.2.1 of EN 15512 [11]. This experimental procedure is designed to accurately capture the phenomena of local buckling and the structural implications of perforations under uniform compressive loading. Consequently, the effective area is calculated using Eq. 1, based on the ultimate compressive resistance exhibited by the test specimen:

$$A_{\text{eff}} = \frac{N_u}{f_y} \tag{1}$$

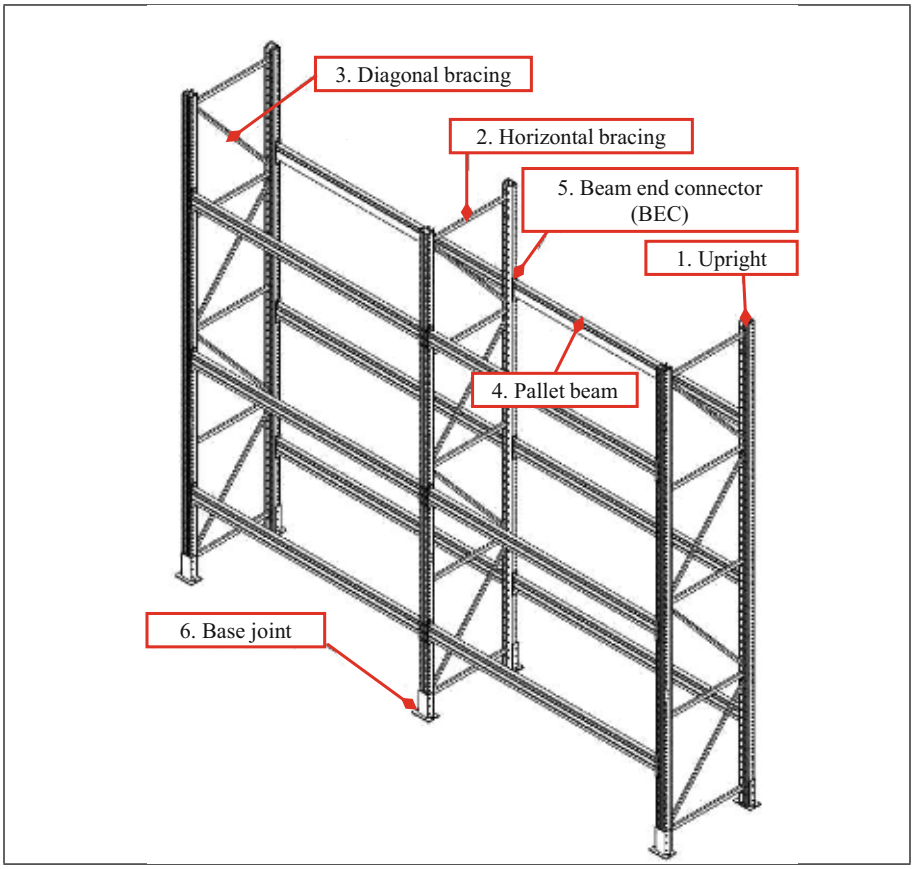


Fig. 1. Schematic drawing of a pallet racking system

where N_u represents the ultimate compressive force obtained from the stub-column test and f_y denotes the actual yield strength of the steel.

This parameter characterizes the fundamental compressive capacity of the upright and is an explicit requirement within the ETA framework.

The distortional buckling behaviour of the upright is assessed through a specific distortional test (detailed in EN 15512 [11], Annex A.2.2 or A.2.3). This procedure evaluates the instability mode induced by flange-web distortion, a distinctive structural phenomenon in perforated rack sections. The corresponding distortional buckling reduction factor, which varies according to the effective length between bracing nodes, is computed using Eq. 2:

$$\chi_{db} = \frac{N_{u,i}}{A_{\text{eff}} f_y} \tag{2}$$

where $N_{u,\,i}$ denotes the adjusted failure load recorded for test i i.

While the EAD does not explicitly itemize χ_{db} this reduction factor among the properties to be directly assessed, it mandates the execution of the distortional test to

derive the upright's buckling curve. Consequently, this factor, χ_{db}, is implicitly integrated into the buckling reduction curve $\chi\left(\bar{\lambda}\right)$ provided in the ETA.

Furthermore, the effective section modulus W_{eff} of the upright, evaluated about its principal axes, is determined via a bending test (EN 15512 [11], Annex A.2.9). This test accurately captures the combined effects of local buckling and perforations under flexural loading. The effective modulus is then derived from the ultimate bending moment using Eq. 3

$$W_{\text{eff}} = \frac{M_u}{f_y} \tag{3}$$

where M_u represents the ultimate bending moment achieved during the test.

These sectional properties are explicitly mandated by the ETA to verify bending resistance.

The lateral-torsional buckling reduction factor, denoted as χ_{LT}, is determined in accordance with Sect. 9.7.4 of EN 15512 [11], which concurrently references the methodologies established in EN 1993-1-3 and EN 1993-1-1. In analytical practice, this factor is conventionally calculated utilizing the effective section properties derived from the bending tests. Conversely, if the experimental bending setup inherently accounts for lateral instability, the measured moment resistance already encompasses this reduction. Furthermore, the EAD explicitly mandates that χ_{LT} be documented within the ETA.

Under EN 15512 [11], the axial buckling behaviour of the uprights is dictated by the more critical condition - that is, the minimum value between the flexural and distortional buckling reduction factors - as formalized in Eq. 4:

$$\chi_{min} = \min\left(\chi_y, \chi_z, \chi_{db}\right) \tag{4}$$

In compliance with the EAD, either the complete upright buckling curve or the equivalent reduction factors must be reported in the ETA. As a result, the distortional reduction factor obtained via Annex A.2.2 or A.2.3 is intrinsically integrated into the overall buckling assessment of the upright provided in the ETA. Finally, Table 1 presents a synthesis of the testing procedures prescribed by EN 15512 [11], outlining the minimum essential upright characteristics that must be declared in the ETA pursuant to EAD 200059–00-0302.

Table 1. Summary of EN 15512 [11] tests and ETA upright characteristics

EN 15512 [11] test	Property obtained	Recalled by the EAD	To be reported in the ETA
Annex A.2.1 Stub-column	Effective area (A_{eff})	Yes	Yes
Annex A.2.2 / A.2.3 Distortional	Distortional factor (χ_{db})	Implicit	Yes (within buckling curve)
Annex A.2.9 Bending	Effective modulus (W_{eff})	Yes	Yes

(*continued*)

Table 1. (*continued*)

EN 15512 [11] test	Property obtained	Recalled by the EAD	To be reported in the ETA
EN 1993-based or A.2.9	LTB factor (χ_{LT})	Yes	Yes

2.2 BEC Characteristics According to EN 15512 [11] and EAD 200059–00-0302 [12]

EAD 200059–00-0302 stipulates that the mechanical behavior of beam-to-upright connections must be characterized within the ETA in strict accordance with EN 15512 [11] protocols. These essential characteristics - specifically, moment resistance and rotational stiffness - are critical as they dictate the global structural response of pallet-racking frames.

Following EN 15512 [11], the mechanical properties of beam-end connectors are extrapolated from the connection bending test detailed in Annex A. This experimental setup accurately simulates the physical behavior of the hook-in connector under vertical beam loading, yielding a comprehensive moment-rotation curve. From this single experimental profile, all parameters mandated by the EAD for ETA documentation can be derived.

The characteristic bending resistance of the beam-end connector, M_k, is directly extracted from this test as the peak moment attained along the monotonic loading curve. Formally, EN 15512 [11] defines this characteristic value based on the test series, generally adopting a statistical lower-bound of the recorded ultimate moments. As the fundamental measure of the connector's strength, M_k must be explicitly documented in the ETA.

Subsequently, the design value M_{Rd} is typically computed using Eq. 5:

$$M_{Rd} = \frac{M_k}{\gamma_M} \tag{5}$$

For connections subjected to rigorous quality control, EN 15512 [11] specifies a dedicated partial safety factor $\gamma_M = 1.1$. The application of the $\gamma_M = 1.25$ value, which is sometimes adopted in practice for connection resistance, is considered overly conservative and contradicts the EN 15512 [11] provisions intended for qualified connectors.

Furthermore, EN 15512 [11] defines the rotation, θ_k, associated with the characteristic moment as the angular deformation measured at the design stiffness point on the moment-rotation curve. This rotational parameter is essential for determining connection stiffness and for accurately modelling the semi-rigid behaviour of beam-to-upright joints. Correspondingly, the EAD foresees the assessment of these deformation properties. The rotational stiffness of the connector is then calculated via Eq. 6:

$$k = \frac{\eta\, M_k}{\gamma_M\ \theta_k} \tag{6}$$

where η denotes a cyclic reduction factor accounting for structural degradation under repeated loading cycles

M_k represents the characteristic bending moment resistance
θ_k is the rotation corresponding to M_k
γ_M defines the relevant partial safety factor.

While the connection tests specified in EN 15512 [11] are strictly monotonic, beam-end connectors in service conditions frequently experience cyclic loading. Experimental investigations conducted by Bernuzzi & Castiglioni [13] demonstrate that, following initial plasticization, the peak moment undergoes a significant reduction during the first few loading cycles, typically stabilizing at 70–85% of its original value. Consequently, the cyclic reduction factor, η, should logically be assigned a value of less than unity. Nevertheless, EN 15512 [11] omits a specific procedural methodology for calculating η. In engineering practice, this omission often results in the default assumption that $\eta = 1$, which subsequently leads to a potential overestimation of the connection's rotational stiffness.

Prior to the 2009 publication of EN 15512 [11], the rotational stiffness of beam-to-upright connections was predominantly evaluated using the FEM 10.2.02 [14] guidelines. This historical document introduced a simplified formulation for connection stiffness, denoted as Eq. 7:

$$k = \frac{\frac{2}{3} M_u}{\theta_u} \tag{7}$$

In this approach, the experimental ultimate moment, M_u, was reduced to two-thirds of its value and divided by the corresponding rotation, θ_u. This methodology inherently accounted for the degradation of connection resistance that occurs post-plasticization.

Subsequently, EN 15512 [11] introduced a revised stiffness formulation predicated on characteristic values and partial safety factors, complemented by explicit limits on the rotation considered for stiffness evaluation. This paradigm shift was presumably driven by the realization that deriving stiffness from a point on the monotonic moment-rotation curve that is too close to the ultimate moment can yield unrealistically high stiffness values if cyclic degradation is ignored.

From a numerical standpoint, a correlation between the legacy FEM approach and the current EN 15512 [11] formulation can be established by assuming:

$$\frac{\eta}{\gamma_M} \approx \frac{2}{3} \tag{8}$$

This relationship, expressed in Eq. 8, facilitates the estimation of the cyclic reduction factor that aligns with the historical FEM assumptions. Specifically:

- For $\gamma_M = 1.25$, achieving 2/3 requires $\eta \approx 0.83$;
- For $\gamma_M = 1.1$, achieving 2/3 requires $\eta \approx 0.73$.

These calculated values align consistently with the empirical range of cyclic moment reductions observed in pallet-racking connections [13]. Therefore, the legacy FEM formulation can be understood as implicitly embedding a cyclic degradation effect, a phenomenon that EN 15512 [11] now addresses explicitly through the parameter η, the determination of which is ultimately left to the structural designer's discretion.

3 Inconsistencies Between EN 15512 [11] and EAD and Proposed Revisions to EAD 200059–00-0302 [12]

The analysis reveals two principal inconsistencies within the regulatory framework. Firstly, although EN 15512 [11] strictly requires the distortional reduction factor χ_{db} for upright structural verification, the EAD mandates the corresponding test without requiring the factor itself to be reported in the ETA. Thus, a parameter essential for safe design is experimentally quantified but kept functionally unavailable to designers.

Secondly, EN 15512 [11] introduces the cyclic reduction factor η for connection stiffness but provides no operational definition for determining or expressing it within the ETA. Consequently, ETAs typically publish a single stiffness value, implicitly assuming $\eta = 1$, thereby neglecting the cyclic degradation phenomena clearly demonstrated in experimental studies.

Ultimately, EN 15512 [11] demands parameters that the EAD framework either obscures or leaves entirely undefined.

To address the inconsistency regarding uprights, it is proposed that the EAD explicitly require the assessment of distortional buckling effects. This could be implemented through two viable pathways. The most direct solution is to report the distortional reduction factor χ_{db} itself for specific upright configurations. Given that distortional buckling is a function of brace spacing (the effective length between bracing nodes), the ETA must clearly specify the applicable structural range based on the tested specimen length. This would enable designers to execute EN 15512 [11] verifications directly and accurately.

Alternatively, while retaining the EAD's current buckling curve format, the regulation could require a governing upright buckling curve, $\chi_{min}(\overline{\lambda})$, defined according to Eq. 9:

$$\chi_{min}(\overline{\lambda}) = \min(\chi_y, \chi_z, \chi_{db}) \tag{9}$$

This modification must explicitly state that distortional buckling effects are accounted for within the curve. Even in this scenario, the ETA must rigorously define the range of applicable brace spacing. Such clarification is critical because χ_{db} is an inherently member-dependent characteristic rather than a purely cross-sectional one, and therefore cannot be indiscriminately applied to different bracing architectures without defined applicability limits.

Both proposed approaches ensure complete alignment between the design prerequisites of EN 15512 [11] and the characteristics evaluated within the ETA. Crucially, this alignment is achieved without imposing any additional experimental burden, as the distortional test is already mandated by the EAD. Consequently, the suggested modifications significantly enhance the transparency and practical utility of ETA data while keeping

the established experimental framework intact. By rendering distortional effects explicit and directly traceable to the tested configurations, the revised EAD facilitates a more robust application of EN 15512 [11] verification protocols. Furthermore, it improves the comparability of upright performance across various pallet-racking systems. Regarding the beam-end connectors (BEC), given that the cyclic reduction factor, η, cannot be uniquely predefined, it is recommended that the ETA reports the rotational stiffness parametrically, as a function of η. This is formalized in Eq. 10:

$$k(\eta) = \frac{\eta\, M_k}{\gamma_M\ \theta_k} \tag{10}$$

This methodological shift prevents the arbitrary assumption of $\eta = 1$, a default often adopted in engineering practice due to the absence of explicit guidelines for quantifying cyclic degradation. By formally expressing stiffness as a function of η, the inherent uncertainties tied to the cyclic behaviour of beam-to-upright connections are transparently addressed. Simultaneously, this parametric formulation remains entirely consistent with the EN 15512 [11] definition of stiffness, as it is mathematically derived from the normative relationships governing moment, rotation, and partial safety factors. Additionally, this representation ensures backward compatibility with legacy FEM-type stiffness values, which inherently accounted for cyclic reductions. Ultimately, supplying stiffness data in a parametric format equips designers with a transparent and flexible set of connection properties, empowering them to select appropriate values based on specific cyclic demands and overall design contexts.

4 Numerical Validation

To substantiate the practical implications of the previously identified discrepancies between EN 15512 and EAD 200059-00-0302, a simplified numerical analysis has been conducted at the component level, focusing specifically on uprights and beam-to-upright connections.

4.1 Influence of Distortional Buckling on Upright Resistance

The design axial resistance, denoted as N_{Rd}, of a pallet-racking upright is calculated according to Eq. 11:

$$N_{Rd} = \chi_{min}\, A_{eff}\, \frac{f_{yk}}{\gamma_M} \tag{11}$$

where A_{eff} is the effective cross-sectional area, f_{yk} is the characteristic yield strength of the steel, γ_M is the partial safety factor, and χ_{min} is the governing buckling reduction factor. In accordance with EN 15512, the design resistance is determined by the most critical instability mode, according to Eq. 9.

This formulation explicitly accounts for both flexural and distortional buckling phenomena. Under EN 15512 provisions, the overall design resistance is dictated by the more critical condition that is, the minimum value between the corresponding buckling reduction factors.

To illustrate the influence of distortional buckling, a representative cold-formed pallet-racking upright with nominal dimensions of approximately 90 × 70 × 2.0 (length × height ×depth) mm is considered.

The following design parameters are adopted:

$A_{eff} = 520\ mm^2$
$f_{yk} = 350\ MPa$
$\gamma_M = 1.10$

The corresponding design resistance of the effective cross-section is evaluated according to Eq. 11:

$N_{,Rd} = 165.5\ kN.$

Two design scenarios are subsequently evaluated.

Case 1 (Flexural buckling only):

$\chi_x = 0.68;\ N_{,Rd} = 112.5\ kN$

Case 2 (Including also distortional buckling):

$\chi_{db} = 0.53;\ N_{,Rd} = 87.7\ kN$

The inclusion of distortional buckling therefore reduces the calculated axial resistance by 22.0%

This numerical example demonstrates that distortional buckling may significantly affect the load-carrying capacity of cold-formed pallet-racking uprights. Neglecting the distortional reduction factor would lead to a non-conservative overestimation of the design axial resistance. Therefore, the explicit provision of the distortional buckling reduction factor χ_{db} within the European Technical Assessment (ETA) documentation is essential to ensure a reliable and consistent structural design in accordance with EN 15512.

4.2 Influence of Cyclic Reduction Factor on Connection Stiffness

To assess joint behaviour, the rotational stiffness is calculated using Eq. 6 based on the following assumed mechanical parameters:

$$M_k = 10\ kNm$$

$$\theta_k = 0.02\ rad$$

$$\gamma_M = 1.1$$

The connection stiffness is then evaluated across varying values of the cyclic reduction factor, η, with the detailed results tabulated in Table 2. The analysis clearly illustrates that defaulting to the standard assumption of $\eta = 1$ yields a significant overestimation of

connection stiffness. When properly accounting for cyclic degradation, the actual stiffness reduction can reach approximately 30%. Such a drastic decrease inevitably alters the global structural stiffness and significantly impacts the internal load distribution throughout the entire pallet-racking frame.

Table 2. Influence of η on connection stiffness k

η	k (kNm/rad)	Variation
1.00	455	0%
0.85	387	−15%
0.70	318	−30%

4.3 Discussion

The simplified numerical analysis corroborates that both the distortional buckling reduction factor χ_{db} and the cyclic reduction factor η exert a substantial influence on the mechanical behaviour of pallet-racking components. Specifically, while χ_{db} directly governs the axial resistance of the uprights, η dictates the rotational stiffness of the beam-to-upright connections, thereby shaping the global structural response of the frame. These findings offer a robust quantitative foundation for the proposed revisions to the EAD framework. Crucially, they illustrate how the omission of explicit χ_{db} values, coupled with the lack of an operational definition for η, engenders significant discrepancies between component-level assessments and global structural design.

5 Conclusions

This study has critically evaluated the methodological consistency between EN 15512 [11] and EAD 200059–00-0302 [12] regarding the characterization and reporting of pallet-racking component properties. Although the EAD framework is fundamentally anchored in EN 15512 [11], notable discrepancies emerge when these standards are examined through the lens of component-based assessment.

Regarding uprights, EN 15512 [11] mandates the use of the distortional buckling reduction factor, χ_{db}, for structural verification. Conversely, while the EAD requires the physical execution of the distortional test, it does not compel the reporting of χ_{db} within the ETA. Consequently, a parameter paramount to safe structural design remains inaccessible to practicing engineers, severely restricting the transparency and direct applicability of ETA data.

Concerning beam-end connectors, EN 15512 [11] introduces the cyclic reduction factor, η, into the stiffness formulation but fails to provide a specific methodology for its quantification. In engineering practice, this regulatory void often leads to the default assumption that $\eta = 1$. This assumption categorically ignores experimentally proven cyclic degradation and risks a dangerous overestimation of connection stiffness.

Collectively, these issues highlight a systemic misalignment: critical parameters necessitated by EN 15512 [11] design protocols are either concealed (in the case of uprights) or operationally undefined (in the case of connectors) within the current EAD documentation. As a result, the characteristics detailed in the ETA do not always align with the direct verification needs of EN 15512 [11].

To rectify these critical gaps, targeted revisions to EAD 200059–00-0302 [12] are proposed. For uprights, it is recommended that distortional effects be explicitly detailed, either by directly reporting χ_{db}, or by providing a governing buckling curve that inherently integrates distortional behaviour alongside its applicable brace-spacing limits. For beam-end connectors, rotational stiffness should be documented parametrically as a mathematical function of η.

Importantly, these proposed modifications necessitate no supplementary experimental testing, as the prerequisite laboratory procedures are already embedded within the current EAD framework. Instead, these adjustments would drastically improve the transparency, traceability, and immediate utility of ETA data, ensuring seamless compatibility with EN 15512 [11] design methodologies. Ultimately, a revised EAD that integrates these clarifications would bolster the reliability and comparability of component assessments, fostering more rigorous and uniform structural design practices across the European framework.

References

1. Freddi F et al (2025) Seismic retrofitting of existing steel frames with external BRBs: pseudo-dynamic hybrid testing and numerical parametric analysis. Earthq Eng Struct Dyn 54(3):1064–1083
2. Tartaglia R, Monte F, Demonceau JF, Maddaloni G (2026) Monotonic behaviour of 4-bolt row connections: analytical and numerical analyses. J Constr Steel Res 236:110048
3. Milone A, D'Aniello M, Landolfo R (2024) Advanced fatigue assessment of riveted railway bridges on existing masonry abutments: an Italian case study. Buildings 14(8):2271
4. Gnazzo M, Mahmoudi B, D'Aniello M, Imanpour A, Landolfo R (2026) Seismic design and response of inverted-V CBFs compliant with European and Canadian standards. Eng Struct 363:123071
5. Dubina D, Ungureanu V, Landolfo R (2012) Design of cold-formed steel structures: Eurocode 3—design of steel structures, part 1–3. Ernst & Sohn, Berlin
6. Landolfo R (2019) Lightweight steel framed systems in seismic areas: current achievements and future challenges. Thin-Walled Struct 140:114–131
7. Prota A, Fiorino L, Landolfo R (2026) Quantification of seismic performance factors according to FEMA P695 for Eurocode DC2-compliant lightweight steel shear walls with gypsum board sheathing. Thin-Walled Struct 230:115297
8. Fiorino L, D'Addesa V, Landolfo R (2024) Seismic design rules for lightweight steel shear walls with wood panel sheathing within the Eurocode format. Thin-Walled Struct 204:112293
9. Schafer BW (2008) Review: the direct strength method of cold-formed steel member design. J Constr Steel Res 64(7–8):766–778
10. Godley MHR (2002) The behaviour of drive-in storage structures. In: 16th international specialty conference on cold-formed steel structures, Orlando, FL. University of Missouri–Rolla, Rolla
11. European Committee for Standardization (CEN) (2009) EN 15512:2009, steel static storage systems—adjustable pallet racking systems—principles for structural design. CEN, Brussels

12. European Organisation for Technical Assessment (EOTA) (2018) EAD 200059–00-0302, Steel components for pallet racking systems. EOTA, Brussels
13. Bernuzzi C, Castiglioni CA (2001) Experimental analysis on the cyclic behaviour of beam-to-column joints in steel storage pallet racks. Thin-Walled Struct 39(10):841–859
14. European Materials Handling Federation (FEM) (2001) FEM 10.2.02, the design of static steel pallet racking: racking design code. FEM Section X, West Bromwich

M-N Interaction in Steel Storage Pallet Rack Base Joints

Nadia Baldassino(✉), Arianna Serraiotto, Martina Bernardi, and Riccardo Zandonini

University of Trento, Trento, Italy
nadia.baldassino@unitn.it

Abstract. Adjustable steel storage pallet racks are framed structures used for logistic purposes. Despite their non-strategic role in construction, several collapses in recent years have clearly highlighted the need for a holistic design approach to address the variety of parameters affecting their structural performance. These framed systems are usually made with cold-formed steel profiles, characterized by slender elements and by the absence of bracing systems along the corridor. Stability in this plane is governed by the behaviour of both the beam-to-upright and the base connections. Both connection types exhibit remarkable nonlinear behaviour, with the base connection performance significantly depending on the axial force applied to the upright. The connections' behaviour plays a fundamental role in structural design. However, very few studies focused on the performance of base joints. This paper presents the results of an experimental work conducted on a commercial base joint connection. The joint's response to combined axial force and bending moment was investigated under monotonic and cyclic loading. Tests were carried out in the two main directions of the rack system: the cross-aisle and down-aisle directions. The axial force influence on the joints' flexural behaviour was first investigated. The experimental outcomes enabled the development and calibration of *Pinching4* models to numerically appraise the hysteretic performance of the joint. The paper describes the main features of the study and discusses the key findings.

Keywords: Steel storage racks · Cold-formed steel · Design by testing · Base-plate joints · Cyclic and monotonic tests · Pinching4 model

1 Introduction

Steel storage pallet racks are framed structures composed of cold-formed steel (CFS) members, widely utilized for logistics and storage purposes. The framework consists of uprights—usually monosymmetric, open cross-section members perforated along their length—and beams, which feature either an open or closed cross-section. Typically, a hooked end-connector is welded to both ends of these beams to enable a mechanical connection with the uprights. Base joints, consisting of a prefabricated assembly welded or bolted to the uprights, anchor the structure to the floor. To provide stability against lateral forces and second-order effects, bracing elements are employed. However, to facilitate pallet handling, they are usually placed only along the cross-aisle direction.

© The Author(s), under exclusive license to Springer Nature Switzerland AG 2026
R. Zanon et al. (Eds.): CTA 2026, LNCE 942, pp. 369–380, 2026.
https://doi.org/10.1007/978-3-032-39505-4_32

Consequently, down-aisle rack stability entirely relies on the rotational continuity provided by both the beam-to-upright and the base joints. Given the relatively low stiffness typically exhibited by beam-end connectors, the rotational stiffness of the base plate assembly plays a crucial role in governing global rack response [1].

Base plate joints are typically classified as semi-rigid joints [2], and their moment-rotation relationship is strongly non-linear. To date, no reliable analytical tools are available to predict their performance, primarily due to the complexity of the underlying physical phenomena and the vast variety of commercial configurations. Consequently, an experimental approach is widely adopted to determine the joints' moment-rotation relationships, which are essential for global frame analysis. This methodology, known as 'Design by Testing', is also prescribed by the main rack design standards [3–5]. From the experimental results, it is possible to obtain the parameters to develop reliable numerical models capable of capturing the primary sources of geometric and mechanical non-linearity that influence the rack structural response [6].

In line with this approach, existing literature has predominantly focused on investigating the mechanical behaviour of the base joints through experimental testing. The axial load acting on the upright is one of the primary factors influencing their flexural behaviour [2, 7–9], to the extent that design standards require its explicit consideration during experimental analysis. Other geometric and mechanical parameters affecting the flexural behaviour of these joints include the geometry of the base plate [7, 10], the configuration and characteristics of the anchorage devices [11, 12], the mechanical properties of the floor material [8, 9], and the geometry of the bracket element [2, 7, 10]. Scientific work devoted greater attention to the down-aisle behaviour of the base joint, precisely because it is in this direction that, as previously mentioned, base joints play a fundamental role in ensuring the stability of racking systems. Studies conducted in recent years on the flexural behaviour of base-plate joints in the cross-aisle direction have begun to fill this gap [9, 11]. Furthermore, while monotonic behaviour is relatively well documented, another largely unexplored area is their cyclic performance. Research interest within the scientific community regarding these topics has recently increased due also to several post-earthquake collapses. To date, the cyclic behaviour of base joints has been investigated mainly within the framework of the RFCS European Research Projects SEISRACKS [9] and SEISRACKS2 [13]. Regarding the numerical modelling of base joints, to the best of the authors' knowledge, only [14] provides a numerical characterization of a specific base-plate joint for implementation in the global structural model of a steel storage pallet rack.

To address the gap in the literature, studies on the behaviour of base-plate pallet racks have been carried out at the University of Trento in both the down-aisle and cross-aisle directions under monotonic and cyclic loading. This paper presents the results of the experimental campaigns conducted in recent years and describes the numerical calibration of the joints' hysteretic behaviour using the *Pinching4* model [15]. The paper is structured as follows: Sects. 2 and 3 describe the experimental program and the test setup, respectively. Sections 4 and 5 present and discuss the experimental results along with the derived numerical parameters. Finally, Sect. 6 provides some concluding remarks.

2 The Experimental Program

The study investigated the response of a typical commercial seismic rack base-plate joint, shown in Fig. 1. This joint comprises a prefabricated assembly consisting of a base plate, anchored to the floor by means of four anchor bolts, and two brackets, connected to the upright via eight bolts. Due to confidentiality requirements imposed by the manufacturer, the geometric properties of the components are not explicitly disclosed herein.

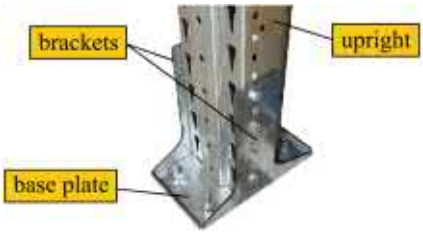


Fig. 1. Base-plate joint: case study

The base-plate joint is monosymmetric; therefore, a complete characterization of its flexural behaviour requires testing in both the down-aisle (i.e., parallel to the aisle) and cross-aisle (i.e., orthogonal to the aisle) directions. Furthermore, because the joint response in the cross-aisle direction is asymmetric, three distinct test configurations, shown in Fig. 2, were considered:

- Configuration A: characterization in the down-aisle direction;
- Configuration B1: characterization in the cross-aisle direction with the lateral force F_2 directed toward the web;
- Configuration B2: characterization in the cross-aisle direction with the lateral force F_2 directed toward the rear flanges;

where F_2 is the force that generates the bending effect.

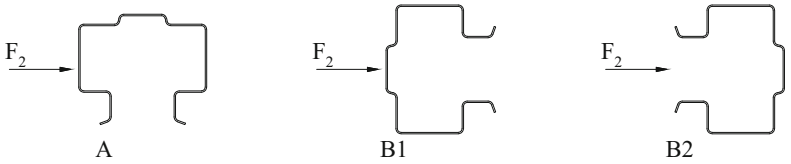


Fig. 2. Test configurations of the base-plate joint

The experimental characterization of the base-plate joint response was carried out in two distinct phases:

1. The joint was initially characterized under both monotonic and cyclic loading protocols in both directions (down-aisle and cross-aisle) at three axial load levels (5 kN, 50 kN, and 80 kN). For each direction and test type, three tests were performed. These

tests were originally conducted within the research work by Bernardi [16]; however, the raw data collected have been completely reprocessed in the present study to ensure a homogeneous calibration of the mechanical parameters.

2. The testing campaign was subsequently complemented by cyclic tests in the down-aisle direction at two additional axial load levels (30 kN and 65 kN). In this phase, a single monotonic test was performed for each axial load level solely to define the loading history for the corresponding cyclic tests, for which three tests were again carried out for each axial load level.

3 Test Set-up

The experimental tests were conducted in accordance with the requirements specified in [3], adopting the 'Alternative A' test method. In this arrangement, the specimen consists of two upright sections of equal length, not less than four times the dimension of the upright in the direction perpendicular to the bending axis, connected via the base plates to a concrete block. The loading scheme adopted is defined by [3] and shown in Fig. 3: the axial force F_1 is applied to the uprights via a hydraulic jack (jack 1 in Fig. 4), while the bending moment is generated by the lateral force F_2, applied to the concrete cube via a second hydraulic jack (jack 2 in Fig. 4).

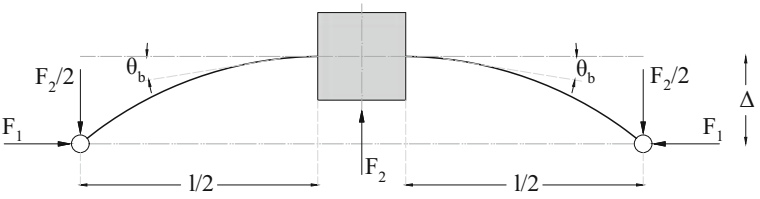


Fig. 3. Forces and deflections in the base-plate test [3]

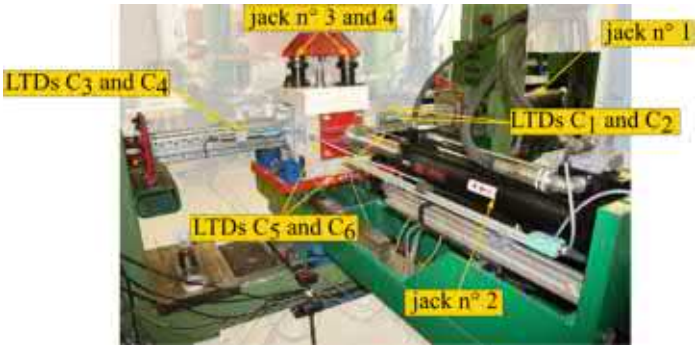


Fig. 4. Experimental testing set-up adopted for the study

In compliance with the provisions of [3], a pinned connection was provided both between jack 1 and the upright and between jack 2 and the concrete cube. The latter was mounted on a rail system that allows translations in the horizontal plane, while rotations around its vertical axis were prevented by two vertical hydraulic jacks (jacks 3 and 4 in Fig. 4). The measurement of the horizontal displacements of the concrete cube and the rotations of the base joint was carried out via displacement transducers (LTDs from C_1 to C_6 in Fig. 4), according to the scheme specified in [3].

4 The Test Results

4.1 Monotonic Tests

Three tests were performed under monotonic loading conditions for each axial load level (5 kN, 50 kN, and 80 kN) and configuration (A, B1, and B2), for a total of 27 tests. Two additional monotonic tests performed exclusively for configuration A—one at an axial level of 30 kN and the other at 65 kN—were carried out during the second phase of the experimental campaign. The experimental results are in the following presented in the form of moment-rotation curves, calculated as prescribed by [3].

Down-Aisle. The experimental joint's mechanical response and failure modes exhibited a strong dependence on the applied axial load (Fig. 5).

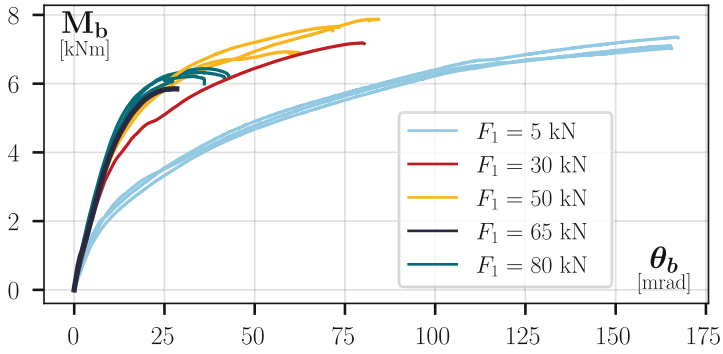


Fig. 5. Monotonic test results for configuration A

At 5 kN, collapse was governed by local buckling of the upright webs and base plate deformation. Specifically, the thin-walled upright webs experienced out-of-plane distortion near the base plate, while the presence of the web perforations led to severe edge distortion and ovalization of the holes. This failure mode provided significant ductility, yielding the highest rotational capacity. Conversely, under higher loads (65 and 80 kN) collapse was driven by failure of the uprights at the bracket ends, a mechanism that prematurely limited both the rotational capacity and the moment capacity. Intermediate load levels (30 and 50 kN) exhibited a transitional behaviour, characterized by a combination of both upright buckling at the bracket ends and base plate deformation. As shown in Fig. 5, the initial stiffness values for the 30 kN, 50 kN, 65 kN and 80 kN

loads are comparable, and significantly higher than those observed for the 5 kN load. The curves also denote a clear trade-off between stiffness and rotational capacity: high initial stiffness corresponds to limited rotational capacity. The specimens tested at 5 kN, 30 kN and 50 kN are the ones that exhibit the highest peak moment. Finally, it can be observed that the scatter of results for each level of axial load is modest.

Cross-Aisle. In configuration B1, the behaviour of the assemblies was consistent across all tested axial loads, exhibiting local deformation of the uprights near the base (characterized by significant buckling deformations of the upright web) and non-negligible deformation of the two brackets. Furthermore, specimens subjected to the highest axial load experienced upright failure at the bracket extremities.

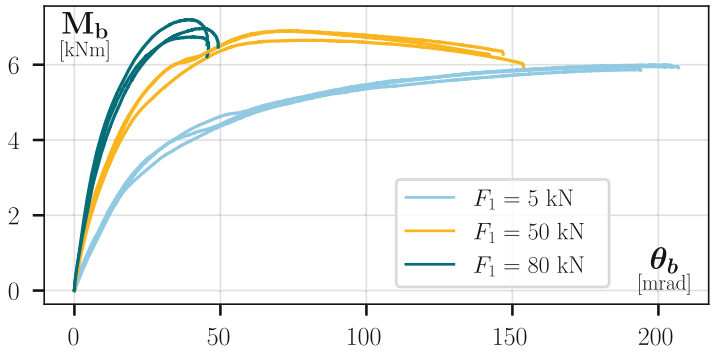


Fig. 6. Monotonic test results for configuration B1

As shown in Fig. 6, the initial stiffness increases with the applied axial load, but in contrast to configuration A, the 50 kN and 80 kN tests clearly show different initial stiffness values. Another major difference is observed in the maximum bending moment. Specifically, in configuration B1, the highest peak bending moment occurs at the highest axial load, while the lowest one is recorded for the 5 kN tests. Besides, the specimen under 50 kN axial load reaches a peak moment comparable to the highest one. Finally, as previously observed for configuration A, the correlation between axial load and rotational capacity is confirmed, along with the limited scatter of the results.

In configuration B2 (Fig. 7), a consistent collapse mode was observed across all three axial load levels, triggered by significant distortional buckling of the uprights. Additionally, under the maximum axial load, the uprights exhibited remarkable deformations also near the brackets, in a similar manner as for configurations A and B1. The analysis of the moment-rotation curves for configuration B2 reveals that the initial stiffness shows a similar trend to that of configuration A. Consistent with previous findings, the curves corresponding to the 50 kN and 80 kN axial loads exhibit nearly coincident initial slopes, far higher than the slope observed for the 5 kN load. In contrast to the results obtained for configuration B1, the specimens that exhibited the highest maximum bending moment are those subjected to the minimum and intermediate axial loads. Furthermore, in line with all previous configurations, the trend of decreasing joint rotational capacity with increasing axial load remains unchanged, along with the limited scatter of the results.

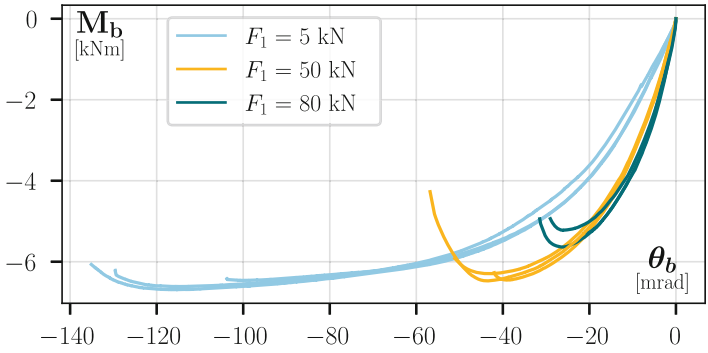


Fig. 7. Monotonic test results for configuration B2

4.2 Cyclic Tests

Under cyclic loading, a total of 24 tests were carried out, 18 of which were part of the first experimental campaign and 6 from the supplementary campaign. In the first campaign, three tests were performed for each axial load level (5 kN, 50 kN and 80 kN) and for each test configuration (A and B). In the second experimental campaign, which focused solely on configuration A, three tests were carried out for each axial load level (30 kN and 65 kN). The cyclic loading history was defined on the basis of the monotonic tests results and the ECCS n°45 [17] recommendations. Test results, calculated as prescribed by [3], are in the following presented in the form of moment-rotation curves. For each loading condition, all three cyclic curves are plotted; these closely overlap owing to the low data scatter. Furthermore, the cyclic curves are 'superimposed' with those from the corresponding monotonic tests; however, to maintain visual clarity given the low variance, only a single representative monotonic curve is displayed for each loading condition.

Down-Aisle. The failure modes in the cyclic tests were consistent with the ones exhibited by the specimens in the monotonic tests, for each level of axial load. The analysis of the moment-rotation curves in Fig. 8 allows three key observations to be made. The first concerns the pinching effect which intensity becomes more pronounced as the axial load decreases. This phenomenon is likely due to the lack of fit between the base plate and the upright, as well as between the base plate and the concrete block. Under high axial loads, the contact between the elements is indeed consistently maintained, and the failure of the upright occurs at lower lateral displacement values. The second observation regards ductility, which under cyclic conditions is generally lower than that observed in monotonic tests; this reduction becomes increasingly evident as the axial load increases. An exception is the 30 kN case, which displays greater ductility in the cyclic regime. It is worth noting that, for this load level, only one monotonic test was performed. Finally, it can be noted that the monotonic curve lies below the cyclic curves. In this case as well, the phenomenon magnitude depends on the axial force, becoming more significant as the axial load increases.

Cross-Aisle. The collapse modes were quite similar for each level of applied axial load and can be associated with a mix of the failure modes exhibited during the monotonic

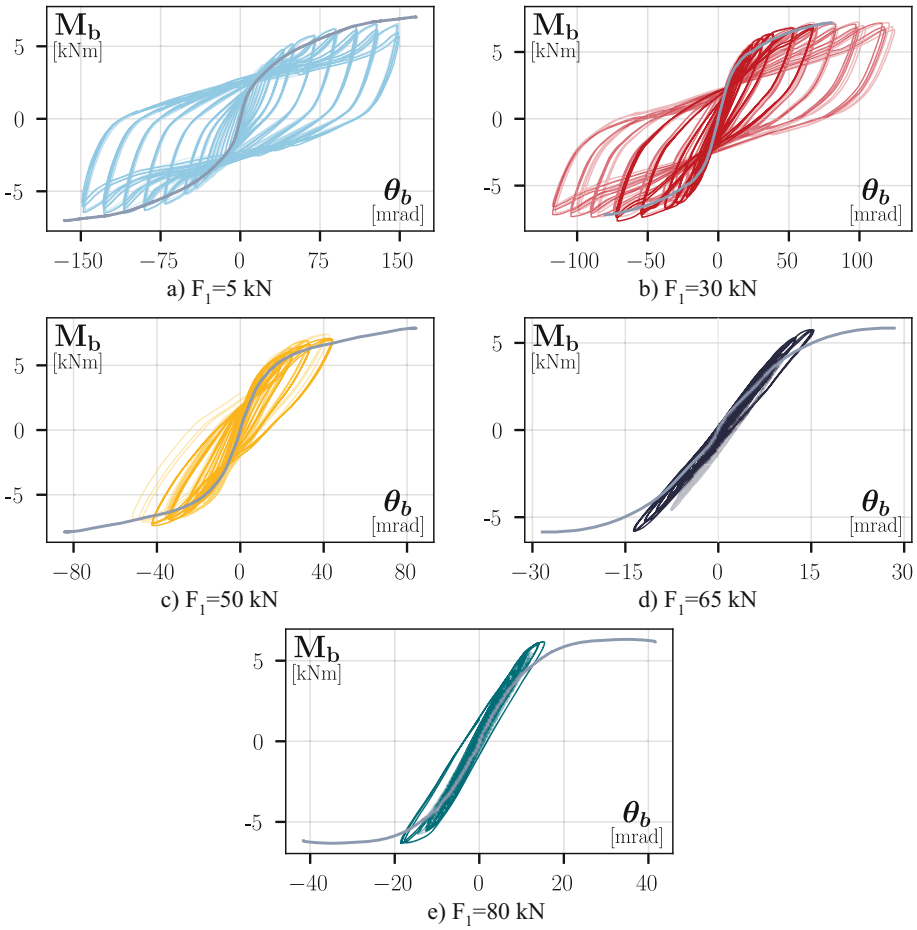


Fig. 8. Cyclic test results for configuration A

tests in configurations B1 and B2. Similarly to configuration A, the pinching effect is more pronounced at low axial load levels. Conversely, for higher loads (50 kN and 80 kN), this phenomenon is significantly limited, and the specimens exhibit a nearly elastic response. This configuration also confirms the trend of a progressive reduction in deformation capacity as the axial load increases. Furthermore, the cyclic deformation capacity is also reduced if compared to the monotonic one (Fig. 9).

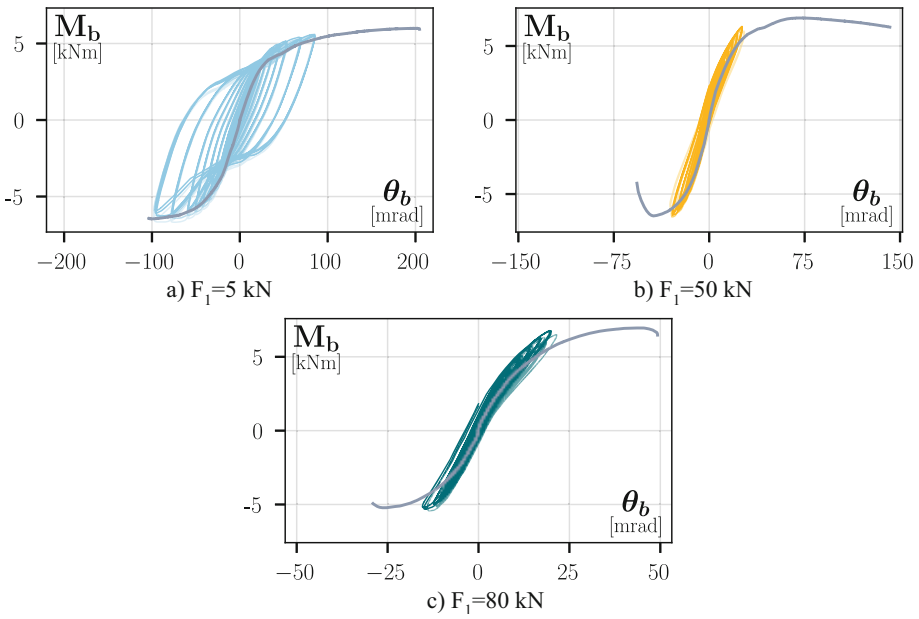


Fig. 9. Cyclic test results for configuration B

5 Numerical Modelling of the Hysteretic Response

Given the significant influence of base connections in the global structural response of pallet racking systems, accurate numerical modelling requires a precise representation of their moment-rotation behaviour. As highlighted by the experimental results, the numerical model of the base joint must be capable of adequately capturing nonlinearities, asymmetries, pinching effects, and degradation phenomena. OpenSees [15] provides a versatile computational tool for this purpose. Within this framework, the joints can be modelled using *zeroLength* elements, whose flexural behaviour can be defined by a *Pinching4* material model. This model is characterized by a backbone curve (the black lines in Fig. 10), unload-reload paths that account for the pinching effect (the red lines in Fig. 10). Specifically, these paths consist of an unloading branch, a pinching branch and a reloading branch. For the unload path, point (b) defines the end of the unloading branch, segment (b)-(c) defines the pinching branch, and segment (c)-(d) represents the reloading branch. Similarly, for the reload path, the same branches are defined by point (e), segment (e)-(f), and segment (f)-(a), respectively. In addition, three distinct damage rules govern unloading stiffness, reloading stiffness, and strength degradation.

The calibration of the parameters defining the backbone curve and the pinching parameters is based on the conservation of the dissipated energy. Specifically, the backbone curve was obtained from the experimental envelope curve of the cyclic tests. This approach allows to implicitly account for the phenomena associated with the damage rules. Furthermore, due to the nearly absent softening branch in the experimental curves, the coordinates of the fourth point of the backbone curve were conventionally set at a rotation equal to 120% of the maximum recorded rotation and a moment value equal to 10%

of the maximum moment. This approach provides a simplified strategy for numerically simulating a post-peak performance of the joint, avoiding convergence problems.

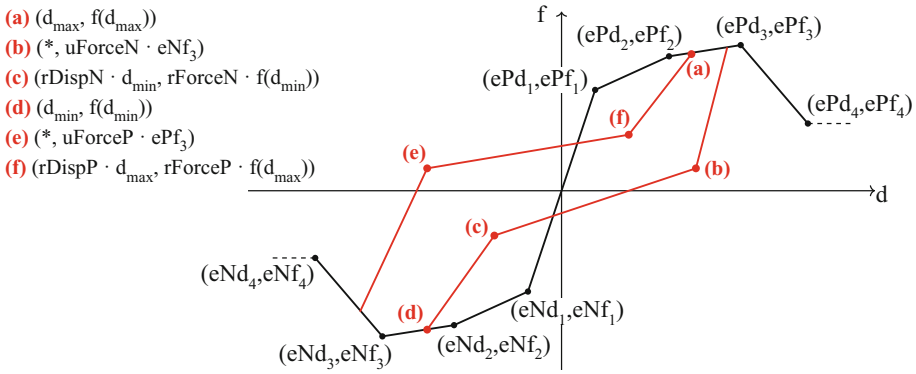


Fig. 10. *Pinching4* model [15]

For configuration A, owing to the symmetric behaviour observed experimentally, the positive (P) backbone and pinching parameters (Table 1) were also applied for the negative (N) counterpart with a sign reversal. Conversely, this symmetry was not observed for configuration B, thus requiring separate definitions for the positive (Table 2) and negative parameters (Table 3).

Table 1. *Pinching4* positive (P) parameters for base joints in configuration A

F_1	ed_1	ef_1	ed_2	ef_2	ed_3	ef_3	ed_4	ef_4	uForce	rDisp	rForce
[kN]	[mrad]	[kNm]	[mrad]	[kNm]	[mrad]	[kNm]	[mrad]	[kNm]			
5	17.0	3.6	83.2	6.3	170.0	6.4	200.0	0.6	−0.1	0.5	0.7
30	12.4	5.0	53.0	7.0	125.0	7.5	150.0	0.7	−0.4	0.8	0.9
50	8.3	4.3	27.4	6.8	45.0	7.2	75.0	0.7	−0.5	0.8	0.9
65	2.2	1.4	9.5	4.7	15.5	6.0	20.0	0.5	−0.7	0.7	0.8
80	3.5	2.3	10.5	5.7	20.0	6.3	30.0	0.6	−0.6	0.8	0.9

The parameters presented in Tables 1, 2 and 3 can be directly applied to the global numerical modelling of pallet racking systems. An analysis routine can be established, taking so benefit from the implementation flexibility of OpenSees [15]. First, a preliminary analysis determines the axial force acting on the uprights; subsequently, the routine assigns the calibrated *Pinching4* material model to each *zeroLength* element based on the closest matching axial force value.

It should be noted that, due to the intrinsic formulation of the *Pinching4* model and the calibration approach adopted, the presented parameters are applicable to joints that exhibit cyclic experimental behaviour and cycle-by-cycle energy dissipation capability analogous to those reported in this paper.

Table 2. *Pinching4* positive (P) parameters for base joints in configuration B

F_1	ed_1	ef_1	ed_2	ef_2	ed_3	ef_3	ed_4	ef_4	uForce	rDisp	rForce
[kN]	[mrad]	[kNm]	[mrad]	[kNm]	[mrad]	[kNm]	[mrad]	[kNm]			
5	15.0	3.0	35.0	5.0	100.0	5.8	120.0	0.6	0.2	0.4	0.7
50	4.0	2.0	20.0	6.0	37.0	6.8	40.0	0.6	−0.7	0.3	0.6
80	5.0	3.0	10.0	5.1	22.0	6.8	25.0	0.6	−0.5	0.3	0.5

Table 3. *Pinching4* negative (N) parameters for base joints in configuration B

F_1	ed_1	ef_1	ed_2	ef_2	ed_3	ef_3	ed_4	ef_4	uForce	rDisp	rForce
[kN]	[mrad]	[kNm]	[mrad]	[kNm]	[mrad]	[kNm]	[mrad]	[kNm]			
5	−20.0	−5.0	−55.0	−6.5	−100.0	−6.7	−120.0	−0.6	0.2	0.5	0.6
50	−5.0	−2.5	−20.0	−6.0	−32.0	−6.5	−40.0	−0.6	−0.8	0.8	0.9
80	−4.5	−3.0	−10.0	−5.0	−15.0	−5.5	−20.0	−0.5	−0.9	0.5	0.5

6 Conclusions

In this study, an experimental campaign was conducted on a base plate joint type of steel storage pallet racks, following the procedure proposed by [3]. Monotonic test results confirmed that the axial load level significantly influences the joint performance in terms of failure modes, stiffness, and both flexural and rotational capacities. Additionally, cyclic testing demonstrated that the axial load magnitude explicitly affects the hysteretic pinching behaviour.

To exploit the collected experimental data for practical applications, the numerical calibration of the *Pinching4* [15] material model was presented for the investigated base joint. In the context of full-scale rack modelling, these parameters are crucial for defining the joint moment-rotation relationship across different axial load levels and along both principal directions.

Acknowledgments. The authors would like to thank Mr. Stefano Girardi, of the Testing laboratory for light structural metals systems of the University of Trento, for his valuable technical assistance and support during the experimental testing.

References

1. Baldassino N, Bernuzzi C (2000) Analysis and behaviour of steel storage pallet racks. Thin-Walled Struct 37(4):277–304
2. Baldassino N, Zandonini R (2004) Performance of base-plate connections of steel storage pallet racks. In: Dubina D, Grecea T (eds) Recent advances and new trends in structural design. Proceedings of the international colloquium dedicated to the 70th anniversary of professor Victor Gioncu. Editura Orinzonturi Universitare, Timisoara, pp 11–20

3. European Committee for Standardization (2022) Steel static storage systems – Adjustable pallet racking systems – Principles for structural design, EN 15512 + A1.
4. Rack Manufacturers Institute (2012) Specification for the design, testing and utilization of industrial steel storage racks, ANSI MH16.1.
5. Standards Australia (2012) Steel storage racking, AS 4084.
6. Baldassino N, Zandonini R (2011) Design by testing of industrial racks. Adv Steel Constr 7(1):27–47
7. Zhao X, Huang Z, Wang Y, Sivakumaran S (2019) Flexural behavior of steel storage rack base-plate upright connections with concentric anchor bolts. Steel Compos Struct 33(3):357–373
8. Godley MHR, Beale G, Feng X (1998) Rotational stiffnesses of semi-rigid baseplates. In: Yu WW, LaBoube RA (eds) 14th international specialty conference on cold-formed steel structures. University of Missouri-Rolla, St. Louis, pp 323–334
9. Rosin I, Calado L, Proença J et al (2009) Storage racks in seismic areas. Final research report RFCS Project SEISRACKS. Publications Office of the European Union, Luxembourg
10. Huang Z, Wang Y, Zhao X, Sivakumaran S (2021) Determination of the flexural behavior of steel storage rack baseplate upright connections with eccentric anchor bolts. Thin-Walled Struct 160:107375
11. Yazici C, Gürbüz M, Orhan N, Solak K, Özkal FM (2025) Structural performance of different baseplate configurations in storage rack systems. Arab J Sci Eng 50(16):13209–13223
12. Furukawa MN, Malite M (2026) Performance of baseplate connections in steel storage rack systems: an experimental and theoretical study. Structure 88:111954
13. Castiglioni CA, Kanyilmaz A, Bernuzzi C et al (2014) Seismic behaviour of steel storage pallet racking systems (SEISRACKS2). Final research report RFCS Project SEISRACKS2. Publications Office of the European Union, Luxembourg
14. Gabbianelli G, Cavalieri F, Nascimbene R (2019) Seismic fragility curves of steel storage pallet racks. In: Proceedings of the fourth international workshop on seismic performance of non-structural elements (SPONSE), Pavia, pp 363–377
15. OpenSees command language manual. https://opensees.berkeley.edu/wiki/index.php/Command_Manual. Accessed 01 July 2026
16. Bernardi M (2021) Industrial steel storage racks subjected to static and seismic actions: an experimental and numerical study. PhD Thesis. University of Trento, Trento
17. European Convention for Constructional Steelwork (ECCS) (1986) Recommended testing procedure for assessing the behaviour of structural elements under cyclic loads, ECCS Publication 45

Buckling and Strength Performance of CFS Back-to-Back Folded-Flange Beams: A Numerical Study

Ward Alarab Safarani(✉), Francesco Tondolo, and Donato Sabia

Department of Structural, Geotechnical and Building Engineering, Politecnico di Torino, Turin, Italy
ward.safarani@polito.it

Abstract. Growing global challenges and the escalating urgency of climate change have intensified the demand for structural systems that are both efficient and sustainable. Within this context, Cold-Formed Steel (CFS) has gained prominence due to its high strength-to-weight ratio, manufacturing efficiency, and inherent recyclability, positioning it as a compelling alternative to traditional construction materials. Among the emerging innovations in CFS design is the use of Folded-Flange Beams (FFBs) in moment-resisting beam-column connections. It is a potential application that offers promising structural advantages but remains insufficiently explored due to limited experimental evidence. This study presents a comprehensive numerical investigation into the flexural behaviour, strength, and stability of CFS FFBs. The research addresses a critical gap in current knowledge by providing an insight about the structural response of FFBs and identifying their dominant strength and deformation characteristics. By expanding the limited database on CFS beam systems, this study contributes essential evidence supporting the integration of Folded-Flange Beams into modern moment-resisting structures. The outcomes not only enhance understanding of their structural feasibility but also reinforce their potential role in promoting resource-efficient and environmentally responsible building solutions.

Keywords: Cold-formed steel · Folded-flange beam · Flexural behaviour and buckling

1 Introduction

The construction sector is increasingly required to respond to two parallel demands: the need for structurally efficient building systems and the need to reduce the environmental impact associated with material consumption, fabrication, and construction processes. As climate-change concerns continue to influence engineering practice, greater attention has been directed toward structural solutions that can deliver adequate strength and serviceability while using fewer resources. In this context, lightweight steel construction has become an important area of research and development because it offers opportunities for material efficiency, prefabrication, ease of transportation, and improved

© The Author(s), under exclusive license to Springer Nature Switzerland AG 2026
R. Zanon et al. (Eds.): CTA 2026, LNCE 942, pp. 381–388, 2026.
https://doi.org/10.1007/978-3-032-39505-4_33

recyclability at the end of a structure's service life [1, 2]. The structural behaviour of CFS members is often more complex than that of traditional steel sections. Because CFS elements are typically thin-walled, they are susceptible to local buckling, distortional buckling, lateral-torsional instability, and interactions among different failure modes. These stability-related phenomena can significantly influence the strength, stiffness, ductility, and deformation capacity of CFS members. Therefore, a reliable understanding of their behaviour requires not only theoretical and numerical assessment but also experimental validation, particularly when new cross-sectional configurations or connection arrangements are proposed [3]. Recent developments in CFS construction have encouraged the exploration of enhanced beam sections capable of improving flexural resistance and connection performance. One such development is the Folded-Flange Beam (FFB), in which the flange geometry is modified through folding to improve sectional efficiency and stability [2]. The folded flange can provide additional stiffness to the compression region of the beam and may help delay or reduce certain buckling effects. As a result, FFBs have potential for use in moment-resisting beam-column connections, where the beam must transfer bending moments while maintaining adequate deformation capacity and structural integrity [4]. However, the use of CFS FFBs in moment-resisting systems remains relatively underdeveloped. Although the concept offers promising structural advantages, the available experimental evidence is still limited. Most existing research on CFS members has focused on conventional channel, lipped-channel, or other standard open sections, while less attention has been given to folded-flange configurations under flexural loading. This lack of full-scale experimental data restricts the ability to evaluate their strength, stiffness, failure mechanisms, and suitability for practical design. Consequently, further investigation is needed to clarify how FFBs respond under bending and to determine whether their performance can meet the demands of modern structural applications [5, 6].

2 Numerical Model

Numerical model of four-point bending test on CFS FFB sections has been developed to simulate the actual experimental test and study the flexural behaviour of CFS FFBs. The analysis has been carried out using ABAQUS software. The test setup is show in Fig. 1. The beam length is 3300 mm and the distance between the supports is 3100 mm while the distance between loading points is 1100 mm. An adjustable lateral-restraining system (in yellow shown in Fig. 1) was designed to limit the lateral deformation of the beam due to global buckling.

2.1 Geometry

The cross-section of FFB shown in Fig. 1 was selected with an overall depth of 270 mm and a width of 80 mm. The web depth is 200 mm, and the flanges are folded at an internal angle of 120°. The thickness of FFB under study is of 3 mm [2].

To select the radii value suitable to manufacture this cross-section, three different corner radii were studied: 1 t, 2 t, and 3 t, where t represents the thickness of the beam section. The findings reported in Table 1 show that increasing the radius has no major

impact on the flexural capacity of the cross-section. For this reason, corner radii of 2 t = 6 mm was adopted.

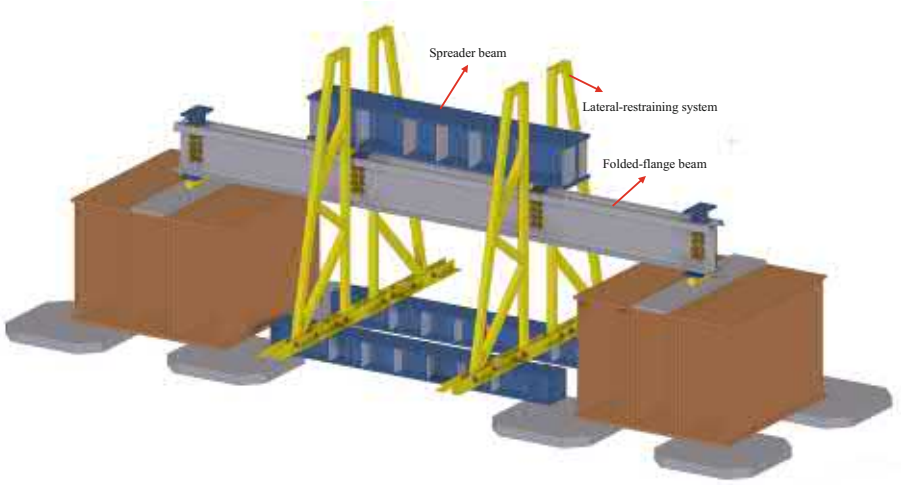


Fig. 1. Four-point bending test setup for back-to-back FFB

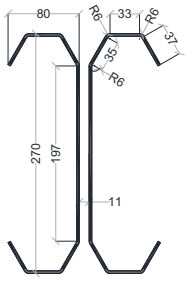


Fig. 2. Geometry of the folded-flange back-to-back beam section as specified for fabrication (t = 3 mm, R = 6 mm)

Table 1. FFB Parametric study summary

Cross section	Thickness	Radius	Mp	Buckling Half-Wavelength		Modelling Length
	[mm]	[mm]	[kNm]	LB [mm]	DB [mm]	[mm]
Folded	3.0	t	66.232	90	700	2100
		2 t	66.255			

(*continued*)

Table 1. (*continued*)

Cross section	Thickness	Radius	Mp	Buckling Half-Wavelength		Modelling Length
		3 t	66.299			

2.2 Material Properties

The model incorporates non-linear stress-strain behaviour from coupon tests. Uniaxial tensile stress was carried out on steel tensile coupons (as shown in Fig. 3) extracted from flat web regions of 1.5 m long and 3 mm thickness from a folded-flange spare beam piece prepared specially to carry out material testing. The beam component was produced from a 1500x3 mm steel coil with a grade of S355J2 + N. The material provides a minimum guaranteed yield strength (Rp0.2) of 355 MPa, and the minimum tensile strength (Rm) required is 470 MPa. The coupon testing was in accordance with [7].



Fig. 3. Coupon test a) Steel coupon under testing, b) Flat coupons after failure

The material model that was incorporated into ABAQUS is represented by true stress-strain curve obtained from the original engineering stress-strain curve. The latter two curves as well as the elastic modulus slope are illustrated in Fig. 4.

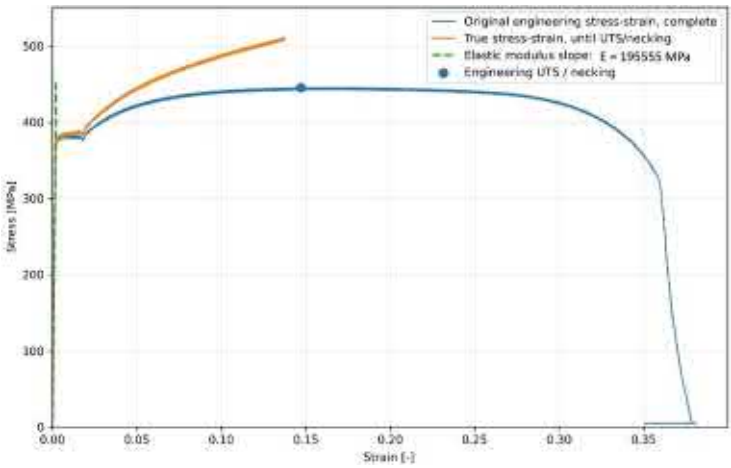


Fig. 4. Coupon Test 1 W Results: Engineering vs. True stress-strain curve

2.3 Element, Mesh and Analysis Type

The type of analysis performed is general static analysis. The mesh size of 5x5 mm was selected with S4R general-purpose finite element which is a 4-node, quadrilateral, stress/displacement shell element with reduced integration and a large-strain formulation.

2.4 Loading and Boundary Conditions

T-sections in between the back-to-back FFB were used to transfer the loads through bolts directly to the web as shown in the test configuration in Fig. 1. To simulate the configuration of four-point bending, reference points were used to introduce boundary and loading conditions, at loading points and supports regions, and coupled to the corresponding t-section flange. Vertical displacements were applied at the reference points at the location of loading. Pinned and roller boundary conditions were introduced into the model at the related reference points of the supports. The lateral-restraining system were also considered by limiting the displacement of FFB section in X direction as shown in Fig. 5.

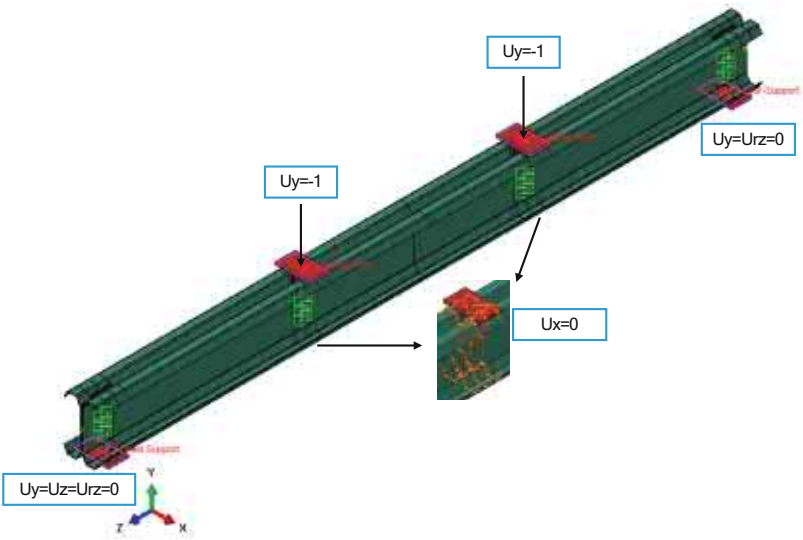


Fig. 5. Boundary and loading conditions for four-point bending configuration

3 Results

The critical buckling mode for FFB cross-section in Fig. 2 is distortional as illustrated in the signature curve in Fig. 6. The critical buckling moment is 2.92 times the yielding moment. This means that the FFB section with thickness 3 mm is fully effective. The yielding moment around the strong axis considering two back-to-back FFB is about 65.58 kN.m. The failure shape resulted from finite strip analysis shows that the critical buckling mode consists of a distortion in the compression flange followed by a local buckling in the web. This aligns with the failure shape obtained by finite element analysis of four-point bending configuration shown in Fig. 7. The moment capacity of the FFB section is 81.91 kN.m.

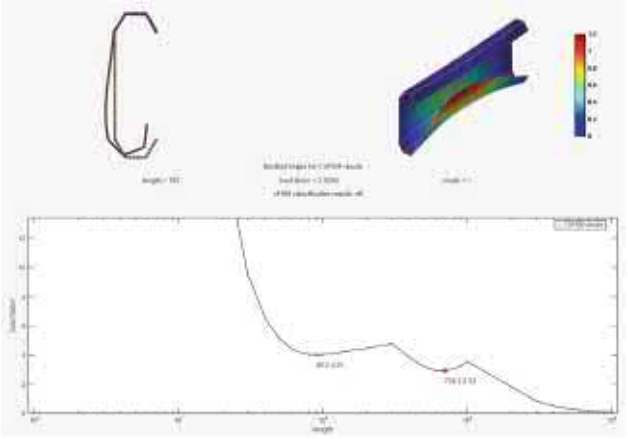


Fig. 6. Signature curve of FFB section

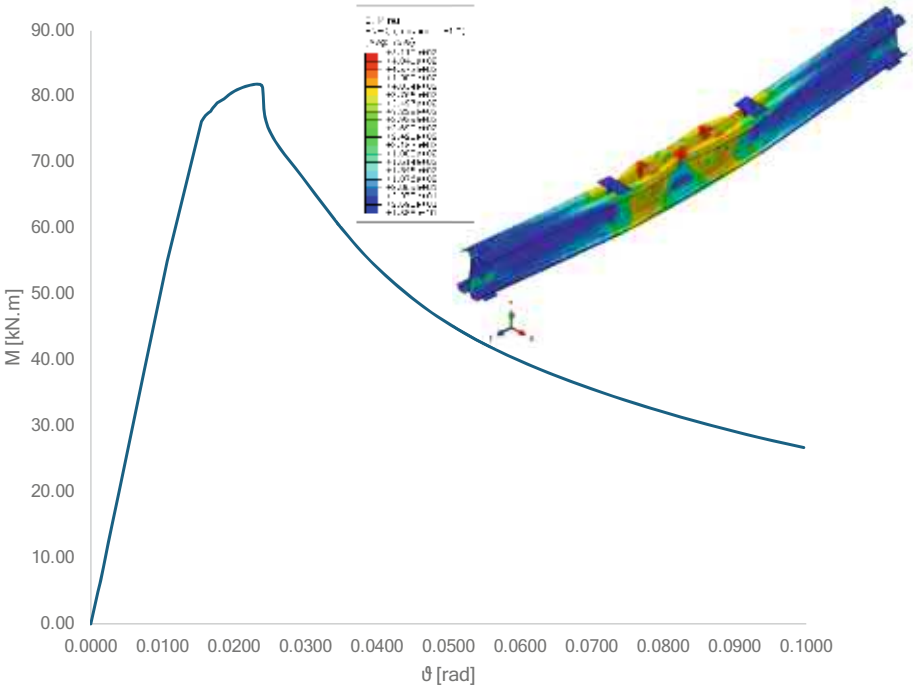


Fig. 7. Moment-Rotation curve and failure shape of FFB

4 Conclusion

- This study investigated the flexural and buckling performance of CFS back-to-back FFBs using numerical modelling supported by material testing.
- The proposed FFB configuration showed potential as an efficient CFS beam solution, especially for applications requiring improved flexural resistance and enhanced stability.
- The folded-flange geometry improved the effectiveness of the compression region and contributed to delaying instability effects under bending.
- The critical buckling moment was 2.92 times the yielding moment, indicating that the 3 mm thick FFB section is fully effective under bending.
- The back-to-back FFB section achieved a yielding moment of approximately 65.58 kNm and a plastic moment capacity of 81.91 kNm, confirming its reliable flexural resistance.
- The findings confirm that folded-flange geometry can enhance the flexural performance and stability of CFS beams while preserving the lightweight, material-efficient, and sustainable advantages of CFS construction.
- Future work should include full-scale experimental validation, connection-level testing, and broader parametric studies to support reliable design recommendations for practical use of FFBs in moment-resisting systems and lightweight steel structures.

Acknowledgments. The authors gratefully acknowledge DAMILANO GROUP S.R.L. for its research support and for providing the material and beam sections used in the experimental tests. The authors also acknowledge Laboratorio MastrLAB, in the DISEG Department at Politecnico di Torino, where all material testing was performed.

References

1. Hasanali M, Roy K, Mojtabaei SM et al (2022) A critical review of cold-formed steel seismic resistant systems: recent developments, challenges and future directions. Thin-Walled Struct 180:109953. https://doi.org/10.1016/j.tws.2022.109953
2. Ye J, Hajirasouliha I, Becque J, Pilakoutas K (2016) Development of more efficient cold-formed steel channel sections in bending. Thin-Walled Struct 101:1–13. https://doi.org/10.1016/j.tws.2015.12.021
3. Ye J, Mojtabaei SM, Hajirasouliha I et al (2018) Strength and deflection behaviour of cold-formed steel back-to-back channels. Eng Struct 177:641–654. https://doi.org/10.1016/J.ENGSTRUCT.2018.09.064
4. Ye J, Mojtabaei SM, Hajirasouliha I (2019) Seismic performance of cold-formed steel bolted moment connections with bolting friction-slip mechanism. J Constr Steel Res 156:122–136
5. Safarani WA, Tondolo F (2024) Computational study on moment-resisting connections in cold-formed steel structures. Fondazione Promozione Acciaio, Milano
6. Safarani WA, Tondolo F (2024) Cold-formed steel moment-resisting connection: numerical study. The Swedish Institute of Steel Construction, Stockholm
7. CEN (2019) BS EN ISO 6892-1:2019. Metallic materials-Tensile testing-Part 1: Method of test at room temperature

Influence of Inherent Damping in Modelling Steel Storage Racks

Jorge Ruiz-Oronia[1(✉)], Bryan Chalarca[2], and Giammaria Gabbianelli[2]

[1] University School for Advanced Studies IUSS, Pavia PV 27100, Italy
jorge.ruiz@iusspavia.it
[2] Department of Civil Engineering and Architecture, University of Pavia, Pavia PV 27100, Italy

Abstract. Steel pallet rack systems are widely used for industrial storage, yet past earthquakes have exposed their vulnerability to seismic effects. Eurocode EN 16681 permits their seismic design by modal response spectrum analysis (MRSA) and, for the loaded case, allows up to 10% inherent damping ratio attributed to sliding of the pallets on the rack beams. However, guidelines do not specify how the inherent damping should be represented in nonlinear time history analysis (NTHA). This study explores the seismic response of a steel rack using seven approaches to model the inherent damping and compares the results among them and the MRSA. The results show that in the down-aisle direction the MRSA and NTHA responses are of similar magnitude, although the trends in the lateral storey-drift profiles differ. In the cross-aisle direction the profile trends are consistent across all NTHA models, but their magnitudes differ considerably, and MRSA exhibited the lowest results, especially in the lateral story drift at the first floor. These findings indicate that the inherent damping model must be carefully selected, and that there is still room for further improvements on this regard.

Keywords: Steel storage pallet racks · Inherent damping models · Seismic response · Steel racks systems · Rayleigh damping

1 Introduction

Steel pallet rack systems are an effective solution for storage due to their fast construction, ease of assembly, and versatility of use and configuration, making them widely adopted wherever storage demands arise, particularly in industrial settings. Regarding their structural topology, steel racks systems present key differences from conventional structures: (a) a high disparity in lateral stiffness between the longitudinal (down-aisle) and transverse (cross-aisle) directions; (b) very low self-weight, which rarely exceeds about 5% of the total load capacity [1]; (c) beam-to-column (upright) connections that are typically plug-in connections, sometimes fitted with a safety pin to prevent beam uplift; (d) cold-formed steel sections; and (e) slender elements whose elastic capacity usually governs, making it difficult to develop any significant plasticity [2] and susceptible to buckling or warping effects [3].

© The Author(s), under exclusive license to Springer Nature Switzerland AG 2026
R. Zanon et al. (Eds.): CTA 2026, LNCE 942, pp. 389–400, 2026.
https://doi.org/10.1007/978-3-032-39505-4_34

These differences raise the question of whether the analysis procedures used to assess buildings — particularly for seismic forces — are equally reliable for this type of structure, or whether care must be taken in applying them to obtain a reasonable prediction of the response. As is commonly established in building codes worldwide, the European code EN 16681 [4] prescribes modal response spectrum analysis (MRSA) as the standard seismic design procedure, and for certain structures nonlinear time history analysis (NTHA) may additionally be required. This paper compares the two analyses to assess how accurately the MRSA response reproduces the NTHA behavior. The comparison is carried out in terms of lateral storey drift.

In both types of dynamic analysis, the inherent damping was taken as 10%, as established in EN 16681; such high damping is attributed to the sliding of pallets on the rack beams when loaded [5]. This paper offers some insights into how to model inherent damping in the NTHA. Seven approaches were considered, each calibrated to produce an equivalent viscous damping of 10%: mass-proportional damping; initial-stiffness-proportional damping; tangent-stiffness-proportional damping; and Rayleigh damping characterized by the 1st mode and the mode that captures at least 90% of the seismic mass, and by the 1st and 2nd modes, each considered with either initial or tangent stiffness.

The main purpose of the paper is the identification of (1) whether the inherent damping model produces significant differences in the seismic response, and (2) how these differences compare against MRSA, in which a 10% inherent damping ratio is assumed when computing the response spectrum.

2 Case Study Steel Storage Pallet Rack and Inherent Damping Models

The case study steel storage pallet rack was adapted from the SEISRACKS2 project [6]. A three-dimensional model was considered with a down-aisle length of 10.8 m divided into four bays, a cross-aisle length equal to 1.1 m, and a total height of 8.2 m divided into four stories of 2.0 m each, plus 0.20 m at the top of the upright (see Fig. 1). The pallet loads were applied by a uniform linear force equal to 4.3 kN/m in all the pallet beams of the steel rack. The modal properties of the case study rack are summarized in Table 1.

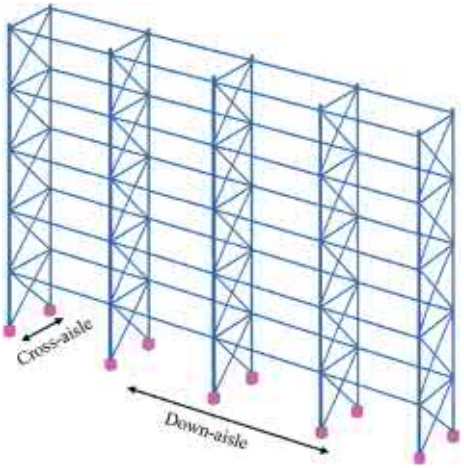


Fig. 1. Isometric view of the case study steel rack

Eurocode EN 1998–1 specifies that the MRSA should include the number of modes required to reach 90% of the seismic mass of the structural model. Accordingly, for the MRSA the first 42 modes were considered, which account the following participating mass in each direction: 100% for down-aisle translation, 95.91% for cross-aisle translation, and 92.58% for rotation about the Z axis. Table 1 and Table 2 report the three modes contributing most to the mass participation in each of the translational and rotational directions, together with their natural periods and frequencies.

Table 1. Natural frequencies of the three modes with highest mass participation in each direction

Mode	Period	Down-aisle	Cross-aisle	Torsion
1	2.50	82.12%	–	–
3	0.73	–	68.68%	–
4	0.68	–	–	57.03%
5	0.65	12.49%	–	–
7	0.58	–	6.59%	–
8	0.47	–	–	12.78%
39	0.29	4.31%	–	–
25	0.34	–	10.55%	–
24	0.36	–	–	7.73%
		98.93%	**85.82%**	**77.54%**

2.1 Numerical Analysis

The numerical analyses were performed in OpenSeesPy [7]. The members (uprights, beams, and braces) were modelled with elastic beam-column elements including geometric nonlinearity, and the warping effect is incorporated in the beam-column element formulation [8]. To represent the plug-in connection between the beam and the upright, a zero-length element with the uniaxial Pinching4 material was used. Its hysteretic behavior was calibrated against experimental results from cyclic tests on the beam-upright connection (see Fig. 2).

For confidentiality reasons, absolute values are not reported; the backbone curve is normalized by the maximum moment and rotation capacity, as the figure is intended only to illustrate the shape of the hysteretic response. Consistent with the nature of this connection, the stiffness, the moment and rotational capacities differ depending on the direction of loading: the positive quadrant of the curve corresponds to the response under vertical loads. The *Hysteretic* material was used to model the nonlinear shear and axial behavior of the beam-upright and upright-beam connections. Further information on the materials, section properties, and modelling assumptions can be found in [9].

2.2 Ground Motions

The case study rack is assumed to be in a high seismicity area in Colombia with a soil type C. A set of 11 ground motions was selected from the far-field ground motion set proposed in the FEMA P695 document [10] and scaled following the recommendation of the ASCE 7–22 [11] to match the design spectrum NSR-10. Figure 3 shows the envelope and median spectra of the scaled response spectrum for all the ground motions considering a critical damping ratio of 10%. More information regarding the definition and scaling of the ground motions can be found in [1].

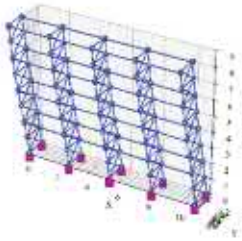
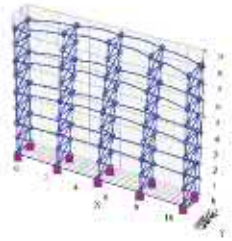
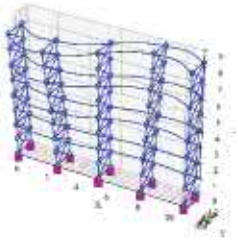
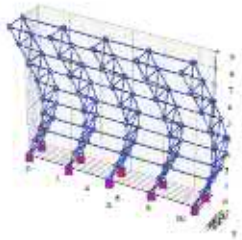
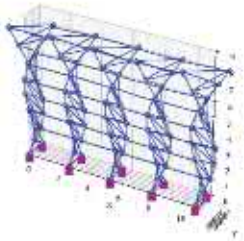
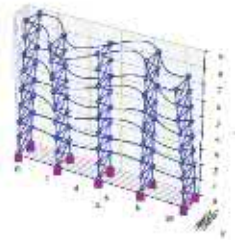
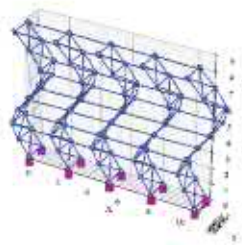
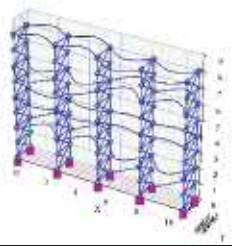
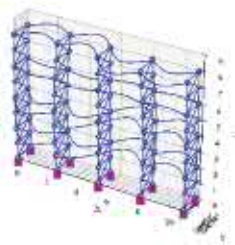
2.3 Inherent Damping

In the NTHA, inherent damping is represented through the damping matrix C, which accounts for the sources of energy dissipation that are not explicitly modeled. These include nonlinearities within the elastic range, foundation damping, material nonlinearity and radiation damping, damping from non-structural elements, among others [12]. In the present case, as noted earlier, most of the inherent damping is presumed to arise from the sliding of pallets on the beams.

In this work, the damping matrix used to solve the dynamic equations is built from mass-proportional terms, stiffness-proportional terms, or both, following the Rayleigh procedure (Eq. (1)) [13]. In this approach the damping forces are taken to be velocity-dependent for mathematical convenience; however, this procedure has well-known drawbacks that must be kept in mind when applying it [14]. Despite this, Rayleigh damping serves as a general tool to assess the effects of inherent viscous damping in the structure, as described in Eq. (1).

$$\boldsymbol{c} = a_0\boldsymbol{m} + a_1\boldsymbol{k} \tag{1}$$

Table 2. Mode shapes

Mode	**1**	**3**	**4**
T = [s]	2.50	0.73	0.68
w = [rad/s]	2.52	8.59	9.20
MPMR* = [%]	82.12	68.68	57.03
			
Mode	**5**	**7**	**8**
T = [s]	0.65	0.58	0.47
w = [rad/s]	9.68	10.80	13.49
MPMR* = [%]	12.49	6.59	12.78
			
Mode	**39**	**25**	**24**
T = [s]	0.29	0.34	0.36
w = [rad/s]	17.63	18.73	21.79
MPMR* = [%]	4.31	10.55	7.73
			

*MPMR = Modal Participation Mass Ratio

Where a_0 and a_1 represent the mass-proportional and stiffness-proportional factors, respectively.

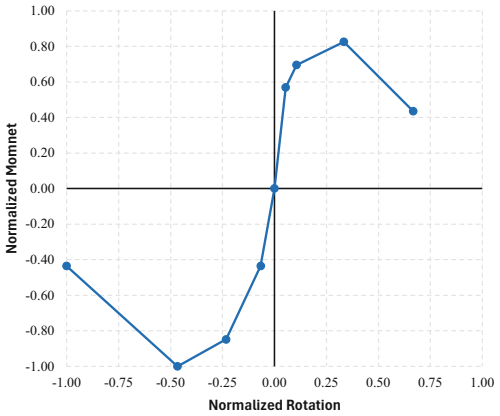


Fig. 2. Normalized backbone curve of the beam-upright connection

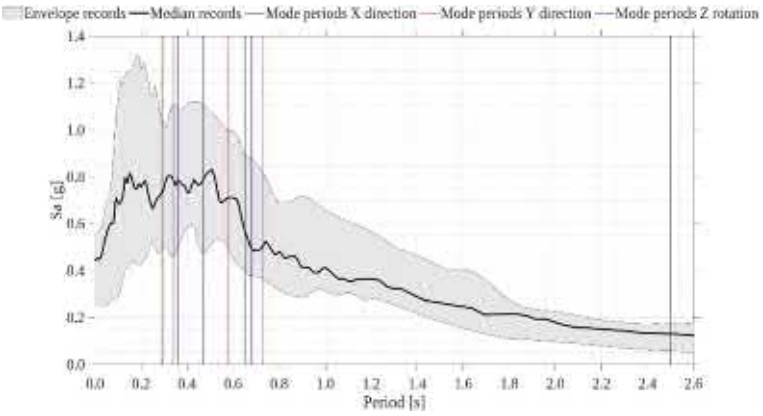


Fig. 3. Seismic input 10% damping spectra. X direction = Down-aisle; Y direction = Cross-aisle

A series of analyses was performed by varying the approach used to model the inherent damping; while the percentage critical damping value was kept as 10% for all models, as recommended by EN 16681 [4]. As summarized in Fig. 3 and represented in Fig. 4, the seven inherent damping models evaluated correspond to:

- A mass proportional damping (***M-Model***) computed using the 1st mode.
- Stiffness proportional damping models are characterized by the initial stiffness (i.e., the stiffness matrix is read at the very beginning of the analysis), and by the tangent stiffness (i.e., the stiffness matrix is read after each analysis iteration) (***S_I / S_T – Models***).
- Rayleigh damping models (i.e., based on a combination of both mass and stiffness proportional damping). Similar to the stiffness proportional model, initial and tangent stiffness assumptions were also taken for the formulation of Rayleigh damping. In addition, the two modes considered to compute the proportional factor values were assumed as the 1st and the 42th modes (***$R_{I\text{-}142}$ / $R_{T\text{-}142}$ – Models***) and the 1st and 2nd

modes (***R*I-12 / *R*T-12 – Models**). The mode selection for the formulation of Rayleigh damping could be misleading, as they are commonly labeled as mode 1 and mode 2, especially in commercial software. This can lead to the use of the 1st and 2nd modes of structure, instead of using two modes that cover at least 90% of the seismic mass.

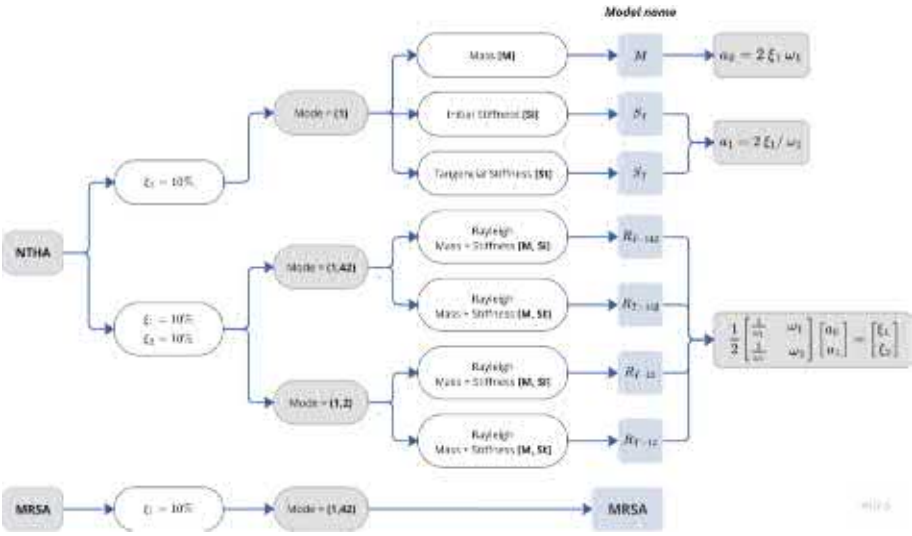


Fig. 4. Summary of the inherent damping models evaluated

Then, using the aforementioned formulations, the equivalent viscous damping can be calculated using Eq. (2) for a given mode frequency (w_n). Table 3 reports the computed equivalent damping values of the different inherent damping models (Fig. 5).

$$\xi_n = \frac{a_0}{2}\frac{1}{w_n} + \frac{a_1}{2}w_n \tag{2}$$

Based on the values reported in Table 3, the following remarks can be drawn: (i) for the mass- proportional damping model, the inherent damping associated with the first mode is 10%, however because of the large separation between the first mode and the others (see Table 1), the subsequent modes are only lightly damped - 2.9% and 2.7% for the modes 3 and 4 respectively, falling to 1.2% for the last mode reported (mode 24); (ii) on the contrary for the stiffness proportional damping model, there is a highly increment of the equivalent viscous damping at subsequent modes, being 34% in mode 3 and 86% in mode 24; (iii) for the Rayleigh damping model with the 1st and 42th modes, the equivalent viscous damping for the first nine modes vary between 8–10%, (iv) meanwhile, the Rayleigh damping model with the 1st and 2nd mode, in the 24th mode the damping rise to 20%. These results highlight the sensitivity of the inherent damping modelling assumptions.

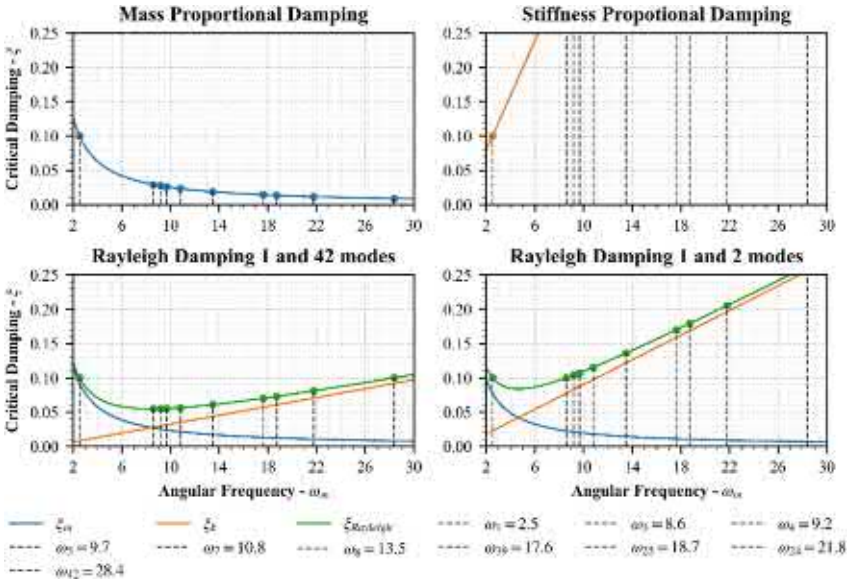


Fig. 5. Equivalent viscous damping values based on the evaluated inherent damping models

Table 3. Percentage of critical damping for the different modes and inherent damping models

Mode	Percentage critical damping [ζ]			
	M	S_I, S_T	$R_{I\text{-}142}$, $R_{T\text{-}142}$	$R_{I\text{-}12}$, $R_{T\text{-}12}$
1	0.100	0.10	0.100	0.10
3	0.029	0.34	0.055	0.10
4	0.027	0.37	0.055	0.10
5	0.026	0.38	0.055	0.11
7	0.023	0.43	0.056	0.11
8	0.019	0.54	0.061	0.14
39	0.014	0.70	0.070	0.17
25	0.013	0.74	0.073	0.28
24	0.012	0.86	0.081	0.20

Finally, according to EN 16681 [4], the seismic design of steel storage racks can be performed using a modal response spectrum analysis (MRSA), for which the code specifies an inherent damping ratio of up to 10% of critical damping to account for pallet sliding. To assess how MRSA represents the structural response, the respective MRSA is performed alongside the Nonlinear Time-History Analysis (NTHA), using the response spectrum of each record computed with an inherent damping of 10% of critical damping.

3 Results

An initial result follows directly from running the nonlinear time history analyses with the different inherent damping models: in some cases, the ground motions caused the collapse of the case-study rack. The mass-proportional and tangent-stiffness-proportional models produced the most collapses, with three each. The initial-stiffness-proportional model produced two. Two of the Rayleigh models produced one collapse each: the one based on initial stiffness anchored at the 1st and 42nd modes, and the one based on tangent stiffness anchored at the 1st and 2nd modes. It should be noted that the median values exclude the responses for the ground motions that produced collapse.

3.1 Storey Drifts

The median peak story drifts of all inherent damping models are presented in Fig. 6. For the down-aisle direction, the following is observed: (i) the lateral story drift profile of the ***M-Model*** shows the participation of higher modes in the response, as for the upper levels, the story drift tends to increase instead of reducing as can be expected for a first mode governed structure; (ii) as shown in Table 3, there is an important reduction in the percentage critical damping for the higher modes, this increase their participation in the seismic response of the system. In addition, the higher modes correspond to the high acceleration zone demand of the response spectrum (see Fig. **3**) triggering their participation in the total response; (iii) on the $\boldsymbol{S_I}$ / $\boldsymbol{S_T}$ - ***Models***, higher modes are overdamped. This considerably reduces their participation. For these models, the total response of the structure seems mainly controlled by the first mode, which results in a consistent expected lateral story drift profile for a first mode governed structure; (iv) on the $\boldsymbol{R_{I\text{-}142}}$ / $\boldsymbol{R_{T\text{-}142}}$ - ***Models***, the critical damping ratio across the covered modes ranges between 8% and 10%. For the $\boldsymbol{R_{I\text{-}142}}$ / $\boldsymbol{R_{T\text{-}142}}$ - ***Models***, the critical damping ratio across the covered modes ranges between 8% and 10%. Despite the higher modes are slightly more damped than in the ***M-Model***, the lateral drift profile shows that these modes still contribute to the overall response, the lateral profile ends up similar to the ***M-Model***.; (v) the $\boldsymbol{R_{I\text{-}12}}$ / $\boldsymbol{R_{T\text{-}12}}$ – ***Models*** confirm that higher modes may have an important impact on the response, the equivalent damping values for these modes are even greater than those of the $\boldsymbol{R_{I\text{-}16}}$ / $\boldsymbol{R_{T\text{-}16}}$ - ***Models*** and still the profile has similar shape and magnitude; (vi) for the MRSA, the storey drift magnitude are close to those obtained by NTHA. However, the lateral profile shows that the response is dominated by the first mode; with the contribution of higher modes not clearly observed.

In the cross-aisle direction, it was noted that for all inherent damping models, the lateral peak story drifts remain with the same profiles but different magnitudes, which suggests that the fundamental mode for this direction (i.e., 3rd mode) is governing the response. Moreover, as reported in Table 3, the inherent damping values associated with the 3rd mode are: 2.9% for the mass proportional model; 5.5% and 10% for the Rayleigh 1st and 42th modes models, and the Rayleigh 1st and 2nd modes models respectively; and finally, 34.0% for the stiffness proportional model. For all cases, the maximum lateral storey drifts occurred in the first floor, following the same order of the level of inherent damping: 2.63%, 2.34%, 1.94%, 1.71%, 1.55%, 1.48%, and 1.36% are the peak story drift for each model. The inherent damping clearly reduces the magnitude of the

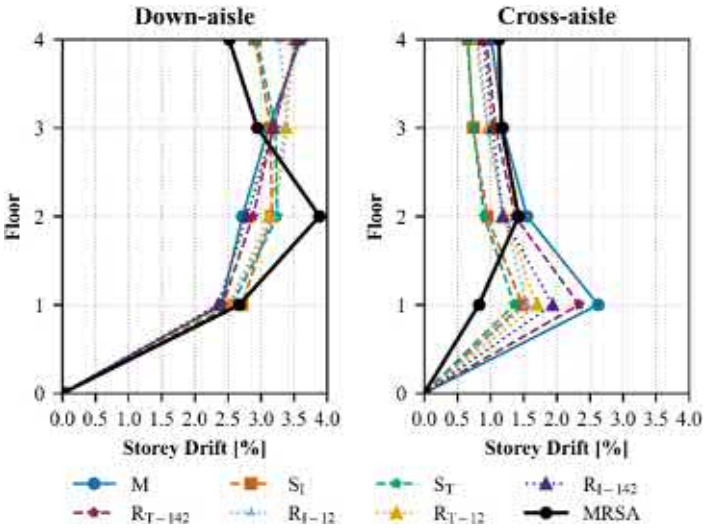


Fig. 6. Median Peak Story Drifts

lateral peak story drifts; the smaller the damping, the higher the magnitude of the lateral peak story drift (see Fig. 6). The modelling assumption of the inherent damping has the potential to increase or reduce the structural response. Moreover, for MRSA the lateral profile exhibits a flexural behavior, with the drift increasing along the height of the building. The drift magnitudes from both analyses agree well over most of the height, except at the first floor, where a significant difference appears. MRSA fails to capture the large drift at the first floor, which may lead to an inaccurate estimation of the structural behavior.

4 Conclusions

The seismic assessment of steel pallet storage racks depends on the ability to build mathematical models that reproduce the structural behavior. In this study, the seismic response of a case-study rack was evaluated using seven approaches to model the inherent damping for nonlinear time history analysis (NTHA) and compared against modal response spectrum analysis (MRSA) in terms of peak storey drifts. Given the results presented, the following conclusions are derived:

- The way inherent damping is modeled in the NTHA directly affects the response, as the contribution of the higher modes is sensitive to the level of damping assigned through the damping model. Care must therefore be taken in defining how inherent damping is represented. Experimental campaigns are needed to determine which modeling approach best estimates the real response, so that guidelines can be developed recommending appropriate procedures for accounting for inherent damping.
- The global response from the two dynamic analyses differs in shape even where the magnitudes are similar. In the down-aisle direction, MRSA does not capture the higher-mode contribution that is clearly observed in the NTHA profiles; in the

cross-aisle direction, the NTHA profiles show a pronounced amplification at the first floor that MRSA fails to reproduce. This limitation of MRSA should be kept in mind when interpreting its results. Further analysis and experimental campaigns are needed to identify adjustments to the MRSA procedure that could account for the effects observed in the NTHA, and to validate if the real behavior of the structure is as we expect from both approaches the MRSA and the NTHA.

- In the cross-aisle direction, the peak storey drift profile remained similar in shape across the inherent damping models, but its magnitude varied with the model. The drift magnitude therefore depends on the technique used to represent inherent damping: the minimum was 1.36%, for the initial-stiffness-proportional model, which assigns 34% damping to the third mode, whereas the maximum was 2.63%, for the mass-proportional model, which assigns only 2.9% to the third mode.
- In the cross-aisle direction, the response is controlled by the third mode and above. The periods of these modes fall within the high-acceleration range of the response spectrum, where the response is most sensitive to damping. The definition of inherent damping therefore becomes critical, since it can lead to underdamping or overdamping of the system.

Further investigation is needed to understand the notable difference in storey drift between the two analyses — particularly MRSA's inability to capture the drift concentration at the first floor in the cross-aisle direction and the higher-mode contribution in the down-aisle direction. The results presented here demonstrate the effect of the inherent damping modeling technique on the response of steel rack structures, expressed in terms of lateral displacement. The way inherent damping is represented in nonlinear time history analysis should therefore be decided with care.

Acknowledgments. The work presented in this paper has been developed within the framework of the project "SAVERACK", funded by the Research Programme of the Research Fund for Coal and Steel (RFCS) of the European Commission under Grant Agreement No. 101216407.

References

1. Rodas S, Herrera JP, Chalarca B, Gabbianelli G, Bedoya-Ruiz D (2025) Seismic demand on steel storage pallet racks located on upper floors. In: Presented at the 10th international conference on computational methods in structural dynamics and earthquake engineering, Greece. https://doi.org/10.7712/120125
2. Gabbianelli G, Cavalieri F, Nascimbene R (2020) Seismic vulnerability assessment of steel storage pallet racks. Ing Sismica Int J Earthq Eng 37(2)
3. Bernuzzi C, Gobetti A, Gabbianelli G, Simoncelli M (2014) Warping influence on the resistance of uprights in steel storage pallet racks. J Constr Steel Res 101:224–241. https://doi.org/10.1016/j.jcsr.2014.05.014
4. European Committee for Standardization (CEN) (2016) EN 16681: steel static storage systems - adjustable pallet racking systems - principles for seismic design
5. European Commission (2009) Directorate-general for research, storage racks in seismic areas (SEISRACKS). Publications Office, LU. https://doi.org/10.2777/60886

6. Castiglioni CA et al (eds) (2014) Seismic behaviour of steel storage pallet racking systems (SEISRACKS2): final report. Publications Office, Luxembourg. https://doi.org/10.2777/931597
7. Zhu M, McKenna F, Scott MH (2018) OpenSeesPy: python library for the OpenSees finite element framework. SoftwareX 7:6–11. https://doi.org/10.1016/j.softx.2017.10.009
8. Gabbianelli G (2016) Numerical model for framed structures with thin-walled cross-section members.," PhD thesis. University of Pavia, Pavia
9. Mucedero G, Gabbianelli G, Rapone A, Monteiro R (2025) A practice-oriented methodology for seismic loss assessment of steel storage pallet racks. Eng Struct 333:120187. https://doi.org/10.1016/j.engstruct.2025.120187
10. FEMA P695 (2009) Quantification of Building Seismic Performance Factors United States
11. ASCE 7-22 (2021) Minimum Design Loads and Associated Criteria for Buildings and Other Structures
12. Petrini L, Maggi C, Priestley MJN, Calvi GM (2008) Experimental verification of viscous damping Modeling for inelastic time history Analyzes. J Earthq Eng 12(sup1):125–145. https://doi.org/10.1080/13632460801925822
13. Chopra AK (2012) Dynamics of structures. Pearson Education
14. Hall JF (2006) Problems encountered from the use (or misuse) of Rayleigh damping. Earthquake Engng Struct Dyn 35(5):525–545. https://doi.org/10.1002/eqe.541

Stub-Column Tests on Pallet Racks Uprights with and Without Reinforcements

Marina Pastore[1](✉), Francesco Pisciottano[1], Rosario Montuori[2], and Elide Nastri[1]

[1] Department of Civil Engineering, University of Salerno, Fisciano, (SA) 84084, Italy
marpastore@unisa.it

[2] Department of Pharmacy, University of Salerno, Fisciano, (SA) 84084, Italy

Abstract. This paper presents an experimental and numerical investigation into the axial compression behaviour of cold-formed steel uprights used in adjustable pallet rack systems. The study focuses on the influence of locally applied reinforcements on the load-bearing capacity, post-peak response, and failure mode of perforated upright sections. The experimental campaign comprised 400-mm-long specimens, including three nominally identical unreinforced uprights and three reinforced uprights characterized by different reinforcement layouts. Monotonic stub-column tests were performed in accordance with the design-assisted-by-testing provisions of EN 15512:2020 + A1:2022. The experimental response was assessed in terms of load–displacement behaviour, maximum resistance, post-peak degradation, and observed deformation patterns. The results show a consistent response among the unreinforced specimens and indicate that the reinforcement arrangement affects the post-peak behaviour and residual load-carrying capacity more markedly than the initial stiffness and peak resistance. A geometrically and materially nonlinear finite element model was subsequently developed in ABAQUS. The model explicitly included the upright perforations, elastic–plastic material behaviour, and initial geometric imperfections derived from linear buckling modes. A dynamic implicit solution procedure was adopted to reproduce the complete experimental response. The numerical results show good agreement with the experimental curves in terms of initial stiffness, maximum load, post-peak trend, and deformation pattern. The proposed experimental and numerical framework provides component-level data and modelling tools for subsequent robustness and progressive-collapse assessments of pallet rack systems.

Keywords: Pallet racks · Cold-formed steel uprights · Stub-column tests · Reinforcements · Post-buckling behaviour · Finite element modelling · EN 15512

1 Introduction

Adjustable pallet rack systems are widely used in logistics and warehouse facilities because they provide high storage capacity, rapid assembly, operational flexibility, and efficient use of the available space. Their structural efficiency is achieved through the extensive use of lightweight cold-formed steel members. However, the limited thickness,

© The Author(s), under exclusive license to Springer Nature Switzerland AG 2026
R. Zanon et al. (Eds.): CTA 2026, LNCE 942, pp. 401–409, 2026.
https://doi.org/10.1007/978-3-032-39505-4_35

open cross-sectional shape, and regular perforation patterns of rack uprights make their structural response particularly sensitive to local, distortional, flexural, and flexural–torsional buckling phenomena [1–7].

The mechanical behaviour of rack uprights is further influenced by material nonlinearity, residual stresses, initial geometric imperfections, perforation geometry, and the interaction between different buckling modes [8–15]. These characteristics make the prediction of their axial resistance more complex than that of conventional hot-rolled steel columns. Consequently, the principal international design standards for pallet rack systems rely extensively on design-assisted-by-testing procedures to determine the resistance and stiffness of upright members and components [16].

A reliable assessment of upright capacity is also relevant to the robustness of the complete rack system. Following accidental damage or the loss of a load-bearing component, the redistribution of internal forces may substantially increase the axial and bending demands on adjacent uprights. Although current rack design standards provide detailed procedures for member, connection, and system verification, they do not establish dedicated assessment procedures for progressive-collapse scenarios [16]. Stub-column tests do not reproduce this system-level phenomenon directly; nevertheless, they provide essential component-level information on axial resistance, deformation capacity, buckling behaviour, and post-peak degradation, which is required for subsequent robustness and progressive-collapse analyses.

Experimental stub-column testing has therefore been widely employed to investigate the response of cold-formed steel members and pallet rack uprights under axial compression [17–23]. Previous studies have examined the influence of cross-sectional geometry, perforations, intermediate stiffeners, built-up configurations, and geometric imperfections on the ultimate resistance and failure mode of thin-walled members [23–25]. At the same time, geometrically and materially nonlinear finite element analyses have increasingly been adopted to reproduce the interaction between local and distortional buckling and to support the interpretation and extension of experimental results [26–28].

Within this framework, the present study investigates the axial compression behaviour of 400-mm-long perforated pallet rack uprights, considering both unreinforced specimens and specimens equipped with different reinforcement layouts. Monotonic stub-column tests are carried out in accordance with EN 15512:2020 + A1:2022 [16]. A geometrically and materially nonlinear finite element model is then developed and calibrated against the experimental response. The study focuses on the influence of the reinforcement arrangement on the maximum resistance, load–displacement response, post-peak degradation, and observed failure mode.

2 The Experimental Campaign

In accordance with EN 15512:2020 + A1:2022 [16], an experimental campaign was carried out at the University of Salerno on pallet rack upright specimens of different lengths. Within this broader programme, the present study focuses on 400-mm-long specimens, tested in both unreinforced and reinforced configurations. The tests provide experimental evidence on their axial response, failure modes, and post-peak behaviour,

while also establishing a consistent basis for the calibration and assessment of nonlinear finite element models. The resulting dataset contributes to addressing the still limited experimental information available for perforated thin-walled rack uprights.

The 15512:2022 setup for conducting stub column tests is explicated as in Fig. 1

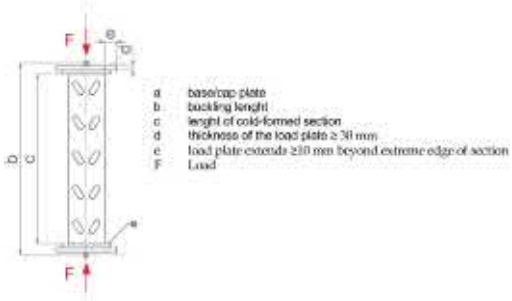


Fig. 1. Setup for stub column tests extrapolated by EN 15512:2022

The test setup specified in EN 15512:2020 + A1:2022 [6] was reproduced at the Structural Engineering Laboratory of the University of Salerno using purpose-built loading and support devices. The tests were performed with an ITALSIGMA hydraulic testing machine having a maximum compressive capacity of 3000 kN and an actuator stroke of 250 mm. A Class 1 load cell with a nominal capacity of 600 kN and a full-scale error of 0.1% was used to improve the accuracy of the force measurements within the load range relevant to the present tests.

The specimen ends were welded to steel bearing plates and positioned between custom-fabricated devices designed to reproduce the end conditions prescribed by EN 15512. Before each test, the alignment of the specimen with the loading axis was checked using a magnetic spirit level in order to minimize unintended load eccentricities. The distance between the welded end plates was measured before testing and adopted as the specimen length. The recorded load–displacement curves were subsequently corrected by removing the initial seating and preload phase associated with stabilization of the test setup.

The experimental program was conducted in two stages. First, three nominally identical unreinforced specimens, designated 400-N1, 400-N2, and 400-N3, were tested to assess the repeatability of the reference response. Subsequently, three reinforced specimens, designated 400-P1, 400-P2, and 400-P3, were tested. Each specimen was characterized by a different reinforcement layout, defined by the position of the reinforcement connections along the upright. The three layouts are schematically illustrated in Fig. 2.

The results of the experimental tests are reported in Fig. 3 (a) and (b).

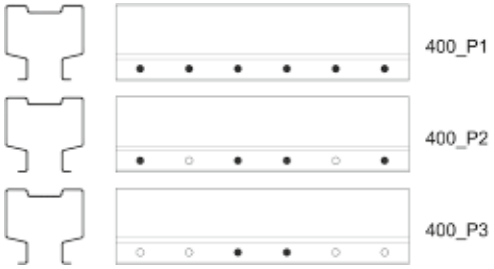


Fig. 2. Simplified adopted scheme of reinforcement

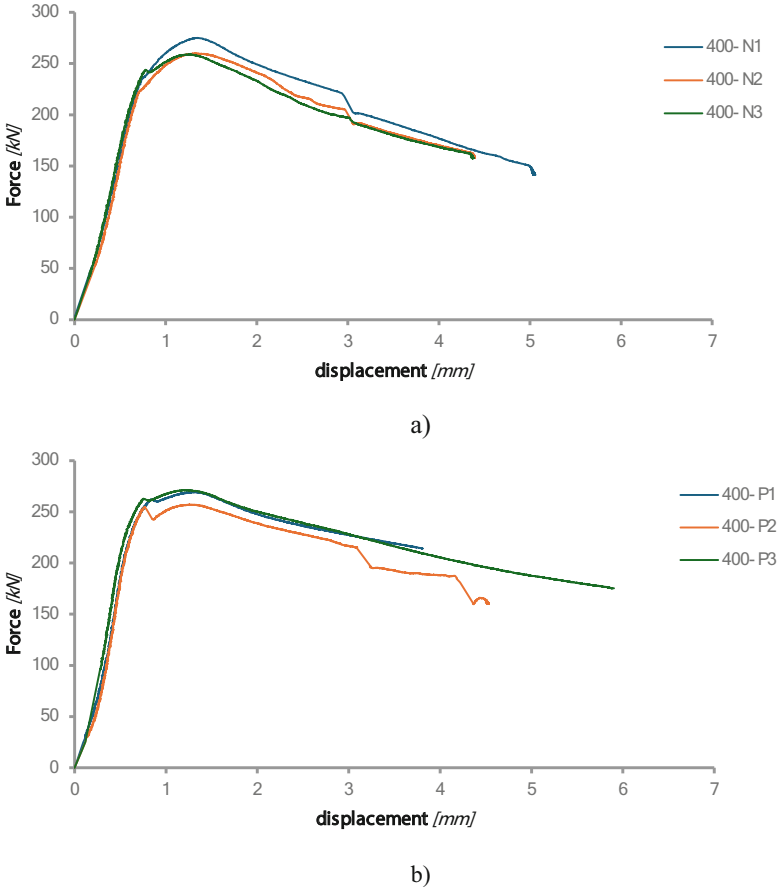


Fig. 3. Load-displacement curves about the 400 specimens. a) without stiffeners b) with stiffeners

3 FEM Simulation

To complement the experimental campaign, a non-linear numerical investigation was developed using the commercial Finite Element (FE) software (ABAQUS). The main objective was to create a robust FE model capable of replicating the experimental failure modes and ultimate load capacities, thereby providing a reliable tool for future parametric studies.

3.1 Non-linear Modelling

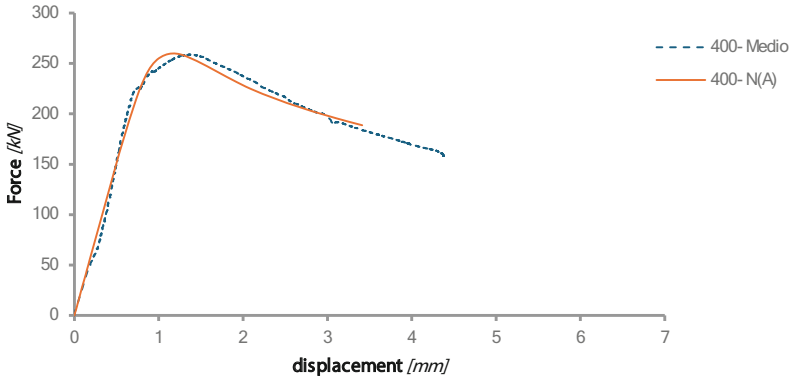
The non-linear numerical investigation was conducted using a Dynamic Implicit solver approach, which yielded the most promising and stable convergence results. The parametric FE testing strictly mirrored the experimental protocol, dividing the specimens into two primary macro-groups: unreinforced uprights and uprights equipped with stiffeners.

The thin-walled perforated uprights were modelled using a 3 mm CDR4 mesh, with no partition; this type of mesh subsequently was proved to be particularly suitable for capturing both local and distortional buckling phenomena involving warping deformations, given a suitable statistical treatment of experimental data. Given the complexity of the analysis, perforations were explicitly modelled in their exact geometry to account for the localized stress concentration and net area reduction. To simulate the experimental boundary conditions, the nodes at the specimen ends were coupled to reference points representing the custom-fabricated spherical hinges, restricting translations while allowing the intended rotations: in order to do so, coupling constraint were adopted, and both boundary conditions and imposed displacements were applied through the reference points (RPs). This modelling strategy ensured consistency with the experimental setup, preventing unintended local deformation at the loading and support regions while accurately reproducing the applied boundary conditions. A critical aspect of the numerical strategy involved the implementation of material and geometric non-linearities (GMNIA). The material behaviour was incorporated using an elastic-plastic formulation based on the true stress-strain curves derived from the tensile coupon tests. To account for initial structural geometric imperfections—which severely affect thin-walled open sections—a two-step analysis was performed. First, an elastic buckling (eigenvalue) analysis was executed to identify the critical local and distortional buckling modes. Then, these shapes were introduced into the subsequent non-linear dynamic implicit analysis as initial geometric imperfections, scaling their amplitudes according to the thresholds suggested by the literature and code provisions [16]. Stiffeners were modelled with simple coupling constraint localized in the pre-existing holes in the model: had not be proven experimentally, said assumption could appear extreme. Needs to be said that the only difference between the three models with stiffeners analysed was the positioning of the coupling constraints, which strictly followed the layout previously implemented in the experimental phase. The same imperfection was used for also the specimen with stiffeners, providing a solid starting benchmark for the dynamic implicit analysis.

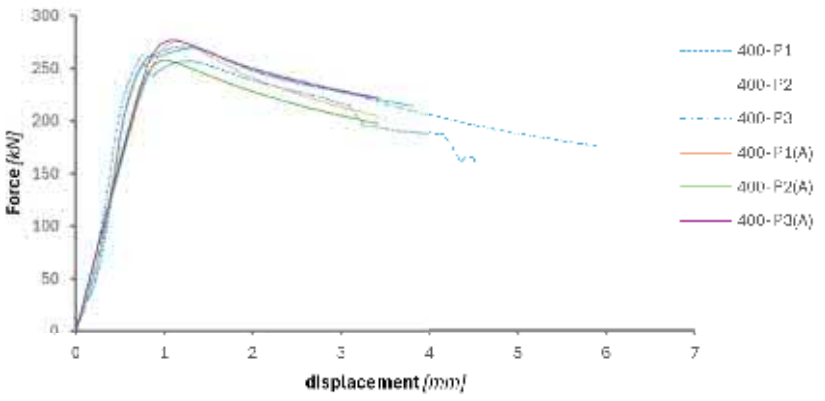
3.2 The Outcome of Dynamic Implicit Analysis

Figure 4 compares the numerical and experimental load–displacement responses of the unreinforced and reinforced specimens. As shown in Fig. 4, the finite element model reproduces the main features of the experimental response, including the initial stiffness, the onset of yielding, the maximum load, and the subsequent post-peak behaviour. The agreement is satisfactory for both the unreinforced and reinforced configurations, although the accuracy of the numerical prediction should be further quantified through direct comparison of the main response parameters.

Figure 5 compares the experimentally observed deformation pattern with the corresponding numerical deformed shape and von Mises stress distribution. The model captures the location and overall form of the dominant deformation mechanism observed in the test.



(a)



(b)

Fig. 4. Load-displacement curves comparisons about the 400 - P specimens. (a) without stiffeners (b) with stiffeners



(a) (b)

Fig. 5. Comparisons between real specimen without reinforcements (a); Abaqus FE model results (b) (Von Mises Stress Contour)

4 Conclusions

This study investigated the axial compression behaviour of 400-mm-long cold-formed steel pallet rack uprights through experimental stub-column tests and nonlinear finite element analyses. Both unreinforced specimens and specimens characterized by different reinforcement layouts were considered.

The unreinforced tests showed a reasonably consistent load–displacement response, providing a reference for assessing the effect of the reinforcement arrangements. The reinforced configurations exhibited differences mainly in the post-peak response and residual load-carrying capacity, whereas the variations in initial stiffness and maximum resistance were less pronounced. This indicates that the position and arrangement of the reinforcement connections may influence the deformation mechanism and the progression of local and distortional buckling more significantly than the elastic response of the upright.

A geometrically and materially nonlinear finite element model was developed by explicitly representing the upright perforations, the elastic–plastic material behaviour, and initial geometric imperfections derived from linear buckling modes. The numerical analyses reproduced the main features of the experimental response, including the initial stiffness, maximum load, post-peak trend, and dominant deformation pattern. The model should therefore be regarded as a calibrated component-level tool suitable for supporting the interpretation of the present tests and for developing subsequent parametric investigations.

The results are relevant to the assessment of pallet rack upright capacity and provide mechanical information that may be used in future system-level robustness and progressive-collapse analyses. However, the present tests do not reproduce progressive collapse directly, since they are limited to monotonic axial compression of isolated upright segments.

The main limitations of the study concern the relatively small number of specimens, the use of a single upright cross-section and specimen length, and the absence of repeated tests for each reinforcement configuration. In addition, the numerical representation of the reinforcements through simplified coupling constraints does not explicitly account for their local deformability, contact behaviour, clearance, or possible connection failure. The model also relies on detailed geometric and material characterization, including coupon-test data and assumptions regarding the amplitude and shape of initial imperfections.

Future work will extend the experimental campaign to additional upright geometries, perforation patterns, reinforcement layouts, and specimen lengths. Further investigations will also address the sensitivity of the numerical response to geometric imperfections, loading rate, mesh refinement, and reinforcement modelling. The final objective is to develop simplified and sufficiently robust modelling procedures that can be applied in parametric studies and, subsequently, in the assessment of complete pallet rack systems.

Acknowledgments. The research was conducted within the PRIN 2022 project PC-RACKS, coordinated by the University of Salerno in collaboration with the University of Campania and the University of Sannio, with funding from the Italian MUR. The authors also gratefully acknowledge Dalmine Logistic Systems for providing the materials used in the experimental programme.

References

1. Ghersi A, Landolfo R, Mazzolani FM (2002) Design of metallic cold-formed thin-walled members. Spon Press, London and New York
2. Hancock GJ, Kwon YB, Bernard ES (1994) Strength design curves for thin-walled sections undergoing distortional buckling. J Constr Steel Res 31(2–3):169–186. https://doi.org/10.1016/0143-974X(94)90009-4
3. Batista EM, Rodrigues FC (1994) Buckling curve for cold-formed compressed members. J Constr Steel Res 28(2):121–136. https://doi.org/10.1016/0143-974X(94)90038-8
4. Batista EM, Camotim D, Prola LC, Vazquez E (1998) On the stability and strength of steel columns affected by distortional buckling. J Constr Steel Res 46(1–3):129–131. https://doi.org/10.1016/S0143-974X(98)00048-0
5. Baldassino N, Bernuzzi C (2000) Analysis and behaviour of steel storage pallet racks. Thin-Walled Struct 37(4):277–304. https://doi.org/10.1016/S0263-8231(00)00021-5
6. Schafer BW (2002) Local, distortional, and Euler buckling of thin-walled columns. J Struct Eng 128(3):289–299. https://doi.org/10.1061/(ASCE)0733-9445(2002)128:3(289)
7. Freitas AMS, Freitas MSR, Souza FT (2005) Analysis of steel storage rack columns. J Constr Steel Res 61(8):1135–1146. https://doi.org/10.1016/j.jcsr.2005.02.004
8. Chen J, He Y, Jin WL (2010) Stub column tests of thin-walled complex sections with intermediate stiffeners. Thin-Walled Struct 48(6):423–429. https://doi.org/10.1016/j.tws.2010.01.008
9. Roure F, Pastor MM, Casafont M, Somalo MR (2011) Stub column tests for racking design: experimental testing, FE analysis and EC3. Thin-Walled Struct 49(2):167–184. https://doi.org/10.1016/j.tws.2010.09.002
10. Crisan A, Ungureanu V, Dubina D (2012) Behaviour of cold-formed steel perforated sections in compression: part 1—experimental investigations. Thin-Walled Struct 61:86–96. https://doi.org/10.1016/j.tws.2012.07.016

11. Crisan A, Ungureanu V, Dubina D (2012) Behaviour of cold-formed steel perforated sections in compression: part 2—numerical investigations and design considerations. Thin-Walled Struct 61:97–105. https://doi.org/10.1016/j.tws.2012.07.013
12. Ungureanu V, Dubina D (2013) Sensitivity to imperfections of perforated pallet rack sections. Mech Mech Eng 17(2):207–220
13. Bernuzzi C, Gobetti A, Gabbianelli G, Simoncelli M (2014) Warping influence on the resistance of uprights in steel storage pallet racks. J Constr Steel Res 101:224–241. https://doi.org/10.1016/j.jcsr.2014.05.014
14. Bernuzzi C, Pieri A, Squadrito V (2014) Warping influence on the static design of unbraced steel storage pallet racks. Thin-Walled Struct 79:71–82. https://doi.org/10.1016/j.tws.2014.01.024
15. Taranu G, Iacob S, Taranu N (2025) Buckling behavior of perforated cold-formed steel uprights: experimental evaluation and comparative assessment using FEM, EWM, and DSM. Buildings 15(9):1561. https://doi.org/10.3390/buildings15091561
16. European Committee for Standardization (CEN) (2022) EN 15512:2020+A1:2022, steel static storage systems—adjustable pallet racking systems—principles for structural design. CEN, Brussels
17. Pu Y, Godley MHR, Beale RG (1998) Experimental procedures for stub column tests. In: Proceedings of the 14th international specialty conference on cold-formed steel structures. University of Missouri–Rolla, St Louis, MO, pp 311–322
18. Gilbert BP, Rasmussen KJR (2009) Experimental tests on steel storage rack components. Research Report R899,. University of Sydney, Sydney
19. Torabian S, Zheng B, Schafer BW (2014) Experimental study and modeling of cold-formed steel lipped channel stub beam-columns. In: Proceedings of the annual stability conference. Structural Stability Research Council, Toronto, Canada, 25–28 March 2014
20. Liu JZ, Fang H, Chan TM (2022) Experimental and numerical investigations on stub column behaviour of cold-formed high-strength steel irregular octagonal hollow sections. Thin-Walled Struct 180:109770. https://doi.org/10.1016/j.tws.2022.109770
21. Ma JL, Chan TM, Young B (2016) Experimental investigation on stub-column behavior of cold-formed high-strength steel tubular sections. J Struct Eng 142(5):04015174. https://doi.org/10.1061/(ASCE)ST.1943-541X.0001456
22. Manikandan P, Arun N (2016) Behaviour of partially closed stiffened cold-formed steel compression members. Arab J Sci Eng 41(10):3865–3875. https://doi.org/10.1007/s13369-015-2015-0
23. Vijayanand S, Anbarasu M (2017) Effect of spacers on ultimate strength and behavior of cold-formed steel built-up columns. Procedia Eng 173:1423–1430. https://doi.org/10.1016/j.proeng.2016.12.205
24. Baldassino N, Bernuzzi C, di Gioia A, Simoncelli M (2019) An experimental investigation on solid and perforated steel storage rack uprights. J Constr Steel Res 155:409–425. https://doi.org/10.1016/j.jcsr.2019.01.008
25. Zucco G, Weaver PM (2020) The role of symmetry in the post-buckling behaviour of structures. Proc R Soc A 476(2233):20190609. https://doi.org/10.1098/rspa.2019.0609
26. Zhang P, Alam MS (2017) Experimental investigation and numerical simulation of pallet-rack stub columns under compression load. J Constr Steel Res 133:282–299. https://doi.org/10.1016/j.jcsr.2017.02.023
27. Lyu Z, Zhang J, Zhao N, Xiang Q, Song Y, Li J (2020) A comparative study on the performance of FEM, RA and ANN methods in strength prediction of pallet-rack stub columns. Int J Steel Struct 20(5):1509–1526. https://doi.org/10.1007/s13296-020-00386-6
28. Plaitano F, Stratan A, Nastri E (2022) Simplified modelling of failure in high-strength bolts under combined tension and bending. J Compos Sci 6(10):302. https://doi.org/10.3390/jcs6100302

Experimental Tests and Fem Simulations of Pallet Racks Beam-to-Column Joints

Marina Pastore[1](✉), Tahir Ahmad[2], Francesco Pisciottano[1], Roberto Tartaglia[3], Massimiliano Ferraioli[2], Rosario Montuori[4], and Elide Nastri[1]

[1] Department of Civil Engineering, University of Salerno, Fisciano, (SA) 84084, Italy
marpastore@unisa.it
[2] Department of Civil Engineering, University of Caserta "Luigi Vanvitelli", Caserta, (CE) 81100, Italy
[3] Department of Civil Engineering, University of Sannio, Benevento, (BN) 82100, Italy
[4] Department of Pharmacy, University of Salerno, Fisciano, (SA) 84084, Italy

Abstract. This study investigates the flexural response and weld-dominated failure of beam-to-upright connections in cold-formed steel pallet rack systems through an integrated experimental and numerical approach. Six monotonic flexural tests, comprising three left-hand and three right-hand connection specimens, were performed in accordance with EN 15512. The specimens exhibited closely comparable moment–rotation responses, indicating that connector orientation had no significant influence on the initial stiffness, peak resistance or overall rotational behaviour of the investigated connection. In all tests, failure initiated at the upper horizontal weld seam of the beam-end connector and subsequently extended towards the adjacent vertical weld.

A detailed three-dimensional finite element model was developed in Abaqus using solid elements, experimentally derived material properties, surface-to-surface contact interactions and ductile damage modelling in the welded region. Dynamic implicit and dynamic explicit solution procedures were investigated as complementary modelling strategies. The implicit formulation effectively reproduced the global response up to peak resistance and identified the experimentally observed damage-initiation region. The explicit formulation additionally captured progressive weld damage, element deletion and the associated post-peak loss of load-carrying capacity. The numerical-to-experimental ratios were approximately 1.04 for the peak moment and 0.98 for the corresponding rotation.

The results demonstrate that agreement with the global moment–rotation response alone is insufficient when connection failure is governed by highly localised weld damage. An adequate representation of the welded region, contact interactions and damage evolution is required to reproduce both the resistance and the governing collapse mechanism. The proposed framework provides a basis for extending design-assisted-by-testing procedures towards failure-oriented numerical assessment of pallet rack connections.

Keywords: steel pallet racks · beam-to-upright connections · finite element modelling · weld failure · ductile damage · design assisted by testing

© The Author(s), under exclusive license to Springer Nature Switzerland AG 2026
R. Zanon et al. (Eds.): CTA 2026, LNCE 942, pp. 410–418, 2026.
https://doi.org/10.1007/978-3-032-39505-4_36

1 Introduction

Steel pallet rack systems are highly sensitive to the mechanical behaviour of beam-to-upright connections [1–16], which govern both global stiffness and ultimate resistance. In current practice, this behaviour is addressed through Design Assisted by Testing (DAT), as formalized in EN 15512:2022 [17]. Experimental flexural tests are employed to derive global moment–rotation relationships, which are subsequently used for structural modelling and safety verification.

While DAT provides a practical and robust design basis, it inherently relies on a limited set of experimental configurations and on simplified joint representations. In particular, the ability of standard approaches to capture localized failure mechanisms—often governing the ultimate capacity—remains limited. Among these, fracture of welded components within the beam-end connector has been repeatedly observed as a critical and often governing mode, yet it is rarely addressed explicitly in numerical design models.

Accurate finite element modelling of pallet rack connections therefore represents a key step toward extending DAT methodologies beyond their empirical scope. However, reproducing the structural response of these joints poses significant numerical challenges: thin-walled members, contact interactions, material nonlinearity, and highly localized stress concentrations combine to make conventional implicit solution schemes often inadequate for capturing fracture initiation and evolution [18–21].

The present study goes beyond conventional FE models used solely to reproduce global moment–rotation response. Its novelty lies in the development and validation of a weld-failure-oriented FE framework specifically conceived to reproduce the experimentally observed local collapse mechanism.

The main objectives are:

- development of a 3D failure-oriented FE model capable of reproducing the weld-dominated collapse mechanism;
- validation against monotonic flexural tests performed according to EN 15512:2022;
- assessment of key modelling assumptions (mesh refinement, material modelling, contact definition, geometric representation);
- comparison between Dynamic Implicit and Dynamic Explicit solution strategies to clarify their respective capabilities in simulating localized nonlinearities and fracture evolution.

By combining these aspects, the study provides not only a calibrated numerical model, but also a methodological framework for predictive, failure-oriented analysis of cold-formed steel pallet rack connections, bridging the gap between design-oriented testing and local failure simulation.

2 The Experimental Campaign (According to EN15512:2022)

In accordance with the prescription of the EN15512:2022 [17], an experimental campaign was carried out on both left (SPX) and right (DXP) beam to upright connections according to the test setup reported in Fig. 1.

Furthermore, the test program included a full material characterization test on materials, in compliance with the UNI EN ISO 6892-1 [19].

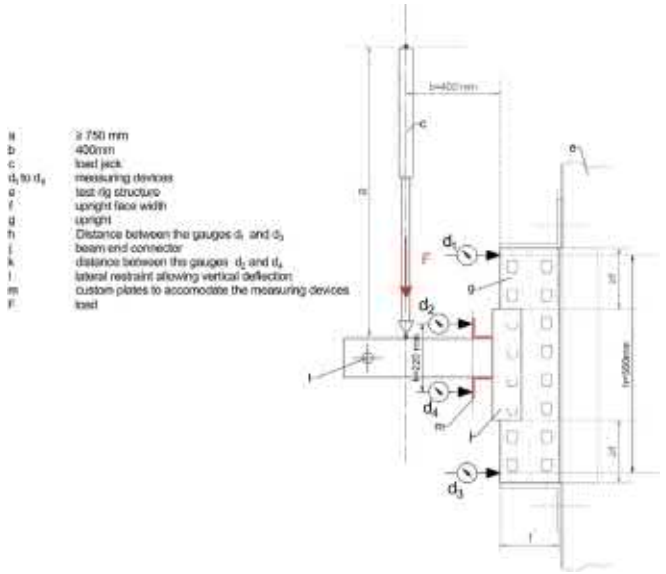


Fig. 1. Setup for flexural tests according to EN 15512:2022

Experimental evidence underlines that the flexural response is governed by highly localized non-linear phenomena, usually (though in general non exclusively) concentrated in the welded region of the beam-end connector (Figs. 3a and 3b).

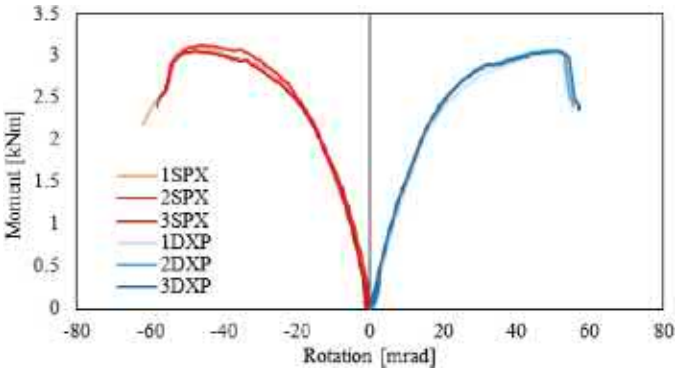


Fig. 2. Experimental tests results in terms of Moment-Rotation curves of left and right connections under in plane bending



Fig. 3. Rupture of the weld in the end-beam connector. a) for left joint, b) for right joint

3 FEM Simulations

The experimental observations highlighted the need for a numerical model capable of reproducing not only the global moment–rotation response, but also the local mechanisms governing connection failure. Accordingly, detailed three-dimensional finite element models (FEM) of the beam-to-upright subassembly were developed, with particular attention to the welded region of the beam-end connector.

Dynamic implicit and dynamic explicit procedures were investigated to assess their respective capabilities in capturing localised plastic deformation, damage initiation and post-peak degradation. The numerical predictions were compared with the experimental moment–rotation curves and observed failure modes, with particular emphasis on the localisation of plastic strains and the identification of the damage-initiation region.

Three-dimensional solid elements were adopted because the local response of the connection involves through-thickness stress gradients, contact-induced bearing, plastic strain localisation at the weld toe and non-negligible stress triaxiality. These phenomena cannot be represented adequately through simplified joint models focused solely on the global response. Geometric nonlinearity was included in all analyses by activating the "Nlgeom" option. The weld material was defined using a yield strength of 500 MPa and an ultimate tensile strength of 600 MPa, based on the inspection certificate. Weld failure was simulated using the Abaqus ductile damage model. Damage initiation was defined in terms of equivalent plastic strain as a function of stress triaxiality and plastic strain rate. Damage evolution was governed by a linear displacement-based law, with an equivalent displacement at failure of 0.05 mm.

Surface-to-surface contact was adopted between interacting steel components. Normal behaviour was defined as hard contact allowing separation, while tangential behaviour was represented through a penalty formulation with a friction coefficient of 0.3. Welded interfaces were modelled using tie constraints.

3.1 The Dynamic Implicit Approach

The beam-to-upright subassembly was modelled using three-dimensional solid elements, optimizing the balance between computational efficiency and accuracy in stress gradient resolution:

- Beam, Connector, Stopper, and Welds: Discretized using 8-node linear hexahedral elements with incompatible modes (C3D8I) to mitigate shear and volumetric locking in regions governed by bending and localized plasticity.
- Upright Profile: Due to its complex geometry and perforations, 10-node quadratic tetrahedral elements (C3D10) were selected for superior geometric adaptability.

A component-specific mesh sensitivity analysis was conducted, monitoring moment–rotation curves and Von Mises stresses at 20 mrad and 40 mrad rotations (with element sizes ranging from 0.5 to 15 mm). While the global elastic stiffness and load-carrying capacity remained mostly independent of element size, local stress variations were observed in the upright and connectors (particularly for upright mesh sizes at large rotations, where coarse meshes reduced accuracy around the perforations).

To ensure mesh-independent results while limiting computational cost, the final optimized mesh sizes were established as:

- Beam and Upright: 5.0 mm
- Connectors: 2.5 mm
- Welds: 2.0 mm

The FE model was validated against experimental data from the 2DPX test using a dynamic implicit solver. The numerical model demonstrated excellent agreement with experimental evidence across multiple parameters:

- Global Response: Accurate replication of the joint's elastic stiffness, yielding resistance, and maximum load-carrying capacity.
- Local Response and Failure: The modelling approach successfully predicted the critical stress concentrations, equivalent plastic deformation (PEEQ) distribution, and the exact fracture initialization site within the welded zone.

The numerical model successfully reproduced the experimental behaviour in terms of elastic stiffness, yielding resistance, and maximum capacity. The assumptions adopted to model the weld behaviour allowed accurate prediction of the maximum stressed point and fracture initiation. The comparison of moment–rotation curves, failure mode, and stress/strain distributions confirmed the capability of the implicit formulation to capture the global response up to peak resistance and to identify the location of fracture onset Fig. 4.

3.2 The Dynamic Explicit Approach

To capture severe contact nonlinearities, material degradation and post-peak response, a dynamic explicit solution procedure was also adopted. This formulation uses a central-difference time-integration scheme, which is particularly suitable for analyses involving complex contact interactions, progressive stiffness degradation and element deletion.

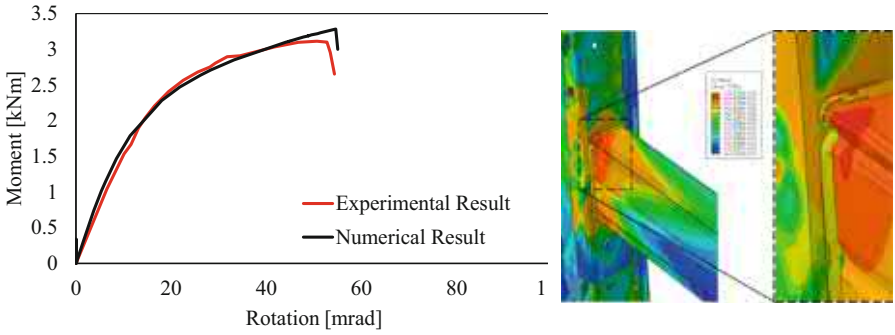


Fig. 4. a) Comparison of moment rotation curves b) Dynamic explicit failure mode in terms of von Mises stress contours

Quasi-static loading conditions were pursued by applying a smooth-step amplitude to the imposed displacement and by selectively using mass scaling. The validity of the quasi-static assumption was checked by monitoring the energy balance and ensuring that the kinetic energy remained below 5% of the internal energy throughout the analysis.

Unlike the implicit model, the explicit model employed eight-node linear hexahedral elements with reduced integration (C3D8R) for all components. This element formulation was selected because of its robustness in large-deformation analyses involving severe contact and progressive damage. Consistently with the mesh sensitivity study, a global mesh size of 5 mm was adopted for the beam and upright, whereas a refined mesh size of 1.0 mm was used for the connector tabs and welded regions in order to improve the resolution of stress triaxiality, plastic strain localisation and damage initiation.

The explicit model reproduced the experimentally observed failure mechanism, which was characterised by pronounced plastic deformation and damage localisation within the connection region. The von Mises stress contours showed a highly stressed zone at the welded interface, in agreement with the experimentally observed failure area. The equivalent plastic strain distribution further confirmed that plastic deformation was mainly concentrated at the weld toe and in the adjacent base material. Progressive degradation was represented through the deletion of highly damaged weld elements, corresponding to the numerically simulated development of damage within the welded region.

The moment–rotation comparison showed good agreement with the experimental response in terms of initial stiffness, peak moment capacity and overall nonlinear behaviour. The post-peak reduction in load-carrying capacity was associated with plastic strain accumulation and progressive deletion of weld elements. This confirms that the explicit formulation is able to reproduce not only the global response, but also the degradation mechanism observed experimentally, as shown in Fig. 5.

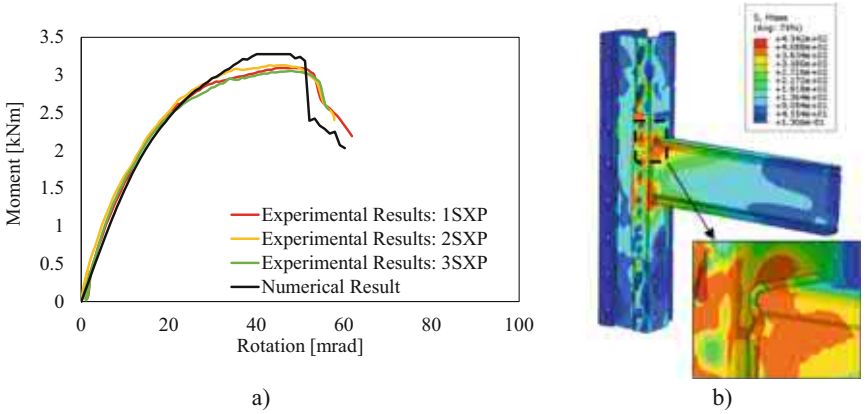


Fig. 5. a) Comparison of moment rotation curves b) Dynamic explicit failure mode in terms of von Mises stress contours

4 Conclusions

This study presented an experimental and numerical investigation of the flexural behaviour and failure mechanism of beam-to-upright connections in cold-formed steel pallet rack systems. Six monotonic flexural tests, comprising three left-hand and three right-hand connection specimens, were performed in accordance with EN 15512.

The experimental results showed closely comparable moment–rotation responses for the two connector orientations, with no appreciable differences in initial stiffness, peak resistance or overall rotational behaviour. For the investigated connection geometry, failure consistently initiated at the upper horizontal weld seam of the beam-end connector and subsequently extended towards the adjacent vertical weld. The ultimate response was therefore governed by a highly localised damage mechanism in the welded region rather than by failure of the stopper or by extensive deformation of the upright.

A detailed three-dimensional finite element model was developed to reproduce both the global connection response and the local phenomena leading to failure. The modelling strategy incorporated experimentally derived material properties, solid elements, geometric nonlinearity, surface-to-surface contact interactions and ductile damage modelling in the welded region. The comparison with the experimental results showed that the numerical model satisfactorily reproduced the initial stiffness, peak moment and corresponding rotation, with numerical-to-experimental ratios of approximately 1.04 and 0.98 for the peak moment and peak rotation, respectively. The model also identified the experimentally observed damage-initiation region.

The implicit and explicit solution procedures provided complementary information. The implicit formulation efficiently reproduced the pre-peak response and the onset of damage and is therefore suitable for model calibration and analyses in which the global response is of primary interest. The explicit formulation was more effective in following severe contact nonlinearities, progressive damage, element deletion and the associated post-peak loss of load-carrying capacity. The two procedures should therefore

be regarded as complementary components of a failure-oriented numerical workflow rather than as interchangeable alternatives.

The results demonstrate that agreement with the global moment–rotation curve alone is not sufficient to assess the reliability of a numerical model when connection failure is controlled by highly localised weld damage. An adequate representation of the welded region, contact interactions and damage evolution is required to reproduce both the resistance and the governing collapse mechanism.

The conclusions are limited to the connector geometry and monotonic loading conditions investigated in this study. Moreover, the weld strength parameters were derived from the available inspection certificate, while the damage parameters adopted in the numerical model require calibration. Further research should therefore investigate additional connector geometries, independently characterise the weld and heat-affected-zone properties, and assess the modelling strategy under cyclic and seismic loading conditions.

Acknowledgments. The research was conducted within the PRIN 2022 project PC-RACKS, coordinated by the University of Salerno in collaboration with the University of Campania and the University of Sannio, with funding from the Italian MUR. The authors also gratefully acknowledge Dalmine Logistic Systems for providing the materials used in the experimental programme.

References

1. Yazıcı C, Gusella F, Özkal FM (2026) Effect of beam-to-connector weld position on the flexural response of boltless rack connections. J Constr Steel Res 237(B):110141
2. Bernuzzi C, Castiglioni CA (2001) Experimental analysis on the cyclic behaviour of beam-to-column joints in steel storage pallet racks. Thin-Walled Struct 39(10):841–859
3. Baldassino N, Bernuzzi C, Zandonini R (2001) Performance of joints in steel storage pallet racks. In: Connections in steel structures IV: steel connections in the new millennium, pp 382–392
4. Prabha P, Marimuthu V, Saravanan M, Jayachandran SA (2010) Evaluation of connection flexibility in cold-formed steel racks. J Constr Steel Res 66(7):863–872
5. Wang T, Zhao X, Chen Y (2012) Experimental analysis of beam-to-upright connections in cold-formed steel storage pallet racks. In: proceedings of the 21st international specialty conference on cold-formed steel structures
6. Shah SNR, Sulong NHR, Shariati M, Jumaat MZ (2016) State-of-the-art review on the design and performance of steel pallet rack connections. Eng Fail Anal 66:240–258
7. Rosli NAM, Tan CG, Hashim H, Sulong NHR (2025) Experimental investigation and parameter analysis of boltless steel pallet rack beam-to-column connection. J Constr Steel Res 231:109578
8. Aguirre C (2004) Structural properties of connections for rack structures. In: Federico V (ed) Connections in steel structures. Santa Maria University, Valparaíso
9. Bajoria KM, Talikoti RS (2006) Determination of flexibility of beam-to-column connectors used in thin-walled cold-formed steel pallet racking systems. Thin-Walled Struct 44(3):372–380
10. Mohan V, Prabha P, Rajasankar J et al (2015) Cold-formed steel pallet rack connection: an experimental study. Int J Adv Struct Eng 7:55–68
11. Giordano S, Gusella F, Lavacchini G, Orlando M, Spinelli P (2017) Experimental tests on beam-end connectors of cold-formed steel storage pallet racks. ce/papers 1:669–678

12. Dai L, Zhao X, Rasmussen KJR (2018) Flexural behaviour of steel storage rack beam-to-upright bolted connections. Thin-Walled Struct 124:202–217
13. Baldassino N, Bernuzzi C, Di Gioia A, Simoncelli M (2019) An experimental investigation on solid and perforated steel storage rack uprights. J Constr Steel Res 155:409–425
14. Chen C, Shi L, Shariati M et al (2019) Behavior of steel storage pallet racking connection—a review. Steel Compos Struct 30(5):457–469
15. Vujanac R, Miloradović N, Vulović S, Pavlović A (2020) A comprehensive study into the boltless connections of racking systems. Meta 10(2):276
16. Yazıcı C, Arık E, Özkal FM (2023) Influence of design parameters on beam-to-column connections of steel storage rack systems. Eng Fail Anal 152:107439
17. European Committee for Standardization (2022) EN 15512:2020+A1:2022. Steel static storage systems—adjustable pallet racking systems—principles for structural design. CEN, Brussels
18. Jing Y, Jiang K, Su A, Liang Y, Zhao O (2025) Testing, numerical modelling and design of stainless steel built-up box sections under interior-one-flange loading. Eng Struct 343:121087
19. UNI (2020) In: UNI (ed) EN ISO 6892-1:2020. Metallic materials—tensile testing—Part 1: Method of test at room temperature, UNI, Milan
20. Piskulić M, Vujanac R, Vulović S, Miloradović N, Blagojević M, Djordjević Z (2026) Structural performance of semi-rigid beam-to-column connections in steel storage racks: a review focused on FEM analysis. Meta 16(1):2
21. Dassault Systèmes Abaqus Analysis User's Guide Version. dassault systèmes, providence RI

Shear Behaviour of Gypsum Board-to-CFS Profile Screw Connections

Vito D'Addesa(✉), Alessandro Prota, Luigi Fiorino, and Raffaele Landolfo

Department of Structures for Engineering and Architecture, University of Naples Federico II, 80134 Naples, Italy
vito.daddesa@unina.it

Abstract. Drywall partitions may be subjected to significant in-plane displacement demands under seismic loading. Under such conditions, the shear behaviour of screw connections between gypsum boards and cold-formed steel (CFS) profiles governs the response and damage evolution of the partitions. This paper presents the results of an experimental study investigating the shear behaviour of these connections under monotonic and cyclic loading. Shear tests were performed on specimens with one or two boards on each side to evaluate the influence of sheathing layout. Complementary material and interaction tests were also carried out, including tensile and bending tests on screws, as well as gypsum embedment and screw head pull-through tests. The results provide a consistent experimental dataset describing the shear response and failure mechanisms of gypsum board-to-CFS profile screw connections. The findings show the influence of sheathing layout and loading conditions on strength, stiffness, ductility, and dissipated energy. Overall, these results may support improvements in modelling and design approaches for gypsum board-to-CFS profile screw connections.

Keywords: Cold-Formed Steel · Gypsum Boards · Lightweight Steel · Screw Connections · Shear Tests

1 Introduction

Non-structural building components often sustain significant damage during earthquakes, resulting in substantial economic losses and loss of functionality. While these elements are not intended to contribute to the primary load-bearing system, failure of these components can pose a risk to occupants and affect the building's operability after an earthquake. Consequently, the seismic qualification and performance assessment of non-structural components require increasing attention. Previous studies have shown that repair costs for non-structural finishes and building services may exceed those for the structural system following a seismic event [1].

Extensive experimental, numerical, and analytical research has been devoted to structural steel systems and their connections, addressing topics such as connection behaviour, seismic response, structural assessment, and fatigue performance [2–7]. By contrast, less attention has been paid to gypsum board-to-CFS profile screw connections employed

© The Author(s), under exclusive license to Springer Nature Switzerland AG 2026
R. Zanon et al. (Eds.): CTA 2026, LNCE 942, pp. 419–431, 2026.
https://doi.org/10.1007/978-3-032-39505-4_37

in non-structural drywall systems. Drywall partitions are recognized as one of the most critical non-structural building components under seismic loading, and their in-plane response is largely governed by the shear behaviour of screw connections between gypsum boards and CFS framing members. To improve the understanding of this behaviour, an experimental campaign was conducted at the University of Naples "Federico II" to investigate the shear behaviour of gypsum board-to-CFS profile screw connections under monotonic and cyclic loading conditions.

The experimental programme included shear tests on connections with either one or two gypsum boards on each side. This allowed the influence of the sheathing configuration on the behaviour of the connection to be evaluated. Additionally, a series of complementary tests were performed to characterize the mechanical properties of the individual components and their interactions. This included screw tensile and bending tests, gypsum embedment tests, and screw head pull-through tests. The resulting experimental data provide a comprehensive description of the connection response and associated failure mechanisms. These data provide a basis for developing or validating analytical models intended to predict the shear behaviour of gypsum board-to-CFS profile screw connections.

2 Gypsum Board-to-CFS Profile Screw Connections in Drywall Partitions

Drywall partitions are widely used as non-structural interior systems in residential, commercial and public buildings. These assemblies generally consist of a lightweight CFS framing system comprising vertical studs and horizontal tracks, to which gypsum boards are mechanically attached. The studs typically have a C-shaped cross-section and are installed at regular intervals ranging from 300 to 600 mm. The tracks have a U-shaped profile, which provides support and alignment to the framing system.

Gypsum boards are typically 12.5 mm thick and connected to the steel frame with self-drilling or self-tapping screws. This fastening system ensures interaction between the sheathing and the supporting frame. In standard practice, screws typically have diameters of up to 3.5 mm. Figure 1 shows a typical drywall partition configuration.

From a seismic perspective, the in-plane response of drywall partitions is strongly influenced by the behaviour of the screw connections between the gypsum boards and the CFS framing members. Previous experimental investigations have shown that damage in drywall partitions is often initiated by the degradation of these localized connections [8]. Consequently, the shear response of gypsum board-to-CFS profile screw connections has received increasing attention in recent years.

Rahmanishamsi et al. (2016) [9] investigated the monotonic and cyclic behaviour of gypsum board-to-steel stud screw connections, highlighting their significant influence on the seismic performance and damage evolution of drywall partition systems. Experimental evidence also demonstrated the sensitivity of the connection response to loading history, stud thickness and screw spacing. In a subsequent experimental study, Fiorino et al. (2017) [10] performed monotonic tests on a wide range of screwed board-to-CFS profile connections incorporating gypsum- and cement-based boards, evaluating

the effects of board type, profile thickness, screw diameter, and number of board layers on the connection behaviour.

Although previous studies have improved the understanding of gypsum board-to-CFS profile screw connections, further experimental evidence is still required to clarify the combined influence of the number of board layers and cyclic loading on the behaviour of connections representative of typical drywall partition systems.

Despite the growing body of research on this topic, design provisions for gypsum board-to-steel screw connections remain limited.

Since the overall response of the connection results from the interaction among different mechanisms, involving the screw, the gypsum board, and the steel profile, the development of reliable analytical formulations requires a thorough understanding of both the global connection behaviour and the contribution of the individual components. Therefore, shear tests on connections should be complemented by component-level investigations specifically aimed at characterizing the mechanical response of the screw, the gypsum board, and the CFS profile. This experimental approach is consistent with the methodology adopted for analytical modelling of timber board-to-CFS profile screw connections [11] and may provide the basis for validating its applicability to gypsum board-to-CFS profile screw connections.

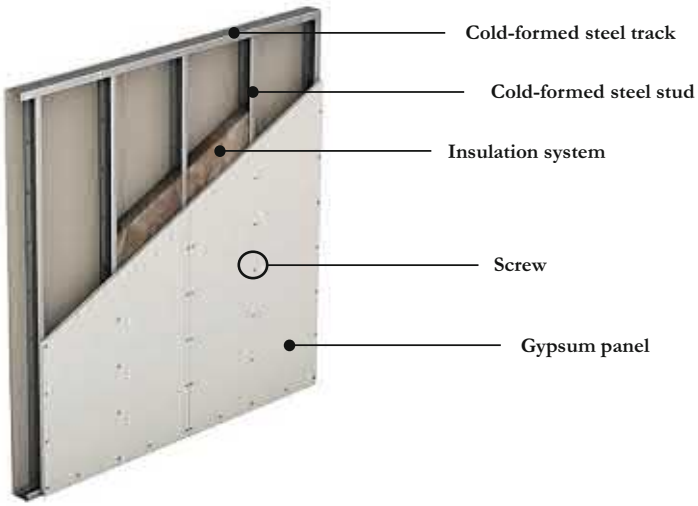


Fig. 1. Drywall partition configuration

3 Experimental Programme

An experimental campaign was carried out to investigate the shear behaviour of gypsum board-to-CFS profile screw connections. The programme included shear tests on connections, together with component-level tests performed to characterize the mechanical properties of the individual components and their interactions.

3.1 Component-Level Experimental Programme

The mechanical response of gypsum board-to-CFS profile screw connections is governed by the combined contribution of several resisting mechanisms associated with the screw, the gypsum board, and the steel profile. To characterize these individual contributions and provide the parameters required for the subsequent interpretation of the connection behaviour, a series of component-level tests was performed. The experimental programme comprised both material characterization tests, namely screw tensile and screw bending tests, and interaction tests, including gypsum embedment and screw head pull-through tests.

Table 1 summarizes the component-level testing programme, reporting the number of nominally identical specimens tested for each configuration together with the reference standards adopted. Figure 2 illustrates the test arrangements used for the different experimental configurations.

Throughout the experimental programme, self-tapping screws having a nominal diameter of 3.5 mm and a 8 mm nominal diameter countersunk flat head were employed. The gypsum boards had a nominal thickness of 12.5 mm, whereas the CFS profiles were manufactured from 0.60 mm nominal thick steel sheets.

The main results obtained from the component-level tests are illustrated in Fig. 3. Figure 3a presents the stress–strain curves obtained from the screw tensile tests, where the stress was calculated by dividing the applied load by the cross-sectional area corresponding to the screw minor nominal diameter (2.2 mm). The average ultimate tensile stress was 1457 MPa, with a coefficient of variation (COV) of 0.02.

Figure 3b shows the load–displacement response measured during the screw bending tests. The average peak load was equal to 0.53 kN, while the corresponding COV was 0.05.

The stress–displacement curves obtained from the gypsum embedment tests are shown in Fig. 3c. In this case, the embedment stress was determined as the applied load divided by the contact area, defined as the product of the nominal screw diameter and the nominal gypsum board thickness. According to EN 383:2007 [12], the average embedment strength, evaluated at a displacement of 5 mm, was 7.3 MPa with a COV of 0.04.

Finally, Fig. 3d illustrates the load–displacement curves obtained from the screw head pull-through tests. An average maximum load of 0.45 kN was recorded, with a COV equal to 0.05.

Table 1. Summary of the component-level experimental programme

Test	Number of nominally identical specimens	Reference standard
Screw tensile	4	ISO 898–1:2013 [13]
Screw bending	6	ASTM F1575/F1575M-21 [14]
Gypsum embedment	4	EN 383:2007 [12]
Screw head pull-through	4	EN 1383:2016 [15]

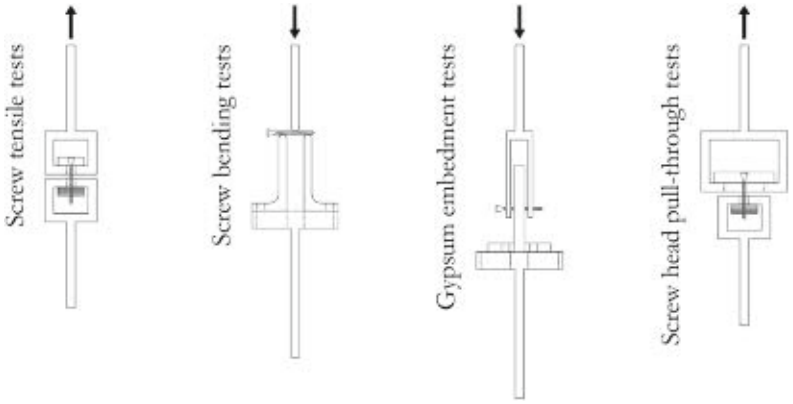


Fig. 2. Component-level tests setups

3.2 Shear Tests on Connections

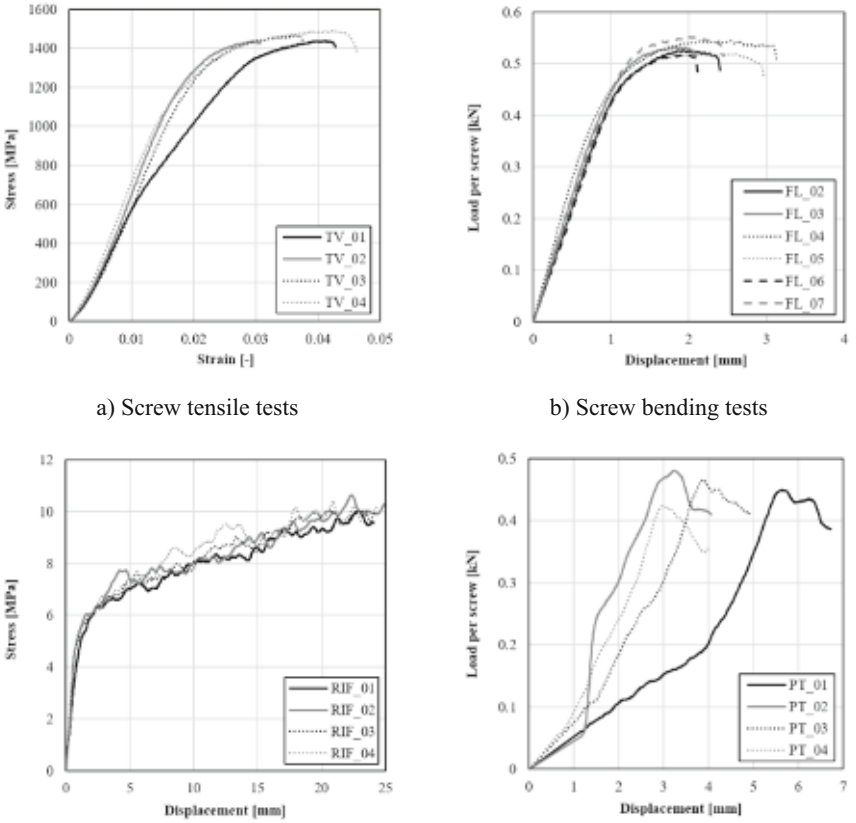
Specimens, Test Setup and Loading Protocol.
The experimental campaign included 14 shear tests on gypsum board-to-CFS profile screw connections. 8 specimens incorporating one gypsum board on each side were tested, comprising 4 monotonic and 4 cyclic tests. The remaining 6 specimens, sheathed with two gypsum boards on each side, included 3 monotonic and 3 cyclic tests. The test configuration was based on the procedure specified in EN 520:2009 [16], originally developed for gypsum board-to-timber connections and adapted for the steel-framed specimens considered in this study.

A schematic view of the test specimens is shown in Fig. 4. Each specimen consisted of two lipped CFS channel sects. (75 × 50 × 6 × 0.6 mm, corresponding to web depth, flange width, lip length and thickness) connected through gypsum boards installed on both flanges. The boards were 12.5 mm thick and were attached using 3.5 mm diameter self-tapping screws with an 8 mm countersunk flat head. The steel studs were positioned at a distance of 160 mm. The upper and lower profiles had lengths of 340 mm and 280 mm, respectively, resulting in an overall specimen length of 980 mm.

The three screws located along the upper edge of each board represented the connections under investigation. These fasteners were spaced at 50 mm, measured parallel to the loading direction. To prevent premature failure outside the test region, the lower edge of the boards was connected using six overstrength screws arranged in two rows. These screws were placed 30 mm from the loaded edge, with a spacing of 40 mm parallel and 15 mm perpendicular to the loading direction.

The monotonic tests were displacement-controlled and were performed at a constant rate of 0.15 mm/s until failure. The data were acquired at a sampling frequency of 10 Hz.

The cyclic tests followed the "CUREE Ordinary Ground Motion Reversed Cyclic Loading Protocol" proposed by Krawinkler et al. (2001) [17] for wood-frame structures (see Fig. 5). The loading history consists of displacement cycles with progressively increasing amplitudes defined from a reference displacement, $\Delta = \gamma \bullet \Delta_m$, where Δ_m corresponds to the average conventional ultimate displacement obtained from the monotonic



a) Screw tensile tests

b) Screw bending tests

c) Gypsum embedment tests

d) Screw head pull-through tests

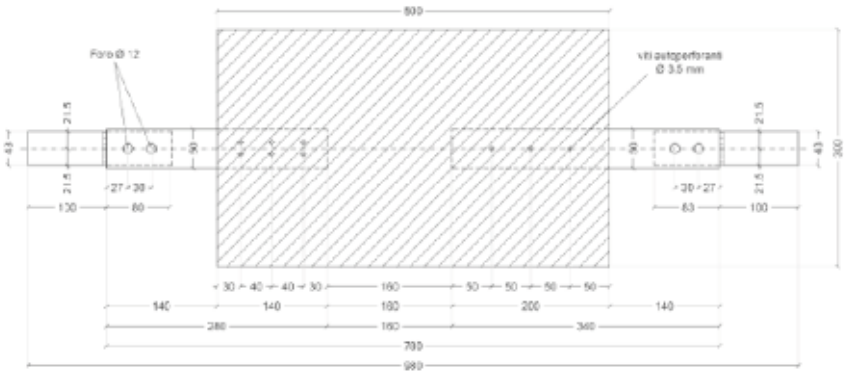
Fig. 3. Component-level tests results

tests, measured at a load equal to 80% of the peak resistance on the descending branch of the load-displacement curve. Following the CUREE recommendations, γ was taken equal to 0.60. Consequently, the reference displacement was set to 7.30 mm for specimens with one gypsum board per side and to 13.30 mm for specimens with two gypsum boards per side. Cyclic loading was applied at a constant frequency of 0.25 Hz, while the acquisition frequency was equal to 25 Hz.

The relative displacement between the gypsum boards and the CFS profiles was monitored by means of two linear variable differential transducers (LVDTs), installed at the upper corners of the specimens. Each transducer had a measurement range of 50 mm.

Test Results.

The load recorded during each test was converted into the average load carried by a



a) Geometry of the specimen



b) Specimen with one board per side

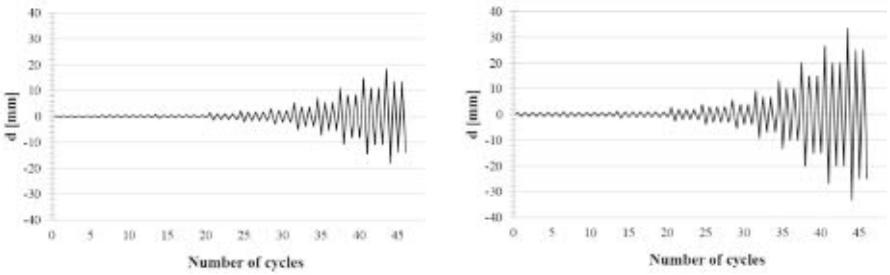


c) Specimen with two boards per side

Fig. 4. Shear test assembly

single screw (i.e., load per screw) by dividing the total measured force by six, corresponding to the number of screw connections involved in the test region. The resulting load-displacement relationships were subsequently used to evaluate the mechanical response of the individual connections. Figure 6 compares the monotonic load-displacement curves obtained for specimens incorporating either one or two gypsum boards on each side. A typical cyclic response is presented in Fig. 7, showing hysteretic loops characterized by pronounced nonlinear behaviour and significant pinching. The backbone curves extracted from all cyclic tests are reported in Fig. 8.

Regardless of the loading protocol or sheathing configuration, all specimens exhibited the same governing failure mode. Failure was consistently associated with the combined occurrence of gypsum board embedment, caused by screw tilting within the board, and screw head pull-through.



a) Specimen with one board per side b) Specimen with two boards per side

Fig. 5. CUREE loading protocol

The experimental response was quantified through a set of conventional parameters derived from the load-displacement curves. For the monotonic tests, these parameters included the peak load (F_p) and the corresponding displacement (d_p); the conventional elastic load (F_e), assumed equal to 40% of the peak load, and its associated displacement (d_e) measured on the ascending branch; the conventional elastic stiffness (k_e), calculated as the ratio between F_e and d_e; the conventional ultimate load (F_u), taken as 80% of the peak load, and the corresponding displacement (d_u) measured on the descending branch; the displacement ductility (μ), defined as the ratio d_u/d_e; and the dissipated energy (E), computed as the area under the load-displacement curve up to d_u. The results obtained from the monotonic tests are summarized in Table 2 for specimens with one gypsum board per side and in Table 3 for specimens with two gypsum boards per side.

The same parameters were adopted to characterize the cyclic response. In this case, they were evaluated from the positive and negative backbone curves and reported as the average of the two. The corresponding results are presented in Table 4 and Table 5 for specimens with one and two gypsum boards per side, respectively. In addition, the tables report the cumulative dissipated cyclic energy (E_c), calculated as the sum of the areas enclosed by all hysteresis loops.

The test results indicate that the average peak load increased from 0.44 kN to 0.74 kN under monotonic loading and from 0.32 kN to 0.55 kN under cyclic loading when the sheathing configuration changed from one to two gypsum boards per side. This corresponds to an increase in resistance of approximately 68% and 70% for monotonic and cyclic tests, respectively. Conversely, for both sheathing configurations, the peak load measured under cyclic loading was approximately 25% lower than that obtained under monotonic loading, mainly due to the degradation induced by repeated load reversals and the associated cyclic screw tilting.

Regarding the conventional elastic stiffness, average values of 0.73 kN/mm and 0.36 kN/mm were obtained from the monotonic tests for specimens with one and two gypsum boards per side, respectively. The corresponding values under cyclic loading were 0.77 kN/mm and 0.40 kN/mm. Therefore, doubling the number of boards produced a reduction in stiffness of about 50% under monotonic loading and 48% under cyclic loading. A possible explanation for this behaviour is the increased thickness of the sheathing, which increases the free length of the screw and consequently its bending deformability during

the initial loading stage. In addition, relative slip between the two gypsum boards may contribute to the initial deformation of the connection. These effects may reduce the initial stiffness, even though the presence of the additional board leads to a higher connection resistance. For both configurations, the stiffness evaluated from the cyclic backbone curves was approximately 10% higher than that obtained from the monotonic response.

A similar trend was observed for the dissipated energy. Under monotonic loading, the average energy increased from 4.49 kNmm to 13.35 kNmm when passing from one to two gypsum boards per side, while under cyclic loading the corresponding values increased from 2.78 kNmm to 8.85 kNmm. These results correspond to increases of approximately 198% and 218%, respectively. However, the energy dissipated up to the conventional ultimate displacement under cyclic loading remained about 35% lower than that measured in the monotonic tests.

Finally, the cumulative dissipated cyclic energy increased from an average value of 20.30 kNmm for specimens with one gypsum board per side to 47.25 kNmm for specimens with two gypsum boards per side, corresponding to an increase of 133%.

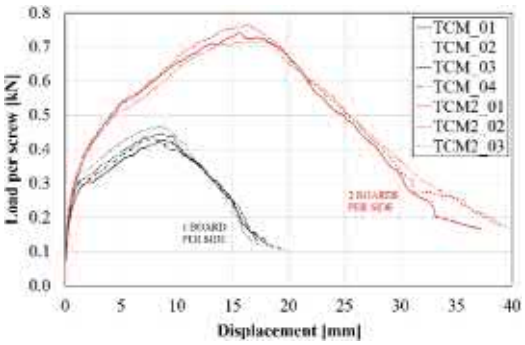


Fig. 6. Monotonic shear tests

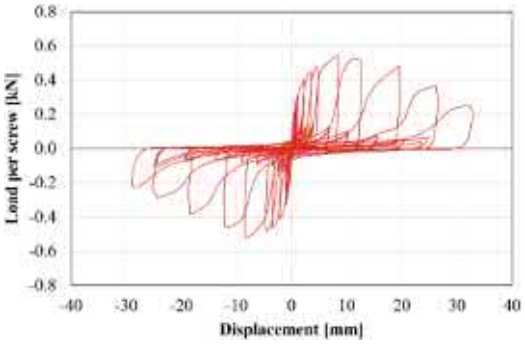


Fig. 7. Typical cyclic response

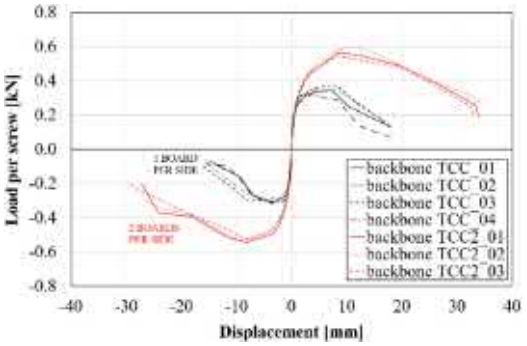


Fig. 8. Backbone curves from cyclic shear tests

Table 2. Monotonic tests results (specimens with one board per side)

Specimen	F_e [kN]	d_e [mm]	k_e [kN/mm]	F_p [kN]	d_p [mm]	F_u [kN]	d_u [mm]	μ [−]	E [kNmm]
TCM_01	0.17	0.28	0.61	0.43	8.86	0.34	12.30	43.93	4.35
TCM_02	0.19	0.21	0.89	0.47	8.39	0.37	11.52	54.86	4.58
TCM_03	0.18	0.23	0.77	0.44	8.61	0.36	12.11	52.65	4.53
TCM_04	0.17	0.27	0.64	0.43	7.75	0.34	12.37	45.81	4.49
average	0.18	0.25	0.73	0.44	8.40	0.35	12.08	49.31	4.49
COV	0.040	0.133	0.177	0.040	0.057	0.040	0.032	0.107	0.023

Table 3. Monotonic tests results (specimens with two boards per side)

Specimen	F_e [kN]	d_e [mm]	k_e [kN/mm]	F_p [kN]	d_p [mm]	F_u [kN]	d_u [mm]	μ [−]	E [kNmm]
TCM2_01	0.30	0.93	0.32	0.74	15.60	0.59	21.84	23.48	13.14
TCM2_02	0.29	0.69	0.42	0.72	17.65	0.57	23.16	33.57	13.71
TCM2_03	0.31	0.86	0.36	0.76	16.20	0.61	21.50	25.00	13.21
average	0.30	0.83	0.36	0.74	16.48	0.59	22.17	27.35	13.35
COV	0.032	0.149	0.134	0.032	0.064	0.032	0.040	0.199	0.023

Table 4. Cyclic tests results (specimens with one board per side)

Specimen	F_e [kN]	d_e [mm]	k_e [kN/mm]	F_p [kN]	d_p [mm]	F_u [kN]	d_u [mm]	μ [−]	E [kNmm]	E_c [kNmm]
TCC_01	0.13	0.17	0.81	0.32	5.89	0.26	8.56	52.83	2.49	17.18
TCC_02	0.13	0.15	0.86	0.32	3.71	0.25	10.30	69.15	3.03	21.29
TCC_03	0.14	0.19	0.73	0.34	5.94	0.27	10.42	55.97	3.23	23.08
TCC_04	0.13	0.18	0.69	0.32	3.49	0.25	8.39	45.58	2.38	19.66
average	0.13	0.17	0.77	0.32	4.76	0.26	9.42	55.88	2.78	20.30
COV	0.032	0.101	0.096	0.032	0.282	0.032	0.116	0.176	0.147	0.123

Table 5. Cyclic tests results (specimens with two boards per side)

Specimen	F_e [kN]	d_e [mm]	k_e [kN/mm]	F_p [kN]	d_p [mm]	F_u [kN]	d_u [mm]	μ [−]	E [kNmm]	E_c [kNmm]
TCC2_01	0.22	0.58	0.38	0.55	8.28	0.44	18.96	32.43	9.12	47.83
TCC2_02	0.23	0.58	0.39	0.57	10.35	0.46	17.86	30.55	8.75	48.66
TCC2_03	0.21	0.50	0.43	0.54	8.23	0.43	18.68	37.29	8.67	45.26
average	0.22	0.55	0.40	0.55	8.95	0.44	18.50	33.43	8.85	47.25
COV	0.032	0.088	0.064	0.032	0.135	0.032	0.031	0.104	0.027	0.038

4 Conclusions

The in-plane response of drywall partitions is primarily governed by the shear behaviour of the gypsum board-to-CFS profile screw connections. Despite their key role in the seismic performance of these systems, current standards do not provide analytical formulations for predicting the shear resistance of gypsum board-to-steel screw connections, highlighting the need for dedicated design approaches. The development and validation of such analytical models require not only shear tests on connections but also component-level tests capable of characterizing the individual resisting mechanisms contributing to the overall connection response.

The experimental results showed that cyclic loading significantly influences the mechanical behaviour of the connections. Compared with monotonic loading, the average connection resistance decreased by approximately 25%, while the dissipated energy was reduced by about 35%. Conversely, the conventional elastic stiffness increased by approximately 10%. The influence of the sheathing configuration was also found to be significant. Increasing the number of gypsum boards from one to two on each side resulted in an increase in the average connection resistance of approximately 68% under monotonic loading and 70% under cyclic loading. At the same time, the conventional elastic stiffness decreased by about 50% and 48%, respectively, whereas the dissipated

energy increased by approximately 198% and 218%. Moreover, the cumulative dissipated cyclic energy increased by approximately 133% for specimens incorporating two gypsum boards per side.

The present findings are limited to the investigated connection configuration. Further studies on different screw, gypsum board, and CFS profile configurations would provide a more comprehensive understanding of the shear behaviour of gypsum board-to-CFS profile screw connections.

References

1. Whittaker AS, Soong TT (2003) An overview of nonstructural component research at three U.S. earthquake engineering research centers. In: Proceedings of seminar on seismic design, performance, and retrofit of nonstructural components in critical facilities, Redwood City, CA
2. Milone A, Prota A, Landolfo R (2026) Ultimate and repairability performance of steel eccentrically braced frames designed according to the 2nd generation of Eurocode 8: a parametric study for medium-rise buildings. Eng Struct 365:123283
3. Freddi F et al (2025) Seismic retrofitting of existing steel frames with external BRBs: pseudo-dynamic hybrid testing and numerical parametric analysis. Earthq Eng Struct Dyn 54:1064–1083
4. Milone A, D'Aniello M, Landolfo R (2024) Advanced fatigue assessment of riveted railway bridges on existing masonry abutments: an Italian case study. Buildings 14(8):2271
5. Tartaglia R, Monte F, Demonceau JF, Maddaloni G (2026) Monotonic behaviour of 4-bolt row connections: analytical and numerical analyses. J Constr Steel Res 236:110048
6. Gnazzo M, Mahmoudi B, D'Aniello M, Imanpour A, Landolfo R (2026) Seismic design and response of inverted-V CBFs compliant with European and Canadian standards. Eng Struct 363:123071
7. Tartaglia R, D'Aniello DJF, Landolfo R (2025) Seismic design and testing of EC8-1-2-compliant unstiffened end-plate beam-to-column joints. J Constr Steel Res 235:109916
8. Fiorino F, Campiche A, Grzesik P, Landolfo R (2024) Experimental evaluation of in-plane seismic demand on power actuated fasteners (PAF) connecting CFS drywall partitions and concrete surrounding elements. Bull Earthq Eng 22(2025):2057
9. Rahmanishamsi E, Soroushian S, Maragakis M (2016) Cyclic shear behavior of gypsum board-to-steel stud screw connections in nonstructural walls. Earthquake Spectra 32(1):415–439
10. Fiorino L, Pali T, Bucciero B, Macillo V, Terracciano MT, Landolfo R (2017) Experimental study on screwed connections for sheathed CFS structures with gypsum or cement based panels. Thin-Walled Struct 116:234–249
11. Vella N, Gardner L, Buhagiar S (2021) Analytical modelling of cold-formed steel-to-timber connections with inclined screws. Eng Struct 249:113187
12. CEN EN 383 (2007) Timber structures - test methods - determination of embedding strength and foundation values for dowel type fasteners. European Committee for Standardization, Brussels
13. ISO 898-1 (2013) Mechanical properties of fasteners made of carbon steel and alloy steel - part 1: bolts, screws and studs with specified property classes - coarse thread and fine pitch thread. International Organization for Standardization, Vernier
14. ASTM F1575/F1575M (2021) Standard test method for determining bending yield moment of nails. ASTM International, West Conshohocken, Pennsylvania

15. CEN EN 1383 (2016) Timber structures - test methods - pull-through resistance of timber fasteners. European Committee for Standardization, Brussels
16. CEN EN 520 (2009) Gypsum plasterboards - definitions, requirements and test methods. European Committee for Standardization, Brussels
17. Krawinkler H, Parisi F, Ibarra L, Ayoub A, Medina R (2001) Development of a testing protocol for Woodframe structures. Report W-02, CUREE/Caltech woodframe project Richmond, CA

On the Seismic Performance of Large-Area Lightweight Steel Suspended Ceilings: Experimental Set-Up

Alessandro Prota(✉), Vito D'Addesa, Luigi Fiorino, and Raffaele Landolfo

Department of Structures for Engineering and Architecture, University of Naples Federico II, 80134 Naples, Italy
alessandro.prota@unina.it

Abstract. Suspended ceilings are among the most common non-structural components in buildings and may govern post-earthquake functionality in facilities where immediate occupancy is required. Concealed-grid systems are of particular interest because their seismic response is controlled by the interaction between cold-formed steel profiles, hangers, boards, perimeter details and, when present, lateral restraint devices. The experimental characterisation of these systems is therefore most meaningful when it is carried out at a sufficiently large scale, so that global deformation patterns, construction tolerances and progressive damage mechanisms can be reproduced. This paper presents the development of a large-scale shaking-table test set-up designed for suspended ceilings with a plan area of up to approximately 50 m^2. The steel supporting frame is conceived to extend the effective test area beyond the 3.0 m x 3.0 m table footprint while remaining within the payload and stroke limits of the facility. The paper also introduces the numerical modelling strategy adopted for the bare frame. Preliminary modal analyses indicate horizontal translational frequencies of about 31.0 Hz and 31.1 Hz, and a torsional frequency of about 32.0 Hz, confirming that the supporting frame is sufficiently stiff to act as a nearly rigid boundary for the ceiling specimen. In addition to the experimental design, the revised study will include detailed descriptions of the base anchorage, constructional detailing and numerical dynamic simulations. The latter will be based on table-level input accelerograms generated and checked against an ICC AC156-compatible target spectrum.

Keywords: dynamic testing · large-scale testing · shaking-table testing · suspended ceilings · test set-up

1 Introduction

Non-structural components have a direct influence on the safety, serviceability and economic performance of buildings during and after earthquakes. Although they are not normally part of the primary load-bearing system, their damage may lead to falling hazards, interruption of evacuation routes, loss of building services and prolonged downtime. Suspended ceilings are particularly relevant in this respect, because they are widely adopted in commercial buildings, hospitals, schools, airports and other facilities in which architectural finish, acoustic performance and service integration are required.

© The Author(s), under exclusive license to Springer Nature Switzerland AG 2026
R. Zanon et al. (Eds.): CTA 2026, LNCE 942, pp. 432–443, 2026.
https://doi.org/10.1007/978-3-032-39505-4_38

The seismic vulnerability of suspended ceilings has been repeatedly observed after damaging earthquakes [1, 2]. Their response is generally governed by floor acceleration demands rather than by inter-storey drift alone, and therefore even relatively stiff buildings with limited lateral deformation may experience damage to ceiling panels, suspension devices, grid members or perimeter supports. The consequences are not limited to repair costs: in essential facilities, ceiling failure may also compromise operational continuity and the use of mechanical, electrical and fire-safety systems installed above or within the ceiling void.

From an experimental viewpoint, suspended ceilings are difficult to investigate because they are assemblies of many light components, local connections and boundary details. Their seismic response may involve sliding, impact at the perimeter, local disengagement, screw or hanger damage, progressive panel cracking and the mobilisation of global vibration modes. These mechanisms are strongly affected by workmanship, tolerances and the actual plan dimensions of the installation. For this reason, small specimens are useful for component characterisation but may not be sufficient to reproduce full-system behaviour.

Recent studies on steel and lightweight steel systems have also shown the importance of constructional detailing, local connection behaviour and calibrated analytical or numerical assessment procedures in different structural applications, including bolted steel connections, seismic-resistant CFS wall systems and existing steel infrastructure [3–8]. Within this broader methodological context, the present work focuses on the development and preliminary numerical verification of a large-scale testing set-up for suspended ceilings.

Shaking-table testing remains one of the most effective approaches for assessing acceleration-sensitive non-structural components. However, large ceiling specimens are often incompatible with conventional laboratory equipment because of limits in table footprint, payload, displacement capacity and available construction time. The present work addresses this issue by proposing a steel testing frame that allows a ceiling area of approximately 50 m2 to be installed and tested using a single 3.0 m x 3.0 m shaking table. The frame is intended to provide a stiff and stable boundary condition while extending the usable ceiling plan well beyond the table platform.

Dedicated sections are introduced for the base connections, the anchorage to the shaking table, the ceiling installation details and the numerical simulation.

2 Lightweight Steel Suspended Ceilings and Seismic Restraint

2.1 System Layout and Seismic Behaviour

Suspended ceiling systems may be broadly divided into exposed-grid and concealed-grid configurations. In exposed-grid, or lay-in, systems, panels are placed within a visible network of main runners and cross tees. This arrangement facilitates inspection and maintenance of building services, but the panels may be vulnerable to uplift, sliding and dislodgement when subjected to horizontal and vertical accelerations.

Concealed-grid systems, usually consist of cold-formed steel profiles suspended from the structural slab by hangers and connected to secondary members that support the finishing boards. The boards are typically screwed to the profiles, producing a continuous

lower surface. The seismic response is therefore influenced by both the global motion of the suspended assembly and the local behaviour of screws, hangers, profile intersections and perimeter details.

In seismic qualification, suspended ceilings are commonly treated as acceleration-sensitive components. The inertial forces induced by floor motion are transferred through the boards and grid to the suspension and restraint system. Depending on the boundary condition, these forces may be resisted by perimeter connections, by internal bracing connected to the slab above, or by a combination of both. When clearances are insufficient, impacts between the ceiling and the surrounding walls may become a critical damage mechanism.

2.2 Lateral Restrain

Three idealised restraint strategies are generally considered in experimental and design studies: fully perimeter-fixed systems, partially perimeter-fixed systems and floating systems. In a fully perimeter-fixed configuration, all edges are connected to the surrounding walls or boundary members. This solution may be appropriate for small ceiling areas, but it can transmit wall displacements and impact forces directly into the ceiling grid.

A partially perimeter-fixed arrangement typically restrains two adjacent sides while allowing movement along the remaining sides. The aim is to provide lateral stability while reducing the risk of force transfer caused by incompatible wall movement. Adequate gaps and carefully detailed free edges are essential for this approach to perform as intended.

For larger ceiling areas, floating systems with independent back-bracing are often preferred. In this configuration, the ceiling is laterally separated from the surrounding walls and horizontal seismic forces are transferred to the floor or roof slab above through dedicated bracing elements. The experimental set-up described in this paper is conceived so that different restraint layouts can be accommodated in future testing programmes.

3 Background from Previous Shaking-Table Studies

A growing experimental database is available on the seismic response of suspended ceilings, although the range of ceiling typologies, boundary conditions and test rigs remains broad. Previous studies have shown that representative large-area tests are essential when the objective is to capture global vibration, progressive damage and interaction with the surrounding support system [9]. At the same time, they have highlighted the practical difficulty of testing ceiling specimens whose plan dimensions exceed the physical dimensions of the available shaking table.

Large experimental programmes on exposed-grid systems have demonstrated the importance of boundary conditions, panel mass and multi-directional excitation. Ryu and Reinhorn tested ceiling areas from approximately 36 m2 to more than 90 m2 using one or two synchronised shaking tables and steel mock-up frames [10]. Their work remains a key reference because it combined realistic ceiling dimensions, different lateral restraint strategies and extensive instrumentation.

Other investigations have focused on discontinuous or concealed systems. Very large ceiling specimens, in some cases reaching approximately 150 m2, have been tested using paired shaking tables and purposely built steel rigs [11]. These programmes confirmed that the dynamic properties of the supporting frame cannot be ignored: if the rig is not sufficiently stiff, the measured response may include interactions between the test structure and the ceiling rather than the behaviour of the ceiling alone.

A further group of studies addressed the problem of testing specimens larger than the table footprint [12, 13]. In these cases, steel frames were designed to overhang or extend beyond small-to-medium shaking tables, increasing the usable plan area while maintaining a controlled boundary condition. Although these solutions considerably improved experimental representativeness, reported bare-frame natural frequencies varied significantly, indicating that the stiffness of the test rig should be explicitly assessed and, where possible, designed to remain outside the frequency range of interest for the ceiling system.

The set-up proposed in the present study follows the same methodological direction but targets a larger ratio between ceiling area and table footprint. The main design requirement is to achieve a sufficiently rigid steel frame while respecting the 200 kN payload capacity of the facility. The resulting solution allows a ceiling plan of about 7.7 m x 6.5 m to be installed on a single 3.0 m x 3.0 m table, leading to a ceiling-to-table area ratio of approximately 5.6.

4 Proposed Large-Scale Experimental Set-Up

4.1 Shaking-Table Facility

The experimental campaign is planned at the laboratory of the Department of Structures for Engineering and Architecture of the University of Naples Federico II. The facility is equipped with two identical shaking tables, each having a plan dimension of 3.0 m x 3.0 m and a maximum payload of 200 kN. The tables can operate in the two horizontal directions, with a frequency range up to 50 Hz, a peak velocity of 1.0 m/s, a peak acceleration of 1.0 g and a maximum stroke of +/−250 mm. Vertical excitation is not available.

Although two tables are present in the laboratory, the proposed configuration is based on the use of a single table. This choice makes the set-up simpler, reduces synchronisation issues and provides a demanding design case because the supporting frame must extend significantly beyond the table footprint while maintaining adequate stiffness and stability.

4.2 Design Objectives and Global Concept

The main objective of the test set-up is to reproduce a medium-to-large suspended ceiling while remaining compatible with the limitations of a standard laboratory shaking table. Four design requirements were considered. First, the ceiling plan should be sufficiently large to allow global response mechanisms to develop. Secondly, the steel supporting frame had to remain dynamically stiff with respect to the ceiling assembly, thereby limiting undesired interaction between the rig and the specimen. In this regard, the bare

supporting frame was designed to achieve fundamental lateral frequencies higher than 20 Hz [14].Thirdly, the total mass should remain safely below the table payload. Finally, the frame should be modular and practical to assemble, inspect and dismantle.

The selected solution consists of a three-dimensional steel frame mounted on the 3.0 m x 3.0 m table. The frame acts both as a support for the ceiling hangers and as the boundary structure used to reproduce the desired perimeter conditions. The maximum ceiling installation area is approximately 7.7 m x 6.5 m, corresponding to about 50 m2. The largest plan dimension of the frame is therefore around 2.5 times the side length of the table, while the ceiling area is about 5.6 times the table area.

4.3 Geometry and Member Arrangement

The upper portion of the set-up is formed by steel trussed beams that carry the secondary members used for suspending the ceiling. The trussed beams include angle profiles for vertical and diagonal web members and paired angle profiles for the chords. The total depth of the trussed beams is 0.8 m. The beams are supported by lateral resisting systems made of paired UPN 300 profiles, giving a support height of 1.7 m.

The distance between the lower chord of the trussed beam and the top of the lateral resisting system creates a free zone for positioning and inspecting the ceiling grid. This gap is equal to approximately 0.6 m. The arrangement allows ceilings to be suspended either from the upper chord or from the lower chord of the trussed beams. In the first case, the resulting suspension height is expected to range from about 0.9 m to 1.3 m; in the second case, the height can be reduced to approximately 0.1 m to 0.5 m. This flexibility is useful for reproducing different practical installation conditions (see Fig. 1).

The choice of structural sections was mainly governed by stiffness requirements. At the same time, open sections such as angles and channels were preferred because they facilitate bolting, access to connections and adjustment during assembly. The global layout also provides sufficient space for instrumentation, visual inspection and future changes in boundary restraints or ceiling typology.

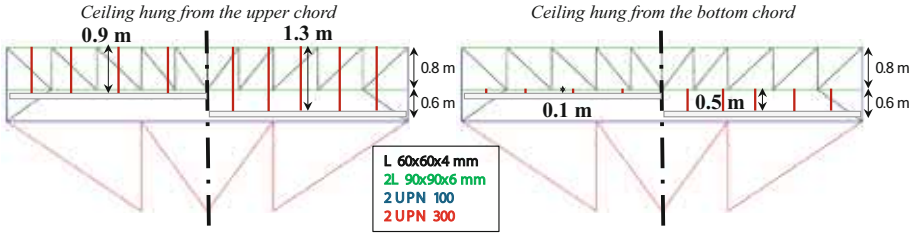


Fig. 1. Set-up geometry and member arrangement

4.4 Base Connection Layout

The supporting frame is connected to the shaking table by means of a dedicated bolted steel interface. The anchorage system consists of stiffened adapter plates, arranged to

match the regular threaded-hole grid of the table, with a nominal spacing of 0.25 m. Multiple bolts are used to transfer the horizontal inertial forces and overturning effects from the steel frame to the table, while the welded stiffeners limit local plate deformation. This solution provides a rigid, removable and inspectable base connection without requiring any modification to the shaking table (see Fig. 2).

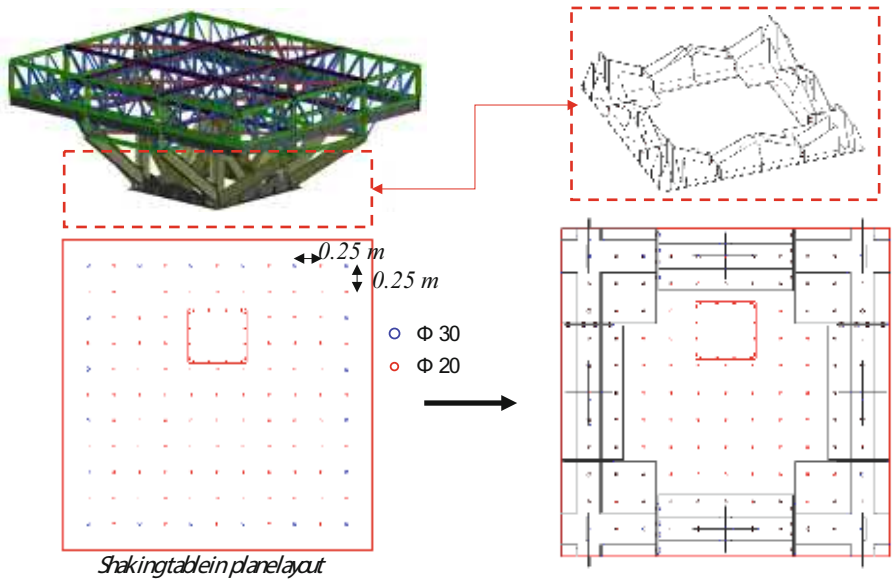
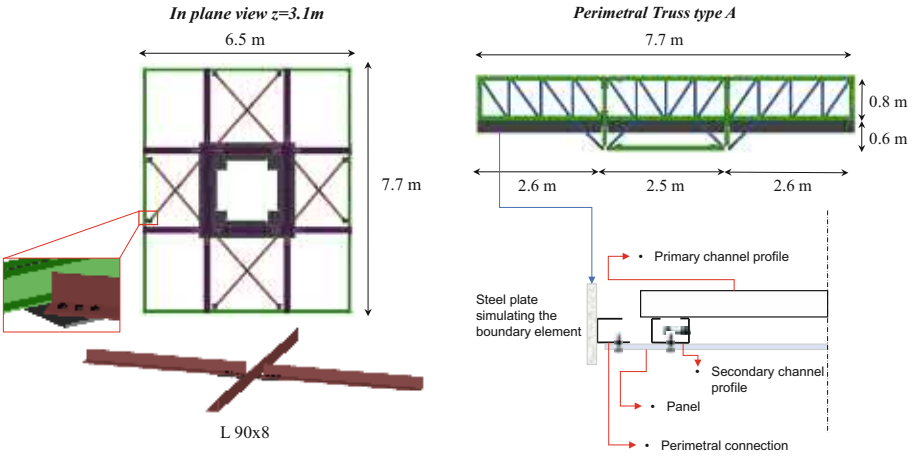


Fig. 2. Base connection layout

4.5 Constructional Details and Ceiling Installation

The testing frame is conceived as a modular steel assembly, with horizontal bracing systems provided at two different elevations, namely at approximately z = 1.7 m and z = 3.1 m. The upper horizontal bracing level contributes to the global in-plane stiffness of the supporting frame, whereas the lower bracing level improves the lateral stability of the system close to the ceiling installation zone. For practical reasons, the horizontal braces located at z = 1.7 m are designed as removable elements, so that they can be temporarily dismantled during the installation of the suspended ceiling and subsequently re-installed before testing (see Fig. 3a). The ceiling specimens are suspended from secondary steel members placed at the upper part of the set-up. These secondary members provide the anchorage points for the hangers and allow different hanger layouts and ceiling configurations to be accommodated. Along the perimeter of the specimen, below the lower chord of the main truss beams, steel plates are installed to reproduce the desired boundary condition of the ceiling system. Depending on the specific test configuration, these plates can be used either to restrain the ceiling edge, simulating a fixed perimeter condition, or to provide the required clearance for a free/floating edge condition (see

Fig. 3b). In this way, the same supporting frame can be adapted to different seismic restraint layouts while maintaining a consistent global testing configuration.



a) Horizontal bracing b) Detailing for boundary condition

Fig. 3. Constructional details

4.6 Mass and Payload Assessment

The estimated self-weight of the steel set-up, including the main supporting members and secondary elements required for suspending the ceiling, is approximately 120 kN. For a relatively heavy ceiling configuration with a unit weight between 0.35 kN/m2 and 0.40 kN/m2, the additional mass associated with a 50 m^2 specimen is expected to range from about 17.5 kN to 20.0 kN. The resulting total vertical load is therefore approximately 140 kN, leaving a significant margin with respect to the 200 kN payload of the shaking table.

This mass margin is important because it allows different ceiling typologies to be investigated, ranging from lightweight mineral-fibre or metal panel systems to heavier gypsum-board assemblies. It also provides allowance for instrumentation, local reinforcement, anchorage devices and possible changes in the final test configuration.

5 Numerical Modelling and Simulation

5.1 Bare-Frame Numerical Model

A numerical model of the steel testing frame was developed in SAP2000 [15] to assess the dynamic properties of the bare set-up before the installation of any ceiling specimen (see Fig. 4). The structure was modelled using frame elements, including the cross-sectional properties selected during the design phase and representing the principal trussed beams and the lateral resisting systems. The material was assumed to be S275 structural steel, consistently with the steel grade adopted for the realised set-up.

At this preliminary stage, the ceiling specimen was not included in the model, so that the intrinsic stiffness of the supporting structure could be evaluated separately. The seismic masses were automatically derived from the self-weight and dead loads of the steel members included in the model. The base nodes of the frame were assumed to be pinned to the shaking table, in accordance with the intended anchorage layout. In the final version of the study, this assumption may be refined to account for the actual stiffness of the base plates and bolted connections, if relevant.

The beam-to-column and truss connections were modelled either as pinned or continuous restraints, depending on the corresponding design detail. Modal analysis was then carried out as a first verification that the frame can be regarded as a stiff support with respect to the suspended ceiling system. For the subsequent dynamic analyses, Rayleigh damping equal to 5% was assigned on the basis of the first two vibration modes.



Fig. 4. 3D finite element model of the proposed set-up

5.2 Modal Analysis Results

The first two modes of the bare frame are mainly translational in the horizontal plane, while the third mode is predominantly torsional about the vertical axis. The corresponding frequencies are close to each other and exceed 30 Hz. These values are significantly higher than those reported for several previous large-area ceiling test rigs, confirming the high global stiffness of the proposed set-up.

The modal results suggest that the dynamic contribution of the supporting frame should be limited within the frequency range expected for the ceiling assembly. This is a key requirement because the aim of the experimental programme is to measure the response of the suspended ceiling rather than the flexibility of the test rig. The high bare-frame frequencies also reduce the likelihood that the target shaking-table input will be distorted by amplification of the supporting structure (Table 1).

Table 1. Modal analyses results

Mode	Dominant shape	Frequency
1	Horizontal translational	31.0 Hz
2	Horizontal translational	31.1 Hz
3	Torsion about the vertical axis	32.0 Hz

5.3 Preliminary Dynamic Verification Under ICC AC156-Compatible Input

A preliminary numerical verification of the testing frame was carried out through linear time-history analyses. The main aim was not to assess the seismic performance of the ceiling specimen, which will be investigated in the forthcoming experimental campaign, but rather to check the dynamic suitability of the steel set-up itself when subjected to a severe shaking-table input. The adopted input motion was an artificial accelerogram defined to be compatible with the requirements of ICC-ES AC156 (see Fig. 5) [16]. According to this protocol, the required response spectrum is derived from the design short-period spectral acceleration, SDS, the component location within the building height, and the distinction between the amplified and rigid spectral regions. The test response spectrum is generally evaluated assuming 5% critical damping and is checked over the frequency range from 1.3 to 33.3 Hz. In the present preliminary assessment, a value of SDS equal to 1.0 g was assumed, consistently with severe seismic qualification conditions and with the input motion adopted in a previous shaking-table experimental programme on drywall partitions, façades and suspended ceilings [17]. ICC-ES AC156 defines the drive signal as a non-stationary broadband random excitation with energy content in the 1.3–33.3 Hz range; the corresponding test response spectrum should envelope the required response spectrum within the specified acceptance limits. The accelerogram was applied at the base of the finite element model of the bare steel frame, considering separately the two principal horizontal directions of the set-up. For each excitation direction, the response was monitored at eight representative nodes located at the top level of the supporting frame: the four corner nodes and four internal nodes. This selection was intended to capture both the global horizontal response of the set-up and possible local vertical movements associated with the fact that the upper reticular frame extends significantly beyond the shaking-table footprint.

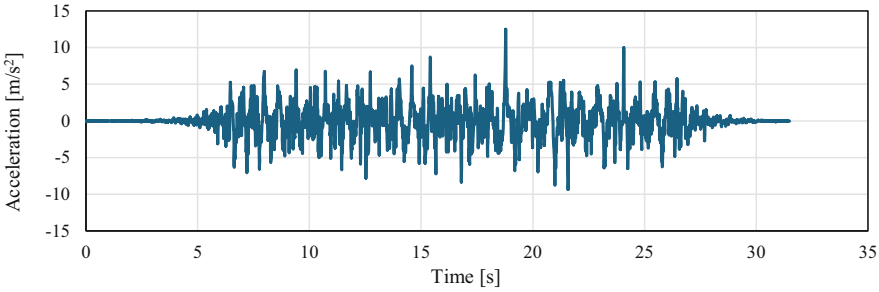
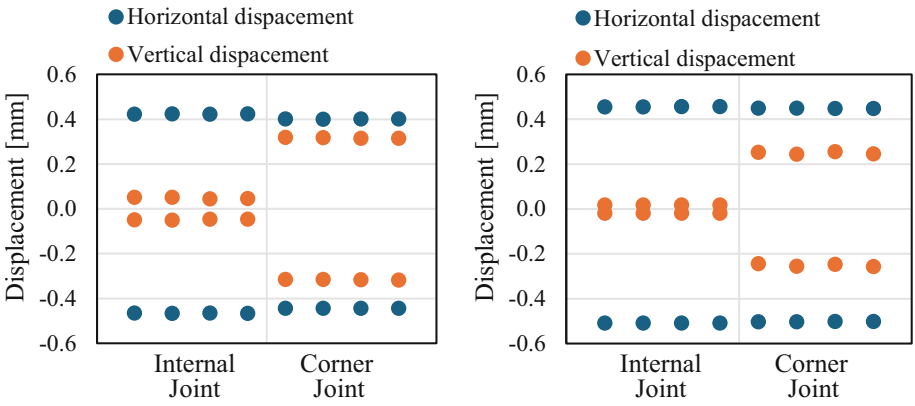


Fig. 5. Input acceleration time-history

The monitored quantities included the maximum horizontal displacement in the direction of excitation (relative displacement between the test set-up and the shaking table) and the corresponding vertical displacement at the selected control nodes. When the input was applied along the X direction (parallel to largest set-up dimension), the maximum absolute horizontal displacement was equal to 0.47 mm, while the maximum vertical displacement was 0.32 mm (see Fig. 6a). For excitation along the Y direction (parallel to shortest set-up dimension), the corresponding maximum values were 0.51 mm in the horizontal direction and 0.26 mm in the vertical direction (see Fig. 6b). These results confirm that the frame works within a very low displacement range under the selected input motion.



a) Time-history Dir. X b) Time-history Dir. Y

Fig. 6. Maximum roof displacements from time-history analyses

The checks were therefore considered satisfactory. The maximum relative horizontal displacements between the set-up roof and shaking table are negligible in both testing directions, confirming that the dynamic tests can be safely performed without excessive relative movement of the supporting frame. Moreover, the vertical displacements induced by the overhanging configuration of the upper structure remain very limited,

with maximum values close to or lower than 0.4 mm for the corner joints, and can therefore be considered negligible for the purposes of the planned shaking-table tests.

The numerical model was also used to estimate the maximum overturning moments transmitted to the shaking table. Peak values of approximately 266 kNm and 244 kNm were obtained for excitation along the X and Y directions, respectively. These values are lower than those recorded during previous experimental campaigns carried out on the same equipment and remain well below the nominal overturning moment capacity of the shaking table, which is approximately 800 kNm. This further confirms that the proposed testing configuration is compatible with the operational limits of the facility.

6 Conclusions

This paper presents a revised framework for the large-scale shaking-table assessment of concealed-grid suspended ceilings. The proposed steel set-up allows a ceiling area of approximately 50 m^2 to be tested using a single 3.0 m $\times$ 3.0 m shaking table, thereby overcoming one of the main limitations related to laboratory footprint. The layout provides flexibility in terms of suspension height, boundary condition and ceiling typology, while keeping the total mass within the 200 kN payload capacity of the facility.

The constructional detailing was also developed to ensure practical installation and testing. Horizontal bracing systems are provided at different elevations, with removable lower braces to facilitate ceiling installation. Secondary steel members allow the ceiling hangers to be connected at the upper part of the frame, while perimeter steel plates below the lower chord make it possible to reproduce fixed or free/floating edge conditions. The frame is connected to the shaking table through stiffened bolted interface plates, arranged to match the existing threaded-hole grid.

Preliminary modal analyses of the bare frame showed that the first three modes occur at frequencies slightly above 30 Hz. The first two modes are mainly horizontal translations, whereas the third is torsional. This confirms that the supporting frame is sufficiently stiff to act as an almost rigid boundary for the ceiling specimen, limiting undesired dynamic interaction between the test rig and the component under investigation.

Finally, time-history analyses were carried out using an ICC AC156-compatible artificial accelerogram. The maximum horizontal displacements were 0.47 mm and 0.51 mm for excitation along the X and Y directions, respectively, while the corresponding vertical displacements were 0.32 mm and 0.26 mm. In addition, the estimated overturning moments transmitted to the shaking table, equal to 266 kNm and 244 kNm for X- and Y-direction excitation, respectively, remained significantly lower than the nominal table capacity, further confirming the suitability and safety of the proposed set-up for the planned dynamic tests.

Overall, the set-up provides a flexible and robust platform for future full-scale seismic testing of LWS suspended ceilings, allowing the investigation of dynamic response, damage mechanisms and boundary-condition effects under realistic shaking-table conditions.

References

1. Salkhordeh M, Soroushian S (2026) Seismic performance of suspended ceiling systems; A literature review. J Earthq Eng 30(1):301–333
2. Dhakal RP, MacRae GA, Hogg K (2011) Performance of ceilings in the February 2011 Christchurch earthquake. Bull NZ Soc Earthq Eng 44(4):379–389
3. Tartaglia R, Monte F, Demonceau JF, Maddaloni G (2026) Monotonic behaviour of 4-bolt row connections: analytical and numerical analyses. J Constr Steel Res 236:110048
4. Fiorino F, Campiche A, Tartaglia R, Landolfo R (2025) Seismic-resistant CFS walls braced with pre-tensioned UHS steel bars: design and construction of a building mockup. Thin-Walled Struct 208:112818
5. Milone A, D'Aniello M, Landolfo R (2024) Advanced fatigue assessment of riveted railway bridges on existing masonry abutments: an Italian case study. Buildings 14(8):2271
6. Fiorino F, D'Addesa V, Landolfo R (2024) Seismic design rules for lightweight steel shear walls with wood panel sheathing within the Eurocode format. Thin-Walled Struct 204:112293
7. Tartaglia R, Monte F, Maddaloni G (2025) Seismic performance of stiffened end-plate steel joints with non-symmetric octagonal bolts arrangement. J Constr Steel Res 234:109770
8. Monte F, Tartaglia R, Maddaloni G (2026) Extended stiffened end-plate steel joints with octagonal bolt arrangement under column loss scenario. Appl Sci 16(2):735
9. Landolfo R, D'Aniello M, Safaei S, Fiorino L, Sarno DI, L, Le Maoult A, Rastiello G. (2025) Shake table test on a steel moment resisting frame with nonstructural elements. Eng Struct 333:120191
10. Ryu KP, Reinhorn AM (2019) Experimental study of large area suspended ceilings. J Earthq Eng 23(6):1001–1032
11. Jiang H, Wang Y, He L (2021) Study of seismic performance of chinese-style single-layer suspended ceiling system by shaking table tests. Adv Civ Eng 2021:9861722
12. Ozcelik O, Misir IS, Saridogan S (2016) Performance evaluation of suspended ceiling systems using shake table tests. Struct Eng Mech 58(1):121–142
13. Matale SV, Kumar M, Rai DC (2022) Experimental and numerical study of a plasterboard suspended ceiling system with free perimeter supports. J Struct Eng 149(1):04022217
14. Reinhorn AM, Ryu KP, Maddaloni G (2010) Modelling and seismic evaluation of nonstructural components: testing frame for experimental evaluation of suspended ceiling systems. Technical Report MCEER-10-0004,. University at Buffalo, State University of New York
15. Computers and Structures Inc (2026) SAP2000 integrated software for structural analysis and design, Berkeley, CA
16. AC156 Acceptance criteria for the seismic qualification of nonstructural components. international code council evaluation service, whittier, california. year and edition to be confirmed in the final manuscript
17. Fiorino L, Bucciero B, Landolfo R (2019) Evaluation of seismic dynamic behaviour of drywall partitions, façades and ceilings through shake table testing. Eng Struct 180:103–123

Aluminium H-Sections under Uniform Compression: Initial Imperfection Modelling

Ida Pia Parzanese[1](✉), Alessandro Pisapia[1], Francesco Fabbrocino[1], Vincenzo Piluso[2], Elide Nastri[2], and Francesco Pisciottano[2]

[1] Pegaso University, Naples, Italy
idapia.parzanese@unipegaso.it
[2] University of Salerno, Salerno, Italy

Abstract. The main goal of this work is to provide numerical study on the aluminium H-sections under to compression. Finite Element (FE) models were developed based on specific modelling assumptions; subsequently, nonlinear analyses were carried out, including initial imperfections. The results obtained were validated through comparison with experimental data available in the literature. This study allowed for the definition of the imperfection model to be adopted in subsequent parametric analyses, which were used to investigate the local buckling behaviour of aluminium H-section profiles. The numerical and experimental results were compared with those obtained by the main standards (European, American and Chinese codes). This comparison was carried out to assess the applicability and accuracy of the design provisions prescribed by these standards for predicting the local buckling resistance of aluminium H-shaped sections.

Keywords: Aluminium alloys · H-section stub columns · Local buckling · Finite Element Analysis · Design methods · Imperfection modelling

1 Introduction

Aluminium alloys are widely used in numerous industrial sectors, including transportation, packaging, consumer goods, and electrical engineering. Over the past two decades, these materials have also attracted growing interest among structural engineers, architects, and builders, thanks to their excellent physical and mechanical properties. Currently, it is estimated that about 25% of global aluminium production is destined for the construction sector [1]. Among the various alloy families, those belonging to the 6000 series, commonly referred to as structural alloys, are distinguished by their low density and high strength-to-weight ratio. These properties enable the fabrication of lightweight structural members that are also economically efficient [2]. Consequently, these alloys represent a particularly suitable material choice for applications in high-rise buildings and long-span structures, where low self-weight and high mechanical performance are key design requirements. The widespread use of aluminium alloys in the construction sector has stimulated scientific research aimed at understanding the structural response of elements made from these materials through experimental and numerical approaches

© The Author(s), under exclusive license to Springer Nature Switzerland AG 2026
R. Zanon et al. (Eds.): CTA 2026, LNCE 942, pp. 444–455, 2026.
https://doi.org/10.1007/978-3-032-39505-4_39

[3–5]. To expand the database on structural performance and to achieve a more rigorous understanding of the compressive mechanical behaviour of aluminium alloy H-shaped members, an extensive numerical study was carried out. Based on the results obtained from an experimental campaign conducted at the University of Salerno, a finite element model was developed using the ABAQUS software. Based on this previous model, a parametric study was performed with the aim of assessing the accuracy of the main design recommendations currently available in literature with respect to the evaluation of the ultimate load.

2 State of Art

Despite the growing interest in the structural use of aluminium alloys, experimental studies on the compressive behavior of H-shaped members remain limited. To address this gap, an experimental campaign was carried out at the University of Salerno [6], the results of which served as the basis for the calibration and validation of the finite element model developed in ABAQUS.

Specifically, 17 stub column tests were conducted on 5 H-shaped members, made from three different aluminium alloys and featuring various width-to-thickness ratios, under uniform compression.

The alloys tested were 6060-T66, 6082-T6, and 6005A-T6. The experimental tests were carried out on 5 different sections: H90, H100, H120, H140, and H160. To ensure failure due to local instability, a length equal to or less than three times the web plate width was adopted. The mechanical properties of the specimens were determined through tensile tests according to UNI EN ISO 6892-1-1 [7]. The results are reported in Table 1, where the values for each specimen refer, respectively, to the lower flange plate, the upper flange plate, and the web [6].

Specifically, E is the Young's modulus, $\sigma_{0.1}$ is the 0.1% proof stress, $\sigma_{0.2}$ is the 0.2% proof stress, σ_u is the ultimate tensile strength, and n_p is the Ramberg–Osgood strain-hardening exponent. The compression tests were carried out using a Schenck RBS 4000-E2 testing machine. Two tests under displacement control have been performed for each specimen. A summary of the results is presented in Table 2, where $N_{u.exp}$ denotes the maximum compressive resistance and δ_m the corresponding displacement.

Table 1. Material properties of tested specimens.

Specimen		E [MPa]	$\sigma_{0.1}$ [MPa]	$\sigma_{0.2}$ [MPa]	σ_u [MPa]	n_p [−]
H90	P_b	65698.37	157.16	162.84	19.52	22.81
	P_t	68005.45	167.99	172.66	25.28	21.32
	P_w	65434.86	167.64	171.88	27.75	22.26
H100	P_b	76564.13	302.18	308.26	34.80	39.21
	P_t	71965.64	314.96	318.33	65.13	39.25
	P_w	68055.87	302.00	307.17	40.84	36.37

(*continued*)

Table 1. (*continued*)

Specimen		E [MPa]	$\sigma_{0.1}$ [MPa]	$\sigma_{0.2}$ [MPa]	σ_u [MPa]	n_p [−]
H120	P_b	78896.46	169.59	171.41	64.93	24.37
	P_t	65873.24	168.61	171.19	45.64	25.59
	P_w	68474.20	164.58	168.89	26.81	26.68
H140	P_b	72267.14	253.09	258.28	34.15	40.95
	P_t	74986.19	255.38	259.95	39.08	44.98
	P_w	69290.51	256.74	261.85	35.17	42.41
H160	P_b	69776.81	261.51	267.29	31.71	27.97
	P_t	70839.20	262.37	268.87	28.32	30.48
	P_w	68135.23	258.79	264.29	32.96	28.29

Table 2. Summary of the experimental results.

Specimen	$N_{0.2}$ [kN]	$N_{u.\,exp}$ [kN]	δ_m [mm]
H90–1	157.95	171.90	2.50
H90–2	159.05	174.63	2.53
H90–3	158.22	180.64	2.70
H90–4	159.06	185.85	2.74
H100–1	855.39	1023.27	11.16
H100–2	871.44	1010.21	9.98
H100–3	873.88	1015.07	10.22
H100–4	856.06	1023.26	11.51
H100–5	868.45	1029.50	11.95
H120–1	466.81	530.54	7.78
H120–2	469.27	513.45	5.01
H120–3	473.62	518.36	5.63
H120–4	473.62	534.12	6.40
H140–1	700.13	763.10	5.96
H140–2	700.13	790.98	5.77
H160–1	749.32	819.89	2.71
H160–2	749.32	814.89	2.64

3 Validation of the Finite Element Model

For the finite element modeling of aluminium alloy H-shaped sections, the ABAQUS software was employed. This section describes the main features of the FE models, including the discretization methodology, boundary conditions, and the material assumptions adopted. After model validation through comparison with experimental data, 64 parametric numerical analyses were carried out, systematically varying cross-sectional aspect ratios, local slenderness, and types of aluminium alloy, in order to thoroughly evaluate the mechanical behaviour of the sections.

3.1 General Modeling Assumptions

Based on experimental tests conducted at the University of Salerno, the ABAQUS software was set up and refined through targeted numerical analysis. By systematically comparing numerical and experimental results, the modeling assumptions were defined and validated, leading to an improved agreement between the numerical and experimental curves.

Shell elements were employed for numerical modeling. The use of shell elements to represent thin-walled components is a well-established practice in the modeling of the members. In the context of the present study, this choice proved consistent with the adopted modeling assumptions and allowed for a good agreement between the numerical and experimental curves.

A mesh convergence study was performed to determine the optimal element size, allowing a balance between accuracy and computational efficiency. In particular, the mesh size was parameterized based on the height of the H-shaped specimen, evaluating the influence of the discretization level on the numerical response. The comparative analysis showed that the best agreement between numerical and experimental results is obtained by adopting a discretization with an element size equal to $H/20$, a configuration that ensures solution convergence.

Geometrically and materially nonlinear analyses were performed using the Riks method, which accurately captures post-critical behavior and instability in thin-walled structures. This arc-length control approach overcomes the limitations of traditional load or displacement-controlled methods, ensuring reliable prediction of the system's nonlinear response [1].

Appropriate boundary conditions were applied at the ends of the member. Specifically, the lower end was fully restrained, with all translational and rotational degrees of freedom fixed, while the upper end was allowed to translate only along the longitudinal direction.

3.2 Material Modeling

The most widely used model for describing the stress–strain curve of aluminium alloys is the Ramberg–Osgood model, as it allows for an accurate representation of the material's elastic-plastic behavior, capturing the characteristic gradual and continuous transition

from the elastic to the plastic phase. This curve is described by the analytical Eqs. (1) and (2).

$$\varepsilon = \frac{\sigma}{E} + 0.002\left(\frac{\sigma}{\sigma_{0.2}}\right)^{n} \tag{1}$$

$$n = \frac{\ln 2}{\ln\left(\frac{\sigma_{0.2}}{\sigma_{0.1}}\right)} \tag{2}$$

where ε is the strain, σ the stress, E the Young's modulus, n the Ramberg–Osgood exponent, and $\sigma_{0.1}$ and $\sigma_{0.2}$ denote the stresses corresponding to strains of 0.1% and 0.2%, respectively. In accordance with ABAQUS guidelines, the nominal stress and strain values were converted into true stress and true strain through Eqs. (3) and (4).

$$\sigma_{true} = \sigma_{nom}(1 + \varepsilon_{nom}) \tag{3}$$

$$\varepsilon_{true} = \ln(1 + \varepsilon_{nom}) - \frac{\varepsilon_{nom}}{E} \tag{4}$$

3.3 Numerical Results

The developed FE models were validated against the experimental data presented in the previous section. Figure 1 (a) shows a comparison between the ultimate load values obtained using the FE model and the experimental results reported in Table 2, corresponding to the experimental campaign conducted at the University of Salerno [6]. The comparison highlights a high correlation between the results obtained from the FE model and the experimental data. This indicates that the finite element model is capable of accurately reproducing the ultimate response observed experimentally over the entire analyzed load range. The minor discrepancies observed fall within an acceptable margin, confirming the reliability and robust-ness of the proposed FE model for the prediction of ultimate loads. The value of the initial geometric imperfection was de-fined through a specific parametric analysis, conducted by varying the amplitude of the initial imperfection within the finite element model. This analysis allowed for the evaluation of the imperfection's influence on the numerical structural response and the identification of the most representative value, capable of ensuring a better agreement between numerical and experimental results. The adopted procedure provides a systematic definition of the initial geometric imperfection, consequently improving the overall reliability of the FE model. Figure 1 (b) illustrates the comparison between the experimental curve and the numerical curves obtained by varying the amplitude of the initial geometric imperfection for the H90–3 specimen [6], clearly showing the effect of this parameter on the structural response. The parameter α is a scaling factor applied to the buckling eigenmode shape, used to define the amplitude of the initial geometric imperfection introduced in the numerical model. As the value of the initial geometric imperfection α increases, the numerical curves progressively deviate from the experimental response, showing a reduction in load-carrying capacity. This result confirms the importance of correctly calibrating the initial geometric imperfection to achieve an accurate prediction

of the structural response, highlighting that excessively high values of α may lead to an overestimation of imperfection effects. Figure 2 shows the deformed configuration of the H90–3 H-shaped profile obtained from nonlinear analysis in ABAQUS at the ultimate load (a), together with the buckling deformation associated with the first buckling mode (b).

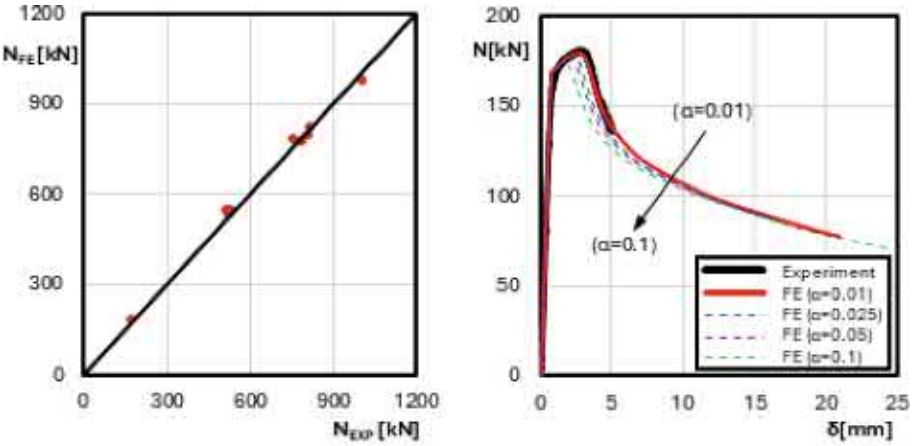


Fig. 1. Comparison between experimentally measured ultimate loads and finite element model predictions. (a). Comparison between numerical and experimental curves for varying values of the initial geometric imperfection for specimen H90-3. (b)

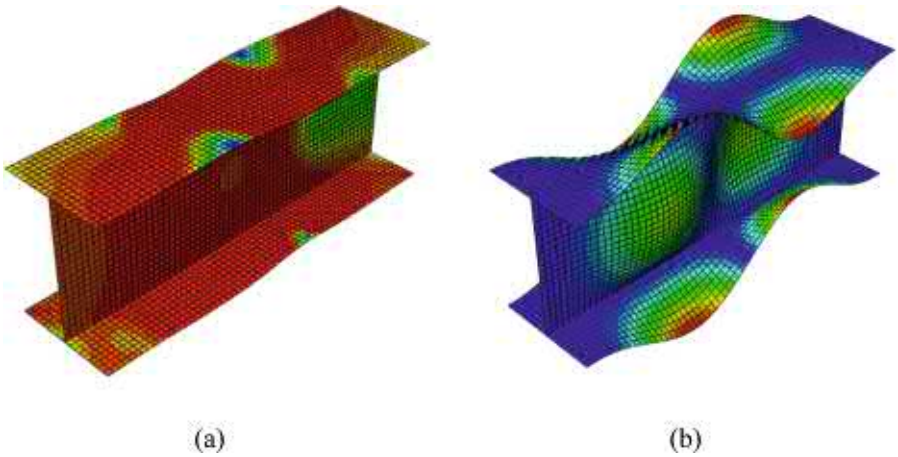


Fig. 2. Deformed configuration of the H90–3 H-shaped profile (a) deformation associated with the first buckling mode (b)

4 Parametric Study

Following the validation of the developed finite element model, a series of parametric analyses was conducted on aluminium alloy H-shaped sections subjected to axial compression. A total of 64 parametric numerical analyses were conducted. Four types of aluminium alloys were considered: 5083-O/H111, 6060-T66, 6082-T6, and 7020-T6, whose properties are reported in Table 3.

Table 3. Material properties of aluminium alloys adopted in the parametric study according to Eurocode 9

alloy	σ_{02}	σ_u	n_p	thickness limits
	[MPa]	[MPa]	[−]	
5083-O/H111	110	270	5	–
6060-T66	160	215	16	$t \leq 5$
	150	195	18	$5 < t < 25$
6082-T6	250	290	32	$t \leq 5$
	260	310	25	$5 < t < 15$
7020-T6	290	350	23	$t \leq 15$
	275	350	19	$15 < t < 40$

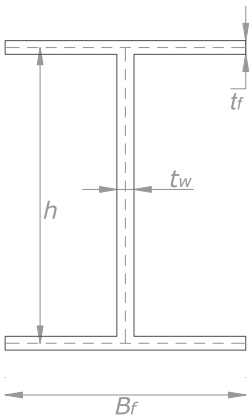


Fig. 3. Geometric scheme of H-section

The base of the cross-section was fixed at $B_f = 100\,mm$ and the height of the specimen is three times the width to prevent the global buckling phenomena. The ratio between the base B_f and the flange thickness t_f was varied, generating profiles with different slenderness. The web thickness t_w was set equal to the flange thickness t_f. Additionally,

the ratio between the base B_f and the section height h was varied, thus obtaining profiles of different heights (Fig. 3). The range of B_f/t_f and B_f/h ratios are reported in Table 4.

Table 4. Examined parameters in parametric studies

B_f/h:	0.5	1.00	1.25	2.00
B_f/t_f:	50	25	20	10

The analysis showed that the ultimate compressive load of aluminium alloy H-shaped members increases as the B_f/h and B_f/t_f ratios decrease. As an illustrative example, Fig. 4 present the stress–displacement curves obtained for 6060-T6 aluminium alloy sections, clearly highlighting these trends. In particular, sections with lower B_f/h ratios have taller webs, resulting in a higher moment of inertia and, consequently, greater compressive load-carrying capacity. Similarly, lower B_f/t_f ratios correspond to thicker flanges, which are less susceptible to local instability and therefore lead to higher ultimate loads. The same trends were consistently observed for all the other section types investigated in this study.

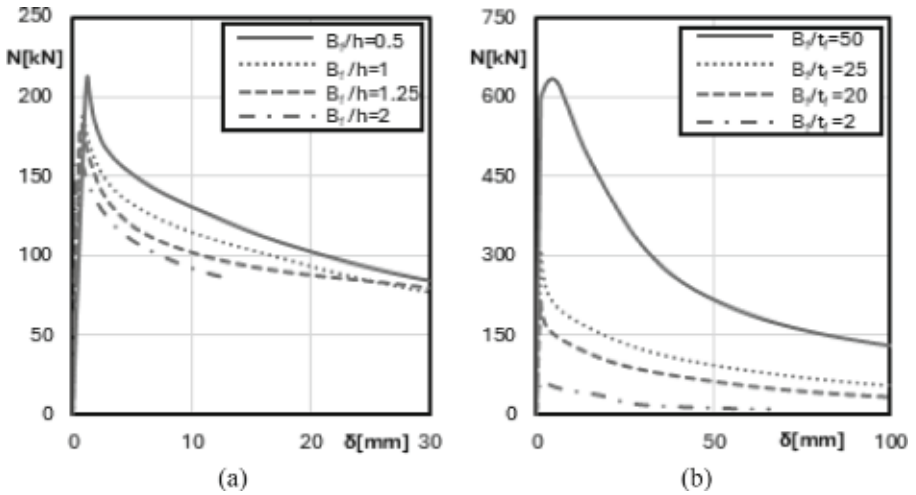


Fig. 4. Stress–displacement curves of 6060-T6 aluminium alloy H-sections for varying: (a) $\boldsymbol{B_f/h}$, with $\boldsymbol{B_f/t_f = 25}$; (b) $\boldsymbol{B_f/t_f}$, with $\boldsymbol{B_f/h = 0.5}$.

4.1 Design Recommendations

In this section, the ultimate strength values obtained from the numerical parametric study, together with experimental results available in the literature [6–9], are compared with the corresponding predictions provided by the main current design codes, with reference to the European standard EN 1999-1-1 (EC9), the Chinese code for aluminium structures

GB 50429, and the American Aluminium Design Manual (ADM). This comparison aims to evaluate the applicability and accuracy of these design rules.

According to Eurocode 9 [10], the ultimate compressive load of a section is determined based on the material yield stress and the section's resistant area. Depending on the section classification, assessed according to the slenderness of the plate elements, the resistant area corresponds either to the gross area for fully effective sections or to the effective area, obtained by reducing the gross area to account for local instability effects in accordance with Eq. (6). The ultimate load is then calculated as the product of the yield stress and the section's resistant area in accordance with Eq. (5).

$$\begin{aligned} N_{EC9} &= A\sigma_{02} \quad \text{for class 1, 2, 3} \\ N_{EC9} &= A_{eff}\sigma_{02} \text{ for class 4} \end{aligned} \tag{5}$$

where:

$$A_{eff} = A\rho_c \tag{6}$$

ρc is the local buckling factor, defined in the standard and calculated according to Eqs. (7), which reduces the effective plate thickness.

$$\begin{aligned} \rho_c &= 1 \qquad\qquad\qquad \text{if } \frac{\beta}{\varepsilon} \leq \left(C_1 + \sqrt{C_1^2 - C_2(3+\psi)}\right) \\ \rho_c &= \frac{C_1}{\beta/\varepsilon} - \frac{(3+\psi)C_2}{4(\beta/\varepsilon)^2} \text{ if } \frac{\beta}{\varepsilon} > \left(C_1 + \sqrt{C_1^2 - C_2(3+\psi)}\right) \end{aligned} \tag{7}$$

According to the Chinese standard GB 50429 [11], the calculation of the compressive ultimate load follows a conceptually similar approach to that of Eurocode 9. The section resistance is determined based on the material yield stress and the resistant area, which may correspond to either the gross area or the effective area. The effective area is calculated as the section's net area multiplied by the local buckling factor ρ_e, defined in Eq. (8).

$$\rho_e = \alpha_1 \frac{1}{\overline{\lambda}} - \alpha_2 \frac{0.22}{\overline{\lambda}^2} \leq 1 \tag{8}$$

where α_1 and α_2 are calculation constants defined in the standard, and $\overline{\lambda}$ is the normalized slenderness of the section, defined in Eq. (9).

$$\overline{\lambda} = \sqrt{\frac{\sigma_{0.2}}{\sigma_{cr}}} \tag{9}$$

where the elastic critical stress σ_{cr} can be determined depending on the elements composing the section.

According to the American Aluminium Design Manual (ADM) [12], the ultimate load is calculated as shown in Eq. (10).

$$N_{ADM} = \sum_{i=1}^{n} \sigma_{ci} A_i + \sigma_{02}\left(A_g - \sum_{i=1}^{n} A_i\right) \tag{10}$$

where A_i is the area of the i-th element composing the cross-section, A_g is the gross cross-sectional area, and σ_{ci}, the local buckling stress, is determined through Eqs. (11) and (12) for internal and external plate elements, respectively.

$$\begin{aligned}
\sigma_{ci} &= \sigma_{02} && \text{if } \frac{b}{t} \leq S_1 \\
\sigma_{ci} &= B_p - 1.6 D_p \frac{b}{t} && \text{if } S_1 < \frac{b}{t} < S_2 \\
\sigma_{ci} &= \frac{k_2 \sqrt{B_p E}}{1.6 b/t} && \text{if } \frac{b}{t} \geq S_2
\end{aligned} \tag{11}$$

$$\begin{aligned}
\sigma_{ci} &= \sigma_{02} && \text{if } \frac{b}{t} \leq S_1 \\
\sigma_{ci} &= B_p - 5 D_p \frac{b}{t} && \text{if } S_1 < \frac{b}{t} < S_2 \\
\sigma_{ci} &= \frac{\pi^2 E}{(5 b/t)^2} && \text{if } \frac{b}{t} \geq S_2
\end{aligned} \tag{12}$$

The American Aluminium Design Manual defines both the slenderness limits (S_1 and S_2) and the buckling constants (B_p and B_p) depending on the type of section element.

Table 5 summarizes the obtained results, where the main statistical indicators—the mean value (μ), standard deviation (σ), and coefficient of variation (COV)—are reported for the ratios between the ultimate load predicted by each method and the theoretical load.

Table 5 Summary of the results obtained

	$\frac{N_{EC9}}{N_{u.th}}$	$\frac{N_{GB}}{N_{u.th}}$	$\frac{N_{ADM}}{N_{u.th}}$
$\boldsymbol{\mu}$	0.82	0.82	0.77
$\boldsymbol{\sigma}$	0.10	0.10	0.18
COV	0.12	0.13	0.24

Figure 5 provides a graphical representation of the results. Specifically, the main vertical axis (left) shows the mean value, while the secondary vertical axis (right) reports the standard deviation and the coefficient of variation.

From the graph, it can be observed that the methods based on Eurocode 9 and the Chinese standard (GB 50429) yield, in terms of mean value, ratios between the results obtained with the respective methodologies and the FE model prediction that are less conservative than those of the ADM, as the mean values are closer to unity. Moreover, the ADM method produces results with higher standard deviation and coefficient of variation, indicating lower reliability of its predictions.

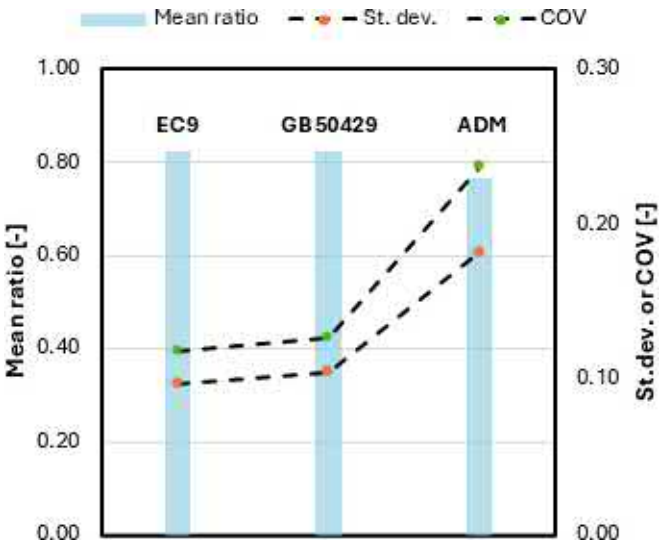


Fig. 5. A graphical summary of the comparison between analytical and experimental values

5 Conclusions

A numerical study was carried out on the compressive behavior of aluminium alloy H-shaped stub columns governed by local buckling. The Finite Element models developed in ABAQUS were successfully validated against experimental results, demonstrating their ability to accurately reproduce both the structural response and the load-bearing capacity of the members. The study also highlighted the importance of a proper definition of the initial geometric imperfections to obtain reliable numerical predictions. Based on the validated models, a parametric study was performed to evaluate the influence of the section aspect ratio, local slenderness, and alloy type on the compressive resistance of H-shaped sections. The results confirmed that local buckling is the dominant failure mode for the investigated members and significantly affects their load-carrying capacity. The numerical database was further used to assess the applicability of the main international design standards for aluminium structures. Comparisons between numerical results and codified predictions showed that all the considered design procedures (Eurocode 9, ADM, and GB 50429) are applicable to aluminium alloy H-shaped sections governed by local buckling. Among them, Eurocode 9 and GB 50429 provided more accurate and less conservative predictions, while the ADM exhibited a greater scatter in the estimated resistances. Overall, the study confirms the reliability of the developed numerical model and supports the use of the current design provisions for the design of aluminium alloy H-shaped sections subjected to local buckling.

References

1. Georgantzia E, Gkantou M, Kamaris GS (2021) Numerical modelling and design of aluminium alloy angles under uniform compression. Civil Eng 2:632–651

2. Montuori R, Nastri E, Piluso V, Pisapia A (2022) The influence of the material properties on the ultimate behaviour of aluminium H-shaped beams. Open Constr Build Technol J 16:176–188
3. Piluso V, Pisapia A (2024) Interactive local instability of aluminium angles. Thin-Walled Struct 202:112159
4. Yuan X et al (2024) A review of research on aluminium alloy materials in structural engineering. Dev Built Environ 17:100319
5. Čudina I, Skejić D (2025) Extruded aluminium alloy members subjected to axial compression—a comprehensive review. Eng Struct 326:119536
6. Pisapia A, Fabbrocino F, Piluso V (2026) Testing and analysis of aluminium H-sections subjected to local buckling. J Constr Steel Res 236:110025
7. UNI (2020) UNI EN ISO 6892-1: metallic materials—tensile testing—part 1: method of test at room temperature. Ente Italiano di Normazione, Milan
8. Yuan HX, Wang YQ, Chang T, Du XX, Bu YD, Shi YJ (2015) Local buckling and postbuckling strength of extruded aluminium alloy stub columns with slender I-sections. Thin-Walled Struct 90:140–149
9. Zhi X, Wang Y, Zhang Y, Li B, Ouyang Y (2022) Study of local buckling performance of 7075-T6 high-strength aluminium alloy H-section stub columns. Thin-Walled Struct 170:109925
10. CEN (2004) prEN 1999-1-1: Eurocode 9—Design of aluminium structures—Part 1–1: General structural rules. European Committee for Standardization, Brussels
11. Ministry of Construction of the People's Republic of China (2007) GB 50429–2007: code for design of aluminium structures. China Architecture & Building Press, Beijing
12. The Aluminium Association (2020) Aluminium Design Manual. The Aluminium Association, Arlington, VA

Modular System in Lightweight Alloy for the Restoration of the Leaning Tower of Pisa: Design Innovations for Monument Preservation

Giuseppe Carluccio[1] and Guido Maccone[2(✉)]

[1] BCD Progetti srl, Rome, Italy
[2] Structural engineer, consultant for BCD Progetti srl, Rome, Italy
solutions@guidomaccone.it

Abstract. The restoration of the external marble surfaces of the Leaning Tower of Pisa called for a support structure that conventional scaffolding could not provide. The monument's fragility and inclination, a strict limit on the additional overturning moment imposed by the International Committee for the Safeguard of the Tower of Pisa — a maximum in-service weight of about 100 kN — and the requirement that the Tower remain visible and open to visitors throughout some two years of work together ruled out any heavy, ground-based or anchored solution. This paper describes the modular structure developed in response, built in an aluminium–zinc–magnesium alloy. Three ideas define it. First, the light alloy brought the total in-service load to about 90 kN — roughly 60 kN of permanent load and 30 kN of live load — within the Committee's ceiling. Second, a polar configuration of thirty radial truss modules, closed by circumferential cables into a self-equilibrating "spoked wheel", gives the structure its rigidity and lets it hold onto the Tower through compression supports (hardwood wedges) and tension straps alone, without any drilled, bolted or bonded fixings. Third, a single adjustable joint accommodates the inclined, position-dependent geometry, so that the structure is assembled from interchangeable, repetitive elements and can be relocated "aerially", level by level, in about ten days, without closing the monument. The result is a reversible, minimally invasive structure that is an instrument of conservation as much as of construction.

Keywords: Scaffolding system · Lightweight alloy · Monument restoration · Leaning Tower of Pisa · Modular design · Minimum intervention · Polar structural system · Heritage preservation

1 Introduction

The bell tower of Pisa Cathedral — universally known as the Leaning Tower — is among the most recognisable monuments in the world, and its inclination, long regarded primarily as a structural threat, has become part of its identity. Any intervention must therefore reconcile technical requirements with the preservation of the historical, structural and perceptual values acquired over eight centuries.

© The Author(s), under exclusive license to Springer Nature Switzerland AG 2026
R. Zanon et al. (Eds.): CTA 2026, LNCE 942, pp. 456–467, 2026.
https://doi.org/10.1007/978-3-032-39505-4_40

This paper concerns the temporary support structure conceived for the restoration of the Tower's external stone surfaces — a campaign promoted by the "Opera della Primaziale Pisana" and carried out with the "Istituto Superiore per la Conservazione e il Restauro (ISCR)" under the direction of architect Gisella Capponi. Unlike the localised scaffolds of previous centuries, it called for a systemic, scientifically documented restoration of the entire surface, with several operators working on every band of the Tower.

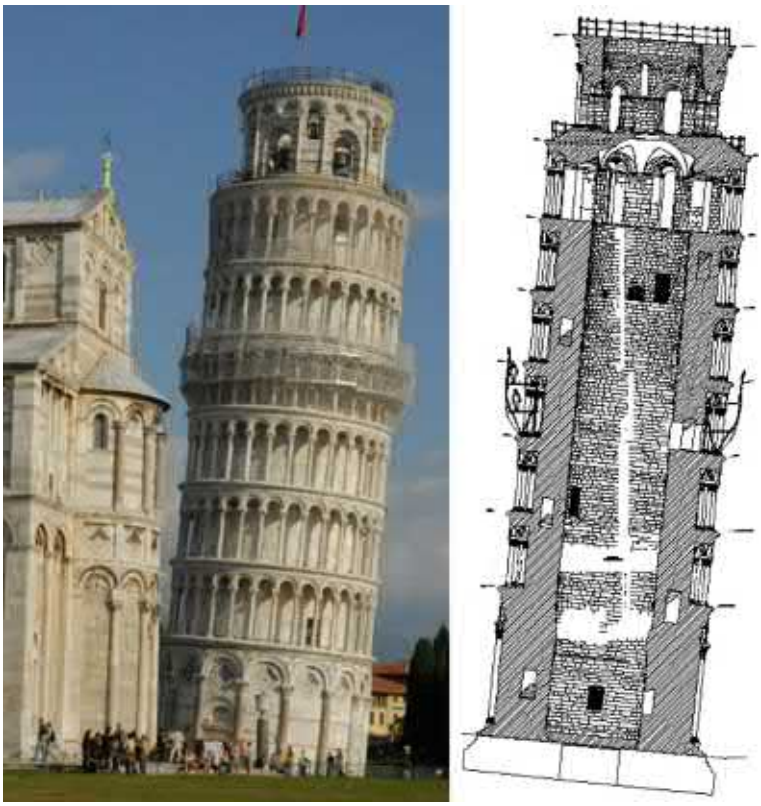


Fig. 1. The Leaning Tower of Pisa: (a) general view with the modular support structure installed on the fifth order during the restoration campaign; (b) general cross-section with the modular support structure

A conventional, ground-based solution was unacceptable on two counts: the monument's fragility and the strict limit on any additional overturning effect ruled out a heavy structure, while a ground-based scaffold would have concealed the Tower for the roughly two-year duration of the works. The design therefore had to deliver a structure that was light, reversible and minimally invasive, keeping the monument visible and accessible to visitors throughout.

The structural design was conceived by the Rome-based studio BCD Progetti; the structure was manufactured and first installed by Icras of Rovereto, while the subsequent

"aerial" relocations from one loggia to the next were carried out by Aeredile of Rome, a firm specialised in suspended works.

The following sections describe how these requirements shaped a modular structure in aluminium–zinc–magnesium alloy that engages the Tower without any mechanical or chemical anchoring (Fig. 1) — the principle of minimum intervention extended even to the very logistics of the construction site.

2 Conservation Context

For the Tower of Pisa, conservation has historically meant, first and foremost, confronting the progressive inclination caused by the unevenly compressible soil beneath the bell tower. Between 1909 and 1990 sixteen expert commissions sought possible remedies, many invasive and disproportionate; as settlement worsened, the Tower was closed to the public in 1990 [1]. The seventeenth commission adopted a deliberately restrained solution: between February 2000 and June 2001, soil was extracted in small, controlled volumes from beneath the higher, northern side of the foundation through 41 boreholes — under-excavation — reducing the inclination by about half a degree and stabilising the Tower, which reopened in 2001 [1, 2]. A minimally invasive operation achieved what decades of more aggressive proposals had not, setting the interpretive key for all subsequent work on the monument.

At Pisa, moreover, the inclination is no longer only a risk to be managed: it has become a constitutive part of the monument's image, at once a hazard and a quality — a duality that any intervention must respect.

The inclination has equally constrained access for restoration. Between 1398 and 1950, work on the architectural surfaces consisted of the localised replacement of isolated elements — columns or capitals — served by equally localised scaffolds allowing only a few operators at a time. Such arrangements were incompatible with a systematic, scientifically documented treatment of the entire surface: they would have prevented parallel working and multiplied costs and time through constant dismantling and re-erection. The campaign demanded a fundamentally different kind of structure — the subject of this paper.

3 Design Objectives and Constraints

The brief for the structure was defined at the outset of the design (begun in 2003) around four priority objectives, which together shaped every subsequent technical decision.

The first was to keep the Tower visible: the structure had to minimise its visual impact, preserving the monument's architectural and figurative qualities from the outside — a requirement of direct economic significance for the city. The second was to preserve tourist access, with visitors able to climb the Tower for all but very short, unavoidable interruptions (Fig. 2). The third concerned the work itself: the restoration proceeded in horizontal bands corresponding to the successive orders (loggias) of the Tower, each requiring generous, stable working space — which excluded local cantilevers and suspended baskets.

The fourth, and structurally the most demanding, was the limit on the additional overturning effect. Because the monument presents an eccentricity of about 5 m at the summit, any added weight acts on a long lever arm; the International Committee for the Safeguard and Architectural Restoration of the Leaning Tower of Pisa therefore set a ceiling of about 500 kN·m on the additional overturning moment, corresponding to a maximum in-service weight of roughly 100 kN. Meeting this limit — rather than any conventional strength or stiffness requirement — became the governing constraint of the design and the reason for the radical pursuit of lightness described in the following sections.



Fig. 2. The Tower remained visible and open to visitors throughout the works; the support structure engaged only the order under restoration

4 From the First to the Definitive Solution

The design of the structure began in 2003 and evolved through two successive proposals. Both shared three founding ideas that already distinguished the approach from any conventional scaffold: the use of a light aluminium alloy in place of steel; a structure that wrapped around the full circumference of the Tower without ever resting on the ground; and a phased vertical movement, engaging one band of the monument at a time in step with the progress of the restoration.

The first proposal occupied two orders at once, with three working planes per order (Fig. 3a), cantilevered from the order immediately above the one under restoration; its total dead weight was about 80 kN and it was relocated by running the whole assembly on dedicated rails along the Tower. Measured against the objectives it showed two

weaknesses: the greater weight and leverage consumed much of the overturning budget, sharply reducing the usable capacity, while the rails, anchored to the masonry, conflicted with the requirement of minimal contact with the monument.

The second proposal — the one actually built — kept the three founding ideas within a more radical configuration confined to the single order under restoration (Fig. 3b). This markedly reduced the structure's own weight and removed the bottleneck on capacity, the only remaining ceiling being the Committee's overturning budget: in service the structure carries about 60 kN of permanent and 30 kN of live load — some 90 kN in all, comfortably below the 100 kN limit. The working planes, adjustable in height, remain horizontal under the variable inclination without made-to-measure components; the structure was assembled from interchangeable, limited-weight modular elements, relocated by dismantling and re-erecting them on the next order through the "aerial" handling described in Sect. 8.

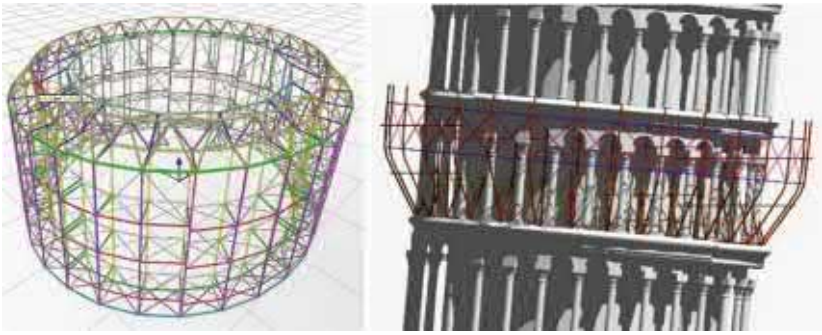


Fig. 3. Calculation model of the structure: (a) first proposal, developed over two orders; (b) definitive single-order solution actually built

5 Material Selection

The overturning limit made lightness the prerequisite of the entire design and immediately raised the question of material selection. Steel, the obvious candidate, was too heavy: a structure of equivalent function in steel would have exhausted the overturning budget through its dead weight alone. The choice therefore fell on an aluminium–zinc–magnesium alloy (UNI 7020/7003, commercially known as Carpental), already proven in demanding lightweight applications such as motorcycle frames.

Table 1 compares the alloy with the two alternatives examined. Titanium, although both lighter and stronger than steel, offered no decisive advantage over the aluminium alloy in this application and carried far higher costs and fabrication difficulty.

The advantage is smaller than the density ratio alone would suggest. At 2700 kg/m^3 against 7850 kg/m^3 for steel, a naïve substitution might promise a threefold weight reduction; in practice the alloy's much lower elastic modulus (about 71 GPa against 210 GPa) and lower allowable stress require appreciably thicker cross-sections to satisfy

Table 1. Comparison of the structural materials considered

Material	Yield strength [MPa]	Density [kg/m^3]	Elastic modulus, E [GPa]	Elongation, A_5 [%]
Al–Zn–Mg alloy (UNI 7020)	~160–180	2700	70	6–12
Steel	~235–355	7850	210	10–15
Titanium alloy	~800–900	4500	105	20–30

the stability and deformation criteria governing aluminium design [3], so the structure weighs distinctly more than one third of its steel equivalent. The saving was nonetheless decisive: the structure's own weight is about 50 kN and the total in-service weight about 90 kN — within the 100 kN ceiling, where an equivalent steel structure could not have arrived. The lower yield strength was not binding, the design being governed by overturning rather than member strength; the low elastic modulus, by contrast, demanded particular attention to deformation and stability, addressed through the configuration described next.

6 Structural Concept: The Polar System

The structure could neither rise from the ground nor add appreciable weight, and so it had to be supported by the Tower itself; yet the fragility of the marble and the principle of minimum intervention forbade drilling, bolting or bonding anything into it. The central problem of the design was therefore how to make a structure secure itself to the Tower without being fixed to it. The solution was a polar system: thirty radial truss modules arranged around the Tower like the spokes of a wheel (Fig. 5) — one for each column of the order under restoration — cantilevering from the shaft and carrying the two working planes (Fig. 4).

Rigidity comes from the closure of the system upon itself, achieved through circumferential elements that all work in tension only. On the external perimeter, the thirty radial modules are connected by an annular trussed ring — two orders of horizontal bars running above and below a layer of diagonals — with redundant steel cables closing another circle at the head of the external uprights; on the internal perimeter, the ring of nylon belts that fixes the internal uprights is tightened around the shaft. During erection, the external ring also doubles as a template guaranteeing the correct geometry of the finished assembly. The behaviour is similar to that of a tensioned spoked wheel: the Tower is the hub, the radial modules are the spokes, and the circumferential elements form the rim that closes the system. Horizontal loads therefore balance around the Tower rather than being discharged into it, and it is this self-equilibrium that allows the structure to stand without anchorage.

Contact with the monument is reduced to the strict minimum and is of two kinds only, compression and tension. Each radial module bears on the stone at two points through compression supports — hardwood wedges with a neoprene interlayer that distributes the load and protects the marble — while the assembly is held against outward rotation

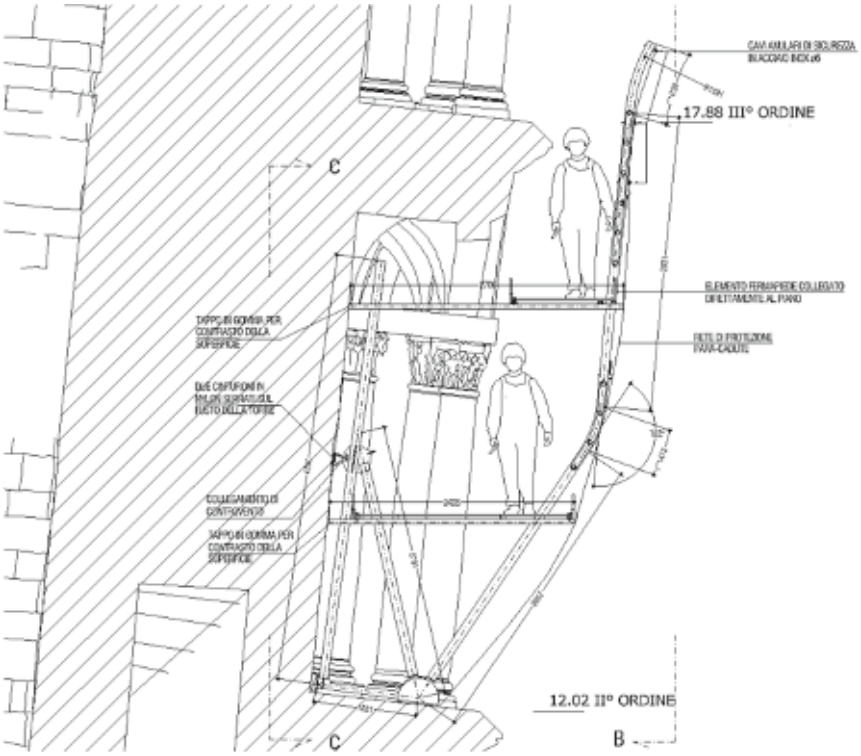


Fig. 4. Cross-section on the maximum tilt plane

by nylon straps wrapped around the shaft, chosen in this material for their gentleness to the marble and their full reversibility. The external protective net is likewise of nylon. No element is drilled, glued or chemically fixed to the masonry. All these circumferential members are slender elements working in tension only, and were modelled accordingly as non-resisting in compression in a non-linear structural analysis.

In conceptual terms, the polar system turns an apparent obstacle — the impossibility of anchoring to a monument that must not be touched — into the organising principle of the design: by balancing its own thrusts, the structure reduces its interaction with the Tower to gentle, fully reversible contact.

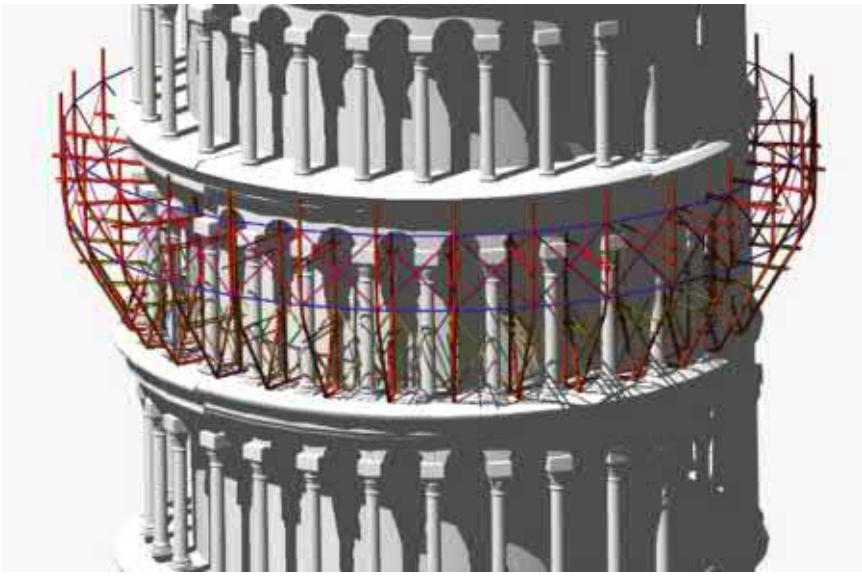


Fig. 5. The polar ("spoked-wheel") system in plan: thirty radial modules, one per column, closed by circumferential elements into a self-equilibrated ring

7 The Adjustable Joint

The greatest geometric difficulty arose from the inclination itself. The axis is not vertical and its tilt varies from one order to the next; around any given order, the thirty radial positions each meet the inclined shaft at a slightly different angle, while the working planes had to remain horizontal and at a constant distance from the Tower. In principle, almost every radial module would have required a geometry of its own.

Thirty made-to-measure modules would have defeated the whole approach — multiplying cost and fabrication time, abandoning the interchangeability on which rapid relocation depended, compromising the reuse of the elements. The design therefore concentrated the entire geometric variability into a single component: an adjustable joint, settable to the thirty distinct configurations required, so that one repeated module type could adapt to every radial position and be reset at each relocation.

The adjustment relies on slotted connections, which allow the relative angle between the converging elements to be varied within the required range and then locked (Fig. 6). The inclined, position-dependent geometry is thus absorbed entirely at the joints, the elements remaining identical and repetitive; the working planes, in turn, are kept horizontal and at constant spacing by stepped sectors that take up the transverse slope.

The consequences reach beyond geometry: fabrication was simplified and its cost contained, assembly and dismantling were made faster and more reliable, and the elements can be stored and reused for any future intervention on the Tower — an economy of means that is itself a form of sustainability.

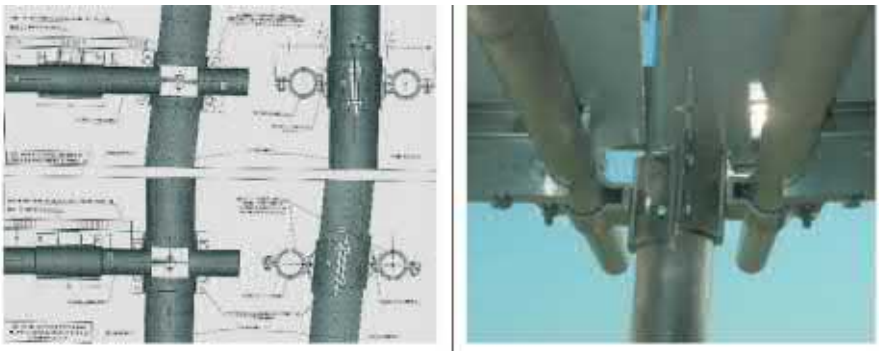


Fig. 6. The adjustable joint with slotted connections, set to the configuration required at each of the thirty radial positions

8 Assembly and Aerial Relocation

Conceived as a single band engaging one order at a time, the structure was relocated repeatedly as the restoration climbed the Tower. Assembly proceeded entirely from the interchangeable modular elements: the thirty radial modules were erected around the order under restoration and tied together by the circumferential tension elements; as already noted, the external trussed ring served during erection as a template fixing the correct geometry, the adjustable joint being set at each position to its required configuration.

The structure worked in turn on each of the six loggia orders above the basement. The first installation, on the lowest order, was carried out from the ground by Icras using a mobile crane; thereafter the structure was dismantled into its elements and re-erected, in the same arrangement, on the order above — the elements lifted in elevation around the Tower by Aeredile, specialists in suspended works (Fig. 7). Five such relocations were performed, each taking on the order of ten days.

This method was decisive for two of the founding objectives. A ground-based scaffold would have concealed the Tower and largely closed it for the whole of the works, which concluded in early 2011 after about two years; the aerial relocation left the monument visible except for the single order under restoration and kept it open throughout — during relocations, only the two loggias involved and the perimeter areas below were placed off-limits against falling objects. Only a structure this light and modular could be moved through the air in days, with all lifting and assembly carried out entirely by hand, without electric winches or hoists (Fig. 8).



Fig. 7. "Aerial" relocation of the dismantled elements from one loggia order to the next, performed by Aeredile



Fig. 8. Working planes in use during the restoration of the external stone surfaces

9 Sustainability and the Conservation Framework

The technical choices described so far align closely with the principles of heritage conservation. The first is minimum intervention: the philosophy that guided the stabilisation of the Tower — non-invasive, strictly proportionate measures — carried over to the site

itself [4, 5]; a structure holding onto the monument without a single drilled, bolted or bonded connection extends it to site logistics.

Closely bound to it are reversibility and material compatibility: the structure leaves the marble untouched and can be wholly dismantled without trace, the only materials in contact with the historic fabric — wood, neoprene, nylon — being inert and not aggressive for the stone surfaces. A third theme is the economy of means: built from interchangeable elements, the structure can be stored and reused for future campaigns, its lightness reducing material consumption and handling effort.

Finally, the project respects the monument as it is perceived. The inclination — which Viollet-le-Duc's isolated nineteenth-century view judged a defect "infinitely better" removed — is today integral to the Tower's identity and memory, the "value of antiquity" that conservation theory, from the Venice Charter to ICOMOS [4, 6], asks us to safeguard [1]. By keeping the Tower visible and accessible, the structure protected not only the fabric but the public's perceptual relationship with the monument, itself part of what is conserved.

These themes align with the framework articulated by UNESCO for World Heritage and sustainable development [7], with the ICOMOS principles of minimum intervention and reversibility [4] and with the European quality principles for cultural heritage [8]; the Italian tradition — from Brandi to the Carta del Restauro — points the same way [9, 10].

10 Conclusions

The restoration of the external surfaces of the Leaning Tower of Pisa required a support structure for which conventional scaffolding offered no adequate answer: a fragile, inclined monument that could not be drilled or anchored, a strict ceiling on the additional overturning moment, and a Tower to be kept visible and open to the public throughout some two years of work. The structure described here met all of these constraints at once.

Beyond its immediate purpose, the project illustrates a wider point: lightness, reversibility, material compatibility and the economy of reusable elements are the operative form, at the scale of the site, of the principles of minimum intervention that governed the safeguarding of the Tower itself. The temporary structure thus became an instrument of conservation as much as of construction — and a transferable model for monuments where weight, fixings and visual impact are as constrained as at Pisa.

Acknowledgements. The restoration campaign was promoted by the Opera della Primaziale Pisana, which owns and manages the monumental complex, and carried out together with the Istituto Superiore per la Conservazione e il Restauro under the direction of architect Gisella Capponi. The support structure was manufactured and first installed by Icras (Rovereto); the subsequent aerial relocations between the loggia orders were performed by Aeredile (Rome). The authors gratefully acknowledge their contribution to the realisation of the project.

References

1. International committee for the safeguard of the tower of Pisa (2002) Safeguard and stabilisation of the leaning tower of Pisa 1990–2001. In: Proceedings 13th ICOMOS general assembly and scientific symposium. ICOMOS, Madrid, pp 199–207
2. Burland JB, Jamiolkowski M, Viggiani C (1998) Stabilising the leaning tower of Pisa. Bull. Eng. Geol. Environ. 57:91–99. https://doi.org/10.1007/s100640050025
3. CEN (2007) EN 1999-1-1 Eurocode 9: design of aluminium structures — part 1–1: general structural rules. European Committee for Standardization, Brussels
4. ICOMOS (2003) Principles for the analysis, conservation and structural restoration of architectural heritage. In: Ratified by the 14th ICOMOS general assembly, Victoria Falls, Zimbabwe
5. Presidenza del Consiglio dei Ministri (2011) Linee Guida per la valutazione e riduzione del rischio sismico del patrimonio culturale allineate alle nuove Norme tecniche per le costruzioni. Direttiva P.C.M. 9 febbraio 2011 Roma
6. ICOMOS (1964) International charter for the conservation and restoration of monuments and sites (The Venice Charter). ICOMOS, Venice
7. UNESCO (2015) Policy document for the integration of a sustainable development perspective into the processes of the world heritage convention. UNESCO, Paris
8. ICOMOS (2019) European quality principles for EU-funded interventions with potential impact upon cultural heritage. ICOMOS, Paris
9. Brandi C (1963) Teoria del restauro. Edizioni di Storia e Letteratura, Roma
10. Ministero della Pubblica Istruzione (1972) Carta del Restauro 1972. Circolare n. 117, 6 aprile 1972, Roma

Fire Protection and Thermal Effects

Optimisation of Fire Passive Protection for Steel Buildings Based on Vulnerability and Cost-Benefit Analysis

Antonio Cibelli[1(✉)], Paola De Santis[1], Donatella de Silva[1], Andrea Miano[2], and Emidio Nigro[1]

[1] University of Naples "Federico II", Naples, Italy
antonio.cibelli@unina.it
[2] University Pegaso, Naples, Italy

Abstract. The thermal vulnerability of structural steel represents one of the main risk factors in the design of industrial buildings, with direct implications on load-bearing capacity and structural integrity under fire conditions. The adoption of passive protection systems constitutes the most widespread strategy to mitigate this risk. However, current design practices predominantly rely on prescriptive requirements, neglecting a quantitative assessment of the actual structural performance in fire, with the associated economic implications. This contribution addresses this gap by proposing a probabilistic assessment of the fire vulnerability of a typological steel industrial building used for vehicle storage, through the derivation of fragility curves obtained from non-linear thermo-mechanical analyses conducted on a wide set of realistic fire scenarios. The investigated configurations, including unprotected and protected configurations using spray-applied fire-resistive material (SFRM), are compared both in terms of structural response and economic sustainability, through a cost-benefit analysis based on the Present Value of Life Cycle Costs (PVLCC). The results highlight how, as fire intensity increases, passive protection becomes the most economically advantageous solution, with the thickness of the passive protective playing a decisive role.

Keywords: steel structures · passive protection · thermo-mechanical analysis · fragility curves · cost-benefit analysis

1 Introduction

Structural steel is widely used in industrial construction due to its high strength-to-weight ratio and construction versatility. However, its high thermal conductivity makes it particularly vulnerable to fire: exposure to high temperatures causes a rapid degradation of mechanical properties, resulting in a reduction in strength and stiffness that can compromise the global stability of the structure. To address this vulnerability, construction practice commonly resorts to passive protection systems, such as fire-resistant coatings, insulating panels, or spray-applied plasters, optionally integrated with active protection measures. Despite the widespread use of these systems, their design is still predominantly

© The Author(s), under exclusive license to Springer Nature Switzerland AG 2026
R. Zanon et al. (Eds.): CTA 2026, LNCE 942, pp. 471–481, 2026.
https://doi.org/10.1007/978-3-032-39505-4_41

based on prescriptive approaches, which impose minimum fire resistance requirements without explicitly considering either the probability of occurrence of fire scenarios or the economic implications of design choices. The assessment of structural vulnerability through fragility curves represents an effective tool to express the response of a structure, in probabilistic terms, to a as wider as possible range of feasible fire intensities, allowing a quantitative comparison between different vulnerability mitigation strategies. The investigated intensity interval should be conceived to cover the range of intended uses, which directly affect the fire risk. Integrated into a life cycle cost analysis, this approach allows for the evaluation of the economic viability of fire protection measures, comparing initial investment costs with the benefits deriving from the reduction of structural damage.

Although the growing interest in these tools, an approach that explicitly integrates them for protected steel structures is still lacking in the literature. This work aims to fills this gap by proposing a probabilistic fire vulnerability assessment of a typological steel industrial building, in unprotected and protected configurations with spray-applied fire-resistive material (SFRM) of different thicknesses and integrating the results into a cost-benefit analysis based on the Present Value of Life Cycle Costs (PVLCC). To this end, numerous realistic fire scenarios derived from the building's occupancy characteristics are analysed, and the results show how the optimal choice of passive protection strongly depends on the expected fire intensity, with the thickness of the protective playing a decisive role in the economic convenience of the adopted solution. The objective is to provide a rational tool of immediate engineering applicability to support the performance-based design of passive fire protection for steel structures.

2 Structural System and Fire Protection Configurations

The proof-of-concept application is a steel structure (24 m x 17 m), with a pitched roof (inclination 15%), representative of the construction typology commonly adopted for industrial buildings. The transverse frames consist of trusses connected to two 6.00 m high HEB320 columns, fixed at the base. The steel grade used for all structural elements is S275, and the structure is designed in compliance with Eurocodes EN 1993 [1] and EN 1998 [2]. The intended use considered in this application is vehicle storage facility, hence fire scenarios are selected accordingly. The fire vulnerability assessment is conducted on three structural configurations: the unprotected structure and two configurations protected with spray-applied fire-resistive material (SFRM) with thicknesses of 10 mm and 20 mm. The thermophysical properties of the protective material were determined experimentally through cone calorimeter tests, allowing the characterization of the effective thermal conductivity as a function of temperature and capturing the chemical-physical transformations of the material during fire exposure [3]. This conductivity law is implemented up to approximately 300 °C, beyond which it is kept constant, to model the effects of cracking phenomena that occur at high temperatures and lead to a progressive decay of the protective layer's insulating properties [4]. The calibrated properties are introduced into the NL-FE model, ensuring an accurate simulation of the thermal transient in the protected steel profiles (Fig. 1).

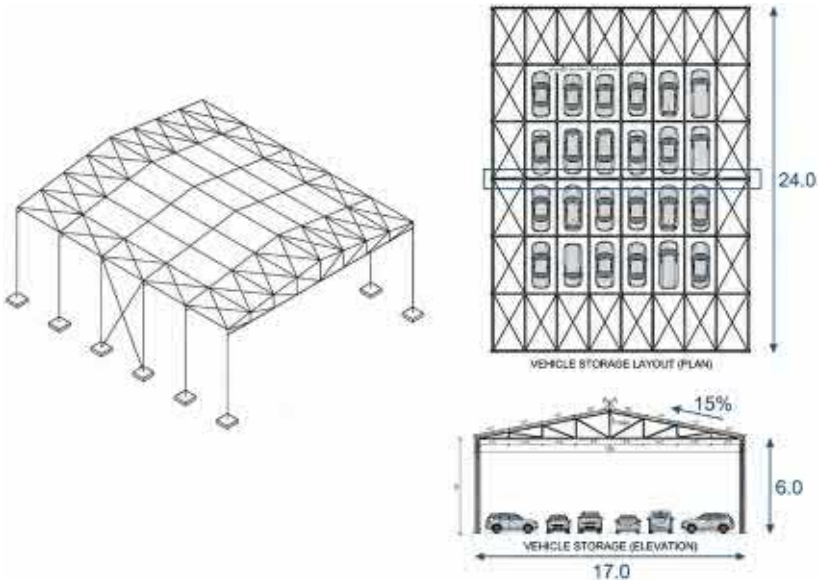


Fig. 1. Proof-of-concept application: steel building used as vehicle storage facility

The definition of structural capacity represents a fundamental step in a performance-based assessment: it can be articulated into progressive damage states that allow the quantification of the structural response as a function of fire severity. To this end, three Performance Levels (PL) [5, 6] are investigated, consistent with the fire safety engineering approach. PL-III represents the limit condition for maintaining load-bearing capacity for the entire duration of the fire, i.e., the threshold beyond which structural collapse occurs. PL-IV identifies a condition of limited damage, in which the structure, despite undergoing significant deformations, preserves a residual structural capacity. Finally, PL-V describes the most restrictive condition, that of full functionality after the fire, where deformations remain within limits that do not compromise the operation of the building (Table 1).

To translate these levels into measurable quantities, specific Key Performance Indicators (KPIs) based on structural deformations are adopted, chosen because they can be directly obtained from numerical analyses and are immediately comparable with regulatory thresholds. For PL-III, the verification remains binary – collapse or no collapse – since beyond this threshold it is not significant to quantify the entity of the deformations. For PL-IV, the limits are set at L/150 for the maximum deflection of the beam and H/150 for the horizontal displacement at the top of the column, while for PL-V the thresholds become more restrictive, equal to L/250 and H/300 respectively, ensuring the full operational capability of the structure.

Table 1. Performance Levels

PL	DESCRIPTION	KPIs
I	no external consequences for structural collapse.	–
II	maintaining the fire resistance requirements for a period sufficient for the safe evacuation of occupants.	–
III	maintaining bearing capacity for entire duration of the fire	collapse/no collapse
IV	structure exhibits limited damage after fire exposure	beam < L/150; column < H/150
V	structure maintains its full functionality after fire exposure	beam < L250; column < H/300

3 Structural Response Assessment

3.1 Fire Scenarios

The structure at issue is used for vehicle storage, which represents the main cause of fire ignition and spread. In this work, 72 fire scenarios are investigated. The latter are defined considering different combinations of involved vehicles, with configurations varying from single to multiple involved vehicles, with the latter arranged along the transverse or longitudinal direction of the building.

Each scenario is analysed considering two fire positions within the layout: at the midpoint of the truss, to maximize the deflection of the truss elements, and near the column, to maximize the displacement at the top of the column. The fire position influences not only the localization of the maximum effects on the structure, but also the characteristics of the fire itself: as the position changes, the initiating vehicle changes, and consequently, the HRR curves and the overall fire load are modified, making each of the 72 scenarios unique in terms of both intensity and position.

For scenarios involving multiple vehicles, the HRR curve is determined as the envelope of the contributions of individual vehicles, taking into account a time delay related to fire spread. Furthermore, the contribution of each vehicle is defined by a reduction factor that takes into account its distance from the ignition point: the closest vehicle to either truss mid-point or column contributes with no reduction, while the input from other vehicles is reduced proportionally to the distance, to realistically represent the actual thermal impact on the structure.

3.2 Structural Modelling

Numerical simulations are conducted using SAFIR® [7], a finite element-based software, developed specifically for the thermo-mechanical analysis of structures exposed to fire. The process is divided into two sequential phases: an initial thermal phase, conducted at

the cross-section level, and a subsequent mechanical phase that uses the obtained thermal histories as input, allowing for an accurate reproduction of the thermo-mechanical transient induced by the fire.

The thermal analyses are conducted by modelling the cross-section of each structural element, defining its geometry, boundary conditions, material properties, and fire exposure. For protected configurations, the protective material is introduced as an additional layer around the steel section, implementing the experimentally calibrated thermal conductivity-temperature relationship. The choice of localized fire models reflects their ability to accurately represent heat distribution in different zones of the structure: the HASEMI [8] model is adopted for the truss elements, while the LOCAFI [9, 10] model is used for the columns. In this work, only the frame experiencing the highest internal forces (i.e., axial force, shear and bending) is analyzed, as it should represent a significant substructure, whose response to fire should approximate the fire resistance of the whole structure with sufficient accuracy. As a matter of fact, the structure of interest does not feature a significant redundancy. This choice reduces the computational burden while preserving the significance of the results, thanks to an accurate calibration of constraints and actions that reproduces the behavior of the complete structure during the thermal transient.

A distributed plasticity model is adopted in order to capture the non-linear response of the material induced by thermal gradients. Fixed supports are applied at the base of the columns to reproduce the rigid connection with the foundation, while all truss elements are modelled as pinned members. Both permanent and accidental loads, determined in compliance with code prescriptions (i.e. quasi-permanent combination), are applied at the nodes of the upper chord. The mechanical behavior of the steel is described by the STEELEC3EN constitutive law implemented in SAFIR®, according to Eurocode 3 [1], which reproduces the progressive degradation of strength and stiffness with increasing temperature. Finally, the thermal histories obtained from the thermal analyses are associated with each structural element, allowing the simulation of the mechanical response for each of the investigated scenarios.

3.3 Thermo-Mechanical Response

The thermo-mechanical analyses conducted made it possible to map the thermal evolution and subsequent mechanical response of the structure for the entire set of investigated scenarios, with respect to the three analyzed configurations. The results highlight significant differences in structural behavior depending on the protection adopted, both in terms of temperatures reached in the elements and global mechanical response.

From a thermal point of view, in the unprotected configuration, the steel reaches temperatures above 700 °C quite rapidly for most scenarios involving heavy vehicles, triggering a rapid degradation of the elastic modulus and yield strength. Conversely, the adoption of spray-applied fire-resistive material (SFRM) proves effective in limiting the heating of the elements: with a thickness of 20 mm, the average temperatures in the critical sections of the columns frequently remain below 400 °C, the threshold beyond which the degradation of steel yielding stress is conventionally assumed to start. From a mechanical point of view, passive protection substantially modifies the collapse kinematics of the structure. In the unprotected configuration, the displacements at the top of

the columns and the deflections at the truss midpoint quickly exceed the limits of full functionality (PL-V) and limited damage (PL-IV), up to reaching local buckling failure for the most severe scenario. Protected configurations, on the other hand, show a significantly stiffer and more controlled response, with a marked reduction in displacements. As the SFRM thickness increases, structural conditions improve further: greater thermal protection translates into a more effective limitation of deformations and a higher probability of maintaining load-bearing capacity for the entire duration of the simulated event, confirming the decisive role of the protective layer thickness in the structural response under fire conditions (Fig. 2).

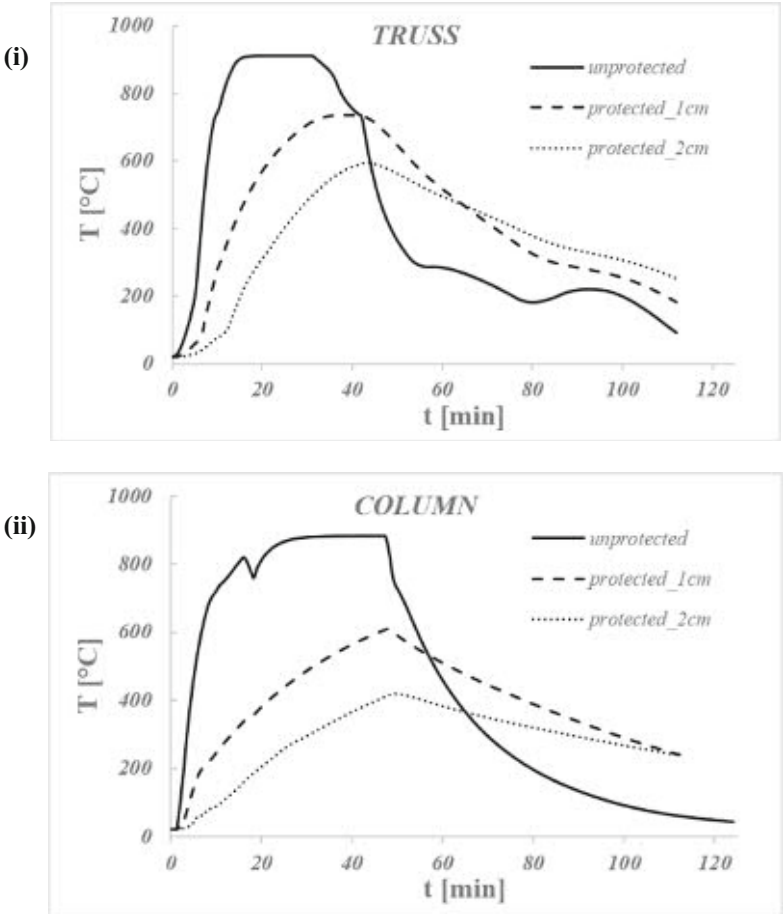


Fig. 2. Time-Temperature curve trends: (i) maximum effect on the beam, (ii) maximum effect at the column head

4 Fire Fragility Analysis

The fire vulnerability of the investigated structural configurations is quantified through the derivation of fragility curves, which express the probability that the structure reaches or exceeds a specific Performance Level as the fire intensity varies. The curves are derived using the Modified Cloud Analysis (MCA) [11], a probabilistic approach that extends the classical Cloud Analysis method to explicitly account for collapse scenarios, combining linear regression on a logarithmic scale with logistic regression. The structural fragility for an assigned Performance Level (PL) is expressed through the total probability theorem as:

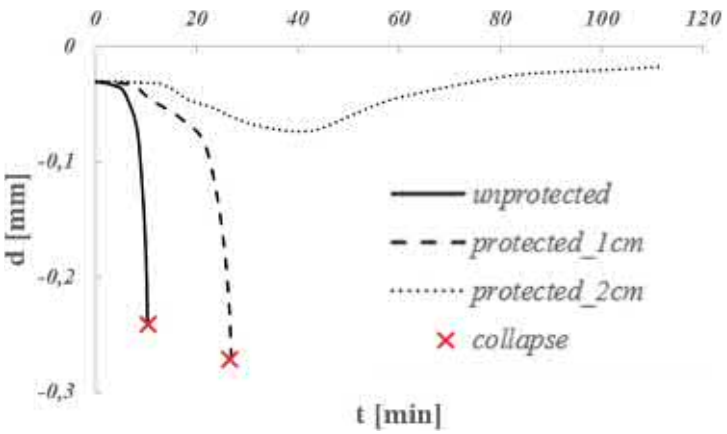


Fig. 3. Displacement trends over time – Scenario 27

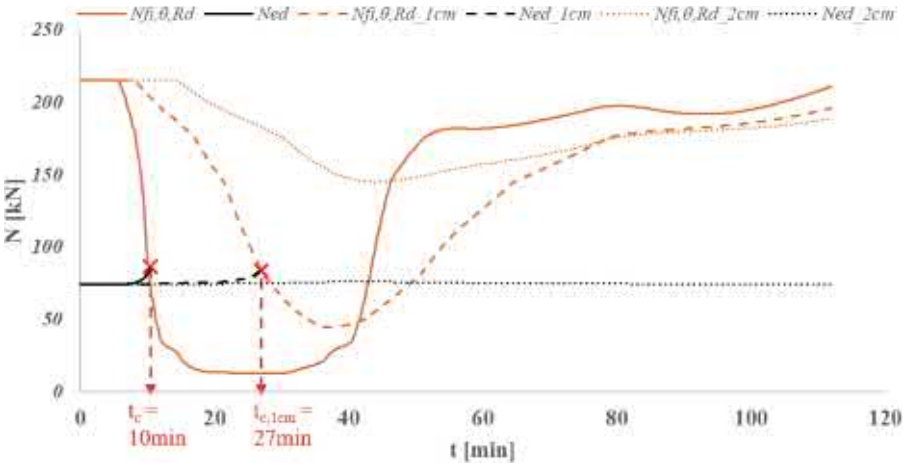


Fig. 4. Local buckling verification of the upper chord – Scenario 27

$$P(DCR_{PL} \geq 1|IM) = P(DCR_{PL} \geq 1|IM, NoC) \bullet (1 - P(C\backslash IM)) + P(DCR_{PL} \geq 1|IM, C) \bullet P(C\backslash IM) \quad (1)$$

where the dataset is divided into two subsets: scenarios that do not induce structural collapse (NoC) and those that cause it (C) (Figs. 3 and 4).

The results, reported in Fig. 5, highlight a significantly higher vulnerability for the unprotected structure compared to the SFRM-protected configurations. The curves relating to PL-V show steeper slopes and lower median values of intensity measures, indicating that even minor fires can compromise the full functionality of the unprotected structure. The adoption of passive protection systematically shifts the curves to the right along the horizontal axis, reducing the probability of exceeding the performance levels for any fire intensity. As the thickness of the SFRM increases, this benefit becomes progressively more pronounced, confirming the decisive role of the protective layer thickness in reducing structural vulnerability to fire.

5 Fragility-Informed Life Cycle Cost Analysis

The economic evaluation of passive protection strategies is conducted by integrating the probabilistic results of the fragility curves into a life cycle cost analysis. The objective is to provide a rational tool to compare the different investigated configurations – unprotected and protected with SFRM of different thicknesses – not only in terms of structural performance but also regarding long-term economic sustainability.

The indicator adopted for this purpose is the Present Value of Life Cycle Costs (PVLCC), which allows aggregating all costs associated with the structure during its service life into a single value, taking into account the time value of money. The PVLCC [12] is expressed as the sum of four main contributions:

$$PVLCC = C_1 + C_M + D_D + D_{ID} \quad (2)$$

where C_1 is the initial construction cost, including any passive protection system; C_M represents the maintenance costs of the structure and the protective layer over time; D_D represents the expected direct losses in the event of a fire, linked to the repair or reconstruction costs of damaged structural and non-structural elements; D_{ID} represents indirect losses, associated with business interruption and the socioeconomic impact of the event.

Maintenance costs [13] are estimated using an approach based on the discounted value of periodic expenses over the service life of the structure:

$$C_m = \int_0^{t_{life}} C_m e^{-\lambda_d t} dt = \frac{C_m}{\lambda_d}\left(1\text{-}e^{-\lambda_d t_{life}}\right) \quad (3)$$

Direct losses, on the other hand, are calculated directly from the fragility curves derived in the previous chapter, associating an expected cost with each Performance Level proportional to the probability of exceedance and the extent of damage, in accordance with the formulations proposed by HAZUS [14] for estimating economic losses as a

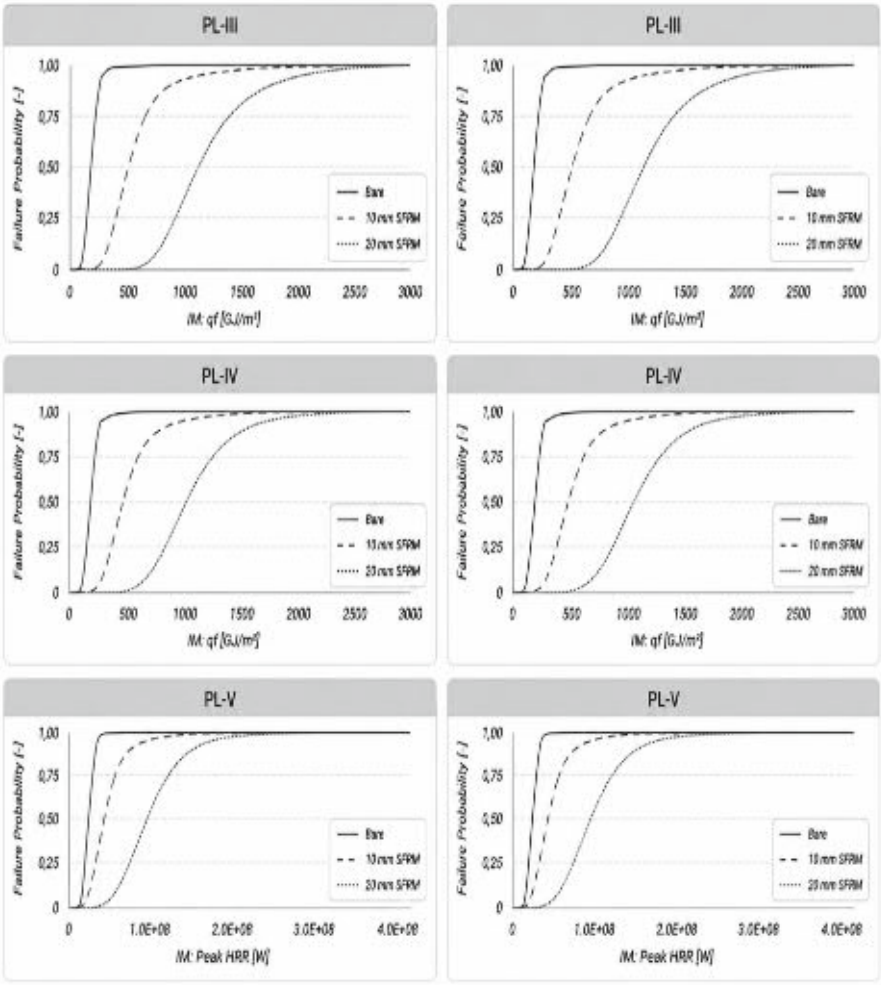


Fig. 5. Fragility curves

function of structural vulnerability. As for indirect losses [16], they are calculated as a function of direct losses.

$$D_D = EL_{STR} = FV_{STR}\, RV_B \sum_{i=0}^{n} (PSTR_{PL\,i} STRD_{PL\,i}) \tag{4}$$

The results, reported in Fig. 6, show how the economic convenience of the different protection solutions strongly depends on the intensity of the fire. For low-intensity scenarios, the unprotected structure represents the most economical solution, as the risk of damage is sufficiently low to not justify the initial investment in passive protection.

As intensity increases, passive protection progressively becomes the most advantageous choice, since the reduction in expected losses compensates and, if the intensity further increases, exceeds the additional cost of the protective system. In this context,

$$D_D = EL_{STR} = FV_{STR}\, RV_B \sum_{i=1}^{n} \left(PSTR_{PL\,i}\, STRD_{PL\,i} \right) \quad (4)$$

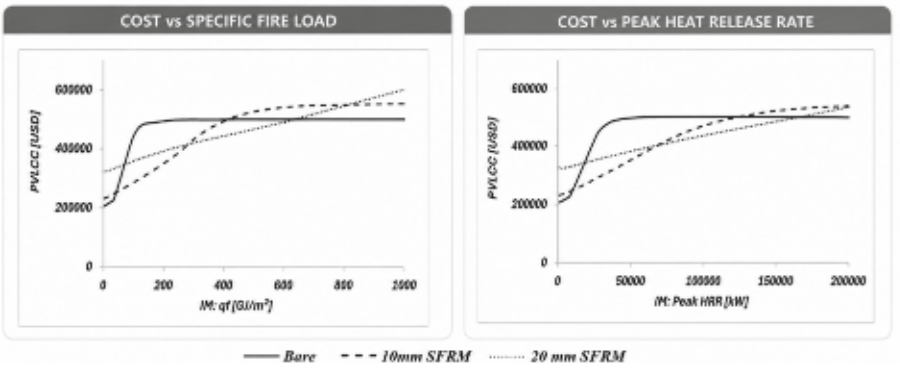


Fig. 6. Life Cycle Cost Analysis (50-year life cycle, 3% discount rate)

the thickness of the SFRM plays a decisive role: for medium-intensity scenarios, the solution with the smaller thickness offers the best compromise between cost and performance, while for high-intensity scenarios, the greater thickness minimizes the overall PVLCC.

Finally, for extreme intensity events, none of the investigated configurations proves to be economically optimal, suggesting the need for more advanced or complementary protection strategies, e.g. active extintion systems, passive protection with higer performance.

6 Conclusions

In this work the fire response of a typological steel industrial building used as vehicle storage facility is investigated, quantitatively evaluating the effect of passive protection on structural vulnerability and identifying the economically optimal protection solution as a function of fire intensity.

- The thermo-mechanical analyses demonstrate that the adoption of spray-applied fire-resistive material (SFRM) substantially modifies the structural response, (i) preventing the occurrence of local buckling failures, observed in the unprotected structure, and (ii) significantly reducing displacements. As the thickness of the protective coating increases, these benefits become further pronounced, confirming the decisive role of SFRM thickness in the structural response under fire conditions.
- The fragility curves derived through the Modified Cloud Analysis allowed to quantify the probability of either reaching or exceeding a performance level relevant to different configurations, showing how passive protection systematically reduces the probability of exceeding each performance level, and how this reduction is progressive with increasing SFRM thickness.

- Finally, the integration of the fragility curves into the life cycle cost analysis allowed for the identification of the optimal protection solution as a function of expected intensity, highlighting how the economic sustainability of passive protection increases progressively as the severity of the scenarios grows.

Future developments will include extending the methodology to other structural typologies and protection systems, as well as integrating it into multi-hazard assessments.

References

1. Eurocode 3 EN 1993 (2005) Design of steel structures. Brussels, Belgium
2. Eurocode 8 EN 1998 (2004) Design of structures for earthquake resistance. Brussels, Belgium
3. Cibelli A et al (2025) Thermal performance of reactive and non-reactive fire protective materials under non-standard heating regimes: an experimental parametric study. Fire Mater
4. Tattukolla Kiran et al (2022). Performance evaluation of lightweight insulating plaster for enhancing the fire endurance of high strength structural concrete.
5. Eurocode 1 EN 1991–1–2 (2002) Actions on structures - Part 1–2: General actions – Actions on structures exposed to fire. Brussels, Belgium
6. Italian National Code for fire prevention - D.M. 03/08/2015 (in Italian)
7. Frannsen J-M, Gernay T (2017) Modeling structures in fire with SAFIR®: theoretical background and capabilities. Journal of structural. Fire Eng
8. Kamikawa D, Hasemi Y, Wakamatsu T, Kagiya K (2002) Experimental flame heat transfer correlations for a steel column adjacent to and surrounded by a pool fire. In: Evans DD (ed) International Association for Fire Safety Science (IAFSS) – proceedings of the 7th international symposium, Worcester (MA, USA) June 16–21 2002
9. Francis P, Baddo N, Hanus F, Thauvoye C (2018) Design of columns subject to localised fires. The Steel Construction Institute (SCI)
10. Tondini N, Thauvoye C, Hanus F, Vassart O (2019) Development of an analytical model to predict the radiative heat flux to a vertical element due to a localised fire. Fire Saf J 105:227–243
11. Jalayer F, Elefante L, De Risi R, Manfredi G (2014) Cloud analysis revisited: efficient fragility calculation and uncertainty propagation using simple linear regression. In: In proceedings of the 10th U.S. national conference on earthquake engineering, frontiers of earthquake engineering, Anchorage (AK, USA) 21–25 July 2014
12. Miano A, Sezen H, Jalayer F, Prota A (2019) Performance-based assessment methodology for retrofit of buildings. J Struct Eng 145(12):04019144
13. HAZUS-MH 2.1 Advaned Engineering Building Module (AEBM) – Earthquake Loss Estimation Methodology
14. SFPE (2002) Handbook of fire protection engineering, 3rd edn

Fire Protection of Steel Structures in High Corrosive Environments

Riccardo Tognaccini[1(✉)], Erik van Schaijk[2], and Roger Soler[3]

[1] Hempel, Genoa, Italy
rito@hempel.com
[2] Hempel, Kampen, The Netherlands
[3] Hempel, Polinya, Spain

Abstract. Modern intumescent coatings have evolved into highly engineered systems capable of de-livering reliable fire protection while simultaneously addressing the practical, aesthetic, and durability demands of contemporary steel construction. This paper examines these ad-vancements through a structured comparison of acrylic and epoxy intumescent technolo-gies, highlighting their respective fire-rating capabilities, achievable surface finishes, appli-cation efficiencies, and performance on complex geometries such as cellular beams and slender steel members. Particular attention is given to the mechanical robustness of current formulations, which significantly reduces transport and handling related damage and there-by minimizes repair work throughout fabrication and installation. Building on this technological overview, the paper evaluates the suitability of intumescent coatings for use in corrosive environments, including exterior exposures up to C5. Recent formulation breakthroughs now allow certain systems to be applied without topcoats or primers, while long term durability of more than 25 years can be achieved when combined with activated zinc technology. These developments position intumescents as multifunc-tional solutions that integrate fire resistance with corrosion protection, even in industrial and coastal environments. Laboratory testing results are presented to substantiate these performance claims, including high-corrosivity exposure data and visual evidence of coating integrity and achievable smooth finishes. The discussion further emphasizes the critical role of approved primers and topcoats in ensuring system compatibility, long term adhesion, and overall protective performance.

Keywords: Fire protection · Coatings · Corrosion · Steel structures · Intumescent · Epoxy

1 Introduction

Steel continues to be one of the most widely utilised structural materials in modern construction due to its favourable combination of high strength-to-weight ratio, ductility, and design adaptability. These inherent advantages enable efficient structural systems and architectural flexibility across a wide range of applications. However, despite its mechanical efficiency, steel is particularly vulnerable to elevated temperatures, which can significantly reduce its load-bearing capacity, making dedicated fire protection strategies essential for ensuring structural safety in the event of a fire.

© The Author(s), under exclusive license to Springer Nature Switzerland AG 2026
R. Zanon et al. (Eds.): CTA 2026, LNCE 942, pp. 482–493, 2026.
https://doi.org/10.1007/978-3-032-39505-4_42

In the context of fire safety, passive fire protection systems based on intumescent coatings have emerged as a widely adopted engineering solution for maintaining structural integrity during fire exposure. These systems are specifically designed to delay the temperature rise of steel elements by forming an insulating char layer when exposed to heat, thereby extending the time to structural failure and enabling safe evacuation and firefighting operations. In parallel, the increasing demand of protection under severe environmental exposure conditions—particularly in industrial, marine, and coastal environments—has placed greater emphasis on the development of coating systems capable of providing sustained corrosion protection over extended service periods [1] (Fig. 1).



Fig. 1. Intumescent coating applied to the roof structure of the Cascina Merlata shopping center

2 Intumescent Technologies

Intumescent coatings function as passive fire protection materials designed to preserve the load-bearing capacity of steel structures during fire exposure. When subjected to elevated temperatures, these coatings undergo a thermochemical reaction that results in substantial volumetric expansion, forming a low-density, carbonaceous char layer. This char acts as an insulating barrier, significantly reducing heat transfer to the underlying steel substrate and thereby delaying the critical temperature rise that leads to loss of structural strength.

Among the available intumescent coating technologies, acrylic systems are the most widely used. These can be broadly classified into water-based acrylics and solvent-based acrylics. Water-based acrylic intumescent coatings are typically used in interior environments and are generally suitable for corrosivity categories up to C3 according to ISO 12944. Solvent-based acrylic systems offer enhanced environmental resistance and can be used in both interior and exterior applications, typically up to corrosivity category C4.

Epoxy intumescent coatings represent a distinct technology from acrylic systems and provide a significantly higher level of durability and environmental resistance. In

addition to their superior mechanical strength, impact resistance, and overall robustness, epoxy intumescent coatings can be used in aggressive exterior environments, typically up to corrosivity category C5 according to ISO 12944. These characteristics make epoxy systems particularly suitable for applications where long-term durability and resistance to severe environmental exposure are critical (Fig. 2).



Fig. 2. Typical use and main characteristics of various intumescent technologies

Fire resistance performance is defined in accordance with standardised classification systems where the required dry film thickness is directly influenced also by the section factor (Hp/A) of the structural steel element. Higher section factors typically require increased coating thickness to achieve equivalent fire resistance durations, making precise specification and application control essential to performance outcomes. Epoxy systems are frequently capable of achieving elevated fire resistance ratings, often up to R240 for some selected massivities and up to R180 for a broader coverage.

Achieving high-quality surface finishes is a key consideration, particularly in architectural steelwork where exposed coatings are visible in service. While epoxy systems can achieve acceptable finishes under controlled conditions, they often require additional sanding, levelling, and application precision to meet higher aesthetic standards. Acrylic systems, by contrast, generally exhibit improved film build characteristics and surface smoothness, reducing the extent of post-application finishing required.

Intumescent coatings are also widely applied to structurally complex geometries such as hollow sections, rods, metal decking and irregular steel profiles. In these contexts, epoxy-based systems demonstrate improved application performance due to enhanced mechanical stability during curing and better resistance to sagging or film disruption, resulting in more uniform coverage on challenging substrates (Fig. 3).

Recent developments in formulation technology have further improved the mechanical resilience of modern intumescent coatings, particularly with respect to resistance against damage during transport, handling, and installation. This reduction in mechanical vulnerability decreases the likelihood of site-based remediation works and contributes to improved construction efficiency.

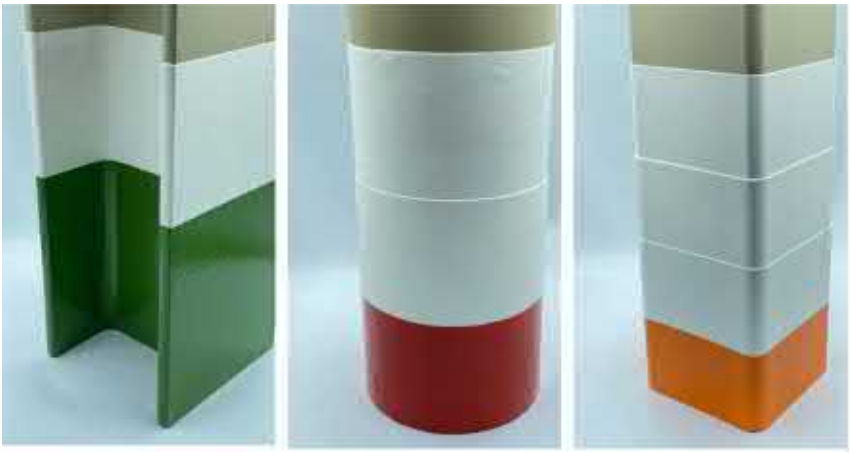


Fig. 3. Demonstration panel showing the complete coating system in a stepped configuration, revealing the individual primer, intumescent coating, and topcoat layers, including final finish

The achievable surface finish varies between acrylic and epoxy technologies. Acrylic intumescent coatings are generally capable of providing a smooth, high-quality architectural finish directly after application, making them well suited to projects where aesthetic appearance is a primary consideration. Epoxy intumescent coatings, while offering superior durability and environmental resistance, typically exhibit a more textured surface profile. Where a high-grade decorative finish is required, additional surface preparation, sanding, and finishing coats may be necessary. Consequently, achieving comparable aesthetic standards with epoxy systems may increase both application time and overall project costs.

From a fire protection design perspective, both acrylic and epoxy technologies can provide solutions for a wide range of steel section factors (massivity Hp/A values). Acrylic systems are often advantageous for conventional open steel sections requiring moderate dry film thicknesses, whereas epoxy technologies are particularly beneficial at higher fire ratings and higher section factors, where the required film build can become substantial.. The char resulting from Epoxy technology is stronger compared the one from Acrylics, thus avoiding detachments and failures under fire. This allows a higher capability of epoxy systems that can protect complex geometries like tension rods or slender hollows. However, the selection of either technology remains dependent on the specific fire design requirements, environmental exposure conditions, and the maximum section factor covered within the relevant product certification.

Transportation, handling, and in-service durability remain important differentiators between the two technologies. Acrylic coatings, particularly at high film thicknesses, are generally more susceptible to mechanical damage, impact, and edge chipping during fabrication, transport, erection and/or use. As a result, repair works following installation are often more frequent and can require careful surface preparation and local reinstatement of the coating system. Epoxy intumescent coatings typically provide greater resistance to abrasion, impact, and mechanical damage, reducing the likelihood of repairs during

construction and throughout the service life of the structure. Where repairs are required, both technologies can generally be repaired effectively in accordance with the manufacturer's procedures, although the extent and complexity of the repair may vary depending on the severity of the damage and the environmental exposure conditions.

Overall, the combined improvements in durability, application efficiency, and reduced maintenance requirements contribute to enhanced lifecycle performance and sustainability credentials of modern intumescent coating systems when compared with earlier-generation technologies. The selection between acrylic and epoxy technologies should therefore consider not only fire performance requirements but also environmental exposure, aesthetic expectations, project programme constraints, transportation and handling considerations, and long-term maintenance objectives.

3 Intumescent in Corrosive Environments

Steel structures operating in environments classified typically from C3 to C5, and in extreme cases CX according to ISO 12944, are subject to accelerated degradation mechanisms driven by moisture, chlorides, industrial pollutants, and cyclic environmental loads. In such conditions, the provision of fire resistance alone is insufficient, and robust corrosion protection strategies must be integrated into the overall coating design to ensure long-term structural integrity and service life [2].

Epoxy-based intumescent technologies have enabled the development of simplified coating systems that, under defined and manufacturer-approved conditions, can be applied without the need for additional primer or topcoat. In such configurations, corrosion protection can typically be achieved up to corrosivity category C3-H according to ISO 12944. For more demanding environments, the use of an approved primer can extend the system performance up to C5-H, while a complete coating system comprising both an approved primer and an approved topcoat can provide protection up to C5-VH. This flexibility represents a significant evolution in system architecture, reducing application complexity, minimizing potential compatibility issues between coating layers, and improving overall installation efficiency while maintaining the required levels of both corrosion protection and fire resistance. All primers and topcoats used within the system must be approved by the intumescent coating manufacturer. Epoxy intumescent technology is also widely used for offshore and marine structures, where its superior durability, resistance to harsh environmental conditions, and long-term corrosion protection are particularly advantageous.

Where enhanced durability is required, the combination of activated zinc-rich primers with epoxy intumescent coatings represents a highly effective integrated corrosion and fire protection system. The zinc-rich primer provides cathodic protection to the steel substrate, while the epoxy intumescent layer delivers fire resistance and additional barrier protection. When correctly specified and applied within certified systems, such configurations can achieve service lives in the range of 25 to 35 years, depending on environmental severity, coating thickness, and maintenance conditions.

In the assessment of long-term performance, durability is primarily governed by the effectiveness of corrosion protection rather than superficial aesthetic changes. Variations in colour, gloss level, or surface appearance over time are generally considered

cosmetic in nature and do not necessarily indicate a loss of functional integrity, provided that the coating system maintains adhesion, barrier properties, and structural protection capabilities.

4 Laboratory Test Results

The fire performance of intumescent coating systems is assessed through standardized furnace testing procedures conducted under strictly controlled regimes, in accordance with internationally recognized classification standards for structural fire resistance. These tests include fire exposure of structural steel elements coated with an intumescent coating system to prescribed standardised fire conditions to determine the ability of coated steel elements to maintain load-bearing capacity for specified durations, expressed as R ratings (e.g., R30 to R180). The methodology ensures repeatability and comparability across different coating technologies by maintaining defined heating curves, loading conditions, and failure criteria (Fig. 4).



Fig. 4. A column covered in intumescent prior to be tested in a furnace (left) and after the test (right)

Corrosion resistance is evaluated through accelerated cyclic corrosion testing combined with exposure protocols aligned with ISO 12944 standards, extending to highly aggressive environments classified as C5 and C5VH. These test regimes replicate alternating conditions of humidity, salt spray, drying cycles, and temperature fluctuations, thereby providing a more realistic simulation of long-term environmental exposure than continuous exposure methods. Such testing could lead to degradation of a coating system and is essential for assessing the durability of integrated coating systems intended for use in marine, offshore, and industrial environments.

In addition to protective performance, surface quality is a critical parameter in the evaluation of modern intumescent systems, particularly for architectural steel applications. Surface assessments focus on parameters such as smoothness, uniformity, and visual consistency, confirming the ability of advanced formulations to achieve aesthetically acceptable finishes without compromising protective performance. This aspect is increasingly important in exposed structural steelwork where coatings must meet both engineering and architectural requirements.

Mechanical performance is characterised through a series of standardised tests including adhesion strength, impact resistance, and abrasion resistance. These tests evaluate the coating system's ability to withstand mechanical stresses during fabrication, transport, installation, and service life. High adhesion values are particularly important for ensuring long-term system integrity, while impact and abrasion resistance directly influence resistance to handling damage and operational wear.

Overall, laboratory findings consistently demonstrate that epoxy-based intumescent systems exhibit superior mechanical robustness, adhesion performance, and long-term exterior durability when compared to traditional acrylic-based formulations. This enhanced performance is attributed to the higher crosslink density and improved structural integrity of epoxy matrices, which contribute to greater resistance against both mechanical damage and environmental degradation over extended service periods.

5 Importance of Approved Primers and Topcoats

The long-term performance and regulatory compliance of intumescent fire protection systems are fundamentally dependent on the chemical and physical compatibility of all constituent layers, namely the primer, the intumescent coating, and the protective topcoat. In multilayer intumescent coatings systems applied to structural steel, each layer performs a distinct but interdependent function, and any incompatibility at the interfaces can significantly compromise both corrosion resistance and fire performance. For this reason, system approvals and manufacturer-certified combinations are critical to ensuring predictable long-term behaviour under both environmental exposure and fire conditions.

Amongst zinc primers, activated zinc-rich primers are a key component in high-performance corrosion protection systems, particularly in aggressive environments such as C5 and CX under ISO 12944. These primers provide cathodic protection through the electrochemical activity of zinc particles, significantly reducing the onset and propagation of corrosion at the steel substrate. When properly integrated into certified coating systems, activated zinc-rich primers enhance the overall durability of the protective system and contribute to extended service life expectations in excess of several decades under controlled exposure conditions.

Topcoats serve a dual function within intumescent systems, acting both as a protective barrier against environmental degradation and as a stabilising layer for long-term aesthetic performance. Their primary role includes resistance to ultraviolet (UV) radiation, moisture ingress, and atmospheric pollutants, all of which can degrade exposed intumescent coatings over time (Figs. 5 and 6).

In this context, polysiloxane-based topcoats have demonstrated superior long-term performance compared to conventional polyurethane systems, particularly in terms of gloss retention, colour stability, and resistance to environmental ageing. These properties are especially relevant in architectural applications where both functional and visual durability are required (Figs. 7 and 8).

Conversely, the use of non-approved or chemically incompatible primer–intumescent–topcoat combinations has been consistently associated with premature system failure. Such failures may manifest as interlayer adhesion loss, reduced corrosion resistance,



Fig. 5. Sample panels at different stages of testing



Fig. 6. Approved and compatible primer to the left and incompatible failed primer to the right 8due to detachment)

cracking, or delamination under thermal or mechanical stress. More critically, deviation from approved system configurations can invalidate fire certification, thereby undermining compliance with regulatory standards and potentially compromising structural safety in fire scenarios. Consequently, adherence to tested and certified coating systems is not only a matter of durability but also a fundamental requirement for ensuring verified fire performance and structural integrity.



Fig. 7. Qualitative performance of conventional zinc primer to the left and activated zinc primer to the right

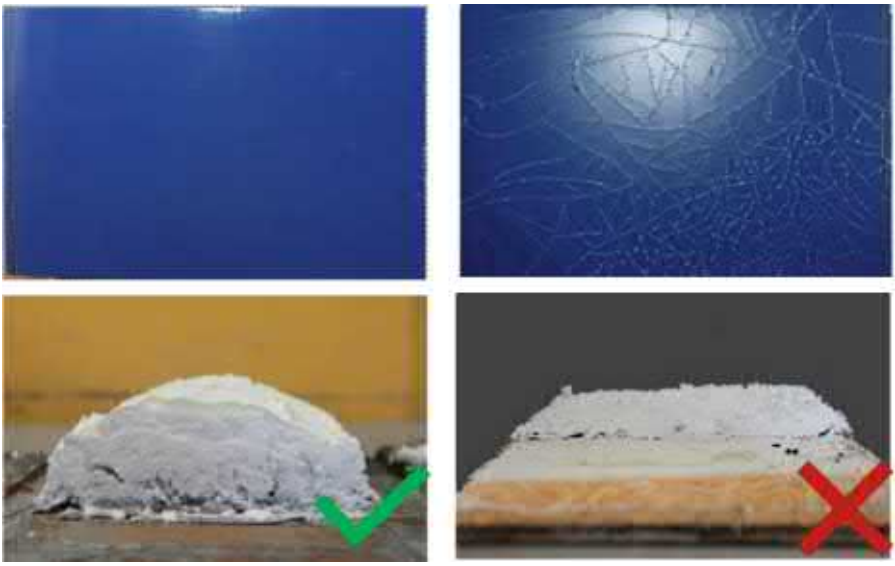


Fig. 8. Approved and compatible topcoat to the left and incompatible failed topcoat to the right. The expansion of the intumescent coating was affected by affected water permeability as a result of cracking

6 Durability Considerations

The long-term durability of intumescent coatings is one of the most important considerations in the specification and lifecycle management of passive fire protection systems for structural steel. Unlike conventional protective coatings, where durability is primarily associated with corrosion protection and maintenance intervals, the principal function of an intumescent coating is to maintain its fire protection performance throughout the service life of the structure. Consequently, durability assessment must consider the ability of the coating system to preserve its fire resistance characteristics over time [3].

The principal European reference document for the assessment of intumescent coatings is EAD 350402–00-1106 [4], Reactive Coatings for Fire Protection of Steel Elements. This document defines exposure categories and corresponding laboratory conditioning procedures intended to evaluate the long-term stability of reactive fire protection systems. According to the EAD, successful completion of the prescribed durability testing demonstrates a service life greater than 10 years. However, unlike standards commonly used for protective coatings, the EAD does not establish multiple durability classes and does not provide a clear analytical methodology to formally classifying systems beyond this minimum period.

The durability statement associated with an ETA-approved intumescent coating should therefore be interpreted as a demonstrated minimum performance period rather than as an indication of the maximum achievable service life. In practice, the actual durability of intumescent systems is strongly influenced by environmental exposure conditions, maintenance practices, mechanical damage, and the quality of the original application. For many indoor applications, particularly in conditioned environments characterised by low humidity, stable temperatures, and limited mechanical exposure, the functional service life of an intumescent coating will normally substantially exceed the minimum life time expectation claimed in EAD requirements.

To provide additional confidence regarding long-term performance beyond the 10-year period demonstrated by the EAD, some manufacturers might perform supplementary durability assessments that exceed the requirements of the European approval framework. These investigations typically employ accelerated ageing procedures derived from ISO 12944, followed by furnace testing to verify that the fire protection performance of the aged intumescent coating remains unchanged. Although such assessments are not part of the formal ETA approval process and therefore do not constitute an official extension of the EAD durability classification, they provide valuable evidence regarding the long-term stability of the coating system. In many cases, these accelerated ageing programmes are designed to simulate environmental exposure periods equivalent to 25 years or more, thereby providing additional confidence that the intumescent properties remain effective throughout an extended service life.

A second approach to long-term durability verification has recently been introduced in Italy through UNI 11947:2024, which establishes procedures for the inspection and maintenance of passive fire protection systems. For ETA-approved intumescent coatings, the standard requires that specific inspections be initiated after the tenth year of service. These inspections include measurements of coating thickness and adhesion to verify that the installed system continues to satisfy the fundamental performance requirements upon which the original fire design was based. In addition to routine visual inspections, further checks are required at regular intervals depending on the exposure category of the structure. This methodology represents an important evolution in durability management because it relies on direct verification of the installed system rather than solely on laboratory predictions of long-term performance. The approach provides objective evidence that the coating system remains capable of fulfilling its intended fire protection function throughout its service life. Aside from the technical requirements, it is typically recommended to visually inspect the conditions of the coating at least once per year from the initial application throughout the whole like of the structures.

A further strategy that may be considered by structural designers involves the installation of sacrificial reference panels coated simultaneously with the main structure using the same materials, surface preparation procedures, application methods, and environmental conditions. These panels are then exposed to the same service environment as the protected structure and periodically removed for inspection and testing. Depending on project requirements, the panels may be assessed annually or at longer intervals through measurements of coating thickness, adhesion, mechanical integrity, and, where appropriate, fire performance testing. Because the panels are representative of the actual installed system, this approach provides a direct empirical assessment of coating performance over time and can offer a particularly high level of confidence regarding long-term durability. Although not currently required by European regulations, the use of sacrificial panels may be considered for critical infrastructure, high-value assets, or structures designed for exceptionally long service lives.

The current European framework therefore provides a demonstrated minimum durability exceeding 10 years for ETA-approved intumescent coatings, while recognising that substantially longer service lives may be achieved in practice. Supplementary accelerated ageing programmes, periodic in-service inspections in accordance with UNI 11947:2024, and empirical monitoring through sacrificial panels provide complementary approaches for assessing long-term performance beyond the minimum requirements of the EAD. Collectively, these strategies support a durability-based approach to passive fire protection management, helping to ensure that the fire resistance performance established at the time of installation is maintained throughout the operational life of the structure.

7 Conclusions

Modern intumescent coatings have evolved from purely passive fire protection materials into multifunctional engineering systems capable of simultaneously addressing fire resistance, durability, constructability, and architectural requirements. The comparison presented in this paper demonstrates that both acrylic and epoxy technologies provide effective fire protection solutions, although their respective characteristics make them suitable for different applications and exposure conditions. Acrylic systems remain the preferred choice for many interior applications where high-quality decorative finishes and ease of application are key requirements, whereas epoxy technologies offer superior mechanical robustness, environmental resistance, and suitability for demanding industrial, marine, and exterior environments.

Recent developments in formulation technology have significantly improved the durability and lifecycle performance of intumescent systems. Enhanced resistance to mechanical damage during transportation, handling, and installation has reduced maintenance requirements and improved overall project efficiency. Furthermore, advances in epoxy intumescent technology have enabled simplified coating architectures, including systems requiring fewer coating layers while maintaining both fire and environmental protection performance.

The long-term durability of intumescent coatings remains a critical consideration for asset owners and designers. While the European assessment framework currently

demonstrates a minimum service life exceeding 10 years through EAD 350402–00-1106 testing, additional evidence can be obtained through accelerated ageing programmes, in-service inspection methodologies such as those defined by UNI 11947:2024, and empirical monitoring through sacrificial test panels. Collectively, these approaches provide increasing confidence that properly specified, applied, and maintained intumescent systems can continue to deliver their intended fire protection performance for periods substantially exceeding the minimum regulatory requirements.

Overall, the continued development of intumescent coating technologies, combined with increasingly sophisticated durability assessment methodologies, is expanding the role of these systems in modern steel construction. Future developments are expected to focus on further extending service life, reducing maintenance requirements, improving sustainability credentials, and providing greater confidence in long-term fire protection performance throughout the operational life of structures.

References

1. Anees SM, Dasari A (2018) A review on the environmental durability of intumescent coatings for steels. J Mater Sci 53(1):124–145
2. Jimenez M, Bellayer S, Revel B, Duquesne S, Bourbigot S (2013) Comprehensive study of the influence of different aging scenarios on the fire protective behavior of an epoxy-based intumescent coating. Ind Eng Chem Res 52(2):729–743
3. Häßler D, Mund M, Daus LH, Hothan S, Schaumann P, Schartel B (2024) Durability of intumescent coatings and recommendations for test concepts for a working life of more than 10 years. Fire Saf J 146:104173
4. European Organisation for Technical Assessment (EOTA) (2017) EAD 350402–00-1106, reactive coatings for fire protection of steel elements. EOTA, Brussels

Strengthening of RC Structures with Steel Plates: Fire Behaviour Analysis Between State-of-the-Art and Practical Applications

Nunzia Gargiulo(✉), Antonio Cibelli, Donatella de Silva, and Emidio Nigro

Department of Structures for Engineering and Architecture, University of Naples Federico II, Naples, Italy
nunzia.gargiulo@unina.it

Abstract. The use of external steel plates represents a versatile and effective strengthening strategy to enhance the bearing capacity and ductility of RC beams and columns. However, the inherent vulnerability of steel to high temperatures raises critical safety concerns in case of fire, as the degradation of mechanical properties of both the reinforcement and the connection systems (epoxy resins or mechanical anchors) can severely compromise the effectiveness of the intervention. This paper presents the results of an extensive literature survey aimed at outlining the state-of-the-art on the thermo-mechanical behaviour of steel-strengthened RC members under fire conditions. The study critically analyzes both the behaviour of the individual components of the steel-concrete-connection system and the global response of the strengthened element, highlighting how factors such as the glass transition temperature of resins and thermal gradients influence failure mechanisms. Furthermore, the paper examines how current international codes and standards deal with the mechanical decay of the strengthening system under fire conditions. To bridge the identified knowledge gap, the methodology of a representative case study of the Italian construction landscape is presented. Starting from the seismic vulnerability assessment of an existing building, steel plate reinforcements were designed and subsequently evaluated under thermal loading using both prescriptive and performance-based approaches. The results emphasize the need to integrate static and seismic design with specific fire resistance verifications to ensure the global safety of strengthened structures.

Keywords: Structural strengthening · Steel plates · Reinforced concrete (RC) · Fire resistance · Thermo-mechanical behaviour · Retrofitting · Vulnerability assessment

1 Introduction

While the European structural engineering community has spent decades perfecting retrofitting strategies to mitigate seismic risk in post-war reinforced concrete (RC) buildings [1–3], a critical secondary vulnerability has inadvertently been introduced. Among the available localized interventions, externally bonded or mechanically anchored steel

© The Author(s), under exclusive license to Springer Nature Switzerland AG 2026
R. Zanon et al. (Eds.): CTA 2026, LNCE 942, pp. 494–501, 2026.
https://doi.org/10.1007/978-3-032-39505-4_43

plates have become a benchmark solution due to their execution speed and mechanical reliability [4]. However, this widespread reliance on structural steel creates a severe multi-hazard conflict: a system optimized for ambient temperature geohazards (earthquakes) is exceptionally vulnerable to thermal hazards (fire). Above 400 °C, the rapid degradation of steel stiffness, combined with the thermal degradation of the connection system-particularly temperature-sensitive epoxy adhesives-threatens trigger premature, catastrophic failures that are often overlooked during the initial seismic upgrading phase.

To bridge the gap between seismic resilience and fire safety, this paper shifts the focus toward a holistic thermo-mechanical evaluation of steel-strengthened RC members. The study is structured around three interconnected objectives: first, a comprehensive critical review maps the state-of-the-art knowledge on the failure modes of these hybrid systems under thermal loading; second, an international comparative analysis uncovers the inconsistencies and regulatory gaps in how current structural codes handle strengthening systems in fire scenarios; and finally, the practical implications of these gaps are demonstrated through an advanced case study of an existing building, where the fire performance of retrofitted RC beams is evaluated by contrasting traditional prescriptive limits against realistic performance-based fire engineering (PBFE) frameworks.

2 State of the Art: Steel-Plated RC Elements Under Fire Conditions

The structural retrofitting of existing reinforced concrete (RC) elements using external steel plates is a highly effective and widely adopted technique to remedy deficiencies in flexural capacity, shear resistance, and structural ductility. The primary technical configurations implemented for such flexural retrofitting fall into two main categories: Externally Bonded (EB) plates and Mechanically Bonded (MB) plates. EB systems typically utilize structural epoxy adhesives to laminate the steel plates to the tension face or shear webs of the RC member. To mitigate the risk of premature, brittle failure modes at ambient temperature—such as plate-end debonding or intermediate crack-induced (IC) debonding [5]—EB schemes are frequently supplemented with post-installed mechanical steel anchors [6]. Conversely, purely MB systems (commonly referred to as Bolted Steel Plates, BSP) rely exclusively on mechanical fasteners, such as expansion anchors or concrete screws, to transfer shear stresses via mechanical interlock and friction, allowing for relative sliding between the steel plate and the concrete substrate. Despite their proven efficacy under ambient static and seismic loading conditions, the fire performance of steel-strengthened RC members remains a critical structural vulnerability. The overall thermo-structural response of these retrofitted systems under elevated temperatures is fundamentally dictated by two interdependent factors: the severe mechanical degradation of the external steel plate—which experiences a dramatic loss of yield strength and stiffness at temperatures exceeding 400 °C—and, crucially, the rapid thermal degradation of the connection interfaces. The existing literature highlights markedly different high-temperature failure modes depending on the chosen connection technology.

2.1 Comparative Fire Behaviour of EB and MB Strengthening Systems

The high-temperature failure modes and structural endurance of the system vary drastically depending on the chosen connection technology (EB vs. MB).

When retrofitted RC members rely solely on Externally Bonded (EB) epoxy resins for interfacial shear transfer, their fire endurance is critically compromised. Structural epoxies widely utilized in civil engineering exhibit a low glass transition temperature (Tg), typically ranging from 54 °C to 60 °C [7]. Above this narrow thermal threshold, the transition of the polymer induces a rapid, non-linear degradation of its mechanical properties. This process effectively nullifies the composite action between the steel plate and the concrete substrate long before any macroscopic thermal decomposition of the resin occurs. Experimental investigations conducted by Tadeu and Branco [8] demonstrated that the shear strength of epoxy-bonded steel joints decreases by approximately 50% at a temperature of just 60 °C. As the interfacial temperature rises to 90 °C and 120 °C, the residual bond strength plunges to 25% and less than 10%, respectively [9]. Furthermore, during thermal exposure, the vaporization of free pore water within the concrete substrate generates localized, out-of-plane vapor pressure at the concrete-adhesive interface. This hydrothermal pressure field significantly accelerates the premature debonding of the steel plate, leading to a catastrophic and sudden loss of structural capacity [8].

In contrast, Mechanically Bonded (MB or BSP) systems utilizing mechanical anchors provide a much more robust, albeit structurally complex, thermo-mechanical response under fire exposure. Su et al. [10] observed that external bolted steel plates function as a partial thermal shield, delaying the heat flux into the underlying concrete core. Although the steel plate inevitably suffers thermal degradation above 400 °C, BSP-strengthened beams exposed to the standard ISO 834 fire curve exhibit enhanced crack control and a highly favourable shift in failure mode, transitioning from a brittle shear failure to a ductile flexural collapse. Post-fire residual capacity characterizations by Liu et al. [11] confirmed that, despite thermal damage and loss of stiffness, BSP-strengthened elements retain significantly higher residual ductility and ultimate load-bearing capacity compared to unreinforced concrete members.

Nevertheless, the metallic connectors themselves constitute a critical thermal bridge in MB systems. Due to their high thermal conductivity, the anchors undergo rapid heating, which can result in localized concrete crushing, shear failure of the bolts, or pull-out [12]. Furthermore, the cooling phase introduces severe structural hazards; subsequent thermal contraction generates high tensile stress fields, which can lead to bottom weld cracking or bolt failure via nut tearing [13, 14]. Finally, the differential thermal expansion between the high-conductivity external steel plate and the low-conductivity concrete substrate induces significant longitudinal shear and creep stresses on the connectors. This complex interfacial interaction strongly dictates the ultimate load-bearing capacity of the system, yet comprehensive design criteria and analytical models to quantify this effect under fire conditions remain scarce in current literature [14].

2.2 The Scientific Knowledge Gap in Global Structural Response

Despite the consolidation of robust prescriptive frameworks for ambient-temperature design, a profound scientific gap persists regarding the high-temperature characterization of these retrofitting systems at the macro-scale. It is crucial to highlight that the current understanding of the high-temperature failure mechanisms detailed in Sect. 1.1 is predominantly derived from experimental studies aimed at characterizing the local behaviour of isolated connections. While the thermal degradation kinetics of individual

materials and the phenomenological response of isolated steel-concrete-anchorage sub-assemblies are relatively well-documented, existing analytical paradigms consistently fail to scale up these local phenomena. Specifically, the complex non-linearities arising from the combined thermo-mechanical degradation of both the steel plate and the connectors in a full structural member - such as differential thermal expansion, localized high-temperature creep, and the consequent loss of kinematic compatibility at the interface - remain inadequately modelled.

As visually synthesized in Fig. 1, the current research landscape is characterized by a striking methodological dichotomy. The overwhelming majority of available high-temperature literature is strictly confined to localized tests on connection components. While a notable fraction of research explores the phenomenological response of isolated sub-assemblies at elevated temperatures, there is an almost complete absence of full-scale experimental research dedicated to the global, integrated thermo-structural response of the strengthened elements under realistic fire conditions. This critical literature gap renders the comprehensive fire safety assessment and performance-based design of steel-strengthened RC members fundamentally unresolved, thereby underscoring an urgent imperative for holistic, macro-scale structural fire analyses.

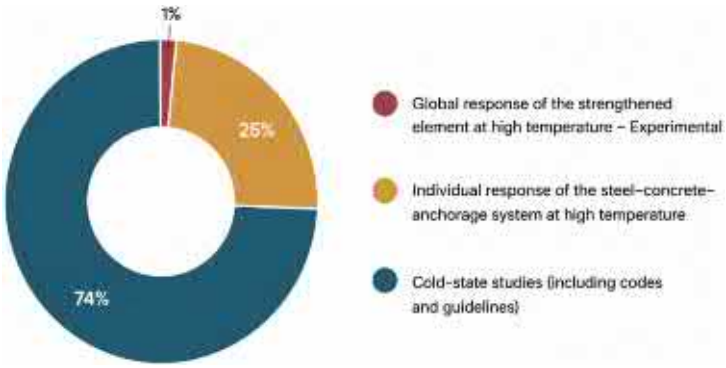


Fig. 1. Classification of the reviewed studies by response level.

3 Case Study Definition and Parametric Setup

To bridge the knowledge gap identified in Sect. 2 and evaluate the global response of steel-strengthened RC beams under elevated temperatures, a comprehensive analytical framework was developed. The methodology is based on the construction of advanced Moment-Curvature diagrams to evaluate the evolution of cross-sectional stiffness, flexural strength, and structural ductility prior to and during simulated fire exposure. The selected structural element is a typical RC beam extracted from a representative pre-1980s frame building. The cross-section is rectangular ($b = 300$ mm, $h = 400$ mm) with a concrete cover of 30 mm.

In accordance with the structural assessment procedures for existing buildings (e.g., Italian Building Code NTC 2018), the lack of exhaustive original construction details

and limited in-situ testing dictates the assumption of a low Knowledge Level (LC1). Consequently, a Confidence Factor (FC) equal to 1.35 is applied to the mean mechanical properties of the existing materials to determine the design strengths for the sectional analysis. The assumed average concrete compressive strength is fcm = 21 MPa, and the average internal steel yield strength is fym = 380 MPa.

The external retrofitting consists of a structural steel plate (S275) bonded to the tension soffit. To evaluate the efficiency of the strengthening technique, the parametric analysis focuses on a lightly reinforced configuration (As = 2ϕ16 at the tension face, A's = 2ϕ12 at the compression face), which is highly representative of obsolete structures designed primarily for gravity loads without modern seismic detailing. For this specific baseline configuration, the thickness of the external steel plate (ts) was parametrically increased from 1 mm to 5 mm (with a 1 mm step). This approach enables a detailed assessment of how the geometric reinforcement ratio influences the structural efficiency at ambient temperature, as well as the consequent reduction in ductility prior to, and during, fire exposure.

3.1 Effect of Plate Thickness on Cold Sectional Response

Before extending the framework to the fire domain, the analytical model was utilized to map the ambient-temperature performance of the selected configurations. Figure 2 illustrates the Moment-Curvature envelopes for the unreinforced baseline beam and the retrofitted sections with increasing plate thicknesses (*ts*). The observation of these global envelopes reveals a clearly definable structural behaviour that can be synthesized into three main aspects: strength, ductility, and yielding sequence. First, the externally bonded steel plates prove highly efficient, significantly raising the ultimate flexural capacity from approximately 40 kNm for the bare beam to over 150 kNm for the maximum retrofitting thickness. However, this substantial strength gain is offset by a drastic reduction in ultimate rotational capacity and energy dissipation. Visually resulting in a distinct "fan-shaped" trend, thicker plates cause the composite section to fail at very low curvatures, primarily governed by premature concrete crushing. Finally, the yielding behaviour is characterized by an upward shift of the elastic limit as plate thickness increases. In these heavily plated sections, the elastic-plastic transition becomes more gradual, indicating a sequential plasticization process where the external steel plate yields prior to the internal longitudinal rebars.

3.2 Impact of ISO 834 Fire Exposure on Flexural Performance

To evaluate the impact of elevated temperatures, the Moment-Curvature analysis was extended into the thermal domain by applying the standard ISO 834 fire curve to both the unreinforced baseline beam and the retrofitted configurations (evaluated under the rigorous theoretical assumption of a perfect bond to exclude premature heat-induced debonding), as comprehensively illustrated in Fig. 3. The initial observation of the structural envelopes highlights a progressive reduction in the elastic stiffness across all sections. As the external concrete cover rapidly heats up, the material experiences a severe degradation of its elastic modulus, rendering the section highly deformable even at low load levels.

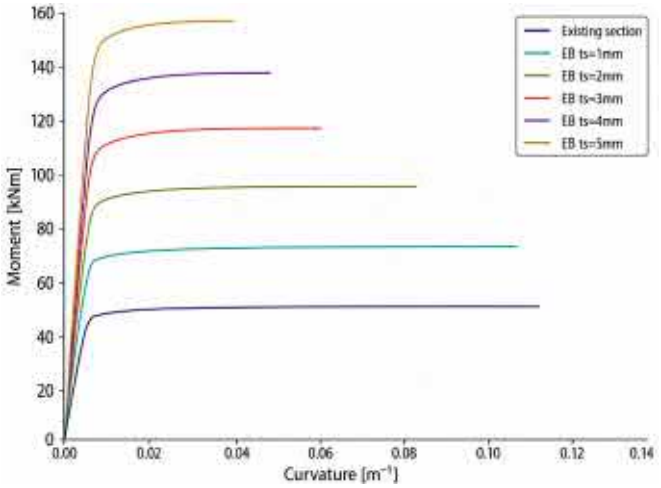


Fig. 2. Moment-Curvature diagrams of the existing section and the externally bonded (EB) retrofitted configurations at ambient temperature.

A profound analysis of the high-temperature envelopes reveals a striking thermo-mechanical paradox: a severe reduction in flexural strength accompanied by an apparent, yet significant, increase in sectional ductility. On one hand, unlike the internal rebars protected by the 30 mm concrete cover, the externally bonded steel plates are directly exposed to the heat source. This triggers a rapid degradation of their yield strength and a consequent, drastic loss of ultimate bending moment across all investigated reinforcement thicknesses (ts = 1–5 mm). By the end of the 60-min exposure (t = 3600 s), the structural benefit of the external plating is almost entirely negated. The residual capacity drops heavily, converging towards a narrow range (approximately 50 to 60 kNm) that asymptotically approaches the baseline unreinforced capacity, rendering the initial geometric over-design futile.

Conversely, this catastrophic loss of strength occurs simultaneously with a massive amplification of the ultimate curvature, which shifts from 0.05 m^{-1} at 60 s to nearly 0.14 m^{-1} at 3600 s. This apparent gain in ductility is directly governed by the thermal degradation of the underlying concrete core. At elevated temperatures, the concrete softens and its ultimate compressive strain capacity increases substantially. Consequently, the cross-section can undergo extreme flexural deformations prior to ultimate crushing. While this thermal softening elongates the curves along the abscissa and prevents a sudden brittle collapse of the concrete, it fundamentally masks the severe structural vulnerability of the strengthening system, which entirely loses its load-bearing function.

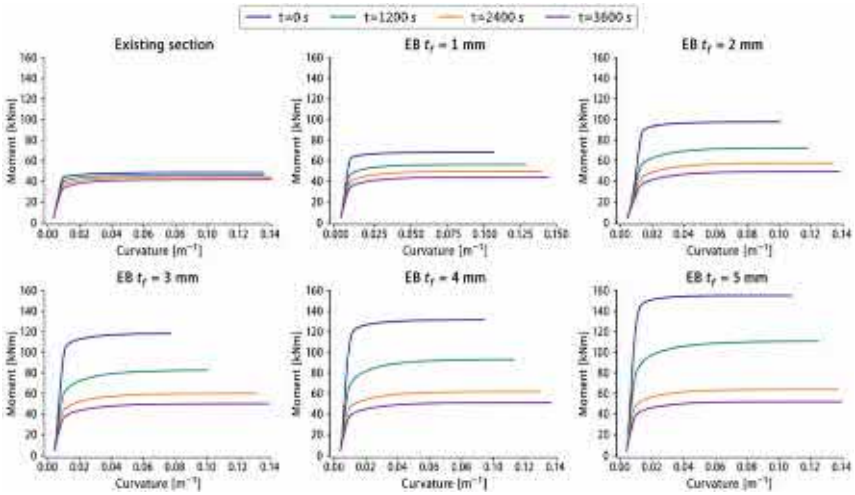


Fig. 3. Moment-Curvature analytical diagrams under the standard ISO 834 fire curve at progressive exposure times (from t = 0 s to t = 3600 s).

4 Conclusions

This study investigated the thermo-mechanical vulnerability of reinforced concrete (RC) elements strengthened to improve flexural strength with external steel plates, aiming to highlight the critical gap between retrofitting effectiveness at ambient temperature and severe performance degradation under fire conditions. The integration of a rigorous systematic literature review with an analytical framework based on temperature-dependent non-linear constitutive laws allowed for the quantification of bearing capacity loss and the identification of dominant failure mechanisms under the standard ISO 834 fire curve. Based on the conducted research, the following main conclusions can be drawn:

- Lack of full-scale experimental evidence: The state-of-the-art review revealed a marked fragmentation of research in this field. Although the thermo-mechanical characterization of individual materials or bonded joints under pure shear is well documented, there is a drastic and concerning lack of experimental fire tests on fully strengthened structural elements (e.g., full-scale beams or columns). To date, this absence of data regarding global flexural behaviour precludes the empirical validation of robust predictive models and the observation of actual macro-scale failure mechanisms.
- Critical vulnerability of the connection interface: In purely externally bonded (EB) systems, the low glass transition temperature of the epoxy adhesive constitutes the true performance limit of the system. Exceeding this thermal threshold, which occurs in the very early stages of fire exposure, triggers a premature and almost instantaneous loss of bond, deactivating the structural contribution of the plate long before the steel or concrete undergoes significant mechanical degradation.

- Ineffectiveness of geometric over-design: The parametric analyses conducted in the case study unequivocally demonstrated that increasing the reinforcement thickness (*ts*) does not confer any additional resilience to the structural element. Being directly exposed to the incident heat flux and lacking the thermal protection provided by the concrete cover, the metal plate rapidly loses its structural effectiveness. After 60 min of ISO 834 exposure, the residual bearing capacity of all strengthened sections asymptotically converges toward that of the unreinforced baseline element, rendering the initial static upgrading entirely futile.
- Crucial need for connection system characterization: The findings underscore the urgent necessity to experimentally and numerically characterize the connection interfaces under fire conditions. Whether dealing with temperature-sensitive epoxy adhesives or mechanical fasteners (e.g., bolted steel plates), the load-transfer mechanism at elevated temperatures ultimately governs global structural survivability. Future research must prioritize the development of temperature-dependent bond-slip models and the assessment of fastener degradation to enable reliable performance-based fire engineering applications.

References

1. Gevorgian A et al (2021) European building stock analysis. Eurac Research
2. Del Grosso A, Inaudi D, Pardi L (2002) Overview of European activities in the health monitoring of bridges. In: Proceedings of the first international conference on bridge maintenance, safety and management, Barcelona
3. Wang Y et al (2025) Multi-physics simulation of adhesives for structural joints in hygrothermal environments considering mechanical degradation. Compos Struct 357:118928
4. Napoli A, Martinelli E, Pecce MR (2024) RC beams externally strengthened by steel plates: experimental database and preliminary analysis. Procedia Struct Integr 64:975–982
5. Teng JG, Smith ST, Yao J, Chen JF (2003) Intermediate crack-induced debonding in RC beams and slabs. Constr Build Mater 17:447–462
6. Seo S, Lim J, Jeong S (2021) Evaluation on the bond capacity of the fire-protected FRP bonded to concrete under high temperature. Int J Concr Struct Mater 15:9
7. Tadeu AJB, Branco FJFG (2000) Shear tests of steel plates epoxy-bonded to concrete under temperature. J Mater Civ Eng 12:74–80
8. Correia ACM (1993) Estudo térmico e envelhecimento higrotérmico de um adesivo de epóxido: comportamento mecânico de juntas coladas. Master's thesis,. University of Coimbra
9. Su RKL, Cheng B, Wang L, Siu WH, Zhu Y (2011) Use of bolted steel plates for strengthening of reinforced concrete beams and columns. IES J Part A Civ Struct Eng 4:55–68
10. Liu X, Li LZ, Lu ZD, Cai ZW (2017) Fire resistance of RC beams strengthened with bolted side-plates. In: Proceedings of the world congress on advances in structural engineering and mechanics
11. Akagwu P, Ali F, Nadjai A (2020) Behaviour of bolted steel splice connections under fire. J Constr Steel Res 170:106103
12. Santiago A, Da Silva LS, Real PV, Vaz G, Lopes AG (2009) Experimental evaluation of the influence of connection typology on the behavior of steel structures under fire. Eng J 46:81–98
13. Lou T, Wang W (2022) Post-fire seismic behaviour of a self-centring connection with buckling-restrained plates and pre-stressed bars. Eng Struct 269:114814
14. Shahabi SEM, Ramli Sulong NH, Shariati M, Shah SNR (2016) Performance of shear connectors at elevated temperatures—a review. Steel Compos Struct 20:185–203

Effects of Temperature on the Dynamic Characterization of Composite Steel-Concrete Highway Decks

Giuseppe Mugnos(✉)

DISMAT s.r.l., Canicattì (AG), Italy
ing.giuseppemugnos@gmail.com

Abstract. Variations in experimentally identified modal parameters are commonly used as indicators of the structural condition of bridges, both during acceptance testing and structural health monitoring. However, interpreting these variations becomes complex when environmental effects - particularly temperature - are not explicitly considered, as they can significantly influence the dynamic response of steel structures. This study analyses the impact of daily temperature fluctuations on the natural frequencies of a composite steel-concrete highway deck, utilizing a dynamic testing campaign conducted over the course of a summer day characterized by high temperatures and marked differences between daytime and evening conditions. Twelve consecutive data acquisition sessions were performed using Operational Modal Analysis techniques based on ambient excitation. The results demonstrate a clear sensitivity of the dynamic parameters to temperature, even in the absence of structural changes. The first natural frequency decreases by approximately 13% as the temperature rises from 38 °C to 46 °C, returning to its initial value during the evening hours. The case study thus highlights the necessity of recording and normalizing thermal conditions when planning and interpreting dynamic tests and monitoring systems for steel and composite decks.

Keywords: Dynamic characterization · steel bridge decks · temperature effects · Operational Modal Analysis · structural health monitoring · thermal influence

1 Introduction

Dynamic characterization tests are a well-established tool for the comprehensive assessment of the structural behaviour of bridges and viaducts. By identifying natural frequencies, mode shapes, and damping coefficients, it is possible to obtain concise information regarding mass distribution, effective stiffness, and the boundary conditions of the structure. Consequently, modal parameters are frequently used both during acceptance testing - to verify the behaviour predicted in the design - and within structural health monitoring systems aimed at detecting potential changes over time.

For major structures, the Technical Standards for Construction (NTC) highlight the value of supplementing static tests with dynamic tests to compare the experimental fundamental period with the design-predicted value [1]. Similarly, the Guidelines for

© The Author(s), under exclusive license to Springer Nature Switzerland AG 2026
R. Zanon et al. (Eds.): CTA 2026, LNCE 942, pp. 502–511, 2026.
https://doi.org/10.1007/978-3-032-39505-4_44

the classification and risk management, safety assessment, and monitoring of existing bridges - along with the UNI 10985 standard - emphasize the importance of proper test planning, the selection of the instrumentation layout, and the interpretation of results [2, 3].

However, using natural frequencies as an indicator of structural condition requires careful interpretation of the experimental data rather than a purely automated analysis.

A change in frequency does not unequivocally indicate an alteration in the structure's health, as it may stem from variations in mass, stiffness, or boundary conditions, or from reversible environmental factors. Among the latter, temperature is particularly significant for steel and steel-concrete composite decks, where restrained thermal expansion, the interaction between the slab and steel girders, and changes in contact conditions can alter the system's apparent stiffness. This paper analyzes this issue with reference to the Himera viaduct on the A19 Palermo-Catania motorway, which was the subject of a dynamic characterization campaign conducted over the course of a full summer day. High daytime temperatures and the temperature fluctuation extending into the evening made it possible to observe significant variations in the identified frequencies on the same structure, without any permanent modifications having been made.

The case study thus offers practical insights for interpreting thermal effects during dynamic testing and for ensuring the repeatability of comparisons over time.

2 Natural Frequencies, Stiffness, and Environmental Variability

In a linear dynamic system, natural frequencies depend on the mass distribution and stiffness. In a simplified form, for a single-degree-of-freedom oscillator, this dependence can be expressed by Eq. (1).

$$f_n = \frac{1}{2\pi}\sqrt{\frac{k}{m}} \tag{1}$$

where k represents the equivalent stiffness and m the participating mass. Although real structures are continuous systems with multiple degrees of freedom, Eq. (1) highlights a fundamental concept: for a given mass, a reduction in effective stiffness leads to a reduction in natural frequencies. For this reason, in structural monitoring, a drop in frequency is often interpreted as a possible sign of deterioration or damage.

This interpretation is valid only when the comparison is made under identical boundary and operating conditions. Thermal variations can cause differential expansion, modify the degree of restraint, alter steel-concrete interaction, and induce reversible strain or stress states. In composite decks, these effects can be particularly pronounced, as materials with different thermal and inertial behaviours contribute jointly to the structural response.

It follows that dynamic testing retains high diagnostic value only if modal data are interpreted in conjunction with environmental conditions. Consequently, during acceptance testing, periodic inspections, and Structural Health Monitoring operations, temperature must be measured, recorded, and - whenever possible - used to normalize dynamic parameters before comparing them against thresholds or reference values [6, 7].

Experimental literature has extensively documented this issue. Annual monitoring of the Z24 Bridge highlighted the need to model environmental variability - specifically thermal effects - to distinguish normal frequency fluctuations from damage events [8]. Analyses of the Ting Kau Bridge revealed correlations (including non-linear ones) between structural temperatures and modal parameters identified through long-term monitoring [9]. With specific regard to steel decks, Ding and Li observed a general decrease in frequencies as temperature rose, as well as varying sensitivity among individual modes [10]. This study is situated within this context, focusing on the intra-day frequency variability of a composite steel-concrete highway deck through twelve consecutive OMA acquisitions.

3 Case Study: The Himera Viaduct

The Himera viaduct is located along the A19 Palermo-Catania motorway, near the Scillato interchange, on the carriageway heading towards Catania. The new deck replaces the previous viaduct and consists of three continuous spans using a composite steel-concrete system. The structural configuration features two main steel girders with variable cross-sections, connected transversely by vertical and horizontal bracing, and a reinforced concrete deck slab (Figs. 1 and 2).

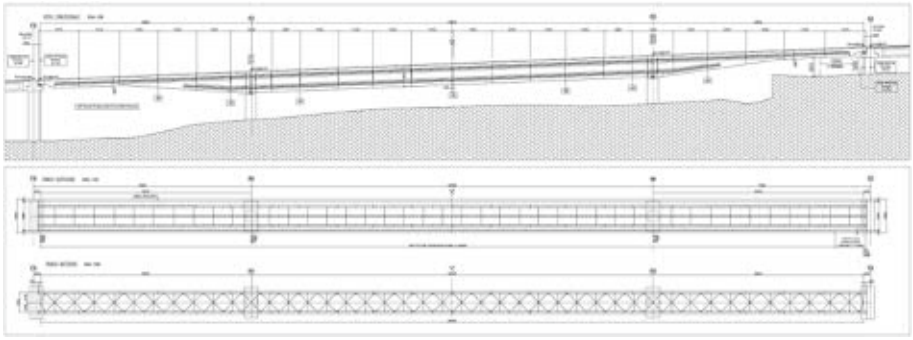


Fig. 1. Plan and longitudinal profile of the Himera viaduct

The two side spans have a span length of 68.00 m, measured between the bearing axes, while the central span has a length of 129.63 m. The roadway is 9.30 m wide, with 0.75 m edge curbs; the spacing between the two main girders is 6.30 m. The girder depth varies from a minimum of 2.50 m to a maximum of 6.50 m. These characteristics make the structure particularly suitable for assessing the dynamic sensitivity of a long-span composite deck, in which the steel component, the concrete slab, and the boundary conditions all contribute to defining the overall stiffness (Fig. 3).



Fig. 2. General view of the motorway deck during the testing campaign

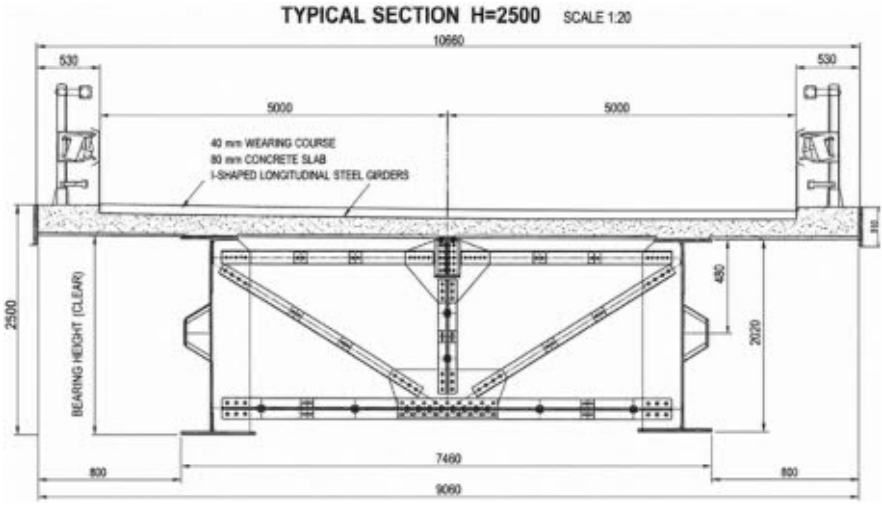


Fig. 3. Cross-section of the bridge deck

4 Experimental Campaign

The testing campaign was conducted on July 30, 2020, through dynamic ambient data acquisition in the absence of vehicular traffic. Structural excitation relied on ambient forces and natural vibrations present during the test, following an approach consistent with Operational Modal Analysis techniques [4, 5].

Twelve consecutive acquisitions were performed, each lasting 2,700 s (45 min). The first measurement began at 11:04 and the last concluded at 23:16, allowing the structural

response to be monitored from the hottest daytime hours through to evening conditions (Fig. 4).



Fig. 4. Timeline of the dynamic acquisitions carried out during the testing day

The transition from the first to the second setup took place between the sixth and seventh data acquisition runs. Three reference accelerometers were kept in the same positions to link the data from the two layouts and reconstruct the overall behaviour of the entire deck (Fig. 5).

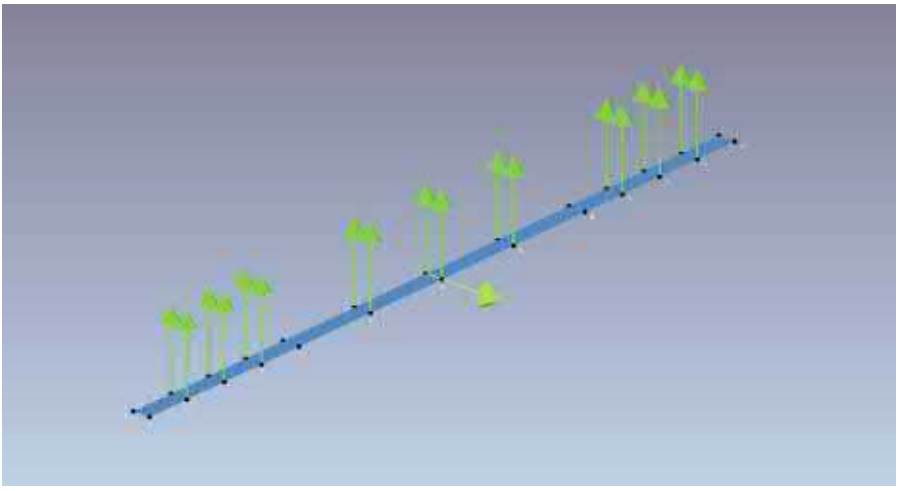


Fig. 5. Overall layout of the accelerometers after merging the two test setups

The main acquisition parameters remained constant throughout all measurements: ambient excitation in the absence of vehicular traffic, two experimental setups, ten vertical channels and one transverse horizontal channel per setup, a sampling frequency of 100 Hz, and an acquisition duration of 2700 s. Measurement points were located at significant sections - such as quarter-spans and mid-spans - to reconstruct the primary

mode shapes. Signal processing enabled the identification of natural frequencies, mode shapes, and damping ratios.

5 Modal Identification and Experimental Results

Analysis of the acquired signals made it possible to identify the deck's principal natural frequencies. The mean values derived from the entire set of acquisitions were 1.16, 1.84, 2.10, 2.49, 3.16, and 4.02 Hz. The average damping factor, estimated in the time domain using the logarithmic decrement method on signal windows characterized by sufficiently distinct oscillations, was found to be in the order of 1.7% (Fig. 6).

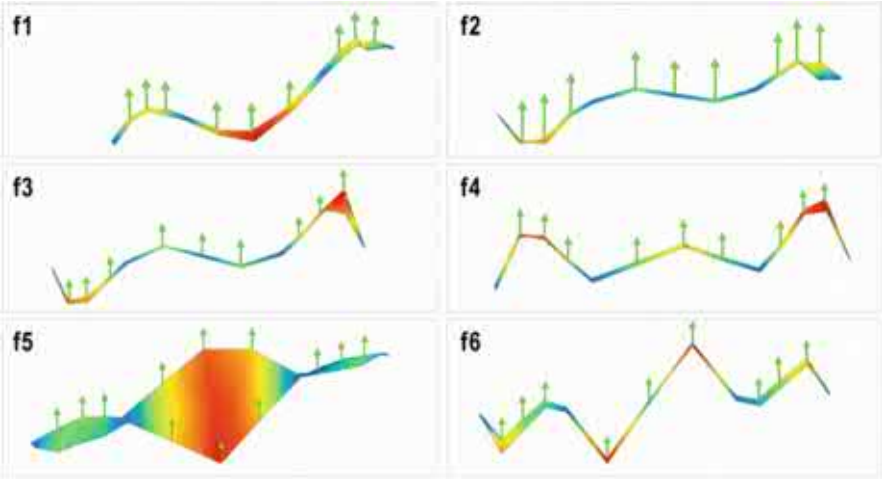


Fig. 6. Main modal shapes identified on the deck and associated average frequencies

The identified frequencies provide a comprehensive description of the deck's response. However, using them as reference values for tests conducted at different times requires taking into account changes in environmental conditions. In the case at hand, the test day was characterized by high temperatures and significant differences between midday and evening hours.

6 Effects of Temperature on the Identified Frequencies

The influence of temperature on the dynamic response of a bridge deck cannot be attributed solely to variations in the mechanical properties of the materials. In composite steel-concrete structures, thermal effects operate at multiple levels: they induce longitudinal expansion, can generate thermal gradients between the slab and the steel girders, alter the deck's deformation state, and may temporarily modify contact and boundary conditions at the supports and connection devices. From a dynamic perspective, these phenomena result in a change in the effective stiffness experienced by the

structure during vibration. Since natural frequencies depend on the ratio of stiffness to mass, even reversible thermal fluctuations can produce measurable shifts in modal parameters, despite the absence of permanent changes to the structural state.

The effect of temperature does not necessarily manifest with the same intensity across all vibration modes. Each mode engages different portions of the structure and is affected differently by stiffness distribution, boundary conditions, and the interaction between primary and secondary elements. Consequently, the analysis must critically evaluate the sensitivity of individual modes to thermal conditions, rather than assuming a uniform shift in frequencies.

To highlight the influence of temperature, three datasets representative of the daily thermal cycle were selected: Acquisition 1, recorded between 11:04 and 11:49 with an external temperature of 38 °C; Acquisition 4, recorded between 14:18 and 15:03 with a temperature of 46 °C; and Acquisition 12, recorded between 22:31 and 23:16 with a temperature of 33 °C. The comparison is particularly significant because it involves the same structure over the course of a few hours, during which it is not reasonable to assume permanent structural changes (Table 1).

Table 1. Comparison of representative acquisitions at different temperatures

Acq.	Time	T [°C]	f1 [Hz]	f2 [Hz]	f3 [Hz]	f4 [Hz]	f5 [Hz]	f6 [Hz]
1	11:04–11:49	38	1,16	1,81	2,05	2,49	3,18	4,03
4	14:18–15:03	46	1,01	1,75	2,01	2,29	3,02	3,97
12	22:31–23:16	33	1,17	1,83	2,12	2,49	3,13	4,03

The comparison reveals a reduction in frequencies during the hottest hours, followed by a recovery in the evening. Specifically, the first frequency drops from 1.16 Hz in the first acquisition to 1.01 Hz in the fourth—a reduction of approximately 13%—before rising back to 1.17 Hz in the twelfth acquisition. Similar behavior is observed for other modes; for instance, the fourth frequency shifts from 2.49 Hz to 2.29 Hz and subsequently returns to 2.49 Hz.

The reversibility of this phenomenon is the most significant aspect from an interpretive standpoint. Since the variation was observed in the same structure over the course of just a few hours, it cannot reasonably be attributed to the progression of damage or a permanent structural alteration. Consequently, the experimental data must be interpreted as the result of varying thermal conditions, which temporarily alter the apparent stiffness of the deck and, in turn, the identified frequencies.

To allow for a direct comparison of the results, Fig. 7 presents frequencies normalized against Acquisition 1, while Fig. 8 quantifies the reductions observed at the peak representative temperature. All selected modes exhibit a decrease during Acquisition 4 followed by a recovery in the evening hours, albeit with varying magnitudes. The first mode proves to be the most sensitive, showing a 12.9% reduction, followed by the fourth and fifth modes with variations of 8.0% and 5.0%, respectively. Variations in the other modes are more limited. This non-uniform response suggests that the thermal

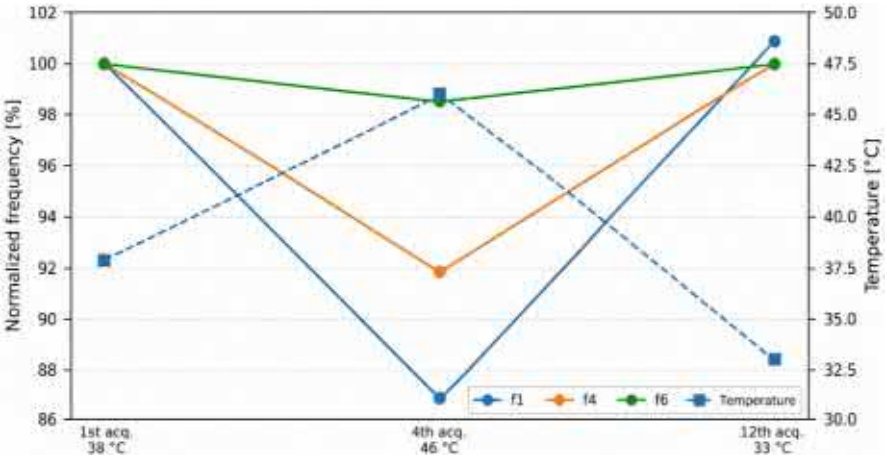


Fig. 7. Evolution of external temperature and normalised frequencies in three representative acquisitions

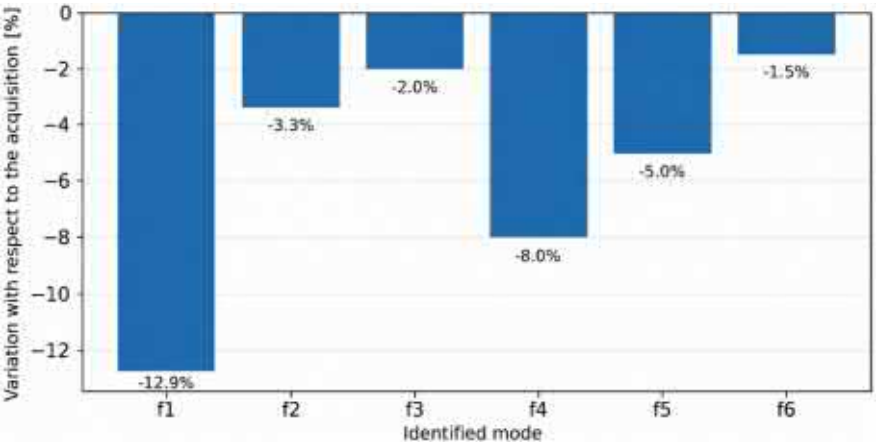


Fig. 8. Percentage variation of the frequencies in the fourth acquisition with respect to the first acquisition

effect depends on the varying degrees to which global and local stiffnesses, boundary conditions, and steel-concrete interaction contribute to each mode shape.

7 Discussion

The case of the Himera viaduct clearly demonstrates the role of environmental conditions in the interpretation of modal parameters. Frequency variations were observed on the same structure, on the same day, and without any intervening structural modifications between tests. Temperature thus acts as a contextual variable capable of significantly altering the dynamic response of the bridge deck.

This finding is particularly significant in the context of dynamic acceptance testing and structural health monitoring. A reduction in natural frequencies could be interpreted as a loss of stiffness associated with deterioration, damage, or changes in boundary conditions. However, without measuring or correcting for thermal conditions, such an interpretation could be misleading. Although dynamic data are highly informative, they should not be viewed as absolute indicators independent of the operational context.

From a practical standpoint, comparing dynamic tests conducted at different times should involve planning to replicate climatic conditions as closely as possible. When this is not feasible, it is necessary to record air temperature—and preferably the surface temperature of structural elements—to assess the potential normalization of modal parameters. This requirement is especially important for steel or composite steel-concrete decks, which can be highly sensitive to daily temperature fluctuations.

The available dataset is limited to a single summer day and to measurements of external air temperature. Consequently, the results do not allow for the development of a general predictive model for the temperature-frequency relationship, nor do they enable the separation of effects attributable to uniform temperature, thermal gradients, and bearing conditions. Long-term monitoring, supplemented by sensors distributed across the deck, the steel beams, and at the supports, would allow for a more comprehensive characterization of environmental variability and its comparison with any changes in structural condition.

8 Conclusions

This study analysed the influence of thermal conditions on the dynamic characterization of a continuous composite steel-concrete highway deck, using the Himera viaduct on the A19 Palermo-Catania motorway as a case study. The experimental campaign, conducted over the course of a full summer day involving twelve sets of ambient dynamic measurements, made it possible to observe the evolution of modal parameters in relation to temperature.

A comparison of representative measurements revealed a significant reduction in frequencies during the hottest period, followed by a recovery during the evening hours. The first natural frequency dropped by approximately 13% between measurements taken at 38 °C and 46 °C, subsequently returning to its initial value when the temperature fell to 33 °C. Other modes also exhibited reversible variations, albeit with varying degrees of sensitivity.

Since these variations were observed on the same structure within a limited timeframe, they must be interpreted as a reversible environmental effect rather than an indicator of permanent structural changes. Consequently, dynamic testing must be accompanied by accurate monitoring of thermal conditions, and longitudinal comparisons should be performed under comparable climatic conditions or by employing appropriate environmental normalization procedures.

Acknowledgments. The author gratefully acknowledges DISMAT Laboratory s.r.l. for supporting the experimental activities and for providing the technical material used in this study.

References

1. Ministry of Infrastructure and Transport (2018) Ministerial Decree of 17 January 2018: update to the technical standards for construction. Official Gazette No. 42, Rome
2. Ministry of Sustainable Infrastructure and Mobility (2022) Guidelines for the classification and management of risk, safety assessment, and monitoring of existing bridges. Ministerial Decree No. 204 of 1 July 2022, Rome
3. UNI (2002) UNI 10985:2002, vibrations on bridges and viaducts – guidelines for performing dynamic tests and measurements. Italian Standards Body (UNI), Milan
4. Brincker R, Zhang L, Andersen P (2001) Modal identification of output-only systems using frequency domain decomposition. Smart Mater Struct 10:441–445
5. Peeters B, De Roeck G (2001) Stochastic system identification for operational modal analysis: a review. J Dyn Syst Meas Control 123:659–667
6. Farrar CR, Worden K (2013) Structural health monitoring: a machine learning perspective. Wiley, Chichester
7. Sohn H (2007) Effects of environmental and operational variability on structural health monitoring. Philos Trans R Soc A 365:539–560
8. Peeters B, De Roeck G (2001) One-year monitoring of the Z24-bridge: environmental effects versus damage events. Earthq Eng Struct Dyn 30(2):149–171
9. Ni YQ, Hua XG, Fan KQ, Ko JM (2005) Correlating modal properties with temperature using long-term monitoring data and support vector machine technique. Eng Struct 27(12):1762–1773
10. Ding YL, Li AQ (2011) Temperature-induced variations of measured modal frequencies of steel box girder for a long-span suspension bridge. Int J Steel Struct 11(2):145–155

Fire Assessment of Steel–Concrete Composite Bridges: Fragility and Life-Cycle Cost Evaluation of Alternative Passive Fire Protection System

Donatella de Silva[1], Andrea Miano[2(✉)], Gabriella De Rosa[1], and Emidio Nigro[1]

[1] University of Naples "Federico II", Naples, Italy
donatella.desilva@unina.it
[2] University Pegaso, Naples, Italy
andrea.miano@unipegaso.it

Abstract. Steel and steel-concrete composite (SCC) bridges are highly vulnerable to fire due to the rapid heating of steel, which significantly reduces its mechanical properties. This study evaluates the effectiveness of passive fire protection systems for SCC bridges by combining probabilistic fragility analysis with life-cycle cost assessment. The methodology includes realistic fire scenarios based on vehicle fires beneath the bridge deck, nonlinear thermo-mechanical simulations performed with SAFIR, and the development of fragility curves relating structural performance to fire intensity measures. A representative SCC bridge is analyzed under five configurations: one unprotected and four protected with different thicknesses of spray-applied fire-resistant material. Results show that passive fire protection significantly improves bridge fire performance, reducing the probability of exceeding critical performance thresholds. While greater insulation thickness generally increases effectiveness, the additional benefits diminish at higher thickness levels. The life-cycle cost analysis also highlights the potential economic advantages of implementing passive fire protection strategies.

Keywords: Fire resistance · passive fire protection · bridges · life-cycle cost

1 Introduction

Bridges are key components of transportation infrastructure and may be significantly affected by fire events, leading to structural damage, safety risks, and high economic losses [1–4]. Steel and steel-concrete composite bridges are particularly vulnerable due to the high thermal conductivity of steel, which causes rapid temperature increase and a consequent reduction in stiffness and load-bearing capacity [5–7]. Fire is often given less attention than hazards such as earthquakes, wind, or snow loads in bridge design practice. Nevertheless, several studies have highlighted that fire-related bridge failures occur more frequently than failures associated with some traditional environmental hazards

© The Author(s), under exclusive license to Springer Nature Switzerland AG 2026
R. Zanon et al. (Eds.): CTA 2026, LNCE 942, pp. 512–524, 2026.
https://doi.org/10.1007/978-3-032-39505-4_45

[8]. The consequences of bridge damage extend beyond repair costs. Bridge closures disrupt transportation networks, increase travel times, generate detours, and produce significant economic losses for both road users and local economies [9–11]. These impacts demonstrate the need for more effective fire safety strategies in bridge engineering. Passive fire protection systems offer a practical solution for improving structural resilience during fire exposure. Although their implementation involves additional construction and maintenance costs [12, 13], these measures can substantially reduce the likelihood of collapse and the associated social and economic consequences. Within this context, Performance-Based Fire Safety Design (PBFSD) provides a flexible framework for developing optimized protection strategies tailored to specific fire scenarios. This study proposes an integrated methodology combining fire fragility analysis and life-cycle cost-benefit assessment to evaluate passive fire protection solutions for bridges. By linking structural vulnerability, fire performance, and economic efficiency, the framework supports informed decision-making and the optimization of fire protection strategies for critical infrastructure.

2 Methodology

The proposed methodology consists of an integrated approach for the assessment of structural fire fragility and cost-benefit analysis. As shown in the Fig. 1, it is organized into five steps: (1) general setting, (2) fire modelling, (3) thermo-structural modelling, (4) fragility assessment, and (5) cost–benefit analysis.

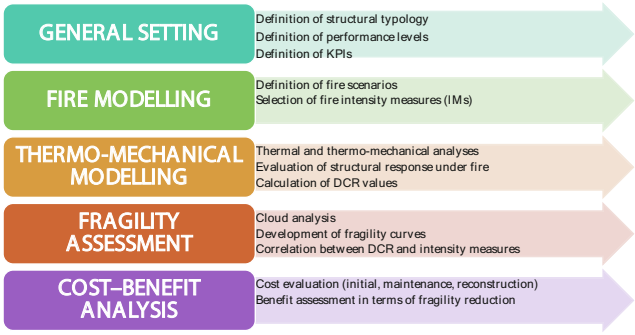


Fig. 1. Flowchart illustrating the methodology followed in the study.

In the first step, the structural typology and the performance levels are defined, along with the reference Key Performance Indicators (KPIs), such as deformations and displacements. In the second phase, the representative fire scenarios for the considered structural typology are established, and the corresponding intensity measures (IMs) are defined to quantify the fire demand and correlate it with the fragility curves developed in the subsequent steps. The third step involves performing thermal analyses of the structural sections and thermo-mechanical analyses of the structure, in order to obtain the corresponding DCR values. The fourth step consists of a Cloud Analysis [14] aimed

at developing fragility curves for the selected performance levels as a function of the defined intensity measures. The final phase applies to a cost-benefit approach, considering initial, maintenance, and reconstruction costs, and evaluating the benefits in terms of the reduction of structural fire fragility.

2.1 Performance Levels Definition

The definition of performance levels for bridge structures under fire conditions remains an open issue, as international [15] and national standards [16] do not provide specific criteria for this type of infrastructure. To overcome this gap, the performance classification proposed by de Silva et al. [17] is adopted, as it was specifically developed for the bridges exposed to fire. The methodology defines four performance levels (PLs) based on damage and serviceability requirements, see the Table 1.

Table 1. Performance levels for bridge under fire conditions.

PL	Description
I	The bridge must be held for the time required for evacuation
II	The bridge must withstand the duration of the fire
III	Max displacement should be limited to L/100 for the duration of the fire and residual displacement should be limited to 50% Δin
IV	Max displacement should be limited to L/250 for the duration of the fire and residual displacement should be limited to 20% Δin

The assessment is performed through two KPIs: the maximum vertical displacement during the heating phase (SC1) and the residual vertical displacement after cooling (SC2), where Δin represents the initial displacement due to vertical loads. Among the performance levels, PL III and PL IV are considered, corresponding respectively to a limited damage state and the full post-fire functionality. In this study, only the SC1 criterion is adopted as the governing KPI, since the maximum displacement reached during fire represents the most critical condition for the structural response.

2.2 Fire Modelling and Thermo-mechanical Analyses

The definition of representative fire scenarios is a key step in structural fire engineering to evaluate the thermal and mechanical response of bridges under realistic fire conditions. Representative scenarios may include single or multiple vehicle fires and are used as input for thermo-mechanical analyses. Different fire modelling approaches may be applied depending on the nature of the fire scenario. In open environments such as bridges and outdoor car parks [18], flashover conditions are generally unlikely, which makes localized fire models more appropriate. Also simplified methods such as the Hasemi [19], provided in Annex C of EN 1991–1-2 [15], are usually adequate to estimate the heat flux acting on structural elements. When the assumptions underlying simplified models

are not satisfied, more advanced Computational Fluid Dynamics (CFD) simulations are required to capture the complex behavior of the fire. Finally, temperature-dependent material properties are defined in accordance with EN 1992-1-2 [20] and EN 1993-1-2 [21], accounting for the progressive degradation of strength and stiffness at elevated temperatures. Thermo-mechanical analyses are performed using SAFIR [22] to evaluate the structural behavior under different fire scenarios. Both protected and unprotected configurations are considered, including the influence of passive fire protection systems. The sprayed plaster was modelled using thermo-physical properties derived from experimental studies reported in the literature, such as those by Venezia et al. [23] and Cibelli et al. [24]. These works provide temperature-dependent correlations for thermal conductivity, specific heat, and density, enabling a realistic representation of the protective layer within the SAFIR numerical framework.

2.3 Fragility Assessment

Fragility curves for both unprotected and protected configurations are developed for Performance Levels III and IV through Cloud Analysis. This approach combines results from thermo-mechanical simulations with a probabilistic formulation based on log-linear regression models [14]. The limit state function is defined in terms of the demand-to-capacity ratio (DCR), calculated as the ratio between the maximum vertical deck displacement and the corresponding limiting displacement associated with each Performance Level. The probability of exceedance is then expressed as a function of two fire IMs: fire load Q and HRR peak. The fragility assessment is performed considering both IMs and both PLs, and it is extended to five structural configurations: the unprotected case and four different thicknesses of passive fire protection (10 mm, 14 mm, 20 mm and 30 mm). This allows the influence of protective systems on fire structural vulnerability to be quantified.

2.4 Life Cycle Cost-Benefit Analysis

The life cycle cost-benefit analysis was used to evaluate the overall effectiveness of passive fire protection systems for a bridge subjected to fire exposure. The adopted methodology follows the model proposed by Ma et al. [25], in which the total structural life-cycle cost is defined as follows:

$$PVLCC = C_I + C_M + D_D + D_I \tag{1}$$

C_I represents the initial costs, including the structure itself, labour, scaffolding, and the fire protection system when present. C_M denotes the maintenance costs associated with both the structure and the passive protection system; it was evaluated according to the formulation proposed by Miano et al. [26], expressed by (2):

$$C_M = \int_0^{t_{life}} C_m \, e^{-\lambda_d \, t} dt = \frac{C_m}{\lambda_d}\left(1 - e^{-\lambda_d \, t_{life}}\right) \tag{2}$$

The total cost also includes both direct D_D and indirect damages D_I. Direct costs are evaluated are estimated based on the repair or reconstruction costs associated with the

damage levels experienced by the structure, using fragility curves that relate performance levels to proportional economic losses. The quantification of direct damage follows the Eq. (3) and datasets provided in [27]:

$$D_D = EL_{STR} = FV_{STR}\, RV_B \sum_{i=1}^{n} (PSTR_{PLi} \cdot STRD_{PLi}) \tag{3}$$

EL_{STR} denotes the expected structural repair cost, while FV_{STR} represents fraction of the total replacement value associated with the structural components. RV_B is the overall replacement value of the structure. $PSTR_{PLi}$ indicates the probability that the structure reaches the performance level PLi, whereas $STRD_{PLi}$ defines the corresponding repair cost ratio, expressed as a percentage of the total structural replacement cost. PL III corresponds to a complete damage state, associated with a repair/reconstruction cost equal to 100% of the replacement cost, while PL IV corresponds to a moderate damage state, associated with 50% of the replacement cost. The Indirect Cost D_I accounts for the wider socio-economic consequences of a fire, including downtime and loss of functionality. Its estimation is based on the empirical formulation proposed in [28]:

$$D_I = c\,(D_D)^b \tag{4}$$

where c and b are parameters that depend on the scale and consequences of the event.

In this study, the coefficients corresponding to the local scale are adopted with $c = 0.203$ and $b = 1.146$.

The uncertainties in the life-cycle cost assessment mainly derive from the probabilistic fragility analysis and the adopted economic models. Additional uncertainties related to cost variability due to market conditions and project-specific factors are not explicitly considered in the present study.

3 Application

The proposed methodology is applied to a representative case study of a steel-concrete composite (SCC) bridge, previously analyzed [17]. The fire fragility analysis is carried out considering five configurations: the unprotected bridge and four protected cases, corresponding to sprayed plaster thicknesses of 10 mm, 14 mm, 20 mm and 30 mm. The aim is to evaluate the effectiveness of passive fire protection in reducing the fire bridge vulnerability while supporting the optimal design of the protection system through an integrated consideration of both structural performance and life-cycle costs.

3.1 Typological Steel-Concrete Bridge Description

The case study concerns a SCC bridge composed of four simply supported spans. The analysis focuses on the longest span (32.23 m), which also has the lowest clearance to the ground (7.95 m), making it the most vulnerable to fire exposure. The deck consists of two main longitudinal girders and five cross-beams spaced at 5 m intervals. The structural system is modelled as simply supported beam with one end restrained and the

other allowed to slide longitudinally. The bridge was designed in accordance with [28]. The structural materials adopted in the case study consist of Fe510 (S355) structural steel, concrete with characteristic compressive strength Rck > 40 MPa (C32/40), and reinforcing steel bars Feb44k (B450C). Material properties and loading conditions in case of fire are defined in accordance with Eurocodes [15, 20, 21, 29, 30] and Italian Standards [31], and a localized mid-span fire scenario is considered.

3.2 Fire Scenarios and Fire Modelling

The fire scenarios were defined considering vehicle-induced fires occurring beneath the bridge deck. Each vehicle type is represented by a specific heat release rate (HRR) curve derived from experimental data or literature sources [32, 33], including heavy goods vehicles, buses, cars, tankers, half-loaded HGVs, and motorcycles, shown in the Table 2.

Table 2. Fire scenarios (FS).

FS	Vehicles	HRR Peak (kW)	Q (GJ)	FS	Vehicles	HRR Peak (kW)	Q (GJ)
S1	HGV	206500	240.0	S4	TANKER	296430	472.0
S1.1	HGV.HGV	413000	480.0	S4.4	TANKER.TANKER	592860	944.0
S1.2	HGV.BUS	225323	292.0	S4.5	TANKER.1/2HGV	399680	592.0
S1.3	HGV.CAR1	210397	245.0	S5	1/2HGV	103250	120.0
S1.4	HGV.TANKER	502930	712.0	S5.5	1/2HGV. 1/2HGV	206500	240.0
S1.5	HGV.1/2HGV	309750	360.0	S6	MOTO	1324	0.6
S2	BUS	39500	52.0	S6.6	MOTO.MOTO	2643	1.2
S2.2	BUS.BUS	79000	103.0	S6.6.6	MOTO.MOTO.MOTO	3972	1.8
S2.3	BUS.CAR1	43830	57.0	S6.6.6.6	MOTO.MOTO.MOTO.MOTO	5296	2.4
S2.4	BUS.TANKER	335930	523.0	S6.3	MOTO.CAR1	5719	5.6
S2.5	BUS.1/2HGV	122073	172.0	S6.3.3	MOTO.CAR1.CAR1	10114	10.6
S3	CAR1	4395	5.0	S6.6.3.3	MOTO.MOTO.CAR1.CAR1	11438	11.2
S3.3	CAR1. CAR1	8790	10.0	S6.2	MOTO.BUS	39500	52.6
S3.3.3	CAR1. CAR1.CAR1	13185	15.0	S6.6.2	MOTO.MOTO.BUS	38782	53.2
S3.4	CAR1.TANKER	300825	477.0	S7	CAR2	1473	4.0
S3.5	CAR1.1/2HGV	107147	125.0				

Temperature development in the near-field region is evaluated using the Hasemi [19] model in accordance with EN 1991–1-2 Annex C [15]. For scenarios exceeding the validity range of the analytical model, computational fluid dynamics simulations are performed using the Fire Dynamics Simulator (FDS) [34], allowing the determination of spatial temperature distributions around the structural members. The resulting thermal

fields are subsequently applied as boundary conditions in the thermo-mechanical analysis of the bridge.

3.3 Passive Protection Modelling

The thermo-mechanical analyses were performed considering two structural configurations: unprotected structure and structure protected with sprayed plaster. The thermal properties, including thermal conductivity, specific heat, and density, used in the simulations are defined as temperature-dependent parameters and calibrated against experimental results [23, 24] obtained from cone calorimeter tests (see Table 3).

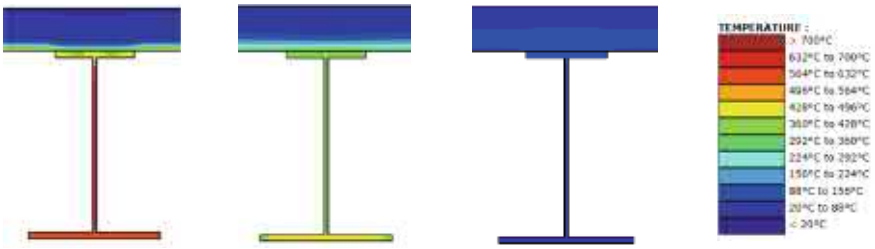
Table 3. Input physical and thermal properties of protective material in the numerical model.

c [J/kgK]	ρ_{dry} [kg/m^3]	w [kg/m^3]	θ_{start} [°C]	θ_{end} [°C]	h_c [W/m^{2}K]	ε [−]
1000	423	210	100	105	25	0.65

4 Results and Discussion

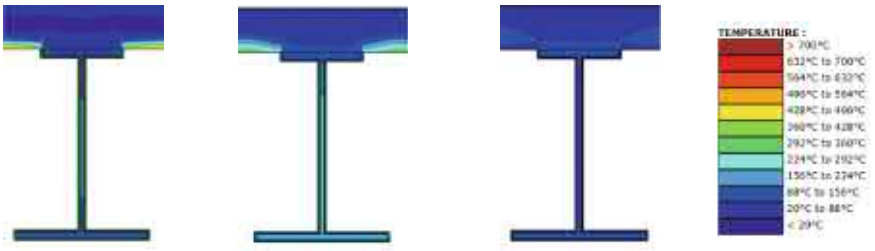
4.1 Thermal Analyses

Thermal analyses were performed for the 31 fire scenarios on the structural cross-sections, evaluating both the unprotected configuration and the protected configuration with four different thicknesses of passive fire protection (10 mm,14 mm, 20 mm and 30 mm). The transient thermal simulations were carried out over a total duration of 36 h, allowing the structural sections to return to ambient temperature after fire exposure. The results highlight the effectiveness of passive protection systems. Increasing the thickness of the protective layer produces a progressive reduction in the temperature increase of the steel section, see the Fig. 1. However, the improvement in thermal performance tends to decrease beyond a certain thickness, indicating that the benefits associated with additional insulation become progressively less significant. Furthermore, the presence of the protection layer influences not only the heating phase but also the cooling phase. Due to its low thermal conductivity, the protective material slows down heat dissipation from the steel components. Protected sections exhibit a lower cooling rate compared with unprotected sections, maintaining higher temperatures for a longer period after the end of fire exposure, see the (Figs. 2 and 3).



t= 30 min *t= 90 min* *t=180 min*

a) *unprotected main beam*



t= 30 min *t= 90 min* *t= 180 min*

b) protected main beam (10 mm)

Fig. 2. Thermal analyses output for fire scenario S2 fore a) bare and b) 10 mm protected configurations.

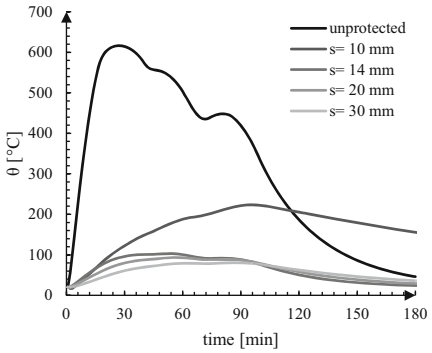


Fig. 3. Temperature in the bottom flange of steel main profile for unprotected configuration and for protected ones; fire scenario S2.

4.2 Thermo-mechanical Analyses

Thermo-mechanical analyses were carried out on both the unprotected and protected structure in order to understand the structural response to fire, in terms of the demand-to-capacity ratio of vertical midspan displacement. The results show, as in the thermal analyses, a reduction in the demand-to-capacity ratio and therefore an improvement in the structure's fire performance as the thickness of the protective material increases. The Fig. 4 shows the vertical midspan displacement for the unprotected and the protected configurations. The results highlight a reduction in vertical displacement with increasing protection thickness, confirming the effectiveness of passive fire protection in improving the structural response under fire conditions.

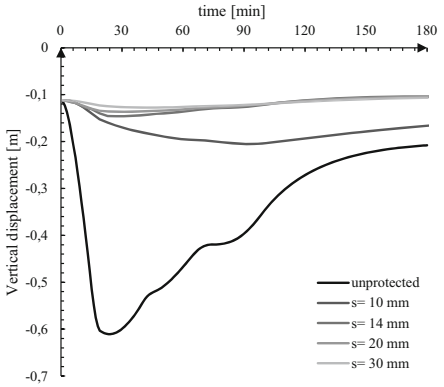


Fig. 4. Vertical midspan displacement for the Scenario S.2.

4.3 Fragility Curves

The fragility curves were developed from the DCR results associated with the 31 fire scenarios for the two performance levels investigated, PL III and PL IV. The analyses were carried out for both the unprotected configuration and the protected ones with four different protective thicknesses. A logarithmic linear regression was performed to establish a relationship between the DCR values, and the fire intensity measures, the fire load and the peak value of the HRR curve. The results show that increasing the thickness of the protective layer leads to a reduction in the fragility curve and a shift of the curve towards higher values of the intensity measure, see the (Figs. 5 and 6). The protective material reduces the fire-induced fragility of the structure; as the thickness of the protection increases, the probability of exceeding a given performance level decrease.

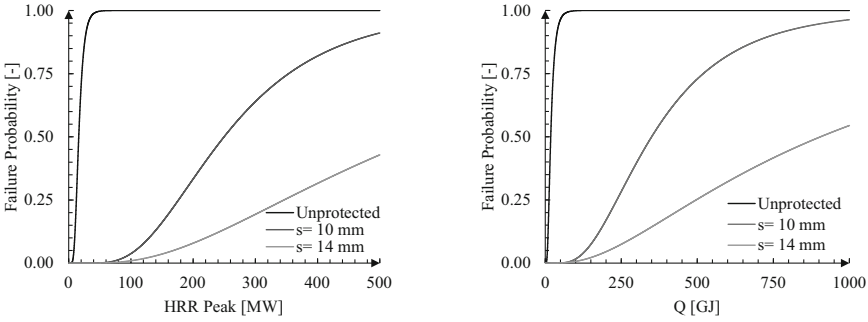


Fig. 5. Fragility curve for PLIII: a) HRR peak as IM; b) Q as IM.

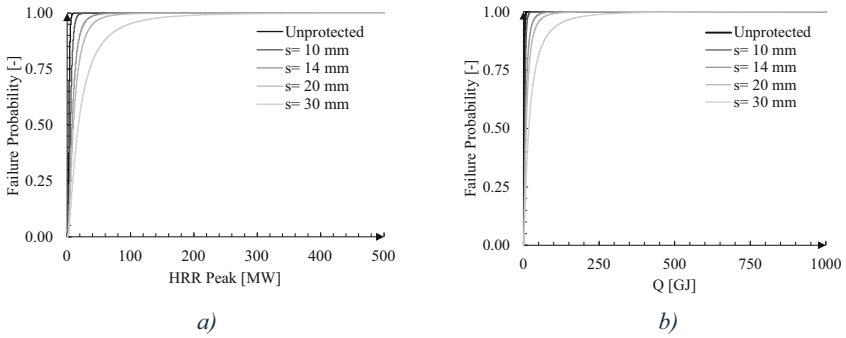


Fig. 6. Fragility curve for PL IV: a) HRR peak as IM; b) Q as IM.

4.4 Life Cycle Cost Analysis

A Life Cycle Cost Analysis (LCCA) was performed to evaluate the economic effectiveness of passive fire protection solutions over the service life of the bridge, 100 years.

The total life-cycle cost was evaluated by combining the initial construction cost of the fire protection system with the expected damage-related costs obtained from the probabilistic fire assessment. The results, shown in Fig. 7, indicate that the unprotected configuration exhibits a significant increase in LCC, reaching high values as the fire intensity increases. This result confirms the high vulnerability of the bridge when no passive protection is provided.

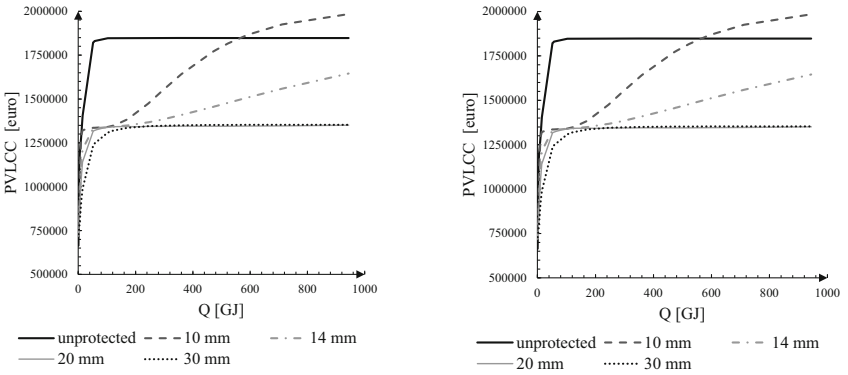


Fig. 7. LCCA curves: a) HRR peak as IM; b) Q as IM.

The use of protection leads to a considerable reduction in LCC, with the effectiveness increasing for larger thickness. In particular, the 20 mm and 30 mm protection layers show almost constant costs with increasing fire severity, demonstrating their ability to limit structural damage even under severe fire scenarios. Instead, the lower thicknesses (10 mm and 14 mm) provide only a partial reduction in costs. Although they improve the structural response compared to the unprotected case, the LCC still increases for more severe fires. These solutions may therefore be suitable for moderate fire scenarios but are less effective for high-intensity events. Overall, the results underline the importance of selecting an appropriate fire protection thickness through a performance-based approach, considering both structural safety and economic efficiency.

5 Conclusions

This study presented an integrated framework for the assessment of bridge performance in fire condition, combining thermo-mechanical simulations, fragility curves, and life-cycle cost evaluation. The thermal analyses showed that the use of passive fire protection reduces the temperature rise in steel cross-sections, with increasing thickness leading to improved insulation performance. However, the marginal benefit decreases for higher thickness values, and the presence of insulation also delays the cooling phase due to its low thermal conductivity. The thermo-mechanical results confirmed these trends, showing a progressive reduction in the demand-to-capacity ratio, as the thickness of the protective material increases. This demonstrates a clear improvement in the structural fire performance when passive protection is adopted. Based on these results, fragility curves were developed for two performance levels, PL III and PL IV. The results highlight a consistent reduction in structural vulnerability with increasing protection thickness, together with a shift of the curves toward higher fire intensity values, indicating a lower probability of exceeding damage states.

Finally, the life-cycle cost analysis demonstrated the economic benefits of passive protection. The unprotected configuration exhibits a rapid increase in LCC with fire severity, while thicker protection layers (20 mm and 30 mm) maintain nearly constant

costs across all scenarios. In contrast, thinner layers (10 mm and 14 mm) provide only partial economic benefits, being effective mainly under moderate fire conditions.

Overall, the study highlights the importance of a performance-based approach that integrates thermal response, structural behaviour, fragility assessment, and economic analysis to identify efficient fire protection strategies for bridges.

References

1. Kodur VKR, Gu L, Garlock MEM (2010) Review and assessment of fire hazard in bridges. Transp Res Rec 2172(1):23–29
2. Hu J, Carvel R, Usmani A (2021) Bridge fires in the 21st century: a literature review. Fire Saf J 126:103487. https://doi.org/10.1016/j.firesaf.2021.103487
3. Garlock M, Payá-Zaforteza I, Kodur V, Gu L (2012) Fire hazard in bridges: review, assessment and repair strategies. Eng Struct 35:89–98. https://doi.org/10.1016/j.engstruct.2011.11.002.0
4. Calvi GM et al (2019) Once upon a time in Italy: the tale of the Morandi bridge. Struct Eng Int 29(2):198–217
5. Izhar-Ul-Haq SNS (1992) Thermal conductivity and its temperature dependence in selected steel samples. Int J Energy Res 16(6):489–496. https://doi.org/10.1002/er.4440160606
6. Neuenschwander M, Scandella C, Knobloch M, Fontana M (2017) Modeling elevated-temperature mechanical behavior of high and ultra-high strength steels in structural fire design. Mater Des 136:81–102
7. Chen J, Young B, Uy B (2006) Behavior of high strength structural steel at elevated temperatures. J Struct Eng 132(12):1948–1954
8. Lee GC, Mohan SB, Huang C, Fard BN (2013) A study of U.S. bridge failures (1980–2012). Technical Report MCEER-13-0008. Multidisciplinary Center for Earthquake Engineering Research, University at Buffalo, Buffalo, NY
9. Xie F, Levinson D (2011) Evaluating the effects of the I-35W bridge collapse on road-users in the twin cities metropolitan region. Transp Plan Technol 34(7):691–703. https://doi.org/10.1080/03081060.2011.602850
10. Aydin SG, Shen G, Pulat P (2012) A retro-analysis of I-40 bridge collapse on freight movement in the U.S. highway network using GIS and assignment models. Int J Transp Sci Technol 1(4):379–397
11. Arkansas Department of Transportation (2021) Daily impacts of a bridge closure: a case study of the 2021 I-40 bridge in Arkansas. Research Problem Statement No. 13. Arkansas Department of Transportation, Little Rock, AR
12. Zhuang J, Payyappalli VM, Behrendt A, Lukasiewicz K (2017) Total cost of fire in the United States. Fire Protection Research Foundation, Quincy, MA
13. Van Coile R, Lucherini A, Chaudhary RK, Ni S, Unobe D, Gernay T (2022) Economic impact of fire: cost and impact of fire protection in buildings. Technical Report FPRF-2022-13. Fire Protection Research Foundation, Quincy, MA
14. Jalayer F, Ebrahimian H, Miano A, Manfredi G, Sezen H (2017) Analytical fragility assessment using unscaled ground motion records. Earthq Eng Struct Dyn 46(15):2639–2663
15. European Committee for Standardization (CEN) (2002) EN 1991–1-2:2002, Eurocode 1: actions on structures—part 1–2: general actions—actions on structures exposed to fire. CEN, Brussels
16. Ministero dell'Interno (2015) Decreto 3 agosto 2015: approvazione di norme tecniche di prevenzione incendi, ai sensi dell'articolo 15 del decreto legislativo 8 marzo 2006, n. 139. Gazzetta Ufficiale della Repubblica Italiana, Serie Generale 192, Supplemento Ordinario 51, Rome

17. de Silva D, Miano A, De Rosa G, Di Meglio F, Prota A, Nigro E (2025) Analitycal fire fragility assessment for bridges considering fire scenarios variability. Eng Struct 325:119442. https://doi.org/10.1016/j.engstruct.2024.119442
18. de Silva D, Sassi S, De Rosa G, Corbella G, Nigro E (2023) Effect of the fire modelling on the structural temperature evolution using advanced calculation models. Fire 6(3):91. https://doi.org/10.3390/fire6030091
19. Pchelintsev A, Hasemi Y, Wakamatsu T, Yokobayashi Y (1997) Experimental and numerical study on the behavior of a steel beam under ceiling exposed to a localized fire. In: Hasemi Y (ed) Fire safety science—proceedings of the fifth international symposium. International Association for Fire Safety Science, Melbourne, pp 1153–1164
20. European Committee for Standardization (CEN) (2004) EN 1992-1-2:2004, Eurocode 2: design of concrete structures—part 1–2: general rules—structural fire design. CEN, Brussels
21. European Committee for Standardization (CEN) (2005) EN 1993-1-2:2005, Eurocode 3: design of steel structures—part 1–2: general rules—structural fire design. CEN, Brussels
22. Franssen JM, Gernay T (2017) Modeling structures in fire with SAFIR®: theoretical background and capabilities. J Struct Fire Eng 8(3):300–323
23. Venezia V et al (2025) Morphological, physico-chemical, and thermal characterization of non-reactive protective materials for steel structures. Fire Mater 49(6):936–950. https://doi.org/10.1002/fam.3304
24. Cibelli A et al (2025) Thermal performance of reactive and non-reactive fire protective materials under non-standard heating regimes: an experimental parametric study. Fire Mater. https://doi.org/10.1002/fam.70023
25. Ma C, Van Coile R, Gernay T (2024) Fire protection costs in composite buildings for cost-benefit analysis of fire designs. J Constr Steel Res 215:108517. https://doi.org/10.1016/j.jcsr.2024.108517
26. Miano A, Sezen H, Jalayer F, Prota A (2019) Performance-based assessment methodology for retrofit of buildings. J Struct Eng 145(12):04019144. https://doi.org/10.1061/(ASCE)ST.1943-541X.0002419
27. Federal Emergency Management Agency (FEMA) (2003) HAZUS-MH MR1 technical manual: multi-hazard loss estimation methodology—earthquake model. Federal Emergency Management Agency, Washington, DC
28. Hicks HL, Liebermann RR (1979) A study of indirect fire losses in non-residential properties. FoU Brand 1:8–15
29. European Committee for Standardization (CEN) (2004) EN 1994-1-1:2004, Eurocode 4: design of composite steel and concrete structures—part 1–1: general rules and rules for buildings. CEN, Brussels
30. European Committee for Standardization (CEN) (2002) EN 1990:2002, Eurocode: basis of structural design. CEN, Brussel
31. Ministero delle Infrastrutture e dei Trasporti (2018) Decreto 17 gennaio 2018: Aggiornamento delle «Norme tecniche per le costruzioni». Gazzetta Ufficiale della Repubblica Italiana, Serie Generale 42, Supplemento Ordinario 8, Rome
32. Chen CJ, Tsai MJ, Ji BC, Wu CW, Pu JY, Lin TH (2005) Burning analysis of motor scooters. Fire Saf Sci 8:671–680. https://doi.org/10.3801/IAFSS.FSS.8-671
33. SFPE (2016) Handbook of fire protection engineering. 5th edn. Springer
34. McGrattan KB, McDermott RJ, Vanella M, Mueller E, Hostikka S, Floyd J (2024) Fire dynamics simulator user's guide. In: NIST special publication 1019, 6th edn. National Institute of Standards and Technology, Gaithersburg, MD

Steel and Composite Structures

Structural Robustness of Steel-Timber Composite Frames Under Column Loss Scenarios

Nikolaos Anagnostou[1,2], Cristiano Loss[3(✉)], and Dan V. Bompa[3]

[1] University of Surrey, Guildford GU2 7XH, UK
[2] JNP Group Consulting Engineers, Aylesbury HP19 8DB, UK
[3] University of British Columbia, Vancouver, BC V6T 1Z4, Canada
cristiano.loss@ubc.ca

Abstract. This study examines the influence of composite action between steel beams and cross-laminated timber (CLT) slab on progressive collapse behaviour. A six-storey steel frame, originally designed as a bare steel frame (BSF) for steel-concrete composite floors, was first validated and then redesigned as a steel-timber composite (STC) system. Floors were modelled using CLT shell elements in both configurations. In the STC model, composite action was enabled through nonlinear spring connectors between CLT slab and steel beams, calibrated using experimentally validated load-slip relationships for coach screws. Progressive collapse performance was evaluated through nonlinear static push-down assessments under edge, corner, and internal column removal scenarios. The STC frame with 30% composite action exhibited up to 48% lower displacements and up to 14% higher vertical load resistance than the BSF for internal and edge column removals. For corner column removals, ultimate capacities were similar, but the STC frame achieved up to 44% lower displacements. Sensitivity studies were carried out in which the composite action was varied between 15–70%. Increasing the composite action from BSF to 15% and 30%, reduced displacements by 21% and 38% on average, respectively, and increased vertical load resistance by up to 14%, while 60–70% composite action mainly improved deformation capacity. The results indicate that moderate levels of composite action provide the greatest benefit to robustness.

Keywords: Steel-timber composite frames · progressive collapse · composite action · cross-laminated timber floors · structural robustness

1 Introduction

Steel-timber composite (STC) systems are emerging as a low-carbon alternative to conventional steel or concrete structures because they combine the strength, stiffness and ductility of steel with the low self-weight, carbon efficiency, aesthetic quality, and biophilic benefits of engineered timber. Their structural performance is governed by composite action at the steel-timber interface, typically achieved through mechanical shear

© The Author(s), under exclusive license to Springer Nature Switzerland AG 2026
R. Zanon et al. (Eds.): CTA 2026, LNCE 942, pp. 527–539, 2026.
https://doi.org/10.1007/978-3-032-39505-4_46

connectors between steel beams and panelised CLT or LVL slabs [1]. When this interaction is effective, STC systems develop higher stiffness and strength, lower deflections and better material utilisation. Conversely, limited composite action results in interface slip, connector deformability and timber heterogeneity limit system performance [2]. Although steel-concrete composite behaviour is well established, fundamental knowledge and design guidance for steel-timber systems is lacking, although existing steel-concrete composite design guidance for ultimate limit state can be applied for STC [1].

Composite action is particularly important for structural robustness. Robustness requires structures to sustain local damage without triggering progressive failure, while redundancy and continuity provide alternative load paths and enable force redistribution after the loss of a vertical load-bearing element [3]. Collapse resistance depends on the mobilisation of moment redistribution, membrane, catenary and floor diaphragm actions [4]. In STC structures, composite action is central to all four mechanisms because the steel beams and timber panels act integrally for the floor system to redistribute loads and stabilise the damaged frame. Existing studies at shear connection level indicate that dynamic effects can alter load transfer and failure development in steel-timber systems subjected to extreme actions [5]. This is largely because the yield point and ultimate strength of steel are affected by strain rates, and the mechanical properties of timber depend on dynamic effects.

Progressive collapse is commonly assessed by removing a critical vertical load-bearing element and evaluating the residual structural response using methods ranging from simplified static to nonlinear dynamic analysis. Among these methods, nonlinear static or pushdown analysis provides a practical balance between simplicity and fidelity, capturing load redistribution, strength degradation and deformation capacity under increasing vertical loading [6]. This makes it well-suited for assessing the influence of composite action on STC frame robustness, as it can capture yielding, slip and large deformations and is already established for steel-concrete composite frames [7].

This paper addresses that gap by investigating the influence of validated steel-CLT composite action under column loss scenarios. Nonlinear static modelling is used to quantify the effect of composite action, expressed through degree of fixity, relative to bare steel frames (BSF). Furthermore, targeted sensitivity studies on connector spacing are performed to inform practical and economical robustness-oriented design.

2 Methodology

2.1 STC Structure Details and Design

A six-storey steel office building was used as the basis for analysis (Fig. 1a). The plan layout consists of six equal 8 m spans along the y-axis and three equal 12 m spans along the x-axis. The floor-to-floor height was 4 m. Gravity loads are resisted by the primary beams aligned with the structural grid and secondary beams evenly spaced between them (2.67 m spacing). Lateral loads are resisted by the V-Bracing system located within the internal core, specifically between grids 3B-C and 5B-C. All connections between elements, including column bases, are assumed to be nominally pinned, transferring

shear and axial forces only. The structural layout was adopted from a validated steel-concrete composite (SCC) structure designed for non-seismic regions [7]. The structure was initially analysed under limit states and column scenarios (nonlinear pushdown) for validation purposes, then redesigned in STC. The structure is categorised as Consequence Class 2b to BS EN 1991-1-7 [8].

All frame members were assigned S355 steel grade. The STC structure was initially sized with a 160 mm-thick C24 5-ply CLT floor slab, consistent with standard for mid-rise STC construction and sufficient to meet strength and serviceability requirements, and minimum 1 h fire-rating resistance (Fig. 1b, c). The floor build-up comprised a 30 mm acoustic mat and a minimum 80 mm concrete screed. The CLT panels were oriented with the outer layers parallel to the beam span, as previous experimental and numerical studies have shown that this configuration maximise shear connection stiffness and strength [5]. The steel-to-CLT connection was assumed to comprise galvanised M20 × 140 Grade 4.8 hexagon head coach screws, with a 20 mm diameter and 120 mm CLT penetration length.

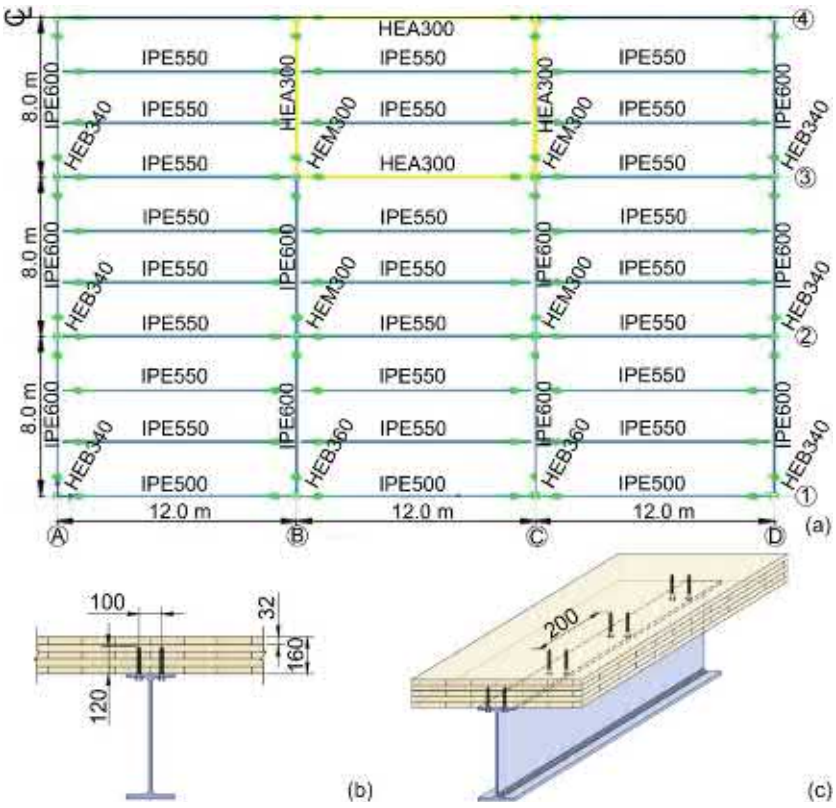


Fig. 1. a) Floor plan layout and steel section sizes, b) STC beam section, c) 3D view.

The gravity loads applied to the STC structure include a total permanent action of 3.0 kN/m^2 and a variable action of 3.0 kN/m^2. The perimeter façade load is assumed unchanged, and a value of 4.0 kN/m is maintained based on the original SCC design. Load combination for the accidental column removal scenario followed the guidance of BS EN 1990 ($G_k + 0.3Q_k$) [9]. Referred to herein as the total static load (TSL), the resulting value for the entire structure was 48830 kN. TSL provides the reference basis for interpreting the force-displacement curves of the four column loss scenarios. Comparing the applied load with the ultimate resistance from each curve shows whether the structure can sustain the accidental action without disproportionate collapse in each scenario. For column removal locations, this study adopts the approach outlined in the GSA guidelines due to the absence of a specific Eurocode procedure [10]. Therefore, considered scenarios comprise a corner (Grid 1D), an edge (Grid 4D), an internal (Grid 2C), and a core internal column (Grid 4B).

For the composite beam design, in lack of specific guidance for steel-timber composite beams, the effective flange width was determined based on BS EN 1994-1-1 [11]. The 100 mm spacing of screws in a row satisfies the minimum requirement of 4d, where d is the diameter of connector, as specified in BS EN 1995-1-1 [12]. The internal force distribution across the composite section was established based on plastic stress distributions in the steel and timber constituents. The ultimate resistance of the CS connector was estimated as $P_u = 20$ kN, corresponding to ductile failure modes governed by yielding of connectors [12].

The comparative results for the composite bending resistance of the primary steelwork are listed in Table 1. Composite action was assessed based on the spacing of the CS connectors along the length of the beam, varying from 100 mm to 400 mm. The internal steelwork assumed two CS fixings per row (Fig. 1b, c) while the perimeter steelwork one per row. The results indicate low composite action, between 15–18%, when CS connectors are spaced at 400 mm. The degree increases to 20–25% at 300 mm spacing, 30–37% at 200 mm and 60–74% at 100 mm spacing. Although 100 mm spacing provides a moment resistance increase of approximately 5–25% compared to 200 mm spacing, it significantly raises costs due to the increased number of connectors and associated installation labour. A spacing of 200 mm offers a more practical balance between structural performance and installation efficiency.

Table 1. Steel-timber composite floor section sizes.

Beam Size	Span (m)	$M_{pl,Rd,y}$ (kNm)	CS Spacing (mm)	Composite action (%)	$M_{COMP,pl,Rd,y}$ (kNm)	Neutral Axis (−)
IPE 550	12	990	100; 200; 300; 400	74%;37%; 25%; 18%	1668; 1456; 1328; 1282	CLTF; STF; SW; SW

(*continued*)

Table 1. (*continued*)

Beam Size	Span (m)	$M_{pl,Rd,y}$ (kNm)	CS Spacing (mm)	Composite action (%)	$M_{COMP,pl,Rd,y}$ (kNm)	Neutral Axis (−)
HEA300	12	491	100; 200; 300; 400	74%; 37%; 25%; 18%	922; 737; 667; 631	CLTF; STF; STF; STF
IPE 500	12	779	100; 200; 300; 400	62%; 31%; 21%; 15%	1187; 1046; 969; 923	STF; SW; SW; SW
HEA300	8	491	100; 200; 300; 400	63%; 31%; 21%; 16%	807; 667; 620; 596	STF; STF; STF; STF
IPE 600	8	1247	100; 200; 300; 400	63%; 31%; 21%; 16%	1869; 1659; 1604; 1467	STF; SW; SW; SW
IPE 500	8	779	100; 200; 300; 400	60%; 30%; 20%; 15%	1011; 969; 906; 870	SW; SW; SW; SW

2.2 Nonlinear Modelling Procedures and Validation

Floor Composite Action Modelling

To model the steel-timber composite floor, the orthotropic and layered characteristics of the CLT panel were considered. The panels were represented as single thin orthotropic shell elements using the equivalent single-layer approach based on the Modified Gamma Method [13]. The resulting properties, determined for both principal bending directions (xx and yy), account for the reduced flexural rigidity of the CLT panels. In SAP2000 [14], this stiffness reduction is implemented via the stiffness modifiers $k_{mod,x}$ and $k_{mod,y}$, which are applied to the shell element's bending equivalent directions. The in-plane stiffness of the CLT diaphragm was reduced to 75% of its theoretical elastic value [15]. The remaining panel properties, including elastic modulus, Poisson's ratio, density, and mass per unit volume, were based on design datasheets for C24 timber grade. The shell elements were discretised using a uniform mesh of 500 mm × 500 mm.

To simulate the longitudinal shear interaction between the CLT slab and the steel beam (i.e., the partial composite action), non-linear spring (link) elements were introduced between the two components. The shell elements were oriented so that their strong axis (parallel to the grain) aligned parallel to the span of the steel beams on grids 1 to 7. The spring links were aligned to act in the intended shear transfer direction. The spring

connectors were defined to connect the centroid of the steel beams to the centroid of the CLT panel (Fig. 2).

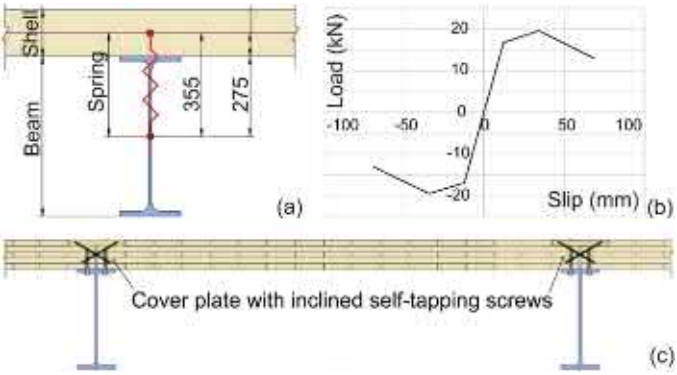


Fig. 2. a) STC modelling procedure, b) CS load-slip curve, c) Panel-to-panel detail.

For modelling purposes, the spring elements were spaced at 1.0 m intervals along the beams in the X and Y direction, with the constitutive response of tributary connectors lumped in a single load-slip curve. For example, for internal beams (X direction-12 m span) a total of 120 physical connectors considering 200 mm spacing and two screws per row were converted into 11 nonlinear spring connectors. All other degrees of freedom were fixed to prevent unrealistic relative movements or rotations between the steel beam and the CLT slab. It should also be noted that the selected mesh in shell elements (500 mm × 500 mm) ensured nodal alignment with the spring links positioned at 1000 mm centres, allowing each link to connect directly at every second node. The constitutive response of the connection between the steel beam and the CLT slab was obtained using a closed-form model validated for coach screws [6]. A similar connector-modelling approach, although based on experimental test data, was adopted in previous studies [16].

The CLT floor system consists of adjacent panels supported by the primary and secondary steelwork, with panel dimensions of 12 m in length and 2.67 m in width. To ensure horizontal and vertical shear transfer between the panel-to-panel contact regions, a single cover plate with inclined self-tapping screws, which is assumed to provide also full moment transfer, was utilised. In the numerical model, this corresponds to continuity of the shell elements at the supports, schematically captured by panel-to-panel connection detail from Fig. 2c. This modelling approach provides a reasonable representation of the assumed continuity above beams.

To validate the composite interaction, a 3D floor model incorporating the above-described modelling approaches was developed to replicate a floor subassembly of the six-storey STC structure. A nonlinear gravity analysis was performed to monitor the vertical displacement at the midspan of the central beam, capture the plastic hinge formation, and assess shear forces and slip response between the CLT slab and the steel

beams. Close inspection of the results indicated that the plastic hinges yielded at mid-span, at approximately 155 kN, matching 12 mm connector slip (Fig. 3a). Connector forces exhibited maximum shear demand near the beam ends, as expected (Fig. 3b). In addition, a single-span beam model was analysed both with and without partial composite action. The resulting deflections were cross validated against analytical assessments, showing around 30% lower deflections for the composite configuration with respect to the bare steel beam.

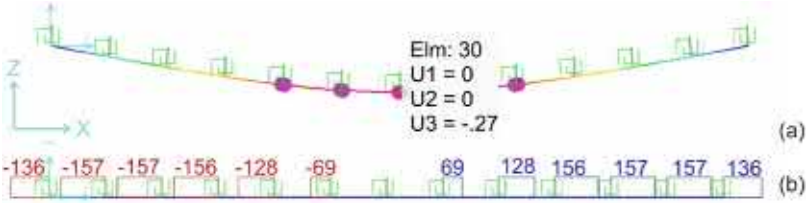


Fig. 3. STC beam validation: a) Plastic hinges and deflections (in m), b) CS forces (in kN).

STC Structure Modelling

To enable a consistent comparison between the STC and BSF (bare steel frame) system, shell elements were assigned to BSF to represent the floor diaphragm, with CLT characteristics identical to those used for STC, as previously described. This ensures that in-plane load distribution can be simulated in a manner comparable with the STC model, but in non-composite configuration. The CLT diaphragm was assumed to remain elastic, and both BSF and STC models adopted a constant in-plane stiffness in the nonlinear analysis. This approach ensures that the comparative behaviour of the two systems can be benchmarked on a consistent basis, thereby isolating the additional influence of composite interaction in the STC.

Nonlinear static (pushdown) analyses were performed in SAP2000 on full structures [14]. Such analyses were conducted to assess whether the composite action enhances load redistribution through the development of alternative load paths, and vertical resistance following a localised failure. A nonlinear static gravity load case was defined incorporating P-Delta effects and large deformations formulations to be able to capture geometric nonlinearity and second-order effects. Incremental vertical displacement was then applied to a control node located at the joint immediately above the removed column, acting along the vertical axis. The Newton-Raphson technique was employed to solve the nonlinear equilibrium.

Plastic hinges were assigned to the beam (flexural), column (axial - biaxial flexural), and bracing steel elements (axial) according to the FEMA 356 (2000) guidelines [17]. In the STC frame, additional plastic hinges were introduced on either side of each spring link to ensure the model captures the full nonlinear response of the composite floor. The plastic hinge stages are elastic (stage A-B), yielding (point B), hardening (stage B-C), failure/ultimate (point C), post-peak softening (stage C-D), residual capacity (stage D-E). In terms of FEMA performance levels are immediate occupancy (IO) including the elastic stage and early inelastic deformations, life safety (LS) characterised by moderate

inelastic deformations, and collapse prevention (CP) represented by severe deformation (beyond point C).

3 Modelling Results

3.1 Load-Displacement Response

The load-displacement curves and deformed shapes of the STC frame are shown in Fig. 4. Under edge column removal at Grid 4D, both the BSF and STC frames developed plastic hinges after column loss (Fig. 4a). In the BSF, hinges formed mainly at the two adjacent columns on Grids 3 and 5, whereas in the STC frame they were distributed more widely across the surrounding columns, indicating a more dispersed plastic mechanism and a more ductile, stable response (Fig. 4b). Both systems reached final maximum displacements of approximately 900–950 mm. Under the TSL, however, the STC developed a displacement of approximately 400 mm compared with about 600 mm for the BSF, a 33% reduction that confirms the higher initial stiffness of the STC system. The BSF reached a peak resistance of about 140 MN at 920 mm, while the STC reached about 160 MN at a similar displacement, representing a 14% increase in vertical load capacity. This improvement is attributed to steel-CLT composite action, which enhances load redistribution.

For corner column removal at Grid 1D, the load-displacement response is shown in Fig. 4c. The BSF and STC systems developed similar hinge patterns. In the STC frame, an additional hinge formed at the top of the removed corner column, at the beam-column junction, indicating combined effects of increased major axis bending and axial demand (Fig. 4d). This redistribution highlights the limited ability of the corner region to mobilise membrane or catenary action and develop alternative load paths. The STC frame reached a peak capacity of about 125 MN, whilst the BSF around 108 MN (difference of around 14%). Under the TSL, the BSF displaced about 1240 mm, whereas the STC displaced about 700 mm, or around 44% less. Both systems ultimately reached displacements above 1500 mm, with the BSF showing larger values (1790 mm), likely due to broader beam bending participation before full hinge development. In the STC frame, composite action accelerates hinge formation in the corner column and limits redistribution through the wider frame.

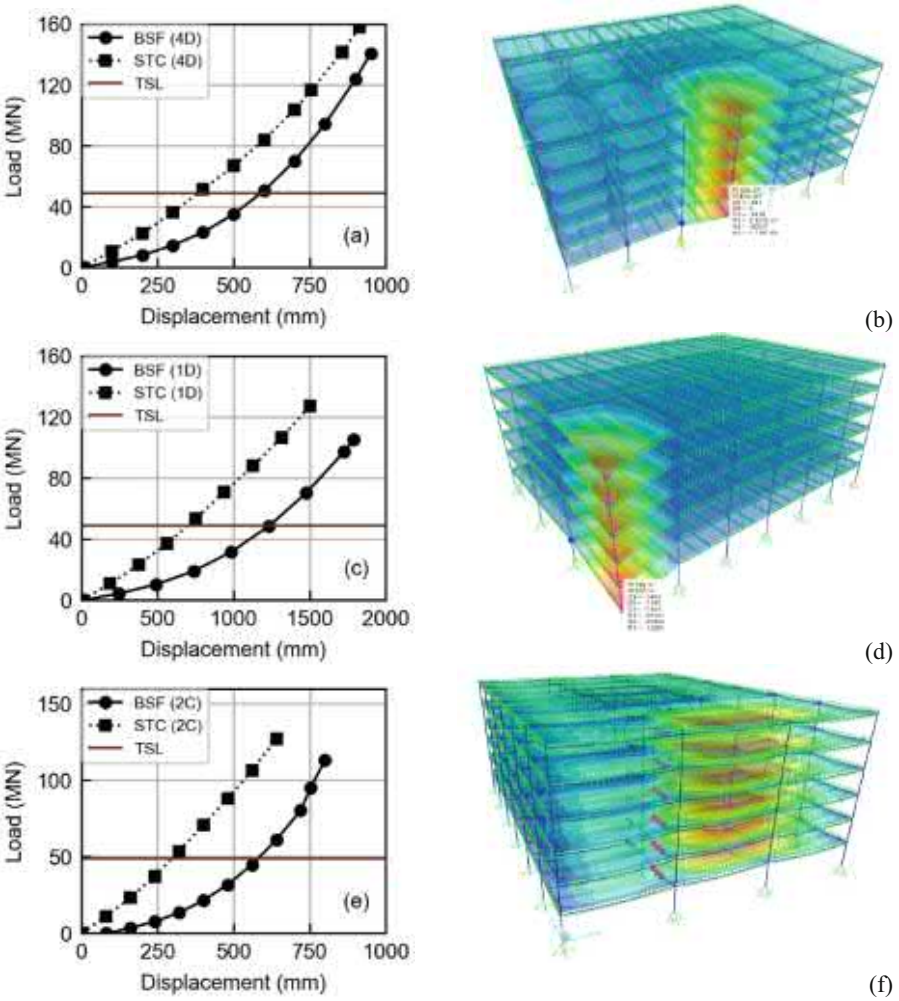


Fig. 4. Edge column (4D) removal: a) Load-displacement curve, b) STC deformed shape; Corner column (1D) removal: c) Load-displacement curve, d) STC deformed shape; Internal column (2C) removal: e) Load-displacement curve, f) STC deformed shape.

The load-displacement response for internal column removal at Grid 2C is shown in Fig. 4e. In both the BSF and STC frames, plastic hinges formed in the adjacent columns at Grids 2B and 2D. The STC frame, however, also developed additional hinges in the primary beams spanning Grid B, a feature not observed in the BSF (Fig. 4f). This indicates that composite action attracts a greater proportion of the redistributed load into the beams, leading to localised plasticity. Under the TSL, the BSF developed a displacement of approximately 575 mm, whereas the STC reached only about 300 mm, corresponding to a 48% reduction in deformation. The STC sustained 127 MN, compared with 113 MN for the BSF, representing an 11% increase in capacity. As in the edge column case, this configuration enables more effective redistribution of gravity loads

back to the core, with bending and axial beam actions contributing more efficiently to load transfer. For internal column removal at braced bays (Grid 4B), close inspection showed that the bracing attracted significant axial forces, restricting redistribution to the rest of the frame and governing the structural response from the early stages of deformation.

3.2 Column Axial Force Distribution

In both the BSF and STC frames, vertical loads were redistributed to the surrounding members; however, close inspection of the results indicate that the STC consistently developed higher axial forces. The magnitude of the increase depends on proximity to both the removed column and the braced core. At the frame perimeter, including columns 3A-5A, 1B-7B, 1C-2C and 6C-7C, the increases are relatively modest, typically about 10%. Closer to the removed column and the core, the increases become more pronounced. Columns 1A-2A, 6A-7A, 4C, 2D and 6D show increases of 15–18%, while the largest increases, around 20%, occur in columns 3C, 5C, 1D and 7D. This confirms that the core zone (Grids 3-5C) attracts the greatest share of the redistributed load, with the STC floor system enabling more balanced and effective interaction between the surrounding vertical elements compared with the BSF. In contrast, the columns immediately adjacent to the removed support (3D and 5D), exhibited axial forces differing by only 0.3% between BSF and STC. This behaviour indicates activation of catenary action in the beams spanning the removed bay.

Close inspection of the results for corner column removal at Grid 1D indicates that the differences in column axial forces between the STC and BSF frames are generally within 0–2%, suggesting a broadly similar global redistribution pattern. Along Grids 1A and 3A-7A, and along Grids 3D-7D, the STC columns withstand slightly higher axial forces, whereas along Grids 3B-7B and 3C-7C the BSF columns carried marginally greater loads. At columns 2A, 1B and 2B, the BSF attracted approximately 5–9% more load than the STC. In contrast, column 2C developed approximately 21% higher axial force in the STC, showing that composite action drives greater load transfer into the internal frame (1-2C) through increased bending and axial action in the secondary and primary beams, consistent with the previously identified beam plastic hinges. The opposite trend was observed at column 2D, where the BSF carried approximately 18% more load than the STC. For internal column removal at Grid 2C, the STC frame generally attracted 10–15% higher axial forces than the BSF across most of the structure, confirming that composite action improves redistribution capacity. This increase is evident at columns 2A, 4A-7A, 2B-6B, 1C, 4C-7C and 3D-7D, while smaller increases of about 7–10% occur at columns 1A, 3A, 1B and 7B.

3.3 Sensitivity Study

To examine the influence of composite action on progressive collapse response, three sensitivity studies were undertaken with details given below: (S1) reduced floor steel member sizes with 30% composite action, (S2) optimised floor beams with 15% composite action, and (S3) optimised floor beams with 60–70% composite action. In S1, the BSF model was re-analysed for a reduced dead load of 3 kN/m^2 using linear static

analysis, with floor beams reduced to IPE400 and IPE500 for the interior beams in the X and Y directions, respectively, and IPE240 for all core beams. Composite action was maintained at 30% using 200 mm CS spacing to assess whether the smaller sections could mobilise full bending capacity before column hinges formed, and how this affected robustness. S2 retained the reduced beam sizes but lowered composite action from 30% to about 15% by increasing CS spacing to 400 mm, to assess whether a lower cost arrangement could still provide comparable robustness and whether frame stiffness continued to govern the response. In S3, CS spacing was reduced to 100 mm, giving about 60–70% composite action and representing a theoretical upper bound. The load-displacement curves are shown in Fig. 5a–c, and the plastic hinge formation for internal column removal in Fig. 5d.

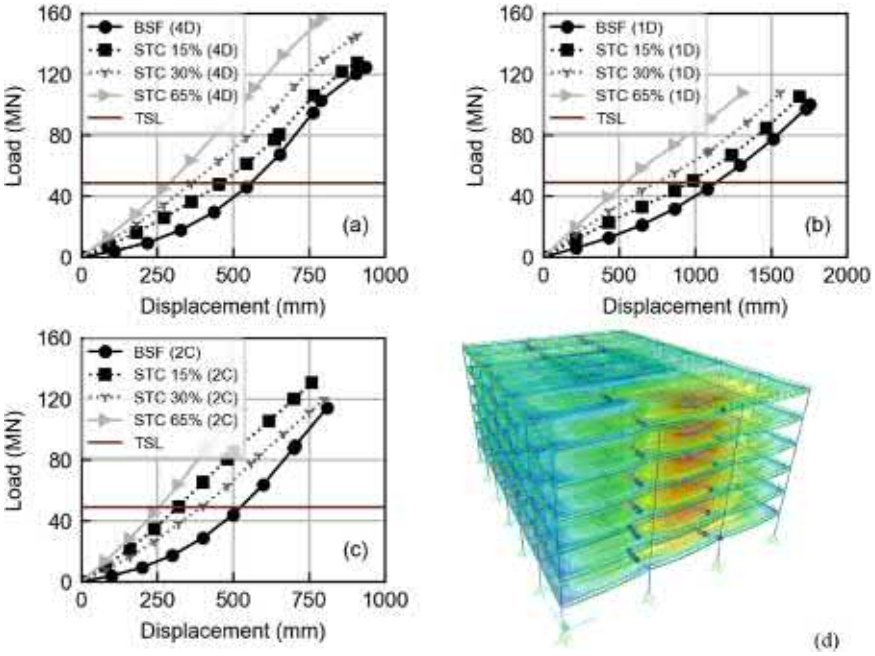


Fig. 5. Load-displacement curves for removal of the a) edge column (4D), b) corner column (1D), c) internal column (2C); d) plastic hinge formation for internal column (2C) removal.

For edge column removal at Grid 4D, the TSL displacement reduced from 600 mm in the BSF to 500 mm in STC 15% (−17%), 400 mm in STC 30% (−33%), and 300 mm in STC 60–70% (−50%). Ultimate resistance increased from 125 MN in the BSF to approximately 130 MN (+4%) at 15%, 145 MN (+16%) at 30%, and 155 MN (+24%) at 60–70%. Final displacements were approximately 1000 mm for the BSF, STC 15% and STC 30%, and slightly lower at 875 mm for STC 60–70%, showing that composite action increases stiffness and ultimate resistance, while maximum deformation capacity remains governed mainly by composite stiffness.

For corner column removal at Grid 1D, the TSL displacement reduced from 1100 mm in the BSF to 900 mm (−18%), 700 mm (−36%) and 500 mm (−55%) for STC 15%, 30% and 60–70%, respectively. Ultimate capacity increased only modestly, from 100 MN in the BSF to 105 MN (+5%), 107 MN (+7%) and 108 MN (+8%), while final displacements were 1625, 1550, 1450 and 1200 mm, respectively, confirming that geometry restricts redistribution to the core and that composite action improves stiffness and deformation resistance more than strength.

For internal column removal at Grid 2C, the TSL displacement reduced from 550 mm in the BSF to 400 mm (−27%), 300 mm (−45%) and 250 mm (−55%) for STC 15%, 30% and 60–70%, respectively. Ultimate capacity increased from 114 MN in the BSF to 120 MN (+5%) at 15% and 130 MN (+14%) at 30% but showed no further gain at 60–70%, remaining at 114 MN. Final displacements were 700–800 mm for the BSF, STC 15% and STC 30%, but only 525 mm for STC 60–70%, indicating that beyond moderate composite action, ultimate resistance is limited by full beam bending and hinge formation in the adjacent beams before further redistribution can develop throughout the frame.

4 Concluding Remarks

This paper presented a focused study on the robustness of a steel-timber composite (STC) frame under standard column loss scenarios. Nonlinear static modelling was adopted to quantify the effect of composite action (CA) on the structural robustness of STC frames relative to bare steel frames (BSF). In addition, targeted sensitivity studies on connector spacing were carried out to inform practical and economical robustness-oriented STC design. The main remarks are outlined below.

At 30% CA, the STC frame had 33% and 48% reduced displacement for edge and internal column removal, respectively, compared with BSF. The resistance increased by 14% and 11%, respectively, for the same cases. Axial forces in columns adjacent to the removed column increased by 10–20% due to redistribution.

For corner column removal, the resistance remained essentially unchanged, whereas the displacement reduced by 44%. CA improved stiffness and enhanced load redistribution towards the internal frame despite the restricted geometry.

For core column removal, the BSF and STC behaved almost identically because the response was governed by early hinging in the bracing members. In this case, CA had negligible influence on the structural response.

In the sensitivity studies, increasing the CA from BSF to 15% and 30% reduced the displacement by 21% and 38% on average, respectively, and increased the ultimate resistance by up to 15%. Increasing CA to 60–70% reduced displacement and increased strength yet at a lower rate; thus 30% CA provides best balance.

Acknowledgements. This research was partly supported by The Royal Society International Exchanges 2025 Global Round 1 under the project “Development of Net-positive Buildings with Steel and Engineered Timber” (IES\R1\251042).

References

1. Bompa DV, Elghazouli AY (2025) Non-linear composite response of steel-timber floors. In: 10th international conference on composite construction-CCX 2025, pp 111–122
2. Zhao E, Song Q, Yao J-R, Zhang X (2024) Study of shear performance of steel-timber composite connection with different shear connectors. Case Stud Constr Mater 21:e04066
3. Elkady N, Augusthus Nelson L, Weekes L, Makoond N, Buitrago M (2024) Progressive collapse: past, present, future and beyond. Structures 62:106131
4. Zandonini R, Baldassino N, Freddi F, Roverso G (2019) Steel-concrete frames under the column loss scenario: an experimental study. J Constr Steel Res 162:105527
5. Bompa DV, Chira A, Zwicky D (2024) Constitutive modelling of deformation rate dependent response of steel timber shear connections. J Build Eng 98:111159
6. Stephen D, Lam D, Forth J, Ye J, Tsavdaridis KD (2018) An evaluation of modelling approaches and column removal time on progressive collapse of building. J Constr Steel Res 153:243–253
7. Demonceau JF et al (2021) D3–1: design recommendations against progressive collapse in steel and steel-concrete buildings. ECCS
8. BS EN 1991-1-7:2006+A1:2014. Eurocode 1. Actions on structures. General actions. BSI, London
9. BS EN 1990:2002 + A1:2005. Eurocode 0. Basis of structural design. BSI, London
10. GSA (2016) Alternate path analysis and design guidelines for progressive collapse resistance. U.S. General Services Administration, Washington, DC
11. BS EN 1994-1-1:2004. Eurocode 4. Design of composite steel and concrete structures. General rules and rules for buildings. BSI, London
12. BS EN 1995-1-1:2004+A1:2008. Eurocode 5. Design of timber structures. General rules and rules for buildings. BSI, London
13. Deeves BP, Woods J (2026) Structural behavior of steel-timber composite beams with mass plywood panels and self-tapping screw shear connections. SSRN 6614348
14. CSI (2016) CSI Analysis Reference Manual. CSI Inc., Berkeley, CA
15. D'Arenzo G, Casagrande D, Reynolds T, Fossetti M (2019) In-plane elastic flexibility of cross laminated timber floor diaphragms. Constr Build Mater 209:709–724
16. Loss C, Piazza M, Zandonini R (2016) Connections for steel-timber hybrid prefabricated buildings. Part II: innovative modular structures. Constr Build Mater 122:796–808
17. FEMA (2000) Prestandard and commentary for the seismic rehabilitation of buildings (FEMA 356). FEMA, Washington, DC

Classification of Shear Connection Systems for Composite Action in Steel-Timber Floor Systems

Dan V. Bompa[1] and Cristiano Loss[2(✉)]

[1] University of Surrey, Guildford GU2 7XH, UK
[2] University of British Columbia, Vancouver, BC V6T 1Z4, Canada
cristiano.loss@ubc.ca

Abstract. Hybrid steel-timber floor systems combine the standardisation, strength and ductility of steel with the prefabrication, low self-weight and biogenic carbon storage potential of engineered timber, offering a promising solution for low-carbon and circular construction. Their mechanical response and system-level performance are governed largely by the steel-to-timber shear connection, which controls load transfer, slip, stiffness, strength, ductility, fire response, and the feasibility of disassembly and reuse. This paper develops a component-informed design framework for hybrid steel-timber floor systems through a critical review of current research and practice on steel-timber shear connection systems. Material configurations and connector typologies are reviewed and classified in relation to structural performance objectives and sub-component circularity. The review is further refined through practitioner survey and workshop findings to assess practical applicability and implementation barriers. Particular attention is given to two representative connection families, namely dry demountable systems and wet-grouted bolted systems, for which the main load-transfer components, governing failure modes, key detailing parameters, and implications for fire performance and reuse are identified. The study provides a basis for the subsequent development of pre-normative, Eurocode-aligned design guidance for hybrid steel-timber floor connections.

Keywords: Steel-timber frames · shear connections · composite action

1 Background

Hybrid Steel-Timber (HST) systems offer a critical route to achieve wider sustainability targets, all calling for low-carbon, demountable, and resource-efficient structural systems. HST systems reduce whole-building embodied carbon by ~5–35% compared with steel-concrete systems while maintaining span capacity and stiffness; the addition of demountable connectors further enhances reuse [1]. HST systems demonstrated life-cycle cost reductions of 3–5% relative to pure steel or timber alternatives through reuse and modular construction [2]. In HST construction, a major part of the vertical

© The Author(s), under exclusive license to Springer Nature Switzerland AG 2026
R. Zanon et al. (Eds.): CTA 2026, LNCE 942, pp. 540–553, 2026.
https://doi.org/10.1007/978-3-032-39505-4_47

or lateral load-bearing system is made of steel; common steel components include lateral force-resisting systems such as steel-framed cores, buckling-restrained braces, and perimeter-frame or exoskeleton bracing systems, while the gravity system usually comprises steel columns and beams working compositely with timber floors or wall panels [3].

Whilst early hybridisation of steel beams and timber materials for structural members has been documented for more than a century, a renewed interest in steel-timber systems is driven by the urgent need for decarbonisation of the built environment. Coordinated industry activity indicates increasing demand for harmonised design principles, comparable performance data, and guidance suitable for routine practice [4]. The publication of conceptual design guidelines for steel frame buildings with timber floors in the US, together with comprehensive state-of-the-art reviews of steel-timber composite elements in Europe, signals consolidation of these systems [5, 6].

Within the academic research, a bibliographic scan of peer-reviewed studies investigating steel structural members (e.g., frames, beams or girders) in combination with timber-based materials (timber, wood, mass timber, CLT, glulam or LVL) indicates a significant increase of published work. A Scopus analysis of 441 peer-reviewed papers for the 2000–2026 period indicates a 41.7%, 40.6% and 17.7% distribution between member-type studies (connection mechanics, composite behaviour, shear transfer and load-slip response), system-type studies (floor systems, frames, seismic response, vibration, fire or whole-structure performance) and mixed papers, respectively. The diversity indicates that there is now comparable momentum towards whole-system behaviour, codification-relevant performance and integrated structural design.

Within the wider remit of HSTs, steel-timber floor systems are a hybrid configuration in which the combination of steel and timber can provide benefits in terms of structural performance and sustainability [7]. Steel-timber floors may be either non-composite or composite, with the latter offering reduced deflection, improved vibration response, and efficient material utilisation [8]. Currently, design expressions governing the composite action in steel-timber floors are lacking. Within this background and considering the need for specific design rules for composite steel-timber floors, a mixed-methods horizon-scanning approach combining an international stakeholder survey with an in-person validation workshop was adopted to capture practitioner views on this structural form. After describing the existing steel-timber shear connection systems (STSCs), the results of the end-user engagement activities are briefly described. Furthermore, a review of the existing literature on the selected STSCs is given.

2 Steel-Timber Shear Connection (STSC) Systems

2.1 Initial Classification

STSCs may be dry, using mechanical fasteners, or wet, employing grouts or epoxy resins [9]. Dry connections support circularity through disassembly and reuse; common solutions include screws, bolts, and dowels [10]. Wet connections hinder disassembly and circularity but typically provide higher stiffness and strength owing to the larger grout-timber contact area [11]. Wet STSCs typically use cementitious grouts cast in pockets. Shear-connection stiffness governs the degree of composite action in composite floors,

controlling flexural stiffness, load sharing, and serviceability behaviour. Higher slip modulus reduces interfacial slip, increases bending stiffness, lowers mid-span deflections, and raises natural frequencies, improving vibration performance [12].

In steel-timber floors, demountable shear connectors enhance deconstructability and material reuse while maintaining structural integrity [13]. During a building's service life, repeated loading-unloading cycles may arise from impacts, vibration, damage, and changes in permanent loads due to functional modifications such as repartitioning. In STSCs, cyclic loading can cause timber hole ovalisation due to back-and-forth movement of connectors, reducing mechanical properties, particularly connection stiffness [10]. This degrades both the composite floor behaviour and the reuse potential of steel-timber floors. Accordingly, STSCs must retain their structural performance during both the initial service life and after reassembly.

It is shown that STSCs require to be designed for serviceability and ultimate limit states, extreme conditions, as well as for disassembly. Experimental validation and design guidance for all STSCs based on multi-criteria requirements are currently lacking or very limited. Based on a previous review, Fig. 1 lists common shear connection systems, while Fig. 2 shows typical connectors used in steel-timber floors [10]. STSCs are grouped as dry with partial or full embedment (DPE and DFE, respectively), wet grouted with bolts or studs (WGB and WGS, respectively), and wet epoxied with plates or at the interface (WEP and WEI, respectively). Connector types include self-tapping screws (STS), dog screws (DS), coach screws (CS), shield anchor bolts (SAB), bare bolts (BB), encased bolts (EB), welded studs (WS) and welded plates (WP).

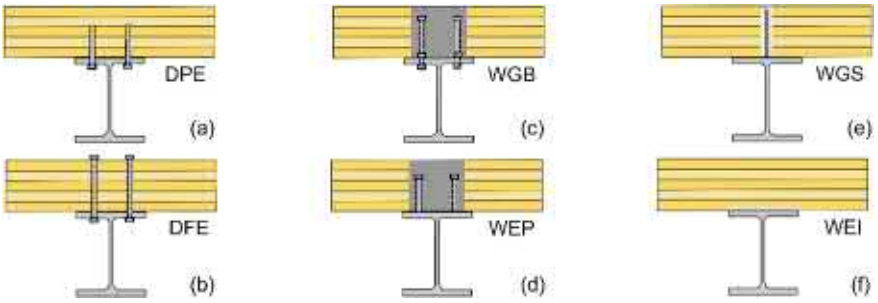


Fig. 1. Shear connection types: a) DPE - dry partial embedment, b) DFE - dry full embedment, c) WGB - wet grouted with bolts, d) WGS - wet grouted with studs, e) WEP - wet epoxied with plates, f) WEI - wet epoxied interface

2.2 Practitioners Ranking

A mixed-methods horizon-scanning approach was adopted, combining an international stakeholder survey with an in-person validation workshop. The survey phase was designed to capture practitioner and academic insights regarding current practices, technical barriers and future research needs in hybrid steel-timber systems, with particular emphasis on steel-framed buildings incorporating timber floors and composite



Fig. 2. Connector types: a) STS - self-tapping screw, b) DS - dog screw, c) CS - coach screw, d) SAB - shield anchor bolt, e) BB - bare bolt, f) EB - encased bolt, g) WS - welded stud, h) WP - welded plate

floor action. The survey targeted practitioners, researchers and industry stakeholders with demonstrable engagement in structural design, detailing, construction or guidance development. A total of 46 participants (Canada, 45.7%; United Kingdom 28.3%; United States 4.3%; Italy, New Zealand, Denmark and Germany each 3.4%; 8.7% did not specify a country) responded to 26 questions. Most respondents were employed in design consultancies (60.9%), followed by manufacturers/suppliers (15.2%), research organisations/universities (6.5%) and specialist fabricators (4.3%), while other roles each accounted for 2.2%. A total of 60% of participants had more than 10 years of experience.

Regarding hybrid steel-timber floor systems and STSC, participants were asked to indicate: (i) the assumed level of composite action adopted in the design of steel-timber floors (none/partial/full/other), (ii) commonly used connector systems, (iii) the perceived structural performance and disassembly/reuse potential of the STSC systems shown in Fig. 1, and (iv) the perceived structural performance and disassembly/reuse potential of the connector systems shown in Fig. 2 . A total of 42.2% of responses indicated that no composite action was assumed in their design approach, followed by partial composite action (33.3%), "depends" (13.3%), and full composite action (8.9%), with one respondent (2.2%) indicating an alternative assumption. In terms of popularity, the results indicate that self-tapping screws (STS) were selected by 33% of respondents, followed by welded plates (WP, 18%) and coach screws (CS, 13%). Bare bolts (9%) and welded studs (6%) were seldomly adopted, while dog screws (4%), encased bolts (3%) and shield anchor bolts (3%) were selected less frequently.

Ranking data were analysed using a Borda count aggregation method to convert individual ordinal rankings into a collective preference score. Using this method, for each respondent ranking *m* connector systems, the top-ranked option was assigned *m* points, the second-ranked option *m-1* points, down to one point for the lowest-ranked option. Total scores were obtained by summing points across all respondents, after which the options were ordered according to their aggregated scores. The ranking of perceived structural performance shown in Fig. 3, places WPs (243) and WS (237) at the top, closely followed by STS (231), suggesting that although STS are most widely used, welded systems are perceived as structurally superior. The ranking for disassembly and reuse potential illustrated in Fig. 4, shows that STS lead (308), followed by BB (281) and DS (269), while WP (96) and WS (93) rank lowest. Regarding STSCs the ranking

for perceived structural performance favours wet and more integrated systems. WGS (204) ranks highest, followed closely by DFE (197) and WGB (195), while DPE (163) occupies a mid-range position. Bonded plates (WEP 146) perform moderately, whereas WEI (82) is again lowest. For perceived disassembly, there is a clear preference for dry systems, with DPE (252) and DFE (252) jointly ranked highest. Wet grouted systems follow at a moderate distance (WGB 170; WGS 123). Bonded solutions rank lowest.

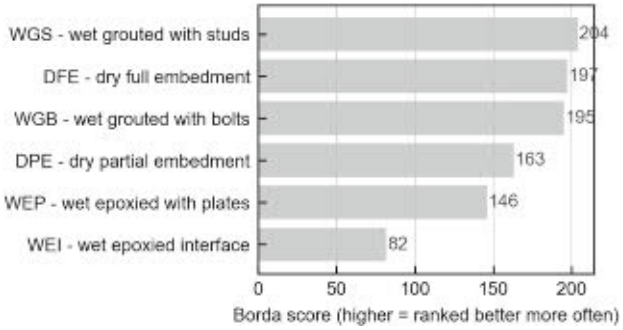


Fig. 3. Ranking of STSC systems for perceived structural performance

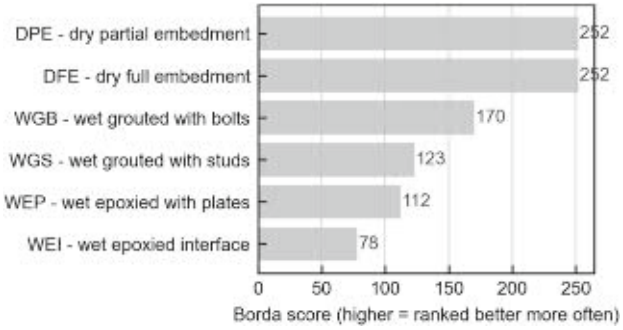


Fig. 4. Ranking of STSC systems for perceived disassembly/reuse capability

2.3 Selected STSCs

The quantitative results demonstrate a clear divergence between systems preferred for structural performance and those favoured for circularity and demountability, highlighting an inherent trade-off between strength-driven and reuse-driven design. These trade-offs are further reflected in the qualitative feedback provided by respondents. It was shown that stiffness, strength and ductility represent distinctive performance criteria, thus, an additional classification based on ductility expectation is advisable. Where grouted systems are intended to form timber-concrete-steel composites, respondents

noted that longitudinal shear transfer between timber and concrete must be explicitly addressed within the classification framework. WEI was viewed as difficult to inspect post-installation and potentially vulnerable to delamination. Grouted systems were also associated with risk of water ingress if not properly sequenced during construction.

Wet and bonded systems were considered problematic for demountability, with WEI viewed as particularly challenging from a reuse perspective. Conversely, DPE and DFE were generally perceived as more practical and widely adopted in current practice. DPE was considered the quickest and most flexible system to install, provided diaphragm shear and uplift demands are adequately reinforced using screws. Comments also noted potential heat conduction through embedded steel (DFE, WEP), the absence of fire resistance in bonded interfaces (WEI), and uncertainty regarding charring behaviour and hot-gas passage between floors. Grouted systems were perceived as more fire-resistant.

To identify a limited number (2–4) of shear-connector families for focused experimental and pre-normative development, a structured multi-criteria decision-making (MCDM) framework using, the (i) Borda-aggregated rankings of perceived structural performance and disassembly/reuse potential, and (ii) frequency of current use of connectors. First, criteria were normalised using min-max scaling to ensure comparability across heterogeneous metrics. A Pareto frontier analysis was then conducted using structural performance and circularity (disassembly/reuse) as primary benefit criteria. An alternative was considered Pareto-dominated if another connector exhibited equal or superior performance in both dimensions and strictly better performance in at least one [14]. Subsequently, ranking within the Pareto-efficient subset was performed using the Technique for Order Preference by Similarity to Ideal Solution (TOPSIS). TOPSIS identifies the alternative closest to a hypothetical ideal solution (maximising all benefit criteria) and furthest from an anti-ideal solution.

Based on this assessment, the WGS and DFE have maximum normalised scores for structural performance and disassembly/reuse, respectively. On an orthogonal structural-reuse coordinate pair (x, y), DFE = (0.94, 1.00), DPE = (0.66, 1.00), WGS = (1.00, 0.26) and WGB (0.94, 0.54) (Fig. 5). Considering the geometric mean, $g = (x \times y)^{0.5}$ as unique index, it results g = 0.97 for DFE, g = 0.51 for WGS, g = 0.71 for WGB, and g = 0.81 for DPE. The quantitative results indicate that DFE for dry and WGB for wet systems offer the best trade-off between structural performance and circularity and

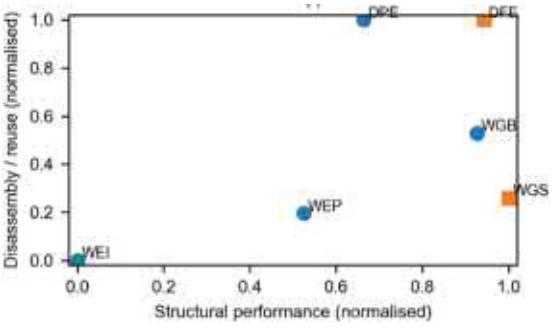


Fig. 5. Pareto trade-off for STSC systems

are selected for further detailed review. The selection of these two STSC systems also is further supported by the qualitative observations provided by respondents.

3 Performance of Selected STSCs

3.1 Dry Fully Embedded (DFE) Bolted STSCs

Dry fully embedded (DFE) bolted shear connections are defined as dry steel-timber shear-transfer systems in which a bolt or threaded shank passes through the full thickness of the timber slab or panel (Fig. 6). Several studies have investigated these systems with different names and variations, including bolt-based steel-CLT [15, 16], concealed and reversible CFS-CLT [17], demountable steel-LVL [13], demountable prestressed steel-CLBT [18]. DFE bolted shear connectors consistently exhibit a staged load-slip response. In prestressed configurations, friction generated by bolt post-tensioning governs the initial no-slip stage, after which the response transitions to shank bearing, timber embedment, and plastic deformation of the bolt [15, 16]. The performance of DFE systems can be enhanced by adding embedded restraint components such as threaded inserts and T-nuts, which in turn consistently increased stiffness by 59–94% and often improved ductility relative to the reference bolted solution [17]. Increasing the bolt diameter from 16 to 18 and 20 mm increased the strength by around 24%, and 67%, respectively [18]. Recessed or concealed bolt heads were also reported to improve both resistance and slip behaviour [18]. For DFE the main failure mode is characterised by timber crushing due to direct bolt-timber interaction, accompanied by the formation of one or two plastic hinges in the steel components [19]. DFE systems with bolts embedded in steel sleeves in direct contact with the timber delay severe local timber damage and promote a more ductile failure mechanism [13]. DFE shear connections can therefore be characterised as friction-assisted dowel systems, in which the overall behaviour is governed by bolt-timber interaction, as well as local restraint conditions at the head, washer, and outer lamellae.

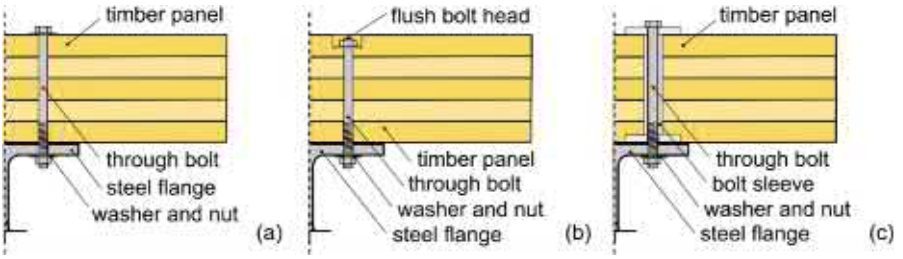


Fig. 6. DFE STSCs: (a) conventional through bolt with or without washers, (b) concealed bolt head with through bolt with or without washers, (c) sleeve encased through bolt system.

The main DFE bolted STSC components identified from the review are listed in Table 1. In addition to the individual components, the implication of loading relative to the grain direction and/or characteristic ply properties should also be considered.

Within a component-method formulation, stiffness should therefore be assembled from the elastic compliance of steel, bolt, grout and substrate components, while resistance should be governed by the weakest component, consistent with Eurocode philosophy.

DFE bolted STSC exhibit strong circularity potential because they are assembled through dry, reversible operations and can therefore support disassembly, replacement of local steel parts, and potential reuse of the timber slab or panel without the irreversible bonding associated with adhesive-based systems [10]. Demountable bolt connectors with embedded steel devices further indicate that circular design depends on controlling damage during both installation and dismantling, since bolt preloading in timber can otherwise cause local crushing that compromises reuse potential [13]. The main limitation is that existing research demonstrate demountability, replaceability and low-damage detailing, but does not provide direct quantitative evidence on residual mechanical properties after disassembly and reassembly. Consequently, reuse potential is presently supported primarily at the detailing and first-life performance levels rather than through second-life re-testing [17, 18]. The latter represents a critical aspect, and quantitative assessment of circularity-related properties remains essential [13]. The fire and thermal performance of DFE is yet to be evaluated. Tests on elevated-temperature load-slip response, pretension loss in fire, residual capacity after heating, or thermo-mechanical degradation of concealed through-bolt details, are currently non-existent.

Table 1. DFE shear connection components

Component	Behaviour	Failure mode
Bolt shank in bending (single hinge)	Plastic development near the steel-timber interface under embedment restraint.	Single plastic hinge with timber crushing / local bearing.
Bolt shank in bending (double hinge)	Plasticity through the embedded length when rotational restraint and layer strength permit a two-hinge mechanism.	Two-hinge bolt yield mode; ductile force redistribution.
Bolt axial tension / rope effect	Axial force generated by rotation, withdrawal restraint and washer/head bearing.	Head pull-through, local crushing at head / nut.
Pretension-induced friction component	Initial no-slip branch before shank bearing develops; serviceability-controlled component.	Slip / relaxation of clamp force.
Steel plate / flange bearing at bolt hole	Local compressive deformation of the steel member at the loaded hole edge.	Hole ovalisation, local bearing, local yielding of plate or flange.

(*continued*)

Table 1. (*continued*)

Component	Behaviour	Failure mode
Steel-side local bending / sheet distortion	Out-of-plane or local flexural deformation of thin steel around the hole, reducing rotational restraint and stiffness.	Local deformation of CFS around hole; reduced slip modulus.
Timber embedment - loaded outer lamella	Bearing of bolt / sleeve / device against the first loaded lamella; primary timber compression component.	Local crushing, indentation, beginning of slip.
Timber embedment - internal effective lamellae	Progressive load transfer to inner layers as local damage grows; key in full-thickness DFE joints.	Layer-specific crushing, split, rolling shear, delamination.
Head / nut / washer / bearing plate compression component	Surface compression beneath bolt head or nut, including washers and external bearing plates.	Local crushing under washer/head; loss of pretension; surface pull-in.
Embedded steel insert / sleeve / tube / T-nut / threaded insert component	Local confinement and rotational restraint added by embedded or semi-embedded steel accessory.	Device yielding, local crushing around device, loss of confinement or bearing.
Panel splitting / rolling shear / interlaminar failure component	Secondary timber-panel damage caused by eccentricity, layer mismatch or over-strength connector.	Split parallel to grain; rolling shear of cross-layers; delamination.

3.2 Wet-Grouted Bolt (WGB) STSCs

Wet-grouted systems have been investigated in several studies (Fig. 7). It was shown that grout pockets enlarge the effective load-transfer surface, compared to bolt-timber cases [20–23]. In terms of structural response, the grout layer increases bearing area in the wood, engages grout-steel composite action, and can enable capacity protection of the surrounding timber by externalising plasticity away from the timber panel [23]. Thus, grout confinement modifies both the resistance hierarchy and the stiffness hierarchy of the connection. The connector diameter governs elastic mechanical properties, whereas grout thickness governs strength resistance and failure mode [23]. Smaller grout pockets resulted in a steeper post-peak softening response because of more severe grout crushing [20]. Increasing the bolt diameter from 12 mm to 20 mm produced an increase in stiffness and strength of 107.8% and 109.7%, respectively [20]. Increasing the bolt grade enhanced the strength without significantly influencing the stiffness. Changing the plate material from cross-laminated timber to cross-laminate bamboo-timber altered the governing failure mode from grout crushing, timber crushing, and bolt bending to

bolt shear, highlighting that the grout-wood interface acts as an active resistance and deformation component [22].

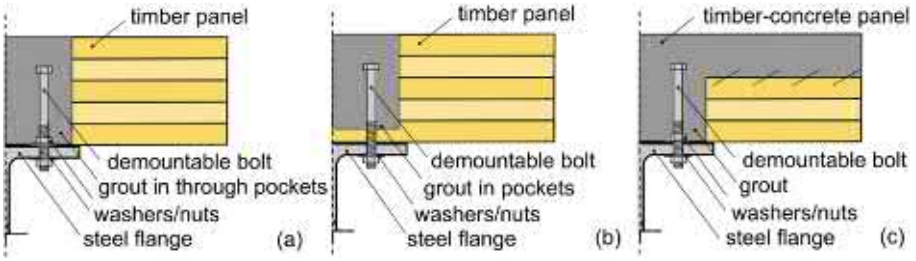


Fig. 7. WGB STSCs; demountable bolt in (a) grouted through pockets, (b) grouted pockets with support, (c) grouted through pockets and composite timber-concrete slab

Failure modes can develop with CLT crushing, grout cracking/crushing, plastic hinging of the bolt, and, for the stronger/larger arrangements, bending and plastic deformation of the steel flange [20]. Elsewhere, bolt fracture, single-hinge behaviour, and mortar compression failure, with additional panel splitting, delamination and local steel deformation, were observed [21]. It is shown that the structural response of WGB shear connections results from the interaction of four deformable connection components: bolt, grout, timber panel, and steel flange. The main WGB STSC components are shown in Table 2. The implications of loading relative to the grain direction should also be considered. As for DFE systems, stiffness should therefore be assembled from the elastic compliance of steel, bolt, grout, and substrate components, while resistance should be governed by the weakest component or component interaction.

Direct experimental evidence regarding the reversibility of wet-grouted systems, residual capacity after disassembly, removability of the grout, and second-life performance of the recovered components is currently lacking. However, some qualitative observations that can provide a useful basis for incorporating disassembly, reuse and circularity into design, are available. It is indicated that grout-pocket bolts can minimise overhead work while preserving the possibility of prefabrication and deconstruction [20]. For the system in Ref. [23] damage to timber is avoided, fuse elements can be replaced, and the system is therefore better aligned with deconstruction and reuse. Elsewhere, it is noted that demountable bolts (DFE) in steel-CLBT remain more ductile but substantially less stiff than grouted variants (WBG), which implies a trade-off between reversibility and mechanical efficiency [22]. At present, the circularity dimension should currently be treated as a design objective informed by mechanistic reasoning. Although no studies have investigated the fire and thermal characteristics of these connections, at least three thermally sensitive subsystems can be identified, namely the steel fastener, the grout phase, and the timber substrate, together with interfaces whose compatibility under heating remains unknown.

Table 2. WGB shear connection components

Component	Role	Failure
Bolt shank in shear	Dominant where substrate confinement governs and bending is restrained.	Bolt shear fracture or bolt-dominated shear resistance.
Bolt plastic hinge at steel interface	Localised at the steel-grout/timber interface when bolt bending is mobilised.	Single hinge formation.
Bolt plastic hinge within grout / embedded zone	Secondary hinge within the embedded length caused by end restraint from grout/substrate and distributed bearing.	Two-hinge mechanism in weaker substrate systems.
Bolt axial tension / rope effect	Axial force contribution mobilised by pretension, anchorage and nut/washer restraint.	Bolt tensile resistance, anchorage limit, bearing beneath head.
Steel flange/web local bearing	Compression/bearing at the hole where the bolt transmits force to the steel section.	Local steel bearing/yielding.
Steel local yielding / buckling	Steel member becomes the weak component once bolt and grout are strong enough to shift demand into the beam flange.	Local flange yielding, flange buckling or beam-local instability.
Grout core in compression	Compressive bearing zone directly beneath the bolt inside the grout pocket/annulus	Grout compressive failure beneath bolt.
Grout shell cracking / crushing / confinement degradation	Outer grout body provides lateral restraint to the fastener and stabilises the load path into the substrate.	Fragmentation or severe crushing of the grout shell.
Grout-steel composite interaction / bond-assisted restraint	Partial composite action between steel rod/bolt and grout increases effective embedded stiffness and restrains rotation.	Loss of effective bond-assisted composite action.
Grout-timber bearing transfer	Load spread from grout perimeter into timer over a larger effective area than a dry bolt.	Failure of the grout-to-substrate bearing block.

(*continued*)

Table 2. (*continued*)

Component	Role	Failure
Timber embedment or crushing	Substrate-side bearing component for steel-timber systems, governing when timber provides weak support to grout.	Timber crushing, embedment growth.
Timber panel-level limit states	Ultimate panel-side limit states that cap connector performance and define capacity-protection requirements for the panel.	Panel splitting, rolling shear, delamination or local crushing.
Washer / nut local bearing and seating	Local compression beneath nut/washer and seating of pretensioned hardware.	Local bearing beneath washer/nut.

4 Concluding Remarks

This paper developed a component-informed classification and review framework for steel-timber shear connections in hybrid floor systems, combining literature synthesis with practitioner input to identify connector families that best reconcile structural performance, disassembly potential and codification needs. The main remarks are below.

The survey results demonstrate a clear trade-off between structural efficiency and circularity. For perceived structural performance, wet grouted with studs (WGS) achieved a Borda score of 204, followed by dry full embedment (DFE) at 197 and wet grouted with bolts (WGB) at 195. In contrast, for disassembly and reuse potential, dry partial and full embedment systems (DPE and DFE) jointly ranked highest at 252, followed by WGB at 170 and WGS at 123; while bonded solutions consistently ranked lowest. DFE and WGB were confirmed as the most promising solutions.

For DFE systems, embedded restraint devices such as sleeves and T-nuts can increase stiffness by 59–94%, while increasing bolt diameter from 16 mm to 18 mm and 20 mm raises strength by about 24% and 67%, respectively, with associated gains in ductility. For WGB systems, the grout pocket enhances the effective load-transfer area and improves mechanical performance, increasing bolt diameter from 12 mm to 20 mm increased stiffness by 107.8% and strength by 109.7%.

DFE systems exhibit strong potential for demountable composite action, although the current evidence base primarily relates to first-life performance. The study shows that circularity and fire remain the main unresolved verification domains for both DFE and WGB systems. Direct evidence regarding residual performance after disassembly/reassembly is lacking and no dedicated fire or thermo-mechanical connection data are yet available. A list of governing connection components was identified for both shear-connection types, providing a basis for the future development of design rules.

Acknowledgements. This research was partly supported by The Royal Society International Exchanges 2025 Global Round 1 under the project "Development of Net-positive Buildings with Steel and Engineered Timber" (IES\R1\251042).

References

1. Becker I, Anderson F, Phillips AR (2023) Structural design of hybrid steel-timber buildings for lower production stage embodied carbon emissions. J Build Eng 76:107053
2. Pimentel R, Simões R, da Silva LS (2024) Hybrid steel frames with mass timber floors: performance, challenges and sustainability benefits. ce/papers 7(1–2):228–239
3. Loss C, Frangi A (2017) Experimental investigation on in-plane stiffness and strength of innovative steel-timber hybrid floor diaphragms. Eng Struct 138:229–244
4. Vertical Urbanism website (2026). https://verticalurbanism.org/resources/research-projects/the-future-potential-of-steel-timber-hybrid-buildings/. Accessed 4 Dec 2026
5. AISC (2022) Design guide 37: hybrid steel frames with wood floors
6. ECCS TC11/WG6 (2024) State of the art on steel-timber-(concrete) structures, 287–291
7. Laboy MM, Eckelman MJ, Hajjar JF, Webster MD (2025) Carbon reduction strategies with steel-CLT hybrid structures. In: Structures and architecture. CRC Press, pp 581–588
8. Owolabi D, Aloisio A, Loss C (2025) Vibration attenuation in cross-laminated timber-steel composite floors using loose sand as a passive damping mechanism. Eng Struct 340:120642
9. Bompa DV, Chira A, Zwicky D (2024) Constitutive modelling of deformation rate dependent response of steel timber shear connections. J Build Eng 98:111159
10. Bompa DV, Kariuki M, Ungureanu V, Elghazouli AY (2025) Disassembly capability and circularity potential of steel-timber floor connections. J Constr Steel Res 235:109806
11. Feujofack KBV, Loss C (2024) Predicting the structural behaviour and failure mechanism of hybrid steel-grout connectors for cross-laminated timber panels using high-fidelity finite-elements modelling. Constr Build Mater 447:138121
12. Chiniforush AA, Alamdari MM, Dackermann U, Valipour HR, Akbarnezhad A (2019) Vibration behaviour of steel-timber composite floors, part (1): experimental & numerical investigation. J Constr Steel Res 161:244–257
13. Romero A, Odenbreit C (2024) Experimental investigation on novel shear connections for demountable steel-timber composite (STC) beams and flooring systems. Eng Struct 304:117620
14. Marler RT, Arora JS (2004) Survey of multi-objective optimization methods for engineering. Struct Multidiscip Optim 26(6):369–395
15. Hassanieh A, Valipour HR, Bradford MA (2016) Load-slip behaviour of steel-cross laminated timber (CLT) composite connections. J Constr Steel Res 122:110–121
16. Lu J, Wei Y, Chen Z, Chen J, Huang S, Huang L (2026) Shear performance of welded stud and detachable bolt in steel-CLT composite structures. J Constr Steel Res 243:110381
17. Moritani FY, Santos P, Carneiro L, Dias AM (2025) Experimental assessment of bolt-based connections for cold-formed steel and cross-laminated timber composite floor systems. Constr Build Mater 492:143004
18. Gong S et al (2025) Shear characteristics of demountable bolt connectors in steel-cross laminated bamboo and timber composite beams. Eng Struct 336:120489
19. Yang R, Li H, Lorenzo R, Ashraf M, Sun Y, Yuan Q (2020) Mechanical behaviour of steel timber composite shear connections. Constr Build Mater 258:119605
20. Hassanieh A, Valipour HR, Bradford MA (2017) Composite connections between CLT slab and steel beam: experiments and empirical models. J Constr Steel Res 138:823–836

21. Gong S et al (2025) Experimental and theoretical study on mechanical behavior of high strength bolt connections for prefabricated steel-CLBT composite floors. Structures 82:110477
22. Lu J, Wei Y, Du H, Zhao K, Huang S, Chen J (2026) Experimental evaluation on the shear performance of grouted bolt connections in steel-CLT and steel-CLBT composite structures. Thin-Walled Struct 114573
23. Shulman S, Loss C (2023) High-performance grout-reinforced shear connectors for hybrid steel-cross-laminated timber building systems: experimental study. J Build Eng 67:106014

A Novel Concept of Steel Timber Concrete Composite Slim Floor Beams: Experimental and Analytical Investigations

Adil Ahmad[1], Teodora Bogdan[1], Jie Yang[2], Riccardo Zanon[2(✉)], Edoardo Benvenuti[3], Micael Bello[3], Francesco Profico[4], and Christoph Odenbreit[1]

[1] University of Luxembourg, Esch sur Alzette, Luxembourg
teodora.bogdan@uni.lu
[2] Arcelormittal Global R&D, Esch sur Alzette, Luxembourg
riccardo.zanon@arcelormittal.com
[3] ArcelorMittal Steligence® Engineering, Esch sur Alzette, Luxembourg
[4] ArcelorMittal – Long Europe - CTO – Reliability, Esch sur Alzette, Luxembourg

Abstract. This study examines the structural behaviour of a novel floor beam solution AB-SFB (Asymmetric Box - Slim Floor Beam), developed as a low-carbon alternative to conventional steel–concrete systems within the framework of sustainable construction objectives set by the European Green Deal and the EU Taxonomy Regulation. The presented experimental program aims to assess the bending capacity, stiffness and failure mechanism of a full-scale steel-timber-concrete composite beam (STCC). The cross-laminated timber (CLT) in the STCC configuration replaces most of the concrete and eventually the steel sheeting, enabling reduced floor weight and improved material efficiency. The beam consists of two parallel welded HE 200 A HISTAR® 460 steel sections filled with concrete, flanked by CLT panels on the left and right sides. The top fibre of the CLT panel is aligned with the top of the steel flange. Both are covered by a 60 mm reinforced concrete slab to achieve composite action. A strain-controlled method was employed to estimate the bending resistance. The results were validated against the experimentally determined values. The findings demonstrate that STCC beams offer a promising solution for low-carbon flooring designs.

Keywords: steel-timber-composite beams · shallow floor beams · CLT panels · composite action

1 Introduction

The construction sector faces increasing pressure to reduce greenhouse gas emissions, improve material efficiency, and accelerate construction processes. Within this context, hybrid structural systems combining steel and engineered timber have emerged as promising alternatives to conventional reinforced concrete solutions. Steel–timber composite systems exploit the high strength, durability, and recyclability of steel together with the renewability and low embodied carbon of timber, offering a favourable balance between structural performance and sustainability.

© The Author(s), under exclusive license to Springer Nature Switzerland AG 2026
R. Zanon et al. (Eds.): CTA 2026, LNCE 942, pp. 554–566, 2026.
https://doi.org/10.1007/978-3-032-39505-4_48

Above that, slim-floor systems represent a particularly attractive application due to their reduced structural depth, and improved fire performance. While steel–concrete slim floors are well established, comparable systems incorporating timber as a structural component remain scarce. Existing concepts are limited, [1–3], and demonstrate advantages such as reduced floor depth, integrated fire protection, and minimised cladding requirements. The absence of standardised design rules and reliable experimental datasets remains a key barrier to wider adoption.

This study addresses this gap by investigating a newly developed asymmetric box slim-floor beam (AB-SFB) combining steel, CLT panels, and concrete. The objective is to experimentally quantify its flexural performance and composite behaviour and to validate simplified analytical design approaches suitable for engineering practice.

2 AB SFB Beams Experimental Test Campaign

2.1 System and Section

The experimental campaign was conducted at the University of Luxembourg within the ArcelorMittal Chair of Steel Construction. The objective of the beam tests was to study the bending capacity of the novel defined slim floor solution and if sufficient composite action of the system can be reached. The initial geometry of the testing campaign was provided by ArcelorMittal Global R&D. Materials used in the AB-SFB testing campaign are summarised in Table 1. The experimentally determined values are presented in Sect. 3. The cross section used for longitudinal beams tests is presented in Fig. 1.

Table 1. Summary of material properties.

Material	Details
Steel Section	S460 XCarb® [4] box girder formed by two HE 200 A rolled sections welded together. The steel is provided by ArcelorMittal.
CLT Timber	5-Layer spruce KLH® - CLT Panel [5]; seated on the bottom steel flange (450 mm × 180 mm). The CLT planks are provided by KLH.
Concrete	C 25/30 low-carbon concrete slab (60 mm × 1200 mm)
Reinforcement	Reinforcement rebar (Ø8–150), and U-bars over the steel beam to resist uplift (Ø12–150)
Shear Connector	mechanical shear connectors (Rothoblass CTC screws) providing composite action between concrete to timber (Ø7 mm × 160 mm length, every 150 mm), and 220 mm × 20 mm × 20 mm rectangular bars every 150 mm welded on top of the steel beam.

The experimental program consists of three 5,25 m long longitudinal tests (LT-1, LT-2, and LT-3) each consisting of two HE 200 A steel profiles, low-carbon C25/30 concrete, KLH® CLT panels and Ø8 reinforcement bars spaced at 150 mm. The structural system consists of a simply supported beam with an effective length of 4.75 m between supports, as shown in Fig. 2. The longitudinal tests were performed in the Laboratory of the University of Luxembourg using the vertical frame (PP4000) that has a pressing force of up to 4 MN (2 Hz) and a maximum stroke of 400 mm. The beam is tested as a 4-point bending loading tests to evaluate the bending behaviour and flexural stiffness. The load was applied symmetrically at two points 750 mm apart on the top concrete surface using a spreader beam. The spreader beam's self-weight was 17.5 kN and was implemented in the loading procedure, as shown in Fig. 3.

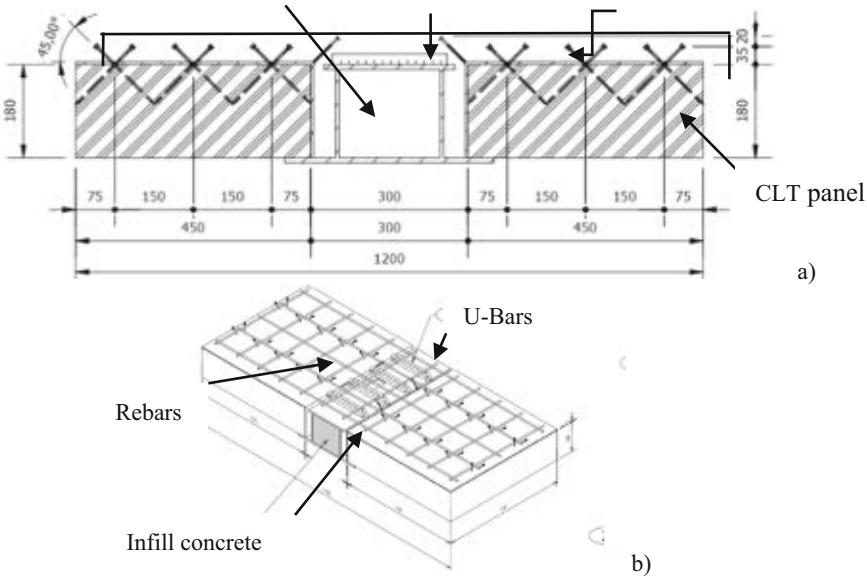


Fig. 1. Beam tests –a) Cross-section without rebars; b) cut perspective view without concrete.

2.2 Loading Communications Protocol

The loading protocol followed Eurocode 4, Annex B [6]. It comprised an initial load ramp from 0% to 5% of the maximum estimated load, followed by 25 cyclic loadings between 5% and 40%. After these cycles, the load was successively increased with unloading and reloading cycles separated by a 5-min pause, as shown in Fig. 3.

After reaching a level of 80% of estimated maximum load, the beam was loaded without unloading up to failure.

The position of the applied force was chosen such as to convert easily the force values into bending moments. To avoid local failure of the concrete surface, a spreader beam was used to apply the loads as shown in Fig. 2b).

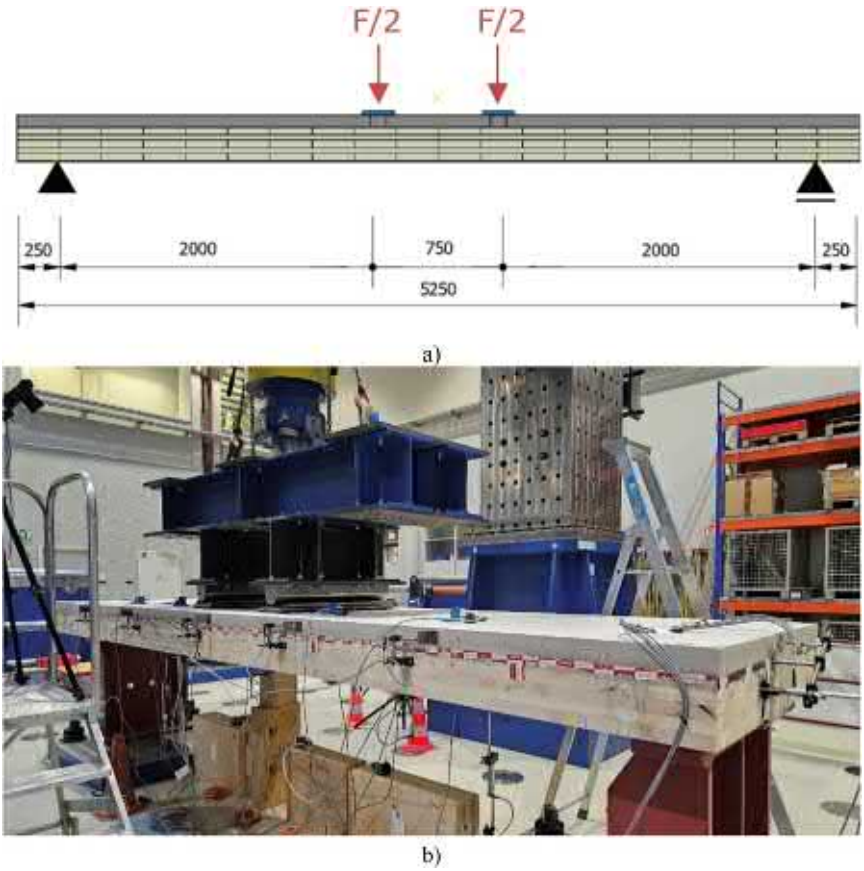


Fig. 2. Beam test –a) structural system; b) specimen before testing.

The test setup and instrumentation were designed to capture the global response, composite interaction, and local strain behaviour of the specimen. Deflections were measured at five locations, including midspan and load introduction points, using wire displacement sensors beneath the beam. Strains were monitored with gauges on the steel beam, while LVDTs on the slab's top surface measured compression-zone strains. Relative displacements between materials were recorded using LVDTs positioned at the bottom, along the sides, and ends of the specimen, see Fig. 2b).

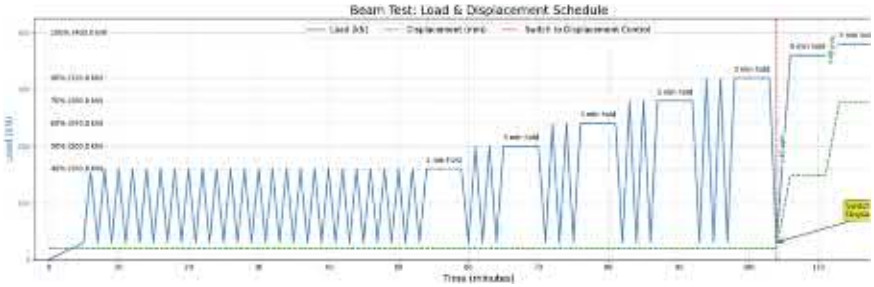


Fig. 3. Beam test – a) beam measurements and load introduction; b) loading procedure.

2.3 Results

The bending moment–deflection curves at midspan for specimens LT-1, LT-2, and LT-3 are presented in Fig. 4. All specimens exhibit similar deflection behaviour, with an average maximum bending capacity of 548 kNm at a midspan deflection of 73.4 mm (L/65), as summarised in Table 2. The beam failed due to concrete crushing at midspan, see Figs. 8b) and 9b).

The plastic bending capacity of the steel section, based on experimentally determined yield strength of steel flanges, is Mpl.a.emat =352.15 kNm, while the composite steel–concrete capacity reaches Mpl.sc. emat =466.9 kNm for specimen LT-1, considering the measured concrete strength on the test day. These values were obtained using the strain-limited approach described in Sect. 3. The results confirm that the AB-SFB slim-floor system develops composite action, with the timber component in compression contributing also to the overall bending resistance of the system.

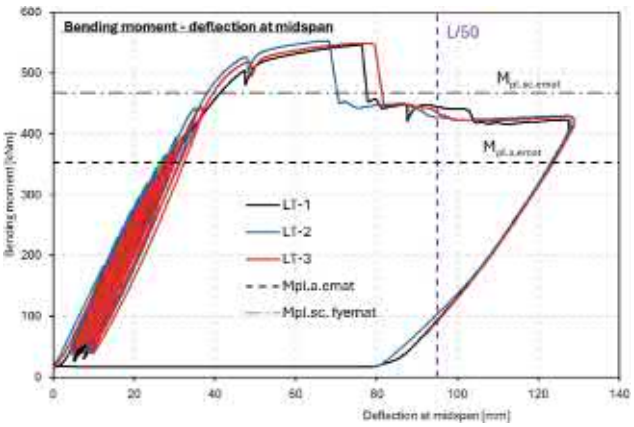


Fig. 4. Beam tests: Bending moment vs. mid span deflection - comparison.

The strain at the midspan of the steel profile, in both the bottom and upper flanges, is presented in Fig. 5 and Table 3. The steel grade is S460JR + M, with a yield strain of 2.24% determined from tensile coupon tests conducted on the flange. Similar strain values are observed on both the left and right sides of the specimens. At ultimate load, yielding of the bottom flanges occurs in all three specimens, approximately coinciding with the onset of concrete crushing at midspan.

Table 2. Beam tests – maximum bending moment and deflection – experimental values.

Specimen	Max bending moment M_{max} [kNm]	Deflection at M_{max} [mm]
LT-1	545.5	76.0 (L/62.5)
LT-2	552.4	67.8 (L/70.0)
LT-3	548.0	76.3 (L/62.0)

Table 3. Longitudinal tests – steel profile yield strains values at ultimate load.

Spec.	DMS_T_3 [%]	DMS_T_4 [%]	DMS_B_3 [%]	DMS_B_4 [%]
LT-1	1.64	1.59	6.30	5.31
LT-2	1.42	1.38	5.82	7.46
LT-3	1.55	1.45	5.89	5.40

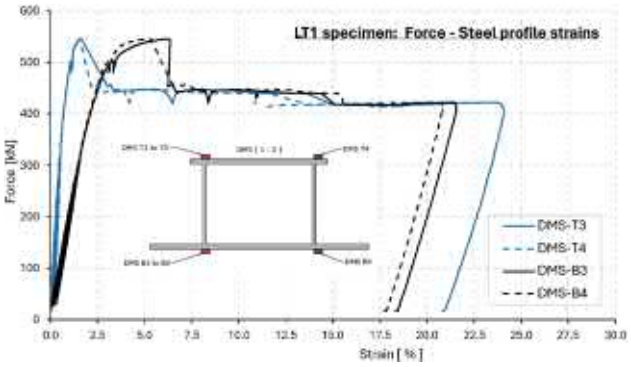


Fig. 5. LT-1 Specimen: Force – steel profile strains.

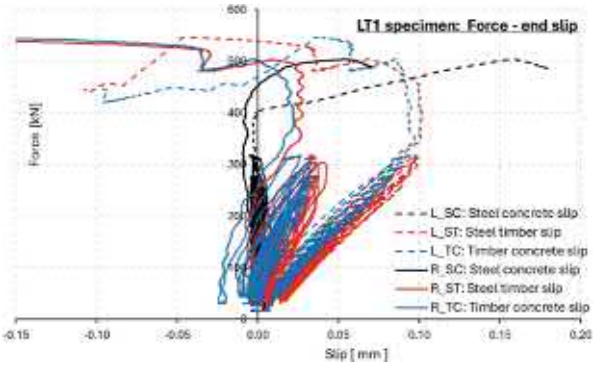


Fig. 6. LT-1 Specimen: Force – end slip between structural components: measured values.

End slips at the steel–timber (ST), steel–concrete (SC), and timber–concrete (TC) interfaces were measured at both ends of each specimen, on the left and right sides. The resulting force–slip relationships are presented in Fig. 6. It can be observed that the measured slips remained very small, on the order of 0.1 mm, up to specimen failure. This confirms that full composite action was maintained and that the shear connections at all three interfaces were fully mobilised throughout the loading process. Figure 7 provides a visual indication of the relative slip between the timber and concrete layers observed after failure.



Fig. 7. LT-1 Specimen: concrete timber end slip, post failure.

The vertical displacement distribution along the beam at different load levels for all three specimens is presented in Fig. 8a). The sensors were positioned on the bottom flange of the steel profile. All specimens exhibit a similar deflection pattern and comparable maximum midspan deflections.

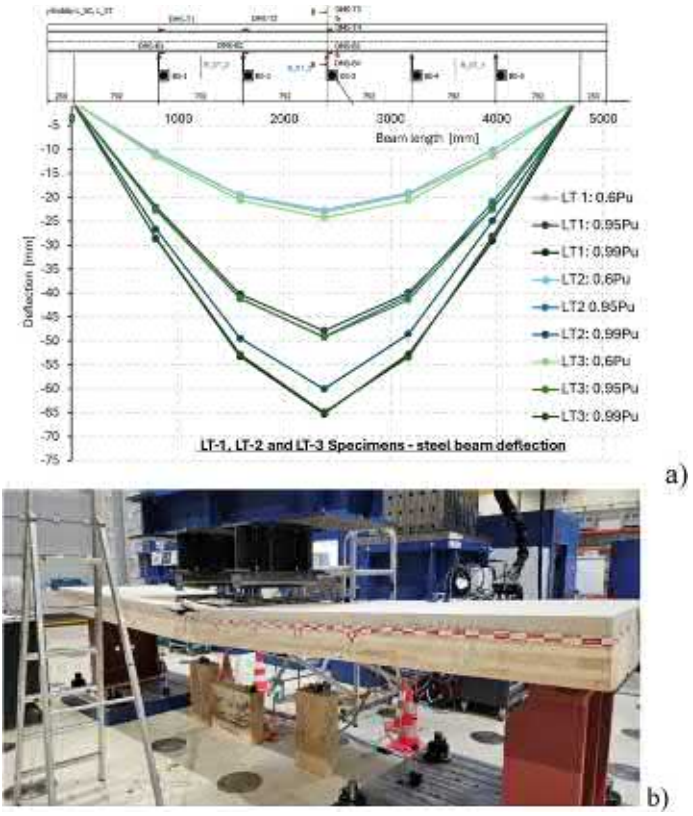


Fig. 8. Beam tests: a) vertical deflection; b) LT-1 specimen at failure

The LVDT measurements converted into strains are shown in Fig. 9. They were installed on the top surface of the concrete specimens and had a gauge length of 100 mm. The compressive strain in concrete at peak stress, $\varepsilon c1$ was evaluated acc. to EN 1992-1-1:2004 [7] yielding an average value of $\varepsilon c1 \approx 0.0021$ (i.e. 0.21%), as shown in Table 5. It can be observed that the LVDTs located at the extremities (TC_1 and TC_2) did not reach the strain corresponding to the maximum compressive stress in any of the three specimens.

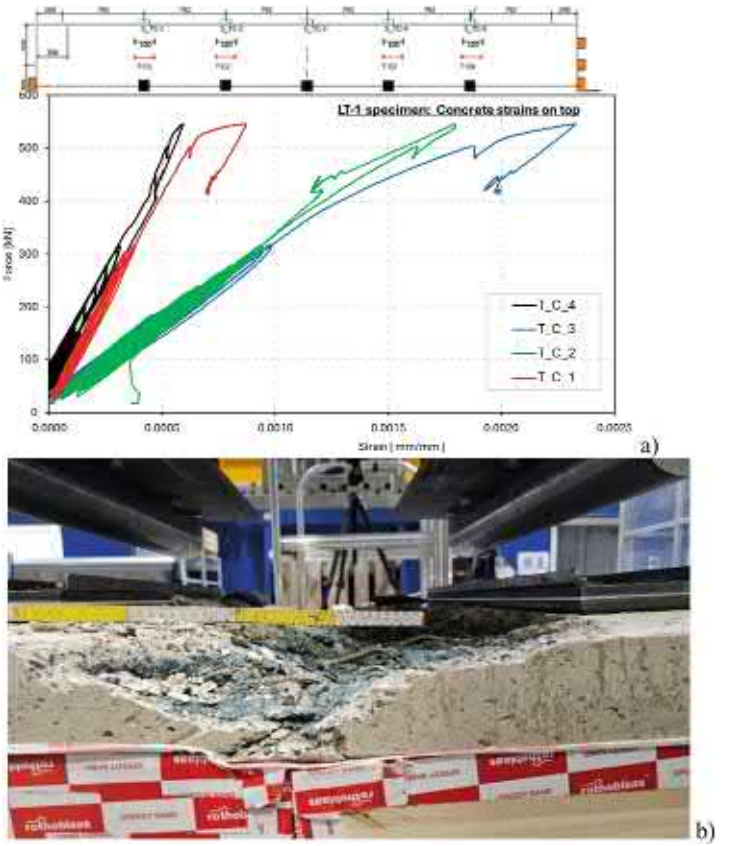


Fig. 9. Beam tests: a) strain values at the top of the concrete surface; b) concrete crushing failure at midspan

3 Analytical Investigations

To assess the bending moment capacity of the composite beam, a strain-based method based on the assumption that the section remains plane and the cross section has the same curvature was used [11]. The section is divided into "fibers" for all concerned materials: steel profile (ε_a), concrete slab (ε_c) and CLT layers (ε_{ti}). The strain limits of each material are considered while the neutral axis is evaluated by force equilibrium. The bending moment capacity is obtained by stress integration across the section under the following assumptions: i) plane sections remain plane; ii) one fibre reaches its ultimate strain; and iii) full composite action ($\eta = 1.0$) is assumed. For each prescribed strain state of the cross section, the neutral axis is iterated until $\Sigma F = 0$, then stresses are integrated to obtain the bending moment values, Fig. 10. The stiffness of the cross section at any given acting moment can be derived from the respective curvature that corresponds to the actual strain distribution. The respective midspan deflection is obtained by integrating the curvature distribution $\kappa(x)$ along the beam by direct numerical integration of $\kappa(x)$.

Partial shear connection ($\eta < 1.0$) can be incorporated via reduced compressive force in the slab.

In the analytical model presented here, full composite action ($\eta = 1.0$) is assumed due to very small slip between materials, see Fig. 6. For concrete and timber materials only the compression contribution is considered. The contribution of the CLT panels in tension is neglected due to the discontinuity of the panels at midspan (see Fig. 8b), while the tensile strength of concrete is neglected, in line with the EN 1992-1-1:2004 [7] recommendations.

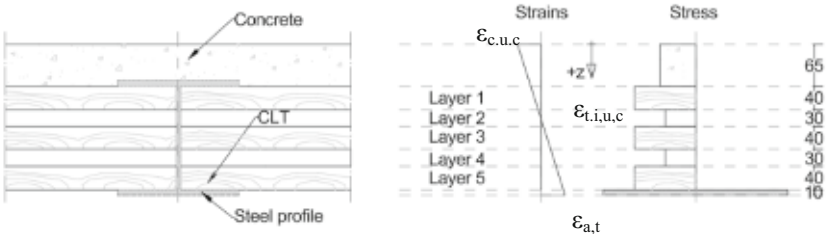


Fig. 10. Analytical strain based method for steel-timber-concrete composite slim floor.

Experimental values for concrete and steel materials were used. The steel profile is defined using a material law with yielding plateau and strain hardening according to EN 1993-1-14 [8] and results obtained experimentally on tensile coupon tests. The tensile test results in flanges and respectively web are shown in Table 4.

Table 4. HE 200 A profile – definition of the material law based on EN 1993-1-14 [8].

Position	E [GPa]	f_y [MPa]	f_u [MPa]	ε_y [%]	ε_{sh} [%]	ε_u [%]	c_1	c_2	E_{sh}
Flange	210	472.4	598.9	0.0022	0.0239	0.1267	0.39	0.51	3075.1
Web	210	501.1	592.3	0.0024	0.0296	0.0924	0.49	0.59	3630.5

Longitudinal and transverse rebars are modelled with an elastic–perfectly plastic stress–strain law, with modulus of elasticity 200 GPa and yield stress 500 MPa.

The timber was modelled as an orthotropic elastic-plastic material. Its elastic properties were defined by the engineering constants provided in [5]. The onset of plastic yielding was governed by the Hill yield criterion [9].

The stress-strain relationship for concrete in short term loading is defined according to FIB Model Code 2010 [10]. The compressive strain in concrete at peak stress $\varepsilon c1$ has been evaluated according to EN 1992-1-1:2004 [7]. Cube and cylinder compressive strengths were determined at 28 days, and the resulting cube-to-cylinder conversion ratio was applied to the cube specimens tested on the day of each beam test, as reported in Table 5.

Figure 11 presents a comparison between the experimentally and analytically derived bending moments and their midspan displacement. The results indicate that the analytical

Table 5. Compression strength values converted to cylinders based on experimental values.

Spec.	Measured cube stress [MPa]	Converted cylinder values [MPa]	ε_{c1} [%]
LT-1	29.15	24.41	0.00205
LT-2	30.80	27.90	0.00212
LT-3	31.21	28.21	0.00212

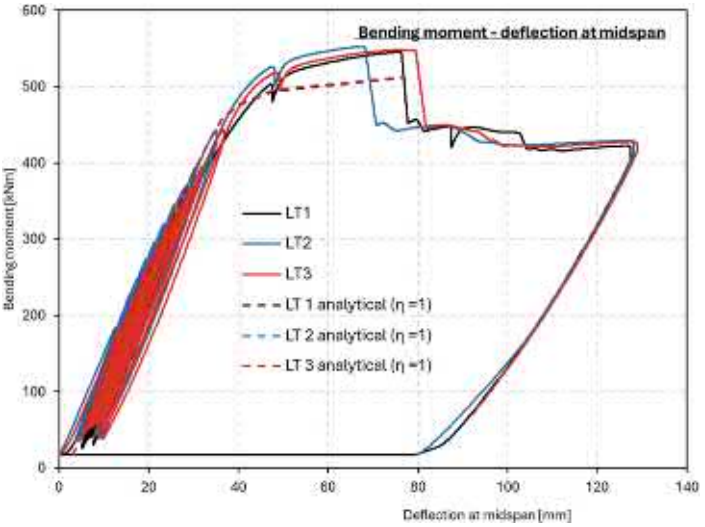


Fig. 11. Experimental curves vs. M_(η = 1) strain controlled analytical curve.

approach provides a high level of accuracy in predicting the experimental response, particularly in terms of maximum bending moment, corresponding midspan deflection, and overall stiffness.

As shown in Table 6, the discrepancies between the analytical predictions and experimental results are below 10% for both the maximum bending moment and the associated midspan deflection.

Table 6. Ultimate bending moment vs. deflection values – analytical vs. experimental.

Spec.	Experimental values		Analytical values		Ratio M_{max} [%]	Ratio d_{Mmax} [%]
	M_{max} [kNm]	d_{Mmax} [mm]	M_{max} [kNm]	d_{Mmax} [mm]		
LT-1	545.5	76.0	511.9	76.7	93.8%	100.9%
LT-2	552.4	67.8	511.9	76.7	92.7%	113.0%
LT-3	548.0	76.3	513.1	76.9	93.6%	100.8%

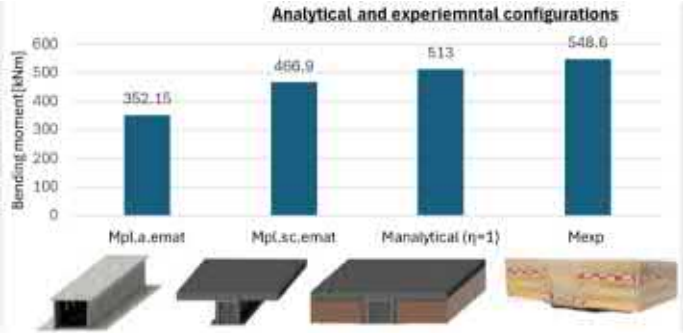


Fig. 12. Bending moment values for different cross section configurations.

Figure 12 presents an overview of several configurations and their corresponding bending capacity related to the experimental beam: i) steel profile alone (HE 200 A box I S460); ii) steel and concrete ($\eta = 1$), iii) AB-SFB composite system; iv) steel, concrete and timber panels ($\eta = 1$); iv) LT-1 experimental specimen. It can be observed that all structural materials: steel, timber and concrete materials contribute to the bending capacity of the system.

4 Conclusions

The experimental campaign conducted on the AB-SFB (Asymmetric Box - Slim Floor Beam) slim floor solution provides a comprehensive and consistent assessment of the structural performance of a steel–timber–concrete composite solution. The tested specimens exhibited repeatable behaviour, composite interaction, and predictable failure mechanisms, confirming the effectiveness of the system's geometry, material configuration, and connection detailing.

The bending tests demonstrated a consistent bending capacity, with all three full-scale beams reaching an average ultimate bending moment of approximately 548 kNm and midspan deflections ranging between L/62 and L/70 at failure. The bending moment–deflection curves displayed limited variation in stiffness, confirming the stability of the system and the reliability of the experimental setup. The principal failure mechanism was governed by concrete crushing in the compression zone, accompanied by rebar yielding and yielding of the bottom steel flange, indicating appropriate strain redistribution within the composite cross-section. No substantial failure was observed in the CLT panels.

The analytical strain-controlled predictions captured the ultimate capacity and the stiffness of the AB SFB slim floor system. This confirms that a strain-based approach can be used to predict the bending capacity of the newly defined structural beam.

References

1. Nordec slim-floor beams – Nordec. https://nordec.com/nordec-slim-floor-beams/. Accessed 11 May 2026

2. DELTABEAM® slim floor structure with timber constructions: DELTABEAM® enables open spaces and slim floors with timber slabs. https://www.peikko.com/references. Accessed 12 Feb 2026
3. Aspila A, Lepikonmäki L, Pajunen S (2023) Suitability of slim-floor steel–timber composites as intermediate floor constructions: case study based on projects in Finland. In: 13th world conference on timber engineering, WCTE 2023, vol 7, pp 4247–4252. https://doi.org/10.52202/069179-0552
4. ArcelorMittal Europe (2021) EPD-ARC-20210132-CBB2-EN: Environmental product declaration as per ISO 14025 and EN 15804+A1. ArcelorMittal Europe, July 2021. https://www.ibu-epd.com; https://epd-online.com
5. Österreichisches Institut für Bautechnik (OIB) (2021) ETA-06/0138 of 18 January 2021: European technical assessment for the construction product KLH®–CLT. Österreichisches Institut für Bautechnik, Vienna. https://www.oib.or.at
6. CEN (2004) EN 1994-1-1, Eurocode 4: design of composite steel and concrete structures—part 1–1: general rules and rules for buildings. European Committee for Standardization, Brussels
7. CEN (2004) EN 1992-1-1, Eurocode 2: design of concrete structures—part 1–1: general rules and rules for buildings. European Committee for Standardization, Brussels
8. CEN (2025) EN 1993-1-14, Eurocode 3: design of steel structures—part 1–14: design assisted by finite element analysis. European Committee for Standardization, Brussels
9. Hill R (2009) The mathematical theory of plasticity. Oxford University Press, Oxford
10. Kordina K, Mancini G, Schäfer K, Schießl A, Zilch K (2010) Structural concrete textbook on behaviour, design and performance, fib Bulletin 54, vol 4, 2nd edn. International Federation for Structural Concrete, Lausanne. https://doi.org/10.35789/fib.BULL.0055
11. Romero A, Odenbreit C (2024) Experimental investigation on novel shear connections for demountable steel–timber composite beams and flooring systems. Eng Struct 304:117620. https://doi.org/10.1016/j.engstruct.2024.117620

Types of Hybrid Steel-Timber Structural Systems for Sustainable Constructions

Giacomo Iovane(✉), Raffaele Landolfo, and Beatrice Faggiano(✉)

Department of Structure for Engineering and Architecture, University of Naples Federico II, P.le Tecchio, 80, 80125 Naples, Italy
{giacomo.iovane,faggiano}@unina.it

Abstract. The increasing demand for sustainable construction practices has encouraged the development of structural systems capable of reducing the environmental impact. In this context, timber has gained significant attention as a renewable material characterized by a low embodied carbon footprint. Timber use has expanded considerably in recent decades, not only in all-timber buildings, but also in hybrid configurations where it is combined with other structural materials such as steel, concrete and glass to enhance overall structural performance. In particular, hybrid steel-timber systems represent promising structural solutions, as they enable the synergistic combination of the environmental benefits, lightness and favorable fire performance of timber with the high strength, stiffness and ductility provided by steel elements. Such hybridization can therefore provide improved structural efficiency while contributing to sustainability objectives. The present paper presents a brief critical review of the main state of the art on hybrid steel–timber structural systems, with particular emphasis on applications for seismic design. Based on the available literature, the main structural types are identified and a comparative assessment is then performed to highlight common trends, differences among the configurations and the main knowledge gaps that should be filled for the development of consistent design methodologies and broader structural applications.

Keywords: Timber structures · Steel structures · Hybrid steel-timber structures · sustainable constructions · seismic resistant steel-timber structures

1 Introduction

The growing demand for sustainable buildings has significantly promoted the use of timber as a primary structural material. Recent advances in engineered wood products have considerably improved the mechanical performance of timber, enabling the construction of multi-storey [1] and long-span buildings that were traditionally realized using steel or reinforced concrete. Consequently, timber has become an increasingly competitive solution for modern structural applications, combining low environmental impact with high levels of prefabrication and construction efficiency. Despite these advantages, the structural performance of timber buildings may be enhanced by integrating steel components into the load-resisting system. Steel provides high strength, stiffness and ductility,

© The Author(s), under exclusive license to Springer Nature Switzerland AG 2026
R. Zanon et al. (Eds.): CTA 2026, LNCE 942, pp. 567–575, 2026.
https://doi.org/10.1007/978-3-032-39505-4_49

while timber offers lightweight and sustainability. The combination of these complementary properties has led to the development of hybrid steel-timber structural systems, in which the two materials cooperate at the member, connection or structural-system levels to improve both structural and seismic performance [2]. During the last decade, several hybrid solutions have been proposed, including steel frames coupled with timber shear walls, composite steel-timber floor systems, hybrid framed structures and timber buildings equipped with steel dissipative devices or buckling-restrained braces. These systems have demonstrated significant potential in terms of stiffness, strength, energy dissipation, construction efficiency and environmental performance. Nevertheless, the available studies are generally focused on individual structural configurations, while a comprehensive structural evaluation of hybrid steel-timber framed systems is still missing. A preliminary classification of the structural types, based on literature review has recently been proposed [3]. Furthermore, although current design standards provide comprehensive rules for steel and timber structures separately, specific provisions for hybrid steel-timber systems remain limited, particularly under seismic actions, where capacity design criteria and dissipative mechanisms are not yet consistently addressed within existing codes. In this context, the present paper reviews the current state of the art in the scientific literature on hybrid steel-timber framed structural systems, proposes a classification of the main typological categories and discusses the current design framework together with the main research needs toward the development of dedicated design guidelines.

2 Identification of the Typological Categories for Hybrid Framed Structural Systems from Literature

Based on the structural role assigned to steel and timber components, five main types of steel-timber composite and hybrid structural systems can be identified from the analysis of the state of the art (Fig. 1):

Type 1. Steel frame or hybrid steel-timber frame with timber shear panels;
Type 2. Timber frame with steel seismic resisting systems;
Type 3. Steel-timber dual framed systems;
Type 4. Steel-timber hybrid and composite floor diaphragms;
Type 5. Timber Buckling-Restrained Brace (T-BRB).

Among Type 1 (Figs. 1 and 2), the following configurations can be identified: (1.1) *steel edge frame with mass timber panel*; (1.2) *steel edge frame with light-weight timber wall*; (1.3) *cold-formed steel frame with timber-based panel*; (1.4) *hybrid frame with steel columns and timber beams, slabs and walls*. Despite their different constructional details, all systems use timber panels to increase the lateral stiffness and resistance of the steel frame. This contribution has been demonstrated for CLT infills [4], lightweight timber walls [5] and wood-sheathed CFS frames [6]. The cyclic response is mainly governed by panel-to-frame connections, which control force transfer, deformation capacity and energy dissipation. Recent studies have therefore investigated improved connection details. For Type 1.1, concealed steel plates with drift pins [7], friction-type high-strength bolted joints [8] and dissipative annular connectors [7, 9] were examined. These solutions

increased lateral resistance, initial stiffness and energy dissipation while concentrating damage at the panel-to-frame connections [7]. For Types 1.2 and 1.3, low-damage techniques based on friction-based devices, post-tensioning and self-centering systems were proposed to reduce damage and residual drift to the lightweight timber walls and facilitate post-earthquake repair [10–12]. Moreover, alternative fastening layouts and refined hysteretic models were instead examined to account for pinching and progressive stiffness and strength degradation. In Type 1.4 systems, steel columns and timber beam resist gravity loads while the timber wall resists horizontal actions. Even in this case the dissipative role is entrusted to panel-to-frame connections [12].

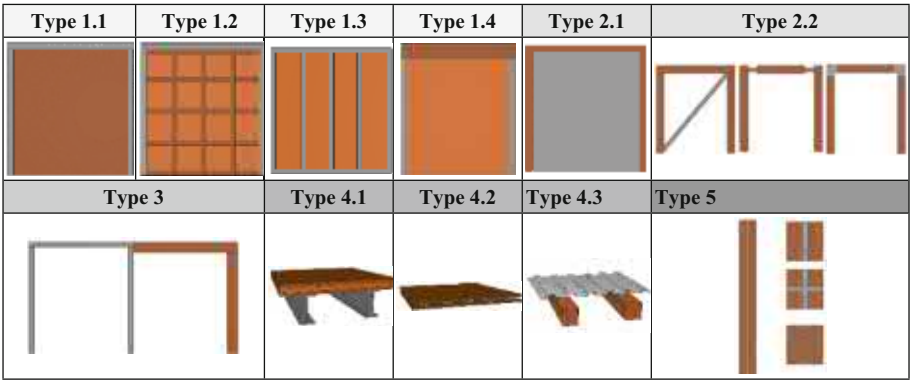


Fig. 1. Types of hybrid and composite structural systems.

Among Type 2 (Figs. 1 and 2), the following configurations can be identified: (2.1) *timber edge frame with mass Steel Plate Shear Walls (SPSWs)*; (2.2) *timber frame with steel members and joints*; In Type 2.1, timber frame mainly resist gravity loads, whereas the steel walls provide lateral stiffness, resistance and energy dissipation. The interaction between the two subsystems is mainly governed by wall-to-diaphragm connections. Preliminary studies showed that the SPSWs can resist most of the lateral demand while limiting deformation and damage in the timber frame [13]. In Type 2.2 systems, steel members or dissipative devices are introduced within timber frames to concentrate inelastic deformation in replaceable components rather than in conventional timber connections. Recent studies have investigated the use in timber frames of friction braces, Additional Damping and Stiffness devices, post-tensioned systems and dissipative steel links [14 – 17]. These devices increase lateral stiffness, resistance and energy dissipation while limiting damage to timber members. Steel links have been applied to timber Moment-Resisting Frames, Concentric and Eccentric Braced Frames and studied through both numerical and experimental investigations, allowing for the definition of capacity-design principles [15, 16].

Type 3 hybrid systems (Figs. 1 and 2) separate the structural functions into a dual system, where gravity loads are resisted by the timber frame and horizontal actions are resisted by the steel frame [17]. Full-scale shake-table tests confirmed the feasibility of such structural combination [18]. Comparative studies also showed that this

hybrid solution can achieve seismic performance comparable with all-steel systems while significantly reducing embodied carbon emissions and structural mass [19].

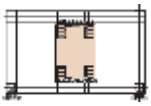
Type 1.1	Type 1.2	Type 1.3	Type 1.4	Type 2.1	Type 2.2
					
Too and Isoda, 2023	Zheng et al., 2024	Fiorino et al., 2024	Jamil et al., 2015	Wang et al., 2026	Iovane et al., 2023b
Type 3	**Type 4.1**	**Type 4.2**	**Type 4.3**	**Type 5**	
					
Li et al., 2023	Laughery et al., 2025	Kyvelou et al., 2021	Boucher and Lamarche, 2019	Wang et al., 2023	

Fig. 2. Research studies on hybrid and composite structural systems.

Among Type 4 (Figs. 1 and 2), it is possible to identify the following most common system configurations: (4.1) *steel beams with mass timber diaphragm*; (4.2) *composite lightweight steel-timber diaphragm*; (4.3) *timber beams with steel-based composite floor diaphragm.* In all types, the structural response is mainly governed by the connections between the steel and timber components, which control force transfer, interface slip, diaphragm stiffness and the degree of composite action [20]. For Type 4.1 recent research has focused on more efficient and demountable connections, including reversible bolted connectors [21], optimized connector layouts for long-span composite floors [22] and improved shear-transfer devices designed to enhance composite action and facilitate disassembly and reuse [20]. Similar developments have been pursued for Type 4.2 systems, through the optimization of prefabricated lightweight floor assemblies for modular construction [23], whereas for Type 4.3 systems recent research has highlighted the potential of steel-based composite diaphragms to increase span capability, diaphragm stiffness and construction efficiency, although further studies are still required to characterize the cyclic response and the behavior of the diaphragm-to-frame connections [24].

Finally, Type 5 hybrid system (Figs. 1 and 2) is the Timber Buckling-Restrained-Brace (T-BRB), applicable to both steel and timber structures. T-BRB consists of a steel core, which can be made of profiles of various shapes or bars and is responsible for axial energy dissipation, enclosed in a timber shell, generally made of radiata pine or Douglas fir, which provides restraint against buckling. Stable hysteretic behavior can be obtained through an appropriate design of the steel core, timber casing and end connections [25]. Recent studies have extended the development of T-BRBs from component tests to complete timber structural systems. Engineered timber casings have shown adequate

buckling restraint and stable cyclic response in qualification tests [26]. Numerical and experimental studies on multi-storey timber frames also showed that BRBs increase lateral stiffness, resistance and energy dissipation while concentrating damage in the replaceable steel core [27]. Applications to high-rise glulam buildings demonstrated satisfactory seismic and collapse performance under severe ground motions [28]. Large-scale shake-table tests further confirmed the effectiveness of combining BRBs with mass-timber structural systems, provided that adequate overstrength is assigned to the brace-to-frame connections and the surrounding timber members [29].

Table 1. Structural characteristics of the identified hybrid steel-timber types.

Type	Role of timber elements	Role of steel elements	Dissipative role	Main advantages	Current research focus	Main research gaps
1.1	Shear wall	Gravity frame	Panel-frame connections	High stiffness	Panel-frame dissipative connections	Capacity design, global cyclic response, dissipative devices other than connections
1.2		Gravity and horizontal load resisting frame		High stiffness, modularity	Panel-frame dissipative connections, modular prefabrication	
1.3						
1.4	Gravity frame and shear wall	Gravity frame		Damage control	Hybrid beam-column and beam-panel connections	Design rules
2.1	Gravity frame	Shear wall		High energy dissipation	Panel-frame dissipative connections	Reduced number of experimental tests and design rules
2.2	Gravity and horizontal load resisting frame	Horizontal load resisting element	Steel elements or dissipative devices	Damage control	Steel links, PT, friction	Capacity hierarchy and design rules
3	Gravity frame	Horizontal load resisting frame		Structural decoupling	System interaction	System-level validation
4.1	Compression side of the composite section, floor diaphragm	Tension side of the composite section	/	High stiffness-to-weight ratio	Shear connector types	Cyclic diaphragm response
4.2	Composite flexural action				Modular floor systems	Long-span performance

(*continued*)

Table 1. (*continued*)

Type	Role of timber elements	Role of steel elements	Dissipative role	Main advantages	Current research focus	Main research gaps
4.3	Tension side of the composite section	Compression side of the composite section, floor diaphragm			Shear connector types	Seismic diaphragm response
5	Core	Shell	Steel core	Stable hysteresis	System integration	Frame interaction

Table 1 provides a synoptic overview of the hybrid steel-timber structural types identified. In particular for each case the role of timber and steel elements, the dissipative role, main advantages, current research focus and main research gaps are pointed out. Across all types, the principal limitation is the strong dependence of global performance on connections and subsystem interaction, which remain the main gap of current research.

3 Current Design Framework and Research Gaps

Although hybrid steel–timber structural systems have attracted increasing research interest in recent years and several building realizations, dedicated design provisions are still unavailable. The design is generally carried out by combining standards for steel and timber structures, according to the structural function performed by each material. While this approach provides adequate rules for the verification of individual members, it does not address the behavior of the hybrid structural system as a whole. In particular, no harmonized procedures are currently available for the classification of hybrid structural systems, the design of steel-to-timber connections, the definition of dissipative mechanisms or the application of capacity-design principles. As highlighted by the literature review, hybrid steel–timber systems include a wide range of structural solutions, differing in terms of load-transfer systems, interaction between materials and seismic response. Despite the increasing number of experimental and numerical studies, the design still relies mainly on project-specific approaches rather than on standardized code provisions. This issue is particularly relevant for seismic-resistant systems, where the location of the dissipative zones, the hierarchy of resistance and the interaction between steel and timber members play a fundamental role in the structural response. The development of dedicated design recommendations therefore represents one of the main challenges for the practical implementation of hybrid steel-timber structures. Future standards should provide a consistent framework for the classification of hybrid systems, the definition of structural and dissipative typologies, the design of steel-to-timber connections and the application of capacity-design criteria, enabling a unified design approach comparable to that currently available for steel, timber and steel-concrete composite structures. Future developments should also address life-cycle assessment.

4 Conclusive Remarks

From the review of hybrid timber-steel framed structural systems based on scientific literature, at first, four typological categories are identified, then the most significant research contributions are critically examined, including experimental investigations, numerical analyses and innovative design approaches for both global structures and connection details. Several hybrid solutions are addressed, also equipped with special devices for seismic protection, such as steel dissipative links, friction connections, advanced self-recentering systems, etc. The reviewed studies demonstrate that combining timber with steel can give rise to efficient structural systems, with stable hysteretic behavior, enhanced energy dissipation capacity, controlled damage mechanisms and, in some cases, self-recentering capabilities that minimize residual deformations after seismic events. Definitely, hybrid timber-steel seismic-resistant structures are promising for future construction, combining sustainability with favorable structural performance. However, further research is recommended, going from numerical and experimental investigations, joint details conception and evaluation, long-term behavior assessment, towards the development of design guidelines to facilitate the practical implementation of the hybrid systems.

Acknowledgments. The research project DPC–ReLUIS 2024-2026–WP12 – Sub Task 12.3.2 Buildings with steel-timber composite structures is acknowledged.

References

1. Ascione F, Esposito F, Iovane G, Faiella D, Faggiano B, Mele E (2024) Sustainable and efficient structural systems for tall buildings: exploring timber and steel–timber hybrids through a case study. Buildings 14(2):524. https://doi.org/10.3390/buildings14020524
2. ECCS TC11 WG6 (2024) State of the art on steel–timber–(concrete) structures. Interim Report of ECCS TC11/WG6. European Convention for Constructional Steelwork (ECCS), Brussels. ISBN 978–92–9147-199-7
3. Iovane G, Landolfo R, Faggiano B (2026) Potential of hybrid steel-timber frames as sustainable seismic structures. Procedia Struct Integr 78:528–535. https://doi.org/10.1016/j.prostr.2025.12.068
4. Loss C, Piazza M, Zandonini R (2016) Connections for steel–timber hybrid prefabricated buildings. Part I: experimental tests. Constr Build Mater 122:781–795. https://doi.org/10.1016/j.conbuildmat.2015.12.002
5. He M, Li Z, Lam F, Ma R, Ma Z (2014) Experimental investigation on lateral performance of timber-steel hybrid Shear Wall systems. J Struct Eng 2014. https://doi.org/10.1061/(asce)st.1943-541x.0000855
6. Landolfo R, Fiorino L, Della Corte G (2006) Seismic behaviour of sheathed cold-formed structures: physical tests. J Struct Eng. ASCE. ISSN 0733-9445/2006/4. https://doi.org/10.1061/(ASCE)0733-9445(2006)132:4(570)
7. Too Je RY, Isoda H (2023) Seismic performance of CLT shear wall infilled hybrid steel moment frame with concealed steel plate and drift-pin connections. In: Proceedings of the world conference on timber engineering. https://doi.org/10.52202/069179-0455

8. Zhang Q, Li Z, Wang X, He M (2024) Experimental and parametric study on friction-type high-strength bolted connections between steel frames and cross-laminated timber infill walls. Structure 69:107412. https://doi.org/10.1016/j.istruc.2024.107412
9. Shen Y, Dong R, Nie Z, Sun G (2026) Connection and seismic performance of a hybrid steel–cross-laminated timber wall system. J Build Eng. https://doi.org/10.1016/j.jobe.2026.115322
10. Dong H, He M, Christopoulos C, Li Z (2021) Quasi-static tests and parametric simulations of hybrid steel frame and light wood shear walls with frictional dampers. Eng Struct 228:111485. https://doi.org/10.1016/j.engstruct.2020.111485
11. Fiorino L, D'Addesa V, Landolfo R (2024) Seismic design rules for lightweight steel shear walls with wood panel sheathing within the Eurocode format. Thin-Walled Struct. https://doi.org/10.1016/j.tws.2024.112293
12. Jamil M, Quenneville P, Clifton GC (2015) Scaled shake table tests of a novel gravity rocking moment frame system. Proceedings of the new Zealand Society for Earthquake Engineering Annual Conference. Rotorua, New Zealand
13. Wang Z, Li Z, He M (2026) Development and experimental validation of deformable wall-to-floor connection for seismic resilient steel-timber hybrid structures. Eng Struct 349:121898. https://doi.org/10.1016/j.engstruct.2025.121898
14. Chen F, Li Z, Li M, Shu Z (2023) Experimental testing of post-tensioned steel–timber hybrid frames equipped with energy-dissipating braces. Eng Struct 296:116960. https://doi.org/10.1016/j.engstruct.2023.116960
15. Iovane G, Oliva V, Faggiano B (2023) Design and analysis of dissipative seismic-resistant heavy timber frame structures equipped with steel links. Procedia Struct Integr 44:1864–1869. https://doi.org/10.1016/j.prostr.2023.01.238
16. Iovane G, Rodrigues L, Branco J, Faggiano B (2023) Monotonic tests on beam-to-column joints with steel links for timber seismic-resistant structures. In: Proceedings of the world conference on timber engineering. https://doi.org/10.52202/069179-0288
17. Li Z, Wang Z, He M, Shu Z (2023) Direct displacement-based design of steel–timber hybrid structures with separated gravity and lateral resisting systems. J Build Eng 69:106216. https://doi.org/10.1016/j.jobe.2023.106216
18. Field TJ et al (2025) Full-scale shake table test of a resilient six-story hybrid mass timber and steel structure. In: Proceedings of the world conference on timber engineering. https://doi.org/10.52202/080513-0301
19. Hsu CC, Chen SW, Yeh MC, Tsai MT (2025) Structural performance, economic benefits and environmental impact of steel, steel–timber hybrid and timber structures in a high seismic zone. In: Proceedings of the world conference on timber engineering. https://doi.org/10.52202/080513-0219
20. Laughery D, Fischer E, Phillips A (2025) Investigating novel steel–timber connections and the effects of knurling through experimental direct shear testing. In: Proceedings of the world conference on timber engineering. https://doi.org/10.52202/080513-0536
21. Romero A, Odenbreit C (2024) Experimental investigation on novel shear connections for demountable steel–timber composite (STC) beams and flooring systems. Eng Struct 304:117620. https://doi.org/10.1016/j.engstruct.2024.117620
22. Hicks SJ, Woodward A, Hamad W (2025) Development of an innovative composite steel and cross laminated timber floor system. In: Proceedings of the IABSE symposium
23. Kyvelou P, Reynolds T, Beckett C, Huang Y (2021) Experimental investigation on composite panels of cold-formed steel and timber. Eng Struct. https://doi.org/10.1016/j.engstruct.2021.113186
24. Boucher S, Lamarche CP (2019) Performance of three dowel type steel connectors on the strength and stiffness of hybrid steel deck to wood frame diaphragms. In: Proceedings of the CSCE annual conference

25. Luo L, Sun X, Song X, Ou Z, Zhang L (2022) Experimental and numerical study on the hysteretic behaviour of a hybrid timber buckling-restrained brace with a cross-shaped steel core. Soil Dyn Earthq Eng 162:107461. https://doi.org/10.1016/j.soildyn.2022.107461
26. Uprety R, Pantelides CP, Blomgren HE, Rammer DR (2026) Design and qualification of timber buckling restrained brace for mass timber-braced frames. Eng Struct 348:121832. https://doi.org/10.1016/j.engstruct.2025.121832
27. Wang M, Zhou B, Harries KA, Chen X, Zhang F, Xu Q (2023) Seismic performance evaluation of a five-story column-and-beam glulam frame with steel-timber buckling restrained braces. J Build Eng. https://doi.org/10.1016/j.jobe.2023.108045
28. Badal PS, Tesfamariam S (2024) Seismic collapse performance of high-rise mass timber buildings with buckling-restrained braced frames. Soil Dyn Earthq Eng 177:108358. https://doi.org/10.1016/j.soildyn.2023.108369
29. Williamson E, Pantelides CP, Blomgren HE, Rammer DR (2025) Seismic performance and nonlinear model of mass timber buckling restrained braced frame. In: Proceedings of the world conference on timber engineering. https://doi.org/10.52202/080513-0348

Structural Performance of Steel–Concrete Composite Slabs Incorporating Recycled Concrete Aggregates

Flavio Stochino[1](✉), Marta Saccone[1], Alireza Alibeigibeni[1], Marco Zucca[1], Monica Valdes[1], Giovanna Concu[1], Marco Simoncelli[2], Marco Andrea Pisani[2], and Claudio Bernuzzi[2]

[1] Department of Civil, Environmental Engineering and Architecture, University of Cagliari, Cagliari, Italy
fstochino@unica.it

[2] Department of Architecture, Built Environment and Construction Engineering, Politecnico di Milano, Milan, Italy

Abstract. The transition toward circular construction requires structural solutions capable of integrating recycled materials without compromising mechanical reliability. In this context, recycled concrete aggregates (RCA) derived from construction and demolition waste represent a promising alternative to natural aggregates. This study investigates the structural performance of steel–concrete composite slabs incorporating RCA through an extensive experimental program carried out within the SARCOS research framework. A total of 48 full-scale composite slabs were produced with RCA replacement ratios ranging from 0% to 100% and tested under four-point bending with span lengths of 2.40 m, 2.80 m, and 3.20 m. The results highlight a consistent three-stage structural response characterized by an initial elastic phase, followed by interface debonding and a post-peak flexural stage with stable residual capacity. Composite slabs with moderate RCA contents exhibited collapse loads comparable to, or slightly higher than, those of conventional slabs, indicating that enhanced aggregate roughness improves mechanical interlock and friction at the steel–concrete interface. Conversely, full RCA replacement produced reductions in stiffness and peak resistance in the most recent test series, although a more ductile post-peak response was observed. Overall, the findings demonstrate that recycled aggregate concrete can be effectively employed in composite floor systems, particularly for short- and medium-span applications where longitudinal shear transfer governs structural behavior. The experimental evidence contributes to the understanding of bond mechanisms in sustainable composite structures and provides useful insights for the refinement of Eurocode-based design approaches.

Keywords: composite slabs · recycled concrete aggregates · longitudinal shear · steel–concrete interface · circular construction · SARCOS project

© The Author(s), under exclusive license to Springer Nature Switzerland AG 2026
R. Zanon et al. (Eds.): CTA 2026, LNCE 942, pp. 576–585, 2026.
https://doi.org/10.1007/978-3-032-39505-4_50

1 Introduction

Steel–concrete composite slabs [1] are widely used in building structures because they combine rapid construction, efficient use of materials and high load-bearing capacity. Their response depends on the interaction between the concrete layer and the profiled steel sheeting. In particular, the longitudinal shear transfer mechanism at the steel–concrete interface governs the transition from full composite action to partial interaction and, eventually, to debonding [2].

The use of recycled concrete aggregates (RCA) in structural concrete is generally associated with a reduction in compressive strength, tensile strength and elastic modulus [3]. This reduction is mainly related to the presence of adhered mortar, higher porosity and a weaker interfacial transition zone around the recycled particles. However, RCA particles are also more angular and rougher than natural aggregates. This feature may improve frictional resistance and mechanical interlock at the steel–concrete interface. For composite slabs, this aspect is particularly relevant because the ultimate response is not governed by concrete strength alone, but by the coupled behavior of concrete, steel sheeting and interface bond [4, 5].

The SARCOS project was developed to investigate whether recycled aggregate concrete can be effectively used in steel–concrete composite slabs [6]. The experimental campaign included full-scale specimens with different RCA replacement ratios and different span lengths. This paper summarizes the main structural mechanics results, focusing on load-bearing capacity, debonding, post-peak behavior and the influence of RCA content on longitudinal shear performance.

The objective is to provide a concise synthesis of the experimental evidence obtained within the SARCOS project and to discuss its implications for the design of composite slabs incorporating recycled aggregates.

2 Experimental Program

2.1 Materials

The concrete mixes were produced using Portland limestone cement CEM II/A-LL 42.5 R. Natural fine and coarse aggregates were partially or totally replaced by recycled concrete aggregates obtained from construction and demolition waste. Since recycled aggregates present higher water absorption than natural aggregates, they were presaturated before mixing in order to keep the effective water available for cement hydration approximately constant, see Table 1.

The same profiled steel sheeting was used for all specimens. The steel deck was a cold-formed SG110–600 profile supplied by Spinelli srl, with a nominal thickness of 0.75 mm and rib height of approximately 110 mm, see Fig. 1. Tensile coupon tests gave an average yield strength of 338.18 MPa, an ultimate strength of 593.16 MPa and an elastic modulus of approximately 195 GPa.

Table 1. Concrete mixes adopted in the experimental campaign

Mix	RCA replacement in fine aggregates	RCA replacement in coarse aggregates	Cement [kg/m^3]	w/c ratio
M0	0%	0%	366	0.51
M20	20%	20%	366	0.51
M30	30%	30%	366	0.51
M50	50%	50%	366	0.51
M70	70%	70%	366	0.51
M100	100%	100%	366	0.51

2.2 Concrete Mechanical Properties

The mechanical properties of the concrete mixes were assessed through compressive strength, splitting tensile strength and elastic modulus tests, see Table 2. The most recent campaign showed that the reference mix M0 reached a 90-day compressive strength of 43.8 MPa, while M100 reached 36.1 MPa. The elastic modulus decreased significantly with increasing RCA content, from about 34.4–34.7 GPa for the reference concrete to about 16.7–18.2 GPa for the fully recycled concrete.

Table 2. Main concrete mechanical properties.

Mix	28-day compressive strength [MPa]	90-day compressive strength [MPa]	Elastic modulus [GPa]
M0	38.2–43.0	43.8	34.7
M20	38.1	44.2	30.4
M30	32.3	–	22.5
M50	34.5	–	23.7
M70	39.9	46.2	24.6
M100	32.9	36.1	16.7

Note: values summarize the experimental campaigns carried out within the SARCOS project. Differences between campaigns are related to casting series, curing age and tested specimens.

2.3 Specimens and Test Matrix

A total of 48 full-scale composite slabs were tested. The experimental program combined two campaigns. The preliminary campaign (2023) [5] included 12 slabs with RCA replacement ratios of 0%, 30%, 50% and 100%. The second campaign (2024) included 36 slabs with RCA replacement ratios of 0%, 20%, 70% and 100%. Three span lengths were investigated: 2.40 m, 2.80 m and 3.20 m, see Table 3.

Table 3. Experimental matrix.

Campaign	Mixes	Span lengths	Number of slabs
Preliminary campaign (2023)	M0, M30, M50, M100	2.40, 2.80, 3.20 m	12
Main campaign (2024)	M0, M20, M70, M100	2.40, 2.80, 3.20 m	36
Total	M0, M20, M30, M50, M70, M100	2.40, 2.80, 3.20 m	48



Fig. 1. Geometry of the steel–concrete composite slab with trapezoidal steel decking.

2.4 Test Setup and Loading Protocol

All slabs were tested under four-point bending. The specimens were simply supported, with loads applied symmetrically at a distance of L/4 from the mid-span, see Fig. 2. The test setup was designed to reproduce the mechanical conditions required for evaluating flexural response and longitudinal shear behavior.

Eight displacement transducers were used for each specimen. Vertical LVDTs measured mid-span deflection and local displacement under the loading points. Additional horizontal LVDTs monitored the relative displacement between the concrete and steel sheeting, allowing direct identification of debonding and longitudinal slip.

The loading protocol included two preliminary cycles up to approximately 30% and 50% of the expected collapse load. These cycles were followed by monotonic loading up to debonding and then continued until the development of the post-peak flexural mechanism.

3 Results and Discussion

3.1 General Structural Response

All tested slabs showed a consistent three-stage response, see Fig. 3. The first stage was almost linear and corresponded to the initial composite behavior of the steel deck and concrete slab. During this phase, horizontal slip was negligible and the interface ensured effective load transfer.

The second stage was characterized by a sudden load drop associated with the onset of longitudinal debonding. This event corresponded to the loss of full composite action and was confirmed by the horizontal LVDTs, which recorded a rapid increase in relative displacement between concrete and steel.



Fig. 2. Four-point bending test setup with LVDT position.

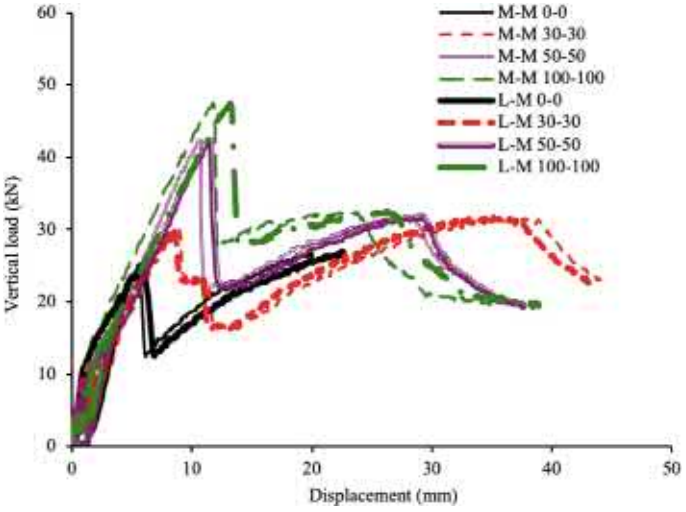


Fig. 3. Representative load–midspan displacement curves for specimens with 3.20 m span (preliminary campaign) showing the three-stage response: elastic phase, debonding drop and post-peak flexural branch.

The third stage was a post-peak flexural phase. After debonding, the slabs did not collapse suddenly. Instead, they developed a residual load-bearing capacity governed by

flexural deformation, progressive cracking and frictional interaction along the interface. This post-peak branch is particularly important because it indicates structural robustness and ductility.

3.2 Collapse Loads in the Main Campaign

The main 36-slab campaign provides the clearest comparison among M0, M20, M70 and M100. Average collapse loads are reported in Table 4.

Table 4. Average collapse loads of the main SARCOS campaign.

Mix	2.40 m span [kN]	2.80 m span [kN]	3.20 m span [kN]
M0	48.23	41.96	36.56
M20	54.69	41.97	36.59
M70	42.12	40.36	35.58
M100	46.37	42.40	32.17

For the 2.40 m span, the highest average collapse load was achieved by M20, with 54.69 kN. This value is approximately 13% higher than the reference mix M0. This result suggests that, for short spans where longitudinal shear transfer is particularly relevant, a moderate RCA replacement ratio can improve interface efficiency.

For the 2.80 m span, all mixes showed very similar average collapse loads. M0, M20 and M100 were close to 42 kN, while M70 reached 40.36 kN. This indicates that the structural performance remained practically comparable even with high RCA content, at least in terms of peak resistance.

For the 3.20 m span, the effect of RCA became more evident. M0, M20 and M70 remained close to each other, with values between 35.58 and 36.59 kN. Conversely, M100 dropped to 32.17 kN, corresponding to a reduction of about 12% compared with M0. This confirms that full replacement may become more critical when flexural deformation and reduced concrete stiffness play a stronger role.

3.3 Comparison with the Preliminary Campaign

The preliminary campaign investigated M0, M30, M50 and M100. Its results showed that RCA can increase the apparent longitudinal shear strength, with ratios up to 1.7 compared with the reference mix. The collapse loads obtained in that campaign are summarized in Table 5.

Table 5. Collapse loads of the preliminary campaign.

Mix	2.40 m span [kN]	2.80 m span [kN]	3.20 m span [kN]
M0	48.20	41.96	26.98
M30	55.91	38.01	31.67
M50	47.53	52.24	42.41
M100	53.05	49.23	47.45

The preliminary results should be interpreted together with the larger main campaign. They confirm that the relationship between RCA content and structural performance is not governed by compressive strength alone. The enhanced roughness of RCA can improve mechanical interlock with the profiled steel deck. However, the larger 36-slab campaign also shows that the beneficial effect has an optimum range and that full replacement may reduce stiffness and peak load, especially for longer spans.

3.4 Role of RCA in the Steel–Concrete Interface

The most relevant structural result of the SARCOS project is that RCA modifies the interface response. In ordinary reinforced concrete, the reduction in compressive strength and elastic modulus caused by RCA is generally considered a disadvantage. In composite slabs, however, the interface behavior is decisive.

RCA particles are rougher and more angular than natural aggregates. The adhered mortar increases surface irregularity and may enhance friction and mechanical interlock between concrete and steel sheeting. This effect can compensate for moderate reductions in concrete strength. This explains why M20 and M70 achieved structural performance similar to the reference mix, and why M20 produced the highest peak load in the 2.40 m span configuration.

Nevertheless, at very high replacement ratios, the lower elastic modulus and higher porosity of recycled aggregate concrete become dominant. This leads to lower initial stiffness, earlier slip initiation and, in some cases, reduced peak load. The M100 mix is therefore mechanically interesting: it is less efficient in terms of stiffness and maximum resistance, but it can show a stable and prolonged post-peak branch, indicating ductile redistribution after debonding.

3.5 Horizontal Slip and Debonding

Horizontal displacement measurements confirmed the interpretation of the collapse mechanism, see Fig. 4. During the initial elastic phase, relative slip between steel and concrete remained almost zero. When the peak load was reached, slip increased rapidly, confirming that the sudden load drop corresponded to longitudinal debonding.

The location and intensity of initial slip were not always perfectly symmetric. This is consistent with the heterogeneous nature of the steel–concrete interface, local imperfections, small differences in support conditions and variability of recycled aggregate

distribution. After debonding, the slabs were still able to sustain load through residual bond, friction and flexural action.

This behavior is relevant for design. It shows that the peak load is not the only meaningful parameter. The post-peak branch and the residual capacity after debonding are essential to describe the real structural response of RCA composite slabs.

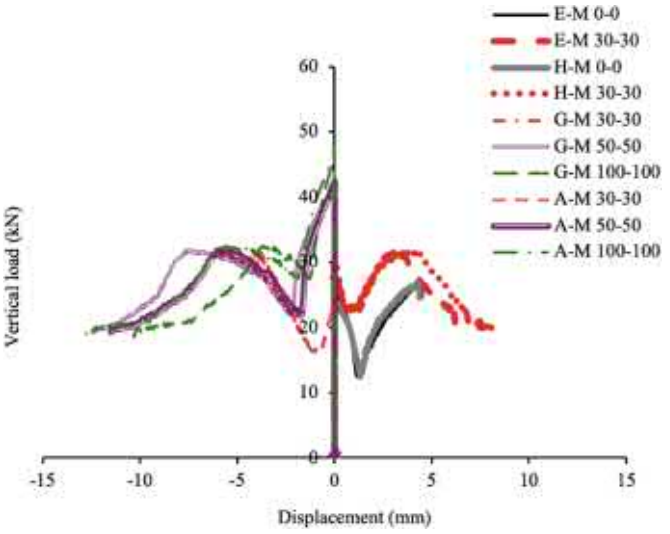


Fig. 4. Load–horizontal displacement curves for 3.20 m span specimens, showing negligible slip before debonding and rapid slip development after peak load.

3.6 Influence of Span Length

The span length affected both collapse load and failure evolution. As expected, peak load decreased as span increased. However, the effect of RCA replacement was not identical for all spans.

For short spans, longitudinal shear transfer plays a dominant role. Under this condition, the beneficial roughness of RCA can improve the interface mechanism, as observed for M20 at 2.40 m.

For medium spans, the response was more balanced. At 2.80 m, all mixes showed similar average peak loads, indicating that RCA replacement up to 100% did not produce a major reduction in ultimate capacity in that configuration.

For longer spans, flexural deformation and stiffness became more relevant. At 3.20 m, M100 showed a clear reduction in collapse load. This suggests that full RCA replacement should be used with caution in longer-span composite slabs unless specific mix design optimization or design recalibration is performed.

4 Design Implications

The experimental results show that recycled aggregate concrete can be used in steel–concrete composite slabs, but the design approach should explicitly account for its influence on interface behavior.

Current Eurocode-based design procedures for composite slabs are mainly calibrated on natural aggregate concrete. The m–k method and partial shear connection approach are effective tools, but they do not explicitly include the effect of RCA on bond–slip response, aggregate roughness, friction and post-peak residual capacity.

The SARCOS results suggest that moderate RCA replacement can enhance longitudinal shear transfer. Therefore, using only compressive strength reduction as a design criterion may be overly conservative for some RCA composite slabs. Conversely, for full RCA replacement, the reduced elastic modulus and higher deformability may affect serviceability and peak resistance, particularly in longer spans.

Future design formulations should consider: RCA replacement ratio, concrete elastic modulus, steel deck geometry, interface friction, bond–slip response, residual capacity after debonding, span-to-depth ratio or different recycled aggregates [7].

A recalibration of longitudinal shear parameters for RCA-based composite slabs appears necessary to extend current design rules toward circular construction materials.

5 Conclusions

This paper presented the main structural mechanics results of the SARCOS experimental campaign on steel–concrete composite slabs incorporating recycled concrete aggregates. Based on 48 full-scale tests, the following conclusions can be drawn.

All tested slabs exhibited a consistent three-stage response: initial elastic behavior, sudden debonding at the steel–concrete interface and post-peak flexural response with residual load-bearing capacity.

RCA reduced the mechanical properties of concrete, particularly elastic modulus. However, this reduction did not automatically imply a reduction in slab collapse load, confirming that composite slab behavior is strongly governed by the steel–concrete interface.

Moderate RCA replacement was structurally effective. In the main campaign, M20 achieved the highest average collapse load for the 2.40 m span, reaching 54.69 kN compared with 48.23 kN for the reference mix.

For the 2.80 m span, all mixes showed comparable collapse loads, with values close to 40–42 kN. This confirms that RCA can be incorporated without significant loss of ultimate capacity in medium-span composite slabs.

For the 3.20 m span, full RCA replacement produced a more evident reduction in peak load. M100 reached 32.17 kN, compared with 36.56 kN for M0. This indicates that full replacement becomes more critical when flexural deformation and reduced stiffness are dominant.

The use of RCA can improve mechanical interlock at the steel–concrete interface because of the rougher and more angular surface of recycled aggregates. This mechanism is particularly beneficial at moderate replacement ratios.

The results support the feasibility of using RCA in steel–concrete composite slabs, especially for short- and medium-span applications. However, current design procedures should be refined to include the specific bond–slip behavior of RCA-based concretes.

Acknowledgements. The financial support of the PRIN2022 SARCOS project, CUP F53D23002030006, Prot. 2022WWN3TC, is gratefully acknowledged. The authors thank Spinelli srl for supplying the steel sheeting and Heidelberg Materials for supporting the concrete production and casting activities.

References

1. Wang Q, Yang J, Zhang Y, Fang Y, Ren Q (2022) Analysis and design of long-term responses of simply-supported steel–concrete composite slabs. J Build Eng 53:104496
2. Ahmed SM et al (2019) Prediction of longitudinal shear resistance of steel-concrete composite slabs. Eng Struct 193:295–300
3. Bai G, Zhu C, Liu C, Liu B (2020) An evaluation of the recycled aggregate characteristics and the recycled aggregate concrete mechanical properties. Constr Build Mater 240:117978
4. Saccone M, Stochino F, Zucca M, Simoncelli M (2025) Longitudinal shear behaviour in recycled aggregate concrete composite slabs: a state-of-the-art review. J Build Eng 113:114002
5. Stochino F et al (2024) Mechanical behavior of composite slabs with recycled concrete aggregates: a preliminary study. Structure 70:107838
6. SARCOS Steel and recycled concrete slab project. https://projectsarcos.it/. Accessed 30 May 2026
7. Coviello CG, Lassandro P, Sabbà MF, Foti D (2023) Mechanical and thermal effects of using fine recycled PET aggregates in common screeds. Sustainability 15:16692

Experimental Analysis of a Novel Hybrid Timber-Concrete-Steel Flooring System

Carmen Amaddeo[1], Raffaele Pucinotti[2(✉)], and Wit Derkowski[1,3]

[1] Building Technology Department, Linnaeus University, Växjö, Sweden
[2] Diceam Department, Mediterranean University of Reggio Calabria, Reggio Calabria, Italy
raffaele.pucinotti@unirc.it
[3] RC and PC Structures Department, Cracow University of Technology, Krakow, Poland

Abstract. This study investigates a sustainable, novel composite floor system integrating steel, concrete, and timber members in a prefabricated unit, with the aim of evaluating both structural and environmental performance. Preliminary investigations included numerical analyses, the fabrication of two mock-ups, and an experimental campaign to assess the dynamic and static behavior of a floor unit. The mock-ups differed in the timber chord configuration and the arrangement of the steel diagonals, while the geometry of the upper concrete slab remained unchanged.

This paper presents only the results of the experimental static tests conducted until failure, conducted at the Laboratory of the Department of Building Technology at Linnaeus University in Växjö (Sweden). Two specimens were tested under a four-point bending test to investigate the flexural behavior and failure modes. Initially, the specimens were subjected to serviceability limit state (SLS) loading, applied in three cycles. Subsequently, three loading cycles were applied under the design ultimate limit state (ULS). Finally, each specimen was loaded under monotonic static loading until failure.

Both Specimen S1 and Specimen S2 showed consistent behavior during all three SLS loading cycles. At collapse, detachment of the diagonals from the bottom chord was observed, while the steel diagonal connections to the upper concrete slab performed as intended throughout the test duration.

The discussion focuses primarily on the behavior of the connections between the timber bottom chords and the thin-walled steel diagonal members, as these elements governed the global response and failure mechanisms.

Based on the observed failure modes, the paper also discusses possible improvements to enhance the overall system performance.

Keywords: Composite Floor System · Timber-steel Connections · Experimental Investigation · Serviceability Limit State (SLS) · Ultimate Limit State (ULS)

1 Introduction

The construction industry is facing increasing pressure to reduce environmental impact by enhancing material efficiency, reducing carbon emissions, and enabling circular use of resources. Floor systems, which contribute significantly to the structural mass, play a key

© The Author(s), under exclusive license to Springer Nature Switzerland AG 2026
R. Zanon et al. (Eds.): CTA 2026, LNCE 942, pp. 586–597, 2026.
https://doi.org/10.1007/978-3-032-39505-4_51

role in this transition. Conventional solutions, such as reinforced concrete slabs, hollow-core elements, and steel–concrete composites, tend to be material-intensive, difficult to disassemble, or constrained by production and transportation limitations. Timber-based systems present environmental advantages but may not meet structural and acoustic requirements, especially for longer spans.

To overcome these challenges, this research investigates a new Hybrid Floor System (HFS) that incorporates prefabricated timber–concrete–steel elements designed for sustainable construction. The aim of this concept is to merge structural efficiency with a diminished environmental impact while promoting local production and effective on-site assembly. The proposed system is intended as a cost-competitive alternative to conventional floor solutions for commercial buildings.

Previous studies show that the performance of composite floor systems mainly depends on how shear connections behave and their effect on overall failure mechanisms. In timber-concrete composite (TCC) systems, effective connectors are crucial to maintain composite action. They directly impact stiffness, load-bearing capacity, and deflection response [1, 2]. Experimental studies have demonstrated that poor connection performance can result in slip, decreased stiffness, and early failure. In contrast, optimized solutions can exhibit nearly linear behavior until failure, with minimal interface displacement [3].

Advanced numerical studies confirm that while global flexural behavior can be predicted with good accuracy, capturing connection slip and local failure modes, such as timber fracture, connector failure, and concrete cracking, remains challenging [4, 5]. Several investigations show that connection design not only affects stiffness but also governs failure modes, including brittle fracture in adhesive joints, shear failure in connectors, and tension failure in timber elements [6, 7].

Recent developments in hybrid and prefabricated systems further underline the importance of connection detailing, as different configurations of steel, timber, and concrete components lead to distinct load-transfer mechanisms and failure patterns [8–11]. Overall, the literature indicates that improving connection behavior is critical for enhancing both the structural performance and reliability of composite floor systems, particularly with respect to ductility and failure control.

2 Experimental Tests

The objective of the experimental campaign was to investigate the potential of an innovative composite floor system as a sustainable and efficient alternative to traditional floor systems such as hollow-core concrete, concrete slabs, and timber floors.

2.1 The Test Specimens and Setup

The structural performance of the two prefabricated steel–timber–concrete composite floor specimens was evaluated through full-scale four-point bending tests. Both specimens had a span length of 8100 mm and were tested using a hydraulic loading frame. The four-point bending configuration was selected to reproduce the maximum bending moment generated by a uniformly distributed floor load while maintaining a constant

moment region between the loading points. The two-line loads were applied 3100 mm from each support (≈0.38 L), creating a 1900 mm constant-moment region and 3100 mm shear spans. This four-point bending configuration was adopted to reproduce the mid-span bending effects of a uniformly distributed floor load. It is consistent with EN 408 [17] and previous full-scale tests on prefabricated timber–concrete–steel composite floors [18, 19]. During testing, the specimens were positioned upside down because the hydraulic actuator applied the load in an upward direction (Fig. 1).

A comprehensive instrumentation system was installed to monitor the structural response. Electrical resistance strain gauges were attached to the concrete slab to measure surface strains. Linear potentiometers were placed at the supports and mid-span to record vertical displacements, while additional potentiometers were mounted along the timber chords to measure axial deformations. Slippage gauges were installed at the timber–steel connections near the supports to quantify relative displacements between the steel diagonals and timber members. For the second specimen, supplementary sensors were used to monitor strains in the steel diagonals and slip in the steel plate connections between timber segments (Fig. 2).

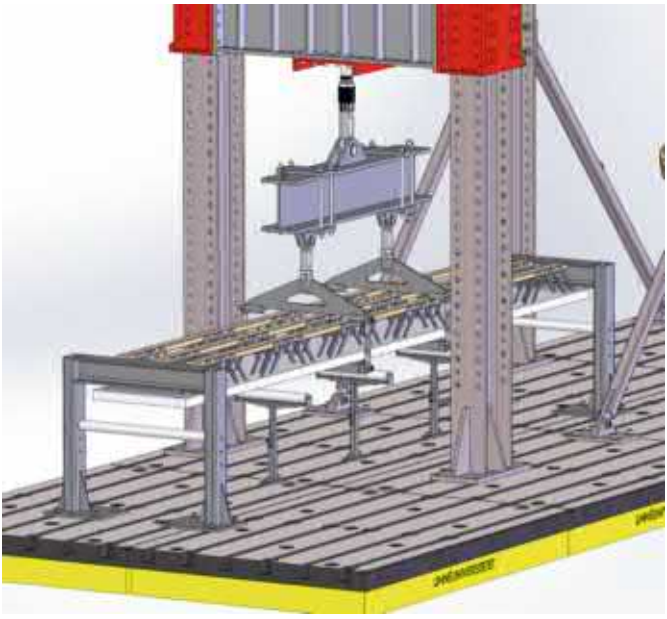


Fig. 1. Experimental setup: testing machine

Two different floor systems were designed and fabricated in collaboration between MiTek Industries AB, Torps Byggelement AB and Linnaeus University (Fig. 3). The floor system was conceived so that the timber-to-steel connection would act as the controlling, comparatively ductile element, while the steel diagonals and the steel-to-concrete connection were expected to remain undamaged up to and beyond the design ULS load according to EN 1995-1-1 [20].These samples are based on a novel floor

system consisting of top concrete chords, bottom timber chords, and steel diagonals, referred to as Posi-Joists/Posi-strut (PS12), which are produced by MiTek Industries AB [12]. Both Specimens, 1 and 2, have identical dimensions: 900 mm in width, 8100 mm in length, and an overall height of 370 mm. The thickness of the concrete slab varies, ranging from 120 mm near the supports to 70 mm near the mid-span.

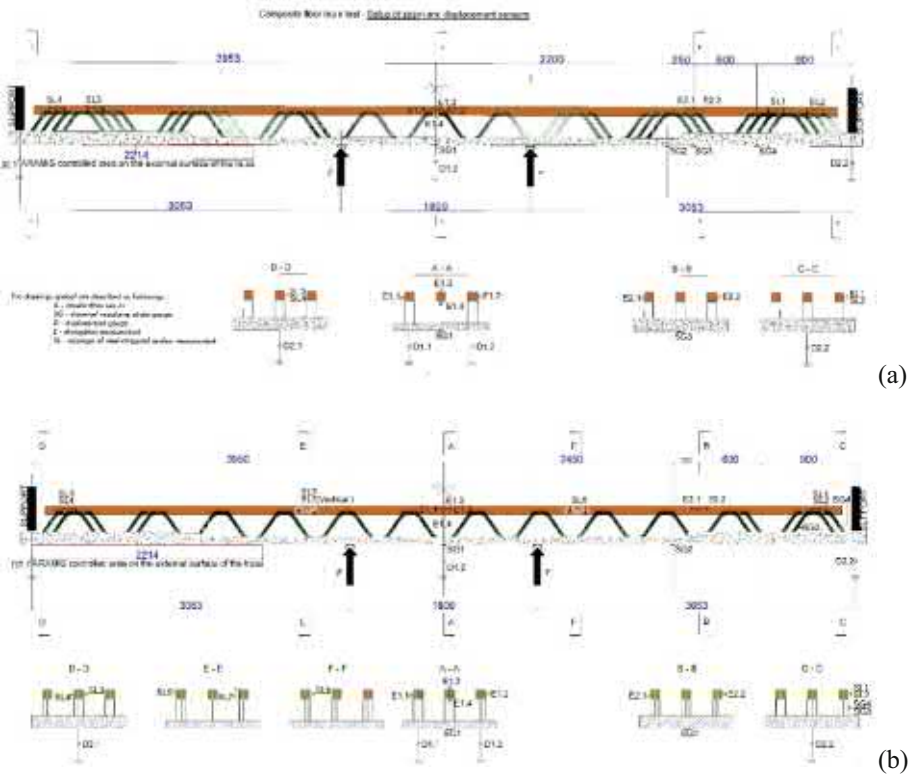


Fig. 2. Experimental setup instrumentation: (a) Specimen 1 (S1); (b) Specimen 2 (S2)

For both specimens, the characteristic self-weight of the floor system was estimated as $g_k = 3\text{kN/m}^2$, whereas the characteristic imposed load was taken as $q_k = 5\text{kN/m}^2$.

The load combinations considered in the experimental program are reported in Table 1.

The tests were conducted under displacement control, using the MTS actuator displacement as the reference. The loading protocol was designed in accordance with the general principles of EN 26891 [15] for the monotonic phase and EN 12512 [16] for the cyclic phases. The loading protocol was divided into three phases. First, cyclic loading was applied within the Serviceability Limit State (SLS) range to evaluate the stiffness, repeatability, and potential degradation of the structural response. This loading condition was applied three times, resulting in three complete loading–unloading cycles.

Table 1. Loads applied on specimens.

	Load Combination	Load value (kN/m^2)	Total line load (2F – kN)
SLS	$g_k + q_k$	8.00	37.16
QP	$g_k + 0.8q_k$	7.00	32.51
ULS	$1.35g_k + 1.5q_k$	11.55	53.64

Subsequently, the specimen was loaded up to the Quasi-Permanent (QP) load level and subjected to a semi-creep test. The load was maintained constant for approximately 6 h in order to assess the time-dependent deformation response of the system.

Following the semi-creep phase, the specimen was unloaded and then reloaded up to the Ultimate Limit State (ULS) load level. As in the SLS phase, three loading–unloading cycles were performed to investigate the onset of nonlinear behavior and any associated stiffness degradation.

Finally, the specimen was subjected to monotonically increasing loading until failure, allowing the determination of the ultimate load-carrying capacity, deformation capacity, and governing failure modes.



Fig. 3. Designed and fabricated specimens

The primary variables that differentiate the two specimens are the type of structural timber used and the configuration of the steel elements throughout the specimens; moreover, the arrangement of the steel diagonals was different between the two slab mock-ups. Specimen 1 (S1) utilized three glulam timber chords of strength class GL30h as the bottom flange elements.

The timber chords were connected to the concrete slab through PS12 steel diagonal members, forming a prefabricated composite truss floor system. The specimen represented the original structural configuration proposed for the floor concept (see Fig. 4). Specimen 2 (S2) was made with structural timber class C24, which was utilized, with the timber chord made up of two elements joined together on each truss. For this specimen, to connect the timber chord elements, steel nail plates (type GNT-100S with dimensions

76 × 218 mm [13] and steel bolts (type B125 with 12.7 mm diameter and 127 mm length [14]) were employed, as shown in Fig. 5.

At the timber–steel interface, the punched-teeth end plates of the PS12 steel diagonals (MiTek Industries AB) are pressed into the glulam (S1) or C24 (S2) bottom chords, following the fastening principle of punched metal plate fasteners as covered by EN 14250 [21] and tested according to EN 1075 [22]. In addition, each punched-teeth end plate is strengthened with two 3 × 40 mm flat-head nails, as it is visible in Fig. 5. At the steel–concrete interface, the upper ends of the same diagonals are directly embedded in the cast concrete slab during casting, providing anchorage through bond and mechanical interlock. In the central regions of the specimens, where the reinforced concrete slab thickness is 70 mm, the embedment depth is equal to the height of the punched-teeth end plate. In the support regions, where the slab thickness increases to 120 mm, the same PS12 Posi-Strut members are used; consequently, the embedment depth extends an additional 50 mm beyond the punched-teeth end plate, encasing the upper portion of the steel diagonal. This additional embedment also reduced the effective buckling length of the most highly stressed compression diagonals. No discrete mechanical connector (e.g. headed stud) is used at this interface.

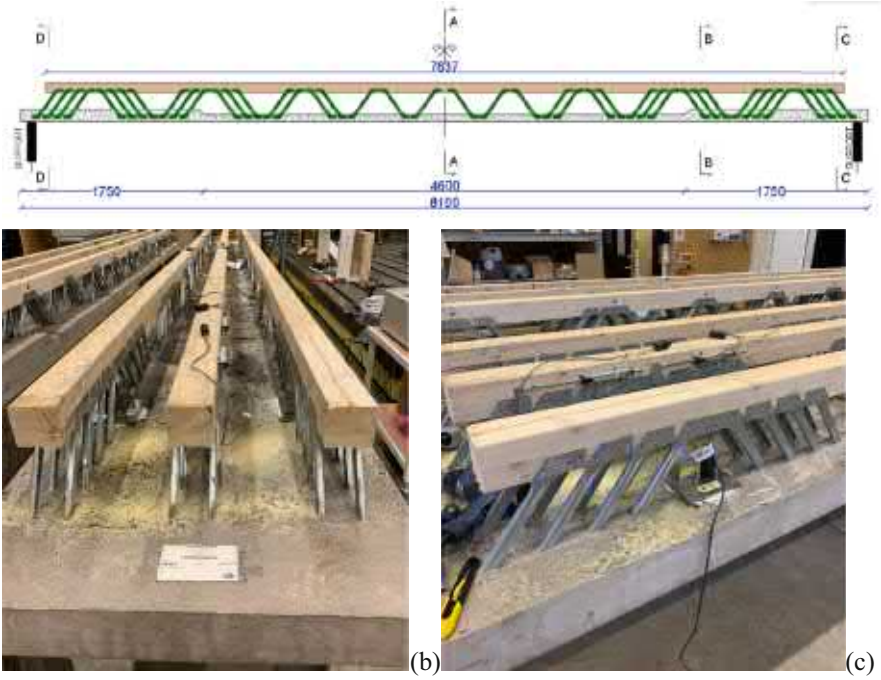


Fig. 4. Specimen S1

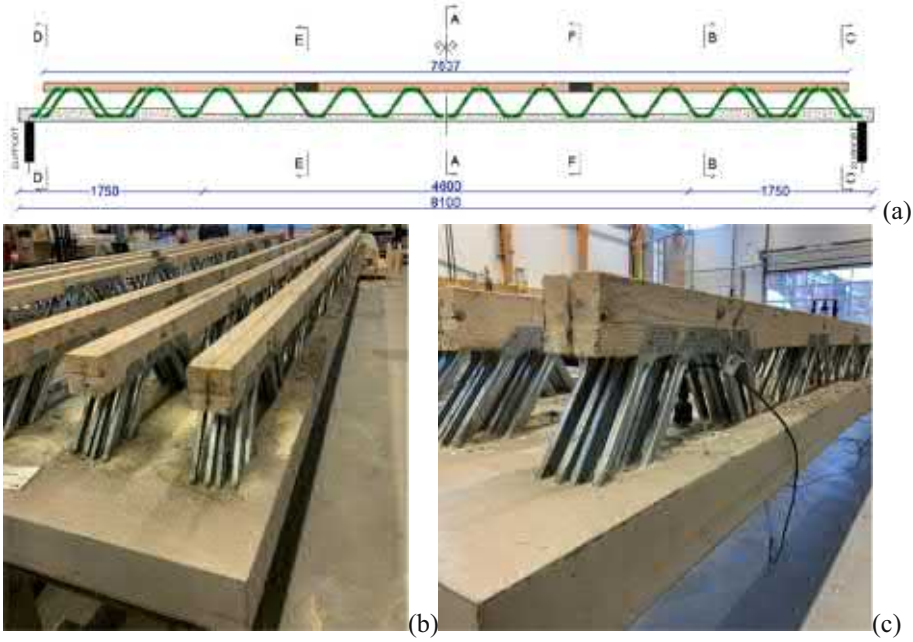


Fig. 5. Specimen S2

2.2 Experimental Test Results and Discussion

The MTS actuator displacement as a function of time for both tested specimens, following the loading protocol described in the previous section, is shown in Fig. 6. In fact, it is possibly clearly identify four phases:

(i) The initial SLS cyclic stage (t ≈ 0–700 s), with three loading–unloading cycles reaching approximately 27 mm;
(ii) The semi-creep plateau held at around 25–27 mm for approximately 20,000 s;
(iii) The ULS cyclic phase, marked by larger-amplitude oscillations;
(iv) The final monotonic loading stage, which drove the actuator displacement up to approximately 87 mm and 62 mm for S1 and S2, respectively, before failure.

The experimental results obtained from both specimens are presented in terms of global force–displacement response (Fig. 7) and local force–slip behavior at the steel–timber interface (Fig. 8).

During the SLS cyclic phase, both specimens show a predominantly linear, quasi-elastic response within the SLS load range (~37 kN), consistent with effective composite interaction between the concrete slab, timber chord, and steel diagonal members, with negligible slippage observed at the interface (Fig. 8), equal to approximately 0.4 mm for Specimen 1 and 0.1 mm for S2. The loading–unloading cycles were highly repeatable, with no appreciable stiffness degradation between consecutive cycles, confirming the structural integrity of both floor configurations under serviceability conditions.

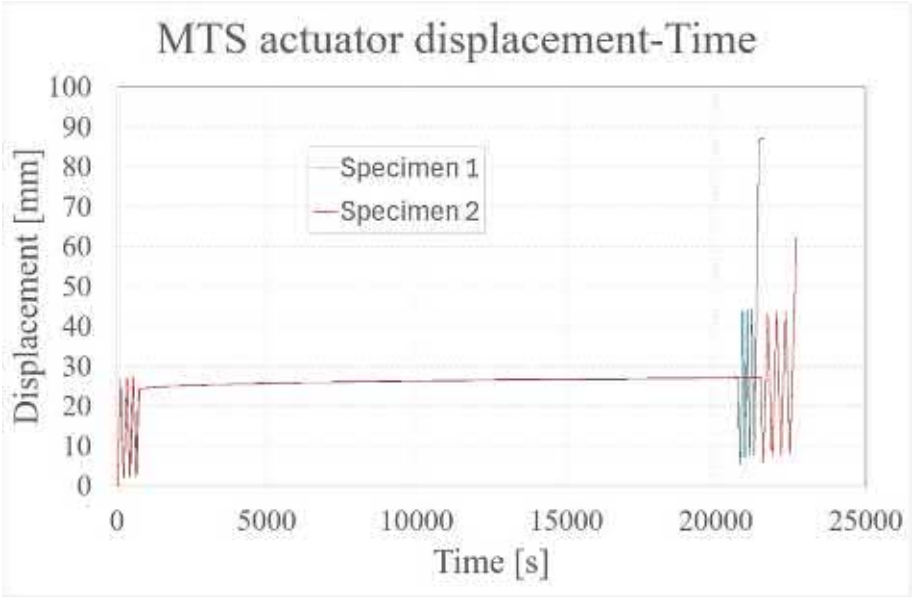


Fig. 6. MTS actuator displacement–Time curves for Specimen 1 and Specimen 2

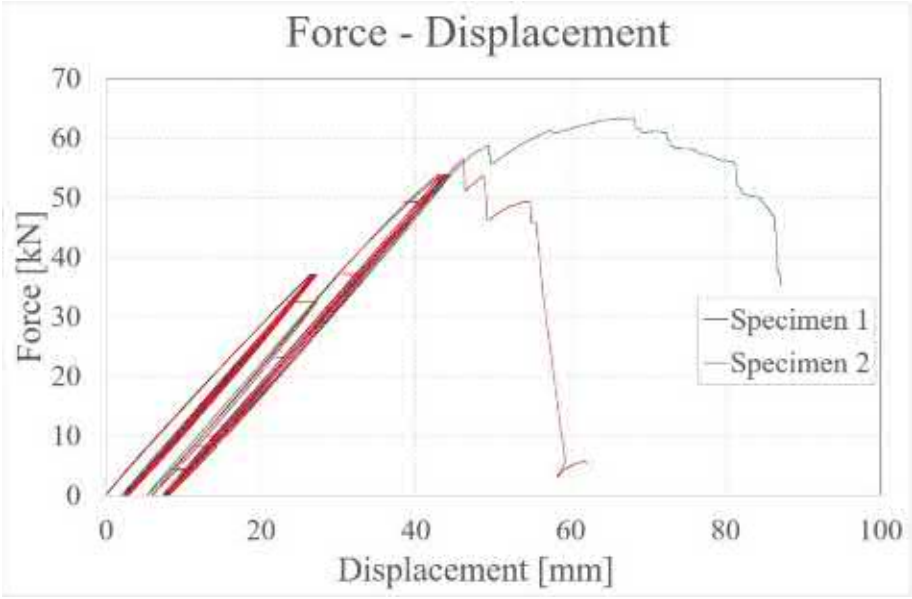


Fig. 7. Force–Displacement curves for Specimen 1 and Specimen 2 over the full loading history (SLS cycles, semi-creep phase, and final monotonic loading to failure).

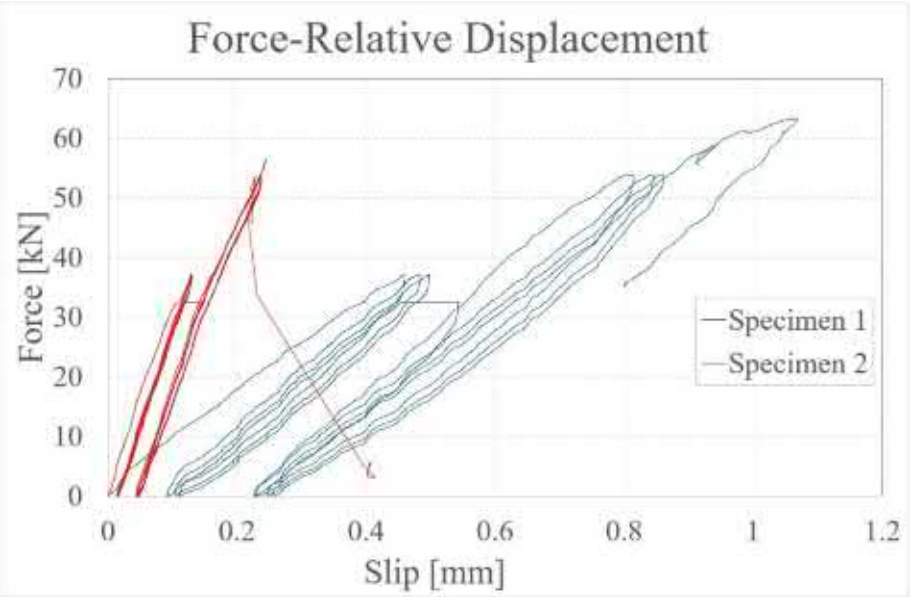


Fig. 8. Force–Slip curves (relative displacement at the steel–timber interface, sensor SL3) for Specimen 1 and Specimen 2 over the full loading history

Under monotonic loading to failure, the two specimens displayed markedly different behaviors, reflecting the influence of timber grade and chord detailing on the overall structural response. As loading progressed beyond the SLS range, the contribution of the steel system (particularly the diagonal members and their connections) became increasingly significant in governing the global response.

Specimen S1, made of GL30h glulam chords and the original PS12 diagonal arrangement, shows a relatively uniform load distribution across the steel diagonal system, with the Posi-struts effectively transferring forces between the concrete slab and the continuous glulam bottom chord. As the load approached the ULS threshold (53.64 kN), localized nonlinearities developed primarily at the steel-to-timber connections, with progressive slip and stiffness reduction leading to a peak load of approximately 63 kN, above the ULS level, thus demonstrating a clear overstrength reserve.

Failure was ultimately governed by detachment of the steel diagonals from the timber chord, indicating that connection capacity, rather than the steel members themselves, limited the system's load-carrying potential. The post-peak response was gradual and progressive, extending over a large displacement range up to approximately 95 mm, indicative of a ductile failure mode with significant deformation capacity. Slip at the steel–timber interface grew steadily up to approximately 1.1 mm at peak load, with progressively wider hysteretic loops reflecting increasing energy dissipation and gradual softening of the connection's slip stiffness. Notably, the steel-to-concrete connections remained intact and continued to transfer forces effectively up to collapse.

Specimen 2, realized with C24 timber with a spliced chord configuration connected through nail plates and bolts, exhibited a more pronounced nonlinear response from an

earlier stage of loading. The built-up timber chord and mechanical fasteners introduced additional compliance at the steel–timber interface, resulting in earlier slip initiation and reduced effectiveness of the steel diagonals in load transfer compared to S1. The specimen reached a peak load of approximately 55 kN — marginally exceeding the ULS level — but exhibited a sudden and brittle load drop at around 55–60 mm of displacement, with interfacial slip arrested at approximately 0.4 mm. As with S1 failure occurred through connection-related mechanisms, with detachment and localized damage concentrated at the steel–timber interfaces, while the steel-to-concrete connections performed satisfactorily throughout the entire loading history.

Overall, the results confirm the adequacy of both floor systems under all considered design limit states. However, the markedly different post-peak behaviors underline the critical role of timber grade and chord detailing in determining the ductility and overstrength reserves of the system. The brittle response of S2 highlights the sensitivity of timber–steel–concrete composite floor systems to connection configuration and material quality, with the steel–timber interface governing both load-carrying capacity and failure mode.

3 Conclusions

Preliminary experimental investigations of a novel composite floor system integrating steel, concrete, and timber members in a prefabricated unit were presented. In particular, two different floor systems were investigated.

Overall, the results confirm the adequacy of both floor systems under all considered design limit states. The markedly different post-peak behaviors underline the critical role of timber grade and chord detailing in determining the ductility and overstrength reserves of the system. The brittle response of Specimen S2 highlights the sensitivity of timber–steel–concrete composite floor systems to connection configuration and material quality, with the steel–timber interface governing both load-carrying capacity and failure mode. The observed failure modes confirm that these interfaces govern both stiffness degradation and ultimate capacity, emphasizing the need for improved connection design to enhance ductility and ensure a more reliable structural response. The present results refer to an 8100 mm span; for floor spans differing significantly from this value, two size-related effects should be considered in future work: (i) the number and spacing of steel diagonals along the chord, which scales with span length and affects the load demand per timber–steel connection, and (ii) the statistical size (length/volume) effect on timber strength, whereby longer continuous chords are expected to exhibit a lower characteristic bending/tensile strength.

Acknowledgements. The authors gratefully acknowledge the financial support from Smart Housing Småland and thank Torps Byggelement AB and MiTek Industries AB for their valuable collaboration, technical input, and support throughout the research.

References

1. Adema A, Santa Maria H, Guindos P (2022) Analysis of instant and long-term performance of timber–concrete floors with boundary conditions other than simply supported. Eng Struct 254:113827. https://doi.org/10.1016/j.engstruct.2021.113827
2. Shahnewaz M, Jackson R, Tannert T (2022) CLT concrete composite floors with steel kerf plate connectors. Constr Build Mater 319:126092. https://doi.org/10.1016/j.conbuildmat.2021.126092
3. Tao H, Yang H, Zhang J, Ju G, Xu J, Shi B (2022) Nonlinear finite element analysis on timber–concrete composite beams. J Build Eng 51:104259
4. Tao H, Shi B, Yang H, Wang C, Ling X, Xu J (2022) Experimental and finite element studies of prefabricated timber–concrete composite structures with glued perforated steel plate connections. Eng Struct 268:114778. https://doi.org/10.1016/j.engstruct.2022.114778
5. Ferrara G, Laurent M, Ferrier E (2023) Flexural behaviour of timber–concrete composite floor systems linearly supported at two edges. Eng Struct 281:115782
6. Pang S, Zhang Y, Li H, Wang Z (2022) Prediction of bending performance for a separable CLT–concrete composite slab connected by notch connectors. J Build Eng 49:103900
7. Jiang Y, Crocetti R (2019) CLT–concrete composite floors with notched shear connectors. Constr Build Mater 195:127–139. https://doi.org/10.1016/j.conbuildmat.2018.11.066
8. Lárusson LH, Ohlsson U, Johansson M (2013) Prefabricated floor panels composed of fiber reinforced concrete and a steel substructure. Eng Struct 46:104–115
9. Huo BY, D'Mello C, Uy B (2013) Push-out tests and analytical study of shear transfer mechanisms in composite shallow cellular floor beams. J Constr Steel Res 88:191–205. https://doi.org/10.1016/j.jcsr.2013.05.007
10. Tian L, Liu Y, Zhang S, Yu Z (2019) Flexural performance of a lightweight composite floor comprising cold-formed steel trusses and a composite mortar slab. Thin-Walled Struct 144:106361
11. Qiao W, Wang X, Li Y, Zhang Z (2020) Flexural properties of new cold-formed thin-walled steel and concrete composite slabs. J Build Eng 31:101441
12. MiTek Sweden (n.d.) Posi-Joist. https://www.mitekab.se/produkter/posi-joist/. Accessed 31 May 2026
13. MiTek Sweden (2021) Nail plate GNT-100S. https://www.mitekab.se/product/spikplat-gnt-100s/. Accessed 31 May 2026
14. MiTek Residential Construction Industry (2021) B SERIES bolts. https://www.mitek-us.com/products/fastener/bolts/b/. Accessed 31 May 2026
15. CEN (1991) EN 26891:1991; Timber structures – joints made with mechanical fasteners – general principles for the determination of strength and deformation characteristics. European Committee for Standardization, Brussels
16. CEN (2001) EN 12512:2001; Timber structures – test methods – cyclic testing of joints made with mechanical fasteners. European Committee for Standardization, Brussels
17. CEN (2012) EN 408: 2010; Timber structures – structural timber and glued laminated timber – determination of some physical and mechanical properties. European Committee for Standardization, Brussels
18. Lukaszewska E, Fragiacomo M, Johnsson H (2009) Laboratory tests and numerical analyses of prefabricated timber-concrete composite floors. J Struct Eng ASCE 136(1)
19. Frohnmuller J, Fischer J, Seim W (2021) Full-scale testing of adhesively bonded timber-concrete composite beams. Mater Struct 54:187
20. CEN (2004) EN 1995-1-1:2004; Design of timber structures – Part 1–1: general – common rules and rules for buildings. European Committee for Standardization, Brussels

21. CEN (2010) EN 14250:2010 – Timber structures – product requirements for prefabricated structural members assembled with punched metal plate fasteners. European Committee for Standardization, Brussels
22. CEN (2014) EN 1075:2014 – Timber structures – test methods – Joints made with punched metal plate fasteners. European Committee for Standardization, Brussels

Integrated Experimental Procedures for the Static Load Testing of Steel-Concrete Composite Highway Decks

Giuseppe Mugnos(✉)

Dismat s.r.l., Canicattì (AG), Italy
ing.giuseppemugnos@gmail.com

Abstract. The static acceptance testing of road and highway bridge decks traditionally relies on load tests aimed at measuring global deflections. While essential, this information alone is insufficient to fully describe the structure's behaviour—particularly for composite steel-concrete decks, where the global response must be interpreted alongside the local deformations of the main girders and the behaviour of the bearings. This paper proposes an integrated experimental procedure for the acceptance testing of a highway overpass, combining multidimensional static load tests with dynamic characterization under service conditions. The testing campaign involved the coordinated use of inclinometers, strain gauges, displacement transducers, and accelerometers, enabling the reconstruction of the deck's deformed shape, the assessment of local stress levels, the monitoring of bearings, and the identification of key modal parameters via Operational Modal Analysis and Enhanced Frequency Domain Decomposition. The results demonstrate a response consistent with the applied load scenarios, negligible residual deformations, and dynamic parameters suitable for establishing an experimental baseline for future monitoring. This integrated approach strengthens the acceptance assessment by reducing interpretive uncertainty compared to procedures based solely on deflection measurements.

Keywords: Static load testing · Composite steel-concrete decks · Load tests · Operational Modal Analysis · Enhanced Frequency Domain Decomposition · Structural monitoring

1 Introduction

The static acceptance testing of road structures marks the final stage of the process leading from design to the structure's entry into service. At this stage, it is not enough merely to verify the physical construction of the work; it is also necessary to confirm—through a technical assessment based on experimental evidence—that the structural response aligns with design assumptions and expected performance levels.

For bridge decks, load testing has traditionally been the primary tool supporting the acceptance decision. In practice, however, assessments often focus on mid-span deflections, treating them as a summary indicator of overall behavior. While deflection

© The Author(s), under exclusive license to Springer Nature Switzerland AG 2026
R. Zanon et al. (Eds.): CTA 2026, LNCE 942, pp. 598–610, 2026.
https://doi.org/10.1007/978-3-032-39505-4_52

is a significant parameter, it does not provide a complete picture of the deck's response—particularly when the aim is to verify local behaviour and the actual functioning of bearing devices.

The Technical Standards for Construction and the associated explanatory circular emphasize the need to conduct tests that monitor the evolution of deformations. For major structures such as bridges and viaducts, they also require supplementing the acceptance test with additional investigations, including dynamic characterization tests [1, 2]. This approach calls for procedures that combine global, local, and dynamic measurements, moving beyond assessments based solely on vertical displacement.

International literature on bridge monitoring and dynamic identification highlights how vibration-based techniques can provide information complementary to static tests, particularly for establishing baseline conditions and monitoring performance changes over time [3, 4, 8, 9]. Recent reviews of Structural Health Monitoring approaches also highlight the benefits of integrating displacement, strain, and acceleration measurements, as each class of sensor captures a different aspect of the structural response [9, 10].

The specific contribution of this study lies in applying this integrated approach to the static load testing of a composite steel-concrete highway overpass. The aim is not merely to present the results of a single testing campaign but to demonstrate the methodological value of a coordinated use of instrumented static tests and operational dynamic tests. The proposed procedure transforms the load test from a point-in-time check of a single parameter into a multidimensional, more robust, and thoroughly documented experimental process.

2 Case Study: Composite Highway Deck

The case study concerns an overpass on the A20 Messina-Palermo motorway, featuring a composite steel-concrete deck. The structural scheme consists of a continuous beam supported at three points, comprising two identical spans of 40 m each, for a total length of 80 m.

The cross-section consists of two steel I-girders spaced 5.00 m apart, with a constant depth of 2.00 m. The girders are connected by truss cross-bracing and lateral bracing systems, while the reinforced concrete deck slab—cast in situ over precast panels—acts compositely with the steel girders via Nelson-type shear studs. The total width of the roadway deck is approximately 10.00 m, including the carriageway, shoulders, edge curbs, and safety barriers.

Elastomeric bearings are used at the abutments and the central pier. Given this configuration, it was deemed appropriate to supplement the measurement of the global deformed shape with direct monitoring of displacements at the bearing locations, in order to assess the compatibility between the spans' structural response and the local behavior of the supports (Figs. 1, 2 and 3) (Table 1).

Table 1. Main geometric and structural characteristics of the case study.

Parameter	Value / description
Type	Highway overpass with composite steel–concrete deck
Structural scheme	Continuous beam on three supports
Spans	Two spans of 40 m
Total length	80 m
Main girders	Two steel I-girders, 2.00 m depth, 5.00 m spacing
Slab	Cast-in-place reinforced concrete slab, made composite through steel shear connector
Bearings	Elastomeric devices on abutments and pier

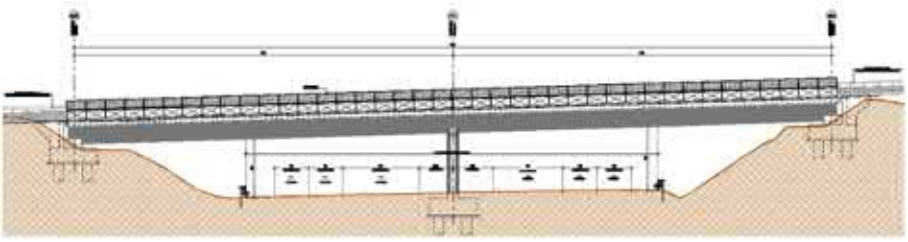


Fig. 1. General overview of the bridge deck.

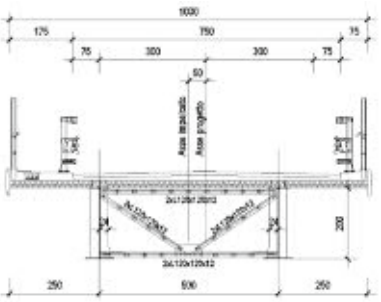


Fig. 2. Typical cross-section of the overpass

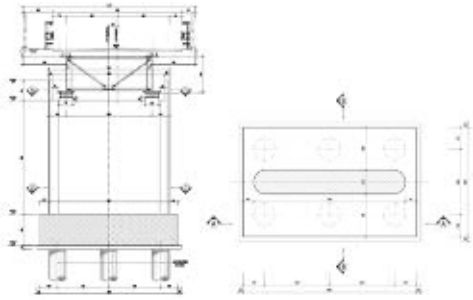


Fig. 3. Foundation section and plan of the pier

3 Integrated Experimental Procedure

The experimental procedure was designed to acquire—in a single, coordinated campaign—data representing the global behaviour, local response, and dynamic characteristics of the deck. The adopted strategy relies on three levels of observation: measurement of global deformation using inclinometers, direct measurement of local strains using strain gauges, and dynamic identification via accelerometers installed on the deck.

3.1 Static Load Tests

Static load tests were conducted prior to reopening the structure to traffic, following the standard procedure for the static acceptance testing of structural works [1, 2], using four-axle trucks with a gross weight of approximately 42 t each, verified beforehand by weighing. Two main loading configurations were considered, defined to induce representative and mutually complementary static conditions.

In the first scenario, six trucks were positioned on a single span to maximize the positive bending moment—and thus the flexural response—of the loaded span. In the second scenario, eight trucks were distributed across the two spans in a 4 + 4 arrangement to increase the negative bending moment at the section above the central pier (Figs. 4 and 5).

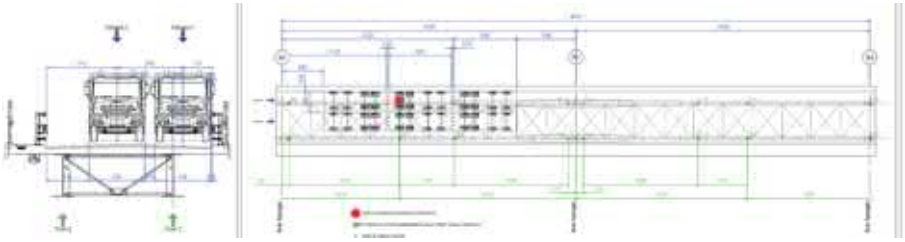


Fig. 4. Loading configuration: Scenario 1 — 6 trucks on a single span.



Fig. 5. Loading configuration: Scenario 2 — 8 trucks on two spans.

3.2 Static Measurement System

The static measurement system was configured to go beyond an assessment limited solely to mid-span deflection. To this end, three types of sensors were employed, each associated with specific structural data.

Electronic inclinometers, installed symmetrically on both sides of the deck, enabled the measurement of elastic line rotations and the reconstruction of the deformed shapes of the two spans. Electrical strain gauges were applied to the top and bottom flanges of the main girders at the central support section to measure local strains in the extreme fibers

and derive the corresponding stress levels. Finally, displacement transducers installed at the supports allowed for the recording of settlements and potential differential rotations of the elastomeric bearings (Fig. 6) (Table 2).

Table 2. Summary of the instrumentation used for static tests.

System	Number / arrangement	Measured quantity	Function in the load test
Electronic inclinometers	18 sensors, distributed along both sides of the deck	Rotations	Reconstruction of the global deflected shape
Electrical strain gauges	8 sensors on the top and bottom flanges	Local strains	Control of extreme fibres and estimation of stress levels
Displacement transducers	3 sensors per bearing, arranged at 120°	Local displacements	Monitoring of bearings and residual movements

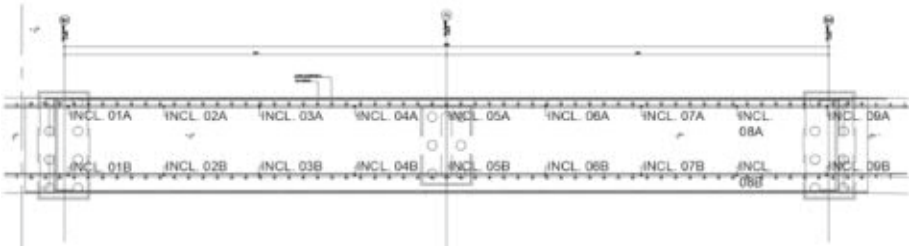


Fig. 6. Inclinometers: plan view of the sensor layout.



Fig. 7. Installation of strain gauges and transducers on the bearings.

3.3 Dynamic Tests Under Ambient Excitation

Dynamic characterization was performed under ambient excitation conditions—without the use of artificial forcing—following the Operational Modal Analysis approach [4]. This choice aligns with the need to describe the deck's global behaviour under near-service conditions and to establish an experimental baseline for comparison with future measurements.

The dynamic testing campaign utilized 15 PCB 393-A03 accelerometers connected to an NI cDAQ-9172 unit equipped with 24-bit USB-9234 modules. The final configuration comprised 12 vertical accelerometers distributed at the quarter-span and mid-span points of the two spans, along with 2 transverse accelerometers and 1 longitudinal accelerometer at mid-span. Positioning the sensors along the vertical axes of the main girders prioritized the identification of the deck's global modes while minimizing interference from potential local vibrations of the lateral cantilevers (Fig. 8).

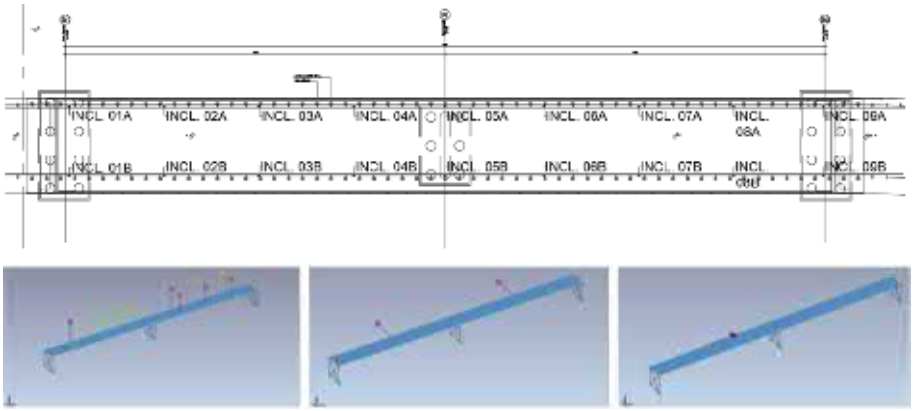


Fig. 8. Accelerometer placement layout and experimental model for dynamic analysis.

4 Processing of Experimental Data

4.1 Reconstruction of the Deformed Shape

Inclinometric measurements provide the discrete field of rotations along the axis of the deck. Assuming small rotations, the relationship between rotation and vertical displacement can be expressed by Eq. (1):

$$\theta(x) \simeq dv(x)/dx \tag{1}$$

The deformed shape is thus obtained by numerically integrating the rotation field, imposing the appropriate boundary conditions at the supports in accordance with Eq. (2):

$$v(x) = \int \theta(x)\, dx + C \tag{2}$$

In this way, the discrete measurement of rotation is transformed into a continuous description of the deformed configuration, useful for comparison with computational model predictions and for assessing the consistency of the global response..

4.2 Local Deformations and Stresses

The strains measured by the strain gauges were used to evaluate the local response of the top and bottom fibres of the main girders at the central support section. Assuming linear elastic behaviour for the steel, the stresses were estimated using Hooke's law, given in Eq. (3):

$$\sigma = E\,\varepsilon \tag{3}$$

where E represents the elastic modulus of the steel and ε the measured strain. This analysis makes it possible to verify not only the sign and distribution of the strains in relation to the loading scheme but also the order of magnitude of the stresses actually reached during the test.

4.3 OMA/EFDD Modal Identification

The accelerometer signals were processed using Operational Modal Analysis techniques [4]. In particular, the Enhanced Frequency Domain Decomposition algorithm was used, derived from the Frequency Domain Decomposition and based on the singular value decomposition of the spectral density matrix of the responses [6]. The estimation of the spectral densities was carried out using procedures based on the average of successive periodograms, according to the commonly adopted approach for the reduction of variance in spectral estimation [7].

In synthetic form, for each discrete frequency, the decomposition can be expressed as in Eq. (4):

$$S_{\gamma\gamma}(\omega_k) = U(\omega_k)\,\Sigma(\omega_k)\,U^*(\omega_k) \tag{4}$$

where $S_{\gamma\gamma}(\omega_k)$ is the power spectral density matrix of the response, evaluated at the discrete frequency ω_k; $U(\omega_k)$ is the unitary matrix whose columns are the singular vectors, taken as estimates of the mode shapes; $\Sigma(\omega_k)$ is the diagonal matrix containing the singular values ordered in descending order; and $U^*(\omega_k)$ represents the conjugate transpose of the matrix $U(\omega_k)$.

5 Experimental Results

5.1 Global Static Response

The deformed shapes reconstructed from inclinometer measurements revealed a response consistent with the applied load configurations. In the first scenario, the greatest deflection is concentrated in the loaded span, while the adjacent span exhibits a deformed shape consistent with the continuity of the deck. In the second scenario, the load distribution across the two spans produces a more symmetrical response and subjects the central support zone to significant stress.

A comparative analysis of the two sides of the deck made it possible to assess the transverse regularity of the response. The differences observed between the Messina side and the Palermo side are consistent with the eccentricities of the load configurations and do not indicate any global anomalies in static behaviour. Furthermore, a joint examination of the four deformed shapes shown in Fig. 7 allows for the verification of response continuity between the two spans and the correct reversal of curvature in the zones near the central pier (Figs. 9, 10, 11 and 12).

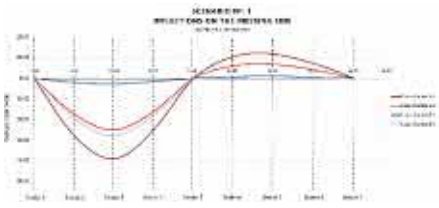


Fig. 9. Deflected configuration of the deck, Scenario 1 – Girder on ME side

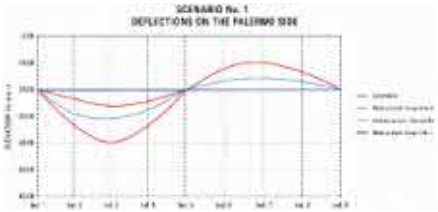


Fig. 10. Deflected configuration of the deck, Scenario 1 – Girder on PA side



Fig. 11. Deflected configuration of the deck, Scenario 2 – Girder on ME side

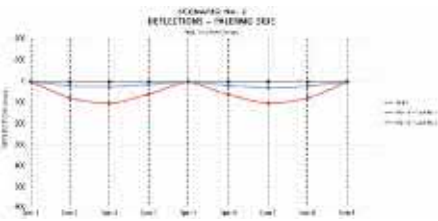


Fig. 12. Deflected configuration of the deck, Scenario 2 – Girder on PA side

5.2 Local Deformations, Stresses, and Supports

Strain gauge measurements at the central pier section yielded trends consistent with the expected flexural behaviour. In particular, the strain distribution between the top and bottom flanges confirmed the sign reversal associated with negative bending moments in the support zone. Converting strains into stresses revealed values within the elastic range, confirming the absence of experimental evidence of non-linear behaviour during the testing phases.

Monitoring the bearings completed the assessment of the static response. Displacement transducer readings were low, and measurements taken after unloading showed negligible residual values compared to those at full load. The average maximum value recorded at full load was 0.42 mm, while the maximum residual value after final unloading was in the order of 0.05 mm. These findings make it possible to distinguish the deformation of the spans themselves from the local contribution of the bearing devices (Table 3).

Table 3. Average support settlements recorded by displacement transducers.

Scenario	Phase	Bearing	Average reading [mm]
1	Full load	PA	0,42
1	Full load	ME	−0,32
1	Final unloading	PA	−0,02
1	Final unloading	ME	−0,04
2	Full load	PA	0,35
2	Full load	ME	−0,02
2	Final unloading	PA	0,01
2	Final unloading	ME	−0,05

5.3 Dynamic Response

The OMA/EFDD analysis [4, 6] enabled the identification of the deck's principal global modes in the vertical, transverse, and longitudinal directions. Data processing was performed using Artemis Modal 7.2 by constructing a 24-node experimental model, comprising 12 nodes corresponding to measurement points and additional nodes representing external constraints. This representation allowed the mode shapes to be projected onto the observed degrees of freedom and the main modal families to be distinguished.

The identified vertical modes include flexural and torsional shapes, with frequencies ranging from 2.488 Hz to 7.614 Hz and damping ratios between 0.480% and 1.249%. Transverse and longitudinal modes—falling within a similar frequency range for the fundamental modes—complete the global dynamic description. The highest damping value was observed for the second longitudinal mode (8.750%), indicating greater dissipation associated with global motion components along the bridge axis (Figs. 13, 14, 15, 16, 17 and 18) (Tables 4 and 5).

Table 4. Main modal parameters identified using OMA/EFDD.

Direction	f [Hz]	zeta [%]	Mode description
Vertical	2,488	1,249	Out-of-phase bending
Vertical	3,643	1,011	In-phase bending
Vertical	4,002	0,850	Out-of-phase torsion
Vertical	4,487	0,970	In-phase torsion
Vertical	7,614	0,480	Double bending with mid-span inflection
Transverse	2,486	1,324	Out-of-phase transverse translation
Transverse	2,735	2,313	In-phase transverse translation
Transverse	3,633	1,061	In-phase transverse translation

(*continued*)

Table 4. (*continued*)

Direction	f [Hz]	zeta [%]	Mode description
Longitudinal	2,484	1,367	Longitudinal translation
Longitudinal	3,694	8,750	Longitudinal translation

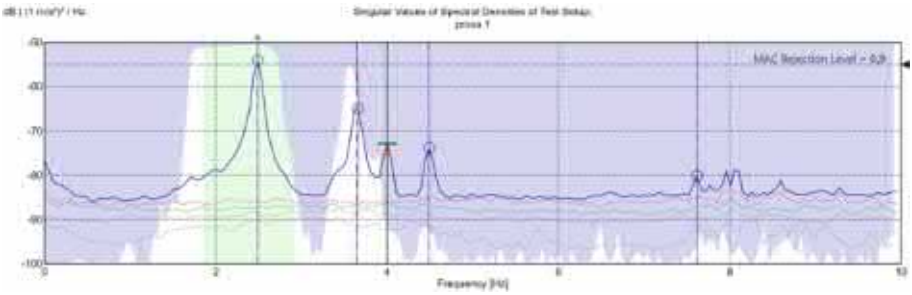


Fig. 13. Singular values of the PSD in the vertical direction.

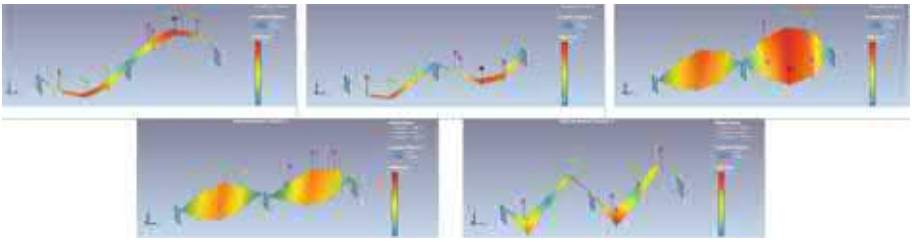


Fig. 14. Modal shapes obtained from the analysis of signals in the vertical direction.

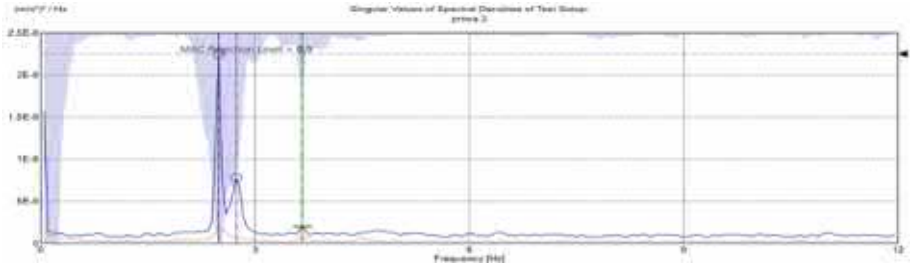


Fig. 15. Singular values of the PSD in the transverse direction.

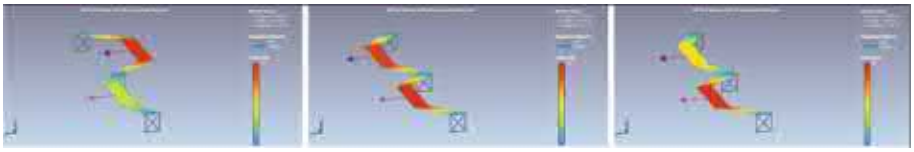


Fig. 16. Modal shapes obtained from the analysis of signals in the transverse direction.

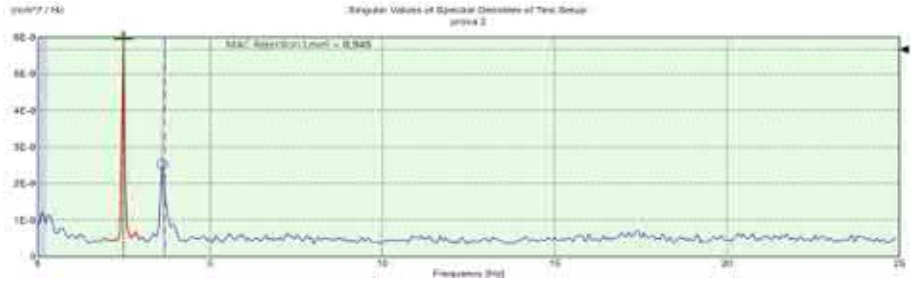


Fig. 17. Singular values of the PSD in the longitudinal direction.



Fig. 18. Modal shapes obtained from the analysis of signals in the longitudinal direction.

Table 5. Quantitative summary of the main experimental indicators.

Indicator	Observed value	Interpretation
Maximum average displacement of supports at full load	0,42 mm	Limited constraint response
Maximum residual displacement at final unloading	0,05 mm	Negligible residues
Identified vertical frequency range	2,488–7,614 Hz	Presence of global flexural and torsional modes
Vertical damping range	0,480–1,249%	Values consistent with global elastic response
Identified maximum damping	8,750%	Associated with the second longitudinal mode
Maximum average displacement of supports at full load	0,42 mm	Limited constraint response

6 Considerations Regarding the Integration of Tests

Experimental evidence highlights that integrating static and dynamic tests yields a more comprehensive interpretive framework than relying on a single type of measurement alone. While static testing provides a direct verification of the structure's response to controlled loads, measuring deflections alone is not always sufficient to characterize the local behaviour of the most highly stressed sections and the support devices.

In this context, inclinometers allow for the reconstruction of the deck's global deformed shape, strain gauges enable the assessment of local deformations and stress levels in the main girders, and transducers installed on the bearings provide insights into support behaviour. Dynamic characterization completes the picture by identifying frequencies, mode shapes, and damping ratios—data that also serve as an experimental baseline for future monitoring [3, 4].

Unlike approaches found in the literature—where modal analysis is often treated as a standalone monitoring or model-updating activity [8, 9]—this study proposes integrating it directly into the acceptance testing procedure. In the case at hand, the consistency among static response, local deformations, bearing behaviour, and modal parameters strengthened the assessment of the structure's performance, thereby reducing interpretive uncertainty and transforming the acceptance test into a multidimensional experimental evaluation.

7 Conclusions

This study presented an integrated experimental procedure for the load testing of a composite steel-concrete highway bridge deck, based on the coordinated use of instrumented static tests and dynamic tests under ambient excitation.

The static tests—utilizing inclinometers, strain gauges, and displacement transducers—enabled a simultaneous assessment of the deck's global deformed shape, local strains in the main girders, and the behaviour of the bearings. The results demonstrated a response consistent with the applied loading schemes, showing negligible residual displacements and stress levels within the elastic range.

The dynamic tests analysed using OMA/EFDD techniques [4, 6], allowed for the identification of key modal parameters, providing a comprehensive description of the dynamic response and an experimental baseline for future monitoring [3, 8]. Integrating static and dynamic testing thus enhanced the reliability of the load test assessment, moving beyond evaluations based solely on deflection measurements.

The proposed approach is applicable to other road and highway bridge decks, particularly for structures requiring a simultaneous assessment of global response, local strains, support behaviour, and dynamic characteristics.

References

1. Ministry of Infrastructure and Transport (2018) Technical standards for construction. Ministerial Decree of 17 January 2018

2. Superior Council of Public Works (2019) Circular No. 7 of 21 January 2019. Instructions for the application of the updated technical standards for construction
3. Doebling SW, Farrar CR, Prime MB (1998) A summary review of vibration-based damage identification methods. Shock Vib Dig 30(2):91–105
4. Brincker R, Ventura C (2015) Introduction to operational modal analysis. Wiley, Chichester
5. Allemang RJ (2003) The modal assurance criterion (MAC): twenty years of use and abuse. Sound Vib 37(8):14–23
6. Brincker R, Zhang L, Andersen P (2000) Modal identification from ambient responses using frequency domain decomposition. In: Proceedings of the 18th international modal analysis conference (IMAC XVIII), San Antonio
7. Welch PD (1967) The use of fast Fourier transform for the estimation of power spectra: a method based on time averaging over short, modified periodograms. IEEE Trans Audio Electroacoust 15(2):70–73
8. Rainieri C, Notarangelo MA, Fabbrocino G (2020) Experiences of dynamic identification and monitoring of bridges in serviceability conditions and after hazardous events. Infrastructures 5(10):86
9. Hasani H, Freddi F (2023) Operational modal analysis on bridges: a comprehensive review. Infrastructures 8(12):172
10. Rizzo P, Enshaeian A (2021) Challenges in bridge health monitoring: a review. Sensors 21(13):4336

Sagging Bending Moment Resistance of Steel-Concrete Composite Beams with Hot-Rolled Stock Sections: Extension of the Simplified Analytical Method to High-Strength Steel and Steel Fiber Reinforced Concrete

Francesco Profico[1(✉)], Riccardo Zanon[2], and Markus Schäfer[2]

[1] ArcelorMittal, Esch-Sur-Alzette, Luxembourg
francesco.profico@arcelormittal.com
[2] University of Luxembourg, Luxembourg, Luxembourg
riccardo.zanon.001@student.uni.lu, markus.schaefer@uni.lu

Abstract. A simplified analytical method of high interest for practitioners is proposed in Eurocode 4 to calculate the plastic bending moment resistance of steel-concrete composite beams. A reduction factor "beta" is applied to correlate the sagging bending resistance with the plastic bending resistance calculated with a full material utilization without considering strain compatibility. This correction accounts for the fact that the ideal condition of fully yielded materials does not occur. This influence is particularly relevant for deep plastic neutral axis and becomes more pronounced for steels with a high yield limit. This paper presents the results of a parametric analysis aimed at extending the applicability of the methodology for higher yield strength structural steels (higher than S460 and up to S690) and use of Steel Fiber Reinforced Concrete, which presents a modified stress-strain constitutive law. The study is limited to double symmetrical hot-rolled sections and is therefore applicable only for these dimensions. The analysis compares, for several typical cross-section configurations, the value of the bending moment resistance obtained through a strain-limitation procedure with the corresponding plastic bending resistance obtained with the simplified rigid–plastic analysis. Based on the ratio between the two values, formulations for the beta factor are proposed.

Keywords: Composite Sections · Plastic Resistance · Sagging Bending Moment · Steel Fiber Reinforced Concrete · High Strength Steel

1 Introduction

In the frame of the first generation of Eurocode 4 (EC4) [1] the plastic bending resistance of composite steel-concrete sections is calculated by means of a simple stress block distribution based on the translation equilibrium condition. This is an effective

© The Author(s), under exclusive license to Springer Nature Switzerland AG 2026
R. Zanon et al. (Eds.): CTA 2026, LNCE 942, pp. 611–620, 2026.
https://doi.org/10.1007/978-3-032-39505-4_53

and practical procedure that allows a simple assessment of the bending resistance of composite elements. The simplicity of the method implies in the most common and simple configurations to evaluate the bending resistance by hand calculation and simple implementations in spreadsheets and calculation tools. In the rigid-plastic model all fibers composing the sections are stressed at their limit. Full yielding on the steel is considered. The compression side of the section is delimited from the tension part by the plastic neutral axis (PNA). This situation ideally occurs when an infinite curvature is applied on the section in simple bending, with perfectly rigid-plastic materials. This hypothesis is ideal and adopted to significantly simplify the calculation process. Correction factors were needed only for S420 and S460 grades.

Differently, a strain-limitation methodology [2] considers the full non-linear stress-strain material relations and can be used as alternative to the stress block method (full-plastic resistance). It represents a more reliable procedure to assess the bending resistance thanks to the fact that the allowable strain limits are properly accounted for in the analysis. This, however, implies higher computational effort and reduced accessibility in the common design practice. This is why Eurocode 4 preserves in the second-generation version [3] the applicability of the stress-block method.

In many cases the direct output of the stress-block model provides good alignment with results obtained with more refined methodology as the strain-limitation. Nevertheless, there are several cases where the stress distribution over the section's fibers cannot be approximated by a constant value. These cases include deep-neutral axis sections or configurations where the bending failure mode is often governed by concrete crushing in compression, thus a limited rotation capacity. Under these circumstances a significant portion of the steel part is still below the yield limit, thus in the elastic phase. The utilization of higher strength steel grades encourages the possibility of premature concrete crushing before the development of the full plastic capacity of the steel portion [4]. To account for this effect an adjustment factor is implemented in the current version of Eurocode 4. The factor known as "beta" was firstly introduced in the code for sections using S420 and S460 steel grades based on studies by Hanswille, Sedlacek and al [5]. The reduction factor is dependent on the relative PNA position obtained from the full-plastic resistance (stress block). This factor reduces the plastic bending resistance obtained with the rigid-plastic methodology. More recent studies by Schäfer, Zhang and Banfi [6–9] extended the research, leading to the updated methodology contained in the forthcoming prEN1994-1-1 [3]. In this new version of the code, the beta reduction factor is provided as well for lower steel grades (S235, S275, S355). The multi-linear curve to determine the beta factor is a safe-sided envelope of the ratios between the bending moment resistance (M_{Rd}) divided by the plastic bending moment resistance ($M_{pl,Rd}$). The studies for the introduction in prEN1994-1-1 were focused on typical down-stand and shallow-floor beams commonly used in building applications [6–9].

To date, relations covering higher steel grades are in the Eurocode missing. Research studies are available up to S550 steel grade [7]. The objective of the present work is to propose equivalent relations for steel grades up to S690. Moreover, the use of SFRC (Steel Fiber Reinforces Concrete) is also treated. The provision of such formulations covering the calculation of these materials can encourage and open the construction market in implementing innovative design configurations. SFRC applied in composite

beams constitutes an innovative solution; one of the motivation for its use can be the enhanced concrete ductility [10, 11]. This allows for larger strain limits and improved ductility properties of the cross-section, reducing or solving the premature failure due to concrete crushing. A parametric study is used to derive lower-bound formulations, replicating the same methodology already used by Schäfer, Zhang and Banfi [6–9], thus comparing the bending moment resistance (M_{Rd}) obtained with strain-limitation analysis with the outcome of the stress-block analysis (plastic bending resistance, $M_{pl,Rd}$). An analogous work exists for filler-beam type composite sects [12].

2 Analysis

A parametric study is performed varying multiple parameters. Every combination of parameters defines a specific configuration. In total 14252 configurations have been analyzed. For each, separately, the bending resistance M_{Rd} is derived using the strain-limitation method and the full-plastic bending resistance $M_{pl,Rd}$ from the stress-block model. The ratio between the two is derived and related to the relative position of the neutral axis (z_{pl}/h_{TOT}). The generic configuration studied is highlighted in Fig. 1, where the geometric variables are identified.

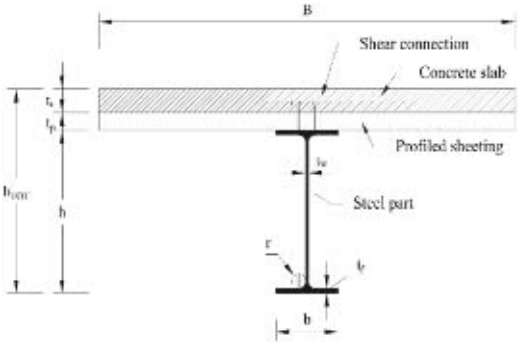


Fig. 1. Typical cross-section with geometric parameters.

The geometries of the steel sections are defined starting from the designation based on the standard EN 10365 [13] (Hot rolled steel channels, I and H sections – Dimensions and masses). From here all the nominal dimensions of the flange and web thicknesses (t_f, t_w), section height (h) and flange width (b), fillet radius (r) are determined. The ultimate deformative state such that the axial force resultant is zero is imposed and the bending resistance is derived as consequence (Fig. 2). No relative strain slip exists at the concrete-steel interface. Further the sequence of loading is not considered, and the composite action is effective already under self-weight. The varied parameters are described in Table 1.

Table 1. List of varied parameters and related values.

Parameter	Symbol and M.U.	Values list
Concrete strength	f_{ck} [MPa]	[20, 35, 50]
FRC		[True, False]
Steel grade		[S355M, S460M, S500, S550, S620, S690]
Steel section		[HE 200 M, HE 220 A, HE 240 AA, HD 400 × 187, HD 400 × 382, HD 400 × 634, HE 600 AA, HE 600 B, HE 600 M, HE 600 × 399, HE 1000 AA, HE 1000 B, HE 1000 M, HE 1000 × 584, HL 920 × 787, HL 1100 A, HL 1100 × 607, UB 762 × 267 × 134, UB 762 × 267 × 220, UB 610 × 325 × 551, UB 610 × 229 × 101, IPE A 220, IPE A 300, IPE A 450, IPE A 600, IPE 600, IPE A 500, IPE 500, HE 300 B, HE 400 M, HE 500 M, HE 800 A, HE 800 M]
Profiled sheeting height or any gap between steel and participating slab	t_p [mm]	[0, 135]
Slab thickness	t_{slab} [mm]	[0.15 h − $t_p \geq$ 50 mm, 0.70 h − $t_p \geq$ 50 mm] where h = steel profile height
Slab width	B [mm]	[500, max(500, 10 h_{TOT}), max(500, 0.5 (10 h_{TOT} + 500))]

The material laws used for the strain limitation analysis are described in Fig. 3. The material properties of the standard EN 10025 [14] are used for the structural steel. A quadrilinear stress-strain curve is adopted according to prEN1994-1-14 [15]. Reinforcement steel is not considered in the analysis. Normal reinforced concrete properties are derived from prEN1992-1-1 [16]. The assigned model is a parabola-rectangle relation. In case Steel Fibre Reinforced Concrete is considered, the mechanical behaviour is modelled with reference to FprEN1992-1-1 [16] and multiple research studies characterizing the mechanical behaviour [17–20].

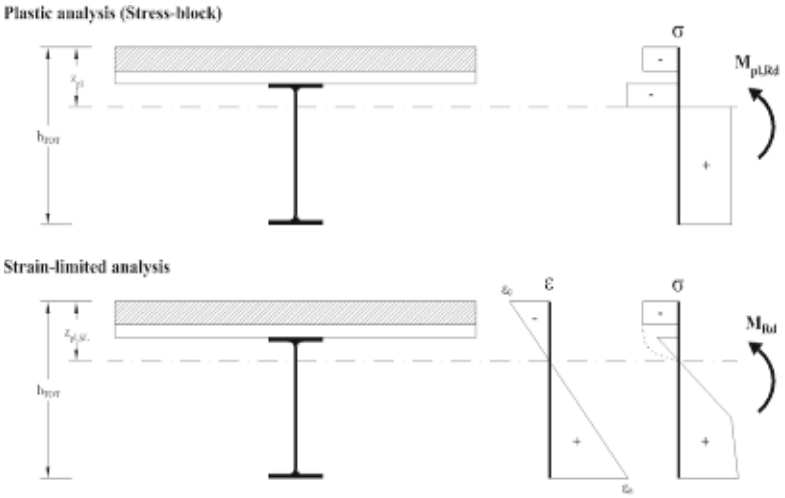


Fig. 2. Plastic analysis and strain-limited analysis

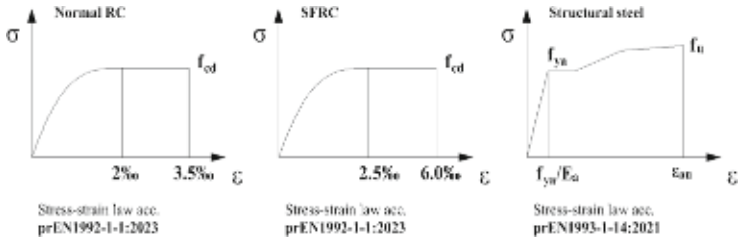


Fig. 3. Adopted material laws.

3 Results and Discussion

The analysis results are illustrated in (Figs. 4, 5, 6, 7, 8, and 9). For each combination of parameters studied, the point represented by the couple "relative position of PNA" (z_{pl}/h) and "ratio between bending moment resistance and plastic bending moment resistance" is showed. A direct comparison with the multi-lines of the beta-factor of next version of EC4 is offered.

The significant influence of the plastic neutral axis position is clearly visible in the graphs as well as the effect of increased steel grade. The ratio between the bending resistance and the related plastic one decreases with deeper plastic neutral axis and higher steel grade. The analysis results show good agreement and coherency with the existing formulations of the beta factor provided in the next version of EC4 for steel grades S355 and S690 with the use of normal concrete.

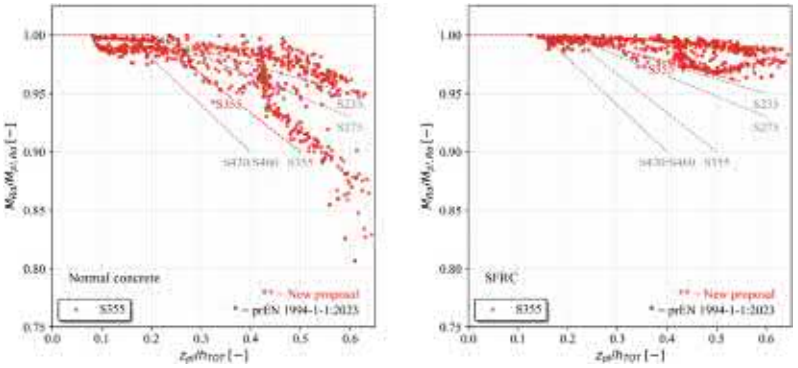


Fig. 4. Results of the parametric analysis for grade S355, for normal concrete and SFRC.

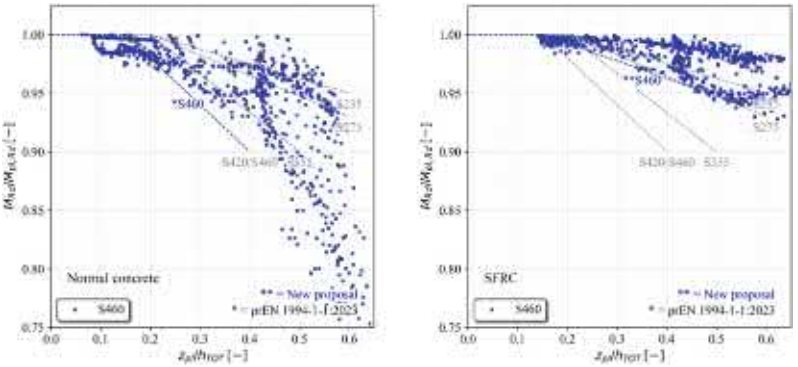


Fig. 5. Results of the parametric analysis for grade S460, for normal concrete and SFRC.

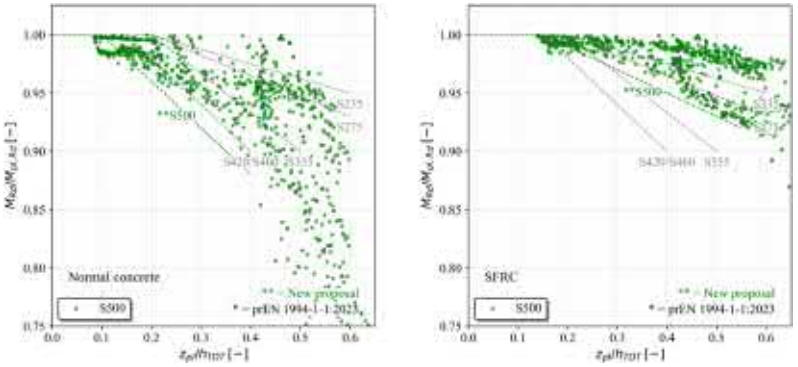


Fig. 6. Results of the parametric analysis for grade S500, for normal concrete and SFRC.

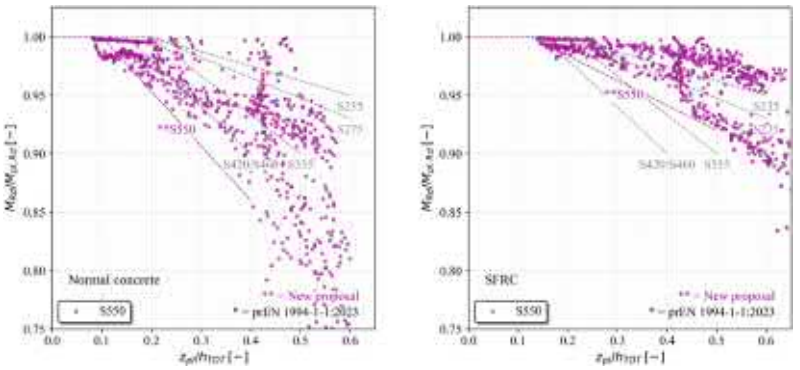


Fig. 7. Results of the parametric analysis for grade S550, for normal concrete and SFRC.

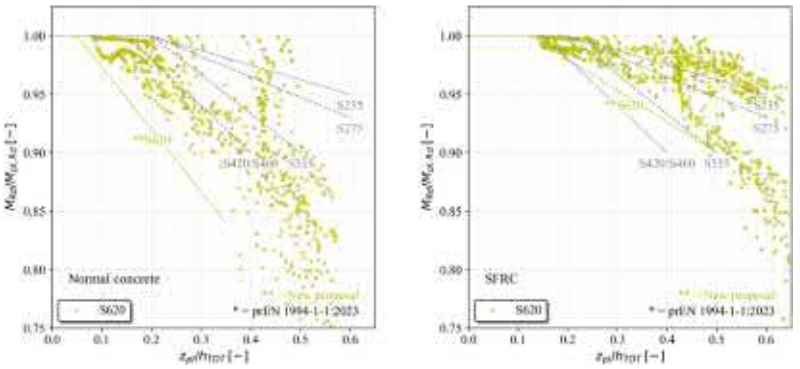


Fig. 8. Results of the parametric analysis for grade S620, for normal concrete and SFRC.

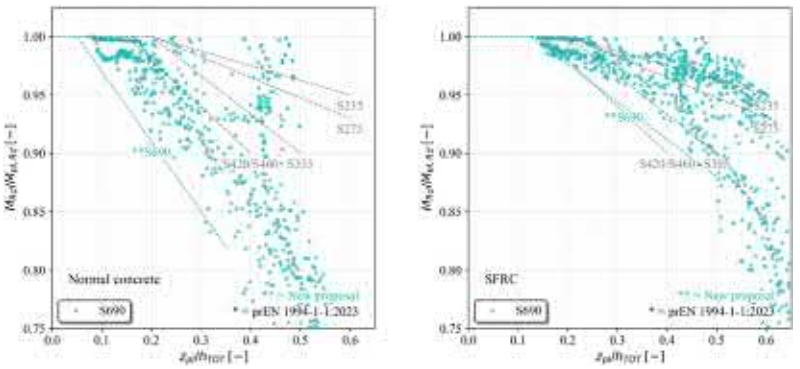


Fig. 9. Results of parametric analysis for grade S690, for normal concrete and SFRC.

A sharp difference can be observed between the results related to normal concrete respect to the correspondent with SFRC. The ratio between the bending moment resistance and the same derived in fully plastic condition systematically presents larger values for the use of SFRC. This reflects the improved deformation capacity of SFRC, implying a possibility for the steel part to reach more extended portions which are fully yielded before the section fails under concrete crushing. It is evident that an increase in steel grade tends, for both cases of normal concrete and SFRC, to lower the ratio. This is an expected result that testifies the lower amount of steel part yielded with increasing steel grade.

For each grade, a beta factor multi-line curve is proposed in Table 2 and graphically illustrated in the results graphs. The definition is provided based on the coordinates of points P1 and P2, identified in Fig. 10. The criteria for defining the lines, beside setting, were the following:

– Population of points below the line: $< 7\%$
– Maximum difference: $< 3\%$

These criteria are coherent with the approach used for grades S355 and S460 with normal concrete. The proposed formulations are in line with the existing approach of the code and easy to implement in it. These would extend the applicability of rigid-plastic methodology for higher steel grades and the use of SFRC.

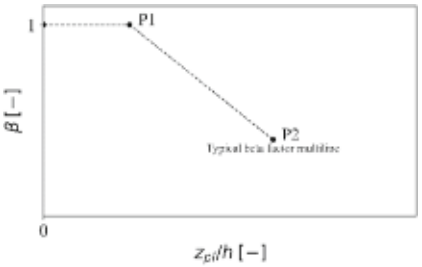


Fig. 10. Definition of multiline curves for beta-factor proposals with relevant points P1 and P2.

Table 2. Proposal of points determining the linearly descending branch of the multi-line curve for the beta factor for different steel grades and concrete type. (*): Already implemented in prEN1994-1-1:2023; (**): New proposal.

	Normal concrete		SFRC	
Steel grade	P1 (z_{pl}/h, β)	P2 (z_{pl}/h, β)	P1 (z_{pl}/h, β)	P2 (z_{pl}/h, β)
S355	*(0.20, 1.000)	*(0.50, 0.900)	**(0.20, 1.000)	**(0.55, 0.960)
S460	*(0.15, 1.000)	*(0.40, 0.900)	**(0.15, 1.000)	**(0.55, 0.940)
S500	**(0.10, 1.000)	**(0.40, 0.880)	**(0.15, 1.000)	**(0.55, 0.920)
S550	**(0.10, 1.000)	**(0.40, 0.860)	**(0.125, 1.000)	**(0.50, 0.920)

(*continued*)

Table 2. (*continued*)

	Normal concrete		SFRC	
S620	**(0.05, 1.000)	**(0.35, 0.840)	**(0.125, 1.000)	**(0.50, 0.900)
S690	**(0.05, 1.000)	**(0.35, 0.820)	**(0.125, 1.000)	**(0.50, 0.880)

4 Conclusions

The study focuses on the effect of the steel grade and use of SFRC on the derivation of the bending moment resistance in composite beams under sagging. With the objective to extend the analytical method approach of EC4 [3] to steel grades up to S690 and to the use of SFRC, the plastic bending resistance is compared to the related bending resistance derived with strain-limitation approach. Following a parametric analysis performed on several typical composite double symmetrical hot-rolled section configurations, the effect of the PNA position, steel grades and use of normal concrete or SFRC is described. With increasing steel grade, there is a progressive increase in the strain limitation impact and therefore a more prominent correction factor. The use of SFRC, on the contrary, acts favorably with a lower impact of the correction factor thanks to the improved deformation capacity of the concrete part. Deeper plastic neutral axis reflects in a reduction of the ratio.

Based on the results, conservative beta-factor formulas are proposed for the combinations of steel grade and concrete type not yet covered by the next EC4 version [3]. The proposed formulations are dependent on the steel grade, the plastic neutral axis position and the use of SFRC.

References

1. EN 1994-1-1 (2004) Eurocode 4: design of composite steel and concrete structures – Part 1–1: General rules and rules for buildings
2. Schäfer M, Zhang Q (2019) Zur dehnungsbegrenzten Momententragfähigkeit von Flachdecken in Verbundbauweise – Grenzen der plastischen Bemessung. Stahlbau 88(7)
3. prEN 1994-1-1 (2025) Eurocode 4: design of composite steel and concrete structures – Part 1–1: general rules and rules for buildings. Draft working group WG 4
4. Goralski C, Hegger J (2007) Zur Verbundsicherung von kammerbetonierten Verbundträgern. Stahlbau 76:805–814
5. Hanswille G, Sedlacek G, Anderson D (1996) The use of steel grades S460 and S420 in composite structures. Technical Report, ECCS-EUROFER improvements by TC11 to Eurocode 4
6. Schäfer M (2017) Review of plastic moment resistance for composite beams. In: Development of second generation of Eurocode 4 – harmonization with Eurocode 2, composite construction in steel and concrete CCVIII, Jackson Hole, Wyoming, USA
7. Zhang Q (2020) Moment and longitudinal resistance for composite beams based on strain limited design method. PhD Thesis,. Université du Luxembourg
8. Schäfer M, Zhang Q, Braun M, Banfi M (2021) Limitations of plastic bending resistance for composite beams deviated from strain-limitation. J Constr Steel Res 180

9. Schäfer M, Zhang Q, Banfi M (2022) Background document on materials and limits for plastic moment resistance. Technical Report, European Mandate M515, CEN/TC250/SC4.T6, CEN Documents CEN/TC250/SC4
10. Zanon R, Schäfer M, Ruiz G, De La Rosa Á, Zhang Q (2022) Steel-fibre reinforced concrete in composite structures as a mean to increase resistance and ductility – outlook in a new generation of composite structures. Stahlbau 91(12)
11. Zanon R, Schäfer M, Ruiz G, De La Rosa Á, Masih VW, Wolf S (2024) Experimental bending tests on encased steel-concrete composite beams with SFRC. In: BEFIB conference, Dresden
12. Zanon R, Profico F, Schäfer M, Ruiz G, De La Rosa Á (2026) Plastic resistance to sagging bending of filler beam decks: extension to S500 grade and steel fibre reinforced concrete. Steel Constr 19(2):123–134
13. EN 10365 (2017) Hot rolled steel channels, I and H – Dimensions and masses
14. EN 10025-4 (2019) Hot rolled products of structural steels – Part 4: Technical delivery conditions for thermomechanical rolled weldable fine grain structural steels
15. prEN 1993-1-14 (2022) Eurocode 3: design of steel structures – Part 1–14: design assisted by finite element analysis. Draft working group WG 3
16. FprEN 1992-1-1 (2025) Eurocode 2: design of concrete structures – Part 1–1: general rules – rules for buildings, bridges and civil engineering structures
17. Neves J, Fernandes de Almeida J (2005) Compressive behaviour of steel fibre reinforced concrete. Struct Concr
18. Ruiz G, De La Rosa Á, Wolf S, Poveda E (2018) Model for the compressive stress-strain relationship of steel fiber-reinforced concrete for non-linear structural analysis. Hormig. Acero 69(Suppl. 1)
19. De La Rosa Á, Ruiz G, Poveda E (2019) Study of the compression behavior of steel-fiber reinforced concrete by means of the response surface methodology. Appl Sci
20. Ruiz G, De La Rosa Á, Poveda E, Zanon R, Schäfer M, Wolf S (2023) Compressive behavior of steel-fiber reinforced concrete in annex L of new Eurocode 2. Hormig Acero

Analysis of Steel-Concrete Composite Spiral-Confined Slabs According to the Second-Generation Eurocodes

Irene Polesel, Marco Fasan, and Chiara Bedon(✉)

University of Trieste, 34127 Trieste, Italy
chiara.bedon@dia.units.it

Abstract. Joints and frames in steel-concrete composite systems represent complex mechanical assemblies that require specific calculation procedures to optimize their detailing and structural capacity, particularly under seismic loads. To this aim, simplified analytical component-based approaches can be used to account for the most relevant mechanisms and resistance/stiffness behaviors of individual members, as well as their mechanical interaction. In this paper, the performance of spiral-confined slabs is investigated analytically and numerically. The preliminary design of the load-bearing components is developed according to both the Italian design standard NTC2018 and the second-generation Eurocodes, to account for their effective contribution and interaction. More in detail, spiral-confined slabs are designed to improve the resisting mechanism 2 of steel-concrete composite systems. The analysis of preliminary analytical results is further extended by Finite Element (FE) numerical analyses developed in ABAQUS, to study the progressive evolution of resisting and damage mechanisms.

Keywords: Steel-concrete Joints · Confinement · Resisting Mechanisms · Numerical Analysis · Second-Generation Eurocodes

1 Introduction

The behavior of steel-concrete composite joints and frames represents a major challenge for designers, especially against seismic loads, due to the optimization need for multiple interconnected load-bearing components and associated resisting mechanisms [1].

In practice, the available design standards are based on the use of simplified analytical component-based models, which can be used to quantify the expected stiffness and resistance of the governing mechanisms [2]. These component-based models can be efficiently used to numerically investigate the performance of steel-concrete composite frames, where a multitude of equivalent springs can be possibly optimized [3].

However, these simplified modelling strategies are not able to capture the detailed response of interconnected load-bearing components, and the use of computationally expensive but more accurate refined 3D Finite Element (FE) numerical models can provide a robust support for understanding and improving the activation of resisting mechanisms and detailing of components [4, 5].

© The Author(s), under exclusive license to Springer Nature Switzerland AG 2026
R. Zanon et al. (Eds.): CTA 2026, LNCE 942, pp. 621–632, 2026.
https://doi.org/10.1007/978-3-032-39505-4_54

Regarding for example the so-called 'mechanism 2' of the slab in compression, it was shown in [6] that the use of confinement steel components (such as spirals) is efficient and promising, in terms of increase of overall resistance and ductility of the composite system. Besides, many other interaction phenomena should be considered to maximize the resisting mechanisms [4, 5]. Even more attention is required for the use and possible refinement of those component-based, simplified analytical strategies that are suggested by design standards, especially in consideration of possible updates [7, 8], as it is for the second-generation Eurocodes [9].

In this paper, following the past promising results reported in [6], the attention is focused on the analysis of spiral-confinement of steel-concrete composite slabs in compression. Through the parametric study, variations are made in terms of geometrical details, to further exploit the contribution of the load-bearing components and particularly the optimization of the mechanism 2 for the slab in compression. The herein reported study is carried out by taking into account preliminary analytical estimates based on the provisions of the Italian technical standard NTC2018 [10] and the second-generation Eurocode 2 (EC2 [11]). The analytical estimates are assessed more in detail by means of refined FE numerical models described in ABAQUS [12], to account for the progressive evolution of resisting and damage mechanisms.

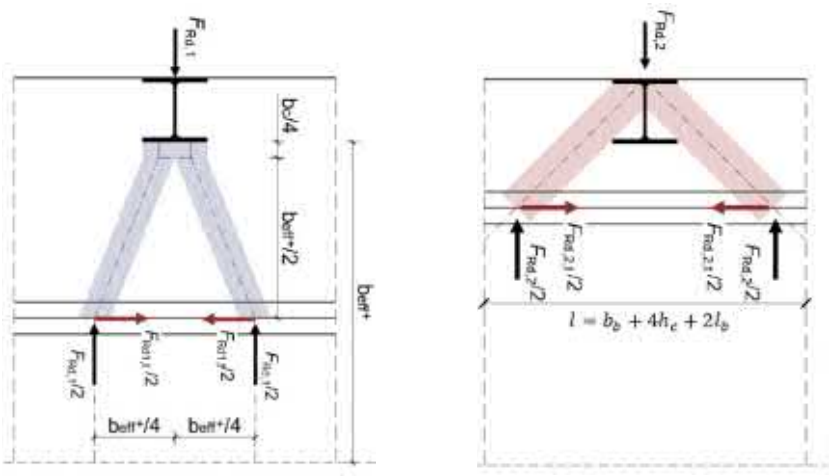
2 Parametric Study

2.1 Examined Configurations

The analytical and numerical study was carried out considering that for the slab under positive bending moment, the possible governing phenomena are associated to the ductile mechanism 1 of transversal rebars and the crushing of concrete in compression, for the mechanism 2 [1, 2], see Fig. 1. However, when the slab is fully isolated, the mechanism 1 vanishes and mechanism 2 governs the compressive response [5].

For the purpose of the present study, the reference system was schematized as reported in Fig. 2. It basically consisted of a HEB280 steel column and a concrete slab (C35/45 its resistance class) with 100 mm thickness, 1400 mm effective width and length. The transversal reinforcement was set in $A_{T1} = 2\Phi16$ and $A_{T2} = 3\Phi16$ (or $5\Phi16$) steel members (B450C type), centered respectively $L_{x1} = 770$ mm and $L_{x2} = 560$ mm apart from the column flange. Moreover, $A_L = (3 + 3)\Phi12$ steel members were used as longitudinal reinforcement.

Following [6], the confinement was obtained by means of Φ8 mm circular steel spirals (one ("1" in the following) or two ("2") respectively), with $D_0 = 70$ mm or 80 mm the diameter of the confined core, see Fig. 2a. Various struts inclinations β_2 were considered through the parametric study, starting from the layout of Fig. 2b and c. in particular, a 40 mm gap between the column and the slab was taken into account [5] to isolate the slab, as schematized in Fig. 2b, so as to better emphasize the contribution and the key influencing parameters for the mechanism 2 only.

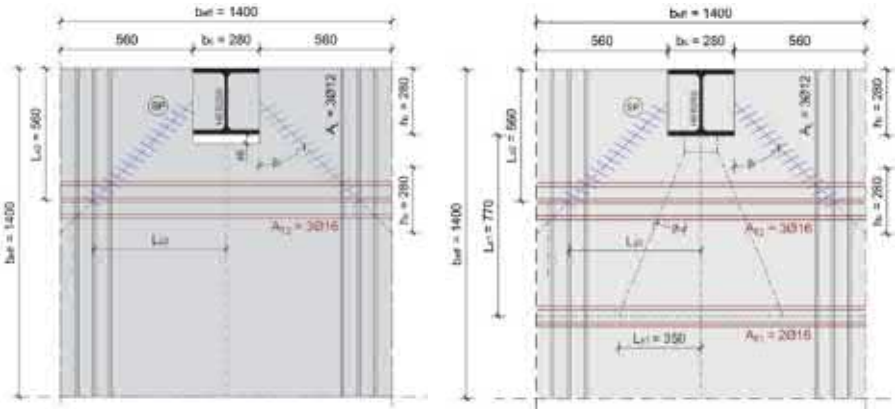


(a) (b)

Fig. 1. Schematic representation of (a) mechanism 1 and (b) mechanism 2 for the slab in compression (dimension in mm).



(a)



(b) (c)

Fig. 2. Nominal geometry and layout details of the examined slab for the compressive performance assessment: (a) setup with 1Φ8 steel spirals ($D_0 = 70$ mm and $D_0 = 80$ mm respectively); (b) slab configuration with mechanism 2 only and (c) slab configuration with both mechanisms 1 and 2 (dimension in mm).

2.2 Preliminary Analytical Estimates for the Mechanism 2

In general, the layout of confining spirals as in Fig. 2c should be designed to optimize the expected benefits for the concrete slab, in particular increasing the maximum resistance and the ultimate strain (i.e., ductility) of concrete, due to confinement.

Ideally, the smaller is the diameter D_0 of the spirals and the smaller is the confined concrete core, but the higher may be the associated lateral pressure. However, the overall resistance and ductility of mechanism 2 also depend on the area of the confined concrete core and on the spiral detailing. To maximize this effect, the layout of confining spirals is set to coincide with the concrete struts of mechanism 2 as in Fig. 2b. Behind that, based on Fig. 2a, the detailing of spirals can be improved in terms of diameter, length and step. Moreover, in consideration of the limited thickness of the slab, the number of spirals can be increased from 1 to 2. In any case, it is important to remind that there is a reciprocal interaction between spirals detailing, confined concrete core, struts inclination β_2, layout/amount of longitudinal rebars (A_L) and layout/amount of transversal rebars (A_{T2}). This aspect should be properly taken into account in design, considering that – depending on these details – the collapse of mechanism 2 can in fact be governed by concrete crushing or steel yielding.

In support of these considerations, an extensive parametric analytical study was carried out for the typical configuration schematized in Fig. 2b. In particular, the attention was focused on the effects due to:

- Variations in the struts inclination β_2, based on the layout of longitudinal rebars (A_L), for both unconfined and confined slabs, where:

$$\beta_2 = \arctan\left(\frac{L_{y2} - h_c/2}{L_{x2} - b_c/2}\right) \tag{1}$$

- Detailing of the confining spirals, by changing number of spirals, diameter, step, and diameter of the confined concrete core;
- And detailing of the associated transversal reinforcement (A_{T2}).

For the analytical comparisons herein reported, the material safety factors for steel and concrete were set equal to the unit.

Resistance. The analytically calculated resistance of the mechanism 2, $F_{Rd,2}$, is presented in Fig. 3 as a function of the strut inclination β_2 (ranging between 29.74° and 50.53°), as obtained with the analytical models provided by NTC2018 or EC2 standards.

Four different confined configurations are considered in Fig. 3, and compared towards the unconfined "NC" configuration, which was used as a benchmark only. In particular, the reported scenarios are designed to include one ("1") or two ("2") steel spirals. Also, according to Fig. 2a, two different diameters of the confined concrete core are taken into account, namely $D_0 = 70$ mm ("70") or $D_0 = 80$ mm ("80").

For the NC configurations, the analytical results of Fig. 3a and b diverge for most of the inclination values β_2. The reason is represented by the resistance contribution of the slab, which follows two different formulations to take into account the contribution of struts. In particular, the NTC2018 assumes that the compressive design strength of

concrete struts is given by:

$$f_{cd,NTC2018} = \alpha\ \nu\ f_{cd} = 0.6\left(1 - \frac{f_{ck}}{250}\right) f_{cd} \tag{2}$$

while the EC2 specifies that:

$$f_{cd,EC2} = \nu' f_{cd} \tag{3}$$

with:

$$\nu' = f(\beta_2) \tag{4}$$

For the same reason, the two analytical models are again aligned for high β_2 values, when the steel yielding prevails in the mechanism 2.

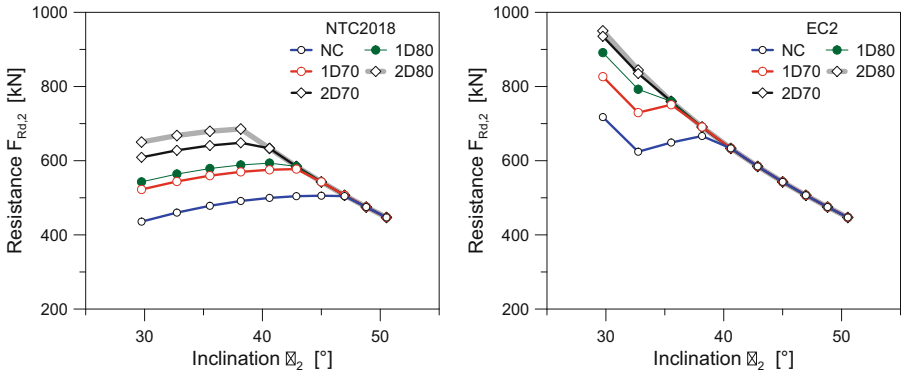


Fig. 3. Variation of the resistance of mechanism 2 ($F_{Rd,2}$) as a function of the strut inclination β_2, for various spiral arrangements, as obtained according to (a) NTC2018 and to (b) the second-generation EC2 ($A_{T2} = 5\Phi16$ the transversal reinforcement).

Regarding the confined slab configurations in Fig. 3, it is possible to see a marked increase in the analytically calculated resistance values $F_{Rd,2}$, especially when compared to the NC system. Such an effect primarily derives from the optimal arrangement and layout design of the confining spirals, as well as from the sensitivity of this contribution to β_2. As it can be seen from Fig. 3a and b, especially for small strut inclinations β_2, the analytical model proposed by the second-generation EC2 predicts resistance values $F_{Rd,2}$ up to approximately 65% higher than those obtained according to the NTC2018 approach.

The NTC2018 and EC2 analytical formulations predict indeed to the same resistance values for all those spiral-confined scenarios associated to a ductile mechanism. As such, as the strut inclination β_2 further increases, the confinement effect and benefit vanish, and the predicted resistance values are insensitive to the confinement arrangement and design.

Yielding and Ultimate Displacements. Displacement amplitudes at yielding and failure were analytically derived from the stiffness calculations for the mechanism 2 ($k_{c,2}$), see [5, 6]. In particular, Fig. 4 shows the evolution of the yielding displacement $u_{y,2}$, as a function of the strut inclination β_2.

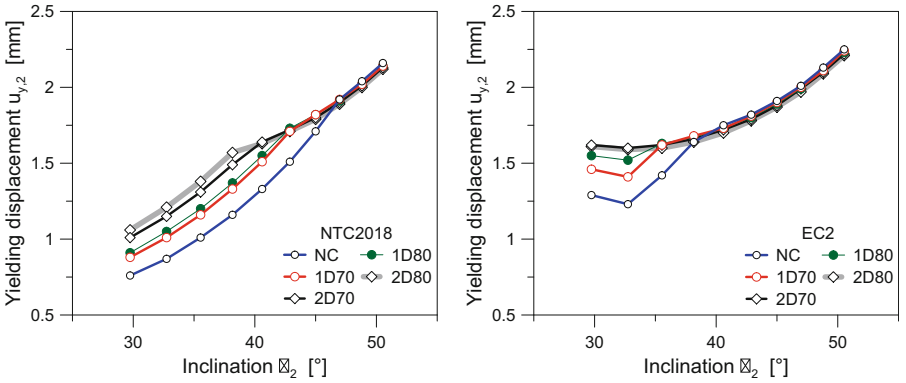


Fig. 4. Variation of the yielding displacement of mechanism 2 ($u_{y,2}$) as a function of the strut inclination β_2, for various spiral arrangements, according to (a) NTC2018 and to (b) the second-generation EC2 ($A_{T2} = 5\Phi16$ the transversal reinforcement).

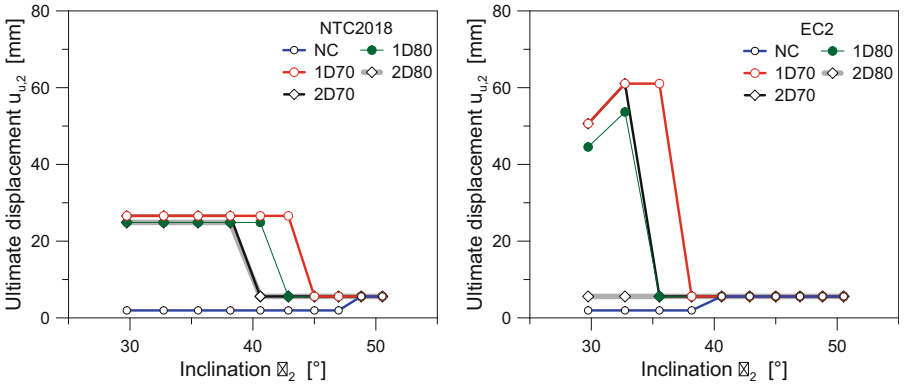


Fig. 5. Variation of the ultimate displacement of mechanism 2 ($u_{u,2}$) as a function of the strut inclination β_2, for various spiral arrangements, according to (a) NTC2018 and to (b) the second-generation EC2 ($A_{T2} = 5\Phi16$ the transversal reinforcement).

Basically, $u_{y,2}$ linearly increases with β_2, and minor effects are observed in correlation with the confinement detailing. The trends of Fig. 4 can be indeed more efficiently commented in combination with Fig. 5, which illustrates the corresponding ultimate

displacements $u_{u,2}$. For this study, the calculations were carried out assuming an ultimate steel strain equal to $\varepsilon_{su} = 1\%$. As it can be seen from Fig. 5, the analytical trends show a clear variation in the predicted $u_{u,2}$ values, depending on the governing collapse mechanism (i.e., confined or unconfined slab). For the NC system, the transition from a concrete-governed to a steel-governed collapse mechanism is associated to an increase in the ultimate displacement $u_{u,2}$, which is characterized by higher ductility. Conversely, for all the examined confined configurations, the concrete-governed mechanism can achieve some ductility thanks to the increase of the ultimate compressive strain of the confined concrete, ε_{cu}. For this reason, the transition to a steel-governed collapse mechanism leads to a reduction in the associated ultimate displacement $u_{u,2}$.

3 Numerical Analysis

3.1 Modelling

The modelling strategy proposed in [6] was used to study the selected configurations, by taking advantage of the past validation and simulation experience.

A set of quasi-static, displacement-controlled, monotonic analyses was performed in ABAQUS/Explicit, to assess the local and global resisting and damage mechanisms of spiral-confined slabs in compression. Model features and calibration parameters were defined in accordance with [6]. The maximum imposed displacement of the assembled model shown in Fig. 6 was set in $u = 4.5$ mm, to ensure the activation of mechanism 2.

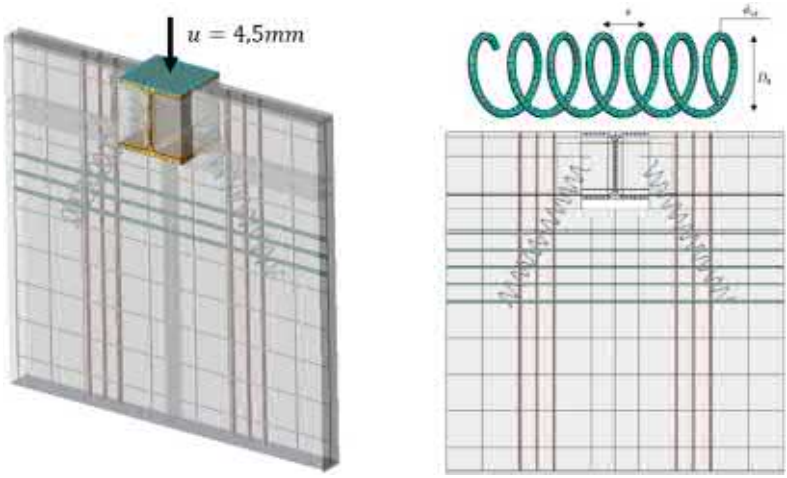


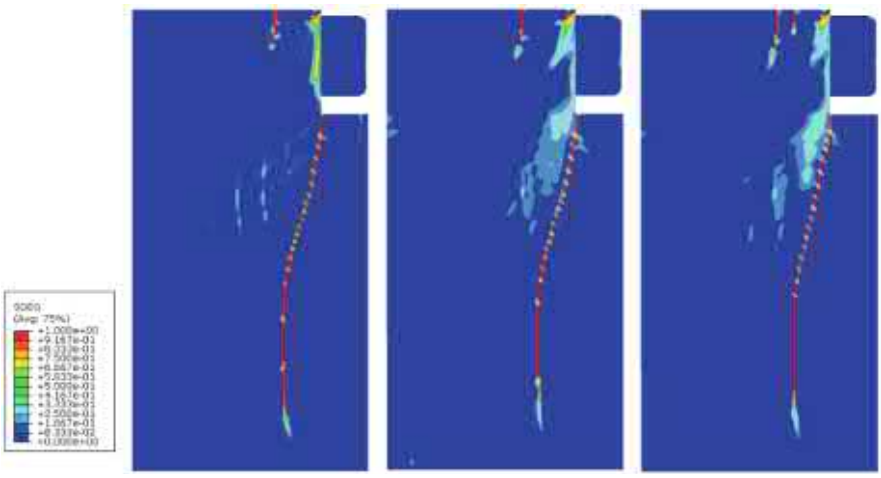
Fig. 6. Typical FE model for the analysis of spiral-confined slabs in compression (ABAQUS).

3.2 Qualitative Damage Evolution

Among the numerically examined configurations, the load-bearing performance of the compressed confined slabs looked severely affected by the propagation of cracks in

concrete, in combination with high tensile stress peaks in the transversal rebars, and followed by (for some configurations only) yielding of the steel rebars. In particular, the first cracks in the concrete slab were observed to initiate prematurely, i.e. at about ≈0.6 mm of imposed vertical displacement.

In this sense, no marked variations were numerically captured in terms of displacement amplitude for the concrete fracture initiation, by changing the confinement arrangement. On the other side, the positive contribution of the steel confining components was more emphasized when increasing further the imposed displacement amplitude. Figure 7, in this regard, shows the non-dimensional SDEG parameter in the slab (SDEG = 0 for undamaged concrete and SDEG = 1 for fully degraded concrete), at a vertical displacement of 2.7 mm (i.e., ≈4.5 times the yielding displacement), by comparing three different configurations. In all of them, the spiral inclination was set in $\beta_2 = 30°$, with 5Φ16 the amount of transversal reinforcement, and $D_0 = 70$ mm for the Φ8 spirals (1 or 2). From the left to the right, it can be seen that compared to the NC system without confinement (Fig. 7a), the presence of 1 (Fig. 7b) or 2 (Fig. 7c) spirals can progressively reduce and delay crack propagation in the slab, postponing the damage evolution in concrete.



(a) NC-30-5Φ16 (b) 1D70-30-5Φ16 (c) 2D70-30-5Φ16

Fig. 7. Comparison of the SDEG parameter in the (a) unconfined (NC) or (b)-(c) spiral-confined concrete slabs ($D_0 = 70$ mm, $\beta_2 = 30°$, $A_{T2} = 5\Phi16$), for a vertical imposed displacement of 2.7 mm, as obtained from a selection of examined configurations (ABAQUS). The mesh pattern and steel column are hidden from the contour plots.

4 Analysis of Analytical and Numerical Results

4.1 Load-Displacement Trends

The numerical analysis helped to investigate more in detail the evolution of the governing resisting mechanisms, as well as to assess the accuracy and potential of the simplified analytical estimates. A typical comparative example is shown in Fig. 8 for slab specimens with 2 steel spirals, with $\beta_2 = 30°$ and $A_{T2} = 5\Phi16$ transversal reinforcement.

Variations are proposed in terms of diameter of the confined core, with $D_0 = 70$ mm (Fig. 8a) and $D_0 = 80$ mm (Fig. 8b). The configuration with $D_0 = 70$ mm, in particular, corresponds to the concrete damage evolution presented in Fig. 7c.

For the system of Fig. 8a, it can be seen that the analytical estimates according to NTC2018 and EC2are closely aligned with each other in terms of initial stiffness. However, a major scatter can be seen in terms of predicted resistance values. The analytical calculations based on EC2, in particular, match rather well the results of the FE numerical analysis. Behind that, the numerical initial stiffness of the system diverges from and underestimates both the NTC2018 and EC2 analytical results. This outcome reminds that the load-bearing response of the examined systems is affected by many influencing parameters and interconnected phenomena that should be further explored in detail.

In Fig. 8b, the analytical and numerical results are compared after increasing the diameter of the confined core to $D_0 = 80$ mm, and keeping fix the other input features. Also in this case, it is possible to see that the analytical estimates based on EC2 are still rather well aligned with the estimates from the FE numerical analysis. An improved correlation can be observed also in terms of initial stiffness. On the other side, a major scatter arises for the comparison of the FE numerical results with the analytical estimates based on NTC2018, both in terms of predicted initial stiffness and maximum resistance of the system. In both Fig. 8a and b, the NTC2018 estimates largely underestimate the expected load-displacement compressive performance of the examined systems, which are indeed well captured by EC2 estimates.

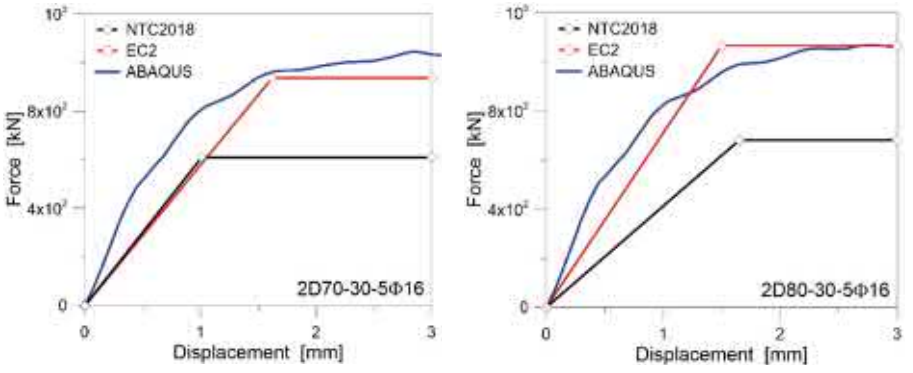


Fig. 8. Selection of load-displacement results for spiral-confined slabs in compression (2 steel spirals, with $\beta_2 = 30°$ and $A_{T2} = 5\Phi16$ transversal rebars): (a) $D_0 = 70$ mm and (b) $D_0 = 80$ mm (ABAQUS).

4.2 Transversal Steel Reinforcement

When the composite confined-slab is subjected to compression, the load-bearing components are required to balance the propagation of possible damage mechanisms. This is the case of the transversal reinforcement, A_{T2}, which is directly affected by the opening of cracks in the slab.

Based on the parametric numerical analysis, the stress evolution in steel reinforcement was separately investigated, as a function of the imposed vertical displacement. In this regard, it is important to remind that both the NTC2018 and EC2 analytical estimates (for most of the examined configurations) were found governed by concrete crushing, and an associated elastic response was always predicted for the transversal rebars. In this sense, the FE numerical models were used to help capturing more in detail such complex interconnected and progressive damage mechanisms. Interestingly, also in the numerical models the steel rebars were found to behave elastically, for most of (not all) the examined scenarios, which is an outcome in good agreement with the NTC2018 and EC2 analytical observations. However, it is important to highlight that high stress peaks were generally predicted in the transversal reinforcement at relatively small amplitudes of imposed vertical displacement. Also, these stress peaks were mostly located in the region of concrete cracks (i.e., Fig. 7).

Considering that cracks in concrete were numerically observed for an average vertical displacement of ≈0.6 mm, the corresponding stress peaks in the steel rebars were measured in about ≈150 MPa. After concrete cracking, the stress peaks in the reinforcement linearly increased with the imposed vertical displacement. Moreover, for few configurations only (i.e., the 1D70 and 2D80 systems), premature steel yielding was also numerically predicted at about ≈2.2 mm and ≈3.1 mm of imposed displacement, respectively. Certainly, a direct correlation of such a kind of stress estimates and the propagation of cracks in the concrete slab should be associated to local numerical effects. In any case, these outcomes suggest a general good correlation with the simplified analytical estimates (especially the EC2 ones), but also enforces the need of additional studies for robust validation and design optimization purposes.

5 Conclusions

The design of steel-concrete composite joints and frames is notoriously challenging, especially against seismic loads.

In this paper, the attention was primarily focused on the possible contribution of steel confining spirals for the improvement of the mechanism 2 of the compressed concrete slab, which can be maximized especially under positive bending moment.

The parametric analysis was carried out on a selection of geometrical configurations of technical interest, by taking into account the Italian technical standard (NTC2018) and the second-generation Eurocode 2 (EC2) for the detailing of the concrete confinement. In parallel, a more detailed FE numerical study was carried out for selected scenarios, in order to obtain a more detailed view of the interconnected resisting and damage mechanisms for the slab in compression.

In general, a rather good match was obtained for several geometrical configurations, when considering the load-displacement response predicted by the analytical model of

EC2 and the results from the more refined FE analysis. The best match was obtained in presence of $\beta_2 \approx 30°$ inclined steel spirals, both in terms of initial stiffness and overall resistance. A major scatter was indeed found for the analytical predictions based on the NTC2018 provisions, compared to EC2 estimates and numerical results.

Among the examined scenarios, the numerical models showed a rather premature crack initiation in the slab (i.e., at about ≈0.6 mm of imposed displacement). Behind that, the positive contribution of the confining spirals was emphasized especially in terms of postponed crack propagation, for higher displacement amplitudes. The stress peak trends in the transversal rebars, as a direct effect of the crack propagation in the slab, also showed a consistent trend between the numerical and the analytical estimates, for most of the examined scenarios. Besides, large discrepancies were also obtained for a few of the investigated configurations, and more extended studies are hence required.

Acknowledgements. DPC-ReLUIS is gratefully acknowledged for providing financial support.

References

1. Amadio C, Fasan M, Pecce MR, Logorano G (2018) The guidelines for the design of steel-concrete composite moment resisting frames in seismic areas. In: Landolfo R, Zandonini R (eds) Steel and steel-concrete composite structures in seismic area: advances in research and design. The research project RP3 of the ReLUIS-DPC 2014–2018, pp 211–244. ISBN 978–88–89972-74-8. https://arts.units.it/retrieve/e2913fdd-704d-f688-e053-3705fe0a67e0/chapter.pdf. Accessed 31 May 2026
2. Fasan M, Bedon C, Amadio C, Pecce MR (2024) Non-linear component-based modelling strategy for beam-to-column steel-concrete composite joints under seismic loads. J Constr Steel Res 212:108314
3. Fasan M, Bedon C, Pecce MR (2024) Optimised rotational-spring component-based modelling strategy for seismic resistant steel-concrete composite joints and frames with continuous or isolated slab. Structure 70:107689
4. Amadio C, Bedon C, Fasan M, Pecce MR (2017) Refined numerical modelling for the structural assessment of steel-concrete composite beam-to-column joints under seismic loads. Eng Struct 138:394–409
5. Amadio C, Bedon C, Fasan M (2017) Numerical assessment of slab-interaction effects on the behaviour of steel-concrete composite joints. J Constr Steel Res 139:397–410
6. Fasan M, Bedon C, Troiano N, Amadio C (2022) Improving the seismic capacity of steel–concrete composite frames with spiral-confined slabs. Adv Struct Eng 25(9):1972–1987
7. Seyoum Lemma M, Rebelo C, Simões da Silva L (2022) Eurocode 8 revision – implications on the design and performance of steel moment-resisting frames: case study. Soil Dyn Earthq Eng 161:107411
8. Landolfo R, Fiorino L (2023) Second generation of Eurocode 8: seismic design rules for cold-formed steel buildings. In: Eurosteel 2023, vol 6. https://doi.org/10.1002/cepa.2682
9. Polo Lopez CS, Sciarretta F, Athanasopoulou A, Tsionis G, Denton S et al (2025) The second-generation Eurocodes: key changes and benefits through design examples - technical contributions from the online workshop, 3-5 June 2025. In: Polo Lopez CS, Sciarretta F (eds) . Publications Office of the European Union, Luxembourg. https://data.europa.eu/doi/10.2760/3056713, JRC144386
10. Ministerial Decree of 17 January 2018 – Updating of the technical standards for construction (NTC 2018). Published in the Italian Official Gazette No. 42 of 20 February 2018

11. EN 1992-1-1:2023 (2023) Eurocode 2 — design of concrete structures — Part 1–1: general rules and rules for buildings, bridges and civil engineering structures. CEN, Brussels, Belgium
12. Simulia ABAQUS Computer Software and Online Documentation, version 2025; Dassault Systems: Johnston, RI, USA

Seismic Design and Retrofitting

Design of Steel Moment Resisting Frames with Predetermined Collapse Mechanism

Bruna Barbieri[1], Maria Maglio[1](✉), Rosario Montuori[2], Elide Nastri[1], and Vincenzo Piluso[1]

[1] Department of Civil Engineering, University of Salerno, Fisciano, Italy
mamaglio@unisa.it
[2] Department of Pharmacy, University of Salerno, Fisciano, Italy

Abstract. The Theory of Plastic Mechanism Control (TPMC) is a seismic design methodology for steel structures developed to ensure the formation of a global collapse mechanism in highly ductile moment-resisting frames. The recent evolution of Eurocode 8 introduces different ductility classes associated with distinct seismic performance objectives that do not always require the development of a global mechanism. To address this requirement, a novel TPMC-based design methodology in the α–θ plane has been developed for steel moment-resisting frames, enabling the achievement of a prescribed collapse mechanism involving a predefined number of storeys. Its effectiveness was evaluated through comparisons of equilibrium curves in the α–θ plane, nonlinear pushover analyses, and Incremental Dynamic Analyses (IDA). The results demonstrate that the proposed design approach successfully achieves the target collapse mechanism while preventing the activation of undesired mechanisms involving fewer storeys than prescribed.

Keywords: Steel Structures · Collapse Mechanisms · Seismic Design · Ductility Classes

1 Introduction

The Theory of Plastic Mechanism Control (TPMC) represents an advanced approach to the seismic design of steel structures. This theory extends the kinematic theorem of plastic collapse through the introduction of mechanism equilibrium curves, providing a basis for controlling structural collapse mechanisms [1, 2]. Originally developed in the α–δ plane, TPMC has recently been reformulated in the α–θ plane to improve structural optimization [3]. More recently, TPMC has also been extended to probabilistic performance-based design methodologies for steel moment-resisting frames equipped with innovative dissipative connections, demonstrating its flexibility and applicability to advanced seismic design procedures [4].

According to the latest provisions of Eurocode 8, three ductility classes are defined, each corresponding to a different level of seismic performance [5, 6]. Specifically, structures designed for high ductility (DC3) are required to develop a global collapse mechanism, whereas those belonging to the medium- and low-ductility classes (DC2 and DC1)

© The Author(s), under exclusive license to Springer Nature Switzerland AG 2026
R. Zanon et al. (Eds.): CTA 2026, LNCE 942, pp. 635–645, 2026.
https://doi.org/10.1007/978-3-032-39505-4_55

are permitted to exhibit partial collapse mechanisms [7, 8]. In this framework, this paper proposes a new design method for steel moment-resisting frames based on TPMC in the α–θ plane, specifically aimed at obtaining a predetermined collapse mechanism. The proposed approach introduces the concept of a target storey, enabling direct control of the portion of the structure involved in plasticization at the ultimate limit state. The methodology was applied to six-storey steel moment-resisting frames with a variable number of bays and compared with the conventional TPMC approach designed to achieve a global collapse mechanism. Nonlinear analyses were performed to evaluate the effectiveness of the proposed design procedure. The results confirmed its ability to consistently achieve the intended collapse mechanism, thereby demonstrating the reliability of the adopted methodology.

2 The Theory of Plastic Mechanism Control (TPMC)

The achievement of a controlled collapse mechanism is essential in seismic design because it enhances the overall ductility and energy dissipation capacity of the structure, while minimizing damage concentration in the columns. Structures developing soft-storey or partial collapse mechanisms cannot fully exploit their plastic deformation capacity (Fig. 1)b, c and d. Consequently, the intended seismic performance is achieved through the development of a global collapse mechanism (Fig. 1)a, characterized by the formation of plastic hinges at the beam ends and at the bases of the first-storey columns.

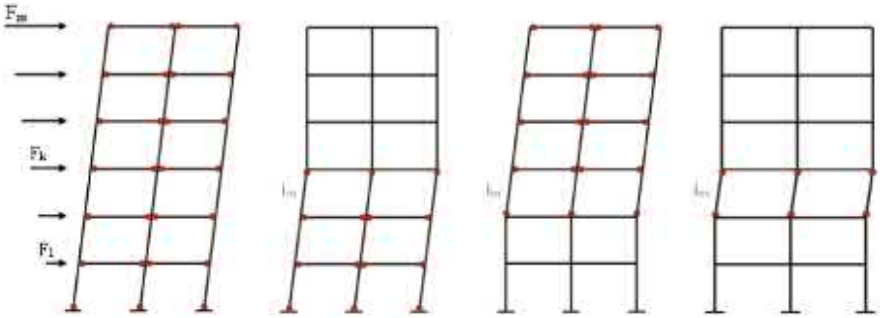


Fig. 1. Global mechanism (a), type 1 (b), type 2 (c) and type 3-mechanism (d)

Introduced by Mazzolani and Piluso in 1997 [1], the Theory of Plastic Mechanism Control (TPMC) was conceived to establish a rigorous seismic design procedure capable of guaranteeing the development of the desired global collapse mechanism. The initial formulation relied on an iterative design procedure, limiting its practical application. A significant advancement was achieved in 2015 [2], when the method was reformulated in closed form, extending its applicability to both steel and reinforced concrete structures. The design procedure compares the equilibrium curves of all admissible collapse mechanisms in the α–δ plane, where α is the seismic load multiplier and δ corresponds to the

horizontal displacement at the top of the structure. The achievement of the global mechanism is guaranteed by imposing that its equilibrium curve remains lower than those associated with all alternative mechanisms up to the ultimate displacement allowed by the local ductility capacity of the structural members, as illustrated in Fig. 2a.

More recently, Montuori et al. (2022) reformulated the TPMC by expressing the equilibrium conditions in the α–θ plane [3], where θ represents the plastic rotation of the first-storey columns instead of the top displacement. In this formulation, the mechanism equilibrium curve assumes the linear form:

$$\alpha = \alpha_0 - \psi\theta \tag{1}$$

where α_0 is the first-order collapse multiplier and ψ represents the slope of the equilibrium curve. The α–θ formulation provides an equivalent but more compact representation of the TPMC design conditions (Fig. 2b) while preserving the theoretical basis of the method.

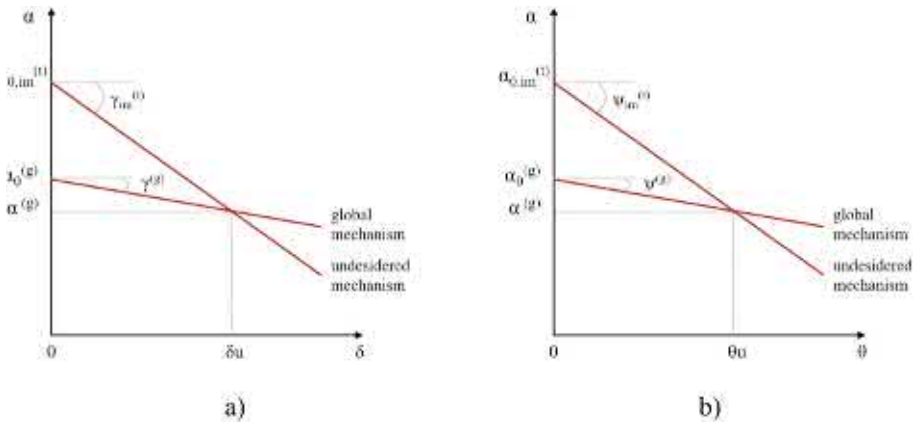


Fig. 2. Design requirements for the activation of the global mechanism represented in the α–δ (a) and α–θ (b) planes

3 Targeted Collapse Mechanism Design Approach

The proposed procedure is developed through an extension of the design principles adopted in the TPMC(θ) approach [3]. Its objective is to provide an intermediate design solution between the two limiting collapse configurations: the global collapse mechanism, which is generally pursued for highly ductile structures, and the undesirable soft-storey mechanism, which must be prevented. Specifically, the proposed procedure enables the designer to predetermine the extent of the structural height involved in the plastic collapse by specifying the number of storeys, t_g, participating in the collapse mechanism. Accordingly, two collapse configurations can be considered: type 1, characterized by a mechanism developing at the tg-th storey (Fig. 3a), and type 2, characterized by a mechanism developing at the $(n_s - t_g)$-th storey (Fig. 3b).

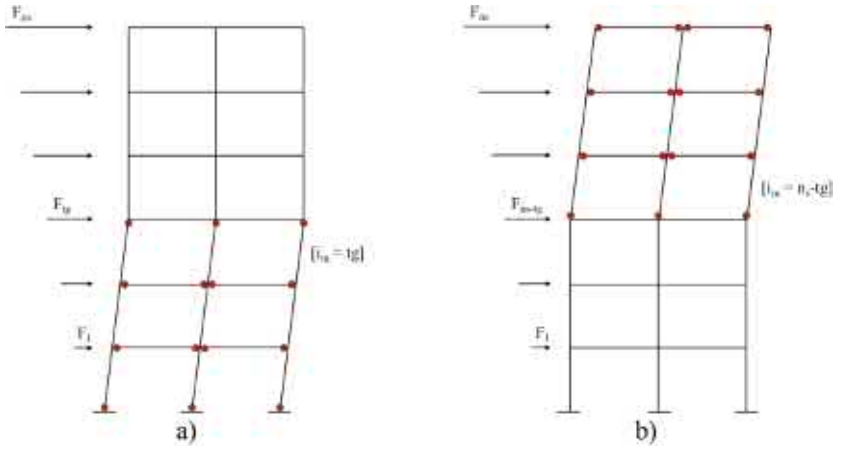


Fig. 3. Admissible collapse mechanisms involving t_g storeys adopted in the proposed design methodology: type 1 mechanism (a), type 2 mechanism (b)

Previous studies have shown that imposing the type 2 collapse mechanism as a target is not cost-effective [9] (Fig. 4). Therefore, the proposed methodology is developed by selecting the type 1 collapse mechanism as the target mechanism for design purposes. In accordance with the kinematic theorem of plastic collapse, the occurrence of a type 1 mechanism at the t_g-th storey is ensured when its equilibrium curve lies below those corresponding to the type 3 mechanism at all storeys, over the entire admissible rotation domain $0 \leq \theta \leq \theta_u$.

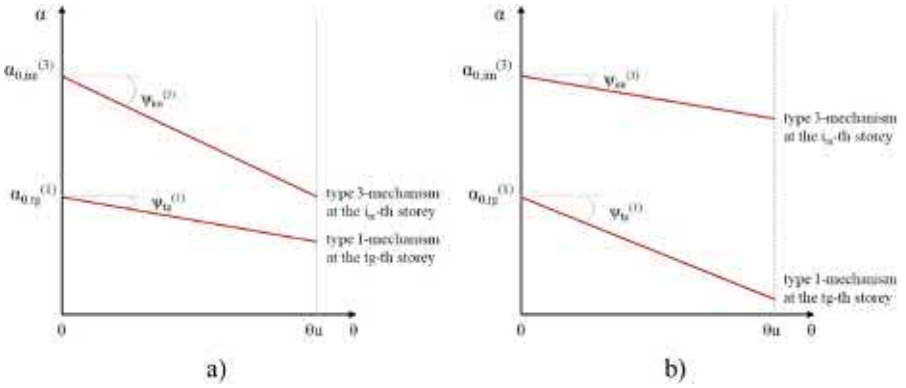


Fig. 4. Graphical representation of the conditions required to avoid the type 3 mechanism

The design requirements can be expressed mathematically in terms of the equilibrium curves of the considered mechanisms, as reported below:

$$\begin{cases} \alpha_{0,tg}{}^{(1)} - \psi_{tg}{}^{(1)} * \theta \leq \alpha_{0,tg}{}^{(3)} - \psi_{tg}{}^{(3)} * \theta \\ \alpha_{0,tg}{}^{(1)} - \psi_{tg}{}^{(1)} * \theta \leq \alpha_{0,1}{}^{(3)} - \psi_{1}{}^{(3)} * \theta \end{cases} \tag{2}$$

4 Design Applications

The applicability of the proposed design methodology for controlling the target collapse mechanism is examined through a case study involving six-storey steel moment-resisting frames. The structures considered are characterized by a storey height of 3.50 m and by a variable number of bays, from three to six, with a uniform bay span of 5.00 m. The analysed frames are composed of HE column sections and IPE beam sections made of S355 steel ($f_{yk} = 355$ N/mm^2). The applied gravity loads consist of a permanent distributed load $G_k = 22.50$ kN/m and a live distributed load $Q_k = 10.00$ kN/m, combined according to the seismic load combination to obtain the design load q_d. The seismic action is represented by a triangular distribution of horizontal forces, starting from 10 kN at the first storey and linearly increasing along the frame height. The ultimate rotation threshold considered in the design procedure is defined as $\theta_u = 0.04$ rad, representing the rotation capacity associated with the ductility requirements of the structural members. Beam design is carried out considering the ultimate limit state load combination, which leads to the selection of an IPE 330 section, with a corresponding bending resistance of $M_{b.\,Rd} = 285.53\ kNm$. The design is described only for the case of a four-storeys target mechanism with the aim of promoting plasticization involving at least four storeys. To satisfy the design objective, the equilibrium curve corresponding to the type 1 mechanism at the fourth storey is required to remain below the curves of the undesired type 3 mechanisms at the first and fourth storeys, as shown in (Fig. 6)a and b. The structural parameters required for the formulation of the design conditions are initially established, including storey elevations, seismic force distribution, and vertical loads. Once these quantities are defined, the slopes of the equilibrium curves associated with the possible collapse mechanisms can be derived (Tables 1 and 2).

Table 1. Structural parameters adopted for the design procedure

n. storeys	h_{int}	h_k	F_k	$F_k\ h_k$	V_k	$V_k\ h_k$
(−)	(m)	(m)	(kN)	(kNm)	(kN)	(kNm)
1	3.50	3.50	10.00	35.00	765.00	2677.50
2	3.50	7.00	20.00	140.00	765.00	5355.00
3	3.50	10.50	30.00	315.00	765.00	8032.50
4	3.50	14.00	40.00	560.00	765.00	10710.00
5	3.50	17.50	50.00	875.00	765.00	13387.50
6	3.50	21.00	60.00	1260.00	765.00	16065.00

The summation of the plastic moment capacities required at the first and fourth storeys is subsequently obtained as follows:

$$\sum_{i=1}^{nc} M_{c,i1} = 2081.19\ \text{kNm} \tag{3}$$

$$\sum_{i=1}^{nc} M_{c,i4} = 1452.45\ \text{kNm} \tag{4}$$

Table 2. Evaluation of the equilibrium curve slopes

n. storeys	ψ_{im} (1)	ψ_{im} (2)	ψ_{im} (3)
(−)	(m^{-1})	(m^{-1})	(m^{-1})
1	21.86	17.65	21.86
2	20.52	16.39	19.13
3	19.45	15.30	17.00
4	18.61	14.34	15.30
5	18.00	13.50	13.91
6	17.65	12.75	12.75

Subsequently, the design procedure is applied to the first and fourth storeys (Tables 3 and 4).

Table 3. Design of the first-storey columns

Col.	Q	N_b	N_{tot}	$M_{req.c.i.1}$	$W_{pl.req}$	Section
(−)	(kN)	(kN)	(kN)	(kN m)	(cm^3)	(−)
1	382.50	746.77	364.27	297.31	837.50	HE 240 B
2	765.00	0.00	765.00	297.31	837.50	HE 260 B
3	765.00	0.00	765.00	297.31	837.50	HE 260 B
4	765.00	0.00	765.00	297.31	837.50	HE 260 B
5	765.00	0.00	765.00	297.31	837.50	HE 260 B
6	765.00	0.00	765.00	297.31	837.50	HE 260 B
7	382.50	746.77	1129.27	297.31	837.50	HE 240 B

The design procedure leads to effective total column plastic moment values of $\sum_{i=1}^{nc} M_{c,i1}{}^* = 3021.87$ kNm and $\sum_{i=1}^{nc} M_{c,i4}{}^* = 1596.61$ kNm for the first and fourth storeys, respectively. These values are then used to derive the required moment demands for the design of the remaining storeys, to prevent collapse mechanisms involving fewer than four storeys (Table 5).

Figure 5 shows the collapse mechanism developed as a result of a pushover analysis performed with SAP 2000 software [10]. It is possible to note that the developed collapse mechanism is consistent with the design conditions imposed.

Table 4. Design of the fourth-storey (target) columns

Col.	Q	N_b	N_{tot}	$M_{req.c.i.1}$	$W_{pl.req}$	Section
(−)	(kN)	(kN)	(kN)	(kN m)	(cm^3)	(−)
1	191.25	368.71	177.46	207.49	584.49	HE 200 B
2	382.50	0.00	382.50	207.49	584.49	HE 200 B
3	382.50	0.00	382.50	207.49	584.49	HE 200 B
4	382.50	0.00	382.50	207.49	584.49	HE 200 B
5	382.50	0.00	382.50	207.49	584.49	HE 200 B
6	382.50	0.00	382.50	207.49	584.49	HE 200 B
7	191.25	368.71	559.96	207.49	584.49	HE 200 B

Table 5. Columns at the remaining storeys

Storey	Exterior columns	Interior columns
2	HE240	HE240
3	HE240	HE240
5	HE180	HE260
6	HE160	HE260

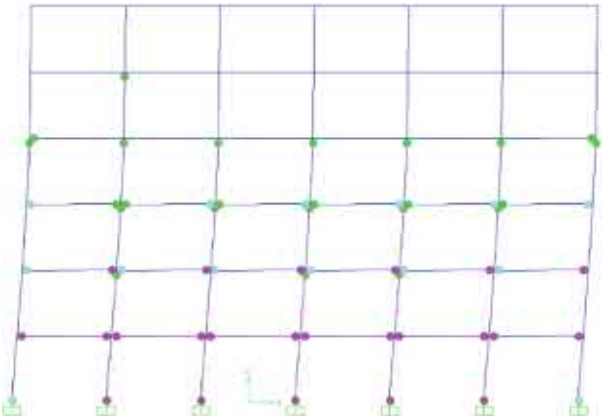


Fig. 5. Hinge pattern for the four-storeys target mechanism

5 Seismic Performance Evaluation

To evaluate the seismic performance, Incremental Dynamic Analyses (IDA) [11] were carried out using the SAP2000 software package [10] and a set of ten natural ground-motion records. The earthquakes were selected to be representative of the seismic hazard

at the reference site and subsequently scaled so that the mean response spectrum of the record set matched the elastic design spectrum corresponding to the Significant Damage (SD) limit state for a Class B subsoil at the Italian site of Reggio Calabria, as shown in Fig. 6.

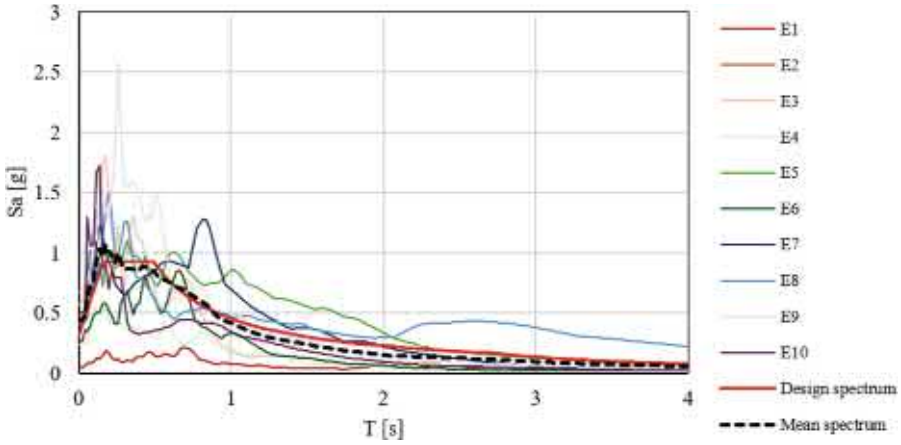


Fig. 6. Selected ground-motion spectra, mean response spectrum, and target spectrum.

For each nonlinear dynamic analysis, the maximum inter-storey drift ratio (MIDR) was computed as the maximum relative lateral displacement between two consecutive storeys divided by the corresponding storey height, considering the entire structural response. The IDA results obtained for the six-bay frame designed to develop a four-storeys target collapse mechanism were then expressed in terms of MIDR versus both peak ground acceleration (PGA) and spectral acceleration at the fundamental period, S_a, this generating the corresponding IDA curves. To facilitate the comparison of the structural response, the PGA and S_a values corresponding to predefined MIDR levels (0.01, 0.02, 0.03, 0.04, and 0.05) were determined by linear interpolation of the individual IDA curves. Finally, the interpolated values were averaged over the ten ground motions to obtain the mean IDA curve, which was adopted as representative of the overall seismic performance of the structure (Figs. 7 and 8).

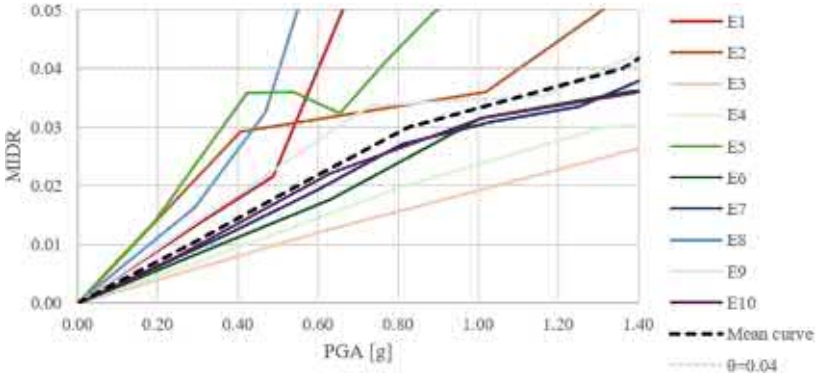


Fig. 7. IDA curves expressed in terms of MIDR versus peak ground acceleration

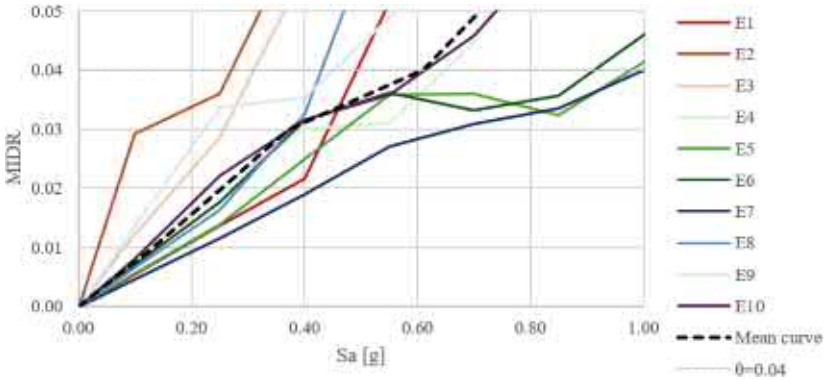


Fig. 8. IDA curves expressed in terms of MIDR versus spectral acceleration

6 Conclusions

In this study, a new design methodology is developed for steel moment-resisting frames to achieve a predetermined collapse mechanism. The proposed procedure allows the minimum number of storeys participating in the plastic collapse mechanism to be defined during the design phase. Consequently, it provides an intermediate design solution between the conventional requirement of a global collapse mechanism for high-ductility structures and the need to prevent undesirable soft-storey mechanisms. The reliability of the proposed methodology was confirmed through equilibrium curve assessments and nonlinear pushover analyses. The numerical results obtained for all case studies confirmed that the proposed methodology reliably achieves the predefined collapse mechanism, ensuring an appropriate control of plastic hinge development throughout the structure. The comparison with frames designed according to the standard TPMC procedure shows that controlling the collapse mechanism location allows for a reduction in structural weight compared with the conventional global mechanism requirement (Fig. 9).



Fig. 9. Comparison of the structural weight resulting from the different collapse mechanism

The seismic response of the designed frames was evaluated through Incremental Dynamic Analyses (IDA) [11]. The comparison was performed by considering the PGA and S_a values associated with the attainment of a MIDR equal to 0.04, as reported in Fig. 10. As expected, the frame designed according to the conventional TPMC(θ), aimed at developing a global collapse mechanism, exhibited the highest seismic capacity. Among the frames designed according to a partial mechanism, the frame with Target 4 shows the best seismic performance. However, all investigated frames achieve the intended collapse mechanism, consistently with the imposed design requirements.

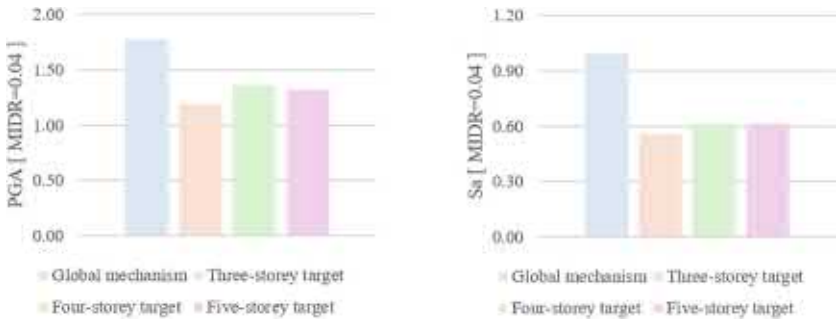


Fig. 10. Comparison of the seismic performance

By normalizing the PGA and S_a values by the corresponding structural weight, the seismic efficiency of the frames designed according to the different target collapse mechanisms can be compared. The results indicate that, in terms of PGA-to-weight ratio, the frame designed to develop a four-storeys target collapse mechanism exhibits the best performance. Conversely, when the S_a-to-weight ratio is considered, the frame designed to develop a global collapse mechanism provides the highest seismic performance (Fig. 11).

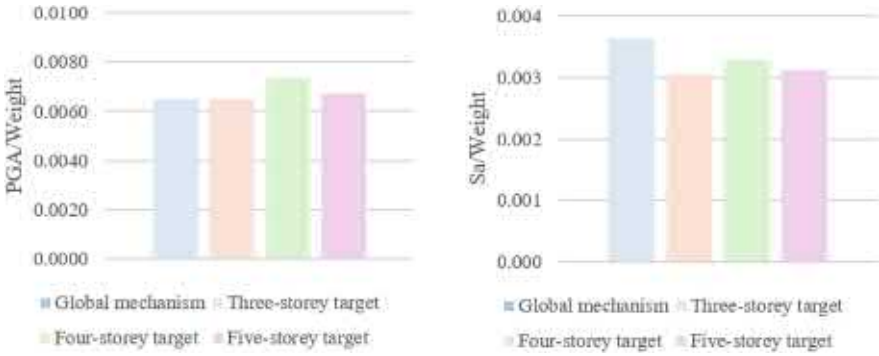


Fig. 11. Comparison of the seismic performance referred to the structural weight

By avoiding unnecessarily conservative member sizing associated with the enforcement of a global collapse mechanism, the proposed approach can reduce steel consumption, fabrication costs, and the environmental impact associated with material production. Consequently, it represents a practical and economically attractive extension of the TPMC design philosophy, particularly for projects where an optimal balance between structural safety, seismic performance, and resource efficiency is required.

References

1. Mazzolani FM, Piluso V (1997) Plastic design of seismic resistant steel frames. Earthq Eng Struct Dyn 26:167–191
2. Montuori R, Nastri E, Piluso V (2015) Advances in theory of plastic mechanism control: closed-form solution for moment resisting frames. Earthq Eng Struct Dyn 44:1035–1054
3. Montuori R, Nastri E, Piluso V (2022) Theory of plastic mechanism control: a new approach for the optimization of seismic resistant steel frames. Earthq Eng Struct Dyn 51:3598–3619
4. Maglio M, Montuori R, Nastri E, Piluso V, Pisapia A (2024) Probabilistic design procedure for steel moment resisting frames equipped with FREEDAM connections. Struct Saf 109:102465
5. European Committee for Standardization (CEN) (2024) FprEN 1998-1-1: Eurocode 8 – design of structures for earthquake resistance – part 1–1: general rules and seismic actions
6. European Committee for Standardization (CEN) (2025) FprEN 1998-1-2: Eurocode 8 – design of structures for earthquake resistance – part 1–2: buildings
7. Maglio M, Montuori R, Nastri E, Piluso V (2023) Critical discussion of DC2 design rules for moment resisting frames in the framework of the prEN 1998 draft. Procedia Struct Integr 44:550–557
8. Maglio M, Montuori R, Nastri E, Piluso V (2023) Design and seismic evaluation of moment resisting frames in DC2 ductility class introduced in the new prEN 1998 draft and comparison with TPMC. Soil Dyn Earthq Eng 168:107833
9. Maglio M, Montuori R, Nastri E, Piluso V (2024) Plastic design of moment resisting frames with low ductility. In: Proceedings of the 11th international conference on behaviour of steel structures in seismic areas (STESSA 2024), Lecture notes in civil engineering, vol 519, pp 1158–1168
10. Computers and Structures Inc. (2024) SAP2000 – Integrated finite element analysis and design of structures: analysis reference manual. Computers and Structures Inc., Berkeley, CA, USA
11. Vamvatsikos D, Cornell CA (2002) Incremental dynamic analysis. Earthq Eng Struct Dyn 31(3):491–514

Dissipative Elliptic-Braced Steel Frames for Seismic Retrofit of RC Buildings

Anna Carmela Ansalone, Salvatore Mottola, Osvaldo Pecorari, and Massimiliano Ferraioli(✉)

University of Campania "Luigi Vanvitelli", Aversa, CE, Italy
massimiliano.ferraioli@unicampania.it

Abstract. Dissipative elliptic-braced steel frames (ELBRFs) represent an innovative solution for the seismic retrofit of reinforced concrete (RC) buildings, combining enhanced structural performance with minimal architectural intrusion. When installed within frame bays, elliptic braces preserve façade openings while providing significant energy dissipation capacity. This study investigates the effectiveness of ELBRFs as a dual lateral force-resisting system, integrating moment-resisting frames with dissipative bracing elements, with the aim of improving the seismic response of existing RC structures. The research combines experimental evidence and advanced finite element modeling to assess the global and local behavior of elliptic-braced systems under seismic loading. Cyclic quasi-static analyses are used to calibrate a refined fem model. A displacement-based design procedure is applied to size all the elements of the elliptic-braced steel frames. Nonlinear simulations are used to evaluate key performance parameters, including stiffness, strength, ductility, hysteretic behavior, and energy dissipation capacity. The results demonstrate that elliptic braces promote stable and symmetric hysteretic responses, with significant enhancement in energy dissipation and delay in the onset of global failure mechanisms.

Keywords: Elliptic-Braced Steel Frames · RC buildings · Seismic Retrofit

1 Introduction

Seismic risk remains one of the most significant threats to structural safety and human life, as evidenced by the numerous earthquakes recorded in recent decades. Reinforced concrete (RC) buildings are particularly vulnerable because many existing structures lack adequate stiffness, strength, ductility, and energy dissipation capacity. During seismic events, these buildings typically dissipate input energy through progressive damage to structural components, leading to substantial economic losses and increased risks to occupants. To mitigate seismic vulnerability, global interventions involve the addition of supplementary lateral-force-resisting systems, such as braced frames or shear walls, to enhance the overall stiffness and seismic load-carrying capacity of the building. These global retrofitting solutions usually involve considerable construction costs, extensive modifications to the existing structure, and significant architectural impact. Furthermore, they can reduce building functionality during construction, causing operational

© The Author(s), under exclusive license to Springer Nature Switzerland AG 2026
R. Zanon et al. (Eds.): CTA 2026, LNCE 942, pp. 646–658, 2026.
https://doi.org/10.1007/978-3-032-39505-4_56

interruptions and social and economic consequences, especially for strategic facilities and critical infrastructure. These limitations have stimulated the search for innovative retrofit solutions capable of substantially enhancing seismic performance while minimizing construction time, architectural intrusion, and disruption to building use. Among the most promising approaches are exoskeleton systems, which are installed externally, can be easily replaced, and contribute to increased structural resilience. Such systems are generally designed to remain elastic during seismic events, thereby ensuring an essentially elastic response of the existing RC structure [1].

In recent years, several dissipative exoskeleton configurations have been proposed for the seismic retrofitting of existing buildings, including Concentrically Braced Frames (CBFs), Eccentrically Braced Frames (EBFs), Buckling-Restrained Braced Frames (BRBFs), and innovative rocking-frame systems [2]. Such systems have proven highly effective in enhancing seismic performance by concentrating energy dissipation and inelastic deformation within dedicated structural components, thereby reducing damage to the existing building. Despite their effectiveness, conventional exoskeleton solutions bracing may significantly affect the building façade, often interfering with architectural features, windows, and openings, and potentially compromising aesthetics, daylighting, and functional requirements. These limitations may restrict their application, particularly in buildings with architectural or heritage constraints. To overcome these limitations, this study proposes a novel dissipative exoskeleton based on Elliptic-Braced Steel Frames (ELBRFs). Thanks to the geometric configuration of the elliptical braces, the proposed system combines effective seismic energy dissipation with improved architectural compatibility. The seismic response of the ELBRF system was first investigated at the single-story level through a calibration process based on experimental tests reported in [3]. Numerical models were developed using Abaqus [4] and SeismoStruct [5] and validated against the available experimental results. The effectiveness of the proposed retrofit solution was then evaluated through its application to a real-world case-study structure. The results demonstrate the potential of ELBRFs as an innovative and practical seismic retrofitting strategy capable of improving structural performance and resilience while minimizing architectural intrusion.

2 Dissipative Elliptic-Braced Steel Frames

2.1 Concept and Structural Rationale

The seismic retrofitting of existing RC buildings using conventional steel bracing systems presents several challenges. Traditional concentric braces are susceptible to buckling under compressive forces, leading to pinched hysteretic behavior and asymmetric tension–compression responses that significantly reduce energy dissipation under cyclic loading. Although this limitation can be mitigated using Buckling-Restrained Braces (BRBs), the resulting systems still require the transfer of substantial axial forces to the existing RC structure. Similarly, eccentric bracing systems enhance seismic performance by concentrating inelastic deformations within dedicated yielding links while maintaining the braces essentially elastic through capacity-design principles. Despite their effectiveness, both concentric and eccentric bracing configurations often impose significant architectural constraints by obstructing openings and limiting the usable space within

structural bays. Furthermore, the transmission of large brace-induced forces to existing non-ductile RC members and beam–column joints remain a critical design and detailing issue, particularly in the retrofit of older structures. To overcome these limitations, this study adopts an external retrofitting substructure based on dissipative elliptic-braced steel frames. The system, originally proposed by Ghasemi Jouneghani *et al.* [3], combines the high lateral stiffness typically associated with Concentrically Braced Frames (CBFs) with the ductility and energy dissipation capacity commonly attributed to Special Moment Resisting Frames (SMRFs). Unlike conventional K-braced configurations, the elliptical brace acts as a structural fuse specifically designed to undergo controlled yielding under seismic loading. Owing to its geometry, the brace dissipates energy through distributed flexural yielding while minimizing the development of severe secondary bending effects in the surrounding frame members. As a result, beams and columns remain predominantly subjected to axial forces, leading to a more efficient force-transfer mechanism and reducing the likelihood of undesirable local stress concentrations. An additional advantage of the proposed solution is its architectural compatibility. The curved geometry of the brace preserves the functional clearance of doors, windows, and circulation paths, thereby minimizing interference with the original building use and improving the feasibility of retrofit interventions in occupied structures.

2.2 Finite Element Modelling and Validation Strategy

To evaluate the cyclic response of the proposed system, detailed finite element models were developed and calibrated against available experimental results. The reference specimen consisted of a scaled steel frame composed of HEB160 beams and columns with lengths of 1820 mm and 1700 mm, respectively, connected to an elliptical tubular brace with a cross-section of 80 × 80 × 10 mm. A high-fidelity numerical model was first developed in Abaqus [4]. The beams and columns were discretized using four-node reduced-integration shell elements (S4R), whereas the elliptical tubular brace was modelled using eight-node reduced-integration solid elements (C3D8R). All structural components were assumed to be fabricated from ASTM Grade 60 steel. Based on a mesh sensitivity study, element sizes of 40 mm and 34 mm were adopted for shell and solid elements, respectively (Fig. 1a). Welded connections were represented through tie constraints to ensure full continuity between adjacent components. The numerical analyses were performed using an implicit nonlinear solution scheme based on the Newmark integration algorithm. Material nonlinearity was modelled through an isotropic linear elastic constitutive law combined with a kinematic hardening plasticity model, allowing the simulation of cyclic yielding and stiffness degradation effects. To further verify the numerical predictions, an independent model of the same specimen was developed in SeismoStruct [5] (Fig. 1b). In this case, the elliptical brace was represented through a simplified discretization consisting of 24 inelastic force-based fiber elements (infrmFB) reproducing the exact geometric profile of the ellipse. Steel behavior was described through the Menegotto–Pinto [6] constitutive model with Filippou isotropic hardening rules [7], which is widely recognized for accurately reproducing cyclic steel behavior under large inelastic deformations.

2.3 Cyclic Behavior and Model Validation

The numerical models were validated against the results of quasi-static cyclic tests conducted under displacement-controlled loading protocols (Fig. 2). The imposed loading history was designed to reproduce the progressive accumulation of inelastic deformations typically observed during severe seismic events. The response predicted by both Abaqus [4] and SeismoStruct [5] was compared with the experimental results in terms of base shear–displacement relationships. Attention was devoted to the reproduction of stiffness degradation, strength development, hysteretic shape, and cumulative energy dissipation capacity. As shown in Fig. 2a and b, both numerical models provide excellent agreement with the experimental observations throughout the loading history. The simulations successfully capture the initial elastic stiffness, the onset of yielding, the post-yield response, and the stable hysteretic behavior exhibited by the dissipative elliptical brace.

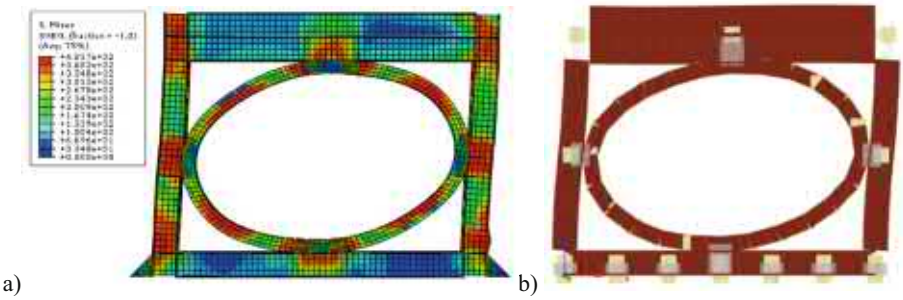


Fig. 1. a) Abaqus numerical model; b) SeismoStruct numerical model.

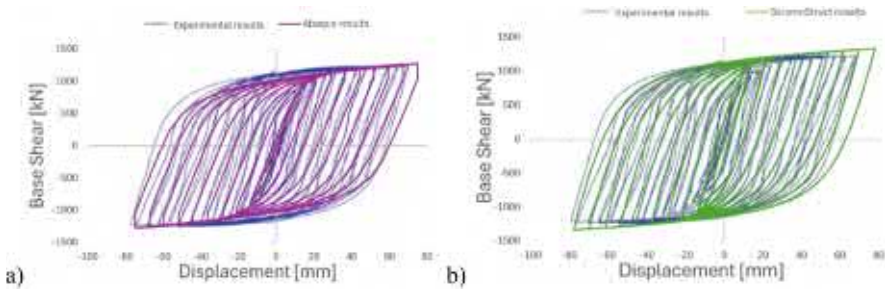


Fig. 2. Force-displacement behavior: a) Abaqus results; b) SeismoStruct results.

Furthermore, the predicted hysteresis loops accurately reproduce the energy dissipation characteristics observed experimentally, confirming the ability of the adopted modeling strategies to represent the cyclic response of the system. The close agreement between experimental and numerical results demonstrates the reliability of the proposed models and provides confidence in their predictive capability.

3 Seismic Retrofit Using Dissipative ELBRFs

3.1 Benchmark Case Study

The benchmark case study is an existing reinforced concrete (RC) building, characterized by a regular square plan (Fig. 3) and rising three stories above ground. The building exhibits regularity in both plan and elevation, with a constant span length of 5.0 m and an inter-story height of 3.0 m. The structure was originally designed for gravity loads only, without any seismic design provisions. The materials utilized consist of C20/25 grade concrete and FeB38k steel reinforcement; the cross-sectional dimensions and corresponding reinforcement details for the various structural elements are summarized in Table 1. The case study was modeled using the software SeismoStruct [5], employing inelastic force-based fiber elements (infrmFB). The cross-sections were discretized into steel, confined concrete, and unconfined concrete fibers [8]. The seismic safety of existing buildings was evaluated through nonlinear static (pushover) analysis following Procedure A of the Italian Building Code [9], which is consistent with the principles of Eurocode 8 – Part 3 [10] for the assessment and retrofitting of existing structures. Nonlinear static (pushover) analyses were performed using two different lateral force distributions applied in the positive and negative directions, i.e., Group 1 (modal pattern) and Group 2 (mass-proportional pattern). The multi-degree-of-freedom (MDOF) structural system is transformed into an equivalent single-degree-of-freedom (SDOF) system through modal participation factors and effective mass properties. The capacity curve is thus converted into the Acceleration–Displacement Response Spectrum (ADRS) format, enabling direct comparison with the seismic demand spectrum. The demand response spectrum was defined in accordance with the Italian Building Code for the site of Grottaminarda (Italy), assuming soil type C, topographic category T_2, and a reference life (V_R) of 75 years. The limit states of Immediate Occupancy (IO), Damage Limitation (DL), and Life Safety (LS) were checked for safety verification. The drift ratio is checked for IO and DL limit states, while the chord rotation is checked for DL and LS limit states. as specified by Equation C.8.7.2.1 [11]. Table 2 presents the results of the seismic assessment at the considered limit states in terms of performance point (target displacement, d, and corresponding normalized base shear, V/W, capacity peak ground acceleration (PGA^{c}), demand peak ground acceleration (PGA^{d}), and seismic safety index ($\zeta_{PGA} = PGA^{c}/PGA^{d}$). For all limit states, the safety index is lower than unity, indicating that the available seismic capacity is insufficient to satisfy the code-prescribed demand. The results therefore highlight the inadequate stiffness, strength, and ductility of the existing structure and confirm the need for seismic strengthening measures to enhance its performance and safety.

Table 1. Cross-section and reinforcement in columns and beams.

Member	Position	Story	Section	Long. bars
Column	External	1 2–3	30 × 45 30 × 35	2ϕ20 along 30 - 3ϕ20 along 45 2ϕ20 along 30 - 2ϕ20 along 35
Column	Internal	1 2–3	40 × 75 35 × 60	2ϕ20 along 40 - 4ϕ20 along 75 2ϕ20 along 35 - 3ϕ20 along 60
Beam	Int. T1	1–3	80 × 25	7ϕ22 top - 7ϕ22 bottom
Beam	Ext. T2	1–3	35 × 35	2ϕ22 top - 2ϕ22 bottom
Beam	Ext. T3	1–3	30 × 42	3ϕ22 top - 3ϕ22 bottom

Table 2. Performance points. Capacity (PGA^c), Demand (PGA^d), Safety index (ζ_{PGA}).

Limit State	d [cm]	V/W [-]	PGA^c [g]	PGA^d [g]	ζ_{PGA}	d [cm]	V/W [-]	PGA^c [g]	PGA^d [g]	ζ_{PGA}
	Modal Load Pattern. X-Direction					Modal Load Pattern. Y-Direction				
IO	3.0	0.151	0.095	0.118	0.802	2.4	0.110	0.075	0.118	0.633
DL	4.2 ara>	0.174	0.115	0.156	0.735	3.6	0.135	0.096	0.156	0.614
LS	11.4	0.230	0.324	0.405	0.800	14.4	0.222	0.347	0.405	0.857
	Uniform Load Pattern. X-Direction					Uniform Load Pattern. Y-Direction				
IO	2.4	0.162	0.09	0.118	0.760	2.4	0.138	0.084	0.118	0.709
DL	3.0	0.180	0.099	0.156	0.633	3.6	0.168	0.107	0.156	0.684
LS	9.0	0.243	0.29	0.405	0.716	12.0	0.251	0.338	0.405	0.835



Fig. 3. a) Plan view; b) Existing building model; c) Retrofitted building model.

3.2 Displacement-Based Design Procedure

The proposed retrofit strategy employs a novel dissipative exoskeleton system composed of Elliptic-Braced Steel Frames (ELBRFs) installed along the building façades in both principal directions. The connections between the exoskeleton and the existing structure are assumed to be sufficiently stiff in translation to ensure full transfer of horizontal forces, while remaining free to rotate about all axes. In practice, the connection details should be designed to provide translational restraint while accommodating

rotational freedom, thereby limiting the interaction between the existing structure and the exoskeleton and preventing local stress concentrations in the structural members. Under these assumptions, the structural system can be idealized as two parallel lateral load-resisting systems acting in conjunction: the existing building and the ELBRF exoskeleton. This simplified representation significantly facilitates the design process. Various seismic retrofitting strategies for reinforced concrete buildings based on dissipative exoskeleton systems have been proposed in the literature [12–18]. In the present study, the displacement-based design (DBD) methodology proposed by Mazza *et al.* [19] is adopted to develop the retrofit design procedure.

Main Structure: Bilinear Equivalent SDOF Idealization

The first phase of the design procedure consists of reducing the existing three-dimensional structural model to an equivalent single-degree-of-freedom (SDOF) system. This idealization is based on the global capacity curve (i.e., base shear versus roof displacement) obtained from nonlinear static (pushover) analysis using a modal lateral load distribution. Once the target design displacement of the existing structure, $d_p{}^{(S)}$, is defined, the corresponding base shear $V_p{}^{(S)}$ is identified on the capacity curve. In the present study, a target displacement of $d_p = 90$ mm, corresponding to a global drift ratio of 1%, was adopted for the design and assessment analyses. A bilinear idealization of the capacity curve is then adopted (Fig. 4a) to derive the principal response parameters of the structure, namely the yield displacement, $d_y{}^{(S)}$, the yield base shear, $V_y{}^{(S)}$ the global ductility capacity, $\mu^{(S)}$, and the post-yield hardening ratio, $r^{(S)}$. These properties are then transformed into the equivalent SDOF system through the modal participation factor, Γ (Fig. 5) (Table 3).

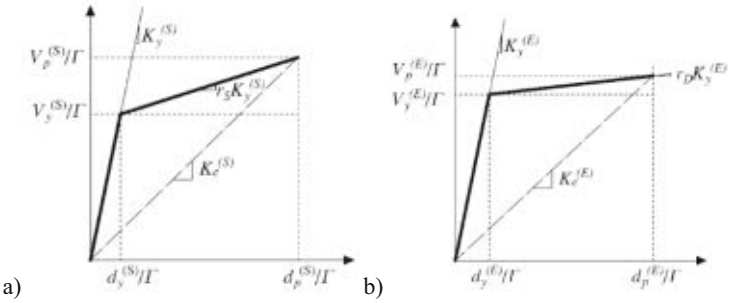


Fig. 4. Bilinear idealization: a) Existing Structure (*S*); b) ELBRF Exoskeleton (*E*).

Finally, the equivalent viscous damping ratio is evaluated by combining the conventional 5% elastic damping with the hysteretic damping component, $\xi_h{}^{(S)}$. The latter is calculated according to ATC-40 [20] using a damping correction factor $\kappa = 0.33$, representative of Type C hysteretic behavior, to account for the limited energy dissipation capacity typically exhibited by existing RC buildings, whose cyclic response is often characterized by significant stiffness degradation and pinched hysteretic loops.

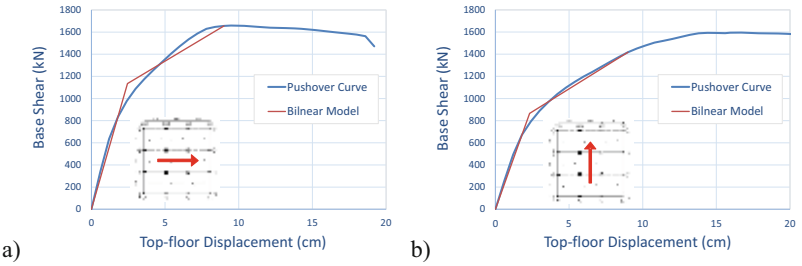


Fig. 5. First-mode pushover curves and corresponding bilinear idealizations.

Table 3. Parameters of the bilinear equivalent SDOF system of the structure (S).

Dir.	$\delta_p^{(S)}$ [mm]	$\delta_y^{(S)}$ [mm]	$V_p^{(S)}$ [kN]	$V_y^{(S)}$ [kN]	$K_e^{(S)}$ [kN/mm]	$T_e^{(S)}$ [s]	$r^{(S)}$ [−]	$\mu^{(S)}$ [−]	$\xi_h^{(S)}$ [%]	$\xi_v^{(S)}$ [%]	m_e^* [kN·s^2/mm]	Γ [−]
X	90.0	24.5	1655	1136	18.39	1.00	0.171	3.67	8.7	5.00	0.470	1.311
Y	90.0	23.2	1417	865	15.75	1.05	0.222	3.88	7.4	5.00	0.436	1.332

Design of ELBRF Exoskeleton

Once the equivalent SDOF representation of the existing structure has been established, the target displacement of the retrofitted system is constrained to coincide with that of the original structure, i.e., $d_p = d_p^{(E)} = d_p^{(S)}$ since the main structure and the exoskeleton are acting in parallel. Owing to the stable hysteretic response exhibited by the ELBRF system (Sect. 2), the exoskeleton can also be represented through a bilinear idealization of its capacity curve (Fig. 4b). However, the corresponding parameters, i.e., the design base shear, $V_p^{(E)}$, the yield displacement, $d_y^{(E)}$, the yield base shear, $V_y^{(E)}$ the ductility ratio, $\mu^{(E)}$, and the post-yield hardening ratio, $r^{(E)}$, are unknown. Therefore, an iterative design procedure is adopted according to the following steps:

1. **Preliminary ELBRF design.** A reference multistorey ELBRF is initially designed to provide a base shear capacity of the same order of magnitude as that of the existing structure, while activating yielding at the lowest possible lateral displacement demand. The structural members are proportioned to ensure a ductile yielding mechanism and to prevent both local and global buckling phenomena.
2. **Nonlinear static analysis.** A pushover analysis of the planar ELBRF model is performed (Fig. 6a and b) using the lateral load distribution proportional to the fundamental mode shape of the existing building. It should be noted that the displacement-based design (DBD) procedure proposed by Mazza *et al.* [19] assumes that the modal shape of the structure remains substantially unchanged after retrofit.
3. **Bilinear idealization.** The ELBRF capacity curve is idealized through a bilinear representation (Fig. 4b). This allows the determination of the principal response parameters of the dissipative system, including the yield displacement, $d_y^{(E)}$, the ductility ratio, $\mu^{(E)}$, the post-yield hardening ratio, $r^{(E)}$, and the equivalent viscous damping due to hysteresis, $\xi_h^{(E)}$calculated according to ATC-40 [20] using $\kappa = 1.00$ representative of Type A stable hysteretic behavior.

4. **Initial estimate of exoskeleton strength.** Since the design base shear of the exoskeleton, $V_p{}^{(E)}$, is initially unknown, the first trial value is estimated from the ELBRF capacity curve.
5. **Evaluation of equivalent damping.** The equivalent viscous damping ratio of the coupled system, $\xi^{(SE)}$, is computed as a weighted average of the equivalent damping ratios of the existing structure, $\xi_h{}^{(S)}$, and the exoskeleton $\xi_h{}^{(E)}$.
6. **Determination of the effective period**. The effective period, T_e, is obtained from the damped design response spectrum through application of the spectral reduction factor, η, as prescribed by both Italian Building Code [9] and Eurocode 8 [10].
7. **Evaluation of the required exoskeleton stiffness.** The stiffness demand associated with the exoskeleton, $(K_e{}^{(E)})$, is determined by subtracting the elastic stiffness of the existing structure, $(K_e{}^{(S)})$ from the total equivalent stiffness (K_e), required for the coupled system. Multiplication of $K_e{}^{(E)}$ by the target displacement d_p provides an updated estimate of the exoskeleton design base shear $V_p{}^{(E)}$. Steps 5–7 are repeated until convergence is achieved.
8. **Updating the ELBRF design.** Once convergence has been reached, the final value of $V_p{}^{(E)}$ is divided by the number of ELBRFs installed along each façade, yielding the design strength required for each individual frame. Using the bilinear idealization, the corresponding mechanical properties—including effective stiffness, yield displacement, ductility ratio, and post-yield hardening ratio—are determined. These parameters are then used to redesign the multistorey ELBRF, and the procedure is repeated from Step 2 until full consistency between the assumed and calculated structural properties of ELBRF is achieved (Tables 4 and 5).

Table 4. Parameters of the bilinear equivalent SDOF system of the Exoskeleton (E).

Dir.	$\delta_p{}^{(E)}$ [mm]	$\delta_y{}^{(E)}$ [mm]	$V_p{}^{(E)}$ [kN]	$V_y{}^{(E)}$ [kN]	$K_e{}^{(E)}$ [kN/mm]	$T_e{}^{(E)}$ [s]	$r^{(E)}$ [−]	$\mu^{(E)}$ [−]	$\xi_h{}^{(E)}$ [%]
X	90.0	30.1	1756	1539	19.51	0.70	0.071	2.99	34.5
Y	90.0	32.0	1701	1548	18.90	0.71	0.050	2.99	36.7

Table 5. Geometric and mechanical characteristics of ELBRF structural members.

Member	Section	Material
1st Floor Column	HEB 120	S450
2nd & 3rd Floor Columns	HEB 120	S450
Beam	HEB 100	S450
Brace	SHS 260 × 14.2	S235

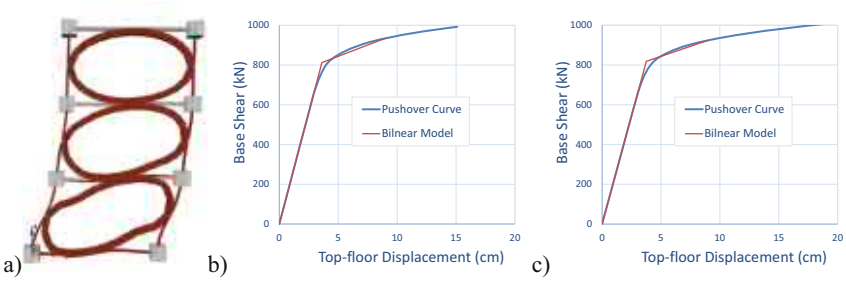


Fig. 6. a) ELBRF model. Pushover Curve: a) ELBRF in X-direction; b) ELBRF in Y-direction.

4 Seismic Assessment

To evaluate the seismic performance of the retrofitted structure, nonlinear response-history analyses were performed using pairs of horizontal ground-motion components applied simultaneously at the base of the model. A suite of seven ground-motion records was selected and scaled using the REXEL software [21] to satisfy the spectrum-compatibility criteria specified by both the Italian Building Code [9] and Eurocode 8 [10] (Fig. 7a and b). The nonlinear time-history analyses (NLTHAs) performed demonstrate the effectiveness of the retrofit strategy. As an example, Fig. 8 compares the responses of the existing and retrofitted buildings, revealing a significant reduction in peak roof displacement and, consequently, in drift-related damage, without increasing the base shear. Figure 9 summarizes the results performed on the retrofitted structure for the LS limit state. The response parameters considered include the peak interstory drift ratio (IDR) and the peak floor acceleration, which are key performance indicators of damage to both structural and non-structural components. For each response quantity, the mean value (μ) and the upper-bound estimate ($\mu + \sigma$), where σ denotes the standard deviation, were computed from the results obtained from the seven ground-motion records. The maximum IDR occurs at the first story in the X-direction and at the second story in the Y-direction. The corresponding $\mu + \sigma$ values are 1.12% in the X-direction and 1.13% in the Y-direction, both well below the CP acceptance threshold of 2% specified by ASCE 41–17 [22] for reinforced-concrete frame structures. The floor acceleration profile tends to increase with height. This behavior is attributed to the reduced interstory drift demands at the upper levels, which limit yielding in the upper-story elliptical braced frames during seismic excitation.

The chord rotation demands in all structural members remained well below their corresponding capacities, with demand-to-capacity ratios lower than unity (e.g., Fig. 9a for EQ313 and Fig. 9b for EQ317). Finally, under the CP-earthquake records, the most highly stressed devices at the first story experienced deformation demands well below the drift ratio range (i.e. ± 0.05) over which the ELBF response was validated through experimental testing and finite-element modeling (Figs. 10 and 11).

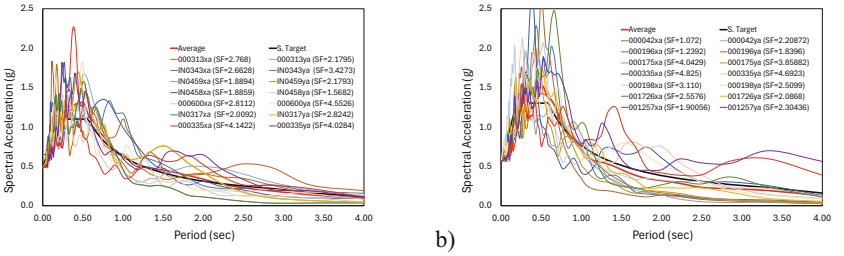


Fig. 7. Spectrum compatibility of the selected ground-motion records with the target response spectrum: a) Life Safety (LS) limit state; b) Collapse Prevention (CP) limit state.

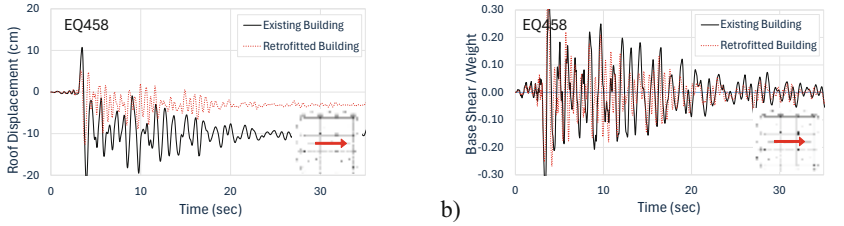


Fig. 8. a) Roof displacement time histories; b) Base shear time histories.

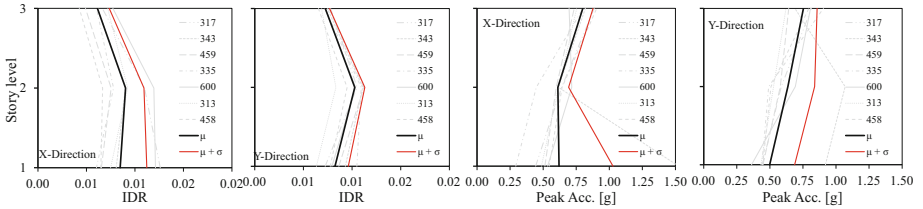


Fig. 9. Distribution of peak interstory drift ratio (IDR) and peak floor acceleration along the building height for the retrofitted building. LS limit state.

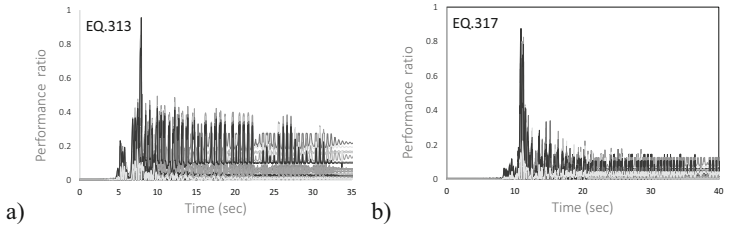


Fig. 10. Demand to Capacity performance ratio. a) EQ313; b) EQ317.

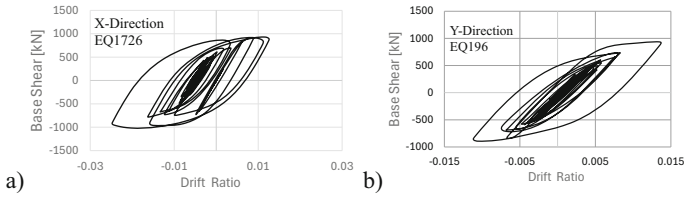


Fig. 11. Base shear vs. first-story drift ratio of ELBRFs. a) EQ1726; b) EQ196.

5 Conclusions

This study investigated the effectiveness of dissipative Elliptic-Braced Steel Frames (ELBRFs) as an innovative exoskeleton system for the seismic retrofit of existing reinforced concrete (RC) buildings. The research combined numerical model calibration against experimental evidence, displacement-based design procedures, and nonlinear seismic assessment of a representative RC case-study building. The main conclusions can be summarized as follows. The finite element models developed in Abaqus and SeismoStruct accurately reproduced the cyclic response observed in experimental tests on elliptic-braced steel frames. The elliptic brace exhibited stable and nearly symmetric hysteretic behavior under cyclic loading, with significant energy dissipation capacity and limited strength degradation. The displacement-based design procedure proved effective for sizing the ELBRF exoskeleton and integrating it with the existing RC structure. Nonlinear time-history analyses confirmed the effectiveness of the retrofit strategy, highlighting a substantial reduction in roof displacement and interstory drift demands. Overall, dissipative ELBRFs represent a promising retrofit solution, combining effective seismic protection with limited architectural impact due to their ability to preserve façade openings and functional spaces.

References

1. Di Lorenzo G, Colacurcio E, Di Filippo A, Formisano A, Massimilla A, Landolfo R (2020) State-of-the-art on steel exoskeletons for seismic retrofit of existing RC buildings. Ing Sismica 37(1):33–50
2. Ferraioli M, Pecorari O, Parolisi S, Mandara A (2025) Controlled rocking steel braced dual-frames for seismic retrofit of rc building structures, pp 3957–3968
3. Ghasemi Jouneghani H, Haghollahi A (2020) Experimental study on hysteretic behavior of steel moment frame equipped with elliptical brace. Steel Compos Struct 34(6):891–907
4. Dassault Systèmes (2026) Abaqus standard/explicit user's manual, version 2026. Dassault Systèmes Simulia Corp., Providence, RI, USA
5. Seismosoft (2026) SeismoStruct—a computer program for static and dynamic nonlinear analysis of framed structures
6. Menegotto M, Pinto PE (1973) Method of analysis for cyclically loaded RC plane frames including changes in geometry and non-elastic behavior of elements under combined normal force and bending. In: Proc IABSE symposium, Lisbon, Portugal
7. Filippou FC, Popov EP, Bertero VV (1983) Effects of bond deterioration on hysteretic behavior of reinforced concrete joints. Report No. UCB/EERC-83/19,. EERC, University of California, Berkeley

8. Mander JB, Priestley MJN, Park R (1988) Theoretical stress-strain model for confined concrete. J Struct Eng 114(8):1804–1826
9. NTC-2018 Guidelines (2018) Technical standards for constructions. G U Rep Ital. 20.02.2018, Rome, Italy (in Italian)
10. EN 1998-3 (2005) Eurocode 8—design of structures for earthquake resistance—part 3: assessment and retrofitting of buildings. CEN, Brussels, Belgium
11. NTC-2019 Instructions (2019) Instructions for the application of the new technical norms on constructions. G U Rep Ital. Circ. 21.01.2019, n.7 (in Italian)
12. Bergami AV, Nuti C (2013) A design procedure of dissipative braces for seismic upgrading structures. Earthq Struct 4(1):85–108
13. Ferraioli M, Lavino A, Mandara A (2020) Seismic retrofit design method of RC buildings using metallic yielding dampers. Ing Sismica 37(1):19–32
14. Ferraioli M, Lavino A, Molitierno C, Di Lauro G (2021) Seismic retrofit of an existing reinforced concrete building with buckling-restrained braces. Open J Civ Eng 15(1):203–225
15. Ferraioli M, Lavino A, De Matteis G (2023) A design method for seismic retrofit of reinforced concrete frame buildings using aluminum shear panels. Arch Civ Mech Eng 23(3):106
16. Ferraioli M, Lavino A (2018) A displacement-based design method for seismic retrofit of RC buildings using dissipative braces. Math Probl Eng 2018:5364564
17. Ferraioli M, Pecorari O, Mottola S et al (2025) Dissipative steel exoskeletons for seismic retrofit of RC buildings. Arch Civ Mech Eng 25(2):134
18. Kasai K, Ito H (2004) JSSI manual for building passive control technology Part-8 peak response evaluation and design for elastoplastically damped system. In: Proceedings of the 13th WCEE, Vancouver
19. Mazza F, Vulcano A (2015) Displacement-based design procedure of damped braces for the seismic retrofitting of RC framed buildings. B Earthq Eng 13(7):2121–2143
20. ATC 40 (1996) Seismic evaluation and retrofit of concrete buildings. Applied Technology Council, Redwood City, California
21. Iervolino I, Galasso C, Cosenza E (2010) REXEL: computer aided record selection for code-based seismic structural analysis. B Earthq Eng 8(2):339–362
22. ASCE 41-17 (2017) Seismic Evaluation and Retrofit of Existing Buildings. American Society of Civil Engineers, Reston, Virginia

Steel Exoskeleton System for Strengthening Infilled RC Frames: Experimental Evidence and Numerical Modelling Under Monotonic and Cyclic Loading

Emilia Meglio(✉) and Antonio Formisano

Department of Structures for Engineering and Architecture, Polytechnic and Basic Sciences School, University of Naples Federico II, Naples, Italy
emilia.meglio@unina.it

Abstract. A significant portion of reinforced concrete (RC) buildings worldwide were designed before the adoption of modern seismic codes and, therefore, lack adequate ductility and energy dissipation capacity. Their seismic response is further complicated by the interaction between RC frames and masonry infill walls, which introduces complex nonlinear behaviors. Enhancing the seismic performance of these structures is particularly challenging when retrofit interventions must be implemented without disrupting building occupancy.

This study investigates the effectiveness of an external strengthening solution designed to improve the lateral performance of infilled RC frame buildings. The proposed system consists of a modular steel exoskeleton made of cold-formed steel members arranged in a regular grid and complemented by diagonal bracing elements. Installed entirely outside the building envelope and connected to the existing structure through mechanical anchors, the system aims to increase seismic capacity while minimizing interference with building use.

An experimental campaign was conducted on two full-scale RC frame specimens with masonry infill walls: one representing the original configuration and the other strengthened with the above-mentioned exoskeleton. Numerical models were also developed and calibrated experimentally through nonlinear static analyses, while cyclic simulations were performed to investigate hysteretic behavior. The results indicate that the retrofitted infilled RC frame exhibits significantly enhanced lateral strength, ductility, and energy dissipation capacity relative to the as-built configuration.

Keywords: Existing Buildings · RC Structures · Seismic Retrofit · Steel Exoskeleton · Full Scale Test

1 Introduction

The seismic upgrading of existing buildings is increasingly required to reduce the vulnerability of ageing urban areas while limiting the social and economic impact associated with rehabilitation works. In practical applications, strengthening interventions are

© The Author(s), under exclusive license to Springer Nature Switzerland AG 2026
R. Zanon et al. (Eds.): CTA 2026, LNCE 942, pp. 659–668, 2026.
https://doi.org/10.1007/978-3-032-39505-4_57

expected not only to improve structural safety but also to minimize construction time, preserve building functionality and reduce disturbance to occupants. These requirements have progressively driven research towards retrofit strategies that combine structural effectiveness with ease of installation.

Among the existing building stock, reinforced concrete (RC) structures represent one of the most critical categories. Their extensive diffusion worldwide is mainly attributable to the favorable mechanical properties, durability and economic convenience of reinforced concrete [1]. Nevertheless, a significant proportion of RC buildings currently in service, particularly in Italy and other European countries, was designed before the introduction of modern seismic regulations. Consequently, these structures generally exhibit inadequate seismic detailing, insufficient confinement of structural members and limited deformation capacity, resulting in poor seismic performance during strong earthquakes [2]. The consequences of these deficiencies have been extensively documented by recent seismic events, which highlighted the high vulnerability of existing RC buildings together with the associated economic and social losses [3–5].

The structural response of these buildings is strongly affected by masonry infill walls. Although usually considered non-structural elements during design, masonry infills actively participate in resisting horizontal actions and significantly influence the global behavior of the surrounding RC frame. Their interaction modifies stiffness, lateral resistance, damage distribution and collapse mechanisms, making both seismic assessment and retrofit design more challenging [6–8]. Reliable strengthening solutions should therefore account for the contribution of the infill to the overall structural response.

Several retrofit techniques have been proposed to mitigate these structural deficiencies, including fibre-reinforced composites, engineered cementitious materials and prefabricated strengthening systems [9–11]. Despite their proven effectiveness, many of these interventions require extensive operations within the building, frequently involving prolonged interruption of normal occupancy and significant architectural modifications. In recent years, external steel exoskeletons have emerged as a promising alternative because they can be installed outside the existing envelope while providing additional stiffness, strength and energy dissipation capacity with limited interference to building use. Within this framework, the Resisto 5.9 Tube system [12] consists of a modular lightweight steel exoskeleton assembled from cold-formed steel members and diagonal braces connected to the existing structure.

The present study evaluates the effectiveness of this retrofit solution through an integrated experimental and numerical investigation. Two full-scale masonry-infilled RC frames representative of pre-code construction practice were tested under quasi-static cyclic loading in both their original and strengthened configurations. The experimental evidence was subsequently used to calibrate nonlinear numerical models developed in SAP2000 and OpenSees, allowing both monotonic and cyclic structural responses to be reproduced. The combined experimental and numerical results provide a comprehensive assessment of the structural behavior of the proposed exoskeleton system and demonstrate its potential for the seismic upgrading of existing RC buildings.

2 Experimental Investigation

2.1 Geometry and Materials

The experimental validation of the proposed retrofit strategy was carried out at the Laboratory of Full-Scale Structures (LaSTRUT) of the University of Naples Federico II. The investigation was conceived to compare the seismic response of an existing masonry-infilled reinforced concrete (RC) frame before and after the installation of the Resisto 5.9 Tube external strengthening system. To ensure that any variation in structural response could be exclusively attributed to the retrofit intervention, two full-scale specimens with identical geometry, reinforcement detailing and masonry infill were constructed and tested. The reference specimen (U-RC) represented the original structural configuration, whereas the second specimen (R-RC) incorporated the external steel exoskeleton.

The structural layout reproduced a typical gravity-load-designed Italian RC frame. The clear span and clear height were 3700 mm and 2650 mm, respectively. Columns had a square cross-section of 300 × 300 mm, while the beam measured 300 × 500 mm. The columns had a square cross-section of 300 × 300 mm and were reinforced with four smooth longitudinal bars (2Ø12 mm on each side), while transverse reinforcement was provided by Ø8 mm stirrups spaced at 300 mm. The beam, with a cross-section of 300 × 500 mm, was reinforced with three Ø12 mm and two Ø8 mm longitudinal bars at the bottom, two Ø8 mm bars at the top, additional Ø8 mm side reinforcement and Ø8 mm stirrups spaced at 300 mm. The use of smooth reinforcement together with the relatively large stirrup spacing was intentionally adopted to reproduce the poor detailing and inadequate confinement typically observed in pre-code RC buildings designed primarily for gravity loads. A 200 mm-thick clay masonry infill panel was built inside each frame using vertically perforated units with an approximate void ratio of 50%. M5 mortar was applied only along the horizontal bed joints, consistently with common construction practice adopted for this typology of infill.

Seismic upgrading was achieved through the installation of the Resisto 5.9 Tube system, consisting of an external modular steel exoskeleton assembled from cold-formed steel members connected by diagonal braces. Two module dimensions (1000 × 500 mm and 1000 × 750 mm) were combined to generate the final strengthening layout, composed of four vertical alignments and four horizontal rows. The columns and beams of the exoskeleton were made of rectangular hollow sections with cross-sectional dimensions of 45 × 60 mm and 25 × 60 mm, respectively. The diagonal members consisted of either steel plates or C-shaped profiles. All structural members were fabricated from S350GD + Z steel with a uniform thickness of 3 mm. Chemical anchorage ensured the connection between the exoskeleton, the existing RC frame and the foundation, allowing the retrofit system to participate in resisting lateral actions.

Concrete strength classes C16/20 and C28/35 were adopted for the frame and the foundation, respectively. Following construction, experimental tests were performed to determine the actual mechanical properties of concrete, reinforcing steel and masonry materials. he measured values adopted in the subsequent numerical analyses are summarized in Table 1.

Table 1. Material properties.

Component	Property	Value
Frame concrete	Average compressive strength	25.9 MPa
Foundation concrete	Average compressive strength	41.6 MPa
Reinforcing steel	Yield strength	340 MPa
Reinforcing steel	Ultimate strength	495 MPa
Masonry units	Nominal compressive strength	15 MPa
Mortar	Class	M5

2.2 Test Setup and Loading Protocol

The structural response of both specimens was evaluated through a displacement-controlled quasi-static cyclic test. Lateral displacements were imposed at beam level by means of a hydraulic actuator following the loading history illustrated in Fig. 1, while each displacement level was repeated for three fully reversed cycles.

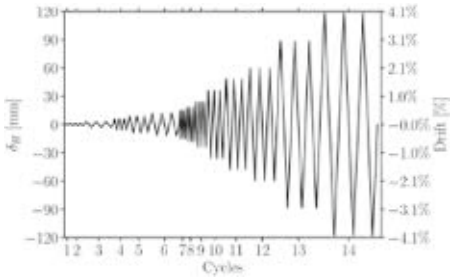


Fig. 1. Experimental loading protocol.

To reproduce the gravity loads acting on a typical multi-storey RC building, a constant axial force of 100 kN was simultaneously applied to each column through hydraulic jacks and maintained unchanged for the entire duration of the test. The actuator velocity progressively increased according to the imposed displacement amplitude, ranging from 0.05 mm/s during the initial loading stages to 1.0 mm/s at the largest displacement levels. Global and local structural responses were continuously monitored throughout the tests. Load cells and displacement transducers were employed to acquire the overall force-displacement response, whereas additional LVDTs positioned along the frame–infill interfaces allowed the relative interaction between the masonry panel and the surrounding RC members to be quantified.

2.3 Experimental Results

The envelope curves of the tested specimens are presented in Fig. 2. Both specimens exhibited an initial stiffness governed by the interaction between the RC frame and the masonry infill. However, significant differences emerged as damage progressed.

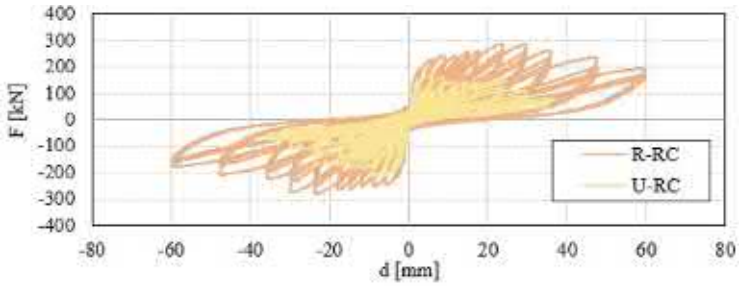


Fig. 2. Experimental lateral force–displacement hysteretic response of the tested specimens.

The unretrofitted specimen (U-RC) reached peak lateral strengths of 170 kN and 209 kN in tension and compression, respectively, at a drift ratio of approximately 0.21%. Following peak resistance, a rapid strength degradation was observed due to extensive cracking and crushing of the masonry infill combined with the onset of damage in the RC columns. The test was terminated at a maximum drift ratio of approximately 1.24%.

In contrast, the retrofitted specimen (R-RC) developed significantly higher lateral capacities, reaching peak strengths of 288 kN and 281 kN in tension and compression, respectively. Peak resistance occurred at a drift ratio close to 0.83%, corresponding to an approximately fourfold increase in displacement capacity at peak load compared with the reference specimen. Moreover, the retrofitted frame sustained drift ratios exceeding 2% before reaching its ultimate condition.

Overall, the Resisto 5.9 Tube system increased peak strength by up to 69%, while significantly enhancing deformation capacity and reducing cyclic degradation. The strengthened specimen also exhibited a more stable hysteretic response, characterized by a smaller difference between tensile and compressive capacities and improved energy dissipation throughout the loading history.

3 Numerical Simulations

3.1 Monotonic Loading

The experimental results provided the basis for the development and calibration of nonlinear numerical models aimed at reproducing the behavior of both the original (U-RC) and retrofitted (R-RC) configurations. Monotonic analyses were performed in SAP2000 using numerical models reproducing the geometry, boundary conditions and material properties measured during the experimental program. The applied loading scheme replicated the laboratory configuration by maintaining the constant axial load on the columns while introducing a monotonically increasing horizontal action at beam level.

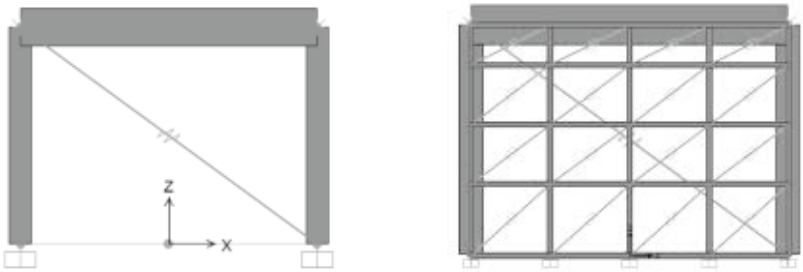


Fig. 3. SAP2000 numerical models adopted for the nonlinear static analyses: (a) unretrofitted specimen (U-RC) and (b) retrofitted specimen with Resisto 5.9 Tube (R-RC).

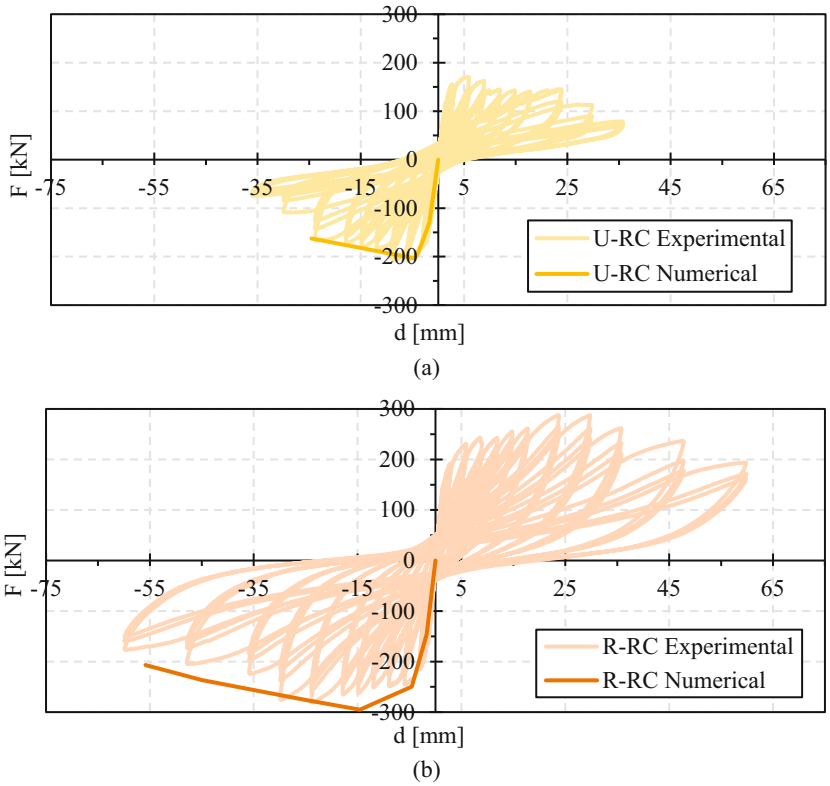


Fig. 4. Comparison between numerical monotonic and experimental results: (a) unretrofitted specimen (U-RC) and (b) retrofitted specimen with Resisto 5.9 Tube (R-RC).

In both models, RC beams and columns were represented by nonlinear frame elements with concentrated plastic hinges located at the member ends. The masonry infill

panel was represented by means of a multilinear nonlinear link, whose properties were defined according to literature-based formulations [13, 14]. For the retrofitted configuration, the Resisto 5.9 Tube system was explicitly included in the model. End releases were assigned to the steel members to accurately represent the real boundary conditions at the connections, whereas fixed restraints were imposed at the base to model the foundation anchorage. The diagonal braces were modelled using multilinear nonlinear links. The resulting SAP2000 models are shown in Fig. 3.

The numerical capacity curves were subsequently compared with the experimental envelope responses derived from the cyclic tests in the pushing direction.

As illustrated in Fig. 4, the proposed modelling approach was able to satisfactorily reproduce the behavior of both specimens, providing a good prediction of the initial stiffness, peak strength, and post-elastic response.

The agreement between numerical and experimental results confirms the reliability of the adopted modelling assumptions and supports the use of the calibrated models for further analyses of RC frames retrofitted with the Resisto 5.9 Tube system.

3.2 Cyclic Loading

To further investigate the cyclic response of the tested system, a detailed numerical model was developed in OpenSees. Unlike the simplified SAP2000 models adopted for the nonlinear static analyses, the OpenSees models were formulated to capture the hysteretic behavior of the structures, including stiffness degradation, strength deterioration, and energy dissipation under cyclic loading. The RC beams and columns were modelled using nonlinear elements with fiber-section discretization. The cross-sections were subdivided into confined concrete, unconfined concrete, and reinforcing steel fibers, allowing the spread of plasticity along the member length to be explicitly represented. The constitutive behavior of concrete and reinforcing steel was simulated through the Concrete02 and Steel02 material models, respectively. The same geometry, material properties, boundary conditions, and loading protocol adopted in the experimental campaign were implemented in the numerical model. The masonry infill was represented through an equivalent nonlinear compression strut calibrated against the experimental response. The Resisto 5.9 Tube exoskeleton was explicitly incorporated into the model by representing vertical and horizontal members with nonlinear beam-column elements, while the diagonal braces were modelled as corotational truss elements governed by the Steel02 constitutive law. The retrofit system was connected to the existing RC frame through rigid compatibility constraints reproducing the experimental mechanical anchorage.

The cyclic response was reproduced through displacement-controlled analyses following the loading history applied during the laboratory tests. Figure 5 compares the experimental and numerical hysteretic force–displacement responses obtained for the unretrofitted (U-RC) and retrofitted (R-RC) specimens.

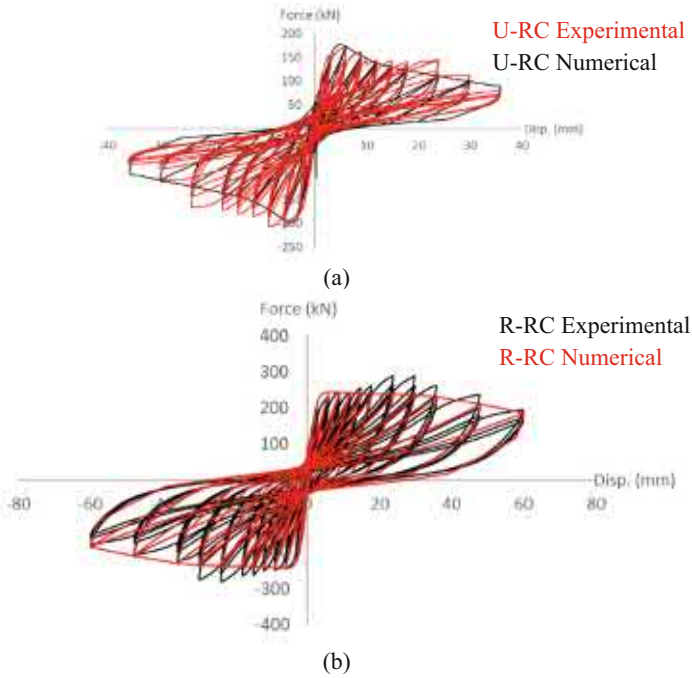


Fig. 5. Comparison between numerical cyclic and experimental results: (a) unretrofitted specimen (U-RC) and (b) retrofitted specimen with Resisto 5.9 Tube (R-RC).

Overall, the numerical model accurately reproduced the main features of the cyclic behavior, including the initial stiffness, peak lateral resistance, post-peak response, and energy dissipation capacity. In particular, the model successfully captured the progressive degradation observed during the tests while maintaining a satisfactory agreement with the experimental hysteretic loops throughout the loading history.

The reliability of the numerical model was quantitatively assessed through the Root Mean Square Error (RMSE), adopted as a measure of the agreement between experimental and numerical results. The resulting discrepancies remained within commonly accepted validation limits, with errors lower than $\pm 2\%$ for stiffness and peak strength, and below $\pm 8\%$ for cumulative dissipated energy. These results demonstrate the effectiveness of the adopted modelling assumptions and confirm the capability of the calibrated model to accurately reproduce the nonlinear cyclic response of RC frames strengthened with the Resisto 5.9 Tube system. Consequently, the proposed numerical model can be reliably employed for further nonlinear dynamic analyses and parametric investigations.

4 Conclusions

This study investigated the effectiveness of the Resisto 5.9 Tube system, a lightweight steel exoskeleton developed for the seismic retrofit of masonry-infilled reinforced concrete (RC) frames. Two full-scale specimens were tested under quasi-static cyclic loading: an unretrofitted frame (U-RC), used as a reference, and a frame strengthened with the proposed retrofit solution (R-RC).

The experimental results demonstrated the significant benefits provided by the strengthening system. Compared to the reference specimen, the retrofitted frame exhibited an increase in lateral strength of up to 77%, while the maximum displacement capacity increased by 67%. Furthermore, the displacement corresponding to peak resistance was approximately four times greater than that of the unretrofitted configuration, reaching a drift ratio of about 0.82%. Despite these improvements, the retrofit produced only a limited increase in the initial lateral stiffness, with a difference of approximately 5% between the two specimens.

The strengthened specimen also exhibited a substantial enhancement in energy dissipation capacity, with cumulative dissipated energy values up to three times greater than those recorded for the as-built frame. Overall, the experimental results confirm the effectiveness of the Resisto 5.9 Tube system in simultaneously improving strength, deformability, and seismic performance while maintaining a lightweight and externally installed retrofit configuration.

The numerical simulations performed in SAP2000 and OpenSees showed good agreement with the experimental observations. The calibrated models accurately reproduced the initial stiffness, peak strength, post-elastic response, and energy dissipation characteristics of the tested specimens. In particular, the advanced OpenSees model successfully captured the cyclic response and degradation mechanisms, with validation errors lower than $\pm 2\%$ for stiffness and peak strength and below $\pm 8\%$ for cumulative dissipated energy. These results confirm the reliability of the adopted modelling strategies and support the use of the calibrated models for future nonlinear dynamic analyses and design-oriented applications.

Acknowledgements. The seismic behavior of the Resisto 5.9 Tube system formed the basis of a research contract between the Department of Structures for Engineering and Architecture at the University of Naples Federico II (Scientific Responsible: A. Formisano) and the Progetto Sisma Srl company, whose contribution is gratefully acknowledged. The Authors would like to express their sincere gratitude to A.D. Costruzioni e Impianti Srl for the construction of the RC samples. Also, the invaluable consulting and assistance activities of Andrea Prota, Ciro Del Vecchio, Antimo Fiorillo, Emanuele Scaiella, Giovanni Manetta and Salvatore Basile in the implementation and preparation of the experimental tests are thankfully acknowledged. Finally, the financial support provided by the DPC-ReLUIS 2024–2026 research project (WP4 research line), which has been instrumental in advancing this study, is gratefully recognized.

References

1. Aïtcin PC (2000) Cements of yesterday and today: concrete of tomorrow. Cement Concrete Res 30(9):1349–1359

2. Crowley H, Despotaki V, Silva V, Dabbeek J, Romão X, Pereira N et al (2021) Model of seismic design lateral force levels for the existing reinforced concrete European building stock. Bull Earthq Eng 19:2839–2865
3. D'Amato M, Laguardia R, Di Trocchio G, Coltellacci M, Gigliotti R (2022) Seismic risk assessment for masonry buildings typologies from L'Aquila 2009 earthquake damage data. Bull Earthq Eng 26: 4545–4579.
4. Laguardia R, D'Amato M, Coltellacci M, Trocchio G, Di Gigliotti R (2023) Fragility curves and economic loss assessment of RC buildings after L'Aquila 2009 earthquake. J Bull Earthquake Eng 27:1126–1150
5. Tatangelo M, Audisio L, D'Amato M, Gigliotti R (2024) Issues related to typological fragility curves derivation starting from observed seismic damage. Eng Struct 307:117853
6. Zovkic J, Sigmund V, Guljas I (2013) Cyclic testing of a single bay reinforced concrete frames with various types of masonry infill. Earthq Eng Struct Dyn 42:1131–1149
7. Wang F, Zhao K, Zhang J, Yan K (2021) Influence of different types of infill walls on the hysteretic performance of reinforced concrete frames. Buildings 11
8. Ricci P, Di Domenico M, Verderame GM (2018) Experimental assessment of the in-plane/out-of-plane interaction in unreinforced masonry infill walls. Eng Struct 173:960–978
9. Kazem Sharbatdar M, Tajari A (2021) Experimental in-plane seismic strengthening of masonry infilled reinforced concrete frames by engineered cementitious composites (ECC). Constr Build Mater 293
10. Erol G, Karadogan HF (2016) Seismic strengthening of infilled reinforced concrete frames by CFRP. Compos Part B Eng 91:473–491
11. Kwon M, Seo H, Kim J (2017) Seismic performance of RC-frame structures with GFRP infill panels. Compos Struct 160:722–733
12. Resisto 5.9 – Progetto Sisma. https://www.progettosisma.it/prodotto/resisto-5-9/. Accessed 8 Apr 2026
13. Cavaleri L, Papia M, Macaluso G, Di Trapani F, Colajanni P (2014) Definition of diagonal Poisson's ratio and elastic modulus for infill masonry walls. Mater Struct 47:239–262
14. Cavaleri L, Di Trapani F (2015) Prediction of the additional shear action on frame members due to infills. Bull Earthq Eng 13:1425–1454

Experimental and Numerical Evaluation of an Aluminium Alloy Exoskeleton for the Seismic and Energy Retrofit of Masonry Buildings

Giovanna Longobardi and Antonio Formisano(✉)

Department of Structures for Engineering and Architecture, School of Polytechnic and Basic Sciences, University of Naples Federico II, Piazzale Tecchio 80, 80125 Naples, Italy
{giovanna.longobardi,antoform}@unina.it

Abstract. Recent seismic events have highlighted the vulnerability of existing masonry buildings, many of which were originally designed to resist gravity loads. At the same time, European initiatives have intensified efforts to reduce greenhouse gas emissions and enhance the energy efficiency of the built environment. These parallel challenges have encouraged the development of integrated retrofit strategies capable of improving structural safety and thermal performance. The MIL15.s system, developed by an Italian company, represents an innovative seismic coat for masonry buildings. The solution integrates seismic strengthening and thermal insulation in a single intervention, addressing both structural deficiencies and energy inefficiencies. The technique is based on aluminium alloy extruded profiles combined with insulated sandwich panels. This configuration improves the structural response while simultaneously reducing heat losses through opaque vertical envelope components. The effectiveness of the system was evaluated through a two-phase experimental campaign conducted on a full-scale masonry panel to investigate both out-of-plane and in-plane behaviour. In the first phase, a partial reinforcement configuration based on aluminium profiles was tested; in the second phase, the complete system was assessed. The results showed a substantial increase in strength, stiffness, and overall stability of the masonry panel. The system was then implemented in a numerical case study involving a masonry building in Italy. Nonlinear static and dynamic analyses demonstrated improvements in global behaviour and seismic safety margins, while the intervention also enhanced the thermal performance. Overall, the study confirms the potential of the system as an integrated solution for the combined seismic and energy retrofit of masonry buildings.

Keywords: Integrated Seismic-Energy Retrofit · Aluminium Alloy Exoskeletons · Masonry Buildings · Experimental Tests

© The Author(s), under exclusive license to Springer Nature Switzerland AG 2026
R. Zanon et al. (Eds.): CTA 2026, LNCE 942, pp. 669–680, 2026.
https://doi.org/10.1007/978-3-032-39505-4_58

1 Introduction

In recent years, the construction market has witnessed an increasing diffusion of innovative retrofit solutions capable of addressing two of the most critical challenges affecting the existing building stock: seismic vulnerability and inadequate energy performance. Unlike traditional strengthening systems, these integrated solutions combine both objectives within a single strategy, thereby reducing construction time, intervention invasiveness, and overall costs [1–3].

The growing interest in such solutions is strongly influenced by European policies aimed at reducing energy consumption and pollutant emissions. Improving the existing building stock is a fundamental step toward achieving decarbonization targets [4–6]. In this context, integrated seismic-energy retrofit systems represent an attractive solution, as they simultaneously improve the thermal efficiency of building envelopes and contribute to reduce seismic risk.

Beyond energy-related issues, these technologies also address the widespread seismic deficiencies characterizing a large portion of existing buildings. In particular, unreinforced masonry (URM) buildings were constructed before the introduction of modern seismic design provisions and were, therefore, designed primarily to resist gravity loads [7, 8]. Observed earthquake damage has revealed inadequate global behaviour, poor connections among structural elements, and the activation of both in-plane and out-of-plane collapse mechanisms, confirming the urgent need for effective retrofitting strategies [9–11].

Within this framework, the present study investigates the effectiveness of an innovative integrated seismic-energy retrofit system, called MIL15.s and developed by the Italian company TM Group S.r.l. [12]. The proposed solution consists of an external exoskeleton made of aluminium alloy profiles combined with thermally insulated sandwich panels. The system is designed to simultaneously enhance the seismic performance and improve the thermal efficiency of the envelope.

The effectiveness of the retrofit solution was assessed through an experimental campaign carried out on full-scale masonry specimens subjected to both in-plane and out-of-plane loading conditions. Different strengthening configurations were investigated, including a partial retrofit consisting solely of the aluminium alloy profiles and a complete configuration incorporating the entire system. Both solutions significantly improved the mechanical response of the unreinforced masonry panels, leading to substantial increases in strength, stiffness, and overall structural performance.

Building upon the experimental evidence, the study further investigated the application of the MIL15.s system to a representative case study represented by a masonry complex located in Southern Italy. The structural effectiveness of the retrofit intervention was evaluated through both nonlinear static and dynamic analyses, allowing the assessment of its influence on the global seismic response of the building. The results provided a comprehensive evaluation of the proposed technology, highlighting its potential as a multifunctional retrofit solution.

2 The Aluminium Alloy-Based MIL15.s System

The novel integrated retrofitting system, known as MIL15.s, was developed in 2022 by TM Group S.r.l., an Italian company. It is an integrated seismic-energy retrofit technology designed to simultaneously enhance the structural and thermal performance of existing buildings through the combination of an aluminium-alloy exoskeleton and thermally insulated sandwich panels.

From seismic viewpoint, depending on the foundation connection and in accordance with the Italian Technical Standards [13, 14], the intervention can be implemented either as a local strengthening measure or as a global retrofit solution. In the latter case, based on the evaluation of the safety index ζ_E, defined as the ratio between structural capacity and seismic demand in terms of peak ground acceleration (PGA), the intervention can be classified as a seismic upgrading or seismic retrofit strategy.

The exoskeleton profiles are manufactured from EN AW-6060 T6 aluminium alloy, an aluminium–magnesium–silicon alloy produced by extrusion and heat treatment. The low density, approximately one third of that of steel, reduces the additional mass applied to the existing structure, limiting the increase in seismic demand. Moreover, aluminium exhibits excellent durability in outdoor environments due to the formation of a stable oxide layer, providing corrosion resistance. From a sustainability perspective, aluminium is fully recyclable without loss of mechanical performance, reducing energy consumption and CO_2 emissions over its life cycle [15].

According to Eurocode 9 [16] and CNR/DT 208-2011 guidelines [17], the material exhibits a characteristic 0.2% proof strength ($f_{0.2}$) of approximately 150 MPa, an ultimate tensile strength (f_u) of about 190 MPa, and an ultimate strain of around 8%, ensuring adequate ductility under cyclic loading conditions. This alloy is classified as buckling class A and durability class B, confirming its suitability for long-term external applications in retrofit interventions.

A schematic representation of the system and its components is reported in Fig. 1.

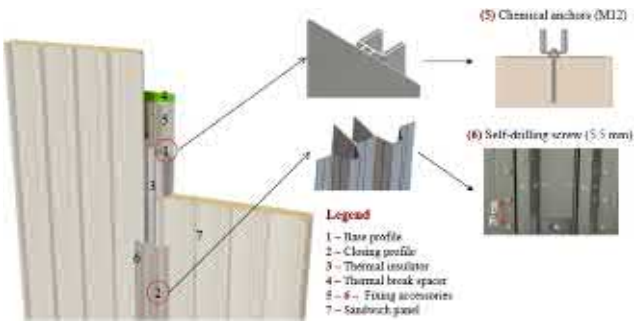


Fig. 1. Schematic view of the combined retrofitting MIL 15.s system.

According to Fig. 1, the system consists of a set of interacting elements.

The installation begins with aluminium alloy profiles (El. No. 1), which are mechanically anchored to the perimeter masonry walls using chemical anchors spaced at approximately 50 cm. The base profiles are spaced at approximately 1 m intervals, forming a

modular grid designed to accommodate the sandwich panels (El. No. 7). The sandwich panel consists of double trapezoidal steel sheeting enclosing a thermal insulation core. After panel installation, an additional thermal insulation layer (El. No. 3) is applied to improve hygrothermal performance, reduce heat transfer between components, and mitigate condensation risks at interfaces. The assembly is completed by installing aluminium closing profiles (El. No. 2), which are inserted into the base profile grooves and mechanically fastened to the external steel sheet of the sandwich panel using self-drilling screws (El. No. 6). This configuration ensures continuity of the external exoskeleton and contributes to the overall mechanical integrity of the system. Additional thermal break spacers are incorporated to reduce thermal bridging between metallic components, while different façade finishing solutions, including plastered and ventilated systems, can be adopted.

3 Experimental Campaign

3.1 Definition of the Setup

The experimental campaign was conducted at the INCERC Laboratory in Timişoara (Romania) to investigate the structural behaviour of the MIL15.s integrated retrofitting system under different loading conditions.

The testing program was organized into two distinct phases addressing both Out-of-Plane (OOP) and In-Plane (IP) responses of a full-scale masonry panel.

In Phase 1, a masonry specimen was tested under OOP loading in both as-built and partially retrofitted configurations, the latter including only the aluminium alloy profiles to assess their contribution in reinforcing the masonry panel.

In Phase 2, a similar masonry specimen was subjected to IP loading considering both unretrofitted and retrofitted configurations. In this case, the complete MIL15.s system, including aluminium profiles and sandwich panels, was installed to evaluate the full integrated response under seismic actions.

Both specimens had identical dimensions of 1.20 m in length, 2.40 m in height, and 0.40 m in thickness and were constructed by assembling two smaller masonry panels (1.20 m $\times$ 1.20 m $\times$ 0.40 m) stacked vertically and connected through a horizontal mortar joint at mid-height.

All laboratory tests were conducted under monotonic loading conditions, providing a reliable assessment of the strength, stiffness, and failure mechanisms of the proposed retrofit system. Although this testing protocol cannot fully reproduce the cyclic response under earthquake actions, it represents a widely adopted approach for a preliminary evaluation of the effectiveness of the solution.

3.2 Results of OOP and IP Laboratory Tests

The OOP experimental program was divided in two stages, involving the same full-scale masonry specimen in both unretrofitted and retrofitted scenarios.

The wall was fully restrained at the base and top to prevent translations, while a constant axial load of 100 kN was applied through a hydraulic actuator and a timber load-distribution beam. The OOP action was imposed by applying a progressively increasing

horizontal load at mid-height on the rear face of the panel using a hydraulic jack. The retrofitted configuration was obtained by installing the two vertical aluminium alloy base profiles of the MIL15.s system along the wall edges and connected to the masonry substrate using M12 chemical anchors spaced at approximately 50 cm. This partial strengthening solution was adopted to assess the contribution of the aluminium profiles only under OOP loading.

The unretrofitted specimen was subjected to a single loading–unloading cycle, reaching a maximum OOP force of 45.94 kN at a horizontal displacement of 12.59 mm. A vertical relative displacement of 3.89 mm between the two masonry sub-panels indicated the activation of a vertical bending mechanism.

The retrofitted specimen was subjected to a double loading–unloading cycle, reaching peak loads of 98.32 kN and 97.09 kN and corresponding displacements of 14.20 mm and 16.66 mm. respectively. The strengthened configuration achieved more than a 100% increase in load-carrying capacity, while maintaining a stable and ductile response.

Figure 2 compares the force–displacement curves up to the peak load. The results clearly demonstrate the beneficial contribution of aluminium profiles. Even in the absence of the complete retrofit configuration, the base exoskeleton significantly enhances the OOP resistance of the masonry panel while preserving adequate deformability. Throughout the tests, the aluminium components exhibited an elastic response, with no evidence of local buckling or plastic hinge formation.

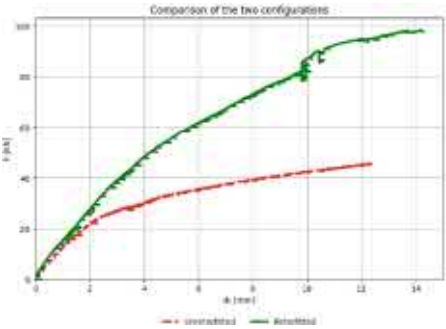


Fig. 2. Comparison of the Force-Displacement (F-d) curves of the two configurations under OOP load (**Legend**: Red Curve = Unretrofitted panel, Green Curve = Retrofitted panel).

At the end of OOP tests, the unretrofitted specimen developed a classical bending mechanism. Cracking initiated close to the mid-height section and progressively propagated through the mortar joints, leading to the formation of a global vertical bending mechanism accompanied by the relative vertical displacement between the two stacked sub-panels. Conversely, the presence of the aluminium profiles effectively restrained the opening of the cracks and limited the deformation of the wall, thus confirming the beneficial interaction between the exoskeleton and masonry substrate.

The second phase of the laboratory test was conducted on a full-scale masonry specimen with the same geometric characteristics adopted in the first phase. The structural response was investigated in unreinforced and reinforced configurations.

The specimen was rigidly restrained at the base, while a constant axial load of 25 kN was applied at the top. The IP lateral action was imposed on the side face of the wall through a hydraulic jack until failure conditions were attained. The strengthened configuration included the complete MIL15.s system, consisting of aluminium alloy base profiles anchored to the masonry through chemical anchors, sandwich panels inserted between the vertical elements, and aluminium closing profiles fixed to the external sheeting using self-drilling screws.

The unreinforced masonry panel exhibited a non-linear response with progressive stiffness degradation due to crack initiation and propagation, reaching a maximum lateral load of 11.45 kN at a corresponding displacement of 23.80 mm. The strengthened configuration reached a peak load of 26.00 kN at approximately the same displacement (24.00 mm), showing effective interaction between the aluminium exoskeleton and the masonry substrate.

Overall, the comparison between the two configurations highlights the significant improvement in structural performance provided by the MIL 15.s system, as illustrated in Fig. 3. Although the ultimate displacement remains essentially unchanged, the lateral load-carrying capacity more than doubles, demonstrating a substantial increase in strength without compromising deformability. These findings confirm the effectiveness of the proposed integrated retrofit solution in enhancing the IP behaviour of existing masonry walls through a stable and effective interaction between the aluminium exoskeleton and the masonry panel.

The unreinforced specimen exhibited the typical damage pattern of URM walls, characterized by progressive diagonal cracking and localized sliding along mortar joints. In the strengthened scenario, the exoskeleton promoted a more uniform redistribution of stress. The sandwich panels and aluminium profiles acted together as an external bracing system, limiting crack opening and delaying stiffness degradation.

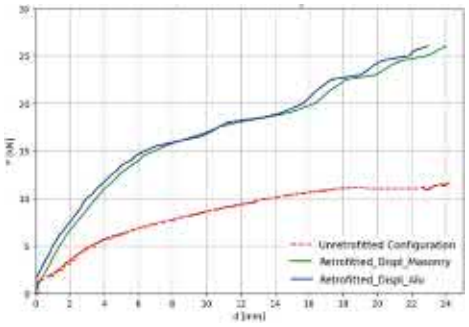


Fig. 3. Comparison of the Force-Displacement (F-d) under IP load (**Legend**: Red Curve = Unretrofitted panel; Green Curve = Masonry; Blue Curve = Aluminium alloy profiles).

Particular attention was devoted to the behaviour of the anchorage system throughout the experimental campaign. No evidence of anchor pull-out was observed during the tests. However, localized cracking developed around some of the holes drilled for the chemical anchors. These cracks remained confined to the anchorage zones and did not

compromise the effectiveness of the connection between the aluminium exoskeleton and masonry substrate.

4 Application of the MIL15.s System to a Masonry Compound

4.1 Placement and Characteristics of the Building Complex

Following the experimental campaign aimed at assessing the performance of the proposed retrofitting system, the methodology was extended to a real case study to evaluate its effectiveness on an existing building. The selected case study is located in the municipality of Campochiaro, a small historic town in the province of Campobasso, in the Molise region of southern Italy.

Building complex case study was selected and studied based on the geometric and structural data available. Its seismic performance was investigated through numerical modelling and nonlinear analyses, both before and after the application of the novel MIL15.s combined system. The selected masonry complex is articulated in six structural units (SUs), which were constructed in continuity along a sloped terrain, resulting in different internal floor elevations. SU1 and SU2 have three storeys, while the remaining units develop on two levels.

4.2 Modelling and Seismic Vulnerability Evaluation

The seismic performance of the Campochiaro masonry aggregate was investigated using a Frame by Macro-Element (FME) approach developed in the 3Muri software (Version 15.0.0.1) by the STA.DATA company [18].

The numerical model was setup assuming the lowest knowledge level (KL1), with a corresponding Confidence Factor of 1.35, in accordance with the Italian Technical Standards [13, 14]. The rough stone masonry was characterized by a tensile strength (f_m) of 2.00 N/mm^2, a shear strength of 0.035 N/mm^2, a Young's modulus (E) of 1230 N/mm^2, and a shear modulus (G) of 410 N/mm^2.

A three-dimensional view of the aggregate both before and after the arrangement of the retrofitting solution is represented in Fig. 4.



(a) (b)

Fig. 4. FME model: a) As-built configuration; b) Retrofitted Configuration.

The exoskeleton system was installed along the perimeter walls of the masonry building, ensuring the continuity of the thermal insulation layer.

The seismic vulnerability evaluation of the case study was carried out both before and after the design of the strengthening solution to provide an effective comparison and estimation of the benefits of the MIL 15.s coating system.

In the FME model, the MIL15.s system was represented as a series of externally braced frames connected to the masonry walls. In particular, while the vertical profiles of the exoskeleton were directly modelled, the sandwich panel was schematized with an equivalent diagonal using a consolidate literature approach. For each diagonal member, assumed to have a solid circular cross-section, the equivalent diameter was determined from the equivalent axial stiffness. The latter was evaluated as the inverse of the total axial deformability of the system, accounting for the contributions of both the sheeting and the fasteners.

4.3 Discussion of Results

First, nonlinear static analyses (NLSAs) were performed by applying two different lateral load distributions, while monitoring the global structural response through a control node located at the top of the structure, corresponding to its centre of mass.

The seismic capacity was evaluated through capacity curves and quantified by the α_{SLV} coefficient, defined as the ratio between the structural capacity and the seismic demand in terms of peak ground acceleration (PGA_C/PGA_D).

Additionally, Nonlinear Dynamic (NLDAs) analyses were carried out in order to achieve a comprehensive knowledge of the seismic performance of the selected case study in Campochiaro. These analyses were performed using a set of spectrum-compatible ground motion records derived from the Rexel web platform [20]. A set of seven earthquake records was considered, and, for each event, the two horizontal components of the ground motion were simultaneously applied to the numerical model, thus accounting for the bidirectional nature of the seismic excitation.

The results of the NLSAs highlighted a significant improvement in the seismic performance of the masonry building following the application of the retrofit system. In particular, the seismic safety index α_{SLV} increased by up to 11.3% and 26.7% in the X and Y directions, respectively. These improvements exceed the indicative threshold of 0.1, which, according to the Italian Technical Standards for Construction, may be considered the minimum increase required for seismic upgrading interventions.

Therefore, the upgraded model exhibited a clear increase in lateral strength and global stiffness in both principal directions, leading to higher values compared to the as-built condition, as reported in Table 1. This confirms the effectiveness of the intervention in enhancing the overall seismic safety of the masonry building compound.

Table 1. Results of the NLSAs in terms of seismic safety index.

Seismic Dir.	Seismic Load	As-Built Conf. α_{SLV}	Retrofitted Conf. α_{SLV}	Δ [%]
+X	Static Forces	0.471	0.584	11.3
−Y	Static Forces	0.361	0.628	26.7

The Base shear vs. Top Displacement capacity curves are provided in Fig. 5. They showed that, in both main directions, the curves associated with the retrofitted scenario reach higher base shear values and exhibit a steeper initial slope compared to the unretrofitted condition, indicating an improvement in both strength and stiffness of the entire structure. The increase in the initial stiffness can be attributed to the effective mechanical interaction between the external aluminium exoskeleton and the existing masonry walls. Owing to the cohesion ensured by the anchorage system, the retrofit progressively acts in combination with the masonry substrate, promoting a more efficient transfer and redistribution of the lateral forces from the early stages of loading. In particular, the retrofitted configuration can sustain higher seismic demands before reaching the same displacement levels, reflecting an overall enhancement of the global structural capacity. The improved post-elastic response is also evident, with a more gradual degradation of stiffness and a delayed attainment of peak strength, providing a more stable and controlled nonlinear behavior.

These results confirm that the retrofit intervention significantly improves the global seismic response of the structure, enhancing the initial lateral stiffness through the composite action between the aluminium exoskeleton and the masonry walls, increasing its strength, stiffness, and deformation capacity under seismic loads.

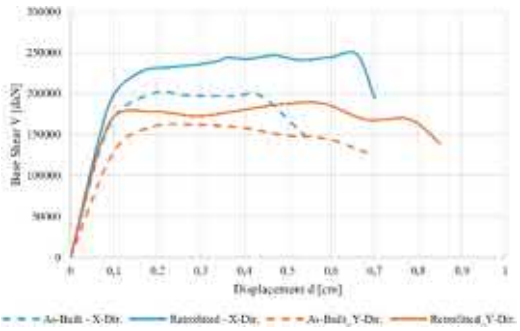
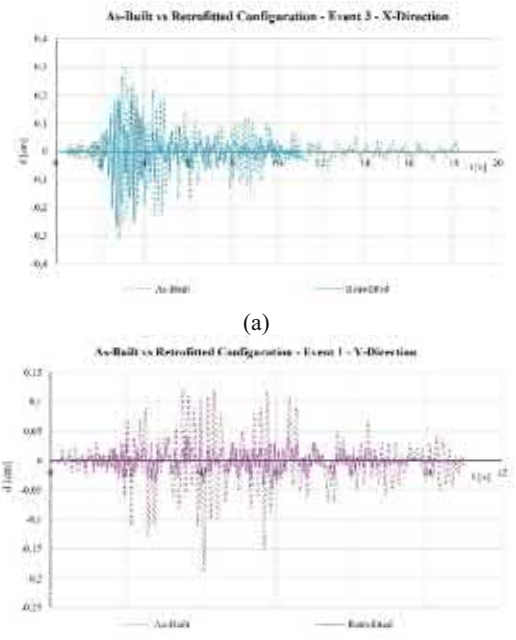


Fig. 5. Comparison among capacity curves. (**Legend**: Dotted Curves = As-Built Configuration; Continuous Curves = Retrofitted Configuration; Blue Curves = X Dir.; Orange Curves = Y Dir.).

For the NLDAs, the results corresponding to the most significant ground motion events in the X and Y directions were depicted in Fig. 6. These figures compare the displacement time histories of the as-built and retrofitted configurations considering real seismic events.

The outcomes demonstrated a clear reduction in displacement demand after the retrofit intervention. In both directions, the retrofitted model exhibited lower peak displacements and reduced oscillation amplitudes throughout the seismic event, particularly evident during the strongest phases of the ground motion.

For Event 3 in the X direction, the strengthening solution led to a noticeable decrease in the maximum displacement response and a faster attenuation of the vibrations after the main peaks. Similarly, for Event 1 in the Y direction, the retrofit significantly reduced displacement amplitudes during the intervals characterized by the highest seismic demand.



(a)

(b)

Fig. 6. Comparison of NLDAs As-Built vs. Retrofitted: a) Event 3 - X-Dir. (**Legend**: Dotted Blue Lines = As-Built Conf.; Continuous Blue Lines = Retrofitted Conf.); b) Event 1 - Y-Dir. (**Legend**: Dotted Purple Lines = As-Built Conf.; Continuous Purple Lines = Retrofitted Conf.).

This behavior can be attributed to the increase in global stiffness and lateral strength provided by the coating system, which limits deformation demand and enhances the overall dynamic response of the aggregate. Overall, the NLDAs confirmed the effectiveness of the intervention in mitigating seismic-induced displacements and improving the stability of the structural response.

The combined results of the nonlinear static and nonlinear dynamic analyses demonstrated that the proposed integrated retrofit system significantly improves the seismic behaviour of the masonry compound. The intervention enhanced both global stiffness and lateral strength, while reducing displacement demand under seismic excitation and promoting a more regular structural response. These improvements were consistently reflected in the increase of the seismic safety indices, the higher base shear capacity, and the lower displacement demands recorded during the time-history analyses.

These findings confirmed the effectiveness of the MIL15.s seismic-energy retrofit solution in improving the seismic performance of existing masonry building aggregates and mitigating the structural vulnerabilities affecting historic urban fabrics.

5 Conclusions

The present study investigated the effectiveness of the innovative MIL15.s seismic–energy retrofit system through an integrated experimental and numerical assessment. The obtained results demonstrated that the proposed solution successfully improved the structural performance of existing masonry buildings.

The experimental campaign confirmed the beneficial contribution of the aluminium exoskeleton under both out-of-plane (OOP) and in-plane (IP) loading conditions. Under OOP loading, the partial retrofit configuration more than doubled the peak resistance of the masonry panel, increasing the maximum load from 45.94 kN to 98.32 kN (+114%) while preserving adequate deformability and maintaining an essentially elastic response of the aluminium profiles. Under IP loading, the complete system increased the lateral load-bearing capacity from 11.45 kN to 26.00 kN (+127%) with virtually unchanged ultimate displacement, demonstrating an effective mechanical interaction between the metal exoskeleton and the masonry substrate.

The numerical application to a masonry building aggregate further confirmed the effectiveness of the proposed intervention. Nonlinear static analyses showed increases in the seismic safety index, α_{SLV}, of 11.3% and 26.7% in the X and Y directions, respectively, exceeding the minimum improvement generally associated with seismic upgrading interventions according to the Italian Technical Standards. Moreover, nonlinear dynamic analyses consistently showed lower displacement demands and a more stable structural response under real earthquake records.

In conclusion, the combined experimental and numerical results demonstrated that the MIL15.s system represented an effective and versatile integrated retrofit solution capable of simultaneously enhancing seismic safety, thermal efficiency, and long-term durability of existing masonry building aggregates, while promoting the use of sustainable insulation materials and minimizing the invasiveness of the intervention.

Acknowledgments. The authors gratefully acknowledge the financial support provided by the DPC–ReLUIS 2024–2026 research project (WP4 research line), which made this research possible.

The authors also gratefully acknowledge TM Group S.r.l. for its contribution to the development and production of the retrofit system presented in this study.

The authors further express their sincere gratitude to the URBAN-INCERC Laboratory in Timișoara (Romania), and to its Managing Director, Eng. Aurelian Gruin, for providing access to the facilities and equipment used during the experimental campaign. Special thanks are also extended to Prof. Marius Moșoarca, from the University of Life Sciences "King Mihai I" in Timișoara, for his invaluable advice and scientific support throughout the experimental campaign.

References

1. https://www.ea-etics.com/etics/about-etics/. Accessed 26 Jan 2026
2. Davino A, Longobardi G, Meglio E, Dallari A, Formisano A (2022) Seismic energy upgrading of an existing brick masonry building by a cold-formed steel envelope system. Buildings 12(11):1918

3. Formisano A (2022) A new seismic coating system for requalification of existing constructions. In: Mazzolani FM, Dubina D, Stratan A (eds) Proceedings of the 10th international conference on behaviour of steel structures in seismic areas (STESSA 2022), lecture notes in civil engineering, vol 262. Springer, Cham
4. European Commission. Factsheet: Energy Performance in Buildings Directive. https://energy.ec.europa.eu/topics/energy-efficiency/energy-performance-buildings/energy-performance-buildings-directive_en. Accessed 26 Jan 2026
5. European Commission (2019) The European Green Deal - Communication from the Commission to the European Parliament, the European Council, the Council, the European Economic and Social Committee, and the Committee of the Regions. European Commission, Brussels. https://eur-lex.europa.eu/legal-content/EN/TXT/?uri=CELEX:52019DC0640. Accessed 26 Jan 2026
6. European Commission. (2021). Fit for 55: Delivering the EU's 2030 Climate Target on the Way to Climate Neutrality. European Commission. https://ec.europa.eu/info/strategy/priorities-2019-2024/european-green-deal/fit-55-package_en. Accessed 26 Jan 2026
7. Caprili S, Del Carlo F, Salvadori G (2023) An enhanced system for the combined seismic and energy retrofit of masonry buildings. Procedia Struct Integrity 44:1030–1037
8. Acito M, Buzzetti M, Chesi C, Magrinelli E, Milani G (2023) Failures and damages of historical masonry structures induced by 2012 northern and 2016–17 Central Italy seismic sequences: critical issues and new perspectives towards seismic prevention. Eng Fail Ana 149:107257
9. Facconi L, Lucchini S, Minelli F, Grassi B, Pilotelli M, Plizzari GA (2021) Innovative method for seismic and energy retrofitting of masonry buildings. Sustainability 13(11):6350
10. Grillanda N, Valente M, Milani G, Chiozzi A, Tralli A (2020) Advanced numerical strategies for seismic assessment of historical masonry aggregates. Eng Struct 212:110441
11. Longobardi G, Formisano A (2021) Seismic vulnerability assessment and consolidation techniques of ancient masonry buildings: the case study of a Neapolitan Masseria. Eng Fail Ana 138:106306
12. https://www.tmgroupsrl.eu/. Accessed 30 Mar 2026
13. Ministry of Infrastructure and Transport (2018) Technical Standards for Construction; Official Gazette (nr. 42 of 20/02/2018): Rome, Italy, 2018 (In Italian)
14. Ministerial Circular n.7/2019 (2019) (M. C., 02/01/2019). Instructions for the application of the "Upgrading of Technical Codes for Constructions" (M. D: 17/01/2018). Official Gazette of the Italian Republic published on 2019 January 2nd
15. https://international-aluminium.org/. Accessed 1 Dec 2025
16. EN 1999-1-1:2003; Eurocode 9—Design of Aluminium Structures. European Committee for Standardization: Brussels, Belgium, 2005
17. CNR-DT 208/2011 (2011) Instructions for the design, execution, and control of aluminium structures. National Research Council
18. https://stadata.com/3-muri-project/. Accessed 17 Mar 2026
19. https://itaca.mi.ingv.it/ItacaNet_40/#/rexel. Accessed 2 Sep 2025

A Simplified Method for the Preliminary Assessment of the Optimal Damping Ratio of Dissipative Exoskeletons

Jana Olivo[1(✉)], Raffaele Cucuzza[2], Goffredo Orsi[1], Gabriele Bertagnoli[1], and Giuseppe Carlo Marano[2]

[1] Politecnico di Torino, Department of Structural, Geotechnical and Building Engineering, Corso Duca degli Abruzzi, 24, Turin 10128, Italy
jana.olivo@polito.it

[2] School of Civil Engineering and Architecture,Henan University of Technology,Zhengzhou, Henan 450001, PR China

Abstract. Steel exoskeletons have emerged as an effective solution for the seismic retrofit of existing buildings, particularly for strategic facilities where rapid, non-invasive interventions are required. When equipped with dissipative devices, these systems can reduce seismic demand through energy dissipation rather than stiffness increase alone, potentially leading to more efficient and economical designs. However, the preliminary design of dissipative exoskeletons remains complex, mainly due to the nonlinear behavior of damping devices and the high computational effort associated with nonlinear dynamic analyses. This study proposes an automated optimization framework for the preliminary design of dissipative steel exoskeletons. A simplified methodology is adopted to correlate the nonlinear damping coefficient of fluid-viscous dampers with an equivalent damping ratio used in linear dynamic analyses, allowing the replacement of nonlinear time-history simulations with spectrum-based analyses. This approach drastically reduces computational time, making it suitable for optimization purposes. A Genetic Algorithm is implemented to determine the optimal exoskeleton layout, member sizing, and damping capacity by minimizing the total intervention cost under drift and strength constraints. The results demonstrate that maximizing the dissipative contribution while reducing steel consumption leads to the most cost-effective solution, satisfying all performance requirements. The proposed framework provides a practical and computationally efficient tool for the early-stage design of dissipative exoskeleton retrofits.

Keywords: Dissipative Exoskeletons · Structural Optimization · Seismic Retrofit · Fluid-Viscous Dampers · Genetic Algorithm

1 Introduction

A large portion of the European building stock was constructed before the introduction of modern seismic regulations and therefore does not satisfy current

© The Author(s), under exclusive license to Springer Nature Switzerland AG 2026
R. Zanon et al. (Eds.): CTA 2026, LNCE 942, pp. 681–689, 2026.
https://doi.org/10.1007/978-3-032-39505-4_59

safety requirements. This condition is particularly critical for strategic and operational facilities in seismic areas, where retrofit interventions must ensure structural safety while limiting downtime and disruption. Consequently, the development of effective, rapid, and minimally invasive strengthening solutions has become a key issue in seismic engineering [6].

Steel exoskeletons represent a promising strategy in this context. They consist of steel frames installed outside the existing building and connected to it, forming a coupled system [14]. Being applied from the exterior, they allow construction with limited interference to internal activities, making them especially suitable for hospitals, airports, and strategic buildings that must remain operational [11]. Key advantages of these systems regard modularity, dry construction, potential reversibility, and compatibility with façade and energy upgrades [5,9,18].

Exoskeletons can be classified as rigid (non-dissipative) or dissipative systems [19]. Rigid exoskeletons improve seismic performance mainly by increasing the global lateral stiffness of the coupled structure [1,3]. Owing to the stiffness difference between the existing building and the external frame, a significant portion of seismic forces is attracted by the exoskeleton, reducing demand on the original structural members [13,16]. While this approach can achieve significant performance improvements, it often requires large steel sections and may lead to increased base shear and foundation demands [20].

Dissipative exoskeletons, instead, combine the external steel frame with localized energy dissipation devices, such as hysteretic or fluid-viscous dampers [10]. In this case, seismic demand is reduced by increasing the equivalent damping of the system rather than by stiffness alone [2]. This mechanism may allow smaller steel sections and improved reparability, as dissipation is concentrated in replaceable components [12]. However, the presence of nonlinear devices introduces design complexity and raises the issue of identifying an optimal balance between structural performance and intervention cost.

Despite growing interest in exoskeleton-based retrofits, efficient procedures for the preliminary design of dissipative configurations remain limited. The main difficulty lies in accounting for the nonlinear behavior of dampers while exploring multiple design alternatives, as required in optimization-based approaches. Performing nonlinear dynamic analyses for each candidate solution would entail prohibitive computational costs.

To address this challenge, the present study proposes a simplified and automated framework for the preliminary design of dissipative steel exoskeletons equipped with fluid-viscous dampers. A Genetic Algorithm is employed to optimize the placement, sizing, and dissipative capacity of the exoskeletons. To ensure computational efficiency, candidate solutions are evaluated through linear dynamic analyses, introducing a correlation between the nonlinear dissipation coefficient of the devices and an equivalent damping ratio used in the linear model. In this way, the nonlinear contribution of the dampers is incorporated indirectly, avoiding time-history analyses while maintaining acceptable accuracy in estimating the global seismic response.

2 Simplified Approach for Damping Coefficient Assessment

The optimization strategy adopted in this work requires the evaluation of a large number of structural configurations, and computational efficiency becomes essential. The procedure proposed by Palermo et al., 2018 [17] establishes a direct correlation between the nonlinear damping coefficient of fluid-viscous dampers (C_{NL}) and the response reduction factor $\bar{\eta}$, used to scale the elastic spectrum. This relationship allows the nonlinear dissipative behavior to be represented through an equivalent damping ratio in linear dynamic analyses, avoiding nonlinear time-history simulations while maintaining adequate accuracy.

The method is applicable to buildings with a fundamental period $T_1 < 1.5s$, regular in plan and elevation, and with dampers uniformly distributed along the height, having identical properties at each storey. These assumptions are consistent with the preliminary design stage addressed in this study.

The method begins with the definition of a target percentage reduction x of the seismic demand. This corresponds to a response reduction factor $\bar{\eta}$, and a target total damping ratio as expressed in Eq. 1. Subsequently, assuming an intrinsic structural damping $\xi_{\text{intr}} = 5\%$, the viscous contribution required from the devices $\bar{\xi}_{\text{visc}}$ can be identified. This value was determined through the optimization process described in the next section and can vary from 0% to 23%.

$$\bar{\eta} = 1 - \frac{x}{100} \quad ; \quad \bar{\xi}_{\text{tot}} = \xi_{\text{intr}} + \bar{\xi}_{\text{visc}} = \frac{10}{\bar{\eta}^2} - 5 \quad ; \quad \bar{\xi}_{\text{visc}} = \frac{10}{\bar{\eta}^2} - 10 \tag{1}$$

Under the initial assumption of linear viscous behavior ($F = C_L.v$), the equivalent damping coefficient and maximum force per device are:

$$C_L = \bar{\xi}_{\text{visc}} \cdot \omega_1 \cdot \frac{W}{g} \left(\frac{N+1}{n} \right) \cdot \frac{1}{\cos^2 \theta} \quad ; \quad F_{L,\max} = 2 \cdot \bar{\xi}_{\text{visc}} \cdot \frac{W}{g} \cdot S_e(T_1, \bar{\eta}) \cdot \frac{1}{n \cdot \cos \theta} \tag{2}$$

where W is the total seismic weight, ω_1 the fundamental circular frequency, N the number of storeys, n the number of dampers per storey, and θ their inclination. $S_e(T_1, \bar{\eta})$ denotes the reduced elastic spectral ordinate at the fundamental period.

For nonlinear velocity-dependent devices, the equivalent coefficient and associated maximum force are obtained through an energy-based criterion, where α is the damping exponent (typically 0.150.30):

$$C_{NL} = C_L \cdot (0.8 \cdot v_{\max})^{1-\alpha} \quad ; \quad F_{NL,\max} = 0.8^{1-\alpha} \cdot F_{L,\max} \tag{3}$$

3 Optimization Tool for the Design of Dissipative Exoskeletons

An optimization framework is developed to identify the cost-optimal retrofit solution using dissipative exoskeletons. The vector of design variables (DVs), defined in Eq. 4, includes three groups: topology, size, and damping variables.

Topology DVs are binary variables that define the number and location of exoskeletons. A value equal to 1 activates an exoskeleton in a given position, whereas 0 leaves the location empty. Size DVs select the steel sections of the exoskeleton members from a set of 150 standard Circular Hollow Sections. Finally, the damping ratio ξ is introduced as a discrete variable. Through the simplified procedure described earlier, it determines the nonlinear damping coefficient C_{NL} of the fluid-viscous dampers. The total damping ratio ξ, used as a design variable, can range from 5% to 28% in accordance with Italian code NTC18 [4] (Sect. 3.2.3.2 and Sect. 7.5). It consists of 5% intrinsic structural damping (ξ_{intr}) and an additional viscous contribution from the devices ($\bar{\xi}_{visc}$) of up to 23%.

$$\mathbf{x} = [\overbrace{x_1 , \dots , x_i , \dots , x_n}^{\text{Topology DVs}}, \overbrace{x_{n+1} , \dots , x_{n+j} , \dots , x_{n+m}}^{\text{Size DVs}} , \xi] \quad (4)$$

The objective function (OF), expressed in monetary terms, represents the total retrofit cost (Eq. 5). It includes the cost of the exoskeletons' steel and the cost of the dissipative devices. The cost of steel, C_{EX}, is computed from the total weight of the exoskeletons, while the dampers' cost, C_{FVD}, is estimated using the empirical formulation proposed in [8].

$$\text{OF} = (C_{\text{EX}} + C_{\text{FVD}})\,\phi_1\,\phi_2 + \phi_3 \;\; ; \;\; C_{\text{EX}} = W_{\text{EX}} \cdot c_{\text{steel}} \;\; ; \;\; C_{\text{FVD}} = 96.88 \cdot F_{\text{NLmax}}^{0.607} \quad (5)$$

where W_{EX} is the total steel weight, $c_{\text{steel}} = 1.9\$/kg$ is the unit steel cost, and F_{NLmax} is the maximum force in the nonlinear dampers.

Design constraints are incorporated through penalty factors. The first penalty term (ϕ_1) limits the maximum storey drift to $H/600$, a threshold associated with negligible damage according to Ghobarah, 2004 [7]. The second penalty (ϕ_2) ensures compliance of exoskeleton members with Eurocode 3 verifications. The third term (ϕ_3) penalizes solutions with a larger number of exoskeletons, promoting more efficient layouts.

The optimization problem is solved using the Genetic Algorithm proposed by Olivo et al., 2024 [15], specifically adapted for structural optimization problems involving topology and size variables, such as the present design problem. For this study, the optimization was set with populations of 100 individuals and 180 iterations per run, encompassing a total of 26 design variables.

4 Case Study

The reference structure is a three-floor reinforced concrete building with a square plan (Fig. 1a), characterized by a storey height of 4 meters and a bay length of 5 meters. The building is located in L'Aquila, Italy, and vertical and seismic loads are defined in accordance with Eurocode provisions.

At the Ultimate Limit State, the structure satisfies all verifications under gravity loads. However, seismic checks are not fulfilled, with a mean Demand-to-Capacity Ratio (DCR) among all the RC elements around 2 and a maximum of 2.87, thus requiring a retrofit intervention.

The proposed retrofit solution consists of steel exoskeletons arranged orthogonally to the building façades and rigidly connected to the existing structure at beamcolumn joints. Each exoskeleton is equipped along one diagonal at each level with a fluid-viscous damper. All potential exoskeleton locations considered in the optimization process are shown in Fig. 1b.

Member sections are selected through the optimization process from a catalogue of standard Circular Hollow Sections (CHS). Nine size variables define the cross-sections of beams, columns, and braces within each exoskeleton (Fig. 1c). For a given configuration, all exoskeletons share identical sectional properties.

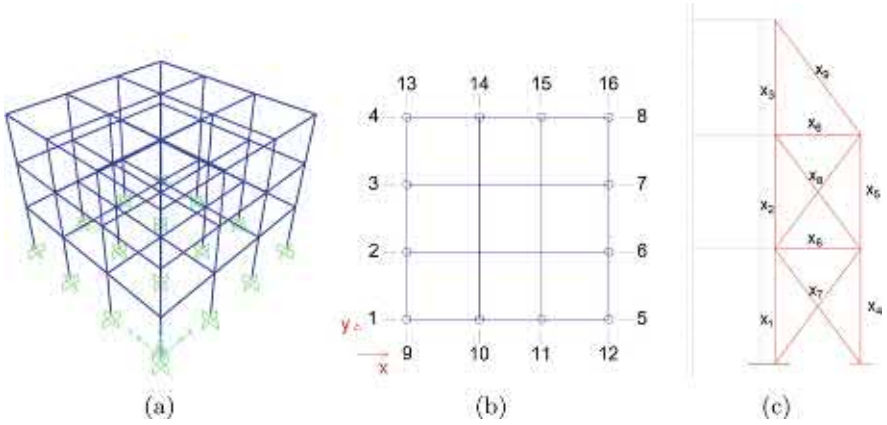


Fig. 1. Design variables in terms of feasible dissipative steel exoskeletons positions

During the optimization phase, energy dissipation is represented indirectly by increasing the global damping ratio, while diagonal braces are modeled as rigid elements. This simplification is necessary because the linear dynamic analyses employed in the optimization framework do not allow explicit modeling of nonlinear dampers. Once the optimal configuration is identified, the equivalent damping ratio (ξ) is converted into the corresponding nonlinear damping coefficient (C_{NL}) according to the relationships presented in Sect. 2, enabling explicit modeling of the dissipative devices for final assessment.

5 Results and Discussion

The optimal retrofit configuration identified by the optimization algorithm is illustrated in Fig. 2, while the corresponding optimal CHS sections for the

exoskeleton members are summarized in Table 1, for the Size DVs illustrated in Fig. 1c. The solution is characterized by an optimal equivalent damping ratio $\xi = 27\%$, very close to the upper bound imposed in the optimization of 28%.

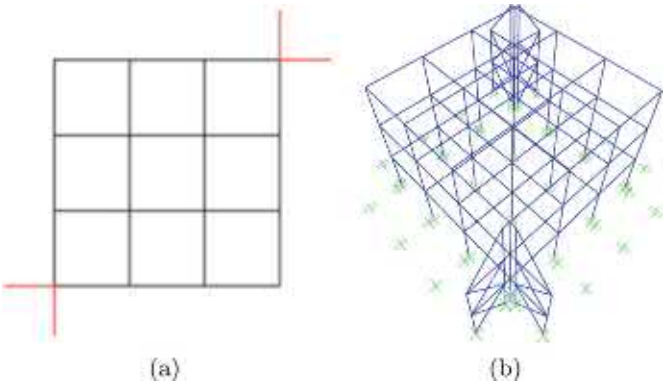


Fig. 2. Optimal layout and sizing optimization of dissipative steel exoskeleton

Table 1. Design variable outputs of the optimization process and associated costs of the exoskeletons (C_{opt}^{Steel}) and dampers ($C_{opt}^{Dampers}$).

$Variable$	x_1	x_2	x_3	x_4	x_5	x_6	x_7	x_8	x_9	ξ
$\phi_e[mm]$	406.4	273.0	244.5	406.4	323.9	177.8	168.3	244.5	273.0	27 %
$s[mm]$	30.0	25.0	14.2	30.0	14.2	10.0	8.0	14.2	14.2	
$Area[cm^2]$	354.8	194.8	102.7	354.8	138.16	52.7	40.3	102.7	115.5	

C_{opt}^{Steel}	$C_{opt}^{Dampers}$	C_{opt}^{Total}
€ 42.445	€ 57.973	€ 97.418

The total intervention cost amounts to € 97.418, including € 42.445 for the exoskeleton steel and € 57.973 for the fluid-viscous dampers, as presented in Table 1. Although the damper cost is higher than in alternative configurations explored during the optimization, the required steel weight is significantly reduced. The algorithm identified this balance—maximizing damping while minimizing steel consumption—as the most cost-effective solution. Configurations with lower damping required heavier steel sections to satisfy drift and strength constraints, resulting in higher overall costs.

From a performance standpoint, the optimal configuration satisfies all imposed constraints. The maximum storey drift is limited to the prescribed

threshold of $H/600$, and all structural verifications are fulfilled for both the exoskeleton members and the existing reinforced concrete elements. The base shear was reduced from 3910 kN in the original building to 1627 kN in the retrofitted configuration.

By applying the procedure described in Sect. 2, the equivalent damping ratio was translated into the mechanical parameters of the fluid-viscous dampers. The resulting nonlinear damping coefficient is $C_{NL} = 806$, with a corresponding maximum force demand of $F_{NL,\max} = 574kN$ per device.

Overall, the results highlight that, within the explored design space, increasing the dissipative contribution proved more economically advantageous than relying on additional steel stiffness. The optimizer consistently favored solutions with higher damping capacity and reduced structural mass, confirming the effectiveness of dissipative exoskeletons in achieving both technical compliance and cost minimization.

6 Conclusions and Future Developments

This study was aimed at addressing the lack of computationally efficient procedures for the preliminary design of dissipative steel exoskeletons. A simplified methodology was adopted to correlate the nonlinear mechanical properties of fluid-viscous dampers with an equivalent damping ratio used in linear dynamic analyses. This approach allowed the replacement of nonlinear time-history simulations with linear dynamic analyses with response spectrum. Such simplification proved essential for enabling the large number of structural evaluations required within an optimization framework.

Building upon this formulation, a Genetic Algorithm was implemented to optimize exoskeleton layout in plan, member sizing, and damping capacity, to minimize the total intervention cost. For the considered structure, the cost-optimal configuration resulted from increasing the dissipative contribution while reducing steel weight. The resulting design satisfied all drift and strength constraints, confirming the technical feasibility of the approach. Overall, the proposed framework provides a practical and automated tool for the early-stage design of dissipative exoskeletons, offering clear advantages in terms of computational efficiency, economic optimization, and structural performance.

Future developments will focus on two main aspects. First, a systematic comparison between the optimal dissipative configuration and alternative solutions based on rigid (non-dissipative) exoskeletons will be carried out, in order to quantitatively assess the relative advantages in terms of structural performance, material consumption, and overall intervention cost. Second, the simplified damping formulation adopted in this study will be validated through nonlinear time-history analyses of the optimal configurations. Such analyses will allow a direct evaluation of the accuracy and applicability limits of the proposed approach, further strengthening its reliability for preliminary design purposes.

References

1. Cucuzza R, Olivo J, Bertagnoli G, Ferro GA, Marano GC (2025) Performance-based optimization of steel exoskeletons: an alternative approach to standard regulations. J. Building Eng. 104:112177
2. Lorenzo, D., Colacurcio, G., Di Filippo, E., Formisano, A., Massimilla, A., Landolfo, A.R.: State-of-the-art on steel exoskeletons for seismic retrofit of existing RC buildings. Int. J. **37**(1) (2020)
3. Di Lorenzo, G., Tartaglia, R., Prota, A., Landolfo, R.: Design procedure for orthogonal steel exoskeleton structures for seismic strengthening. Eng. Struct. **275**, 115252 (2023)
4. DM17/01/2018: Aggiornamento delle "Norme tecniche per le costruzioni". Italian Ministry of Infrastructures and Transportation, Rome, Italy (2018), in Italian
5. D'Agostino, D., et al.: Steel exoskeletons for integrated seismic/energy retrofit of existing buildings-general framework and case study. J. Building Eng. **83**, 108413 (2024)
6. Formisano, A., Galano, S., Meglio, E., Del Vecchio, C., Prota, A.: Experimental investigation on innovative lightweight steel exoskeleton for seismic resilience of masonry-infilled reinforced concrete frames. Eng. Struct. **344**, 121410 (2025)
7. Ghobarah, A.: On drift limits associated with different damage levels. In: International workshop on performance-based seismic design, vol. 28, pp. 321–332. Department of Civil Engineering, McMaster University Ontario, Canada (2004)
8. Gidaris, I., Taflanidis, A.A.: Performance assessment and optimization of fluid viscous dampers through life-cycle cost criteria and comparison to alternative design approaches. Bull. Earthq. Eng. **13**(4), 1003–1028 (2015)
9. Marini, A., et al.: Combining seismic retrofit with energy refurbishment for the sustainable renovation of RC buildings: a proof of concept. Eur. J. Environ. Civ. Eng. **26**(7), 2475–2495 (2022)
10. Mazza F (2021) Dissipative steel exoskeletons for the seismic control of reinforced concrete framed buildings. Struct. Control Health Monit. 28(3):e2683
11. Meglio, E., Formisano, A.: Design and modelling strategy for cold-formed steel exoskeletons for the seismic-energy retrofit of reinforced concrete structures. In: Structures, vol. 69, Dp. 107502. Elsevier (2024)
12. Mottola S, Pecorari O, Ferraioli M (2026) Seismic retrofit of RC structures using performance-spectra design of dissipative exoskeletons. Procedia Struct. Integrity 78:623–630
13. Nigro, F., Corte, G.D., Martinelli, E.: Assessment of alternative design approaches for seismic upgrading of RC frame structures with steel exoskeletons. Eng. Struct. **305**, 117623 (2024)
14. Olivo, J., et al.: Steel exoskeletons for the seismic retrofit of an existing RC building: Optimal design and life cycle assessment. In: International Conference on Resilience, Earthquake Eng. Struct. Health Monit. pp 214–225. Springer (2024)
15. Olivo J, Cucuzza R, Bertagnoli G, Domaneschi M (2024) Optimal design of steel exoskeleton for the retrofitting of RC buildings via genetic algorithm. Comput. Struct. 299:107396
16. Olivo, J., et al.: Stiffness ratio evaluation of steel exoskeletons through performance-based optimal design. In: Material Strength and Applied Mechanics, pp. 438–445. IOS Press (2024)
17. Palermo, M., Silvestri, S., Landi, L., Gasparini, G., Trombetti, T.: A "direct five-step procedure" for the preliminary seismic design of buildings with added viscous dampers. Eng. Struct. **173**, 933–950 (2018)

18. Passoni C, Caruso M, Marini A, Pinho R, Landolfo R (2022) The role of life cycle structural engineering in the transition towards a sustainable building renovation: available tools and research needs. Buildings 12(8):1107
19. Passoni, C., Guo, J., Christopoulos, C., Marini, A., Riva, P.: Design of dissipative and elastic high-strength exoskeleton solutions for sustainable seismic upgrades of existing RC buildings. Eng Struct **221**, 111057 (2020)
20. Reggio, A., Restuccia, L., Martelli, L., Ferro, G.A.: Seismic performance of exoskeleton structures. Eng. Struct. **198**, 109459 (2019)

Seismic Retrofit of RC Buildings Using Self-centering Friction-Damped Steel Exoskeletons Based on P-Spectra Design Methodology

Salvatore Mottola[1(✉)], Annarosa Lettieri[2], Massimiliano Ferraioli[1], and Atsushi Sato[2]

[1] University of Campania "Luigi Vanvitelli", Aversa, Italy
Salvatore.mottola@unicampania.it
[2] School of Engineering, Nagoya Institute of Technology, Nagoya, Japan

Abstract. Existing Reinforced Concrete (RC) buildings designed according to older seismic codes often exhibit inadequate lateral strength and poor deformation capacity, making them particularly vulnerable during strong earthquakes. Modern retrofitting strategies aim not only to limit structural damage by including dissipative components but also to control residual drifts, a key indicator for post-earthquake reparability and rapid functionality recovery. This study investigates the seismic retrofit of an existing RC frame structure through an exoskeleton, equipped with self-centering friction-damped devices. A three-story benchmark RC school building is adopted as a case study and retrofitted with the proposed technology. Performance-Spectra (P-Spectra) approaches are used to design the retrofit intervention, while establishing a direct relationship between target mechanical properties of self-centering exoskeletons, and ensuring a performance-driven design process. Non-linear time history analyses are performed by considering the adopted case study with and without the exoskeleton retrofit intervention and used to assess their seismic response under a compatible set of ground motion. The results highlighted the effectiveness of self-centering exoskeletons and the proposed design methodology in delivering resilient seismic performance while reducing functional disruption.

Keywords: Performance-Spectra-Based Design · Steel Exoskeletons · Self-Centering systems · Seismic Retrofit · Seismic Resilience

1 Introduction

A large portion of RC buildings in Europe was built before the adoption of modern seismic codes [1, 2], leaving many existing structures seismically vulnerable. In recent decades, seismic retrofit of such RC buildings through internal (endoskeleton) or external (exoskeleton) additive systems is increasingly adopted as effective strategy for enhancing their seismic performance [3]. Exoskeletons consist of steel frames placed outside the

© The Author(s), under exclusive license to Springer Nature Switzerland AG 2026
R. Zanon et al. (Eds.): CTA 2026, LNCE 942, pp. 690–701, 2026.
https://doi.org/10.1007/978-3-032-39505-4_60

existing RC structure, connected at beam-column joints and supported by independent foundations. The installation of exoskeletons in existing RC buildings aims to enhance the structural safety level by increasing global stiffness and lateral resistance without altering interior spaces or significantly disrupting occupants. In addition, applications to real RC buildings [4–7] show that integrating energy-dissipating devices in steel exoskeleton can substantially reduce inter-story drifts and floor accelerations, which are closely linked to structural and nonstructural damage. Energy dissipation devices concentrate inelastic deformations within replaceable components, thereby confining seismic damage to sacrificial elements that can be readily inspected and replaced after a strong earthquake [8, 9]. When integrated into exoskeleton systems, such devices enable damage to be confined outside the existing structure. Although these systems effectively reduce the seismic demand on RC buildings, they provide no control over residual deformations, which may compromise the post-earthquake reparability and functionality of the building [10]. To address these limitations, considerable research has focused on the development of low-damage self-centering systems capable of combining efficient energy dissipation with restoring mechanisms [11, 12]. Within this context, Lettieri et al. [13] proposed a Self-Centering link (SC-link) consisting of a pinned device positioned between beams and equipped with post-tensioned high-strength steel bars and disk springs to generate restoring forces, while friction devices provide energy dissipation.

In the present study, a seismic retrofit methodology is developed for RC buildings using an innovative steel exoskeleton equipped with the SC link proposed by Lettieri et al. [13]. The seismic design is based on Performance Spectra (P-Spectra) which allow to directly relate target performance levels (defined in terms of both acceleration and displacement) to the mechanical properties of the SC link. The methodology is applied to a three-story RC school building, providing a realistic context for assessing the effectiveness of the exoskeleton equipped with SC link and illustrating its ability to reduce peak and residual drifts and the influence of torsional effects in irregular structures.

2 Performance Spectra-Based Design Methodology

2.1 Conceptual Decomposition of the Retrofitted Structure

Figure 1 shows the retrofitted system (*SE*). It consists of the bare frame (*S*) and the exoskeletons (*E*), that behaves as a dual system in which both components resist the horizontal actions induced by earthquakes.

For the purposes of applying the proposed design procedure, the Multi Degree of Freedom (MDOF) structures are reduced to equivalent Single Degree of Freedom (SDOF) systems, as shown in Fig. 2. This simplification is similarly adopted in other seismic design methodologies, such as displacement-based design (DBD).

2.2 P-Spectra

P-Spectra are graphical representation of the response of inelastic SDOF systems in terms of peak and residual displacements, as well as acceleration [14]. In this framework, P-Spectra are used to represent the response of the retrofitted structure (*SE*) by

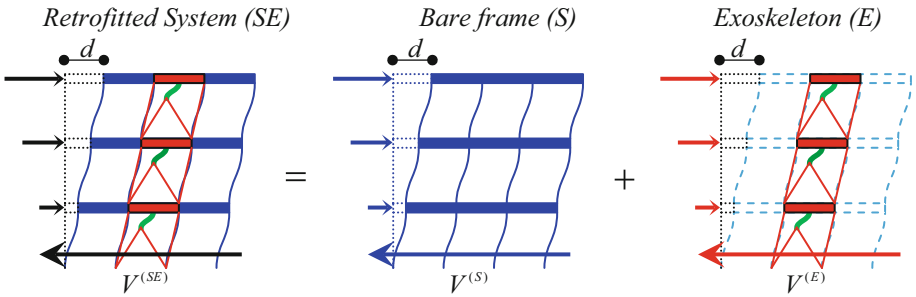


Fig. 1. Decomposition of the retrofitted system into bare frame (*S*) and exoskeleton (*E*).

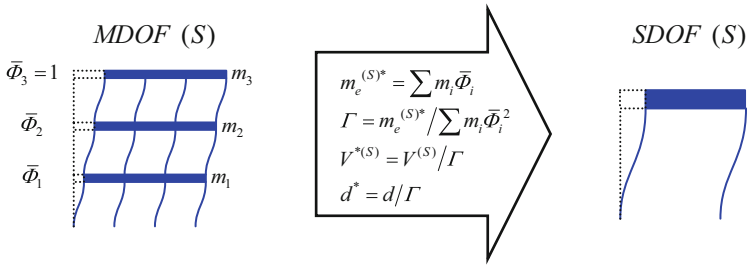


Fig. 2. Procedure for reducing an MDOF system into an equivalent SDOF system.

fixing the properties of the bare frame (*S*), while modifying the characteristics of the retrofit intervention (*E*) in terms of stiffness and strength. In this way, P-Spectra enable direct comparison and selection of alternative retrofit strategies that satisfy prescribed performance objectives, without the need for a full iterative design process. The P-Spectra are obtained from nonlinear time-history analyses (NLTHA) performed on an equivalent SDOF model composed of two parallel nonlinear springs. The first spring represents the bare frame (*S*), characterized by a trilinear Takeda hysteretic behavior [15], while the second spring represents the exoskeleton (*E*), modeled using an elastic-perfectly plastic law (Fig. 3a). The P-Spectra are built by varying the stiffness ratio α, and the ductility of the exoskeleton $\mu^{(E)}$, and deriving three performance parameters: the normalized maximum response factors for displacement and acceleration (R_d and R_a, respectively), and the normalized residual displacement response factor R_s.

The stiffness ratio is quantified as follows:

$$\alpha = K_0^{(S)} / \left(K_0^{(S)} + K_0^{(E)} \right) \tag{1}$$

where ${K_0}^{(S)}$ is the relative stiffness of the structure and ${K_0}^{(S)} + {K_0}^{(E)}$ is the stiffness of the system including the exoskeleton.

R_d, and R_a, are defined as the ratios of the peak responses of the combined system to those of an elastic system with the same natural period ${T_0}^{(S)}$ and damping ${\xi_v}^{(S)}$, as expressed below:

$$R_d = D^{*(SE)} / S_d \left({T_0}^{(S)}; {\xi_v}^{(S)} \right) \tag{2}$$

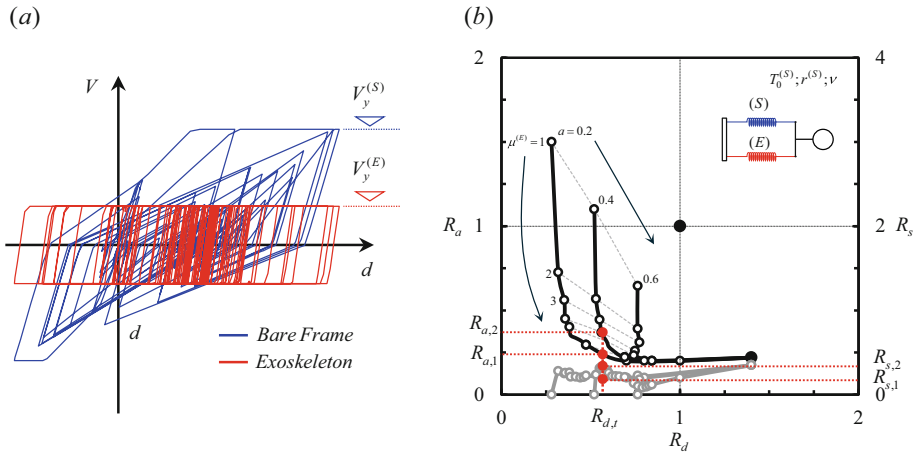


Fig. 3. (a) NLTH Analysis for an elastic perfectly plastic Exoskeleton; (b) P-spectra.

$$R_a = A^{*(SE)}/S_a\left(T_0{}^{(S)};\, \xi_v{}^{(S)}\right) \tag{3}$$

where $D^{*(SE)}$ is the peak relative displacement and $A^{*(SE)}$ is peak absolute acceleration, from which the base shear $V^{*(SE)}$ can be derived, of the equivalent SDOF system corresponding to the retrofitted MDOF (*SE*). The values $S_d(T_0{}^{(S)};\, \xi_v{}^{(S)})$ and $S_a(T_0{}^{(S)};\, \xi_v{}^{(S)})$ denote the spectral displacement and spectral acceleration, respectively, evaluated at the fundamental period $T_0{}^{(S)}$ of the structure and damping ratio $\xi_0{}^{(S)}$ of the existing structure. Finally, R_s is defined as:

$$R_s = D_R^{*(SE)}/D^{*(SE)} \tag{4}$$

where $D_R{}^{*(SE)}$ denotes the displacement corresponding to the intersection of the reloading branch with the horizontal axis.

Figure 3b illustrates the performance spectra for an initial structure characterized by the initial period $T_0{}^{(S)}$, the damping ratio $\xi_v{}^{(S)}$, and the normalized strength $v_y{}^{(S)}$, defined as the ratio between the peak strength $V_y{}^{*(S)}$ and the elastic base shear $m_e{}^{(S)*} \cdot S_a(T_0{}^{(S)};\, \xi_v{}^{(S)})$, and for an exoskeleton characterized by an elastic-perfectly plastic behavior, under a given seismic input. The bold black curves identify systems with the same stiffness ratio α, while the grey dashed lines represent systems with the same ductility $\mu^{(E)}$. The gray curves, on the other hand, represent the R_s factor plotted on the secondary axis, which is always less than unity. In general, R_d is mainly governed by the stiffness ratio α, while R_a is primarily influenced by the ductility $\mu^{(E)}$.

The supplemental damping properties required for the MDOF system are then determined via a direct transformation procedure, enabling an MDOF structure to reproduce the response of the reference SDOF system.

3 Self-Centering Friction-Damped Exoskeleton

The design methodology described in Sect. 2 is applied to retrofit an existing RC building with a steel eccentrically braced frames (EBF) exoskeleton equipped with SC links [13]. Figure 4a shows a representative one-story frame of the exoskeleton equipped with the SC link. In this arrangement, the lateral deformation of the system results from the combined contribution of the elastic brace deformation and the additional displacement provided by the SC-link once activated. Since the device and the braces are arranged in series, the total displacement, D, is given by the sum of these two components. Figure 4b illustrates the hysteretic response of the one-story steel frame equipped with the SC-link, highlighting the transition from the initial elastic behavior of the braces to the activation of the device. Upon activation, the SC-link governs the force–deformation response and provides both energy dissipation and a self-centering contribution that limits residual displacements.

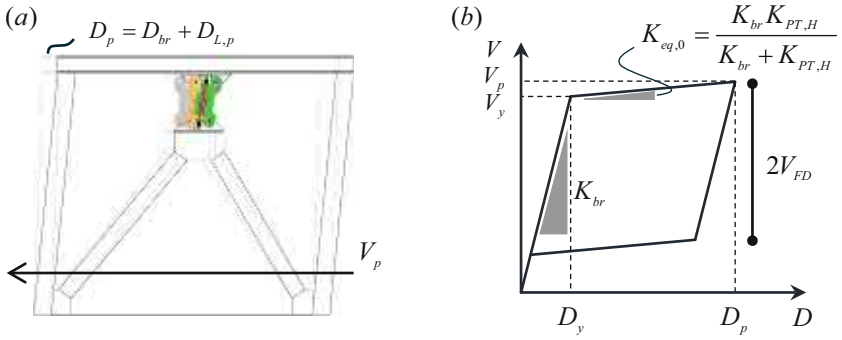


Fig. 4. (a) Friction-damped self-centering one story EBF; (b) Hysteretic behavior.

3.1 Hysteretic Behavior of the SC-Link

Figure 5 illustrates the adopted SC link. Specifically, Fig. 5a shows the forces acting in the SC link, Fig. 5b displays the deformed configuration, while its cyclic response is provided in Fig. 5c. The SC link include friction devices (FD) to dissipate the input seismic energy and post-tensioned high strength bars with disk springs to provide a self-centering mechanism. The SC link cross section consists of T- and L-plates arranged to form an I shaped steel profile. The dissipative mechanism of the SC link is governed by a shear deformation mechanism activated during by the rotation of the SC link, which involves the relative longitudinal sliding (δ_L) between the T- and L-elements. The SC link simultaneously activates the slippage in the FDs and increases the axial force in the PT-bars.

It is noteworthy that compared to the original configuration proposed by Lettieri et al. [13], the SC-link adopted in this study is placed in the vertical direction. This arrangement does not affect the device behavior, since the shear mechanism governing the link response remains unchanged.

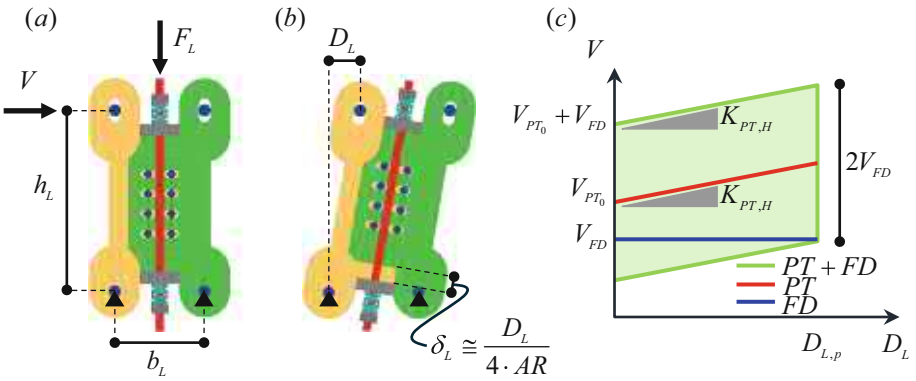


Fig. 5. (a) Schematic of force components; (b) deformed configuration; (c) hysteretic response.

4 Seismic Retrofit of a Real Case-Study Building

To validate the proposed design procedure, an existing L-shaped school building located in a high-seismicity area (Vibo Valentia, Calabria) was selected as case study. A numerical model of the existing structure was developed in SeismoStruct [16], following the modelling assumptions described in [4]. The same building was previously investigated in reference [4], with a seismic retrofit based on steel hysteretic braced frame (HBF) exoskeleton. Figure 6 shows the pushover curves corresponding to the modal load pattern and their trilinear idealization in both X and Y directions.

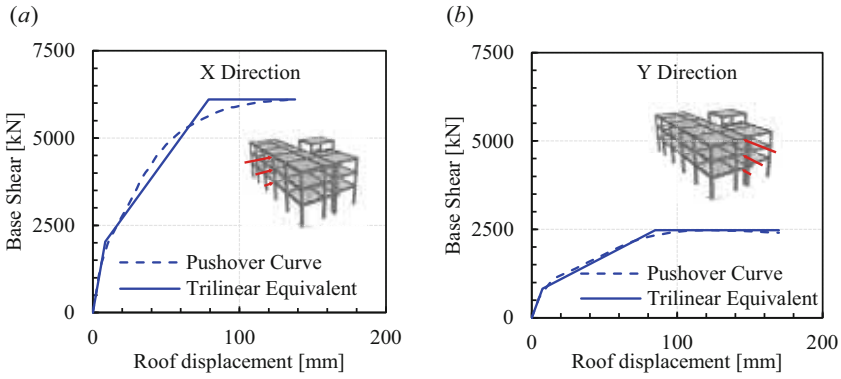


Fig. 6. Pushover curves and trilinear idealization: (a) X direction; (b) Y direction.

The retrofit EBFs equipped with SC links were placed along the façades in a parallel configuration as indicated in Fig. 7a and b, which respectively show the plan and 3D view of the retrofitted building.

The system is designed according to the procedure described in Sect. 2. The target displacement of the combined system (*SE*) is defined as follows: in the X direction, it is governed by seismic pounding with an adjacent building ($d_{pT,\,x} = 50$ mm), while in the

Y direction, a total drift ratio of 1.5% is considered ($d_{pT,\,y} = 73$ mm). NLTHA of the idealized SDOF model were carried out using a suite of spectrum-compatible 7 ground-motion records, each with 2 horizontal components, for a total of 14 accelerograms. The selected motions were chosen and scaled in accordance with the Italian building code [17] and Eurocode 8 [18]. Spectrum compatible records were identified using the REXEL software [19]. NLTHAs of the equivalent SDOF representing the combined system (*SE*) were performed to generate the P spectra. Figure 8 shows the P-spectra where the red cross marks the intersection between the vertical line corresponding to the target displacement reduction factor and the P-spectra curves. Based on the target displacement reduction factor, the stiffness ratio α_t and the ductility ratio $\mu_t{}^{(E)}$ are obtained, which serve as the starting point for the exoskeleton design.

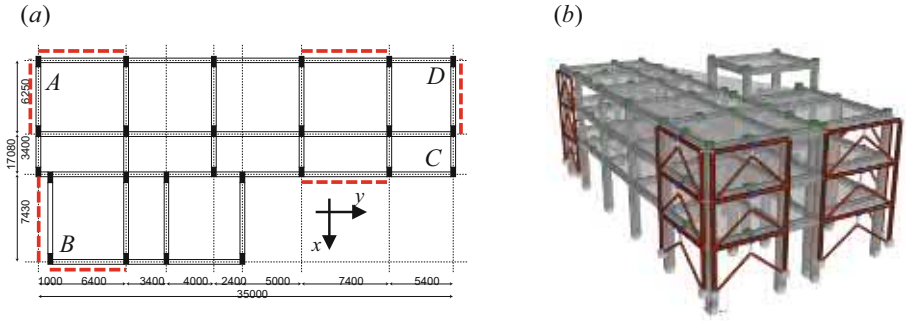


Fig. 7. (a) Layout of EBFs; (b) Analytical 3D Model on SeismoStruct [16].

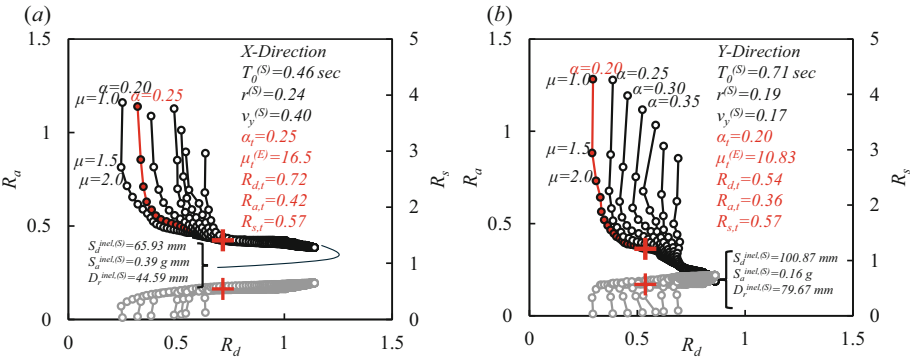


Fig. 8. Performance spectra: (a) X direction; (b) Y direction.

It is worth noting that their behavior differs substantially from the spectra generated for an ideal elastic-perfectly plastic system (Fig. 3b), as reported in previous studies [20–22]. In those works, the curves exhibited a clear reduction in absolute acceleration as the target displacement increased, consistent with the simplified bilinear idealization of the added damping component, consisting of an exoskeleton equipped with steel strip

Table 1. Parameters of the trilinear equivalent system of the structure (S).

Dir	$m_e^{(S)*}$	Γ	$V_c^{(S)*}$	$V_y^{(S)*}$	$d_c^{(S)*}$	$d_y^{(S)*}$	$K_e^{(S)}$	$T_e^{(S)}$	$r^{(S)}$	$\mu^{(S)}$	$\xi_v^{(S)}$
	[kNsec^2/mm]	[−]	[kN]	[kN]	[mm]	[mm]	[kN/mm]	[s]	[−]	[−]	[%]
X	1.28	1.26	1619.33	4857.98	6.80	62.89	238.06	0.46	0.24	1.75	5.00
Y	1.45	1.18	700.58	2101.73	6.15	72.12	113.83	0.71	0.19	2.00	5.00

Table 2. Parameters of the bilinear equivalent system of the exoskeleton (E).

Dir	$V_y^{(E)*}$	$V_p^{(E)*}$	$d_y^{(E)*}$	$d_{p,t}{}^*$	$K_i^{(E)}$	$r^{(E)}$	$K_{eq,0}^{(E)}$	$\mu^{(E)}$
	[kN]	[kN]	[mm]	[mm]	[kN/mm]	[−]	[kN/mm]	[−]
X	1827.29	2094.16	2.41	39.78	714.17	0.01	7.14	16.50
Y	2635.84	2892.11	5.73	62.01	455.32	0.01	4.55	10.83

Table 3. Properties of SC-link in X-Direction.

						Long Side ($\rho = 0.6$, $n_{EBF} = 2$)				*Short side* ($\rho = 0.4$, $n_{EBF} = 2$)			
Story	h_L	b_L	AR	L_{bar}	SC	V_y	V_{FR}	$V_{PT,0}$	$K_{PT,H}$	V_y	V_{FR}	$V_{PT,0}$	$K_{PT,H}$
	[mm]	[m]	[−]	[mm]	[−]	[kN]	[kN]	[kN]	[kN/mm]	[kN]	[kN]	[kN]	[kN/mm]
1	400	200	2	600	1	689.06	344.53	344.53	5.19	459.37	229.69	229.69	3.46
2	400	200	2	600	1	540.49	270.25	270.25	5.35	360.33	180.16	180.16	3.56
3	400	200	2	600	1	276.78	138.39	138.39	4.20	184.52	92.26	92.26	2.80

Table 4. Properties of SC-link in Y-Direction ($n_{EBF} = 4$).

Story	h_L	b_L	AR	L_{bar}	SC	V_y	V_{FR}	$V_{PT,0}$	$K_{PT,H}$
	[mm]	[m]	[−]	[mm]	[−]	[kN]	[kN]	[kN]	[kN/mm]
1	400	200	2	600	1	775.76	387.88	387.88	1.86
2	400	200	2	600	1	567.87	283.94	283.94	3.42
3	400	200	2	600	1	274.81	137.41	137.41	3.25

dampers [23, 24]. In contrast, the spectra developed in this study show higher values of absolute acceleration R_a (see Fig. 8). The parameters of the idealized nonlinear models of the structure and the exoskeleton are reported in Tables 1 and 2, respectively. Tables 3 and 4 provides the story strength $V_{y,i}$ and stiffness K_i of each SC-link as well as the assumed geometrical properties, according to the number EBFs (n_{EBF}) present in each direction.

4.1 Seismic Assessment

To assess the effectiveness of the retrofitting strategy, NLTHA results of the retrofitted building were compared with the results related to the existing bare frame.

Figure 9 compares the time-history of the global drift ratio in the Y direction for the 1999 Düzce earthquake. In particular, the global drift ratio was computed as the ratio between the roof displacement (D_{roof}) and the height of the building (H_{tot}). The results show that the retrofit substantially reduces peak displacements (from nearly 1.5% to less than 0.3%) and, eliminates residual drifts, demonstrating the strong self-centering capability of the system. Figure 10 reports the time-history of the base shear to seismic weight ratio, V/W, i.e., the seismic response coefficient [26], again in the Y direction for the same ground motion. The results show that the retrofitted configuration exhibits higher base-shear demands, which is attributed to the increased global stiffness introduced by the exoskeleton. As the structure becomes stiffer, a larger portion of the earthquake's frequency content is transmitted into the system, which in turn increases the demand in terms of V.

Figure 11 shows the response in terms of peak interstory drift (Peak IDR), residual interstory drift (Residual IDR), and peak absolute acceleration (Peak AA) along the height of the four corner columns (A, B, C, and D) in the X and Y directions, respectively. Each curve represents the mean response obtained as mean value over all selected ground-motion records, while the thicker lines denote the envelope. Across all stories, the retrofitted configuration exhibits lower Peak IDRs than the bare frame, as reported in Fig. 11a, d. The most pronounced reduction occurs at the first story in the Y direction (Fig. 11d), where values decrease from 2% for the bare frame to 0.2% for the retrofitted configuration. In the X direction, the reduction at the first story is more modest (from 1.2% to 0.3%). Figure 11b, e show that the Residual IDR are nearly eliminated by the retrofit, with values along the height approaching zero compared to those of the bare frame, confirming the self-centering capability of the system. The response in terms of Peak AA indicates that the retrofit leads to increased acceleration demands along the building height at the third story, with values rising from 0.23 g to 0.62 g in the Y direction (Fig. 11f), and from 0.48 g to 0.60 g in the X direction (Fig. 11c). The accelerations for all the ground motions never exceed the 0.7 g threshold above which building occupants may experience severe discomfort [25].

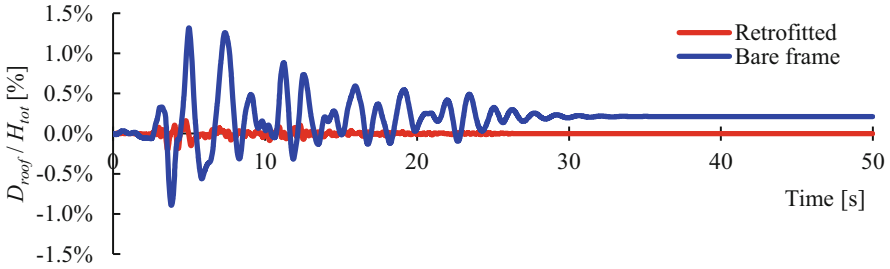


Fig. 9. Global drift ratio time-history for the Düzce earthquake (1999).

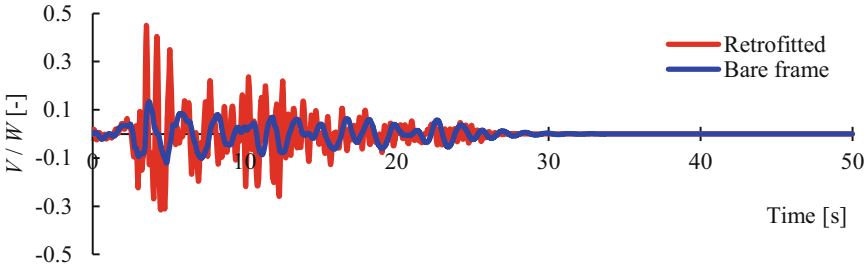


Fig. 10. Base-shear to weight ratio time-history for the Düzce earthquake (1999).

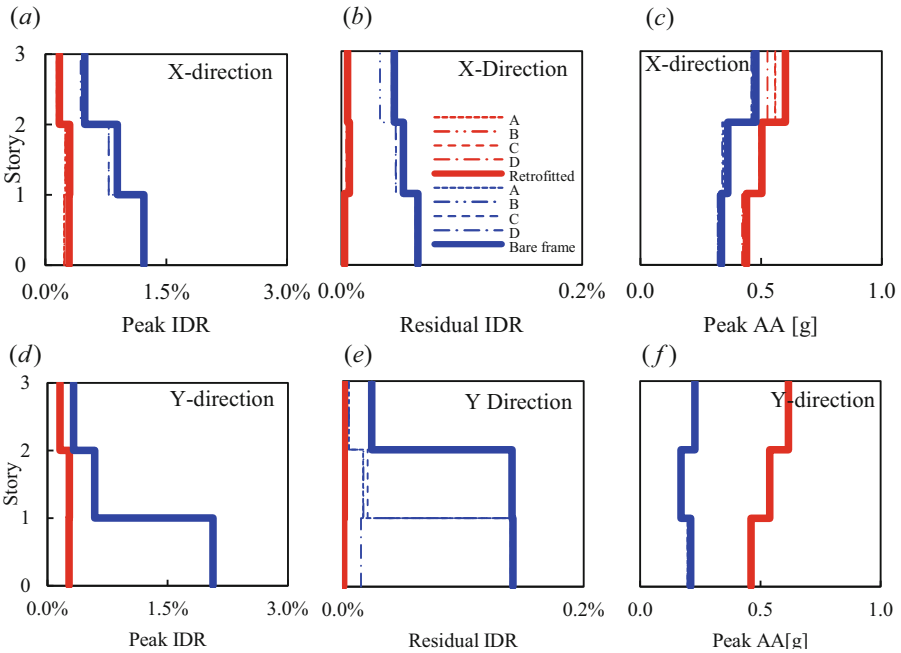


Fig. 11. Peak interstory drift ratio (IDR), residual interstory drift ratio (RIDR), and peak absolute acceleration (PAA) profiles along the building height.

5 Conclusion

This study introduces an effective design methodology for the seismic retrofit of reinforced concrete buildings using innovative self-centering friction-damped steel exoskeletons, a solution particularly suited to strategically important, seismically vulnerable structures that must remain operational during retrofit interventions. The approach leverages P-Spectra to directly link target performance levels with the mechanical properties of SC-links, and its effectiveness was demonstrated through numerical application to a three-story RC school building. The retrofit successfully reduced both peak and residual

interstory drifts while amplifying peak absolute accelerations, with values in the Y direction reaching 0.62 g at the third story. This increase is attributed to the introduction of the friction-damped, self-centering exoskeleton, which modifies the dynamic characteristics of the structure. The resulting change in stiffness and energy-dissipation distribution likely made the system more sensitive to the frequency content of the ground-motion set used in the NLTHA.

In conclusion, the proposed design methodology proved to be effective in sizing the exoskeleton system, and the adopted technology is fully consistent with emerging performance-based objectives, which emphasize not only deformation control but also resilience and reliable recentering after major seismic events.

References

1. CEN (2004) Design of structures for earthquake resistance—part 1: general rules, seismic actions and rules for buildings. In: Eurocode 8, EN 1998–1. CEN, Brussel, Belgium
2. ASCE (2017) Minimum design loads and associated criteria for buildings and other structures. ASCE/SEI 7–16. ASCE, Reston, VA
3. Di Lorenzo G, Colacurcio E, Di Filippo A, Formisano A, Massimilla A, Landolfo R (2020) State-of-the-art on steel exoskeletons for seismic retrofit of existing RC buildings. Int J 37(01)
4. Ferraioli M, Lavino A (2018) A displacement-based design method for seismic retrofit of RC buildings using dissipative braces. Math Probl Eng 5364564
5. Ferraioli M, Concilio A, Molitierno C (2022) Seismic performance of a reinforced concrete building retrofitted with self-centering shape memory alloy braces. Earthq Eng Eng Vib 21(03):785–809
6. Ferraioli M, Laurenza B, Lavino A, Frattolillo C, De Matteis G (2022) Seismic retrofit of a steel-reinforced concrete hospital building using continuous energy-dissipative steel columns. Steel and composite structures 467–488.
7. Ferraioli M, Lavino A, De Matteis G (2023) A design method for seismic retrofit of reinforced concrete frame buildings using aluminum shear panels. Arch Civ Mech Eng 23(02):106
8. Clifton GC, Bruneau M, MacRae GA, Leon R, Fussel A (2011) Steel structures damage from the Christchurch earthquake series of 2010 and 2011. Bull NZ Soc Earthquake Eng 44(4):297–318
9. Freddi F et al (2021) Observations from the 26th November 2019 Albania earthquake: the earthquake engineering field investigation team (EEFIT) mission. Bull Earthq Eng 19(5):2013–2044
10. McCormick J, Aburano H, Nakashima M (2008) Permissible residual deformation levels for building structures considering both safety and human elements. In: 14th world conference of earthquake engineering. Seismological Press, Beijing, pp 12–17
11. Chancellor NB, Eatherton MR, Roke DA, Akbas T (2014) Self-centering seismic lateral force resisting systems: high performance structures for the city of tomorrow. Buildings 4(3):520–548
12. Fang C, Qiu C, Wang W, Alam S (2023) Self-centering structures against earthquakes: a critical review. J Earthq Eng 27(15):4354–4389
13. Lettieri A, Freddi F, Latour M (2025) Experimental response of damage-free self-Centering links for seismic resilient eccentrically braced frames. J Struct Eng 151(11):04025173
14. Guo JWW, Christopoulos C (2013) Performance spectra based method for the seismic design of structures equipped with passive supplemental damping systems. Earthq Eng Struct Dyn 42(06):935–952

15. Takeda T, Sozen MA, Nielsen NN (1970) Reinforced concrete response to simulated earthquakes. J Struct Div 96(12):2557–2573
16. SeismoSoft (2025). SeismoStruct: A computer program for static and dynamic analysis of framed structures. www.seismosoft.com.
17. NTC (2018). Technical standards for constructions. Official Journal of the Italian Republic, Rome (in Italian).
18. EN 1998–3 (2005). Eurocode 8: Design of structures for earthquake resistance – Part 3: Assessment and retrofitting of buildings.
19. Iervolino I, Galasso C, Cosenza E (2010) REXEL: computer aided record selection for code based seismic structural analysis. Bull Earthq Eng 8:339–362
20. Ferraioli M, Mottola S, Pecorari O (2025) Performance-spectra design of dissipative exoskeletons for seismic retrofit of RC building structures. In: In: 10th ECCOMAS thematic conference on computational methods in structural dynamics and earthquake engineering (COMPDYN 2025). Rhodes Island
21. Ferraioli M, Mottola S, Pecorari O (2025) A design method for seismic retrofit of RC buildings using dissipative exoskeletons. In: International conference on protection of historical constructions. Springer Nature Switzerland, Cham, pp 78–86
22. Mottola S, Pecorari O, Ferraioli M (2026) Seismic retrofit of RC structures using performance-spectra design of dissipative exoskeletons. Procedia Struct Integr 78:623–630
23. Mottola S, Ferraioli M, Mistakidis E, De Matteis G (2024) Behavior and design of dumbbell-shaped steel strip dampers. In: International conference on the behaviour of steel structures in seismic areas. Springer Nature Switzerland, Cham, pp 174–186
24. Ferraioli M, Mottola S, Mistakidis E, De Matteis G (2025) Lateral torsional buckling design of dumbbell-shaped steel strip dampers. Structure 77:109080
25. ISN-TG046–2023 (2023) Technical guideline for maintaining normal functionality of buildings in earthquakes. China Architecture and Building Press, Beijing
26. ASCE/SEI 7–10 (2010) Minimum design loads for buildings and other structures. American Society of Civil Engineers, Reston, Virginia

Seismic Improvement of an Existing School Building Through Supplemental Energy Dissipation, Local Strengthening and Continuous Structural Monitoring the Case Study of the "G. Galilei" Science High School in Ancona

Matteo Giuseppe Blasi(✉)

Blasi Ingegneria & Architettura, Pesaro, Italy
matteogiuseppe.blasi@blasiingegneria.com

Abstract. This paper presents the seismic improvement of Building A of the "G. Galilei" Science High School in Ancona, Italy. The project addresses the retrofit of an existing reinforced-concrete school while limiting disruption to teaching activities, architectural finishes and building services. The adopted performance-based strategy combines supplemental energy dissipation with selective local strengthening. Rotational friction dampers are installed in modified chevron braces and are intended to concentrate cyclic demand in inspectable and replaceable components, while the existing frame remains as far as practicable within a substantially elastic response range. The paper summarises the identified vulnerabilities, including the squat members generated by split-level floors, the numerical modelling assumptions, the Fast Nonlinear Analysis procedure, and the definition of spectrum-compatible accelerograms. Device qualification tests performed in accordance with EN 15129 are discussed together with the influence of connection clearance on damper activation. The results are interpreted through energy balance, hysteretic cycles, base response and local utilisation ratios. The intervention is completed by a continuous structural-monitoring system and by BIM-supported coordination of the steel exoskeletons, existing structure and services. The case study demonstrates that dissipation, local capacity enhancement, construction detailing and monitoring must be developed as a single integrated retrofit strategy.

Keywords: seismic improvement · supplemental energy dissipation · rotational friction dampers · chevron braces · nonlinear dynamic analysis · structural monitoring · BIM

1 Introduction

Italy has a widespread seismic hazard and a large stock of public buildings constructed before the development of modern capacity-design and detailing rules. School buildings are especially sensitive because of their daily occupancy and public role. Their retrofit

© The Author(s), under exclusive license to Springer Nature Switzerland AG 2026
R. Zanon et al. (Eds.): CTA 2026, LNCE 942, pp. 702–711, 2026.
https://doi.org/10.1007/978-3-032-39505-4_61

is frequently constrained by continuity of use, limited construction time, architectural compatibility and the need to avoid extensive wet works. Under these conditions, seismic improvement cannot be reduced to the isolated strengthening of members: it requires a global response mechanism that reduces demand on vulnerable components and makes the expected damage controllable [1].

The case study concerns Building A of the "G. Galilei" Science High School in Ancona. Blasi Ingegneria & Architettura was appointed by the Province of Ancona for the structural seismic-improvement and energy-efficiency design and subsequently for construction supervision. The continuity between design and site activities allowed the analytical assumptions, device characteristics, connection details and actual installation tolerances to be checked consistently.

The intervention was developed from an existing vulnerability assessment and a dedicated knowledge campaign. Knowledge Level 2 was achieved; the available tests indicated an average concrete compressive strength of 27.30 MPa, a mean steel yield strength of 441 MPa and a coefficient of variation of approximately 11%. These data were considered sufficiently representative for design, with the applicable confidence factor used in the verification of ductile and brittle mechanisms (Fig. 1).



Fig. 1. Internal view of the completed supplemental energy-dissipation intervention.

2 Existing Building and Design Strategy

2.1 Structural Configuration and Vulnerabilities

The building has an approximately rectangular plan, about 30 × 27 m, three above-ground storeys, a partially underground level and a roof-level stair tower. The average clear storey height is close to 3 m. A major feature is the presence of floor offsets of about 1.70 m, connected by reinforced-concrete stairs with solid slabs. At these intermediate elevations, columns and lift-shaft walls terminate locally, creating squat members with unfavourable shear behaviour.

The vulnerability analyses identified widespread seismic deficiencies and particularly severe local conditions at the split levels. This result ruled out both a simple global stiffening solution and the exclusive use of supplemental damping. The design therefore combines a global reduction of seismic demand with force-based strengthening of the members for which the residual shear or interaction demand remains excessive.

2.2 Performance Objectives and Intervention Concept

The project follows a performance-based approach. The primary reinforced-concrete system is protected by assigning most of the intended inelastic demand to dedicated components with stable cyclic response, accessibility and replaceability. Rotational friction dampers are arranged within steel exoskeletons and modified chevron braces. The

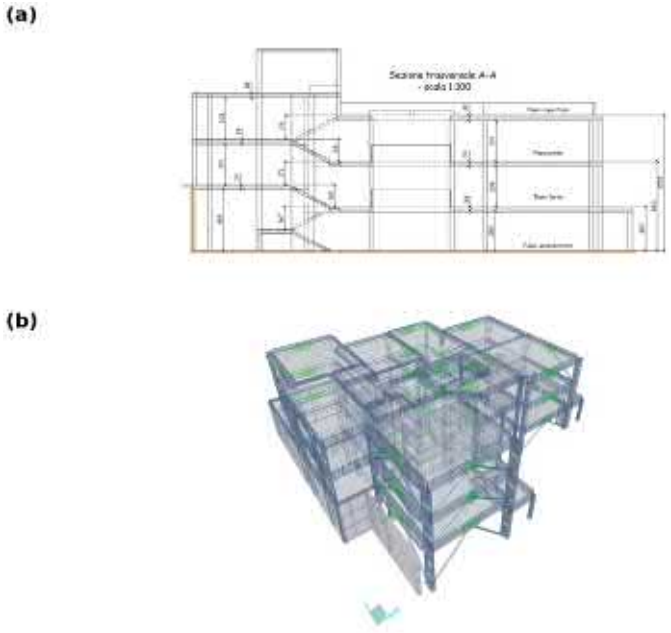


Fig. 2. Existing building and numerical model: (a) transverse section showing the split-level configuration; (b) global FEM model.

system increases the energy-dissipation capacity, controls displacement and acceleration demand, limits plastic rotations in the existing members and establishes a clearer hierarchy between dissipative and non-dissipative components.

The strategy is deliberately integrated: the dampers reduce the global demand, whereas local strengthening restores capacity where geometric singularities remain dominant. This distinction is important for the transferability of the method. Supplemental dissipation is not treated as a universal device-based solution, but as one component of a retrofit calibrated to the actual structural weaknesses (Fig. 2).

3 Dissipative System, Qualification and Detailing

3.1 Rotational Friction Dampers

Rotational friction dampers dissipate energy through controlled sliding between steel plates and composite friction pads. Disc springs maintain the clamping force and hardened washers support a sufficiently uniform contact pressure. Below the activation threshold the device remains in the sticking phase; above it, relative rotation produces an approximately rectangular hysteretic loop. This displacement-dependent behaviour provides high dissipative capacity with no working fluids, limited sensitivity to velocity and temperature, and straightforward inspection [2, 3].

In the numerical model, the device response was represented by a Wen-type hysteretic relationship. The elastic stiffness, activation force and post-activation stiffness ratio were calibrated to reproduce the tested cyclic behaviour. The selected activation forces were differentiated along the height—20, 30 and 40 kN—to obtain balanced engagement at the various levels and maximum design displacements of approximately ±15 mm at the Collapse Limit State.

3.2 Experimental Qualification

A test campaign documented in Report LB/05/24–01 was performed on 29 October 2024 at the Testing Laboratory for Building Materials and Structures of the Cracow University of Technology. Sixteen V-shaped rotational friction dampers were tested. Three representative specimens of the 20, 30 and 40 kN classes underwent the complete sequence required for displacement-dependent devices: five cycles at ±5 mm, five cycles at ±10 mm, ten cycles at ±20 mm, and a subsequent low-velocity ramp to 24 mm. The procedure was consistent with Clause 6.4.4 of EN 15129:2009 [4] (Table 1).

Table 1. Measured forces for the three devices subjected to the complete qualification sequence.

Nominal class	±5 mm 5 cycles	±10 mm 5 cycles	±20 mm 10 cycles	24 mm ramp
20 kN	19.3 kN	20.3 kN	21.1 kN	19.7 kN
30 kN	29.7 kN	29.3 kN	30.1 kN	30.1 kN
40 kN	37.2 kN	36.0 kN	39.7 kN	40.9 kN

The measured forces remained consistent with the nominal classes and the recorded loops were regular and stable. The remaining thirteen devices were subjected to a reduced sequence of five cycles at ±20 mm. Their measured capacities ranged from 20.5 to 24.6 kN, 31.3 to 34.0 kN and 42.0 to 44.6 kN for the 20, 30 and 40 kN classes, respectively, confirming repeatability across the production set (Fig. 3).

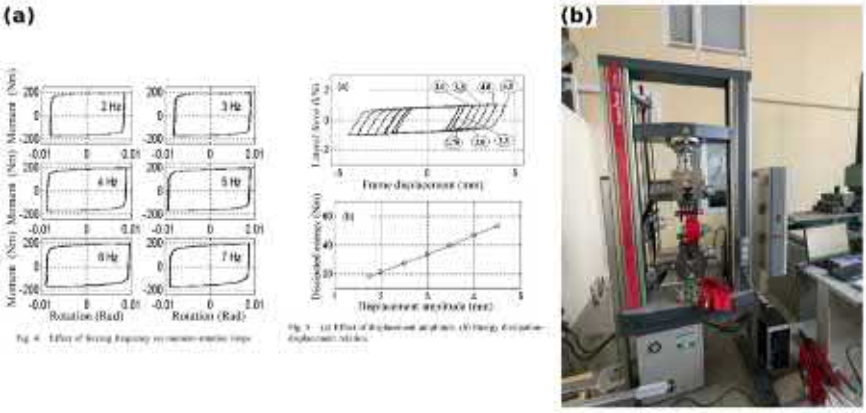


Fig. 3. Device behaviour and qualification: (a) representative friction-damper hysteresis from the literature; (b) laboratory test configuration.

3.3 Modified Chevron Configuration

The devices are positioned horizontally rather than along the braces. A diagonal device would intercept only the projected component of the inter-storey displacement, whereas the adopted horizontal arrangement mobilises almost the full storey drift. The larger useful stroke improves dissipation for a given device size and is advantageous where architectural and installation constraints are decisive.

The benefit depends on the stiffness and freedom of movement of the surrounding components. Collectors, brackets and connections must transmit the floor movement without significant parasitic deformation; braces are intended to work primarily in axial force; and the damper must be restrained against out-of-plane displacement while remaining free to operate along its working axis. Pins, gusset plates, spacers, centring devices and temporary installation bolts were consequently detailed to reproduce the intended kinematics in the completed structure. The elastic components were governed not only by resistance but also by stiffness, because their deformation would directly reduce the effective damper stroke (Fig. 4).

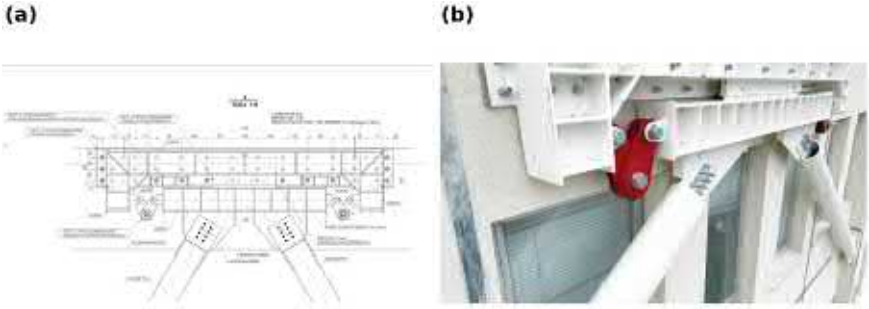


Fig. 4. Modified chevron system: (a) connection and restraint detail; (b) installed horizontal friction damper and braces.

4 Numerical Modelling and Seismic Input

4.1 Global Model and Stiffness Assumptions

Several variants of the global finite-element model were developed to represent a plausible range of structural responses. The parameters included the stiffness of the existing members, boundary conditions, reductions of member inertia, construction tolerances, connection clearance and, in sensitivity analyses, nonlinear links representing the engagement of infill panels. The main load-bearing components were modelled as linear elements, while concentrated nonlinearities were assigned to the dampers and to specific activation mechanisms.

The effective inertias of the reinforced-concrete members were reduced to account for cracking. Gross-section stiffness would underestimate deformation demand, distort the natural periods and produce an unrealistic distribution of internal actions. The adopted values were informed by ACI 318–14 and ASCE 41–13, which distinguish member types and account for axial-force effects in columns [6, 7]. The objective was not to identify a single exact model, but to avoid optimistic assumptions and test the robustness of the retrofit over a credible stiffness range.

4.2 Fast Nonlinear Analysis

Nonlinear dynamic analyses were performed using the Fast Nonlinear Analysis (FNA) procedure implemented in SAP2000 [5]. FNA separates the linear part of the system from a limited number of nonlinear degrees of freedom. The mass, damping and linear stiffness matrices remain constant, while the hysteretic forces of the links are updated incrementally at each time step. This approach is efficient when nonlinearity is deliberately concentrated in supplemental devices and allowed multiple records, directional combinations and sensitivity studies to be evaluated.

The method assumes that the global stiffness of the primary structure does not change substantially during the analysis. This condition was considered consistent with the project objective, because the existing reinforced-concrete frame was intended to remain essentially within a linear response range and the dissipative demand was concentrated

in the friction devices. The expected drift levels and conventional stability indicators were checked to confirm that geometric nonlinearities did not control the response.

4.3 Spectrum-Compatible Accelerograms

The seismic input was based on local seismic-response analyses. The resulting normalised spectrum was slightly higher than the code spectrum for ground type C. Seven artificial spectrum-compatible accelerograms were generated for the relevant limit states, with a pseudo-stationary phase of at least 10 s and compatibility of the mean spectrum over the period range prescribed by the applicable code [1]. The response spectrum was sampled at 0.01 s intervals.

For assessment of seismic improvement, the spectrum was scaled by 0.8 while the peak ground acceleration was retained. The existing structure was treated with the minimum behaviour factor consistent with the adopted substantially non-dissipative response, whereas the steel exoskeletons, connections and dampers were checked at the Collapse Limit State without relying on the reduction associated with the improvement target. This conservative hierarchy protected the existing frame while preventing premature failure of the newly introduced load path.

5 Response Assessment and Design Implications

5.1 Energy Balance, Hysteresis and Validation

The response was interpreted through energy balance, device hysteresis, base response and local utilisation ratios. Energy histories are especially informative for supplemental-damping systems because they reveal whether the input energy is actually directed to the intended devices rather than being absorbed by numerical damping or by uncontrolled structural damage. At the end of the records, the cumulative results showed that the hysteretic contribution of the friction dampers was dominant, while the remaining share was mainly associated with the equivalent linear damping of the model.

The loops confirmed repeated activation and a reasonably balanced distribution of demand among storeys. Differentiating the activation forces prevented both under-utilisation and excessive concentration at a single level. For the seismic-improvement analyses, the maximum dimensionless accelerations were approximately 0.14 g in the X direction and 0.16 g in the Y direction, compared with values close to 0.30 g in the upgrading scenario. With a fundamental period of approximately 0.29 s, the response-spectrum interpretation indicated equivalent damping levels of about 55% in X and 40% in Y. These values are consistent with the high energy-dissipation contribution observed in the time histories (Fig. 5).

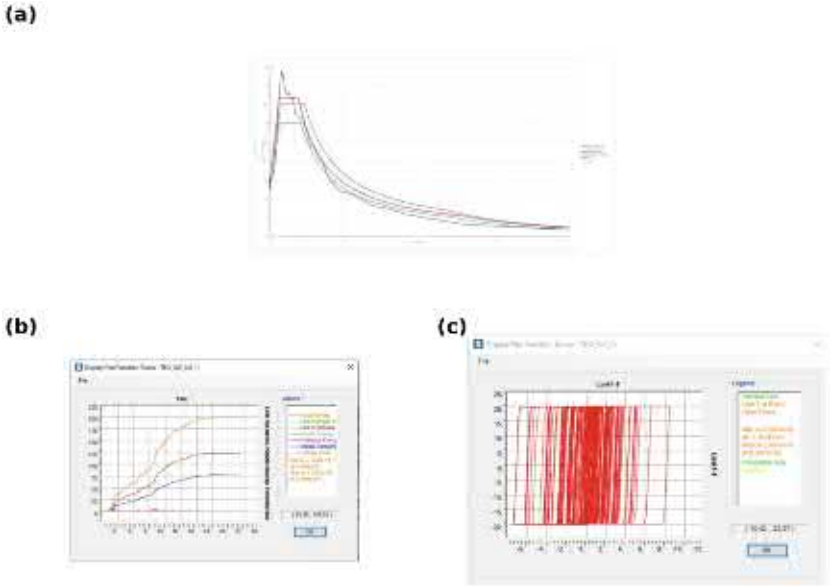


Fig. 5. Seismic input and representative response: (a) comparison of reference spectra; (b) cumulative energy balance; (c) damper hysteretic response.

5.2 Influence of Bolt-Hole Clearance

Connection clearance was modelled explicitly because even a few millimetres of free movement delay device engagement and remove useful displacement from every reversal. A multilinear elastic link represented the initial gap and was placed in series with the Wen damper element. Three configurations—zero, 2 mm and 4 mm clearance—were compared using the same structural model and seismic input (Table 2).

Table 2. Effect of connection clearance on input and dissipated energy.

Clearance	Input X (kJ)	Dissipated X (kJ)	Input Y (kJ)	Dissipated Y (kJ)	Efficiency X / Y
0 mm	200	125	240	150	62.5% / 62.5%
2 mm	240	120	273	145	50.0% / 53.2%
4 mm	260	95	270	110	36.5% / 40.7%

With 2 mm clearance, the absolute dissipated energy decreased by only about 3–4%, but the dissipative efficiency fell to approximately 50–53% because the input energy increased. At 4 mm, the absolute loss reached about 24% in X and 27% in Y, and the efficiency reduced to roughly 36–41%. The result led to a construction requirement to minimise in-situ slip by means of controlled tolerances, adjustment washers or shims,

without compromising assembly. The study demonstrates that connection detailing is part of the energy-dissipation mechanism rather than a secondary fabrication issue.

5.3 Structural Verifications and Local Strengthening

Combined axial force and bending, shear, joint behaviour and the response of the most highly stressed members were checked for the existing structure and the new steel system. The dampers reduced global demand substantially, but residual deficiencies remained at the split levels and in squat members. Selective local strengthening was therefore introduced where the reduced demand still exceeded available capacity. This confirmed the initial design premise: global dissipation and local capacity enhancement must operate together.

6 Structural Monitoring and BIM-Supported Construction

The intervention includes continuous structural monitoring as a permanent component of risk management. An initial dynamic-identification phase is performed before the works and repeated after completion to establish the baseline modal parameters and support calibration of the numerical model. The permanent system includes triaxial accelerometers, acquisition nodes and sensors for relative displacements at selected dampers. Data are transmitted to a central platform, and predefined thresholds generate alerts for post-event assessment and maintenance planning [8, 9].

BIM modelling was essential for coordinating the existing structure, the steel exoskeletons, the dissipative devices and the energy-efficiency systems. The three-dimensional information model supported clash detection, connection development, verification of installation tolerances and coordination with ducts, electrical systems, windows and parapets. It also reduced the risk of site variations and allowed complex components to be checked before fabrication. For exoskeleton retrofits, this design-to-construction continuity is a major condition for reliably reproducing the analytical load path [10] (Fig. 6).

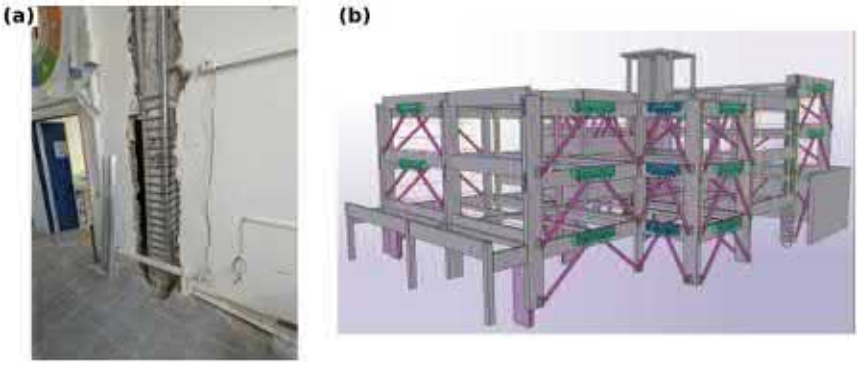


Fig. 6. Integrated design and construction process: (a) local strengthening at a vulnerable member; (b) BIM model used for exoskeleton and connection coordination.

7 Conclusions

The seismic improvement of Building A of the "G. Galilei" Science High School demonstrates a retrofit method suited to operational public buildings. Rotational friction dampers in modified chevron braces reduced the global seismic demand and concentrated cyclic response in accessible, replaceable components. Their effectiveness depended on realistic modelling, experimental qualification, connection stiffness and control of installation clearance.

The case study also shows the limits of a device-only approach. Severe local vulnerabilities generated by the split-level configuration required selective strengthening even after the global demand had been reduced. FNA analyses with spectrum-compatible accelerograms, energy-based interpretation and sensitivity studies provided a coherent basis for calibrating the intervention. Continuous monitoring and BIM coordination extended the project from structural verification to life-cycle management and construction-quality control.

The transferable result is therefore not a standard brace layout, but an integrated process: understand the actual building, define the desired response mechanism, concentrate damage in qualified devices, protect non-dissipative components, detail the real activation path and observe performance over time.

References

1. Ministero delle Infrastrutture e dei Trasporti (2018) Decreto 17 gennaio 2018: Aggiornamento delle Norme tecniche per le costruzioni. In: Gazzetta Ufficiale della Repubblica Italiana, Serie Generale 42, Supplemento Ordinario 8, Rome
2. Mualla IH, Belev B (2002) Performance of steel frames with a new friction damper device under earthquake excitation. Eng Struct 24(3):365–371
3. Wen YK (1976) Method for random vibration of hysteretic systems. J Eng Mech Div 102(2):249–263
4. European Committee for Standardization (CEN) (2009) EN 15129:2009. Anti-seismic devices, CEN, Brussels
5. Wilson EL (2002) Three-dimensional static and dynamic analysis of structures: a physical approach with emphasis on earthquake engineering, 3rd edn. Computers and Structures, Berkeley, CA
6. ACI Committee 318 (2014) Building code requirements for structural concrete (ACI 318–14). American Concrete Institute, Farmington Hills, MI
7. American Society of Civil Engineers (ASCE) (2014) Seismic evaluation and retrofit of existing buildings (ASCE/SEI 41–13). American Society of Civil Engineers, Reston, VA
8. Pierdicca A, Mattiauda F (2021) Il monitoraggio dinamico delle strutture: Identificazione dinamica e vibrazioni di edifici e infrastrutture. Maggioli Editore, Santarcangelo di Romagna
9. Pinho R, Bianchi F, Nascimbene R (2022) Valutazione sismica e tecniche di intervento per edifici esistenti in c.a. 2nd edn. Maggioli Editore, Santarcangelo di Romagna.
10. Passoni C, Guo J, Christopoulos C, Marini A, Riva P (2020) Design of dissipative and elastic high-strength exoskeleton solutions for sustainable seismic upgrades of existing RC buildings. Eng Struct 221:111057

Nonlinear Response of EC8-Compliant Dissipative Steel Concentrically Braced Frames Under Seismic Loading

Massimino Gnazzo[1,2(✉)], Mario D'Aniello[1], and Raffaele Landolfo[1]

[1] University of Naples Federico II, Naples, Italy
massimino.gnazzo@unina.it
[2] University of Alberta, Edmonton, AB, Canada

Abstract. This paper assesses the effectiveness of the design provisions for dissipative cross concentrically braced frames (X-CBFs) provided in the second generation of Eurocode 8. A parametric study was conducted on a set of low- and mid-rise frames designed in accordance with code design rules, considering different seismic intensity levels and ductility classes. The preliminary results presented in this paper focus on a group of medium-dissipative (DC2) and high-dissipative (DC3) frames designed for the same seismic intensity. Nonlinear static and dynamic analyses were performed using refined numerical models. The results show that the examined frames generally develop the intended dissipative mechanism, with inelastic demand mainly concentrated in the braces through yielding in tension and buckling in compression. However, nonlinear dynamic analyses indicated that CBF columns may be prone to global buckling in both ductility classes. Therefore, further studies are needed to investigate this aspect in more detail and, eventually, to support the refinement of the design provisions for non-dissipative members.

Keywords: Steel Structures · Concentrically Braced Frames · Seismic Response · Eurocode 8 · Columns

1 Introduction

Steel concentrically braced frames (CBFs) are widely used as seismic-resistant systems in multi-storey buildings due to their high lateral stiffness and energy dissipation capacity. In dissipative CBFs, the nonlinear response is expected to be mainly concentrated in the diagonal braces, which are designed to yield in tension and buckle in compression under severe seismic actions. Capacity design rules are therefore required to promote the intended behaviour while preventing premature damage in other structural members and connections. The global and local response of steel CBFs is strongly influenced by connection detailing and component-level damage mechanisms. In particular, the mechanical behaviour of steel connections [1, 2] and the degree of restraint provided by beam-to-column joints in the braced bays may affect the lateral stiffness, strength, and energy dissipation capacity of the system through the secondary frame effect [3]. Moreover, steel members and connection details may be affected by damage accumulation

© The Author(s), under exclusive license to Springer Nature Switzerland AG 2026
R. Zanon et al. (Eds.): CTA 2026, LNCE 942, pp. 712–722, 2026.
https://doi.org/10.1007/978-3-032-39505-4_62

under repeated cyclic actions [4], and, with reference to the braces, repeated inelastic cyclic loading may lead to fracture due to low-cycle fatigue phenomena [5]. Costanzo et al. [6] proposed revised design rules to improve the seismic response of cross concentrically braced frames (X-CBFs) within the framework of the Eurocodes. Further studies on chevron and two-storey X-CBFs [7, 8] highlighted that column flexural demand generally exceeds the design code value. Recent research has also addressed the calibration and assessment of design rules provided for traditional seismic-resistant systems [3, 9–11] in the framework of Eurocodes, as well as the use of enhanced bracing solutions, such as buckling-restrained braces, for new construction and seismic retrofit applications [12]. Within the second generation of EC8, EN 1998-1-2 (EC8-1-2) [13], the code that provides material-dependent rules for the seismic design of different structural materials and seismic-resistant systems, introduced several improvements to the design of both dissipative and non-dissipative members and connections in braced frames. Nonetheless, recent studies have shown that the seismic demand on CBF columns remains particularly relevant and warrants further investigation. Bosco et al. [14] have shown that premature buckling of columns still occurs for chevron CBFs designed in accordance with the second generation of the EC8, while Gnazzo et al. [3] have shown that the flexural demand in columns systematically exceeds the EC8-1-2 design value. In light of these considerations, this paper presents a preliminary discussion on the effectiveness of the EC8-1-2 design rules for medium- and high-dissipative X-CBFs. A parametric numerical study was conducted on 3-storey and 6-storey frames designed in accordance with the code, under different seismic intensity levels and ductility classes. The preliminary results discussed herein focus on the comparison between medium-dissipative (DC2) and high-dissipative (DC3) frames designed for a seismic action index, S_δ, equal to 6.5 m/s^2, which corresponds to the upper applicability limit for DC2 design. The lateral performance and seismic response of the selected frames were evaluated through nonlinear static and dynamic analyses performed on refined numerical models.

2 EC8-1-2 Design Rules for Dissipative X-CBFs

The design rules provided in the second generation of Eurocode 8 for dissipative X-CBFs are briefly summarised in this section. The reference seismic action for ordinary buildings, namely those belonging to consequence class CC2 according to EC8-1-1 [15], corresponds to a 475-year return period and is associated with the Significant Damage (SD) limit state. The recommended values of the behaviour factor, q, which accounts for the overstrength, redundancy, and ductility capacity of the seismic-resistant system, are equal to 2.5 and 4.0 for medium-dissipative (DC2) and high-dissipative (DC3) CBFs satisfying the regularity criteria provided by EC8. For DC2 CBFs, simplified capacity design provisions are provided to ensure a moderate dissipative response. For this reason, EC8-1-2 limits the applicability of DC2 to building sites characterised by a seismic action index, S_δ, not exceeding 6.5 m/s^2. The seismic design of DC3 CBFs requires the application of more rigorous global and local capacity design rules, together with stricter ductility requirements than those prescribed for DC2.

2.1 Design of Dissipative Members

EC8-1-2 requires the adoption of a tension-compression model of the braces to evaluate the seismic effects on structural members and components. Hence, regardless of the ductility class, both tensile and compressive diagonals are explicitly considered in the structural model, and the brace buckling resistance, $N_{b,Rd,br}$, has to be larger than the corresponding axial force, $N_{Ed,br}$, obtained from the seismic design combination. To limit the degradation of the brace response under cyclic loadings, the non-dimensional slenderness of braces should be lower than 2.5, and class 1 or 2 cross-sections are required for braces in DC2.

In DC3, the non-dimensional slenderness of braces should be lower than 2.0, and only class 1 cross-sections are allowed. More stringent requirements on the local slenderness are provided by the code in the case of circular, rectangular, and square hollow sections. A further requirement for DC3 frames concerns the distribution of brace overstrength along the building height. EC8-1-2 stipulates that, with the exception of the top storey, the i-*th* storey buckling overstrength ratio, $\Omega_{b,i} = N_{b,Rd,br,i}/N_{Ed,br,i}$, should not exceed $1.25\ \Omega_b$, where Ω_b is the minimum buckling overstrength ratio of the dissipative braces along the building height. For DC3 frames, top-storey braces may be excluded from the set of dissipative bracings, provided that they are designed to remain elastic under the design seismic action.

2.2 Design of Non-dissipative Members

Beams, columns, and connections are designed as non-dissipative components and should remain essentially elastic while the braces develop the intended dissipative mechanism. For DC2 CBFs, simplified capacity design rules are adopted. The seismic axial force in non-dissipative members is amplified by a seismic overstrength factor, Ω, equal to 1.5 for concentrically braced frames, whereas bending moments and shear forces are obtained directly from the seismic design combination.

Beams and columns of DC3 CBFs are designed on the basis of the following conditions:

(i) the most severe combination of axial force, shear force and bending moment in the seismic design combination, where each seismic design effect is amplified by the product of $\omega_{rm}\ \omega_{sh}\ \Omega_d$, being ω_{rm} and ω_{sh} the material overstrength and strain-hardening coefficients, and Ω_d the minimum overstrength ratio of braces in tension along the building height;
(ii) the internal forces obtained considering a free-body distribution of axial forces in the braces equal to their expected buckling resistance;
(iii) the internal forces obtained considering the expected tensile resistance in the braces in tension and the expected post-buckling resistance for the braces in compression.

An additional uniform bending moment in the direction of the braced bays, and equal to 0.20 times the plastic moment resistance of the gross section of the column, should be included in the design of columns under condition (iii).

3 Design of the Structural Archetypes

The plan layout of the residential building considered as the structural archetype in this study is shown in Fig. 1. The lateral load-resisting system consists of four perimetral X-CBFs in each horizontal direction of the building plan. Two building heights were considered, namely 3-storey and 6-storey configurations, in order to investigate the effectiveness of the EC8-1-2 design rules for low- and medium-rise steel braced frames. The interstorey height is 3.50 m, except for the first storey, which is 4.00 m, while the span length of the braced bay is 6.00 m. The seismic intensity was identified through the seismic action index, S_δ, namely the pseudo-acceleration of the constant branch of the elastic response spectrum according to Eurocode 8. Three values of S_δ were considered in the design, namely 5.0, 6.5, and 7.5 m/s^2. The ductility class was selected in accordance with the seismic intensity level and the applicability limits of the EC8-1-2 design provisions. In particular, the medium-dissipative (DC2) ductility class was selected for $S_\delta = 5.0$ m/s^2, since the adoption of the high-dissipative (DC3) ductility class would generally result in an uneconomical design for this seismicity level. Conversely, for $S_\delta = 7.5$ m/s^2, frames were designed in DC3, since this seismic intensity exceeds the applicability range of DC2. Finally, for $S_\delta = 6.5$ m/s^2 frames were designed in both DC2 and DC3, as this seismic intensity level represents the upper bound for the design in DC2 and therefore provides a meaningful basis for comparing the two ductility classes. Overall, a total of eight frames was considered in the parametric study. Dead (G_k) and live (Q_k) loads were assumed equal to 4.7 kN/m^2 and 3.0 kN/m^2 for the intermediate storeys, and 1.40 kN/m^2 and 1.0 kN/m^2 for the roof, respectively. The design of structural members for gravity loads complies with the provisions of EN 1993-1-1 [16]. The seismic design of the selected CBFs was carried out according to the relevant EC8-1-1 and EC8-1-2 design provisions.

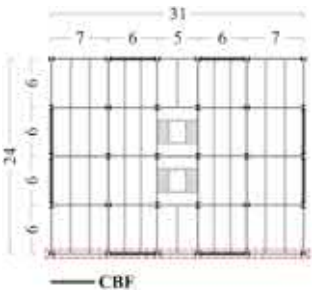


Fig. 1. Plan layout of the building

Cold-formed circular hollow sections (CHS) were adopted for the diagonal braces, while IPE and HE profiles were used for beams and columns, respectively. S355 steel grade was assumed for all structural members. The lateral response and seismic performance of the DC2 and DC3 frames designed for $S_\delta = 6.5$ m/s^2 are discussed in the following section. These frames were selected as representative cases for a preliminary assessment and comparison of the influence of different ductility classes on the nonlinear response of such systems. The member sizes of these frames are given in Table 1.

Table 1. Member cross-sections of the DC2 and DC3 CBFs designed for $S_\delta = 6.5$ m/s^2

	Medium-dissipative (DC2)			**High-dissipative (DC3)**		
Storey	**Columns**	**Beams**	**Braces**	**Columns**	**Beams**	**Braces**
3	HE 220 B	IPE 360	88.9 × 6	HE 240 B	IPE 360	76.1 × 5
2	HE 220 B	IPE 360	114.3 × 6	HE 240 B	IPE 360	88.9 × 6
1	HE 220 B	IPE 360	139.7 × 6	HE 240 B	IPE 360	101.6 × 6
	Medium-dissipative (DC2)			**High-dissipative (DC3)**		
Storey	**Columns**	**Beams**	**Braces**	**Columns**	**Beams**	**Braces**
6	HE 220 B	IPE 360	76.1 × 6	HE 280 B	IPE 360	114.3 × 5
5	HE 220 B	IPE 360	101.6 × 6	HE 280 B	IPE 360	76.1 × 6
4	HE 240 B	IPE 360	101.6 × 6	HE 320 B	IPE 360	88.9 × 5
3	HE 240 B	IPE 360	114.3 × 6.3	HE 320 B	IPE 360	101.6 × 5
2	HE 280 B	IPE 360	114.3 × 6.3	HE 360 B	IPE 360	101.6 × 5
1	HE 280 B	IPE 360	139.7 × 6	HE 360 B	IPE 360	114.3 × 5

4 CBF Response Evaluation

4.1 Numerical Model

The response of the selected braced frames was evaluated by means of numerical models developed in *OpenSees* [17]. The modelling assumptions are consistent with previous studies carried out by the Authors [3] and are briefly recalled in this section. Figure 2 depicts the main features of the 3D planar model used in the numerical study. Force-based beam-column elements [18] with fibre cross-sections were used to reproduce the behaviour of structural members. Each brace was discretised into 6 sub-elements, with an initial sinusoidal out-of-plane camber of peak amplitude $L/1000$, where L is the unbraced length of the brace, to accurately mimic its nonlinear behaviour under cyclic loading [19, 20]. To account for potential global flexural buckling, each column was discretised into 10 sub-elements, with an initial out-of-plane camber equal to 1/1000 of the column's unbraced length. The out-of-plane displacements of the beam nodes were restrained to take into account the continuous lateral support provided by the floor slab. The out-of-plane flexural behaviour of gusset plates was simulated by means of nonlinear rotational springs positioned at brace ends, while rigid links were modelled to account for the dimensions of gusset connections as outlined in [21]. At the same time, the beam-to-column joints were assumed to be fixed due to the presence of the gusset plate and its connections. The Steel02 uniaxial material model [22] was assigned to reproduce the steel stress-strain relationship and the parameters were assigned with the data reported in [23]. Brace fracture due to low-cycle fatigue was simulated by wrapping the Steel02 material model with the Fatigue material model [24]. The model parameters were calibrated according to the equations proposed in [25].

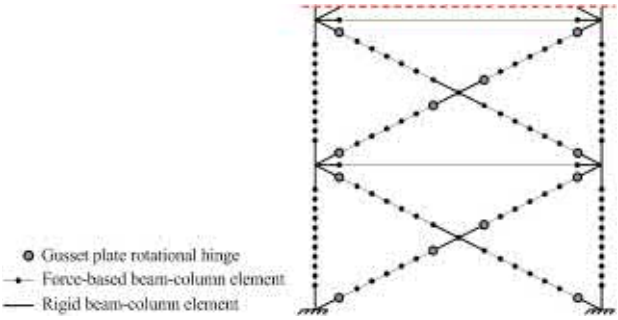


Fig. 2. Main features of the numerical model

The gravity loads applied to the gravity columns tributary to the examined CBF and not directly considered in the model were imposed on a leaning column coupled to the frame at each storey for horizontal translation to simulate large *P*-Δ effects. CBF tributary seismic masses were lumped at the top end of columns of each storey. The Rayleigh approach was used to estimate the damping forces for the time-history analyses. For this purpose, a damping ratio of 2% of the critical damping was used for the first two vibration periods of the frame to compute the Rayleigh damping parameters.

4.2 Pushover Curves

Nonlinear static analyses were carried out to evaluate the lateral performance of the investigated frames. The pushover curves, shown in Fig. 3a for the 3-storey X-CBFs and in Fig. 3b for the 6-storey X-CBFs, were derived by considering both first-mode and mass-proportional lateral load patterns. The results are expressed in terms of the normalised base shear, $V_b/V_{b,des}$, where V_b is the total base shear and $V_{b,des}$ is the base shear adopted in the design procedure, as a function of the maximum interstorey drift ratio, *IDR*. The pushover curves show that all the examined frames exhibit a significant lateral design overstrength. Peak values of $V_b/V_{b,des}$ are slightly larger than 2 for DC2 frames and approximately equal to 3 for DC3 frames, with limited influence of the number of storeys. It is worth noting that this result is primarily due to the lower design seismic forces associated with the larger behaviour factor adopted in the design of DC3 systems, together with the stricter capacity design rules for this ductility class, which promote more ductile behaviour of the system. All frames also exhibit post-peak degradation of lateral strength and stiffness for drift ratios larger than approximately 1.5–2.0%. This degradation is more pronounced in the 6-storey frames, where second-order effects play a more relevant role in the nonlinear response.

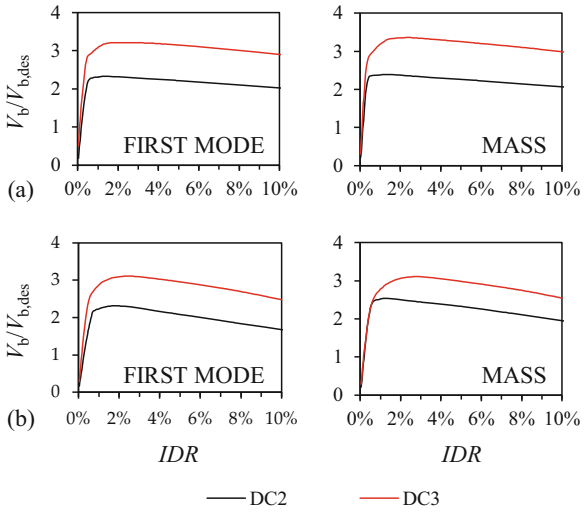


Fig. 3. Pushover curves: (a) 3-storey CBFs and (b) 6-storey CBFs

4.3 Dynamic Analyses

To further investigate the seismic behaviour of the designed frames, nonlinear dynamic analyses were performed using a set of 14 natural ground motions matched to the elastic response spectrum at the NC limit state, as shown in Fig. 4. The selected ground-motion set satisfies the compatibility criteria provided by EC8-1-1 over the period range of interest for the examined structures.

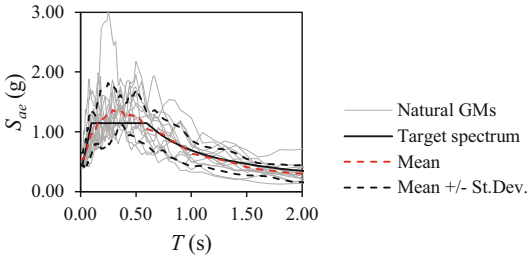


Fig. 4. Response spectra of selected records vs. the EC8 target spectrum

Figure 5a and b show the mean values of the maximum and minimum interstorey drift ratios, *IDR*s, and the brace ductility demand profiles, μ, respectively. The brace ductility demand in tension and compression was evaluated as $d_{br}/d_{pl,br}$ and $d_{br}/d_{b,br}$, respectively, where d_{br} is the maximum brace elongation or shortening, $d_{pl,br}$ is the brace elongation at yielding, and $d_{b,br}$ is the brace shortening at buckling. Overall, the 3-storey DC2 and DC3 frames exhibited similar drift distributions, with peak *IDR* values below 1.5%. Referring to the 6-storey CBFs, the stricter capacity design rules

in DC3 resulted in a significantly more uniform *IDR* distribution than in DC2. Indeed, the DC2 frame shows a more pronounced concentration of drift and damage demand at the second storey, associated with brace fracture due to low-cycle fatigue phenomena. The brace ductility demand profiles confirm that the CBF dissipative response is mainly governed by brace buckling in compression and yielding in tension, consistently with the intended seismic behaviour of the system. As expected, the largest brace ductility demands are generally observed in the storeys with the highest drift demands. It is also worth noting that, consistently with the design assumptions, the roof-storey braces of the 6-storey DC3 frame remain essentially elastic. In accordance with past studies [3], the resistance of beams and columns was monitored at each analysis step by means of the interaction equations provided by EN 1993-1-1 under the combined axial force and bending moment actions. No plastic hinging was observed in beams or columns in any of the examined frames, as the corresponding interaction indices remained below 1 throughout the analyses. Therefore, the discussion of non-dissipative member demand only focuses on potential global buckling phenomena in columns. The mean values of the flexural-torsional buckling index, $I_{b,col}$, are given in Fig. 6. Values of $I_{b,col}$ equal or larger than 1 indicate that the column buckling verification is not satisfied at the corresponding storey. The results show that $I_{b,col}$ values greater than 1 occur in both the DC2 frames and the 3-storey DC3 frame. This indicates that although plastic hinging of non-dissipative members is effectively prevented, columns may still be prone to global buckling. This outcome suggests that the current design provisions may not be fully effective in preventing column instability under severe seismic demand.

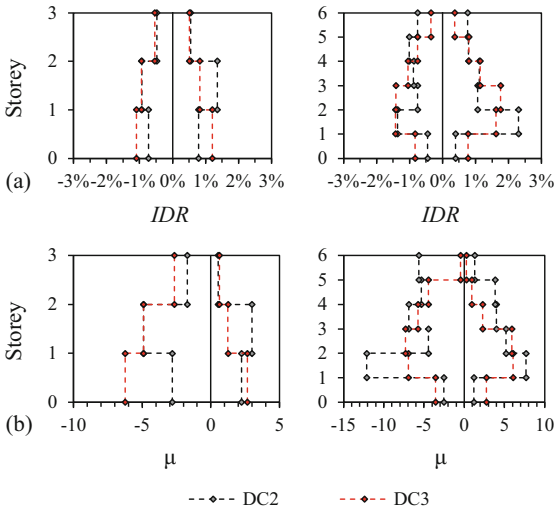


Fig. 5. Mean values of (a) interstorey drift ratios, *IDR*s, and (b) brace ductility demand, μ

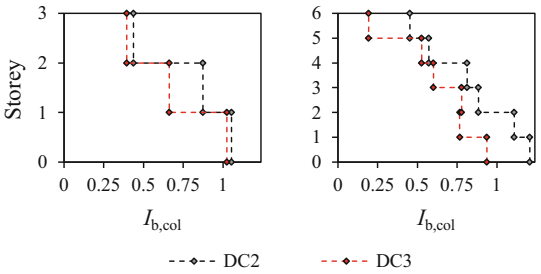


Fig. 6. Mean values of flexural-torsional buckling indexes, $I_{b,col}$, for columns

5 Conclusions

This paper aimed to assess the effectiveness of the design provisions for medium-dissipative (DC2) and high-dissipative (DC3) CBFs provided in the second generation of Eurocode 8. To this end, a numerical study was carried out on a set of 3-storey and 6-storey X-CBFs designed for different levels of seismicity. The preliminary results of this parametric study were discussed with reference to the DC2 and DC3 frames designed for $S_\delta = 6.5$ m/s^2, with the aim of providing an initial comparison between the two ductility classes. The lateral performance and seismic response of the designed frames were evaluated through nonlinear static and dynamic analyses performed on 3D planar models developed in *OpenSees*. The preliminary results showed that the EC8-1-2 design rules generally promote the intended dissipative behaviour of the examined braced frames. The comparison between DC2 and DC3 frames also indicated that the stricter design provisions for DC3 systems resulted in a more regular distribution of interstorey drift and brace ductility demand along the building height. Conversely, DC2 frames may exhibit more localised demands, with larger concentrations of drift and damage demand at specific storeys. At the same time, the results of the time-history analyses highlighted that global buckling phenomena occurred for CBF columns in both ductility classes. This suggests that, although the second-generation EC8 design rules are effective in promoting the intended dissipative mechanism of X-CBFs, they may still be insufficient to fully prevent column instability under the target seismic demand. Further studies are therefore needed to more comprehensively evaluate the effectiveness of the current design provisions and to support their possible refinement. Particular attention should be devoted to the design scenarios governing column demand in dissipative X-CBFs, with the aim of improving the protection of non-dissipative members against global buckling phenomena.

References

1. Tartaglia R, D'Aniello M, Demonceau JF, Landolfo R (2025) Seismic design and testing of EC8-1-2-compliant unstiffened end-plate beam-to-column joints. J Constr Steel Res 235:109916

2. Tartaglia R, Monte F, Demonceau JF, Maddaloni G (2026) Monotonic behaviour of 4-bolt row connections: analytical and numerical analyses. J Constr Steel Res 236:110048
3. Gnazzo M, Mahmoudi B, D'Aniello M, Imanpour A, Landolfo R (2026) Seismic design and response of inverted-V CBFs compliant with European and Canadian standards. Eng Struct 363:123071
4. Milone A, D'Aniello M, Landolfo R (2024) Advanced fatigue assessment of riveted railway bridges on existing masonry abutments: an Italian case study. Buildings 14(8):2271
5. Nip KH, Gardner L, Elghazouli AY (2010) Cyclic testing and numerical modelling of carbon steel and stainless steel tubular bracing members. Eng Struct 32:424–441
6. Costanzo S, D'Aniello M, Landolfo R (2019) Proposal of design rules for ductile X-CBFs in the framework of Eurocode 8. Earthquake Engng Struct Dyn 48:124–151
7. Barbagallo F, Bosco M, Marino EM, Rossi PP (2021) Proposal and validation of a design procedure for concentrically braced frames in the chevron configuration. Earthquake Engng Struct Dyn 50:3041–3063
8. Mahmoudi B, Imanpour A (2025) Seismic design of steel chevron and split-X concentrically braced frames. Earthquake Engng Struct Dyn 54:2565–2585
9. Milone A, Prota A, Landolfo R (2026) Ultimate and repairability performance of steel eccentrically braced frames designed according to the 2nd generation of Eurocode 8: a parametric study for medium-rise buildings. Eng Struct 363:123283
10. Fiorino L, D'Addesa V, Landolfo R (2024) Seismic design rules for lightweight steel shear walls with wood panel sheathing within the Eurocode format. Thin-Walled Struct 204:112293
11. Fiorino L, Campiche A, Tartaglia R, Landolfo R (2025) Seismic-resistant CFS walls braced with pre-tensioned UHS steel bars: design and construction of a building mockup. Thin-Walled Struct 208:112818
12. Freddi F et al (2025) Seismic retrofitting of existing steel frames with external BRBs: pseudo-dynamic hybrid testing and numerical parametric analysis. Earthquake Engng Struct Dyn 54(3):1064–1083
13. EN 1998-1-2, Eurocode 8: Design of structures for earthquake resistance – Part 1–2: Buildings, CEN (2026)
14. Bosco M, Fiamingo A, Massimino MR, Rossi PP (2024) An assessment of the seismic performance of EC8-compliant CBFs taking into account the role of soil: a case study. Buildings 14:2161
15. EN 1998-1-1, Eurocode 8: Design of structures for earthquake resistance – Part 1–1: General rules and seismic action, CEN (2025)
16. EN 1993-1-1, Eurocode 3: Design of steel structures – Part 1-1: General rules and rules for buildings, CEN (2023)
17. McKenna F, Scott MH, Fenves GL (2010) Nonlinear finite-element analysis software architecture using object composition. J Comput Civ Eng 24(1):95–107
18. Spacone E, Filippou FC, Taucer FF (1996) Fibre beam-column model for nonlinear analysis of R/C frames: part I. Formulation. Earthquake Engng Struct Dyn 25:711–725
19. D'Aniello M, La Manna Ambrosino G, Portioli F, Landolfo R (2013) Modelling aspects of the seismic response of steel concentric braced frames. Steel Compos Struct 15(5):539–566
20. D'Aniello M, La Manna Ambrosino G, Portioli F, Landolfo R (2015) The influence of out-of-straightness imperfection in physical theory models of bracing members on seismic performance assessment of concentric braced structures. Struct Des Tall Spec Build 24(3):176–197
21. Hsiao PC, Lehman DE, Roeder CW (2012) Improved analytical model for special concentrically braced frames. J Constr Steel Res 73:80–94

22. Menegotto M, Pinto PE (1973) Method of analysis of cyclically loaded R.C. Plane frames including changes in geometry and non-elastic behaviour of elements under combined normal force and bending. In: IABSE symposium on resistance and ultimate deformability of structures acted on by well defined repeated loads. IABSE, Lisbon, pp 15–22
23. Ashrafi A, Imanpour A (2021) Seismic response of steel multi-tiered eccentrically braced frames. J Constr Steel Res 181:106600
24. Uriz P, Mahin SA (2008) Toward earthquake-resistant design of concentrically braced steel-frame structures. PEER Report 2008/08,. Pacific Earthquake Engineering Research Center, University of California, Berkeley
25. Karamanci E, Lignos DG (2014) Computational approach for collapse assessment of concentrically braced frames in seismic regions. J Struct Eng 140:A401401

Towards Smart Steel Structures: Active Mass Dampers for Wind Comfort and Torsional Control in the Genoa Port Control Tower

Fabio Menardo[1](✉), Leonardo Bandini[2], Barbara Zulian[1], Valentina Bellotti[1], and Stefani Cii[1]

[1] ISAAC s.r.l., Milan, MI, Italy
fabio.menardo@isaacsrl.com
[2] CSi Italia, Pordenone, Italy

Abstract. The new Port Control Tower of the Port of Genoa, designed by Renzo Piano and completed in 2024, represents a case study of a highly slender steel structure with a long span roof at the top and stringent comfort requirements under wind actions. Optimized for lightness and global stiffness, the structural configuration exhibits a dynamic response governed by the first bending modes in the two main directions and by a significant torsional component, resulting in critical acceleration levels at the control cabin.

To control the in-service response, an active vibration control system with four Active Mass Dampers (AMDs) installed at roof level was adopted. This solution enables simultaneous mitigation of bending and torsional components with reduced mass and limited space requirements compared to equivalent passive devices, proving effective for slender and performance-sensitive structures.

The paper describes AMD integration within the structural design, the performance verification framework, target-mode definition, modelling of structure, control-system interaction, and the outcomes of dynamic identification and on-site tuning, highlighting significant acceleration reduction and experimental validation of the active control system in meeting serviceability requirements.

Keywords: active mass damper · wind-induced vibrations · serviceability · slender steel tower · modal control · occupant comfort · structural monitoring · Port of Genoa

1 Introduction

The new Genoa Port Control Tower, designed by Renzo Piano Building Workshop [5], was conceived as a critical infrastructure for navigation safety and, at the same time, as a highly recognizable architectural presence on the city waterfront. The project replaces the previous tower, which collapsed in 2013 after the impact of the vessel Jolly Nero, and is located in a context strongly exposed to wind, with particularly stringent serviceability requirements to ensure continuous operation of the control cabin.

From the earliest design stages, it became clear that the main critical issue was not the ultimate resistance of the structure, but rather its dynamic behaviour in service. The high

© The Author(s), under exclusive license to Springer Nature Switzerland AG 2026
R. Zanon et al. (Eds.): CTA 2026, LNCE 942, pp. 723–734, 2026.
https://doi.org/10.1007/978-3-032-39505-4_63

slenderness of the system, the large roof at the top, and the need to guarantee comfort levels compatible with continuous use of the cabin required an integrated approach combining structural concept, dynamic analysis and active vibration control.

This contribution summarizes that process, focusing on the definition of the performance problem, the criteria that led to the choice of an Active Mass Damper (AMD) system, the related modelling, and the results obtained during commissioning.

An overview of the Port Control Tower together with its main structural configuration is shown in Fig. 1.

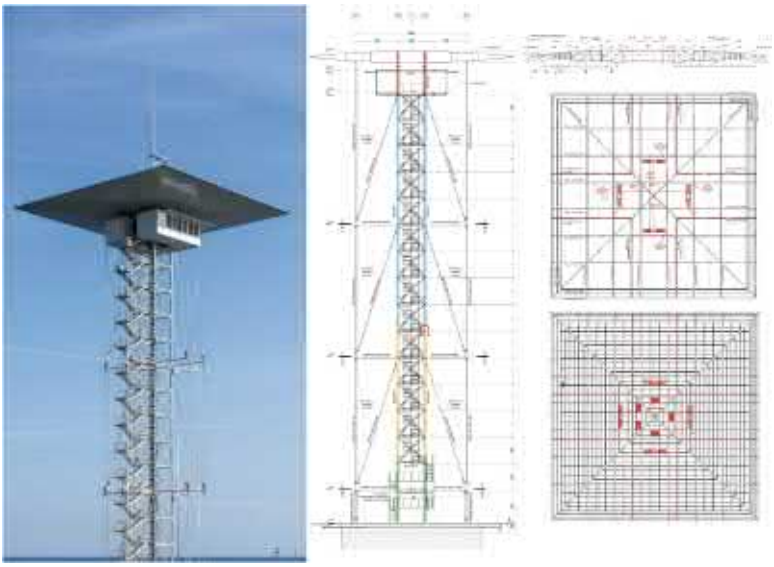


Fig. 1. (a) General view of the Genoa Port Control Tower; (b) elevation of the structural system; (c) roof plan showing the structural layout and the preliminary locations of the Active Mass Dampers (AMDs).

2 The Tower and the Performance Problem

2.1 Structural Configuration and Dynamic Model

The Port Control Tower consists of a steel core formed by four tubular columns arranged on a 3.6 × 3.6 m square plan. The control cabin is located at approximately 60 m elevation, while a 30 m-span lenticular roof supports the active-control system. The overall height reaches about 95 m.

A three-dimensional finite-element model was developed in SAP2000® [7] to perform modal and Fast Nonlinear Analyses (FNA). Frame elements represented the primary structural members, whereas secondary components, floors and the roof were modelled through equivalent shell elements or lumped masses. The model was developed to reproduce the global mass, stiffness and modal properties governing the wind response.

The pursuit of architectural lightness and functional transparency produced a mechanically efficient configuration, but one with intrinsically low damping. The total mass of the structure is approximately 370 t, distributed mainly between the lenticular roof, approximately 191 t, the control cabin, approximately 47 t, and the tower shaft, approximately 135 t. For the un-controlled structure, an initial viscous damping ratio of 0.3% was assumed for all modes, a conservative value consistent with the design assumptions. The first three natural modes governing the wind-induced response are illustrated in Fig. 2, while their corresponding natural frequencies and initial damping ratios are summarized in Table 1. The dominant modes consist of the first torsional mode (0.265 Hz) and the first two global bending modes in the principal directions (0.617 Hz and 0.634 Hz) [1].

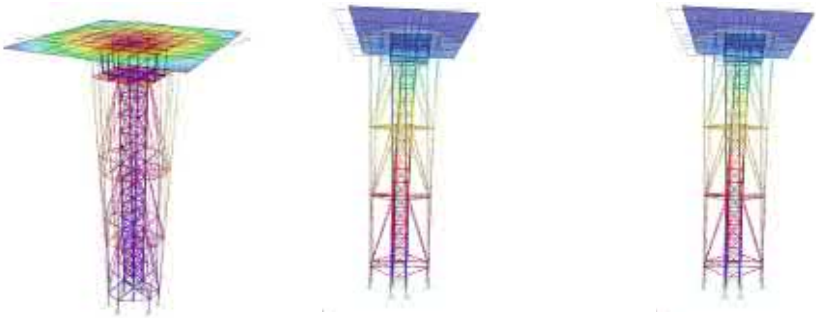


Fig. 2. First vibration modes of the tower: (a) first torsional mode; (b) first bending mode in the X direction; (c) first bending mode in the Y direction.

Table 1. Frequencies of the main modes and target design damping.

Mode	Direction	F [Hz]	ξ_0 [%]
1	Torsional	0.265	0.3
2	Translational in X	0.617	0.3
3	Translational in Y	0.634	0.3

2.2 Comfort Requirements

The main critical issue for the tower is not associated with safety at the ultimate limit state, but with its dynamic response under service conditions. The combination of high slenderness, mass concentrated at the top, low intrinsic dissipation and strong exposure to wind may produce accelerations that are incompatible with continuous use of the control cabin.

The design verifications, based on wind-tunnel results and on the comfort criteria referenced in the detailed design, showed that, at the most critical translational frequency,

the acceleration limit adopted for operator comfort is about 0.08 m/s^2. In the absence of control, the expected accelerations may instead reach values of about 0.58–0.60 m/s^2 at cabin level, and are therefore well above the reference threshold [4]. The performance requirement to be met is consequently the reduction of the accelerations perceived by operators, rather than an increase in the structural resistance capacity.

The comfort criterion adopted in the design, derived from the reference standards, is illustrated in Fig. 3.

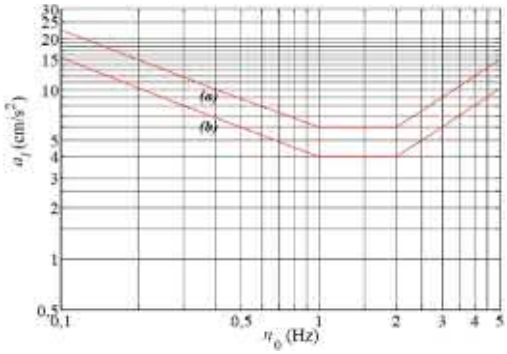


Fig. 3. Comfort acceleration level, return period $T_R = 1$ year.

Passive TMDs were initially considered [2]. However, controlling the first bending modes would have required approximately 30 t of moving mass, making the solution impractical because of space limitations and poor effectiveness in torsional control.

For these reasons, an active-control strategy based on four Active Mass Dampers installed in the roof was adopted. Compared with a passive solution, the active system makes it possible to generate controlled inertial forces using much smaller masses and to act simultaneously on the dominant bending and torsional modes. The design problem was therefore formulated in performance terms: to identify the additional damping required to bring the cabin accelerations back within comfort-compatible values, and to translate that requirement into the mechanical and control characteristics of the AMD devices.

2.3 Definition of the Equivalent Dynamic Wind Action

For the preliminary sizing of the AMD system, an equivalent dynamic wind action was defined for time-history analyses. Rather than reproducing the complete aerodynamic field, already investigated through wind-tunnel testing, the adopted input was calibrated to reproduce the target cabin accelerations specified in the design verification framework.

The excitation consisted of a zero-mean random signal filtered according to the von Kármán spectrum and normalized before being scaled to match the acceleration levels derived from wind-tunnel tests and CNR-DT 207/2008. The adopted excitation is shown in Fig. 4, while the corresponding target acceleration levels are summarized in Table 2.

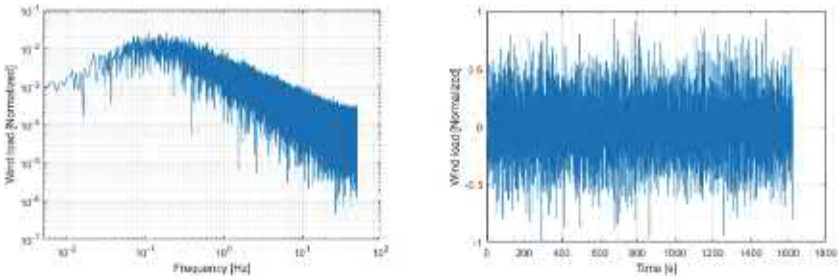


Fig. 4. Equivalent wind excitation adopted in the numerical analyses: (a) normalized von Kármán spectrum; (b) normalized time-history.

The reference design case corresponds to a wind event with a 200-year return period, producing a transverse cabin acceleration of approximately 0.600 m/s^2, in agreement with the maximum value obtained from wind-tunnel tests (about 0.580 m/s^2). The same excitation was subsequently scaled to represent return periods of 1 and 10 years [6].

Table 2. Reference accelerations at cabin level according to CNR-DT 207/2008.

T_R [yr]	Longitudinal acc [m/s^2]	Transverse acc [m/s^2]	Torsional acc [m/s^2]
1	0.130	0.160	0.005
10	0.220	0.290	0.007
200	0.390	0.600	0.011

For the numerical model, the wind action was represented by equivalent concentrated forces applied at four perimeter roof nodes, corresponding to the preliminary locations of the AMDs. The force amplitudes were iteratively calibrated until the uncontrolled model, assuming 0.3% damping, reproduced the target cabin accelerations. The resulting loading was then adopted for comparison of the uncontrolled and controlled responses and for sizing the required damping, force, stroke and moving mass of the AMD system.

3 Active-Control Strategy

The active-control system was conceived as part of the tower's global dynamic response, with the aim of introducing controlled additional damping rather than increasing structural strength. Since the response is governed by two closely spaced bending modes and a significant torsional component, a distributed solution with four AMD devices installed in the roof was adopted instead of a single concentrated unit.

The devices were placed at perimeter positions within the top lens, corresponding to the nodes used in the numerical model for the equivalent wind forces. This layout improves control effectiveness in both principal bending directions and in torsion by generating controlled force couples through the motion of the moving masses.

3.1 Device Layout and Sizing Criteria

During the preliminary design stage, each AMD was represented by an equivalent single-axis viscous damper connected to the roof, expressed by Eq. (1). This simplified model enabled the translation of the comfort requirement into equivalent modal damping, from which the required actuator force was derived through time-history analyses.

$$F_{AMD} = G\left(\dot{x}_r - \dot{x}_g\right) \tag{1}$$

where G is the equivalent viscous coefficient, or Gain, $\dot{x}_r$ is the velocity of the roof node and $\dot{x}_g$ is the velocity of the reference node. This idealization made it possible to translate the comfort requirement into an increase in modal damping and to estimate, through time-history analyses, the mechanical demand on the devices.

The relationship between the Gain value and the additional modal damping can be expressed, in simplified form, according to Eq. (2).

$$n_i G = 2m_i\omega_i\left(\xi^*{}_i - \xi_{0,i}\right) \tag{2}$$

where m_i and ω_i are, respectively, the modal mass and the circular frequency of the i-th mode, $\xi_{0,i}$ is the initial damping of the uncontrolled structure, $\xi^*{}_i$ is the target damping, and n_i represents the number of actuators effective on the considered mode. For the bending modes, n_i is equal to 2, while for the torsional mode the contribution of all four actuators can be exploited in a coupled manner.

Gain was iteratively tuned and calibrated until the target comfort requirements were satisfied, resulting in a final value of $G = 50$ *kNs/m*.

The resulting target modal damping ratios are summarized in Table 3 [6].

Table 3. Modal damping targets of the AMD system.

Mode	Direction	ξ_0 [%]	ξ^* [%]
1	Torsional	0.3	6.3
2	Translational in X	0.3	4.4
3	Translational in Y	0.3	4.0

After calibration of the equivalent viscous model, the force time histories required of the individual devices were extracted from the time-history analyses for the most severe case, corresponding to the wind event with a nominal return period of 200 years. The most severe profile was taken as the design cycle for the mechanical sizing of the AMD. The analyses identified a peak force of approximately 2.6 kN and an RMS force, evaluated over a 5 s moving window, of approximately 1.5 kN [1].

The equivalent modelling strategy adopted during the preliminary design stage is schematically illustrated in Fig. 5.

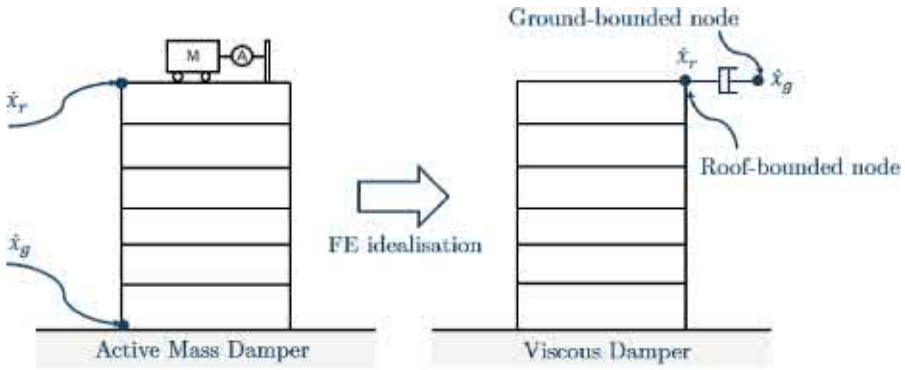


Fig. 5. Preliminary modelling of the AMDs as equivalent viscous dampers for the definition of damp-ing targets.

3.2 Sizing of the Actuator and Moving Mass

The force demand obtained from the numerical analyses defines the primary requirement for the actuator. In the case of an AMD, however, the choice of machine cannot be based on maximum force alone, but must also consider attainable velocity, available stroke, inertial mass and margins with respect to saturation and end stops.

To maximize reliability and reduce maintenance requirements, the choice was oriented towards electric linear motors, which generate the motion of the moving mass directly along the control direction while limiting mechanical motion-conversion components. The selected motor is characterized by a peak force of 5.0 kN, sustainable for 1 s, and a continuous force of 1.979 kN, values greater than the demand identified by the analyses, equal to 2.6 kN peak and 1.56 kN RMS, respectively.

The moving mass was sized by identifying the minimum value compatible with the velocity and stroke constraints, according to Eq. (3):

$$M = \max\left(M_V, M_S\right) \tag{3}$$

where M_V is the minimum mass required to avoid velocity saturation of the motor and M_S is the minimum mass required to keep the displacement of the mass within the allowable stroke.

Velocity and stroke constraints were checked through integration of the force histories. The velocity criterion required a minimum moving mass of 285 kg, whereas the stroke limitation governed the design, leading to the final value of 340 kg [1]. The outcome of the sizing procedure is illustrated in Fig. 6, showing both the force–velocity verification and the resulting displacement response.

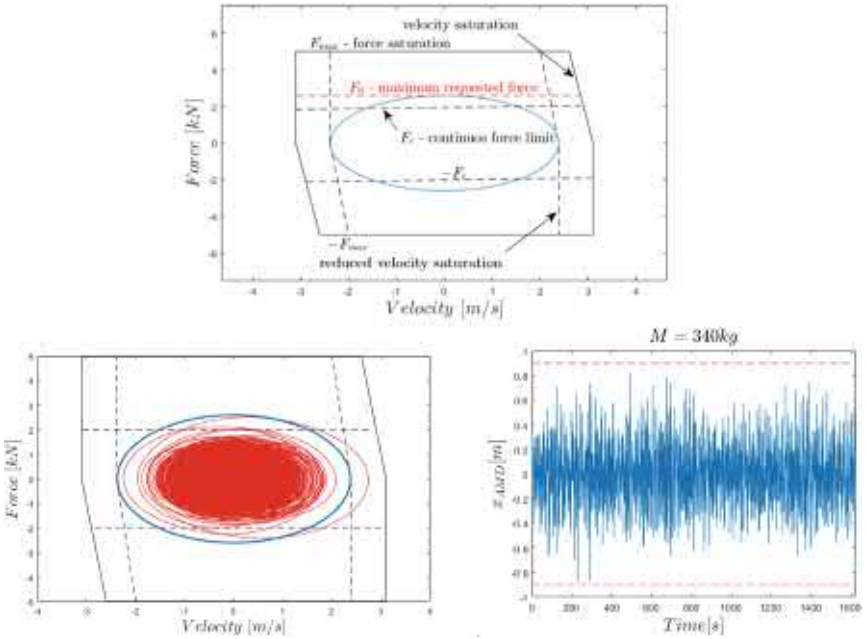


Fig. 6. Verification of the AMD sizing procedure: (a) force–velocity domain of the selected linear motor; (b) force–velocity trajectory of the moving mass; (c) displacement response compared with the allowable stroke.

The final configuration of each device therefore includes a moving mass of 340 kg, a useful stroke of 1.8 m and an overall length of approximately 3.0 m. Including the frame, guides, motor and auxiliary components, the total mass of each AMD is approximately 500 kg; the four devices therefore add approximately 2 t to the structure, corresponding to about 0.5% of the total mass of the tower [6].

The main characteristics of the AMD configuration are summarized in Table 4.

Table 4. Main design parameters of the installed AMD system.

Parameter	Value
Number of devices	4
Moving mass per device	340 kg
Total moving mass	1.36 t
Total installed mass	approximately 2.0 t
Peak force per device	2.60 kN
RMS force per device	1.56 kN
Selected motor	5.00 kN peak; 1.98 kN continuous
Useful stroke	1.8 m
Machine length	3.0 m

3.3 MMNAF Control Logic

The adopted controller is based on the Multi-Modal Negative Acceleration Feedback (MMNAF) strategy [3], which converts measured structural accelerations into displacement commands for the moving masses. The control law reproduces the behaviour assumed in the numerical design model and allows simultaneous control of the two bending modes and the first torsional mode. Final controller tuning was performed during on-site commissioning.

4 Experimental Validation and Performance

4.1 Modal Identification and Damping Increase

The active system was installed inside the tower roof during the final completion phase of the work. In addition to the four actuators, the configuration includes a central control unit, four feedback accelerometers placed at the roof control nodes, three monitoring accelerometers distributed along the tower height, and an ultrasonic anemometer installed at the top. The same measurement network also provides a basis for dynamic monitoring of the structure in service and for the future correlation between measured wind and structural response.

The installation layout of the four AMD units and the monitoring system is shown in Fig. 7.

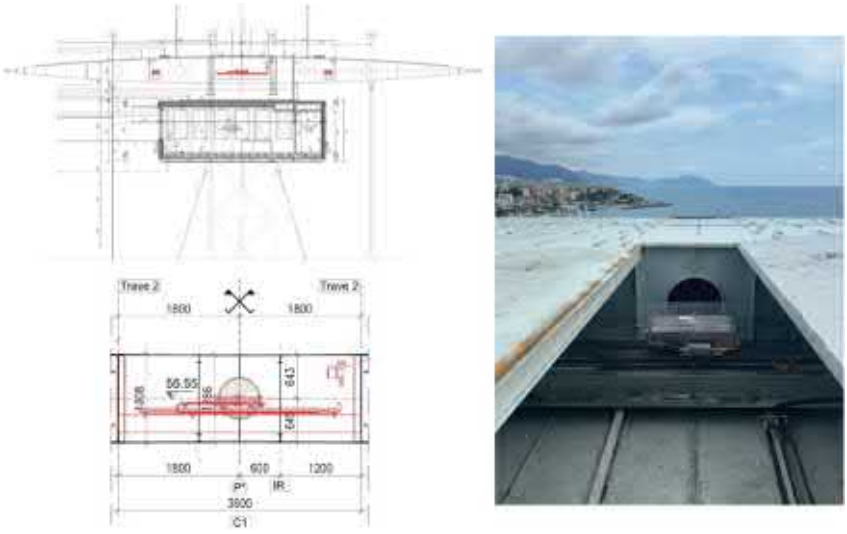


Fig. 7. Integration of the AMD system within the roof structure: (a) cross-section of the roof showing the AMD location; (b) installation detail of the actuator within the roof lens; (c) installed AMD unit during commissioning.

The experimental commissioning campaign had a twofold objective: on the one hand, to identify the actual dynamic properties of the uncontrolled structure; on the other, to

verify the effectiveness of the AMD system once activated. The tests included frequency sweeps, resonance excitations in the two principal directions, and tests dedicated to the torsional mode, both with the active system switched off and with the active system engaged. In total, 20 tests were performed, with harmonic forces applied by the AMDs themselves used as dynamic exciters.

The experimental modal identification was carried out starting from the Frequency Response Functions obtained in a MIMO configuration, using the signals from the different accelerometers simultaneously. The comparison with the numerical model confirmed that the response of the tower is governed by the first three modes. The experimental frequencies are approximately 0.32 Hz for the torsional mode and approximately 0.67 Hz and 0.69 Hz for the two principal bending modes; the intrinsic damping ratios of the uncontrolled structure range between 0.37% and 0.65%.

With the active system engaged, the damping of the three principal modes increases significantly. The torsional mode increases from 0.61% to 8.31%, the first bending mode from 0.65% to 6.07%, and the second bending mode from 0.37% to 5.34%. As shown in Table 5, the experimental values are higher than the minimum targets defined during the design phase, confirming the robustness of the numerical calibration and subsequent on-site tuning [6].

Table 5. Experimental modal parameters before and after activation of the AMD system.

Mode	Direction	Fexp [Hz]	ξ_0 [%]	ξ^* [%]
1	Torsional	0.32	0.61	8.31
2	Translational in X	0.67	0.65	6.07
3	Translational in Y	0.69	0.37	5.34

The numerical analyses performed with the calibrated AMD system show a significant reduction in accelerations at cabin level. As reported in Table 6, for the case associated with a return period of 1 year, taken as the reference for in-service comfort, the peak accelerations decrease from 16.0 cm/s^2 to 4.1 cm/s^2 in the X direction and to 5.4 cm/s^2 in the Y direction. The values are therefore below the comfort threshold of 8 cm/s^2. For more severe events, corresponding to return periods of 10 and 200 years, the absolute accelerations increase, but the relative reduction remains between 66% and 75% [6].

Table 6. Accelerations from numerical analyses at the control-room level of the tower equipped with AMDs.

Direction	$T_R = 1$ year		$T_R = 10$ year		$T_R = 200$ year	
	UC a_{peak}[cm/s^2]	C a_{peak}[cm/s^2]	UC a_{peak}[cm/s^2]	C a_{peak}[cm/s^2]	UC a_{peak}[cm/s^2]	C a_{peak}[cm/s^2]
X	16.0	4.1 (−74%)	29.0	7.5 (−74%)	60.0	15.1 (−75%)

(*continued*)

Table 6. (*continued*)

Direction	$T_R = 1$ year		$T_R = 10$ year		$T_R = 200$ year	
	UC a_{peak}[cm/s^2]	C a_{peak}[cm/s^2]	UC a_{peak}[cm/s^2]	C a_{peak}[cm/s^2]	UC a_{peak}[cm/s^2]	C a_{peak}[cm/s^2]
Y	16.0	5.4 (−66%)	29.0	9.8 (−66%)	60.0	19.6 (−67%)

4.2 Reduction at Cabin Level

The resonance tests experimentally confirmed the effectiveness of the system. Sinusoidal forces were applied at the identified natural frequencies under both uncontrolled and controlled conditions, with amplitudes up to 4 kN for the bending modes and 900 N for the torsional mode. The comparison of the responses showed a marked reduction in oscillation amplitude when active control was engaged.

A distinctive feature of the experimental campaign is that the AMDs were used both as excitation sources and as control devices. During selected tests, three actuators operated as active dampers while the fourth applied a known excitation, allowing validation of the tower dynamics without external shakers and making the commissioning procedure fully representative of the operational system.

The experimental and numerical results consistently demonstrate that the AMD system significantly increases modal damping and reduces cabin accelerations, effectively controlling both bending and torsional vibrations.

Representative time histories from the experimental campaign are reported in Figs. 8 and 9. Figure 8 presents the response during bending-mode excitation (Tests T7 and T13), whereas Fig. 9 shows the response during excitation of the first torsional mode (Test T18).

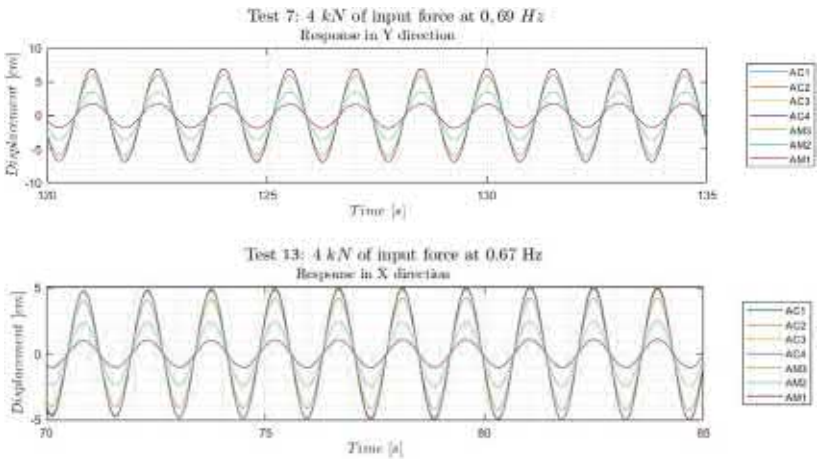


Fig. 8. Representative displacement time histories of tower displacement in tests T7 and T13.

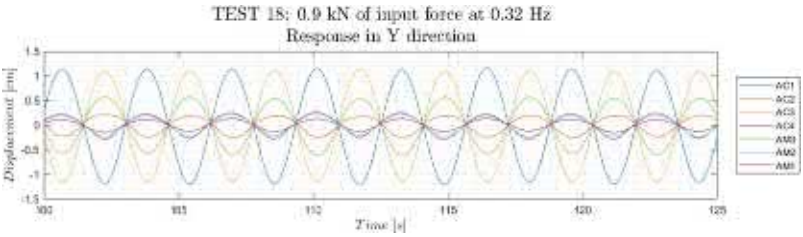


Fig. 9. Representative torsional displacement time history response of tower displacement in test T18, in which the torsional mode was excited.

5 Conclusions

This paper presented the design, sizing and experimental validation of the Active Mass Damper (AMD) system installed in the new Genoa Port Control Tower. The adopted solution, based on four compact actuators governed by a Multi-Modal Negative Acceleration Feedback (MMNAF) control law, was specifically developed to control the coupled bending and torsional response of the slender steel structure.

The numerical design procedure, based on equivalent viscous dampers, enabled the definition of the required damping targets and proved consistent with the results of the experimental commissioning. Modal identification and on-site testing confirmed a significant increase in modal damping and a substantial reduction of cabin accelerations, while requiring considerably less installed mass and space than an equivalent passive solution.

The proposed approach demonstrates that active-control systems represent an effective solution for slender structures governed by multimodal dynamic behavior, where serviceability and occupant comfort are the primary design requirements. Beyond the presented case study, the methodology provides a practical framework for integrating structural design, control engineering and experimental validation in future high-performance structures.

References

1. TO.RE.4210 (2022) Realizzazione Nuova Torre Piloti, Progetto Esecutivo Opere Civili: Analisi delle Azioni del Vento sulle Strutture. Ports of Genoa
2. Kareem A, Kijewski T, Tamura Y (1999) Mitigation of motions of tall buildings with specific examples of recent applications. Wind Struct 2(3):201–251
3. Resta F, Ripamonti F, Cazzulani G, Ferrari M (2010) Independent modal control for nonlinear flexible structures: an experimental test rig. J Sound Vib 329(8):961–972
4. ISAAC. (2024), Progetto esecutivo nuova Torre Piloti di Genova.
5. Renzo Piano Building Workshop. (2015), New Genoa pilot tower project.
6. Calvi P.M., Bogni L., Bussini A., Cii S., Bandini L., Ripamonti F. (2025), Implementation of active mass damping for wind-induced vibration mitigation: the Genoa control tower.
7. Computers and Structures, Inc (2024) SAP2000 integrated software for structural analysis and design, version XX. User's Manual, Berkeley, California, USA

Behaviour Factors for the Seismic Design of Steel Frames Equipped with Pinching-Free Devices

Rio Saito[1], Annarosa Lettieri[1](✉), Atsushi Sato[1], and Massimo Latour[2]

[1] School of Engineering, Nagoya Institute of Technology, Nagoya, Japan
lettieri.annarosa@nitech.ac.jp
[2] Department of Civil Engineering, University of Salerno, Fisciano, Italy

Abstract. Concentrically Braced Frames (CBFs) are widely used in seismic design due to their high stiffness and strength. However, their performance is often limited by brace buckling under cyclic loading, which leads to strength and stiffness degradation and pinched hysteretic behaviour. This results in unstable energy dissipation and significant damage concentrated in the bracing members, often requiring post-earthquake repair or replacement. To overcome these issues, an innovative replaceable Aluminium Foam Damper (AFD) has been proposed for X-braced CBFs. The system improves seismic performance by eliminating pinching and enhancing energy dissipation through aluminium foam layers combined with a wedge-based mechanism that ensures stable hysteretic behaviour. Since such systems are not yet covered by seismic design codes, key parameters like the behaviour factor (q) must be investigated. A parametric study was conducted on single-story steel parking structures designed in accordance with Eurocode 8 and upgraded with AFDs. Nonlinear models were developed in OpenSees, and Incremental Dynamic Analyses (IDAs) were performed using 44 ground motion records from FEMA P695. Three different behaviour factors were examined to determine the optimal value that balances seismic performance and design efficiency.

Keywords: Concentrically Braced Frame · Aluminium foam damper · Wedge device · Seismic design · Incremental dynamic analysis · Fragility curve

1 Introduction

Concentrically Braced Frames (CBFs) are commonly designed to dissipate input seismic energy through axial yielding of the diagonal bracing [1–3]. However, recent earthquakes have shown that brace buckling can lead to severe structural damage, stiffness and strength degradation, pinched hysteretic behaviour, and significant economic losses [4, 5].

To overcome these limitations, several replaceable dissipative devices have been proposed for CBFs, such as slotted bolted connections [6], buckling-restrained braces [7], and shear dampers [8]. These systems are generally installed in series with the braces to concentrate damage in replaceable components while protecting the main structural members. In parallel, increasing attention has been devoted to innovative

© The Author(s), under exclusive license to Springer Nature Switzerland AG 2026
R. Zanon et al. (Eds.): CTA 2026, LNCE 942, pp. 735–746, 2026.
https://doi.org/10.1007/978-3-032-39505-4_64

materials with enhanced energy dissipation capabilities. Among them, Aluminium Foam Material (AFM) [9] is characterised by low density, high deform-ability, and excellent energy absorption under compression.

Recently, Lettieri et al. [10] proposed the use of AFM to develop an innovative damper for X-braced Concentrically Braced Frames (X-CBFs). The proposed device consists of AFM layers, designed to dissipate the incoming seismic energy through compressive deformation, and a wedge mechanism [11] that prevents the brace from developing compressive forces. In this configuration, the system behaves as a tension-only device, thereby avoiding pinching effects and strength degradation associated with buckling phenomena in compressed elements.

In this paper, a preliminary parametric study is conducted on single-storey steel parking structures designed in accordance with Eurocode 8, with different behaviour factors and upgraded with AFDs (Pinching-Free CBF, PF-CBF). Experimental tests on the proposed device, carried out in collaboration between the Nagoya Institute of Technology (Japan) and the University of Salerno (Italy), are presented. Subsequently, a numerical model is validated in OpenSees and used to conduct the study. Incremental Dynamic Analysis (IDA) [12] is conducted in OpenSees [13] using 22 ground motion records in accordance with FEMA P695 [14]. Interstorey drift and local deformation parameters of the AFD are monitored in the analyses. Furthermore, fragility curves are constructed to probabilistically evaluate the seismic response performance and appropriate behaviour factors of the proposed PF-CBF. The results provide insight into the acceptable ranges for designing the proposed system.

2 Aluminium Foam Damper (AFD)

2.1 Configuration Details and Hysteretic Response

Figure 1 illustrates the details of the proposed AFD. The AFD is intended to be installed in series with bracings in X-Braced CBFs. The configuration equipped with AFDs is hereafter referred to as Pinching-Free CBF (PF-CBF).

The bracing, realised with a steel rod in this study, is split into two portions by a clearance δ_{gap}, and both parts are anchored to the device. δ_{gap} ensures that the axial deformation in the bracing is released, allowing a tension-only behaviour. is composed of two primary components: (1) AFM layers, which are expected to dissipate the seismic energy by accumulating plastic compressive deformation; (2) a wedge system equipped with springs [11], which guarantees a ratchet behaviour of the bracings (bracings are able to immediately sustain tensile forces after experiencing a compressive axial deformation). Additionally, a bearing plate is installed between the AFM layers and the wedge mechanism to distribute compressive stresses uniformly across the foam layers and facilitate the integration of the wedge assembly within the device; an external tube with endplates ensures that the two rod portions behave as a single bracing element.

Figure 2 illustrates the dissipative mechanism of a PF-CBF subjected to a fully symmetric lateral displacement cycle, including the dissipative behaviour of the AFD and its hysteretic response.

When the PF-CBF experiences a lateral displacement $\Delta_{(+)}$ $\Delta_{(+)}$ during Phase 0–1, a tensile force develops in Rod 1. This force is transmitted to the AFM layers, resulting

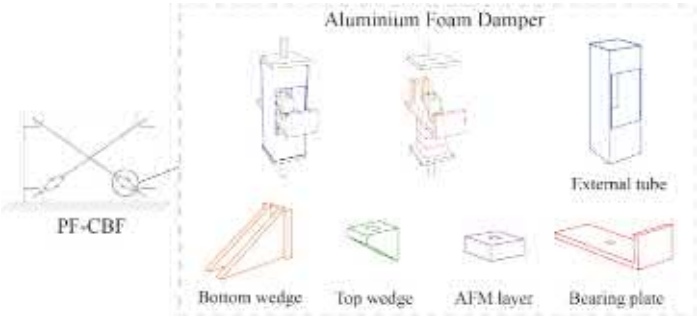


Fig. 1. AFD's main components.

in a compressive deformation of the AFM, denoted as $\delta_{Foam1(+)}$. At this stage, sufficient friction between the wedge components prevents any relative sliding. Simultaneously, Rod 2 remains disengaged due to the gap δ_{gap}, allowing both the rod and the upper wedge to move upward and create a separation from the lower wedge equal to $\delta_{Foam1(+)}$. This separation is accommodated by the horizontal penetration of the lower wedge, driven by the tension in the spring system.

When the loading direction reverses, the behaviour of the bracing system also reverses: tensile force develops in Rod 2, while Rod 1 slides in compression. Phase 2–3 represents the stage in which both rods return to their initial configuration. In this phase, the compressive sliding of Rod 1 is equal to $\delta_{Foam1(+)}$, while Rod 2 undergoes tensile deformation, with the AFM layers accommodating $\delta_{Foam1(-)}$. This mechanism is consistently repeated in subsequent loading cycles.

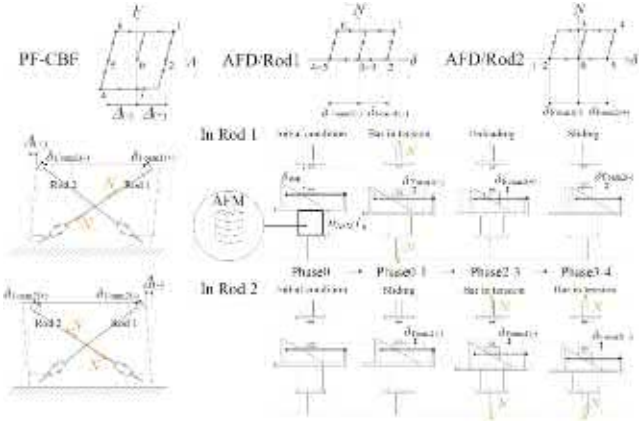


Fig. 2. Dissipative mechanism of a PF-CBF system.

2.2 Experimental Tests

AFM layers and the AFD were experimentally investigated, as shown in Fig. 3(a) and (b). Monotonic compression tests with unloading-reloading phases were carried out on four AFM layers with nominal dimensions of 90 × 90 × 42 mmThe results showed that the material exhibits a stable constitutive response during the reloading phase, maintaining a consistent stress-strain behaviour (Fig. 3(a)).

The monotonic test results were further used to define a constitutive law adopted for the AFM layers, also depicted in Fig. 3(a). In particular, E_{AFM} denotes the AFM stiffness; $f_{y,AFM}$ is the corresponding yielding stresses; $f_{u,AFM}$ is the maximum stress; the overstrength factor is defined as $\Omega_{AFM} = f_{u,AFM} / f_{y,AFM}$; and $\varepsilon_{u,AFM}$ is the ultimate strain. The numerical values are 2077 MPa, 7.1 MPa, 10.8 MPa and 1.5, respectively for $E_{AFM}, f_{y,AFM}, f_{u,AFM}$, and Ω_{AFM}.

Subsequently, the six-layer configuration was implemented within the AFD device and experimentally tested under cyclic loading conditions. Figure 3(b) shows the relationship between the applied load and the deformation of the AFM layers obtained from the displacement transducers. The results confirmed the capability of the AFD to effectively dissipate seismic energy through the deformation of the AFM layers, with a stable hysteretic behaviour.

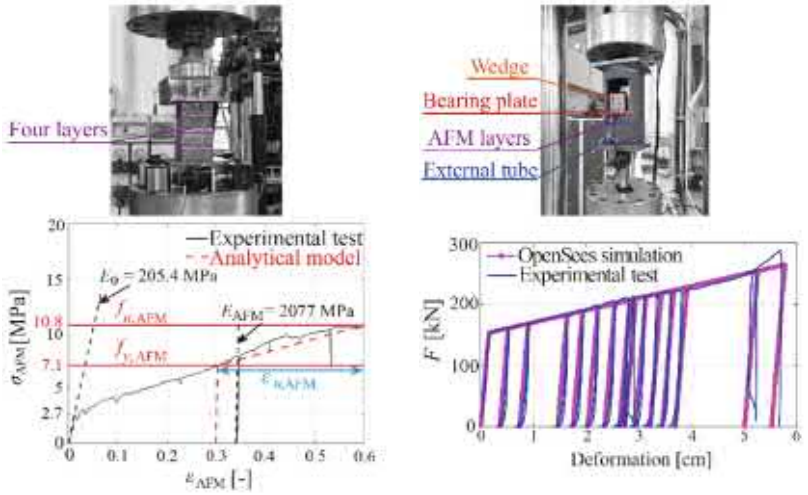


Fig. 3. (a) AFM layers and (b) AFD device experimental characterisation.

3 Design of the Case-Study Structures

3.1 Case-Study Structures

Figure 4 presents the plan layout and elevation view of the reference building configurations. X-braced CBFs, with a bay width of 5000 mm and a storey height of 3500 mm, are arranged in both the x- and y-directions, whereas the internal framing system is designed to resist only gravity loads.

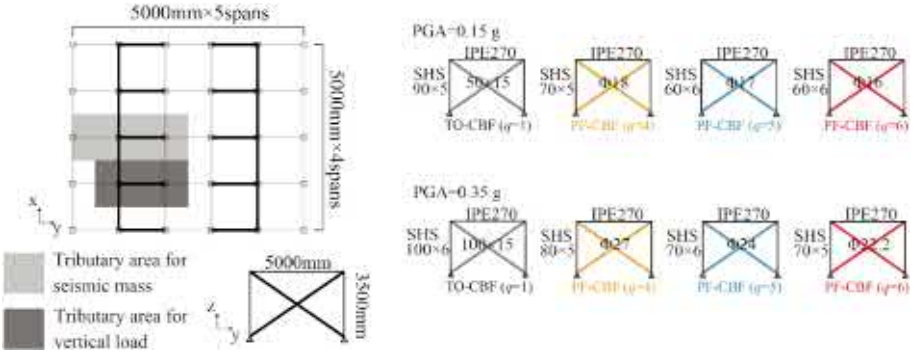


Fig. 4. Plan and elevation views of the case-study structures.

The parametric study includes a reference structure in a conventional configuration (denoted as TO-CBF) and several innovative PF-CBF configurations designed with different behaviour factors q.

The structures were designed in compliance with the provisions of Eurocode 8, accounting for permanent and imposed loads of 2.5 kN/m^2 each. All structural components are fabricated from S275 structural steel. The columns consist of square hollow sections (SHS), whereas the beams are formed using IPE profiles. In the conventional TO-CBF system, the bracing members are steel strap plates, whereas the PF-CBF configuration employs high-strength steel rods.

In PF-CBF systems, the high-strength steel rods are proportioned by applying an overstrength factor, Ω_{AFM}, derived from the compressive behaviour of the AFM layers. This criterion ensures that the rods remain elastic until the AFM layers reach their maximum compressive resistance. The structures are designed for two seismic intensity levels. Figure 5 illustrates the Type 1 elastic response spectra corresponding to the Ultimate Limit State (ULS) design earthquake, considering ground type C and peak ground acceleration (PGA) values of 0.15 g and 0.35 g. The seismic demand at the Collapse Limit State (CLS) is assumed to be 1.5 times that adopted for the ULS. A behaviour factor of $q = 1$ is adopted for the conventional TO-CBF systems, in accordance with Eurocode 8. For the PF-CBF configurations, the parametric study considers $q = 4$, 5, and 6 to evaluate the influence of this parameter on the structural seismic response and to identify the seismic demand compatible with the mechanical properties of the AFM

layers obtained from the compression tests. The analyses assume the AFD configuration experimentally investigated in Sect. 2.2. Further details of the PF-CBF design methodology are provided in [10].

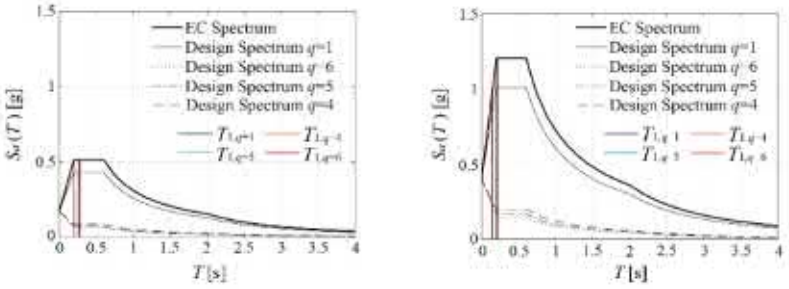


Fig. 5. Design spectrum for PGA equal to (a) 0.15 g and (b) 0.35 g.

3.2 Numerical Modeling

The seismic performance of the TO-CBF and PF-CBF configurations was investigated through two-dimensional numerical models developed in OpenSees. The finite element idealisation adopted for the analyses is illustrated in Fig. 6. Frame members and braces are discretised using force-based beam-column elements with distributed plasticity, employing four integration points. Material nonlinearity associated with flexural and shear behaviour is captured by combining fibre sections with the *Aggregator* section command. All steel structural members are assigned the *Steel01* constitutive model, assuming a yield strength of 275 MPa and a strain-hardening ratio of 0.2%. The nonlinear axial response of the bracing systems is modelled using zero-length elements placed in series with the braces. Different constitutive formulations are adopted for the two structural configurations. In the conventional TO-CBF models, the cyclic degradation and gap-closing behaviour are represented by an *ElasticPPGap* material. For the PF-CBF systems, the mechanical response of the AFD is reproduced by coupling an *ElasticPP* material in series with a *Steel01* material. Within this arrangement, the *ElasticPP* component provides compressive resistance while preserving tensile stiffness, thereby reproducing the bracing's tension-only response. The *Steel01* component is calibrated from the experimental compression tests on the AFM layers (Fig. 3(a)) and governs the inelastic deformation associated with energy dissipation.

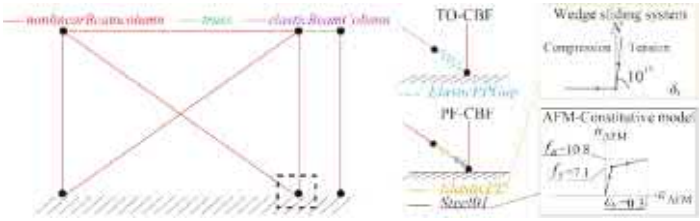


Fig. 6. OpenSees modelling for TO-CBFs and PF-CBFs.

4 Seismic Response of the Case-Study Structures

4.1 Ground Motion Selection and Monitored Parameters

To assess the seismic performance of the proposed structures, Incremental Dynamic Analyses (IDAs) were performed using a set of 22 ground-motion pairs selected in accordance with the FEMA P695 protocol [14]. Since each record includes two orthogonal horizontal components, a total of 44 accelerograms were analysed. The response spectra of the selected records are presented in Fig. 7.

The intensity measure adopted in the analyses is the spectral acceleration at the fundamental vibration period, $S_a(T_1)$. During the IDA procedure, the ground motions were scaled in increments of 0.1 g to investigate the structural response under DLS, ULS, and CLS limit states. To facilitate the comparison of the results, the seismic intensity is expressed in terms of the normalised intensity measure, IM_N, defined as the ratio between $S_a(T_1)$ and the corresponding value at the ULS.

The structural response is evaluated in terms of the maximum interstorey drift ratio, θ_{peak}. Although 44 IDA curves were obtained for each structural configuration, only the median response, along with the 16th and 84th percentile envelopes, is presented in the following sections to improve the readability of the results. For the PF-CBF systems, additional local response quantities are monitored to assess AFD performance. In particular, the accumulated compressive stress (σ_{damper}), the accumulated compressive strain (δ_{damper}), and the corresponding compressive displacement (δ_V) of the damper are recorded throughout the analyses.

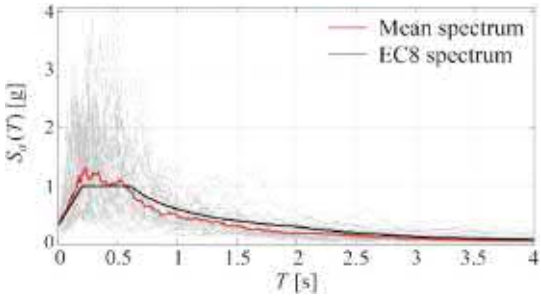
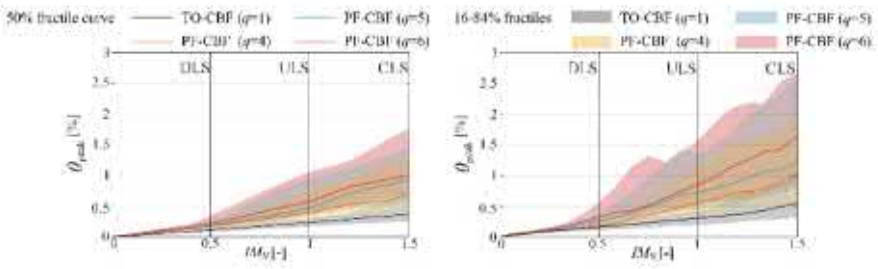


Fig. 7. Spectra of the ground motion records.

4.2 Incremental Dynamic Analysis (IDA)

Figures 8, 9, 10 and 11 present the results obtained from the IDAs. In each plot, the 50% fractile responses are depicted with bold lines, whereas the 16% and 84% fractiles are represented by shaded areas. Vertical solid lines are included to demarcate the DLS, ULS and CLS and facilitate a direct evaluation across the different demand levels.

Figure 8(a) and (b) compare θ_{peak} values obtained for the TO-CBF ($q = 1$) and PF-CBF ($q = 4$, 5, 6) designed with PGA = 0.15 g and PGA = 0.35 g, respectively. The results show that, compared with TO-CBF, the PF-CBF systems exhibit larger θ_{peak} values due to their higher plastic deformation capacity. Moreover, the θ_{peak} values generally increase as the behaviour factor q increases, consistently with the expected structural behaviour. At the ULS, the 50% fractile values of θ_{peak}, remain below the 2% threshold prescribed by ASCE/SEI 7–22 [2], indicating that all PF-CBF configurations satisfy the required performance. At CLS, the θ_{peak} values for the structures designed with PGA = 0.15 g also remain below 2%. In contrast, for PGA = 0.35 g, the 84% fractile curves for $q = 5$ and 6 exceed 2.5%.



(a) **(b)**

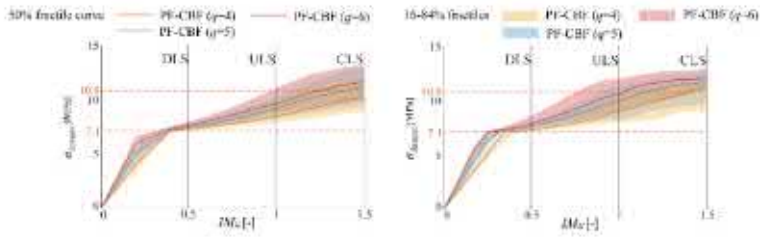
Fig. 8. IDA comparison in terms of θ_{peak} for PGA equal to (a) 0.15 g and (b) 0.35 g.

Figure 9(a) and (b) compare the σ_{damper} values, calculated by dividing the compressive force by the cross-sectional area. In addition, the values of $f_{y,AFM}$ and $f_{u,AFM}$ are reported with horizontal lines. Similarly, Fig. 10(a) and (b) compare the ε_{damper} values accumulating in the AFM layers of the AFD. The maximum compressive deformation $\varepsilon_{u,AFM}$ $\varepsilon_{u,\,AFM}$ is also reported. It is important to note that the values of $f_{y,AFM}$, $f_{u,AFM}$ and $\varepsilon_{u,AFM}$ are reported to verify that the seismic demand quantified by IDAs aligns the expected capacity of the AFM layers.

Figures 9 and 10 indicate that, for PGA = 0.15 g, the 50% fractile curves at ULS remain below the allowable limits for all values of q; however, the 84% fractile curve for $q = 6$ exceeds such limits. Furthermore, for PGA = 0.35 g, not only the 84% fractile curve for $q = 6$ but also that for $q = 5$ exceed the allowable values at ULS, while the 50% fractile curve for $q = 6$ remains only slightly below the limits.

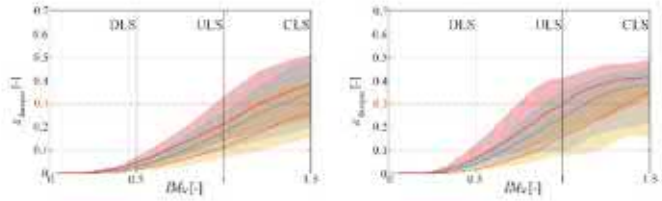
Figure 11(a) and (b) display the δ_V values, respectively, for PGA = 0.15 g and 0.35 g. For PGA = 0.15 g, all 50% fractile curves at ULS remain below 20 mm, and no significant differences are observed in the 84% fractile curves with changes in the

value of q. For PGA = 0.35 g, the 50% fractile curves at ULS also remain below 20 mm; however, the 84% fractile curves for $q = 5$ and $q = 6$ exceed 20 mm. At CLS, the maximum PGA values of 0.15 g remain below 40 mm, whereas those for PGA = 0.35 g increase to nearly 80 mm.



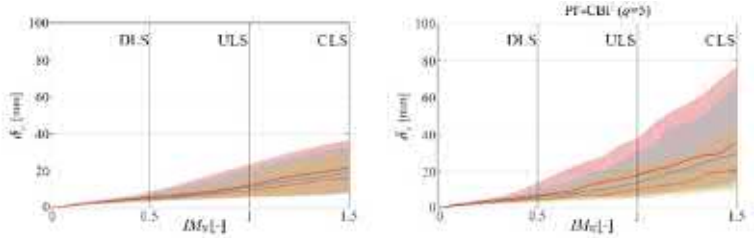
(a) **(b)**

Fig. 9. IDA comparison in terms of σ_{damper} for PGA equal to (a) 0.15 g and (b) 0.35 g.



(a) **(b)**

Fig. 10. IDA comparison in terms of ε_{damper} for PGA equal to (a) 0.15 g and (b) 0.35 g.



(a) **(b)**

Fig. 11. IDA comparison in terms of δ_V for PGA equal to (a) 0.15 g and (b) 0.35 g.

4.3 Fragility Curves

The fragility curves provide a probabilistic meaning of the IDA curves and describe the probability that the seismic demand exceeds a specified limit state under a given level of seismic intensity. Figure 12(a) and (b) show the fragility curves representing the probability that σ_{damper} exceeds $f_{u,AFM} = 10.8$ MPa, while Fig. 13(a) and (b) show the fragility curves representing the probability that ε_{damper} exceeds $\varepsilon_{u,AFM} = 0.3$. The IM used on the horizontal axis is the same as that adopted in IDA.

The results show that at the DLS, the exceedance probabilities P_f are negligible, confirming that the capacity of the AFD in terms of both σ_{damper} and ε_{damper} is fully satisfied. At the ULS, the P_f values associated with both σ_{damper} and ε_{damper} increase as the behaviour factor q increases. In particular, P_f remains almost negligible for $q = 4$, whereas it approaches values of approximately 40–50% for $q = 6$. Intermediate values are observed for $q = 5$. A similar trend is obtained for both PGA levels, although slightly higher exceedance probabilities are observed for PGA = 0.35 g.

Finally, at the CLS, the exceedance probabilities become significantly higher. In particular, for PGA = 0.35 g, the P_f values associated with $q = 6$ and $q = 5$ become relatively close, indicating a lower sensitivity of the AFM response to variations in the behaviour factor q at this seismic intensity level. Conversely, for PGA = 0.15 g, more noticeable differences between the considered configurations are still observed. Nevertheless, the reasons for the similarity in exceedance probabilities at PGA = 0.35 g require further dedicated investigation.

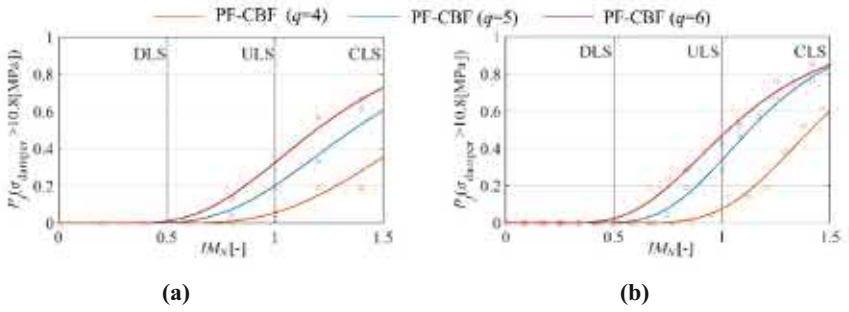
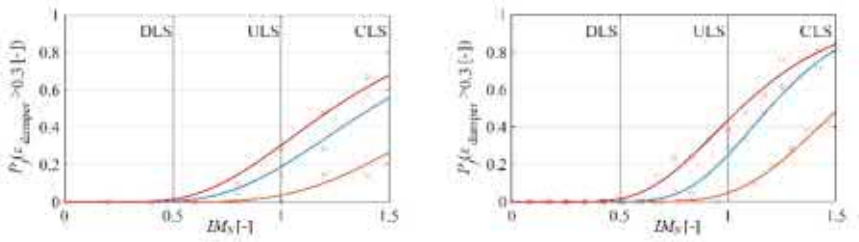


Fig. 12. Fragility curves for σ_{damper} for PGA equal to (a) 0.15 g and (b) 0.35 g.



(a) **(b)**

Fig. 13. Fragility curves for ε_{damper} for PGA equal to (a) 0.15 g and (b) 0.35 g.

5 Conclusions

This work examined the feasibility of employing replaceable Aluminium Foam Dampers (AFDs) in Pinching-Free Concentrically Braced Frames (PF-CBFs) and investigated the behaviour factor that can be adopted for their seismic design. The proposed solution combines a wedge mechanism with Aluminium Foam Material (AFM) layers to provide stable energy dissipation while preventing the pinching behaviour commonly observed in conventional tension-only braced systems. The experimental campaign confirmed the favourable compressive response of both the AFM layers and the complete AFD assembly, which was subsequently reproduced through numerical models implemented in OpenSees. These models were employed to analyse single-storey steel parking structures designed according to Eurocode 8 and equipped with PF-CBF systems, considering behaviour factors of $q = 4$, 5, and 6. Seismic performance was assessed by means of Incremental Dynamic Analyses (IDAs) performed using 44 horizontal ground-motion components selected following the FEMA P695 protocol, while fragility analyses were used to quantify the probability of exceeding the stress and strain capacities of the AFM layers. Based on the obtained results, the following observations can be made. 1) The introduction of the AFD significantly improves the cyclic response of concentrically braced frames by providing stable hysteretic behaviour and increasing the energy dissipated during seismic loading. This improvement results from the combined action of the wedge mechanism, which ensures tension-only behaviour, and the large compressive deformation capacity of the AFM layers. 2) All investigated PF-CBF configurations satisfy the interstorey drift requirements at the Ultimate Limit State. Nevertheless, increasing the behaviour factor from $q = 4$ to $q = 6$ progressively amplifies both the global deformation demand and the local demand imposed on the aluminium foam damper. 3) Among the analysed cases, the configuration designed with $q = 4$ exhibits the most favourable compromise between global seismic performance, local demand on the damper, and record-to-record variability.

The findings presented in this study are restricted to the single-storey archetype and to the specific AFD configuration considered herein. Consequently, further experimental and numerical investigations involving multi-storey structures and alternative AFM layer configurations are required before general design recommendations for PF-CBF systems can be established.

References

1. CEN (European Committee for Standardization) (2004) Eurocode 8: design of structures for earthquake resistance – part 1: general rules, seismic actions and rules for buildings. In: EN 1998–1. CEN, Brussel, Belgium
2. ASCE/SEI7–22 (2022) Minimum design loads and associated criteria for buildings and other structures. American Society of Civil Engineers. https://doi.org/10.1061/9780784415788
3. BCJ (2016) The Building Standard Law of Japan.
4. Freddi F et al (2021) Observations from the 26th November 2019 Albania earthquake: the earthquake engineering field investigation team (EEFIT) mission. Bull Earthq Eng 19:2013–2044. https://doi.org/10.1007/s10518-021-01062-8
5. Roeder CW, Lumpkin EJ, Lehman DE (2012) Seismic performance assessment of concentrically braced steel frames. Earthquake Spectra 28(2):709–727. https://doi.org/10.1193/1.4000006
6. Fitzgerald TF, Anagnos T, Goodson M, Zsutty T (1989) Slotted bolted connections in aseismic design for concentrically braced connections. Earthquake Spectra 5(2):383–391. https://doi.org/10.1193/1.1585528
7. Atlayan O, Charney FA (2014) Hybrid buckling-restrained braced frames. J Constr Steel Res 96:95–105. https://doi.org/10.1016/j.jcsr.2014.01.001
8. Ghamari A, Almasi B, Kim CH, Jeong SH, Hong KJ (2021) An innovative steel damper with a flexural and shear–flexural mechanism to enhance the CBF system behavior: an experimental and numerical study. Appl Sci 11(23):11454. https://doi.org/10.3390/app112311454
9. Smith BH, Szyniszewski S, Hajjar JF, Schafer BW, Arwade SR (2012) Steel foam for structures: a review of applications, manufacturing and material properties. J Constr Steel Res 71:1–10. https://doi.org/10.1016/j.jcsr.2011.10.028
10. Lettieri A, Sato A, Latour M, Rizzano G (2026) Seismic performance assessment of pinching-free tension-only CBFs equipped with aluminium metal foam dampers. Eng Struct 352:122126. https://doi.org/10.1016/j.engstruct.2026.122126
11. Tamai H, Takamatsu T (2005) Cyclic loading tests on a non-compression brace considering performance-based seismic design. J Constr Steel Res 61(9):1301–1317. https://doi.org/10.1016/j.jcsr.2005.01.009
12. Vamvatsikos D, Cornell CA (2002) Incremental dynamic analysis. Earthquake engineering structural. Dynamics 31(3):491–514
13. Mazzoni S, McKenna F, Scott MH, Fenves GL (2009) Computer program OpenSees: open system for earthquake engineering simulation, Pacific earthquake engineering research Center (PEER). University of California, Berkeley, California. http://opensees.berkeley.edu
14. FEMA P-695 (2009) Quantification of building seismic performance factors. Federal Emergency Management Agency, Washington, DC

Influence of Connection Design on the Seismic Response of School Building Retrofitted with Steel Orthogonal Exoskeletons

Alessandro Prota[1(✉)], Roberto Tartaglia[2], and Raffaele Landolfo[1]

[1] Department of Structures for Engineering and Architecture, University of Naples Federico II, 80134 Naples, Italy
{alessandro.prota,landolfo}@unina.it
[2] Department of Engineering, University of Sannio, 82100 Benevento, Italy
rotartaglia@unisannio.it

Abstract. Steel orthogonal exoskeletons represent an effective strategy for the seismic retrofit of existing buildings, as they allow significant structural upgrading while limiting intrusive interventions on the original structure. Within this strategy, the design of the connections between the exoskeleton and the existing structure plays a fundamental role in the correct functioning of the intervention. The connections govern the interaction between the external steel structure and the existing building, controlling the transfer of forces and the global distribution of stiffness and strength. For this reason, they must be carefully designed not only to ensure the effectiveness of the seismic retrofit, but also to comply with the main conceptual advantage of exoskeleton interventions. In this perspective, the connection system is conceived to allow easy installation from the outside and to ensure the potential reversibility of the intervention, minimizing the impact on the existing structure. To investigate this aspect, a case study consisting of a steel school building retrofitted with an orthogonal steel exoskeleton is considered. The structural performance of the retrofitted system is evaluated by comparing two modelling approaches: an ideal configuration assuming rigid and infinitely resistant connections, and a more realistic model in which the specifically designed connection system is explicitly represented and its behaviour is assessed through detailed finite element analyses. The comparison highlights the influence of connection behaviour on the global seismic response of the retrofitted structure.

Keywords: Steel exoskeleton · seismic retrofit · connection design · steel joints · non-linear dynamic analysis · existing steel buildings

1 Introduction

The seismic upgrading of existing buildings is a major issue in earthquake engineering, especially for structures designed according to older codes and lacking modern capacity-design provisions. Among global retrofit strategies, external seismic-resistant systems are particularly attractive because they reduce the demand on the existing structure

© The Author(s), under exclusive license to Springer Nature Switzerland AG 2026
R. Zanon et al. (Eds.): CTA 2026, LNCE 942, pp. 747–757, 2026.
https://doi.org/10.1007/978-3-032-39505-4_65

while limiting interference with building use. Steel exoskeletons belong to this category. They are installed outside the structural envelope, are usually supported by independent foundations and can be combined with architectural or energy refurbishment measures, such as double-skin facades or photovoltaic cladding. For these reasons, they are well suited to integrated renovation strategies in which seismic safety, sustainability and functionality are addressed simultaneously [1, 2].

Previous studies have shown that external steel systems can increase lateral stiffness, reduce inter-storey drifts and control structural and non-structural damage [3–5]. The effectiveness of external steel devices for the seismic retrofit of existing steel frames has also been confirmed by recent pseudo-dynamic hybrid testing and numerical studies on external BRB retrofit solutions [6].

Several layouts have been proposed, including concentrically braced frames, dissipative systems, self-centring solutions and optimised exoskeleton configurations. Concentrically braced steel systems remain a key reference solution within modern seismic design frameworks [7]. Design approaches have also moved from conventional force-based procedures towards displacement-based and performance-based methods, which allow a clearer control of target seismic response [2, 8]. Nevertheless, the connection between the existing structure and the external exoskeleton remains a critical aspect that is often simplified.

The connection is the component through which floor inertia forces are transferred to the retrofit system. In many global models, the existing structure and the exoskeleton are assumed to act in parallel, with negligible relative displacement at each storey. This assumption is acceptable only if the connection is sufficiently stiff, resistant and properly detailed. In real applications, the link is neither infinitely rigid nor necessarily elastic. Depending on the exoskeleton layout, it may be subjected mainly to shear or axial force, and its deformability may modify the distribution of actions between the existing building and the external frames. If the connection is poorly designed, it may become the weakest part of the retrofit, producing inefficient force transfer or undesirable brittle damage. Local force-transfer mechanisms are also crucial in the cyclic response of structures, as connection behaviour may govern stiffness, strength and damage distribution [9].

This paper focuses on connection systems for orthogonal steel exoskeleton interventions. An integrated framework is proposed in which the global retrofit demand, local connection design and final global verification are treated consistently. The procedure is applied to an existing steel school building and verified through non-linear static and bidirectional non-linear dynamic analyses. Particular attention is given to a dry, bolted and pinned steel connection whose cyclic response is investigated by refined finite element modelling and then introduced into the global model through calibrated non-linear links.

2 Research Significance and Objectives

The significance of the study lies in treating the connection as a primary design component of exoskeleton-based retrofit systems. Although the external frames provide the added stiffness and strength, their contribution can be fully mobilised only if the interface devices transfer diaphragm forces without excessive deformation or premature

damage. The connection is therefore not a secondary construction detail, but a governing part of the retrofit mechanism. The objectives are: (i) to formulate a design procedure that includes connection stiffness and resistance in the equivalent retrofit system; (ii) to develop a capacity-designed, inspectable and replaceable connection suitable for dry steel interventions; (iii) to evaluate the monotonic and cyclic behaviour of the connection through refined finite element analyses; and (iv) to quantify whether explicitly modelling the connection affects the global seismic performance of the strengthened building.

3 Methodology and Case Study

3.1 Integrated Design Approach

The proposed procedure extends displacement-based exoskeleton design by modelling the retrofit system as the series combination of the external exoskeleton and the connection link. Accordingly, the equivalent stiffness of the retrofit system, K_{Retr}, depends on both the exoskeleton stiffness, K_{Exo}, and the connection stiffness, K_{Link}, as follows:

$$K_{\text{Retr}} = \frac{K_{\text{Exo}}\, K_{\text{Link}}}{K_{\text{Exo}} + K_{\text{Link}}} \tag{1}$$

A coupling parameter, β, is introduced to express the relative contribution of the two components. Therefore:

$$K_{\text{Exo}} = \beta K_{\text{Retr}} \tag{2}$$

$$K_{\text{Link}} = \frac{\beta}{\beta - 1} K_{\text{Retr}} \tag{3}$$

When β approaches 1, the connection tends to behave as a rigid link. Conversely, as β increases, a larger exoskeleton stiffness is required to obtain the same equivalent retrofit stiffness. The design process starts with the assessment of the as-built structure through non-linear static analyses and the N2 method [10]. The capacity curve is idealised as an elastic-perfectly plastic equivalent SDOF system. For each limit state, the displacement demand is compared with the available displacement capacity. If the target performance is not achieved, the required stiffness and strength of the strengthened system are derived in the ADRS domain. The retrofit demand is then obtained as the difference between the target response of the strengthened system and the capacity of the as-built structure. The corresponding base shear is finally distributed along the building height, providing the storey diaphragm forces to be transferred by the connection devices.

The connection is designed according to the component method of EN 1993-1-8 [11]. The combination of analytical design rules and refined numerical modelling is consistent with recent research [12]. Two design philosophies may be adopted: an over-resistant elastic connection, or a ductile connection with a controlled local plastic mechanism. The latter strategy is adopted in this study. The ductile component is designed to resist the diaphragm force, whereas all the other components are capacity-designed using overstrength factors accounting for material randomness and strain hardening:

$$R_{\text{d},i} \geq \omega_{\text{sh}}\, \omega_{\text{rm}}\, R_{\text{d,ductile}} \tag{4}$$

where $R_{d,\,i}$ is the design resistance of the generic non-ductile component, while $R_{d,\,ductile}$ is the design resistance of the selected ductile component. In the investigated connection, bearing deformation and progressive ovalisation of the pin holes in the fork plates are selected as the intended ductile mechanism. The general connection design workflow is presented in Fig. 1.

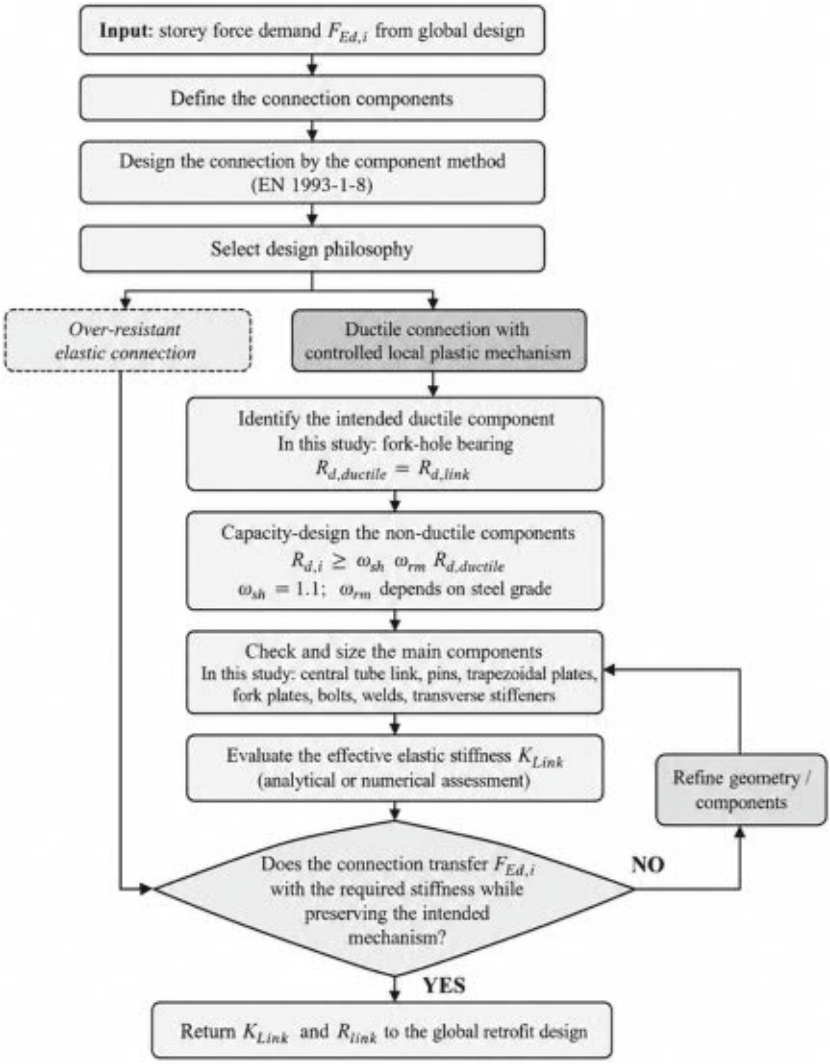


Fig. 1. Connection design workflow

3.2 Case-Study Building

The procedure is applied to a two-storey steel school building located in Avellino, Italy. The site has a peak ground acceleration of 0.238 g for a 10% probability of exceedance in 50 years on rock soil. The building has an irregular plan, an approximate floor area of 2,500 m^2 and a total height of 7.2 m. It was constructed between 1982 and 1987. Vertical loads are mainly carried by the primary framing system, whereas horizontal actions are resisted by tension-only X-braced concentrically braced frames.

The braced-frame columns are HEB160 profiles, the remaining columns are HEA160 profiles and the beams are IPE sections with depths between 220 and 360 mm. The original steel grade was Fe360, corresponding to S235. For assessment, a mean yield strength of 310 MPa was adopted together with the confidence factor associated with the available knowledge level [13, 14]. A three-dimensional SAP2000 [15] model was developed using frame elements, rigid floor diaphragms and non-linear elements for the braces. Modal analysis showed first translational periods of approximately 0.38 s in both principal directions, with participating masses close to 77–78%, and a shorter torsional period of about 0.32 s. The building can therefore be considered torsionally stiff despite its irregular plan.

Before the global assessment, the existing brace-to-column connections were checked against brittle failure. Their capacity was compared with the maximum force transferable by the diagonal braces at full plasticisation. Since the demand-to-capacity ratios were below unity for the relevant checks, these connections were considered over-resistant with respect to brace failure and were not explicitly included in the global model.

3.3 Numerical Programme

Three global configurations were analysed: the as-built structure; an effective strengthened configuration (ESC) in which the actual connection behaviour was represented by calibrated non-linear links; and an ideal strengthened configuration (ISC) with rigid links between the existing building and the exoskeleton.

Pushover analyses were performed in both principal directions using modal and uniform lateral load patterns. The investigated performance levels were Damage Limitation and Significant Damage. Damage Limitation checks were based on a maximum inter-storey drift ratio of 0.5% and prevention of yielding in steel members. Significant Damage checks were based on a 1.5% drift limit for X-CBFs and on local deformation limits in the steel components. In addition, bidirectional non-linear time-history analyses were performed using 20 natural records selected and scaled through REXELweb to match the target spectra and seismological parameters [16].

The local connection response was analysed in Abaqus [17] using refined solid finite element models. The modelling strategy adopted for the local assessment is consistent with recent refined finite element studies on existing steel details [18]. S355 steel was adopted for the new connection components, while S235 was used for the existing column. Class 10.9 M20 bolts and M30 pins were modelled, including bolt preload and contact interactions. Both monotonic and quasi-static cyclic displacement histories based on the ECCS procedure [19] were applied. This allowed the local response and the

associated redistribution mechanisms under repeated in-plane demand to be consistently assessed [20]. The resulting force-displacement curves were used to calibrate multilinear plastic links with Pivot hysteresis for the global effective model [21].

4 Main Results and Discussion

4.1 As-Built Seismic Performance

The pushover analyses showed similar stiffness and strength in the two principal directions, consistently with the balanced distribution of the existing X-CBFs. However, the seismic safety ratios, expressed as PGA_C/PGA_D, were lower than unity for all load patterns and directions. At Damage Limitation, the ratios ranged from 0.48 to 0.62; at Significant Damage, they ranged from 0.54 to 0.65. These values indicate that the building does not satisfy the target seismic performance and requires global strengthening [13, 14]. The time-history analyses confirmed this deficiency. The maximum inter-storey drift ratios exceeded the code limits at both performance levels, and plastic deformations developed in the existing diagonal members. The average drift demand in the as-built configuration was approximately 0.763% and 0.826% at the first and second storeys for Damage Limitation, increasing to approximately 1.9% and 2.0% for Significant Damage. The structure is therefore excessively flexible for the considered seismic demand.

4.2 Exoskeleton and Connection Design

The retrofit intervention consisted of 24 external tapered Y-shaped concentrically braced frames, equally distributed along the two principal directions. The frames were positioned along the perimeter to provide a diffuse transfer of horizontal actions and to keep the stiffness centre of the external system close to the mass centre of the existing building. S355 CHS 244.5 × 16 mm profiles were selected for the exoskeleton columns, while CHS 219.1 × 12.5 mm profiles were adopted for beams and diagonals (see Fig. 2). After retrofit, the first two translational periods reduced to approximately 0.25 s, with participating masses close to 90–91%.

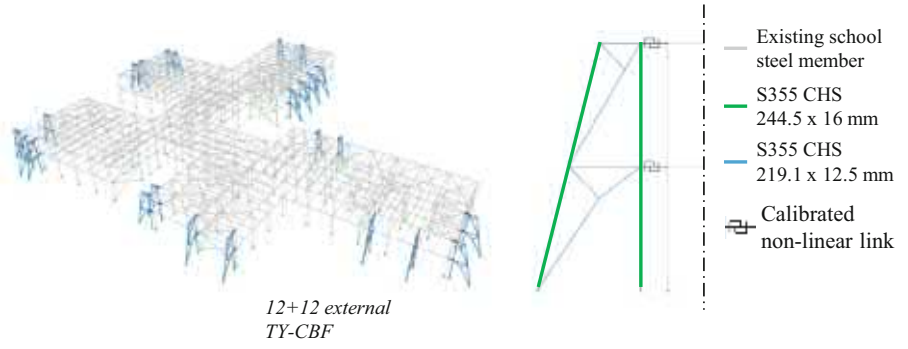


Fig. 2. Strengthened building 3D FEM model

The maximum design force transferred by the connection was $F_{Ed,Max}$ equal to 945 kN, obtained from the Significant Damage demand. The adopted connection includes a 0.5 m long CHS 139.7 × 10 mm central steel link, connected through pins to fork plates and trapezoidal plates attached to the existing column and to the exoskeleton (see Fig. 3). The building-side interface includes a bolted end-plate system, continuity plates and an additional S355 plate welded to the existing column flange. The fork-plate bearing mechanism governs the design. The design resistance was 945.2 kN in both tension and compression, while the initial axial stiffness from the component method was 690 kN/mm in tension and 757 kN/mm in compression. The resulting β values were close to unity, indicating a connection sufficiently stiff with respect to the target retrofit stiffness.

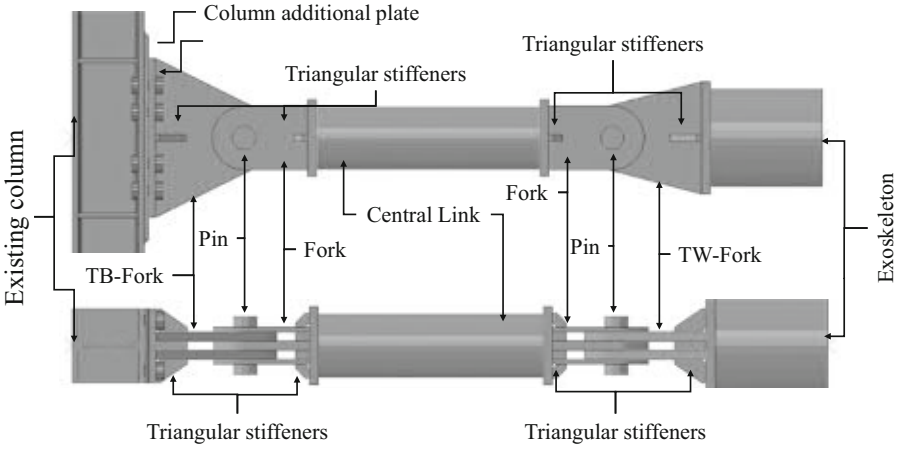


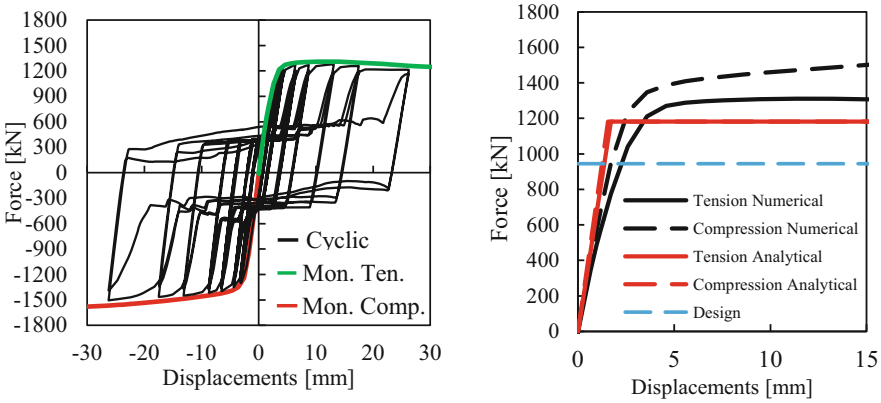
Fig. 3. Designed connection's main components

4.3 Local Connection Performance

The refined numerical analyses showed a slightly asymmetric response in tension and compression (see Fig. 4a). Tensile stiffness and resistance were lower because of the bolted end-plate system, although the stiffness reduction remained below 17%. No significant gap opening was observed in the bolted interface up to 30 mm of axial displacement.

The connection fulfilled the design requirements in both loading directions. The yielding force exceeded the design demand of 945 kN, with overstrength factors of 1.34 in tension and 1.47 in compression. Plastic deformation was concentrated in the intended fork-plate region, mainly through bearing deformation and pin-hole ovalisation. Other components, including welds, tube link, pins and bolted column interface, remained essentially elastic. Under cyclic loading, the connection showed stable hysteretic behaviour and relevant energy dissipation without failure up to 30 mm of imposed displacement.

The comparison between analytical and numerical results confirmed that the component method provides a satisfactory estimate of resistance, especially in tension (see Fig. 4b). However, it overestimates elastic stiffness, with analytical-to-numerical stiffness ratios of 1.38 in tension and 1.30 in compression. This difference suggests that refined numerical modelling or experimental calibration is advisable when connection deformability may influence the global response.



a) Numerical results

b)Comparison with analytical evaluation

Fig. 4. Local connection performance

4.4 Global Performance of the Strengthened Building

The pushover analyses of the effective strengthened configuration showed that the retrofit system achieves the target performance levels. The PGA_C/PGA_D ratios increased to 1.30–1.35 at Damage Limitation and to 1.59–2.08 at Significant Damage. Compared with the as-built condition, the PGA capacity increased from about 0.6–0.8 m/s^2 to about 1.65–1.72 m/s^2 at Damage Limitation, and from about 1.66–1.99 m/s^2 to about 4.85–6.34 m/s^2 at Significant Damage.

The main outcomes of the non-linear static and dynamic analyses are synthetically reported in Table 1, which summarises the seismic safety indicators and the drift response before and after the retrofit intervention.

The dynamic analyses confirmed the effectiveness of the intervention. At Damage Limitation, the average maximum drift decreased from 0.763% to 0.175% at the first storey and from 0.826% to 0.085% at the second storey. At Significant Damage, it decreased from approximately 1.9% to 0.435% at the first storey and from approximately 2.0% to 0.173% at the second storey. The drift demand was therefore reduced by about 77% at the first storey and by about 90–91% at the second storey.

Table 2 compares the global seismic response of the strengthened structure obtained by modelling the exoskeleton-to-building connections either as rigid links or as calibrated non-linear links. The explicit modelling of the connection produces a moderate increase

in the mean first-storey drift demand, whereas the response at the second storey remains practically unchanged. In all cases, the resulting drift demand remains well below the SD limit, and the axial forces developed in the links confirm that the connections remain within their intended elastic performance range.

Table 1. Summary of nonlinear analysis results for the as-built and ESC configurations

Analysis	LS	Demand/ limit	As-built configuration	ESC configuration	Effect of retrofit
Pushover — PGA_C	DL	$PGA_D = 1.27$ m/s^2	0.61–0.79 m/s^2	1.65–1.72 m/s^2	Verified
Pushover — PGA_C/PGA_D	DL	≥ 1.00	0.48–0.62	1.30–1.35	Safety ratio > 1
Pushover — PGA_C	SD	$PGA_D = 3.05$ m/s^2	1.66–1.99 m/s^2	4.85–6.34 m/s^2	Verified
Pushover — PGA_C/PGA_D	SD	≥ 1.00	0.54–0.65	1.59–2.08	Safety ratio > 1
NLTHA — mean IDR_{max}, 1st floor	DL	0.50%	0.763%	0.175%	−77%
NLTHA — mean IDR_{max}, 2nd floor	DL	0.50%	0.826%	0.085%	−90%
NLTHA — mean IDR_{max}, 1st floor	SD	1.50%	1.90%	0.435%	−77%
NLTHA — mean IDR_{max}, 2nd floor	SD	1.50%	2.00%	0.173%	−91%

These results indicate that, for the investigated connection system, the rigid-link assumption provides a reasonable approximation of the global response. However, this simplification is acceptable only because the designed connection is sufficiently stiff and resistant with respect to the seismic demand.

Table 2. Influence of connection modelling on the global seismic response

Response quantity	Floor	Rigid-link model, ISC	Non-linear-link model, ESC	ESC / ISC
Mean $IDR_{\max}$	1st floor	0.36%	0.43%	1.20
Mean $IDR_{\max}$	2nd floor	0.18%	0.17%	0.98
Mean peak axial force in links from THs	All links	–	$F_{avg} = +456/-452$ kN	–
Connection design resistance	–	–	$R_{\mathrm{d,\,Link}} = 945.2$ kN	–

5 Conclusions

An integrated design and modelling procedure for the connection between an existing steel building and an orthogonal steel exoskeleton has been presented and applied to a real school building. The following conclusions can be drawn.

The external steel exoskeleton is effective for the investigated structure. Both pushover and time-history analyses show that the intervention satisfies the Damage Limitation and Significant Damage performance requirements and reduces inter-storey drift demand by approximately 80–90%.

The proposed procedure incorporates connection stiffness and resistance into the equivalent retrofit system. Modelling the exoskeleton and the link as components in series provides a rational basis for verifying whether the connection is sufficiently stiff or whether the exoskeleton design must be updated.

The adopted dry steel connection, based on bolted interfaces, pins, fork plates and a short tubular link, satisfies the intended capacity hierarchy. Plastic deformation is concentrated in bearing and pin-hole ovalisation of replaceable fork-plate components, while brittle or unstable failure modes are avoided.

Refined finite element analyses show that the connection remains elastic up to the design demand and provides overstrength factors of 1.34 in tension and 1.47 in compression. For larger imposed displacements, it develops stable ductile behaviour and dissipates energy through the intended mechanism.

The component method gives a reliable estimate of resistance but overestimates elastic stiffness. Therefore, when connection deformability is relevant, analytical design should be complemented by refined numerical modelling or experimental calibration.

For the investigated configuration, the difference between rigid and non-linear link modelling is limited. Hence, a rigid-link assumption may be acceptable only after verifying that the connection is sufficiently stiff, resistant and elastic at the design limit states. Further work should include experimental validation of the proposed pin-fork sub-assemblies and the extension of the modular link to alternative dissipative or shock-transmitting devices.

References

1. Marini A et al (2017) Combining seismic retrofit with energy refurbishment for the sustainable renovation of RC buildings: a proof of concept. Eur J Environ Civ Eng 26(7):2475–2495
2. Di Lorenzo G, Tartaglia R, Prota A, Landolfo R (2023) Design procedure for orthogonal steel exoskeleton structures for seismic strengthening. Eng Struct 275:115252
3. Prota A, Tartaglia R, Di Lorenzo G, Landolfo R (2024) Seismic strengthening of isolated RC framed structures through orthogonal steel exoskeleton: bidirectional non-linear analyses. Eng Struct 302:117496
4. Lee H-J, Lee H-B, Park H-G, Lee J-K (2023) Cyclic lateral load test for RC moment frames retrofitted with external steel frames. J Struct Eng 149(5)
5. Cao X-Y, Feng D-C, Wu G (2019) Seismic performance upgrade of RC frame buildings using precast bolt-connected steel-plate reinforced concrete frame-braces. Eng Struct 195:382–399
6. Freddi F et al (2025) Seismic retrofitting of existing steel frames with external BRBs: pseudo-dynamic hybrid testing and numerical parametric analysis. Earthquake Engineering & Structural Dynamics 54:1064–1083
7. Gnazzo M, Mahmoudi B, D'Aniello M, Imanpour A, Landolfo R (2026) Seismic design and response of inverted-V CBFs compliant with European and Canadian standards. Eng Struct 363:123071
8. Mazza F (2021) Dissipative steel exoskeletons for the seismic control of reinforced concrete framed buildings. Struct Control Health Monit 28(3):e2683
9. Fiorino F, D'Addesa V, Landolfo R (2024) Seismic design rules for lightweight steel shear walls with wood panel sheathing within the Eurocode format. Thin-Walled Struct 204:112293
10. Fajfar P (2000) A nonlinear analysis method for performance-based seismic design. Earthquake Spectra 16(3):573–592
11. CEN. EN 1993-1-8: Eurocode 3: Design of steel structures - Part 1–8: Joints. Brussels: European Committee for Standardization; (2024).
12. Ascione F, D'Aniello LA (2026) Numerical and analytical modelling of a novel hybrid ductile connection between FRP composite elements. Thin-Walled Struct 227:115008
13. C.S.LL.PP (2018) Aggiornamento delle Norme Tecniche per le Costruzioni. Gazzetta Ufficiale della Repubblica Italiana, Rome
14. C.S.LL.PP. Circolare 21 gennaio 2019, n. 7: Istruzioni per l'applicazione dell' Aggiornamento delle Norme tecniche per le costruzioni" di cui al decreto ministeriale 17 gennaio 2018. Rome: Gazzetta Ufficiale della Repubblica Italiana.(2019).
15. Computers and Structures Inc (2026) SAP2000 integrated software for structural analysis and design, Berkeley, CA
16. Sgobba S et al (2019) REXELweb: a tool for selection of ground-motion records from the engineering strong motion database. In: Proceedings of the 7th international conference on earthquake geotechnical engineering; 2019
17. Dassault Systemes. Abaqus 6.13 User's Manual; (2013)
18. Milone A, D'Aniello M, Landolfo R (2024) Advanced fatigue assessment of riveted railway bridges on existing masonry abutments: an Italian case study. Buildings 14(8):2271
19. ECCS (1986) Recommended testing procedure for assessing the behaviour of structural steel elements under cyclic loads. Publication no. 45. Brussels, European Convention for Constructional Steelwork
20. Fiorino F, Campiche A, Grzesik P, Landolfo R (2024) Experimental evaluation of in-plane seismic demand on power actuated fasteners (PAF) connecting CFS drywall partitions and concrete surrounding elements. Bull Earthq Eng 22(2025):2057
21. Dowell RK, Seible F, Wilson EL (1998) Pivot hysteresis model for reinforced concrete members. ACI Struct J 95(5):607–617

Seismic Retrofit of Pre-code RC Structures Using a Hybrid Timber-Aluminium Exoskeleton: Numerical Definition of the Earthquake-Resisting System and Reduced-Scale Testing

Emilia Meglio[1](✉), Marco Domaneschi[2], and Antonio Formisano[1]

[1] Department of Structures for Engineering and Architecture, Polytechnic and Basic Sciences School, University of Naples Federico II, Naples, Italy
emilia.meglio@unina.it

[2] Department of Structural, Building and Geotechnical Engineering, Politecnico di Torino, Turin, Italy

Abstract. The RESUME research project investigates an innovative external seismic-energy retrofitting solution consisting of a hybrid exoskeleton composed of a timber frame and aluminium panels as seismic-resistant part, and cork insulation panels to improve thermal performance of the building envelope.

The seismic effectiveness of the proposed solution is investigated through a numerical and experimental study carried out on reduced-scale RC frame structures. Both numerical simulations and laboratory tests were performed on 1:3 scale models representing a typical pre-code RC building. Two structural configurations were considered: the original unretrofitted frame and the same structure strengthened with the hybrid exoskeleton system. A preliminary numerical investigation was first carried out to identify the most effective strengthening configuration. Two alternative retrofit solutions of the hybrid exoskeleton system were considered: aluminium panels and aluminium X-shaped bracing, both acting as shear-resistant devices. The outcome of this study indicated that the aluminium panel configuration provided the most favourable structural response and was therefore selected for the subsequent experimental phase.

Shaking table tests were then carried out at the IZIIS Laboratory in Skopje on the 1:3 scale specimens. The experimental campaign aimed to investigate the dynamic behaviour, damage mechanisms, and global response of the structure under increasing seismic input, allowing a direct comparison between the original and strengthened configurations. The combined numerical and experimental results contribute to a deeper understanding of the interaction be-tween the RC frame and the external hybrid exoskeleton system.

Keywords: Aluminium Shear Panels · Existing Buildings · RC Structures · Seismic Retrofit · Exoskeleton · Shaking Table Test

© The Author(s), under exclusive license to Springer Nature Switzerland AG 2026
R. Zanon et al. (Eds.): CTA 2026, LNCE 942, pp. 758–769, 2026.
https://doi.org/10.1007/978-3-032-39505-4_66

1 Introduction

The large stock of existing buildings constructed before the introduction of modern seismic regulations is characterized by significant structural deficiencies and inadequate energy performance. This issue is particularly critical in countries with high seismic hazard, where vulnerable reinforced concrete and masonry buildings are exposed to substantial earthquake risk. Consequently, improving both structural safety and energy efficiency has become a major objective for researchers, engineers, and policymakers. Recent earthquakes in Italy and other European countries have further emphasized the necessity of developing effective retrofit strategies capable of increasing the resilience of the existing building stock. At the same time, the transition toward more sustainable and energy-efficient buildings, together with rising energy costs and increasingly stringent environmental targets, has encouraged the adoption of integrated retrofit solutions. Previous studies have shown that simultaneously addressing seismic vulnerability and thermal inefficiency can provide technical and economic advantages compared with carrying out the two interventions separately [1].

Several integrated retrofit techniques have therefore been proposed in recent years, combining structural strengthening systems with energy-efficient envelope solutions. These include fiber-reinforced mortars coupled with thermal insulation layers [2], as well as laminated timber systems that simultaneously improve the seismic response, architectural appearance, and thermal behaviour of buildings [3]. Among the available approaches, external exoskeleton systems installed along building façades have attracted increasing interest because they allow seismic upgrading while minimizing disruption to occupants and facilitating the integration of insulation components. Different structural configurations have been investigated, including cast-in-place reinforced concrete walls, timber-cement composite panels providing both lateral resistance and thermal insulation, timber solutions and steel exoskeletons designed to improve lateral stiffness and strength [4–8].

Within this framework, the present study investigates an innovative integrated retrofit solution based on an external exoskeleton composed of laminated timber members combined with aluminium braces or aluminium panels. A comprehensive research methodology is adopted, starting with numerical analyses aimed at identifying the most efficient structural configuration.

The selected solution is subsequently assessed through an experimental campaign involving shaking table tests performed at the IZIIS Laboratory in Skopje. The experimental program considers two geometrically identical 1:3 scale reinforced concrete frame specimens with the same mechanical properties. The first specimen, tested in its original unretrofitted condition, provides the reference response, while the second specimen is strengthened using the optimized timber-aluminium exoskeleton identified through the numerical investigation. The comparison between the two structures allowed to assess the effectiveness of the proposed retrofit system in terms of seismic performance while also assessing its potential for integrated seismic and energy rehabilitation of existing reinforced concrete buildings.

2 Numerical Optimization

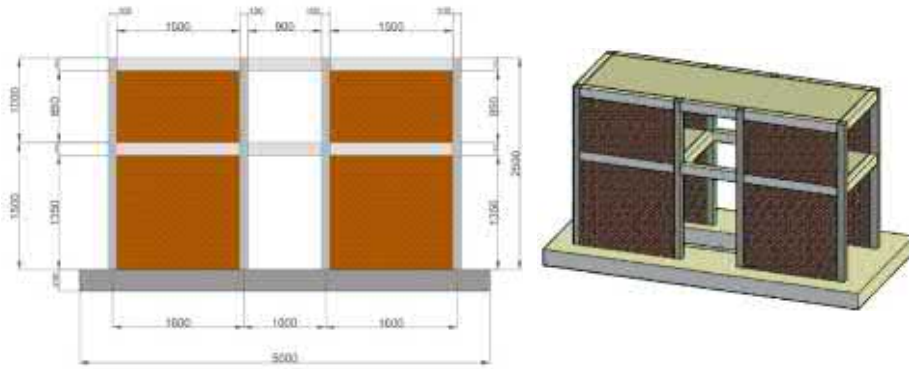
2.1 Geometry and Material Properties of the Unretrofitted Structure

The reference building selected for this study is a 1:3 scale reinforced concrete (RC) structure representative of existing buildings designed according to obsolete design practices, in which seismic actions were either neglected or only marginally considered. Such a configuration reproduces the structural characteristics of a large portion of the pre-code building stock and therefore provides an appropriate benchmark for assessing the effectiveness of retrofit solutions.

The structural system comprises two parallel longitudinal RC frames connected by a reinforced concrete floor slab and spaced at 1.4 m. No internal transverse beams are provided, so the slab represents the only connection between the two frames. Each longitudinal frame consists of three bays, resulting in an overall building length of 4.2 m. The prototype includes two stories, with a story height of 1.5 m at the ground floor and 1.0 m at the upper level. Masonry infill panels made of hollow clay bricks are installed only in the external bays of the longitudinal frames.

The frame is supported by a 25 cm thick reinforced concrete foundation slab, ensuring a uniform base restraint during testing. Beam members have a rectangular cross-section of 10 × 15 cm, whereas the columns have a square cross-section of 10 × 10 cm. Both beams and columns are reinforced with four 8 mm diameter longitudinal bars located at the section corners, while 4 mm diameter stirrups are arranged at 100 mm spacing. The concrete adopted for the specimen has a cube compressive strength of 20 MPa, corresponding to strength class C16/20, which is representative of the relatively low-strength concrete commonly found in older reinforced concrete buildings.

The geometrical configuration and a three-dimensional view of the reference, unretrofitted structure is presented in Fig. 1.



(a) (b)

Fig. 1. Unretrofitted structure: (a) geometrical properties; (b) three-dimensional view.

2.2 Geometry and Properties of the Retrofitted Structure

The proposed retrofit strategy consists of two alternative external exoskeleton solutions designed to simultaneously enhance the seismic performance and energy efficiency of existing reinforced concrete buildings. Both solutions combine laminated timber and aluminium alloy components, taking advantage of the high strength-to-weight ratio of aluminium and the sustainability of engineered timber.

The two retrofit systems share the same primary supporting framework, which is formed by laminated timber members connected through galvanized steel plates and screws. The exoskeleton is mechanically linked to the existing RC structure by means of steel anchors installed at the beam-column joints, ensuring effective force transfer while maintaining a reversible and minimally invasive intervention.

The investigated configurations differ only in the type of aluminium lateral-load-resisting system adopted: (i) X-braced configuration, where concentric aluminium diagonal braces provide the required lateral stiffness and strength; (ii) Shear panel configuration, in which thin aluminium panels replace the diagonal bracing and act as continuous shear-resisting elements.

The exoskeleton is installed along the external perimeter of the building, with the exception of the central bay on the longitudinal façades, which is intentionally left unobstructed to facilitate visual inspection and experimental monitoring during the laboratory tests.

The aluminium structural components are connected to the timber frame through galvanized steel angle brackets. The same brackets also support external insulation panels made of recycled cork, thereby integrating structural upgrading with thermal retrofit. All aluminium elements, including both the diagonal braces and the shear panels, are manufactured from EN AW-5754 H111 aluminium alloy with a constant thickness of 2 mm, whereas the primary frame is fabricated from Gl24h laminated timber.

The construction details of the proposed retrofit system, together with the assembly sequence and the two investigated exoskeleton configurations, are shown in Fig. 2, illustrating the interaction between the external reinforcement system and the existing reinforced concrete frame.

2.3 Numerical Analyses

The numerical investigation was carried out using the commercial finite element software Pro_SAP v.22, developed by 2SI (Ferrara, Italy). The analysis was aimed at assessing the influence of the proposed retrofit solutions on the global structural response and at identifying the most effective exoskeleton configuration for the subsequent experimental campaign. To this end, modal analyses were first performed to evaluate the dynamic characteristics of the structure in its as-built and retrofitted conditions, followed by nonlinear static analyses to quantify the improvements in strength and stiffness. Masonry infill panels were represented through the equivalent diagonal strut approach, following modelling procedures available in the literature [9]. Seismic actions were defined according to the Italian building code [10], assuming the structure to be located in L'Aquila (Abruzzo, Italy), with topographic category T1 and soil class A.

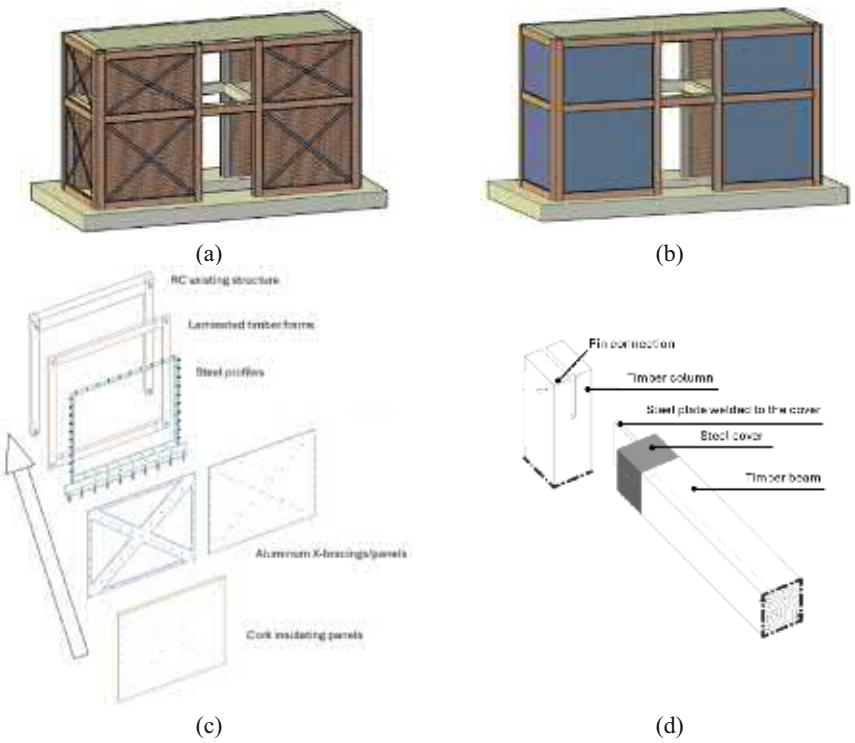
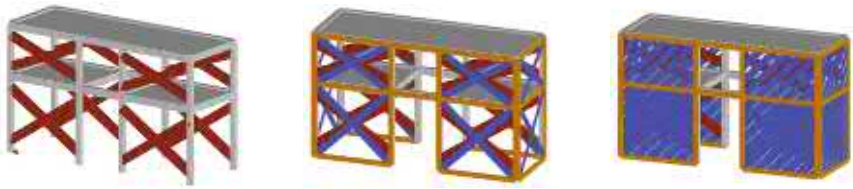


Fig. 2. Retrofitted structure: (a) three-dimensional view of the X-bracings solution; (b) three-dimensional view of the panel solution; (c) assembly scheme of the hybrid exoskeleton; (d) detail of the timber beam-column connection.

The first numerical model reproduced the existing reinforced concrete frame with masonry infill walls, representing the as-built configuration. Two additional models were subsequently developed to simulate the proposed retrofit alternatives: (i) X-braced configuration, in which the aluminium diagonal braces were explicitly represented by structural frame elements; (ii) Shear panel configuration, where the aluminium panels were idealized using an equivalent strip model composed of ten diagonal elements. Each strip was assigned the same thickness as the actual panel, while its width was determined according to the strip-model formulation proposed in the literature [11]. The three-dimensional view of the structural models is depicted in Fig. 3.

The modal analyses showed that the installation of the exoskeleton did not alter the sequence or nature of the dominant vibration modes. In all configurations, the first mode corresponded to transverse translation (Y direction), the second exhibited a predominantly torsional response, and the third was characterized by longitudinal translation (X direction). Nevertheless, both retrofit solutions produced a significant reduction in the fundamental vibration periods, reflecting the increase in global lateral stiffness provided by the external reinforcement system (Fig. 4).



(a) (b) (c)

Fig. 3. Numerical models of the three structures: (a) unretrofitted; (b) retrofitted with X-bracing; (c) retrofitted with shear panels.

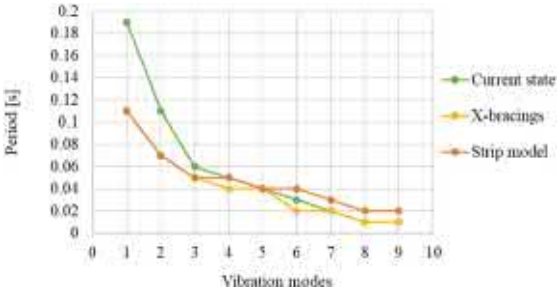


Fig. 4. Results of the modal analysis: vibration periods.

Consistently, lower peak displacements and reduced inter-story drifts were obtained for the strengthened models, with the shear panel configuration providing the largest improvements (Fig. 5).

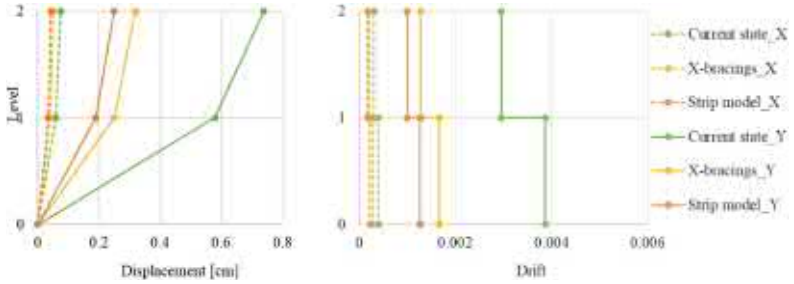


Fig. 5. Results of the modal analysis: peak displacements and inter-story drifts.

The results of the nonlinear static analyses are summarized through the capacity curves reported in Fig. 6. Both retrofit solutions substantially enhanced the lateral strength and initial stiffness of the structure compared with the unretrofitted configuration. The most pronounced improvements were observed in the transverse (Y) direction, where the original frame lacked the beneficial contribution of masonry infill walls. Among the two alternatives, the exoskeleton incorporating aluminium shear panels

achieved the highest increase in both lateral resistance and stiffness, outperforming the X-braced solution and therefore representing the most effective retrofit configuration.

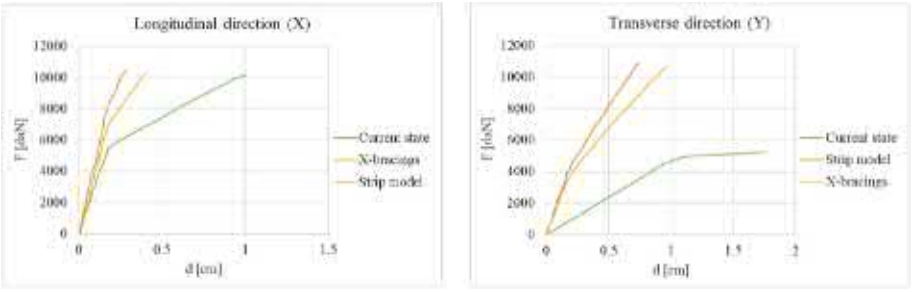


Fig. 6. Results of the nonlinear static analysis: capacity curves.

Overall, the analyses confirm the effectiveness of both exoskeleton systems in enhancing the stiffness, strength, and overall seismic performance of deficient RC buildings. Among the investigated solutions, however, the configuration incorporating aluminium shear panels consistently provided the largest performance gains, outperforming the X-braced alternative in both the modal and pushover analyses. On the basis of these results, the shear panel exoskeleton was selected for the subsequent experimental validation through shaking table testing, as it represents the most promising retrofit strategy.

3 Reduced-Scale Testing

3.1 Specimens and Test Set-Up

The experimental campaign was designed to assess the effectiveness of the proposed timber–aluminium exoskeleton through shake table testing on two identical 1:3 scale reinforced concrete (RC) specimens, referred to as Model X and Model Y (see Fig. 7). Both models were characterized by the same geometry, reinforcement details, and material properties described in the previous numerical investigation. The testing program was divided into three consecutive phases to investigate the influence of the retrofit when applied before and after earthquake-induced damage.

In Phase 1, Model Y was tested in its original unretrofitted configuration by applying ground motions with progressively increasing intensity until significant damage developed. In Phase 2, the damaged specimen was retrofitted using the selected exoskeleton system and tested again to evaluate its ability to restore and improve the structural performance. Finally, Phase 3 involved testing Model X after installing the exoskeleton before any seismic excitation, allowing a direct comparison between a preventive retrofit and a post-damage strengthening intervention.

To ensure dynamic similitude with the prototype structure, the experimental models were designed as lumped-mass systems with artificially distributed masses. Additional inertial mass was provided by placing eight steel blocks, each weighing approximately



(a) (b)

Fig. 7. Tested specimens: (a) Model Y unretrofitted; (b) Model X retrofitted.

400 kg (≈3.9 kN), on the upper floor slab, resulting in a total vertical load of about 31 kN. This configuration allowed the reduced-scale models to reproduce the inertial effects expected in the full-scale prototype during seismic excitation.

The experimental tests were performed using a multi-degree-of-freedom shaking table capable of reproducing one horizontal and one vertical translational motion together with three rotational degrees of freedom. Each specimen was rigidly anchored to the platform to guarantee accurate transmission of the imposed base excitation.

A total of 66 dynamic tests were carried out throughout the experimental program. The testing sequence combined resonant frequency measurements and earthquake simulations. Resonant frequency tests were periodically conducted to monitor the evolution of the dynamic properties and quantify stiffness degradation as damage accumulated. Earthquake tests, on the other hand, were performed using seismic records applied at progressively increasing intensity levels, enabling the structural response to be investigated from the elastic range up to severe nonlinear behaviour.

Three input motions were selected for the experimental campaign: EQ1, corresponding to the 1998 Adana earthquake (Mw 6.3); EQ2, a synthetic accelerogram generated to match the Eurocode 8 design spectrum for Soil Type C; and EQ3, recorded during the 2016 Umbria earthquake (Mw 6.2). These ground motions were chosen because of their representative spectral characteristics and frequency content for the considered structural typology. To satisfy the similitude requirements of the 1:3 scale model, the earthquake records were appropriately scaled, including time compression according to the relationship $t_m = t_p/\sqrt{3}$.

The excitation amplitude was progressively increased, from low seismic intensity up to 200% of the reference input motion, in order to investigate the evolution of the structural response under increasingly demanding loading conditions. The same loading protocol was adopted for all three experimental phases, ensuring a consistent comparison between the as-built, post-retrofitted, and pre-strengthened configurations.

The structural response was monitored through an extensive instrumentation system. Fifteen accelerometers were distributed over the structure to record its global dynamic

behaviour, while four linear potentiometers measured the inter-storey displacements. Local deformations were monitored by ten LVDTs, including two positioned between the specimen and the shaking table to measure the imposed base motion and eight installed near the beam-column joints. In addition, thirty strain gauges were employed, of which twenty-four were attached to the longitudinal reinforcement of the columns at different elevations and six were bonded to the concrete surface.

Following each seismic test, the specimen was visually inspected to document crack development and damage progression, allowing the observed failure mechanisms to be correlated with the corresponding excitation level.

The recorded measurements were subsequently processed to evaluate the evolution of the principal structural response parameters, including the variation of the natural frequencies and the inter-storey drift demand, which are discussed in the following section.

3.2 Results of the Experimental Investigation

During the initial stage of the investigation, the unretrofitted specimen was subjected to the EQ1 and EQ3 records at low intensity levels. Under these loading conditions, no visible cracking or other signs of structural deterioration were detected, confirming that the response remained within the elastic range.

The first evidence of damage appeared during the application of the EQ2 ground motion, which served as the reference record for the progressive seismic loading protocol. Initial cracking was observed in the masonry infill panels, marking the onset of stiffness degradation. As the intensity of EQ2 gradually increased, the damage evolved steadily, leading to widespread cracking of the ground-floor infill walls and their subsequent collapse (see Fig. 8a). At the same time, cracking developed in the reinforced concrete columns, particularly in the beam-column joint regions. The progressive loss of the lateral contribution provided by the infill walls produced a marked reduction in the overall lateral stiffness of the structure, reflected by a significant decrease in the fundamental frequency and a corresponding increase in the inter-story drift demand.

After completing the first testing phase, the damaged masonry panels were repaired, and the selected exoskeleton system was installed. The subsequent experimental campaign showed a substantial improvement in structural performance. Damage was mainly limited to the reopening and extension of previously formed cracks, while no collapse of the repaired infill walls was observed throughout the prescribed loading sequence (see Fig. 8b).

The best structural performance was achieved when the exoskeleton was installed before the application of any seismic excitation. In this configuration, only minor cracking developed within the masonry infills, even under the highest prescribed input levels. The EQ2 record was progressively amplified up to the maximum acceleration achievable by the shaking table without causing collapse of the infill walls or significant damage to the reinforced concrete frame. These results demonstrate the ability of the retrofit system to effectively control both global and local structural response under severe seismic loading.

To further increase the seismic demand beyond the operational limits of the standard testing protocol, additional random excitation signals were subsequently applied. Under

these more demanding conditions, localized damage gradually accumulated until the collapse of one masonry infill wall occurred (see Fig. 8c). Despite the extensive loading history, the timber-aluminium exoskeleton remained fully functional. No evidence of local buckling, yielding, or in-plane deformation of the aluminium panels was detected, indicating that the retrofit system remained within the elastic range throughout the entire experimental program.



(a) (b) (c)

Fig. 8. Damages after testing: (a) Phase I; (b) Phase II; (c) Phase III.

The evolution of the fundamental frequency measured during the three testing phases is summarized in Table 1. The unretrofitted configuration exhibited a pronounced reduction in frequency as the seismic intensity increased, reflecting the progressive degradation of structural stiffness associated with cracking and the eventual loss of the infill wall contribution. Following retrofit, the frequency increased considerably owing to the combined effect of masonry repair and the installation of the exoskeleton, while the subsequent rate of degradation became significantly less pronounced. The specimen strengthened before testing showed the highest initial frequency together with the most stable dynamic response up to 180% (Phase 3), confirming the effectiveness of the proposed system in enhancing global stiffness and delaying damage progression.

Table 1. Experimental results: evolution of fundamental frequency.

Intensity Level (EQ2)	Phase 1 (Hz)	Phase 2 (Hz)	Phase 3 (Hz)
Initial	10.2	7.4	11.9
50%	8.6	7.0	11.1
75%	7.6	6.8	12.5
100%	4.0	6.6	11.9
120%	3.3	6.1	10.6
140%	2.0	5.5	9.9
160%	–	5.2	9.7
180%	–	4.8	8.9
200%	–	–	2.7

The corresponding interstory drift demands are reported in Table 2. For the original structure, drift values increased rapidly with increasing seismic intensity and reached their maximum at the 140% EQ2 level, coinciding with the collapse of the ground-floor masonry infill walls. Retrofitting the previously damaged specimen resulted in a substantial reduction in lateral deformations, demonstrating the ability of the exoskeleton to improve the global stability of the structure. The lowest drift demands were recorded for the specimen strengthened prior to testing, further confirming the superior performance achieved when the retrofit is applied before earthquake-induced damage occurs.

Table 2. Experimental results: inter-story drifts.

Intensity Level (EQ2)	Phase 1 (%)	Phase 2 (%)	Phase 3 (%)
18%	0.04	0.05	0.03
27%	0.06	0.07	0.04
50%	0.10	0.14	0.07
75%	0.14	0.23	0.10
100%	0.35	0.34	0.15
120%	0.51	0.43	0.22
140%	2.49	0.53	0.26
160%	–	0.62	0.28
180%	–	0.78	0.32
200%	–	–	0.51

4 Conclusions

This study investigated the effectiveness of an innovative hybrid timber-aluminium exoskeleton for the seismic upgrading of existing reinforced concrete buildings through a combined numerical and experimental approach.

A preliminary numerical investigation compared two retrofit solutions based on the same timber supporting frame but adopting different aluminium lateral resisting systems, namely X-bracing and shear panels. Modal and nonlinear static analyses demonstrated that both configurations significantly improved the global structural response by increasing lateral stiffness and strength. However, the shear panel solution consistently outperformed the X-braced configuration, particularly in the transverse direction where the original structure lacked the contribution of masonry infill walls. Consequently, the aluminium shear panel system was selected for experimental validation.

The shaking table tests confirmed the effectiveness of the proposed retrofit strategy. The unretrofitted specimen experienced progressive stiffness degradation, extensive cracking of the masonry infills, and collapse of the ground-floor infill walls under increasing seismic demand. Conversely, the retrofitted specimens exhibited significantly improved behaviour, characterized by higher natural frequencies, lower inter-story drift demands, and a substantial delay in damage development.

An additional finding of the experimental campaign is the excellent performance of the hybrid exoskeleton itself. Despite being subjected to severe seismic loading, the timber-aluminium system showed no evidence of local buckling, yielding, or permanent deformation of the aluminium panels, demonstrating that the retrofit remained within the elastic range while effectively controlling the structural response.

Acknowledgements. This work is part of the transnational access project "ERIES-RESUME", supported by the Engineering Research Infrastructures for European Synergies (ERIES) project (www.eries.eu), which has received funding from the European Union's Horizon Europe Framework Programme under Grant Agreement No. 101058684. In this framework the contribution given to the experimental activity from the IZIIS team of the University of Skopje in North Macedonia is gratefully acknowledged.

References

1. Pertile V, Stella A, De Stefani L, Scotta R (2021) Seismic and energy integrated retrofitting of existing buildings with an innovative ICF-based system: design principles and case studies. Sustainability 13(16):9363
2. Bournas D (2018) Concurrent seismic and energy retrofitting of RC and masonry building envelopes using inorganic textile-based composites combined with insulation materials: a new concept. Compos Part B Eng 148:166–179
3. Margani G, Evola G, Tardo C, Marino EM (2020) Energy, seismic, and architectural renovation of RC framed buildings with prefabricated timber panels. Sustainability 12(12):4845
4. Ecosism. https://www.ecosism.com/moduli/geniale/. Accessed 24 Oct 2025
5. Betonwood. https://www.betonwood.com/. Accessed 24 Oct 2025
6. Martelli L, Restuccia L, Ferro GA (2020) External systems for seismic upgrading of buildings. Procedia Struct Integrity 26:213–220
7. Margani G, Evola G, Marletta L et al (2020) Energy and seismic retrofitting using prefabricated timber panels. Sustainability 12:4842
8. Badini L, D'Ayala D, Palermo A (2022) Seismic retrofit of RC buildings using timber systems. Bull Earthq Eng
9. Al-Chaar G (2002) Evaluating strength and stiffness of unreinforced masonry infill structures. US Army Corps of Engineers, Engineer Research and Development Center
10. Ministry of Infrastructure and Transport. (2018) Technical Standards for Construction. In Official Gazette; Number 42 of 20 February; Ministry of Infrastructure and Transport: Rome, Italy, 2018 (In Italian)
11. Formisano A, Mazzolani FM, De Matteis G (2007) Numerical analysis of slender steel shear panels for assessing design formulas. Int J Struct Stab DynDyn 7(02):273–294

Visual Scripting-Based Design Methodology for Lattice-Structured Metallic Dampers Produced via Additive Manufacturing

Francesca Romana Andreacola[1], Marco Di Cristofano[1], Valentino Sangiorgio[1,2], and Giuseppe Brando[1,2(✉)]

[1] Department of Engineering and Geology, University "G. d'Annunzio" of Chieti-Pescara, 65127 Pescara, Italy
giuseppe.brando@unich.it

[2] UdA-TechLab, Research Center, University "G. d'Annunzio" of Chieti-Pescara, 66100 Chieti, Italy

Abstract. In recent years, the convergence of design optimization, parametric modeling, and metal additive manufacturing has opened new opportunities for the development of passive seismic energy dissipation devices, enabling performance-driven geometries beyond the constraints of conventional solutions. In this context, lattice-based architectures are particularly promising, as they allow stiffness, strength, and dissipative capacity to be finely tuned through a limited set of governing geometric parameters. This study introduces an innovative typology of metallic energy dissipation devices designed for the passive seismic protection of structures. The proposed methodology leverages design optimization to transform conventional geometries into lattice structures tailored to specific performance targets regarding strength, stiffness and energy dissipation. Engineered for metal additive manufacturing, the complex geometries discussed in this study are generated through visual scripting algorithms within Rhinoceros-Grasshopper. The workflow begins by converting a standard geometric solid shape into a lattice structure while maintaining its global dimensions. Key geometric parameters influencing structural response are identified and analyzed through Finite Element Modeling in Abaqus. By employing statistical analysis of the resulting data to evaluate parameter sensitivity, the optimal configuration in terms of stiffness, strength and dissipative capacity is determined. The effectiveness of this approach is illustrated through a case study involving a spherical geometry. The result is a damper designed to withstand axial forces typically transmitted via diagonal bracing in a steel frame during a seismic event. Ultimately, this work aims to bridge the gap between design optimization, advanced manufacturing methods and seismic engineering through an innovative approach.

Keywords: Additive manufacturing · 3D printing · Optimization process · Metal dampers · Lattice structures · Visual scripting algorithms

© The Author(s), under exclusive license to Springer Nature Switzerland AG 2026
R. Zanon et al. (Eds.): CTA 2026, LNCE 942, pp. 770–781, 2026.
https://doi.org/10.1007/978-3-032-39505-4_67

1 Introduction

In today's civil engineering practice, seismic risk mitigation has firmly established itself as a key concern for both academic research and professional application. Consequently, earthquake engineering has come to occupy an increasingly central position within structural design frameworks. The core goal of seismic design procedures continues to be achieving safety standards strict enough to prevent catastrophic failure and the resulting loss of life.

Within this context, current design codes require that structures guarantee occupant safety and the possibility of evacuation by keeping damage within acceptable limits while strictly preventing collapse of primary structural elements [1, 2]. To meet these requirements, installing dedicated energy dissipation devices has become standard practice, since these elements concentrate plastic deformation and energy absorption, thereby preserving the integrity of the main structure [3, 4].

To improve structural performance under earthquake loading, a range of energy dissipation systems has been developed, generally classified according to their activation mechanism [5]. Depending on how they respond to seismic demand, these systems fall into two broad categories: active or semi-active systems — such as Active Mass Dampers, Active Bracing Systems, Variable Stiffness or Damping Systems, and Smart Materials — and passive systems, including Friction Dampers, Viscoelastic Dampers, Viscous Fluid Dampers, Metallic Dampers, Tuned Mass Dampers, and Tuned Liquid Dampers [4, 6–9]. Each of these technologies relies on a distinct mechanical principle to effectively reduce the impact of seismic events on structures [1, 3, 10, 11].

While these devices have long been employed to mitigate earthquake effects, the rise of additive manufacturing is now enabling a new generation of passive metallic dampers featuring complex, optimized geometries. Building on this premise, the present study proposes a novel seismic dissipation device designed through a performance-driven parametric visual scripting procedure. Unlike conventional topology optimization approaches, which are based on material subtraction, this work exploits the geometric properties of the Schwarz Primitive (P) Triply Periodic Minimal Surface (TPMS) to rationally define the internal core of the component.

Through visual scripting, the starting solid geometry is converted into a complex lattice structure, allowing precise calibration of energy absorption capacity without compromising the original stiffness needed to attract seismic loads. The fabrication of such intricate geometries is made possible by additive manufacturing, which overcomes the constraints of conventional manufacturing methods to produce shapes that enhance plasticization mechanisms. Moreover, TPMS surfaces possess an inherent geometric continuity, a feature that ensures a uniform distribution of plastic strain and maximizes the volume of material actively engaged in energy dissipation.

This research presents a preliminary assessment of this design workflow — from mathematical generation to numerical validation under target displacement demands — specifically developed for steel components manufactured using Atomic Diffusion Additive Manufacturing (ADAM) technology. At the current stage of the study, the proposed lattice-structured metallic damper is intended solely as a proof-of-concept prototype. However, the device is conceptually envisioned for real structural applications in seismic energy dissipation. To bridge the gap between this initial concept and practical

deployment, future work will mandate extensive experimental laboratory testing, focusing first on characterizing the raw printed material and subsequently on evaluating the actual structural response of the full-scale printed dampers. Consequently, the comprehensive reliability and process parameters variability of the ADAM technology—and their direct implications for safety-critical structural performance—will be thoroughly assessed alongside the experimental investigation of the mechanical properties of the 3D-printed devices.

2 Methodological Approach

2.1 Parametric Design Framework

The design of the dissipative device follows a parametric workflow created in the Rhinoceros-Grasshopper visual scripting environment, adopting a top-down approach. The process starts from a baseline solid sphere of predefined dimensions. This shape was chosen for its strategic structural advantages: its intrinsic compactness and high resistance to global buckling, a critical requirement for energy dissipation components. The spherical geometry is conceived for integration into steel Concentrically Braced Frames (CBF).

After defining the initial spherical volume, its internal layout was optimized via Rhinoceros-Grasshopper visual scripting in order to attain enhanced structural efficiency. Through this mathematical approach, the original solid sphere was converted into a high-performance hybrid configuration, in which the internal architecture is defined by a Triply Periodic Minimal Surface — specifically, the Schwarz P unit cell shown in Fig. 1.



Fig. 1. Single unit cell of the Schwarz Primitive (P) Triply Periodic Minimal Surface.

This geometry displays triple periodicity along the three spatial directions and is free of sharp edges or abrupt transitions. These characteristics make it particularly well suited for generating lattice structures able to fill complex volumes while avoiding the stress concentration points typically associated with conventional truss-like topologies. The letter “P” stands for “Primitive”, reflecting the Simple Cubic (SC) lattice symmetry

of the structure, which is composed of a network of orthogonally intersecting channels along the principal axes, forming independent yet interconnected labyrinths [12].

This mathematical surface belongs to a special class of geometries with zero mean curvature at every point, and it is mathematically described by the implicit Eq. (1), in which the parameter c governs the level-set definition of the TPMS and, together with the assigned wall thickness, determines the relative density of the resulting lattice.

$$\cos(x) + \cos(y) + \cos(z) = c \tag{1}$$

To generate the core, the unit cell is replicated n times along each of the three principal directions until it occupies the entire spherical volume previously defined. This produces an integrated geometry in which the lattice nucleus is fully enclosed within the spherical envelope, with a smooth and continuous junction linking the internal struts to the outer surface. Both the external spherical shell and the internal Schwarz P lattice share the same wall thickness, ensuring geometric consistency throughout the component.

2.2 Optimization Method

In contrast to conventional topology optimization tools (e.g., Abaqus ATOM), which operate through algorithmic removal of material, the present work adopts a parametric methodology implemented via a visual scripting platform. The underlying aim of this approach is to achieve a deliberate decoupling between stiffness and strength: maintaining the elevated initial stiffness necessary to attract seismic loads, while at the same time calibrating the ultimate strength to trigger stable and controlled dissipative behavior.

Within this framework, structural performance is controlled primarily by the relative density of the internal Schwarz P core, rather than by the outer boundary alone. This allows the response to move away from the stiff, brittle behavior typical of the solid baseline geometry, toward a more favorable, optimized dissipative curve. The definitive configuration is identified through a subsequent evaluation of the finite element analysis outcomes, by tracking ductile damage at the most critical locations and verifying that the device can withstand the target displacement without experiencing premature failure.

Compared with the irregular, non-periodic geometries typically produced by traditional topology optimization tools, the Schwarz P architecture offers notable benefits. Material-subtraction methods tend to generate organic, branch-like structures that are susceptible to unpredictable stress concentrations. The Schwarz P surface, by contrast, is defined by a mathematically continuous curvature that promotes a more even stress distribution across the entire volume, helping to avoid the localized stress "hot spots" that often lead to early failure in optimized components. This regular geometric pattern also results in an "open-cell" configuration that proves particularly advantageous for the ADAM process: by eliminating the isolated internal pockets or inaccessible cavities frequently found in algorithmically generated shapes, it facilitates the essential chemical debinding and sintering stages of the workflow. Overall, this parametric strategy offers a more predictable, manufacturing-friendly approach, granting direct control over the trade-off between geometric complexity and structural performance.

3 Numerical Modelling and Case Study

3.1 Material Characterization and FE Setup

For this study, 17–4PH stainless steel was selected, a martensitic precipitation-hardening alloy commonly employed in additive manufacturing applications, owing to its outstanding combination of high strength, hardness, and corrosion resistance [13, 14].

The mechanical properties used in the FEM analysis were obtained from the manufacturer's technical datasheet for the filament spool, with particular reference to the H900 (ASTM A564) heat-treated condition, selected to maximize structural performance. The nominal characteristics of the feedstock material are summarized in Table 1 [15].

Since mechanical characterization specifically for the ADAM-printed material has not yet been conducted by the authors, and given the preliminary nature of this proof-of-concept study, the nominal values provided by the filament manufacturer's datasheet were adopted for the initial FEM analysis.

To reduce computational demand, the elastic-plastic behaviour of the 17–4PH steel was represented using a bilinear stress-strain relationship, offering an appropriate balance between numerical accuracy and computational efficiency.

Table 1. Nominal mechanical properties of 17–4PH steel feedstock in the H900 condition [15].

Properties	Value
Offset yield strength $\sigma_{y,0.2\%}$	1050 MPa
Ultimate tensile strength σ_u	1230 MPa
Fracture strain ε_u	13%
Young's Modulus E	170 GPa

All numerical simulations were carried out using the Abaqus/CAE finite element software [16].

To capture the onset of failure in the devices, a progressive damage approach was adopted based on the *Ductile Damage* criterion. This formulation requires the definition of the following input parameters to characterize the initiation of material degradation:

- Fracture Strain, representing the plastic strain value at which damage begins;
- Stress Triaxiality, defined as the ratio between hydrostatic pressure and the Von Mises equivalent stress;
- Strain Rate, describing the rate at which the load is applied.

Since the loading conditions are quasi-static, the influence of strain rate on the ductile damage model was disregarded (set to zero). Once the material reached the critical threshold associated with damage initiation, a *Damage Evolution law* was applied to capture the gradual reduction in material stiffness and the subsequent removal of damaged elements. A linear, displacement-based softening law was used, with the plastic

displacement at failure defined so as to realistically represent the energy dissipated during fracture.

Given the considerable geometric complexity of the shapes produced through the visual-scripting workflow, the specimens were meshed using C3D4 elements (4-node linear tetrahedral elements), with an average element size of 7 mm. Although these elements exhibit greater stiffness than higher-order alternatives, they provide significantly better meshing robustness for irregular and intricate topologies, such as TPMS lattices, which are not easily partitioned into hexahedral meshes.

To reproduce the operating conditions of the metallic damper, the boundary conditions consisted of a fully fixed (*encastre*) constraint at the base of the specimen, eliminating all degrees of freedom. A monotonic displacement of 10 mm along the longitudinal axis was imposed at a *Reference Point* (RP) located on the top surface, simulating a compressive loading condition. A kinematic *Coupling* constraint was defined between the RP and the top surface of the damper to ensure a uniform load distribution and prevent localized stress concentrations at the loading point. The structural capacity and failure initiation were evaluated through a quasi-static, displacement-controlled analysis. This preliminary investigation made it possible to determine the yield point, together with the corresponding strength and displacement values, as well as the ultimate strength and displacement capacity, for both the baseline solid geometry and the visual scripting-optimized configuration.

3.2 FE Analysis and Case Study

The structural behavior of the 3D-printed dampers was investigated through a series of numerical simulations run within the Abaqus/Explicit environment. The choice of a *Dynamic, Explicit* procedure was motivated by the need to adequately material plasticity and geometric non-linearity. Both are indispensable for accurately reproducing the large deformations and the intricate contact phenomena undergone by the lattice ligaments before the point of failure.

Unlike implicit solution strategies, the explicit approach solves the equations of motion through a central difference integration method, thereby eliminating the need for iterative processes such as the Newton-Raphson algorithm. This ensures greater robustness and convergence stability when dealing with the pronounced non-linear response and material degradation introduced by the ductile damage model.

From each simulation, Force-Displacement (F-d) curves were obtained for both the solid sphere and the TPMS-based geometry. These curves constituted the main output for evaluating device performance, as they allowed the relevant mechanical indicators to be systematically derived and compared. On this basis, the configuration best aligned with the specific seismic energy dissipation requirements was identified.

The proposed design methodology was applied to a specific metallic damper prototype intended for seismic protection in steel Concentrically Braced Frames (CBF). The device is built around a spherical volume with an outer diameter of 150 mm: this dimension is dictated by the maximum build envelope of the 3D printer available at the Department of Engineering and Geology of the University “G. d’Annunzio” of Chieti-Pescara (Metal X, Markforged Inc.). As a result of this process, the entire device could be fabricated as a single, monolithic part through Atomic Diffusion Additive Manufacturing

(ADAM). Despite its compactness, the 150 mm diameter provides a highly dissipative core, capable of undergoing substantial plastic deformation without triggering global instability.

The internal architecture is defined by a Schwarz P TPMS core, generated by tiling two unit cells in each spatial direction (see Fig. 2). A uniform wall thickness of 6 mm was applied to both the internal lattice and the outer enclosing shell. This value was selected to ensure structural robustness and consistent energy dissipation, while simultaneously satisfying the manufacturing constraints imposed by the ADAM process. In particular, it facilitates the polymer binder removal during the chemical debinding phase and promotes full-density sintering of the 17–4PH stainless steel. Although this 6 mm value represents the baseline configuration adopted for preliminary validation, it constitutes only an initial step in the research; future work will include a thorough parametric investigation into how changes in wall thickness affect the overall dissipative behavior.

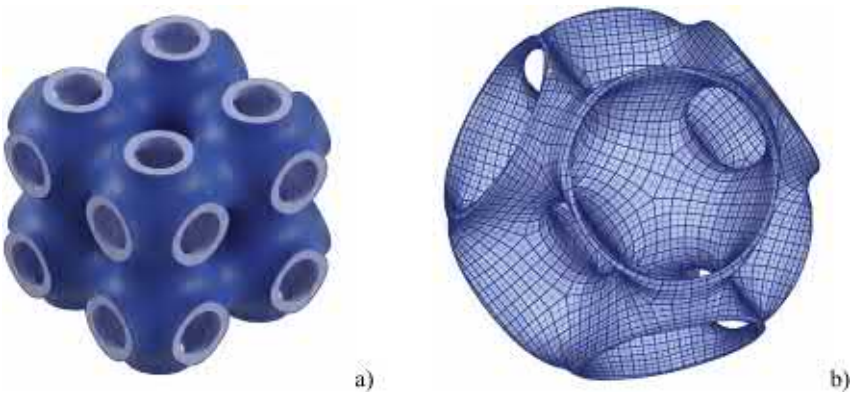


Fig. 2. Schwarz P TPMS: a) 2 × 2 × 2 unit cell configuration; b) Internal lattice core of the prototype.

The geometry is completed by two truncated cones positioned at the poles of the sphere, functioning as connection interfaces with the bracing system (Fig. 3). For numerical validation purposes, the device was subjected to a target axial displacement of 10 mm. This case study specifically examines how the interaction between the 6 mm thick Schwarz P ligaments and the spherical outer boundary shapes the Force-Displacement response, with a focus on the effectiveness of the resulting energy dissipation mechanism.

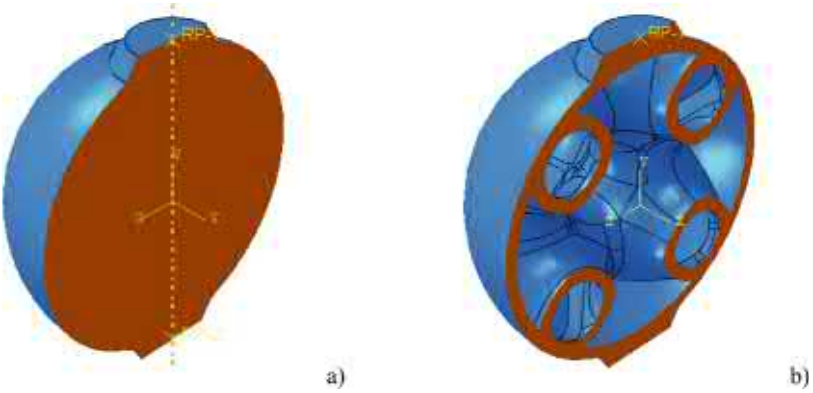


Fig. 3. Cross-sectional views of the two configurations modelled in Abaqus: a) Baseline solid sphere; b) Optimized geometry featuring the 2 × 2 × 2 Schwarz P internal core.

4 Results and Discussion

4.1 Comparative Performance Assessment

The Force-Displacement monotonic curves obtained from the numerical analyses of both models are presented in Fig. 4.

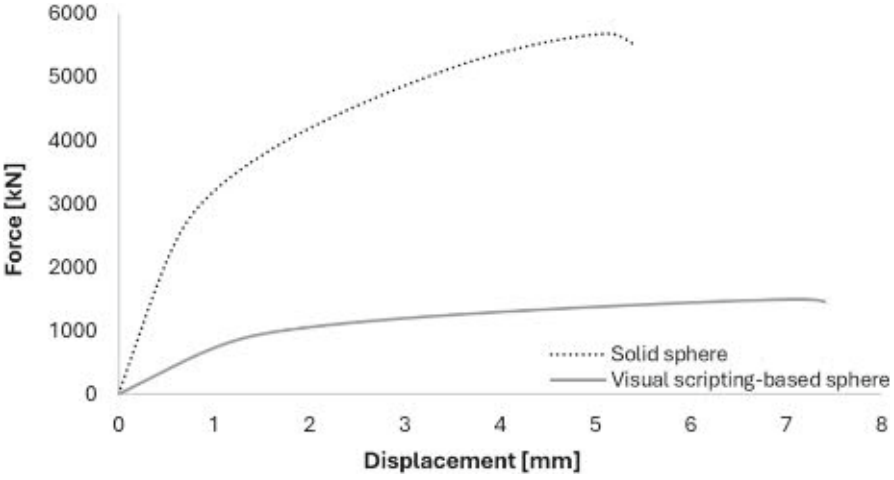


Fig. 4. Comparison of the numerical Force - Displacement curves under monotonic loading between the baseline solid sphere and the TPMS Schwarz P configuration.

The comparative evaluation clearly highlights how the internal topology exerts a decisive influence on the mechanical behavior of the device, with the two configurations exhibiting markedly different responses.

The solid sphere, adopted as a theoretical reference, displays very high elastic stiffness and considerable load-bearing capacity, reaching a yield force F_y of 2193 kN. However, its response is characterized by an abrupt elastic-to-plastic transition, with failure occurring at a displacement d_f of just 5.4 mm. This brittle behavior makes it largely unsuitable for seismic protection applications in steel frames, where a gradual and sustained energy dissipation capacity is essential.

The introduction of the TPMS internal core substantially modifies the device performance: the elastic stiffness is reduced and the yield force F_y is brought down to 635 kN, a level more compatible with the capacity of the surrounding bracing members. This adjustment is strategically beneficial, as it allows the damper to activate — and thus plasticize — at force levels that protect the main structural frame from excessive seismic demands. Although the ultimate force F_u drops from 5533 kN to 1452 kN, the TPMS-based configuration exhibits a considerably improved post-yield response, with the displacement at failure d_f extending to 7.4 mm. These findings confirm that the 6 mm wall thickness configuration successfully delivers a wider plastic range relative to the brittle response of the solid baseline, representing a key step in the transformation of a rigid mass into a fully functional dissipative component.

The effectiveness of the proposed approach is further supported by the substantial weight reduction achieved relative to the starting geometry. The solid sphere has a mass of 14.00 kg, whereas the visual scripting-based model weighs only 4.98 kg — a reduction of approximately 64%. This material saving demonstrates the ability of the lattice architecture to eliminate structurally redundant material. The resulting weight reduction brings direct practical benefits: it enhances manufacturability via ADAM technology by cutting printing time and associated costs, enables a more precise calibration of the device activation force, and preserves a favorable stiffness-to-weight ratio. The most significant implication of these results, however, lies in the tunability of the proposed design strategy. The 6 mm thickness is treated here as an initial reference point, and the stable post-yield behaviour observed suggests that future parametric variations of the TPMS wall thickness could be used to tailor the device response to specific seismic demand spectra. Accordingly, the focus of the ongoing research is shifting away from the comparison with the solid baseline and toward a sensitivity study among different TPMS configurations, with the aim of identifying the optimal trade-off between initial stiffness and plastic deformation capacity.

4.2 Parametric Evaluation and Performance Index

A performance index was introduced to quantify the parametric variability across the different damper configurations. This index is defined as the ratio of the mass-normalized stiffness to the mass-normalized yield force — both quantities being normalized with respect to the mass of the full solid sphere. As such, it provides a comparative measure of damper efficiency by relating the mass-normalized stiffness response to the mass-normalized yielding capacity.

To ensure a rigorous and detailed presentation of the proposed numerical workflow, Sect. 3 focused exclusively on the 6 mm wall thickness configuration, treating it as the baseline case study to thoroughly document the FE modelling procedure. However, to

showcase the flexibility of the visual scripting methodology and to evaluate how geometric variations influence the structural response, the exact same numerical framework was parametrically extended to generate and analyze three additional configurations (3, 9, and 12 mm). This section presents these performance index results to provide a broader comparative outlook, demonstrating the sensitivity of the passive dissipation device to scale and wall thickness variations.

The results reveal a gradual decline in the performance index as wall thickness increases from 3 mm to 9 mm, with values ranging from 0.65 to 0.62. This trend indicates that, within this thickness range, adding more material does not translate into a proportional improvement in relative damper performance. A notable exception is observed for the 12 mm configuration, which yields an index of 0.78. This outcome suggests that the 12 mm wall thickness achieves the most favorable balance between mass-normalized stiffness and mass-normalized yield force. On this basis, the 12 mm configuration is identified as the best-performing solution within the 2×2 damper layout (see Fig. 5).

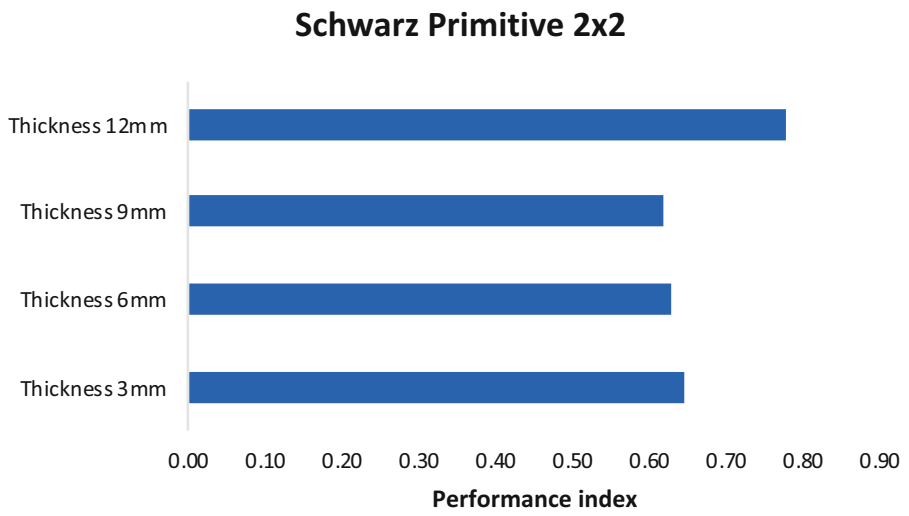


Fig. 5. Performance index variation across Schwarz P TPMS configurations.

5 Conclusions

The present work addressed the conception and numerical validation of an innovative seismic dissipation device, whose internal architecture draws on the geometric properties of the Schwarz Primitive TPMS and whose fabrication is enabled by Atomic Diffusion Additive Manufacturing. Through this investigation, it was shown that a parametric, performance-oriented design workflow can effectively address the shortcomings of traditional passive protection solutions while avoiding the manufacturability constraints that commonly affect algorithmically generated geometries.

The main outcomes of this work can be summarized as follows:

- The incorporation of the Schwarz P geometry enabled a strategic decoupling of stiffness and strength. Relative to the solid baseline, the visual scripting-based 6 mm configuration achieved a mass reduction of 64.4%, while bringing the yield threshold down to 635 kN from an initial value of 2193 kN. This ensures that the device activates at force levels compatible with those of standard steel frames;
- The numerical simulations, carried out using a damage-driven explicit solver, confirmed that the geometric regularity of the TPMS architecture allows the device to withstand extensive plastic deformation, considerably extending the functional stroke prior to the onset of ductile damage — with strength values shifting from 5533 kN to 1452 kN and displacement at failure increasing from 5.4 mm to 7.4 mm;
- The open-cell character of the Schwarz P core proved well suited to the requirements of the ADAM process, effectively supporting the chemical debinding and sintering stages.

Although the 6 mm wall thickness configuration serves as a solid baseline for this preliminary validation, the present work represents the first phase of a broader optimization framework. While a preliminary parametric comparison across different wall thicknesses has been presented in Sect. 4.2, future investigations will focus on a comprehensive multi-parameter optimization. This will examine how the simultaneous variation of wall thickness, cell scale, and TPMS volume fraction affects the energy dissipation capacity, ultimately validating these numerical trends through the upcoming experimental testing campaign. These efforts will contribute to refining the design space and providing deeper insight into the adaptability of the TPMS-based approach to a wider range of seismic protection scenarios.

Acknowledgements. The authors gratefully acknowledge the support of Uda-TechLab Research Center and the Digital Fabrication Lab of the Department of Engineering and Geology at the University “G. d’Annunzio” of Chieti-Pescara.

References

1. Saaed TE, Nikolakopoulos G, Jonasson JE, Hedlund H (2015) A state-of-the-art review of structural control systems. J Vib Control 21(5):919–937
2. De Domenico D, Tubaldi E, Takewaki I, Karavasilis T, A D’A, Lavan O (2020) Editorial: recent advances and applications of seismic isolation and energy dissipation devices. Front Built Environ 6:126
3. Brando G, D’Agostino F, De Matteis G (2015) Seismic performance of MR frames protected by viscous or hysteretic dampers. Struct Des Tall Spec Build 24(9):653–671
4. Pu W, He C (2022) Seismic design framework for steel structures with hysteretic and viscous dampers. J Constr Steel Res 194:107330
5. Symans MD et al (2008) Energy dissipation systems for seismic applications: current practice and recent developments. J Struct Eng 134(1):3–21
6. Talley PC, Javidialesaadi A, Wierschem NE, Denavit MD (2021) Evaluation of steel building structures with inerter-based dampers under seismic loading. Eng Struct 242:112488
7. Farsi A, Amiri HR, Dehghan Manshadi SH (2021) An innovative C-shaped yielding metallic dampers for steel structures. Structure 34:4254–4268

8. De Matteis G, Brando G, Caldoso F, D'Agostino F (2018) Seismic performance of dual steel frames with dissipative metal shear panels. Ingegneria Sismica 35(2):124–141
9. De Matteis G, Brando G (2016) Metal shear panels for seismic protection of buildings: recent findings and perspectives. Ingegneria Sismica 33(3):5–27
10. Yang J, Jing H, Li P (2022) Shaking table test and simulation of 12-story buildings with metallic dampers located on soft soil. J Build Eng 46:103585
11. Housner GW et al (1997) Structural control: past, present, and future. J Eng Mech 123(9):897–971
12. Maskery I et al (2018) Insights into the mechanical properties of several triply periodic minimal surface lattice structures made by polymer additive manufacturing. Polymer 152:62–71
13. Andreacola FR, Capasso I, Langella A, Brando G (2023) 3D-printed metals: process parameters effects on mechanical properties of 17-4PH stainless steel. Heliyon 9(7):e17698
14. Eskandari H, Lashgari HR, Ye L, Eizadjou M, Wang H (2022) Microstructural characterization and mechanical properties of additively manufactured 17–4PH stainless steel. Mater Today Commun 30:103075
15. Markforged Inc (2018) 17–4 PH stainless steel: Material datasheet. Revision 2.0. Markforged Inc, Watertown, MA.
16. Inc ABAQUS (2006) ABAQUS analysis user's manual, version 6.6. ABAQUS Inc, Providence, RI

Seismic Design in Greece and Italy: A Comparative Study of a Steel Frame

Maria Liapopoulou[1](✉) and Maria Maglio[2]

[1] University of Cambridge, Cambridge CB2 1TN, UK
ml2204@cam.ac.uk
[2] University of Salerno, 84084 Fisciano, SA, Italy

Abstract. Greece and Italy adopt distinct approaches within the Eurocode 8 framework to define the seismic action. The Greek National Annex uses a uniform-hazard map with fixed spectral shapes per Ground Type, while the Italian Technical Standards for Construction (NTC 2018) define the hazard at grid points of a national map with site- and hazard-dependent corner periods and soil amplification factors. This paper examines how these approaches influence the seismic performance of a typical residential steel building. A three-storey moment resisting steel frame is modelled in SAP2000 and analysed using the response spectrum method for two equivalent Greek–Italian site pairs, matched at the reference peak ground acceleration for relatively high (Athens–L'Aquila) and low (Thessaloniki–Napoli) seismicity. The design spectra differ by up to 26% at the plateau, with the NTC 2018 spectra showing higher accelerations, while the corner periods show smaller differences and the spectra converge at longer periods. A recently proposed revision of the Greek National Annex is also examined, revealing notable changes in the design spectra for the Greek sites, with a 10% reduction in plateau spectral acceleration for Athens and a 60% increase for Thessaloniki. The resulting bending moment utilisation ratios are 6–12% higher for beams and 10–16% higher for columns at the Italian sites. The implications of the two codified approaches are discussed, highlighting the importance of considering site- and hazard-dependent soil amplification and spectral shape.

Keywords: Seismic Design · Steel Structures · Eurocode 8 · Greek National Annex · Technical Standard for Construction NTC

1 Introduction

Greece and Italy are among the most seismically active European countries, with a long history of devastating earthquakes that have shaped structural engineering practice, driving the evolution of seismic standards. In Greece, the first national seismic design code was published in 1959 and updated as the Seismic Code for Building Structures in 1984 [1], following the catastrophic 1978 Thessaloniki and 1981 Alkionides earthquakes. This was later refined to incorporate European pre-standards, leading to the Greek Seismic Code (EAK 2000) [2], before the full mandatory enforcement of Eurocode 8 [3] alongside its National Annex (NA) in 2012 [4]. The second-generation Eurocode 8 [5] will

© The Author(s), under exclusive license to Springer Nature Switzerland AG 2026
R. Zanon et al. (Eds.): CTA 2026, LNCE 942, pp. 782–792, 2026.
https://doi.org/10.1007/978-3-032-39505-4_68

be adopted by September 2027, while the Greek NA is currently being revised with a notable proposal for this presented by Pitilakis et al. [6].

In parallel, the first seismic provisions in Italy appeared in the 1909 building code following the 1908 Messina earthquake [7]. Lateral design forces were introduced in 1915, the response spectrum concept and dynamic analysis in 1975, and limit state design and ductility considerations in 1996 [7]. The 2002 San Giuliano di Puglia earthquake triggered a major shift towards the Eurocode 8 methodology, leading to Ordinance OPCM 3274 in 2003 [8]. This was followed by the Technical Standards for Construction (NTC 2008) [9], which fully aligned Italian practice with Eurocode 8, introducing probabilistic seismic hazard analysis and performance-based seismic design. A revised version of this code, NTC 2018 [10], is currently enforced.

Previous studies have investigated the implementation and compared the codes in the two countries. Panagiotakos and Fardis [11] presented one of the earliest comparisons of Eurocode 8 and EAK 2000, assessing the design and performance of 4-, 8- and 12-storey reinforced concrete frames to both codes. They found comparable performance, despite large differences in material quantities and detailing, and they showed that Eurocode 8 enabled more cost-effective designs than EAK 2000. Liapopoulou et al. [12] evaluated 3- and 7-storey moment resisting frames to the first- and second-generation Eurocode 8, showing that the revised code results in higher column design loads, while second-order effects are usually less critical. Maglio et al. [13, 14] examined the design rules proposed for the newly introduced DC2 (medium) ductility class, designing and assessing steel moment resisting frames of varying span length and height through pushover and incremental dynamic analyses. Iervolino et al. [15] assessed the seismic reliability of cast-in-place and precast reinforced concrete, masonry, steel, and base-isolated buildings designed according to NTC 2008 across three Italian sites, finding lower seismic reliability indices at sites of higher hazard. More recently, Iervolino et al. [7, 16] demonstrated that fatality and failure rates decreased with the evolution of design codes, with the largest improvement attributed to NTC 2018.

This paper presents a comparative study of the current Greek and Italian seismic codes for the seismic performance assessment of a three-storey steel moment resisting frame designed in previous studies [17, 18]. The effect of the seismic action definition in the two codes is isolated by matching the hazard level for two equivalent site pairs in Greece and Italy. The proposed revision of the Greek NA by Pitilakis et al. [6], alongside the second-generation Eurocode 8, is also examined. The differences in the resulting spectra and member utilisation ratios are discussed, highlighting the distinct philosophies of the two codes and their implications in seismic design.

2 Seismic Action Definition

2.1 Greek and Italian Codes

The current Greek and Italian seismic codes can be regarded as national implementations of Eurocode 8, with the Greek NA defining the Nationally Determined Parameters (NDPs) and NTC 2018 being largely based on Eurocode 8. The principal differences between the two codes lie in the definition of hazard, spectral shape, and site amplification.

The Greek NA [4] defines three uniform-hazard seismic zones with constant reference peak ground acceleration (PGA) on rock at 475-year return period (a_{gR} of 0.16 g, 0.24 g, and 0.36 g), as shown in Fig. 1a. In contrast, NTC 2018 [9] defines the hazard at grid points of a national map, capturing the spatial variability of three parameters (peak ground acceleration on reference rock a_g, maximum amplification factor F_0, and upper bound of the constant velocity branch T_C*) at nine return periods (see Fig. 1b).

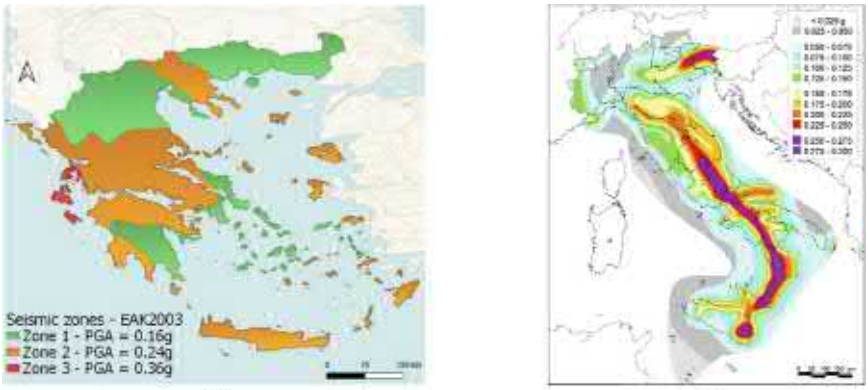


Fig. 1. a) Zone-based seismic hazard definition in Greece [6], and b) site-specific seismic hazard definition in Italy [19].

The spectral shape and soil amplification also differ between the two codes. In the former, the corner periods T_B, T_C and T_D and soil factor S depend only on Ground Type. Hence, for a given soil class, the same spectral shape is adopted and only the spectral ordinates scale with a_{gR}. On the other hand, NTC's corner periods T_B, T_C and T_D and the stratigraphic factor S_S are site- and hazard-dependent, resulting in a varying-width plateau and spectral shape. The maximum spectral amplification depends on F_0, while the corner periods are computed from Eqs. (1)–(3):

$$T_C = C_C \cdot T_C^* \tag{1}$$

$$T_B = T_C/3 \tag{2}$$

$$T_D = 4 \cdot a_g/g + 1.6 \tag{3}$$

where C_C is a coefficient that depends on the soil category and T_C*.

In Greece, the second-generation Eurocode 8 [5] and the proposed Greek NA update [6] align with recent progress towards improved seismic action definition. The revised Eurocode 8 shifts from a single-parameter spectrum anchored by PGA to a more robust two-parameter formulation anchored by S_α at the short-period acceleration plateau and S_β at $T_\beta = 1.0$ s. These two parameters are derived by multiplying the reference spectral acceleration on rock at 475-year return period ($S_{\alpha,475}$ and $S_{\beta,475}$) by the short-period and

intermediate-period amplification factor (F_α and F_β). The proposed NA [6] incorporates a five-zone hazard map with recommended values for $S_{\alpha,475}$ and $S_{\beta,475}$, based on the European Seismic Hazard Model 2020 (ESHM20) [20]. A novel site categorisation scheme is also included, as well as intensity-dependent F_α and F_β factors. The corner periods are also site- and hazard-dependent, as shown in Eqs. (4)–(7).

$$T_A = 0.02\ s \tag{4}$$

$$T_C = S_\beta / S_\alpha \cdot T_\beta \tag{5}$$

$$0.05\ s \leq T_B = T_C/4 \leq 0.10\ s \tag{6}$$

$$T_D = 1.0 + S_{\beta,475} \geq 2.0\ s \tag{7}$$

2.2 Site Pairs

Two Greek - Italian equivalent site pairs are selected to represent two levels of relatively high (Athens–L'Aquila) and low seismicity (Thessaloniki–Napoli), with the reference PGA at 475-year return period approximately equal within each pair, as shown in Table 1. For the Italian sites, the parameters a_g, F_0 and $T_C{}^*$ are interpolated from the national hazard map at the nominal coordinates of the city centre.

Table 1. Definition of equivalent site pairs based on the current Greek and Italian codes.

Greek site	a_{gR} (g)	Italian site	a_g (g)	F_0	$T_C{}^*$ (s)
Athens	0.24	L'Aquila	0.27	2.4	0.35
Thessaloniki	0.16	Napoli	0.17	2.4	0.34

The soil class is Ground Type C, representing deposits of dense or medium-dense sand, gravel, or stiff clay, with the corner periods and soil amplification shown in Table 2.

Table 2. Corner periods and soil amplification factors for equivalent site pairs based on the current Greek and Italian codes.

Greek site	T_B (s)	T_C (s)	T_D (s)	S	Italian site	T_B (s)	T_C (s)	T_D (s)	S
Athens	0.2	0.6	2.0	1.15	L'Aquila	0.17	0.52	2.66	1.32
Thessaloniki	0.2	0.6	2.0	1.15	Napoli	0.17	0.51	2.27	1.46

The parameters for the definition of the response spectra for the Greek sites with the revised Eurocode 8 and NA [5, 6] are summarised in Table 3, considering soil class C2.

Table 3. Spectral acceleration at the plateau and at 1.0 s period at 475-year return period, corner periods, and soil amplification factors based on the revised Eurocode 8 and proposed NA.

Greek site	$S_{\alpha,475}$ (g)	$S_{\beta,475}$ (g)	T_A (s)	T_B (s)	T_C (s)	T_D (s)	F_α	F_β
Athens	0.47	0.15	0.02	0.10	0.49	2.47	1.32	2.02
Thessaloniki	0.58	0.18	0.02	0.10	0.48	2.77	1.27	1.97

3 Structural System

The case study consists of a three-storey steel building which was designed to Eurocodes 3 and 8 by Liapopoulou et al. [17, 18]. The plan configuration is shown in Fig. 2a, with the lateral force-resisting system including moment resisting frames (MRFs). The building is symmetric and regular in plan and elevation; therefore, a two-dimensional model is adopted. The interior MRF is selected as the representative structural system, as it is subjected to the highest gravity loads due to the contribution of the tributary areas from both adjacent sides. The bay length is 6 m, while the storey heights are 4.5 m for the first storey and 3.5 m for the upper storeys (Fig. 2b).

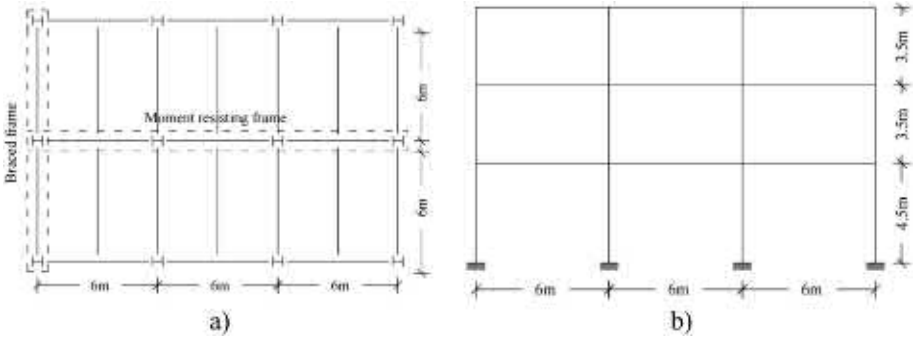


Fig. 2. Structural configuration: (a) plan view, and (b) elevation [17, 18].

The characteristic gravity loads considered in the design included dead load of 5.75 kN/m^2 at the first two storeys and 4.75 kN/m^2 at the third, as well as imposed load of 2.00 kN/m^2 at the first two storeys and 1.00 kN/m^2 at the third [17, 18]. European steel profiles manufactured from S275 structural steel are used, as shown in Table 4.

Table 4. Beam and column sects [17, 18].

Storey	*Beam sections*	*Column sections*
1	IPE500	HE500B
2	IPE500	HE500B
3	IPE360	HE340B

The examined MRF is modelled in SAP2000 [21], assuming rigid connections. Its first-mode period is 0.48 s, which falls within the plateau region of the design response spectra, where the differences between the seismic demands defined by the Greek and Italian regulations are more pronounced.

4 Response Spectrum Analysis

4.1 Response Spectra

The design acceleration response spectra for the equivalent Greek and Italian site pairs are evaluated based on Eurocode 8 and NTC 2018, respectively. The Importance Class is defined as II in both codes ($\gamma_I = 1.0$, $C_U = 1.0$), the damping ratio as 5%, and the behaviour factor as 4.0. The design response spectra, computed according to the respective code for each site, are plotted in Fig. 3.

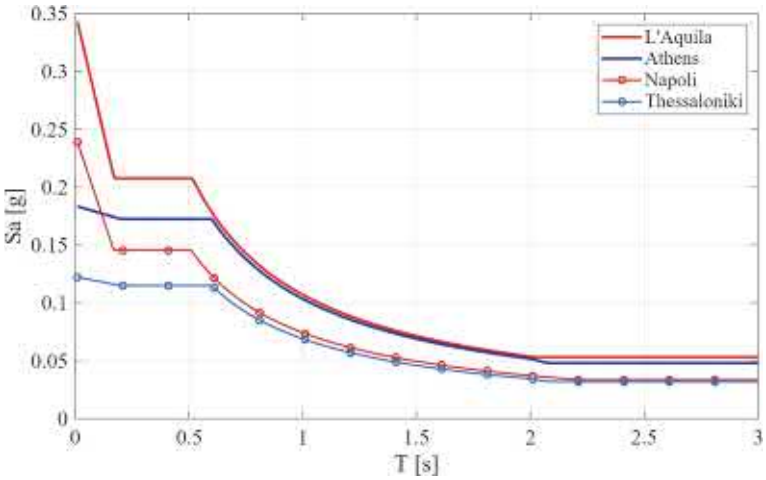


Fig. 3. Design response spectra for the equivalent site pair of relatively high seismicity (Athens–L'Aquila), and low seismicity (Thessaloniki–Napoli).

Although the reference PGA at the 475-year return period is kept constant between the Greek and Italian sites within each pair, the spectra exhibit notable differences due to the distinct code approaches in defining the seismic action. The largest divergence

is observed at $T = 0$ s, where the design spectral acceleration is 0.34 g for L'Aquila and 0.24 g for Napoli, compared with 0.18 g for Athens and 0.12 g for Thessaloniki, corresponding to differences of 47% and 50%. The Italian code does not apply any reduction of the elastic spectral ordinate for very stiff structures ($T = 0$ s) on the basis that they do not exhibit ductility, while Eurocode 8 employs a reduction factor of 2/3.

Significant differences are also observed at the plateau, where the design spectral acceleration is 24% higher for L'Aquila (0.21 g) than Athens (0.17 g), and 26% higher for Napoli (0.15 g) than Thessaloniki (0.12 g). This arises from the hazard dependence of the Italian stratigraphic factor as opposed to the fixed soil amplification in Eurocode 8, which disregards the intensity dependence of nonlinear soil response.

The corner periods T_B, T_C and T_D are less different between the two codes. As shown in Table 2, for the Greek sites they are fixed, while for the Italian sites T_B and T_C are slightly shorter than the Eurocode 8 values and T_D is longer. The overall spectral shape is similar, following the Eurocode 8 equations, and the equivalent spectra converge in the medium-to-long period range.

To assess the impact of the second-generation Eurocode 8 [5] and proposed Greek NA [6], the corresponding design response spectra for Athens and Thessaloniki are evaluated and compared against those based on the current provisions in Fig. 4. The revised Eurocode 8 spectra are not used in further analyses, however, as they are not defined as equivalent to those from NTC 2018, and they are only examined herein to provide insights into the proposed spectra for the two Greek sites.

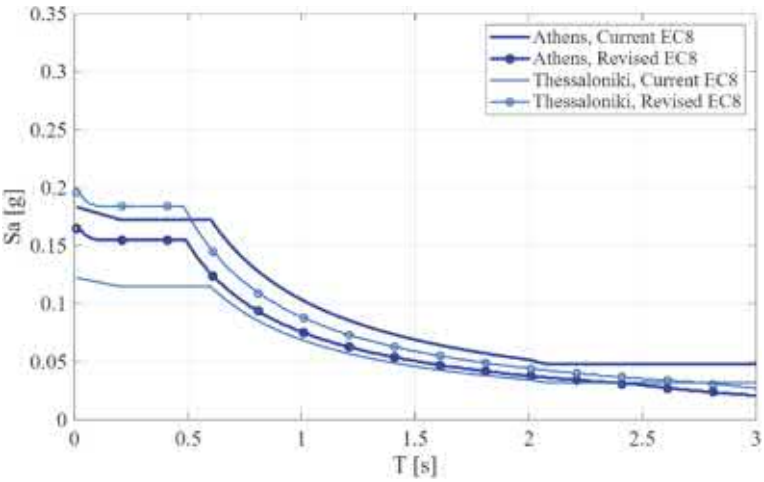


Fig. 4. Design response spectra for the Greek sites (Athens and Thessaloniki) based on the current Eurocode 8 and NA [3, 4] and the revised Eurocode 8 with the proposed NA [5, 6].

As shown in Fig. 4, the revised Eurocode 8 leads to lower spectral ordinates for Athens and substantially higher for Thessaloniki, due to the refined hazard definition through the ESHM20-based zonation [20]. The current NA [4] assigns Athens to Zone 2 (PGA = 0.24 g) and Thessaloniki to Zone 1 (PGA = 0.16 g), incorporating the EAK

2000 [2] hazard zonation. In contrast, the proposed five-zone scheme, based on the ESHM20 model, assigns Athens in Zone 2 (PGA = 0.19 g) and Thessaloniki in Zone 3 (PGA = 0.23 g). Hence, the revised Eurocode 8 plateau spectral acceleration reduces by 10% for Athens, while it increases by 60% for Thessaloniki. The revised framework defines the seismic action with due account of site- and hazard-dependent corner periods and soil amplification, similar to NTC 2018 [10].

4.2 Results

The MRF under consideration is analysed using the Response Spectrum Method (RSM) with each of the design response spectra based on the current seismic codes for the equivalent Greek and Italian sites. The seismic performance was verified for all examined sites, and the results presented in the following focus on bending moments, where the largest differences were observed.

The bending moment utilisation ratio (UR) is defined as the ratio of the design bending moment demand M_{Ed} to the design flexural resistance $M_{pl,Rd}$, as shown in Eq. (8):

$$UR = M_{Ed}/M_{pl,Rd} \tag{8}$$

For columns, the design bending moment demand is evaluated from Eq. (9), adopting the Eurocode 8 [3] approach to account for overstrength requirements imposed by capacity design. Although the effect of gravity loading is considered in NTC 2018 [10], it is disregarded herein, as the intention is to examine how the different definition of the seismic action in the two codes affects the RSM results.

$$M_{Ed} = M_{Ed,G} + 1.1\ \gamma_{ov}\ \Omega\ M_{Ed,E} \tag{9}$$

where $M_{Ed,G}$ is the column design bending moment due to gravity loads, $M_{Ed,E}$ is the column design bending moment due to seismic loads, γ_{ov} is the overstrength factor (γ_{ov} = 1.25 for S275 steel [3]), and Ω is the minimum overstrength ratio ($M_{pl,Rd}/M_{Ed}$) of the dissipative members [3].

The values of the overstrength factor for each examined site are given in Table 5. Within each pair, the Italian site exhibits lower Ω by approximately 7%, reflecting the larger seismic demands corresponding to the Italian design spectra.

Table 5. Overstrength factors.

Greek site	Ω	Italian site	Ω
Athens	2.55	L'Aquila	2.40
Thessaloniki	2.84	Napoli	2.66

The beam and column URs for the higher seismicity (Athens–L'Aquila) and lower seismicity (Thessaloniki–Napoli) pair are presented in Figs. 5 and 6, respectively.

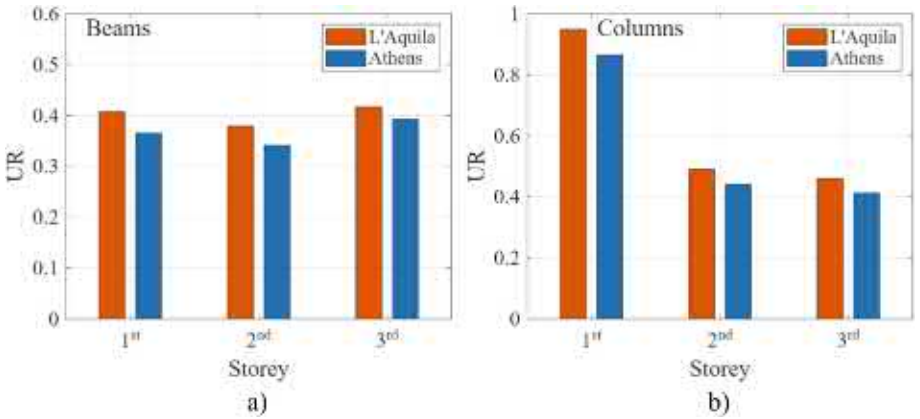


Fig. 5. a) Beam, and b) column bending moment utilisation ratios of the frame based on Athens and L'Aquila design response spectra.

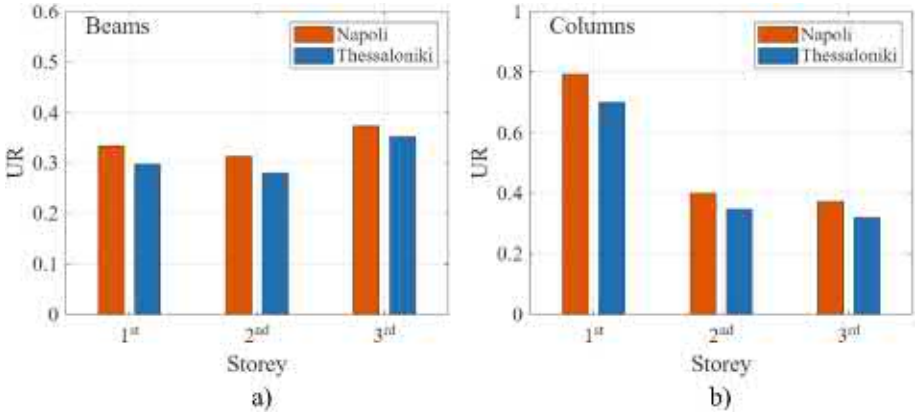


Fig. 6. a) Beam, and b) column bending moment utilisation ratios of the frame based on Thessaloniki and Napoli design response spectra.

For all locations, columns govern the design, with their first-storey URs being close to unity for L'Aquila, while beam URs are lower, as they are governed by serviceability rather than strength criteria. Beam URs are 6–12% higher for Italian sites, exhibiting smaller changes than the plateau accelerations, due to the contribution of gravity loads. For columns, although the gravity contribution is lower, overstrength requirements partially reduce spectral effects, resulting in 10–16% lower URs for Greek sites, with the upper limit corresponding to third-storey columns for Thessaloniki–Napoli. These results indicate that disregard of site and hazard effects on soil amplification and spectral shape may underestimate member utilisation, potentially leading to unsafe designs.

5 Conclusions

A comparative study of the seismic action definition in the current Greek and Italian codes was presented, through response spectrum analysis of a three-storey MRF steel frame. Two Greek-Italian equivalent site pairs were selected, matched at PGA levels of relatively high (Athens–L'Aquila) and low (Thessaloniki–Napoli) seismicity to isolate the effect of code approach from that of hazard magnitude. The design spectra of equivalent pairs differ by up to 26% at the plateau, mainly due to the hazard- and site-dependent corner periods and stratigraphic factor of NTC 2018. These differences translate into less pronounced changes in beam and column utilisation ratios, which are up to 12% and 16%, respectively, higher for the NTC-based spectra, due to the substantial gravity load contribution for beams and the overstrength requirements for columns. This suggests that disregarding the site and hazard dependence of soil amplification and corner periods may lead to unsafe designs. A recently proposed revision of the Greek NA based on the ESHM20 model, which addresses this limitation and represents more accurately the seismic hazard and its variability, resulted in reduced plateau spectral ordinates by 10% for Athens and increased values by 60% for Thessaloniki, correcting the current EAK-based hazard underestimation for the latter.

Acknowledgements. The first author would like to acknowledge the support provided by the Royal Commission for the Exhibition of 1851 through the Brunel Fellowship.

References

1. Greek Seismic Code (1959) Royal Decree on the Seismic Code for Building Structures. Government's Gazette Issue A No. 36, Revision in 1984 (in Greek).
2. EAK (2000) Greek seismic code. Greece, Athens
3. CEN (2004) Eurocode 8: design of structures for earthquake resistance. CEN, Brussels
4. ELOT (2010) National annex to EN 1998-1:2004. Hellenic Organization for Standardization (ELOT), Athens, Greece. (in Greek).
5. CEN (2026) Eurocode 8: design of structures for earthquake resistance. CEN, Brussels
6. Pitilakis K, Riga E, Apostolaki S, Danciu L (2024) Seismic hazard zonation map and definition of seismic actions for Greece in the context of the ongoing revision of EC8. Bull Earthq Eng 22(8):3753–3792
7. Iervolino I, Pacifico A (2026) Design code Progress and conventional seismic safety improvement in Italy. J Earthq Eng:1–9
8. OPCM 3274 (2003). Italian seismic classification criteria and technical norms for construction in seismic zones. Gazzetta Ufficiale della Repubblica Italiana n. 105. (in Italian).
9. NTC (2008) Italian technical norms for construction. Decreto Ministeriale 14 January 2008. Gazzetta Ufficiale della Repubblica Italiana n 29. (in Italian).
10. NTC (2018) Update of the Italian technical norms for construction. Decreto Ministeriale 17 January 2018. Gazzetta Ufficiale della Repubblica Italiana n. 42. (in Italian).
11. Panagiotakos TB, Fardis MN (2004) Seismic performance of RC frames designed to Eurocode 8 or to the Greek codes 2000. Bull Earthq Eng 2(2):221–259
12. Liapopoulou M, Stafford PJ, Elghazouli AY (2023) Comparative assessment of steel moment frames designed to Eurocode 8. In: SECED Proceedings. Cambridge, UK

13. Maglio M, Montuori R, Nastri E, Piluso V (2023) Critical discussion of DC2 design rules for MR-frames in the framework of the prEN1998 draft. Procedia Struct Integrity 44:550–557
14. Maglio M, Montuori R, Nastri E, Piluso V (2023) Design and seismic evaluation of MRFs in DC2 ductility class introduced in the new prEN1998 draft and comparison with TPMC. Soil Dyn Earthq Eng 168:107833
15. Iervolino I, Spillatura A, Bazzurro P (2018) Seismic reliability of code-conforming Italian buildings. J Earthq Eng 22:5–27
16. Iervolino I, Baraschino R, Spillatura A (2023) Evolution of seismic reliability of code-conforming Italian buildings. J Earthq Eng 27(7):1740–1768
17. Liapopoulou M, Stafford PJ, Elghazouli AY (2024) Duration-dependent seismic collapse capacity prediction for steel moment-resisting frames. J Build Eng 86:108810
18. Liapopoulou M (2018) Ultimate seismic response of steel framed structures. PhD thesis,, Imperial College London, UK
19. Stucchi M, Meletti C, Montaldo V et al (2004) Pericolosità sismica di riferimento per il territorio nazionale MPS04. Istituto Nazionale di Geofisica e Vulcanologia (INGV)
20. Danciu L, Nandan S, Reyes CG et al (2021) The 2020 update of the European seismic Hazard model-ESHM20: model overview. EFEHR Technical Report 1
21. CSI (2024) SAP2000 structural analysis and design. CA, USA, Berkeley

Comparative Analysis and TPMC (θ) Design Approach for a Moment-Resisting Frame Structure

Rosario Montuori[1], Elide Nastri[2], Vincenzo Piluso[2], and Chiara Scafuri[2(✉)]

[1] Department of Pharmacy, University of Salerno, Fisciano, Italy
[2] Department of Civil Engineering, University of Salerno, Fisciano, Italy
cscafuri@unisa.it

Abstract. The anti-seismic design of moment-resisting frame structures (MRFs) based on the Theory of Plastic Mechanism Control (TPMC) assures the absence of undesired collapse mechanisms and the development of a specific number of plastic hinges in all dissipative zones of the structure. The purpose of this work is to design and optimize a regular steel MRF structure in plan and height, comparing design solutions in the case of beams sized for gravitational loads or seismic actions. From the analysis of the 3D structure and the acting loads, two orthogonally plane structural schemes with different stresses were obtained, and the TPMC (θ) procedure was adopted for the design of the most stressed one, verifying the geometric and mechanical compatibility of the orthogonal scheme. To validate the obtained results, non-linear static analyses were conducted on both the 3D-structure and the plane schemes, as well as a bi-component non-linear dynamic analysis, the results of which, expressed in terms of plastic hinge distribution patterns, confirmed the validity of the proposed procedure. The absence of undesired collapse mechanisms confirmed the efficacy of TPMC(θ), and the size reduction of columns on all storeys highlighted the technical and economic advantage of reducing the overall structural weight.

Keywords: TPMC · Moment Resisting Frames · Steel structures · Collapse mechanisms

1 Introduction

The Theory of Plastic Mechanism Control (TPMC) first emerged in the 1990s [1] as an iterative procedure for seismic structural design. It is a methodology based on a solid theoretical background, specifically the extension of the kinematic theory of plastic collapse to the concept of the mechanism equilibrium curve, in the context of a second-order rigid-plastic analysis. It allows for the design of structures able to collapse by exhibiting global collapse mechanisms, which assure the dissipation of the greatest amount of input seismic energy due to the yielding of all dissipative zones of the structure. The original kinematic design parameter of the TPMC was the top sway displacement of the structure δ, TPMC (δ), while recent works have improved the procedure by replacing δ

© The Author(s), under exclusive license to Springer Nature Switzerland AG 2026
R. Zanon et al. (Eds.): CTA 2026, LNCE 942, pp. 793–805, 2026.
https://doi.org/10.1007/978-3-032-39505-4_69

with the plastic rotation of the dissipative zones θ, namely TPMC (θ) [5]. This adjustment improved the method, obtaining technical and economic benefits thank to a significant decrease in structural weight resulting from the reduction of column cross-sections on all storeys. To assure that the structural collapse mechanism is the global one, the design algorithm of the closed-form solution presented in 2015 is applied [2], ensuring the yielding of the beam ends on all storeys and of the base sections of the columns at the first storey, in the case of MR-frames. The procedure, which has demonstrated its accuracy and reliability, is applicable to various structural typologies and construction materials, and is independent of the specific force distribution [3–4], [4–13]. The purpose of this work is to confirm the validity of the TPMC method for the design of MR-frames, by proposing optimized structural solutions derived from the analysis of frames subjected primarily to gravitational loads and seismic actions and optimizing beam cross-sections under both load conditions. The obtained results were validated performing static and nonlinear dynamic analyses using finite element analysis software.

2 TPMC (θ) Design Approach of MR-Frames

The theoretical basis of TPMC design approach, overcomes the uncertainties associated with the application of the Hierarchy Criteria suggested by the codes [14], which are based on simple equilibrium considerations that do not assure the absence of undesired collapse mechanisms. The closed-form solution presented in 2015, however, introduced the design algorithm to be used to prevent the development of partial collapse mechanisms. Furthermore, in recent years, research has brought significant improvements to TPMC procedure by modifying the kinematic design parameter, ensuring a reduction in the structure's overall weight. From a theoretical point of view, the procedure is based on the extension of the kinematic theorem of plastic collapse to the concept of the mechanism equilibrium curve derived from a second-order rigid-plastic analysis, by equating the external and internal work of the plastic hinges, also taking into account the second-order work of the external loads. In the case of global-type collapse mechanisms:

$$a = a_0 - \psi\theta = \frac{\sum_{k=1}^{n_c} M_{c,i,1} + 2\sum_{k=1}^{n_s}\sum_{j=1}^{n_b} M_{b,jk}}{\sum_{k=1}^{n_s} F_k h_k} - \frac{\sum_{k=1}^{n_s} V_k h_k}{\sum_{k=1}^{n_s} F_k h_k}\,\theta \qquad (1)$$

Where a_0 represents the kinematically admissible multiplier of the horizontal forces according to the first-order rigid-plastic analysis, ψ the slope of the mechanism equilibrium curve in the (α−θ) plane, θ the plastic rotation of the dissipative zones, $M_{c,\,i,\,1}$ the required plastic moment of the columns at the I storey reduced by the contemporary action of the axial force, and $M_{b,\,jk}$ the plastic moment of the beams, designed to resist both gravitational loads and seismic actions, also satisfying the deformability and stability checks. F_k and h_k are, respectively, the seismic force applied to the k-th floor and the height of the k-th floor from the foundation level; V_k is the total vertical load acting on the k-th floor; and n_c, n_s, and n_b are the number of columns, storeys, and bays, respectively. Similarly, it is possible to obtain the mathematical expression of the theoretical curve associated with undesired collapse mechanisms that could occur in MR-frame structures (Tables 1 and 2).

Table 1. I order rigid-plastic multiplier of the mechanism equilibrium curves of undesired mechanisms.

Mechanism	a_{0,i_m}
Type-1	$\frac{\sum_{k=1}^{n_c} M_{c,i,1}+\sum_{k=1}^{n_c} M_{c,i,i_m}+2\ \sum_{k=1}^{i_m-1}\sum_{j=1}^{n_b} M_{b,jk}}{\sum_{k=1}^{i_m} F_k\ h_k+h_{i_m}\sum_{k=i_m}^{n_s} F_k}$
Type-2	$\frac{\sum_{k=1}^{n_c} M_{c,i,i_m}+2\ \sum_{k=i_m}^{n_s}\sum_{j=1}^{n_b} M_{b,jk}}{\sum_{k=i_m}^{n_s} F_k(\ h_k-h_{i_m-1})}$
Type-3	$\frac{2\sum_{k=1}^{n_c} M_{c,i,i_m}}{(h_{i_m}-h_{i,i_m-1})\ \sum_{k=i_m}^{n_s} F_k}$

Table 2. Slope of the mechanism equilibrium curves of undesired mechanisms.

Mechanism	ψ_{i_m}
Type-1	$\frac{\sum_{k=1}^{i_m} V_k\ h_k+h_{i_m}\sum_{k=i_m+1}^{n_s} V_k}{\sum_{k=1}^{i_m} F_k\ h_k+h_{i_m}\sum_{k=i_m+1}^{n_s} F_k}$
Type-2	$\frac{\sum_{k=i_m}^{n_s} V_k\ (h_k-h_{i_m-1})}{\sum_{k=i_m}^{n_s} F_k(\ h_k-h_{i_m-1})}$
Type-3	$\frac{\sum_{k=i_m}^{n_s} V_k}{\sum_{k=i_m}^{n_s} F_k}$

The design requirement necessary to prevent undesired collapse mechanisms requires that the equilibrium curve associated to the collapse mechanism of global type has to be positioned below all those corresponding to the undesired mechanisms (Fig. 1):

$$a_0^{(g)} - \psi^{(g)}\theta \le a_{0,i_m}^{(t)} - \psi_{i_m}^{(t)}\theta \tag{2}$$

For $i_m = 1, 2, 3, \ldots, n_s$ storey index and t = 1,2,3 mechanism index, in the interval $[0, \theta_u]$.

Given the cross-sections of the beams on all storeys, which, as will be seen below, will be obtained with reference to load cases dominated by gravity loads or seismic actions, by applying the TPMC (θ) design algorithm, the set of steel profiles to be assigned to the columns is derived in order to satisfy the reduced plastic resistance requirement for the contemporary action of the axial force at storey I, to avoid undesired collapse mechanisms:

$$\sum_{i=1}^{n_c} M_{c,i1} \ge \frac{2\sum_{k=1}^{n_s}\sum_{j=1}^{n_b} M_{b,jk} + \left(\psi_1^{(t)} - \psi^{(g)}\right)\theta\ \sum_{k=1}^{n_s} F_k h_k}{2\frac{\sum_{k=1}^{n_s} F_k h_k}{h_1\sum_{k=1}^{n_s} F_k} - 1} \tag{3}$$

By applying the design requirement (Eq. (2)) and changing the mechanism index, we also obtain the sum of the reduced plastic moment required for storeys above the I, to prevent the development of Type 1, 2, and 3 collapse mechanisms:

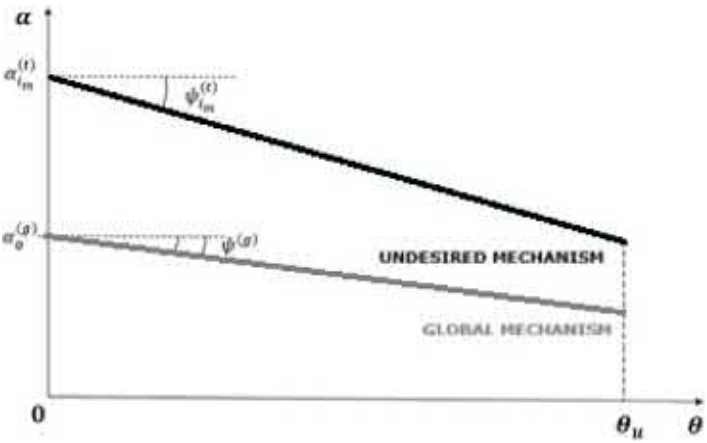


Fig. 1. Design requirement to avoid undesired collapse mechanisms.

$$\sum_{i=1}^{n_c} M_{c,ii_m}{}^{(1)}(\theta) \geq \left(a^{(g)} + \psi_{i_m}^{(1)}\theta\right)\left(\sum_{k=1}^{i_m} F_k h_k + h_{im} \sum_{k=i_m+1}^{n_s} F_k\right) - \sum_{i=1}^{n_c} M_{c,i1}{}^{*} - 2\sum_{k=1}^{i_m-1}\sum_{j=1}^{n_b} M_{b,jk} \tag{4}$$

$$\sum_{i=1}^{n_c} M_{c,ii_m}{}^{(2)}(\theta) \geq \left(a^{(g)} + \psi_{i_m}^{(2)}\theta\right)\left(\sum_{k=i_m}^{n_s} F_k(h_k - h_{im-1})\right) - 2\sum_{k=i_m}^{n_s}\sum_{j=1}^{n_b} M_{b,jk} \tag{5}$$

$$\sum_{i=1}^{n_c} M_{c,ii_m}{}^{(3)}(\theta) \geq \left(a^{(g)} + \psi_{i_m}^{(3)}\theta\right)\frac{(h_{im} - h_{im-1})}{2}\left(\sum_{k=i_m}^{n_s} F_k\right) \tag{6}$$

Where $M_{c,i1}{}^{*}$ is the effective plastic moment of the columns on floor I, i.e., the available plastic resistance obtained from profiles derived from standard shapes. From a design perspective, the choice of cross-sections is obviously a function of the maximum among the values previously calculated. The selection is also influenced by the need to satisfy the technical requirement that prevents column cross-sections from increasing with height.

3 Case Study

3.1 Numerical Approach

To assure the validity of the TPMC (θ) procedure for the seismic design of moment-resisting steel frames, several numerical simulations were performed. The seismic system consists of spatial truss structures made of S355 steel, as shown in Fig. 2.

To get a detailed understanding of the structural behaviour, the number of stories was varied, analysing configurations with 4, 6, and 8 stories. It was observed that, due to the deformation of the slab, two distinct configurations emerged in which the orthogonal systems were subjected to different stress conditions; From the two configurations obtained,

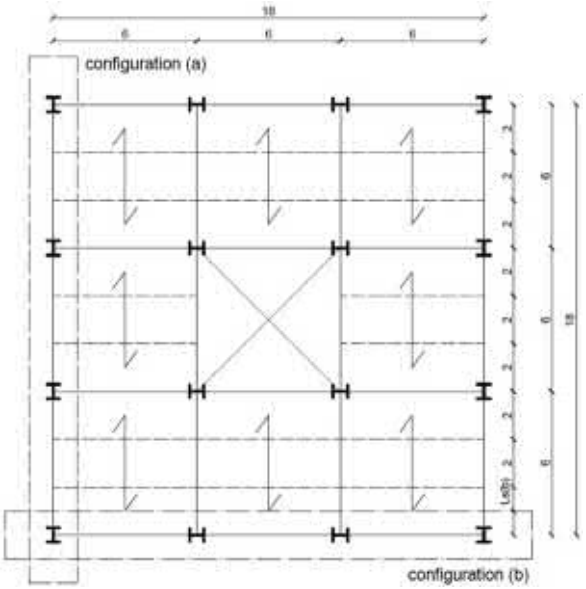


Fig. 2. Plan configuration of investigated MRFs.

a predominance of stresses resulting from gravitational loads was observed for frames arranged orthogonally to the secondary beams (configurations: (a)) (Fig. 3), where the effects of gravitational loads prevail, while in the other one (Fig. 4), stresses of a predominantly seismic type prevail in the frames arranged parallel to the secondary beams (configurations: (b)). Therefore, the design of the beams depended on the specifically considered layout.

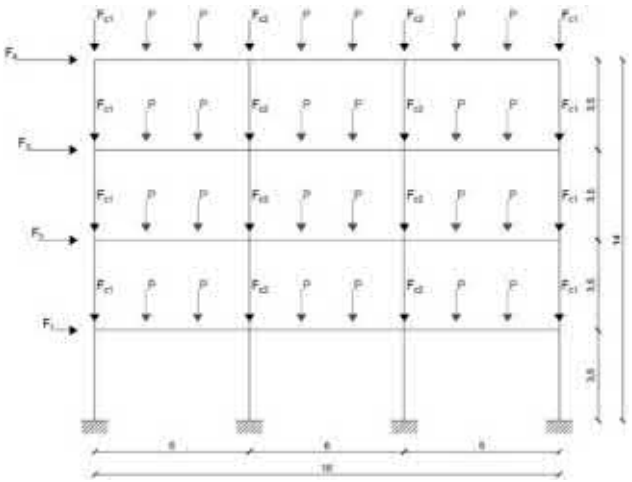


Fig. 3. Transversal scheme of the most stressed 4-storeys frame-configuration(a).

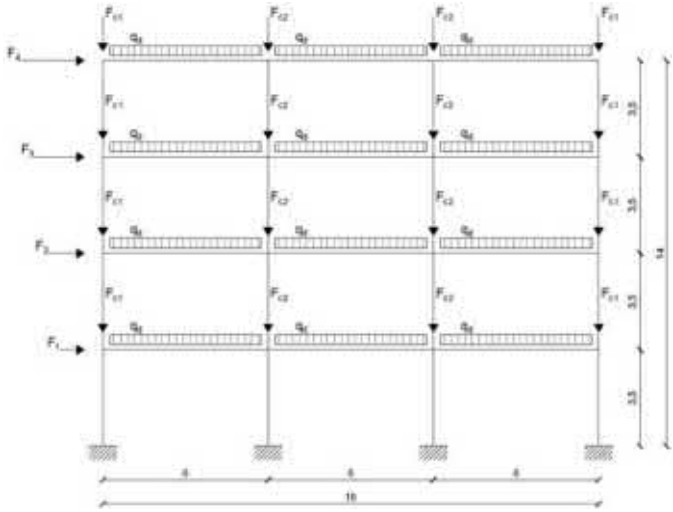


Fig. 4. Transversal scheme of the less stressed 4-storeys frame-configuration(b).

The main design work focused on the structure subjected to the highest load conditions, namely configuration (a), by performing a preliminary sizing of the beams subjected to gravitational loads and distributing the seismic forces derived from the spectrum associated with the "Full Operation" requirement. The resulting cross-sections were, of course, checked for phenomena of excessive deformability. To achieve the correct distribution of forces among the frames subjected to different loads in the two principal directions, the "Train of Frames" approach was applied, followed by the TPMC design procedure, selecting the column cross-sections based on the design algorithm. The transverse frame, which is subject to lower stresses, was only verified by checking that the column cross-sections previously identified by the analysis of configuration (a) satisfied the strength verification by comparing the required plastic moments in the columns at each storey and the available strength. The beams in configuration (b) were assigned the minimum cross-sections that simultaneously satisfied the SLU condition for both gravitational loads and the seismic load combination. In both cases, the TPMC design requirement (θ) (Eq. (2)) is satisfied, therefore all undesired collapse mechanisms are avoided.

3.2 Validation

The validity of the TPMC (θ) design procedure was confirmed by performing nonlinear static and dynamic analyses using the SAP 2000 finite element software [15]. Pushover analyses were conducted both in two dimensions, on both orthogonal configurations, the more stress-loaded (a) and the less one (b), both by analysing the three-dimensional



Fig. 5. 3D-model of the 4-storeys MRf.

structure, not only to confirm the achievement of the design goal, i.e., the development of a damage pattern according to the global collapse mechanism, but also to evaluate the interaction between the differently stressed orthogonal frames and their contribution to the overall seismic behaviour of the structure (Fig. 5). The pushover analyses on the Train of frame and the 3D structure were performed under displacement control. For comparative purposes, the 3D pushover analyses were conducted in both directions for both configuration (a) and (b). The 3D analyses, in particular, were performed by assigning three-dimensional plastic hinges as PMM-type to the columns to capture the correct compression-bending stress state occurring in these elements, and by accounting for the nonlinearities of the beams with M-type plastic hinges, representative of a simple bending regime. A comparison of the mechanism's equilibrium curve with the pushover curve confirmed the accuracy of the TPMC (θ) design procedure, as evidenced by the overlap of the two curves, both in the pushover analysis conducted on the Train of frames and, in particular on the three-dimensional structure (Figs. 6, 7 and 8). The corresponding distribution of plastic hinges, not reported in this work for aim of brevity, also assures that undesired collapse mechanisms are avoided.

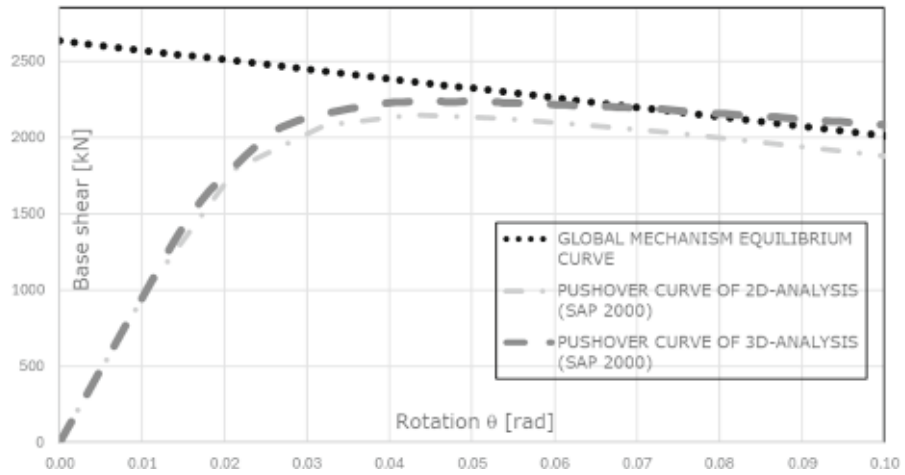


Fig. 6. Comparison between theoretical and pushover curve of 4-storeys MRF in configuration (a).

Although the pushover curves from the 2D and 3D analyses remain parallel to the mechanism's equilibrium curve, the 2D curve is lower. This is due to the different plastic redistribution in the 3D model, caused by the interaction between the orthogonal frames in configurations (a) and (b). In all cases, the resulting collapse mechanism remains of the global type. The 3-dimensional model already investigated with pushover analyses, had been tested with bi-component dynamic analyses, without going into detail of the structural behaviour of the model, but with the main purpose of validating the TPMC (θ) design procedure, i.e., demonstrating that all the analyzed schemes do not develop undesired collapse mechanisms. Directly integrated nonlinear time history analyses were performed with a damping value proportional to the Period of Vibration obtained from the

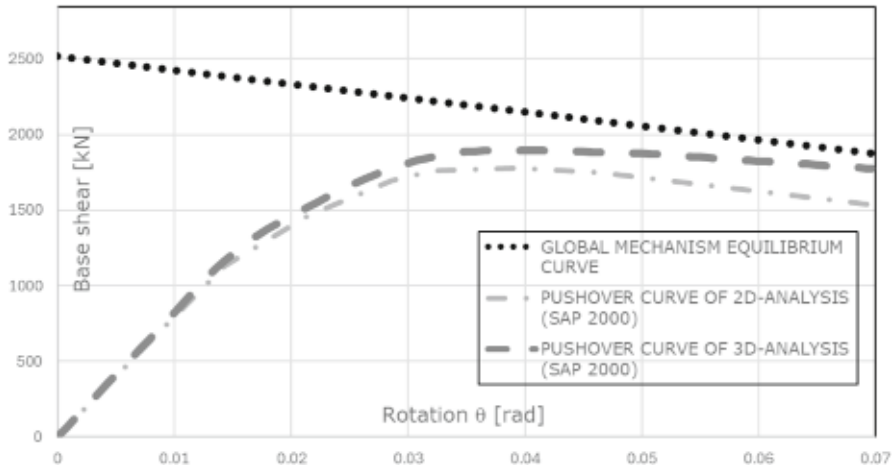


Fig. 7. Comparison between theoretical and pushover curve of 6-storeys MRF in configuration (a).

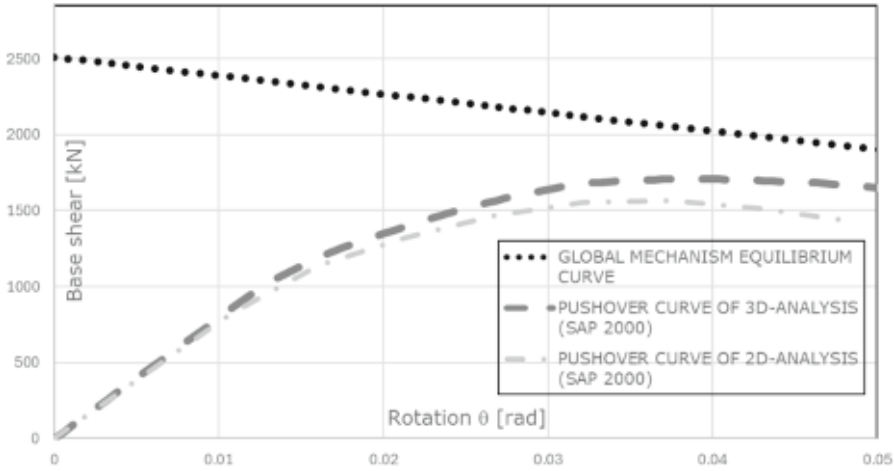


Fig. 8. Comparison between theoretical and pushover curve of 8-storeys MRF in configuration (a).

modal analysis of the 3-dimensional model of the structure. The 3-dimensional models of the 4, 6, and 8-storeys MRFs have been stressed by the two E-W and N-S components of 7 selected earthquakes, the results of which are here reported with reference to the most intense one, i.e. the Norcia-Castelluccio earthquake (Fig. 9) as examples of the all analyses, the main characteristics of which are given in Table 3.

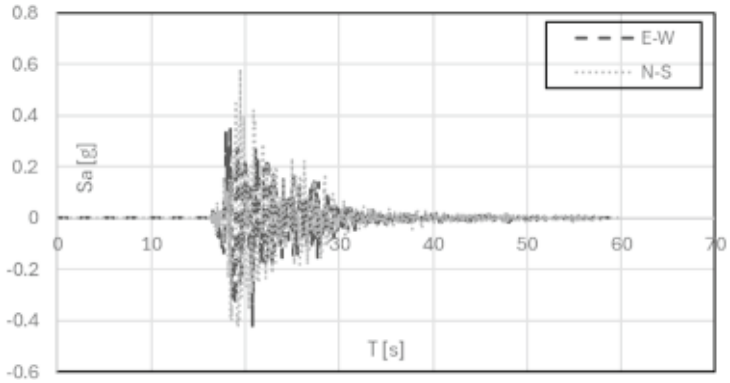


Fig. 9. Norcia-Castelluccio earthquake accelerogram.

Table 3. Norcia-Castelluccio earthquake characteristics.

Norcia-Castelluccio earthquake	
Magnitude W	6.5
Magnitude L	6.1
Site classification (EC-8)	A*
Duration (s)	60
PGA E-W (cm/s2)	−418,6
PGA N-S (cm/s2)	571,4

The bi-component dynamic analyses confirmed the results obtained from the non-linear static analysis. Analyzing the distribution of active plastic hinges at the end of the earthquake, for both dominant earthquakes applied in X and Y directions, it is observed that the structure does not develop undesired collapse mechanisms, confirming the achievement of the design objective of TPMC (θ). To illustrate, the mechanisms that develop in the 3-dimensional models of the analyzed schemes are reported (Figs. 10, 11 and 12), with reference to the most stressed frames.

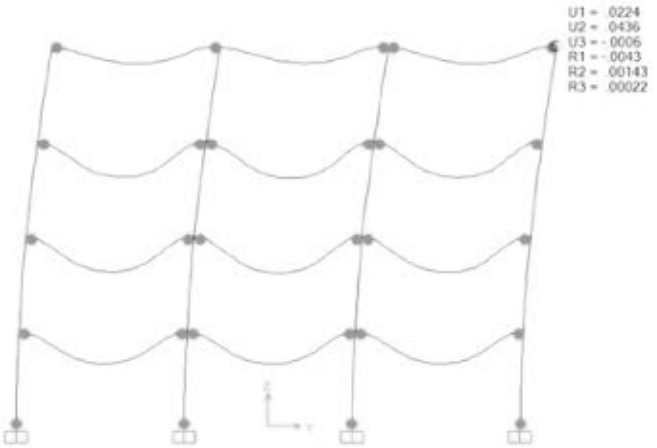


Fig. 10. Bicomponent dynamic analyses of 4-storeys MRF - Plastic hinges distribution for X-direction dominant earthquake at 60 s.

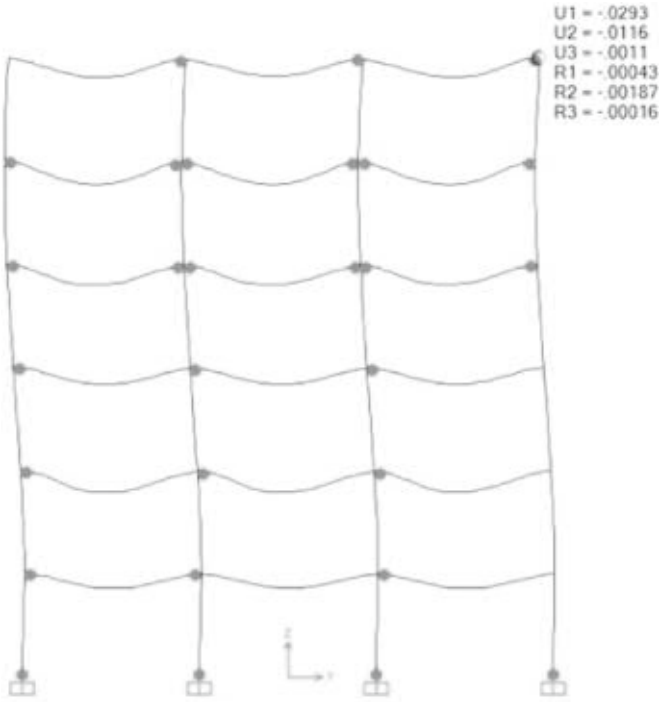


Fig. 11. Bicomponent dynamic analyses of 6-storeys MRF - Plastic hinges distribution for Y-direction dominant earthquake at 60 s.

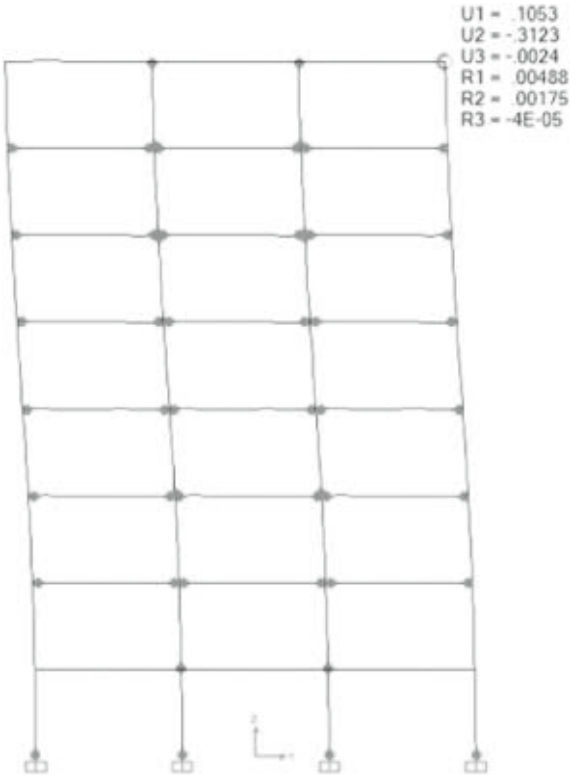


Fig. 12. Bicomponent dynamic analyses of 8-storeys MRF - Plastic hinges distribution for X-direction dominant earthquake at 60 s.

4 Conclusion

The aim of this study was to demonstrate the validity and accuracy of the TPMC (θ) procedure for the design of moment-resisting steel structures, showing its perfect applicability both in structural design where gravitational loads predominate and in cases involving seismic actions. From the design step, it was found that the orthogonal frames, subjected to different stresses, exhibited two distinct structural behaviors due to the effect of the slab. In relation to this, it was selected to subject the more stressed one to design procedure and limit the orthogonal frame to a check for strength and stability. The validation phase, through nonlinear analyses, particularly those conducted on the three-dimensional structure, not only demonstrated the structure's overall seismic behavior but also confirmed the achievement of the design goal, i.e., that for both load cases, the application of the TPMC (θ) prevents undesired collapse mechanisms.

References

1. Mazzolani FM, Piluso V (1997) Plastic design of seis-mic resistant steel frames. Earthq Eng Struct Dyn 26:167–191

2. Montuori R, Nastri E, Piluso V (2015) Advances in theory of plastic mechanism control: closed form solution for MR-Frames. Earthq. Eng. Struct. Dyn. 44(7), 1035–1054. https://doi.org/10.1002/eqe.2498
3. Castaldo P, Nastri E, Piluso V, Pisapia A (2017) Stochastic approach for theory of plastic mechanism control. In: Associazione Italiana di Meccanica Teorica e Applicata (AIMETA), pp 2408–2420
4. Montuori R, Nastri E, Piluso V, Pisapia A, Todisco P (2024) Application and validation of a simplified approach to evaluate the seismic performances of steel MR-frames. Appl Sci 14(3):art.no. 1037
5. Montuori R, Nastri E, Piluso V (2022) Theory of Plas-tic mechanism control: a new approach for the optimization of seismic resistant steel frames. Earthq Eng Struct Dyn 51(15):3598–3619
6. Montuori R, Nastri E, Piluso V, Pisapia A (2023) Design procedure for failure mode control of linked column frames. Eng Struct 296: art. no. 116937.
7. Montuori R, Nastri E, Piluso V (2016) Theory of plastic mechanism control for MRF–EBF dual systems: closed form solution. Eng Struct 118:287–306
8. Montuori, R, Gabbianelli G, Nastri E, Simoncelli M (2019) Rigid plastic analysis for the seismic performance evaluation of steel storage racks. Steel Compos. Struct. 32(1): 1–19. https://doi.org/10.12989/scs.2019.32.1.001
9. Montuori R, Nastri E, Piluso V, Pisapia A, Scafuri C (2024) Seismic design approach for steel K-shaped 1 eccentrically braced frames. Structures 70:107852. https://doi.org/10.1016/j.istruc.2024.107852
10. Maglio M, Montuori R, Nastri E, Piluso V (2023) Design and seismic evaluation of MRFs in DC2 ductility class introduced in the new prEN1998 draft and comparison with TPMC. Soil Dyn Earthq Eng 168:107833
11. Maglio M, Montuori R, Nastri E, Piluso V, Pisapia A (2024) Probabilistic design procedure for steel moment resisting frames equipped with FREEDAM connections. Struct Saf 109:102465
12. Maglio M, Montuori R, Nastri E, Piluso V (2024) Plastic design of moment resisting frames with low ductility. In: STESSA Proceedings, Lecture Notes in Civil Engineering
13. Maglio M, Montuori R, Nastri E, Piluso V (2022) Design, analysis and assessment of MRFs equipped with FREEDAM connections and designed by TPMC: comparison with traditional connections. In: STESSA Proceedings, Lecture Notes in Civil Engineering
14. EN 1998-1:2004- EUROCODE 8: Design of structures for earthquake resistance – PART 1: General rules, seismic actions and rules for buildings
15. CSI (2023) SAP 2000: integrated finite element analysis and design of structures. Analysis reference. Computer and Structure Inc., University of California, Berkeley

Robustness

Nonlinear Response of Steel Storage Racks Under Progressive Collapse Scenarios

Tahir Ahmad, Massimiliano Ferraioli(✉), Angelo Lavino, and Alberto Mandara

University of Campania "Luigi Vanvitelli", Aversa (CE), Italy
massimiliano.ferraioli@unicampania.it

Abstract. Steel storage racks, widely used in industrial and commercial facilities, are lightweight yet highly stressed structures composed of thin-walled cold-formed steel members. Their susceptibility to progressive collapse arises from semi-rigid connections, local instabilities, asymmetric bracing layouts, and limited ductility, which may trigger disproportionate failure under accidental actions such as impacts or abnormal loads. This study investigates the progressive collapse behavior of braced pallet racking systems through an integrated experimental–numerical approach. The results highlight the critical role of connection behavior and bracing configuration in governing collapse mechanisms. While systems with limited bracing exhibit more ductile responses and develop catenary action, highly braced configurations may experience brittle failure due to constrained deformation capacity. The comparison between static and dynamic analyses enabled the evaluation of dynamic amplification effects through the derivation of Dynamic Increase Factors. The findings emphasize the need for performance-based design approaches that explicitly account for connection ductility, axial–flexural interaction, and load redistribution mechanisms. This study provides new insights into the progressive collapse response of cold-formed steel rack systems and contributes to the development of resilience-oriented design strategies for enhancing their robustness under accidental loading conditions.

Keywords: Steel Storage Racks · Progressive Collapse · Axial–Flexural Interaction · Catenary Effects

1 Introduction

Industrial steel storage racks are specialized structures designed for high-density warehousing. Unlike standard buildings, they are constructed from cold-formed, thin-walled steel profiles. Under Eurocode 3, these are classified as Class 4 sections because they tend to experience local and distortional buckling before the material can fully yield. The overall behavior of the racking system depends heavily on perforated uprights, semi-rigid proprietary connections, and cross-aisle bracing that is frequently asymmetrical. While this engineering approach maximizes material efficiency, it also minimizes structural redundancy and the system's ability to dissipate energy. Consequently, these racks are

© The Author(s), under exclusive license to Springer Nature Switzerland AG 2026
R. Zanon et al. (Eds.): CTA 2026, LNCE 942, pp. 809–819, 2026.
https://doi.org/10.1007/978-3-032-39505-4_70

highly vulnerable to progressive collapse, meaning that localized damage from routine operational risks such as forklift collisions, seismic activity, or fire can easily trigger a catastrophic, full-scale structural failure [1, 2]. When a primary load bearing upright suddenly fails, it triggers a rapid "domino effect." The weight of the structure is instantly transferred to neighboring, intact columns, overloading them with severe axial forces and accelerating a total collapse of the system. To mitigate these vulnerabilities, extensive structural research over the past two decades has focused heavily on component-level performance. Specifically, studies have quantified how upright perforations alter and exacerbate local buckling behavior [3], while also demonstrating how beam-to-column joint capacities are strictly limited by connector tab deformation and ultimate disengagement [4]. On a global scale, numerical and pushover analyses emphasize that accurate frame simulations must explicitly account for semi-rigid joint flexibility, material and geometric nonlinearities, and structural imperfections [5–7]. Additionally, it has been reported that baseplate performance is highly sensitive to anchor eccentricity [8] and axial compression demands [9]. Meanwhile, braced cross-aisle joints exhibit severely pinched hysteretic loops, which drastically limits the system's overall energy dissipation capacity [10]. Specifically, conventional models overlook how semi-rigid beams transition into catenary action, how abrupt load reversals damage connector tabs, and how complex combined tension and bending forces interact during large structural shifts. Consequently, there is an urgent demand for studies that connect individual component mechanics to broader, system-wide behavior during sudden upright failures. Also, in the design codes, including RMI and EN 15512 [11, 12], the issue of the progressive collapse of these structures is not sufficiently considered. As a result, investigations are needed concerning how industrial racks handle progressive collapse [13]. This study addresses these research gaps by evaluating the progressive collapse performance of a typical industrial pallet rack framework. Utilizing an advanced numerical approach, the global structural model directly incorporates the nonlinear behaviors of the beam-to-upright, baseplate, and brace connections that were previously established and validated in prior research [13]. By simulating sudden column-removal scenarios through both nonlinear static (pushdown) and dynamic analyses, this paper quantifies the framework's internal force-redistribution capacity, effect of bracings and connections, and evaluates transient inertial effects through the derivation of Dynamic Increase Factors (DIF).

2 Methodology

2.1 Non-linear Rack Modelling Approach for Components

An integrated experimental–numerical investigation was carried out to characterize the nonlinear response of key rack components to provide a physically based foundation for system-level progressive collapse analysis. The behavior of beam-to-column connections was first examined through a high-fidelity numerical framework validated against experimental observations. A series of cantilever tests on representative specimens (namely Exp S1, Exp S2 and Exp S3) subjected to displacement-controlled loading was conducted to determine the moment–rotation (M–θ) characteristics, as shown in Fig. 1a, and identify failure mechanisms at the beam to upright connection. These tests were subsequently reproduced in ABAQUS [14] using detailed finite element models discretized

with C3D8R solid elements and a refined mesh size of 5 mm to accurately capture local stress concentrations and deformation patterns. A Dynamic Explicit solver was employed to efficiently handle material degradation and complex contact nonlinearities. Following validation (Fig. 1a), the numerical model was used to generate an extended database of M–θ responses under different axial tension loadings. In accordance with EN 15512 [12], the resulting curves were idealized into bilinear representations using the equal-energy approach. To capture the demands associated with progressive collapse, interaction domains were developed to describe the coupled relationship between axial force and bending moment.

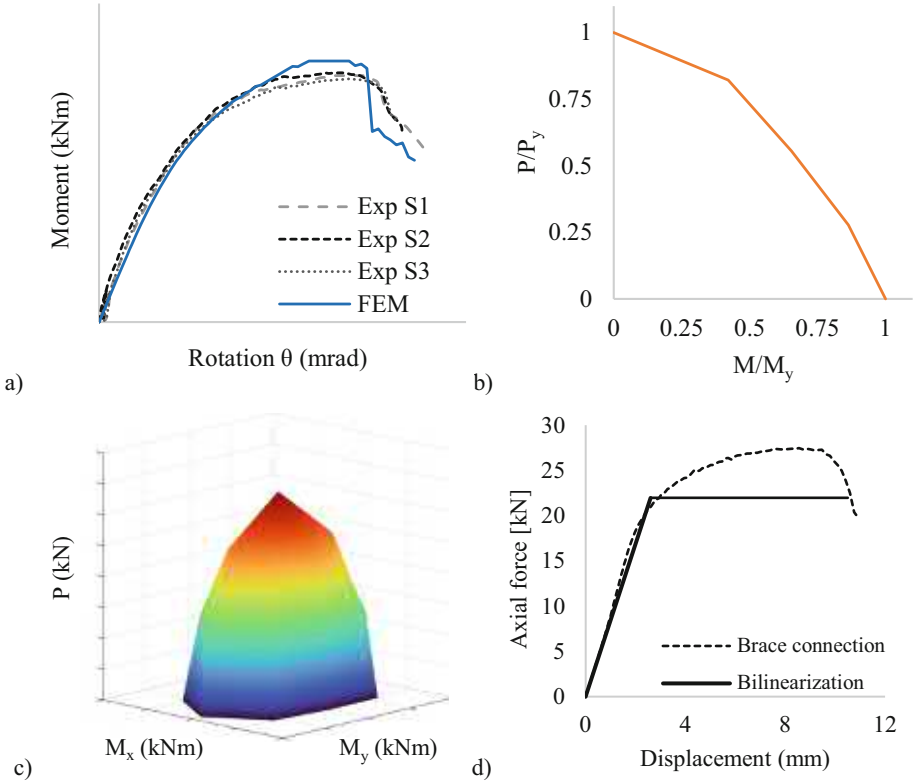


Fig. 1. a) M–θ curves of beam to upright connection; b) PM interaction of beam to upright connection; c) PMM interaction surface of base-plate connection; d) F-D curve of brace connection.

The M–θ characteristics of the beam to upright connection and the corresponding PM interaction relationship is presented in Fig. 1a and b. The base-plate connection was modeled considering the combined effects of axial compression (P) and biaxial bending (M_x,M_y). The models incorporated bolt behavior as well as local buckling phenomena in perforated uprights. A comprehensive PM_xM_y interaction surface was established by applying a sequence of compressive axial loads and biaxial displacements, from

which M–θ curves corresponding to different axial force levels were obtained. The resulting PMM interaction surface is shown in Fig. 1c. In addition, the brace-to-upright connection was investigated to evaluate the performance of the bracing system. The analysis revealed that failure occurs through localized bearing or tearing around the bolt holes before the brace reaches its buckling capacity. This indicates that the load-carrying capacity of the bracing system is governed by the connection strength, confirming its non-dissipative nature. The capacity curve and bilinear idealized curve of the brace connection is presented in Fig. 1d. Further details regarding the component-level modeling can be found in [13].

2.2 Global Modelling Approach for Progressive Collapse

Steel Rack Description

A full-scale steel storage rack representative of a real warehouse system was selected as the case study. The details of the case study are given in Table 1 and shown in Fig. 2. A global finite element model of the storage rack was developed in SAP2000 [15], into which the nonlinear moment–rotation relationships and axial–moment interaction characteristics obtained from the component-level analyses were incorporated as user-defined hinges. Accurate representation of the nonlinear behavior of the various structural components was essential to ensure the reliability of global analysis. Specifically, beam-to-upright connections were assigned axial-moment (PM) hinges and base plates were defined with coupled axial-moment (PM_xM_y) hinges. Brace connections were represented by axial plastic hinges located along the brace joints. Since the axial strength of the braces exceeded the strength of the brace connections, only the connection hinges were considered in the brace model.

Table 1. Case study details

Parameter	Details
Number of stories	5
Story height	2.29 m
Bays in Y-direction	2 bays (span = 1.0 m)
Bays in X-direction	19 bays (span = 2.82 m)
Steel grade	S350
Yield strength (fy)	350 MPa
Ultimate strength (fu)	420 MPa
Dead load	1.0 kN/m
Live load	5.28 kN/m

Progressive Collapse and Dynamic Increase Factor Evaluation

Progressive collapse performance was assessed by considering three distinct column-loss scenarios: Scenario 1, involving the removal of a corner; Scenario 2, internal column

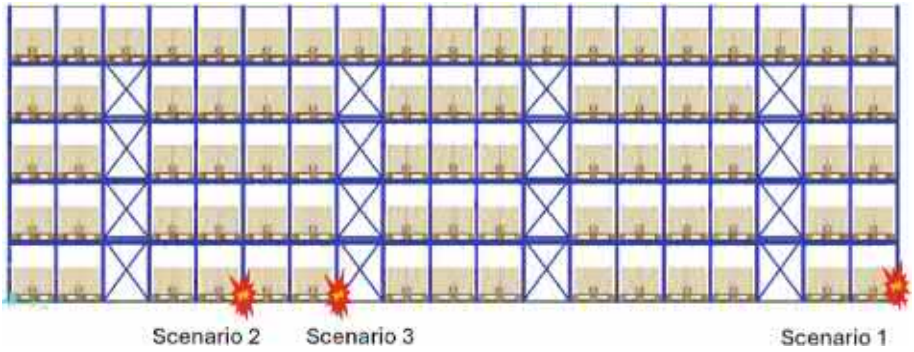


Fig. 2. Model of the Steel Storage Rack.

involving a column removal in an unbraced bay; Scenario 3, where the removed column was located within a bay reinforced with additional transverse bracing as shown in Fig. 2. For the nonlinear static pushdown analysis, a displacement-controlled strategy was adopted to evaluate the global structural response as a function of increasing vertical deformation. In accordance with the General Services Administration [16] and Unified Facilities Criteria [17] guidelines, the gravity loading for bays unaffected by the column removal was defined according to Eq. (1), while the loading for bays directly impacted by the localized failure was defined according to Eq. (2).

$$P_{unaffected} = LF \times (1.2DL + 0.5LL) \tag{1}$$

$$P_{affected} = DIF \times LF \times (1.2DL + 0.5LL) \tag{2}$$

Here, DL and LL represent the nominal dead and live loads, respectively. LF is the Load Factor, and DIF denotes the dynamic amplification factor. Numerous empirical expressions for the DIF have been proposed in the literature [18–25]; however, their predictive capability is often inconsistent across different structural systems and loading configurations. While earlier provisions recommend adopting a conservative value of $DIF = 2.0$, this study explicitly incorporates both P-Delta and geometric nonlinear (large-displacement) effects to realistically capture the large-displacement behavior and catenary stiffening mechanisms essential for accurate collapse resistance evaluation. Furthermore, a three-stage nonlinear dynamic (ND) analysis procedure was employed to account for transient inertial effects. In stage 1, the intact structure was initially stabilized under standard gravity loading. In stage 2, the target column was substituted with equivalent internal reaction forces while the amplified gravity loads were gradually applied over 5 s and maintained for 25 s to ensure complete numerical stabilization given the inherent flexibility of the racking system. In the final stage, the equivalent reaction forces were abruptly removed to simulate sudden column loss, thereby capturing the inertia-driven force redistribution. Finally, the specific DIF was also determined using an energy-based, two-step pushover procedure [26] as shown in the Fig. 3. First, the unamplified gravity loads, defined by Eq. (1), were applied to the intact structure (Push

1) before removing the target column, thereby generating the initial load–displacement branch. Second, the incremental amplified load, corresponding to (DIF − 1)× Eq. (1), was applied exclusively to the spans directly affected by the column loss (Push 2). Thereby obtaining the total gravity loads defined by Eq. (2). By superimposing these two loading phases, the total load equals the standard progressive collapse combination characterized by amplified loads in the affected bays and unamplified loads elsewhere. The final *DIF* was established at the intersection of the static pushdown curve and the Incremental Dynamic Analysis (IDA) response envelope, representing the exact amplification factor required for the static analysis to replicate the peak transient dynamic displacement.

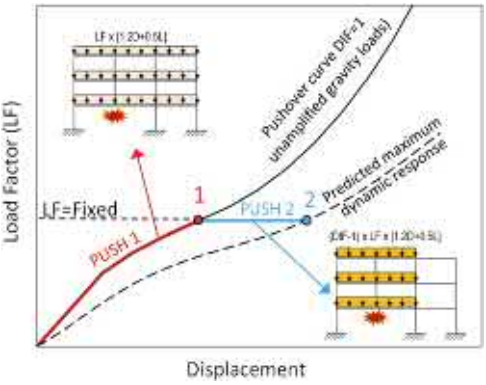


Fig. 3. Dynamic increase factor evaluation method [26].

3 Results and Discussions

The nonlinear static pushdown and dynamic time-history analyses reveal distinct behavioral patterns that are fundamentally governed by the location of the removed column and the localized stiffness of the frame. In Scenario 1, involving the removal of a corner column, the structure exhibits its lowest load-bearing capacity, with initial beam connection yielding occurring early at a Load Factor (*LF*) of 0.4. The perimeter location severely limits the availability of alternative load paths, forcing the system to reach its peak capacity at a modest *LF* of approximately 1.0 before experiencing total beam connection failure at a lateral displacement of 32 mm as shown in Fig. 4a. This vulnerability is mirrored in the corresponding dynamic response, which records the largest transient peak displacement of 65 mm and a prolonged period of oscillation before settling at a residual displacement of 55 mm as shown in Fig. 4b. The lack of geometric continuity at the corner ensures that the system is heavily reliant on large, unconstrained deformations to stabilize the gravity loads. When the column loss occurs in an internal unbraced bay (Scenario 2), the structural configuration permits more effective load redistribution, significantly enhancing the ultimate capacity to an *LF* exceeding 2.0 as shown in Fig. 4c. Although initial beam-to-upright joint yielding initiates at the same low threshold ($LF \approx 0.4$), the surrounding intact framework provides superior redundancy.

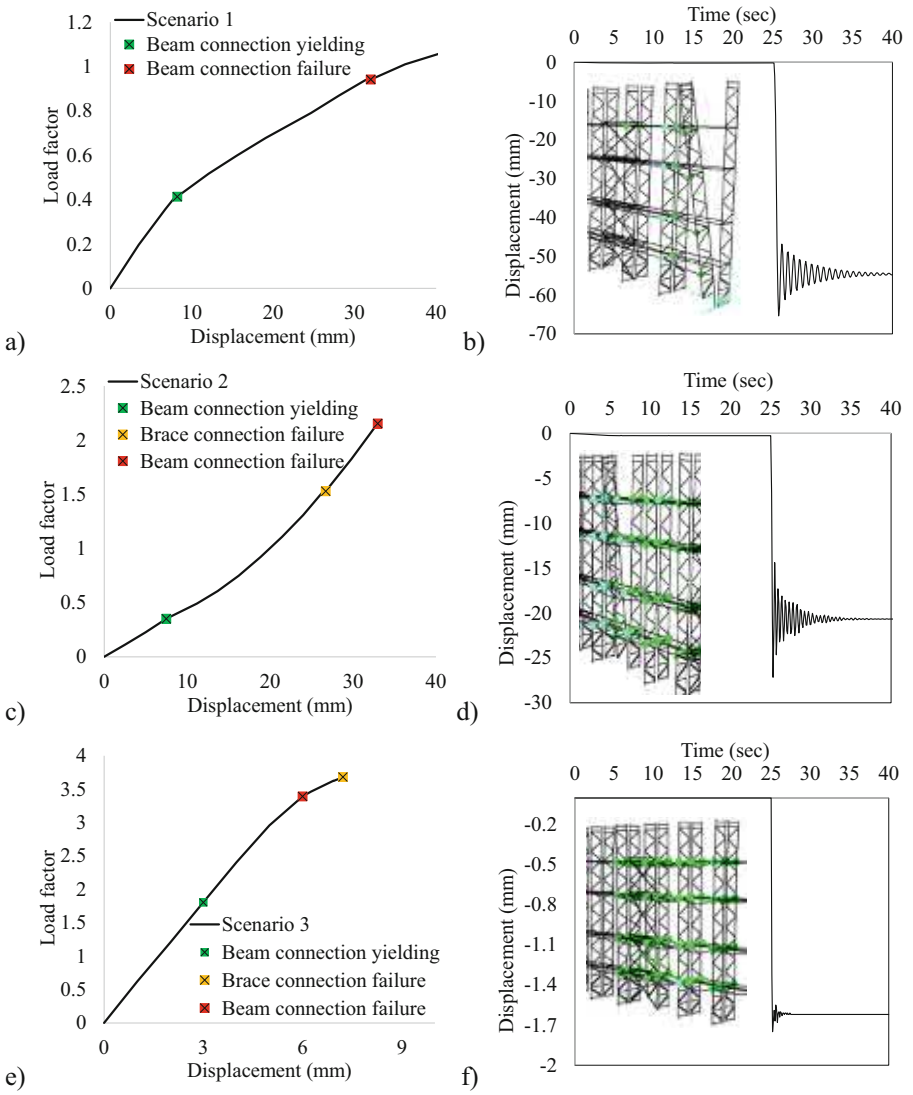


Fig. 4. Pushdown curve: a) Scenario 1; c) Scenario 2; e) Scenario 3 and Dynamic response: b) Scenario 1; d) Scenario 2; f) Scenario 3.

However, the progression of damage is critical; the brace connections reach their capacity and fail at an *LF* of approximately 1.5, which accelerates the force concentrations on the surrounding joints until final beam connection failure occurs at $LF \approx 2.2$. Dynamically, this internal unbraced scenario results in a well-controlled peak displacement of 27 mm and rapid stabilization near 21 mm as shown in Fig. 4d. The extensive formation of plastic hinges across multiple levels demonstrates a high capacity for energy dissipation despite the flexible nature of the unbraced bay.

In contrast, Scenario 3 represents the stiffest and structurally strongest configuration, where the column is removed from a bay reinforced with additional transverse bracing. Here, the high initial stiffness successfully delays the onset of beam connection yielding until a much higher load level ($LF \approx 1.8$), ultimately driving the static capacity to an *LF* of nearly 3.7 as shown in Fig. 4e. Dynamically, this massive elastic resistance results in negligible inertial effects, restricting the peak dynamic displacement to less than 2 mm as shown in Fig. 4f. However, the static pushdown curve exposes a highly brittle global mechanism: the margin between the first connection failure and total structural compromise is exceptionally narrow, with brace and beam connection failures occurring almost simultaneously at minimal displacements below 9 mm. The high stiffness due to additional bracings in Scenario 3 restricts the deformation capacity needed to mobilize catenary action, leading to localized force concentrations.

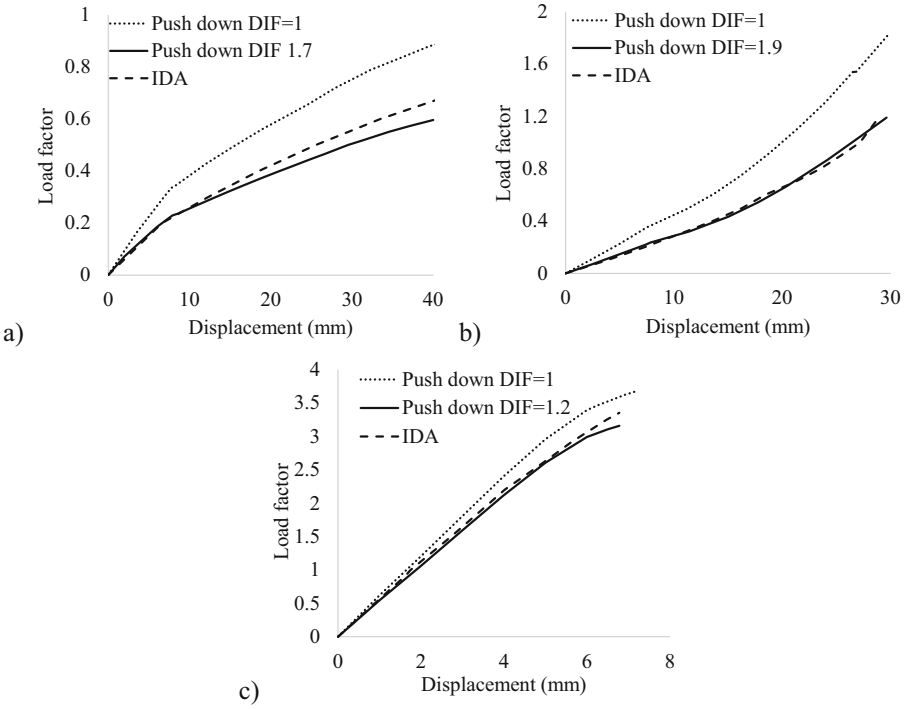


Fig. 5. Dynamic increase factor: a) Scenario 1; b) Scenario 2; c) Scenario 3.

This complex trade-off between strength and ductility is further illuminated by the Dynamic Increase Factors (*DIF*) derived at the intersection of the amplified pushdown curves and the Incremental Dynamic Analysis (IDA) envelopes. Scenario 1 (Fig. 5a) demands a substantial *DIF* of 1.7, which highlights the vulnerability of the corner column loss, where the lack of structural continuity leads to large dynamic response. while Scenario 2 (Fig. 5b) requires the highest amplification with a *DIF* of 1.9, approaching the theoretical maximum of 2.0.

Because the transition from an unbraced intact state to a damaged state involves a major release of kinetic energy, a large static load multiplier is mandatory to accurately replicate the dynamic peak. Conversely, the highly rigid braced system in Scenario 3 (Fig. 5c) limits dynamic amplification to a minor *DIF* of 1.2. These findings indicate that while standard design codes often recommend a uniform *DIF* of 2.0, such an assumption is overly conservative for heavily braced configurations but highly accurate for internal unbraced bays. Ultimately, the results underscore that while additional bracing in such scenario significantly improves static capacity, it can unexpectedly compromise progressive collapse robustness by generating highly localized stress concentrations and brittle failure sequences.

4 Conclusions

This study investigated the progressive collapse behavior of steel storage racks through nonlinear static and dynamic analyses considering different column-removal scenarios. The results showed that the collapse resistance of rack systems is strongly influenced by both the location of the removed column and the local stiffness provided by the bracing layout.

Among the investigated cases, corner column removal was identified as the most critical scenario due to the lack of structural continuity and limited alternative load paths, resulting in the largest dynamic displacement demands and the lowest collapse resistance. In contrast, the removal of an internal column within an unbraced bay exhibited the most favorable redistribution mechanism, characterized by extensive plastic hinge development, enhanced energy dissipation, and effective activation of alternative load paths.

The analyses also highlighted a significant trade-off between strength and robustness. Although additional bracing substantially increased the static load-carrying capacity and delayed connection yielding, it reduced deformation capacity and inhibited the development of catenary action, leading to localized force concentrations and a more brittle failure mechanism.

The derived Dynamic Increase Factors ranged from 1.2 to 1.9 depending on the structural configuration. These results indicate that the commonly adopted value of DIF = 2.0 provides a reasonable estimate for flexible unbraced configurations but may be overly conservative for highly braced rack systems.

Overall, the findings demonstrate that the progressive collapse resistance of cold-formed steel storage racks cannot be assessed solely on the basis of strength. Robustness depends on the combined effects of redundancy, connection ductility, deformation capacity, and load redistribution mechanisms. Consequently, performance-based design approaches that explicitly account for these factors are required to improve the resilience of rack structures against accidental column-loss events.

References

1. McConnel R, Kelly S (1983) Structural aspects of the progressive collapse of warehouse racking. Struct Eng 61:343–347

2. Montuori R, Gabbianelli G, Nastri E, Simoncelli M (2022) Rigid plastic analysis for the seismic performance evaluation of steel storage racks. Steel Compos Struct 42:1–19
3. Baldassino N, Bernuzzi C, di Gioia A, Simoncelli M (2019) An experimental investigation on solid and perforated steel storage racks uprights. J Constr Steel Res 155:409–425
4. Shah S, Sulong NR, Khan R, Jumaat M, Shariati M (2016) Behavior of industrial steel rack connections. Mech Syst Signal Process 70:725–740
5. Rasmussen K, Gilbert BP (2013) Analysis-based design provisions for steel storage racks. J Struct Eng 139(5):849–859
6. Sangle KK, Bajoria KM, Talicotti RS (2012) Elastic stability analysis of cold-formed pallet rack structures with semi-rigid connections. J Constr Steel Res 71:245–262
7. Ungureanu V, Dubina D (2013) Sensitivity to imperfections of perforated pallet rack sections. Mech Mech Eng 17(2):207–220
8. Huang Z, Wang Y, Zhao X, Sivakumaran KS (2021) Determination of the flexural behavior of steel storage rack baseplate upright connections with eccentric anchor bolts. Thin-Walled Struct 160:107375
9. Castiglioni CA (2016) Seismic behavior of steel storage pallet racking systems. Springer, Heidelberg
10. Gusella F, Orlando M, Peterman K (2022) Stiffness and resistance of brace-to-upright joints with lipped channel braces assembled flange-to-flange. J Constr Steel Res 193:107258
11. Rack Manufacturers Institute (RMI) (2008) Specification for the design, testing and utilization of industrial steel storage racks. RMI, Charlotte
12. CEN (2020) EN 15512: steel static storage systems - adjustable pallet racking systems - principles for structural design. European Committee for Standardization, Brussels
13. Ahmad T et al (2026) Performance assessment of steel storage racks under progressive collapse scenarios. Procedia Struct Integrity 78:631–638
14. Dassault Systèmes Simulia Corp (2024) SIMULIA Abaqus FEA (Version 2025). Dassault Systèmes Simulia Corp, Providence
15. Computers and Structures Inc (2025) SAP2000: Linear and Nonlinear Static and Dynamic Analysis of Three-Dimensional Structures, Research Ultimate Version 26.2.0, Analysis Ref. Manual. Computers and Structures Inc, Berkeley.
16. General Services Administration (GSA) (2016) Alternate path analysis & design guidelines for progressive collapse resistance. GSA, Washington DC
17. United States Department of Defense (DoD) (2024) Unified facilities criteria: design of buildings to resist progressive collapse. UFC 4-023-03, DoD, Washington DC
18. Ferraioli M (2016) Dynamic increase factor for pushdown analysis of seismically designed steel moment-resisting frames. Int J Steel Struct 16(3):857–875
19. Ferraioli M (2019) Evaluation of dynamic increase factor in progressive collapse analysis of steel frame structures considering catenary action. Steel Compos Struct 30(3):253–269
20. Ferraioli M (2019) A modal pushdown procedure for progressive collapse analysis of steel frame structures. J Constr Steel Res 156:227–241
21. Ferraioli M (2019) Dynamic increase factor for nonlinear static analysis of RC frame buildings against progressive collapse. Int J Civ Eng 17(3):281–303
22. Ferraioli M, Lavino A, Mandara A (2018) Assessment of dynamic increase factors for progressive collapse analysis of steel frames subjected to column failure. Ing Sismica 35(2):67–77
23. Mashhadi J, Saffari H (2017) Effects of postelastic stiffness ratio on dynamic increase factor in progressive collapse. J Perform Constr Facil 31(6):04017107
24. McKay A, Marchand K, Diaz M (2012) Alternate path method in progressive collapse analysis: variation of dynamic and nonlinear load increase factors. Pract Period Struct Des Constr 17(4):152–160

25. Tsai MH, Lin BH (2009) Dynamic amplification factor for progressive collapse resistance analysis of an RC building. Struct Design Tall Spec Build 18(5):539–557
26. Ferraioli M, Laurenza B, Lavino A, De Matteis G (2024) Progressive collapse analysis and retrofit of a steel-RC building considering catenary effect. J Constr Steel Res 213:108364

A Hybrid SDOF Model for Thin Steel Plates Under Dust-Explosion Loading: Dynamic Response and Preliminary Collapse Assessment

Francesco Pinna[1](✉), Marco Zucca[1], Marco Simoncelli[2], and Flavio Stochino[1]

[1] Department of Civil and Environmental Engineering and Architecture, University of Cagliari, Via Marengo 2, 09123 Cagliari, Italy
francesco.pinna4@unica.it

[2] Department of Architecture, Built Environment and Construction Engineering, Politecnico di Milano, Via G. Ponzio 31, 20133 Milan, Italy

Abstract. Dust explosions represent a major hazard in industrial environments where combustible powders are generated, handled, transported, or stored. In partially or fully confined equipment, the rapid pressure rise associated with dust deflagrations may impose severe impulsive loads on thin-walled steel components such as panels, walls, covers, and closure elements. Under these conditions, the structural response may evolve from bending-dominated behavior to a strongly nonlinear regime in which membrane effects become significant and classical linear formulations are no longer adequate. This paper proposes a hybrid single-degree-of-freedom (SDOF) model for the rapid prediction of the dynamic response of thin steel plates subjected to pressure-time histories representative of dust-explosion scenarios. The proposed formulation combines an elastic branch enhanced by a membrane-stiffness contribution with a subsequent global elastic-plastic branch, enabling efficient simulation of displacement-time histories with limited computational effort. In addition, a preliminary collapse-oriented classification is introduced to identify response regimes compatible with large plastic deformation, tensile tearing and shear-sensitive behavior. The model is conceived as a fast-engineering tool for preliminary assessment, parametric studies and early-stage design. The proposed approach provides a physically informed link between dust-explosion load definition, nonlinear plate response and simplified collapse interpretation.

Keywords: Dust Explosions · Thin Steel Plates · Impulsive Loading · SDOF Model · Membrane Effects · Collapse Classification

1 Introduction

Dust explosions remain a major industrial hazard wherever combustible powders are generated, handled, transported, filtered, or stored [1]. When fine particles are dispersed in air and encounter a suitable ignition source within partially or fully confined equipment, the resulting deflagration may generate rapid pressure growth, severe impulsive

© The Author(s), under exclusive license to Springer Nature Switzerland AG 2026
R. Zanon et al. (Eds.): CTA 2026, LNCE 942, pp. 820–831, 2026.
https://doi.org/10.1007/978-3-032-39505-4_71

loading, and potentially catastrophic structural consequences. In industrial practice, these effects are especially relevant for thin-walled steel components such as panels, covers, walls, and closure elements, whose structural response may govern the integrity of the equipment during an explosion event [2].

This issue is particularly important because modern dust-handling equipment is often characterized by thin steel enclosures, internal obstacles, local congestion, and vented configurations, all of which can significantly influence the pressure-time evolution and, consequently, the structural demand [3]. Recent collector-focused studies have shown that internal congestion, filter arrangement, turbulence amplification, and venting configuration may strongly modify both reduced pressure and pressure-pulse duration, indicating that structural loading cannot be inferred reliably from oversimplified assumptions alone. Accident surveys and equipment-specific reviews further confirm that dust collectors and similar dust-processing units are among the most recurrent sources of dust explosions in practice [1–3].

From the structural point of view, the dynamic behavior of thin plates under impulsive loading has long been recognized as a nonlinear problem [4]. Early formulations were mainly bending-dominated, whereas later developments showed that membrane effects become increasingly important as the deflection grows, particularly for thin plates under short-duration severe loading. Reviews of impulsively loaded plates have also shown that the response may evolve through different damage or collapse families, commonly associated with large plastic deformation, tensile tearing, and shear-dominated failure [5–7]. These observations are highly relevant in the present context, since the structural problem associated with dust explosions is not limited to estimating a maximum displacement, but also concerns the interpretation of the response regime reached by the plate.

1.1 Dust-Explosion Loading and Structural Behavior

Although combustion, vent sizing, reduced pressure prediction, and protection strategies for dust explosions have been widely investigated, a rapid structural tool specifically conceived for thin steel elements subjected to dust-explosion-induced impulsive loading is still lacking. In current practice, engineers can either rely on advanced CFD analyses and high-fidelity finite-element simulations, which are often too demanding for preliminary design and broad parametric studies, or on simplified linear approaches, which do not explicitly account for membrane stiffening, post-yield evolution, and the progressive transition from global deformation to more severe collapse-sensitive regimes [8]. As a result, there is still no reduced-order structural model that is both fast enough for engineering use and sufficiently rich in physical content to support the preliminary assessment of thin-walled steel components under dust-explosion loading.

The present work addresses this need through a hybrid single-degree-of-freedom formulation for thin steel plates subjected to pressure-time histories representative of dust-explosion scenarios. The proposed model combines a membrane-enhanced elastic branch with a subsequent global elastic-plastic branch [9], allowing rapid simulation of displacement-time histories with limited computational effort. In addition, a preliminary collapse-oriented interpretation is introduced to distinguish between response regimes compatible with large plastic deformation, tensile tearing, and shear-sensitive

behavior. The proposed approach is conceived as a fast-engineering tool for preliminary structural assessment and screening, providing a physically informed bridge between dust-explosion loading, nonlinear plate response, and simplified collapse interpretation.

After this introduction, Sect. 2 presents the proposed hybrid SDOF model and its main assumptions. Section 3 discusses the model response and its interpretation in terms of nonlinear structural behavior and collapse-sensitive regimes under dust-explosion loading. Finally, the main conclusions of the study are drawn in Sect. 4.

2 Model Formulation

The proposed structural formulation is based on a hybrid single-degree-of-freedom (SDOF) idealization aimed at providing a rapid yet physically informed prediction of the response of thin steel plates subjected to dust-explosion-induced impulsive loading. The plate is represented through a single generalized displacement w(t), identified with the transverse deflection at the plate center, while the distributed pressure acting on the panel is transformed into an equivalent generalized force. The formulation is hybrid because it combines two distinct stages of structural response. In the first stage, the plate response is described by an elastic branch in which both bending stiffness and membrane-induced geometric hardening are explicitly included. In the second stage, once a first-yield threshold is exceeded, the response is described through a global elastic-plastic branch with reduced tangent stiffness. The model is further complemented by a collapse-oriented interpretation intended to distinguish between response regimes compatible with large plastic deformation, tensile tearing, and shear-sensitive behavior.

This strategy was adopted to fill the gap between detailed numerical approaches and overly simplified linear checks. On the one hand, nonlinear plate response under impulsive loading is known to depend strongly on membrane action, especially for thin plates undergoing large deflections [8]. On the other hand, preliminary structural assessment in engineering practice requires a compact model that can be used rapidly for parametric studies and early-stage screening. The present formulation therefore connects dust-explosion loading, nonlinear plate response, and simplified collapse interpretation within a unified reduced-order framework.

2.1 Equivalent Pressure-Time History for Dust-Explosion Loading

A key feature of the model is the definition of an equivalent pressure-time history representative of dust-explosion loading. In the present work, the pressure pulse is not idealized through purely triangular law or through a classical external-blast Friedlander decay. Instead, a two-stage pulse is adopted to satisfy four requirements that are essential for preliminary structural assessment: the pressure must start from zero, reach a prescribed peak value P_0 [2], vanish at the end of the positive phase t_d, and preserve a controllable total impulse.

The equivalent pulse is therefore defined as the combination of a nonlinear rising branch and a linear descending branch. The rising branch is described by a reversed-Friedlander-type law,

$$p_{eq}(t) = P_0\left(\frac{t}{t_r}\right)^n \exp\left[-\beta\left(1-\frac{t}{t_r}\right)\right], \quad 0 \le t \le t_r \tag{1}$$

where t_r is the time peak, n is a shape exponent, and β is a curvature parameter. This expression was selected because it allows a smooth and monotonic increase from zero to the prescribed peak pressure, while avoiding the unrealistic abrupt rise associated with idealised instantaneous pulses. In the present context, the purpose of this law is not to reproduce a free-field blast wave, but to provide a compact nonlinear representation of the progressive pressure build-up that may develop in dust-explosion scenarios inside confined or partially vented equipment.

The parameter β is not assigned arbitrarily but is obtained by imposing the value of the pressure at mid-rise: $p_{eq}(0.5t_r) = f_{mid}P_0$. where f_{mid} is a prescribed nondimensional parameter controlling the curvature of the rising branch. In this way, the shape of the pulse is calibrated through a transparent condition, and the rise phase can be made sharper or more gradual depending on the desired engineering representation.

The descending branch is defined over the final interval T_{fall} through a linear decay law:

$$p_{eq}(t) = P_0\left(1 - \frac{t - t_r}{T_{fall}}\right), \quad t_r < t \leq t_d \tag{2}$$

with $t_d = t_r + T_{fall}$. This choice was made deliberately. Once the peak has been reached, the main requirement for the descending phase is to preserve the total positive duration and to provide a stable and easily interpretable contribution to the impulse. A linear tail meets this requirement without introducing unnecessary additional parameters. The adopted pulse thus combines a nonlinear and physically meaningful rise with a simple and robust unloading phase, making it suitable for reduced-order structural assessment.

The corresponding equivalent generalized force is written as:

$$F(t) = \alpha_p A p_{eq}(t) \tag{3}$$

where $A = ab$ is the plate area and α_p is the load transformation factor used to convert the uniformly distributed pressure acting on the plate into the corresponding generalized force of the SDOF system. In the present formulation, α_p is branch-dependent because different equivalent deformation assumptions are adopted in the membrane-enhanced elastic branch and in the global elastic-plastic branch. For the membrane-enhanced elastic branch, the load transformation factor is obtained from the same normalized displacement shape used in the nonlinear elastic thin-plate formulation. For the fully clamped square plate with immovable in-plane edges considered in the present implementation, this gives $\alpha_{p,\,e} = 1/4$. For the global elastic-plastic branch, the load transformation factor is taken from the tabulated SDOF transformation coefficients for clamped rectangular plates reported by Biggs [4]. It is denoted here as K_{L2} and depends on the aspect ratio $\lambda = a/b$. Accordingly, $\alpha_{p,\,pl} = K_{L2}(\lambda)$. In the reference square-plate case adopted in this study, $\lambda = 1.0$ and therefore $\alpha_{p,\,pl} = K_{L2} = 0.460$. Thus, the generalized force is computed as $F_e(t) = \alpha_{p,\,e} A p_{eq}(t)$ in the elastic branch and as $F_{pl}(t) = \alpha_{p,\,pl} A p_{eq}(t)$ in the global elastic-plastic branch. This clarification ensures consistency between the generalized load, the equivalent mass, and the restoring-force representation adopted in each response branch and improves the reproducibility of the proposed model. This form allows the pressure-time history to be coupled directly with the SDOF equation of motion while preserving a clear mechanical interpretation of the loading input. The

importance of pulse shape in impulsive structural response has long been recognized in the literature, and this is one of the reasons why the present model does not rely on purely impulsive idealization with instantaneous load application.

2.2 Elastic Branch with Membrane Hardening

In the elastic range, the plate response is described through a Duffing-type nonlinear SDOF equation [8]:

$$m_e\ddot{w}(t) + k_b w(t) + k_m w^3(t) = F_e(t) \tag{4}$$

where m_e is the equivalent mass, k_b is the linear bending stiffness, k_m is the cubic membrane stiffness, and $F_e(t)$ is the equivalent generalized force in the elastic branch. The cubic term represents membrane-induced hardening and is the essential feature distinguishing the present formulation from conventional bending-only reduced-order models.

For the present implementation, the elastic branch is specialized in the case of a square plate with fully clamped flexural boundary conditions and immovable in-plane edges. This choice follows the nonlinear SDOF formulation proposed for thin rectangular elastic plates undergoing large deflections, in which membrane action appears explicitly as a separate nonlinear term rather than being embedded indirectly into an equivalent linear stiffness. The equivalent elastic coefficients are written as: $m_e = \frac{9}{64}\rho abh$, $k_b = m_e K_1$, $m_e K_3$ where K_1 and K_3 are the normalized coefficients of the nonlinear elastic plate model, while the plate flexural rigidity is: $D = \frac{Eh^3}{12(1-\nu^2)}$. Because $k_m > 0$, the elastic branch exhibits hardening behaviour. Physically, this means that as the transverse displacement increases, the in-plane restraint progressively contributes to the restoring action, and the apparent stiffness becomes larger than that predicted by a bending-only model. This effect is especially important for thin plates, for which large amplitudes may develop before local failure takes place.

2.3 Transition to the Elastic-Plastic Branch

The transition from the elastic membrane-enhanced regime to the global elastic-plastic regime is governed by a first-yield resistance R_y, obtained from a strain-rate-sensitive stress level and transformed into an equivalent generalised force. Because the elastic branch contains the cubic membrane term, the corresponding first-yield displacement is not obtained through a linear ratio R_y/k. Instead, the threshold displacement w_y is obtained from the positive real solution of:

$$k_b w_y + k_m w_y^3 = R_y \tag{5}$$

Once this threshold is exceeded, the model switches to a global elastic-plastic branch with reduced tangent stiffness k_{pl}. Consistently with the branch-dependent SDOF transformation factors defined in Sect. 2.1, the generalized load in the post-yield branch is evaluated using $\alpha_{p,\,pl} = K_{L2}(\lambda)$, where K_{L2} is the load transformation coefficient associated with the equivalent plastic deformation mechanism of the clamped plate. The

post-yield restoring force is described through a bilinear law with offset, so that the plastic branch starts from the yield resistance and evolves with a smaller slope up to a limiting plastic displacement. In this way, the model preserves continuity between the end of the elastic stage and the beginning of the post-yield response, while maintaining the simplicity of a reduced-order formulation. It is important to note that this branch is not intended to reproduce a detailed local plastic mechanism. Rather, it provides a compact engineering representation of the global deformation response after yielding. The purpose is to maintain an interpretable and computationally efficient description of the structural response, suitable for rapid preliminary analyses. For clarity, a schematic representation of the main ingredients of the proposed formulation is shown in Fig. 1. The figure summarizes both the equivalent pressure-time history adopted for dust-explosion loading, with a nonlinear rising branch followed by a linear descending branch, and the idealized resistance function of the hybrid SDOF model, consisting of a membrane-enhanced nonlinear elastic branch followed by a linear post-yield branch with reduced tangent stiffness.

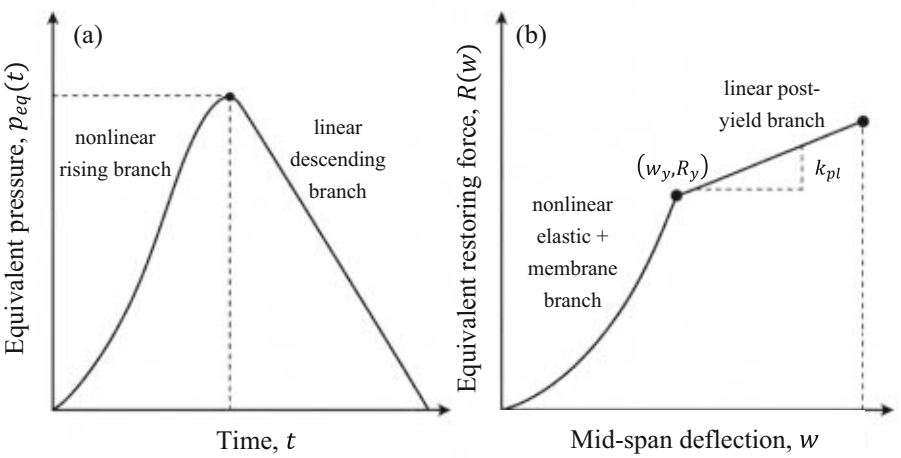


Fig. 1. Schematic representation of the proposed analytical framework: (a) equivalent pressure-time history adopted for dust-explosion loading, with nonlinear rising branch and linear descending branch; (b) idealized resistance function of the hybrid SDOF model, including the membrane-enhanced nonlinear elastic branch and the subsequent linear post-yield branch with reduced tangent stiffness.

This schematic representation is intended to facilitate the interpretation of the analytical framework and the transition between the two response stages.

2.4 Collapse-Oriented Interpretation

Beyond the prediction of the displacement-time history, the proposed model incorporates a collapse-oriented interpretation of the structural response [10]. This additional layer relates the computed global response of the plate to the main collapse families commonly

reported in the literature on impulsively loaded thin plates, namely large plastic deformation, tensile tearing, and shear-dominated failure. In this sense, the present formulation should be regarded as a reduced-order structural model equipped with a physically informed interpretation of the response regime, rather than as a local damage or crack-propagation solver. The first regime, denoted here as Mode I, corresponds to large plastic deformation [9]. Physically, this is the case in which the plate undergoes significant irreversible global deflection while remaining a continuous load-carrying surface. The panel bends, stretches, and dissipates energy through plastic deformation, but no local rupture mechanism is assumed to dominate the response. Within the present model, this regime is associated with the post-yield response after the first-yield threshold has been exceeded, provided that the deformation remains below the adopted tearing-sensitive condition. Accordingly, Mode I should not be interpreted as failure in the strict sense, but rather as a severe yet still globally deformable response regime. The second regime, denoted as Mode II, is associated with tensile tearing or severe local thinning. In the literature on impulsively loaded plates, this regime is commonly linked to the progressive localization of deformation, in which the global plate response is accompanied by pronounced stretching, necking and eventually tearing. In the present formulation, Mode II is therefore introduced as a collapse-sensitive candidate based on the global transverse displacement response. This classification identifies a response range in which severe thinning and tearing-sensitive behavior may become relevant. The adopted interpretation is based on the observation that, once the deflection-to-thickness ratio becomes sufficiently large, the response is no longer adequately described as pure global plastic deformation and becomes increasingly compatible with severe thinning and tearing-sensitive behavior. The transition to Mode II therefore marks the loss of confidence in a purely global deformation description and indicates that local rupture mechanisms may become relevant. The third regime, denoted as Mode III, is associated with shear-sensitive collapse. This case is more delicate than the previous two because, unlike large plastic deformation and tensile tearing, shear-dominated failure is not governed primarily by the magnitude of the central deflection. Instead, it is typically related to strong local demand at boundaries or support and may occur before the panel develops very large global displacements. For this reason, Mode III cannot be inferred reliably from the displacement amplitude alone. In the present model, a shear-sensitive classification is therefore assigned only through a conservative multi-condition logic, in which the exceedance of the global plastic capacity is treated as a prerequisite and is combined with additional indicators related to the timing of the event and the limited extent of the global deformation. This approach reflects the fact that a true shear-dominated failure should be interpreted as a more abrupt and localized collapse process than a deformation-dominated one. For clarity, the collapse-oriented interpretation adopted in the present work is summarized in Table 1. The table does not describe exact local fracture mechanisms, but rather the physical meaning assigned to each response regime within the proposed reduced-order model.

Mode I identify a globally deformable plastic response. Mode II identifies a response compatible with severe thinning and tensile tearing. Mode III identifies a response compatible with a more abrupt, shear-sensitive collapse. This distinction is particularly useful

Table 1. Collapse-oriented interpretation adopted in the proposed hybrid SDOF model.

Regime	Physical meaning	Structural response in the present model	Engineering interpretation
Mode I	Large plastic deformation	The plate exceeds the first-yield threshold and develops significant permanent global deflection, while remaining below the adopted tearing-sensitive limit.	Global plastic response of the panel; the plate is severely deformed but still treated as a continuous load-carrying surface.
Mode II	Tensile tearing / severe thinning candidate	The post-yield response is accompanied by large deflection-to-thickness ratios, indicating that the global deformation is becoming increasingly compatible with local thinning, necking and tearing-sensitive behavior.	The reduced-order model is no longer interpreted as purely deformation-based; local rupture mechanisms may become relevant.
Mode III	Shear-sensitive collapse candidate	The global plastic capacity is exceeded, and the response satisfies additional conditions associated with an early and relatively localized collapse tendency, without requiring very large global displacement.	Response compatible with a shear-dominated or abrupt boundary-sensitive collapse; this is treated as a conservative screening classification rather than a direct local shear prediction.

in preliminary structural assessment, because it allows the analyst to move beyond a single maximum-displacement criterion and to attach a physical meaning to the response history predicted by the reduced-order model.

3 Discussion

To illustrate the behavior of the proposed hybrid SDOF model, a single reference configuration was considered. The aim of this section is not to provide an exhaustive parametric investigation, but rather to discuss how the formulation behaves when applied to a representative thin steel plate subjected to a dust-explosion-type pressure pulse. The selected case, reported in Table 2, is intended to show, in a compact way, how the model links equivalent loading, nonlinear structural response, and collapse-oriented interpretation within a single reduced-order framework.

For the reference case reported in Table 2, the pressure pulse was first transformed into an equivalent pressure-time history defined by a nonlinear rising branch and a linear

Table 2. Reference input parameters adopted for the discussion case.

Parameter	Symbol	Value	Unit
Short side	a	1000	mm
Long side	b	1000	mm
Plate thickness	h	1	mm
Steel density	ρ	7850	kg/ m^3
Dynamic yield stress	f_{dy}	275	MPa
Young's modulus	E	210	GPa
Poisson's ratio	v	0.30	–
Dust explosion index	K_{St}	250	bar • m/s
Maximum explosion pressure	P_{max}	8	bar(g)
Filter-side volume	$V_{Filters}$	4	m^3
Dirty-side volume	V_{Dirty}	8	m^3
Vent area	A_{v0}	1	m^2
Predicted reduced pressure	P_0	41.8	kPa
Positive phase duration	t_d	0.150	s

descending branch. The resulting structural response shows that the model can reproduce a strongly nonlinear displacement evolution even within a reduced-order setting. In particular, the predicted displacement-time history highlights a rapid initial increase in transverse deflection followed by a progressively more severe response, indicating that the plate does not remain in a purely bending-dominated regime. Instead, the response is influenced by the combined action of bending, membrane hardening, and subsequent post-yield evolution. A relevant aspect of the model is that the elastic range is not treated as purely linear. The inclusion of the cubic membrane term modifies the restoring force already before the onset of global yielding, so that the structural response becomes progressively stiffer as the displacement grows. This is consistent with the expected behavior of thin plates undergoing large transverse deflection, for which in-plane restraint contributes increasingly to the resistance. In the present framework, this effect is clearly visible in the equivalent force-displacement relationship, where the initial branch deviates from a straight line and develops a hardening curvature before the transition to the post-yield regime. For the thinnest plate configuration considered in this study, the predicted displacement-time history, reported in Fig. 2, shows that the response rapidly evolves toward a collapse-sensitive regime. The panel undergoes a marked increase in mid-span deflection and reaches the tearing-sensitive threshold adopted in the present formulation. Accordingly, this case is classified as a Mode II candidate, meaning that the response is no longer interpreted as merely large global plastic deformation, but as a regime compatible with severe thinning and tensile tearing sensitivity. In this sense, the role of the model is not to simulate local crack initiation explicitly, but to indicate

when the global structural response enters a range in which local rupture mechanisms may become physically relevant.

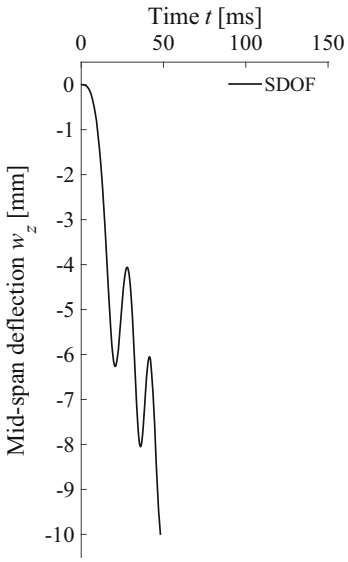


Fig. 2. Predicted displacement-time history for the thinnest plate configuration (h = 1 mm) under the reference dust-explosion loading case.

A second configuration, obtained by increasing the plate thickness to $h = 5$ mm while keeping the remaining parameters unchanged, is shown in Fig. 3.

In this case the structural response remains much more controlled. Although the panel still experiences a transient downward displacement, the deformation amplitude remains limited and the response is followed by a recovery toward the undeformed configuration, with subsequent oscillations of relatively small magnitude. Within the proposed interpretation, this behavior is representative of an admissible or near-elastic response regime, since the predicted displacement does not approach the collapse-sensitive thresholds used for Mode II and Mode III classification.

The comparison between Figs. 2 and 3 clearly highlights the role of plate thickness within the proposed framework. For the thinner plate, the same impulsive load leads to a rapid transition toward a tearing-sensitive condition, whereas for the thicker plate the response remains globally stable and structurally admissible. This comparison is important because it shows that the model is able not only to estimate the magnitude of the displacement response, but also to distinguish between different structural regimes under the same loading scenario.

From an engineering perspective, this is one of the main strengths of the proposed hybrid SDOF formulation. The model combines a compact equivalent representation of the pressure pulse with a membrane-enhanced elastic branch and a subsequent global elastic-plastic branch, thus retaining the essential nonlinear features of thin-plate response without resorting to high-fidelity numerical simulations. At the same time, the

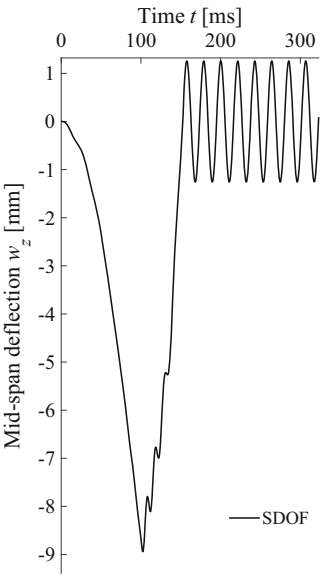


Fig. 3. Predicted displacement-time history for the thicker plate configuration (h = 5 mm) under the same reference dust-explosion loading case.

collapse-oriented interpretation provides a direct and physically meaningful framework for screening whether a given panel remains in a globally admissible regime or tends toward a more critical collapse-sensitive condition. Finally, it should be emphasized that the present discussion is intended as an illustrative application of the model rather than as a complete parametric investigation. Even so, the two representative cases discussed here are sufficient to show the capability of the proposed approach to connect equivalent dust-explosion loading, nonlinear structural response and simplified collapse interpretation within a single reduced-order engineering tool.

4 Conclusion

This paper presented a hybrid single-degree-of-freedom model for the rapid prediction of the dynamic response of thin steel plates subjected to dust-explosion-type impulsive loading. The proposed formulation combines a membrane-enhanced elastic branch, based on a Duffing-type representation, with a subsequent global elastic-plastic branch with reduced tangent stiffness. In this way, the model provides a compact but physically informed description of the transition from bending-dominated response to strongly nonlinear plate behavior. A further contribution of the work lies in the definition of an equivalent pressure-time history specifically conceived for preliminary structural assessment under dust-explosion loading. The adopted pulse combines a nonlinear rising branch with a linear descending branch, allowing the peak pressure, positive phase duration and overall impulse to be represented in a transparent and computationally efficient way. This makes the formulation suitable for early-stage analyses, rapid comparisons and parametric investigations, without the need for detailed CFD or high-fidelity

finite-element simulations at the preliminary level. The results discussed for the reference configurations showed that the model can distinguish between markedly different structural regimes under the same loading framework. In the thinner plate case, the predicted response rapidly evolved toward a tearing-sensitive condition, leading to a Mode II candidate classification. In the thicker plate case, the response remained controlled and compatible with an admissible or near-elastic regime. These results confirm that the proposed framework can provide more information than a simple estimate of the maximum displacement, since it also supports a physically meaningful interpretation of the structural regime reached by the plate. The proposed approach is conceived as a fast-engineering tool for preliminary assessment and screening, capable of bridging equivalent dust-explosion loading, nonlinear plate response and preliminary collapse-oriented interpretation within a unified reduced-order procedure. Future developments should focus on systematic validation against experimental evidence and higher-fidelity numerical models, as well as on the extension of the method to different plate geometries, boundary conditions and loading scenarios relevant to industrial dust-explosion protection.

References

1. Pinna F, Zucca M, Simoncelli M, Stochino F (2025) Explosion venting in dust collectors: a critical review of standards for reduced pressure and reaction force duration. J Loss Prev Process Ind 97:105670
2. Pinna F, Zucca M, Simoncelli M, Stochino F (2025) A new logarithmic congestion model for vent sizing and reduced pressure prediction in baghouse dust collectors. J Loss Prev Process Ind 105829
3. Pinna F, Zucca M, Simoncelli M, Stochino F (2026) Dust explosions in baghouse dust collectors: a state-of-the-art review. J Loss Prev Process Ind 105958
4. Biggs, J. M. (1964). Introduction to structural dynamics.
5. Nurick GN, Martin JB (1989) Deformation of thin plates subjected to impulsive loading—a review: part I: theoretical considerations. Int J Impact Eng 8(2):159–170
6. Nurick GN, Martin JB (1989) Deformation of thin plates subjected to impulsive loading—a review part II: experimental studies. Int J Impact Eng 8(2):171–186
7. Yuen SCK, Nurick GN, Langdon GS, Iyer Y (2017) Deformation of thin plates subjected to impulsive load: part III–an update 25 years on. Int J Impact Eng 107:108–117
8. Feldgun VR, Yankelevsky DZ, Karinski YS (2016) A nonlinear SDOF model for blast response simulation of elastic thin rectangular plates. Int J Impact Eng 88:172–188
9. Pinna F, Stochino F (2025) Nonlinear SDOF model for dynamic response and fragility analysis of steel plates under blast loads. Eur J Environ Civ Eng 29(14):3048–3071
10. Yao S, Zhang D, Lu F, Zhao N, Li Y (2021) Fast prediction method of failure modes for steel box structures under internal blast loading. Eng Fail Anal 120:104919

Bridges and Large-Span Structures

Design, Fabrication and Erection of a Large-Span Steel Vierendeel Girder: The New SCC Railway Control Centre in Turin

Andrea Imbrenda[1] and Giuseppe Vigoriti[2(✉)]

[1] Proges Engineering S.r.l., Rome, Italy
a.imbrenda@progesengineering.com
[2] Proges Engineering S.r.l., Venosa, (PZ), Italy
g.vigoriti@progesengineering.com

Abstract. The new operational control centre (SCC) of the Italian railway network in Turin is a mission-critical, importance-class IV building that supervises rail traffic across the Piedmont and Aosta Valley regions. The functional brief required the ground-floor control room to be entirely free of vertical structure, which along the east elevation translated into a clear span of about 60 m. The structural answer is a three-storey-deep welded steel Vierendeel girder in S460 steel that runs along the facade and hangs the upper floors, leaving the control room column-free. The paper concentrates on the constructional aspects that governed the design: workshop fabrication of the heavy built-up sections under execution class EXC3, segmentation for transport into modules below ten tonnes, ground pre-assembly, the connections that carry the girder actions into the reinforced-concrete cores through embedded steel frames, the multidirectional bearings, and the shored erection sequence with construction counter-cambers carried out alongside live railway tracks.

Keywords: Large-span steel structures · Vierendeel girder · Steel–concrete connections · Embedded steel frame · Structural bearings · Segmental fabrication · Erection sequence · Railway control building

1 Introduction

Railway traffic control buildings belong to a small family of civil works whose structural design is dominated less by the magnitude of the loads than by the requirement that the facility remain operational at all times. The new SCC (Command and Control System) control centre of Turin, commissioned by RFI – Ferrovie dello Stato for the south-west quadrant of the city, supervises the rail traffic of the Piedmont and Aosta Valley regions through ACCM, SCCM and CTC technologies. Because of its function it is classified in importance class IV

© The Author(s), under exclusive license to Springer Nature Switzerland AG 2026
R. Zanon et al. (Eds.): CTA 2026, LNCE 942, pp. 835–844, 2026.
https://doi.org/10.1007/978-3-032-39505-4_72

under the Italian building code (NTC 2018) [1,2], with a nominal design life of 50 years.

The functional brief placed a single, dominant constraint on the structure: the ground-floor control room had to be entirely free of internal columns and walls. On the west side of the main body the vertical loads could be carried comfortably by reinforced-concrete walls, but on the east side the same arrangement was not admissible, and the column-free requirement produced a clear span of about 60 m over the full height of three storeys. Steel was the natural material for the large-span elements, and the device that makes the brief feasible is a deep Vierendeel girder running along the east facade.

For a structure of this kind the real difficulty is as much constructional as analytical. A heavy welded girder of this size cannot be fabricated, transported and lifted in one piece; it must be broken down, pre-assembled, registered against the tolerances of the concrete cores, and erected on temporary supports while working immediately beside tracks that remain in service. The present paper therefore gives only a concise account of the analysis and concentrates on fabrication, transport, pre-assembly, the connections to the reinforced-concrete structure and the erection strategy (Fig. 1).

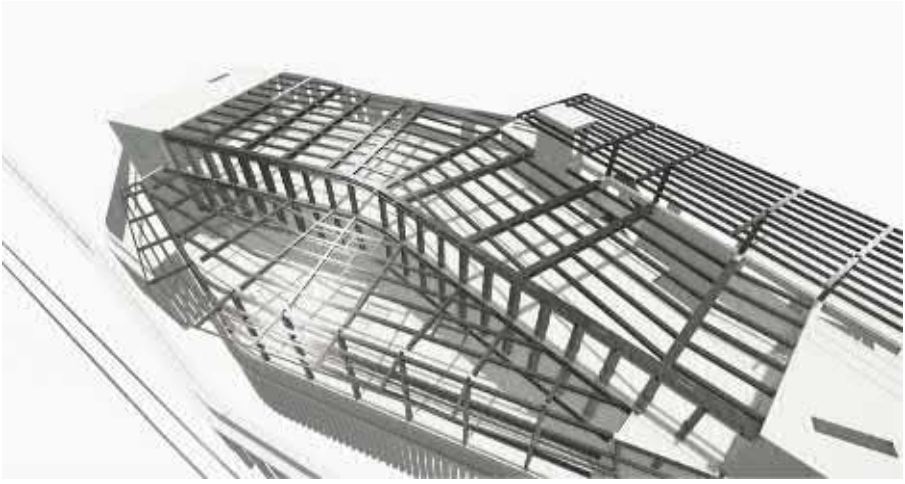


Fig. 1. Overall BIM view of the steel structure of the main body (Body A).

2 The Building and the Structural Concept

The complex is divided by structural joints into two independent bodies: the main building (Body A), on which this paper focuses, and a smaller technical building (Body B, the SIAP), built entirely in reinforced concrete. Body A

develops over four levels – a services basement, the control-room ground floor and two office floors – with interstorey heights of 4.20, 5.10 and 4.60 m. The roof is accessible and carries photovoltaic panels and a steel canopy.

Lateral stability is provided by massive reinforced-concrete cores at the south and north heads of the building, complemented by perimeter walls 30 to 55 cm thick with local thickenings up to 80 and 140 cm where the steel girder is supported. The horizontal floors are composite steel-concrete slabs. The seismic design follows a capacity-design philosophy, with a hierarchy of strengths and ductility detailing intended to drive plastic engagement towards the dissipative elements and to keep brittle mechanisms in reserve.

The principal structural materials are steel grade S460 N/NL for the Vierendeel girder and the main floor beams, and S355 for the remaining steelwork (terrace frame, embedded guide frames and canopy); class 10.9 preloaded bolts; Nelson studs for the composite action; and concrete up to class C40/50 in the most stressed walls. The steelwork is assigned execution class EXC3, determined from production category PC2, consequence class CC3 and service category SC1 under EN 1090-2 [7]. The member design follows the Eurocode 3 [3] and NTC 2018 provisions and the established literature on steel structures [9–11]. The foundations are reinforced-concrete rafts modelled on a Winkler soil.

3 The Steel Vierendeel Girder

Along the east elevation the floors are carried by a Vierendeel girder spanning about 60 m and articulated over three levels, with vertical members at 2.50 m centres. The three chords are welded double-T Sects. 600 mm wide and 800 mm deep, with plate thicknesses varied along the span according to the internal forces; the verticals are welded plated members of 600 × 600, 500 × 500 and 400 × 400 mm. The three chord levels effectively stack two Vierendeel panels over the building height, so that the girder behaves as a deep three-chord beam that hangs the intermediate and upper floors and leaves the control room below free of structure.

A Vierendeel layout, rather than a conventional braced truss, was preferred because its open rectangular panels allow the floors, the continuous glazed facade and the building services to pass through the depth of the girder without interference from diagonals, and because the regular, repetitive geometry of its nodes is well suited to workshop fabrication and to a modular erection. The price of removing the diagonals – higher local bending in the chords and verticals, analysed with the classical methods for Vierendeel girders [12] – is paid with the generous member depths and the S460 grade.

In the static scheme the girder is supported near its two ends: a fixed bearing at the south head provides the longitudinal restraint, while a multidirectional sliding bearing at the intermediate support near the north head shortens the free span and reduces both the vertical deflection and the peak internal forces. As a consequence the south side, farther from the intermediate support, carries the larger reactions and required the more substantial anchorage. Deflections were

limited to $L/250$ under variable loads and $L/200$ under the rare combination. The bearings are of the anti-uplift type and carry a vertical reaction up to about 13 200 kN; the sliding bearing decouples the slow thermal movement of the girder from the fast transfer of seismic and wind actions, with a longitudinal travel of ± 50 mm and a transverse travel of ± 25 mm, including the 40 mm margin required by EN 1337 [8].

The structure was analysed by the finite-element method with the Pro_SAP code. A complete model of the building was used to extract the actions, and dedicated steel submodels with conservative rigid restraints were then used to size the members and connections. All elements of the girder satisfy the ultimate and damage-limitation checks with utilisation ratios below unity, and the serviceability deflections fall within the limits above (Figs. 2 and 3).

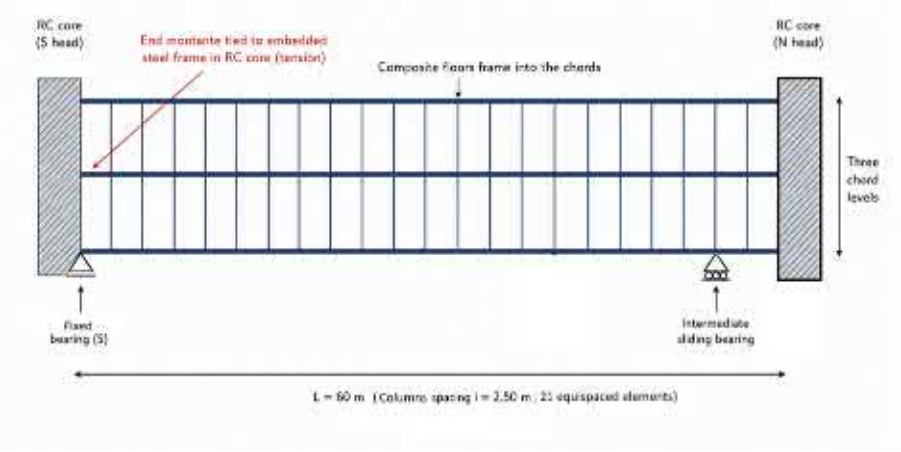


Fig. 2. Structural scheme of the east-facade Vierendeel girder (schematic, not to scale).

4 Connections to the Reinforced-Concrete Cores

The transfer of the girder actions into the concrete cores is the most distinctive aspect of the design. At each chord level a steel frame fitted with shear studs is cast into the core – the embedded frame – which performs two tasks: during construction it centres and guides the girder against the as-built tolerances of the concrete, and in service it provides the pull-out resistance of the connection. The embedded frames carry rows of headed studs designed as shear connectors in accordance with EN 1994-1-1 [5], sized on the maximum tie force that can be transferred to the wall.

At the north head the connection is a continuous bolted joint between the end vertical of the girder and the matching vertical of the embedded frame. The holes



Fig. 3. BIM view of the column-free control room, spanned by the Vierendeel girder above.

in the end vertical are vertically slotted, so that the vertical reaction is delivered to the bearing seated below while the bolted joint works in tension only; the flexural stiffness of the end vertical spreads the tie force over the full height of the connection and prevents it from concentrating at the individual chords. For a design tension of about 1 590 kN per metre the joint uses M30 class 10.9 bolts, with twelve bolts per metre adopted against a calculated minimum of eight.

At the south head, where the forces are larger but the nearby intermediate support reduces them, the connection is made by plates welded on site to inserts embedded in the wall and bolted at each chord. Because a full-height thickening of the wall could not be provided here, the bearing is housed on a corbel cast on top of the wall, whose projecting zones act as short cantilevers and were verified with a strut-and-tie model on C40/50 concrete. Throughout, the embedded frames are what make a 60 m welded girder geometrically compatible with the cast-in tolerances of the cores – a constructional rather than a purely static function (Fig. 4).

5 Fabrication, Transport and Pre-assembly

The chords and verticals are heavy welded built-up sections fabricated in the workshop, with full-penetration first-class welds where explicitly required and fillet welds elsewhere. The EXC3 execution class imposes the corresponding tolerances, welding qualification and inspection extent, which in turn drove the detailing of the splices and the handling of the pieces.

Segmentation was governed by the maximum lifting and transport weight of ten tonnes and by the road-transport width. The girder is therefore cut both vertically and horizontally: vertically at mid-length of each chord, and horizontally at one third of each vertical. Because the chords run continuous through the



Fig. 4. End of the girder during erection: the end vertical and the bolted connection to the embedded frame in the RC core.

verticals, every vertical is split into three parts – in the proportion 2/6, 1/6+1/6, 2/6 – so that each transported piece carries one third of a vertical together with its chord segment. The operation yields a set of comparable modules roughly 2.50 m wide and not heavier than ten tonnes; the field joints between them are made with bolted web and flange cover plates.

To limit work at height and crane occupancy, the transported pieces are bolted together on the ground into larger multi-storey modules before lifting. Figure 5 shows one such three-level module standing on temporary props during ground pre-assembly, ready to be hoisted; Fig. 6 shows the bolted cover-plate splices that close the joints between modules once they are in place.

6 Erection Sequence

The modules are raised onto temporary shoring towers and the girder is assembled bay by bay on these supports. Construction counter-cambers are built into the fabrication so that, once the permanent loads are in place and the shoring is released, the girder settles to its intended, near-horizontal profile. The whole operation is conditioned by the proximity of railway tracks that remain in service throughout the works, which restricts crane positions, lifting windows and site logistics.

The sequence can be summarised as follows. The pre-assembled modules are placed on the shoring and connected to one another through the cover-plate splices; the connections to the concrete cores are then completed – bolting to



Fig. 5. A pre-assembled three-level Vierendeel module on temporary props, ready for lifting.



Fig. 6. Bolted web and flange cover-plate splices between girder modules, on the temporary shoring.

the embedded frame at the north head and welding the plates at the south head; the shoring is released, so that the girder takes up its self-weight and the permanent loads on the intermediate sliding bearing and on the core connections; the multidirectional bearing is then activated; and finally the composite floors are cast and, framing into the chords, stiffen the completed system. Figures 7 and 8 show the girder fully erected on its shoring, beside the live tracks, before the floors were cast.



Fig. 7. The Vierendeel girder along the curved east elevation, carried during construction by the rows of temporary props.

7 Complementary Aspects

The horizontal floors are steel-concrete composite slabs on HI-BOND A55/P600 profiled sheeting, 13 cm thick, made composite with the steel beams by a triple row of Nelson studs and a C28/35 topping; the main floor beams span 15 to 18 m at about 5 m centres. The steelwork is fire-protected to R60: the S460 girder and floor beams are treated with sprayed lightweight high-resistance plaster (Monokote MK-6/HY) or, where preferred, with an intumescent paint, the thickness being set from the section factor and the critical temperature – conventionally 550 ° C for class 1 to 3 sections and 350 ° C for class 4, in accordance with EN 1993-1-2 [4,13]; the composite slabs are checked for the same fire rating and the additional reinforcement provided following EN 1994-1-2 [6]. As an accidental action, a dedicated wall protects the building from the impact of a derailed train on the adjacent tracks, designed under the accidental combination of NTC 2018 (Fig. 9).



Fig. 8. The three-storey Vierendeel girder on its shoring, beside the railway tracks, before casting of the composite floors.



Fig. 9. The completed column-free control room, with the double-height glazed volume on the east side.

8 Conclusions

The requirement for a column-free control room in a mission-critical railway building drove a 60 m, three-storey steel Vierendeel girder along the east elevation. The interest of the project lies less in its elastic analysis than in making the girder buildable: the workshop fabrication of heavy S460 built-up sections under EXC3, their segmentation into transportable modules below ten tonnes, the ground pre-assembly, the embedded-frame connections that both register and tie

the girder to the reinforced-concrete cores, and a shored erection with construction counter-cambers carried out beside live tracks. Steel made the architectural brief feasible and, equally important, made the construction controllable.

Acknowledgment. The authors gratefully acknowledge the general contractor Brancaccio Costruzioni S.p.A., whose work is documented in the site photographs.

References

1. Ministero delle Infrastrutture e dei Trasporti: D.M. 17 gennaio 2018 – Aggiornamento delle Norme tecniche per le costruzioni (NTC 2018). Rome (2018)
2. Consiglio Superiore dei Lavori Pubblici: Circolare 21 gennaio 2019, n. 7 – Istruzioni per l'applicazione dell'Aggiornamento delle Norme tecniche per le costruzioni di cui al D.M. 17 gennaio 2018. Rome (2019)
3. EN 1993-1-1: eurocode 3 – design of steel structures, part 1-1: general rules and rules for buildings. CEN, Brussels (2005)
4. EN 1993-1-2: eurocode 3 – design of steel structures, part 1-2: general rules – structural fire design. CEN, Brussels (2005)
5. EN 1994-1-1: eurocode 4 – design of composite steel and concrete structures, part 1-1: general rules and rules for buildings. CEN, Brussels (2004)
6. EN 1994-1-2: eurocode 4 – design of composite steel and concrete structures, part 1-2: general rules – structural fire design. CEN, Brussels (2005)
7. EN 1090-2: execution of steel structures and aluminium structures, part 2: technical requirements for steel structures. CEN, Brussels (2018)
8. EN 1337: structural bearings (all parts). CEN, Brussels
9. Ballio, G., Mazzolani, F.M.: Theory and design of steel structures. Taylor & Francis, London (1983)
10. Salmon, C,G., Johnson, J.E, Malhas, F.A: Steel structures: design and behavior, 5th edn. Pearson Prentice Hall, Upper Saddle River (2009)
11. ANSI/AISC 360-16: specification for structural steel buildings. American Institute of Steel Construction, Chicago (2016)
12. Lightfoot E (1951) a method of analysis of the continuous vierendeel girder. Struct. Eng. **29**(11) (1951)
13. Franssen, J-M., Vila Real, P.: Fire Design of Steel Structures, 2nd edn. ECCS Eurocode Design Manuals, Ernst & Sohn, Berlin (2015)

Environmental Assessment of a Suspended Pedestrian Bridge Built with Mostly Recovered Materials: The Marangara School Bridge, Rwanda

Edoardo Benvenuti[1], Riccardo Zanon[2(✉)], Nicola Turrini[3], Godfrey Uwiringiyimana[3], and Tina Gunnarsson[3]

[1] ArcelorMittal Steligence® Engineering, Esch-sur-Alzette, Luxembourg
edoardo.benvenuti@arcelormittal.com
[2] ArcelorMittal Global R&D, Esch-sur-Alzette, Luxembourg
riccardo.zanon@arcelormittal.com
[3] Fika (Formerly Bridges to Prosperity), Kigali, Rwanda

Abstract. The article presents the Life Cycle Assessment (LCA) of a suspended pedestrian bridge located in Marangara, Rwanda, constructed through the reuse of reclaimed materials and without the use of heavy machinery during the construction phase. The case study represents an example of lightweight infrastructure developed according to the principles of the circular economy, enhancing the value of components that had reached the end of their original life cycle.

The analysis considers the environmental impacts associated with the maritime and land transportation of the reused materials, assuming that the impacts resulting from their production are attributed to the previous life cycle. This approach makes it possible to quantify the environmental impacts directly associated with the operations required for the reuse of the materials in the construction of the structure.

The results show that the climatic impact of the bridge allows it to be classified in one of the best categories proposed in the international literature (SCORBS A+).Furthermore, the analysis makes it possible to compare the environmental contribution of the entire structure with that of the deck alone, highlighting the role of the different structural components in the overall emissions balance. The study confirms the potential of material reuse in the construction of infrastructures with reduced environmental impact, particularly in contexts characterized by limited economic and technological resources.

Keywords: Life Cycle Assessment · Reuse · Suspended Bridges · Global Warming Potential · Embodied Carbon

1 Introduction

Sensitivity to environmental issues has increased significantly in recent years, and this has also had an important impact on the field of civil engineering and, more generally, on the construction sector. Indeed, the construction sector is one of the main contributors to

© The Author(s), under exclusive license to Springer Nature Switzerland AG 2026
R. Zanon et al. (Eds.): CTA 2026, LNCE 942, pp. 845–857, 2026.
https://doi.org/10.1007/978-3-032-39505-4_73

global green-house gas emissions worldwide [1]. Many commonly used materials, such as concrete and steel, have a significant environmental footprint associated with their production, and reducing their use results in more sustainable structures.

The circular economy is a model that aims to minimize waste generation and the consumption of raw materials by maintaining the value of materials within the economic system. This objective is pursued through practices of reuse, recycling, and recovery, which make it possible to extend the life cycle of materials and reduce the need for new resources, thereby promoting the transition towards closed-loop production systems [2]. Within the context of the circular economy, it is important to distinguish between reuse, recycling, and recovery. In the case of steel, the term reuse is defined as the process by which an existing structural element is used for a new project without the need to be melted down to create a new one. By contrast, recycling is the process by which metal waste is melted down to create new material, as in the case of steel produced by Electric Arc Furnaces (EAF). Finally, recovery refers to the reuse and adaptation of structural elements in existing buildings [3].

As highlighted in this article, the concepts of reuse and circular economy can be applied to the construction of infrastructure in developing countries. Suspended pedestrian bridges can be built using cables recovered from other structures at the end of their service life and, if they are in good condition, these cables can be reused as the main structural elements of such infrastructure.

Furthermore, bridges and road infrastructure are essential for communities living in rural areas, especially in hilly and volcanic regions such as those of Central Africa. The economic benefits provided by well-designed pedestrian connections are remarkable: a 75% increase in agricultural profits, a 36% increase in labor income, and a 60% increase in women's participation in the labor market [4, 5]. Moreover, the local population can benefit from additional advantages, such as easier access to schools and hospitals.

The methodology most commonly used for the assessment of environmental impact is the Life Cycle Assessment (LCA), which aims to measure the entire environmental footprint of a structure throughout its life cycle. The analysis begins with the production phase of the main structural materials, including the processes of raw material procurement, processing, and transportation, as well as on-site construction activities. Subsequently, the impacts associated with the use phase of the building or infrastructure are considered, including energy consumption and any maintenance operations. Finally, the analysis includes the end-of-life phase, which comprises demolition activities, waste management, and the potential recovery of materials. The integration of the contributions associated with each phase makes it possible to determine the overall environmental footprint of the system under analysis and to identify the main environmental hotspots, thereby providing designers with useful information for optimizing design choices and reducing impacts throughout the entire life cycle.

This article presents the case study of a suspended pedestrian bridge located in the rural area of Marangara, in the western part of Rwanda. The infrastructure was built with the aim of creating a 95-m-long connection linking the existing rudimentary infrastructure with the Marangara primary school, crossing the Nyamutera stream below, which during the rainy seasons can reach a water discharge that makes it impossible to ford.

This bridge can be considered an excellent example of sustainability and circular economy, since the main structural cables were reused for structural purposes. In addition, rocks and sand for the construction of the access ramps and abutments were recovered from the riverbank, while the cement and steel deck were purchased from local producers. Another distinctive feature of this infrastructure is that it was built without the use of heavy machinery, relying solely on manual labor and involving the local population in construction work, in order to teach them the use of simple tools.

The objective of this article is to assess the environmental impact of the life cycle of the bridge built in Rwanda by applying the Life Cycle Assessment (LCA) methodology and quantifying the amount of carbon dioxide equivalent (CO_2-eq) emitted.

2 Description of the Bridge

The suspended pedestrian bridge is located in the Nyabihu District, Rwanda, and connects the two banks of the Nyamutera stream by means of a span of approximately 95 m (Fig. 1). The structure was built to provide a safe crossing of the watercourse for the local population and, in particular, for the students and teachers at the primary school located in the immediate vicinity of the northern abutment of the bridge. This need is particularly significant during the rainy season, when the river may represent a major obstacle to local mobility.

From a structural point of view, the bridge consists of two pairs of main cables, two lowers and two uppers, designed to transfer the permanent loads of the deck and the variable loads due to pedestrian traffic. The steel cables are anchored to reinforced concrete anchor beams located inside the abutments. The two upper cables are supported by reinforced concrete towers and rest on saddles obtained through the reuse of automobile wheel rims (Fig. 2). The deck consists of steel angle sections connected to UPN100 cross-beams, which are suspended from the main cables by means of hangers made of 10 mm diameter reinforcing bars and subsequently connected to the lower main cables by means of U-bolts (Fig. 3).

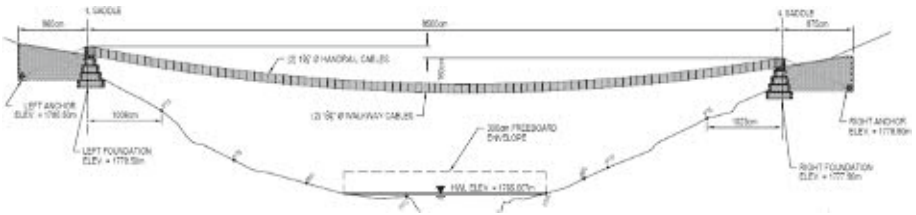


Fig. 1. Layout of the suspended pedestrian bridge in Marangara, Rwanda

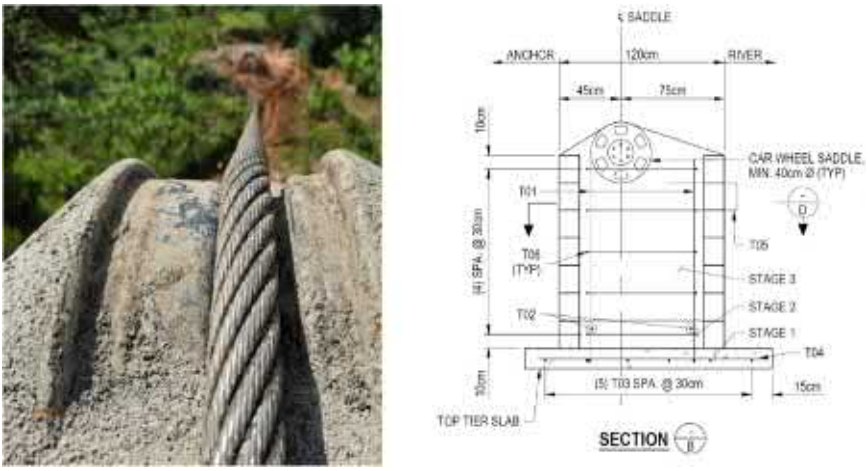


Fig. 2. Technical detail of the seating of the upper main cables

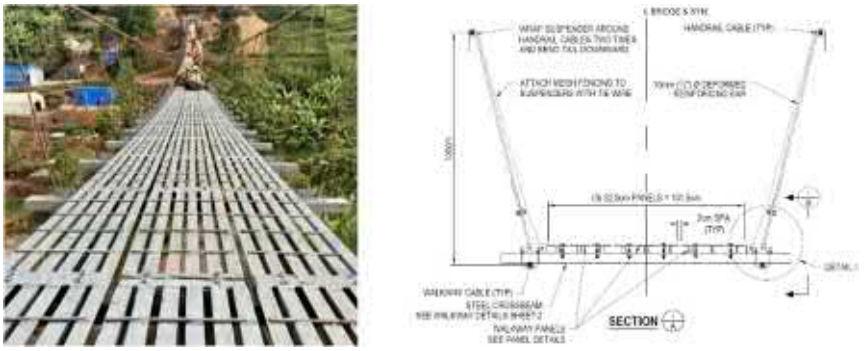


Fig. 3. Technical detail of the deck and steel crossbeams

3 Material Used and Design Assumptions

The materials used for the construction of the bridge can be divided into three categories: reused materials (provided by international donors), materials sourced locally on the construction site, and materials purchased on the local market. Among the reused materials are the main cables, the lifeline cable, and the clamps used for cable anchorage. In addition, a significant portion of the materials required for the construction of the abutments and access ramps was sourced directly along the Nyamutera river, including sand, rocks, and gravel. The remaining construction materials, such as cement, reinforcing bars, hangers, paints, bitumen, bolts, fences, plastic pipes, and metal profiles, were purchased locally in the cities of Kigali and Musanze (Fig. 4 and Table 1). For the LCA assessment, it was assumed that the impacts associated with modules A1–A3 of the reused materials are entirely attributable to the previous life cycle. The bridge has an expected lifespan of 50 years.

Consequently, only the environmental impacts associated with module A4, relating to transport to the construction site, were attributed to these materials. As regards the materials collected along the river course, a zero impact was instead assumed for modules A1–A5, since these do not require industrial production processes or mechanized transport, having been collected and handled exclusively by manual labour. For all materials purchased locally, the entire life cycle, comprising modules A1–A5, was considered. The installation activities and waste generation associated with module A5 of the LCA were considered equal to 5% and 1% of modules A1–A4 for concrete and metallic materials, respectively [6]. All the remaining contributions of module A5, such as the demolition of existing buildings, construction activities, and workers' transport, were considered negligible, since every type of operation was carried out without the use of heavy machinery or internal combustion vehicles, but using only manual labour and electric tools powered by portable photovoltaic systems. The reused materials, namely cables and clamps, were shipped by sea from the port of Dubai and arrived at the port of Mombasa, Kenya, covering approximately 4700 km. Subsequently, they were transported to the construction site by road transport, covering approximately 2300 km. All other construction materials sourced locally were transported overland to the construction site. In particular, the transport distance of cement was 342 km, that of reinforcing bars was 184 km, and that of the steel deck was 120 km. Table 2 summarises all the quantities of materials used for the construction of the Marangara bridge:

Table 1. Categories of materials used

Reused	New	Recovered along the river course
Main cables	Cement	Sand
Cable for safety line	Rebars	Gravel
Clamps	Suspenders	Rocks
	Paint / Bitumen	
	Bolts	
	Metallic fencing	
	Plastic pipes	
	Steel profiles	



Fig. 4. Categories of materials used: reused, new, and recovered along the river

Table 2. Quantities of materials divided by parts and components

Element	Weight (kg)	Total	Weight (kg)
Left Abutment	**451121,28**	Anchor	17988,99
Anchor	8994,55	Approach ramp	645186,07
Approach ramp	298551,03	Cable	5201,97
Foundation	135699,00	Crossbeam	1672,94
Tower	7876,70	Decking	3828,16
Right Abutment	**498057,48**	Fencing	825,00
Anchor	8994,45	Foundation	270250,00
Approach ramp	346635,03	Miscellaneous	54,00
Foundation	134551,00	Suspenders	278,55
Tower	7877,00	Tower	15753,70
Superstructure	**11860,63**	**Total**	**961039,39**
Cable	5201,97		
Crossbeam	1672,94		
Decking	3828,16		
Fencing	825,00		
Miscellaneous	54,00		
Suspenders	278,55		
Total	**961039,39**		

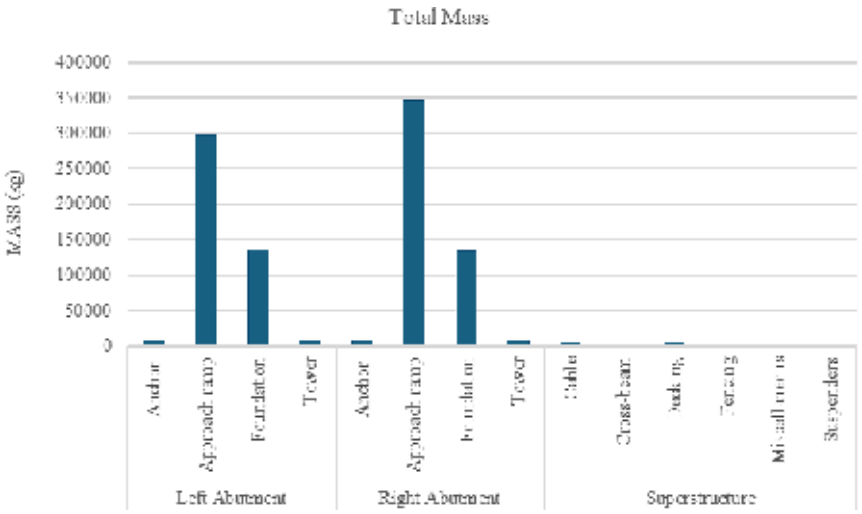


Fig. 5. Bill of masses by structural element

4 Life Cycle Inventory

The inventory of carbon dioxide equivalent emissions for each material is summarized in Table 3: as(EPDs) are not available for materials produced in Rwanda, all Global Warming Potential (GWP) values considered were estimated and obtained from OneClickLCA. the For module A4, GWP were assumed to be equal to 0.1555 $kgCO_2e$/tkm and 0.01154 $kgCO_2e$/tkm, respectively for land and maritime transport [7].

Table 3. Life Cycle Inventory of the materials used

	Unit	A1-A3
Cement CEM II	kgCO2e/kg	0,91
Sand	kgCO2e/kg	0,00
Gravel	kgCO2e/kg	0,00
Stones	kgCO2e/kg	0,00
Rebar	kgCO2e/kg	2,86
Plastic pipe	kgCO2e/kg	2,50
Steel pipe	kgCO2e/kg	2,86
Steel wire	kgCO2e/kg	2,86
Steel clips	kgCO2e/kg	2,86
Black tar	kgCO2e/kg	2,00
Profiles	kgCO2e/kg	2,86
Plate	kgCO2e/kg	2,86

(*continued*)

Table 3. (*continued*)

	Unit	A1-A3
Bolts	kgCO2e/kg	2,86
Fence	kgCO2e/kg	2,86
Anticorrosion paint	kgCO2e/kg	1,79

5 Life Cycle Assessment

The environmental impact in terms of carbon dioxide equivalent is obtained by multiplying the emission factor value of each module by the quantity of materials used for the construction of the structure. The total emission values associated with the different structural elements and the different structural components are in Figs. 6 and 7:

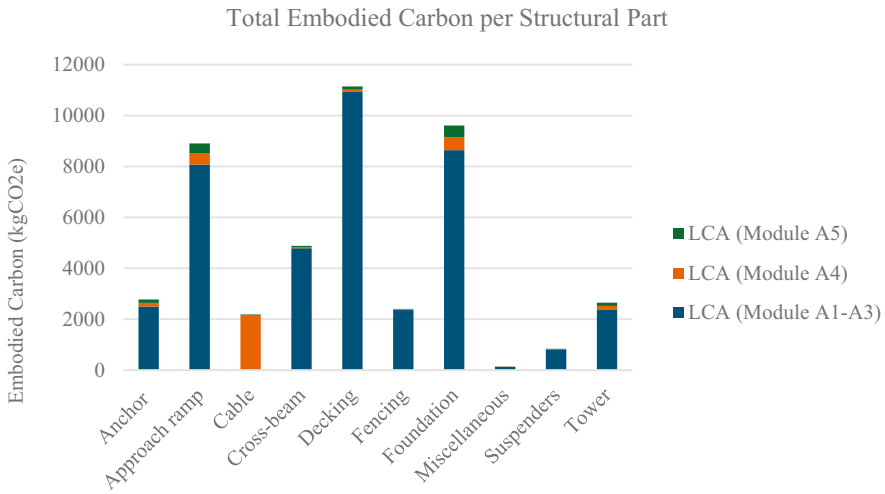


Fig. 6. Total embodied carbon by structural element

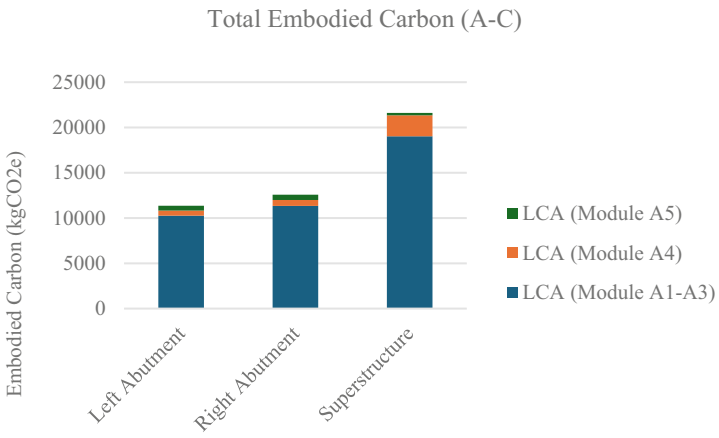


Fig. 7. Total embodied carbon by structural component

6 Interpretation of the Results

By observing Figs. 5, 6 and 7, several aspects regarding the environmental impact of the Marangara bridge can be discussed. First, despite an extremely high mass compared to that of the deck, the abutments show a low-er environmental impact (11361,56 and 12575,77 $kgCO_2e$ compared to 21602,65 $kgCO_2e$). This result highlights that structural mass is not necessarily a reliable indicator of environmental impact. Although the abutments represent the heaviest part of the structure, they are mainly composed of locally sourced stone materials, characterized by significantly lower embodied emissions compared to the steel elements that make up the deck. Another relevant aspect of this analysis is that the most impactful module from an environ-mental point of view is A1–A3 (approximately 88%). The predominance of this module con-firms that, even in lightweight infrastructures, material production represents the main source of greenhouse gas emissions. This result is consistent with numerous LCA studies on bridges and civil works, where the contribution of structural materials is generally dominant.The A1–A3 module has a strong impact on the abutments due to the large quantities of cement used, and on the deck and cross-beams due to the steel present.

Transport contributes in a limited but not negligible way, representing about 7.8% of total emissions. The main cables constitute the only component for which transport plays a significant role. This suggests that, in the case of reused materials coming from remote locations, the environmental benefits of reuse may be partially offset by emissions associated with logistics. The A5 module has an environmental impact that is considered negligible, amounting to only 3%. This article presents the SCORBS evaluation, which aims to communicate how sustainable a bridge is from an environmental point of view [8]. This indicator is based on modules A1–A5 and includes the superstructure, foundations, and access ramps. The assigned rating ranges from A++ to F considering the functional area of the deck (Figs. 8 and 9). In the case of the Marangara bridge, the total length of the bridge is 95 m, while its functional width is 1.3 m.

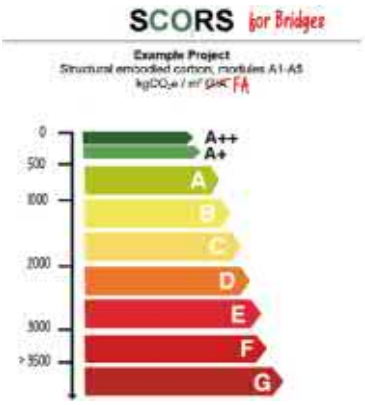


Fig. 8. Evaluation SCORBS [8]

The resulting value is 368.74 $kgCO_2e/m^2$, lower than the threshold value of 500 $kgCO_2e/m^2$, classifying the Marangara bridge as A+ and placing it in one of the best categories provided by the SCORBS method. The obtained result demonstrates that designing with reused materials and with limited resource use is possible and highly beneficial from an environmental point of view. It should be noted that the obtained value considers relatively high embodied carbon values for steel (2.86 $kgCO_2e/kg$), which have a significant influence on the overall environmental sustainability of the bridge. Assuming instead the use of more favourable values, typical of steel produced in electric arc furnaces (EAF), with equivalent emissions of 0.70 $kgCO_2e/kg$, the final result would have been 246.81 $kgCO_2e/m^2$ (Fig. 10), thus receiving the SCORBS A++ rating.

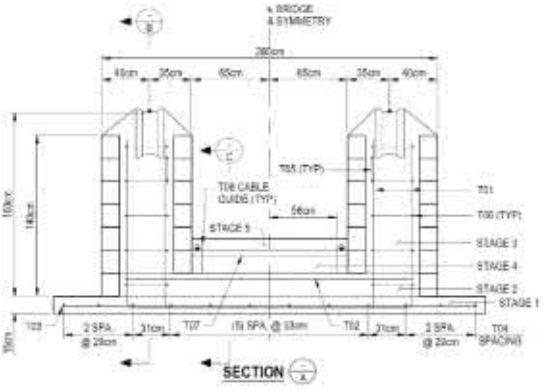


Fig. 9. Functional width at the lowerst point considered for the Marangara Bridge

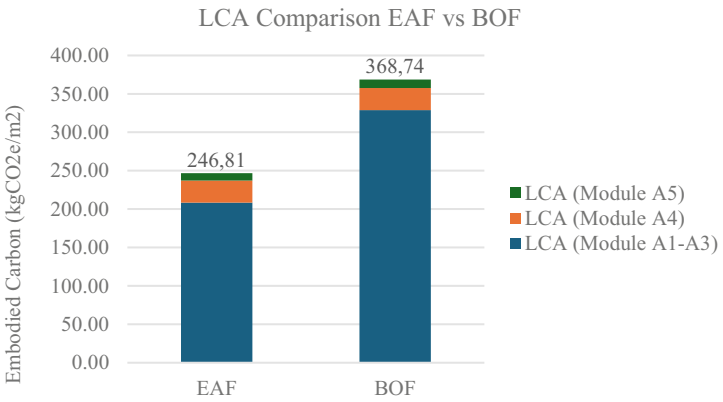


Fig. 10. Embodied carbon comparison considering EAF steel

7 Conclusions

This article presented the assessment of the environmental impact of a suspended pedestrian bridge throughout its entire life cycle. The distinctive feature of this work lies in the fact that it was constructed through the reuse of materials and without the use of heavy machinery powered by internal combustion engines. Despite these characteristics, it was possible to build a 95-m-long connection in a rural area of Rwanda, providing significant social benefits.

The work carried out demonstrates that the environmental impact of such a structure can be very low, below 500 $kgCO_2e/m^2$, receiving an SCORBS A+ rating. Nevertheless, it can be observed that the material production phase accounts for 88% of the total environmental impact, highlighting the importance of reusing materials at the end of their life cycle. However, although transport has an overall limited impact, for reused cables this contribution is significant due to the long transport distances involved.

The study presented in this article assumes module A5 as a percentage of modules A1–A4, excluding all contributions related to the installation of the structure, since all construction works were carried out using only manual labor and without the use of internal combustion machinery. Furthermore, for reused materials, all their environmental impact from modules A1–A3 was assigned to the previous life cycle.

Comparing the obtained value of 368.74 $kgCO_2e/m^2$ with the COWI database (Fig. 11) for built bridges, whose average is 2300 $kgCO_2e/m^2$ [8], it can be inferred that bridges such as the Marangara one, therefore constructed with reused materials and without the use of heavy machinery, are significantly more environmentally sustainable. The article also shows that the use of steel with a low embodied carbon content significantly improves the final result, placing the structure in the highest SCORBS category (A++) with a normalized value of 246.81 $kgCO_2e/m^2$ (Table 4).

Furthermore, it is possible to compare the results obtained in this article with those of previously constructed works, as reported in the table:

Table 4. Embodied carbon for the same type of suspension bridges

	Units	Marangara	Kugasumo	Kabingo	Hanika
Bridge Span	m	95	90	98	98
Walkway width	m	1.3	1.3	1.3	1.3
Functional Area (FA)	m^2	123.5	117	127.4	127.4
SCORBS	$kgCO_2e/m^2$	369	417	366	381

In conclusion, the reuse and use of locally sourced materials prove to be an environmentally advantageous choice, and transport is a factor that must be considered within the life cycle of the structure, although it has a secondary contribution. Given the limited availability of Environmental Product Declarations (EPD) for Rwanda, average values from international databases were adopted. They introduced a certain level of uncertainty but it can be kept in a +/−20% confidence boundary.

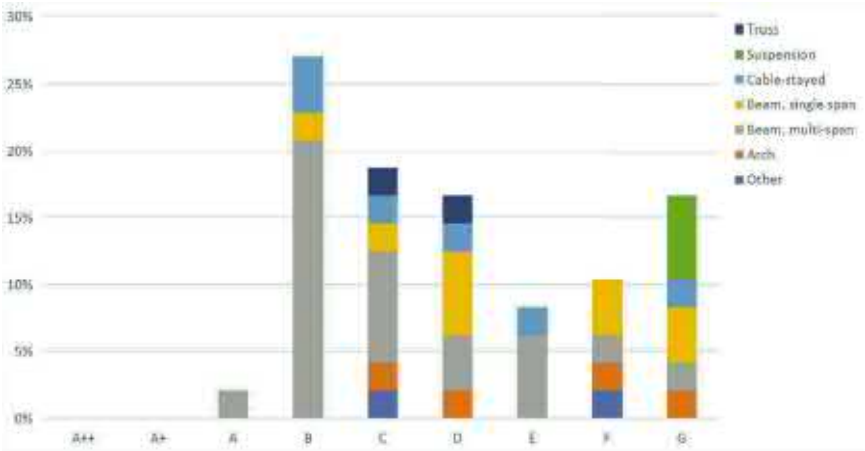


Fig. 11. Evaluation SCORBS for bridges of COWI's database [8]

Acknowledgements. Special thanks are due to all the individuals and companies who contributed to the construction of this extraordinary work, starting with the Collegio dei Tecnici dell'Acciaio, who enthusiastically proposed this sustainability initiative, genuine and comprehensive. We thank all the partner companies that financially supported the project: Anas, ArcelorMittal, CSI Italia, DCR Progetti, DMN Ingegneria, Fhecor, Fincantieri Infrastrutture, Franchetti, Hempel, IIS, Innoventions, Nord-Lock Group, Politecnica, Seteco Ingegneria S.r.l., Sina, Steel Projects Engineering, and Studio De Miranda S.r.l.

Great gratitude is also extended to all the volunteers from the partner companies who chose to dedicate their experience, time, and effort to the Rwandan population, as well as to help the author of this article experience a wonderful and unforgettable experience: Marco Cipani, Gianmarco Marani, Simone Pardini, Rocco Raimo, Alessandro Rosti, and Gianluca Villanova.

Finally, thanks are given to the non-profit organization Fika and all its collaborators, without whom there would have been no organization or management of the logistical and construction aspects of the bridge.

References

1. UNEP and GlobalABC (2025) Global status report for buildings and construction 2025–2026
2. Bakker C et al (2019) Circular product design: addressing critical materials through design. In: Critical materials - underlying causes and sustainable mitigation strategies. World Scientific, pp 179–192
3. Bartsch H (2025) Reuse of reclaimed steel components in construction: a systematic review of potential, challenges and future directions. Structure 80:108391
4. Brooks W, Donovan K (2020) Eliminating uncertainty in market access: the impact of new bridges in rural Nicaragua. Econometrica 88:1965–1997
5. Yale School of Management (2023) Measuring return of Investment for a Footbridge in Nicaragua and Rwanda. Yale School of Management
6. RICS (2024) Whole life carbon assessment for the built environment
7. ÖKOBAUDAT: ÖKOBAUDAT – sustainable construction information portal. https://www.oekobaudat.de/en.html.
8. Archer-Jones C, Green D (2020) Carbon targets for bridges: a proposed SCORS-style rating scheme. Struct Eng 99:34–42

Steel Roof for the "PALARICCIARDI SPORTS HALL": Design and Construction Process

Marco Stizzo, Vito Elia, and Aldo Giordano(✉)

iDeas s.r.l., Naples, Italy
info@ideas-ea.com

Abstract. This paper describes the design and construction process of the steel roof for the new "PalaRicciardi" Sports Hall in Taranto, Italy. The elliptical-based shell structure is composed of a system of primary and secondary steel trusses, covered by a tensioned PVDF membrane. Advanced structural analyses has been performed to ensure structural stability in all the construction stages. Computational fluid dynamics (CFD) simulations were used to evaluate wind pressure loads, while buckling analyses assessed lateral instability. The interaction between the main steel structures and the PVDF membrane, modeled as a net a of cable element, has been also investigated in a non-linear analysis. Furthermore, a Construction Stage Analysis was implemented to monitor the construction process. FEM elements and boundary conditions were sequentially "activated and deactivated" to replicate the evolving structural configurations during its assembly. By following the construction sequence, stresses and deformations were evaluated and compared to the predicted final state. This approach allowed the identification and implementation of any necessary adjustments or variants as the project progressed on site. The results confirmed that the structural element stresses and deformations are significantly influenced by the specific construction sequence, highlighting the importance of the construction sequence assessment for complex steel structures.

Keywords: Steel Structures · Steel Trusses Arch · PVDF Membrane Cover · FEM Analysis · Erection Sequence · Structures Assessment

1 Introduction

As part of a broader program to enhance the city of Taranto -which will host the 20th edition of the Mediterranean Games- the new "**Amatori Ricciardi**" complex has been developed. This multi-purpose facility is designed to provide an indoor, multi-disciplinary sports space for track and field and other indoor sports, as well as a venue for public performances, cultural events, and leisure activities, including the 20th Mediterranean Games. The building has a gross footprint of approximately 6,250 m^2 and consists of an elliptical structure covered by a tensile roof-supported by a steel framework-housing the sports activity area (Figs. 1 and 2).

The roof structure consists of a series of primary trusses spanning the transverse direction with a height of 2.0 m and a spacing of approximately 6 m—interspersed

© The Author(s), under exclusive license to Springer Nature Switzerland AG 2026
R. Zanon et al. (Eds.): CTA 2026, LNCE 942, pp. 858–869, 2026.
https://doi.org/10.1007/978-3-032-39505-4_74



Fig. 1. External aerial view



Fig. 2. Internal vies

with a series of secondary trusses running longitudinally at a spacing of approximately 8 m. The ellipsoidal shape is irregular, formed by the union of two semi-ellipsoids: a larger one (major axis of 120 m, semi-minor axis of 37 m, and maximum height of approximately 25 m) and a smaller one (major axis of 111 m, semi-minor axis of 30 m, and maximum height of approximately 23 m). Along the junction between the two forms, a continuous change in elevation occurs along the building's longitudinal axis; at this point, the bottom chord of the larger semi-ellipsoid transitions into the top chord of the smaller semi-ellipsoid. Additionally, a deeper central truss is inserted longitudinally at the point of this elevation change. A perimeter truss runs along the edge of the roof, where the tensile structure reaches a minimum height of approximately 7 m (Fig. 3.

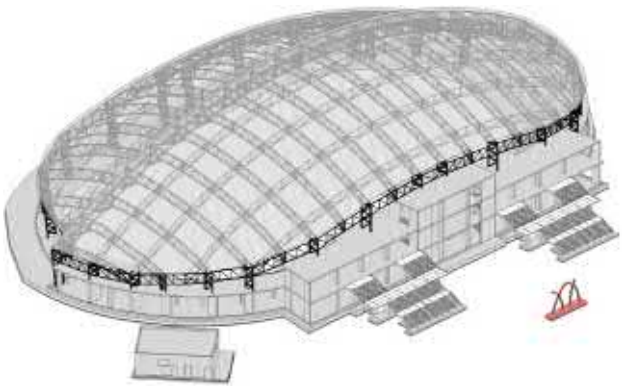


Fig. 3. Structural REVIT 3D Model with substructure

The roof structure is enclosed by an upper PVDF membrane and rests on a series of inclined steel truss columns. On the north, northwest, and northeast sides of the building, the columns are directly connected to the foundation structure, whereas on the south, southwest, and southeast sides, they rest on the roof structure of a reinforced concrete building that varies in height from one to three stories.

2 Design Assumptions

2.1 Structural Load Pattern

The main resisting elements of the new Palaricciardi roof structures are the transversal steel trusses arches placed each 6,0 m, placed parallel to the minor axis of the ellipsoidal shape of the roof. All the Main arches trusses are connected at the top by a double height (4,0 m) big trusses arch which is equivalent to the maximum axis of the ellipse, and at the base by a perimetral steel truss that follow the ellipse perimeter in plan while change the level along its length due to the presence of the building only in one of the side of the construction.

The main trusses arches are directly connected with the PVDF cover and are able to support the design load in terms of strength, while some retain structures are needed to avoid buckling. So, secondary steel trusses orthogonal to the above mentioned were placed which are not supporting vertical load.

These secondary elements have been designed neglecting the load transmission by the covering. Considering the cover system is made by a PVDF tensioned membrane, with a typical span of about 6,0 m, those elements has been placed below the minimum level the membrane could reach under the external loads to avoid any contact between structures and membrane and so load transmission. The gap necessary to avoid contact between PVDF membrane and secondary elements was about 500 mm, to reach that dimension more than the underlying of the secondary elements some spacers made by trapezoidal steel plates welded on the top chord, with a continue secondary steel 40 mm diameter CHS profile. All the elements of each assembly were studied incorporating the secondary structures, taking into account the joint position even in the secondary tube and in leaving some expansion gap in the members (Figs. 4 and 5)

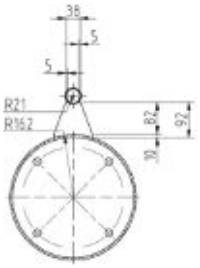


Fig. 4. Top chord Connections

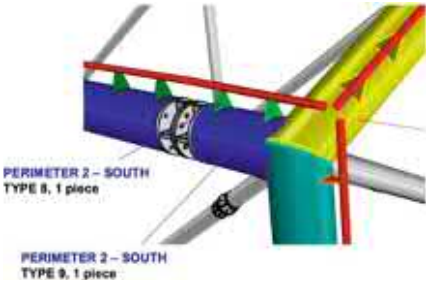


Fig. 5. Top chord connection stresses

2.2 Joint Design Strategy

The Executive design was performed before the choice of the executors of the steel roof. So, all the erection sequence and all the bolted connection, which lead to a specific assembly and to a specific sequence of construction were supposed in the design stage. To minimize changing into the joint design all splice connections were designed considering the dimensioning emerging forces each steel profile section type of all the roof structural elements. So, changing the position of the bolted connection along the members the connection remains valid and with sufficient strength and stiffness (Figs. 6 and 7).

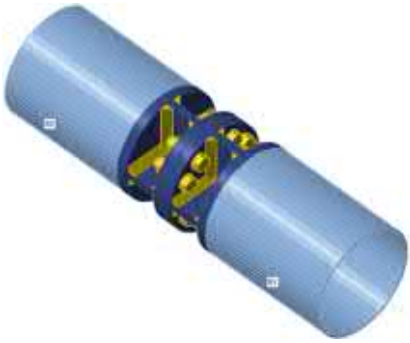


Fig. 6. CHS splice connection

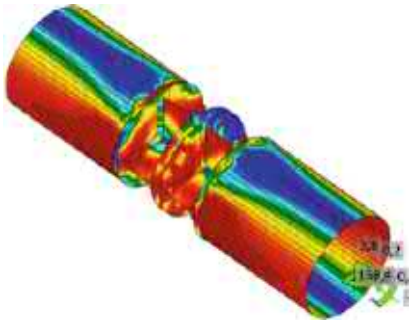


Fig. 7. CHS splice stresses

Such strategy allowed to change the assemblies according to the sequence of construction chosen by subcontractors to speed up the erection without changing type or resizing members/ joint even if some other splice connection were included.

3 CFD Analysis

To evaluate the wind loading on the sports hall structure, a computational fluid dynamics simulation was carried out in accordance with Sect. C3.3.8.1 of the Implementing Circular: "For shapes not covered by the cited documents, reference may be made to literature data, specific wind-tunnel tests or, finally, computational fluid dynamics simulations using tools of proven scientific validity". The analyses were performed using VENTO [2] AEC computational fluid dynamics (CFD) soft-ware, developed by Vento CFD. CFD is a computational discipline that employs numerical methods to solve the Navier–Stokes equations. These comprise a system of five partial differential equations governing fluid motion and representing, respectively, the conservation of mass, momentum and energy (Figs. 8 and 9).

When all five balances reach equilibrium throughout the computational domain and in every cell, the numerical method is said to have converged; in other words, the steady-state solution has been obtained. The code has undergone so-called validations, i.e. its results have been compared with wind-tunnel measurements and with the results of the most widely used CFD software packages. The data and results are documented in

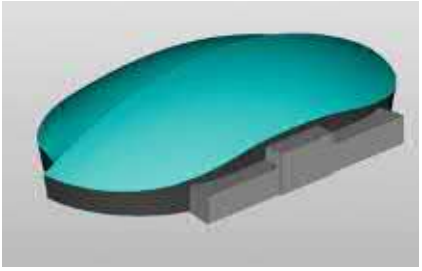


Fig. 8. Building Model

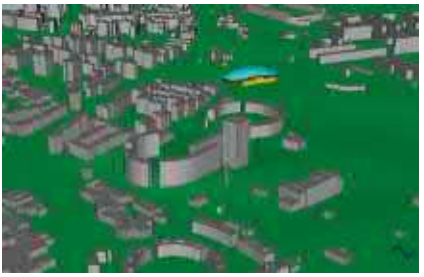


Fig. 9. Context overall model

international scientific publications. In the specific case of the new PalaRicciardi, two computational models were implemented to determine the wind pressure coefficients acting on the roof: one representing the isolated building, and another including the surrounding urban context in order to assess shielding effects. Eight wind directions were analysed for each model, comprising the four cardinal directions and the four intermediate directions. This was necessary because of the asymmetrical roof geometry, which consists of one shell larger than the other and has an ap-proximately 2 m step along the major axis (Figs. 10 and 11).

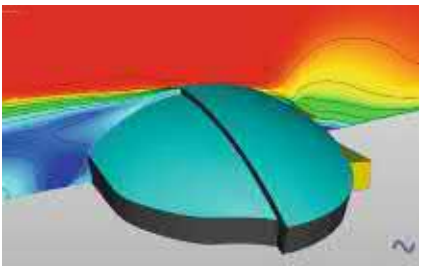


Fig. 10. Section plot

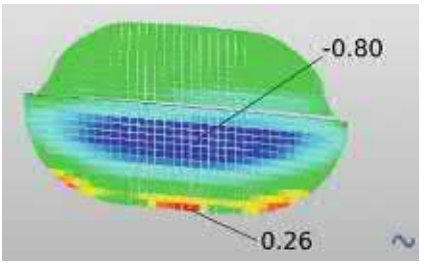


Fig. 11. Pressure diagram

As shown in the table below, the analyses of the wind actions on the roof surface yield sub-stantially lower values when the urban context is included than for the isolated-building model (Table 1).

Conservatively, and taking account of possible future urban changes that cannot currently be predicted, the results obtained for the isolated-building model were adopted.

Table 1. Sum of the wind action for each direction [kN]

Direction	Shell 1			Shell 2		
	Without context	With context	Reduction	Without context	With context	Reduction
North	725	260	64%	−330	125	138%
North-East	730	170	77%	15	55	−267%
East	524	32	94%	434	32	93%
South-East	735	220	70%	532	196	63%
South	800	345	57%	370	213	42%
South-West	840	77	91%	665	115	83%
West	560	255	54%	448	177	64%
North-West	1000	148	85%	220	115	48%

4 FEM Analisys Strategy

4.1 Fem Models Implemented

Main Results from different FEM model were compared to assess the correct structural behavior of the steel roof structures, to understand the compliance with the standard code (NTC 2018) [1] for each one of them. A global 3D model including foundation system was implemented to control deflection limit cause of the reduction of the base stiffness of the truss columns in front of a fixed base model with fully restrained at the base.

The model with fixed base were implemented in the stability calculation and were stress checks were performed.

To understand the interaction between PVDF Tensioned Membrane and steel primary structures were performed two different analysis a linear elastic analysis in a model of the roof cover with with a membrane-like shell elements, and a non- linear analysis in a model where the roof covere were modeled as a grillage with cable elements at a preset value of sagging or pretension (Figs. 12 and 13).

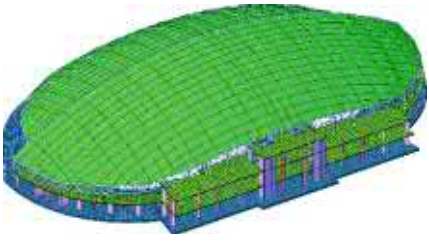


Fig. 12. FEM Model with Mat Found and elastic soil

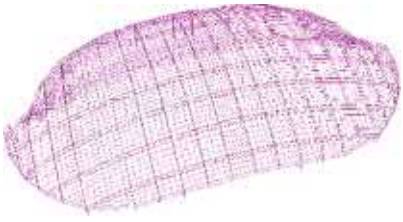


Fig. 13. Cable Net Model

In the first model the pretension of the PVDF membrane included as external load applied to the elements where the tensioned membrane was connected acting along the direction of the membrane plane with the intensity became from the subcontractor stability calculation of the membrane itself.

In the second model the roof cover was modeled with a net made by nonlinear cable elements, in which the pretension were applied to cable elements to reach the correct initial sagging. After that the external load has been applied as nodal loads at each intersection between the perpendicular cables.

The main differences between the two models is related to the direction of the action which the shell transfers to the substructures that is vertical, due to FEM Shell element definition while the action transferred by the cable elements is tangent to the effective deformed shape, typically sub-horizontal. So, the external loads could lead to an high variation for the out of plane forces on the substructures between the results obtained from the two models. To understand the intensity of the variations between the out of plane behavior (Figs. 14 and 15).

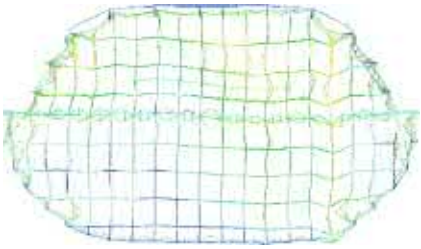


Fig. 14. XY Displ – Rigid Cover Model



Fig. 15. XY Displ – Cable Net Model

4.2 Elastic Buckling Assessment

An additional check of possible lateral instability modes of the members was carried out by means of an elastic buckling analysis using the following load combination:

Permanent loads:

- Structural self-weight;
- Superimposed permanent load (0.30 kN/m^2)
- PVC membrane prestressing actions (where unfavourable)

Variable loads, for which the critical load multiplier was calculated:

- Uniform snow load (0.48 kN/m^2)
- Increase in membrane tensile forces transmitted to the structure due to snow loading (Figs. 16 and 17)

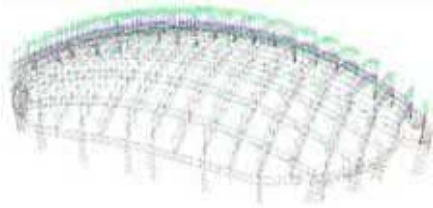


Fig. 16. Load applied for B.A

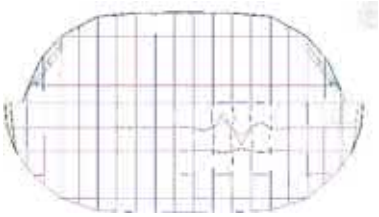


Fig. 17. First mode of Buckling

The minimum Euler critical load multiplier for member instability obtained from the analyses under the assumed load conditions is **11.13 > 10**, which indicates that global instability effects are sufficiently remote and may therefore be neglected in the elastic analysis.

5 Erection Sequence Assesment

5.1 Construction Stage Analisys

In the numerical models considered, the structure was subjected to a staged-construction analysis (*Construction Stage Analisys*): it was subdivided according to the erection stages, and FEM elements and/or restraints were sequentially "activated and deactivated" to reproduce the restraint and loading conditions experienced by the various structural components during erection.

This type of analysis was required because construction is a continuous process in which the structure is assembled progressively, and both the internal forces and deformations in the final service configuration are directly affected by the erection sequence. The construction process was therefore analysed and simulated, and the results were compared with those obtained from the design-stage analyses, in order to identify possible deviations from the assumed final configuration and avoid issues that would not have emerged from conventional analyses alone. The numerical simulation of the construction process was therefore intended to monitor sudden changes in internal forces and deformations in the primary structure before the final configuration was reached [3, 4].

The analysis also accounts for the cumulative effects of internal forces and deformations throughout the construction process. It was also considered that, during erection, some truss segments would be bolted together at elevation through the specified continuity connections; until the bolts are tightened, however, the continuity restraint represented in the design model is not fully developed. This temporary condition was reproduced in the staged model by assigning rotational releases at the ends of the newly installed truss segments; these releases were subsequently deactivated in later stages. This procedure allows for the rotations that the newly installed elements may undergo (Figs. 18 and 19).

A comparison between the staged model (Construction Stage Analysis) and the design model (one-time model) shows a difference between the deformations calculated using the two approaches ($\delta_{z,C.S.} = 32.94 > \delta_{z,O.T.} = 18.09$ ➔ +45% deformation due to self-weight).

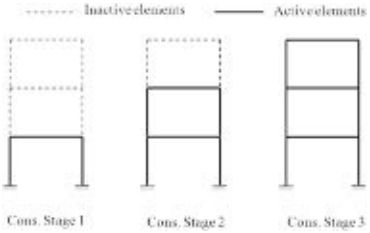


Fig. 18. CS analysis process

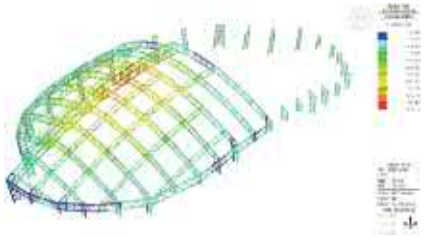
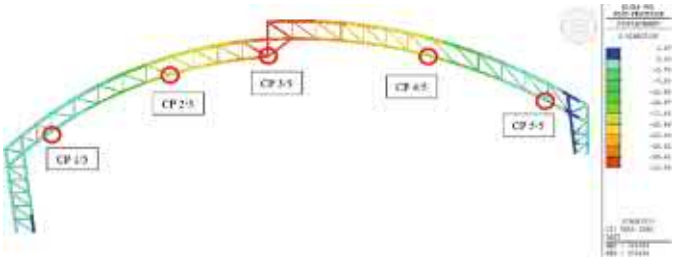


Fig. 19. Intermediate Stage of Roof Erection

However, this variation is not considered significant, since it remains within the code limits and does not adversely affect erection of the structure (Table 2).

Table 2. Differences between CS and OT Analisys

Differences between CS and OT Analisys – Structural Grid SN			
	[cm]	[cm]	Δ
CheckPoint 1/5	0.13	0.15	+13%
CheckPoint 2/5	1.19	1.84	+35%
CheckPoint 3/5	1.81	3.29	+45%
CheckPoint 4/5	1.06	1.68	+37%
CheckPoint 5/5	0.25	0.29	+14%



A series of monitoring points is also defined (located on the top chord of truss X at its intersections with gridlines SA to SU) to enable displacement monitoring and, where necessary, to establish additional control measures based on the tolerances to be met during erection (Figs. 20 and 21).

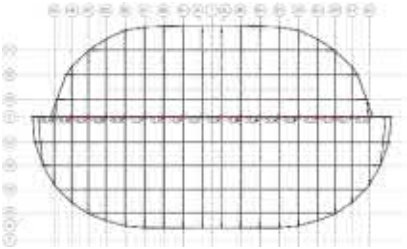


Fig. 20. Check points location

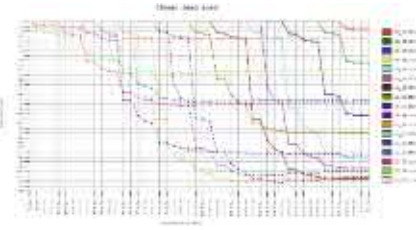


Fig. 21. Disp. Of check points vs. Stage

5.2 Site Acceptance Tests

As stated in NTC 2018 and in Section §C9.2 of the Implementing Circular, load tests "*are intended to establish the correspondence between theoretical and experimental behaviour*".

It is proposed to test the truss along gridline SI (which has the greatest span and is least affected by edge restraints) by comparing the measured maximum deflections with the predicted values following the application of equivalent forces reproducing the load associated with the rare serviceability limit state (SLS) combination.

Concentrated loads are therefore proposed at the positions indicated below, so as to reproduce the stress state described above.

The loads are applied not only to the central truss being tested, but also, at lower levels, to the adjacent trusses SH and SL, in order to avoid excessive differences in stress and deformation between neighbouring members.

The adopted loading arrangement, including the nodal loads, is shown below (Figs. 22 and 23).

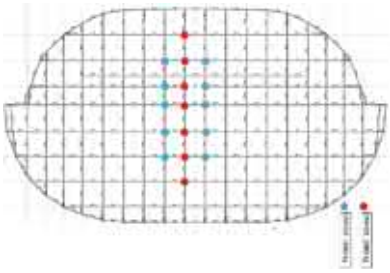


Fig. 22 Loads Test location



Fig. 23. Loads application on site

A local model of the top chords of the trusses was developed to verify that the 20 kN concentrated force applied to the steel section would not cause an increase in the existing stress state (under self-weight) sufficient to compromise member stability (Figs. 24 and 25).

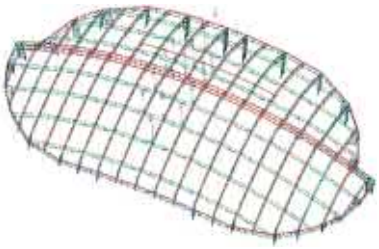


Fig. 24. FEM Model – SAT loads

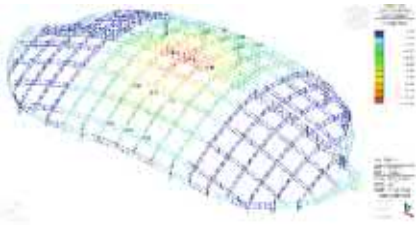


Fig. 25. FEM Model, SAT Displacement

In view of the small stress increase resulting from the application of the concentrated load, this action is considered compatible with the global stress state; however, particular care is recommended when applying and distributing the concentrated loads during the test (Figs. 26 and 27).

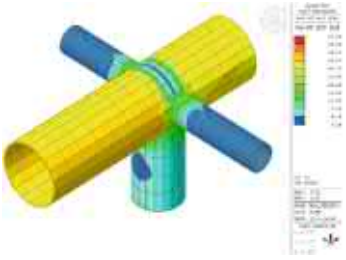


Fig. 26. $\sigma_{VM} = 41.84$ MPa

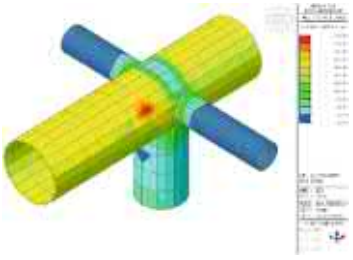


Fig. 27. $\sigma_{VM} = 51.23$ MPa

6 Conclusions

As a results of the design and construction process of the steel roof of the new Palaricciardi sport hall, the main achievements were related to the necessity, in not ordinary steel structures, to implement various Structural Analysis of the same construction in order to assess the correct behavior of the structure, both during construction and in operation. Several FEM model with different types of analysis and FEM elements were thus utilized, also taking advantage of Computational Fluid Dynamics for the assessment of wind induced forces.

A global FEM model was implemented including the Mat foundation with elastic boundary at the base comparing the results in terms of steel members stresses and deflections with a Fix base global model.

The presence of a PVDF membrane as a roof covering, tensioned at a certain value of tensile force, were considered modelling the membrane with a grillage of cable elements, tuning the pretension with the sagging obtained by a local membrane analysis made by the producers. The emerging results were compared with another global model where the roof cover was modelled as a membrane-type shell element.

Acknowledgments. Vento CFD s.r.l – CFD Analisys
Diaferia SRL — Tensostrutture & Membrane

References

1. Ministero delle Infrastrutture e dei Trasporti (2018) Norme Tecniche per le Costruzioni 2018. Gazzetta Ufficiale della Repubblica Italiana. Decreto Ministeriale, Rome, Italy
2. Vento CFD S.r.l. (2016) Determinazione dei carichi del vento sulla copertura del progetto del Pala Ricciardi di Taranto. Technical Report
3. Wu LL, Gao G, Ye BR, Zhang HD, Lu Q (2021) Analysis on accumulated deformation and stress of the steel roof of Beijing opera house during construction. In: Proceedings of the 10th global conference on materials science and engineering (CMSE 2021)
4. Yang X, Zheng J, Zhou G, Yang B (2018) Mechanical simulation and analysis of the construction process of a large-span space latticed structure in coal yard. In: Proceedings of the 7th international conference on energy, environment and sustainable development (ICEESD 2018), Advances in engineering research, vol 163, pp 707–711

New Termini Bridge: Design and Construction of a Steel Deck Integrated Within a Historic Structure

Giorgio Rizzo[1(✉)], Salvatore Condurso[2], Federico Panighel[1], and Enrico Parcianello[1]

[1] Gefyra Engineering Srl STP, Oderzo, Italy
info@gefyraengineering.com

[2] "Direttore dei Lavori", ANAS Catania, Road Network Management Area, Misterbianco, Italy

Abstract. The Termini Bridge is an important link between the municipalities of Barcellona Pozzo di Gotto and Terme Vigliatore (Messina). Inaugurated in December 2024, it complies with current NTC18 standards, with a widening of the carriageway of the old masonry arch bridge.

The bridge has 13 mixed-structure spans with a total length of 193.4 m and a width of 10 m. The project had to integrate architecturally with the existing structure but bypass it structurally, as it was no longer suitable for modern traffic loads.

The deck was separated from the arches by the insertion of friction pendulum isolators, which reduce seismic loads that are particularly intense in the Messina area. The piers were reinforced with micropiles to independently transfer the foundation loads.

The construction phases were geared towards extensive prefabrication to ensure a rapid reopening of the road: this result was achieved through the extensive use of bolted connections and prefabricated slabs.

Keywords: Composite bridge · Precast slab · Historic architectural integration · Seismic isolation

1 Introduction

The rehabilitation of existing masonry arch bridges requires reconciling structural safety with architectural preservation. In Italy, a large share of the road network relies on early twentieth-century masonry structures no longer adequate for modern traffic loads [1], many of which are located in areas of high seismic hazard.

This paper presents the design and construction of the new Termini Bridge (Messina, Italy), inaugurated in December 2024, in which a composite steel-concrete deck with friction pendulum isolators and micropile foundations was integrated into a thirteen-arch masonry structure. This structural-decoupling approach — inserting a new independent load-carrying system within an existing structure without altering its appearance — has proven effective [2], and pairs naturally with seismic isolation techniques, such as friction pendulum bearings, that reduce force demand on deteriorated substructures [3].

© The Author(s), under exclusive license to Springer Nature Switzerland AG 2026
R. Zanon et al. (Eds.): CTA 2026, LNCE 942, pp. 870–877, 2026.
https://doi.org/10.1007/978-3-032-39505-4_75

Moreover, to minimize the construction time and costs while maximizing quality and reliability, extensive prefabrication was adopted for the slab, following internationally acknowledged techniques [4]. While this prefabrication approach is not common for composite bridges in Italy, other notable realizations can be found [5].

2 Bridge Description

2.1 Geometry of the Existing Bridge

The existing structure features a series of opposing segmental arches in solid brick masonry, with bases resting on stocky rectangular piers terminated at their ends by semicircular cutwaters. The load-bearing masonry of the arch barrel has a thickness of 1.00 m, over which inert fill material consisting of rubble stone and soil is placed; similarly, the piers are constructed of solid brick masonry with dressed stone in the perimeter zone of the cutwaters, and are internally filled with coarse-grained inert material. The bridge comprises thirteen spans with a clear opening of 12 m each; the piers have plan dimensions of 2.50 × 9.00 m, with the exception of two piers measuring 4.30 × 10.80 m. The pier centreline spacing varies between 14.5 m and 15.4 m. The overall length of the structure, including the two abutments at either end, is 223.26 m (Fig. 1).

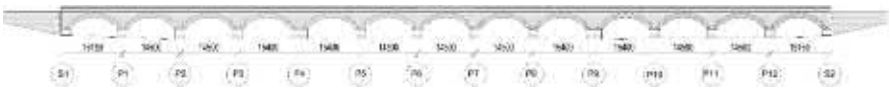


Fig. 1. Existing bridge elevation.

2.2 Evaluation of the Existing Structure and Design Criteria for the New Bridge

Inspection of the existing bridge's condition revealed an advanced state of deterioration, characterized by widespread efflorescence of the masonry and progressive settlement of the arch spans (Fig. 2). The proposed consolidation and restoration intervention was therefore structured around the following objectives: i) elimination of the structural load-bearing function of the arches, piers, and abutments; ii) construction of a new load-bearing structure independent of the aforementioned elements (structural bypass), together with widening of the existing carriageway to meet current design standards; iii) preservation of the bridge's original architectural character through targeted structural consolidation and aesthetic reinstatement of deteriorated areas.

These objectives were achieved through the insertion of a new composite steel-concrete deck within the existing structure, seismic isolation by means of friction pendulum bearings, and consolidation of the piers by micropiles.

In order to preserve the architectural appearance of the bridge, the existing loose fill material was removed down to the extrados of the masonry arches at the keystone cross-section. This operation created a recess, screened by solid brick walls approximately 700 mm in height, within which the new deck was seated, as illustrated in the cross-section shown in Fig. 3.



Fig. 2. Photograph of the bridge in its original condition before the restoration work.

The new road platform required for the deck consists of a 7000 mm wide carriageway accommodating two traffic lanes, flanked by two 950 mm footways protected by guardrails. In order to maintain architectural consistency, the parapets along the footway edges were likewise constructed as solid brick walls.

2.3 New Composite Deck and Prefabrication

The new composite deck consists of 6 longitudinal steel girders in S355W weathering steel, fabricated from standard rolled sections (HEA 600). At the abutments and piers, the HEA 600 girders connect to a welded cross-beam of equal depth — 590 mm — with bottom flanges of 620 × 35 mm, top flanges of 550 × 35 mm, and a 30 mm thick web. The girders are spaced at 1.10 m centers and are interconnected within each span by 3 intermediate cross-frames of HEA 400 section. All steel elements listed above are designed for on-site assembly by bolted connections only, thereby optimizing construction operations.

With the further aim of minimizing construction time and ensuring higher quality control standards, the use of a precast slab was similarly adopted.

The slab was produced as precast panels 10.12 m wide (matching the full deck width), with a maximum length of 2.4 m for transportability requirements, and a thickness of 260 mm. The precast elements incorporate the upstand kerb for guardrail installation and the provisions for the drainage system.

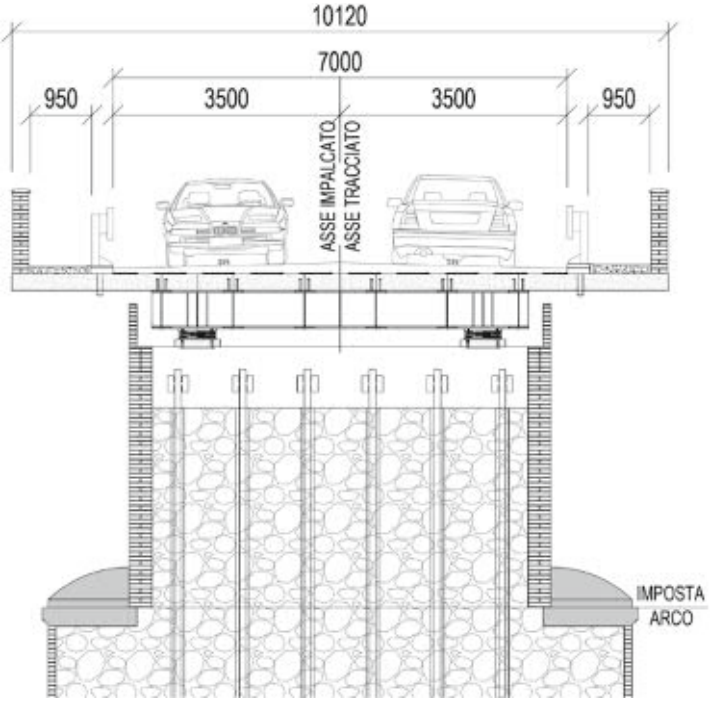


Fig. 3. Typical section of the new composite deck in correspondence of a pier.

Along the abutting edges between adjacent panels, a rebate is formed from which the reinforcement loops project (Fig. 4). Following placement on the steel girders, stitching reinforcement is inserted into this rebate, ensuring structural continuity between panels after casting of the in-situ closure pour.

The shear connection between the slab and the steel girders is achieved using block-and-hoop connectors installed through 90 × 220 mm openings (Fig. 5), in lieu of conventional headed stud (Nelson) connectors. This solution allowed the structural continuity of the precast elements to be preserved while minimizing the number of apertures required for the connection. The resistance of this connector type was calculated in accordance with reference standard [6].

2.4 Seismic Isolation

The most significant horizontal action governing the verification of the piers is seismic loading. The construction site falls within seismic zone 2, with a peak ground acceleration at the Life Safety Limit State (SLV) of $a_g = 0.227$ g. The design of an isolation system capable of minimizing the horizontal forces transmitted to the substructures was therefore of paramount importance. This is achieved by installing two friction pendulum bearings at each support cross-beam at the intermediate piers; double concave friction pendulums are adopted because their compactness better suits the restricted available space (equivalent radius of curvature R = 2500 mm, nominal dynamic friction coefficient



Fig. 4. Precast concrete slabs in the plant.

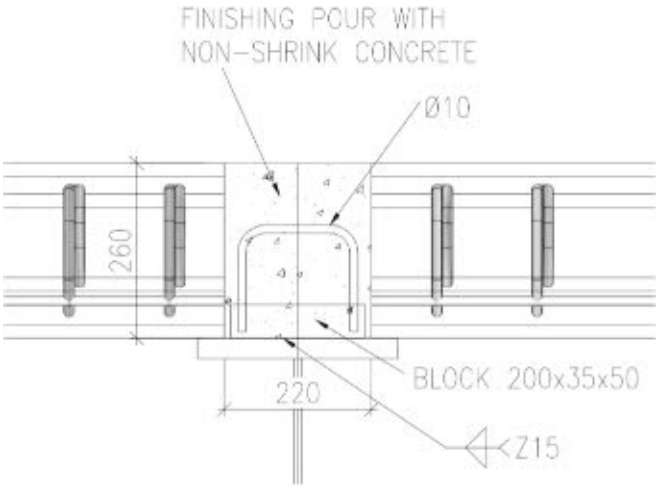


Fig. 5. Detail of the shear connection through block with hook.

$\mu = 4\%$, displacement capacity 300 mm, maximum ULS vertical load $R_{Ed} = 3250$ kN, quasi-permanent vertical load $R_{qp} = 1400$ kN). To limit transverse displacements at the abutments — thereby simplifying the expansion joint arrangement — a unidirectional bearing and a multidirectional bearing are provided at each abutment (Fig. 6).

Friction pendulums suit this case due to their low horizontal stiffness compared to other common isolators, such as rubber bearings, maximizing the reduction of horizontal actions. Other solutions, like fluid dampers, were discarded as less economical for short spans, where multiple small isolator bearings can instead be placed.

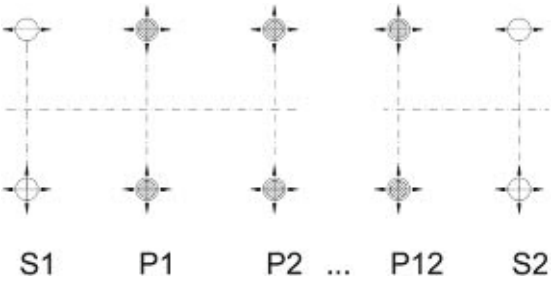


Fig. 6. Seismic isolators layout.

The resulting isolated system exhibits asymmetric behavior under transverse seismic excitation, which necessarily requires a nonlinear time-history analysis by direct integration of the equations of motion. This was performed on seven pairs of spectrum-compatible accelerograms in accordance with the requirements of §3.2.3 of EN 1998–2 [7].

2.5 Foundations

The consolidation of the piers is carried out by means of micropiles 23 m in length, with tubular steel reinforcement of outer diameter Ø101.6 mm and wall thickness 8 mm, installed in a 200 mm diameter borehole. For the purposes of bearing capacity calculations, the effective length below the pier base is 15 m. The micropiles are arranged in a rectangular grid pattern of 1.0 × 0.8 m centers, with a total of 18 micropiles beneath piers of 2.50 m width and 30 micropiles beneath piers of 4.30 m width.

The micropile heads are connected by a pile cap 0.95 m thick, on which the bearing pedestals supporting the deck are constructed.

With respect to vertical-action resistance, the micropiles are designed as fully independent of the existing structure.

3 Erection Phases

The initial phase of demolishing the road surfacing and partially removing the infill material between the spandrel walls — down to the exposure of the upper face of the masonry arch at the keystone — is carried out with plant operating directly on the existing bridge structure, as are the micropile and pile cap construction works.

The channel of the watercourse being crossed is characterized by an extensive gravel riverbed under low-flow conditions, making it readily accessible to construction plant in safe working conditions. The erection operations were therefore carried out by means of straightforward crane lifts performed by a rubber-tyred mobile crane positioned directly in the riverbed, both for the steel deck elements and for the precast slab panels (Fig. 7), allowing a significant reduction in construction time.



Fig. 7. Erection of the Precast concrete slabs.

4 Conclusions

The new Termini Bridge represents a practical application of the structural bypass concept in bridge construction, whereby a new independent structure is integrated within the existing one without altering its architectural appearance, while fully meeting all safety performance requirements set out by current design standards. This objective was achieved primarily through the adoption of a composite steel-concrete deck, seismically isolated from the existing structure by means of friction pendulum bearings.

The bridge was further realized through the extensive application of prefabrication, employing an all-bolted steel framework and a slab composed of precast panels made composite in-situ.

An aerial view of the completed structure is provided in Fig. 8, while summary data are presented in Table 1.

Table 1. Summary of project information.

Client	ANAS S.p.A.
Main contractor	STEEL CONCRETE S.r.l.
Total construction cost	€4 million
Opening Date	17 December 2024



Fig. 8. Aerial view of the completed bridge.

References

1. Niero L, De Matteis G, Pellegrino C, Zampieri P, Zizi M (2025) Structural assessment, repair, and strengthening of masonry arch bridges: modes of operation and open issues. BER Open: Int J Bridge Eng, Manage Res 2(2)
2. Pettorruso C, Quaglini V (2024) Conceptual Design of Seismic Retrofit of existing bridges by deck isolation: assessment of effectiveness. Appl Sci 14(16):7353
3. Zayas VA, Low SS, Mahin SA (1990) A simple pendulum technique for achieving seismic isolation. Earthquake Spectra 6(2)
4. Garber D, Shahrokhinasab E (2019) ABC-UTC guide for full-depth precast concrete (FDPC) deck panels. Florida International University, Accelerated Bridge Construction University Transportation Center
5. Organte M (2008) Tecniche di Prefabbricazione nella Realizzazione del Ponte sul Piave. Strade Autostrade (4)
6. BSI (2012) Background paper to BS EN 1994–2 and the UK National Annex to BS EN 1994–2
7. CEN (2005) 1998–2 Eurocode 8: Design of structures for earthquake resistance – Part 2: Bridges



AI-Driven Composite Bridge Design Using Machine Learning and Genetic Algorithms

Ali Yousefi[1](✉), Valentina Boretti[1], Umberto Folco[1], Pietro Palumbo[2], Rodolfo Epicoco[1], Daniele Cantelmi[1], Gabriele Bertagnoli[2], and Davide Masera[1]

[1] Masera Engineering Group s.r.l., Turin, Italy
ali.yousefi@masera-eg.com
[2] Department of Structural, Geotechnical and Building Engineering, Politecnico di Torino, Turin, Italy

Abstract. The design of steel-concrete composite bridges requires iterative structural analysis, code-based verification, and optimization processes that can become computationally demanding during the early design stages. This study presents an AI-assisted workflow for preliminary design and optimization of composite bridges using a parametric framework developed to automate structural verification according to Eurocode provisions called EFESTO. It combines a spreadsheet-based user interface with a Python computational backend that performs automated verification of ultimate limit states (ULS), serviceability limit states (SLS), and fatigue, while accounting for time-dependent effects such as creep and shrinkage. In the first phase, the framework incorporates a Genetic Algorithm to identify optimal structural configurations for given bridge parameters. In the second phase, it was used to systematically vary key geometric parameters to generate a database of approximately 2500 bridge configurations, including optimal section dimensions, verification demand-capacity ratios, and structural steel consumption. To accelerate the preliminary design phase, machine learning surrogate models were trained on the generated dataset to predict key design outputs directly from geometric parameters. Three approaches of Gradient Boosting, Random Forest, and Polynomial Regression were evaluated in terms of predictive accuracy for parameters such as girder height and steel consumption. The proposed workflow is demonstrated through a case study where machine learning predictions are used to estimate the design of a new bridge configuration. The predicted solution is subsequently verified and validated through finite element analysis, highlighting the potential of integrating machine learning with parametric design tools to accelerate bridge design.

Keywords: Composite bridges · Structural optimization · Genetic Algorithms · Machine Learning · Parametric design · Eurocode

1 Introduction

Steel-concrete composite bridges represent one of the most efficient structural solutions for medium-span highway crossings, typically in the range of 25 to 75 m, offering favorable combinations of span capacity, construction speed, and material economy [1]. Despite these advantages, the early-stage design of composite bridges remains

© The Author(s), under exclusive license to Springer Nature Switzerland AG 2026
R. Zanon et al. (Eds.): CTA 2026, LNCE 942, pp. 878–889, 2026.
https://doi.org/10.1007/978-3-032-39505-4_76

a demanding process, requiring iterative evaluation of structural configurations under complex loading scenarios, time-dependent material behavior, and multiple limit state verifications. Traditional workflows rely heavily on engineering experience and manual iteration, often resulting in conservative solutions that do not fully exploit available material efficiency [2].

The integration of computational optimization and artificial intelligence into structural engineering has opened new possibilities for automating and accelerating this process. Among metaheuristic methods, Genetic Algorithms (GAs) have demonstrated good effectiveness for structural optimization problems involving discrete design variables, non-differentiable objective functions, and extensive constraint sets derived from code-based verification procedures [3, 4]. Recent research has confirmed the versatility of these methods across a broad range of structural design problems, from reinforced concrete frames and bridges to large-scale skeletal systems, as documented in comprehensive reviews of metaheuristic applications in structural optimization [5, 6]. More recently, surrogate-assisted variants in which machine learning models guide the evolutionary search toward promising regions of the design space have further reduced the computational cost of expensive structural evaluations [7]. Applications to composite bridge cross-section design have grown steadily in recent years, with studies confirming the potential of evolutionary strategies to identify material-efficient girder geometries under realistic fabrication and design constraints [8, 9]. However, most existing approaches simplify or omit critical aspects of composite bridge behavior, like time-dependent effects such as creep and shrinkage [10], lateral-torsional buckling, and fatigue assessment, limiting their applicability to full Eurocode-compliant design practice.

A complementary and increasingly active research direction applies machine learning (ML) surrogate models to structural engineering tasks, enabling the rapid prediction of design outputs from geometric and loading parameters without repeated execution of full analysis routines [11]. Surrogate models trained on databases of optimized solutions have shown strong predictive performance for a range of structural systems, offering a promising pathway to knowledge-based preliminary design. However, in the domain of composite bridge design, the combination of a GA-based optimization engine with systematic database generation and ML-based prediction has not yet been demonstrated in an integrated, code-compliant framework.

This paper presents an integrated AI-assisted workflow built on EFESTO, a parametric framework for the automated analysis and optimization of simply supported composite bridges [12]. The framework integrates Courbon's transverse load distribution theory [13], staged construction time-dependent analysis, and full Eurocode verification of ULS, SLS and fatigue limit states within a GA optimization engine. In the work presented here, EFESTO is applied systematically across a broad design space defined by span lengths from 10 to 60 m and deck widths from 6 to 35 m, generating a database of 2,485 optimized bridge configurations. Three machine learning surrogate models of Gradient Boosting, Random Forest, and Polynomial Ridge Regression are trained on this database to predict steel consumption and girder height directly from geometric parameters. The resulting workflow, including a Streamlit-based interactive interface, enables engineers to obtain reliable preliminary design estimates within seconds, subsequently verified and validated through full EFESTO analysis and finite element modeling. The

central idea of the proposed workflow lies in this coupling. The genetic algorithm delivers rigorous, Eurocode-compliant optimization, but to be more compatible with the rapid, exploratory nature of early-stage design, the surrogate models learn to reproduce the optimal outcomes almost instantaneously. This synergy, where optimization generates trustworthy training data and surrogates deliver real-time prediction, is the core contribution of this work.

2 The EFESTO Framework

The system is structured as a modular three-tier architecture that separates user interaction, structural analysis, and optimization logic, providing a transparent and accessible working environment that augments rather than replaces engineering judgment. Specifically, the engineer retains full control over the design process: they define the project requirements, material choices, load scenarios, and admissible design ranges, review the intermediate optimization outcomes, and make the final design decision. The framework supports engineers' decisions by automatically evaluating multiple feasible bridge configurations and presenting their optimized solutions, governing demand-capacity ratios, steel consumption, and geometric characteristics.

2.1 System Architecture

The computational backend is written in Python, while the user interface is implemented in Microsoft Excel with VBA macros, providing an accessible environment for defining all project data without requiring programming expertise. Input parameters include bridge geometry, material properties, environmental exposure conditions, load definitions including permanent loads, traffic Load Model 1 (LM1), Fatigue Load Model 1 and 3 (FLM1 and FLM3), and Genetic Algorithm optimization settings such as population size and number of generations.

2.2 Structural Analysis and Verification Engine

The Python analysis engine performs Eurocode-compliant structural analysis of composite I-girder bridges under all relevant load combinations. Time-dependent behavior is modeled through a staged construction analysis that accounts for concrete hardening, creep, and shrinkage in accordance with EN 1992-1-1 [14]. Permanent and variable loads are evaluated according to EN 1994-1-1 [15] and EN 1993-1-1 [16], with traffic actions applied according to EN 1991-2 [17].

The verification suite performs automated cross-section classification and covers all mandatory limit state checks: ULS bending resistance, shear resistance, lateral-torsional buckling, and interaction effects; SLS stress limits, deflection limits, and web breathing; fatigue verification based on damage-equivalent stress ranges. All checks are expressed as Demand/Capacity ratios $\eta i \leq \eta i, \max$, providing a consistent and quantitative measure of structural adequacy that is directly exploitable within the optimization engine.

To improve material efficiency along the span, EFESTO supports multi-segment girder configurations of 1, 3, or 5 symmetric segments, defined by the user as part of

the project input. This allows each region of the girder to be dimensioned according to local internal force demands: mid-span segments are typically governed by bending and require sections with wider flanges, while support segments are governed by shear, favoring adjusted web thickness and flange proportions. For multi-segment bridges, the optimization is executed sequentially, the mid-span segment first, followed by the support segment, with each optimization run requiring only 2–3 min of computational time. To preserve geometric continuity and avoid abrupt structural steps between adjacent segments, the Beam height is held constant along the entire girder, fixed at the value determined during the mid-span optimization. The support segment consequently retains the same height, while its remaining variables are optimized independently but constrained within a user-defined range around the corresponding mid-span dimensions to limit the magnitude of the cross-sectional transition.

2.3 Genetic Algorithm Optimization Engine

Optimization is performed using a Genetic Algorithm that interacts directly with the analysis engine to evaluate candidate cross-sections. Each individual in the population encodes a design vector of six discrete variables representing the steel I-girder geometry: $x = [b_{f,\,top}, t_{f,\,top}, h_w, t_w, b_{f,\,bot}, t_{f,\,bot}]$, where b_f and t_f are flange widths and thicknesses, and h_w and t_w are web height and thickness respectively. Each variable is restricted to a user-defined discrete set of commercially available values, ensuring that all optimized solutions correspond to manufacturable cross-sections. The total number of possible combinations in the design space typically ranges from 10^{10} to 10^{15}, confirming the suitability of evolutionary search.

The objective function minimizes the total steel cross-sectional area, directly proportional to material cost. The fitness function receives a penalty if constraints are violated. Formally, the fitness of an individual is defined as:

$$F(x) = f(x) + P \times \max\left\{0,\, \eta_i(x) - \eta_{i,\max}\right\} \tag{1}$$

where $f(x)$ is the steel cross-sectional area, $\eta_i(x)$ is the demand-capacity ratio of the verification i, $\eta_{i,\,max}$ is its user-defined admissible limit, and $P = 10^6$ is a large penalty coefficient [12]. Geometric constructability constraints, including flange proportionality rules and slenderness limits consistent with AASHTO provisions, are enforced through a repair function applied after each genetic operation, maintaining population feasibility throughout the search process.

The GA operators consist of tournament selection with a pool size of 3, arithmetic crossover with 70% probability, and a two-stage probabilistic mutation in which each individual enters mutation with 40% probability and each gene is independently replaced with 40% probability if mutation is triggered. Population size and generation count were calibrated through sensitivity studies across multiple bridge configurations, with values of 1,000 individuals and 50 generations selected as providing the best balance between solution quality and computational efficiency.

When the number of main girders is not prescribed by the user, EFESTO automatically generates and independently evaluates multiple framing cases within feasible girder spacing bounds, enabling direct comparison of structural efficiency, expressed as total steel consumption in kg/m^2, across alternative configurations for the same bridge.

3 Database Generation

3.1 Parametric Design Space

EFESTO was applied systematically across a broad parametric design space defined by span length L and deck width W to build a comprehensive dataset of optimized composite bridge configurations. Span lengths varied from 10 to 60 m in steps of 2 m, and deck widths from 6 to 35 m in steps of 1 m. For each combination of L and W, the number of main girders was determined by feasible girder spacing bounds, with a minimum spacing of 1.5 m and a maximum of 8 m. The transverse outer cantilever length of the slab was constrained to a maximum of 2.5 m, with a cantilever-to-spacing ratio not exceeding 0.6. These rules reflect realistic construction practice and ensure that all generated configurations correspond to structurally and geometrically feasible bridge layouts.

A minimum L/W ratio of 1.5 was considered to exclude wide bridges as they are not compatible with Courbon theory. Consequently, the populated region of the parametric space takes a triangular shape, as visible in Fig. 1. This approach generated a total of 2,485 distinct bridge configurations; each treated as an independent optimization problem.

All configurations shared a common set of non-geometric input assumptions, kept constant throughout the database generation process to ensure comparability of results. These include material grades (S355 steel and C35/45 concrete), permanent loads from curbs and barriers, wind load, temperature effects, and traffic actions. Fatigue assessment was performed using Fatigue Load Model 3 in all cases, representing a deliberately uniform verification baseline across the entire database.

3.2 Segmentation and Optimization Strategy

The number of longitudinal segments per girder was assigned based on span length, reflecting a practical design decision aimed at balancing material efficiency with fabrication complexity. Bridges with spans of 10 and 12 m were optimized as single-segment configurations, spans between 14 and 30 m were assigned to three symmetric segments, and spans between 32 and 60 m were assigned to five symmetric segments. These rules represent the choices made for database generation and do not constitute constraints of EFESTO itself, which accepts segmentation as a free user-defined input parameter.

3.3 Database Contents and Output Variables

Each record in the database corresponds to a single optimized bridge configuration and stores the following primary output variables:

- steel consumption in kg/m^2 (*Incidenza* in Italian), defined as the total distributed steel weight per unit deck area, including longitudinal girders, transverse beams, bracing system, and a 15% allowance for connections and secondary elements;
- midspan beam height (m);
- the governing Demand/Capacity ratio and its corresponding verification check;
- the full optimized cross-section dimensions for each segment.

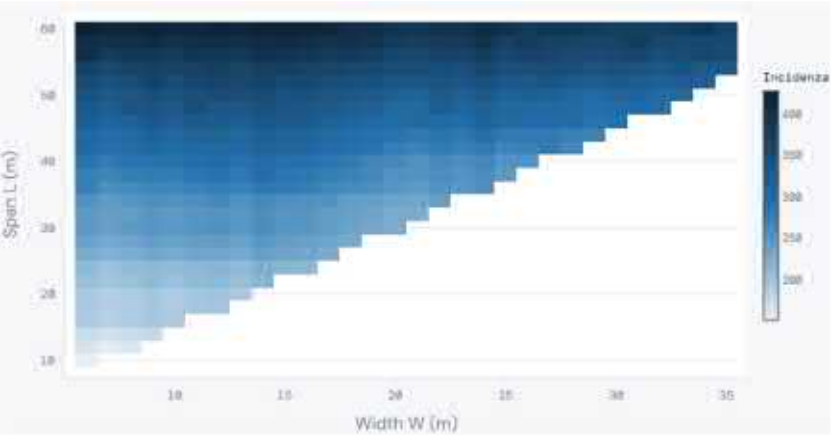


Fig. 1. Average steel consumption (kg/m^2) across the EFESTO database as a function of span length L and deck width W.

Figure 1 presents heatmaps of the average steel consumption across the database, plotted as functions of L and W and averaged over all feasible girder configurations for each L-W pair. Steel consumption increases strongly with span length, driven by the growth of bending moment demand, and shows a slightly decreasing trend with deck width.

4 Machine Learning Surrogate Models

4.1 Motivation and Workflow

During preliminary design, engineers often need to rapidly explore dozens of geometric alternatives before committing to a full optimization campaign. The systematic application of EFESTO across 2,485 bridge configurations produces a rich dataset capturing the nonlinear relationships between bridge geometry and optimized structural outcomes. Machine learning surrogate models address this need by approximating the input-output relationships learned from the database, enabling the prediction of key design outputs within seconds from a compact set of geometric parameters. All models were implemented in Python using the scikit-learn library [18].

4.2 Features and Target Variables

The input feature set was defined to include only parameters available to an engineer at the earliest stage of project definition, before any structural analysis is performed: span length L, deck width W, and the number of main girders n. These three variables collectively characterize the bridge geometry and constitute the minimum information required to obtain a prediction of structural steel demand.

Two target variables were defined for independent regression: steel consumption (kg/m^2), serving as the primary economic indicator for preliminary design comparison;

and beam height (m), representing the governing geometric output for vertical clearance planning and structural depth estimation.

4.3 Model Selection and Training

Three individual regression approaches were evaluated. Gradient Boosting Regression (GBR) constructs an ensemble of shallow decision trees sequentially, where each tree corrects the residual errors of the previous one, capturing complex nonlinear relationships and feature interaction effects without explicit feature engineering [19]. Random Forest Regression (RFR) builds an ensemble of independently trained decision trees on bootstrapped subsamples of the training data and aggregates predictions by averaging, providing natural robustness against overfitting [20]. Polynomial Ridge Regression (PRR) extends linear regression by expanding the feature space with polynomial interaction terms combined with L^2 regularization, providing a smooth and interpretable prediction surface that is advantageous for capturing global trends.

The dataset of 2,485 records was partitioned into training and test sets using an 80/20 stratified split. Hyperparameters for all models were tuned using 5-fold cross-validation on the training set [21], with cross-validation R^2 standard deviations below 0.006 for all models and targets, confirming stable generalization performance across folds.

4.4 Predictive Performance

The predictive accuracy of all models is summarized in Table 1, reporting R^2 and Root Mean Square Error (RMSE) on the held-out test set for both target variables.

Table 1. Predictive performance of surrogate models on the held-out test set.

Model	Steel Consumption [kg/m^2]		Beam Height [m]	
	R^2	RMSE	R^2	RMSE
Gradient Boosting	0.989	7.46	0.958	0.111
Random Forest	0.989	7.55	0.957	0.112
Polynomial Ridge	0.987	7.95	0.955	0.115

All three models achieve very high predictive accuracy for steel consumption, with R^2 values between 0.987 and 0.990 and RMSE values below 8.0 kg/m^2, confirming the strong and learnable structure of steel consumption as a function of bridge geometry. Performance on beam height is slightly lower but remains excellent, with R^2 values between 0.955 and 0.960 and RMSE below 0.12 m across all models. The three individual

models perform comparably, with Gradient Boosting showing a marginal advantage over Random Forest and Polynomial Ridge for both targets.

Analyzing feature importance on the models confirms that span length L is the dominant predictor for both steel consumption and beam height, which is physically consistent with structural behavior and confirms that the models have captured meaningful engineering relationships rather than spurious correlations.

Figure 2 shows the Gradient Boosting model prediction of steel consumption as a function of span length L for W = 10 m and 4 main girders, overlaid on the corresponding EFESTO database points. The model closely follows the database values across the full span range from 10 to 60 m, capturing both the overall increasing trend and the local variations associated with segmentation transitions.

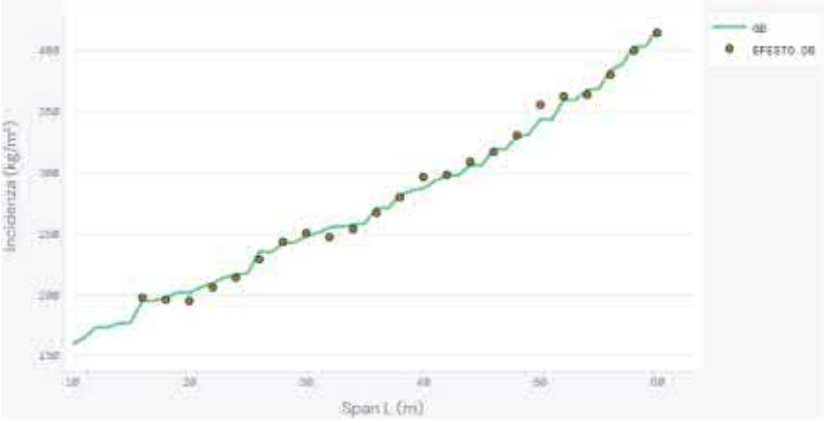


Fig. 2. Gradient Boosting model prediction of steel consumption vs. span length L for W = 10 m and 4 main girders, overlaid on EFESTO database points.

4.5 Interactive Design Interface

A web-based interface was developed using the Streamlit framework to make the surrogate models and the underlying database accessible to practicing engineers without requiring direct interaction with optimization or machine learning code. As shown in Fig. 3 the interface is organized into several integrated panels. The prediction panel accepts L, W, and the number of girders as inputs and returns instantaneous predictions of steel consumption and beam height from all three individual models, ranked by their deviation from the closest database record. When an exact match exists in the database, the corresponding EFESTO-optimized result is displayed as the ground-truth reference alongside the ML predictions, along with the full optimized cross-section geometry rendered as an SVG diagram. Additional panels provide interactive correlation charts including steel consumption vs. L and W for user-selected configurations, and heatmap views of the full database, supporting rapid sensitivity assessment during the scoping phase of a project.



Fig. 3. EFESTO-ML interface showing prediction panel, with ML predictions for steel consumption and beam height, database ground truth, and optimized cross-section diagram.

5 Case Study: AI-Assisted Design

5.1 Bridge Configuration and Design Approach

The case study considers a real simply supported composite bridge project with a span of L = 44 m, a deck width of W = 6 m, and two main steel I-girders acting compositely with a reinforced concrete slab. Given the span length, five symmetric longitudinal segments are adopted. This bridge configuration corresponds to an exact record in the EFESTO database, providing a direct reference between database output, ML prediction, and a dedicated full design run with real project-specific loads. The case study is presented as a three-stage engineering workflow representative of real practice:

1. In the first stage, the database and ML surrogate models provide an immediate preliminary estimate of steel consumption and beam geometry, sufficient for early feasibility assessment and cost budgeting.
2. In the second stage, EFESTO is run with the actual project-specific loads, which differ from the uniform database assumptions in terms of wind intensity, barrier geometry, and curb dimensions, to produce a fully Eurocode-compliant optimized design. This stage corresponds to the feasibility and preliminary design phase (*PFTE* in Italy).
3. In the third stage, corresponding to the executive design phase (*PE* in Italy), a detailed finite element model is developed in MIDAS Civil NX for final verification and design validation.

This workflow reflects the natural progression of bridge design from conceptual estimation to fully verified engineering deliverables.

5.2 Preliminary Estimate from Database and ML Surrogates

The configuration L = 44 m, W = 6 m and n = 2 corresponds to an exact match in the database, thus the interface returns both the database ground truth record and the ML model predictions for direct comparison. The database record reports steel consumption

of 257 kg/m^2 and a midspan beam height of 2.4 m, while the RF model predicts steel consumption of 260 kg/m^2 and a midspan beam height of 2.6 m. These results confirm the good accuracy of the surrogate model. The Stage 1 estimate is obtained within seconds, while the EFESTO run requires 3 min.

5.3 Full EFESTO Design

In the second stage, EFESTO was run with the actual project loads. The GA optimization converged to the optimized cross-section dimensions summarized below, with the midspan and support segments optimized sequentially.

- Midspan segment = [450, 20, 2645, 18, 700, 35] mm,
- Support segment = [450, 20, 2655, 18, 500, 25] mm

The optimized design achieves a total steel consumption of 270 kg/m^2, compared to the database reference of 257 kg/m^2. The difference of 13 kg/m^2 (approximately 5%) is attributable to the heavier project-specific permanent loads. The governing verification is fatigue stress, with a Demand/Capacity ratio of 99.6%, confirming that fatigue governs the design for this span range as consistently observed across the database for long spans.

5.4 FEM Validation for Delivery

In the third stage, the optimized configuration was modeled in MIDAS Civil NX using a grillage approach, incorporating the full deck geometry, loads and design combos. Table 2 reports the results for one of the two main girders.

Table 2. Comparison of bending moments and shear between EFESTO and FEM.

Load case	Bending Moment [kN.m]			Shear [kN]		
	EFESTO	FEM	Δ (%)	EFESTO	FEM	Δ (%)
G1 + G2	9651	9416	2.5	877	871	0.7
Traffic LM1	9253	9011	2.7	847	842	0.5
ULS combination	26591	26217	1.4	2425	2416	0.4

The results demonstrate very good agreement between the simplified Courbon-based analytical model and the detailed finite element analysis across all load cases. EFESTO consistently predicts slightly higher internal forces than the FEM model, with deviations of 2.5% under permanent loads, 2.7% under traffic loading, and 1.4% under the governing ULS combination. This conservative bias results from the Courbon load distribution assumptions. The FEM model confirms the structural adequacy of the optimized solution.

6 Conclusion

This paper presented an integrated AI-assisted workflow for the rapid preliminary design and optimization of simply supported steel-concrete composite bridges, built on a parametric framework combining Eurocode-compliant structural analysis with Genetic Algorithm optimization. The work extends the capabilities of the framework in two significant directions: the systematic generation of a large database of optimized bridge configurations and the development of machine learning surrogate models capable of predicting key design outputs directly from geometric parameters.

The database of 2,485 optimized configurations, generated by applying EFESTO across a broad parametric space of span lengths from 10 to 60 m and deck widths from 6 to 35 m, constitutes a structured and physically consistent repository of composite bridge design knowledge. Each record encodes not only optimized cross-section dimensions but also steel consumption, governing verification checks, and Demand/Capacity ratios, providing a multidimensional resource for both data-driven modeling and direct engineering reference.

Three machine learning surrogate models were trained on the database to predict steel consumption and beam height. All models achieved high predictive accuracy. The analysis confirmed that span length is the dominant predictor for both targets.

A case study demonstrated the practical applicability of the three-phase workflow: ML predictions, full EFESTO optimization, and finite element modelling. Results showed close agreement between all three stages, with deviations below 5% for steel consumption and below 3% for internal forces. The close agreement between all three levels of analysis highlights the potential of this approach to dramatically compress the preliminary design timeline for composite bridge structures, while maintaining full compliance with Eurocode provisions and transparency of the structural verification process. The interactive interface makes the entire workflow accessible to practicing engineers without requiring direct interaction with optimization or machine learning code, allowing an easy professional design adoption.

References

1. Johnson RP (2018) Composite structures of steel and concrete: beams, slabs, columns and frames for buildings, 4th edn. Wiley-Blackwell, Oxford
2. Fragiacomo M, Amadio C, Macorini L (2004) Finite-element model for collapse and long-term analysis of steel-concrete composite beams. J Struct Eng ASCE 130(3):489–497
3. Kaveh A (2017) Applications of metaheuristic methods in civil engineering. Springer International Publishing, Switzerland
4. Bertagnoli G, Giordano L, Mancini S (2014) Optimization of concrete shells using genetic algorithms. Z Angew Math Mech 94(1–2):43–54. ISSN 0044-2267
5. Lagaros ND, Plevris V, Kallioras NA (2022) The mosaic of metaheuristic algorithms in structural optimization. Arch Comput Methods Eng 29(7):5457–5492
6. Kaveh A, Mottaghi L, Izadifard R (2022) Optimal design of a non-prismatic reinforced concrete box girder bridge with three meta-heuristic algorithms. Sci Iran 29(3):1154–1167
7. Prayogo H, Yang I-T (2024) Dynamic gradient boosted metaheuristic approach for efficient reinforced concrete structure optimization. J Build Eng 97

8. Martí JV, González-Vidosa F, Yepes V, Alcaá J (2013) Design of Prestressed Concrete Precast Road Bridges with hybrid simulated annealing. Eng Struct 48:342–352
9. Alberdi R, Murren P, Khandelwal K (2015) Connection topology optimization of steel moment frames using metaheuristic algorithms. Eng Struct 100:276–292
10. Lopes AV, Lopes SMR, Moreira AACM (2015) A parametric study on the optimal design of composite steel-concrete beam systems. Structure 4:49–59
11. Salehi H, Burgueño R (2018) Emerging artificial intelligence methods in structural engineering. Eng Struct 171:170–189
12. Yousefi A et al (2026) A genetic algorithm-based tool for optimizing composite bridge design. In: Proceedings of international structural engineering and construction, vol 13. ISEC Press. [accepted, in press]
13. Courbon J (1940) Calcul des ponts à poutres multiples solidarisées par des entretoises. Ann Ponts Chaussées 17:293–322
14. CEN (2004) Eurocode 2: design of concrete structures — part 1–1: general rules and rules for buildings, EN 1992-1-1. European Committee for Standardization, Brussels
15. CEN (2004) Eurocode 4: design of composite steel and concrete structures — part 1–1: general rules and rules for buildings, EN 1994-1-1. European Committee for Standardization, Brussels
16. CEN (2005) Eurocode 3: design of steel structures — part 1–1: general rules and rules for buildings, EN 1993-1-1. European Committee for Standardization, Brussels
17. CEN (2003) Eurocode 1: actions on structures - part 2: traffic loads on bridges, EN 1991–2. European Committee for Standardization, Brussels
18. Pedregosa F, Varoquaux G, Gramfort A et al (2011) Scikit-learn: machine learning in python. J Mach Learn Res 12:2825–2830
19. Friedman JH (2001) Greedy function approximation: a gradient boosting machine. Ann Stat 29(5):1189–1232
20. Breiman L (2001) Random forests. Mach Learn 45(1):5–32
21. Hastie T, Tibshirani R, Friedman J (2009) The elements of statistical learning: data mining, inference, and prediction, 2nd edn. Springer

Analytical and Empirical Fragility Assessment of Italian Single-Storey Steel Industrial Structures

Antonio Davino, Emilia Meglio, Iolanda Cerbone, Gianmaria Di Lorenzo, Antonio Formisano(✉), and Raffaele Landolfo

Department of Structures for Engineering and Architecture, Polytechnic and Basic Sciences School, University of Naples Federico II, Naples, Italy
antoform@unina.it

Abstract. This study presents a comprehensive numerical investigation aimed at evaluating the seismic vulnerability of single-storey steel industrial buildings representative of the Italian building stock. A simulation framework was developed based on the technological evolution of industrial construction in Italy, considering structural geometry, truss typology, environmental loading conditions, and construction period as the main parameters influencing seismic response. The combination of these variables led to the generation of 336 structural configurations. For each building, member sections were determined through a simulated design procedure consistent with the regulations in force at the time of construction. Finite element models were then developed and subjected to nonlinear static analyses to derive capacity curves in the principal directions. Subsequently, analytical fragility curves were obtained to estimate the probability of reaching different damage states as a function of Peak Ground Acceleration (PGA). These results were compared with fragility curves derived using empirical formulations available in literature. The comparison allowed a critical assessment of the consistency and reliability of different seismic damage estimation approaches. Furthermore, the study validated a new empirical formulation for the derivation of transverse-direction fragility curves, showing improved predictive capability for the considered structural typology.

Keywords: Seismic Vulnerability · Steel Structures · Industrial Buildings · Nonlinear static analysis · Fragility Curves

1 Introduction

A large portion of the existing Italian building stock was constructed before the introduction of modern seismic design provisions. According to ISTAT statistics, nearly 60% of Italian buildings were constructed before the enactment of the first nationwide seismic code in 1974 [1]. While seismic design requirements were formally introduced in that year, a comprehensive seismic classification of the entire national territory was achieved only in 2002, in the aftermath of the San Giuliano di Puglia earthquake. As

© The Author(s), under exclusive license to Springer Nature Switzerland AG 2026
R. Zanon et al. (Eds.): CTA 2026, LNCE 942, pp. 890–900, 2026.
https://doi.org/10.1007/978-3-032-39505-4_77

a consequence, a large share of the existing building stock was conceived and built without specific seismic design provisions, resulting in a significant level of structural vulnerability.

Among these structures, industrial buildings constitute a substantial portion of the national building stock and play a strategic role in the Italian economic and productive system. A large percentage of these facilities were constructed between the 1960s and the 1990s [2], often according to design approaches based exclusively on gravity and wind loads. Their seismic vulnerability became evident during recent earthquake events, particularly during the 2012 Emilia-Romagna seismic sequence, which caused extensive damage to industrial facilities and led to severe economic losses due to production interruptions and building inoperability [3–5]. Despite the generally satisfactory performance exhibited by steel structures compared with other construction typologies, these events highlighted the necessity of developing reliable methodologies for assessing the seismic vulnerability of existing industrial buildings [6, 7].

The present work contributes to this objective through the development and application of a comprehensive simulation framework for single-storey steel industrial buildings representative of the Italian construction practice. The proposed methodology considers buildings originally designed for non-seismic areas and investigates the influence of structural typology, geometric configuration, steel grade, and loading conditions on seismic performance. Nonlinear static analyses are performed to derive capacity curves and analytical fragility functions, which are subsequently compared with empirical fragility relationships available in literature. Particular attention is devoted to the calibration of a modified empirical formulation capable of improving the prediction of seismic damage probabilities for industrial steel buildings characterized by an inverted-pendulum structural behavior.

2 Simulation Framework

The simulation framework was developed to evaluate the seismic vulnerability of single-storey steel industrial buildings representative of the Italian industrial building stock. The proposed approach is based on the definition of prototype building families generated through the systematic combination of a limited number of parameters governing both structural capacity and seismic demand. By adopting a parametric methodology rather than focusing on individual case studies, it is possible to obtain a comprehensive overview of the seismic behavior of this structural typology and to identify recurring vulnerability patterns.

The simulation program is summarized by the matrix shown in Fig. 1. The matrix was established following an extensive review of the technological and typological evolution of industrial steel buildings and covers approximately one century of construction practice. The columns are organized according to the construction period, the associated structural typology, and the steel grades commonly employed during each historical phase. Five construction periods were considered, namely pre-1900, 1900–1930, 1930–1960, 1960–1990, and post-1990. For each period, the structural systems most representative of the prevailing construction practice were identified [8]. In particular, Type 1 and Type 2 refer to Howe and Polonceau trusses, respectively, SPT and DPT denote

single-span and double-span Pratt truss configurations, and P identifies portal-frame structures. The steel grades associated with each period reflect the historical evolution of construction materials, ranging from cast iron and early homogeneous steel to Aq, Fe, and modern S-grade steels.

The rows of the matrix define the parameters governing the structural demand. Three structural grid configurations, denoted as C1, C2, and C3, were considered. These configurations correspond to different combinations of span length, column height, and longitudinal bay spacing, representative of typical industrial layouts. Seven span classes were introduced, identified as L1 to L7 and corresponding to span lengths ranging from 10 m to 50 m. In addition, three loading scenarios were considered, namely low, medium and high, corresponding to equivalent gravity loads of 0.5, 1.0, and 1.5 kN/m^2, respectively. These loading levels were defined to account for different environmental and service conditions, including snow loads and the possible presence of overhead cranes.

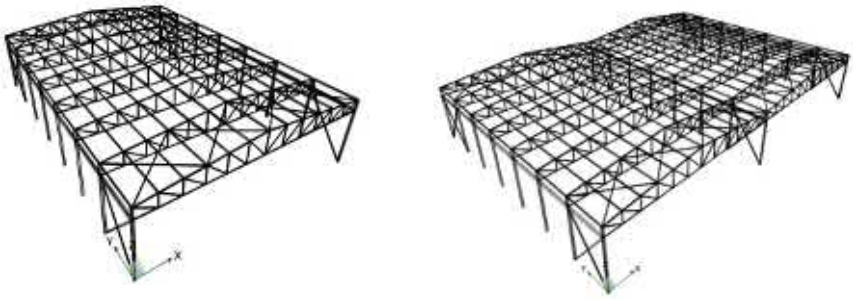
The combination of construction period, structural typology, steel grade, geometric configuration, and loading scenario generates the complete simulation program, consisting of 336 potential structural configurations. Not all combinations were considered physically meaningful or representative of actual construction practice; therefore, the matrix includes excluded configurations, shown by cross-marked cells in Fig. 1. For example, configurations consisting of double-span Pratt trusses (DPTs) with span lengths of 40 m or 50 m are uncommon in the Italian building stock. Consequently, they were excluded from the investigation and are identified by a cross in the matrix.

The remaining cells identify the prototype buildings considered suitable for vulnerability assessment.

The present study focuses on the subset of configurations highlighted in Fig. 1, corresponding to industrial buildings constructed between 1960 and 1990 and characterized by Pratt lattice-girder roof systems. Within this period, two structural typologies were investigated: SPT, consisting of single-span Pratt trusses, and DPT, consisting of double-span Pratt trusses (see Fig. 2). For each typology, different combinations of geometric parameters, loading levels, and steel grades (Fe360, Fe430, and Fe510) were considered, generating the dataset of prototype buildings analyzed in this work.



Fig. 1. Simulation matrix for the parametric investigation of single-storey steel industrial buildings.



(a) (b)

Fig. 2. Structural typologies under investigation: (a) single-span Pratt trusses (SPT), and (b) double-span Pratt trusses (DPT).

3 Structural Modelling and Analyses

3.1 Simulated Design

Before performing the seismic assessment, all prototype buildings included in the investigated subset of the simulation framework were subjected to a simulated design procedure aimed at determining the cross-sections of the structural members. The objective of this phase was to reproduce, as realistically as possible, the design practice adopted during the historical period considered, thereby obtaining structural configurations representative of the actual Italian industrial building stock.

Since the present study focuses on buildings constructed between 1960 and 1990, the design procedure was carried out according to the regulations in force during that period. In particular, the structural members were designed following the allowable stress method prescribed by the CNR-UNI 10011 standard [9]. The design process considered only the actions typically accounted for in non-seismic design practice, namely permanent loads, environmental loads, and wind actions, consistently with the assumption that the analyzed buildings were originally conceived for non-seismic areas.

For each configuration generated within the simulation framework, the design loads were assigned according to the corresponding geometric layout and loading scenario. Three levels of equivalent gravity loads were considered, accounting for different environmental and service conditions. In addition, a uniform wind pressure was applied to all configurations to reproduce the horizontal actions typically governing the design of industrial steel buildings during the considered period.

The structural members were then sized through iterative calculations aimed at satisfying the strength, stability and deformability requirements prescribed by the code. In the generated structural configurations, IPE sections were adopted for roof purlins, HEA sections for columns, while coupled UPN profiles were used for truss members and both roof and vertical bracing systems. The resulting cross-sections, therefore, reflected the combined influence of geometry, loading level, steel grade, and construction practice.

3.2 Nonlinear Static Analyses

Following the simulated design phase, all prototype buildings were modelled in the finite-element software SAP2000 and subjected to nonlinear static analyses. The numerical models were developed using frame elements to represent the primary structural members, including columns, roof trusses, purlins, and bracing systems. The geometry, material properties, and member cross-sections were assigned according to the results of the simulated design procedure described in the previous section.

The nonlinear behavior of the structures was introduced through the assignment of concentrated plastic hinges in the critical members governing the lateral response. In the transverse direction, where the structural response is mainly controlled by the inverted-pendulum seismic scheme, flexural plastic hinges were assigned at the base of the columns. In the longitudinal direction, seismic resistance is primarily provided by the concentric bracing systems located within the vertically braced bays, and, therefore,

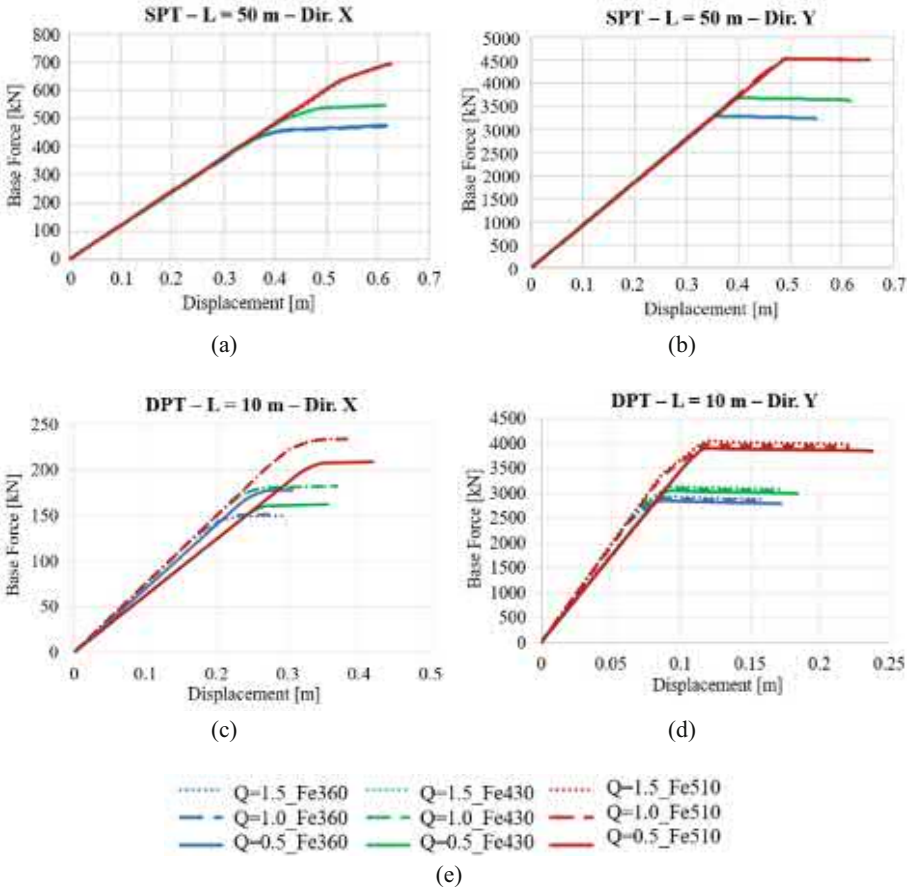


Fig. 3. Representative capacity curves: (a) SPT in X-direction, (b) SPT in Y-direction, (c) DPT in X-direction, (d) DPT in Y-direction and (e) legend.

axial plastic hinges were assigned to the diagonal members to simulate yielding under tension forces.

Nonlinear static analyses were performed independently along the two principal directions of the buildings. Lateral forces proportional to the first-mode shape were progressively applied until significant strength degradation or collapse mechanisms developed. The results of the analyses were expressed in terms of capacity curves relating to the base shear force versus the control-node displacement. These curves provide a synthetic representation of the global nonlinear response and constitute the basis for the subsequent derivation of analytical fragility curves. Overall, both structural typologies exhibit a significantly higher seismic capacity in the longitudinal direction (Y) than in the transverse direction (X). Moreover, the capacity curves clearly demonstrate the influence of steel grade on the structural response, with higher-strength steels generally leading to increased load-carrying capacity. Representative capacity curves for a single span length are shown in Fig. 3 for both the single-span Pratt truss (SPT) and double-span Pratt truss (DPT) configurations, considering the two principal structural directions.

4 Fragility Assessment

4.1 Analytical and Empirical Approaches

The fragility curves represent one of the most effective tools for quantifying the seismic vulnerability of structures, as they express the probability of reaching or exceeding a given damage state as a function of seismic intensity. In the present study, the seismic demand is characterized by the Peak Ground Acceleration (PGA), allowing for the seismic performance of the investigated buildings to be evaluated independently of the specific seismic classification of the site. Three performance levels were considered, namely Immediate Occupancy (IO), Life Safety (LS), and Near Collapse (NC).

To investigate the reliability of different vulnerability assessment procedures, fragility curves were derived using both empirical and analytical approaches [11]. The empirical methodology relies on probabilistic formulations commonly adopted in literature and calibrated on observed damage data from past earthquakes. In particular, the fragility functions were constructed according to the FEMA 365 (2000) formulation [10], in which the probability of exceeding a given damage state is expressed through a lognormal cumulative distribution function, as illustrated in Eq. (1):

$$P\left(d_s \geq d_{si}/PGA\right) = \varphi\left[\left(1/\beta d_s\right)\cdot \ln\left(ag/ag_{dsi}\right)\right] \tag{1}$$

where ag_{dsi} denotes the median PGA associated with the attainment of damage state (d_{si}), β is the logarithmic standard deviation, and φ is the cumulative standard normal distribution function.

The analytical approach was instead based on the nonlinear static analyses described in the previous section. For each structural configuration, fragility curves were derived by comparing seismic demand and structural capacity. The latter was obtained from the pushover analyses, whereas the seismic demand was evaluated through the performance-point procedure. Unlike empirical formulations, this approach explicitly accounts for the

geometry, material properties, structural layout, and nonlinear response of the examined buildings, thus providing a more physically based estimate of seismic performance.

The comparison between empirical and analytical fragility curves constitutes the basis of the proposed methodology. Such comparison enables the evaluation of the applicability of existing empirical formulations to single-storey steel industrial buildings and provides the basis for the calibration of a modified empirical relationship specifically developed for the structural typologies considered in this study.

4.2 Results and Calibration of the Proposed Empirical Formulation

The comparison between the analytical and empirical fragility curves revealed markedly different behavior in the two principal structural directions. In the longitudinal direction (Y), the empirical approach generally provided conservative estimates of the seismic damage probability, yielding fragility curves characterized by higher exceedance probabilities than those obtained through nonlinear analyses. Conversely, in the transverse direction (X), the opposite trend was observed: the analytical curves predicted higher damage probabilities than the empirical ones, indicating that the standard empirical formulation may underestimate the seismic vulnerability of the investigated structures.

This discrepancy can be attributed to the peculiar structural behavior of single-storey steel industrial buildings. In the transverse direction, the seismic response is primarily governed by portal-frame mechanisms characterized by an inverted-pendulum behavior, which differs substantially from that of the multi-storey buildings on which the original Hazus-based formulation was calibrated. As a result, the direct application of the standard empirical model does not adequately reproduce the actual vulnerability of the examined structural typologies.

To overcome this limitation, a modified empirical formulation was introduced and calibrated against the fragility curves derived from the analytical procedure. The proposed expression preserves the lognormal probabilistic framework adopted by the original methodology while introducing corrective factors aimed at improving the agreement with the mechanical results, as illustrated in Eq. (2):

$$P\left(d_s \geq d_{si}/PGA\right) = 0.65 \cdot \varphi\left[\left(1/\beta d_s\right) \cdot \ln\left(ag/ag_{dsi}\right) + 2.5\right] \tag{2}$$

The corrective coefficients were determined through an iterative calibration procedure based on the comparison between the analytical fragility curves and those obtained from the original empirical formulation. The calibration aimed to minimize the discrepancy between the two approaches for the transverse response of the investigated building typologies.

The resulting modified fragility curves exhibit significantly improved correspondence with the analytical predictions and provide a more conservative representation of the seismic damage probability for single-storey steel industrial buildings. Consequently, the proposed formulation represents a practical alternative for large-scale vulnerability assessments, allowing the computational efficiency of empirical methods to be maintained while improving their applicability to industrial steel structures.

Representative fragility curves are shown in Fig. 4 for both the single-span Pratt truss (SPT) and double-span Pratt truss (DPT) configurations, considering the two principal

structural directions and highlighting the difference between the standard and modified empirical formulation in the transverse direction (X). In particular, the same span lengths reported for the capacity curves were selected with medium loads and Fe 430 steel grade.

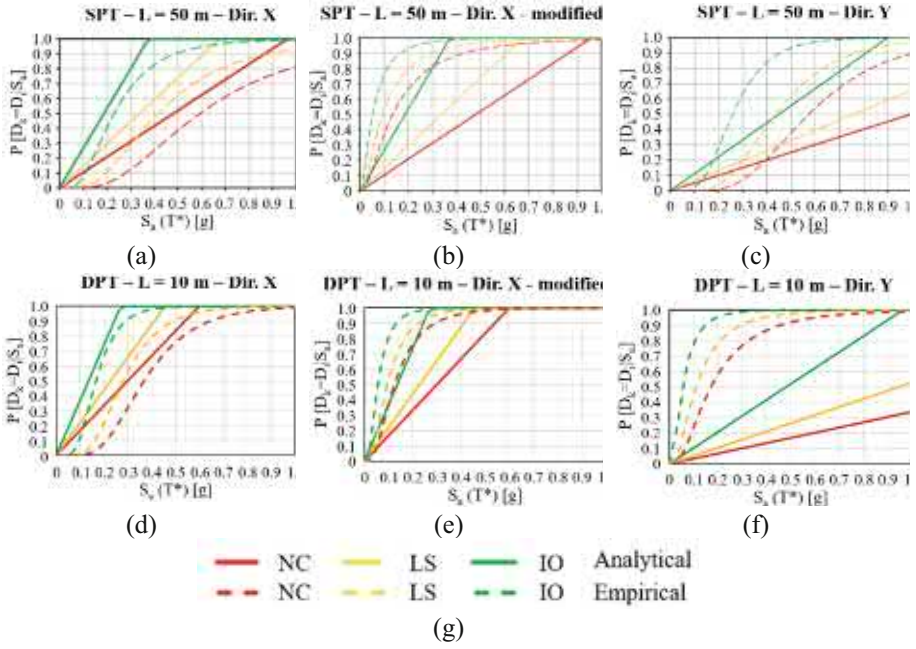


Fig. 4. Representative fragility curves: (a) SPT in X-direction, (b) SPT in X-direction – modified, (c) SPT in Y-direction, (d) DPT in X-direction, (e) DPT in X-direction – modified, (f) DPT in Y-direction and (g) legend.

4.3 Typological Fragility Curves

The large number of structural configurations generated within the simulation framework makes it possible to investigate not only the seismic response of individual prototype buildings but also the vulnerability characteristics of an entire structural typology. To this end, the fragility curves obtained for the different configurations belonging to the same building class were examined jointly to identify common vulnerability trends and evaluate the influence of the considered parameters.

For each damage state, the analytical fragility curves derived for all the investigated configurations were superimposed and compared within the same structural typology. The analysis was performed separately for the SPT and DPT building classes and for the two principal structural directions (X and Y). This procedure allowed the variability associated with span length, steel grade, and loading conditions to be directly visualized, providing a comprehensive overview of the dispersion of the seismic response within each typological class.

The comparison of the superimposed curves enabled the identification of the most vulnerable configuration for each structural typology and loading direction. Rather than defining an average fragility function, the typological fragility curves were conservatively assumed as those corresponding to the most critical configuration within each set of analyzed buildings. This choice ensures that the resulting curves provide a safe-side estimate of the seismic vulnerability of the considered typology while accounting for the variability introduced by the investigated parameters.

The resulting typological fragility curves, therefore, represent the upper-bound vulnerability of the examined SPT and DPT building classes and can be employed in large-scale seismic risk assessments where detailed information on individual structures is not available (see Fig. 5). Furthermore, they constitute a first step towards the development of a national fragility database for Italian single-storey steel industrial buildings designed without seismic provisions.

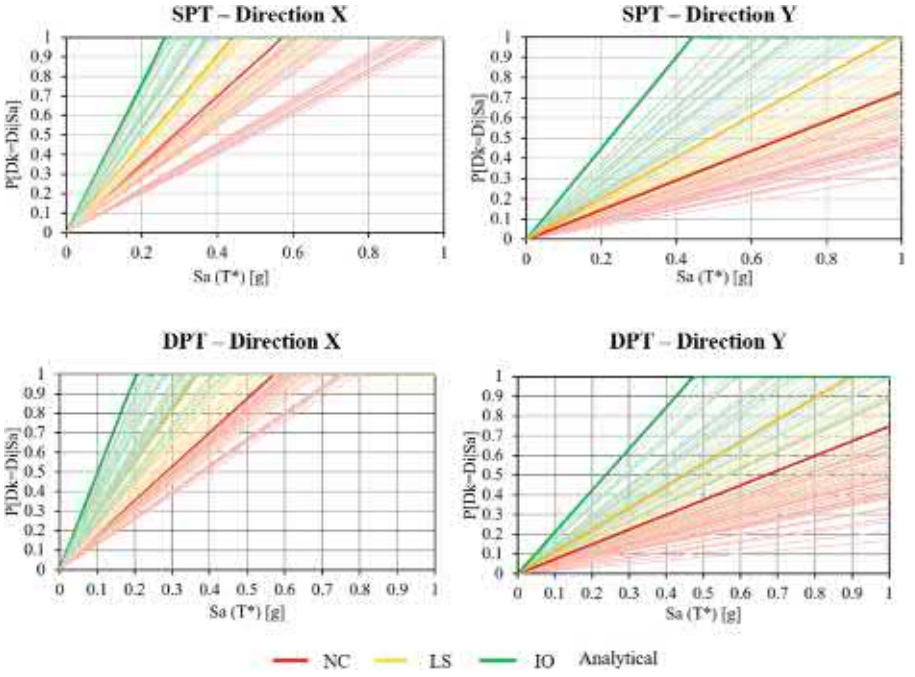


Fig. 5. Superimposed analytical fragility curves for the investigated configurations and identification of the governing typological fragility curve for the SPT and DPT building classes in the X and Y directions.

5 Conclusions

This study presented a comprehensive parametric investigation aimed at assessing the seismic vulnerability of single-storey steel industrial buildings representative of the Italian building stock. A simulation framework consisting of 336 potential structural configurations was developed by systematically combining construction period, structural typology, geometric parameters, steel grade, and loading conditions. The present work focused on single-span (SPT) and double-span (DPT) Pratt truss buildings constructed between 1960 and 1990.

For each investigated configuration, a simulated design procedure consistent with the regulations in force during the considered period was performed, followed by nonlinear static analyses. The obtained capacity curves highlighted the significant influence of both structural direction and steel grade on the seismic response. In particular, the investigated buildings generally exhibited higher strength and displacement capacity in the longitudinal direction than in the transverse direction.

Analytical fragility curves derived from the pushover analyses were compared with empirical fragility functions based on the FEMA 365 (2000) methodology. The comparison revealed a satisfactory agreement in the longitudinal direction, where the empirical approach generally provided conservative estimates of seismic damage. Conversely, in the transverse direction, the standard empirical formulation tended to underestimate the vulnerability of the investigated structures.

To overcome this limitation, a modified empirical formulation was proposed and calibrated against the analytical results. The new expression showed a significantly improved agreement with the analytical fragility curves and provided a more conservative estimation of seismic damage probabilities in the transverse direction.

Finally, the superposition of the analytical fragility curves allowed the identification of governing typological fragility curves for both SPT and DPT building classes in the two principal directions. These curves represent a first step towards the development of a fragility database for Italian steel industrial buildings and may support future large-scale seismic risk assessments where detailed structural information is unavailable.

Future developments will extend the proposed methodology to the remaining structural typologies included in the simulation framework, with the objective of defining a comprehensive set of typological fragility curves representative of the national stock of steel industrial buildings designed without seismic provisions.

Acknowledgements. The Authors would like to acknowledge the DPC-ReLUIS 2024-2026 research project (WP4 research line) for financial support to the current research activity.

References

1. ISTAT 2011: Census of residential and productive buildings. https://www.istat.it/it/files/2015/12/C18.pdf. Accessed 13 May 2026
2. ANCE/CRESME report (2012) The state of the Italian territory 2012: settlement and seismic and hydrogeological risk, Rome

3. Bournas DA, Negro P, Taucer FF (2014) Performance of industrial buildings during the Emilia earthquakes in northern Italy and recommendations for their strengthening. Bull Earthq Eng 12(5):2383–2404
4. Liberatore L, Sorrentino L, Liberatore D, Decanini LD (2013) Failure of industrial structures induced by the Emilia (Italy) 2012 earthquakes. Eng Failure Anal 34:629–647
5. Belleri A, Brunesi E, Nascimbene R, Pagani M, Riva P (2014) Seismic performance of precast industrial facilities following major earthquakes in the Italian territory. J Perform Constr Facil 29(5)
6. Formisano A, Di Lorenzo G, Landolfo R, Iannuzzi I (2017) Seismic vulnerability and fragility of industrial steel buildings. Open Civ Eng J 11:1122–1137
7. Ntaliakouras IA, Pnevmatikos NG (2017) Seismic fragility curves for industrial steel buildings. In: Proceedings of the 9th Hellenic conference of steel structures, Larisa, Greece, October 5–7, 2017
8. Italsider (1986): Structural elements of single-storey industrial steel buildings. monography 8, finsider working group of the european committee
9. CNR 10011 (1997) Steel constructions. Instructions for calculation, execution, testing and maintenance. Italian National Research Council
10. FEMA356 (2000) Prestandard commentary for seismic rehabilitation of building. Federal Emergency Management Agency Report, Washington D.C., USA
11. Chieffo N, Clementi F, Formisano A, Lenci S (2019) Comparative fragility methods for seismic assessment of masonry buildings located in Muccia (Italy). J Build Eng 25:100813

The Braila Suspension Bridge, Erection and Commissioning

Massimo Averardi Ripari[1(✉)], Fabio Brancaleoni[1], Andrea Del Vecchio[1], and Giovanni Massimo Aluffi[2]

[1] E.D.IN., Società di Ingegneria, Rome, Italy
m.averardi@ediningegneria.com
[2] Webuild S.p.A, Milan, Italy

Abstract. The suspension bridge on the Danube River near Braila is the main crossing of the Buzău - Brăila - Tulcea – Costanza motorway in Romania. The deck is a streamlined box girder made of orthotropic steel plates, coherently with the present state of the art. The high strength concrete towers have been erected via slipforming, the main cables, erected via aerial spinning, are composed by high strength steel zinc coated parallel wires. With its main span of 1120 m, it is one of the longest bridges in Europe and the largest in Central Europe. The present paper shall focus on construction methods and sequences, with main attention to the deck, as well as the load testing campaign carried out for commissioning. The bridge was opened to traffic on July 6th, 2023.

Keywords: Large Span Bridges · Suspension Bridges · Load testing · Erection Methods

1 Introduction

The suspension bridge on the Danube River near Braila is the main crossing of the Buzău - Brăila - Tulcea – Costanza motorway in Romania, whose completion is planned within the 2020–2030 decade. The bridge is the last crossing of the Danube before its outflow into the Black Sea, providing a strategic transnational transport link, being located along the corridor closest to the Black Sea (Fig. 1).

The crossing is situated approximately 165 km upstream of the Danube Delta, listed as a UNESCO World Heritage site, between Brăila and Jijila, immediately south of Galați, close to the borders with the Republic of Moldova and Ukraine [1]. The construction works, carried out by the joint venture Webuild S.p.A. and IHI Infrastructure Systems Co., Ltd., commenced in early 2019 with anchor blocks and towers. The erection of the main cable started in March 2021 and was completed in December 2021, while the erection of the deck was carried out between March 2022 and September 2022. The bridge, Fig. 2, was opened to traffic on July 6th, 2023, becoming the longest bridge in Romania and the third longest span in the European Union, with its 1120 m main span, a total suspended length of approx. 1975 m and side spans of 490 m on the Braila side and 365 m on the Jijila side.

© The Author(s), under exclusive license to Springer Nature Switzerland AG 2026
R. Zanon et al. (Eds.): CTA 2026, LNCE 942, pp. 901–913, 2026.
https://doi.org/10.1007/978-3-032-39505-4_78



Fig. 1. Location



Fig. 2. The completed Bridge

2 Design Criteria

A dedicated Design Basis was prepared for the bridge, based on the assumption of a 100-year working life for its primary structural components. The document was based on the Eurocodes, together with the Romanian National Annexes for all aspects of general structural design, supplemented by specific provisions addressing the distinctive requirements of suspension bridges. As for traffic loads, the Norwegian bridge design code FOR-2017 [3], which can be readily used with the Eurocodes, was adopted as the most up-to-date guidance available in Europe for this purpose. For the Braila bridge, the resulting total uniformly distributed traffic load is 36 kN/m, compared with 67 kN/m from the unmodified Eurocode LM1. This reduction is relevant only to the global response of the bridge and structural components governed by global actions, i.e. main cables, towers, and anchor blocks. For local effects, governing the design of the deck, hangers, cable bands, etc., the Load Model 1 as per Eurocode (EN 1991–2) is governing when applied over a loaded length of up to 200 m.

3 Description of the Bridge

3.1 Anchor Blocks and Towers

The anchor blocks [2] are primarily designed to resist the horizontal component of the cable tension, which under permanent loads only is in the order of 250 MN, while ensuring the complex connection to the main cable itself. In fact, in the splay chamber inside the blocks, the bundle of parallel wires forming the main cable is inclined downwards by means of a splay saddle and branches out into individual strands allowing the connection to the block. In the specific geotechnical context [1], a shallow gravity anchorage block was not feasible due to the poor soil properties. It was instead necessary to adopt a shaft-type solution (Fig. 3), less common but with notable international precedents, such as the Akashi Bridge in Japan. In most applications, though, the splay chamber is located above ground level, while in this case, the low height of the profile, essential for connection to the approaches, led to its placement inside the shaft. This entails highly complex internal formwork, with intersections between the shaft perimeter, internal walls and the

chamber, whose rear wall has a spherical configuration to allow the correct arrangement of the anchorages, Figs. 4 and 5. These are formed by anchor plates (cross-head slabs) supporting tension rods connected to the main cable strand shoes. Each cross-head slab is in turn anchored to the concrete by four triplets of 47 mm prestressing bars, about 20 m long and anchored at the rear to prestressing plates located in a low rear chamber with a cylindrical configuration.



Fig. 3. Anchor shaft, general view



Fig. 4. Anchor shaft, internal layout



Fig. 5. Anchorage system

Each tower foundation comprises 76 piles with 1.8 m diameter and 40–45 m long, with large cellular pile caps formed by two intersecting circles, each with a radius of 18 m and a height of 8 m. Two massive, truncated cones provide the connection to the tower legs, which are of high-strength concrete, with an overall height above ground level of 184 m for the Braila tower and 189 m for the Jijila tower, with two hollow rectangular legs measuring 6.5 m × 6.5 m and a large double crossbeam on top.

3.2 Cable System

Each of the two main cables is approx. 2135 m long, with a sag of 130 m, corresponding to a sag/span ratio of 1:8.6, chosen to optimize the quantity of cable steel, which is approx. 6800 t in total, while keeping adequate stiffness in service. In the main span, each cable consists of a bundle of 8,704 parallel zinc coated wires with a diameter of 5.38 mm each, formed using the aerial spinning technique, which during construction provides 16 individual strands of 544 wires each, subsequently compacted to form the single cable with a diameter of approx. 60 cm, Fig. 6. The ultimate strength of the wires is 1860 MPa. In line with the state of the art, the main cables are protected against corrosion by three layers, i.e. wrapping wire, paint coating and dehumidification system. At the tower tops the main cables are deviated by means of large saddles, approximately 6 m long and with a radius of about 5 m, made with cast steel for the upper part and heavy steelwork for the lower part, Fig. 7. Two additional strands per main cable, anchored to strand shoes integrated in the saddles, are provided in the side spans due to the unbalance in the horizontal components of the cable forces. At the entrance to the anchor blocks, in the splay chambers, the cable strands are splayed individually and deviated both downwards and horizontally by means of splay saddles, Fig. 8, also made with an upper cast-steel part and a lower heavy steelwork part, resting on a cylindrical hinge able to rotate around

a transversal axis. The suspension system is completed by 152 hangers connecting the deck to the main cables, which are arranged in a vertical configuration, with lengths between 4 m and 143 m, formed by parallel wire strand (PWS), composed typically by 127 and up to 277 steel wires of 7 mm diameter with a strength of 1770 MPa. The hangers are terminated with fork sockets at both ends and attached to the main cable by pins on cast-steel clamps composed of two half-shells, connected by M42 threaded bars, Fig. 6.



Fig. 6. Main cable and clamp



Fig. 7. Tower Saddle



Fig. 8. Splay Saddle

3.3 Deck

The steel deck is an orthotropic wing-shaped box-girder, Fig. 9, following the international standard established after the first application on the Severn bridge (1966). The advantages are well known: first and foremost the reduced weight, with an average value in this case of 330 kg/m^2, the low aerodynamic drag and the good torsional stiffness which ensures aerodynamic stability in the span range considered here. The total platform width is 22 m, including two dual-lane carriageways of 9.5 m each and a reservation 3 m wide. The box girder has a depth of 3.2 m and a width of 25.5 m, corresponding to the transverse spacing of the main cables and the hanger planes. Outside these, cantilevered maintenance walkways 3.10 m wide are provided on both sides, bringing the overall deck width to 31.7 m. The upper plate is 14 mm thick, stiffened with 7 mm trapezoidal troughs, 360 mm deep and with a spacing of approx. 300 mm in the areas beneath traffic, while bulb flats stiffeners were adopted in areas not directly subjected to wheel loads for reasons of constructability; the lower plate is typically 9 mm thick, increasing to max 16 mm at the towers, and is also stiffened with 6 mm-thick trough stiffeners. The inclined side webs are typically 12 mm thick, increasing to max 18 mm at the towers. The diaphragms, typically spaced at 5 m intervals, are formed by trusses with circular tubes throughout the typical deck and with solid plates in the strengthened deck zones at the towers and at the ends, where additional longitudinal bulkheads are also added to cope with the increased shear and bending at these locations, Fig. 10. The deck connection to the hangers features thick eye plates in strengthened areas, with provisions for temporary ropes for replacement operations. The typical hanger spacing is 25 m, with deck segments for fabrication and transport of the same length. The deck comprises 86 segments, for a total length of 1,977 m and a total weight of around 20 700 t, made in S355 steel. Shop joints are entirely welded, while site joints are welded for skin panels and bottom stiffeners and bolted for the upper plate troughs to ease the

erection. The detail for the bolted connection was developed for this project and envisages cover plates both on webs and flange of the stiffener, so as to restore the bending stiffness at the joints. Access holes are provided to install and tighten the bolts on the surfaces of the stiffeners, Fig. 11.



Fig. 9. Typical deck cross section



Fig. 10. Deck cross section at tower



Fig. 11. Rib connection

3.4 Articulation System

At its ends, the deck is vertically supported by two sliding spherical bearings placed on additional webs at a transverse spacing of 18.5 m, a distance defined to prevent uplift from torsion. The transverse restraint is provided by two preloaded sliding spherical bearings, inserted within a recess in the lower part of the deck and connected to a vertical concrete fin integrated into the upper structure of the anchor blocks. There are no longitudinal restraints, the deck being free to move in accordance with the movements of the suspension system. The longitudinal displacements of the deck are considerable, with the expansion joints accommodating total movement of approximately 1850 mm on the Braila side and 2300 mm on the Jijila side. These are of the modular type, i.e. formed by a series of transversal steel rails with interposed rubber profiles, supported by longitudinal I-beams. The deck passes through the towers without vertical support, with a double transverse restraint provided on the tower legs, leaving longitudinal displacements, approx. ± 800 mm, and vertical displacements, equal to $+400$ mm/-700 mm, and rotations free. The restraint is obtained, as for the deck ends, by means of two preloaded sliding spherical bearings, in this case integral with the deck, with a wide sliding plate fixed to a corbel cantilevering from the tower.

4 Erection Aspects

4.1 Construction of Anchor Blocks and Towers

The anchor blocks shafts were constructed by first installing diaphragm walls on the perimeter, followed by the construction of internal reinforced concrete structures, designed with internal walls and cells, which were subsequently filled with lean concrete, limiting the thickness of the structural concrete and reducing the effects of heat of hydration and shrinkage. The excavation followed a top-down procedure, from the capping beam at the top of the D-walls down to the foundation slab, by alternating excavation and concreting operations for circular lining rings, each approximately 3.0 m high, suspended from the capping beam and cast directly against the D-walls after installation of a waterproofing membrane. Once the bottom was reached, the foundation slab was cast, followed by a bottom-up construction sequence of the internal walls and chambers. The last stages included placing ducts, anchor plates and cross-head slabs for the anchoring system of the main cables, for which temporary assembly steel frames and laser measurements were used to ensure an accurate alignment.

The tower foundations were similarly constructed by realizing first the circular D-walls and the foundation piles. Once the excavation had reached the bottom level, the foundation slab and the radial walls forming the cellular structure were cast. Each internal cell was then filled with compacted granular material prior to casting the top slab and the truncated cones up to the tower base. The tower legs were constructed by slipforms, allowing their completion in approx. three months [5], with an average progress of 2 m per day. The towers were completed by lifting the partially precast crossbeams, weighing 450 t each, into their final position by strand jacks, securing them to the legs by means of temporary steel connections and finally achieving continuity through an in-situ stitch joint. The legs are transversally inclined with a slope of approx. 1:50, with the construction procedure omitting temporary struts and compensating the self-weight induced deformation by adopting a calculated pre-camber during the slip-forming process, so as to achieve the final geometry at the tower freestanding condition while fully respecting the tolerance of 1/2000 of their height.

4.2 Construction of the Cable System

The first step in constructing the cable system was the erection of temporary footbridges, the catwalks, spanning the whole length of the bridge and formed by several strand ropes connected to temporary steel structures at the anchor blocks and towers. The two catwalks are connected at intervals with temporary cross-bridges, which provide torsional stability and crossing points for personnel. The main cables were erected by the aerial spinning method, which implies pulling individual loops of wire across the catwalks by means of "spinning wheels" travelling on an aerial tramway, and is the classical *in situ* strand forming method alternative to the pre-fabricated parallel wire strand method (PPWS), in which full strands are prefabricated with the exact unstressed length, equipped with sockets and then hauled across the span along the catwalks. In particular, the aerial spinning [6] was carried out by the low-tension control method, originally developed for the Shimotsui Seto and Second Bosphorus Bridges in the '80 s,

in which the tension in the wires during spinning, applied by counterweight towers at one anchor block, is around 75% of the free hanging tension in order to avoid individual adjustment of wires, minimize horizontal deformations due to wind and improve the workability especially at the saddles. In the present case the spinning wheel is equipped with two grooves and thus hauls two wire loops per trip, Fig. 12, placing them on cable formers fixed to the catwalk, which supports the remaining 25% of the weight of the spun wires. As the catwalk is flexible, progress of the spinning causes deflections and hence sag variations, effect that was compensated by ballasting the cross-bridges with water counterweights. Since the spinning was operated alternately at upstream and downstream sides, the compensation was done by shifting the water weight to the opposite side of the main cable being spun. When the spinning of the wires forming each strand has been completed, Fig. 13, these are compacted and secured by straps, then the final adjustment of the strand is done during night-time in stable temperature conditions and, considering the difference from the reference temperature, the correct sag is achieved by moving the strand through the saddles and jacking out the strand shoes. At erection and adjustment of all strands completed, compaction is carried out by squeezing the wires together by means of hydraulic machinery, Fig. 14. Finally, the cable clamps are erected, and their bolts are tightened to join the two halves, after which hangers are installed by lifting them vertically from barges or embankments.



Fig. 12. Aerial spinning operations



Fig. 13. Completed strands before compaction



Fig. 14. Main cable compaction

A peculiar aspect for suspension bridge erection is the need to compensate the unbalance in horizontal components of the main cable tension between main and side spans at the towers, where an equilibrium condition is generally achieved only at bridge completion, but not during construction. In fact, in a backward construction analysis, when the weight of the deck is removed to obtain the so called “free hanging” condition, Fig. 15, the main cable has a large upward vertical displacement (approx. 10 m for the Braila bridge) together with outward horizontal deflections of the tower tops, in the order of 1.4 m in this case. As the towers are erected vertically for constructability reasons, if this deflection was not compensated, then the designated geometry would not be obtained at the end of construction and large permanent bending in the towers and risk of slippage of the strands in the saddles would occur. While for bridges with steel towers this is usually carried out by pulling the tower tops apart by temporary ropes before starting cable erection (the so called “tie back”), for concrete towers, which are comparatively stiffer, this procedure is not appropriate as it would cause high bending moments, with risk of cracking and consequent uncertainties in estimating the actual flexural stiffness.

An alternative procedure, called “saddle set-back”, Figs. 16 and 17, is thus adopted, by installing the tower saddles with an initial offset towards the side spans and then, as the erection proceeds, shifting horizontally by hydraulic jacks the tower tops with respect to the main cable, as the latter has a much larger stiffness than the bending stiffness of the tower. At construction end the saddle will be recentered on the tower, which will be free of bending under permanent loads as the equilibrium of the horizontal components of the main cable tension has been reached. For the Braila bridge, the set-back amount was 1.2 m [6], and recentering was achieved by 2000 t capacity jacks before welding the saddle to the base plate, which was fixed to the concrete by shear studs.

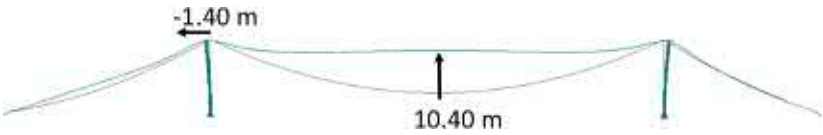


Fig. 15. Free hanging condition deformed shape

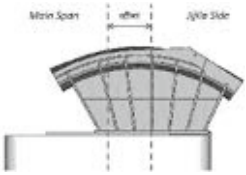


Fig. 16. Initial saddle offset



Fig. 17. Recentering after cable erection

4.3 Deck Erection

The deck erection procedure for a suspension bridge shall be defined considering the large displacements and changes of curvature that occur when adding stepwise the weight of the deck to the free-hanging main cable, in order to avoid overstressing the deck due to imposed bending and occurrence of large secondary stresses in the cables due to angular changes at the saddles and clamps. The sequence generally adopted for suspended box girder decks entails erecting first the segments at the center of the main span, proceeding outwards symmetrically and achieving closure near the towers, with main and side spans being erected simultaneously, to avoid excessive bending at the towers due to unbalanced weight. In the early stages, the main span deck adopts a pronounced sagging profile, and it is not possible to close and connect the bottom flange joints, hence temporary connections are established at top plates and webs only, with segments being essentially free to rotate between each other around the transversal axis. This sequence has the advantage that, as erection proceeds, the final deck profile is quickly achieved, enabling welding of the transverse joints to commence earlier in the center, where subsequent residual rotations will be small. Another advantage is that deck segments close to the towers are erected

only when the main cable is reaching its final configuration, thus reducing the secondary stresses as the final tightening of the cable bands near the towers can be carried out when only small residual angular changes remain [4]. Another significant aspect of deck erection is achieving stability against flutter, considering the low torsional stiffness of the partially erected deck. For the Braila bridge, wind tunnel testing on a 1:150 3D model, carried out at Politecnico di Milano, confirmed that critical wind speeds were larger than 60 m/s with 1/5 of deck erected in the main span and 65 m/s with 2/3 of deck erected, in both cases well above the required threshold for construction. An outline of the deck erection sequence is shown in Fig. 18. As described above, the suspended deck is divided into 86 segments, with a typical length of 25 m and weight of approx. 260 t each. Fabrication of the segments took place at Vard (Fincantieri Group) shipyard in Braila, a few km upstream from the bridge. Shop trial assemblies of three segments at a time were conducted to ensure compliance with the established tolerances. Segments were then loaded onto a barge and transported to the bridge site along the river.

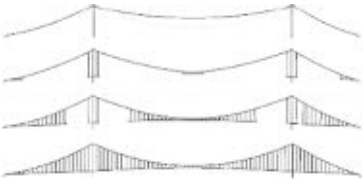


Fig. 18. General outline of the deck erection



Fig. 19. Deck segment at main span

The subsequent lifting operations depended on the location of each segment, with those to be installed above the river lifted directly in their final location (Figs. 19 and 20) and fixed to the hangers. Instead, segments at both side spans and one third area of main span, located on land or over temporary embankments, were lifted from the barge near the tips of embankments by an unloading device, horizontally shifted by an operation called, “swinging”, implying the use of temporary hangers, see Fig. 21, then lowered and loaded onto SPMTs, which transported them to the designated location where they were finally lifted and connected to the hangers, Fig. 22. As the unloading device needed to be kept at both banks until the final stages, deck closures at main span had to be carried out at these locations. An innovative aspect concerned the lifting devices developed for this bridge [7], which were integrated on the deck segments to be lifted, as opposite to the conventional procedure which foresees installing heavy lifting gantries which move along main cables. The lifting device developed consisted of four 200 t strand jacks, a lifting girder, strand recoilers and necessary machinery, which were all grouped into a “Strand jack mobile unit” placed on the deck, except for temporary cable clamps placed on the main cable to support segments during lifting. The main advantage of this solution was lightweight and compactness, which facilitated fast relocation of the lifting device: in fact, it was installed on each segment on the delivery barge and, after lifting, disassembled into parts, moved along the deck and lowered by a small gantry onto the barge again for the next cycle. Moreover, in case of malfunction each part was readily accessible for repair or replacement. For unloading segments on embankments,

instead, a fixed "unloading girder" equipped with strand jacks and suspended from the main cable was used.

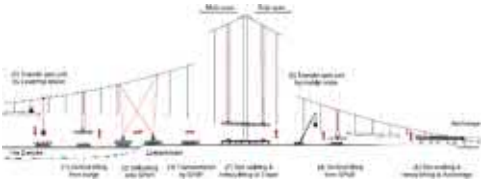


Fig. 20. Main deck erection activities, from [7]



Fig. 21. Swinging operation, from [7]



Fig. 22. Lifting of a side span segment

The segments at towers and deck ends, which would not be suspended by hangers, had to be welded with adjacent segments on the ground and then lifted with a "heavy lifting" operation. The 5 segments at each tower weighed approx. 1000 t and required 8 200 t strand jacks to be installed, while 4 strand jacks were used to lift the 3 segments at anchorages. Throughout the erection process, the as-built geometry of each segment was carefully monitored and compared against theoretical design values to ensure precise alignment [8]. The erection was completed by welding site joints between segments, in enclosed platforms below the deck or shelters above the top plate.

5 Load Testing and Commissioning

Prior to the commissioning of the Bridge, in June 2023, a thorough campaign of static load testing was carried out to verify the structural stiffness, stability and load-carrying capacity, by comparing analytical predictions from the FE model of the bridge to measured values of displacements at selected locations. The number and arrangement of test vehicles were designed to generate effects as close as practicable to those produced by the design traffic loading, so as to provide a meaningful assessment of the structural response. In this regard, the peculiar behavior of a suspension bridge shall be considered: in fact, a preliminary distinction shall be made between the so called "global effects" and "semi-local effects" of traffic loading. Global effects include e.g. maximum axial force in the main cables, maximum vertical deflections, and maximum longitudinal displacements. These effects are produced by long loaded lengths, in the order of several hundred meters for a bridge with a span of 1 km. In the present case, global effects are governed by traffic loading specified in the Norwegian regulations [3]. On the other hand, semi local effects are those concerning the behavior of the suspended deck as a continuous beam supported on flexible supports (hangers), typically spaced at 25.0 m for the present bridge. Such effects include shear and bending in the deck and axial forces in the hangers and are generally associated with shorter loaded lengths, typically less than 200 m. Consequently, the maximum design effects are produced by the full Load Model 1 as per EN 1991–2. The concept of global and semi-local effects is illustrated

below, Fig. 23, via influence lines of bending moment in the deck at midspan and axial force in the main cable.

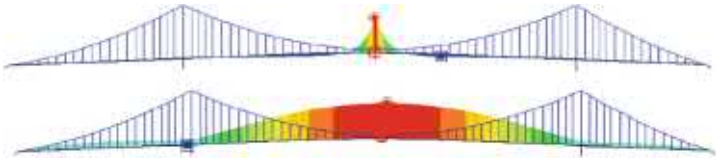


Fig. 23. Influence line of deck bending at midspan (top) and axial load in main cable (bottom)

Thirteen test loading configurations were analyzed, twelve used to verify the semi local behavior in the main and side spans and at towers, while the last load test was aimed at maximizing the main cable forces. The semi-local effects could be satisfactorily reproduced by a reasonable number of vehicles. For typical deck sections and hangers, the static load test has been performed using 16 trucks, each with a gross weight of 40 t, to a total load of 640 t. Additional configurations have been envisaged for the deck zones adjacent to anchor blocks and near towers, where the deck is supported by hangers at larger-than-normal spacing (no hangers are provided along the tower axis, while at bridge ends the distance between the last hanger and the bearings is larger than the standard 25.0 m spacing). For these additional tests, up to 19 trucks of 40 t each were used, to a maximum load of 760 t, Fig. 24. As for the last load test concerning global effects, on the other hand, reproducing the full design traffic loading was not practicable, since achieving the maximum axial force in the main cable would have required a load of approx. 7,400 t over the entire bridge length, or about 185 fully loaded 40 t trucks. As this was deemed unreasonable, the load test was instead carried out by mobilizing sixty 40 t trucks, resulting in a total load of 2,400 t, arranged on a single lane. The spacing between two consecutive trucks was 32.50 m, on a total loaded length of 1,950 m, Fig. 25. The amount of load applied during this test was anyhow sufficient to reach approx. 90% of the design axial force in the main cable under SLS characteristic combination. In fact, it shall be considered that global effects in the main cable are governed by permanent actions, i.e. self-weight and superimposed loads, while traffic provides a comparatively small contribution (approx. 15% of the total axial force at SLS characteristic). The global behavior of the bridge concerning also vertical and horizontal deck displacements was verified by comparing measured deflections with the corresponding analytical predictions for the actual test loads, even though the complete design traffic loading was not reproduced in full. In fact, it is the opinion of the authors that, for a long span bridge, a meaningful load testing shall be aimed at validating the structural response as predicted by the calculation models used for design, rather than focusing on reproducing the global design effects of traffic loads, which are of conventional nature on such long loaded lengths and have a very low probability of being reached during normal operating conditions, considering the percentage of heavy vehicles in the actual traffic mix.

The evaluation of load testing outcome also has peculiar aspects connected to the specific structural behavior of a suspension bridge, whose global stiffness is predominantly geometric, as such depending on the tension in the main cable, which is in turn a



Fig. 24. Side span load test





Fig. 25. Load test for the main cable

function of permanent loads and ambient temperature. As for the superimposed loads, in fact, those considered in the design were, as normal, forfeit values of conservative nature. In order to provide an accurate displacement prediction for the load test, the global non-linear FEM was updated, accounting for the actual loads applied (e.g. installation of barriers was not completed at the time) and removing/updating load assumptions concerning e.g. MEP, drainage, allowance for future supplementary equipment, etc. As for temperature, though no significant variations occurred during the loading-stabilization-unloading cycle of each test, it was necessary to consider that the average temperature at that time was about 30 °C, which is 20 °C higher than the reference average temperature assumed for design (10 °C). This uniform variation also implies a reduction of the force in the main cable and slightly changes its geometric stiffness. A uniform temperature was thus applied in the FE model in the construction stage analysis considering geometrical nonlinearity, prior to applying the loads simulating load tests. The load test campaign was successful, with all the measured deflections below a few per cent variation from the theoretical values, and particularly the main span vertical deflection within 1% of the expected values, confirming a high level of reliability of the design and accuracy of the construction process. Fig. 26 shows the displacements envelopes due to design traffic loads and theoretical and measured displacements for Load Case 1, corresponding to 16 trucks stationed at 1/3 of the main span. This condition produced a deflection of around 2.5 m, which is approx. 50% of the maximum deflection produced by the design traffic load.

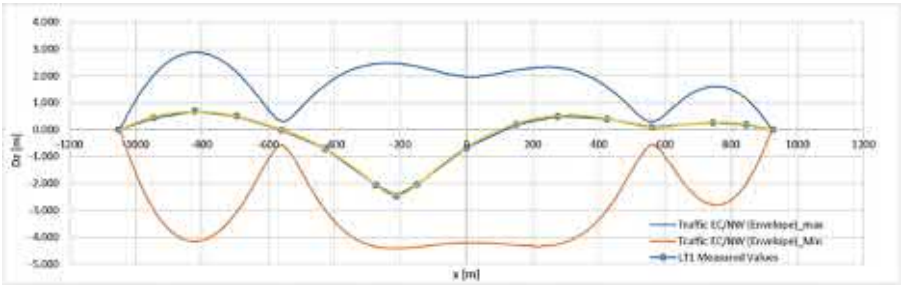


Fig. 26. Example of deflections measured during load tests

6 Conclusions and Acknowledgements

This paper presented construction methods of the suspension bridge on the Danube River near Braila and the load testing campaign carried out for commissioning. The bridge was opened to traffic on July 6th, 2023. The authors wish to express their sincere gratitude to the Association Webuild S.p.A. and IHI Infrastructure Systems Co., Ltd., for their kind permission to publish and contribution to this paper.

References

1. Brancaleoni F et al (2022) Il ponte sospeso sul Danubio a Braila, progetto e stato attuale. Costruzioni Metalliche LXXIV 2:10–45
2. Brancaleoni F et al (2022) Le strutture in calcestruzzo per il ponte sospeso sul Danubio a Braila. In: Proceedings of the 2022 ICC conference, Neaples
3. Norway Ministry of Transport (2017) Regulations for traffic loads on bridges, ferries and other load-bearing structures in the public road network FOR-2017-11-17-1900
4. Gimsing NJ, Georgakis CT (2011) Cable supported bridges. Wiley, New York
5. Berber O et al (2022) Braila suspension bridge: construction methodology of the pylons. In: Proceedings of IABSE symposium Prague, pp 1251–1256
6. Idani T et al (2023) Braila bridge: design and construction of the cable system. In: Proceedings of IABSE symposium Istanbul, pp 995–1002
7. Murano et al (2023) Innovative unloading and lifting system applied for deck erection of new suspension bridge across the Danube River in Romania. In: Proceedings of IABSE symposium Istanbul, pp 560–567
8. Koc C, Shima T (2025) Geometry control of the Braila suspension bridge over the Danube in Romania. In: Proceedings of IABSE symposium Tokyo, pp 2109–2115

Level-4 Safety Evaluation and Subsequent Interventions for the Retrofit of the "Ponte Blu" in Rome

Mario Paolo Petrangeli, Luigi Fieno, Andrea Polastri(✉), and Simone Trentacarlini

Mario Petrangeli & Partners, Rome, Italy
andrea.polastri@mpaing.com

Abstract. The "Ponte Blu", a bridge spanning the Tiber River along the coplanar road of the A90-GRA in Rome, with about 50 years of service, is a 248 m long steel portal frame bridge with inclined struts; the deck is composite with steel girders and a PC slab for the 43.5 m long rear spans, while the 161 m long central span is an orthotropic deck. Recently, a LEVEL-4 safety evaluation, performed because a fire broke out underneath the Flaminia side rear span causing extensive damage to the steel structure with local heat-induced buckling of plates, stiffeners and braces, revealed other additional bridge defects. Among the most noteworthy, significant corrosion damage, produced by water infiltration from the deck and involving the lateral cantilever of the orthotropic deck, near the transition with the PC slab, has been discovered; furthermore, the failure of the bilateral device for one of the abutment bearings was also discovered so that urgent works for installation of provisional tie-down bars have been executed. In view of these findings, as described in the paper, based on the results of the safety evaluation, the bridge has been declared transitable to traffic but with 44-ton load restriction and a reduction in carriageway width; however, considering the general fair level of bridge preservation, after the execution of the designed intervention for bridge repairing, the descriptions of which are also covered by the paper, the imposed restriction will be lifted extending the service life for a further 30 years.

Keywords: VAL-4 · steel portal frame bridge · orthotropic deck · repair

1 Description of the Ponte Blu Bridge

The Rome ring road, built during the decade following the Second World War, was originally a two-way single-carriageway; subsequently, during the 1970s, to construct the inner carriageway required for doubling the lanes so that, at the end of the works, it would become a dual two-lane carriageway - the A90-GRA Highway - the bridge known as "Ponte Blu" was built, downstream of the Castel Giubileo Tiber floodgates, to span the Tiber river between the SS-3 Flaminia and SS-4 Salaria consular roads.

The A90-GRA and the Ponte Blu remained unchanged until the turn of the millennium, when new bridges were built to span the Tiber River in order to introduce a third lane for each carriageway; as a result, the Ponte Blu became a "coplanar" of the outer main carriageway, serving traffic heading toward the SS-3 Flaminia exit (Figs. 1, 2 and 3).

© The Author(s), under exclusive license to Springer Nature Switzerland AG 2026
R. Zanon et al. (Eds.): CTA 2026, LNCE 942, pp. 914–924, 2026.
https://doi.org/10.1007/978-3-032-39505-4_79



Fig. 1. View of the "Ponte Blu" – Coplanar of A90-GRA

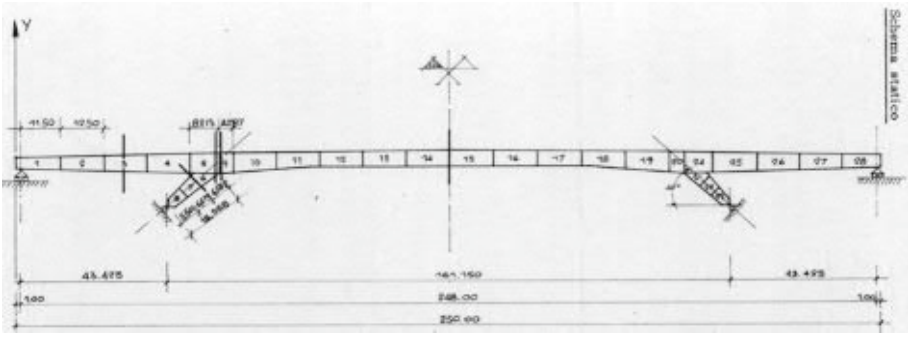


Fig. 2. Longitudinal section

The bridge, with approximately 50 years of service, is a 250 m long steel portal frame supported by two inclined struts.

The deck is a steel-concrete composite structure, with two steel main girders and a post-tensioned prestressed concrete slab for the 43.5 m long rear spans and the first portion of the 161 m long main span; the central portion of the main span, including segments 12 to 17, is instead an orthotropic deck. The two inclined 18.5 m long steel struts are continuous with the deck and hinged at the base.

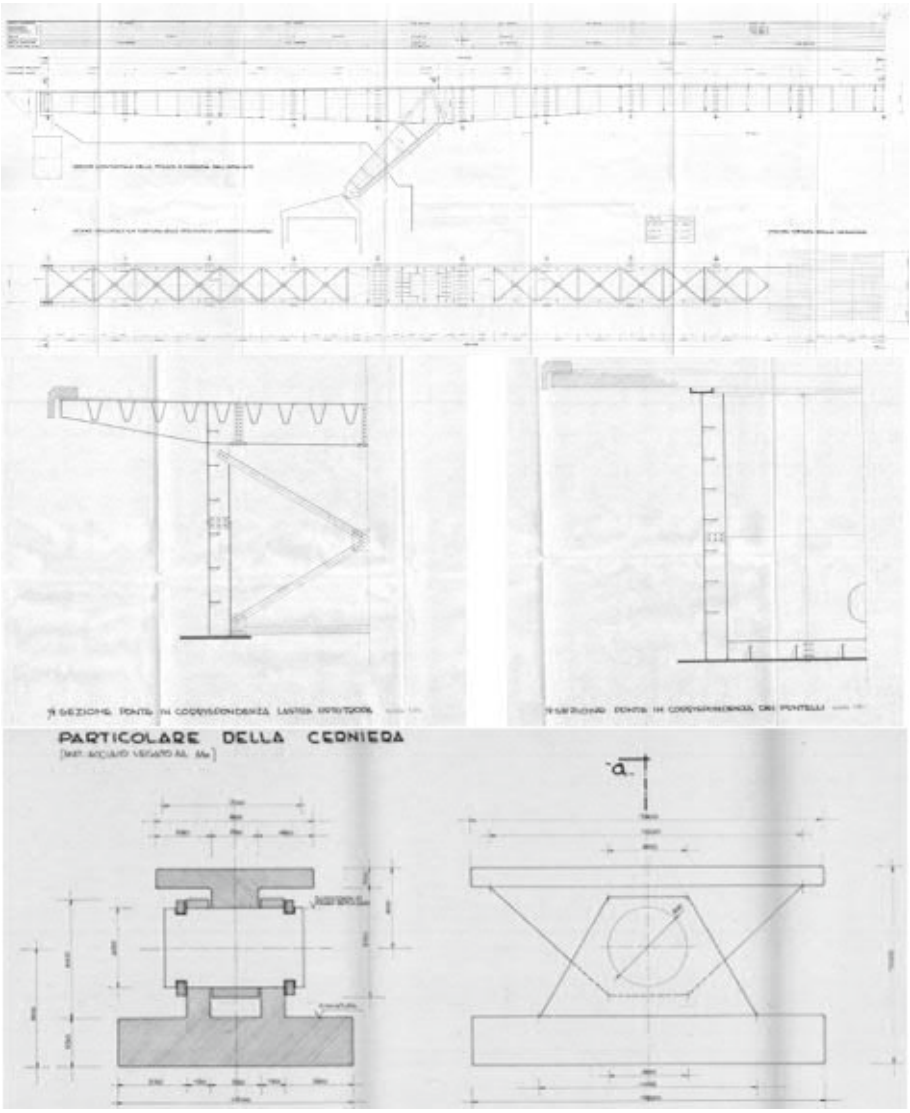


Fig. 3. Drawings of the original design

Due to the unbalanced structural scheme, with the central span significantly longer than the rear spans, the use of an orthotropic deck for the central part was intended to reduce, as much as possible, the uplift effects on the abutments bearing devices.

2 LEVEL-4 Safety Evaluation

Recently, a fire broke out underneath the Flaminia-side rear span, causing heat-induced buckling of the bottom flanges and web stiffeners of the main girders, as well as of the horizontal and cross bracing, over approximately the first 14 m of the rear span (Figs. 4, 5 and 6).



Fig. 4. Damaging of the Flaminia-side rear span caused by a fire

After the event, the required LEVEL-4 Safety Evaluation (L-4), carried out in accordance with D.M. 17-12-2020 No. 578 [1], also revealed additional bridge defects, as described below:

– significant corrosion damage caused by localized water infiltration through the deck, affecting one of the lateral cantilevers of the orthotropic deck at the transition zone with the PC slab;
– the failure of the bilateral device for one of the two guided bearings of the Salaria-side abutment, so that, due to the presence of unexpected uplift under dead-load conditions, a millimetre-sized gap formed between the bearing and the upper sliding plate;

– Further investigations and FEM analyses suggested that, for the rear spans, the effects of creep and shrinkage of the longitudinally prestressed deck slab may have been underestimated at the time of the original design of the bridge.



Fig. 5. Corrosion damage of one lateral cantilever of the orthotropic deck



Fig. 6. Uplift of one of the bilateral guided bearings

– fatigue damage of the hollow longitudinal ribs of orthotropic deck systematically localized: at the end of the additional longitudinal stiffeners present at the transition zone with the concrete slab (Fig. 7A) and at the ends of the longitudinal rib welds, where cut-outs were required for executing the transverse welding of the deck top plate (Fig. 7B);

After the prompt execution of very urgent works, consisting of the installation of provisional tie-down bars to withstand the uplift effects that damaged one of the bilateral abutment bearings and to prevent the failure of the remaining ones, since an uplift of the deck could have produced a step at the level of the expansion joints, posing a significant danger to road traffic, at the end of the L-4 safety evaluation the bridge was declared open to traffic, but with a 44-ton maximum traffic load restriction and a reduction in carriageway width (Figs. 8 and 9).



Fig. 7. Damages due to fatigue effects

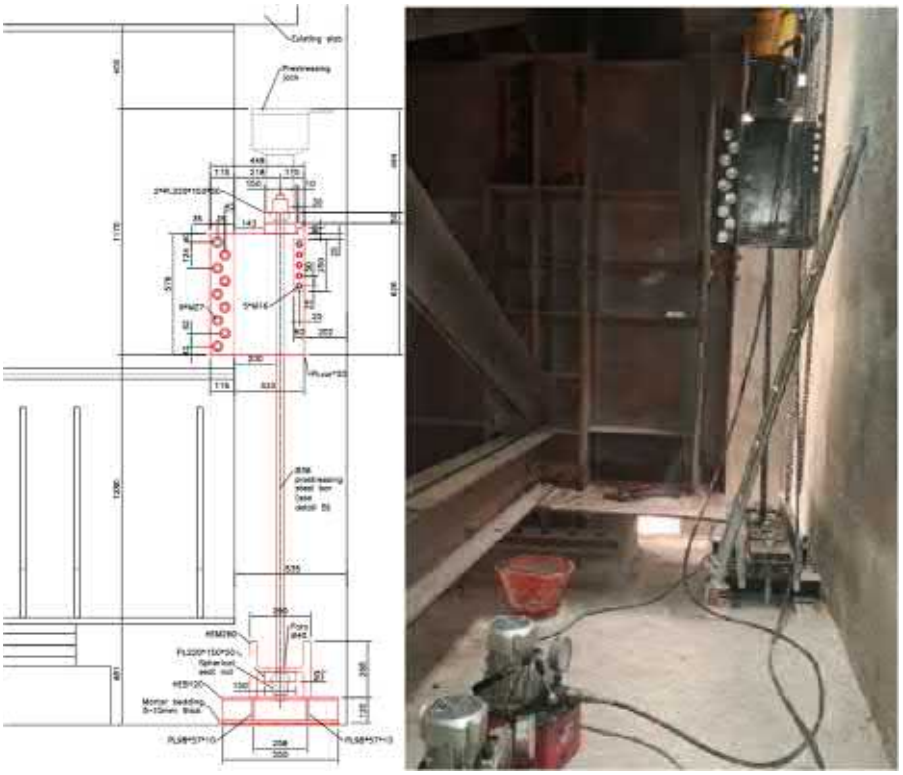


Fig. 8. Provisional tiedown bars

3 Retrofit and Repair Interventions

After more than 50 years of service, in order to remove the 44-ton traffic load restriction imposed as a result of the L-4 assessment, several retrofit interventions became necessary; the ongoing works are described below:

– Bearing Replacement and Uplift Management: as previously noted, for the abutment bilateral bearings, the outcome of the L-4 assessment showed the presence of uplift effects, also under dead-load conditions, a situation that was unlikely to have been intentional in the original design and potentially resulting from underestimated creep and shrinkage effects in the longitudinally prestressed deck slab. During the tensioning of the provisional tie-down bars, it was possible to evaluate the actual permanent uplift force as 330 kN per bearing. The replacement of the existing bearings, which will account for the increased design uplift loads based on updated evaluations, will also be carried out with the help of the installed provisional tie-down bars. After removal of the bilateral devices of the old bearing, the bars can be gradually de-tensioned to allow the minimum required deck lift to facilitate bearing replacement. The bars will then be re-tensioned to secure the connection of the new bilateral devices and finally removed.
– Repair of Fire-Damaged Girders: regarding the bottom flanges and web stiffeners of the main girders, buckled by the fire, additional stiffened plates will be installed using high-strength bolts to sandwich and straighten the buckled plates. Following tightening of the bolts, any residual gaps will be injected with epoxy resin to ensure full structural contact and protection.

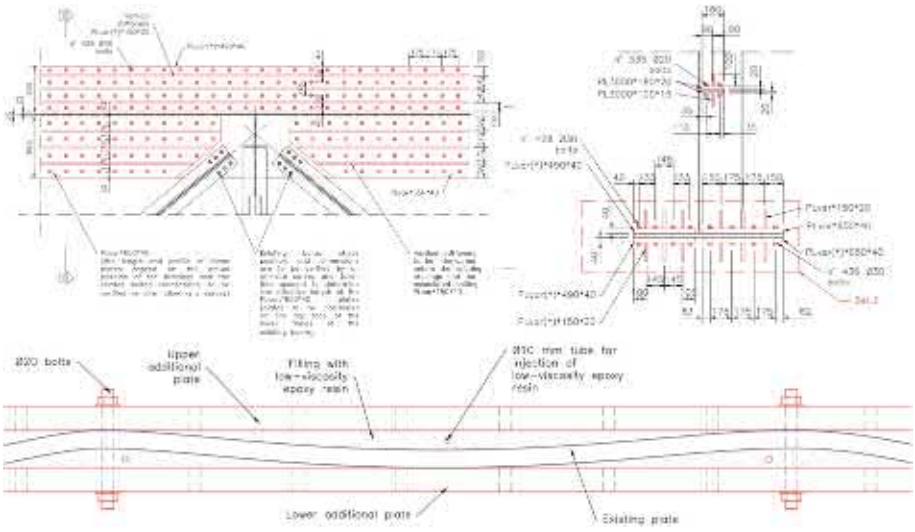


Fig. 9. Repair of bottom flanges and ribs of the main girders, buckled by fire

For the damaged horizontal bracing and crossmembers, full replacement with new elements was found to be more effective.

– Fatigue Resistance Upgrades: to improve the fatigue resistance of the orthotropic deck, specific detail modifications have been introduced: for both cases A and B in the previous paragraph, cut-outs and full-penetration butt welds have been introduced in order to decrease fatigue stress concentrations and, at the same time, increase fatigue

strength (design detail category). Specifically, from the 56 MPa fatigue strength of the original solution referred to Detail 8.4.1 of EN 1993-1-9 [2], for Case A the fatigue strength was increased to 100 MPa (Detail 8.2.7) while for Case B the fatigue strength was increased to 71 MPa (Detail 8.2.9) (Figs. 10, 11 and 12).

– Local Buckling Prevention: at the quarter-spans of the main span, where the bottom flanges of the main girders are subjected to compression under certain load cases, the existing Class 4 plates require retrofitting. To prevent local buckling, which would significantly reduce the cross-sectional resistance, additional plates will be bolt-connected to increase the effective thickness. This intervention is designed to improve the cross-section classification from Class 4 to Class 3.

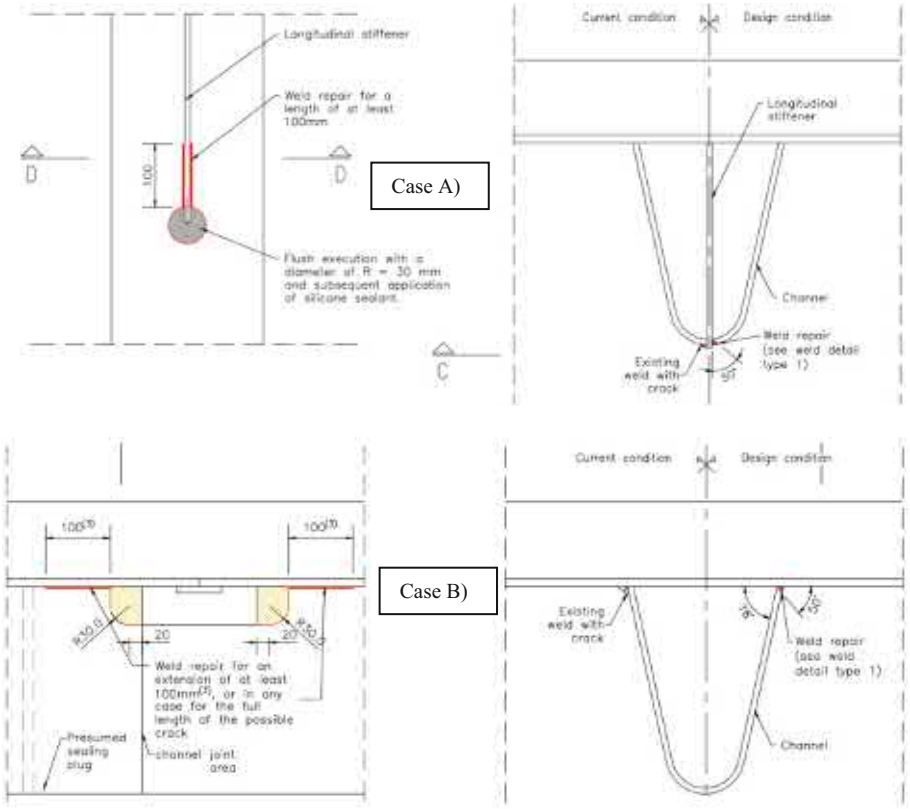


Fig. 10. Variation introduced for increasing fatigue resistance of the orthotropic deck

In addition to the replacement of the cantilever elements damaged by corrosion, the works include the replacement of the expansion joints, deck waterproofing and pavement, as well as general sandblasting and repainting of the entire structure. Upon completion of all these works, the current traffic restrictions will be lifted, and the bridge will become "Operativo" according with the definitions and requirements of GL n.578/2020, the bridge's nominal service will then be extended by an additional 30 years.

4 Conclusions

The so-called "Ponte Blu", spanning the Tiber River between the SS-3 Flaminia and SS-4 Salaria consular roads, was originally built in the 1970s during the construction of the inner carriageway required for doubling the lanes of the Rome ring road; during the works for the last widening of the A-90 GRA platforms, at the turn of the millennium, the original bridge, being a considerable steel portal frame structure with a 180 m long major span, was wisely repurposed as a coplanar of the external main carriageway of the GRA highway serving traffic directed toward the SS-3 Flaminia exit.

The LEVEL-4 safety evaluation executed after a fire broke out underneath the rear span, damaging the main steel girders and several braces, revealed additional defects so that the bridge has been temporarily declared transitable to traffic but with a 44-ton restriction for maximum traffic loads and a carriageway reduction; however, considering the general fair level of bridge preservation after 50 years of service, at the end of the ongoing repairs and retrofits all current traffic restrictions will be lifted and resulting the bridge being "Operativo" according with the definitions and contents of the GL n.578/2020, the bridge's nominal service life shall be extended by an additional 30 years.

5 Main Figures Involved and Project Data

- Owner: "ANAS SpA"
- Contractor: "Consorzio Fenix (Agent) - I.C.O.S. S.r.l. - Cavecon S.r.l. - Gielle Costruzioni e Restauro Soc. Coop.";
- Accurate Safety Evaluation VAL-4: Eng. Luigi Fieno and Eng. Andrea Polastri -Mario Petrangeli & Ass. S.r.l;
- Detailed Design of retrofit interventions: Prof. Eng. Mario Paolo Petrangeli, Eng. Luigi Fieno and Eng. Andrea Polastri - Mario Petrangeli & Ass. S.r.l;
- Responsible for the administrative process and Client's Clerk of Works: Eng. Adriano Massimi - ANAS SpA;
- Project assistant: Eng. Michele Silvestri – ANAS SpA;
- Total cost of works: € 2.804.905,80;

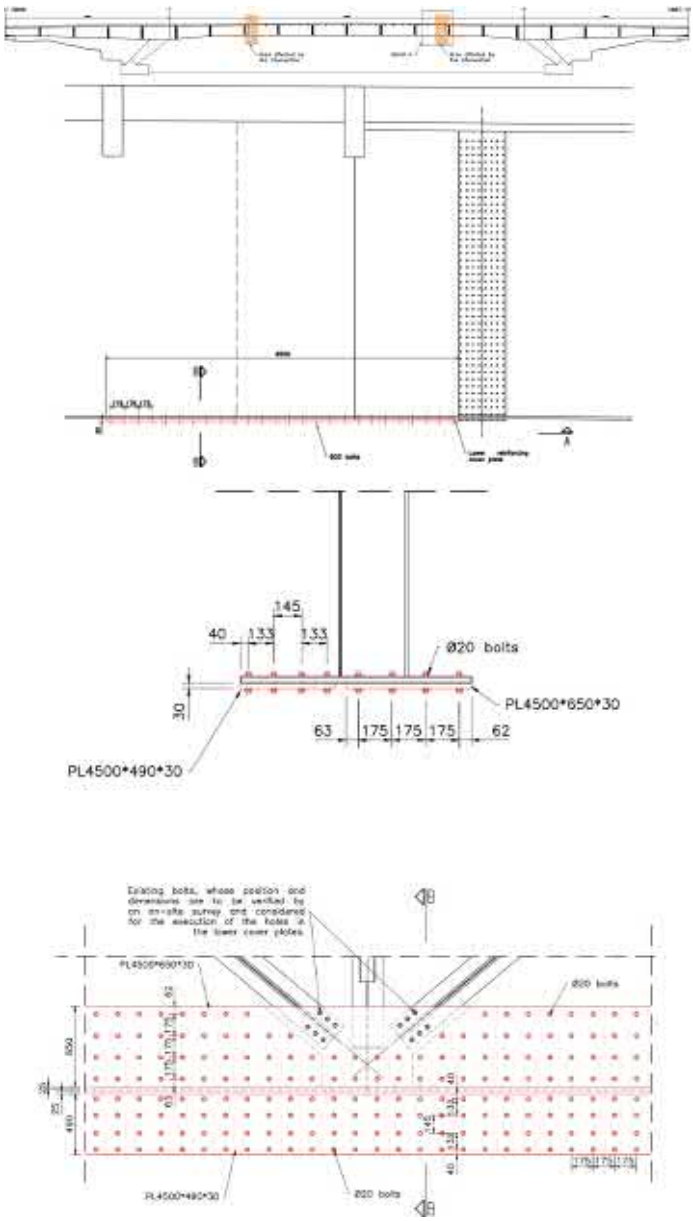


Fig. 11. Retrofit of the bottom plates of main girders against local buckling effects



Fig. 12. View of the "Ponte Blu" from "Castel Giubiuleo" bank – works on going

References

1. Ministero delle Infrastrutture e dei Trasporti (2020) D.M. 17 dicembre n. 578 - Linee guida per la classificazione e gestione del rischio, la valutazione della sicurezza ed il monitoraggio dei ponti esistenti
2. UNI EN 1993-1-9 (2005) Eurocode 3 - design of steel structures - Part 1–9: Fatigue

Geotechnical Steel Works for the Repair of Damage Caused by Landslides and for Infrastructures Protection

Michelangelo Micheloni[1(✉)], Domenico Paldino[2], and Erica Antonuccio[2]

[1] Studio Micheloni Srl, Via dei Servi, 12 Firenze, Italy
michelangelo@micheloni.pro
[2] Officine Maccaferri Italia Srl, Via del Faggiolo 1/12, Bologna, Italy
{d.paldino,e.antonuccio}@maccaferri.com

Abstract. In recent times, Italy's mountainous region has been severely damaged by violent weather events that have caused landslides. The extremely urgent work to restore roads and protect slopes requires rapid and flexible solutions, that can be identified in bulkheads, made of steel piles with metal tie rods and metal rockfall barriers. These technologies have recently been used in specific cases following the landslides, that affected the Campigno Valley in the municipality of Marradi on March 14, 2025.

Keywords: geotechnical steel works · landslides · infrastructure

1 Extraordinary Meteorological Events and Landslides in Italy's Mountainous Region

In recent times, Italy's mountainous region has been severely damaged by violent weather events that have caused landslides and damage to infrastructure.

The Campigno Valley, in the municipality of Marradi, was hit by extraordinary meteorological events on March 14, 2025. A large amount of rain fell in a very short time, causing the collapse of the valley slopes.

Many landslides have compromised local roads and affected large mountain areas, but the main landslide occurred in Ravale area along the Campigno valley, where a large event has modified the orography of the place.

The following aerial image (Fig. 1) shows the extensive hydrogeological instability, that has modified one side of the valley.

The Campigno Ravale landslide involved a large area of mountain damaging a road and a local water line. The meteorological events caused an immediate traffic interruption.

A landslide was triggered in the upper part of the mountain, sweeping away everything further down the mountain. In particular a large rock destroyed the retaining wall of the only connecting road in the area and the aqueduct line was severely damaged.

© The Author(s), under exclusive license to Springer Nature Switzerland AG 2026
R. Zanon et al. (Eds.): CTA 2026, LNCE 942, pp. 925–935, 2026.
https://doi.org/10.1007/978-3-032-39505-4_80



Fig. 1. Orthophoto processed from photogrammetric survey with drone

The landslide affected an area of 6,400 square meters with a total length of 255 m and a difference in altitude of 108 m with 28° slope, as shown in the following image of 3D photogrammetric survey (Fig. 2). To quickly and effectively restore local roads and secure the local aqueduct, it was essential to identify a type of intervention that could be carried out in a very short time.

A program of exploratory investigations and subsequent interventions was therefore developed to allow for very rapid execution.

In this context, steel structures proved to be the quickest to install, achieving a reliable result in a very short time.

2 Diagnostic

In order to plan safe, rapid and economically sustainable interventions, it is important to develop precise diagnostic.

A precise topographic survey was conducted using aerial photogrammetry. The precise geometry of the terrain not only allowed to develop the calculation models for the geotechnical assessments, but also to identify the largest rocks to be considered for the fall simulations

Likewise, it was important to reconstruct the lithotechnical stratification of the subsoil, through seismic refraction and geoelectric surveys, correlated with geognostic surveys.

In the following topographical survey (Fig. 3) the lines of seismic refraction and geoelectric surveys are represented. A total of 48 geophones and 84 electrodes are used.

The longitudinal and transverse sections allow to make three-dimensional reconstructions represented in the following images (Fig. 4).



Fig. 2. Measurement on 3D photogrammetric survey

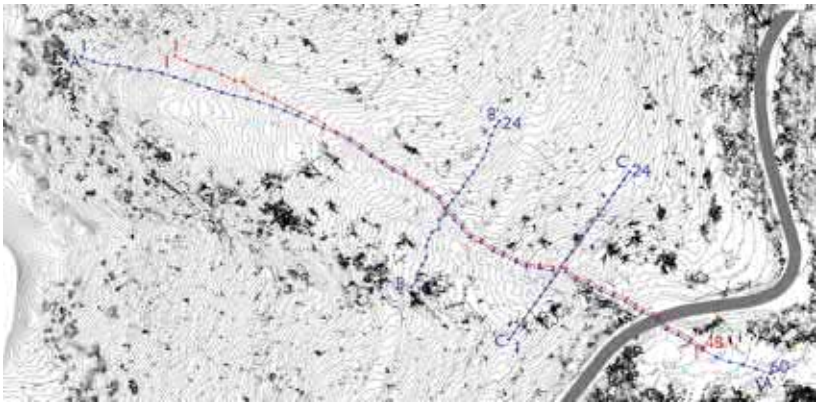


Fig. 3. Seismic refraction lines (in red) and geoelectric lines (in blu) on topographical survey

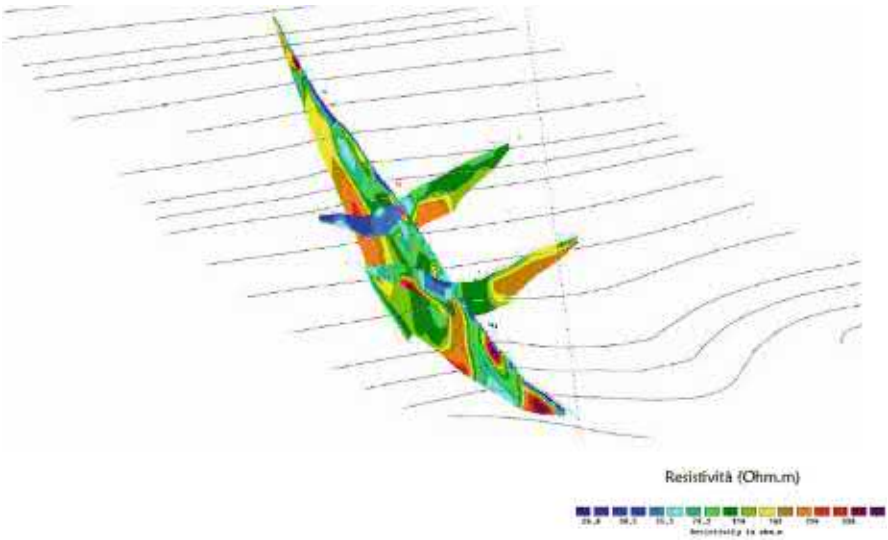


Fig. 4. 3D geoelectric survey

3 Steel Structures as a Quick and Effective Solution

The extremely urgent work to restore roads and protect slopes requires rapid and flexible solutions, that can be identified in bulkheads, made of steel piles, and rockfall barriers, made of pre-assembled steel components.

Specifically, the solutions adopted are calculated in accordance with Italian regulations [1] and can be divided into two parts:

1. bulkheads with steel piles, to restore local roads and the aqueduct line;
2. rockfall barriers, to protect the restored infrastructure and ensure the safety of people in transit.

The old road and the resulting aqueduct were supported by a high stone wall that rose approximately 7 m from the riverbed.

This wall was largely destroyed by the landslide and a large boulder that struck it. The geometry after the impact is shown in the following image (Fig. 5).

The project involves a double bulkhead on the roadside, designed to support both the road and the double aqueduct pipe. Since tie rods cannot be installed at the correct angle, given the geometry and availability of the space, the new bulkhead will be anchored at the top via connections to a second upstream bulkhead fixed into the existing rock. In fact, the rock is shallower in the upstream area of the road, allowing for easier anchoring.

At the same time, the upstream bulkhead forms a framework that can also be used to drain water from the landslide gully. This also addresses the drainage problem of the large amount of water present in the area, as illustrated in the following project section (Fig. 6).

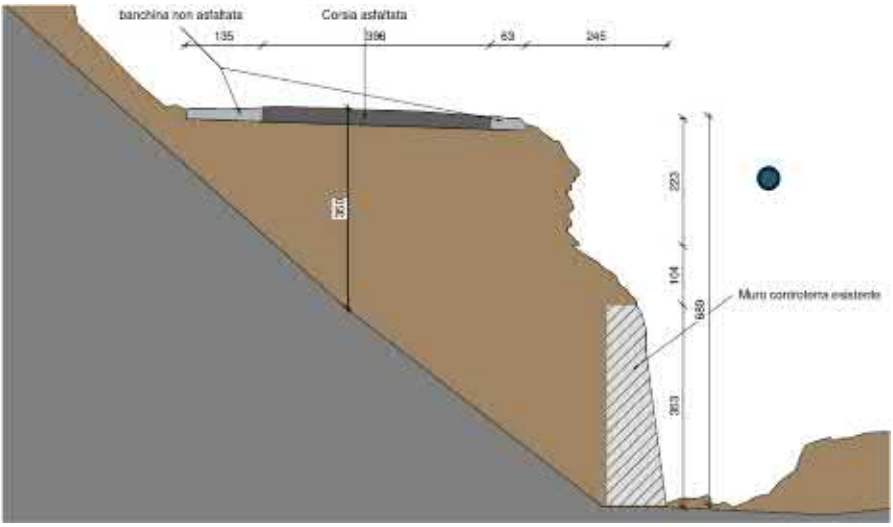


Fig. 5. Caption describing the road and retaining-wall cross section

The large landslide created a risk for the road and the underlying aqueduct, which is being addressed locally with the works described above. However, it is important to prevent further rock blocks from detaching from the mountain and impacting the underlying infrastructure again in the future.

The adopted technical solution comprised rockfall barriers with the aim of intercepting and retaining potential unstable rocks. A rockfall barrier is a flexible protective structure designed to intercept falling rock blocks and dissipate their kinetic energy. During impact, the system is designed to deform in a controlled manner, allowing it to withstand rockfall events up to its specified energy absorption capacity.

A detailed investigation was carried out involving the analysis of the most dangerous trajectories and energy calculation.

In particular, thanks to the precise survey of the landslide, it was possible to identify the maximum dimensions of the rocks present on site and perform a simulation of their fall.

The rockfall barriers were designed considering:

- Use class: III
- Maximum volume of stone blocks: 6.00 m^3
- Weight per unit of rock volume: 25.6 kN/m^3

Under these conditions, a 6.00 m high, “RB 3000” type barrier was designed. “RB 3000” is a rockfall barrier certified by Officine Maccaferri with Maximum Energy Level $\geq$3000 kJ according to EAD 340059-00-0106 [2]. The design of the rockfall barrier has been performed considering the Maximum Energy Level (MEL) of the barrier, according to UNI 11211-4:2018 [3]. The Falling Rock Protection Kit RB 3000 mainly consists of an interception structure made of continuous steel ring panels, energy-dissipating devices installed on the longitudinal cables and steel support posts.

Here below the results of one of the numerical simulations performed using Rocfall software (RocScience Inc.) [4], which led to the design of the 3000 kJ barrier (Fig. 7 and 8).

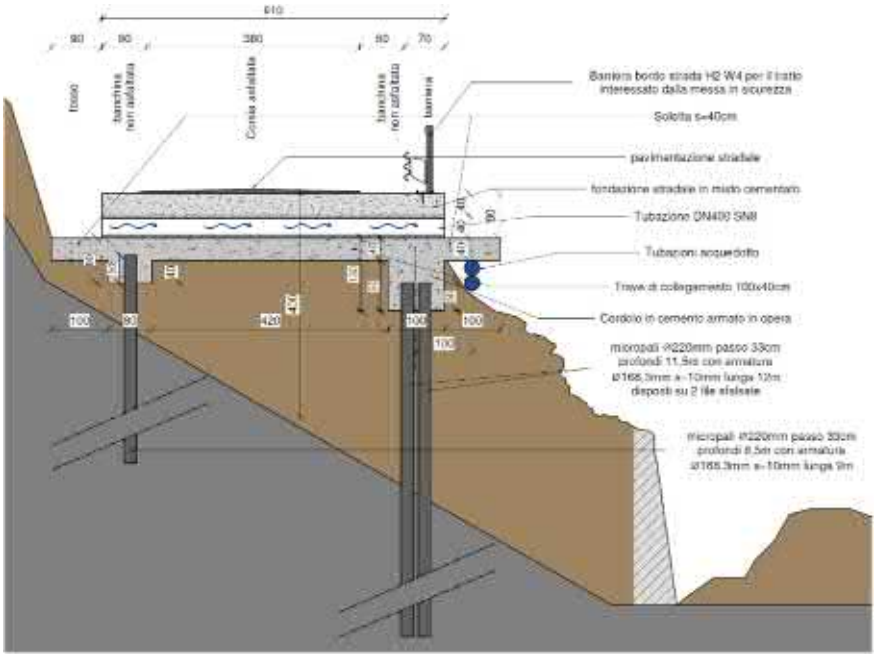


Fig. 6. Project section

Considering the trajectories it is possible to collect the statistics of the heights and speeds with which the boulders hit the barrier as shown in the following graphics (Figs. 9 and 10). From the data obtained, the following values are obtained for 95% of the sample population at the barrier.

– impact height: 3.52 m
– impact velocity: 12.95 m/s

An equivalent simulation was carried out for the downstream barrier. Based on the simulation results, two rockfall protection barriers were designed: a main one upstream barrier with an energy absorption capacity of 3000 kJ and a height of 6,0 m and a further downstream barrier with an energy absorption capacity of 750 kJ and a height of 3,50 m. The two structures are therefore designed to retain, respectively, larger rocks with longer runout distance and smaller rocks with a shorter travel distance (Figs. 11, 12, 13, 14 and 15).

The two barriers shown above will therefore prevent large or small rocks from hitting again the road and aqueduct, supported by new bulkhead, as happened during the events of March 14, 2025.

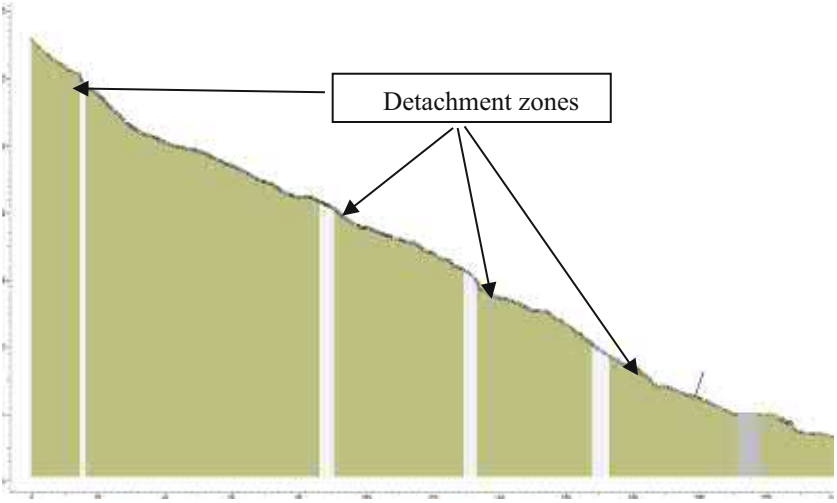


Fig. 7. Project section

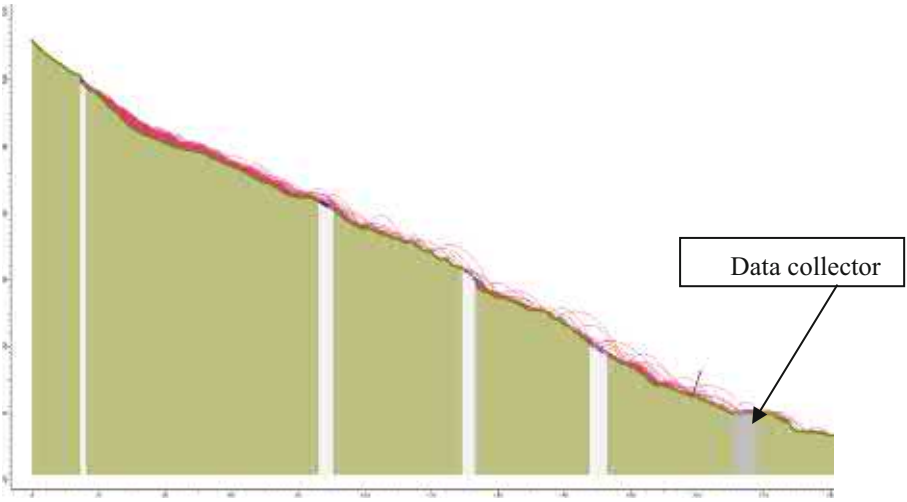


Fig. 8. Rockfall trajectories along the investigated section

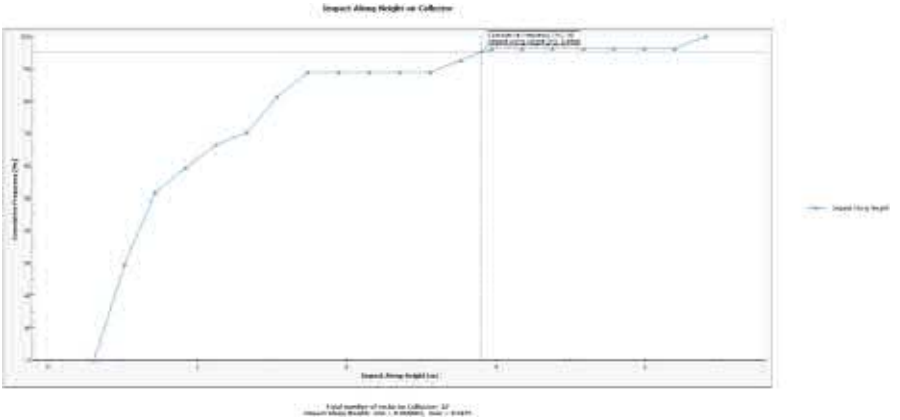


Fig. 9. Distribution of impact heights along the investigated section at the data collector

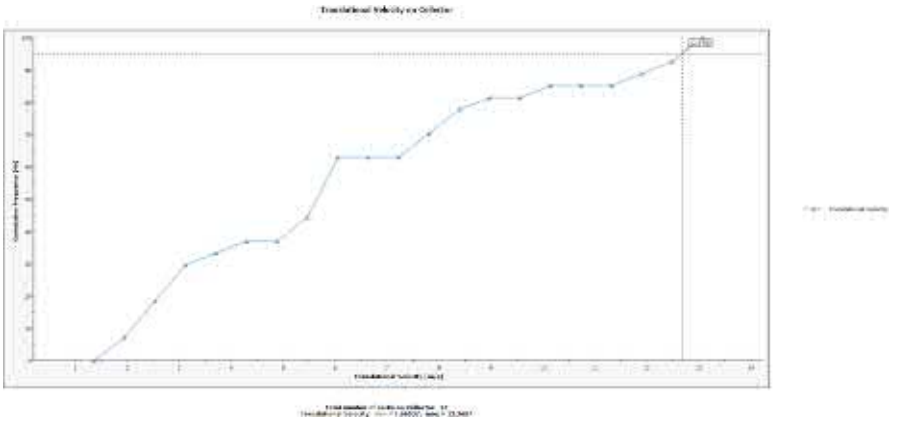


Fig. 10. Distribution of impact velocities along the investigated section at the data collector

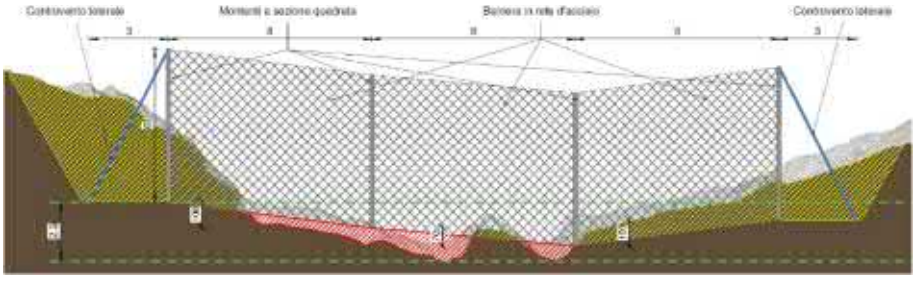


Fig. 11. Upstream metal rockfall barriers with an energy absorption capacity of 3000 kJ



Fig. 12. Upstream rockfall barriers with an energy absorption capacity of 3000 kJ

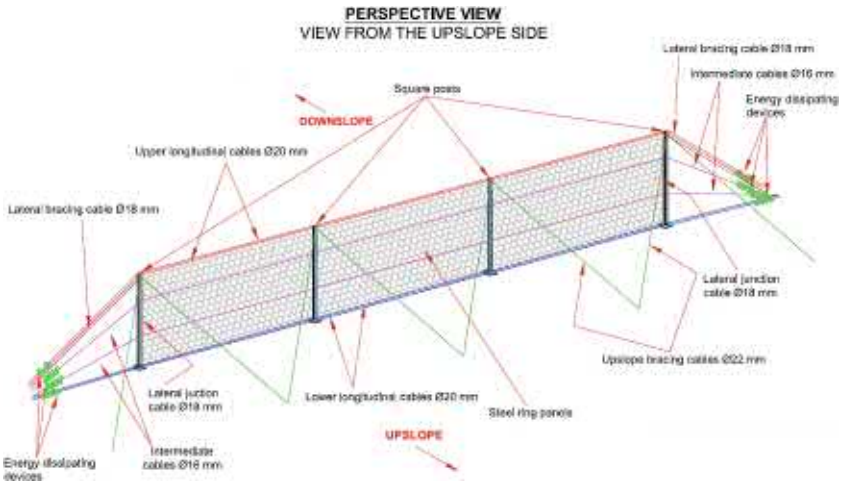


Fig. 13. Perspective view of the 3000 kJ rockfall barrier

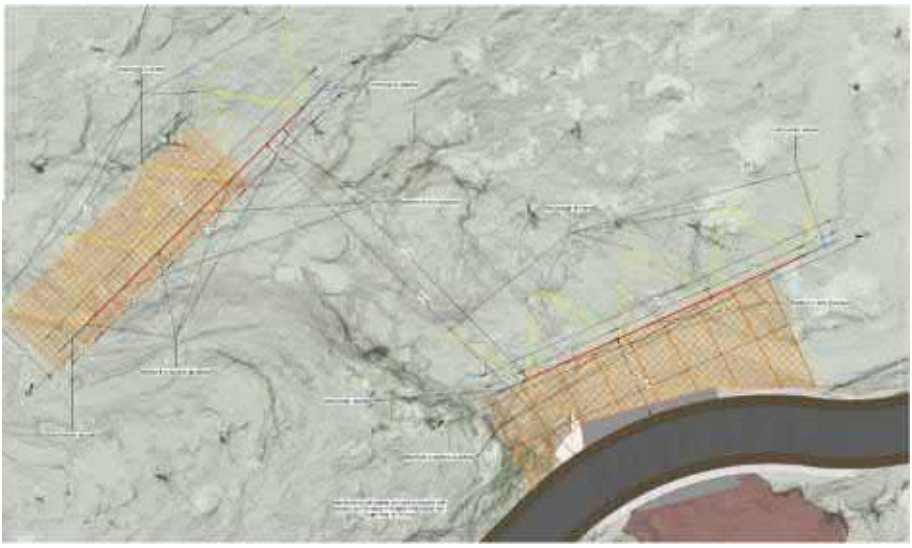


Fig. 14. Plan showing the arrangement of rockfall barriers and soil-nailing interventions



Fig. 15. Starting from the top: 3000 kJ barrier, 750 kJ barrier and double bulkhead supporting the road and the aqueduct

4 Conclusions

Seel piles bulkheads and rockfall barriers represent a fast ed. effective solution to restore roads and to protect slopes after sudden weather events and landslides. The application of these techniques in the case of municipality of Marradi demonstrates the effectiveness of this type of projects and intervention.

References

1. NTC2018, Norme Tecniche per le Costruzioni, D.M. Infrastrutture 17.01.2018, Italian code for structure
2. EAD 340059-00-0106 – Falling rock protection kits
3. UNI 11211-4:2018 Opere di difesa dalla caduta massi - Parte 4: Progetto definitivo ed esecutivo
4. Rocscience Inc., http://www.rocscience.com

Structural Retrofit of Steel Truss Girders Using Prestressing Strands: The Roof of the Nelson Mandela Forum in Florence

Paolo Cioni(✉), Claudia Chioatero, and Alexandra Szokalska

Studio Tecnico Cioni Di Ing. Paolo Cioni, Via Aretina 167 M, 50136 Florence (FI), Italy
studio@ingegneriacioni.it

Abstract. This paper details the structural assessment and subsequent strengthening of the Nelson Mandela Forum's steel roof in Florence, a facility originally designed in the 1960s and completed in 1985. Due to the evolution of structural regulations (NTC) and the transition of the venue into a multi-purpose arena for major concerts, the original steel trusses required upgrading to accommodate increased snow loads, maintenance loads, and heavy suspended stage equipment.

The strengthening strategy focused on an innovative post-tensioning technique. By utilizing unbonded, low-relaxation steel strands, a mid-span upward displacement (camber) of approximately 1/1000 of the span was induced. Numerical modeling, performed with SISMICAD and SAP 2000, validated that this prestressing effectively counteracts compression in the top chords, reducing the need for traditional bolted steel plates. This approach was further refined by applying exploratory upward loads to the digital model to match empirical field measurements, allowing for a 34% reduction in calculated compression for safety verifications. Additionally, web members were reinforced to prevent buckling instability. Material testing was conducted to confirm the steel characteristics. The phased implementation plan (2025–2027) ensures full regulatory compliance while maintaining the facility's operational continuity during the event seasons.

Keywords: Structural Strengthening · Steel Trusses · Prestressing · Seismic Assessment · Nelson Mandela Forum · Unbonded Strands

1 The Mandela Forum Roof

The Florence sports arena, later dedicated as the "Nelson Mandela Forum", was conceived in 1963. The original design was inspired by the Olympic arenas of the 1964 Tokyo Games, featuring prestressed concrete roofs (see the works of Kenzo Tange). Designed by architects Francesco Tizzi and Renzo Paoli, construction began in 1963. As with many contemporary projects, funding was exhausted before completion, leaving only the reinforced concrete (R.C.) substructures up to the roof supports, while the roofing remained unbuilt. These structures remained abandoned and exposed to weathering until 1975. Construction eventually resumed and was completed in 1984, with the official inauguration in 1985.

© The Author(s), under exclusive license to Springer Nature Switzerland AG 2026
R. Zanon et al. (Eds.): CTA 2026, LNCE 942, pp. 936–943, 2026.
https://doi.org/10.1007/978-3-032-39505-4_81

The roof design underwent a drastic modification, being replaced by a steel system consisting of 14 trusses with varying spans and a 6-m spacing (Fig. 1). This choice allowed the use of the existing R.C. structures, as the steel roof's self-weight was significantly lower than that of the original concrete design. The complex seats approximately 8,000 people and has transitioned from a multi-sport venue to a major hub for concerts and shows. This change in use necessitated suspending various equipment from the roof trusses, including stage machinery, lighting, and sound systems.

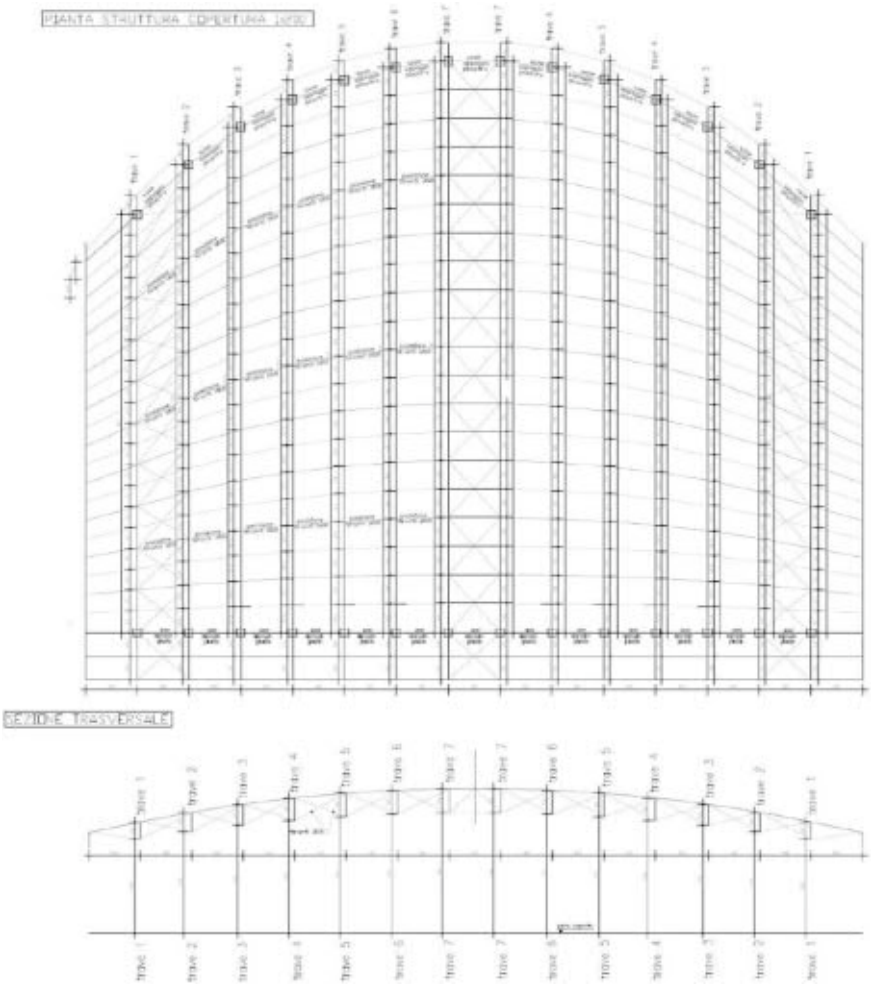


Fig. 1. Mandela Forum layout, with beam numbering

Over the past 40 years, structural regulations regarding live loads have evolved, specifically:

1. Snow load: increased from 0.6 kN/m^2 to 0.8 kN/m^2.

2. Maintenance load: a new requirement of 0.5kN/m^2 was introduced.

Furthermore, the regulatory framework shifted from deterministic maximum loads to probabilistic load combinations. Consequently, safety checks for snow (primary load, factor 1.0) now include maintenance loads (combination factor 0.5), and vice versa. This results in a total design load of:

$$0.5 \times 0.8 + 1 \times 0.5 = 0.9 \text{ kN/m}^2$$

Applying a partial safety factor for loads of 1.5, the total ULS (Ultimate Limit State) load reaches 1.35 kN/m^2. The need to update safety assessments followed inspections by the Prefectural Commission for Public Entertainment. Transitionally, the venue operated under the condition of "no snow," but the increase in occasional loads for concerts prompted a definitive structural strengthening of the roof.

Meanwhile, the Municipality of Florence entered into two research contracts[1] for a rapid seismic vulnerability assessment of approximately 160 municipal school buildings. These contracts, awarded to the Universities of Florence and Pisa, assigned expertise for masonry structures to the University of Pisa and for reinforced concrete (R.C.) and steel framed structures to the University of Florence. As an addendum to this contractual agreement, the team from the University of Pisa was tasked with evaluating the structural safety of the Costoli swimming pool and the Mandela Forum, both also owned by the municipality.

The research contract (formalized by executive provision 2016/DD/05412 on August 30, 2016) concluded that the R.C. structures of the Mandela Forum were safe, even under an acceptable quota of seismic action. However, it noted that several members of the steel roof were inadequate, even when considering vertical static loads alone. A strengthening

[1] Following the Prime Ministerial Decree (OPCM) No. 3274 of March 20, 2003, and the OPCM No. 3431 of May 3, 2005, public administrations were mandated to perform analyses and evaluations of public buildings related to civil protection or specific high-occupancy uses. These assessments focused on the seismic resilience and survival capacity of each structure. The Municipality of Florence proactively addressed this issue, particularly regarding the school buildings within its jurisdiction (nurseries, kindergartens, primary, and middle schools), totaling approximately 180 complexes. The primary challenge was to obtain comparable evaluations across all buildings to manage hazard levels effectively and establish a priority ranking for interventions, decommissioning, or demolition.Entrusting the study of building behavior to various independent professionals would have posed a significant problem regarding the uniformity and comparability of results. Consequently, the decision was made to involve Tuscan universities with extensive experience in assessing the effects of Italian earthquakes. Thus, a research project was commissioned to the Universities of Florence and Pisa (City Council Resolution DCC No. 2016/00281 of July 8, 2016).Specifically, the University of Florence was tasked with studying framed structures (reinforced concrete and steel), while the University of Pisa focused on massive structures (masonry). Due to the steady progress of the study, the scope was extended: the University of Florence was asked to evaluate the Municipal Stadium, while the University of Pisa assessed the Mandela Forum and the Costoli swimming pool.The work was carried out by two teams, coordinated by Prof. Paolo Spinelli and Prof. Gloria Terenzi for the University of Florence, and by Prof. Pietro Croce and Prof. Maria Luisa Beconcini for the University of Pisa.

plan for the Mandela Forum roof[2] was therefore implemented, scheduled during seasonal closures to keep the venue operational.

2 Strengthening Strategy

The first option considered was reinforcing deficient steel sections by bolting on additional steel plates (Fig. 2). However, this posed a challenge: the new material would be attached to elements already under tension, making the stress distribution between old and new material questionable.

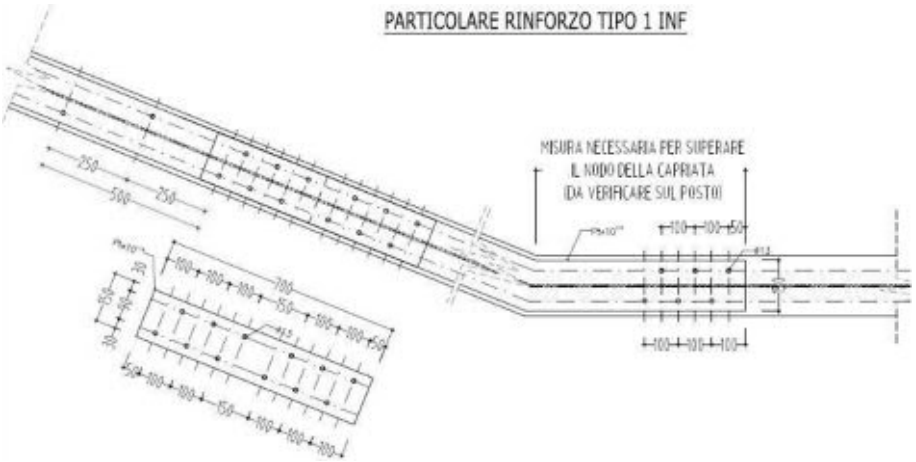


Fig. 2. Structural retrofitting project, with detail of the bottom chord reinforcement of the trusses, achieved by means of bolted plates

We then evaluated partially unloading the sections before reinforcing them. This proved difficult due to the height of the trusses (approx. 30 m above floor level). Consequently, we hypothesized prestressing the trusses using high-strength steel strands positioned near the centroid of the bottom tension chord, with the intent of removing them after reinforcement.

A pilot test was conducted on Truss No. 4. During the tensioning of the strands, a vertical lift (camber) was observed. This suggested that the bottom chord could be strengthened directly by leaving the post-tensioning strands in place. Modeling confirmed these encouraging results, leading to the application of prestressing across all trusses. A mid-span lift of approximately 1/1000 of the span was recorded during tensioning. This behavior prompted an evaluation of how much compression in the top chord could be offset in the design data.

[2] This study phase was commissioned by the Mandela Forum Operator to an external consultant engineer.

2.1 Structural Modeling

The roof trusses were modeled using SISMICAD software. Depending on the tension required in the bottom chord, post-tensioning was applied using 2 to 4 strands of 0.6 in. per truss. with a tensioning level of approximately 80 kN/cm^2. All bottom chords now meet the tension requirements derived from SAP 2000 models, assuming Fe 360 steel (standard at the time of construction), as verified by the University of Pisa. Further SISMICAD modeling validated the strengthening system for the top chord.

In the initial phase of the strengthening project, the required amount of supplementary steel sections was evaluated without considering the effects of prestressing. Once it was decided to maintain the prestressing - achieved through corrosion-protected unbonded strands - an assessment was conducted to determine its impact on the top chord. This was performed by introducing a series of equal, upward-directed exploratory loads at each of the truss's bottom nodes, until a mid-span displacement was achieved that matched the lift observed during the actual prestressing operation.

This system of exploratory loads induced a tensile force in the top chord, which served to counteract and reduce the calculated design compression. It was therefore decided to incorporate this tensile contribution into the safety verification of the top chord (applying a reduction factor of 0.66). This approach is specifically justified by the fact that the previous unfavorable safety checks for the top chord were due to insufficient cross-sectional capacity rather than phenomena of global instability.

Prestressing (Fig. 3 and 4) was implemented using low-relaxation unbonded cables, consisting of 2 to 4 strands of 0.6 in. each, with a tensioning force ranging from 200 kN to 400 kN, depending on the span of the trusses and the specific strengthening requirements. The force was transferred to the structure by welding specialized anchorage blocks near the bottom nodes, located close to the truss curvature near the supports, ensuring an effective and secure anchorage for the strand system.



Fig. 3. The prestressing of beam no. 4 (grandstand side) and the reinforcement of the bottom chord with bolted plates



Fig. 4. The prestressing of the bottom chord, achieved by inserting 0.6″ section PC steel strands

2.2 Diagonals, Web Members, and Supports

For the web members (diagonals and posts), failures were primarily due to buckling instability. These sections were reinforced (Fig. 5) by welding additional material to the original members at a minimum of three points to improve both cross-sectional area and stability.



Fig. 5. Detail of the diagonal reinforcement project using welded steel rods

While prestressing only affects the full-depth section of the truss, the areas near the supports required specific reinforcement and stabilization. Regarding the increase in inertia, the load level at the time of reinforcement was deemed negligible. While all trusses have been prestressed, the reinforcement of web members and compression zones is scheduled in phases between 2025 and 2027.

2.3 Evaluation of the Truss Compression Zones

The assessment of the strengthening requirements for the compression zones of the trusses is based on the analysis conducted by the University of Pisa team and the numerical modeling performed using SISMICAD. During the prestressing of the tension chords, a mid-span upward displacement (camber) equivalent to 0.001 of the span was recorded. Consequently, to quantify the necessary reinforcement for the top chords and diagonals, a system of equal and incrementally increasing exploratory loads was applied to the truss model. These loads were positioned at each of the lower nodes and directed upward, until the mid-span lift matched the empirical values observed during prestressing (approximately 1/1000 of the span).

The resulting tensile force in the top chord was then calculated. The design compression in said chord was reduced by superimposing the force derived from the exploratory load system, adjusted by a partial safety factor of 1.5 for favorable actions.

This methodology demonstrated that only a fraction of the reinforcements initially calculated in the first approach were actually required. Accordingly, the installation of steel plate reinforcements was optimized and reduced based on these evaluated results.

2.4 Material Testing

The original materials from the 1980s used for the steel roof structure were evaluated across different categories:

(a) primary structural sections, mainly HE profiles;
(b) smaller sections, including diagonals, vertical posts, and inspection walkways;
(c) connection bolts.

It was decided not to perform material sampling directly from the truss profiles, as each element is subjected to constant axial force. Instead, a hardness testing campaign consisting of 54 measurements was conducted. The results indicated that the primary trusses, secondary elements, and walkways are all composed of the same steel grade, identified through hardness testing as S275.

This was further verified by testing material extracted from a walkway (an NPU 160 profile). The specimen was subjected to a tensile strength test, which confirmed the steel quality as S275.

3 Final Results

The described interventions ensured that the structure complies with current regulations for snow and maintenance loads. Regarding suspended event loads, while capacity has higly increased, it remains limited. In specific cases, when loads from stage equipment are significantly high, use may be still restricted during heavy snowfall. Given that public access would also be hindered by snow, this limitation is considered acceptable.

This methodology of work allowed the facility to remain operational during all the season. All trusses have been now prestressed. By the summer of 2025, reinforcement was completed on half of the trusses (prioritizing those most exposed to variable event loads), with full completion expected by 2027.

Ultimately, this strengthening technique for existing steel structures could represent an interesting paradigm shift for contemporary structural engineering. The success achieved at the Mandela Forum opens the way to several development perspectives, particularly relevant for long-span structures within a European context where the existing building stock is reaching the end of its nominal service life. From this perspective, the effectiveness of the method lies in its minimal invasiveness: eliminating complex ground-based scaffolding systems not only optimizes logistical costs but also guarantees the full operational continuity of the structure.

References

1. Kingdom of Italy (1939) Regio Decreto 16 novembre 1939, n. 2229: Norme per la esecuzione delle opere in conglomerato cementizio semplice od armato. Gazzetta Ufficiale del Regno d'Italia 92, 18 April 1940
2. Italian Republic (1971) Legge 5 novembre 1971, n. 1086: Norme per la disciplina delle opere di conglomerato cementizio armato, normale e precompresso ed a struttura metallica. Gazzetta Ufficiale della Repubblica Italiana 321, 21 December 1971
3. Italian Republic (1974) Legge 2 febbraio 1974, n. 64: Provvedimenti per le costruzioni con particolari prescrizioni per le zone sismiche. Gazzetta Ufficiale della Repubblica Italiana 76, 21 March 1974
4. Ministero dei Lavori Pubblici (1974) Decreto ministeriale 30 maggio 1974: Norme tecniche per la esecuzione delle opere in cemento armato normale e precompresso e per le strutture metalliche. Supplemento Ordinario alla Gazzetta Ufficiale della Repubblica Italiana 198, 29 July 1974
5. Presidenza del Consiglio dei Ministri (2003) Ordinanza del Presidente del Consiglio dei Ministri 20 marzo 2003, n. 3274: Primi elementi in materia di criteri generali per la classificazione sismica del territorio nazionale e di normative tecniche per le costruzioni in zona sismica. Supplemento Ordinario 72 alla Gazzetta Ufficiale della Repubblica Italiana 105, 8 May 2003
6. Presidenza del Consiglio dei Ministri (2005) Ordinanza del Presidente del Consiglio dei Ministri 3 maggio 2005, n. 3431: Ulteriori modifiche ed integrazioni all'Ordinanza del Presidente del Consiglio dei Ministri n. 3274 del 20 marzo 2003. Supplemento Ordinario 85 alla Gazzetta Ufficiale della Repubblica Italiana 107, 10 May 2005
7. Ministero delle Infrastrutture e dei Trasporti (2018) Decreto 17 gennaio 2018: Aggiornamento delle Norme tecniche per le costruzioni. Gazzetta Ufficiale della Repubblica Italiana 42, Supplemento Ordinario 8, 20 February 2018
8. Bigi M (2018) Il Mandela Forum di Firenze: Valutazione della sicurezza statica e sismica delle tribune e della copertura. Master's thesis,. University of Pisa, Pisa
9. Ariani L, Marcetti C, Poli D (2009) Francesco Tiezzi architetto. Associazione Culturale Villa Classica, Torrita di Siena

Residual Stresses and Corrosion

Assessment of the Influence of Corrosion on the Structural Performance of a Steel Truss Railway Bridge

Giuseppe Mugnos(✉)

Dismat s.r.l, Canicattì (AG), Italy
ing.giuseppemugnos@gmail.com

Abstract. Steel railway infrastructures located in marine environments are particularly vulnerable to corrosion phenomena, which may progressively impair the efficiency of structural connections and boundary conditions, affecting both the static behaviour and the global dynamic response. In such contexts, the assessment of the effectiveness of extraordinary maintenance interventions requires investigation protocols capable of capturing structural changes that are not readily detectable through visual inspections alone.

This work presents an integrated experimental approach for the assessment of the structural performance of steel railway bridges, based on the comparison between testing campaigns carried out before and after maintenance interventions. The protocol combines static load tests, aimed at evaluating structural deformations and stress states, with dynamic characterization tests performed through Operational and Experimental Modal Analysis, allowing the identification of natural frequencies, mode shapes and damping ratios.

The application to the Forgia railway bridge, consisting of steel truss girders affected by an advanced state of corrosion, highlights how restoration interventions on bolted joints and steel surfaces produce measurable effects not only on the static response, but also on boundary conditions and energy dissipation capacity. The results show that dynamic analysis represents a particularly sensitive tool for interpreting the evolution of structural performance and for defining a reliable reference baseline for long-term monitoring.

Keywords: Corrosion · Steel truss railway bridges · Structural dynamics · Experimental assessment · Operational Modal Analysis

1 Introduction

Steel railway bridges constitute a significant part of existing infrastructure assets. Many of these structures feature efficient, lightweight designs where overall behavior depends heavily on the efficiency of bolted connections, bracing systems, and boundary conditions. When located near the coast, the combined effects of humidity, salt spray, and hygrothermal cycles accelerate corrosion, complicating the assessment of residual safety [1, 2].

© The Author(s), under exclusive license to Springer Nature Switzerland AG 2026
R. Zanon et al. (Eds.): CTA 2026, LNCE 942, pp. 947–959, 2026.
https://doi.org/10.1007/978-3-032-39505-4_82

Corrosion causes more than just a localized reduction in cross-sectional area. In truss bridges, it can alter joint behavior, reduce or modify relative slip between connected components, and consequently influence both static and global dynamic responses. Therefore, while visual inspection is essential, it is not always sufficient to quantify the impact of deterioration or the effectiveness of major maintenance interventions.

In this context, a coordinated approach combining static and dynamic testing enables a more comprehensive assessment. Load tests provide direct data on deflections, deformations, and stresses induced by controlled loads. Conversely, dynamic tests—conducted using Operational Modal Analysis (OMA) and Experimental Modal Analysis (EMA)—allow for the identification of natural frequencies, mode shapes, and damping coefficients; these parameters are particularly sensitive to changes in stiffness, boundary conditions, and energy dissipation [3, 4].

This paper describes the application of this approach to the Forgia railway bridge, located on the Trapani-Palermo line. The structure, which exhibited widespread corrosion at bolted joints, underwent an experimental testing campaign both before and after the intervention. Comparing the results makes it possible to interpret the effects of the restoration interventions and to establish an experimental baseline for potential future monitoring (Fig. 1).

2 Case Study and State of Deterioration

2.1 Description of the Work



Fig. 1. Side view of the Forgia Bridge.

The Forgia Bridge is a railway structure on the Trapani-Palermo line, located within the municipality of Balestrate, near the mouth of the stream of the same name and a short distance from the shoreline. Its location results in a harsh environmental exposure, characterized by the presence of salt spray and conditions conducive to the initiation and propagation of corrosion on the metal components.

The structure consists of metal trusses featuring a Warren configuration with a bottom-chord track layout and upper bracing. The main elements are constructed from rolled sections connected by bolted joints—a common design solution for metal railway bridges of that era [1]. The span between the bearing centerlines is 39.93 m; the spacing between the two trusses is 5.20 m, while the truss height is 6.90 m (Fig. 2 and Table 1).

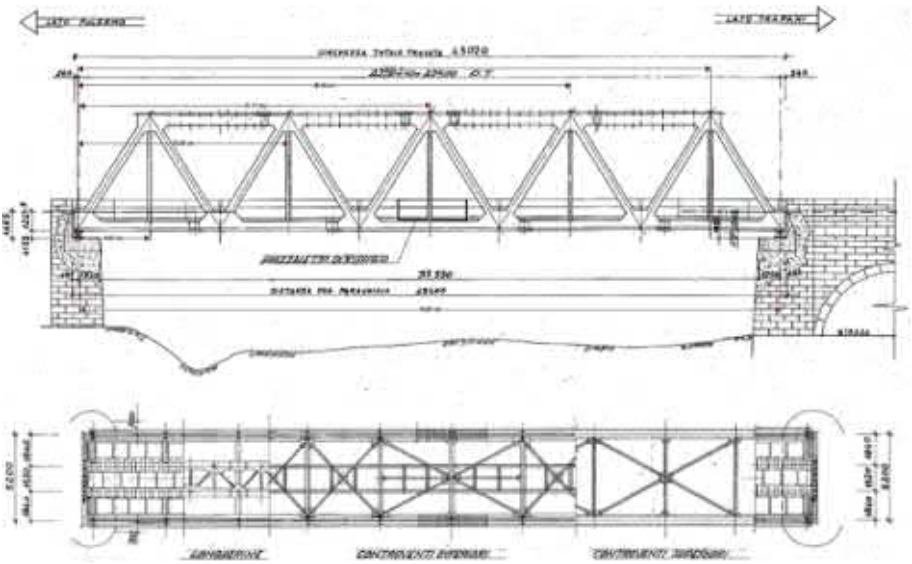


Fig. 2. General layout of the structure and main geometric dimensions.

Table 1. Main geometric and structural characteristics of the Forgia Bridge.

Parameter	Value
Structural scheme	Warren-type metal truss with a bottom chord deck
Clear span between bearing centerlines	39.93 m
Center-to-center distance between the two spans	5.20 m
Height of the truss girders	6.90 m
Connection type	Bolted connections on rolled sections

2.2 Corrosive Degradation and Maintenance Intervention

The deterioration observed prior to the work was primarily attributable to the corrosion of metal surfaces and, more notably, of the bolted connections. In some instances, oxidation had significantly affected the bolts, potentially reducing their load-bearing cross-section and consequently compromising the local efficiency of the connection. This phenomenon is particularly critical in a truss bridge, as the connections facilitate the transfer of axial forces between members and maintain the system's overall structural stiffness.

The major maintenance project involved replacing the bolts, abrasive blasting the metal components, and applying a protective coating. The objective was not only to halt the surface deterioration process but also to restore connection conditions that aligned with the structure's original configuration, thereby enhancing its durability and operational performance (Fig. 3).



Fig. 3. State of corrosive degradation observed on bolted joints and metal surfaces.

3 Influence of Corrosion on Structural Behaviour

In metal elements exposed to marine environments, corrosion can produce diverse and sometimes competing effects. On one hand, it causes material loss, thereby reducing local load-bearing capacity; on the other, it can alter connection behaviour through localized oxidation between plates, splice plates, and bolts.

In bolted joints, oxide formation can increase local friction, partially restrict relative slip, and create boundary conditions that differ from those envisaged in the original design.

These aspects are particularly significant for truss bridges, where force transfer relies on a system of members and connections. Even a localized change in joint efficiency

can affect the apparent stiffness of the entire truss, its deformation under load, and experimentally identified dynamic parameters. Consequently, any change in natural frequencies following maintenance cannot be automatically interpreted as a simple increase or decrease in structural safety.

Dynamic analysis is particularly useful in this context. Frequencies, mode shapes, and damping characteristics not only describe global stiffness but also reflect the system's boundary conditions and energy dissipation capabilities. Comparing pre- and post-intervention data thus makes it possible to assess whether restoring connections yields a more consistent response, even when frequency changes are minor or appear counterintuitive.

4 Pre- and Post-intervention Experimental Protocol

4.1 Investigation Programme

The experimental protocol was organized into two distinct campaigns. The first, conducted in July 2021, documented the condition of the structure prior to the intervention.

The second, carried out in March 2022, took place upon completion of the work. Repeating the same testing scheme allowed for a direct comparison between the two states, thereby reducing uncertainty associated with variations in the test setup (Fig. 4 and Table 2).

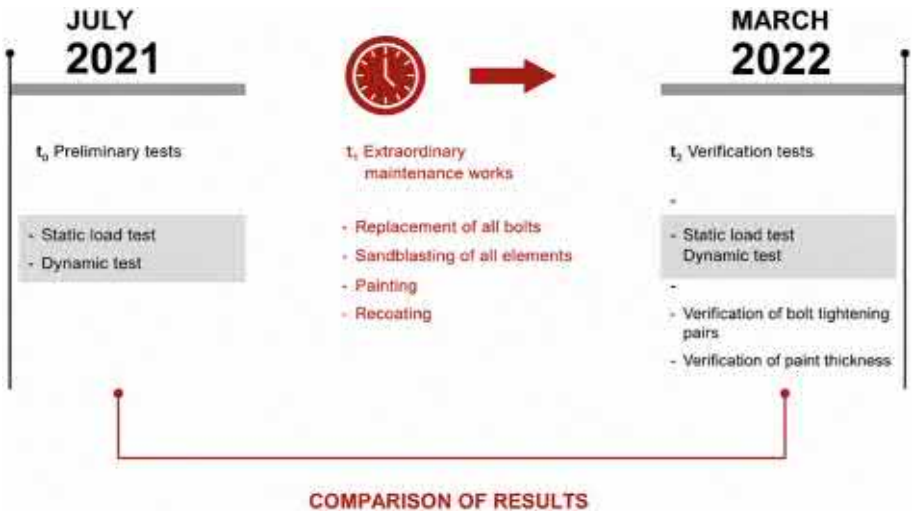


Fig. 4. Timeline of the pre- and post-intervention protocol.

Table 2. Structure of the experimental program.

Phase	Period	Key activities
Before the work begins	July 2021	Static load test; OMA/EMA dynamic characterization
Intervention	2021–2022	Bolt replacement; sandblasting; protective coating
After work	March 2022	Static load test; OMA/EMA dynamic characterization; complementary inspections

4.2 Static Tests

Static load tests were conducted using a hopper car weighing approximately 44 t to simulate the passage of a rail load across the deck. Six configurations were considered, encompassing both loading and unloading phases.

The most representative configurations were established by positioning the load 1.10 m from the axis of the Trapani-side bearing (measured to the front buffer) and 17.40 m from the same bearing; subsequent unloading phases allowed for the assessment of any residual deformation.

Static response was monitored using ten biaxial inclinometers installed on the top surface of the deck, oriented in both longitudinal and transverse directions. This setup enabled the reconstruction of the deformed shape of the two truss girders at mid-span and at the quarter-span points. Local deformation was evaluated using two electrical resistance strain gauges installed on the underside of the bottom chords of the downstream and upstream trusses, designated ER3 and ER6, respectively (Fig. 5 and Fig. 6).

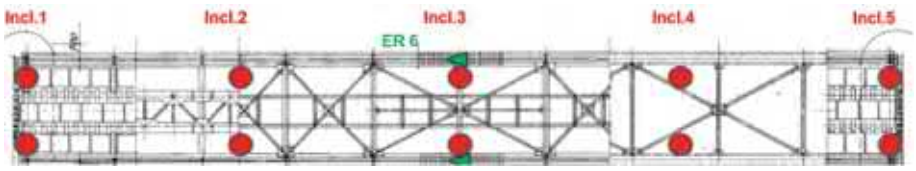


Fig. 5. Layout of static instrumentation: inclinometers and extensometers.

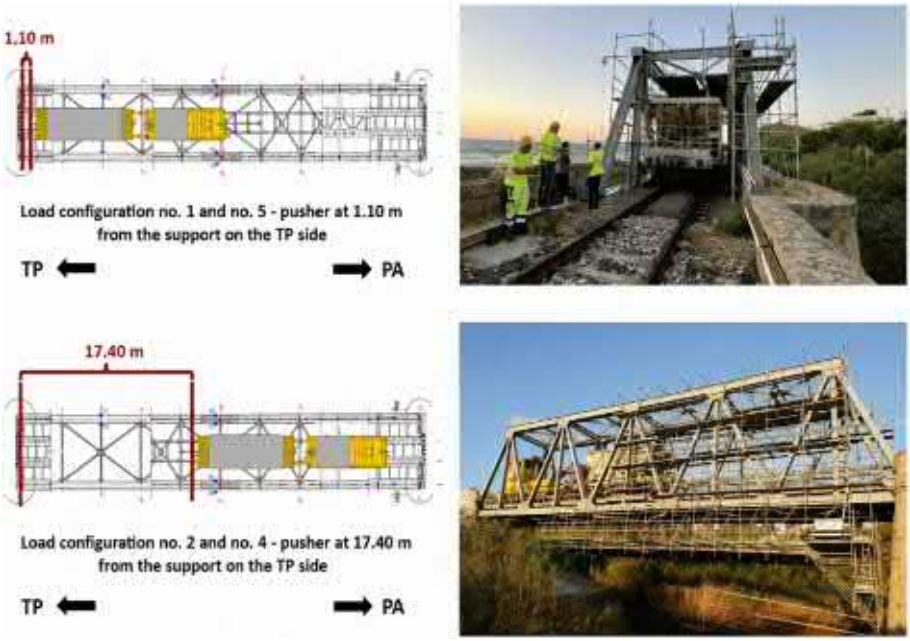


Fig. 6. Testing phases.

4.3 Dynamic Tests (OMA/EMA)

The dynamic tests were aimed at identifying the structure's key modal parameters both before and after the intervention. Accelerometers installed at strategic points on the deck were used for data acquisition, capturing both flexural modes and any torsional components of the response. The sensors were positioned at mid-span and at the quarter-span points on both sides of the girder, measuring in both vertical and horizontal directions to obtain a representative description of the overall dynamic behavior (Fig. 7).

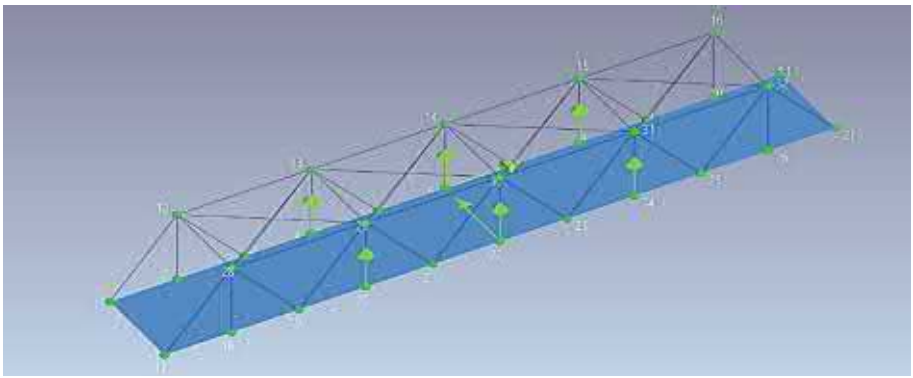


Fig. 7. Layout of the accelerometric instrumentation used for dynamic characterization.

Measurements were carried out using two complementary approaches. Operational Modal Analysis (OMA) was employed using ambient excitation—without artificial forcing—to identify the structure's natural frequencies and mode shapes [4]. Conversely, Experimental Modal Analysis (EMA), conducted using an instrumented hammer, allowed for the analysis of the free-oscillation response following a known input force, thereby supporting the estimation of damping coefficients [3].

The sampling frequency was set at 100 Hz, a value adequate for identifying the structure's first few modes. OMA data acquisition lasted long enough to ensure a stable representation of the dynamic response under ambient conditions; in this case, recordings of approximately 30 min were used. EMA acquisition, however, was limited to the transient phase following the impulse—lasting about 20 s—which was necessary for assessing damping.

The mode shapes identified in the two testing campaigns were compared using the Modal Assurance Criterion (MAC), which assesses the degree of correspondence between experimental modes before and after the intervention [6]. Values close to unity indicate good consistency between the compared mode shapes, whereas lower values may highlight differences in modal response or potential uncertainties in identification. In this instance, the MAC served as a tool to verify modal consistency and assist in interpreting the observed dynamic changes.

The combined use of OMA, EMA, and MAC analysis thus made it possible to evaluate not only changes in natural frequencies but also the stability of mode shapes and the evolution of the structure's energy-dissipation characteristics following maintenance interventions. In this way, the dynamic characterization provided a picture complementary to the static tests—particularly useful for interpreting the influence of the restoration of bolted joints and metal surfaces on the overall behaviour of the deck.

5 Experimental Results

5.1 Static Response

A comparison of the deformed shapes reconstructed using inclinometers reveals a response that is generally consistent with the applied loading patterns. In the configuration with the load applied 1.10 m from the Trapani-side support, the maximum deflection decreased from 8.12 mm during the July 2021 campaign to 4.88 mm during the March 2022 campaign. Conversely, in the configuration with the load at 17.40 m, the maximum values were essentially comparable, measuring 9.61 mm before the intervention and 9.58 mm after. During the unloading phase, the residual value decreased from 1.84 mm to 1.30 mm (Table 3).

Table 3. Summary comparison of maximum deflections in the pre- and post-intervention campaigns.

Test plan	Max deflection 2021 [mm]	Max deflection 2022 [mm]	Variation
Load at 1.10 m from the support on the Trapani side	8.12	4.88	−39.9%
Load at 17.40 m from the support on the Trapani side	9.61	9.58	−0.3%
Unloading after transit to Palermo	1.84	1.30	−29.3%

Strain gauge readings confirm the same pattern. The maximum strain measured at ER3 decreases from 92 με to 71 με, with the associated stress dropping from 19.32 MPa to 14.91 MPa; for ER6, the strain decreases from 74 με to 63 με, with stress falling from 15.54 MPa to 13.23 MPa. These values, referring solely to the added load, are low and consistent with elastic structural behaviour (Table 4).

Table 4. Comparison of maximum strains and stresses measured on the bottom chords.

Sensor	εmax 2021 [με]	σmax 2021 [MPa]	εmax 2022 [με]	σmax 2022 [MPa]	Variation σ
ER3	92	19.32	71	14.91	−22.8%
ER6	74	15.54	63	13.23	−14.9%

The reduction in residual deformation upon unloading is a particularly significant indicator, as it highlights a more consistent system response under loading and unloading cycles. This improvement is not uniform across all configurations; however, a direct comparison of tests repeated using the same protocol makes it possible to distinguish global effects from those dependent on the load position.

5.2 Static Response

Dynamic identification yielded four main modes, attributable to flexural and torsional forms of the deck. The pre- and post-intervention comparison reveals slight variations in natural frequencies—variations that are nonetheless significant from an interpretive standpoint. The first flexural mode shifts from 6.93 Hz to 6.24 Hz; subsequent modes show more limited variations, with frequencies of 14.01 Hz and 13.96 Hz for the second mode, 18.16 Hz and 18.02 Hz for the third, and 21.73 Hz and 21.41 Hz for the fourth (Table 5).

Table 5. Key dynamic parameters identified during the two campaigns.

Mode	Type	f 2021 [Hz]	f 2022 [Hz]	Variation
1	Flexional	6.93	6.24	−9.96%
2	Torsional	14.01	13.96	−0.36%
3	Flexional	18.16	18.02	−0.77%
4	Torsional	21.73	21.41	−1.47%
Damping	–	4.51%	5.26%	+16.6%

The most significant finding concerns the damping coefficient, which increases from 4.51% to 5.26%, representing a relative increase of approximately 17%. This result indicates a change in the structure's dissipative capacity—an aspect particularly useful for interpreting the role of connections and boundary conditions following the restoration.

A summary of the dynamic results is presented in (Fig. 8 and 9)

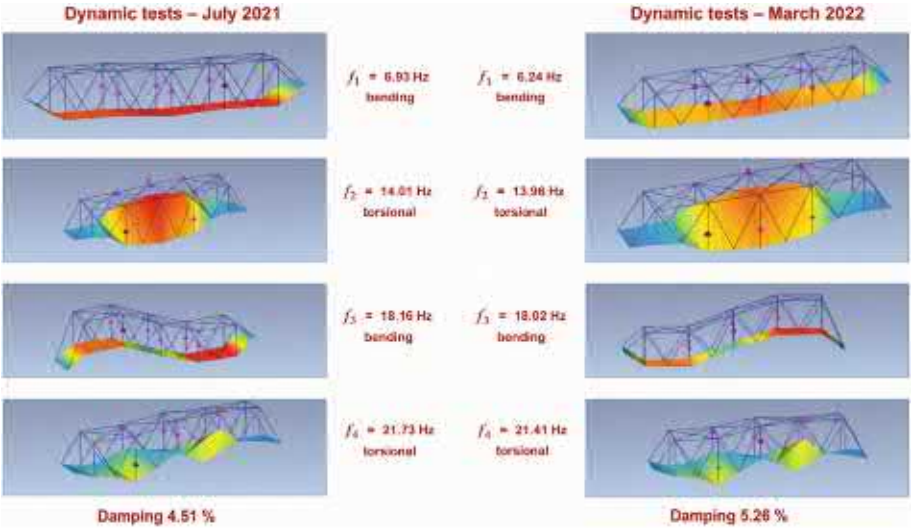


Fig. 8. Comparison of frequencies, mode shapes, and damping across testing campaigns.

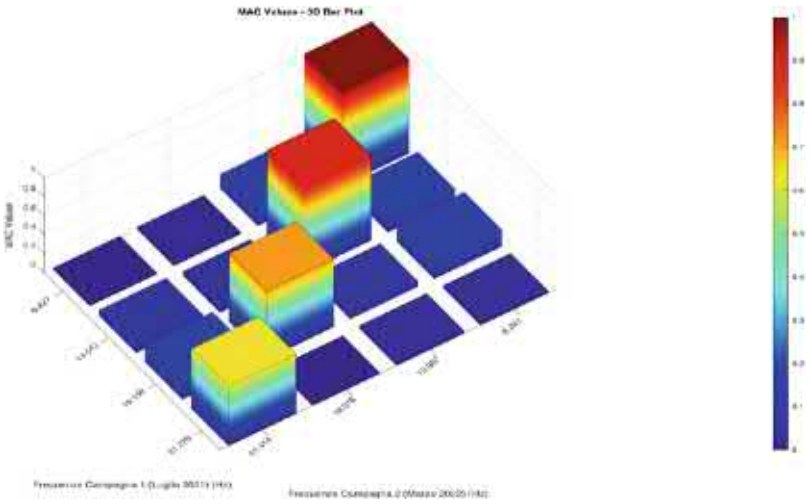


Fig. 9. Comparison of the modes identified in the two campaigns using MAC.

The MAC comparison shows the correspondence between the modal shapes identified in the two campaigns and makes it possible to verify that the observed variations are not due to an arbitrary change in modal identification. In this regard, the MAC serves as a tool for quality control of the comparison and supports the interpretation of frequency and damping variations.

5.3 Diagnostic Discussion

The results indicate that the effect of maintenance interventions cannot be interpreted solely in terms of an increase in global stiffness. In the case of metal truss structures with bolted joints, corrosion can create anomalous local conditions, resulting in apparent stiffening caused by oxide formation and reduced microslip between connected elements. Bolt replacement, sandblasting, and the restoration of surface protection can therefore alter connection behavior, once again allowing for a degree of local deformability within the joints.

From this perspective, the reduction in certain natural frequencies observed after the intervention should not automatically be interpreted as a loss of performance. Instead, it can be viewed as the result of restoring boundary conditions that are less artificially stiffened by corrosion. Concurrently, the increase in damping indicates greater energy dissipation capacity in the structure, consistent with connection behavior that is more regular and less constrained by oxidative phenomena.

It must also be noted that the two testing campaigns were conducted at different times of the year: preliminary tests took place in summer, with high average temperatures, whereas post-intervention tests were performed in March, under significantly lower thermal conditions. Such differences can influence the dynamic response of a metal structure and must be taken into account when interpreting frequency data quantitatively. However, a combined analysis of frequencies, mode shapes, damping, and static results allows for a more robust assessment than relying on a single indicator.

The pre- and post-intervention comparison thus demonstrates that evaluating the effectiveness of maintenance on degraded metal structures cannot rely solely on frequency variations. It is necessary to jointly interpret deformations, residual deflections, stresses, mode shapes, damping, and modal coherence. In this regard, the integration of static and dynamic tests represents an effective tool for distinguishing between actual performance improvement, changes in boundary conditions, and local modifications induced by the interventions.

6 Conclusions

This study presented an integrated experimental procedure to evaluate the influence of corrosion and maintenance interventions on the performance of a steel truss railway bridge. The approach was applied to the Forgia Bridge, located in a marine environment and characterized by widespread corrosion, particularly concentrated at the bolted joints.

Static tests conducted before and after the intervention revealed a reduction in deflection values under certain load configurations and, notably, a decrease in residual deformation upon unloading. Strain gauge measurements showed a reduction in peak strains and stresses in the bottom chords, confirming improved elastic behavior.

Dynamic tests (OMA/EMA) provided complementary insights, showing minor variations in natural frequencies and an increase in damping of approximately 17%. This result suggests that the interventions also affected connection conditions and the structure's energy dissipation capacity—aspects that are difficult to assess through visual inspections or static testing alone.

The case study thus confirms the value of pre- and post-intervention protocols that integrate static and dynamic measurements. The identified parameters establish an experimental baseline useful for both calibrating numerical models and implementing future structural health monitoring programs (Fig. 10).



Fig. 10. Photo of the Forgia Bridge after completion of the work.

References

1. De Miranda F (1989) Steel structure railway bridges. ILVA Monograph

2. International Organization for Standardization (ISO) Paints and varnishes – Corrosion protection of steel structures by protective paint systems. UNI EN ISO 12944.
3. Ewins DJ (2000) Modal testing: theory. Research Studies Press, Practice and Application
4. Brincker R, Ventura C (2015) Introduction to operational modal analysis. Wiley 5
5. Brincker R, Zhang L, Andersen P (2000) Modal identification from ambient responses using frequency domain decomposition. In: proceedings of the 18th international modal analysis conference (IMAC XVIII).
6. Allemang RJ (2003) The Modal Assurance Criterion–Twenty years of use and abuse. Sound Vib 37(8)
7. Welch PD (1967) The use of fast Fourier transform for the estimation of power spectra. IEEE Trans Audio Electroacoust 15(2):70–73

Enhanced Durability for Corrosion Protection of Steel Structures

Riccardo Tognaccini[1(✉)] and José Fernandes[2]

[1] Hempel, Genoa, Italy
rito@hempel.com
[2] Hempel, Barcelona, Spain

Abstract. Activated zinc primer technology has been developed to improve the corrosion protection of steel structures through enhanced zinc activation and optimized material utilization, strengthening the galvanic, barrier, and inhibitor mechanisms compared with conventional zinc-rich and barrier primer systems. Performance has been evaluated using standardized laboratory testing in accordance with ISO 12944-6 together with long-term atmospheric exposure in C5 and CX corrosivity environments. The results show improved resistance to corrosion creep, cyclic degradation, and mechanical damage while maintaining high durabil-ity under severe exposure conditions. The technology is compatible with a range of protec-tive coating systems, including epoxy intumescent coatings, and supports extended mainte-nance intervals. By extending coating service life and reducing maintenance frequency, activated zinc primers can contribute to lower lifecycle costs and embodied CO_2 emissions, supporting circular economy objectives and more sustainable steel use.

Keywords: Durability · Activated zinc paint technology · Corrosion · Performance enhancement · Sustain-ability

1 Introduction

Corrosion of steel is an electrochemical process that leads to progressive material degradation and structural failure if not properly controlled. Protective coating systems are widely used to mitigate this process by isolating the steel from aggressive environments and extending service life. In practice, these systems are typically composed of multiple layers, where overall performance depends on the interaction between each component and the quality of surface preparation.

Within such systems, the primer layer is critical, as it is applied directly onto the steel substrate and provides the primary corrosion protection mechanism. Zinc-rich primers, in particular, have been extensively used for decades and remain a standard solution for protecting steel structures in aggressive environments. Their performance is largely based on galvanic (cathodic) protection, where zinc particles act as sacrificial anodes and preferentially corrode to protect the underlying steel. This requires sufficient electrical connectivity within the coating and adequate zinc dispersion to enable current flow [1, 2].

© The Author(s), under exclusive license to Springer Nature Switzerland AG 2026
R. Zanon et al. (Eds.): CTA 2026, LNCE 942, pp. 960–970, 2026.
https://doi.org/10.1007/978-3-032-39505-4_83

In addition to galvanic action, modern primer technologies increasingly rely on a combination of barrier and inhibitive effects, contributing to overall durability. For instance, recent developments in activated zinc-rich primers demonstrate that corrosion protection is achieved through a synergy of galvanic, barrier, and inhibitor mechanisms, improving long-term performance and reducing degradation phenomena such as rust creep and blistering. These advances highlight that primer functionality extends beyond a simple sacrificial role and is fundamental to the robustness of the entire coating system [3].

Therefore, after surface preparation, the primer can be considered the most decisive element in determining coating system performance, as it governs adhesion to the substrate, controls early-stage corrosion processes, and ensures the effectiveness of subsequent layers.

2 General and Local Technical Standards

The specification and evaluation of corrosion protection systems are governed by a range of international and regional standards. Among these, ISO 12944 provides the principal framework for the selection, application, qualification, and maintenance of protective paint systems for steel structures. The standard classifies atmospheric environments according to their corrosivity, ranging from C1 (very low) to CX (extreme), and defines durability categories based on the expected period before major maintenance becomes necessary. The latest edition also distinguishes between high and very high durability categories (e.g., C5-H, C5-VH), enabling coating systems to be selected more precisely according to the intended service life.

Within ISO 12944, durability is not a warranty period but a technical estimate of the time until the coating system reaches a defined level of deterioration requiring major maintenance. This endpoint is commonly associated with rust grade Ri3, as defined in ISO 4628, corresponding to approximately 10% of the assessed surface exhibiting visible rusting. Importantly, Ri3 does not represent coating failure; rather, it indicates the stage at which maintenance should be scheduled to prevent accelerated substrate corrosion. A visual comparison of rust grades (Ri0–Ri4) is recommended to illustrate this criterion.

ISO 12944 also establishes qualification testing requirements for coating systems. While traditional neutral salt spray testing remains widely used, modern qualification increasingly relies on cyclic corrosion testing, which combines salt fog, humidity, drying, temperature variation, and ultraviolet exposure to better reproduce real service conditions. These accelerated ageing protocols provide a more representative assessment of coating durability and adhesion over time. Illustrations of cyclic corrosion chambers, QUV weathering equipment, and representative coated test panels before and after exposure help demonstrate the differences between the various testing methodologies. The distinction between C5-VH and CX environments is particularly important when specifying coating systems. C5-VH applies to very high durability requirements in severe industrial and marine atmospheres, whereas CX represents the most aggressive atmospheric exposure, including offshore structures and coastal environments subjected to persistent salt deposition and high humidity. Coating systems qualified for CX service therefore require more demanding performance during laboratory qualification testing.

Looking ahead to the next ISO 12944 revision cycle (currently under development and expected to be published progressively around 2028), the focus appears to be on updating several core parts of the standard. The ongoing revisions reflect the industry's increasing need to address new protective coating technologies, sustainability requirements, evolving corrosion environments and improved surface-preparation practices. This direction is consistent with the paradigm shift highlighted in this paper: moving from prescriptive coating-system requirements toward a stronger emphasis on demonstrated performance and durability validation, thereby creating greater opportunities for innovative, lower-carbon corrosion protection solutions [4].

Beyond ISO standards, several sector-specific specifications further define coating requirements. NORSOK M-501, developed for the offshore oil and gas industry, specifies a series of approved coating systems for different service conditions. For example, System 1B incorporates a zinc-rich epoxy primer, providing sacrificial cathodic protection in addition to barrier protection, whereas Systems 1A, 7A, and 7B address other combinations of environmental exposure and surface preparation. Similarly, ZTV-ING BLATT 100 (Module A) specifies coating systems for steel bridges that typically include a zinc-rich epoxy primer, epoxy intermediate coats, and a polyurethane finish, with durability targets approaching 50 years under appropriate inspection and maintenance regimes. Performance evaluation also differs among specification bodies. ACQPA distinguishes between corrosion protection, which determines the functional durability of the coating system, and colour and gloss stability, which relate only to its aesthetic appearance. This distinction recognises that surface fading or gloss loss does not necessarily imply a reduction in corrosion protection, allowing functional performance and visual ageing to be assessed independently.

3 Types of Primers

Primers constitute the first line of defense in a protective coating system and have a decisive influence on the long-term corrosion performance of steel structures. Their primary function is to provide adhesion to the substrate while preventing corrosion through barrier protection, galvanic protection, or a combination of both. Conventional primer technologies generally fall into two categories: barrier primers, which rely on low permeability to isolate the steel from the environment, and zinc-rich primers, which provide sacrificial cathodic protection through electrically connected zinc particles.

Although zinc-rich primers are often considered a single product category, their performance can vary considerably depending on formulation. Factors such as zinc particle size and morphology, zinc loading, resin chemistry, particle distribution, and electrical connectivity all influence the effectiveness of galvanic protection. Consequently, two primers classified as "zinc-rich" may exhibit substantially different corrosion resistance and long-term durability despite having similar nominal zinc contents. Comparative laboratory testing frequently demonstrates significant differences in corrosion creep, adhesion retention, and mechanical integrity between conventional zinc-rich formulations (Fig. 1).

Barrier primers provide excellent protection as long as the coating remains intact but offer limited resistance once mechanical damage exposes the underlying steel.

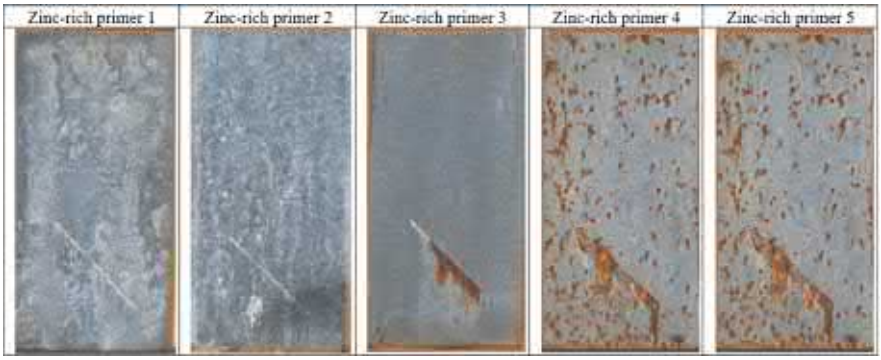


Fig. 1. Qualitative comparison between different primers classified as "zinc-rich". Primers applied between 70–80 μm and exposed to salt spray test (ISO 9227) for 1.800 h.

Conventional zinc-rich primers provide active protection at damaged areas; however, they typically require very high zinc loading to maintain electrical continuity throughout the coating. This high pigment concentration can increase porosity, reduce flexibility, complicate application, and affect overcoating performance. The challenge for modern primer technology is therefore to maximize galvanic efficiency while maintaining good mechanical and application properties.

Activated zinc primer technology represents an important evolution of conventional zinc-rich coatings. Through the synergistic interaction of zinc, hollow glass spheres, and a proprietary activator, these systems combine galvanic, barrier, and inhibitor mechanisms to improve corrosion protection. Activation increases the utilisation of zinc for cathodic protection, while zinc corrosion products enhance barrier performance by reducing water permeability. In addition, the coating captures aggressive ionic species, limiting their transport to the steel substrate. This multi-mechanistic protection results in improved resistance to rust creep, enhanced mechanical performance, and increased coating durability under severe corrosive conditions [5].

Experimental qualification testing has demonstrated the capability of activated zinc-rich primers to meet demanding durability requirements with simplified coating systems. For example, C3-VH performance has been achieved with a single 100 μm coating, C4-VH qualification with a two-coat system having a total dry film thickness of approximately 160 μm, and C5-VH with a two-coat system having a total dry film thickness of approximately 300 μm.

In the case of the single-coat C3-VH system shown in Fig. 3, the activated zinc primer applied at a nominal dry film thickness of 100 μm was tested in accordance with ISO 12944-6 by an independent accredited laboratory and successfully met all requirements for corrosivity category C3 Very High. Following 720 h of neutral salt spray exposure (ISO 9227), the coating exhibited no blistering [0(S0)], no rusting (Ri 0), no cracking [0(S0)] and no flaking [0(S0)]. Adhesion remained high after exposure, with pull-off strengths ranging from 6.7 to 9.7 MPa and panel averages of 7, 8 and 9 MPa, significantly exceeding the ISO 12944-6 minimum requirement of 2.5 MPa. Corrosion propagation from the scribe was measured as 0.0 mm on all three test panels (maximum allowable

limit of 1.5 mm). Furthermore, the system achieved Cross-Cut classifications of 0 and X-Cut classifications of 0 after salt spray exposure, confirming excellent coating adhesion and integrity following accelerated ageing. The visual appearance of the panels after testing, shown in Fig. 2, corroborates the quantitative assessment, with no observable coating defects and no measurable underfilm corrosion originating from the scribe.

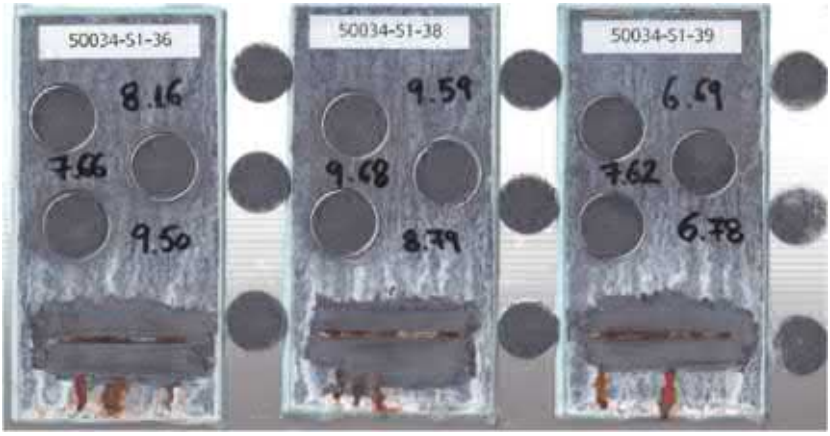


Fig. 2. C3-VH performance requirements were achieved using a single 100 µm coating

For the C5-VH system illustrated in Fig. 3, a coating system comprising an activated zinc-rich primer and a topcoat with a combined dry film thickness of approximately 300 µm was independently tested in accordance with ISO 12944-6 and successfully achieved the requirements for Corrosivity Category C5 Very High. Following 2,688 h of cyclic ageing, consisting of repeated UV/condensation, salt spray, and low-temperature exposure cycles, the panels exhibited no blistering [0(S0)], no rusting (Ri 0), no cracking [0(S0)], and no flaking [0(S0)].

From a quantitative performance standpoint, the system passed the qualification requirements with a substantial margin. Pull-off adhesion values after exposure ranged from 6.8 to 10.5 MPa, with average values between 9 and 10 MPa, representing more than three times the minimum 2.5 MPa acceptance criterion specified by ISO 12944-6. Corrosion creep from the scribe was measured at 2.3 mm, 1.8 mm, and 2.4 mm on the three replicate panels, all well below the maximum allowable limit of 3.0 mm for C5-VH qualification. The average corrosion creep across all panels was approximately 2.2 mm, providing a comfortable compliance margin and demonstrating excellent underfilm corrosion resistance under severe cyclic ageing conditions.

The visual appearance of the panels after testing, shown in Fig. 3, fully supports the quantitative data, with no visible coating degradation, blistering, rusting, cracking, or flaking observed after completion of the exposure programme. Taken together, the visual assessments and measured performance results demonstrate that the activated zinc-rich primer system not only satisfied the C5-VH requirements but did so convincingly, maintaining excellent adhesion, coating integrity, and corrosion protection throughout the full 2,688-h test programme.

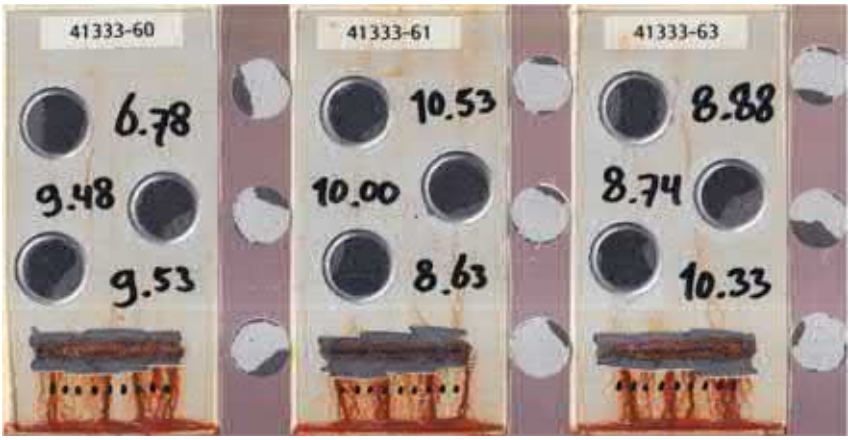


Fig. 3. C5-VH performance requirements were achieved using a two coat 300 µm coating

The examples above demonstrate how activated zinc-rich primers can maximise corrosion protection efficiency by reducing both the minimum number of coats and nominal dry film thickness without compromising durability. Through enhanced zinc utilisation and anticorrosive performance, these systems enable qualification of coating specifications that would traditionally require thicker films and more complex paint systems. Lower paint consumption reduces material use, CO_2 emissions, and VOC releases, while fewer coats improve application efficiency, shorten project schedules, and reduce labour costs. These results show how advances in primer technology can simplify coating specifications while maintaining high corrosion resistance and long-term durability. Simplified coating systems also improve application consistency and reduce the risk of coating defects, helping asset owners achieve long-term durability with a smaller environmental footprint and lower total lifecycle costs.

4 Enhanced Durability

Long-term accelerated corrosion testing further highlights the performance differences between conventional and advanced zinc-rich systems. Whereas many qualification programmes conclude after approximately 2,688 h of cyclic exposure, extended testing beyond 6,000 h provides a more discriminating assessment of coating durability, corrosion creep from artificial defects, adhesion retention, and overall system robustness. Such extended exposure demonstrates that not all zinc-rich primers provide equivalent long-term protection and emphasises the importance of evaluating complete system performance rather than zinc content alone.

This distinction is clearly illustrated by the results shown in Fig. 4. After 6,720 h (280 days) of cyclic ageing in accordance with ISO 12944-9:2018, the activated zinc-rich primer system continued to satisfy the requirements for CX offshore environments. All three test panels achieved Ri0 rust rating, 0(S0) blistering, 0(S0) cracking, and 0(S0) flaking, while corrosion creep from the scribe remained between 2.6 and 2.9 mm, below the 3.0 mm acceptance criterion for CX systems. Adhesion was also well maintained after

exposure, with average pull-off values of 6.9, 10.1 and 8.6 MPa, demonstrating substantial retention of coating integrity following nearly seven thousand hours of accelerated ageing. These quantitative results confirm the excellent long-term durability suggested by the visual appearance of the panels in Fig. 4.

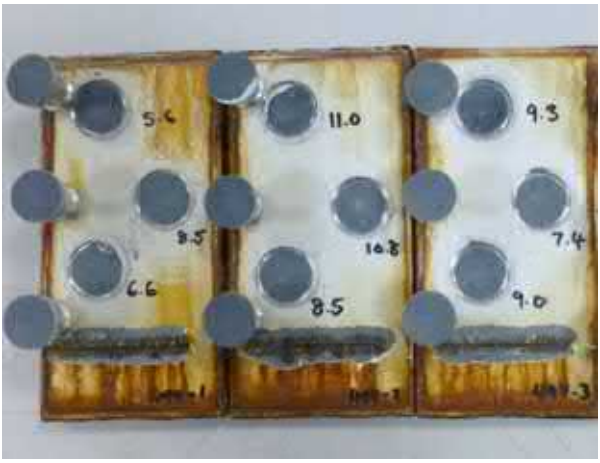


Fig. 4. Third-party results after 6720 h (280 days) cyclic ageing test (Annex B of ISO 12944-9:2018)

Durability is a critical parameter in the evaluation of protective coating systems because it directly influences maintenance intervals, lifecycle costs, asset availability, and environmental impact. Experimental qualification testing has demonstrated that advanced activated zinc-rich primer systems can significantly improve corrosion protection durability through a combination of galvanic protection, barrier properties, and corrosion-inhibiting mechanisms that delay corrosion initiation and propagation.

A key benefit of these systems is their ability to minimise corrosion creep from mechanically damaged areas. By maintaining sacrificial protection around scratches and coating defects, activated zinc-rich primers reduce underfilm corrosion, preserve adhesion, and consistently deliver improved long-term performance in laboratory and accelerated cyclic corrosion testing compared with conventional zinc-rich primer technologies.

Extended experimental testing indicates that these systems can achieve corrosion protection equivalent to service lives of approximately 35 years in appropriately designed coating systems for aggressive atmospheric environments, including C5 and CX exposure classes. This increased durability translates directly into reduced maintenance frequency, lower whole-life costs, and continued protection of the steel substrate.

An important distinction should be made between corrosion durability and aesthetic durability. While weathering may gradually affect colour, gloss, or surface appearance, these changes do not necessarily reduce corrosion protection performance. Functional durability and aesthetic performance should therefore be evaluated independently. Where long-term colour and gloss retention are important, polysiloxane topcoats can offer

advantages over conventional polyurethane finishes through their superior resistance to ultraviolet radiation, providing improved colour stability and gloss retention while maintaining the corrosion protection delivered by the complete coating system.

5 Laboratory Testing Procedure

All accelerated corrosion tests presented in this paper were conducted and assessed by external accredited laboratories in accordance with ISO 12944-9:2018. The test panels consisted of cold-rolled mild steel measuring 100 × 150 × 1.6 mm. Surface preparation was carried out by abrasive blasting to Sa 3 for thermal spray metallization systems and Sa 2½ for activated zinc primer systems in accordance with ISO 8501-1.

The accelerated ageing cycle lasted one week (168 h) and comprised 72 h of QUV weathering, 72 h of salt spray testing (SST), and 24 h of thermal shock at −20 °C (−4 °F). QUV exposure was performed according to ISO 11507 using alternating cycles of 4 h UV exposure at 60 ± 3 °C with UVA-340 lamps and 4 h condensation at 50 ± 3 °C. Salt spray exposure followed ISO 7253 using a continuous 5% NaCl solution at 35 °C, while thermal shock consisted of exposure at −20 ± 2 °C. Total test durations were 25 cycles (4,200 h) for CX, 40 cycles (6,720 h) for CX Extended, and 10 cycles (1,680 h) for C5 High Regime 2.

Before testing, panels were scribed with a 2 mm wide cut through to the substrate, positioned 20 mm from the panel edges. After exposure, corrosion creep from the scribe was measured at nine locations and calculated as $M = (C - W)/2$, where C is the average measured corrosion width and W is the original scribe width.

6 Protection Against Fire

Fire protection is an essential design consideration for many steel structures, particularly in industrial facilities, transportation infrastructure, energy installations, and offshore environments where both corrosion and fire represent significant risks. Passive fire protection is commonly achieved using intumescent coatings, which expand when exposed to elevated temperatures to form an insulating char layer that delays the heating of the steel and preserves its load-bearing capacity during a fire.

The long-term performance of an intumescent coating depends not only on its fire resistance but also on the durability of the underlying corrosion protection system. If corrosion develops beneath the fire protection layer, both structural integrity and the effectiveness of the passive fire protection system may be compromised. For this reason, compatibility between the corrosion protection primer and the intumescent coating is a fundamental requirement when designing integrated protective systems. Among the available intumescent coating technologies, acrylic systems are the most widely used. These can be broadly classified into water-based acrylics and solvent-based acrylics. Water-based acrylic intumescent coatings are typically used in interior environments and are generally suitable for corrosivity categories up to C3 according to ISO 12944. Solvent-based acrylic systems offer enhanced environmental resistance and can be used in both interior and exterior applications, typically up to corrosivity category C4. Epoxy intumescent coatings represent a distinct technology from acrylic systems and provide

a significantly higher level of durability and environmental resistance. In addition to their superior mechanical strength, impact resistance, and overall robustness, epoxy intumescent coatings can be used in aggressive exterior environments, typically up to corrosivity category C5 according to ISO 12944.

Activated zinc-rich primers provide an excellent foundation for both acrylic and epoxy intumescent coatings by combining long-term galvanic corrosion protection with strong adhesion and excellent compatibility throughout the complete coating system. The resulting system protects the steel against atmospheric corrosion during normal service while simultaneously providing certified passive fire protection when exposed to fire.

Experimental qualification and durability testing have demonstrated that coating systems combining activated zinc-rich primers with specifically epoxy intumescent coatings can achieve approximately 35 years of corrosion protection in aggressive atmospheric environments while maintaining the required fire protection performance throughout the service life of the system. This integrated approach reduces maintenance requirements, simplifies specification, and supports lower whole-life costs by addressing both corrosion and fire protection within a single engineered coating solution.

7 Case Study: Santiago Bernabéu Stadium Renovation

The renovation of the Santiago Bernabéu stadium was not just about enhancing its structure but transforming it into the most modern entertainment venue in Europe. This transformation demanded a corrosion and fire protection solution that met the highest standards of safety and efficiency.

Hempel provided a comprehensive passive fire protection system called Hempafire Pro 315, renowned for its accurate dry film thickness (DFT) and exceptional performance in critical fire safety applications. This solution was complemented by Hempadur Avantguard 750 as an activated zinc-rich epoxy primer and Hempathane HS 55610 as a high gloss polyurethane topcoat for the structural elements. The roof cover also utilized Hempadur Mastic 45880 as a primer along with the same intumescent coating and topcoat, ensuring uniformity and the highest safety standards across the entire structure (Fig. 5).

The Hempafire passive fire protection solution has been integral in ensuring that the Santiago Bernabéu stadium meets the current standards and anticipates future safety requirements, affirming its status as Europe's most advanced entertainment venue. The project not only demonstrates Hempel's commitment to innovation and safety but also reinforces our position as a leader in industrial and building construction solutions (Fig. 6).



Fig. 5. View of the painted roof structure of the stadium



Fig. 6. View of the painted roof structure of the stadium

8 Conclusions

Advances in activated zinc primer technology demonstrate that long-term corrosion protection is not solely dependent on high zinc loading or increased coating thickness. By combining galvanic, barrier, and inhibitive protection mechanisms, activated zinc-rich systems provide enhanced resistance to corrosion creep, mechanical degradation, and aggressive environments. Qualification testing and extended cyclic ageing programmes have confirmed that these systems can achieve very high durability classifications with reduced coating complexity and material consumption.

The results presented in this paper show that durability should be assessed through overall system performance rather than individual coating characteristics. Activated zinc-rich primers enable steel structures in C5 and CX environments to achieve corrosion protection equivalent to service lives approaching 35 years while remaining compatible with modern protective solutions, including epoxy intumescent fire protection. The

resulting increase in durability reduces maintenance frequency, improves asset availability, and lowers lifecycle costs. In addition to their technical advantages, activated zinc-rich primer systems support more sustainable and performance-based corrosion protection strategies. By reducing paint consumption, maintenance requirements, and associated CO_2 emissions, they contribute to both economic and environmental objectives and are well positioned to play an important role in the future protection of steel infrastructure.

References

1. Yagüe A, Morton D (2020) Challenging the organic "zinc-rich" primer standard. J Prot Coat Linings 37(3):16–20
2. Hare CH, Steele M, Collins SP (2001) Zinc loadings, cathodic protection, and post-cathodic protective mechanisms in organic zinc-rich metal primers. J Prot Coat Linings 18(9):54–72
3. Prieto A (2016) The Avantguard product range—innovative zinc-rich epoxy primers with outstanding corrosion protection. In: NACE Milano Italia Section International Conference & Expo 2016, Genoa, Italy, 29–31 may 2016.
4. Hempel A (2024) Standards and the adoption of new technologies in corrosion protection. Hempel A/S, Kgs. Lyngby, White paper
5. Hempel A (2025) Avantguard: long-lasting corrosion protection with less environmental impact. Hempel A/S, Kgs. Lyngby, Product brochure

Stress Concentrations in Steel Structural Details: A Linear Strain-Based Approach for Cyclic Plasticity

Marco Gastaldello[1(✉)], Alessandro Catanzano[2], Filippo Berto[3], Anna Saetta[1], and Roberto Scotta[4]

[1] Department of Architecture and Arts, IUAV University of Venice, Santa Croce 191, 30135 Venice, Italy
mgastaldello@iuav.it
[2] Santo Engineering S.r.l., Via San Crispino 12, 35129 Padua, Italy
[3] Department of Chemical Engineering, Materials and Environment, Sapienza University of Rome, Via Eudossiana 18, 00184 Rome, Italy
[4] Department of Civil, Environmental and Architectural Engineering, University of Padua, Via Marzolo 9, 35131 Padua, Italy

Abstract. Fatigue verification of steel structures is commonly carried out using stress-based criteria derived from elastic analyses. This approach is well established for high-cycle fatigue, characterized by predominantly elastic material behavior. However, it becomes less effective when cyclic loading induces localized plasticity at critical structural details, leading to fatigue damage governed by strain-driven mechanisms not explicitly addressed within conventional linear design frameworks.

This work proposes a strain-based methodology to evaluate monotonic and cyclic plastic behaviour, as well as low-cycle fatigue damage, in steel structural details using only the results of linear elastic finite element analyses. The approach is based on Neuber's rule, combined with Ramberg–Osgood monotonic and cyclic material laws, the Smith–Watson–Topper parameter for mean-stress effects, and Miner's rule for cumulative damage. Notch effects are introduced through the fatigue stress concentration factor K_f, enabling a clear distinction between elastic stress amplification K_t and fatigue-relevant local response.

The methodology is applied to two case studies. A perforated plate under monotonic loading is benchmarked against a materially nonlinear finite element solution, clarifying the domain of applicability of the method. A welded beam-to-column joint subjected to seismic loading demonstrates the complete cyclic workflow at structural scale, including rainflow counting, local elasto-plastic correction and cumulative damage evaluation. The results confirm that the proposed approach provides practical and computationally efficient estimates of local fatigue demand at steel structural details.

Keywords: Steel structures · stress concentration · cyclic plasticity · low-cycle fatigue · Neuber rule

© The Author(s), under exclusive license to Springer Nature Switzerland AG 2026
R. Zanon et al. (Eds.): CTA 2026, LNCE 942, pp. 971–981, 2026.
https://doi.org/10.1007/978-3-032-39505-4_84

1 Introduction

Fatigue assessment of steel structures is well established for high-cycle fatigue, but becomes less effective when cyclic loading induces localised plasticity at critical structural details. Under these conditions, fatigue damage is governed by strain-driven mechanisms that standard linear frameworks do not explicitly address.

Current Eurocode provisions for fatigue in steel structures, including the upcoming prEN 1993-1-9 [4], classify structural details through nominal fatigue strength categories and impose stress-range limitations to prevent low-cycle fatigue, but do not provide an explicit procedure to quantify crack-initiation demand at the notch level. The cyclic plasticity limit state LS2 of EN 1993-1-6 [2] addresses plastic strain at a smooth reference point outside the notch field, without transferring this demand to the local detail. This gap is particularly relevant under seismic loading, where few severe cycles may concentrate significant plastic demand at welded joints even when global elastic checks are satisfied.

A direct solution would require materially nonlinear finite element analyses of the full structure, which are computationally demanding and impractical for design-oriented assessments. This motivates the development of simplified procedures capable of estimating local elasto-plastic response and low-cycle fatigue damage from the results of conventional linear analyses.

This paper proposes a strain-based methodology for the low-cycle fatigue assessment of steel structural details using only results from linear elastic finite element analyses. The approach converts nominal elastic stresses into local elasto-plastic quantities through a fatigue notch factor K_f, derived consistently from the fatigue detail categories of prEN 1993-1-9 [4], combined with established strain-life methods within the ISO 19902 initiation-life framework [5].

The methodology is evaluated through two applications. The first considers a perforated steel plate under monotonic loading and serves as a benchmark against a materially nonlinear finite element solution. The second addresses a welded beam-to-column joint subjected to seismic loading and demonstrates the full cyclic workflow at structural scale.

2 Methodology

2.1 Nominal Stress and Fatigue Notch Factor

The procedure operates on nominal elastic stresses S evaluated at a smooth reference location outside the notch field, consistently with prEN 1993-1-9 [4]. The nominal stress location is commonly taken at a distance of approximately $1.5t$ from the stress raiser, where t is the thickness of the adjacent plate, so as to exclude the localised stress field induced by the geometric discontinuity. This assumption is consistent with established practice in the fatigue assessment of welded joints, where the stress at a location 1.0–1.5 times the wall thickness away from the weld toe is commonly taken as nominal stress, since the nonlinear stress peak induced by the weld geometry decays within this region [12].

Two stress concentration factors are distinguished. The theoretical factor K_t captures the purely elastic amplification at a geometric discontinuity:

$$K_t = \frac{\sigma_e}{S} \tag{1}$$

The fatigue notch factor K_f additionally accounts for the material response under cyclic loading and is defined as the ratio between the fatigue strengths of smooth and notched specimens:

$$K_f = \frac{f_{\text{smooth}}}{f_{\text{notch}}} \tag{2}$$

For large notch radii $K_f \approx K_t$; for sharp notches such as weld toes $K_f < K_t$ [7]. In the present work, K_f is derived from the fatigue detail categories of prEN 1993-1-9 [4], interpreting lower categories as more severe notch conditions:

$$K_f = \frac{\text{FAT}_{\text{ref}}}{\text{FAT}_{\text{detail}}} \tag{3}$$

The elastic notch stress used as input to the local correction is:

$$\sigma_e = K_f \cdot S \tag{4}$$

2.2 Neuber's Rule and Cyclic Ramberg–Osgood Relationship

Neuber's rule [6] states that the product of elasto-plastic stress and strain at the notch equals the elastic solution:

$$\sigma\varepsilon = \frac{(K_f S)^2}{E} \tag{5}$$

The notch constitutive response is described by the Ramberg–Osgood relationship [7]. Under monotonic loading:

$$\varepsilon = \frac{\sigma}{E} + \left(\frac{\sigma}{K}\right)^{1/n} \tag{6}$$

Under cyclic loading, the stabilised hysteresis loop is expressed in terms of ranges, with distinct hardening parameters K' and n' accounting for cyclic hardening or softening:

$$\Delta\varepsilon = \frac{\Delta\sigma}{E} + 2\left(\frac{\Delta\sigma}{2K'}\right)^{1/n'} \tag{7}$$

Combining Eqs. (5) and (7) yields the cyclic Neuber equation, solved numerically for $\Delta\sigma$:

$$\Delta\sigma\left[\frac{\Delta\sigma}{E} + 2\left(\frac{\Delta\sigma}{2K'}\right)^{1/n'}\right] = \frac{(K_f \Delta S)^2}{E} \tag{8}$$

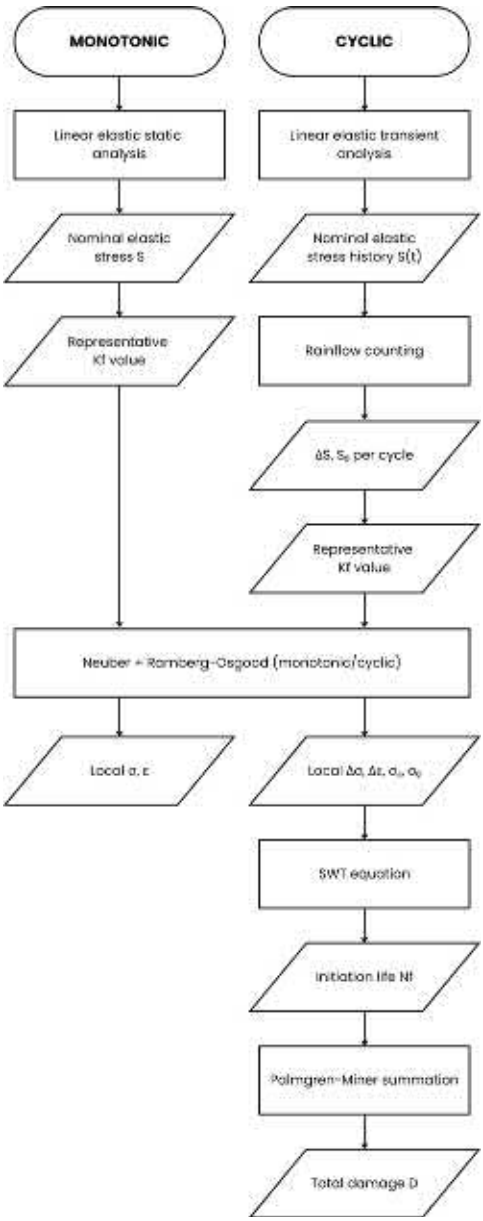


Fig. 1. Computational workflow of the proposed linear global-to-local LCF assessment procedure. The monotonic branch (left) and cyclic branch (right) share the same local correction steps.

2.3 Smith–Watson–Topper Formulation and Life Estimation

The local stress amplitude σ_a and mean stress σ_0 required for the fatigue assessment are recovered from the peak stress σ_p, obtained by applying the Neuber–Ramberg–Osgood combination to the peak elastic quantity:

$$\sigma_p \left[\frac{\sigma_p}{E} + \left(\frac{\sigma_p}{K'} \right)^{1/n'} \right] = \frac{K_f^2}{E} \left(S_0 + \frac{\Delta S}{2} \right)^2 \tag{9}$$

$$\sigma_a = \frac{\Delta \sigma}{2}, \qquad \sigma_0 = \sigma_p - \frac{\Delta \sigma}{2} \tag{10}$$

Mean stress effects are accounted for through the Smith–Watson–Topper (SWT) parameter [8]. The equivalent fully reversed stress amplitude is obtained following ISO 19902 [5]:

$$\sigma_{re} = \left[\frac{\sigma_a}{1 - \sigma_0 / \sigma'_f} \sqrt{(\sigma_0 + \sigma_a)\, \sigma_a} \right]^{0.5} \tag{11}$$

The corresponding strain amplitude follows from the cyclic Ramberg–Osgood law:

$$\varepsilon_{re} = \frac{\sigma_{re}}{E} + \left(\frac{\sigma_{re}}{K'} \right)^{1/n'} \tag{12}$$

The crack-initiation life N_f is obtained by solving:

$$\sigma_{re}\, \varepsilon_{re}\, E = (\sigma'_f)^2 (2N_f)^{2b} + \sigma'_f\, \varepsilon'_f\, E\, (2N_f)^{b+c} \tag{13}$$

2.4 Cumulative Damage and Computational Workflow

For variable-amplitude loading, rainflow counting decomposes the stress history into cycles $(\Delta S_i,\, S_{0,i})$. Each cycle is processed through Sects. 2.1, 2.2 and 2.3 to obtain $N_{f,i}$, and cumulative damage is assembled via Palmgren–Miner summation [9,10]:

$$D = \sum_i \frac{n_i}{N_{f,i}} \tag{14}$$

Failure is assumed at $D = 1$. The complete computational workflow is summarised in Fig. 1.

3 Case Study 1: Perforated Plate Under Monotonic Loading

The proposed procedure is first verified against a materially nonlinear finite element solution on a simple and controlled geometry. A perforated S355 steel plate is subjected to monotonic tensile loading, with net cross-sectional area $A_{\text{net}} = (b - d)\, t = 5000\,\text{mm}^2$ and applied force $F = 1800\,\text{kN}$, giving a nominal stress $S = 360\,\text{MPa}$. The hole radius is sufficiently large to justify $K_f = K_t = 3$

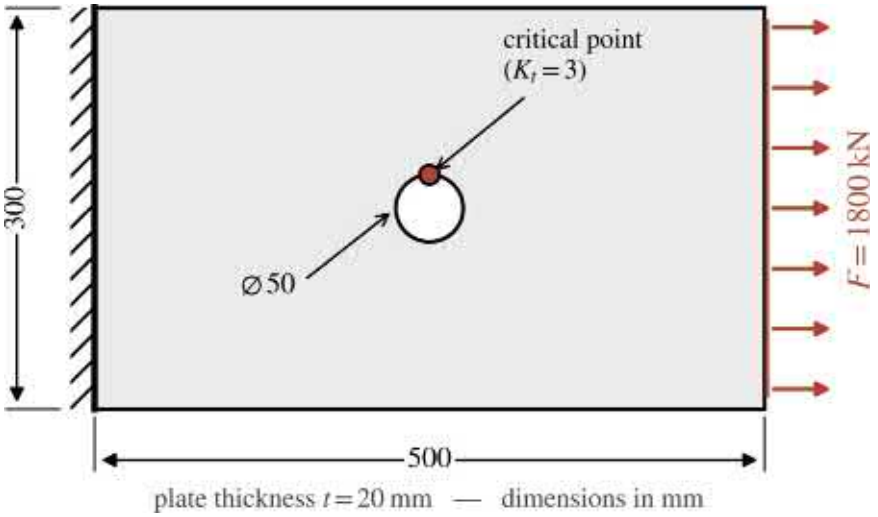


Fig. 2. Geometry, boundary conditions and loading of the perforated plate of Case study 1, fully restrained at one end and subjected to a uniform tensile force at the opposite end (dimensions in mm). The critical point is located at the hole edge on the net section ($K_t = 3$).

Table 1. Monotonic material parameters for S355 steel.

Parameter	Symbol	Value
Yield strength	f_y	355 MPa
Ultimate strength	f_u	490 MPa
Elastic modulus	E	206 000 MPa
Hardening exponent	n	8.00
Second hardening exponent	m	3.49

from Peterson's charts [11], yielding an elastic notch stress $\sigma_e = 1080$ MPa. The geometry, boundary conditions and loading scheme are shown in Fig. 2.

Applying the Neuber–Ramberg–Osgood procedure of Sect. 2 with the monotonic material parameters of S355 (Table 1) gives a local elasto-plastic state of $\sigma = 409$ MPa and $\varepsilon = 1.36\%$. The same result is reproduced by the automated numerical implementation, confirming the correctness of the workflow. A materially nonlinear finite element model of the same plate yields $\sigma = 436$ MPa and $\varepsilon = 4.46\%$ at the same load level, as shown in Fig. 3.

The deviation between the Neuber estimate and the nonlinear solution reflects the progressive spread of plasticity over the net section as load increases—a redistribution that the point-based Neuber procedure does not capture. Agreement is satisfactory while plasticity remains localised near the hole, which is the typical condition for welded details and sharp notches with high

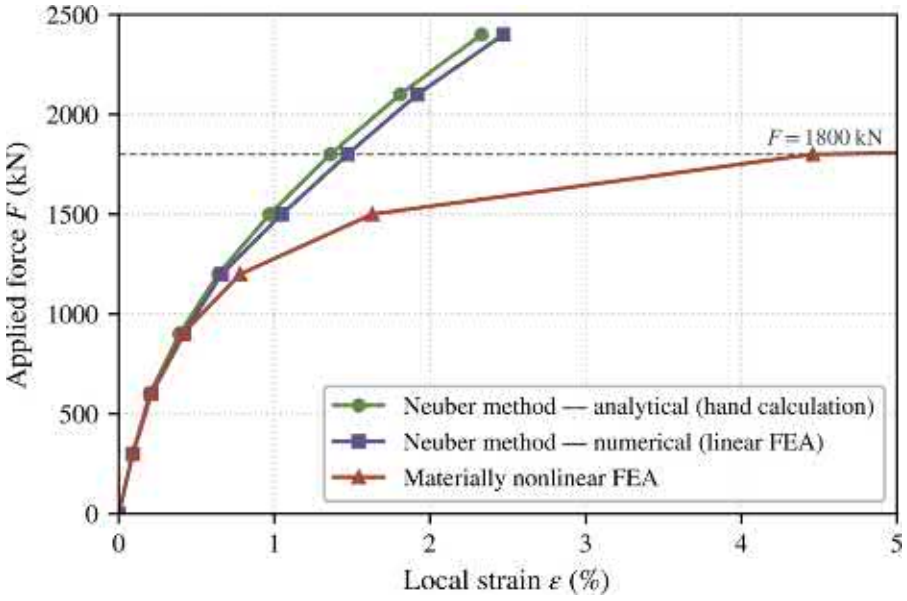


Fig. 3. Force–local strain response at the critical point: analytical Neuber calculation, numerical Neuber implementation based on linear FEA, and materially nonlinear finite element solution.

stress concentration. The benchmark therefore defines the applicability domain of the method and confirms the correctness of its numerical implementation.

4 Case Study 2: Welded Beam-to-Column Joint Under Cyclic loading

4.1 Structural Model and Seismic Input

The proposed workflow is applied to a welded beam-to-column joint of a two-storey S355 steel portal frame with HEA 140 columns and IPE 220 beams, designed according to EN 1993-1-1 [1] and EN 1998-1 [3] with behaviour factor $q = 4$. Three spectrum-compatible accelerograms are applied to the global linear beam model. The resulting displacement and rotation histories at the connection are imposed on a refined local plate model of the joint through kinematic compatibility at the boundary nodes, shown in Fig. 4.

The most critical location is identified at the centre of the top beam flange at $1.5t$ from the weld toe. The nominal stress history is extracted as a signed scalar quantity consistently with Sect. 2.1:

$$S = \sigma_{\mathrm{VM}} \cdot \mathrm{sign}(P_{11} + P_{22}) \tag{15}$$

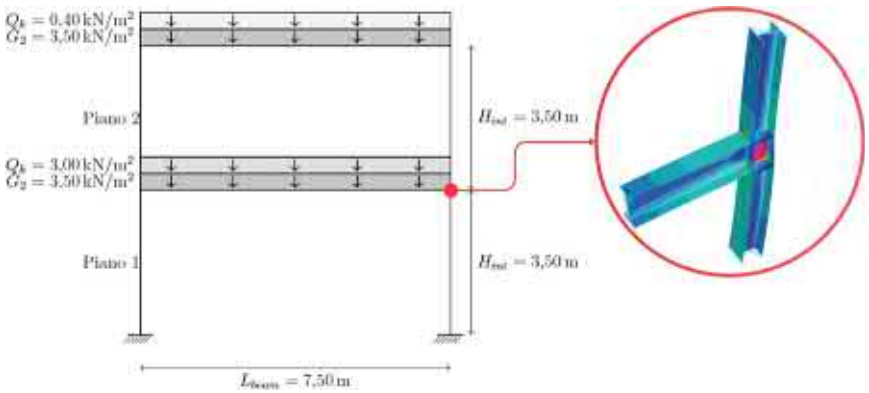


Fig. 4. Structural scheme of the portal frame and local plate model of the beam-to-column joint with the selected assessment point.

4.2 Selection of the Fatigue Notch Factor

The governing detail is classified according to prEN 1993-1-9 [4] as a load-carrying welded attachment with weld toe failure, corresponding to FAT 56 (Fig. 5). The smooth base material reference is FAT 160, giving:

$$K_f = \frac{\mathrm{FAT}_{\mathrm{ref}}}{\mathrm{FAT}_{\mathrm{detail}}} = \frac{160}{56} = 2.86 \tag{16}$$

This derivation is fully code-consistent and avoids dedicated experimental calibration. The sensitivity to K_f is significant: since the elastic notch stress enters Neuber's rule as $(K_f \Delta S)^2$, the correct identification of the detail category is the most influential decision in the assessment workflow.

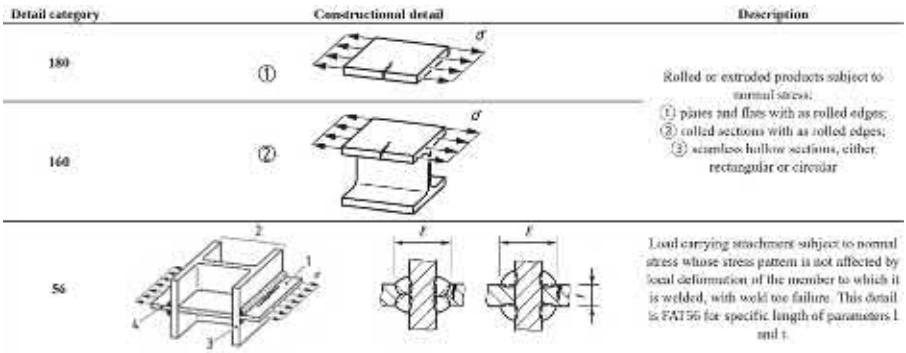


Fig. 5. Fatigue detail categories from prEN 1993-1-9 [4] relevant to the present assessment. FAT 180 and FAT 160 refer to smooth base material (plates and rolled sections respectively); FAT 56 corresponds to the load-carrying welded attachment governing the beam-to-column connection.

4.3 Cyclic Assessment and Results

After rainflow decomposition of the nominal stress history, each cycle is amplified by $K_f = 2.86$, converted into local elasto-plastic quantities through the cyclic Neuber–Ramberg–Osgood correction and assessed through the SWT equation. The equivalent fully reversed stress spectrum is shown in Fig. 6.

Cumulative damage by Palmgren–Miner summation is reported in Table 2. The record-to-record variability confirms that spectral compatibility alone does not uniquely determine local fatigue demand. At the reference input level damage remains limited for all records; when scaled, failure is reached at 4.5 times the reference PGA.

Table 2. Cumulative LCF damage at $\gamma_{\mathrm{PGA}} = 1$.

Accelerogram	Damage D
Record 1	2.08%
Record 2	1.69%
Record 3	0.85%

The case study confirms that a structural design satisfying standard elastic checks does not directly describe the local low-cycle fatigue demand at welded

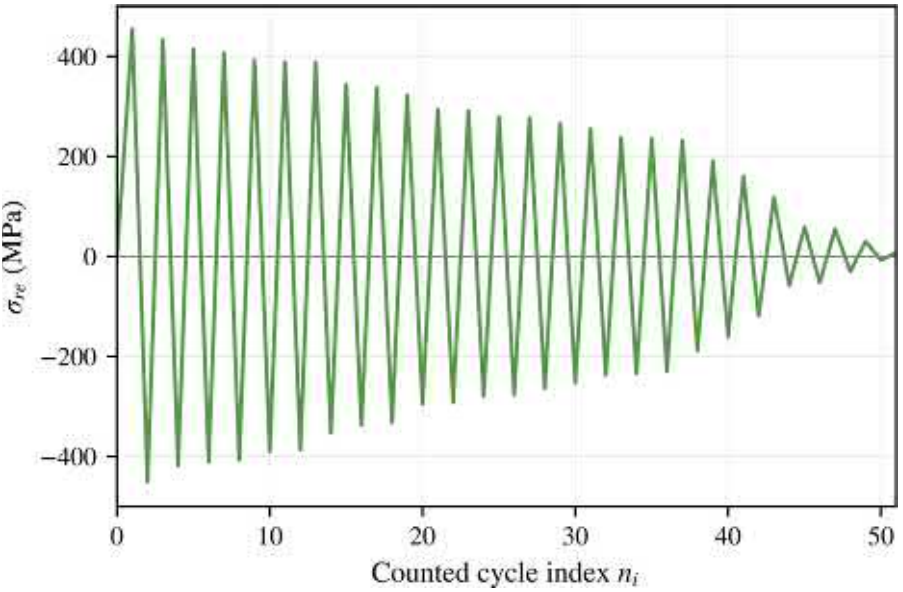


Fig. 6. Equivalent fully reversed stress amplitude σ_{re} for each counted cycle, after Neuber correction and SWT mean-stress adjustment (most damaging accelerogram).

details—a gap that standard Eurocode provisions do not explicitly address at the notch level. The proposed workflow quantifies this demand efficiently, without resorting to nonlinear analyses of the full structure.

5 Conclusions

A linear global-to-local procedure for the low-cycle fatigue assessment of steel structural details has been presented, combining a fatigue notch factor K_f with established strain-life methods to estimate local elasto-plastic demand and cumulative damage from conventional linear analyses, without resorting to nonlinear simulations of the full structure.

The perforated plate benchmark confirmed that the proposed approach provides a satisfactory estimate of the local elasto-plastic response when plasticity remains sufficiently localised. Larger deviations from the nonlinear reference arise when plasticity spreads over a significant portion of the net section, defining the applicability domain of the method. In welded and sharply notched details, where high stress concentration is typically associated with confined plastic zones, the proposed approach is expected to remain representative.

The portal frame application demonstrated that the local low-cycle fatigue demand at a welded beam-to-column joint cannot be inferred from global elastic verifications alone. Even when the structural system satisfies standard code checks, significant cyclic plasticity may develop at fatigue-sensitive details. The proposed workflow quantifies this demand explicitly, starting from a conventional linear analysis and without resorting to materially nonlinear simulations. The results also highlighted a non-negligible record-to-record variability in local fatigue damage among spectrum-compatible accelerograms, confirming that the loading history—and not only its spectral content—governs the local cyclic response of the detail.

Overall, the proposed methodology offers a practical and computationally efficient tool for identifying fatigue-sensitive details in steel structures and supplementing standard design verifications with an explicit local low-cycle fatigue assessment. Future developments should include validation against experimental results, extension to a wider range of structural details, and explicit comparison with Eurocode fatigue detail classifications to assess the conservatism of the procedure across a wider range of structural details.

Acknowledgements. This paper originates from research activities initially developed within a master's thesis carried out during an internship at Cimolai S.p.A. The authors also acknowledge Nicola De Martino for his contribution to the subsequent development of the study.

References

1. European Committee for Standardization (2005) EN 1993-1-1: Eurocode 3 - Design of steel structures - Part 1–1: General rules and rules for buildings. CEN, Brussels

2. European Committee for Standardization (2017) EN 1993-1-6: Eurocode 3 - Design of steel structures - Part 1–6: Strength and stability of shell structures. CEN, Brussels
3. European Committee for Standardization (2013) EN 1998–1: Eurocode 8 - Design of structures for earthquake resistance - Part 1: General rules, seismic actions and rules for buildings. CEN, Brussels
4. European Committee for Standardization (2023) prEN 1993-1-9: Eurocode 3 - Design of steel structures - Part 1–9: Fatigue. CEN, Brussels
5. International Organization for Standardization (2020) ISO 19902:2020 Petroleum and natural gas industries - Fixed steel offshore structures. ISO, Geneva
6. Neuber H (1936) Theory of Notch Stresses: Principles for Exact Stress Calculation. Springer, Berlin
7. Dowling NE, Kampe SL, Kral MV (2019) Mechanical Behavior of Materials: Engineering Methods for Deformation, Fracture and Fatigue, 5th edn. Pearson, Harlow
8. Smith KN, Watson P, Topper TH (1970) A stress-strain function for the fatigue of metals. J. Mater. 5:767–778
9. Palmgren A (1924) Die Lebensdauer von Kugellagern. Zeitschrift des Vereines Deutscher Ingenieure 68:339–341
10. Miner MA (1945) Cumulative damage in fatigue. J. Appl. Mech. 12:A159–A164
11. Pilkey WD, Pilkey DF (2007) Peterson's Stress Concentration Factors, 3rd edn. Wiley, Hoboken
12. Hobbacher, A.F.: Recommendations for Fatigue Design of Welded Joints and Components, 2nd edn. IIW Collection, Springer, Cham (2016)

Residual Stress Distribution in Cold Bent Hot Rolled Shapes: Analytical Model and Numerical Simulation

Francesco Pisciottano[1(✉)] and Riccardo Zanon[2]

[1] Department of Civil Engineering, University of Salerno, Fisciano, Italy
fpisciottano@unisa.it
[2] ArcelorMittal Global R&D, Esch-sur-Alzette, Luxembourg

Abstract. Residual stresses due to the manufacturing process affect the buckling resistance of structural members. This evidence is inexplicitly considered in the various stability curves provided in the design code such as Eurocode 3 and the AISC Specification. The residual stress distribution of typical hot-rolled or welded sections has been studied extensively and can be therefore considered as known. When hot-rolled sections are subjected to a mechanical curving process to obtain a curved structural member, their residual stress distribution is obviously modified. Curving can occur about the strong axis of inertia (in the plane of the web) or about the weak axis of inertia (in the plane of the flanges). This article proposes an analytical model to describe the residual stress distribution in H hot-rolled sections cold bent about the weak axis (also referred to as "easy way" bending). The results are validated against numerical simulation, demonstrating the model's ability to accurately predict the residual stress distribution.

Keywords: Cold bending · Residual stress · Steel section · Arch stability · Sectioning method

1 Introduction

1.1 Residual Stresses in Structural Members

It is well known that residual stresses have a detrimental influence on the behavior and strength of compression members, whether straight or curved. In general, residual stresses are formed in structural members as a result of plastic deformation, which may be due to cooling after hot-rolling (thermal residual stresses), or due to fabricating operations (deformational residual stresses) such as cold-straightening or cold-curving processes. Over the decades, residual stresses in hot-rolled structural sections have been determined both theoretically and experimentally, leading to simplified distribution models considered for the determination of the buckling curves provided in design codes [1–7].

© The Author(s), under exclusive license to Springer Nature Switzerland AG 2026
R. Zanon et al. (Eds.): CTA 2026, LNCE 942, pp. 982–988, 2026.
https://doi.org/10.1007/978-3-032-39505-4_85

With the improved capability of the steel industry to produce increasingly larger sections with higher-performance steel, hot-rolled profiles have become a competitive alternative to welded sections for various applications, such as arch ribs in bowstring bridges [8]. The most common methods to plastically deform hot-rolled straight members into the desired curved members are pyramidal roller bending and gag pressing [9]. Both methods lead to an alteration of the original internal stress state. This new residual stress state depends on both the magnitude of the plastic strain imposed during bending and the axis of bending. Unlike straight members, experimental measurements of residual stresses in curved members are very limited in the literature, and only for strong-axis bending [10, 11]. Accurate numerical simulation of the cold bending process has been shown to be an effective approach for evaluating the residual stress distribution [12]. In this study, a theoretical model for predicting residual stresses in hot-rolled shapes curved about the weak axis is presented and subsequently validated against the results obtained from numerical simulations.

2 Proposed Distribution Model for Weak Axis Curved Beam

In this section, the assumptions and main features of the proposed model are discussed. The proposed model is a function of the section geometry, the yield stress, and the *bending ratio*, defined as the ratio between the final radius of the curved member (assumed to be a circular arch) and the flange width. This ratio is the main parameter governing the degree of plastic deformation achieved during the cold bending process and thus the final residual stress pattern and magnitude. The assumptions underlying the model are:

- Material strain-hardening is neglected.
- Plane section remains plain during bending (Bernoulli hypothesis).
- Initial residual stress states before curving is neglected.
- During the curving process a constant curvature is achieved along the members.

The proposed distribution model is obtained by considering both theoretical aspects and experimental evidence. In particular, for the flanges, the stress distribution arising from the curving process is considered as summation of the loading and unloading stresses. For the web, which is assumed to undergo no deformation in the theoretical analysis, the additional compressive residual stresses are incorporated based on early experimental results presented in [13]. In Fig. 3 are represented the flange and the web residual stresses distribution, where σ_e^- is the compressive stress at the top flange tip (the tip that is stretched during the curving process), σ_e^+ is the tensile stress at the bottom flange tip (the tip that is shortened during the curving process), σ_i^+ is the maximum tensile internal stress, σ_i^- is the maximum compressive internal stress, y_{el} is the location of the peak internal stress from the middle of the flange and σ_w is the maximum web compressive stress. The equations that describe each of the aforementioned parameters are:

$$\sigma_e^- = -f_y\left(0.50 - 4.18 \bullet 10^{-7} \bullet \left(\frac{R_f}{B}\right) + 2.10 \bullet 10^{-7} \bullet \left(\frac{R_f}{B}\right)^2\right) + \frac{0.30 h_i t_w f_y}{A_f} \quad (1)$$

$$\sigma_e^+ = +f_y\left(0.50 - 4.18 \bullet 10^{-7} \bullet \left(\frac{R_\mathrm{f}}{B}\right) + 2.10 \bullet 10^{-7} \bullet \left(\frac{R_\mathrm{f}}{B}\right)^2\right) + \frac{0.30 h_i t_w f_y}{A_f} \quad (2)$$

$$\sigma_i^+ = f_y\left(1 - \frac{2\alpha\varepsilon_y R_0}{B}\right) + \frac{0.30 h_i t_w f_y}{A_f} \quad (3)$$

$$\sigma_i^- = -f_y\left(1 - \frac{2\alpha\varepsilon_y R_0}{B}\right) + \frac{0.30 h_i t_w f_y}{A_f} \quad (4)$$

$$y_{el} = \frac{\varepsilon_y}{\frac{1}{R_f} + \frac{\alpha W_{el} f_y}{EI}} \quad (5)$$

$$\sigma_w = -0.35 f_y \quad (6)$$

where h_i is the web height, t_w is the web thickness, f_y is the yield stress, A_f is the area of a single flange, R_f is the bending radius of the section achieved after the spring-back effect, R_0 is the bending radius of the section achieved before spring-back effect, ε_y is the strain corresponding to f_y, W_{el} is the elastic section modulus, E is the Young's modulus, I is the weak axis inertia modulus of the section and α is the equivalent shape factor of the flanges, which represents the degree of plasticization achieved during the curving process. As the fillet radius are neglected, the flanges are assumed to be rectangular shape, and α ranges between $1 \leq \alpha < 1.50$. When α is equal to the unity, it means no plastic strain is achieved during the bending process, and when α is equal to 1.50 (plastic shape factor of a rectangular section) it corresponds to the limit case (not possible to reach in reality) where half of the flange has reached the yield strain in tension, and the other half has reached the yield strain in compression.

The value of α is expressed by a second-order polynomial, dependent on the bending ratio R_f/B, in which the coefficients are calibrated by regression analysis:

$$\alpha = 1.50 - 4.18 \bullet 10^{-7} \bullet \left(\frac{R_\mathrm{f}}{B}\right) + 2.10 \bullet 10^{-7} \bullet \left(\frac{R_\mathrm{f}}{B}\right)^2 \quad (7)$$

3 Comparison to Numerical Simulations

In this section, the proposed residual stress model is compared with the results of FE model where the curving process is simulated. A four-point bending load scheme was employed to represent the general case of a continuous bending process, ensuring a constant curvature between the loading points. The HD 400x421 steel shape (Table 1) was adopted in the finite element model. The mesh was built using C3D8 brick elements, and fillet radii were neglected. Initial residual stresses from hot rolling were assigned to the integration points according to the triangular distribution proposed in prEN1993-1-14. A bilinear material law with $f_y = 460MPa$ was assumed, with a flat hardening branch. Supports and loading points were modeled as rigid surfaces with hard normal contact and a tangential friction coefficient of 0.3. The analysis was performed using a quasi-static general procedure, consisting of loading and unloading steps. An example

of the longitudinal stresses distribution during the loading steps is shown in Fig. 2. In order to evaluate the proposed model with different cases, four bending ratios belonging to the range $80 < R_f/B < 225$ were analyzed, resulting for the cross section considered in final radius range of $32 < R_f < 90$ meters (Fig. 1).

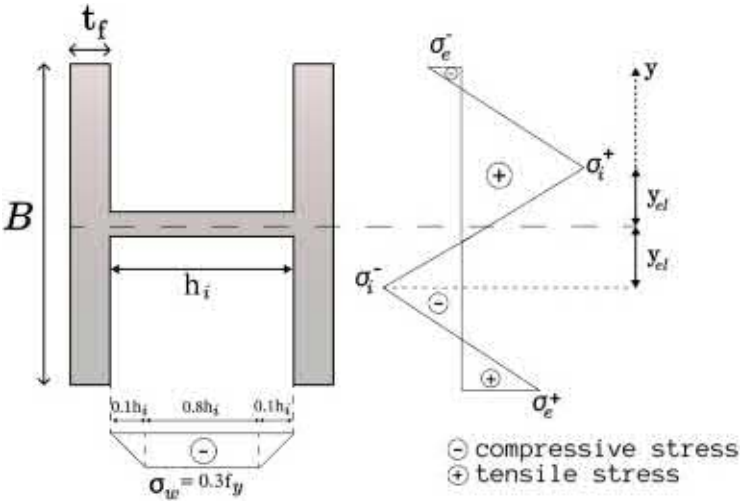


Fig. 1. Residual stresses distribution of the proposed model for weak axis cold bent sections.

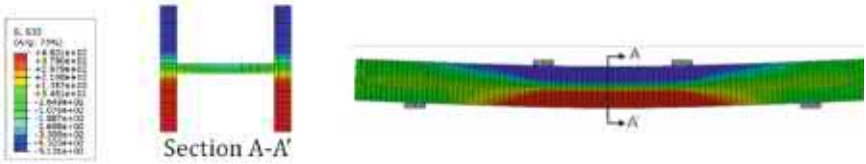
Table 1. Geometrical properties of the selected steel section.

Steel shape	H (mm)	B (mm)	t_f (mm)	t_w (mm)
HD 400x421	425	409	52,6	32,8

The comparison between the suggested model and the FE model results in terms of flange stresses distribution are shown in Fig. 3. A very good agreement in terms of both distribution and magnitude of residual stress can be observed for all the four cases studied. The stress distribution clearly indicates that lower bending ratios correspond to higher residual stress magnitudes, as a result of the higher plastic strain imposed during the bending process. More noticeable discrepancies are observed in the web, which can be attributed to the fact that the numerical model adopts the triangular initial stress state proposed by the Eurocode, which represents only a simplification of the actual residual stress state of a structural member in as-rolled conditions.



(a) Step 0 – Hot-rolling residual stresses from EN1993-1-14



(b) Step 1- Loading step



(c) Step 2- After unloading step

Fig. 2. Longitudinal residual stress distribution during numerical simulation.

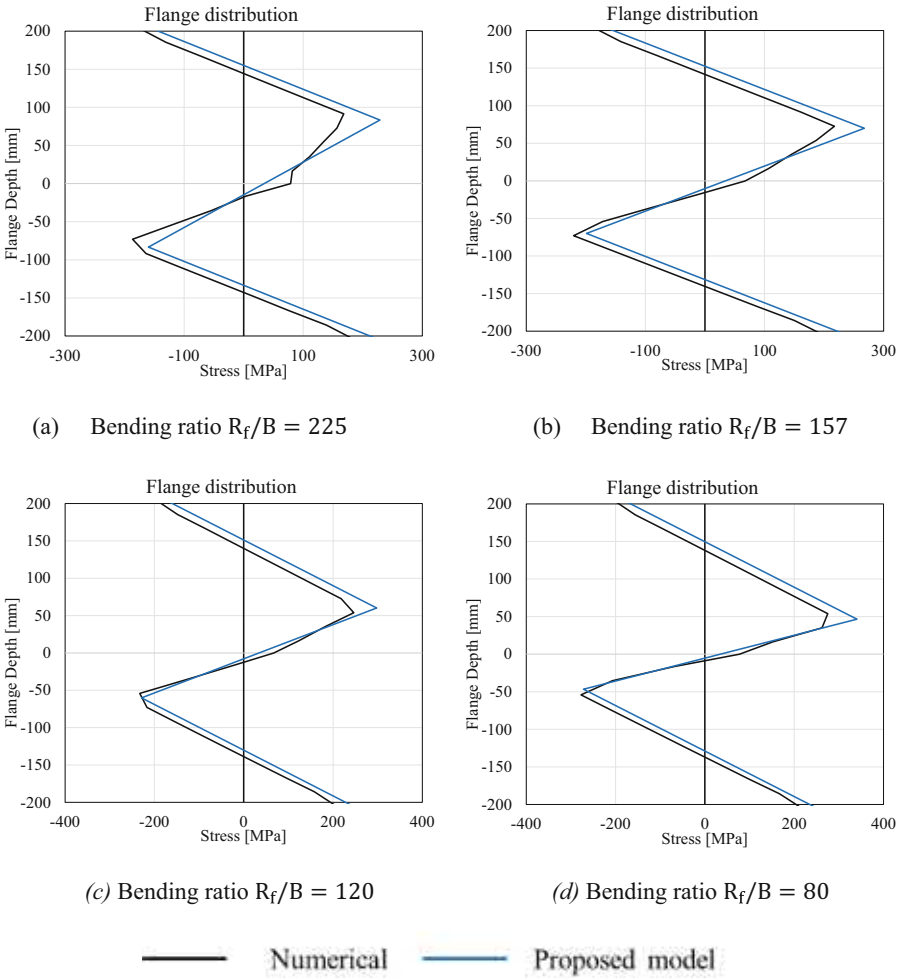


Fig. 3. Flange comparison between proposed stress model and numerical analysis for different bending ratios.

4 Conclusion

In this study, an analytical model to describe the residual stress distribution in hot-rolled sections cold-bent about the weak axis has been presented. By exploiting the linear relationship between section curvature and deformation, the equivalent shape factor α is derived, providing a measure of the degree of plasticity achieved during the curving process. The suggested model depends on the bending ratio, yield stress, and geometrical properties of the section. The results are validated against numerical simulations, demonstrating the model's ability to accurately predict the residual stress distribution. In order to further validate the theoretical model, an experimental campaign

is currently underway to assess the residual stresses in steel section curved through the roller bending process, for different values of bending ratio.

References

1. Beer H, Schulz G (1969) The maximum strenght of axiallly loaded columns with imperfection. VDI-Z, Bd.111
2. Szalai J, Papp F (2005) A new residual stress distribution for hot-rolled I-shaped sections. J Constr Steel Res 61:845–861
3. Sfintesco D (1967) European steel column research. In: ASCE structural engineering conference (preprints 502), Seattle, Washington
4. EN 1993-1-1. Eurocode 3 (2022). Design of steel structures, general rules and rules for buildings. Brussels: CEN European Committee for Standardization
5. ECCS (1976) Manual on stability of steel structures, European Convention for Constructional
6. Young B (1975) Residual stresses in hot rolled members. IABSE Rep Work Commiss 23(1):25–38
7. Galambos TV, Ketter RL (1959) Columns under combined bending and thrust. J Eng Mech Div 85(2):1–301
8. Zanon R, Zaganelli D (2019) Wide flange beams: trends towards higher steel performance. Curr Trends Civil Struct Eng
9. King C, Brown D (2001) Design of curved steel, SCI Publication P281
10. Spoorenberg RC, Snijder HH, Hoenderkamp JCD (2010) Experimental investigation of residual stresses in roller bent wide flange steel sections. J Constr Steel Res 66(6):737–747., ISSN 0143-974X. https://doi.org/10.1016/j.jcsr.2010.01.017
11. Spoorenberg RC, Snijder HH, Hoenderkamp JCD (2011) Proposed residual stress model for roller bent steel wide flange sections. J Constr Steel Res 67:992–1,000
12. Spoorenberg RC, Snijder HH, Hoenderkamp JCD (2011) Finite element simulations of residual stresses in roller bent wide flange sections. J Constr Steel Res 67(1):39–50
13. Leonetti D, Snijder BH, Pisciottano F, Zanon R, Marcinczak K, Lorenc W (2026) Residual stress measurements on wide flange hot rolled profiles cold bent about the weak axis. ce/papers 9:2067–2071. https://doi.org/10.1002/cepa.70788

Structural Optimisation

Identification of Optimal Parameters for Lateral Impact-Resilient Friction Pendulum Isolators

Diego Gino[1](✉), Elena Miceli[1], Gabriele Neri[1], Gaspar Andrés Auad[2], and Paolo Castaldo[1]

[1] Politecnico di Torino, Turin 10129, Italy
diego.gino@polito.it
[2] Universidad Diego Portales, Santiago, Chile

Abstract. Seismic isolation is widely recognized as an effective strategy for protecting structures against high-magnitude earthquakes. However, under extreme seismic events, large isolation displacements may induce internal impacts within friction-based isolators, leading to significant increases in structural ductility demand or even bearing failure. To address these issues, a lateral impact-resilient double concave friction pendulum (LIR-DCFP) isolator has been developed, capable of limiting impact forces while dissipating additional energy during impact events. The LIR-DCFP device is characterized by an enhanced inner slider composed of two rigid bodies in contact, forming a high-friction internal interface with a predefined gap that allows relative displacement. This study aims to identify the optimal combination of frictional properties that minimizes the ductility demand of structures equipped with LIR-DCFP isolators. A parametric investigation is conducted by varying both mass ratio and the superstructure period. The variability of seismic input is accounted for by considering multiple sets of natural ground motion records selected to match site-specific conditional spectra. Nonlinear time-history analyses are performed to evaluate the structural response under extreme seismic loading conditions. The results allow the identification of optimal friction coefficient ratios that effectively reduce ductility demand while maintaining stable isolation performance, providing practical guidance for the design of impact-resilient friction pendulum isolation systems.

Keywords: Seismic Isolation · Friction Pendulum Systems · Impact-resilient Isolators · Optimal Friction Coefficients · Ductility Demand

1 Introduction

In structural engineering field there are various types of interventions aimed at improving the structural response during seismic event phenomena. Among the various potential solutions, one could be increasing the structure's ability to withstand the actions generated by the earthquake, or improving the system's dissipative capacity by operating in its damping capacity, or even reduce the required demand. The first case solution corresponds to structural reinforcement, the second is obtained by means of dissipative bracing systems, whereas the latter approach is achieved via seismic isolation.

© The Author(s), under exclusive license to Springer Nature Switzerland AG 2026
R. Zanon et al. (Eds.): CTA 2026, LNCE 942, pp. 991–1000, 2026.
https://doi.org/10.1007/978-3-032-39505-4_86

Seismic isolation represents a passive protection system that consists of introducing a vertical discontinuity into the structure [1, 2]. This approach divides the structure into two parts: the substructure and the superstructure. The substructure comprises the foundation system and the isolators, bearings with specific characteristics that reduce the seismic energy transmitted to the portion above them. These devices are characterized by a much lower horizontal stiffness than the vertical one, thus significantly reducing the overall stiffness of the system, introducing also a novel protection technique achieving the dynamic decoupling of the structural systems. A suitable design of such devices could provide significant benefits for structural safety on a large scale, enhancing the protection of both individual structures and infrastructure systems [3–5]. Several types of isolation devices are commonly adopted, including High-Damping Elastomeric Bearings (HDEBs), Lead Rubber Bearings (LRBs), and Friction Pendulum Systems (FPSs) [6]. In HDEBs the elastomeric material is replaced with a mixture of an elastomer with special aggregates. This mixture increases the energy dissipation of the device, providing broader hysteretic loops and consequently enhancing the damping capacity. LRBs devices instead are made with a lead-core that arises the energy dissipation capacity; these devices represent the most efficient way to dissipate seismic energy in the elastomeric bearing field. FPS devices comprise a concave stainless rough surface (namely characterized by friction) on which a slider is arranged [7]. During seismic events, the sliding movement on the concave surface ensures dissipation of the seismic energy and also re-centering capability to the devices. Concave sliding surfaces have radii of curvature of the order of approximately 2 m, whereas the friction in the sliding interface is in the range of [0.05–0.1].

FPS devices can be designed with multiple curvature configurations, namely Single Curvature Friction Pendulum (SCFP), Double Curvature Friction Pendulum (DCFP) [8], and Triple Curvature Friction Pendulum (TCFP) [9], depending on the number of sliding interfaces within the device. Compared with the simple curvature device, the DCFP and TCFP systems provide approximately two and three times the displacement capacity respectively. Moreover, the higher is the number of sliding surfaces, the higher is the energy dissipation capacity of the device due to the greater contribution of frictional mechanisms. During seismic phenomena, the isolation system could be subjected to outstanding displacement demands, potentially triggering impacts of the slider with the lateral restraining rims due to displacement capacity exceedance and, in extreme cases, to the failure of the isolation systems. According to their epicentral distance, earthquakes could be classified in near – fault and far – field event [10–12]. The near – faults events are seismic inputs that occur within 10 km from the seismic source and are characterized by strong impulses of displacement and velocity at low frequencies and therefore have a high energy content [13, 14]. Far-field earthquakes, on the other hand, occur at much greater distances. Therefore, the energy contribution is significantly lower due to the attenuation to which seismic waves are subject as they travel through different rock layers. As seismic waves travel through different geological layers, part of their energy is dissipated, effectively reducing the intensity of the motion reaching the structure. Due to their high energy content and pulse-like characteristics, near-fault ground motions can induce exceptionally large displacements in base-isolated structure, making ineffective the isolation devices.

In this work, a novel typology of Double Concave Friction Pendulum (DCFP) bearing equipped with an additive inner sliding surface is investigated, namely the Lateral Impact Resilient Double Concave Friction Pendulum (LIR-DCFP) bearing [15–17]. A simplified single degree of freedom structural system is adopted as reference configuration. Nonlinear dynamic analyses are performed to assess structural response, taking into account record to record variability of seismic ground motions [18, 19]. Structural performance is evaluated in terms of seismic ductility demand, selected as Engineering Demand Parameter (EDP). A parametric analysis is carried out assuming friction as a deterministic parameter, accounting for a given isolation period and gap size, varying mass ratios and superstructure periods. The LIR-DCFP innovative device is expected to provide significant enhancements in the overall seismic performance of structures during high-intensity seismic events by improving the superstructure seismic ductility demand.

The conventional DCFP and the proposed LIR-DCFP share the same geometric characteristics in terms of concave plates and slider dimensions. However, unlike the standard DCFP, the internal slider of the LIR-DCFP consists of two distinct components, referred to as the top and bottom sliders. These elements interact through an internal interface characterized by a higher friction coefficient, resulting in increased energy dissipation capacity.

Furthermore, the presence of an internal gap between the top and bottom sliders allows for additional displacement capacity. The combined effect of the internal gap and the enhanced friction interface contributes to improved energy dissipation and greater displacement accommodation, ultimately leading to superior seismic isolation performance. The results show a trend in the friction coefficient that deserves attention, as it is possible to identify an optimal value. Furthermore, they provide ideas for additive case studies to further explore the relationship between the structure's ductility demands and the isolator's friction coefficient.

2 Lateral Impact Resilient Device

LIR-DCFP isolator is characterized by two spherical inox steel – based sliding with a further internal slider that enhances its displacement and energy dissipation capacity.

The internal additive slider represents the novel feature of this bearing: it consists of two separate components in contact through an interface characterized by a higher friction coefficient which enhances the frictional dissipation mechanism. An internal clearance that permits relative movement between the two components is realized. The top slider is designed with slightly smaller dimensions than the bottom slider, thereby creating an additive displacement capacity.

The additional sliding mechanism is intended to be triggered only when the internal slider reaches the displacement limit and impacts the restraining rim of the concave plates. Thanks to the presence of the internal gap, the device exhibits an increased displacement capacity and enhanced energy dissipation compared with conventional DCFP bearings. Figure 1 represents the simplified model of the LIR – DCFP isolator:

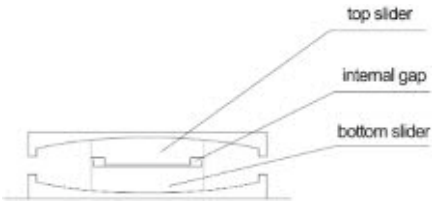


Fig. 1. Simplified model of LIR-DCFP, modified from [16].

2.1 Velocity – Dependent Friction Law

In this section the friction law adopted is shown. For this case study is assumed that friction (μ) is velocity dependent [20], with a non linear relationship, depicted in the following Eq. (1):

$$\mu = \mu_{max} - (\mu_{max} - \mu_{min}) \bullet e^{-\alpha v} \tag{1}$$

The quantities involved in the equation are:

- μ_{max} represents the frictional value corresponding to high sliding velocity;
- μ_{min} represents the frictional value corresponding to low sliding velocity;
- α represents a constant coefficient assumed equal to 30 s/m;
- $\dot{v}$ represents the sliding velocity.

It can be observed that friction law has an exponential trend. Furthermore, it is worth highlighting that for very low sliding velocity (namely when $\dot{v}$ tends to zero) we obtain that the friction coefficient μ tends to μ_{min} value ($\mu = \mu_{min}$), whereas for very high sliding velocity (namely when $\dot{v}$ tends to infinite) the friction coefficient μ tends to μ_{max} value ($\mu = \mu_{max}$).

2.2 Lateral Impact Resilient Device: Forces Transmitted to the Superstructure

During seismic events, some forces of different nature that the isolation system transfers to the superstructure may generate. We can compute the total lateral force F_{tot} with the following Eq. (2):

$$F_{tot} = F_p + F_\mu + F_i \tag{2}$$

where:

- F_p represents the pendular force, namely it originates because of the pendular movement;
- F_μ represents the frictional force, namely the force that develops in presence of friction;
- F_i represents the impact force, namely the force generated if an impact occurs;

The component F_p originates from the pendular motion of the additive internal slider along the spherical sliding surfaces of the upper and lower concave plates. The frictional contribution, F_μ, develops at the interface between the top and bottom parts of the

additive internal slider and is generated by their relative sliding motion. Finally, the impact force, F_i, is activated only when the inner slider comes into contact with the lateral constraining edges of the concave plates. This condition occurs when the relative displacement between the top and bottom sliders exceeds the available internal gap, thereby triggering the impact mechanism. We can distinguish five different steps of the force – displacement behaviour in the LIR bearing, that are the following:

(i) Onset of sliding between concave plates and internal additive slider;
(ii) Impact between the internal additive slider and the lateral constraining edges of the concave plates;
(iii) Relative sliding between top – bottom part of the internal additive slider;
(iv) Impact between the top part of the internal additive slider and the lateral constraining edges of the bottom part;
(v) Bottom part that goes back to its original configuration

The behavior of the three force components introduced above is not uniform throughout the motion cycle, but varies significantly across the different stages. Specifically, during phase i–ii, the pendular force F_p exhibits an approximately linear increase, while the friction force F_μ remains nearly constant. In phase ii–iii, the system reaches a condition in which contact may occur between the inner slider and the edges of the external sliding surfaces. This interaction initiates sliding on the high-friction interface, resulting in a marked increase in F_μ. Subsequently, during phase iii–iv, the two elements composing the internal slider reach the end-of-travel condition, leading to an impact event and a consequent significant rise in the impact force F_i. Finally, in phase iv–v, the pendular force F_p decreases approximately linearly as the slider returns to its initial configuration. In the following Fig. 2 the mechanism of the LIR device is depicted:

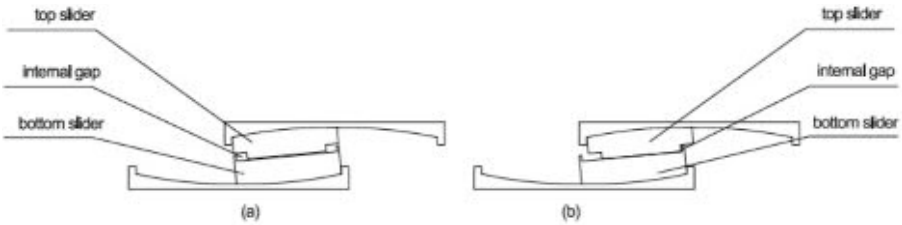


Fig. 2. Mode of operation of the device during a seismic event and activation of the additional sliding surface (a)-(b), simplified from [16].

3 Ground Motions Selection Approach

This section presents the procedure adopted for selecting the seismic input motions used in the dynamic analyses. The methodology has been extensively applied and validated in previous studies reported in the scientific literature [16], supporting its suitability for the purposes of the present work. Seismic hazard disaggregation technique is used to identify the seismogenic zones that gives the major contributes, whereas the definition

of the input features of a representative seismic scenario, namely the earthquake magnitude and source-to-site distance, are obtained using the Unified Hazard Tool [24]. The disaggregation analysis also provided two additional quantities:

- the Conditional Mean Spectrum (CMS) [22, 23] corresponding to the selected return period, conditioned on the isolation period (T_b);
- the associated Intensity Measure (IM) level.

In this work, the adopted IM is the spectral acceleration at the isolation period, ($S_a(T_b)$).

Subsequently, a set of various natural seismic inputs recorded at the reference site of Riverside (California) is adopted, to account for record to record variability. Ground motion records are selected following the methodology proposed in [25–27], ensuring spectral compatibility with the Conditional Spectra (CS), which incorporate both the target CMS and its conditional standard deviation. Finally, the selected records are appropriately scaled to the target IM level adopted.

4 Optimal Friction Study Within a Parametric Framework

A generic base-isolated structure is considered and modeled as a single-degree-of-freedom (SDOF) system in this study. The simplified model consists of a superstructure with lumped mass (m_s) concentrated at its top and a base characterized by its mass (m_b). The LIR isolation device is modeled through a simplified 2D approach, accounting for the rigid systems kinematics. In Fig. 3 the simplified scheme adopted for this case study is represented:

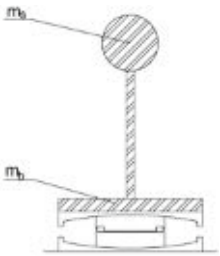


Fig. 3. Simplified SDOF base-isolated model, modified from [16].

To investigate the range of friction coefficients leading to improved seismic performance, a broad parametric analysis is performed using MATLAB environment. The parameters considered include the isolation period (Tb), the superstructure period (Ts), the mass ratio (γ), the hardening ratio (r), the additive gap (g), and the friction coefficient under high-velocity conditions μfast.

To account for inherent record to record variability of seismic inputs, different natural records from the Riverside (California) site are selected and appropriately scaled to satisfy spectrum-compatibility requirements with the target Conditional Spectra (CS). The latter are derived for a return period (Tr = 2475) years, corresponding to the Maximum Considered Earthquake (MCER) hazard level.

The structural response is evaluated in terms of ductility demand, adopted as the Engineering Demand Parameter (EDP), while the spectral acceleration at the isolation period, (Sa(Tb)), is selected as the Intensity Measure (IM). As far as friction is concerned, two different values of friction at high velocity are adopted μfast = 3–4%, whereas the high friction interface of the additive slider is characterized by μh = 3.5–4.5%. The variables Tb, Ts and γ are computed respectively with Eqs. (3), (4) and (5). In Table 1 the corresponding values are reported.

$$T_b = 2\pi \cdot \left(R_{eff}/\mathrm{g}\right)^{0.5} \tag{3}$$

$$T_s = 2\pi \cdot \left(m_s/\mathrm{k_s}\right)^{0.5} \tag{4}$$

$$\gamma = m_s/m_{s+}\, m_b\Big) \tag{5}$$

Table 1. Values of the variables involved in the parametric analysis.

Parameter values	
T_b	3 s
T_s	0.6–0.9 s
γ	0.7–0.9

5 Results

The seismic performance of the base-isolated structures is assessed in terms of ductility demand μ_d, defined as the ratio between the maximum relative lateral displacement of the superstructure with respect to the base ($u_{s,max}$) and the lateral superstructure displacement in yielding conditions (u_y). In Eq. (6) is shown the formula:

$$\mu_d = \mathrm{u_{s,max}}/\mathrm{u_y} \tag{6}$$

Thus, the ductility demand is adopted herein as the Engineering Demand Parameter (EDP) to quantify the maximum displacement demand experienced by the superstructure during seismic excitation. Figure 4 presents the results of the parametric analysis in terms of maximum ductility demand for the considered range of system parameters. Results are shown for a given isolation period $T_b = 3\ s$, a post-yield hardening ratio $r = 10\%$, an internal gap g = 20 cm, two different values of superstructure period $T_s = 0.6$–0.9 s and two different values of mass ratio $\gamma = 0.7$–0.9.

The maximum ductility demand μd is plotted as a function of the parameter Δμh = μh - μfast. The results show that the ductility demand generally decreases as the superstructure period increases, indicating improved performance for more flexible superstructures. In contrast, higher mass ratios are associated with larger ductility demands.

The friction coefficient also plays a significant role in the structural response. Specifically, higher ductility demands are observed for low friction values, whereas an increase in friction leads to a progressive reduction in ductility demand. This behavior can be attributed to the enhanced energy dissipation capacity provided by larger friction coefficients, which reduces the displacement demand.

The observed trends reveal the presence of an optimal friction coefficient corresponding to the minimum ductility demand. Values lower or higher than this optimum result in less favorable structural performance, highlighting the importance of an appropriate calibration of the friction properties in the design of the isolation system.

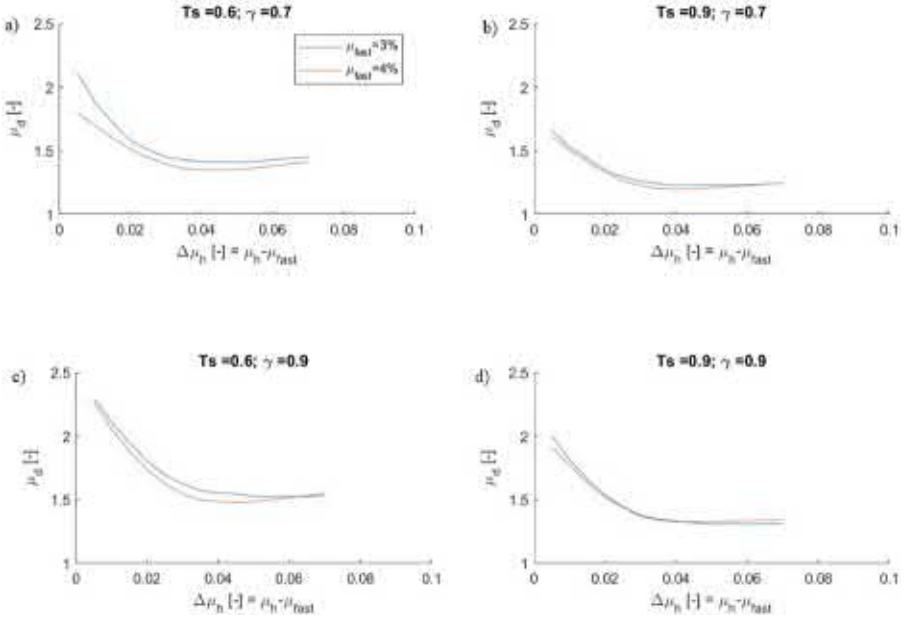


Fig. 4. Comparison between superstructure ductility demand for isolation period Tb = 3 s and post – yield hardening ratio r = 0.10 as function of superstructure period Ts = 0.6 s (a) – (c) and Ts = 0.9 s (b) – (d).

6 Conclusions

This study investigates the optimal friction coefficients of the proposed LIR–DCFP (Lateral Impact Resilient Double Concave Friction Pendulum) isolation system. Unlike conventional DCFP bearings, the LIR–DCFP device comprises an inner slider characterized by high-friction contact interfaces with additional internal gap. These characteristics are intended to enhance both the energy dissipation capability and the displacement capacity of the isolation system.

An extensive parametric analysis is performed in MATLAB environment by varying the main structural and isolation-system parameters. To account for the inherent record

to record variability of earthquake excitation, 50 spectrum-compatible natural ground motions are selected and scaled to the target intensity measure level. The friction coefficient is considered as the primary design variable, while the ductility demand is adopted as the Engineering Demand Parameter (EDP).

The results reveal a non-monotonic relationship between the frictional properties of the LIR–DCFP device and the seismic response of the superstructure. Specifically, the ductility demand initially decreases as the $\Delta\mu_h$ increases and then increases for larger $\Delta\mu_h$. This behavior indicates the existence of a potential optimal friction range capable of minimizing the ductility demand and, consequently, improving the seismic performance of the isolated structure.

These findings highlight the importance of carefully calibrating the frictional characteristics of LIR–DCFP bearings during the design process, as the seismic response of the superstructure is strongly influenced by the selected friction coefficients.

Acknowledgments. This work was developed within the framework of the WP 15 – Task 15.1 – ReLUIS.

This work is also part of the project PNRR - NGEU which has received funding from the MUR - DM630/2024.

References

1. LNCS Homepage. http://www.springer.com/lncs. Accessed 21 Nov 2016
2. Fenz DM, Constantinou MC (2007) Spherical sliding isolation bearings with adaptive behavior: theory. Earthq Eng Struct Dyn 37(2):163–183
3. De Iuliis M, Miceli E, Castaldo P (2025) Information theory-guided machine learning to estimate seismic response of non-linear SDOF structures. Eng Struct 336:120448
4. Miceli E, De Iuliis M, Castaldo P (2025) Robustness assessment of reinforced concrete structures for different failure scenarios. Struct Concrete:1–35
5. Colajanni P, D'Anna J, Mancini S, La Mendola L (2024) Tools aiding decision-making for economic resources allocation in seismic retrofitting of residential buildings. Int J Disaster Risk Reduct 116:105149
6. Castaldo P, Gino D, Mancini G (2019) Safety formats for non-linear analysis of reinforced concrete structures: discussion, comparison and proposals. Eng Struct 193:136–153
7. Pokhrel A, Li J, Li Y, Maksis N, Yu Y (2016) Comparative studies of base isolation systems featured with lead rubber bearings and friction pendulum bearings. Appl Mech Mater 846:114–119
8. Castaldo P, Miceli E (2023) Optimal single concave sliding device properties for isolated multi-span continuous deck bridges depending on the ground motion characteristics. Soil Dyn Earthq Eng 173:108128
9. Fenz DM, Constantinou MC (2006) Behaviour of the double concave friction pendulum bearing. Earthq Eng Struct Dyn 35(11):1403–1424
10. Fenz DM, Constantinou MC (2008) Modeling triple friction pendulum bearings for response-history analysis. Earthquake Spectra 24(4):1011–1028
11. Jangid RS (2005) Optimum friction pendulum system for near-fault motions. Eng Struct 27(3):349–359
12. Mazza F (2018) Seismic demand of base-isolated irregular structures subjected to pulse-type earthquakes. Soil Dyn Earthq Eng 108

13. Hall JF, Heaton TH, Halling MW, Wald DJ (1995) Near-source ground motion and its effects on flexible buildings. Earthquake Spectra 11(4):569–605
14. Jangid RS, Kelly JM (2001) Base isolation for near-fault motions. Earthq Eng Struct Dyn 30(5):691–707
15. Mazza F, Vulcano A (2012) Effects of near-fault ground motions on the nonlinear dynamic response of base-isolated r.c. framed buildings. Earthq Eng Struct Dyn 41(2):211–232
16. Auad G, Castaldo P, Almazán JL (2022) Seismic reliability of structures equipped with LIR-DCFP bearings in terms of superstructure ductility and isolator displacement. Earthq Eng Struct Dyn 51(13):3171–3214
17. Auad G, Almazán JL (2021) Lateral impact resilient double concave friction pendulum (LIR-DCFP) bearing: formulation, parametric study of the slider and three-dimensional numerical example. Eng Struct 233:111892
18. Auad G, Castaldo P, Almazán JL (2023) Comparative seismic performance of a moment frame equipped with lateral impact resilient double concave frictional devices. Procedia Struct Integr 44:1466–1473
19. De Domenico D, Spinella N, Messina D, Mazzeo M, Recupero A (2024) Structural behavior of deteriorated Gerber half-joints in highway overpasses by nonlinear finite element analysis combined with a simplified uniform-corrosion model. Struct Concrete 26:5677–5707
20. De Domenico D, Mazzeo M, Messina D, Santoro R, Recupero A (2025) Structural health assessment of concrete half-joint bridges: from load testing to FEM simulation accounting for material uncertainties. Struct Infrastruct Eng:1–20
21. Boore DM, Stewart JP, Seyhan E, Atkinson GM (2014) NGA-West2 equations for predicting PGA, PGV, and 5% damped PSA for shallow crustal earthquakes. Earthquake Spectra 30(3):1057–1085
22. Mokha A, Constantinou M, Reinhorn A (1990) Teflon bearings in base isolation I: testing. J Struct Eng 116(2):438–454
23. Baker JW (2011) Conditional mean spectrum: tool for ground-motion selection. J Struct Eng 137(3):322–331
24. Unified Hazard Tool https://earthquake.usgs.gov/hazards/interactive/. Accessed 17 June 2021
25. Baker JW, Lee C (2018) An improved algorithm for selecting ground motions to match a conditional spectrum. J Struct Eng 22(4):708–723
26. Lin T, Haselton CB, Baker JW (2013) Conditional spectrum-based ground motion selection. Part I: hazard consistency for risk-based assessments. Earthq Eng Struct Dyn 42(12):1847–1865
27. Lin T, Haselton CB, Baker JW (2013) Conditional spectrum-based ground motion selection. Part II: intensity-based assessments and evaluation of alternative target spectra. Earthq Eng Struct Dyn 42(12):1867–1884

Optimal Seismic Isolation Properties of Multi-Span Bridges Under Asynchronous Earthquakes

Elena Miceli(✉), Diego Gino, Gabriele Neri, Luca Giordano, and Paolo Castaldo

Politecnico di Torino, Turin 10129, Italy
elena.miceli@polito.it

Abstract. The detrimental effects that asynchronous earthquakes may induce on extended infrastructures such as bridges have attracted increasing attention in civil engineering practice and research. A seismic analysis framework is herein adopted, accounting for the aleatory variability of the seismic input and comparing the structural response under uniform and spatially variable ground motions, with specific emphasis on pier response. An existing five-span bridge equipped with friction pendulum system (FPS) isolators, is considered as the reference configuration. A parametric investigation is carried out by deterministically varying the FPS sliding friction coefficient, considering eight values, and two different radii of curvature, corresponding to two isolation periods. Nonlinear time-history analyses are performed in OpenSees, where the nonlinearities are related to the piers and the isolation devices. Seismic response is evaluated under seismic inputs associated with a return period of 475 years, scaled with respect to a spectral displacement-based intensity measure and with an incidence angle equal to 30° with respect to the bridge longitudinal axis. The results are expressed in terms of pier displacement ratios, adopted as engineering demand parameters, plotted against the FPS friction coefficient. The analysis allows the identification of optimal isolation configurations that minimize pier seismic demand. Such findings demonstrate the key role of spatial variability of earthquake ground motion in terms of seismic demand and how friction properties of FPS devices could attenuate such effects on the dynamic seismic response of piers.

Keywords: Friction pendulum system (FPS) · Optimal friction coefficient · Spatially variable ground motion · Multi-span bridges · Pier displacement demand

1 Introduction

Bridges represent some of the most complex civil engineering structures due to their geometric configuration, structural characteristics, and functional requirements. Unlike conventional buildings, which primarily develop in the vertical direction, bridges are designed to overcome natural or artificial obstacles, such as rivers, valleys, and transportation corridors, resulting in a significant horizontal extension.

© The Author(s), under exclusive license to Springer Nature Switzerland AG 2026
R. Zanon et al. (Eds.): CTA 2026, LNCE 942, pp. 1001–1011, 2026.
https://doi.org/10.1007/978-3-032-39505-4_87

This distinctive feature introduces additional challenges in seismic design. In particular, the large distance between supports makes bridges especially susceptible to the effects of spatially variable earthquake ground motion (SVEGM). Variations in the energetic content and arrival time of seismic waves at different support locations may significantly condition the dynamic response of the structure [1].

Consequently, the assumption of synchronous seismic input (namely uniform ground motion), which is often adopted for building structures, may not be appropriate for bridge systems. Neglecting SVEGM effects can lead to an underestimation of seismic demands, potentially resulting in unrealistic design predictions and an increased risk of structural damage or even failure under extreme earthquake events [2, 3]. It is widely recognized that the spatial variability of earthquake ground motion (SVEGM) is mainly governed by three contributing mechanisms: loss of coherence, wave-passage effects, and local site-response effects [4, 5]. Owing to the inherently complex and random nature of these phenomena, probabilistic approaches are typically adopted rather than purely deterministic simulations [6–9]. To account for the spatial variability of seismic excitation, various models have been developed, starting from empirical, semi – empirical and analytical methods up to coherency models and stochastic procedures [10–13]. Among the mathematical and stochastic approaches, the spectral representation method turns out to be one of the most widespread techniques for the generation of spatially variable ground motions in the time domain. Nonlinear time-history analyses represent an effective tool to investigate the effects of SVEGM on bridge performance subjected to asynchronous excitations, highlighting that these seismic inputs may increase the seismic demand in terms of internal forces, deck displacements, and damage concentration, particularly in long-span and multi-span bridge systems [14–17]. Despite these findings, the dynamic response of base-isolated bridges subjected to asynchronous seismic ground motions has received less attention, even though seismic isolation has become a well-established strategy in structural engineering field [18–21]. Seismic isolation is a passive structural protection strategy widely employed in regions exposed to moderate-to-high seismic hazard. Its primary objective is to reduce the amount of seismic energy transmitted from the ground to the structure, thereby limiting structural demand, reducing inter-story drifts, and mitigating damage to both structural and non-structural components [22–24].

This objective is achieved via the installation of isolation devices characterized by low horizontal stiffness, typically placed between the substructure and the superstructure. By decoupling the dynamic response of the structure from that of the ground, these devices significantly reduce the seismic forces and displacements transmitted to the superstructure during earthquake events [25–27].

The introduction of seismic isolators increases the fundamental vibration period of the structure as a consequence of the reduction in its overall lateral stiffness. Among the various isolation technologies currently available, Friction Pendulum System (FPS) are stainless-steel bearings particularly effective because they dissipate seismic energy through frictional mechanisms developed at the sliding interfaces [28–31]. Unlike elastomeric isolation systems, where energy dissipation is primarily associated with the hysteretic behavior of rubber-based materials, FPS devices rely on friction-induced energy dissipation while maintaining stable self-centering capabilities. It is worth highlighting that in the contemporary code rules the dynamic response of isolated bridges equipped

with FPS isolation system accounting for SVEGM conditions is still not comprehensively covered. Thus, this study examines within a seismic scenario the behavior of multi-span bridges equipped with FPS devices subjected to asynchronous ground motions by means of a parametric investigation of the friction coefficients of the isolation devices. Building upon a previously developed numerical model, the analysis aims to identify optimal ranges of friction coefficients defined as the values that minimize the dynamic response of the bridge piers under asynchronous seismic inputs.

These findings illustrate how friction governs FPS isolation performance and provide practical guidance for the calibration and design of such bearings in bridge applications. Furthermore, the findings enlarge the knowledge of the seismic performance of isolated bridges exposed to spatially variable ground motions, supporting the development of more reliable and efficient seismic protection strategies.

2 Bridge Under Study: Description and Modelling

2.1 Description

An existing reinforced concrete (RC) highway bridge is selected as case study, situated close to the border between Marche and Abruzzo, in Central Italy. The bridge is located in a medium to high seismicity zone and was built in the late 1970s following design standards that predated modern seismic design and detailing requirements. Figure 1 shows the location of the existing bridge and the model considered.

The total bridge length is around 163 m, divided into five spans with a simple support static scheme, each one with an average length of approximately 32 m. As far as the substructure is concerned, four reinforced concrete piers and two abutments located at bridge ends are considered. The piers feature circular cross-section with equal diameter of about 2.6 m, while each pier differs from other in height, moving from 9.8 m up to 13.4 m. Consequently, a non-uniform height distribution leads to a non-uniform stiffness distribution in longitudinal direction, which may play a crucial role in the seismic behaviour of the bridge when subjected to asynchronous seismic inputs.

The superstructure comprises of a 12.5 m-wide reinforced concrete deck, supported by five longitudinal RC girders and a reinforced concrete slab with a thickness of approximately 0.27 m.

The abutments are realized as conventional RC structures with a height of approximately 3.5 m and a width equal to that of the deck. Deep foundations constructed using piles are considered for both piers and abutments, with a fully-fixed boundary condition at the base. To account for site-specific geological conditions, rock-like soil properties are assigned to the abutment foundations, while stiffer soil conditions are considered at the pier locations.

The seismic retrofit scheme adopted in this study consists of connecting the original simply supported spans to form a continuous deck and positioning Friction Pendulum System (FPS) bearings at the superstructure–substructure interfaces. FPS isolators are provided at both pier and abutment supports, with one device assigned to each longitudinal girder, ensuring a uniform arrangement of the isolation system along the entire bridge length.

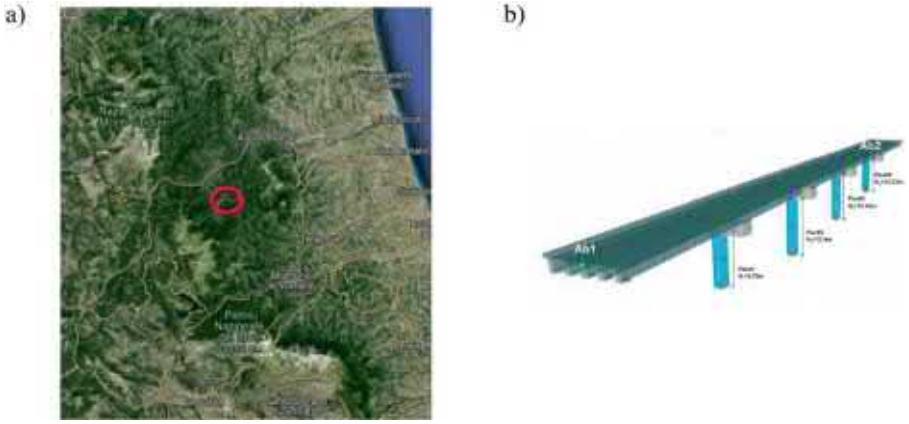


Fig. 1. Location of the existing bridge (1a) [32] and model of the case study bridge (1b) [33].

2.2 Numerical Modelling in the OpenSees Framework

The three-dimensional model is constructed using OpenSees [34], an open-source finite element software for studying the seismic response of structural systems. The model is implemented using OpenSeesPy, a Python library within OpenSees, and adopting a fiber-based nonlinear regime. Since the isolation system is expected to significantly reduce the seismic force transmitted to the superstructure, it is assumed that the deck remains in linear-elastic regime. The bridge deck is modeled using elastic beam-column elements. As far as the substructure is concerned, piers are modeled using force-based beam-column elements with fiber cross-sections, enabling the explicit representation of material nonlinearities. To reach an appropriate trade – off between computational effort and modeling accuracy, each pier is discretized into two beam-column elements.

Material nonlinearities are modeled using the *Concrete02* and *Steel02* constitutive laws available in OpenSees for concrete and reinforcing steel, respectively. The *Concrete02* model accounts for tensile strength and post-cracking behavior, whereas the *Steel02* model incorporates isotropic hardening and accurately captures the cyclic response of reinforcing steel. For *Concrete02*, the following parameters are assumed: a compressive strength $f_c = 29.1$ MPa, the corresponding strain $\varepsilon_c = 0.2\%$, a tensile strength $f_t = 3$ MPa, the ultimate values (f_u and ε_u) $f_u = 0.2 f_c$ and $\varepsilon_u = 0.6\%$ respectively. The elastic modulus $E_c = 2 f_c/\varepsilon_c$, whereas the parameter $\lambda = 0.1$. For *Steel02*, the following parameters are assumed: a yield strength $f_y = 420$ MPa, $E_s = 200000$ MPa, an hardening ratio $b = 0.001$, whereas the parameters that rule the elastic to plastic transition are $R0 = 18$, $cR_1 = 0.925$ and $cR_2 = 0.15$. The ε_{su} is limited to 0.1 via the *MinMax* in OpenSees.

The influence of transverse reinforcement confinement is included by distinguishing between confined and unconfined concrete regions within the fiber sections. Concrete outside the stirrups is modeled as unconfined, while the concrete core enclosed by the transverse reinforcement is assumed to be confined. Owing to the confinement effect, the latter exhibits enhanced compressive strength and ductility, thereby providing a more realistic representation of the nonlinear behavior of reinforced concrete members

under seismic loading. Regarding the abutments, such elements provide a significant contribution to the global stiffness of the structure in both the longitudinal and transverse directions. The numerical model incorporates the soil–structure interaction at the piers, backwalls, and wingwalls. In both directions, these interactions are simulated using nonlinear spring elements.

FPS isolators are positioned at both pier and abutment locations and implemented using the appropriate friction-pendulum bearing elements available in OpenSees. The devices comprise a concave sliding surface whose radius of curvature is chosen to reach the target isolation period. It is assumed that each FPS device withstands the tributary weight of the deck. Energy dissipation is achieved through friction. To compute the friction value of the isolator μ, a velocity-dependent friction law is adopted [35] depicted in Eq. (1):

$$\mu = \mu_{max} - (\mu_{max} - \mu_{min}) \bullet e^{-\alpha v} \tag{1}$$

For this case study, μ_{max} (namely the friction value for high velocity) is assumed as deterministic parameter, considering eight different values in [0.02–0.09] range. The relationship between μ_{min} (namely the friction value for low velocity) and μ_{max} is $\mu_{max}/\mu_{min} = 3$, whereas α is a coefficient assumed equal to 30 s/m. The damping model considered is the proportional Rayleigh's damping model, assuming a 2% value as inherent damping.

3 Generation of Artificial Spectrum – Compatible Seismic Inputs

The starting point of the analysis is the seismic hazard characterizing the reference site of the case study, namely on the border between Marche and Abruzzo, which is located within a region of medium-to-high seismicity. The seismic inputs considered in this work are not derived from recorded natural earthquakes but are artificially generated. To ensure their reliability, the generated records must satisfy the condition of spectral compatibility with the seismic hazard of the site, i.e., with the elastic response spectrum associated with the reference area.

Accordingly, a set of 30 artificial accelerograms is generated using the Spectral Representation Method (SRM), a technique based on stochastic process theory and widely adopted in nonlinear dynamic analyses of structural systems. The analyses are carried out for a single seismic intensity level corresponding to a return period of 475 years (T_R = 475 years).

As regards the intensity measure (IM), the spectral displacement evaluated at two isolation periods, $S_d(T)$, is adopted owing to its direct correlation with the displacement demand of base-isolated structures. To account for Spatially Variability of Earthquake Ground Motion (SVEGM), a multiple-support excitation approach is employed, whereby different acceleration time histories are assigned to each support location. The generated seismic inputs incorporate the three main mechanisms contributing to SVEGM, namely wave-passage effects, loss of coherency, and phase differences along the bridge length. Furthermore, since the seismic wave front is assumed with an incidence angle of 30° with respect to the longitudinal development of the deck, seismic action results almost

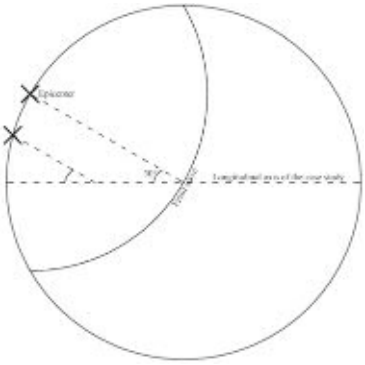


Fig. 2. Wave front modified from [33].

parallel with respect to the longitudinal axis of the bridge. In Fig. 2 the front wave considered for this case study is depicted.

Finally, to evaluate the influence of spatial variability, the results obtained under asynchronous excitation are compared with those corresponding to the conventional uniform excitation case, in which the same acceleration record is applied simultaneously at all support locations.

4 Parametric Analyses

To evaluate the seismic performance of the isolated bridge considered in this case study, a deterministic analysis is carried out with the objective of identifying the friction characteristics of the Friction Pendulum System (FPS) devices that minimize the seismic response of the piers.

Two different isolation periods are considered, corresponding to two radii of curvature of the FPS devices and, consequently, to different levels of seismic isolation. Since the isolation period of FPS bearings T_{is} is independent of the supported mass, it can be expressed as a function of the radius of curvature according to Eq. (2):

$$T_{is} = 2\pi \bullet (R_{device}/g)^{0.5} \tag{2}$$

Where:

- R_{device} represents the radius of curvature of the FPS isolator;
- g is the acceleration due to gravity.

Based on this formulation, two isolation periods are selected, $T_1 = 2$ s and $T_2 = 3$ s, corresponding to radii of curvature equal to $R_1 = 1$ m and $R_2 = 2.25$ m, respectively.

The primary parameter investigated in the analysis is the friction coefficient of the FPS devices, which is treated deterministically. Eight friction coefficient values are considered, ranging from 2% to 9%, covering a range commonly adopted in structural engineering field. The coefficients are varied with a constant increment to systematically investigate response trends and identify possible optimal configurations.

Nonlinear time-history analyses are carried out for all combinations of isolation period, friction coefficient, and seismic input, considering spatially variable ground motions as excitation. In addition, nonlinear time-history analyses under uniform excitation are performed to provide a benchmark for comparison. In this latter case, the acceleration record assigned to the first abutment is applied simultaneously at all support locations.

As regards the Engineering Demand Parameter (EDP), normalized pier displacement (pier drift ratio) is adopted to evaluate the structural response of the isolated bridge, as it provides a direct indicator of damage experienced by the substructure.

5 Results

The dynamic seismic response of the isolated bridge is assessed via the pier drift ratios (θ), selected as EDP in this case study and computed with Eq. (3):

$$\theta = \left(d_i - d_j\right)/\mathrm{H_{pier}} \tag{3}$$

Where:

- d_i represents the displacement at the top of the pier;
- d_j represents the displacement at the bottom of the pier;
- H_{pier} represents the height of the pier.

The pier drift ratio represents its normalized lateral displacement, obtained as the ratio between the relative displacement of the pier ends and its height. This parameter is particularly relevant for seismic performance assessment, as it provides a direct measure of the damage demand experienced by the bridge substructure during earthquake excitation.

For each of the 30 generated ground motions, nonlinear time-history analyses are performed under both asynchronous and uniform excitation conditions. From each analysis, the maximum pier drift ratio is extracted and subsequently, through a statistical lognormal processing, the mean of such peak values is computed and depicted in the results. In Fig. 3 the resulting mean peak drift ratios are then represented as a function of the friction coefficient for each of the four bridge piers.

Each graph reports the pier drift ratios obtained for the two isolation periods considered, and the corresponding radii of curvature, namely $\mathrm{R_1} = 1$ m (blue curves) and $\mathrm{R_2} = 2.25$ m (red curves). Results are presented for both asynchronous excitation (solid lines) and uniform excitation (dashed lines), assuming a seismic-wave front incidence angle of 30° with respect to the bridge longitudinal axis.

The results indicate that spatially variable ground motions generally produce higher seismic demands than the corresponding uniform excitation cases. This behavior is consistently observed for all piers and for both isolation periods considered. Additionally, for a given radius of curvature (and, consequently, a fixed isolation period), the seismic response is influenced by the pier height. Specifically, taller piers, characterized by lower lateral stiffness, exhibit higher drift ratios than shorter and stiffer piers. This trend is consistently observed regardless of the isolation period considered.

Moreover, the relationship between pier drift and friction coefficient shows a non-monotonic trend mainly for $R_2 = 2.25$ m ($T_2 = 3$ s) with a minimum drift in asynchronous conditions, whereas for $R_1 = 1$ m ($T_1 = 2$ s) the response tends to decrease monotonically with increasing friction. Specifically, for $R_2 = 2.25$ m ($T_2 = 3$ s), the seismic demand tends to decrease as the friction coefficient increases up to a certain threshold value, beyond which the trend reverses and pier drift slightly increases. This behavior highlights the existence of an optimal friction coefficient that minimizes the seismic response of the bridge piers.

Overall, the results suggest that the friction properties of the FPS devices play a key role in controlling the effectiveness of the isolation system and that neglecting the spatial variability of ground motion may lead to an underestimation of the seismic demand on the bridge substructure. The mean friction coefficient value that minimizes the response of the substructure—specifically, the piers is around 9% for all the piers for $R_1 = 1$ m ($T_1 = 2$ s), whereas for $R_2 = 2.25$ m ($T_2 = 3$ s) the value is around 6%, 8%, 9%,8% for pier 1, pier 2, pier 3 and pier 4 respectively.

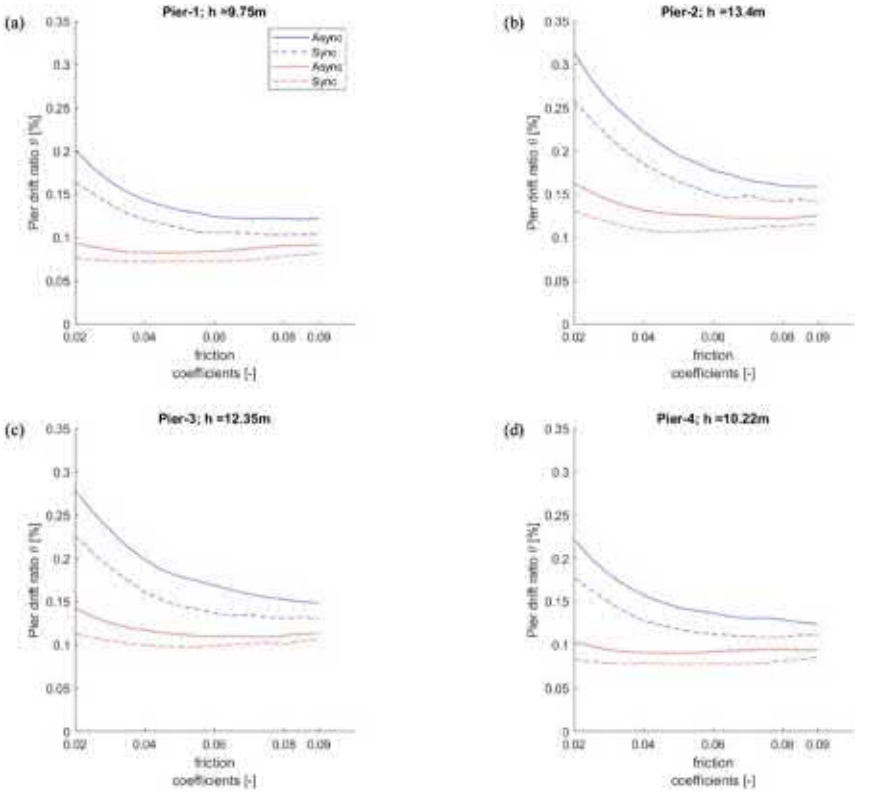


Fig. 3. Mean pier drift ratios for both R1 = 1 m (blue curves) and R2 = 2.25 m (red curves), ac-counting for both asynchronous and synchronous excitation for pier 1 (a), pier 2 (b), pier 3 (c) and pier 4 (d) of the isolated bridge.

Based on the obtained results, increasing the radius of curvature of the FPS device (and consequently the isolation period) leads to a lower optimum friction coefficient. This behavior can be attributed to the higher degree of seismic isolation, which reduces the amount of seismic energy transmitted to the substructure and, consequently, the dissipated energy demand.

6 Conclusions

In this work, the detrimental effects of spatial variability of earthquake ground motion (SVEGM) on extended infrastructures such as bridges are analyzed. An existing five-spans RC bridge located in a medium to high seismicity area in the central part of Italy, near the border between Marche and Abruzzo, is selected as case study. The bridge is subjected to a retrofitting intervention with FPS devices to fulfill seismic requirements and analyze the effects of spatial variability of seismic motion. To assess seismic structural performance of the isolated bridge, nonlinear time domain analyses are performed selecting the pier drift ratios as Engineering Demand Parameter (EDP) and the spectral displacement evaluated at the isolation period, $S_d(T_1)$ as Intensity Measure (IM). The analyses are carried out with a set of 30 artificially generated spectrum – compatible seismic inputs having an incidence angle of 30° with respect to the longitudinal axis of the bridge, accounting for both spatial variability of seismic motion and uniform excitation conditions. Optimal friction coefficients are investigated in a parametric framework, taking into account two different isolation periods (namely two different radii of curvature), eight friction coefficients in the range [2% - 9%]. The results show that spatially variable ground motions generally lead to higher seismic demands up to around 20% compared to the corresponding uniform excitation cases. This trend is consistently observed across all bridge piers and for both isolation periods considered in the study. In addition, for each radius of curvature considered (corresponding to a given isolation period), the seismic response is found to be strongly affected by the pier height. Due to their lower lateral stiffness, taller piers develop larger drift ratios than shorter ones. This observation remains valid across all the isolation periods investigated. Furthermore, pier drift and the friction coefficient exhibits a non-monotonic relationship for $R_1 = 1$ m ($T_1 = 2$ s), whereas for $R_2 = 2.25$ m ($T_2 = 3$ s) the seismic demand decreases as the friction coefficient increases up to a certain threshold, beyond which a slight increase in pier drift is observed. This finding suggests the existence of an optimal friction coefficient capable of minimizing the seismic response of the bridge piers. It should be noted that the findings of the present work rely on a parametric assessment performed on a single case-study bridge, two isolation periods, a single incidence angle.

To overcome this aspect, further studies could extend the proposed framework by considering bridges with different geometric configurations, a larger number of spans, additional ground-motion incidence angles and isolation periods, enabling a more comprehensive assessment on isolated bridge systems.

Acknowledgments. This work was developed within the framework of the WP 15 – Task 15.1 – ReLUIS.

This work is also part of the project PNRR - NGEU which has received funding from the MUR - DM630/2024.

References

1. Luco JE, Wong HL (1986) Response of a rigid foundation to a spatially random ground motion. Earthq Eng Struct Dyn 14(6):891–908
2. Miceli E, De Iuliis M, Castaldo P (2025) Robustness assessment of reinforced concrete structures for different failure scenarios. Struct Concr:1–35
3. Troisi R (2022) The firm and territory: an organizational perspective. Routledge
4. Zerva A (2009) Spatial variation of seismic ground motions: modeling and engineering applications, 1st edn. CRC Press, Boca Raton
5. Harichandran RS (1999) Spatial variation of earthquake ground motion: what is it, how do we model it, and what are its engineering applications? Michigan State University
6. Gino D, Castaldo P, Bertagnoli G, Giordano L, Mancini G (2020) Partial factor methods for existing structures according to fib bulletin 80: assessment of an existing prestressed concrete bridge. Struct Concr 21:15–31
7. Castaldo P, Gino D, Marano GC, Mancini G (2022) Aleatory uncertainties with global resistance safety factors for non-linear analyses of slender reinforced concrete columns. Eng Struct 255:113920
8. Colajanni P, D'Anna J, Mancini S, La Mendola L (2024) Tools aiding decision-making for economic resources allocation in seismic retrofitting of residential buildings. Int J Disaster Risk Reduct 116:105149. https://doi.org/10.1016/j.ijdrr.2024.105149
9. Castaldo P, Gino D, Bertagnoli G, Mancini G (2018) Partial safety factor for resistance model uncertainties in 2D non-linear analysis of reinforced concrete structures. Eng Struct 176:746–762. https://doi.org/10.1016/j.engstruct.2018.09.041
10. Harichandran RS, Vanmarcke EH (1986) Stochastic variation of earthquake ground motion in space and time. J Eng Mech 112(2):154–174
11. Deodatis G (1996) Non-stationary stochastic vector processes: seismic ground motion applications. Probabilistic Eng Mech 11(3):149–168
12. Sextos AG, Pitilakis KD, Kappos AJ (2003) Inelastic dynamic analysis of RC bridges accounting for spatial variability of ground motion, site effects and soil-structure interaction phenomena. Part 1: methodology and analytical tools. Earthq Eng Struct Dyn 32(4):607–627
13. Sextos AG, Kappos AJ (2009) Evaluation of seismic response of bridges under asynchronous excitation and comparisons with Eurocode 8-2 provisions. B Earthq Eng 7:519–545
14. Lupoi A, Franchin P, Pinto PE, Monti G (2005) Seismic design of bridges accounting for spatial variability of ground motion. Earthq Eng Struct Dyn 34(4–5):327–348
15. Tzanetos E, Hamdan A (2000) Inelastic dynamic response of RC bridges subjected to spatial non-synchronous earthquake motion. Adv Struct Eng 3(3):191–214
16. Shinozuka M, Saxena V, Deodatis G (2000) Effect of spatial variation of ground motion on highway structures. Technical Report MCEER-00-0013, New York
17. Papadopoulos SP, Sextos AG (2020) Simplified design of bridges for multiple support earthquake excitation. Soil Dyn Earthq Eng 131:106013
18. Perotti F (1990) Structural response to non-stationary multiple-support random excitation. Earthq Eng Struct Dyn 19(4):513–527
19. De Domenico D, Mazzeo M, Messina D, Santoro R, Recupero A (2025) Structural health assessment of concrete half-joint bridges: from load testing to FEM simulation accounting for material uncertainties. Struct Infrastruct Eng:1–20. https://doi.org/10.1080/15732479.2025.2468199
20. Der Kiureghian A, Keshishian P, Halabian AM (1997) Multiple support response spectrum analysis of bridges including the site-response effect and the MSRS code. University of California, Berkeley

21. Zanardo G, Hao H, Modena C (2002) Seismic response of multi-span simply supported bridges to a spatially varying earthquake ground motion. Earthq Eng Struct Dyn 31(6):1325–1345
22. De Iuliis M, Miceli E, Castaldo P (2025) An energy framework to control viscoelastic semi-active devices in plan-wise one-way asymmetric systems. Struct Control Health Monit:1–34
23. De Domenico D, Spinella N, Messina D, Mazzeo M, Recupero A (2024) Structural behavior of deteriorated Gerber half-joints in highway overpasses by nonlinear finite element analysis combined with a simplified uniform-corrosion model. Struct Concrete 26:5677–5707. https://doi.org/10.1002/suco.202400556
24. De Iuliis M, Miceli E, Castaldo P (2025) Information theory-guided machine learning to estimate seismic response of non-linear SDOF structures. Eng Struct 336:120448
25. Jangid RS (2004) Seismic response of isolated bridges. J Bridg Eng 9(2):156–166
26. Papadopoulos SP, Sextos AG (2018) Anti-symmetric mode excitation and seismic response of base-isolated bridges under asynchronous input motion. Soil Dyn Earthq Eng 113:148–161
27. Buckle I, Constantinou M, Dicleli M, Ghasemi H (2006) Seismic isolation of highway bridges. University of Buffalo, New York
28. Castaldo P, Miceli E (2023) Optimal single concave sliding device properties for isolated multi-span continuous deck bridges depending on the ground motion characteristics. Soil Dyn Earthq Eng 173:108128
29. Hao H, Oliveira CS, Penzien J (1989) Multiple-station ground motion processing and simulation based on smart-1 array data. Nucl Eng Des 111(3):293–310
30. Landi L, Grazi G, Diotallevi P (2016) Comparison of different models for friction pendulum isolators in structures subjected to horizontal and vertical ground motions. Soil Dyn Earthq Eng 81:75–83
31. Castaldo P, Amendola G (2021) Optimal DCFP bearing properties and seismic performance assessment in nondimensional form for isolated bridges. Earthq Eng Struct Dyn 50(9):2442–2461
32. Ozsarac V (2023) Integrated evaluation of earthquake-induced economic losses for multi-span reinforced concrete bridges. PhD Dissertation
33. Amendola G (2024) Seismic reliability of 3D isolated bridges accounting for spatial variability of earthquake ground motions. PhD Dissertation
34. McKenna F, Scott MH, Fenves GL (2010) Nonlinear finite-element analysis software architecture using object composition. J Comput Civ Eng 24(1):95–107
35. Mokha A, Constantinou M, Reinhorn A (1990) Teflon bearings in base isolation I: testing. J Struct Eng 116(2):438–454

Nonlinear Response Prediction for Stock-Constrained Optimized Steel Gridshells

Farzin Kazemi[1,2], Elena Mele[3(✉)], Neda Asgarkhani[1,2], Francesco Esposito[3], and Fabrizio Ascione[3]

[1] Faculty of Civil and Environmental Engineering, Gdańsk University of Technology, Gdańsk, Poland
{farzin.kazemi,neda.asgarkhani}@pg.edu.pl

[2] Department of Architecture, Built Environment and Construction Engineering, Politecnico di Milano, Piazza Leonardo da Vinci 32, Milan, Italy

[3] Department of Structures for Engineering and Architecture, University of Naples Federico II, 80125 Naples, Italy
{elena.mele,francesco.esposito8,fabrizio.ascione2}@unina.it

Abstract. Steel gridshells are lightweight structures particularly suitable for long-span applications, but their design is strongly influenced by geometrical nonlinearities, material nonlinearities and instability phenomena. When the reuse of steel elements is considered, the design problem becomes significantly more complex. The structural grid must be adapted to the available stock of reclaimed elements, whose lengths, cross-section types, and quantities impose additional constraints on the optimization process. However, the need to perform nonlinear structural analyses for each generated configuration, in order to assess capacity - and displacement-related performance indicators, makes large-scale design-space exploration computationally demanding. This paper presents a preliminary study comparing five Machine Learning (ML) models for the prediction of nonlinear response parameters in steel gridshell configurations generated through a stock-constrained optimization workflow. Starting from a FreeGrid barrel-vault benchmark, several geometrical configurations are generated through SAP2000 Open Application Programming Interface (OAPI)-based nodal perturbations, while preserving the analytical reference surface. The target variables are the load factor, LF, and the maximum vertical displacement, Δ_{max}, extracted from nonlinear analyses. The results show that the ML models can provide rapid and sufficiently accurate estimates of these response quantities, supporting future surrogate-assisted optimization workflows.

Keywords: Steel gridshells · steel reuse · stock-constrained optimization · machine learning · nonlinear analysis

© The Author(s), under exclusive license to Springer Nature Switzerland AG 2026
R. Zanon et al. (Eds.): CTA 2026, LNCE 942, pp. 1012–1023, 2026.
https://doi.org/10.1007/978-3-032-39505-4_88

1 Introduction

In recent years, the reuse of structural steel components has emerged as a promising strategy to reduce the environmental impact of the construction sector. Unlike recycling, reuse preserves the geometry and a significant part of the embodied value of existing members, potentially avoiding the energy-intensive processes associated with remelting or with new steel production. However, the design of structures made of reclaimed members is a stock-constrained optimization problem: the designer cannot freely select member lengths, section types and quantities from a catalogue, but must instead work with the characteristics of the available inventory [1, 2].

Gridshell structures are particularly interesting in this context because they are composed of a dense network of discrete members. This makes them suitable for integrating reclaimed elements with different lengths and cross-sections. At the same time, gridshells are highly sensitive to the geometrical arrangement of the grid and to instability phenomena, so their structural response usually requires careful nonlinear assessment [3, 4]. The FreeGrid benchmark provides a useful reference framework for this type of investigation, including benchmark gridshell geometries and performance-oriented design problems [4]. In previous studies, steel reuse in gridshells was investigated through reuse-oriented and stock-constrained optimization workflows. In these studies, the nodal coordinates of selected portions of the grid were used as design variables, while the global reference surface was preserved. This allowed the grid geometry to partially adapt to the available stock, improving the compatibility between required member lengths and reclaimed elements [5]. Related contributions have also addressed topology and sizing optimization strategies for gridshells with reused members, as well as automated design and fabrication workflows aimed at enhancing steel reuse through structural optimization and metal additive manufacturing [6, 7]. These studies showed the potential of reuse-based gridshell design, but also highlighted the computational burden associated with repeated nonlinear analyses.

In this context, Machine Learning (ML) can provide an additional design-support layer by estimating structural responses. Instead of embedding nonlinear analyses directly into every iteration of an optimization process, ML models can be trained to predict relevant response quantities from low-cost descriptors of the structural configuration [8, 9]. This approach is particularly useful when a large number of geometrical and sectional configurations must be explored, as in stock-constrained gridshell design. Recent studies have shown the potential of ML-based surrogate models to provide rapid estimates of structural or resilience-related performance indicators in preliminary design stages [10], and to support multi-objective structural optimization by coupling predictive models, explainability tools and sustainability indicators [11]. However, before developing a full surrogate-assisted optimization workflow, it is necessary to assess whether the available descriptors are informative enough to predict the nonlinear response with sufficient accuracy.

This paper addresses this intermediate step. A dataset of stock-constrained steel gridshell configurations is generated starting from the FreeGrid barrel-vault topology. The geometries are varied through nodal perturbations implemented in Python by means of

the SAP2000 Open Application Programming Interface (OAPI), while the vertical coordinate is recomputed from the analytical barrel-vault surface. For each generated configuration, structural analyses are performed and two response quantities are extracted: the load factor, LF, and the maximum vertical displacement, Δ_{max}. These quantities are then used as target variables for ML models trained on structure-level descriptors. The objective of the paper is therefore not to present a complete surrogate-assisted optimization framework, but to provide a preliminary assessment of ML-based prediction of nonlinear response parameters for stock-constrained steel gridshell configurations.

2 Generation of Gridshell Configurations

2.1 Reference Workflow and Role of Nodal Movements

The dataset adopted in this study builds on the reuse-oriented design workflow previously developed for steel gridshell structures [5]. In such a framework, the design problem is no longer limited to the selection of optimal cross-sections from a standard steel catalogue but is constrained by the characteristics of an available stock of reclaimed members. Member lengths, section types, steel grades and available quantities are therefore fixed a priori by the inventory, and the structural design must adapt to these constraints. This aspect is particularly relevant for gridshell structures, since their performance depends not only on the size of the assigned members, but also on the geometrical arrangement of the grid. In previous reuse-based optimization studies, nodal movements were introduced to allow geometry to partially adapt to the available stock. More specifically, the coordinates of selected nodes were used as design variables, while the global reference surface was preserved. This made it possible to modify member lengths and grid patterns without changing the overall architectural form of the structure [5]. In the same framework, a matching algorithm was used to replace newly designed members with reclaimed steel elements whenever length and mechanical compatibility requirements were satisfied. The rationale behind this strategy is that, in stock-constrained design, the geometry and the material inventory are strongly coupled. Small variations in the nodal layout may significantly affect the compatibility between the required member lengths and the available reclaimed elements, thereby influencing the reuse rate, the number of cutting operations and the final structural response. For this reason, the movement of nodes should not be interpreted only as a geometric perturbation, but as a design mechanism aimed at exploring feasible configurations under stock availability constraints.

2.2 Dataset Generation Strategies

The structural configurations used to build the ML dataset are generated starting from a single reference topology, corresponding to the barrel-vault gridshell selected from the FreeGrid benchmark [4]. The initial model is imported in SAP2000 [12] and used as the reference configuration for all subsequent geometrical variations. In this work, the term generator quarter denotes one of the four symmetric portions of the barrel-vault plan layout. Only the nodes belonging to this quarter are directly assigned independent movement variables; the corresponding nodes in the remaining three quarters are obtained by mirror symmetry. This reduces the number of geometrical variables while preserving the global symmetry of the gridshell.

The admissible nodal movements are defined according to the position of each node within the reference grid. Internal nodes of the generator quarter are allowed to move in both horizontal directions. Nodes located on the symmetry axis $x = 0$ can move only along the y-direction, while nodes located on the symmetry axis $y = 0$ can move only along the x-direction. In the perimeter-compatible generation mode, external boundary nodes are also allowed to move, but only along directions compatible with the boundary: nodes on the external $x = x_{max}$ edge slide along y, whereas nodes on the external $y = y_{max}$ edge slide along x. The external corner is kept fixed to avoid incompatible one-dimensional boundary constraints. This classification is directly implemented in the geometry-generation script, where symmetry axes and external edges are detected through coordinate tolerances.

For each generated configuration, the horizontal position of the movable nodes is modified within a prescribed maximum in-plane displacement. In the present dataset, the maximum nodal perturbation is set equal to ±0.50 m. Depending on the adopted generation strategy, this value is either imposed as a fixed maximum amplitude or sampled within a bounded interval. In all cases, the vertical coordinate is not independently perturbed. Following each horizontal movement, the z-coordinate is updated according to the analytical barrel-vault surface defined by the generatrix equation (Eq. 1) and the directrix equation (Eq. 2).

$$z(x) = -\frac{x^2}{2B} + f \quad -\frac{B}{2} \le x \le \frac{B}{2} \tag{1}$$

$$z(y) = f \quad -\tfrac{B}{2} \le y \le \tfrac{B}{2}, x = 0 \tag{2}$$

where B is the span of the barrel vault, $f = B/8$ is the rise. Representative configurations generated through the adopted perturbation strategies are shown in Fig. 1. Figure 1(a) reports the reference FreeGrid barrel-vault geometry, which serves as the undeformed baseline configuration. Different perturbation strategies were then adopted to enrich the dataset and avoid generating configurations that are too similar to each other. The first strategy, referred to as *chaotic node*, assigns independent high-amplitude movements to each compatible nodal degree of freedom, producing deliberately irregular but bounded geometries, as illustrated in Fig. 1(b). The second strategy follows the same local movement logic, but with a sampled target amplitude, so that the dataset includes both mildly and strongly perturbed configurations; a representative example is shown in Fig. 1(c). A third strategy combines perimeter-compatible boundary conditions with smooth modal displacement fields, allowing the external perimeter to slide along tangent directions while preserving the global barrel-vault geometry, as shown in Fig. 1(d). Finally, Fig. 1(e) shows the *max-compatible* configuration, corresponding to a limiting perturbation case in which the maximum component-wise in-plane nodal movements reach $|\Delta x|_{\max} = |\Delta y|_{\max} = 0.50$ m. These strategies do not define different grids, but different samples of the same parametric configuration space. The resulting configurations were then analyzed in SAP2000 to extract the response quantities used as target variables, namely the load factor, LF, and the maximum displacement, $\Delta_{\max}$.

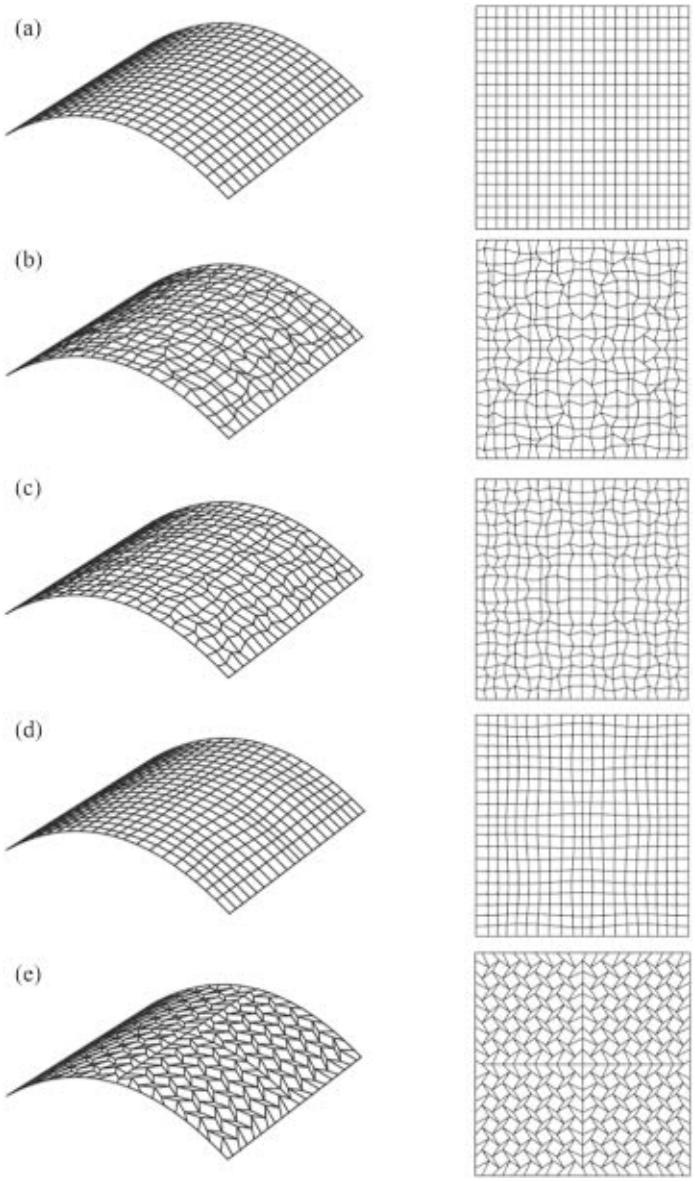


Fig. 1. Representative geometrical configurations generated from the same FreeGrid barrel-vault topology: (**a**) reference geometry; (**b**) *chaotic node* perturbation; (**c**) *chaotic sampled* perturbation; (**d**) *perimeter-tangent* configuration based on smooth modal displacement fields; (**e**) *max-compatible* configuration

3 Dataset for Machine Learning

The dataset generated according to the strategy described in Sect. 2.2 includes 600 complete structural configurations. Each row corresponds to one gridshell solution and stores compact structure-level descriptors rather than member-by-member data. As shown in Fig. 2(a), subset B01 includes 300 perimeter-tangent configurations based on smooth modal displacement fields, subset B02 includes 150 chaotic node configurations, and subset B03 includes 150 chaotic sampled configurations. The max-compatible configuration shown in Fig. 1(e) is used only to illustrate the limiting case of the adopted nodal movement rules and is not considered a different structural topology.

The input descriptors were selected to represent the main factors affecting the nonlinear response of the gridshell. The first group includes geometrical perturbation descriptors. The in-plane nodal perturbation, Δ_p, is defined as:

$$\Delta_p = \sqrt{\left[(\Delta x)^2 + (\Delta y)^2\right]} \tag{3}$$

where Δx and Δy are the horizontal nodal movements imposed. Since the nodes are projected back onto the analytical barrel-vault surface after each horizontal movement, the associated vertical coordinate variation is denoted as Δ_z. Accordingly, Fig. 2(b) reports the mean and maximum values of the in-plane perturbation, $\overline{|\Delta_p|}$ and $|\Delta_p|_{max}$, and of the induced vertical variation, $\overline{|\Delta_z|}$ and $|\Delta_z|_{max}$. The parameter A_p indicates the requested plan-amplitude used during geometry generation, while r_{mov} is the ratio between the number of moved nodes and the total number of nodes.

The second group describes the section assignment. The members are divided into four demand-based groups, g_0, g_1, g_2 and g_3, and one circular hollow section is assigned to each group. This assignment is encoded through the section indices s_{g0}, s_{g1}, s_{g2} and s_{g3}. The corresponding section properties are then aggregated at the structure level. In Fig. 2(b), m_{tot} denotes the total mass proxy, while $\overline{A}$ and $\overline{I}$ denote the mean cross-sectional area and the mean second moment of area of the assigned members. These quantities are member-weighted descriptors of the complete gridshell configuration and not properties of a single group.

The third group includes demand-related descriptors obtained from preliminary linear analyses. These quantities are not intended as formal code-based demand-to-capacity ratios, but only as compact structural indicators. In Fig. 2(b), $\overline{P/A}$ and $(P/A)_{max}$ are axial-force-related proxies, while $\overline{M/I}$ and $(M/I)_{max}$ are bending-related proxies. Finally, member-length statistics are included because nodal perturbations modify the grid geometry and therefore the distribution of member lengths. These are represented by the mean member length $\overline{L}$ and the standard deviation σ_L.

The target variables are the load factor LF and the maximum displacement Δ_{max}, which describe the global nonlinear response of each gridshell configuration. Configurations with $LF < 1.0$ were not removed, since they represent relevant low-capacity cases and help the ML models distinguish safe and unsafe regions of the design space. Figure 2(a) shows the distribution of the dataset in the Δ_{max}– LF target space, while Fig. 2(b) reports the Pearson correlation heatmap between the main input descriptors and the two target variables.

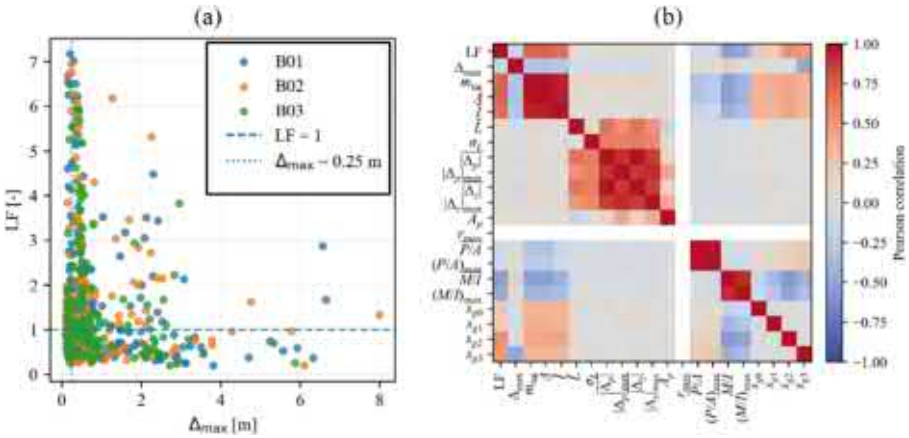


Fig. 2. (**a**) Target space of the ML dataset; (**b**)Pearson correlation heatmap of the main descriptors and target variables included in the ML dataset

3.1 Target Variables

Two target variables are considered in this study: the non-linear load factor LF and the maximum non-linear displacement Δ_{max}. The first target, LF, is used as a global capacity - or stability-related indicator. For each generated gridshell solution and nonlinear load case, LF is defined as the maximum load multiplier reached during the nonlinear push-down analysis. It is computed as the ratio between the maximum vertical base reaction obtained from the nonlinear analysis and the total vertical reference load associated with the corresponding load case. The load factor assigned to each configuration is then taken as the minimum value among the considered nonlinear load cases:

$$LF = \min_{k} \lambda_k \tag{4}$$

where λ_k is the estimated load multiplier associated with the k-th load case. In this way, LF represents the most critical load-amplification capacity among the analysed loading conditions. The second target, Δ_{max}, is the maximum absolute vertical displacement extracted from the nonlinear pushdown analyses. It is defined as

$$\Delta_{max} = \max_{k} |\Delta_k| \tag{5}$$

where Δ_k is the relevant vertical displacement response associated with the k-th nonlinear load case. This quantity provides a deformation-based measure of the structural response and complements the capacity-oriented information given by LF.

The distributions of the two target variables among the dataset presented in sect. 3 are reported in Fig. 3. In particular, Fig. 3(a) shows the distribution of the load factor LF, while Fig. 3(b) reports the distribution of the maximum displacement Δ_{max}. The threshold values $LF = 1.0$ and $\Delta_{max} = 0.15$ m are also shown, highlighting that the dataset includes both configurations below and above the selected capacity and displacement limits. The scalar objective value used during dataset generation was not included among the ML

input descriptors, since it is derived from the same response quantities used as targets. Including it would introduce data leakage and would artificially improve the predictive performance of the models.

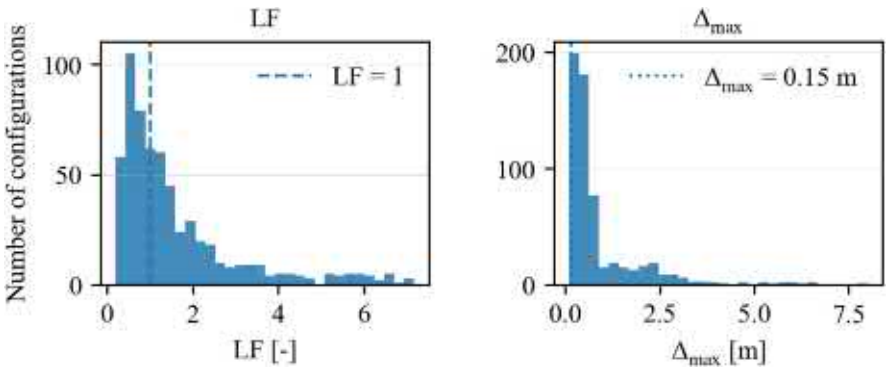


Fig. 3. Distribution of the target variables in the ML dataset: (a) load factor *LF*; (b) maximum displacement Δ_{max}

The simultaneous prediction of *LF* and Δ_{max} allows the ML models to approximate both strength/stability-related and displacement-related aspects of the nonlinear response. This is particularly useful for preliminary screening of generated configurations, where a rapid estimate of structural performance can reduce the number of expensive nonlinear analyses required in later optimization stages.

4 Machine Learning Models

The dataset described in Sect. 3 was used to train and test five regression-based ML models for the prediction of the two target variables, *LF* and Δ_{max}. The selected models are Multilayer Perceptron (MLP), Categorical Boosting (CatBoost), Gradient Boosting Machine (GBM), Random Forest (RF), and Extreme Gradient Boosting (XGBoost). These models were selected because they represent different families of regression algorithms, including neural-network-based learning and ensemble tree-based methods, and have been widely adopted in recent data-driven structural engineering applications [13, 14]. All models were trained using the same structure-level input descriptors and evaluated on the testing dataset using Mean Absolute Error (MAE), Root Mean Square Error (RMSE), and the coefficient of determination (R^2).

4.1 Results and Discussion

The prediction results for estimating *LF* and Δ_{max} are presented in Figs. 4 to 8. To better assess the performance of ML models, the predictive performance was evaluated for two target variables, namely *LF* and Δ_{max}, as presented in Table 1. For the *LF* prediction task, CatBoost demonstrated the best overall performance, achieving the lowest MAE

=0.164 and RMSE =0.331, as well as the highest R^2 value of 0.948, indicating superior accuracy and explanatory capability compared to the other models. MLP and XGBoost showed moderate performance with R^2 values of 0.938 and 0.918, respectively, while GBM and RF exhibited comparatively lower predictive accuracy, reflected in higher error metrics and reduced R^2 values (Figs. 5, 6 and 7).

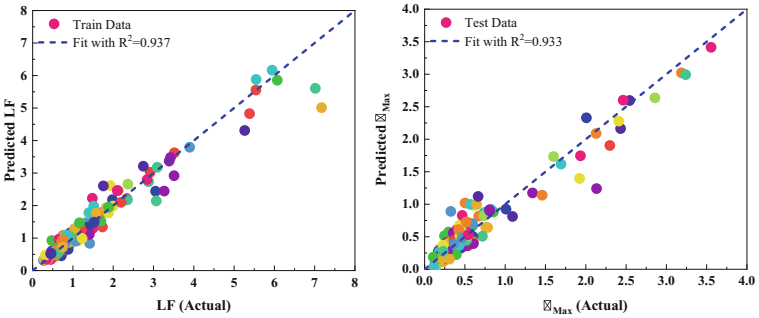


Fig. 4. Scatter plots of prediction results for LF and Δ_{max} using MLP algorithm

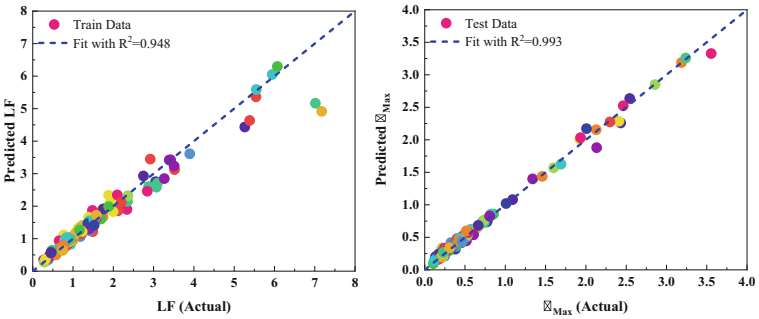


Fig. 5. Scatter plots of prediction results for LF and Δ_{max} using CatBoost algorithm

In the case of Δ_{max} prediction, all models achieved high accuracy; however, GBM provided the most accurate results, with the lowest MAE =0.005 and RMSE =0.017, and an R^2 value of 0.999, indicating near-perfect predictive performance. RF also performed strongly (i.e., MAE = 0.008, RMSE = 0.021, and R^2 = 0.999), closely followed by CatBoost and XGBoost, while MLP showed comparatively higher prediction errors for this target. Therefore, GBM emerged as the most robust model for predicting Δ_{max}, while CatBoost was the most effective for LF prediction. These results indicate that ensemble-based boosting methods generally outperform other approaches, particularly in capturing nonlinear relationships and improving predictive accuracy for structural response parameters.

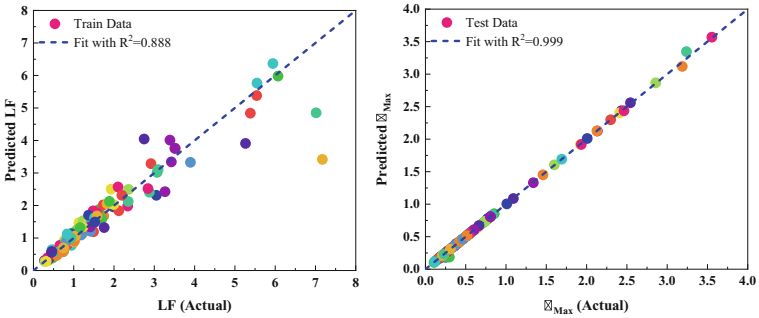


Fig. 6. Scatter plots of prediction results for LF and Δ_{max} using GBM algorithm

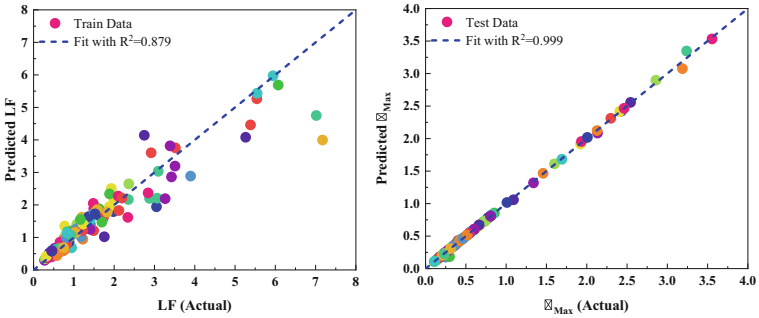


Fig. 7. Scatter plots of prediction results for LF and Δ_{max} using RF algorithm

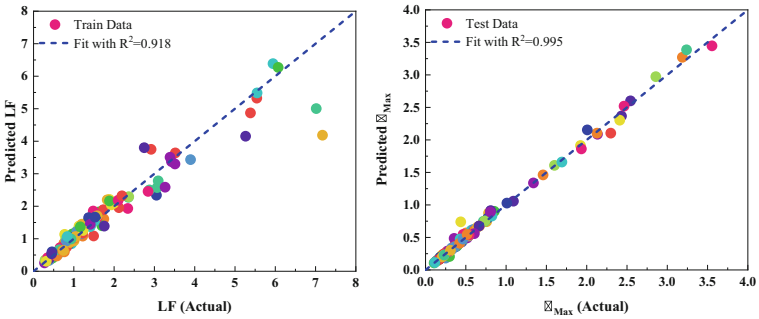


Fig. 8. Scatter plots of prediction results for LF and Δ_{max} using XGBoost algorithm

Table 1. The statistical metrics of ML models for predicting the targets of testing dataset

Model	Target	MAE	RMSE	R^2
MLP	LF	0.219	0.362	0.938

(*continued*)

Table 1. (*continued*)

Model	Target	MAE	RMSE	R^2
	DeltaMax	0.133	0.190	0.934
CatBoost	LF	0.164	0.331	0.948
	DeltaMax	0.041	0.058	0.994
GBM	LF	0.224	0.485	0.888
	DeltaMax	0.005	0.017	0.999
RF	LF	0.280	0.505	0.879
	DeltaMax	0.008	0.021	0.999
XGBoost	LF	0.201	0.415	0.918
	DeltaMax	0.029	0.052	0.995

5 Conclusions

The increasing use of optimization methods in the structural design of gridshells highlights the growing importance of computational approaches in achieving efficient, lightweight, and structurally optimized forms. These methods enable the systematic exploration of complex design spaces, allowing for improved structural performance, material efficiency, and sustainability. As a result, optimization-driven design has become an essential tool in the development of advanced gridshell systems, facilitating the integration of architectural intent with structural rationality. This study evaluated the performance of five ML models for predicting *LF* and Δ_{max} structural response parameters using statistical metrics. The results demonstrate that ensemble-based methods generally outperform the neural network approach, particularly in terms of predictive accuracy and robustness. For *LF* prediction, CatBoost achieved the best overall performance, exhibiting the lowest error values and the highest R^2, indicating strong predictive capability. In contrast, GBM delivered the most accurate results for Δ_{max}, with near-perfect agreement between predicted and observed values. Although all models performed well for Δ_{max}, boosting-based algorithms consistently showed superior performance compared to MLP and RF.

References

1. Brütting J, Senatore G, Schevenels M, Fivet C (2020) Optimum design of frame structures from a stock of reclaimed elements. Front Built Environ 6:57
2. Brütting J, Senatore G, Fivet C (2018) Optimization formulations for the design of low embodied energy structures made from reused elements. In: Smith IFC, Domer B (eds) Advanced computing strategies for engineering. EG-ICE 2018, Lecture notes in computer science, vol 10863. Springer, Cham, pp 139–163
3. Gioncu V (1995) Buckling of reticulated shells: state-of-the-art. Int J Space Struct 10(1):1–46

4. Bruno L et al (2023) Exploring new frontiers in gridshell design: the FreeGrid benchmark. Structure 58:105678
5. Ascione F, Esposito F, Faiella D, Mele E (2025) Steel reuse for sustainable design of large-span structures: the case of gridshells. J Constr Steel Res 234:109743
6. Tomei V, Grande E, Imbimbo M (2024) Topology optimization of gridshells with reused elements. In: Proceedings of the IASS 2024 symposium: redefining the art of structural design, Zurich, paper 163
7. Laghi V, Babovic N, Laccone F, Malomo L, Savino E, Gasparini G (2026) Automated design and fabrication framework to enhance steel reuse through structural optimization and metal 3D printing. Structure 88:111942
8. Asgarkhani N, Kazemi F, Jankowski R et al (2025) Dynamic ensemble-learning model for seismic risk assessment of masonry infilled steel structures incorporating soil-foundation-structure interaction. Reliab Eng Syst Saf 255:111839
9. Asgarkhani N, Kazemi F, Jankowski R (2025) Machine-learning based tool for seismic response assessment of steel structures including masonry infill walls and soil-foundation-structure interaction. Comput Struct 317:107918
10. Tang Q, Cui Y, Jia J (2024) Machine learning-based surrogate resilience modeling for preliminary seismic design. J Build Eng 98:111226
11. Rabie M, Almutairi FF, Tsavdaridis KD, Shaaban IG (2026) Machine learning-driven capacity design and embodied carbon reduction optimization in composite reduced web section (RWS) connections. Adv Eng Softw 217:104145
12. Computers and Structures, Inc (2009) SAP2000: integrated finite element analysis and design of structures. Computers and Structures, Inc, Berkeley
13. Asgarkhani N, Kazemi F, Mirrashid M, Okasha NM, Jankowski R (2026) Seismic performance assessment of reinforced concrete shear walls using data-driven methods. Arch Civ Mech Eng 26(2):75
14. Asgarkhani N, Kazemi F, Lasowicz N, Jankowski R (2026) Evaluation of mechanical behavior of concrete-timber-filled steel tubes using multi-stage machine-learning model. Structure 89:112017

Pre-sizing and Optimal Cross-Section Selection of Steel Gravity-Load Columns in Multi-story Concentrically Braced Frames

Gianmaria Di Lorenzo(✉), Giusy Terracciano, and Raffaele Landolfo

Department of Structures for Engineering and Architecture, University of Naples Federico II, Via Forno Vecchio 36, 80141 Naples, Italy
gianmaria.dilorenzo@unina.it

Abstract. Pre-sizing plays a key role in structural conceptual design, gaining renewed relevance in the current context of integration between Artificial Intelligence (AI) and computational tools, as it allows first-attempt dimensions to be defined in the early stages of the design process. Within the framework of the General Theory of Structural Conceptual Design developed by the authors, this paper focuses on gravity-load steel columns in multi-story buildings with concentrically braced frames. A critical review of the literature shows that the available rules for column pre-sizing are often highly aggregated and only partially account for the main parameters governing axial demand and buckling resistance. The study first discusses the selection of a target cross-section family among European hot-rolled steel sections, identifying the HEB series as a suitable reference for gravity-load columns. A parametric procedure is then developed to correlate the column size with the number of supported stories and the steel grade. The results are expressed through growth laws and reorganized into a semi-empirical tri-linear model. Finally, the equivalent number of stories is introduced to extend the results to systems with different grid dimensions and design loads.

Keywords: Structural conceptual design · optimal cross-section selection · steel gravity-load columns · concentrically braced frame structures · column pre-sizing · tri-linear model

1 Introduction

The advent of Artificial Intelligence (AI) and its integration into Building Information Modeling (BIM) and finite element analysis (FEA) software are marking a paradigm shift in structural design, assigning a central role to structural conceptual design with respect to purely computational aspects. Technological and process-related transformations are accompanied by increasingly demanding performance requirements, which affect contemporary constructions and make a holistic and multidisciplinary design approach unavoidable. Within this context of growing complexity, the General Theory of Structural Conceptual Design (GTSCD), developed by the authors, aims to merge materials engineering, the principles of structural mechanics, namely structural archetypes, and

© The Author(s), under exclusive license to Springer Nature Switzerland AG 2026
R. Zanon et al. (Eds.): CTA 2026, LNCE 942, pp. 1024–1035, 2026.
https://doi.org/10.1007/978-3-032-39505-4_89

the theory of proportions, scientifically reinterpreted by the authors [1]. The GTSCD is founded on its "Postulate", according to which, once the expected performance requirements and target performance levels, architectural and MEP constraints, and general design strategies have been defined, structural conception is articulated through three consecutive and consequential choices, respectively defined as: the technological choice, or the choice of the material for structural use (Step I); the typological choice, or the choice of the load-resisting scheme (Step II); and the dimensional choice, or the choice of the first-attempt dimension (Step III).

The GTSCD, which has a fully general character, has already been applied by the authors to the conceptual design of floor systems in multi-story buildings [1] and of roofs, including complex roof structures [2], as well as to the design methodology of orthogonal steel exoskeletons used for the retrofit of existing constructions [3]. A key role within the GTSCD is played by the dimensional choice, also referred to as "pre-sizing", which consists in assigning a first-attempt dimension. In the case of beams, this dimension is commonly defined through suitable shape ratios, obtained on the basis of experience, by structural analogy, or through parametric analyses performed a priori on systems that are homogeneous in terms of construction technology and structural type.

It should be noted that pre-sizing must not be confused with structural sizing, even when the latter is carried out using simplified schemes. Structural sizing takes place at a later stage of the design process, namely after global or partial structural modeling and analysis, and consists in determining, for non-dissipative systems or for the dissipative parts of earthquake-resistant systems designed according to capacity design criteria, the geometric unknowns strictly required to ensure, for the different limit states (LSi), equality and, more generally, compatibility between demand (D_{LSi}) and capacity (C_{LSi}).

The use of geometric rules based on the depth-to-span ratios ($r_{\mathrm{hL}} = h/L$) of members, or on their inverse, is widespread in the design of beams for single-story or multi-story buildings [4] and bridge decks [5]. The use of shape ratios is not merely good practice for proper structural conception and design. By allowing designers to rapidly orient dimensional choices in the early stages of the design process and to reduce the need for time-consuming preliminary FEM analyses, this approach can be particularly useful in the preparation of technical and economic feasibility studies for public works and infrastructure, where alternative solutions must be compared within limited timeframes and on the basis of still partial information. Despite the importance and effectiveness of this approach, the values provided in the literature for beams are often excessively aggregated [1] and do not allow the optimal choice of member dimensions as the main design parameters vary. These parameters affect the demand due to gravity loads, for example grid spacing, load intensity, and boundary conditions, as well as the resistance, for example steel grade and cross-section type.

Due to the greater complexity involved in characterizing the demand and to the large number of governing parameters, the studies and results available in the technical literature for column pre-sizing are even more limited. When available, such indications provide even more aggregated and uncertain values [6–9]. In particular, they do not specify, or do not systematically vary, column size as a function of material, grid spacing, global structural typology, and adopted cross-section/profile type. Moreover, the role of

horizontal actions is not explicitly clarified, nor is the influence of their intensity on member pre-sizing.

A detailed analysis of the cited sources shows that the ArcelorMittal manual [6] provides useful indications for the concept design stage of multi-story steel buildings, but they are still characterized by a high level of aggregation. In particular, columns are considered as members generally made of H-shaped sections and mainly subjected to axial force; the preliminary selection of the section is suggested on the basis of axial load only, while imposing a utilization level not exceeding 90% of the resistance, in order to account, in a subsequent stage, for nominal moments resulting from beam-to-column connection eccentricities. The typical depths reported are expressed as a function of the number of stories supported by the column, but they are not associated with a specific European section series, such as HEA, HEB, or HEM, nor with a given steel grade, buckling length, or fully defined structural grid. Furthermore, the problem is formulated under the assumption that the lateral stability of the building is provided by cores or vertical bracing systems; consequently, the effect of horizontal actions due to wind or earthquake is neither disaggregated nor related to the position of the column within the overall load-resisting system. This approach therefore does not allow a distinction to be made between ordinary columns mainly subjected to gravity loads and columns belonging to braced bays or otherwise directly involved in the transfer of horizontal actions.

The SCI P365 document [7] is clearer with respect to the structural typology considered, since it refers to medium-rise braced multi-story buildings, up to about 15 stories, designed according to the "simple construction" model, with nominally pinned beam-to-column connections and resistance to horizontal actions provided by vertical bracing systems. In this context, columns are generally made of British rolled Universal Column (UC) sections, selected for their good compression resistance and for the ease of connecting beams to the flanges and web of the section. The pre-sizing table provides UC sizes as a function of the number of supported stories, with reference to grids up to 6 × 7.5 m and composite floor systems with limited spans. Compared with the ArcelorMittal manual, the document also introduces a more rational procedure for the initial selection of the column, based on the determination of the design value of the axial force (N_{Ed}), obtained by multiplying the loads acting on the tributary area by the number of supported stories, without applying live-load reductions at this preliminary stage. For edge columns or columns subjected to asymmetric loading, it is suggested to amplify the axial force demand in order to account for the effects of nominal moments, using coefficients that decrease as the number of supported stories increases. The section is finally sized by requiring that the design buckling resistance ($N_{b,Rd}$), evaluated by assuming a system length equal to the story height, ensures a utilization level not exceeding 90%. Nevertheless, also in this case, the indications remain calibrated on UC sections and on British design practice, are not directly transferable to European HE, HD, or hollow sections, and do not explicitly distinguish between ordinary gravity-load columns and columns belonging to braced bays. Moreover, the influence of horizontal actions is treated at the level of the bracing system and is not translated into disaggregated pre-sizing criteria for individual columns as a function of their position and resisting role.

The AISC tables [8, 9] represent, among the sources examined, the most parameterized approach for column pre-sizing. They are expressly conceived to support architects and designers in the early stages of a project, when it is necessary to rapidly estimate column overall dimensions before the development of detailed structural calculations. Preliminary dimensions are provided for interior columns of buildings from one to six stories, as a function of structural grid, floor system, and design gravity loads. The tables consider square and rectangular bays ranging from 20 × 20 ft. (6.1 × 6.1 m) to 40 × 40 ft. (12.2 × 12.2 m), two floor live-load levels, different floor systems, and a maximum floor-to-floor height of 15 ft. (4.5 m). Moreover, they refer to rolled wide-flange sections made of ASTM A992 steel with a yield strength of 50 ksi and to HSS hollow sections made of ASTM A500-C steel with a yield strength of 46 ksi. These values are comparable, in order of magnitude, with those of European S355 steel, but they are not directly equivalent in terms of design framework, section catalogue, and verification criteria. The main limitation of these tables is, however, explicitly stated by their authors: the columns considered are exclusively interior columns, subjected only to gravity loads, with simple connections and with no contribution to the lateral resistance of the building. Therefore, exterior columns, which are often affected by façade loads and, in some systems, by resistance to horizontal actions, are not considered, nor are columns belonging to frames or braced bays. Moreover, the full application of live loads without reductions, together with the absence of contributions from wind, earthquake, second-order effects, and interaction with the lateral-force-resisting system, makes the AISC tables an effective tool for preliminary space planning, but not a general structural pre-sizing procedure transferable to the European context.

The study on beam depth-to-span ratios therefore represents the methodological reference for the present work [1]. In this paper, the parametric approach developed by the authors and already adopted for members in bending is extended to steel columns, for which the definition of growth laws is more complex because of the cumulative nature of the axial demand along the building height and the possible influence of buckling phenomena. Based on these considerations, and by initially limiting the scope of the study to gravity-load columns in multi-story buildings with concentrically braced frames (CBFs), the aim of the present work is to provide designers with growth laws for column size as the number of stories varies. After first identifying, among European steel sections, the most suitable cross-section family to be used for gravity-load columns, a parametric design procedure is developed and implemented to determine the first-attempt dimension to be adopted as the main design parameters vary. As an example, this fully general approach is applied and presented in this paper with reference to wide-flange sections of the HEB series. The results of the parametric analyses are finally reorganized through tri-linear models, intended to provide practical tools for the rapid pre-sizing of HEB columns as a function of the number of supported stories. It should be noted that the proposed approach overcomes the intrinsic limitations of the existing literature on column pre-sizing, which is typically characterized by a high level of aggregation and does not explicitly capture the influence of the governing parameters. The method provides a rational, parametric, and generalizable formulation directly applicable in conceptual design. As a future development, this procedure will be extended to other cross-section families and

structural systems, such as two-dimensional and three-dimensional moment-resisting frames (MRF2D and MRF3D), also considering the influence of seismic actions.

2 Optimal Cross-Section Selection

In accordance with Step II of the GTSCD Postulate, namely the typological choice, before proceeding with the definition of growth laws for column pre-sizing, it is necessary to identify a target cross-section family with respect to which the parametric procedure can be calibrated. For the different steel grades, the steel industry currently provides designers with a wide range of hot-rolled steel sections, also produced using structural steels with reduced embodied carbon [10]. The selection of the optimal cross-section plays a crucial role in reducing structural weight, cost, and environmental impact [11]. This selection can be performed through a rapid approach based on suitable geometric efficiency ratios (ρ_S) which make it possible, depending on the stress regime, to identify the most efficient profile type for the same cross-sectional area [12]. In the case of members subjected to global flexural or flexural-torsional buckling, the key parameter is (ρ_{Iz}) defined as the ratio between the second moment of area about the weak axis (I_z) and that of the benchmark section, represented by a square section of equal weight ($I_{z.SQ}$). This parameter also expresses the gain, or loss, in terms of geometric property and associated structural performance with respect to the initial semi-finished product, thereby justifying the advantage of the hot-rolling process, whose energy and environmental cost significantly affects the Life Cycle Assessment (LCA) of the product.

Figure 1 shows the trend of the efficiency parameter (ρ_{Iz}) with respect to global flexural or flexural-torsional buckling of European hot-rolled steel sections, as a function of the cross-sectional area and weight.

Once the unit permanent and variable actions (g_k and q_k), as well as the tributary area depending on the structural grid, have been defined, the cross-sectional area can also be correlated, as a first approximation, with the axial force demand and therefore with the number of stories of multi-story buildings. In a fully conventional way and for design-oriented purposes, by adopting a scalar-structural taxonomy, multi-story buildings may be classified, for descriptive and design purposes, into dimensional classes defined as a function of the number of above-ground stories:

- XS Low-rise: up to 3 stories;
- S Low/mid-rise: 4–10 stories;
- M Mid-rise: 11–20 stories;
- L High-rise/Tall: 21–40 stories
- XL Very tall/Supertall: 41–100 stories;
- XXL Ultra-tall/Megatall range: $>$ 100 stories, also to be checked with respect to a height $\geq$ 600 m

As can be observed from Fig. 1, when hollow sections are excluded from the comparison, no profile can be considered optimal in an absolute sense.

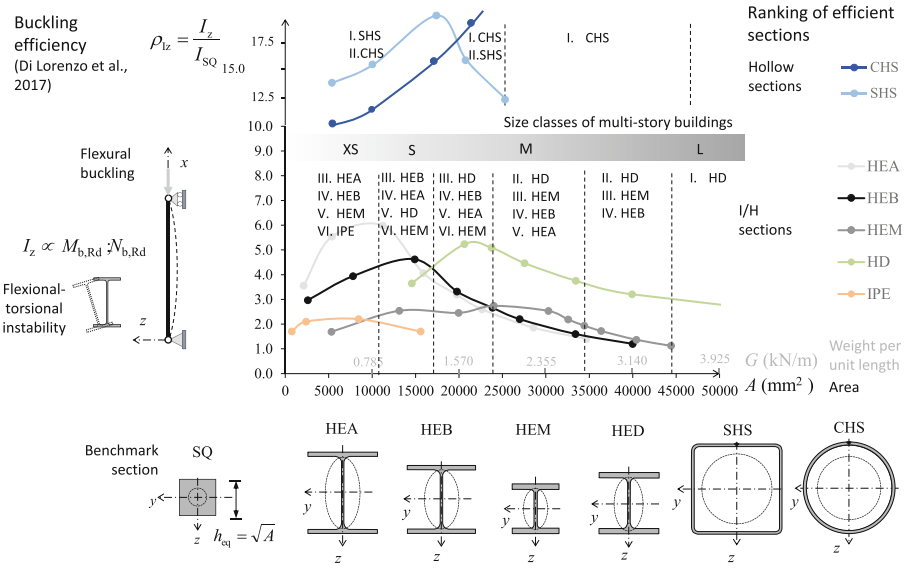


Fig. 1. Rapid selection of efficient cross-sections for slender steel columns subjected to pure compression.

For very low-rise and low-rise buildings, namely up to approximately 10–12 stories, the wide-flange HE sections are particularly efficient. The HEA series is especially suitable for single-story buildings or buildings with a very limited number of stories (XS), whereas the HEB and HEM series are highly efficient for low-rise (S) and medium-rise (M) buildings. These sections are particularly effective in compression up to the HE 300 section, beyond which the flange width no longer increases and remains approximately constant, with a width (b) of about 300 mm. Beyond this size, their efficiency decreases sharply in favor of heavier wide-flange sections, such as the HD series, which also have the advantage of being less sensitive to web local buckling, even for large-size profiles.

Based on the previous considerations, and considering their widespread commercial availability, the HEB section series is adopted in the present work as the reference section family. This choice does not imply that the HEB series represents the optimal solution in an absolute sense for every field of application; rather, it makes it possible to identify a widely used target family, characterized by good compression efficiency, adequate geometric compactness, and ease of use in multi-story steel systems.

3 Methodology and Parametric Analyses for Deriving the Growth Laws of the Target Cross-Section Family: *The Case of HEB Profiles*

Growth laws and, more generally, the shape ratios derived from them can be obtained through three main approaches: design experience, structural analogy, and parametric analyses. The first approach is empirical in nature and is based on the direct knowledge

acquired by the designer through observation and the sizing of a significant number of structural systems. The second, semi-empirical approach consists in the cataloguing and statistical analysis of structural systems or members that are homogeneous in terms of material, load-resisting typology, and performance levels, using both direct sources and data available in the technical-scientific literature or in digital archives. The third and most rigorous approach is represented by parametric analyses, which allow the pre-sizing quantities to be derived through the rapid sizing of representative members or systems as the main parameters governing demand and resistance vary.

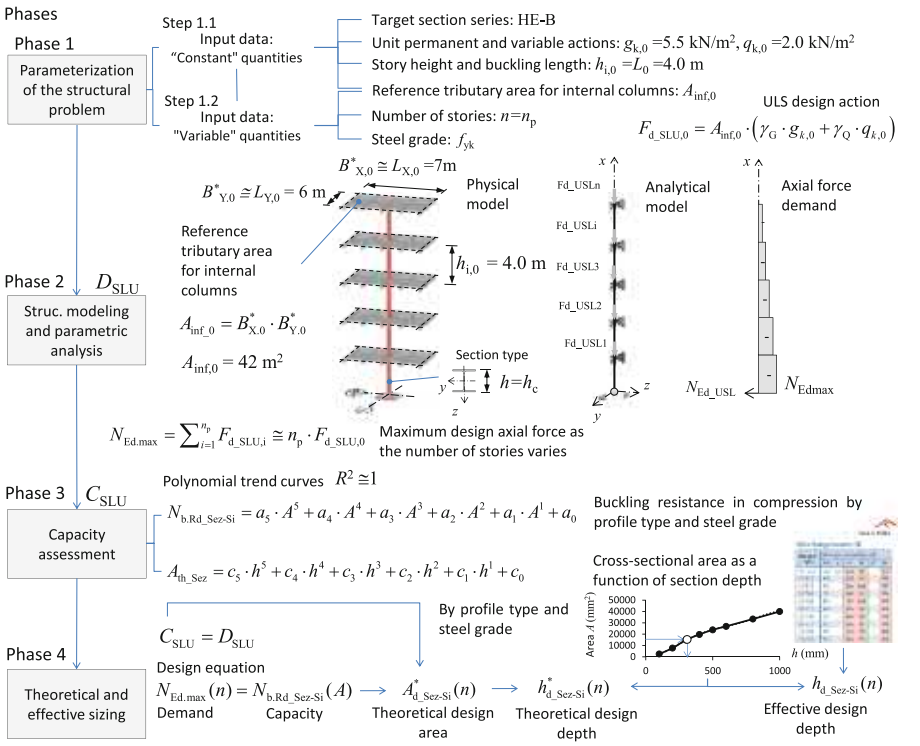


Fig. 2. Flowchart of the parametric algorithm for deriving growth curves of target sections for gravity-load columns in CBF structures.

In the present work, the latter approach is adopted, since it allows the results to be disaggregated as a function of the main design variables and enables growth laws to be derived directly from the mechanical behavior of the target cross-section family. The algorithm used for deriving the growth curves of the target section for gravity-load columns in CBF structures, shown in Fig. 2, is organized into four phases. The first phase consists in the parametrization of the problem, namely the identification of the design quantities, classified as "constant" and "variable" parameters. The first group includes the target cross-section type, in this case HEB, the load per unit floor area associated with permanent actions ($g_{k,0}$) and variable actions ($q_{k,0}$), assumed equal to

reference values considered representative of residential and similar buildings, such as dwellings, hotel rooms, hospital rooms, and offices not open to the public (see Fig. 2). For permanent actions, a value of $g_{k,0} = 5.5\text{kN/m}^2$ was assumed, including the contribution of the structural system weight and of non-structural components. For variable actions, a reference value of $q_{k,0} = 2\text{kN/m}^2$ was adopted, representative of residential and similar buildings. A further constant quantity is the story height ($h_i = 4$ m), coinciding with the buckling length (L_0 or L_{cr}). Although the selected value is typically used for office buildings, it is also representative of residential buildings with commercial premises at the ground floor. Moreover, the possibility of calculating, after the parametric sizing procedure, the column shape ratio $r_{hL} = h/L = h_c/h_i$ allows the results to be extended also to story heights different from the reference value. The variable quantities are the number of stories ($n = n_p$) and the steel grades (S235, S275, S355, S420 and S460), characterized by the yield strength (f_{yk}). Finally, the tributary area, which depends on the structural grid, can be considered either as a constant or as a variable parameter. As discussed below, the possibility of generalizing the results with respect to the parameters affecting demand, such as the grid parameters L_X and L_Y, and the unit actions g_k and q_k, through the concept of equivalent number of stories ($n_{eq,0}$), ensures that the reference values adopted in the analyses do not limit the applicability of the results obtained in the present study.

Once the design parameters have been defined, structural modeling and analysis are carried out (Phase 2). For the type of member considered, namely a gravity-load column, and for the structural system under investigation, namely a CBF building, this can be performed using simplified schemes. After evaluating the maximum demand (D_{ULS}) in terms of design axial force at the base of the reference column ($N_{Ed,max}$) the sizing procedure is carried out by determining the required geometric quantities (A, and therefore h, of the HEB column), equating the design axial force demand to the capacity (C_{ULS}), given by the compression capacity governed by flexural buckling ($N_{b,Rd}$). To overcome the indeterminacy that characterizes the compression sizing of columns affected by buckling, a preliminary characterization and identification of the resistance is performed (Phase 3). The compression resistance ($N_{b,Rd}$) of HEB columns is calculated for the different steel grades and related to the cross-sectional area (A) (Fig. 3). The resulting capacity curves are interpolated by means of a fifth-degree polynomial function, which ensures an excellent coefficient of determination ($R^2 \cong 1$) and allows the capacity trend to be accurately reproduced over the whole section range. By equating the design action effect, as the number of stories varies, to the resistance ($N_{Ed,max}(n) = N_{b,Rd_Sez\text{-}Si}(A)$) it is possible to determine the required theoretical and effective area ($A^*_{d_Sez\text{-}Si}(n)$), (Phase 4). By identifying the variation of the cross-sectional area with the section depth ($A(h)$) the "theoretical" design depth can be determined in continuous form ($h^*_{d_Sez\text{-}Si}(n)$: $A^*_{d_Sez\text{-}Si}(n) = A(h)$) as the number of stories varies. Once the theoretical design depth is known, the shape ratio (r_{hL}) and the effective design depth ($h_{d_Sez\text{-}Si}(n)$) can be obtained by selecting from the steel section catalogue [13] the profiles with a depth immediately greater than the required one. Unlike a conventional catalogue-based parametric sizing procedure, in which the profile is directly selected as the first commercial section whose capacity exceeds the demand, the proposed algorithm first derives a continuous theoretical design depth and only subsequently converts it into an

effective commercial profile. This continuous formulation avoids making the growth laws dependent on the discrete sequence of commercial sections and provides the basis for generalizing the results through the equivalent number of stories.

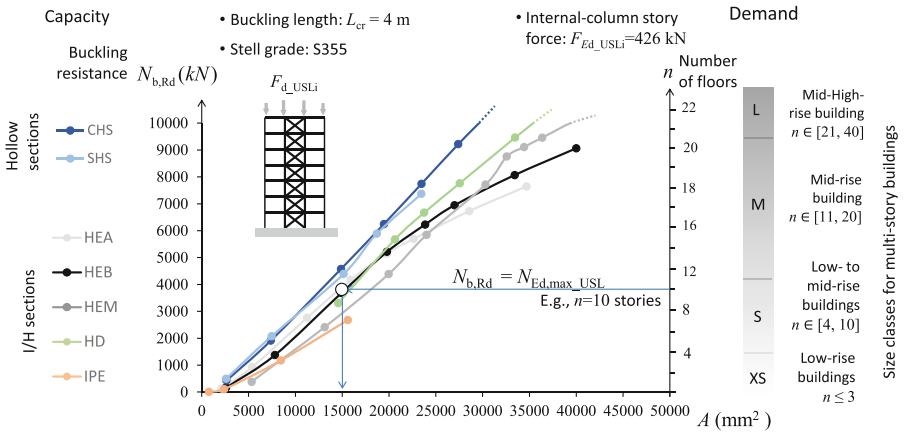


Fig. 3. Buckling capacity curves of S355 steel columns versus cross-sectional area and axial demand related to the number of stories.

In this regard, the results obtained from the above procedure and presented in Sect. 4 can also be generalized to cases in which the design parameters, in terms of tributary area ($A_{inf,d}$) and/or unit actions ($g_{k,d}$ and $q_{k,d}$), differ from those used as reference values among the constant quantities. In this case, the concept of equivalent number of stories ($n_{eq,0}$) is introduced, defined as the number of stories of the benchmark structure, characterized by the tributary area $A_{inf,0}$ and by the reference vertical actions $g_{k,0}$ and $q_{k,0}$, that produces at the base of the gravity-load column the same design axial force as the structure being analyzed.

$$n_{eq,0} = n_d \cdot \frac{A_{inf,d} \cdot \left(\gamma_G \cdot g_{k,d} + \gamma_Q \cdot q_{k,d}\right)}{A_{inf,0} \cdot \left(\gamma_G \cdot g_{k,0} + \gamma_Q \cdot q_{k,0}\right)} \tag{1}$$

where

γ_G is the partial factor for permanent actions, for which a single value equal to 1.3 was assumed for both structural and non-structural permanent actions, considered as well-defined actions;
γ_Q is the partial factor for variable actions, assumed equal to 1.5.

4 Results and Tri-Linear Models for the Pre-Sizing of HEB Columns

The trends of the growth laws for the size of HEB columns ($h^*_{d,HEB} = f(n, f_{yk})$) as a function of the number of stories (n) and the steel grade (f_{yk}), are reported in Fig. 4.

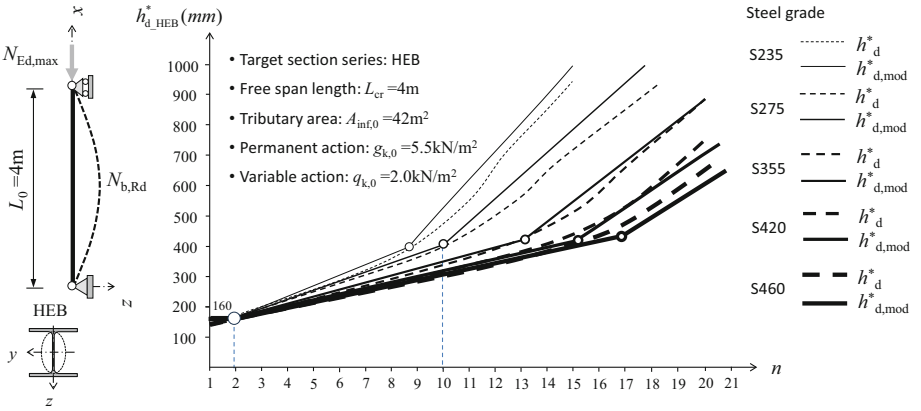


Fig. 4. Parametric results and tri-linear pre-sizing model for HEB gravity-load columns as a function of (n) and (f_{yk}).

In particular, the dashed lines indicate the theoretical trends obtained by applying the algorithm described in Sect. 3, whereas the solid lines indicate the required theoretical values described by a semi-empirical tri-linear model (Eq. (2)), calibrated against the parametric results.

$$h^*_{d,th_HEB} = \begin{cases} h_{0,HEB} & n \le 2 \\ h_{0,HEB} + (n-2)\cdot \Delta h_I \cdot \left(\frac{275\ MPa}{f_{yk}}\right) & 2 < n \le 10\cdot \frac{f_{yk}}{275\cdot MPa} \\ h_{0,HEB} + \left(10\cdot \frac{f_{yk}}{275\ MPa} - 2\right)\cdot \Delta h_I \cdot \left(\frac{275\ MPa}{f_{yk}}\right) + \left(n - 10\cdot \frac{f_{yk}}{275\ MPa}\right)\cdot \Delta h_{II} \cdot \left(\frac{275\ MPa}{f_{yk}}\right) & n > 10\cdot \frac{f_{yk}}{275\cdot MPa} \end{cases} \quad (2)$$

The model, calibrated on S275 steel, consists of three branches: a plateau $h^*_{d,HEB} = h_{0,HEB}$, for $n \le 2$, a first branch with a slope characterized by the coefficient (Δh_I = 30 mm/story), for $n \le 10$ and a second branch whose inclination depends on the coefficient (Δh_{II} = 85 mm/story). The model is extended to other steel grades through the ratio (f_{yk}/275 *MPa*) and its inverse (275 *MPa*/f_{yk}) which respectively modify the number of stories at which the branches join and the slopes of the inclined branches. The model can be regarded as semi-empirical because the three branches account for the change in section efficiency described in Fig. 1, particularly for HEB profiles with depths greater than 300 mm. The third branch is steeper than the second because, for less efficient profiles, the section depth and therefore the cross-sectional area must be significantly increased to satisfy the design axial force demand ($N_{Ed,ULS}$) as the number of stories increases. The plateau ($h_{0,HEB}$ = 160 mm) has a design meaning and is intended to limit, for low-rise buildings, the maximum geometric slenderness ($\lambda_{z,max}$) below a conventional limit value equal to 100. As can be observed, the semi-empirical model is conservative over almost the entire investigated range, except for buildings with a high number of stories made of S420 and S460 steel, for which the column sizes should be increased by about 15%. Moreover, the best fit of the proposed semi-empirical model is obtained for S355 steel, which, owing to its favorable performance-to-cost ratio, is currently among the most widely used steel grades in the construction sector.

The proposed model was finally validated by comparing the growth curves with the results of parametric analyses performed on CBF systems designed for seismic actions [14, 15]. To homogenize the results, the comparison was performed using Eq. (1) for the gravity-load columns, which allows the growth laws to be extended to systems with different structural grids and design loads.

5 Conclusions

In this work, a procedure for the pre-sizing of steel gravity-load columns in multi-story buildings with concentrically braced frames (CBFs) has been proposed within the framework of the General Theory of Structural Conceptual Design developed by the authors. Starting from a critical review of the indications available in the technical literature, the lack of sufficiently disaggregated tools for the preliminary selection of columns was highlighted, especially with respect to the number of stories, structural grid, vertical loads, steel grade, and adopted section family. Among European hot-rolled steel profiles, the HEB series was selected as the target family, owing to its commercial availability, good compression efficiency, and ease of use in multi-story steel systems. The developed parametric procedure allows the design axial demand to be correlated with the compression buckling capacity of HEB profiles, deriving growth laws for column size as the number of stories and steel grade vary. The results were reorganized into a semi-empirical tri-linear model, suitable for immediate design application and capable of representing the different behavior of HEB profiles as the nominal size increases. The introduction of the equivalent number of stories also allows the obtained laws to be extended to configurations with tributary areas and unit loads different from the reference ones. The scope of application remains limited to gravity-load columns in CBF buildings. Therefore, the selected sections should be regarded as first-attempt dimensions, to be validated through structural modeling and limit-state checks. Future developments will address the extension of the procedure to other profile families and structural systems, including two-dimensional and three-dimensional moment-resisting frames (MRF2D and MRF3D), also considering the influence of horizontal and seismic actions.

References

1. Di Lorenzo G, Formisano A, Terracciano G, Landolfo R (2025) Span-depth ratios for the preliminary structural design of steel beams: the case of European hot-rolled I sections without lateral-torsional buckling. Eng Struct 345(B):121504. https://doi.org/10.1016/j.engstruct.2025.121504
2. Di Lorenzo G, Terracciano G, Formisano A, Landolfo R (2025) Innovative V-shaped column design for one-way 3D truss systems in preserving archaeological sites. In: Mazzolani FM, Landolfo R, Faggiano B (eds) Protection of historical constructions. PROHITECH 2025, Lecture notes in civil engineering, vol 595. Springer, Cham. https://doi.org/10.1007/978-3-031-87312-6_37
3. Di Lorenzo G, Tartaglia R, Prota A, Landolfo R (2023) Design procedure for orthogonal steel exoskeleton structures for seismic strengthening. Eng Struct 275(A):115252. https://doi.org/10.1016/j.engstruct.2022.115252
4. Schodek DL, Bechthold M (2014) Structures, 7th edn. Pearson Education, Harlow

5. American Association of State Highway and Transportation Officials (2024) LRFD bridge design specifications, 10th edn. AASHTO, Washington, DC
6. ArcelorMittal, Peiner Träger, Corus (2010) Steel buildings in Europe. Multi-storey steel buildings. Part 2: concept design. Technical content prepared by CTICM and SCI, collaborating as the Steel Alliance. ArcelorMittal, Luxembourg
7. Brown DG, Iles DC, Yandzio E (2009) Steel building design: medium rise braced frames SCI publication P365. The Steel Construction Institute, Ascot
8. American Institute of Steel Construction (n.d.) Guide to using the preliminary beam, girder and column size tables. American Institute of Steel Construction, Chicago. Last Accessed 16 May 2026
9. American Institute of Steel Construction (AISC) (2023) Steel construction manual, 16th edn. American Institute of Steel Construction, Chicago
10. ArcelorMittal Europe – Long Products (2021) Environmental product declaration: XCarb™ recycled and renewably produced structural steel sections and merchant bars (EPD-ARC-20210132-CBB2-EN). Institut Bauen und Umwelt e.V. (IBU)
11. D'Antimo M (2023) Optimised steel structures for a low carbon future. In: Biondini F, Frangopol DM (eds) Life-cycle of structures and infrastructure systems. CRC Press. https://doi.org/10.1201/9781003323020-295
12. Di Lorenzo G, Formisano A, Landolfo R (2017) On the origin of I beams and quick analysis on the structural efficiency of hot-rolled steel members. Open Civ. Eng. J. 11(Suppl-1, M3):332–344. https://doi.org/10.2174/1874149501711010332
13. ArcelorMittal Europe – Long Products (2026) Sections and merchant bars. Sales programme. ArcelorMittal, Luxembourg. sections.arcelormittal.com. Last Accessed 16 May 2026
14. Costanzo S, D'Aniello M, Landolfo R (2019) Proposal of design rules for ductile X-CBFs in the framework of Eurocode 8. Earthq. Eng. Struct. Dyn. 48(1):124–151. https://doi.org/10.1002/eqe.3128
15. Gnazzo M, D'Aniello M, Landolfo R (2024) X-concentrically braced frames designed according to the second generation of Eurocode 8. In: Mazzolani FM, Piluso V, Nastri E, Formisano A (eds) Proceedings of the 11th international conference on behaviour of steel structures in seismic areas. STESSA 2024, Lecture notes in civil engineering, vol 520. Springer, Cham, pp 721–732. https://doi.org/10.1007/978-3-031-62888-7_63

Vibrations

Human-Induced Vibrations on Steel-Glass Floors: Guidelines, Experiments and Modelling of a Case-Study

Chiara Bedon(✉) and Marco Fasan

University of Trieste, 34127 Trieste, Italy
chiara.bedon@dia.units.it

Abstract. Human-induced vibrations are a task of well-known importance in current practice, for floors and pedestrian systems in general. Because of this challenge, this paper focuses on steel-glass floors. There, the relatively high stiffness and resistance of steel members make them suitable for realizing bracings and minimize restraints, in many composite solutions. At the same time, laminated glass panels can be adapted to several modular configurations, covering wide surfaces. However, compared to pedestrian systems made of traditional materials, steel-glass floors have intrinsic geometrical and mechanical features that should be properly taken into account, both at the design stage and in-service. Existing technical guidelines and performance indicators are discussed in this paper, and applied to a case-study steel-glass floor of recent construction in Italy, including analytical calculations, on-site experimental measurements and Finite Element numerical simulations. While the suitability of repeated simplified checks for steel-glass solutions should be verified (considering their sensitivity to a multitude of design assumptions and service conditions), this study shows how the comfort check can be affected by many uncertainties, especially in consideration of human reactions on glass surfaces.

Keywords: Laminated Glass · Steel-glass Floor · Vibration Comfort · Vibration Assessment · Experiments · Numerical Analysis

1 Introduction

Steel-glass systems are frequently used for roofs, both in new and existing buildings. The high rigidity and resistance of steel, combined with the good mechanical performances of structural glass, allows to construct modular solutions and cover large surfaces. Often, these systems are optimally designed for strength and deflection demands, at the Ultimate and Serviceability Limit States [1, 2], disregarding – due to the relatively high frequency – the vibration performances and the associated comfort [3].

The problem increases further for existing steel-glass floors, where the material degradation due to long-term phenomena or unfavourable operating conditions can take place [4]. While steel and glass materials do not suffer for these effects, major sensitivity is in fact associated to the viscoelastic polymeric interlayers that bond glass, as well as

© The Author(s), under exclusive license to Springer Nature Switzerland AG 2026
R. Zanon et al. (Eds.): CTA 2026, LNCE 942, pp. 1039–1051, 2026.
https://doi.org/10.1007/978-3-032-39505-4_90

to the soft gaskets and components that are commonly used to connect steel and glass, preventing stress peaks [5, 6].

An additional concern regards the suitability of existing design guidelines and protocols for the vibration comfort assessment of traditional floors (i.e., [7, 8]), considering that steel-glass solutions are characterized by own geometrical and mechanical features. For example, steel-glass floors can be associated to relatively high vibration frequency, but at the same time to uncomfortable dynamic responses. In some other cases, they could have small thickness-to-size ratios, high flexibility, and unconventional boundary restraints, making them even more sensitive to dynamic excitations [6, 9]. Finally, human behaviour is known to be affected by the dynamic features of transparent floors [10]. This paper examines some of the existing vibration comfort criteria of floors, and their application to a case-study steel-glass floor of recent construction. The analysis is supported by on-site experiments and Finite Element (FE) numerical analyses [11].

2 Comfort Criteria

Vibration verification criteria in terms of pedestrian comfort are provided by several international standards, design codes and guidelines that can be applied to road bridges, rail bridges, pedestrian bridges and floors, i.e [12–15]. and Fig. 1.

For pedestrian systems, it is usually required to perform a more detailed dynamic investigation for those structures with fundamental natural frequency that falls within specific ranges, corresponding to the risk of resonance amplification, when subjected to human-induced vibrations [12]. Specific acceleration limits are recommended by ISO, and adjusted for the intended occupancy (Fig. 1a). The reference indicator for the proposed criterion is expressed in terms of peak acceleration as a percentage of gravity, but is only one among several performance indicators of practical use.

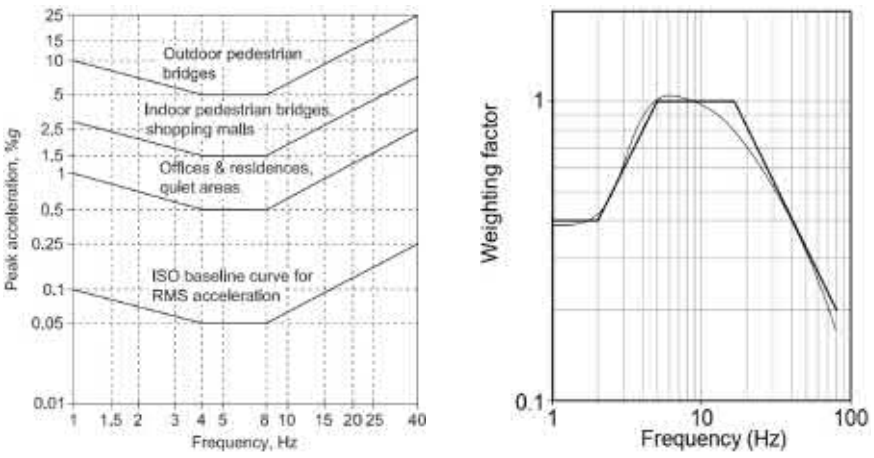


Fig. 1. Vibration comfort assessment based on the specifications by ISO [12]: (a) peak accelerations and (b) weighting factor.

To avoid possible resonance issues, a maximum threshold for the so-called weighted acceleration is often provided. For instance, the Sétra guideline [13] detects four classes of comfort criteria for pedestrian structures, with respect to the measured critical acceleration due to vertical vibrations, specifying (i) maximum, (ii) medium, (iii) minimum and (iv) unacceptable comfort levels for acceleration peaks (i) < 0.5 m/s^2; (ii) between 0.5 and 1.0 m/s^2; (iii) between 1.0 and 2.5 m/s^2; and (iv) > 2.5 m/s^2 respectively.

3 SCI Report P354

3.1 Response Factor for High-Frequency Floors

For high-frequency floors ($f_1 > 10$ Hz), the methodology proposed by SCI Report P354 [14] is elaborated considering that the response is transient, rather than stationary like for low-frequency floors. The method assumes that each step corresponds to an impulsive impact on the floor, equal to:

$$F_I = 60 \frac{f_p^{1.43}}{f_1^{1.3}} \frac{Q}{700} \tag{1}$$

where

- f_p is the pacing frequency, in Hz;
- f_1 is the fundamental frequency, in Hz;
- Q is the static force exerted by an average person, normally taken as 76 kg = 746 N.

The associated maximum weighted acceleration is given by:

$$a_{w,\max,e,r} = 2\pi \ \mu_e \ \mu_r f_1 \sqrt{1-\xi^2} \ \frac{F_I}{M} \frac{Q}{700} W \tag{2}$$

with

- μ_e the mode shape factor at the point of excitation, normalized to the anti-node ($\mu_e \leq 1$, conservatively equal to 1);
- μ_r the mode shape factor at the point of response, normalized to the anti-node ($\mu_r \leq 1$, conservatively equal to 1);
- M the modal mass, in kg;
- ξ the modal damping ratio;
- W the appropriate code-defined weighting factor for human perception of vibrations, based on f_1 (see also Fig. 1b). When $f_1 > 16$ Hz, $W_b = f_1/16$.

Based on Eq. (2), the weighted root mean square acceleration value ($a_{w,rms}$) can be derived for vibration assessment purposes. For practical applications, $a_{w,rms}$ can be calculated based on a simplified approach (in m/s^2):

$$a_{w,rms} = 2\pi \ \mu_e \ \mu_r \ \frac{185}{M \ f_0^{0.3}} \frac{Q}{700} \frac{W}{\sqrt{2}} \tag{3}$$

The corresponding response factor R for vertical vibrations is given by:

$$R = \frac{a_{w,rms}}{0.005} \tag{4}$$

and should not exceed specific limits. For daily activities, these limits span between 1 for critical working areas (i.e., hospitals), to 2–4 for residential buildings, and up to 4 for offices and 8 workshops.

3.2 Vibration Dose Value (VDV)

Generally, when the R value based on Eq. (4) does not exceed the recommended limits, there is no need to investigate the vibration performance associated to the intermittent nature of the dynamic forces. However, the VDV assessment may be in any case particularly useful for high-frequency floors. The VDV of a walking activity of duration T_a that occurs n_a times in an exposure period is given by:

$$VDV = 0.68\, a_{w,rms} \sqrt[4]{n_a\, T_a} \tag{5}$$

where

- T_a is the duration of the activity (in seconds);
- n_a is the number of times the activity will take place in an exposure period.

The VDV result of Eq. (5) must then not exceed the limits of Table 1.

Table 1. VDV limit values.

Place	Low probability of adverse comment	Adverse comment possible	Adverse comment probable
Buildings 16 h day	0.2 to 0.4	0.4 to 0.8	0.8 to 1.6
Buildings 8 h night	0.13	0.26	0.51

Alternatively, the number of times an activity can occur in an exposure period, and correspond to a "low probability of adverse comment", can be expressed as:

$$n_a = \frac{1}{T_a}\left[\frac{VDV_{limit}}{0.68\, a_{w,rms}}\right]^4 \tag{6}$$

where

$$T_a = \frac{L_p}{v_p} \tag{7}$$

$$v_p = 1.67 f_p^2 - 4.83 f_p + 4.50 \tag{8}$$

with L_p (in m) the longest path for walks and VDV_{limit} taken from Table 1, while f_p is assumed in the range 1.5–2.5 Hz for normal walks.

4 AISC Steel Design Guide 11

4.1 Walking Excitation Criterion

The AISC document detects a simplified criterion for steel framed structural systems supporting footbridges or floors with various classes of use [15]. In particular, the method considers high-frequency floors those systems with $f_1 > 9$ Hz.

Floors are satisfactory in terms of vibration comfort if the peak acceleration a_p due to the walking excitation, as a fraction of the acceleration of gravity g, does not exceed the limits a/g given by Fig. 1a for the appropriate occupancy:

$$\frac{a_p}{g} = \frac{P_0 \exp(-0.35 f_1)}{\beta W} \quad \left(\leq \frac{a}{g}\right) \tag{9}$$

where

- P_0 is a constant force representing the excitation;
- β is the modal damping ratio;
- W is the modal weight.

For churches, the recommended values in Eq. (9) are $P_0 = 0.29$ kN and $\beta = 0.02$ (floors with few non-structural components).

4.2 Floor Stiffness

In addition to the walking excitation criterion of Sect. 4.1, the AISC guide recognizes that walking vibration can be annoying in high-frequency floors, even without resonance issues. As such, the stiffness criterion should be also used. It is required that the static deflection of the floor, calculated under a 1 kN concentrated load placed in the most unfavourable configuration, is less than 1 mm.

5 Case-Study Steel-Glass Floor

5.1 Floor Description

The examined steel-glass floor is a refurbishment for the archaeological site located in the historic San Giorgio Martire church, in San Giorgio di Nogaro (UD, Italy). The architectural and structural design of the floor took into account the layout of the existing masonry structures, as well as the general layout of the previous similar steel-glass floor that has been renovated in 2021 (Fig. 2).

More in detail, the examined floor consists of primary steel beams (S235 JR) and 3-ply laminated glass panels on top. The glass panels are composed of three 12 mm thick, extra-clear fully tempered glass layers, bonded by 1.52 mm thick PVB foils. For the steel members, box profiles with 100 × 60 (sp. 5 mm) section are mostly used, in combination with few smaller box profiles (60 × 60, sp. 5 mm).

The floor has an irregular shape (Fig. 2) and spans over a total surface of ≈28 m^2, which can be inscribed in a rectangle with dimensions of 8.1 m by 7.4 m (Fig. 3). Locally, the floor is composed of rectangular modular units that are simply supported on perimetral steel plates, anchored to masonry, that are used to regularize the background surface. Accordingly, each modular unit has a typical 1-bay bending behaviour. The maximum bending span for the steel beams is in the order of 2.2 m or 2.75 m, and they are spaced 0.64 m or 0.55 m respectively. These dimensions correspond to the size of the 3-ply glass panels, which are linearly supported along the longest edges and present a free bending span of 0.64 m or 0.55 m, depending on their location.



Fig. 2. View of the case-study indoor steel-glass floor.

Both the glass panels and steel members have been optimally designed to satisfy the Serviceability and Ultimate Limit State verifications [1, 2]. The connection of glass panels and steel profiles consists of soft rubber-like (EPDM type) layers, 3 mm in thickness, that are interposed along the linear supports and provide the structural interaction of the composite section, but at the same time are flexible restraints for glass [9, 16].

At the edges, the glass panels are also spaced by secondary soft gaskets and spacers (8 mm in thickness), which are used to prevent stress peaks, but without any structural continuity role. Such a slab configuration allows to perform – at least for preliminary considerations – a simplified analysis of a representative modular unit, rather than a vibration assessment of the whole floor.

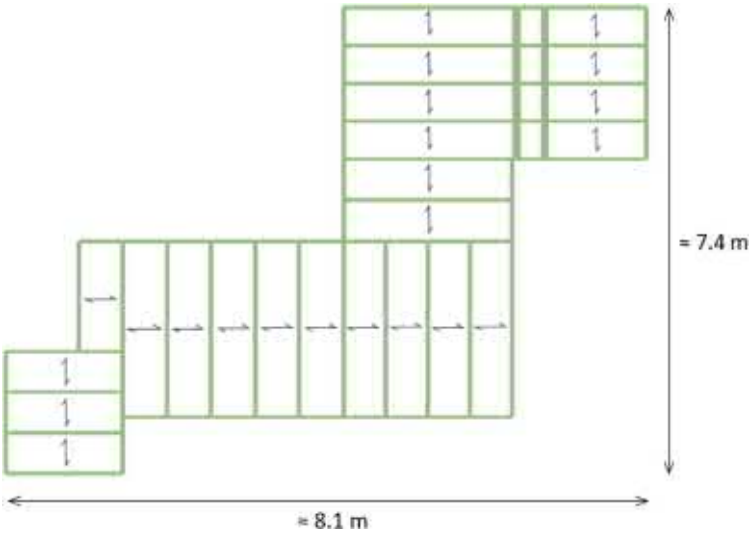
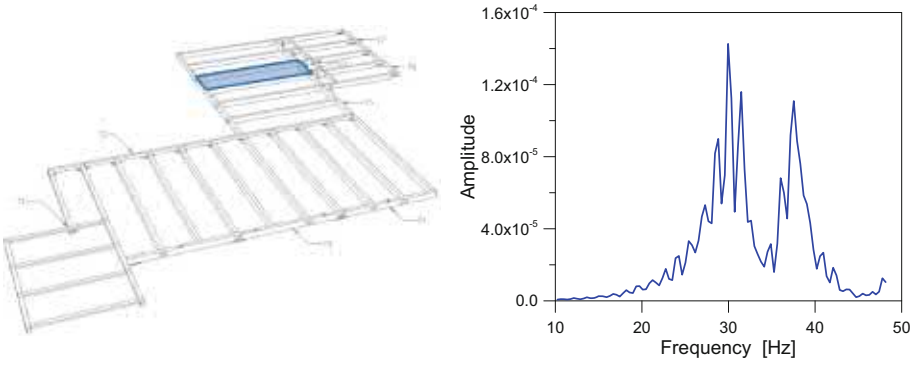


Fig. 3. Plan view of the case-study indoor steel-glass floor.

5.2 On-Site Testing and Experimental Frequency

On-site experimental investigations were carried out, in Winter 2021, to preliminary assess the fundamental vibration frequency of a typical unit, based on traditional OMA techniques [5, 6, 9]. The instrumentation was placed at the centre of the modular unit highlighted in Fig. 4a, to record the acceleration induced by a randomly walking volunteer. A three-axis MEMS accelerometer was used, and the sampling rate was set in 200 Hz. Based on OMA, the fundamental frequency was estimated in $f_{1,exp} = 30.33$ Hz (Fig. 4b), which is a confirmation of the relatively high rigidity of the examined system.



(a) (b)

Fig. 4. On-site OMA experiments: (a) setup and (b) predicted fundamental vibration frequency.

5.3 Numerical Frequency

To validate the experimental fundamental frequency, a FE model was also described in ABAQUS, to reproduce the typical geometry of the examined module (Fig. 5).

In particular, symmetry planes were taken into account to reduce the computational cost of the model, which was assembled as a full 3D system composed of solid brick elements for (i) the steel beam, (ii) the interposed soft layer and (iii) the laminated glass section. For 1/4th the module geometry, the mesh size was set in 4 mm (with additional localized partitions), which resulted in ≈212000 elements and ≈735000 DOFs.

Assuming equivalent linear elastic constitutive laws, and average material properties from literature for steel, glass, PVB and the rubber-like soft layer (Table 2 and [5, 6]), the numerical frequency of the so-called M1 model resulted in $f_{1,FE} = 30.86$ Hz, which matches well the experimental findings (Fig. 4b). It is important to note that the single steel beam has a frequency of ≈60 Hz, which is then properly reduced by the mechanical contribution of the 3-ply laminated glass panel. The cross-section details have indeed a key role.

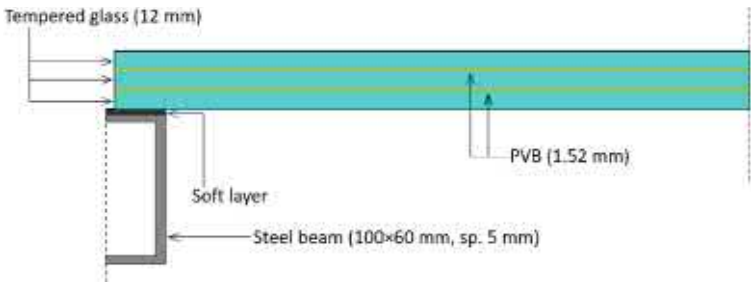


Fig. 5. Layout of the reference (M1) numerical model (ABAQUS).

Table 2. Input material properties for the modal analysis (M1 model, ABAQUS).

	Steel	Glass	PVB	EPDM
E [MPa]	210000	70000	24	10
v [−]	0.30	0.23	0.49	0.49
ρ [kg/m^3]	7850	2450	1000	900

In this regard, it is of technical interest to check the effect of the components detailing on the vibration response of the composite section, as some of the typical materials (in particular the viscoelastic PVB and the soft layer) are sensitive to external conditions, time and loading features. To this aim, the vibration frequency from additional modal analyses is reported in Table 3, where the following assumptions were made:

- M2: ideally rigid steel-glass bond, and other features like M1 (Table 2);

- M3: ideally rigid interlayer, and other features like M1;
- M4: weak interlayer, and other features like in M1.

Table 3. Vibration frequency of the examined floor, based on modal analysis (ABAQUS).

	M1	M2	M3	M4
$f_{1.FE}$ [Hz]	30.86	48.62	32.68	26.50

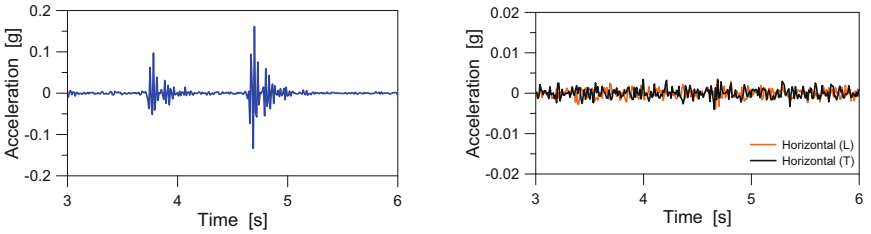
Certainly, several occupancy configurations (i.e., number of pedestrians and walking paths) should be also addressed, combining them with different seasonal scenarios. Globally, it can be in any case seen from Table 3 that the presence of a fully rigid (M3) or weak / degraded viscoelastic PVB interlayer (M4) has clear effects on $f_{1,FE}$. Similarly, the stiffness and bonding efficiency of the steel-glass connection (M1 vs. M2) has major effects. M2 and M3, in particular, represent theoretical upper scenarios only, and frequency values that the steel-glass composite section cannot achieve, due to the typical features of the materials in use. At the same time, M4 can be associated to long-term phenomena and/or unfavourable ambient conditions that typically affect the rigidity of PVB bonds. The fundamental frequency can decrease by ≈15%, with obvious effects in terms of comfort analysis and structural performance of the system.

6 Vibration Comfort Assessment

6.1 Sétra Guidelines

The vibration comfort was first verified considering the vertical acceleration peaks from the experiments. Typical acquisitions (i.e., Fig. 6) resulted in a marked sensitivity of the floor to vertical vibrations (Fig. 6a), and negligible horizontal components (Fig. 6b). This outcome is in line with the typical dynamic response of the system, with a prevailing 1-bay fundamental vibration mode.

More in detail, vertical accelerations were recorded in the order of ≈1.6 m/s^2, in the most unfavourable configurations. Based on Sétra [13], the associated comfort level is "minimum", with experimental acceleration peaks between 1.0 and 2.5 m/s^2.



(a) (b)

Fig. 6. Example (selection) of typical acceleration records based on on-site OMA experiments: (a) vertical and (b) horizontal components.

6.2 SCI Report P354

Analytical calculations were then carried out based on Eqs. 1, 2, 3 and 4. The modal mass of the floor was analytically estimated in $M = 740$ kg. The experimental rms acceleration and response factor are presented in Table 4. $a_{w,rms}$ is weighted according to Fig. 1b, where $W = 0.527$ for the examined experimental vibration frequency.

Table 4. Vibration assessment based on SCI Report P354.

Method	$a_{w,rms}$ [m/s^2]	R	R_{limit}	Comfort check satisfied
Analytical	0.2189	43.78	4	No
Experimental	0.1872	37.44		

Less than 20% scatter was found between the simplified analytical and experimental results, with the first one on the conservative side. However, Table 4 also shows that the response factors R do not satisfy SCI requirements. This means that the church floor should be classified as "unacceptable" for continuous vibrations, and the associated discomfort could be further amplified by typical human reactions on glass surfaces [10].

The effect of intermittent vibrations was hence considered, with the VDV. To this aim, the maximum dimension of the floor region was taken into account ($L_p = 3.64$ m). Considering the building type, the pacing frequency was set in $f_p = 1.5$ Hz, with, $v_p = 1.013$ m/s, $T_a = 3.598$ s, $\text{VDV}_{limit} = 1.6$ m/s$^{1.75}$, and thus:

$$n_a = \frac{1}{T_a}\left[\frac{VDV_{limit}}{0.68\ a_{w,rms}}\right]^4 = \frac{1}{3.598}\left[\frac{1.6}{0.68 \times 0.2189}\right]^4 = 3710 \qquad (10)$$

Equation (10) represents the critical number of activity occurrences that can lead to adverse comments. In practical terms, the floor can be traversed 3710 times in a 16 h day, corresponding to (on average) ≈ 3.85 times per minute.

The analysis based on Eq. (10) – combined with human reactions [10] – can be challenging, as a church can involve crowds (i.e., religious events or visitors). For the specific case-study, such a level of activity is expected to occur rarely, and therefore the floor could be considered at the borderline of a "comfortable" response.

6.3 AISC Steel Design Guide 11

The vibration comfort was finally checked based on the walking excitation criterion of Sect. 4.1, based on Fig. 1a and the experimental acceleration peaks. In this case, the floor would exceed both the limit values of "offices" and "indoor footbridges", being indeed still aligned with the requirements for "outdoor footbridges".

Considering also the floor stiffness criterion of Sect. 4.2, the deflection corresponding to a 1 kN load was indeed assessed numerically, based on a static analysis carried out in ABAQUS on the M1 model. As shown in Fig. 7, the calculated deflection was estimated in ≈2.18 mm, which doubles the limit value of 1 mm and confirms the "uncomfortable" features of the examined floor.

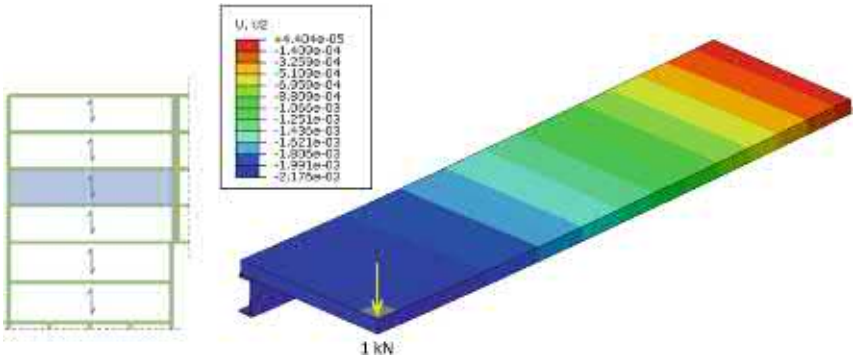


Fig. 7. Numerical analysis (ABAQUS) for the floor stiffness check (legend values in m).

6.4 Discussion

Overall, the output of vibration checks is listed in Table 5. Considering Sétra guidelines, the available acceleration peaks (based on experiments) are associated to a "minimum" comfort. This is also the case of the AISC guide, which – based on experimental accelerations – would result "comfortable" for "outdoor footbridges", but this is not the case of the examined floor. When different indicators are introduced, like the response factor R of SCI report, the performance is "uncomfortable". Similarly, the floor stiffness due to a 1 kN load, based on AISC, does not satisfy (and doubles) the 1 mm limit defection. The VDV based on SCI report is associated to a borderline "comfortable" response. Finally, considering the "perception index" proposed in [10], and calibrated for a different in-service glass walkway (15 Hz its fundamental frequency), to account for human perceptions on transparent floors, the present experimental accelerations would result in "intolerable" vibrations.

Such a result emphasizes the attention required by the vibration assessment of steel-glass floors, and the need of dedicated procedures. While the case-study system has been optimally designed for the Serviceability and Ultimate Limit States [1, 2], major concerns emerge from Table 5. Seel-glass floors have high frequency, and skip the detailed

Table 5. Summary of vibration comfort checks. C = comfortable; U = uncomfortable.

	Sétra [13]	SCI [14]		AISC [15]		Perception Index [10]
Param.	Acceleration peak	*R*	VDV	Acceleration peak	1 kN load stiffness	Acceleration peak
Comfort	C (Minimum)	U	C/U(?)	U	U	Intolerable

checks of low-frequency ones. However, their typical features can involve uncomfortable dynamic responses that should be properly verified and mitigated, and minimized in consideration of human perceptions of pedestrians on glass surfaces [10].

7 Conclusions

The design of steel-glass floors is challenging, but even more is their comfort assessment (both for design and maintenance), due to uncertainties in measurement and data interpretation, towards technical documents in use for traditional floors.

This paper proposed an analytical, experimental and numerical analysis of a case-study steel-glass floor in Italy, by taking into account consolidated approaches. The comparative analysis highlighted the need of more extended investigations for similar systems. The structure, while optimally designed, and being characterized by high frequency, resulted associated to severe indicators for human-induced vibrations. This outcome suggests that the high frequency alone does not exclude comfort mitigation strategies, and suitable indicators should be efficiently calibrated, to take into account the intrinsic features of steel-glass floors. Similarly, the sensitivity of their soft materials to operating conditions (and the effects on comfort) should be properly considered.

Acknowledgements. These research activities are financially supported by the Italian Ministry of University and Research (MUR) via the FIS2021 Starting Grant (FIS00000609), www.hopglaz.it . Seretti Srl is acknowledged for sharing the technical drawings of the floor.

References

1. Ministero delle Infrastrutture e dei Trasporti (2018) Aggiornamento delle Norme Tecniche per le Costruzioni, D 17 gennaio. Gazzetta Ufficiale della Repubblica Italiana. Suppl. Ordinario n. 8 alla n. 42, 20 febbraio 2018
2. CNR-DT 210/2013 (2013) Istruzioni per la progettazione, l'esecuzione ed il controllo di costruzioni con elementi strutturali di vetro. Consiglio Nazionale delle Ricerche, Roma, I
3. Feldmann M et al (2009) Design of Floor Structures for human induced vibrations. In: JRC scientific and technical reports. Publications Office of the European Union, Luxembourg, L
4. Bedon C (2020) Experimental investigation on vibration sensitivity of an indoor glass footbridge to walking conditions. J Build Eng 29:101195

5. Bedon C (2019) Diagnostic analysis and dynamic identification of a glass suspension footbridge via on-site vibration experiments and FE numerical modelling. Compos Struct 216:366–378
6. Bedon C, Noè S (2021) Post-breakage vibration frequency analysis of in-service pedestrian laminated glass modular units. Vibration 4:836–852
7. Xiong J, Liu Z, Duan S, Qian H (2024) A review of evaluation methods of standards for structural vibration serviceability under crowd walking. Buildings 14:675
8. Aloisio A et al (2023) Vibration issues in timber structures: a state-of-the-art review. J Build Eng 76:107098
9. Bedon C, Fasan M, Amadio C (2019) Vibration analysis and dynamic characterization of structural glass elements with different restraints based on operational modal analysis. Buildings 9:13
10. Bedon C, Fasan M (2019) Reliability of field experiments, analytical methods and Pedestrian's perception scales for the vibration serviceability assessment of an in-service glass walkway. Appl Sci 9:1936
11. Simulia (2025) ABAQUS computer software and online documentation, version. Dassault Systems, Johnston, RI, USA
12. ISO 10137 (2007) Basis for Design of Structures - serviceability of buildings and walkways against vibration. International Organization for Standardization, Geneva, CH
13. Association Francaise de Génie Civil (2006) Footbridges - assessment of vibrational behaviour of footbridges under pedestrian loading - practical guidelines. The Sétra, Paris, F
14. Smith A, Hicks S, Devine P (2009) SCI P354: Design of Floors for vibration: a new approach. Bracknell, UK, Steel Construction Institute
15. American Institute of Steel Construction (2016) Design guide 11: vibrations of steel-framed structural systems due to human activity. AISC, Chicago, IL, USA
16. Firmo F, Jordão S, Costa Neves L, Bedon C (2016) The effect of adhesive joints on the performance of hybrid steel-glass beams - an analytical and experimental study. In: Challenging glass conference proceedings 5. https://doi.org/10.7480/cgc.5.2245

Wind-Induced Fragility and Vulnerability of Industrial Steel Buildings: Preliminary Considerations

M. Eteme Minkada[1], A. Belleri[1(✉)], M. Gualdi[1], G. Della Corte[2], G. Cantisani[2], J. Žužul[3], L. Pagnini[3], and A. Ricci[4]

[1] Department of Engineering and Applied Sciences, University of Bergamo, Dalmine, Italy
andrea.belleri@unibg.it

[2] Department of Structures for Engineering and Architecture, University of Naples Federico II, Naples, Italy

[3] Department of Civil, Chemical and Environmental Engineering, University of Genova, Genoa, Italy

[4] Department of Science, Technology and Society, Istituto Universitario di Studi Superiori (IUSS), Pavia, Italy

Abstract. Non-residential single-story steel structures are widely used in industrial and commercial applications. A significant portion of the existing building stock of this type was designed according to pre-1990s wind provisions, generally based on equivalent static approaches and simplified modeling assumptions. With increasing variability and uncertainty in extreme wind events, concerns have arisen regarding the adequacy of these assumptions when assessing the current vulnerability of existing lightweight steel structures. This paper presents preliminary considerations from an ongoing study focused on the nonlinear vulnerability assessment of an existing non-residential steel building subjected to wind loading. The case study building represents an industrial structure with typical characteristics of a facility designed and constructed in the 1980s. Nonlinear dynamic analyses are performed in OpenSees using a 2D structural model, accounting for both material nonlinearity and second-order geometric effects. Wind actions are derived from validated Computational Fluid Dynamics (CFD) simulations and applied as time-dependent force histories, which are incrementally scaled to perform a wind-based incremental dynamic analysis. Structural performance is evaluated through Demand-to-Capacity (D/C) ratios, enabling the quantification of the structural demand under increasing wind intensities. The study provides an initial step toward defining wind-specific intensity measures and developing fragility curves for light-weight steel structural types, paving the way for a unified performance-based framework for multi-hazard vulnerability assessment.

Keywords: Steel structures · CFD · Wind-induced fragility · Structural vulnerability

© The Author(s), under exclusive license to Springer Nature Switzerland AG 2026
R. Zanon et al. (Eds.): CTA 2026, LNCE 942, pp. 1052–1060, 2026.
https://doi.org/10.1007/978-3-032-39505-4_91

1 Introduction

A substantial portion of non-residential single-story steel buildings was designed in accordance with pre-1990s wind provisions, typically using equivalent static approaches and simplified modeling assumptions. As a result, older steel buildings often feature partial-strength or semi-rigid connections, limited control over the hierarchy of resisting mechanisms, and structural details that may promote non-ductile local failures.

Recent studies have shown that the global response of these buildings is strongly influenced by connection behavior, the adopted structural scheme, and the interaction between the primary structure and the envelope system [1]. This sensitivity to connection behavior and system interaction is reflected in designer choices regarding pinned or semi-continuous column bases, truss-to-column connections, and bracing layouts, which can lead to markedly different structural responses, with brittle mechanisms frequently observed in the transverse direction [1–3]. Although these findings originate primarily from seismic investigations, they are directly relevant under wind loading, where lightweight industrial frames with low lateral stiffness, limited inherent damping, and slender members are susceptible to geometric nonlinearity, second-order effects, and instability-driven collapse modes [3, 4].

Wind is one of major natural hazards, often leading to multi-hazard scenarios that cause substantial damage to the built environment. Synoptic winds, such as atmospheric boundary layer (ABL) winds, and non-synoptic winds, such as thunderstorm downbursts and tornadoes, involve primary hazards like extreme winds, heavy rainfall, and lightning, and may also trigger secondary hazards such as flooding, landslides, and debris impacts, thus creating a multi-hazard scenario [5]. Reducing the magnitude of such events is beyond the capabilities of wind and civil engineering experts. However, wind and civil engineers can work to reduce the vulnerability of structures and infrastructure. Performance Based Engineering (PBE) has gained interest in recent years in structural design. Developed by the seismic engineering community, this approach can be adapted to other hazards, such as wind, leading to the development of Performance Based Wind Engineering (PBWE), which provides a robust framework with fragility curves serving as a fundamental component to quantify structural damage [6]. Such curves provide a quantitative relationship between an incident hazard intensity measure and the resulting probability of reaching or exceeding a damage state, supporting the development of loss estimation models, disaster risk assessment, and PBE. In general, low-rise structures are among the most vulnerable to wind-driven hazards [7].

These considerations highlight the need for nonlinear dynamic analyses capable of capturing stiffness degradation, connection behavior, and second-order effects, which are essential for a realistic assessment of the wind-induced vulnerability of existing lightweight steel buildings. In this context, understanding the wind-induced structural demand on older industrial buildings becomes crucial, especially given the increasing variability of extreme wind events and the limitations of past design assumptions.

The long-term goal of this research is to establish a performance-based framework in which wind-induced fragility curves are derived from nonlinear dynamic analyses informed by CFD-based pressure fields and experimental benchmark data. In stage 1, CFD simulations are performed on an industrial steel building under neutral ABL winds. WT and CFD analyses will consider variations in parameters such as terrain roughness

length, roof slope, and other relevant configurations. In stage 2, well-established and publicly available databases from WT tests conducted by other researchers on similar or identical structural archetypes are analyzed for comparison. In stage 3, results from both CFD and experimental benchmark databases are combined with nonlinear analyses, where the outcomes are interpreted in terms of Demand to Capacity ratios (D/C), allowing quantification of structural demand under increasing wind intensities and supporting the development of wind-specific fragility functions.

2 Case Study Building

The case study building is a non-residential, single-story industrial steel structure (Fig. 1) with a rectangular plan measuring 32 m × 30 m, representative of typical Italian design assumptions for industrial facilities built during the 1980s–1990s. Previous research has examined buildings with the same overall geometry and structural scheme, providing a detailed characterization of typical construction details and structural behavior [3, 4].

The structural layout consists of four portal frames equipped with reticular truss beams in the transverse direction and concentric braces in the longitudinal direction, reflecting common design practice for industrial buildings of that period.

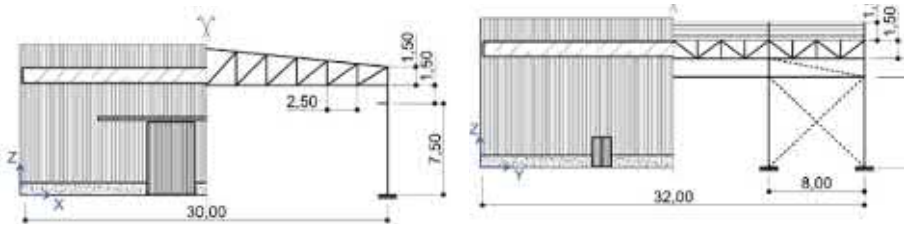


Fig. 1. Transverse (a) and longitudinal (b) views of the case study building.

The vertical load-resisting system consists of hot-rolled steel columns and roof trusses, while the lateral response is governed by the boundary conditions assigned to the columns. Specifically, the columns are pinned at the base in the transverse direction, allowing rotation and preventing significant bending moments at the foundation level. In contrast, in the longitudinal direction, lateral bracing is provided. The main columns use HE 700 M profiles, while the transverse truss consists of paired UPN sections for the chords (2 UPN 140 for the upper chord and 2 UPN 120 for the lower chord) – and double-angle sects. (2 L 60 × 60 × 8) for both the vertical and diagonal members.

3 Wind Action Modeling

3.1 Benchmark Data from Public Database

Experimental data for the benchmark industrial building were obtained from the University of Western Ontario (UWO) [8] and from the Tokyo Polytechnic University database [9]. Both databases provide publicly accessible time-series wind-load data for generic

low-rise gable-roof building models, with full coverage of pressure taps over all building surfaces tested in the wind tunnel: 665 pressure taps for the UWO model and 128 taps for the TPU model. The selected cases correspond to an isolated building with a roof pitch of 4.8°. The height-to-breadth ratio is 1:3 for the UWO model and 1:4 for the TPU model, for both open and suburban exposure conditions.

3.2 CFD Modeling

CFD simulations are carried out on the benchmark case using the large-eddy simulation (LES) approach. To avoid a computationally demanding CFD model unsuitable for developing fragility curves, two initial assumptions are made: (i) only the 0° wind direction is simulated; (ii) pressure coefficient data are extracted on the cross section (*xz* plane) and along a spanwise dimension (*y*) arbitrarily defined by the user (Fig. 2). A high-resolution computational grid is created for both benchmark cases, with a minimum grid size of 0.1 m on the building walls. The computational grid contains approximately 120 million cells. The cell aspect ratio remains below 1.1 throughout the entire domain, while the Courant number varies during the simulation, reaching a maximum of 0.30. The minimum $y+$ value is about 50 across the ground surface and below 1 on the building walls. The simulations are performed in two stages: (1) a precursor domain, including turbulence generators and roughness fetch to replicate a wind-tunnel facility at full scale, is used to properly develop the wind flow; (2) the wind flow field is mapped immediately downstream of the roughness fetch in the precursor domain and applied to the inlet of the actual domain containing the building. The synthetic turbulence inflow generator by Poletto et al. (2013) [10] is used in the precursor domain. For the sub-grid scale turbulence model, the dynamic evaluation of the Smagorinsky constant is used to model small-scale turbulence. The simulation is initialized for about 140 s (precursor and actual domain), after which 300 s (5 min) are used for statistical analysis.

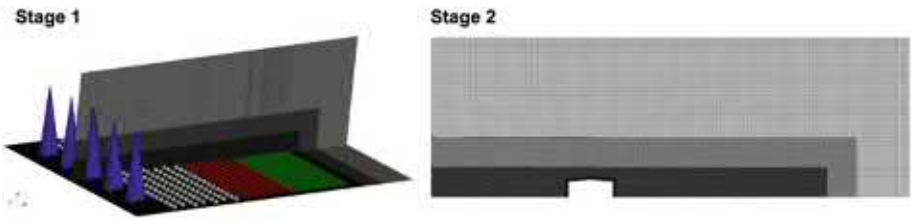


Fig. 2. Computational grid: precursor domain including turbulence generators and roughness fetch (left); actual domain including the simulated industrial building (right).

3.3 LES Results: C_p Contour and Time Histories

Figure 3 shows the contour field of the instantaneous ($t = 300$ s) C_p on the building façades. In general, these contours provide a clear overview of the flow separation and reattachment as well as the occurrence of positive (dark red) and negative (dark blue)

C_p peaks. Figure 4 shows instantaneous (red) C_p and mean (dashed-black line) $C_{p(mean)}$ time histories extracted at four locations on a vertical plane crossing the building across at $y = 0$, for a sampling time of 300 s. The $C_{p(mean)}$ between LES and TPU shows a very good agreement at the four locations (windward façade, windward roof, leeward roof, leeward façade). The instantaneous C_p time histories extracted across the building façades and roof (at $y = 0$), are then used as input on the 2D structural system then analyzed in OpenSees [11], see Sect. 4.

Analyses of $C_{p(peak)}$ values, which are critical for damage assessment and cladding evaluation, are still ongoing.

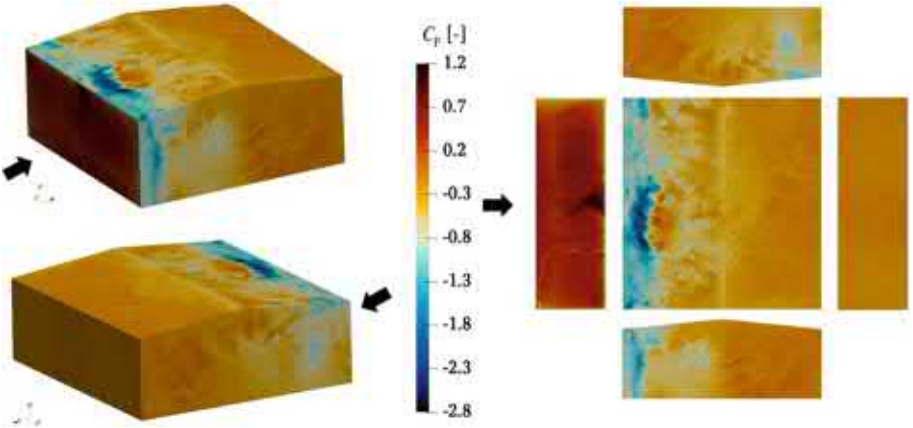


Fig. 3. Instantaneous contour field ($t = 300$ s) of the pressure coefficient (C_p) on the building façades.

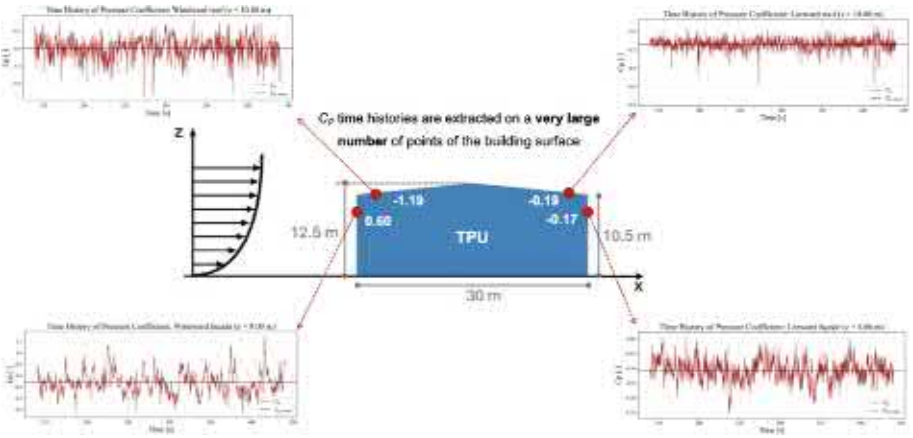


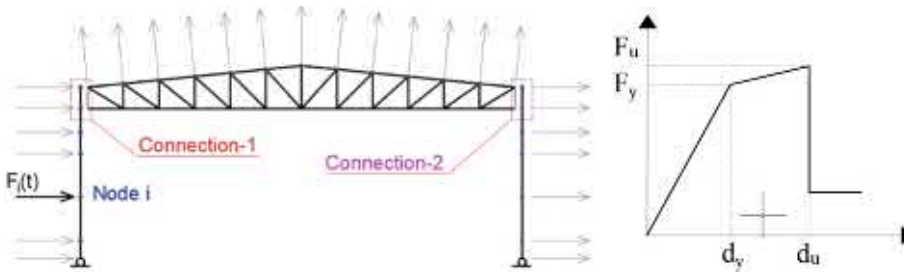
Fig. 4. An example of the instantaneous (red) C_p and mean (dashed-black line) $C_{p(mean)}$ extracted at four locations on a vertical plane crossing the building across at $y = 0$. The white numbers indicate the $C_{p(mean)}$ of the TPU benchmark database.

4 Structural Modelling and Nonlinear Analysis

4.1 Model Description

Structural analyses are performed on a representative 2D portal frame taken from the transverse structural system of the building and modeled in OpenSees [11].

The columns are modeled using "Elastic Beam Column" elements. For the truss beam, a differentiated strategy is used to reflect the structural role of each member: the internal segments of both the upper and lower chords are idealized with "Elastic Beam Column" elements, consistent with their expected elastic response, while the diagonal members are modeled as truss elements. A refined modeling approach is applied to the end regions of the upper and lower chords. These segments are represented with "Corotational Truss" elements, whose nonlinear shear response reproduces the behavior of the truss-to-column connections. Fig. 5a shows the location of the end-chord connections within the portal-frame model, while Fig. 5b depicts the hysteretic law assigned to these regions. The connection shear stiffness and resistance were evaluated according to EN 1993-1-8 [12], and the ductility of bolts in shear was assessed following Henriques et al. [13]. The constitutive parameters adopted for the upper-chord connection are a yield displacement $d_y = 0.00701$ m and yield force $F_y = 371.3$ kN, with an ultimate displacement $d_u = 0.00704$ m and ultimate force $F_u = 375.4$ kN. For the lower-chord connection, the corresponding values are $d_y = 0.00682$ m, $F_y = 374.0$ kN, $d_u = 0.00684$ m, and $F_u = 377.72$ kN.



a) b)

Fig. 5. (a) Schematic representation of the portal-frame model and (b) hysteretic law of the truss-to-column connections.

The wind-induced force histories acting on the portal frame are derived from the pressure time series obtained from the LES simulations. This required a dedicated processing step consisting of interpolating the pressure signals p(t) over the building surfaces and integrating them over the tributary width associated with each structural member, in accordance with the structural discretization used in OpenSees [11] and assuming a uniform distribution along the out-of-plane direction of the 3D LES model. The resulting

nodal forces $F_i(t)$ are computed as:

$$f_i(t) = \int_{Ai} p(t)dA \tag{1}$$

where A_i denotes the influence area associated with element i.

4.2 Nonlinear Structural Analysis Results

The nonlinear dynamic analyses are performed using wind-induced force time histories scaled to progressively increasing values of the reference base wind velocity. The global and local structural responses of the portal frame are evaluated in terms of the Demand-to-Capacity ratio (D/C), where the capacity of each component is defined as the minimum of the element capacity and its connections, thus providing an envelope of possible failure mechanisms.

The results for the truss-to-column connections, shown in Fig. 6, indicate a steady increase in D/C with wind speed. The most critical connection reaches D/C = 1 at approximately 45 m/s, marking the onset of the global collapse mechanism. This confirms that the truss-to-column connections govern the structural capacity under the wind-induced load distribution, as the lateral demand progressively concentrates at this junction. It is also worth noting that collapse initiates at the lower connection.

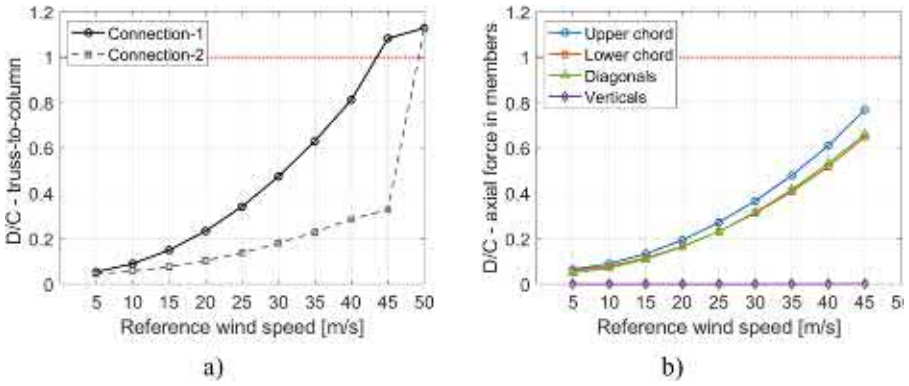


Fig. 6. Demand-to-Capacity ratios for the truss-to-column connections (a) and for the internal members of the reticular truss beam (b). The horizontal dashed line denotes the collapse threshold.

The behavior of the internal members of the reticular truss beam (Fig. 6b) follows a different trend. The upper chord, lower chord, and diagonal members show increasing D/C values with wind intensity, while the vertical members remain essentially unaffected. Throughout the pre-collapse range, all internal members maintain D/C ratios below unity, indicating that they remain within the elastic regime and do not control the failure mechanism. Their contribution remains secondary until the collapse of the truss-to-column connections.

Once the connections reach their capacity at around 45 m/s, the structural system loses its load-carrying ability. Beyond this threshold, the D/C values of the internal truss

members rise abruptly due to force redistribution; however, these post-collapse values are no longer physically meaningful. For this reason, the response beyond the collapse point has been truncated.

5 Conclusions

The study presented preliminary considerations on the wind-induced vulnerability of existing industrial steel buildings. As a case study, a structure representative of pre-1990s design assumptions was selected to reflect typical characteristics of older lightweight industrial facilities. A key contribution of the work is the integration of CFD-derived wind pressure fields with nonlinear time-history analyses, enabling the application of wind-based incremental dynamic analysis to a structural typology for which such approaches remain uncommon.

The results, expressed in terms of Demand-to-Capacity (D/C) ratios, show a progressive increase in structural demand with increasing reference wind velocity. The truss-to-column connections are identified as the most critical components. In contrast, the internal members of the reticular truss beam remain within the elastic range throughout the pre-collapse domain, confirming a clear hierarchy of resisting mechanisms. Although the collapse wind speed is relatively high, the analyses highlight that connection behavior and local detailing influence the nonlinear response and the distribution of wind-induced forces.

Overall, the study demonstrates the feasibility and potential of combining CFD-based wind loading with nonlinear dynamic analysis to investigate the vulnerability of lightweight industrial steel buildings. These preliminary findings are an initial step toward developing wind-specific fragility functions and contribute to the broader effort to establish a performance-based framework for wind assessment of existing structures. Future developments will include extending to three-dimensional models, additional wind directions, and multiple structural archetypes.

Acknowledgements. This study was developed, in part, within the framework of the ReLUIS-DPC 2024-2026 research program, funded by the Italian Presidency of the Council of Ministers - Department of Civil Protection. The opinions expressed herein are exclusively those of the authors and should not be considered as reflecting the position of the research program.

References

1. Cantisani G, Della Corte G (2020) Non-residential single-story older steel buildings: effects of design options and envelope panels on seismic fragility. In: 2020 17th World Conference on Earthquake Engineering, 17WCEE; Sendai, Japan
2. Cantisani G, Della Corte G (2021) Modelling issues and pushover response of single-story older steel buildings. ce/papers 4:1932–1941
3. Cantisani G, Della Corte G (2022) Collapse fragility curves for non-residential older single-storey steel buildings. In: Mazzolani FM, Dubina D, Stratan A (eds) Proceedings of the 10th. STESSA 2022, Lecture Notes in Civil Engineering, vol 262. Springer, Cham. https://doi.org/10.1007/978-3-031-03811-2_44

4. Cantisani G, Della Corte G (2023) Modelling and seismic response analysis of non-residential existing steel buildings in Italy. J. Earthquake Eng. 27(3):623–655. https://doi.org/10.1080/13632469.2022.2030438
5. Sköld Gustafsson V, Hjerpe M, Strandberg G (2023) Construction of a national natural hazard interaction framework: the case of Sweden. iScience 26(4):106501
6. Gavanski E, Kopp GA (2017) Fragility assessment of roof-to-wall connection failures for wood-frame houses in high winds. ASCE-ASME J. Risk Uncertainty Eng. Syst. Part A Civil Eng. 3(4):04017013
7. Spence SMJ, Arunachalam S (2022) Performance-based wind engineering: background and state of the art. Front. Built Environ. 8:830207
8. Ho TCE, Surry D, Morrish D, Kopp GA (2005) The UWO contribution to the NIST aerodynamic database for wind loads on low buildings: Part 1. Archiving format and basic aerodynamic data. J. Wind Eng. Ind. Aerodyn. 93:1–30
9. Tokyo Polytechnic University (TPU) Aerodynamic Database, 2025. https://db.wind.arch.t-kougei.ac.jp
10. Poletto R, Craft T, Revell A (2013) A new divergence free synthetic eddy method for the reproduction of inlet flow conditions for LES flow. Turbul. Combust. 91(3):519–539
11. McKenna F, Fenves GL, Scott MH (2000) Open System for Earthquake Engineering Simulation. University of California, Berkeley, Berkeley, CA, United States
12. CEN (2009) EN 1993-1-8: Eurocode 3: Design of Steel Structures - Part 1–8: Design of Joints. European Committee for Standardization, Brussels, Belgium
13. Henriques J, Jaspart JP, Da Silva LS (2014) Ductility requirements for the design of bolted lap shear connections in bearing. Adv. Steel Constr. 10(1):33–52

Emerging Technologies for Steel Structures

Integrated Approach to the Structural Assessment of the Rai Tower of Caltanissetta

Giuseppe Mugnos(✉)

Dismat s.r.l., Canicattì AG, Italy
ing.giuseppemugnos@gmail.com

Abstract. The structural assessment of unconventional existing structures is often constrained by the limited availability of reliable design documentation, the difficulty of conducting extensive destructive testing, and the absence of specific standardized procedures. Under these conditions, defining an investigation protocol cannot rely on the simple application of standard schemes; instead, it requires an integrated approach combining local observations, global measurements, monitoring, and numerical modeling. This paper describes the methodological framework adopted for the RAI tower in Caltanissetta—a tall, guyed steel structure characterized by high slenderness, a spherical base hinge, and a significant dependence on the tension state of the guy cables. Key experimental activities are outlined, focusing on indirect mechanical characterization, the hole-drilling technique, guy cable tension verification, operational dynamic identification, and the monitoring of tension and environmental conditions. The study highlights the role of cross-validating data in reducing epistemic uncertainties and proposes an operational workflow applicable to other unconventional, data-scarce steel structures.

Keywords: Guyed towers · metal structures · unconventional structures · investigation protocol · Hole Drilling · Operational Modal Analysis · structural monitoring

1 Introduction

The assessment of existing structures is typically based on a progressive investigative process, in which surveying, material testing, analysis of construction details, and numerical modeling combine to define the knowledge level and confidence factors. For standard buildings and many common infrastructure types, designers have access to regulatory standards and technical documents outlining the criteria, minimum objectives, and operational procedures for establishing an investigation plan.

The situation changes significantly when the subject of the assessment is an unconventional metal structure—characterized by large-scale geometry, a unique structural scheme, strong interaction with environmental loads, and design documentation that cannot be fully verified. In such cases, the very concept of "knowledge level" requires reinterpretation: simply increasing the number of tests is insufficient; instead, a coherent information system must be constructed—one capable of linking local measurements, global response, and structural model parameters.

© The Author(s), under exclusive license to Springer Nature Switzerland AG 2026
R. Zanon et al. (Eds.): CTA 2026, LNCE 942, pp. 1063–1074, 2026.
https://doi.org/10.1007/978-3-032-39505-4_92

International literature on guyed towers highlights, in particular, the complex dynamic behavior of these structures and the high sensitivity of their response to guy pretension, boundary conditions, non-linear cable modeling, and wind loads [6–10]. In this context, experimental measurements play a crucial role not only in describing the structure's condition but also in calibrating and validating the numerical model used for subsequent assessments.

The RAI tower in Caltanissetta serves as a prime example of these challenges. It is a very tall steel lattice tower, stabilized by a system of guy wires and anchored at the base via a spherical hinge. This configuration makes the structure's behavior highly dependent on the tension state of the guy wires, boundary conditions, and environmental loads—particularly wind. This paper does not aim to present a final safety assessment of the structure—conducted by other parties based on available data—but rather to illustrate the rationale behind the design and implementation of an integrated investigation protocol.

2 Introduction

2.1 General Description of the Work

The RAI transmitting station at Caltanissetta-Sant'Anna, built between 1949 and 1951, served for decades as one of the region's key radio broadcasting infrastructures. Standing approximately 286 m tall, the tower consisted of a metal lattice mast—comprising primarily angle-section members—stabilized by multiple tiers of radially arranged guy wires and connected to the foundation via a base assembly functioning much like a spherical hinge.

Given its height, the structure was a landmark feature of the Italian landscape; in terms of scale and visual impact, it rivaled some of the world's most famous vertical structures, even though it belonged to a different construction category than skyscrapers or freestanding towers (Figs. 1, 2, and 3).

The presence of the base hinge and the stay cables gives the structure a behavior fundamentally different from that of a freestanding tower. The metal mast cannot be analyzed in isolation: overall equilibrium depends on the distribution of tensile forces in the stays, their geometry, the stiffness of the anchorages, and the dynamic response of the entire system. An uncontrolled change in the tension of one or more stays can alter the equilibrium configuration and, under adverse conditions, compromise the tower's overall stability.

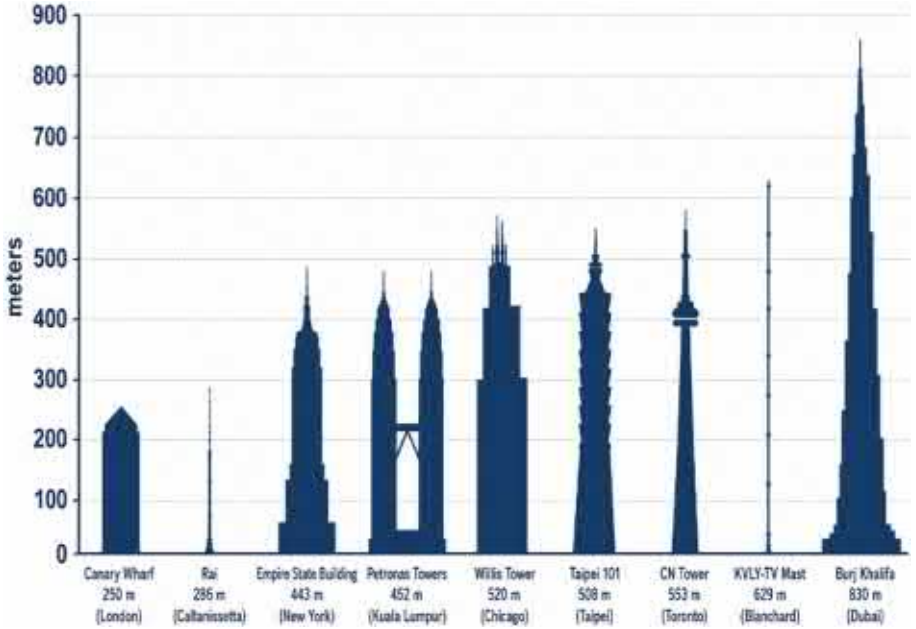


Fig. 1. Size comparison between the RAI tower in Caltanissetta and some major international vertical structures.



Fig. 2. General view of the RAI tower in Caltanissetta, a guyed metal structure.



Fig. 3. Characteristic features of the tower: lattice shaft made of angle sections, spherical base hinge, and stay anchorages.

2.2 Operational and Knowledge-Related Challenges

The design of the investigation protocol was shaped by two main challenges. The first concerns the lack of specific procedural standards for structures of this type. While regulatory guidelines or supporting documents exist for existing buildings and infrastructure such as bridges and tunnels, a tall, guyed metal tower requires specific choices tailored to the structural function of individual components and the risks associated with testing operations.

The second challenge involves the impossibility of adopting an investigation plan based on extensive metal sampling. Removing significant portions of the elements could have compromised local load-bearing capacity or introduced further uncertainties. Furthermore, the absence of laboratory samples made it impossible to calibrate non-destructive tests in the standard manner. The assessment strategy therefore had to rely on indirect or semi-invasive techniques, targeted repetition of measurements, and cross-validation of independent results.

3 Definition of the Integrated Protocol

The general logic of the protocol was to replace the traditional sampling–laboratory testing–result extrapolation scheme with an integrated, redundant process. Each investigation technique was selected not only for the specific data it provided but also for its contribution to verifying the consistency of the overall picture.

Local data provided information on the actual condition of the elements; global data allowed for the interpretation of the structure's response as a whole; and the numerical model served as a synthesis tool to verify the compatibility between hypotheses, measurements, and observed behavior (Table 1).

Table 1. Summary of the integrated investigation protocol.

Scope of the investigation	Learning objective	Main output
Microhardness and local inspections	Indirect estimation of mechanical properties	Classification and comparison of homogeneous elements
Hole Drilling	Assessment of the local in-situ stress state	Principal stresses and orientation
Stay cables and anchorages	Determination of effective pull and monitoring of the unloading procedure	Stay loads and released deformations
OMA dynamic identification	Overall assessment of dynamic behavior	Natural frequencies and principal mode shapes
Tension and wind monitoring	Correlation between environmental actions and variations in stress	Time series of deformation, strain, and wind
FEM modeling	Interpretative synthesis of experimental data	Model calibrable against independent observables

4 Local Investigations: Materials and Stress State

4.1 Mechanical Characterization via Indirect Tests

The mechanical characterization of the metal elements was carried out using microhardness testing—a non-destructive method chosen to assess the variability of the material's properties. As samples could not be extracted for direct mechanical testing, these measurements provided localized, comparable data across different elements, aiding in the definition of homogeneous groups and the selection of parameters for the analytical model.

The value of this test lies not merely in estimating a mechanical property, but in the ability to extend the assessment to multiple points on the structure without causing significant damage. For tall, existing metal structures, this approach increases the density of data gathered during the survey without compromising the local structural integrity of the elements being examined.

4.2 Principles of the Hole-Drilling Technique

The assessment of the in-situ stress state was conducted using the hole-drilling technique. The test principle relies on local stress relief: the controlled removal of a small volume of material via micro-milling causes a redistribution of pre-existing stresses, generating elastic strains that can be measured on the surface using a strain gauge rosette applied around the drilling point.

Assuming a plane stress state and linearly elastic material behavior, the released strains measured along the rosette axes can be related to the principal stress components

using calibration coefficients that account for the hole geometry, drilling depth, and the material's elastic properties. In summary, by using the released strains εa, εb, and εc and the calibration coefficients A and B, the procedure allows for the determination of the principal stresses σ1 and σ2 and the angle θ of the principal directions.

$$p = \frac{\varepsilon_a + \varepsilon_c}{4A} \tag{1}$$

$$q = \frac{\varepsilon_c - \varepsilon_a}{4B} \tag{2}$$

$$t = \frac{\varepsilon_a + \varepsilon_c - 2\varepsilon_b}{4B} \tag{3}$$

$$\sigma_{1,2} = p \pm sqrt(q2 + t2) \tag{4}$$

$$\tan 2\theta = \frac{t}{q} \tag{5}$$

Principal stresses and principal stress directions are particularly useful in lattice structures, where the direction of actual stress can be influenced by eccentricities, connections, local constraints, and redistributions that are not immediately deducible from geometry alone. Compared to more invasive stress-relief methods, this technique allows for a local measurement of the stress state while limiting material removal to a very small volume (Fig. 4).

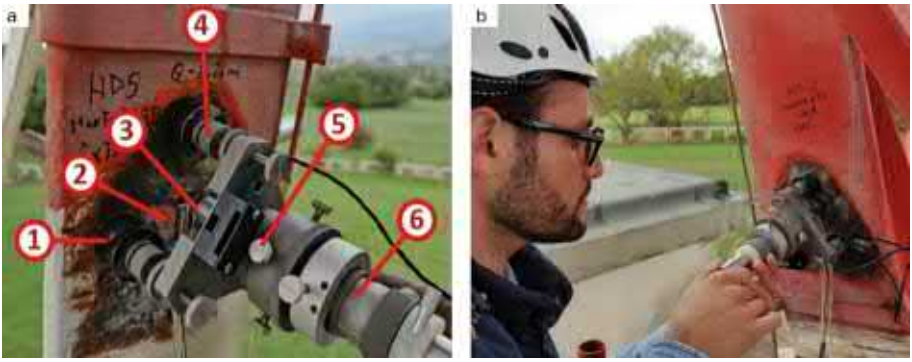


Fig. 4. Execution of the hole-drilling test and details of the measuring device: (1) magnetic bases for attachment to the metal structure; (2) strain gauge rosette; (3) micro-milling cutter; (4) adjustable feet for aligning the device with the measurement surface; (5) device for micrometric adjustment of the drilling point; (6) slider for micrometric adjustment of the milling cutter's removal depth.

A summary of representative results obtained using the hole-drilling method is presented in Table 2. The values confirm the utility of the test in determining not only the magnitude of the local stress state but also the variability across different elements and elevations of the structure.

Table 2. Representative results of Hole Drilling tests.

Trial	Elevation	θ [°]	σ1 [MPa]	σ2 [MPa]	Summary reading
HD1	Elevation 0,00 m	43,94	1,73	−2,60	Limited local stress state
HD2	Elevation 0,00 m	10,63	−4,11	−10,30	Predominant local compression
HD3	Elevation 0,00 m	−38,11	−23,71	−32,46	More pronounced compression
HD4	Elevation 12,10 m	−21,44	−3,93	−2,20	Limited stress state
HD5	Elevation 8,26 m	20,38	38,93	32,79	Higher local dose

5 Verification of Stay Tensile Load

Determining the tensile load in the stay cables was one of the most critical tasks in the protocol. In a stayed tower, cable tension is not a secondary detail but a parameter directly linked to lateral stiffness, natural frequencies, stress distribution, and the structure's overall equilibrium. Experimental determination was therefore essential both for understanding structural behavior and for setting up the numerical model.

The procedure involved instrumenting the anchorage forks with electrical strain gauges. Subsequently, the load was progressively transferred from the fork to a parallel system consisting of hydraulic jacks arranged symmetrically around the stay cable. During this transfer, the strain release in the fork was continuously monitored; once the released strain began to stabilize, the fork was considered fully unloaded, and the load reading from the parallel system was taken as an independent measure of the pre-existing tension.

This approach served a dual purpose: on one hand, it allowed for the estimation of the load originally borne by the fork by comparing the released strain with the load recorded by the jacks; on the other, it acted as an operational safety indicator. The test was designed not to increase the tension in the stay cable, but merely to take over the existing load. An excessive increase in load could have altered the tower's equilibrium state—a particularly sensitive factor given the presence of the spherical hinge at the base (Figs. 5 and 6).

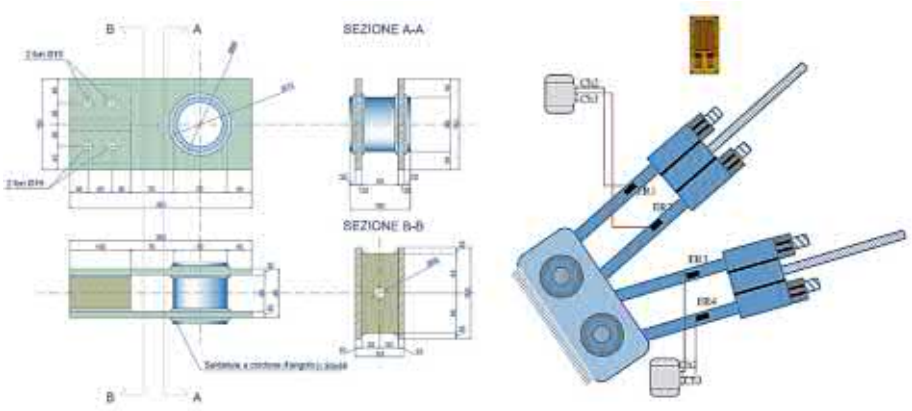


Fig. 5. Verification of stay tension: load transfer scheme to a parallel system.



Fig. 6. Verification of stay tension: anchoring system and instrumentation.

In summary, the operational sequence involved: installation and verification of strain gauges on the forks; gradual activation of the parallel jacks; monitoring of strain release; halting the procedure upon signal stabilization; and a final comparison between the released strains and the load recorded by the jacks. Selected representative values derived from the test records are summarized in Table 3.

Table 3.

Stay group	Stay	Indicative load	Pressure [bar]	Stopping criterion
Upper	1–4	150,0–159,0	437,5–465,0	Stabilization of deformation release
Lower	1–4	168,0–171,0	490,0–500,0	Stabilization of deformation release

6 Dynamic Identification and Monitoring

6.1 Operational Modal Analysis

Local inspections and stay-cable tension checks provide essential information on individual components but are insufficient on their own to describe the tower's global behavior. Consequently, the protocol included an in-service dynamic identification campaign using Operational Modal Analysis, aimed at estimating the structure's natural frequencies and primary mode shapes.

The tower's considerable height and access difficulties necessitated a streamlined experimental setup. Three triaxial accelerometers were installed at different elevations along the shaft to sample the structure's dynamic response across its height. Spectral analysis was performed on both the overall three-dimensional system and the subsystems associated with the principal directions, utilizing singular values of the spectral density to identify dominant modes. From a methodological standpoint, the most significant result is that a limited number of sensors can yield useful dynamic data when their placement is designed based on expected mode shapes and actual operational constraints. For slender, very tall structures, this approach allows for the acquisition of global information without requiring extensive measurement campaigns, which are often unfeasible due to safety concerns or prohibitive costs (Fig. 7).

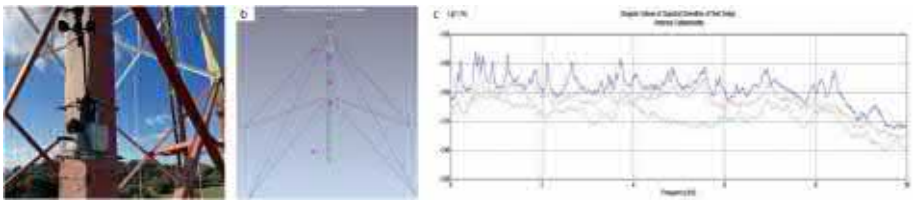


Fig. 7. Dynamic identification phases: accelerometer installation, setup representation, and spectral analysis using singular values of the spectral density.

6.2 Tension and Wind Monitoring

Alongside dynamic measurements, the protocol included continuous monitoring of the strain state of the stay-cable anchorages and wind conditions. The objective was to correlate stress variations observed in the anchorage elements with environmental loads, distinguishing between the system's routine oscillations and variations associated with gusts or specific wind conditions.

This integration is significant for stayed towers, where structural behavior cannot be decoupled from environmental conditions. Simultaneous measurement of strain and wind allows stress peaks to be interpreted not as isolated values, but as the system's response to a specific external load. The monitoring data thus become valuable both for assessing in-service behavior and for calibrating the assumptions made in the numerical model.

7 Role of Experimental Data in FEM Modeling

The numerical modeling of a cable-stayed tower with limited available data is characterized by a large number of uncertain parameters. Key among these are material mechanical properties, the stiffness of truss elements, base boundary conditions, actual geometry, cable tension, and the representation of anchorages. In the absence of comprehensive documentation, these parameters cannot simply be adopted from design drawings; instead, they must be verified and updated based on experimental evidence.

Microhardness tests contribute to defining mechanical parameters; the hole-drilling method provides insights into the local stress state; cable inspection allows for the input of tension values consistent with actual conditions; and dynamic identification offers global observables—such as frequencies and mode shapes—against which the model's consistency can be evaluated. The comparison between measurements and the model can thus be viewed as an iterative process in which a preliminary model is progressively updated by incorporating available experimental data.

In this context, the modeling objective is not to produce a representation that is formally detailed yet unvalidated, but rather to construct an analytical model consistent with the available observables. This approach helps reduce the epistemic uncertainty associated with an unconventional structure by making explicit which experimental data support the adopted assumptions and which require further investigation.

8 Discussion

The case of the RAI tower in Caltanissetta highlights how, for unconventional metal structures, defining the investigation protocol cannot be viewed merely as a preliminary step to the subsequent structural assessment; rather, it must be treated as a genuine design activity. Unlike standard buildings or common infrastructure, the investigative approach must be tailored to the specific characteristics of the load-bearing system, accessibility conditions, and the risks associated with individual testing operations.

The choice of investigation techniques was driven by the need to gather meaningful data without disrupting the structure's equilibrium or resorting to extensive destructive sampling of key elements. The protocol's value lies in the ability to compare diverse types of data: indirect mechanical properties, local stress states, guy-wire tension, global dynamic response, and wind-induced variations. Consistency among these parameters is more significant than the sheer volume of tests, particularly when the structure does not allow for a standard investigation plan.

A particularly significant aspect concerns the procedure adopted to verify the guy-wire tension. In this instance, the measurement system served not only a diagnostic purpose but also an operational control function during the test itself. Monitoring the deformation release at the clevis allowed for the detection of the progressive load transfer to the parallel counter-system, preventing the operation from causing an unintended increase in guy-wire tension. In this sense, the diagnostic process also served as a tool for managing the safety of the test.

Dynamic identification and continuous monitoring completed the assessment process by providing a comprehensive overview of the tower's behavior. Natural frequencies,

primary mode shapes, and variations in stay-cable tension—driven by environmental loads—constitute essential data for constructing and calibrating a numerical model that accurately reflects the structure's actual behavior.

The scope of this paper is limited to defining the investigation protocol, conducting the tests, and generating the experimental data required for modeling and subsequent structural assessment. Management decisions, final safety verifications, and the reasons behind the structure's demolition fall outside the study's objectives. However, the fact that the tower no longer exists—having been brought down via controlled collapse in July 2025—gives this study documentary value as well. The investigations conducted serve as a technical record of one of the most significant cable-stayed steel structures built in Italy; while no longer directly observable, it remains a valuable case study for the assessment of unconventional structures (Fig. 8).



Fig. 8. Images of the demolition phases of the RAI tower in Caltanissetta, carried out in July 2025 via controlled collapse.

9 Conclusions

This study outlines an integrated investigation protocol applied to the RAI tower in Caltanissetta, selected as a case study of a tall, guyed steel structure characterized by significant knowledge uncertainty. The lack of specific procedural guidelines and the impossibility of conducting extensive destructive testing necessitated an approach combining local measurements, global checks, monitoring, and numerical modeling.

The findings demonstrate that, for data-scarce structures, the reliability of the assessment process depends more on the consistency between independent observables than on the sheer volume of tests performed. Local measurements provide data on materials and stress states; checks on the guy cables allow for the determination of parameters essential to global equilibrium; and dynamic identification and monitoring enable the assessment of the structure's overall behavior under actual operating conditions.

The proposed protocol thus serves as an operational framework applicable to other guyed towers and, more broadly, to unconventional steel structures for which no directly applicable standardized procedures exist. Furthermore, the case study underscores the documentary value of experimental investigations when applied to structures of significant technical and historical importance—particularly those that may not be accessible for future direct inspections.

Acknowledgment. The author thanks the technicians and personnel involved in high-altitude operations, measurement campaigns, and instrumentation procedures, whose operational contribution was essential for carrying out the investigations under complex conditions.

References

1. Ministry of Infrastructure and Transport (2018) Ministerial Decree of 17 January 2018, Update to the Technical Standards for Construction. Ministry of Infrastructure and Transport
2. Superior Council of Public Works (2019) Circular No. 7 of 21 January 2019, Instructions for the application of the Update to the Technical Standards for Construction. Superior Council of Public Works
3. Superior Council of Public Works (2020) Guidelines for risk classification and management, safety assessment, and monitoring of existing bridges. Superior Council of Public Works
4. ASTM International (2025) ASTM E837, Standard Test Method for Determining Residual Stresses by the Hole-Drilling Strain-Gage Method. ASTM International
5. ASTM International (2025) ASTM E384, Standard Test Method for Microindentation Hardness of Materials. ASTM International
6. Madugula MKS, Wahba YMF, Monforton GR (1998) Dynamic response of guyed masts. Eng. Struct. 20(12):1097–1101
7. Saudi G (2014) Structural assessment of a guyed mast through measurement of natural frequencies. Eng. Struct. 59:104–112
8. Shi H, Salim H (2015) Geometric nonlinear static and dynamic analysis of guyed towers using fully nonlinear element formulations. Eng. Struct. 99:492–501
9. Pezo ML, Bakić V, Marković Z (2016) Structural analysis of guyed mast exposed to wind action. Therm. Sci. 20(Suppl. 5):S1473–S1485
10. Brincker R, Ventura C (2015) Introduction to Operational Modal Analysis. Wiley, Chichester
11. Ewins DJ (2000) Modal Testing: Theory, Practice and Application. Research Studies Press, Baldock
12. Brownjohn JMW (2007) Structural health monitoring of civil infrastructure. Philos. Trans. R. Soc. A 365:589–622

Steel and BIM for Digital Twins. Information Modelling of the Buildings in the Hall B of LNGS

Matteo Abita[1(✉)], Renato Morganti[1], Alessandra Tosone[1], Daniele Castri[2], Umberto Di Sabatino[2], and Danilo Di Donato[1]

[1] DICEAA Department, University of L'Aquila, L'Aquila, Italy
matteo.abita@univaq.it
[2] Gran Sasso National Laboratory, Assergi (AQ), L'Aquila, Italy

Abstract. Building information models conceived as the foundation of digital twins have become central to the governance of the built environment, and this was among the strategies pursued by the Tecnodigit research project, which sought to embed sensor data within BIM environments so as to raise the safety and sustainability of the assets involved. Among its case studies, the experimental halls of the National Gran Sasso Laboratories stand out for both their subterranean setting and their hybrid typology, in which architectural objects coexist with infrastructural ones. Because the apparatus employed for particle-physics experiments is predominantly of steel, the modelling effort was directed at reproducing the as-built reliability and definition of the structural members, whilst aligning the information structure with the ISO/IEC 81346 classification and its hierarchy. The contribution reports on the information modelling of the constructions housed in the central tunnel of the LNGS and on the procedure devised to assemble a federated model suited to digital-twin applications.

Keywords: BIM · Digital Twin · Deep Underground Laboratories · Steel structure · LOIN · Federated models

1 Technological Development of Digital Twins and the Research Framework

1.1 Policy Drivers and Expanding Role of DT Applications

In many engineering fields the digital replication of physical assets through digital twins (DT) is delivering measurable gains in accuracy, operational oversight, and predictive capacity [1]. Public policy has hastened their adoption: since 2019 the European Commission has counted DTs among the instruments of its "Digital Age" agenda, and the Union's data strategy ties the digital transformation of the built environment to the broader objective of climate neutrality by 2050.

© The Author(s), under exclusive license to Springer Nature Switzerland AG 2026
R. Zanon et al. (Eds.): CTA 2026, LNCE 942, pp. 1075–1086, 2026.
https://doi.org/10.1007/978-3-032-39505-4_93

Across the built-environment disciplines of architecture, engineering and construction (AEC), the virtual reproduction of products, processes, and systems is encouraged on both economic and performance grounds, from energy efficiency to structural safety. Well-planned maintenance and asset management preserve structural integrity and enable timely intervention, curbing deterioration before it becomes a hazard.

The enabling technology here is Building Information Modelling (BIM), which governs the exchange and stewardship of construction data across the asset life cycle and reinforces quality control and the interoperability of the parties engaged in design and upkeep [2]; since 2023 such workflows have been framed internationally by ISO 19650. Contemporary digitalisation increasingly couples BIM with real-time streams from Internet-of-Things devices, so that sensors embedded in the model set up a live correspondence between the physical asset and its virtual counterpart [3].

1.2 Objectives and Case Studies of the Tecnodigit Research Project

Funded by the National Recovery and Resilience Plan (PNRR) and pursued between June 2024 and December 2025 within the Rome Technopole Innovation System, the "Tecnodigit – Technologies for the Creation of Digital Twins" project gathered five partners from industry and academia under the coordination of Best Design Srl [4]. It sought to endow DTs with a monitoring system spanning structural and energy performance, coupling installed and purpose-built smart sensors with advanced data processing and automation to uphold safety and interoperability. Its principal outputs were the digitalisation of selected assets, the infrastructure needed to collect data and route it to a central database, and the planning of management activities, all consolidated in a single visual interface within a smart-city perspective [5]. A central ambition was a DT methodology transferable across building types; among the three case studies, the National Gran Sasso Laboratories (LNGS) offered a notable instance of architecture built expressly for scientific research, whose earlier information-modelling phases the authors have documented [6] (Fig. 1).

1.3 The LNGS Case Study

Buildings dedicated to scientific research form a category shaped by specialised teams pursuing agendas set at national and international level. They are inherently technology-dependent, a trait heightened in underground laboratories, which exploit their subterranean setting for experimental advantage and occupy the threshold between structure and infrastructure [7].



Fig. 1. The arrangement of the underground halls of the Gran Sasso National Laboratory and their connection to the motorway tunnel system. © 2025 LNGS.

The LNGS, the largest underground laboratory engaged in astroparticle physics and rare-event research, is a foremost facility of INFN, the National Institute of Nuclear Physics. Its underground complex comprises three experimental halls — A, B, and C — reached by two tunnels off the L'Aquila–Teramo motorway and joined by minor passages, perpendicular to the motorway axis beneath roughly 1,400 m of rock in the Gran Sasso massif. Over three decades they have hosted experiments across diverse physical phenomena. Structural monitoring is here indispensable, since the main experiments occupy steel structures — framed systems and tanks alike — requiring careful surveillance and management.

Despite the promise Tecnodigit held for safety and monitoring at the LNGS, developing DTs in this context proved demanding: the singular siting and typology of the structures preclude any direct transfer of conventional methods [6].

Validation was to begin with Hall B, a gallery roughly 125 × 14 m in plan and about 15 m high, its rock walls lined with an insulating layer and detached finishing panels and its floor a reinforced-concrete slab cast over the rock and finished in polyurethane resin. At present it accommodates experimental apparatus of large and medium scale — among them IBF, COSINUS, XENON, CRYO-PLATFORM and STELLA — and is served by overhead cranes. The information modelling of these facilities is the subject of the sections that follow.

2 Methodology for the Development of the Federated Model

The University of L'Aquila research unit was charged with conceiving BIM models that would act as vessels for the data streamed from the sensor network.



Fig. 2. The five procedural steps of the methodology for the development of the federated BIM model. © 2025, developed by the authors.

The distinctive character of the objects to be represented called for a purpose-made methodology. Because its scale and spatial features liken Hall B to an infrastructure whilst the items it shelters behave as buildings, this layered configuration was rendered as a federation of models built up through the procedural sequence set out below (Fig. 2). Selecting the exchange format came first: the Industry Foundation Classes (IFC) were adopted, the current phase relying on IFC 2x3 to meet requirements expressed by other research units, whereas the more supple IFC 4x3 is reserved for later investigation. A second stage fixed a georeferencing origin for the gallery and its contents so that their reciprocal placement would be correct. A third defined, for each experiment, the external area recorded in the IFC as a site-level parameter; when several buildings belong to one experiment — as with IBF — that area is attributed to the principal building alone. A fourth addressed the drafting of models able to satisfy the Level of Information Need (LOIN) prescribed by ISO 19650, consistent with the project's evolving demands [8]. The closing stages exported every model to IFC and then federated them. Once assembled, the federated model serves as a valuable means of sharing knowledge, coordinating disciplines, managing interferences, and checking the design.

2.1 From LOD to LOIN: Modelling Requirements and Level of Information

Opting for a federated approach follows inevitably from a considered judgement about the uniform degree of definition to be conferred on every element that populates each model. The strategy was accordingly framed not around reaching a fixed Level of Detail (LOD) but around endowing each model with a fitting Level of Information Need (LOIN), so that the resulting federation would answer four requirements: responsiveness, flexibility, adaptability, and interoperability [9].

Responsiveness was sought not only to ease the navigation and inspection of each model but also to permit live handling of the whole data stream issuing from the sensor network. The geometric resolution given to structural connections was, moreover, calibrated so that model granularity would serve the maintenance, monitoring, and inspection routines foreseen rather than becoming an end in itself. Flexibility arose from the LNGS's wish for a model usable beyond the Tecnodigit project — for asset management and for scheduling the laboratory's maintenance. That aim in turn made adaptability necessary,

obliging the models to carry a level of detail generous enough to absorb later spatial reconfigurations and any further data flows [10].

2.2 From Authoring to Federation: Software Strategy and IFC Implementation

Choosing IFC as the interoperability format through which every tier of information from the sensor network would be integrated was, from the very start, all but unavoidable if the LNGS were to be furnished with a BIM resource reusable for future purposes.

A number of alternatives were weighed beforehand, from proprietary BIM authoring packages to open-source tools able to create and edit IFC files natively [11]. Proprietary environments commend themselves chiefly through smoother workflow management and, on occasion, a readiness to ingest sensor data; yet they labour under two notable constraints — a tight reliance on one software ecosystem, which curtails the reach of the models produced, and a likely rigidity where sensor data formats are unsupported or, as at the LNGS, heterogeneous in origin. Software that edits IFC natively, by contrast, sidesteps the pitfalls of format conversion, though its comparatively recent arrival means it has still to be thoroughly proven in production settings against the longer-established maturity of commercial products.

The course finally taken strikes a balance between these two poles. The project's brief timescale and the obligation to deliver on set objectives argued for a dependable and widely used proprietary authoring tool, whereas the task of integrating data from installed and planned sensor networks was entrusted to bespoke solutions produced by the research units concerned. When each model was exported to IFC from the authoring environment, care was taken to secure the correct identification of every element and the faithful transfer of the data needed for federation: PSETs attached to individual elements were rendered in tabular form, whilst those at project, site, and building level were conveyed through a dedicated text file.

3 Development of BIM Models

The BIM modelling activities encompassed four buildings situated within Hall B of the LNGS together with a federated model integrating all completed structures. Each facility presented distinct typological, geometric, and informational challenges, requiring the adaptation of a shared methodological framework.

3.1 The Pilot Case of IBF Bellotti

The IBF Bellotti was the earliest building to be modelled: sited in the northern part of Hall B, it was realised by the LUNA (Laboratory for Underground Nuclear Astrophysics) collaboration to accommodate a 3.5 MV particle accelerator [12] and is made up of two separate volumes: the Accelerator Room and the Control Room.

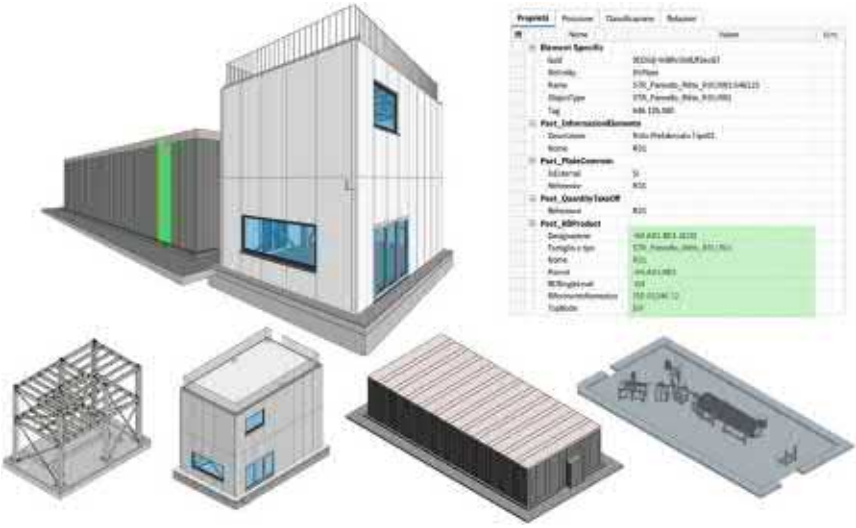


Fig. 3. The federated model of the Ion Beam Facility comprising the architectural, structural, and MEP disciplines. © 2025, developed by the authors.

The former is a heavily shielded box of 26.9 × 12.4 × 5.7 m whose walls and roof are formed of massive T-shaped reinforced-concrete columns and beams, joined by structural adhesive together with exposed bolted steel plates. The latter follows a more ordinary constructional pattern, its skeletal steel frame using HEB 300 columns with IPE 300 and IPE 240 beams as primary and secondary members, all linked through bolted plates and flanges. Its floor build-up couples electro-forged steel grating with a steel sheet and a rubber wearing surface, whilst the enclosure is made of 50 mm sandwich panels faced in galvanised steel and filled with rock wool.

Particular attention was devoted to the modelling of steel connections and joints, reproduced with a high degree of geometric and constructive accuracy to reflect the as-built assembly logic. Prior to the Revit modelling phase, a preliminary structural model was developed in Tekla Structures; this was subsequently retained for comparative purposes only, as the Tekla Structural Designer Integrator did not permit the complete importation of building elements, preventing a full interoperability pipeline between the two platforms. The parametric definition of each connection relied on the Revit structural connection type properties, into which dimensional and material values from both the executive project and as-built survey data were entered, enabling exact geometry reproduction and component reuse across the model. For all bolted joints, a uniform class 8.8 specification and a nominal diameter of 20 mm were adopted throughout; bolt class, plate thickness, stiffener configuration, and weld data were embedded in each parametric assembly. Additional parameters were incorporated into connection assemblies and structural profiles to accommodate future maintenance data integration. Bolted end-plate joints, flange connections, and secondary fixing components were modelled as nested parametric assemblies linked to executive drawings and photographic documentation (Fig. 3).

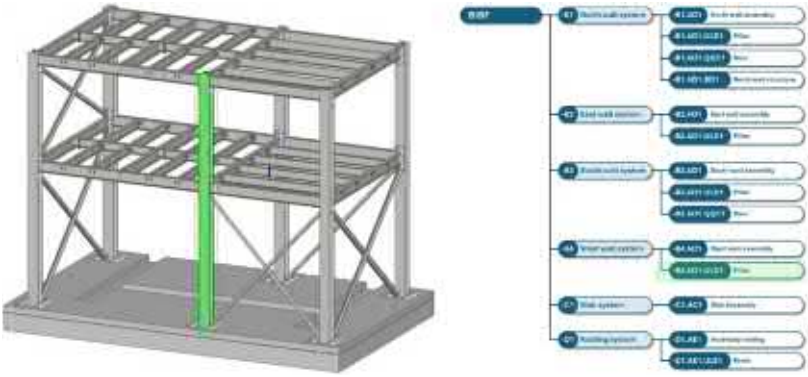


Fig. 4. The structural model of the Control Room of the IBF and the reference designation system developed in accordance with ISO/IEC 81346. © 2025, developed by the authors.

BIM modelling of the IBF Bellotti was developed across architectural, structural, and MEP disciplines. A geometric survey of the exterior and interior of both buildings was conducted with LNGS technical staff to compare the as-built configuration with the original documentation. The survey also informed the modelling of electrical system elements such as primary switchboards, circuits, and individual components, using both Revit software families and custom-made components based on LNGS documentation.

The ISO/IEC 81346 reference designation system was applied as a central element of the modelling strategy. Location Breakdown Structures (LBS) and Product Breakdown Structures (PBS) were developed in consultation with LNGS representatives, and a concentric IFC file structure was adopted, governed by a dedicated Excel file. The ISO/IEC 81346 framework enabled the separation of component designation from material or functional properties, thereby preserving the stability of the coding structure over time despite potential modifications to the components themselves. The designation system was organised according to hierarchical relationships between systems, subsystems, and components, whilst dedicated prefixes and symbols were employed to distinguish functional, product, and locational aspects. This multisectoral approach proved particularly suitable for the Gran Sasso Laboratories, where architectural, structural, plant, and scientific equipment systems coexist within a highly integrated infrastructural environment. Parameter sets were therefore defined not only to support designation, but also to facilitate maintenance tendering procedures and future asset management operations in accordance with ISO 55000 principles (Fig. 4). The resulting IFC organisation preserves the prescribed hierarchy and nomenclature whilst associating electrical system components and circuits with the corresponding architectural spaces.

The sensor network of the IBF Bellotti comprises: triaxial MEMS accelerometers installed at strategic positions on the load-bearing elements of both buildings provide structural and vibrometric monitoring data, whilst sensors measuring temperature, humidity, electromagnetic field intensity, acoustic noise, and radon concentration are deployed within the spaces for environmental monitoring.

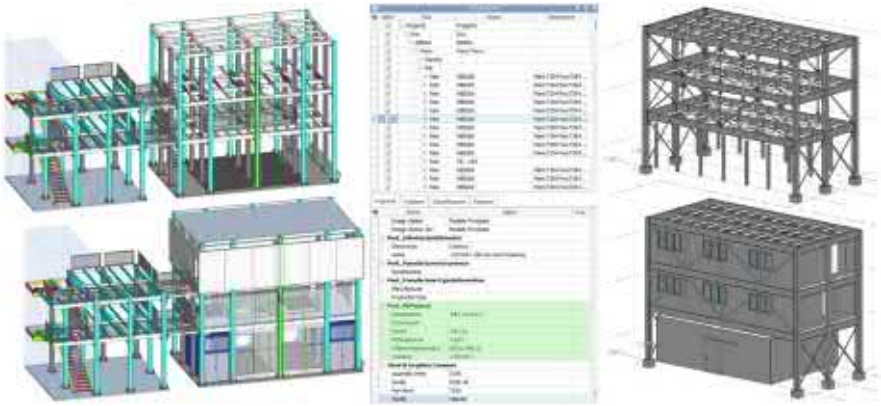


Fig. 5. The structural and architectural models of the Cryo-Platform and Stella facilities with a sample of the Reference Designation System (RDS). © 2025, developed by the authors.

Data transmission follows two distinct pathways: the MEMS accelerometers generate binary files transmitted via SFTP protocol through local gateways to a central processing server, whilst the environmental sensors — operating across heterogeneous communication protocols — are normalised through a Home Assistant-based integration layer before being forwarded to a centralised time-series database. Both data streams are accessible through an interactive monitoring dashboard enabling real-time visualisation of sensor readings directly associated with the corresponding BIM objects in the federated model.

3.2 Cryo-Platform and Stella Facilities

The BIM modelling of the CRYO-PLATFORM and STELLA facilities adopted the same methodological framework developed for the IBF Bellotti case study, particularly regarding interdisciplinary coordination, IFC interoperability, and the implementation of the ISO/IEC 81346 reference designation system.

CRYO-PLATFORM is a scientific infrastructure currently under construction in Hall B, conceived as a large-scale underground cryogenic hub dedicated to the testing of next-generation cryogenic detectors and sensors at temperatures approaching 10 mK. Supported by the PNRR LNGS-FUTURE programme, the facility comprises two structurally independent steel volumes characterized by regular framed systems with HEB 260 columns and primary beams, combined with secondary beams of varying sections. The first building accommodates loading, office, and roof-level technical functions, whilst the second contains storage and circulation spaces connected to adjacent facilities.

As the structure was absent from the available point cloud survey, the BIM reconstruction, developed with the collaboration of UNIBIM based in Pisa, relied primarily on executive documentation integrated through in-situ verification. Particular attention was devoted to the steel structure and its constructive logic, including the modelling of beam-to-column joints, bolted plate assemblies, and secondary framing systems through parametric components suitable for future maintenance and inspection activities. The

IFC structure and parameter organisation were defined in accordance with the ISO/IEC 81346 methodology and LNGS asset management requirements.

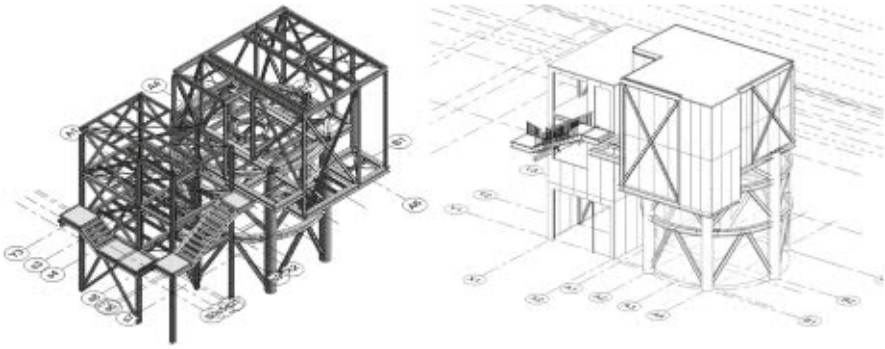


Fig. 6. The structural and architectural models of the Cosinus experimental facility. © 2025, developed by the authors.

The STELLA facility, located at the southern extremity of Hall B, is one of the earliest structures realised within the LNGS complex (Fig. 5). The facility consists of a three-level steel structure connected by metal staircases and gallery walkways, together with a structurally independent watertight steel enclosure at ground-floor level used for service and storage functions. The BIM reconstruction was based on CAD documentation, point cloud surveys and photographic records. Modelling focused initially on the steel framework, including columns, beams, and exposed diagonal bracing systems that define the building facades. Floor assemblies, envelope systems, and structural nodes were subsequently integrated, whilst bolted joints and fastening systems were modelled and parameterised using survey and executive data. The model was prepared for the implementation of the information system.

3.3 Cosinus Experiment

Sited next to the IBF Bellotti, the COSINUS experiment searches for dark matter by gauging the thermal energy that particles release within crystalline materials held at cryogenic temperatures [13]. Three constructions make up the facility — the Control Room, the Clean Room, and the Tank — whose architectural and structural models were built as linked files sharing plan and elevation as fixed references.

For the Control Room and the Clean Room, conventional architectural and structural models were linked and then federated by means of a common survey point, whereas the Tank was treated as a mass, since its atypical contents cannot be described as a building element. The level of detail of the steel structure was intentionally kept lower than that of IBF Bellotti to preserve compatibility with finite element method (FEM) analytical software, COSINUS having been selected as the reference structure for testing BIM-to-FEM interoperability.



Fig. 7. The federated BIM model of Hall B of the LNGS. © 2025, developed by the authors.

The tests required iterative simplifications of the geometric model to produce an analytical configuration in which structural members accurately converge at shared nodes, a prerequisite for the correct transmission of forces in numerical analysis. Compatibility tests were conducted using MIDAS Civil, although the structural analyses were assigned to a separate research unit within the consortium; the IFC export to the FEM platform revealed recurring challenges in the automatic recognition of structural axes and the correct positioning of elements at shared nodes, requiring iterative analytical model corrections. The circular geometry of the Clean Room presented additional modelling challenges, addressed through precise node alignment; bracing elements, window frames, and facade modules were finalised in accordance with the architectural project (Fig. 6).

3.4 Hall B Federated Model

The federated model of Hall B was assembled by linking the individual models within a common reference framework, anchored to the shared survey point and to design points positioned at the vertices of each facility. The XENON experiment, for which no documentation suitable for BIM modelling was available, it is represented in the federated model through a volumetric placeholder element (Fig. 7). The independent construction of the various facilities, spanning different periods and not all captured within the available point cloud, precluded direct verification of the alignment between project reference points and as-built conditions. To address this limitation, additional laser scanning surveys were conducted. The integration of these acquisitions with earlier scans will yield a geolocated point cloud of Hall B, enabling federated model optimisation through verified reference coordinates. Its export to IFC format ensures interoperability with the sensor networks and data infrastructure of the Tecnodigit digital twin system.

4 Conclusion

The research demonstrates the potential of BIM-based methodologies for the development of DTs in highly specialised underground research environments such as the LNGS. The complexity of Hall B required the definition of a dedicated modelling strategy capable of ensuring interoperability, adaptability, and effective information management. The adoption of a federated BIM approach based on IFC exchange formats enabled the integration of heterogeneous models and data sources within a shared digital environment [14]. Particular attention was devoted to the modelling of steel structures and connections, whose geometric and constructive reliability was considered essential for accurate representation of the as-built condition and maintenance, monitoring, and asset

management purposes. The implementation of the reference designation system further supported the organisation of information through stable hierarchical relationships. The case studies highlighted the need to define modelling requirements according to the concept of LOIN and this approach allowed the development of responsive and interoperable BIM models capable of accommodating future modifications, additional sensor networks, and analytical applications [15].

The research also revealed several critical aspects: the management of IFC structures, the manual implementation of ISO/IEC 81346 classifications, and the difficulties associated with georeferencing and survey integration. Nevertheless, the developed methodology constitutes a significant step towards the creation of scalable DT systems for scientific infrastructures and the digital management of complex research facilities [16].

Funding. This work was supported by the research project "Tecnodigit – Technologies for the creation of digital twins" (CUP: B83C22002820006) financed by the PNRR as part of the Next Generation EU (NGEU) through the regional innovation ecosystem Rome Technopole (Spoke 1 and 6, Project code ECS 00000024).

References

1. Grieves M, Vickers J (2017) Digital twin: mitigating unpredictable, undesirable emergent behavior in complex systems. In: Kahlen F, Flumerfelt S, Alves A (eds) Transdisciplinary Perspectives on Complex Systems. Springer, Cham, Switzerland, pp 85–113. https://doi.org/10.1007/978-3-319-38756-7_4
2. European Commission (2021) Supporting Digitalisation of the Construction Sector and SMEs: Including Building Information Modelling. European Construction Sector Observatory (ECSO), Analytical Report. Publications Office of the EU, Luxembourg
3. Assaad R, El-adaway IH, Hastak M (2024) An intelligent BIM-enabled digital twin framework for real-time structural health monitoring using wireless IoT sensing, digital signal processing, and structural analysis. Expert Syst. Appl. 252:124204. https://doi.org/10.1016/j.eswa.2024.124204
4. Sapienza Università di Roma, Bando a cascata Sapienza per progetti collaborativi di Ricerca nell'ambito di Rome Technopole Spoke 1 e 6. https://www.uniroma1.it/it/pagina/bando-cascata-sapienza-progetti-collaborativi-di-ricerca-nellambito-di-rome-technopole-spoke. Accessed 7 Jan 2025
5. Quaquero E, Rubiu G, Gatto G, Perra C (2021) BIM and IoT sensors integration: a framework for consumption and indoor conditions data monitoring of existing buildings. Sustainability 13(8):4496. https://doi.org/10.3390/su13084496
6. Abita M et al (2025) Towards the digital twin of a deep underground laboratory. The information modelling of the LNGS experiment facilities. In: Albatici R, Dalprà M, Gatti MP, Maracchini G, Torresin S (eds) Envisioning the Futures – Designing and Building for People and the Environment. Colloqui.AT.e 2025, Lecture Notes in Civil Engineering, vol 766. Springer, Cham, Switzerland, pp 17–31. https://doi.org/10.1007/978-3-032-06993-1_2
7. Ianni A, Peña Garay C, Hall J, Paling SM (2024) Editorial: science and technology in deep underground laboratories. Front. Phys. 12:6–8
8. ISO 19650-1:2018 (2018) Organization and Digitization of Information About Buildings and Civil Engineering Works, Including Building Information Modelling (BIM) — Information Management Using Building Information Modelling — Part 1: Concepts and Principles. International Organization for Standardization, Geneva

9. Abualdenien J, Borrmann A (2022) Levels of detail, development, definition, and information need: a critical literature review. J. Inf. Technol. Constr. 27:363–392. https://doi.org/10.36680/j.itcon.2022.018
10. Sacks R, Brilakis I, Pikas E, Xie HS, Girolami M (2020) Construction with digital twin information systems. Data-Centric Eng. 1:e14. https://doi.org/10.1017/dce.2020.16
11. Abualdenien J et al (2021) On BIM interoperability via the IFC standard: an assessment from the structural engineering and design viewpoint. Appl. Sci. 11(23):11430. https://doi.org/10.3390/app112311430
12. Boeltzig A, Junghans AR (2025) Underground nuclear astrophysics at LUNA and the bellotti ion beam facility of INFN-LNGS. EPJ Web Con. 340:04006. https://doi.org/10.1051/epjconf/202534004006
13. Angloher G et al (2024) Deep-underground dark matter search with a COSINUS detector prototype. Phys. Rev. D 110:043010. https://doi.org/10.1103/PhysRevD.110.043010
14. Sacks R, Eastman C, Lee G, Teicholz P (2018) BIM Handbook: A Guide to Building Information Modeling for Owners, Designers, Engineers, Contractors, and Facility Managers, 3rd edn. John Wiley & Sons, Hoboken, NJ
15. Fawad M et al (2023) Automation of structural health monitoring (SHM) system of a bridge using BIMification approach and BIM-based finite element model development. Sci. Rep. 13:13215. https://doi.org/10.1038/s41598-023-40363-3
16. Boje C, Guerriero A, Kubicki S, Rezgui Y (2020) Towards a semantic construction digital twin: Directions for future research. Autom. Constr. 114:103179. https://doi.org/10.1016/j.autcon.2020.103179

A Tool for Informed Choices of Post-production Protocols: The Pre-deconstruction Audit Model

Renato Morganti, Laura Ciammitti(✉), Alessandra Tosone, Alessandra Bellicoso, Danilo Di Donato, Matteo Abita, Alessia Panepucci, and Simone Rea

DICEAA Department, University of Study of L'Aquila, L'Aquila, Italy
laura.ciammitti@univaq.it

Abstract. Developed as part of the Project of Significant National Interest "ST3P+L. Buildings and Circular Economy. Steel from production to post-production. Law and responsibility issues" (Next Generation EU), the pre-deconstruction audit model is an operational tool for the reusability assessment of steel components from decommissioned buildings. The tool supports technical decisions, guiding them towards the protocols defined by the standard CEN/TS 1090–201:2024 for structural reuse or towards specific procedures suitable for the Italian context for non-structural reuse. Through progressive phases, the proposed tool introduces the building and organizes its structural components into a schedule describing their production, geometric, and relational characteristics. It proceeds with the verification of the original documentation, which reduces destructive testing and increases the reliability and accuracy of preliminary assessments. Finally, it allows data to be exported to BIM environments, allowing for integration with the Digital Product Passport, ensuring traceability throughout the entire life cycle. Validation on a real case study confirms its effectiveness as a tool to support the reusability assessment of components and highlights its potential to promote building management strategies aimed at optimizing resources and costs, encouraging the spread of steel reuse as a competitive practice in the construction sector.

Keywords: Reuse · Steel structural components · pre-deconstruction audit model · reusability assessment · post-production protocols

1 Introduction

This research is part of the construction sector's transition to circular economy models, with particular reference to the reuse of steel structural components. In this context, developing tools to support and monitor the design process throughout the entire building life cycle is essential for promoting sustainable resource management practices. For this reason, this is one of the goals of the Project of Significant National Interest, funded by Next Generation EU, "ST3P+L. Buildings and Circular Economy. Steel from production to post-production. Law and responsibility issues".

In this context, monitoring component life cycles plays a central role, as it provides reliable information on performance characteristics, usage history and transformations

© The Author(s), under exclusive license to Springer Nature Switzerland AG 2026
R. Zanon et al. (Eds.): CTA 2026, LNCE 942, pp. 1087–1096, 2026.
https://doi.org/10.1007/978-3-032-39505-4_94

over time. From this perspective, audit tools are essential for data collection, management and transmission, contributing to the strengthening of accountability mechanisms and the structuring of circular supply chains.

The evolution of the audit concept highlights the shift from an approach initially limited to the pre-demolition phase, with objectives primarily related to environmental protection and safety [1], to a broader and more systemic vision. European policies on construction and demolition waste have progressively promoted the standardization of auditing as a structured technical process, aimed not only at quantifying and classifying waste, but also at improving the quality of recycling and the traceability of material flows. Community guidelines and protocols have helped define operational phases, competence requirements, and reporting tools transforming it from a voluntary practice to an almost structural element of sector policies [2].

The most recent regulatory and scientific developments mark a further advancement, orienting auditing towards a proactive and integrated function within the design process. In this scenario, the concept of pre-deconstruction audit is emerging, understood as a predictive tool aimed at assessing the reusability of building components [3].

2 Structure and Content of the Pre-deconstruction Audit Model for Steel Components Reuse

Starting from the European theoretical and regulatory framework, the research has developed a pre-deconstruction audit model specifically for steel structural components, following the European pre-deconstruction audit and reusability assessment methodologies recently formalized in the technical standard CEN/TS 1090-201:2024 [4]. The objective is to build a knowledge base capable of supporting the transition from a waste-oriented management to one oriented towards preserving the value embodied in construction products: the building is therefore interpreted as an "urban mine" from which to recover components with residual performance that can be reused through different post-production strategies.

Consistent with European guidelines, the proposed methodology proceeds from the analysis of the building to the characterization of the individual technical element, maintaining the link between the component and its context of origin. The information structure incorporates the contents of CEN/TS 1090-201:2024 regarding data collection, component condition assessment, and inspection and test records, integrating them with the results of the database of structural typologies and industrialized steel construction systems used in Italy from the post-World War II period to the present [5]. This has allowed the proposed tool to be adapted to the specificities of the national building heritage through guided compilation options.

The structure of the Excel template is therefore divided into four main sections, according to an iterative organization inspired by the «reclamation audit» of the European FCRBE project [6]: building identification, inventory and characterization of technical elements, selection of post-production protocols, and data export to digital traceability systems. Each section corresponds to a specific phase of the audit process and contributes to the construction of a progressively more in-depth information framework, aimed at defining technically sound, economically sustainable, and consistent reuse scenarios with the circularity aims promoted by European policies.

2.1 Building Identification

This section corresponds to the *Data Collection* phase required by CEN/TS 1090-201:2024 and represents the information level relating to the donor structure, i.e., the building from which the components intended for recovery originate. The information collected is not intended solely for the description of the work, but constitutes the knowledge base necessary for the subsequent reusability assessment of the structural elements. The European literature on pre-deconstruction audits, promoted by the Steel Construction Institute [7], as well as the results of the PROGRESS research [8], highlight how knowledge of the construction history of the building, its transformations, and its operating conditions represents an essential requirement to ensure the reliability of the decision whether or not to reuse a component.

The description of the building organism through its decomposition according to UNI 8290:1981 [9] responds to the need for a structured and shared reading of the building, functional both for planning de-construction activities and for identifying potentially reusable parts. Therefore, not only the vertical and horizontal load-bearing structures are described, but also the complementary works, such as internal partitions, roofing systems, stairs, and other building elements, with a view to selective and planned deconstruction.

Knowing the year of building allows the project to be immediately linked to the regulatory framework in force at the time of its construction. This allows for the identification of the mandatory documentation that should have accompanied the project and which, therefore, should be available from the competent inspection offices. These mandatory documents can be supplemented by additional ones produced throughout the building's life cycle, such as maintenance reports, inspection ones, or accident reports, which help reconstruct its technical and performance evolution.

The system also allows for the recording of subsequent interventions, for each of which it is necessary to enter general data, which may differ from those of the initial project, and to verify the availability of the relevant documentation, both mandatory and optional, possibly drafted in compliance with a regulatory framework different from that in force at the time of the original construction. This chronological reconstruction of the interventions is aimed at identifying any changes in load conditions, replacements of elements, or reinforcement interventions that may have altered the originally intended structural behavior. In this sense, the building's technical and construction history becomes an integral part of the restored component's identity and constitutes an information asset to be preserved and transferred in subsequent traceability phases (Fig. 1).



Fig. 1. Sheets A and B relating to the building, of which A describes the building system, and B verifies the availability of technical documentation

2.2 Inventory and Characterization of Technical Elements

The second section corresponds to the *Material Inventory* phase required by the European guidelines on C&D waste auditing [2, 3] and aims to transform the building into a set of individually identifiable, quantifiable and assessable components, allowing each element to be associated with a structured set of technical, documentary, and performance data.

The fields relate to:

- **Identification**: each element is identified with a code, which must be retained even during disassembly and reassembly, thus maintaining the connection with its provenance. Its function within the building (vertical, horizontal, inclined structure, etc.), the type (beams, columns, etc.), the construction phase, and its cross-section type (simple, welded, composite) are specified.
- **Production:** This field contains all the product data from the workshop, including the cross-section, type of rolling, manufacturer and steel grade, also using libraries specifically created with commercially available profiles. Furthermore, this field requires the number of profiles per section inventoried within the building, which is then used to estimate the overall weight.
- **Geometry:** Entering profile data via the library allows the geometry field to be automatically populated, with the exception of profile lengths or heights, which can be deduced from the project documents.
- **Weight:** The weight of the profile (kg/m) is also automatically entered; the model also calculates the weight in kg of the element and of the entire class of technical elements identifiable with that specific profile. In addition to geometric characterization purposes, determining weight plays a significant role in the application of the qualification protocols required by European standards: the definition of test units and

sampling lots is in fact correlated to the overall mass of the components belonging to the same production category.

- **Surface treatments:** this field is not descriptive but merely identifies their presence.
- **Connections:** this section indicates both the type of connection and the technical elements that constitute the node, identified with their codes.

Particular attention is paid to verifying the product documentation associated with individual components, introduced by the French protocol *Recommandations Professionnelles Réemploi D'éléments Structuraux En Acier* [10], which significantly influences preliminary assessments, as there is a direct relationship between document completeness and reduction in testing.

The mandatory certificates are directly related to the product standard according to which the steel elements were manufactured (DoP, CE Marking, etc.), while the optional certificates, of which the tool offers a non-exhaustive list derived from a field comparison with companies that deal with metal carpentry, can be useful for conducting specific assessments of the work cycles or other aspects relating to the construction process (Fig. 2).



Fig. 2. Sheets C and D relating to the technical elements, of which C represents an abacus of the structural components, and D a check of the technical product documentation

2.3 Selection of Post-production Protocols

The final datasheet dedicated to protocol selection represents the summary of the audit process. This phase corresponds to the final stage of the *Reusability Assessment*, in which the information collected during the audit is processed within a decision-making matrix aimed at identifying the most appropriate post-production scenario among all those

functional to component reuse [11], which include «remanufacture», «reconditioning», «reuse» and «repurpose», as proposed by the British Standard 8887–2:2009 [12].

The objective is not simply to verify the component's compliance with specific technical requirements, but to identify the enhancement path most consistent with the level of available knowledge and the potentially achievable performance. The auditor is thus guided towards a reasoned and replicable decision, based on assessments conducted on the construction period, knowledge of the component's origin and history, and the availability of documentation, making explicit the conditions leading to each outcome.

Regarding possible post-production scenarios, the research aims to identify and define those most suited to the Italian context at a time when the European Commission for Standardization was still working on them. This research adopts the protocols proposed by the French recommendations, which provide for reuse even in seismic-prone areas, a mandatory requirement for much of Italy. The identified protocols, compatible with those of CEN/TS 1090-201:2024, provide for exclusively structural reuse for components produced after 1970 according to four protocols (A, B, C, and D), which differ in terms of the units to be tested, with the resulting costs. Alongside these, the ST3P + L research proposes the non-structural reuse of components produced before 1970, allocating them to a reuse with "downgrading" (E) or to their repurposing (F), following the appropriate transformations that the new function requires: this allows to consider as a source of reusable resources also that 30% of the metal-structure building heritage which, from the database of structural typologies and industrialized steel construction systems, appears to be made with components produced before 1970, the year of publication of the European standard which defines the technical characteristics of hot-rolled profiles, implemented in Italy in 1972 (Fig. 3) [13].



Fig. 3. Sheet E on post-production protocols, with a matrix that guides the auditor towards an informed choice

2.4 Data Export to Digital Traceability Systems

The model is designed as an open and interoperable tool: data export in CSV format allows for integration with open BIM environments and traceability tools, such as the

Digital Product Passport [14], promoting information continuity throughout the entire life cycle of components. This feature overcomes the traditional audit time limit, transforming the data collected during the pre-deconstruction phase into a reusable information asset during the subsequent phases of disassembly, marketing, and reuse of the component.

From this perspective, the dataset generated by the audit constitutes the initial core of the Digital Product Passport, i.e., the first level of knowledge necessary to build the product's digital identity.

3 Model Validation on the C.A.S.E. Project



Fig. 4. A building of C.A.S.E. project as case study for the model validation (Source: Google maps; Progetto C.A.S.E. L'Aquila - Progetto per la realizzazione di edifici residenziali al di sopra di piastre sismicamente isolate: progetto esecutivo, in Archivio privato Taddei S.p.A.-Gruppo Edimo S.p.A.)

The C.A.S.E. (Sustainable and Eco-Friendly Anti-Seismic Complexes) project, implemented in L'Aquila in 2009 to respond to the post-earthquake housing emergency, represents an excellent case study for validating the pre-deconstruction audit model (Fig. 4) [15].

The database developed within the ST3P + L research project identified two building typologies characterized by metal load-bearing structures, built according to an industrialized frame construction system on seismic isolators. These structures were

selected as the operational validation context because they are characterized by a modular component system and a defined time horizon typical of emergency construction.

The final choice for validating the developed audit system fell on the residential building located on Via Lucio Battisti, in the Bazzano area, with a rectangular plan (54 m × 12 m) and a structural grid of 6 m × 6 m, developed on four floors above ground. From a technical perspective, the structure consists of the following main components:

- Columns: HEA 220 profiles.
- Main beams: IPE 330, IPE 300, and IPE 360 profiles.
- Bracing: UPN 220 with X-shaped geometry.
- Roofing: HEA 200 beams, Omega purlins (200 × 120 × 60 × 3), and lightweight panels.

For this specific case study, it was possible to collect a higher-than-average amount of original information, including the structural design provided by the construction company Taddei S.p.A. [16]. This availability of documentation is crucial for simplifying the audit procedure, as the quality of the data drastically reduces uncertainty and the need for destructive testing of the materials. It also speeds up the reusability assessment, which in this case led to the structural components being placed in Protocol A, with a certificate of structural reuse (execution classes EXC1 or EXC2) based on existing documentation. Finally, it allows for the quantification of resources, which in this building amount to approximately 84 tons of S275JR steel.

Despite the reversibility ensured by the bolted connections, the audit confirmed a critical issue: the presence of corrugated sheet metal floors with concrete casting makes the complete recovery of the beams extremely complex, while confirming the high potential for reuse of the columns. This preliminary assessment allows for the subsequent de-construction and post-production phases to be carefully planned.

The data collected through the audit was finally exported in CSV format to feed the DPP, transforming each technical element into a traceable digital resource ready for reuse on the market.

4 Conclusions

The proposed pre-deconstruction audit model establishes a systematic process that transcends the traditional view of buildings as sources of waste, instead interpreting it as a repository of potentially reusable resources, building a reliable knowledge base for subsequent post-production assessments.

Moreover, this tool could evolve into a governance support system for the transformation of built heritage, with a predictive function useful for more accurate planning of selective deconstruction, handling, qualification and re-marketing of recovered components.

Its implementation with economic evaluation tools capable of estimating deconstruction costs, qualification tests, and post-production treatments would make it extremely attractive to stakeholders involved in the supply chain. Integration with BIM environments and geographic information systems would also enable the creation of territorial inventories of available resources, supporting planning strategies at urban and regional scales.

In this scenario, the pre-deconstruction audit could evolve from a single-building analysis tool to an information platform for the circular management of built heritage, contributing to the definition of new procurement policies, waste reduction and the valorization of existing resources.

Acknowledgments. We would like to thank Taddei S.p.A. - Edimo S.p.A. Group, for providing the material relating to the C.A.S.E. project.

Funding. This work was supported by the research Project of Relevant National Interest (PRIN) "Buildings and Circular Economy. Steel from production to post-production. Law and responsibility issues" financed by the National Recovery and Resilience Plan (PNRR) - Next Generation EU (NGEU) - Mission 4 "Education and Research" - Component C2 Investment 1.1 "Fund for the National Research Programme and Projects of Relevant National Interest (PRIN)", CUP: E53D23003600006.

References

1. European Commission: Directorate-General for Internal Market, Industry, Entrepreneurship and SMEs (2016) EU Construction & Demolition Waste Management Protocol. European Commission. https://ec.europa.eu/docsroom/documents/20509/
2. European Commission: Directorate-General for Internal Market, Industry, Entrepreneurship and SME (2018) Guidelines for the Waste Audits before Demolition and Renovation Works of Buildings. European Commission. https://ec.europa.eu/docsroom/documents/31521/
3. European Commission: Directorate-General for Internal Market, Industry, Entrepreneurship and SMEs (2024) EU construction & Demolition Waste Management Protocol Including Guidelines for Pre-demolition and Pre-renovation Audits of Construction Works – Updated edition 2024. Publications Office of the European Union, Brussels. https://data.europa.eu/doi/10.2873/77980
4. CEN-European Committee for Standardisation (2024) CEN/TS 1090-201:2024, Execution of Steel Structures and Aluminium Structures – Reuse of Structural Steel. CEN-European Committee for Standardisation
5. Morganti R, Ciammitti L, Tosone A, Bellicoso A, Di Donato D, Abita M (2025) Towards a database of structural typologies and construction systems in steel for the components reuse/repurpose. In: Albatici R, Dalprà M, Gatti MP, Maracchini G, Torresin S (eds) Envisioning the Futures - Designing and Building for People and the Environment. Colloqui. AT.e 2025, Lecture Notes in Civil Engineering, vol 766. Springer, Cham. https://doi.org/10.1007/978-3-032-06993-1_36
6. Smeyers T, Deweerdt M, Mertens M (2022) Reuse Toolkit. The Reclamation Audit, Interreg North-West Europe. FCRBE, Brussels
7. SCI P427 (2019) Structural Steel Reuse. Assessment, Testing and Design Principles. The Steel Construction Institute, Silwood Park Ascot
8. Girão Coelho Ana M, Pimentel R, Ungureanu V, Hradil P, Kesti J (2020) PROGRESS Provisions for Greater Reuse of Steel Structures. European Recommendations for Reuse of Steel Products in Single-Storey Buildings. ECCS -European Convention for Constructional Steelwork, Coimbra
9. UNI – Italian Committee for Standardisation (1981) UNI 8290-1:1981 Residential Building. Building Elements. Classification and Terminology. UNI – Italian Committee for Standardisation

10. CTI CM (2024) Recommandations professionnelles. Réemploi d'èlèments structuraux en acier. CTI CM. https://maisondelaconstructionmetallique.com/wp-content/uploads/2024/06/reemploi_elements_structuraux_en_acier_interactif.pdf
11. Morganti R et al (2025) Procedures for the reuse of steel components in building sector. Costruzioni Metalliche 5:41–60
12. BSI (2009) BS 8887-2:2009 Design for manufacture, assembly, disassembly and end-of-life processing (MADE) – Part 2: Terms and definitions. British Standards Institution (BSI), London
13. Ente Italiano di Normazione (1972) UNI 7070:1972 Prodotti finiti di acciaio di uso generale laminati a caldo - Profilati, laminati mercantili, larghi piatti, lamiere e nastri larghi aventi spessore >= 3 mm, UNI, Milano
14. European Commission (2024) Regolamento (UE) 2024/3110 del Parlamento europeo e del Consiglio, del 27 novembre 2024, che fissa norme armonizzate per la commercializzazione dei prodotti da costruzione e abroga il regolamento (UE) n. 305/2011. European Commission. https://eur-lex.europa.eu/legal-content/IT/ALL/?uri=CELEX:32024R3110
15. Turino R (2010) L'Aquila: Il progetto C.A.S.E., Complessi Antisismici ed. Ecocompatibili, 2010. Iuss Press, Milano
16. Progetto C.A.S.E. L'Aquila - Progetto per la realizzazione di edifici residenziali al di sopra di piastre sismicamente isolate: progetto esecutivo, in Archivio privato Taddei S.p.A.-Gruppo Edimo S.p.A.

InSAR-Based Monitoring of the Diego Armando Maradona Stadium

Pier Francesco Giordano(✉), Riccardo Liuzzo, and Maria Pina Limongelli

Department of Architecture, Built Environment, and Construction Engineering, Politecnico di Milano, Piazza Leonardo da Vinci 32, 20133 Milan, Italy
pierfrancesco.giordano@polimi.it

Abstract. Satellite Interferometric Synthetic Aperture Radar (InSAR) offers displacement measurements without permanent on-site instrumentation. However, its use for structural monitoring is complicated when the investigated asset is located in areas affected by ground movements such as subsidence or volcanic deformation. In this regard, this paper investigates the steel roof of the Diego Armando Maradona Stadium, which lies within the Campi Flegrei caldera, in Naples, Italy. High-resolution COSMO-SkyMed Persistent Scatterer (PS) time series from ascending and descending geometries are combined to reconstruct longitudinal and vertical displacements in local reference systems associated with the radial roof trusses. The InSAR measurements are dominated by regional ground uplift and horizontal motion and cannot be directly interpreted as structural response. Two compensation strategies are compared to isolate the structural response: subtraction of the mean displacement of surrounding reference PSs and subtraction of a polynomial approximation of their temporal evolution. The first approach provides smoother residuals and reveals a repeatable seasonal structural response compatible with thermal deformation of the steel roof. A refined correction based on local reference clusters further reduces long-term drift for most roof areas. The results demonstrate that reference-PS selection is decisive for InSAR-based structural monitoring in areas affected by ground deformation.

Keywords: InSAR · COSMO-SkyMed · Remote Sensing · Ground Deformation · Campi Flegrei · Active Caldera · Structural Health Monitoring · Stadium · Steel Structure · Displacement Monitoring

1 Introduction

Structural Health Monitoring (SHM) supports the management of civil structures by providing evidence on serviceability, safety and long-term performance [1]. Conventional systems based on sensors installed on the asset can offer high temporal resolution, but installation, maintenance and data-management costs often limit their application to individual structures [2]. Satellite Interferometric Synthetic Aperture Radar (InSAR) is therefore increasingly investigated as a complementary monitoring technology because it can provide spatially distributed displacement time series over large areas and can retrospectively exploit archived acquisitions [3–6].

© The Author(s), under exclusive license to Springer Nature Switzerland AG 2026
R. Zanon et al. (Eds.): CTA 2026, LNCE 942, pp. 1097–1108, 2026.
https://doi.org/10.1007/978-3-032-39505-4_95

InSAR measures the displacement of radar-reflective targets, commonly referred to as Persistent Scatterers (PSs), along the satellite Line of Sight (LOS). The measured LOS displacement does not directly correspond to a structural degree of freedom but represents the projection of the actual three-dimensional motion onto the satellite viewing direction. Moreover, it may include contributions from environmental effects, ground deformation, and measurement noise. Structural displacement components can be reconstructed by combining InSAR observations acquired from different satellite geometries, provided that suitable preprocessing operations, such as spatial and temporal resampling, are first performed to ensure consistency between the datasets. Multi-geometry displacement reconstruction and the associated propagation of measurement uncertainty have therefore become central topics in the application of InSAR to SHM [7–9].

A particularly demanding situation occurs when the structure is located in a region affected by subsidence, uplift, landslides or volcanic deformation. In such cases, the LOS time series measured on the structure may be dominated by ground-related motion, while the structural response represents only a smaller residual component [10]. Relative-displacement approaches based on nearby reference PSs have been used to remove common motion from bridges and buildings [11, 12]. Their reliability, however, depends on the spatial representativeness and density of the reference targets. A reference area that is too broad may not reproduce local ground motion, whereas a very small reference cluster may be unstable when only a few PSs are available.

The present study considers the Diego Armando Maradona Stadium in Naples, Italy. The stadium is located in the Fuorigrotta district, within the Campi Flegrei caldera, and its steel roof comprises long cantilever trusses with different orientations around an elliptical plan. These characteristics make the case study suitable for investigating three coupled issues: separation of ground and structural motion, sensitivity of two-orbit reconstruction to structural orientation, and identification of a thermally induced seasonal response [13].

The remainder of the paper is organised as follows. Section 2 presents the methodology adopted for displacement reconstruction and ground-motion compensation. Section 3 describes the case study and the COSMO-SkyMed datasets. Section 4 reports and discusses the main results, while Sect. 5 summarises the principal conclusions and outlines future developments.

2 Methodology

Ascending and descending InSAR datasets are acquired from different viewing geometries and processed independently. Consequently, they generally provide PSs at different spatial locations and displacement measurements at different acquisition dates. Spatial and temporal resampling are therefore required before the LOS observations from the two satellite orbits can be combined [3, 8].

In this work, spatial consistency is obtained by subdividing the stadium roof into 28 areas, each corresponding to one radial steel truss. Further details on the definition and orientation of these areas are provided in Sect. 3. For each acquisition geometry k, where $k = A$denotes the ascending orbit and $k = D$the descending orbit, the PSs located within each area are selected. Their displacement time series are then averaged

to obtain a representative LOS displacement for the corresponding structural area. This method allows ascending and descending measurements associated with different PS distributions to be referred to the same physical portion of the roof.

Since ascending and descending acquisitions are also performed on different dates, the representative LOS time series are not directly synchronised. Temporal consistency is obtained by interpolating the measurements of one orbit at the acquisition dates of the other. Linear interpolation is applied only within the common observation period of the two datasets, avoiding temporal extrapolation. Following this procedure, each roof area is associated with paired ascending and descending LOS observations at common time instants. For simplicity, the following equations are written for a generic roof area; the same formulation is applied independently to each of the 28 areas.

The displacement of each roof area is expressed in a local structural reference system comprising longitudinal, transverse, and vertical components:

$$\mathbf{u}(t) = \begin{bmatrix} d_L(t) \\ d_T(t) \\ d_V(t) \end{bmatrix} \tag{1}$$

where $d_L(t)$, $d_T(t)$, and $d_V(t)$are the longitudinal, transverse, and vertical displacement components, respectively. The longitudinal direction is aligned with the axis of the corresponding radial steel truss, the transverse direction is orthogonal to it in the horizontal plane, and the vertical direction coincides with the Up direction. The orientation of each truss is defined by the angle ϕ, measured clockwise from the East direction.

For an acquisition geometry k, the measured LOS displacement is the projection of the local displacement vector onto the satellite look direction, as follows:

$$d_{\mathrm{LOS},k}(t) = \mathbf{h}_k^T(\phi)\mathbf{u}(t) \tag{2}$$

where the projection vector is

$$\mathbf{h}_k(\phi) = \begin{bmatrix} \sin\theta_k \cos(\alpha_k - \phi) \\ -\sin\theta_k \sin(\alpha_k - \phi) \\ \cos\theta_k \end{bmatrix} \tag{3}$$

Here, $\theta_k$is the incidence angle of acquisition k, $\alpha_k$is the corresponding look-azimuth angle measured clockwise from the East direction, and $\phi$is the orientation of the longitudinal axis of the considered roof truss. The three components of $\mathbf{h}_k(\phi)$represent the LOS sensitivities to longitudinal, transverse, and vertical motion, respectively. Positive LOS displacement denotes motion towards the satellite.

The ascending and descending acquisition geometries observe the structure from different look directions and therefore provide complementary information. Combining the two LOS observations gives

$$\begin{bmatrix} d_{\mathrm{LOS},A}(t) \\ d_{\mathrm{LOS},D}(t) \end{bmatrix} = \begin{bmatrix} \mathbf{h}_A^T(\phi) \\ \mathbf{h}_D^T(\phi) \end{bmatrix} \begin{bmatrix} d_L(t) \\ d_T(t) \\ d_V(t) \end{bmatrix} \tag{4}$$

Since Eq. (4) contains two observations and three unknown displacement components, an additional assumption is required. In this study, the transverse structural displacement is assumed to be negligible, $d_T(t) = 0$. The reduced system can therefore be written as

$$\begin{bmatrix} d_{\mathrm{LOS},A}(t) \\ d_{\mathrm{LOS},D}(t) \end{bmatrix} = \mathbf{H}(\phi) \begin{bmatrix} d_L(t) \\ d_V(t) \end{bmatrix} \tag{5}$$

where the observation matrix is

$$\mathbf{H}(\phi) = \begin{bmatrix} \sin\theta_A \cos(\alpha_A - \phi) & \cos\theta_A \\ \sin\theta_D \cos(\alpha_D - \phi) & \cos\theta_D \end{bmatrix} \tag{6}$$

The longitudinal and vertical displacement components are then reconstructed as

$$\begin{bmatrix} d_L(t) \\ d_V(t) \end{bmatrix} = \mathbf{H}^{-1}(\phi) \begin{bmatrix} d_{\mathrm{LOS},A}(t) \\ d_{\mathrm{LOS},D}(t) \end{bmatrix} \tag{7}$$

Because the radial trusses have different orientations around the stadium perimeter, $\mathbf{h}_k(\phi)$and $\mathbf{H}(\phi)$are calculated separately for each roof area.

The LOS displacement measured on the roof includes both the local structural response and the broader ground motion affecting the surrounding area. For each acquisition geometry, roof area, and time instant, the observed LOS displacement is expressed as

$$d_{\mathrm{LOS},k}(t) = d_{\mathrm{str},k}(t) + d_{\mathrm{gnd},k}(t) \tag{8}$$

where $d_{\mathrm{str},\,k}(t)$is the component associated with the local structural response and $d_{\mathrm{gnd},\,k}(t)$represents the ground-related contribution. The latter is estimated independently for the ascending and descending datasets and removed before the two acquisition geometries are combined.

Two approaches are considered to estimate the ground-motion contribution. In the first, the ground-related displacement is evaluated at each acquisition date as the mean LOS displacement of a set of reference PSs located in the surroundings of the stadium. This procedure retains both the long-term deformation trend and the shorter-term variations shared by the roof and the surrounding area.

In the second approach, the ground motion component is modelled as a second-order polynomial in time, constrained to the mean displacement of the reference PSs at the first acquisition date and fitted by least squares to the pooled reference-PS observations. Although this approach provides temporal regularisation, shorter-term ground-motion variations may remain in the roof time series after correction.

The corrected LOS displacement is obtained by subtracting the estimated ground-motion contribution from the measured LOS displacement.

The correction is applied independently to the ascending and descending LOS time series before their fusion. The corrected observations are then spatially and temporally resampled and combined through Eqs. (5)–(7) to reconstruct the residual longitudinal and vertical displacement components of the roof.

3 Case Study and InSAR Data

3.1 Regional Setting and Stadium Roof

The Naples metropolitan area lies between the Campi Flegrei caldera and the Somma–Vesuvius volcanic complex. Campi Flegrei is characterised by bradyseism, i.e. slow and partly reversible ground deformation associated with pressure changes in the magmatic-hydrothermal system. A renewed uplift phase has been observed since 2005 and affects not only the central caldera but also parts of the western Naples urban area [14]. The stadium is located in the Fuorigrotta district, where the deformation field includes both vertical uplift and horizontal motion. The original stadium was inaugurated in 1959. The roof added for the 1990 FIFA World Cup consists of a circumferential steel ring supporting 28 radial trusses and lightweight cladding. Each cantilever extends approximately 41.65 m towards the pitch and reaches an overall elevation of about 33.5 m. Because the trusses are distributed along an elliptical perimeter, their local longitudinal axes cover the full range of plan orientations. The roof was therefore subdivided into 28 areas, one for each radial truss (Fig. 1).

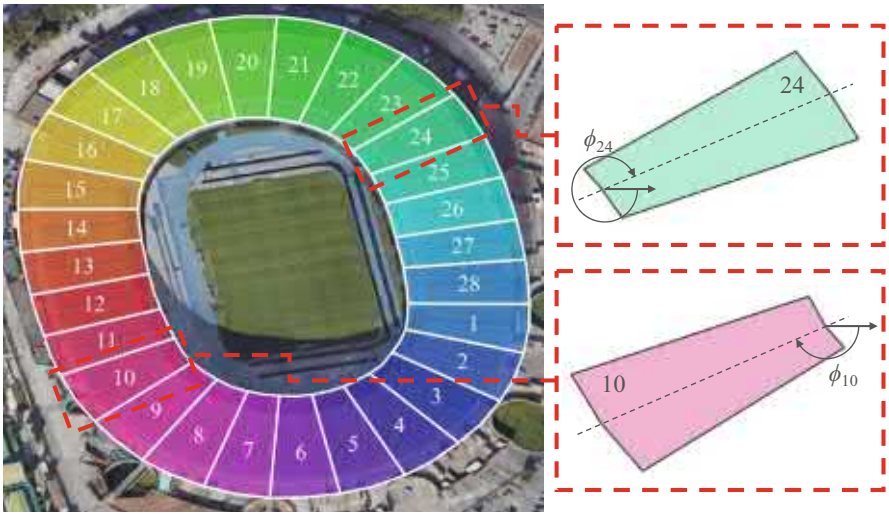


Fig. 1. Discretisation of the stadium roof into 28 areas and definition of the local longitudinal direction for two representative radial trusses.

3.2 COSMO-SkyMed Datasets

The interferometric products were generated by CNR-IREA through the Parallel SBAS processing chain from COSMO-SkyMed Stripmap images [15]. The ascending dataset covers the period from July 2009 to March 2025 and comprises 432 acquisition dates, whereas the descending dataset covers the period from July 2011 to March 2025 and comprises 213 acquisition dates. The analysis was performed over the observation period

common to the two geometries. A 1 km^2 window centred on the stadium was extracted, and PSs on the roof were separated from those in the surrounding urban area. As shown in Fig. 2, both ascending and descending datasets provide dense coverage over the stadium and its surroundings, while the opposite signs of the mean LOS velocities already indicate a substantial horizontal component of ground motion.

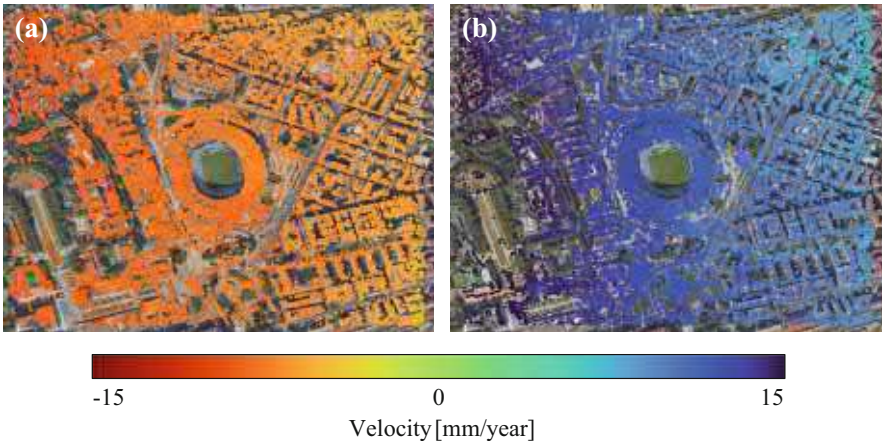


Fig. 2. Spatial distribution of PSs in the 1 km^2 area around the stadium for the (a) ascending and (b) descending tracks.

4 Results and Discussion

4.1 Uncorrected Reconstruction and Orientation Sensitivity

The analysis was first performed using the original LOS displacement time series, without removing the ground-motion contribution. Figure 3 shows the representative LOS displacements obtained for the 28 roof areas from the ascending and descending datasets. In both acquisition geometries, the time series exhibit a pronounced common trend, indicating that the measurements are strongly influenced by a deformation component affecting the entire stadium area. The cumulative LOS variation is approximately −100 mm for the ascending track and exceeds 150 mm for the descending track. The opposite signs observed in the two geometries indicate that the dominant displacement field includes a significant horizontal component, consistent with the regional deformation affecting the Campi Flegrei area.

The uncorrected ascending and descending LOS observations were subsequently combined to reconstruct the longitudinal and vertical displacement components in the local reference system of each radial truss. The results for all 28 roof areas are shown in Fig. 4. For most areas, the reconstructed displacements are dominated by long-term trends common to broad sectors of the roof and are therefore mainly attributable to the regional ground motion rather than to the local structural response.

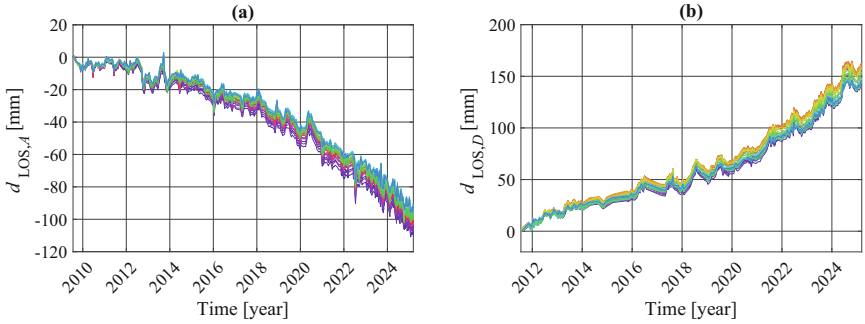


Fig. 3. Mean uncorrected LOS displacement time series of the 28 roof areas for the (a) ascending and (b) descending datasets.

For areas 6, 20, and 21, however, the reconstructed displacement components reach unrealistically large amplitudes. These trusses are oriented approximately along the north–south direction, to which conventional ascending and descending InSAR geometries have limited sensitivity. Consequently, the two LOS observations provide insufficiently independent information to reliably separate the longitudinal and vertical displacement components. Specifically, small differences and measurement uncertainties in the LOS time series are strongly amplified during displacement reconstruction. As realistic longitudinal and vertical displacement time series cannot be obtained for these three areas, they are excluded from the subsequent analyses.

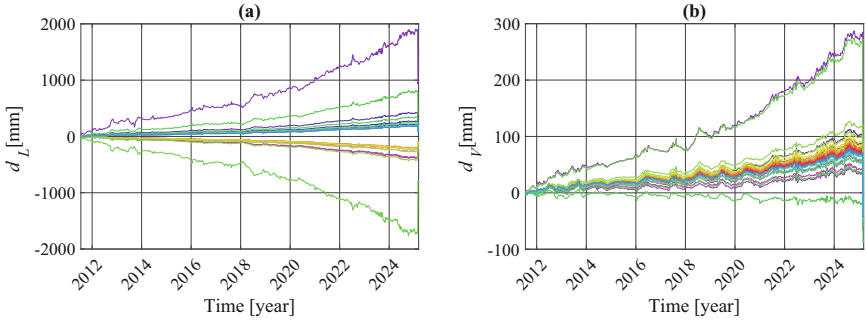


Fig. 4. Longitudinal and vertical displacement components reconstructed from the uncorrected ascending and descending LOS measurements for the 28 roof areas: (a) longitudinal component and (b) vertical component.

For the remaining areas, the longitudinal component exhibits opposite signs in different areas of the roof. This behaviour is primarily related to the definition of the local reference system: because the radial trusses have different orientations around the stadium perimeter, the same regional horizontal displacement is projected with different signs onto their longitudinal axes. The vertical component instead shows a general upward trend, with cumulative displacements of approximately 100–150 mm over the observation period, consistent with the ongoing uplift affecting the surrounding area.

These results demonstrate that the uncorrected LOS measurements are dominated by regional ground deformation and cannot be directly interpreted as representative of the roof response. Ground-motion compensation is therefore required before the reconstructed displacement components can be used to investigate the structural behaviour.

4.2 Comparison of Ground-Motion Compensation Strategies

As a first step, the two compensation strategies are applied using the PSs located within a 1 km^{2}area centred on the stadium, to estimate a ground-motion contribution common to the entire roof. In the following, the discussion focuses on the reconstructed vertical displacements. The reconstructed vertical displacements after correction are shown in Fig. 5. With the mean-reference strategy, a regular annual oscillation emerges across most roof areas. The pattern is compatible with thermal expansion and contraction of the steel trusses: warmer periods are associated with upward movement of the cantilevered roof, while colder periods produce the opposite response. The polynomial correction preserves less coherent seasonality and higher scatter; it is therefore not adopted in the subsequent analysis.

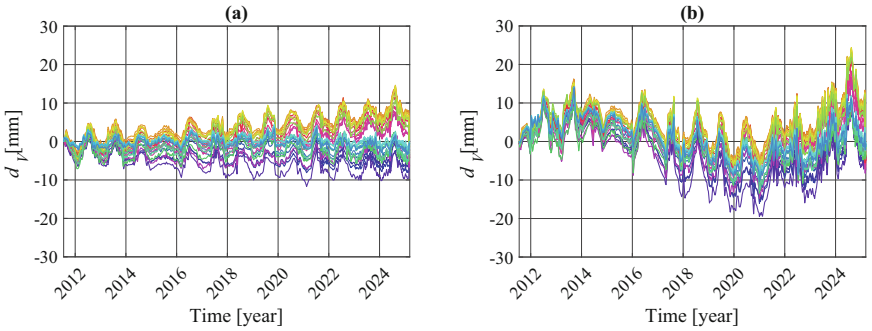


Fig. 5. Reconstructed vertical displacement after removing ground motion using (a) the mean displacement of reference PSs and (b) a polynomial approximation. The mean-reference method reveals a clearer seasonal response.

Although the mean-reference correction removes most of the regional deformation, residual low-frequency trends remain. This indicates that the mean displacement of the PSs within the 1 km^2 area is not fully representative of the local ground movement beneath each roof area. The remaining drift may also include spatially variable PS behaviour, interpolation errors and residual effects of the neglected transverse component. These observations motivated the use of local reference clusters.

4.3 Local Reference Clusters and Residual Trends

For each roof area, neighbouring reference PSs were selected in a 20 m band around the stadium perimeter (Table 1). The number and spatial distribution of PSs vary considerably among areas and between acquisition geometries. Area 13 has no ascending PSs within the local band and is excluded, leaving 24 areas for the final comparison.

Table 1. Number of local reference PSs within the 20 m band for each roof area.

Area n.	1	2	3	4	5	6	7
Asc.	1	3	52	71	130	154	94
Dsc.	43	50	25	22	54	107	161
Area n.	8	9	10	11	12	13	14
Asc.	35	17	31	26	1	0	28
Dsc.	87	61	20	21	18	4	3
Area n.	15	16	17	18	19	20	21
Asc.	24	56	77	79	99	135	119
Dsc.	52	81	71	100	106	112	128
Area n.	22	23	24	25	26	27	28
Asc.	86	52	4	3	6	5	8
Dsc.	103	56	2	8	50	32	28

The local correction leads to a more compact set of reconstructed vertical displacement time series and reduces the residual long-term separation between roof areas, while preserving the annual oscillation observed after the regional correction (Fig. 6). This effect is more evident for areas where the local reference cluster includes a sufficiently large number of PSs. The fact that the seasonal component remains visible after applying two different reference selections indicates that it is not simply an artefact of the adopted ground-motion correction, but is likely associated with the response of the roof structure. Some residual drift is still observed in selected areas, suggesting that the local reference PSs do not always fully capture the ground motion affecting the corresponding roof sector.

The effectiveness of the correction strategies was quantified by fitting a linear trend to each reconstructed vertical displacement time series and considering the absolute value of the corresponding slope, $|m_V|$, which can be interpreted as the residual vertical velocity after ground-motion compensation. As shown in Fig. 7, the correction based on the 1 km^2reference population reduces this residual velocity by approximately two orders of magnitude with respect to the uncorrected reconstruction. The use of local reference clusters generally provides a further reduction, with residual velocities approaching 0.1 mm/year in several areas.

The improvement, however, is not uniform across the roof. In areas where only a limited number of local reference PSs is available, the estimated correction may become

sensitive to the behaviour of individual scatterers. This is particularly evident for areas 24–28 and 1–2, where the local correction does not always outperform the correction based on the larger 1 km^{2}reference population.

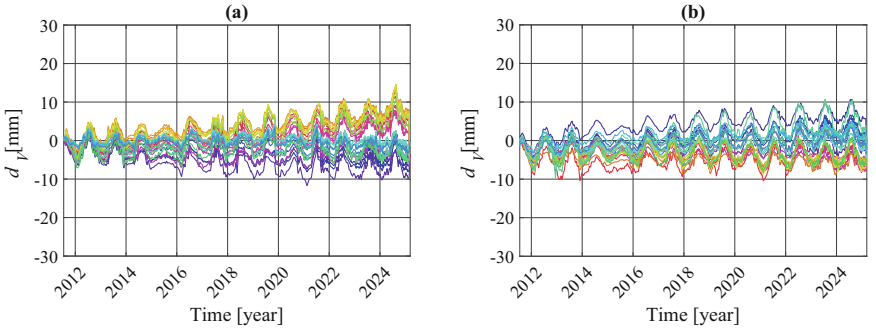


Fig. 6. Vertical displacement reconstructed after correction with (a) reference PSs from the 1 km^2 area and (b) local reference clusters. Local correction reduces the residual drift while preserving the seasonal response.

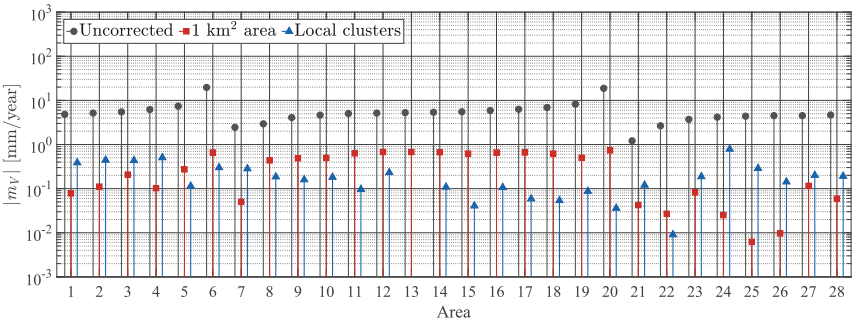


Fig. 7. Absolute velocity of the reconstructed vertical displacements for uncorrected data, correction with the 1 km^2 reference population and correction with local clusters.

5 Conclusions

Separating the local structural response from the ground-deformation component is particularly challenging in areas affected by phenomena such as subsidence, uplift, landslides, or volcanic activity. This study addressed this issue through the analysis of the Diego Armando Maradona Stadium in Naples, whose steel roof lies within the deformation field of the Campi Flegrei caldera.

The results show that the raw COSMO-SkyMed LOS measurements acquired over the stadium are largely dominated by regional ground deformation. Consequently, the

direct combination of ascending and descending observations mainly reconstructs the effects of ground uplift and horizontal motion.

Among the investigated correction strategies, subtracting the mean displacement of surrounding reference PSs proved more effective than removing a polynomial trend. The mean-based correction accounts not only for the long-term deformation trend but also for shorter-term variations shared by the stadium and the surrounding area. After correction, a coherent seasonal oscillation emerged in the reconstructed vertical displacements, consistent with the expected thermal response of the radial steel trusses. The use of local reference clusters selected close to the stadium further reduced residual long-term trends in most roof areas, with estimated slopes approaching 1 mm/year in several cases. The analysis also highlighted two important limitations. First, the orientation of the structural elements relative to the satellite viewing geometries must be considered, since trusses aligned approximately along the north–south direction cannot be reliably reconstructed from conventional ascending and descending observations. Second, local compensation may become less robust where only a limited number of reference PSs is available. The corrected displacement time series should therefore be interpreted together with information on the acquisition geometry and the spatial density of the reference PSs.

Future work should validate the observed seasonal response using independent displacement measurements. Further developments should also focus on adaptive procedures for reference-PS selection that balance spatial proximity to the monitored structure with the statistical robustness of the estimated ground-motion component.

Acknowledgements. The study was carried out within the DPC-ReLUIS 2024–2026 project, WP6 “Monitoring and satellite data”. CNR-IREA is acknowledged for processing and providing the COSMO-SkyMed InSAR datasets.

References

1. Datteo A, Lucà F, Busca G (2017) Statistical pattern recognition approach for long-time monitoring of the G.Meazza stadium by means of AR models and PCA. Eng. Struct. 153:317–333. https://doi.org/10.1016/j.engstruct.2017.10.022
2. Ubertini F, Comanducci G, Cavalagli N (2016) Vibration-based structural health monitoring of a historic bell-tower using output-only measurements and multivariate statistical analysis. Struct. Health Monit. Int. J. 15:438–457. https://doi.org/10.1177/1475921716643948
3. Talledo DA et al (2022) Satellite radar interferometry: Potential and limitations for structural assessment and monitoring. J. Build. Eng. 46:103756. https://doi.org/10.1016/j.jobe.2021.103756
4. Giordano PF et al (2025) Monitoring of a multi-span prestressed concrete bridge using satellite interferometric data and comparison with on-site sensor results. Struct. Concr. 26:5430–5453. https://doi.org/10.1002/suco.202400881
5. Caspani VF, Tonelli D, Bado MF, Rocca A, Perissin D, Zonta D (2026) Bridge monitoring with satellite InSAR technology and clustering algorithm. Measurement. 258:118939. https://doi.org/10.1016/j.measurement.2025.118939
6. Alahmad W, Quqa S, Ubertini F, Gentilini C (2026) Anomaly identification in historical modular structures using satellite data: methodology and application to Portico di San Luca, Bologna. J. Build. Eng. 118:114893. https://doi.org/10.1016/j.jobe.2025.114893

7. Farneti E et al (2023) A method for structural monitoring of multispan bridges using satellite InSAR data with uncertainty quantification and its pre-collapse application to the Albiano-Magra Bridge in Italy. Struct. Health Monit. 22:353–371. https://doi.org/10.1177/14759217221083609
8. Giordano PF, Kamariotis A, Giardina G, Chatzi E, Limongelli MP (2025) Uncertainty propagation in satellite InSAR data analysis for structural health monitoring. Autom. Constr. 177:106371. https://doi.org/10.1016/j.autcon.2025.106371
9. Giordano PF, Liuzzo R, Limongelli MP, Piscini A, Gammino M (2026) Three-dimensional bridge displacement reconstruction through Kalman filter fusion of multi-track InSAR observations. Measurement. 284:122214. https://doi.org/10.1016/j.measurement.2026.122214
10. Striano P et al (2026) National-scale full-resolution P-SBAS processing of large CSK/CSG and SAOCOM-1 SAR datasets for the built-up environment displacements retrieval. In: EUSAR2026
11. Giordano P, Turksezer Z, Previtali M, Limongelli M (2022) Damage detection on a historic iron bridge using satellite DInSAR data. Struct. Health Monit. 21:2291–2311. https://doi.org/10.1177/14759217211054350
12. Giordano PF, Miraglia G, Lenticchia E, Ceravolo R, Limongelli MP (2023) Satellite interferometric data for seismic damage assessment. Procedia Struct. Integr. 44:1570–1577. https://doi.org/10.1016/j.prostr.2023.01.201
13. Liuzzo R, Giordano PF, Bonzani A, Limongelli MP (2026) InSAR-based structural health monitoring within an active caldera: the case study of diego armando Maradona Stadium. Buildings. 16(18):3726. https://doi.org/10.3390/buildings16183726
14. De Martino P, Dolce M, Brandi G, Scarpato G, Tammaro U (2021) The ground deformation history of the Neapolitan Volcanic Area (Campi Flegrei Caldera, Somma–Vesuvius Volcano, and Ischia Island) from 20 years of continuous GPS observations (2000–2019). Remote Sens. (Basel). 13(2725). https://doi.org/10.3390/rs13142725
15. Casu F et al (2014) SBAS-DInSAR parallel processing for deformation time-series computation. IEEE J. Sel. Top. Appl. Earth Obs. Remote Sens. https://doi.org/10.1109/JSTARS.2014.2322671

Strengthening of Metal Thin Plates Through Wire-Arc Additive Manufacturing

Vittoria Laghi(✉), Elisabetta Savino, Neira Babovic, Giada Gasparini, and Tomaso Trombetti

Department of Civil, Chemical, Environmental and Materials Engineering, University of Bologna, Bologna, Italy
vittoria.laghi2@unibo.it

Abstract. Wire-Arc Additive Manufacturing (WAAM) is a metal 3D printing technology suitable to realize medium- to large-scale steel components suitable for applications in Architecture, Engineering and Construction (AEC) sectors. Given the high flexibility of this advanced technology, the additive fabrication of metal parts with almost no geometrical constraints can be adopted either to create new complex-shaped steel elements or to strengthen existing ones. This work proposes a novel approach for the structural strengthening of thin metal plates through WAAM. The study explores the conceptual design, numerical optimization, and fabrication of ribbed stiffening patterns directly deposited onto thin steel substrates. Leveraging the design freedom of WAAM, various rib topologies were parametrically defined and optimized to enhance local stiffness, buckling resistance, and overall load-bearing efficiency while minimizing material use. The optimized configurations were validated through finite element simulations and subsequently fabricated to assess geometric accuracy, material integrity, and adhesion behavior between the substrate and the deposited ribs. Preliminary experimental tests confirmed a significant improvement in mechanical performance compared to flat reference plates, demonstrating the potential of WAAM in structural and industrial applications, offering a pathway to lightweight and tailored metal structures.

Keywords: Wire-Arc Additive Manufacturing · Strengthening · Thin plates, Bead optimization

1 Introduction

Wire Arc Additive Manufacturing (WAAM), also referred to as Directed Energy Deposition - Arc (DED Arc), is one of the most promising solutions for the additive manufacture of large-scale metallic components [1–3]. It relies on an electric arc as the heat source and a metallic wire as feedstock, enabling layer-by-layer deposition of complex geometries with high deposition rates and relatively low costs compared with other metal additive manufacturing technologies [4]. From a scientific perspective, WAAM is the subject of extensive research, ranging from microstructural and mechanical characterization

© The Author(s), under exclusive license to Springer Nature Switzerland AG 2026
R. Zanon et al. (Eds.): CTA 2026, LNCE 942, pp. 1109–1115, 2026.
https://doi.org/10.1007/978-3-032-39505-4_96

of structural steels and titanium alloys to the development of process control strategies, thermo-mechanical numerical models, and WAAM-specific design methodologies, with the aim of ensuring reliable and reproducible structural performance [5–7].

In the construction sector, WAAM is emerging as a key technology for the fabrication of complex structural nodes, topologically optimized elements and large-scale components that are difficult to obtain using conventional manufacturing methods [8, 9]. Remarkable examples include steel nodes for beam–column connections and the "Weaving Love" pavilion in Hong Kong, the first constructional 3D-printed metal pavilion in steel produced by WAAM, demonstrating the combination of geometric freedom, structural efficiency and reduced material waste [7, 10]. At the same time, a growing research avenue is devoted not only to the production of new components but also to interventions on existing structures: the deposition of stiffeners directly onto slender plates, beam webs or existing columns makes it possible to enhance local and global buckling resistance without replacing the member, enabling targeted strengthening strategies that are potentially more sustainable than traditional techniques [11–13]. In this context, the use of WAAM for "on-demand" stiffening of in-service members opens highly attractive scenarios for structural retrofit and for extending the service life of existing constructions.

However, printing directly on very slender plates is not straightforward, as thermal input, distortion and lack of stiffness of the substrate can easily compromise both process stability and structural performance. In particular, when the plate thickness becomes small, conventional WAAM stiffening strategies may lead to excessive out-of-plane deformations, poor bonding or stress concentrations that limit the actual structural benefit of the added material. For this reason, the present study focuses on the stiffening of thin plates through a design optimization process aimed at defining rib geometries and deposition paths that ensure an effective improvement of the in-plane stress field, while remaining compatible with a robust and repeatable manufacturing process. Within this framework, the research objective is to bridge the gap between process feasibility and structural efficiency, demonstrating that WAAM can be effectively employed as a practical solution for the reinforcement of very slender plate-like elements.

2 The Principle of Stiffeners and their Role in Structural Efficiency

The principle of stiffeners (ribs) is based on increasing the bending and membrane stiffness of plates or shells by adding localized material at a distance from the mid-surface, instead of uniformly increasing the plate thickness [14]. This leads to a marked increase of the second moment of area and torsional rigidity of the effective cross section, which in turn enhances buckling resistance and limits deflections under compressive, bending and shear loads [15, 16]. Such an approach is particularly efficient because material is concentrated where it contributes most to structural performance, allowing lighter components for the same load-bearing capacity [17]. This concept is commonly adopted, for example, in aircraft fuselage and wing panels, where thin skins are combined with longitudinal stringers and transverse frames to delay local and global buckling while minimizing structural weight [18, 19]. In civil engineering, similar principles govern the design of orthotropic steel decks and plate girders with longitudinal and transverse

stiffeners, improving the stability of webs and flanges and enabling more slender sections and longer spans [20, 21]. In the context of WAAM, the same structural principle becomes particularly attractive, since ribs with non-standard layouts (curved paths, variable height, branched patterns) can be tailored to follow principal stress trajectories and local demand, thereby maximizing structural efficiency while exploiting the geometric freedom offered by additive manufacturing [3, 4].

3 Analysis of Plate Stiffening Using Rib Reinforcements

The design of rib reinforcement was studied on plate of 300 × 300 mm dimensions with three different thicknesses: 1 mm, 1.5 mm, and 2 mm, made of S235JR steel, as specified by the manufacturer. As per Nervi's theory, here applied on thin steel plates, the strengthening was achieved by adding WAAM material on the principal stress lines for the anticipated boundary conditions of the element being strengthened. In contrast to conceptual nature of Nervi's principal stress lines for rib stiffening, different strengthening approaches that use geometric deformation without added material, such as bead optimization, are mathematical in nature with solution that require minimal further validation.

Initially, bead optimization was performed for the thin plates for boundary conditions of concentrated force at the center and four corner pinned supports using Abaqus TOSCA software, with official software documentation found in Smith (2009), in order to obtain strengthening solution without added material, that resulted in symmetrical force dissipation across the entire plate, with higher stresses concentrated in the central region as shown in Fig. 1. Bead optimization was set to minimize strain energy by controlling the allowed bead height.

Similar resulting output pattern was anticipated for the conceptual Nervi's approach as well, where for the same boundary conditions, extraction of principal stress lines was performed, along which single-layer welded ribs were to be placed.

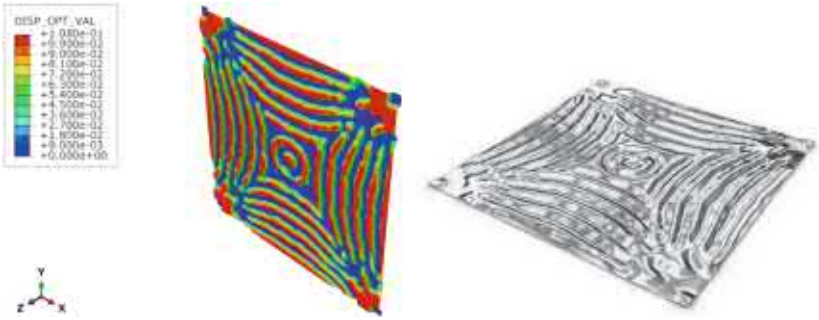


Fig. 1. a) Bead optimization in Abaqus, b) the resulting pattern of beads

The applied load of 1 kN roughly corresponded to the load-bearing capacity of the flat plate of 1 mm whose strength and stiffness were intended to be improved. The symmetrical initial geometry as well as boundary conditions, resulted in all symmetrical

resulting patterns, for either strengthening approaches. Although rib stiffening would be achieved even with relatively simple geometries, the unconstrained movement of the robotic arm allowed ribs to be deposited following the optimal pattern, particularly of higher geometric complexity. The final rib stiffening geometry is presented in Fig. 2.

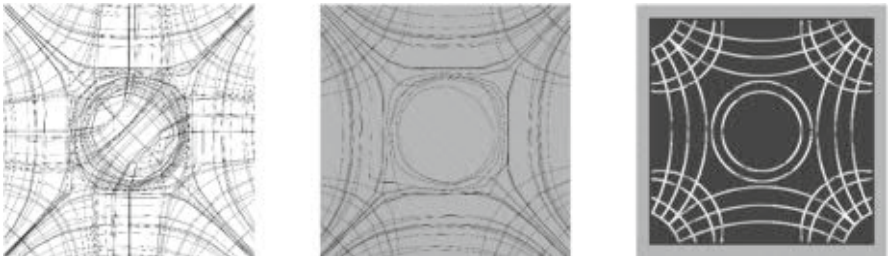


Fig. 2. a) Superimposed principal stress lines of high density, b) reduced density of lines on plate taking into consideration manufacturability, and c) final design for manufacturing.

Both bead and rib method at the end yielded similar final patterns for the boundary conditions of central concentrated load and pinned supports at the corners. They provided stiffening of the plate, one through geometry deformation and other through added material. Depending on the machine constraint, some more complex cold forming as dictated by the mathematical result of bead optimization potentially could be difficult to manufacture, while stiffening with WAAM is theoretically unconstrained for any pattern, ensuring the layer width is taken into consideration. This design study presents single-layer welded rib, however, for further stiffening, increased height of several WAAM layers would be of interest.

4 Manufacturing of Plate Ribs: Process Design and Optimization

4.1 Definition of Printing Processes

The production phase of the plates was carefully prepared due to the continuous WAAM deposition process and the need to control thermal deformations induced by heat input. All stiffening ribs were manufactured using an Omron TM5 collaborative robotic arm integrated with a Fronius welding head operating in Cold Metal Transfer (CMT) mode, enabling stable metal transfer with reduced heat input. An ER70S-6 steel wire with a diameter of 0.8 mm was selected as filler material.

The CMT process was configured with 40 cycles per sequence and a waiting time of 0.02 s to ensure stable droplet transfer and limit overheating. Pre-gas and post-gas times of 0.3–0.4 s and 0.8 s, respectively, were adopted to protect the molten pool. An 82% argon – 18% CO_2 shielding gas mixture was supplied at 13 L/min to minimize oxidation. Finally, the welding speed was set to 10 mm/s and the wire feed speed to 5 m/min, ensuring a balance between thermal control, geometric accuracy and deposition stability.

4.2 Strategic Plate Positioning

As anticipated, the treatment of the plate required a preliminary study concerning the selection of the filler wire, the optimization of the deposition strategy, and the definition of a suitable positioning and clamping methodology. The plate was fixed at its corners to a welding table designed to dissipate electric arcs, reducing out-of-plane deformations caused by shrinkage during solidification. Nevertheless, due to the small plate thickness, limited deformation in the unconstrained regions was unavoidable.

The progressive distortion along the free edges required continuous adjustment of the deposition code during manufacturing. While the initial deposition paths were executed on an undeformed surface with constant Z-coordinate, the following trajectories were modified with variable Z-values according to the evolving deformation of the plate, ensuring dimensional accuracy and consistent layer formation. In addition, the deposition sequence was optimized by first printing the lower side curves, followed by the central circles, and finally the remaining curves and corner regions in alternating stages.

4.3 Post-processing and Quality Consideration

As previously mentioned, at the end of the printing phase the plates were left on the build table to cool, allowing the cooling process to occur without introducing additional deformations beyond those already present. Once the plate had reached complete cooling, the polishing phase was carried out to forcibly remove the oxide layer that had accumulated during the deposition stage. As can be observed, gaps and streaks exhibit visible discontinuities. This is due to the deliberate reduction in power during the ignition phase of the electric arc, implemented to preserve the integrity of the plate as much as possible and to avoid further increasing the deformation that had already occurred. In fact, the reduction in arc power affects the number of cycles and the resulting imperfections; therefore, these defects are attributable to this manufacturing-related constraint. The final result of the entire printing process for the stiffening structure is shown in Fig. 3.



Fig. 3. Final printed result

5 Conclusion and Future Work

This study presented an innovative approach for the stiffening of thin metallic plates using WAAM technology, focusing on computational design optimization and the verification of its manufacturing feasibility. In the first phase of the research, through finite element method (FEM) simulations, an optimized pattern for the reinforcement ribs was developed. Based on the extraction of principal stress lines, in accordance with Nervi's design principle, a geometry capable of symmetrically dissipating the forces resulting from a central concentrated load was defined. This theoretical approach aims to maximize the structural efficiency of the component by placing additional material exclusively along the lines of maximum stress, theoretically improving its overall stiffness and stress distribution. Subsequently, the investigation demonstrated the practical feasibility of translating this mathematical model into a physical component by printing the single-layer ribs directly onto extremely thin substrates (1 mm, 1.5 mm, and 2 mm). The use of a robotic arm integrated with the Cold Metal Transfer (CMT) welding mode allowed for precise control of the thermal input. To address the inevitable challenges related to out-of-plane deformations induced by the intense thermal inputs, specific manufacturing strategies were successfully implemented: the strategic clamping of the substrate corners, the dynamic compensation of the Z-coordinate along the deposition paths, and the adoption of an alternating printing sequence. Although the rib-stiffened design was explicitly conceived to increase the stiffness of the structure, the actual mechanical performance of the component has not yet been tested in this phase of the analysis.

The present work therefore concludes by demonstrating that the structural optimization and the subsequent real-world production via WAAM of these stiffened elements are feasible and controllable. For future work, an experimental testing campaign is planned to empirically validate the numerical results. Both unreinforced reference samples and WAAM-stiffened plates will be manufactured and subjected to physical mechanical flexural tests (with a central point load and pinned supports at the corners). This subsequent phase will allow the measurement of key structural parameters to exactly quantify the actual increase in stiffness, ultimate load-bearing capacity, and resistance to maximum deflection provided by the 3D-printed deposited ribs.

References

1. Almeida A, Williams S (2019) Wire + Arc Additive Manufacturing (WAAM). Materials Science Forum, Trans Tech Publications, Switzerland, pp 1–10
2. Ding D, Pan Z, Cuiuri D, Li H (2015) Wire-feed additive manufacturing of metal components: technologies, developments and future interests. Int. J. Adv. Manuf. Technol. 81:465–481
3. Wu B et al (2018) A review of the wire arc additive manufacturing of metals: properties, defects and quality improvement. J. Manuf. Process. 35:127–139
4. Williams SW, Martina F, Addison AC, Ding J, Pardal G, Colegrove P (2016) Wire + Arc additive manufacturing. Mater. Sci. Technol. 32(7):641–647
5. Xiong J, Yin Z, Zhang W (2024) Intelligent control of arc-based additive manufacturing processes for improved geometric accuracy and mechanical performance. In: Additive Manufacturing. Elsevier, pp 1–12

6. Cong BQ, Ding J, Williams SW (2015) Effect of arc mode in cold metal transfer process on porosity of additively manufactured Al–6.3%Cu alloy. Int. J. Adv. Manuf. Technol. 76:1593–1606
7. Huang RJ, Liew JYR, Chan CH (2025) Structural performance of WAAM-fabricated steel components for construction applications. In: Additive. Manufacturing. Elsevier, pp 101–115
8. García J, Liew JYR, Huang RJ (2025) Additive manufacturing of steel structural nodes by WAAM: current applications and prospects. In: Engineering Structures. Elsevier, pp 104–119
9. Liew JYR, García J, Huang RJ (2025) Wire Arc Additive Manufacturing (WAAM) for large-scale structural steel elements. In: Construction and Building Materials. Elsevier, pp 56–70
10. So DKL, Wong BCP, Siu TSK, Xi N, Chan SL, Liu SW (2025) Design and fabrication of Hong Kong's first constructional 3D-printed metal pavilion "Weaving Love". Sci. Rep. 15:32982
11. Tankova T, Veljkovic M (2023) On-site repair and strengthening of steel members using Wire + Arc Additive Manufacturing. In: Engineering Structures. Elsevier, pp 75–89
12. Tankova T, Ojeda JE, Veljkovic M (2024) WAAM for retrofitting slender steel plates: experimental and numerical studies. In: Additive Manufacturing. Elsevier, pp 91–104
13. Veljkovic M, Tankova T, Ojeda JE (2024) Integrated WAAM-based retrofitting strategies for steel structures. J. Constr. Steel Res.:130–142
14. Timoshenko SP, Woinowsky-Krieger S (1959) Theory of Plates and Shells, 2nd edn. McGraw-Hill, New York
15. Kollbrunner CF, Basler K (1969) Torsion in Structures. Springer-Verlag, Berlin
16. Hancock GJ (1973) Buckling of Thin Plates Under Compression and Shear. University of Sydney Press, Sydney
17. Bruhn EF (1973) Analysis and Design of Flight Vehicle Structures, 2nd edn. SR Jacobs, Indianapolis
18. Niu MCY (1988) Airframe Structural Design: Practical Design Information and Data on Aircraft Structures. Conmilit Press, Hong Kong
19. Swift T, Beaumont PWR (1998) Composite and Metallic Fuselage Design: Analysis, Requirements, and Development. AIAA, Reston (VA)
20. EN 1993-2 (2006) Eurocode 3: Design of Steel Structures – Part 2: Steel Bridges. CEN, Brussels
21. Beg D, Kuhlmann U, Braun B, Davaine L (2010) Design of Plated Structures. ECCS—European Convention for Constructional Steelwork, Brussels

Robotic Repair of Steel Structural Elements by Wire Arc Additive Manufacturing

Alessandro Menghini[1(✉)], Alper Kanyilmaz[1], Saad Waqar[2], Barbara Previtali[2], and Ilchat Sabirov[3]

[1] Department of Architecture, Built Environment and Construction Engineering, Politecnico di Milano, Milan, Italy
alessandro.menghini@polimi.it
[2] Department of Mechanical Engineering, Politecnico di Milano, Milan, Italy
[3] IMDEA Materials Institute, Madrid, Spain

Abstract. This paper investigates the repair potential of Wire Arc Additive Manufacturing (WAAM) for damaged steel structural elements, combining material characterization data with a bridge-scale proof-of-concept assessment and a full-scale experimental beam repair study. The mechanical properties of WAAM-produced low-alloy steel are first presented, highlighting a homogeneous granular bainitic microstructure that provides a favourable combination of strength, ductility, fatigue resistance, and fracture toughness, exceeding the minimum requirements of European construction steels. A proof-of-concept bridge-scale numerical study then demonstrates how WAAM enables an efficient management of stress redistribution throughout the repair process, progressively restoring the local stress field to values closely approaching the undamaged configuration. Finally, a full-scale printing campaign demonstrates the manufacturability of possible WAAM repairs, produced with a high-strength low-alloy wire (AM70), of two representative damage scenarios on a 260 mm deep structural steel I-beam (base grade S355): diffuse damage on the lower flange and localised damage at the lower-flange toe propagating into the lower web.

Keywords: Wire Arc Additive Manufacturing (WAAM) · structural repair · steel bridges · fatigue resistance · fracture toughness · AM70 wire (ER100-G) · over-matching repair

1 Introduction

Extending the service life of ageing metallic infrastructure (bridges, cranes, and industrial facilities) is a central challenge for sustainable construction. In Europe alone, approximately 300,000 railway bridges are currently in operation, many of which have been in service for several decades and are approaching or exceeding their original design life [1]. Widespread replacement of these structures is neither economically nor environmentally viable, making efficient in-situ repair strategies essential. Conventional repair techniques such as stop-hole drilling [2], bolted retrofits, welded steel patches [3], and

© The Author(s), under exclusive license to Springer Nature Switzerland AG 2026
R. Zanon et al. (Eds.): CTA 2026, LNCE 942, pp. 1116–1127, 2026.
https://doi.org/10.1007/978-3-032-39505-4_97

rewelding of fatigue-cracked connections [4] are commonly employed, yet they often introduce new stress concentrations, require complex execution procedures, and lead to considerable downtime.

In recent years, metal additive manufacturing (AM) has emerged as a promising alternative for structural repair. Among the various AM techniques, Wire Arc Additive Manufacturing (WAAM) is particularly attractive due to its high deposition rate, low equipment cost relative to laser-based processes, compatibility with existing welding infrastructure, and suitability for in-situ deposition using robotic arms [5]. WAAM utilizes a continuous metallic wire melted by an electric arc to deposit material in a layer by layer manner, making it inherently scalable to the large dimensions typical of civil engineering structures. Several studies have demonstrated the viability of WAAM-based repair for damaged metallic components [6–8], including the arrest of fatigue cracks through compressive residual stresses generated by the deposition process [9–10].

Despite these advances, the effective use of WAAM for structural repair still rests on two connected requirements that have received comparatively little attention. First, the deposited material must provide mechanical properties (tensile strength and ductility, and above all fatigue and fracture resistance) adequate for the fatigue-prone details that typically govern the repair of structural steel, and these properties must be demonstrated for the specific feedstock and process actually used. Second, the repair cannot be treated as a mere deposition task but must be conceived as a design problem, effective both at the process level (sound, defect-free deposition with controlled heat input and adequate torch accessibility) and at the structural level (a deliberate management of the stress field that restores the load-carrying capacity of the member). To the best of the authors' knowledge, no study in the literature has yet connected these two aspects by linking the mechanical performance achievable with WAAM to a repair concept validated from the bridge scale down to a full-scale physical trial. As a preliminary, proof-of-concept contribution towards this gap, this paper combines the mechanical characterization of the WAAM-produced steel with a bridge-scale numerical assessment of the repair concept and a full-scale experimental WAAM repair of a structural steel beam.

2 Mechanical Characterization of WAAM-Produced Steel

Initially, walls were deposited through WAAM using low-alloy steel wire feedstock (3Dprint AM70, Böhler, 1.2 mm diameter), with nominal composition (wt.%): C 0.08, Si 0.6, Cr 0.2, Mn 1.7, Ni 1.5, Mo 0.5, bal. Fe. These deposited walls were subsequently characterized through microstructural analysis, tensile testing (ASTM E8), high-cycle fatigue testing (ISO 1099), and fracture testing (ASTM E1820). Subsequently, using the same feedstock material (3Dprint AM70, Böhler, 1.2 mm diameter), a beam section was repaired as described in Sect. 4, so that the characterised properties can be used as an orientation to study the deposited repair material.

Test specimens were extracted by electrical discharge machining (EDM) from WAAM fabricated walls with dimensions of approximately 100 × 107 × 10 mm for the tensile specimens and approximately 225 × 190 × 10 mm for the fatigue specimens, in such a way that the gauge sections were aligned with the mid-region of the walls. The specimen surfaces were then finished by standard metallographic techniques

to remove machining defects. Tensile and fracture specimens were machined at 0°, 45° and 90° to the building direction, whereas fatigue specimens were limited to 0° and 90°. For microstructural analysis, samples were ground and polished to a 1 μm diamond and 0.03 μm alumina finish, etched with Vilella's reagent (4–5 s) and examined on the plane parallel to the building direction by light optical microscopy (LOM, Nikon Eclipse LV100ND) and field-emission scanning electron microscopy (FEG-SEM, Thermo Fisher APREO 2S); electron backscatter diffraction (EBSD) was acquired with a 0.075 μm step at 20 kV on 70°-tilted samples and processed with the MTEX toolbox, while transmission electron microscopy (TEM, FEI Talos F200X, 200 kV) was performed on electropolished foils.

2.1 Microstructure

The WAAM material exhibited columnar grains aligned with the building direction. As these columnar dendritic structures tend to grow along the heat dissipation direction, they are aligned with the loading direction (Fig. 1). These columnar grains exhibit a complex microstructure, analogous to the tempered martensite and bainite phases that are often dominant in structural steel alloys.

EBSD analysis revealed an effective bainitic ferrite size of 0.62 μm and a weak crystallographic texture (maximum multiples of uniform density, MUD = 1.95). No retained austenite was detected. TEM analysis identified oxide and oxysulphide inclusions rich in Si, Mn, and Ti (250–450 nm). This homogeneous bainitic microstructure proved to be the key factor behind the good cyclic and dynamic performance of WAAM steel.

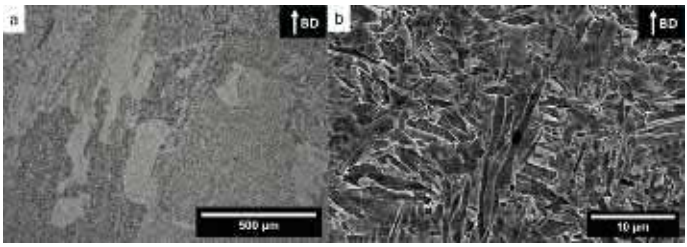


Fig. 1. Microstructure of WAAM-produced steel: a) LOM and b) SEM.

2.2 Tensile Properties

Table 1 summarizes the tensile properties at three orientations relative to the building direction. Sub-size specimens with a 25 mm gauge length and a thickness of 1.33–1.58 mm (ASTM E8) were tested at room temperature on an INSTRON 8808 system using an extensometer. The material exhibited moderate strength (YS 429–517 MPa, UTS 770–807 MPa) combined with high ductility (εu 10.5–11.2%, εf 16.4–17.7%) and substantial strain hardening (n = 0.17–0.19). Tensile properties showed minimal

anisotropy, with only a modest increase in yield strength at 90°. Compared with conventional construction steels (EN 10025-2 and -4, grades S275–S460), the WAAM material exceeds the minimum strength requirements while maintaining adequate ductility.

Table 1. Tensile properties of WAAM-produced steel. Orient.: orientation relative to the building direction; E: Young's modulus; YS: yield strength; UTS: ultimate tensile strength; εu: uniform elongation; εf: elongation at fracture; n: strain-hardening exponent.

Orient. [°]	E [GPa]	YS [MPa]	UTS [MPa]	εu [%]	εf [%]	n
0	176 ± 20	429 ± 22	770 ± 24	10.5 ± 0.6	16.4 ± 1.3	0.19
45	170 ± 18	439 ± 11	771 ± 31	10.6 ± 0.4	16.6 ± 1.9	0.19
90	175 ± 31	517 ± 102	807 ± 51	11.2 ± 1.2	17.7 ± 1.4	0.17

2.3 High-Cycle Fatigue Properties

High-cycle fatigue tests were carried out on flat dog-bone specimens with an overall length of 100 mm, a grip width of 25 mm, a reduced gauge width of 12 mm and a fillet radius of 12.5 mm; the gauge thickness ranged from 1.43 to 1.59 mm (Fig. 2). The tests were performed in pull–pull, stress-controlled mode under a sinusoidal waveform at a load frequency of 50 Hz on an INSTRON 8802 servo-hydraulic system, in accordance with ISO 1099. Both the 0° and the 90° orientations relative to the building direction were investigated, run-out was defined at 10^7 cycles and the fatigue limit was estimated from the resulting S-N curves. Expressed in terms of the maximum stress σmax at a stress ratio $R = 0.1$, the WAAM material exhibited fatigue limits of 590 MPa at 0° and 600 MPa at 90°, corresponding to approximately 77% and 74% of the respective ultimate tensile strengths (Fig. 2). Such a high ratio is remarkable for an additively manufactured steel and indicates a near-isotropic fatigue behaviour. Fractographic analysis showed that the fatigue cracks initiated predominantly at the specimen surface and propagated transgranularly, confirming the absence of critical internal defects.

The excellent fatigue resistance of the WAAM steel can be attributed to three main factors. First, its homogeneous granular bainitic microstructure avoids the sharp phase boundaries and brittle regions typical of martensitic microstructures. Second, the multi-layer deposition provides an inherent in-situ stress relief, as each successive layer partially re-heats and relaxes the residual stresses in the material underneath. Third, the wire-fed arc process is characterised by a low defect density and avoids the lack-of-fusion porosity and entrapped gas defects commonly found in powder-based AM techniques. These characteristics are particularly relevant for structural repair applications, where the deposited material must withstand cyclic loading at the stress levels typically encountered in the fatigue-prone details of steel bridges and welded connections.

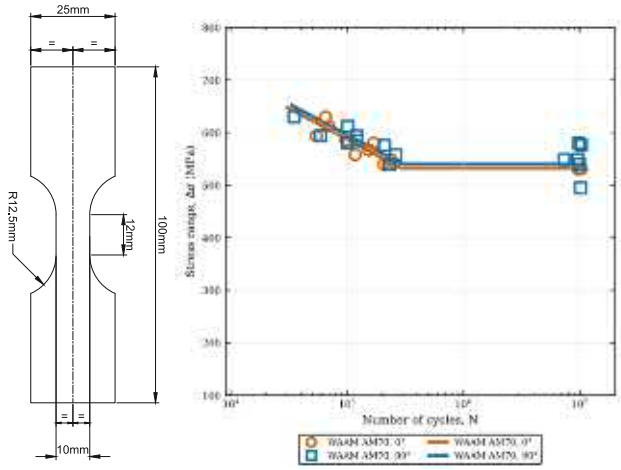


Fig. 2. S-N curves from high-cycle fatigue testing of WAAM-produced steel (R = 0.1).

2.4 Fracture Toughness

Fracture toughness was measured at three orientations on single-edge notch bend (SENB) specimens (120 mm long, 25 mm wide) machined by EDM, with a 12 mm notch sharpened with a razor blade and 1.25 mm symmetric side grooves to promote plane-strain conditions; after fatigue pre-cracking to a crack-length-to-width ratio a_0/W of 0.45–0.55, the tests were run in displacement control (ASTM E1820) with crack growth monitored by the direct-current potential-drop (DCPD) method. The WAAM material exhibited JIC values ranging from 213 kJ/m^2 (0°) to 250 kJ/m^2 (90°), KJIC values of 201–220 MPa·m½, and crack-tip opening displacement (CTOD) values of 0.53–0.60 mm (Table 2). The high CTOD values indicate substantial crack-tip blunting before unstable crack growth, reflecting the material's capacity for plastic deformation. The modest increase in toughness with build angle (17% higher JIC at 90° vs. 0°) indicates reasonably isotropic fracture behaviour, confirming that WAAM material is well-suited for damage-tolerant structural applications.

Table 2. Fracture toughness of WAAM-produced steel. JIC: J-integral fracture toughness; KJIC: fracture toughness derived from JIC; CTOD: crack-tip opening displacement.

Orient. [°]	JIC [kJ/m^2]	CTOD [mm]	KJIC [MPa·m½]
0	213	0.60	201
45	244	0.53	213
90	250	0.56	220

3 Proof-of-Concept: Bridge-Scale Repair Assessment

To demonstrate how WAAM can be employed to efficiently manage stress redistribution during the repair of a real structural component, a proof-of-concept numerical study was carried out on a fatigue-cracked steel bridge girder. The proposed repair methodology (Fig. 3) consists of two steps: (i) installation of a temporary bolted cover plate to maintain load-carrying capacity during material removal, followed by controlled milling to remove crack-affected material; (ii) WAAM cold metal transfer (CMT) deposition to fill the milled cavity with successive beads, re-establishing the original cross-section. The cavity geometry was designed as a trapezoidal groove with corner radii of at least 25 mm to minimize stress concentrations at the groove terminations, and a transverse raster deposition strategy was adopted, consistent with the experimental repair presented in Sect. 4. The numerical study presented here and the physical trial of Sect. 4 are complementary demonstrations at two scales: the former quantifies the stress-management rationale on a representative bridge girder, while the latter proves the manufacturability of a sound repair on a full-scale steel member.

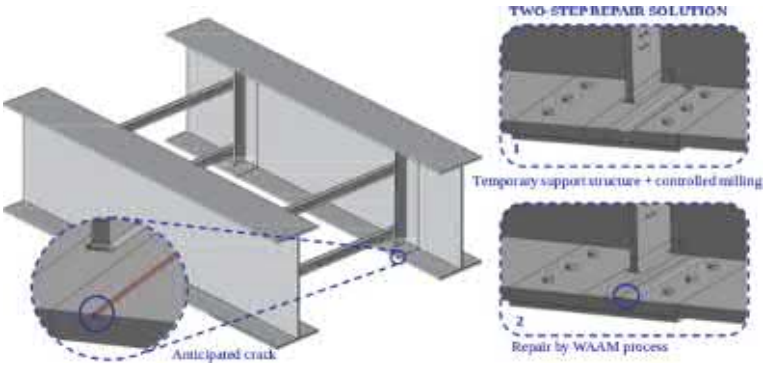


Fig. 3. Proposed WAAM repair methodology for a fatigue-cracked girder bridge.

The analysis was performed on a representative composite bridge cross-section reflecting a typical European single-span railway bridge, with S355 steel I-girders (web height 2480 mm, flange thickness 50 mm) and a C25/30 reinforced concrete deck. The local model was extracted as a submodel from a calibrated global beam-element model, with the global displacement field imposed at the submodel boundaries. The applied loading comprised the structural self-weight together with a representative service train passage with a maximum axle load of 20.5 t. The damaged flange region was discretised with a refined mesh of 5 mm (against a 50 mm global element size), giving approximately 2.75×10^5 nodes. Three configurations were compared (Fig. 4): a cracked state with a 25 mm-deep triangular notch in the lower flange, a temporary repair with trapezoidal groove and bolted cover plate, and the final WAAM-repaired state. The results illustrate the ability of WAAM to govern the stress field during each repair phase. In the cracked state, principal stress peaks reached 50–62 MPa at the crack tip—about 3.1–3.3 times the value of the repaired configurations (a stress-concentration factor of $\approx$3), with the

elevated stresses confined within 30–40 mm of the crack tip and a crack-opening displacement of 0.15 mm under service loads. The temporary bolted repair controlled the stress redistribution at groove edges to approximately 58 MPa, while the final WAAM deposit restored principal stresses to 15–18 MPa—virtually identical to the intact configuration. This demonstrates that WAAM-based repair enables an effective step-by-step management of the local stress distribution, progressively reducing stress concentrations until the original structural performance is recovered. Because it is based on local principal stresses under a representative service load, the present analysis is intended as a qualitative assessment of the elastic stress redistribution achieved by the repair rather than a fatigue-life calculation, which would additionally require the cyclic stress range $\Delta\sigma$. The present model is linear-elastic and therefore neglects the beneficial compressive residual stresses induced by the deposition process; published work on WAAM crack repair attributes to such residual stresses a major share of the stress-intensity reduction [9], so the actual fatigue benefit is expected to exceed the elastic estimate reported here. Quantifying this contribution requires dedicated residual-stress measurement, which is left to future work.

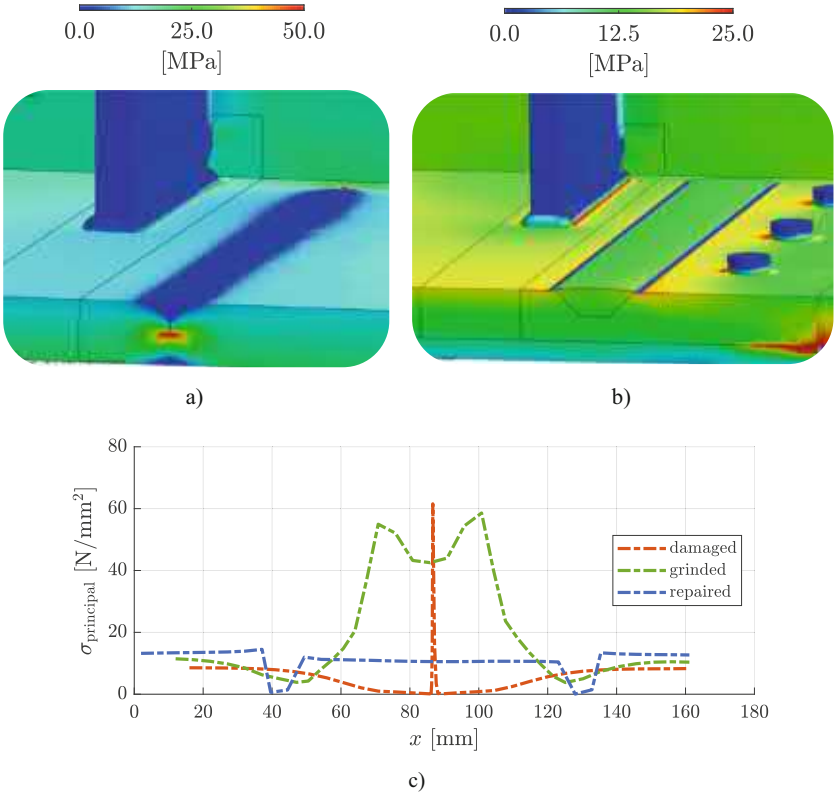


Fig. 4. Bridge-scale numerical analysis: cracked flange (a), repaired configuration (b), and principal stress results (c).

4 Experimental Repair of a Structural Steel Beam

Building on the favourable mechanical properties of the WAAM-produced steel, an experimental repair campaign was carried out on a full-scale structural member. The campaign was conceived as a proof of concept for WAAM-based repair strategies, and two representative damage scenarios were investigated (Fig. 5). The first reproduces a diffuse, large-area damage (namely diffuse corrosion damage on the lower flange of the beam); in this case the repair was carried out with the beam rotated so that the favourable building direction coincided with the direction of gravity during deposition. The second reproduces a localised damage (namely a fatigue crack initiating at the root of the lower-flange toe, where the stress-concentration factor is highest, and propagating partly into the lower portion of the web); in this case the building direction was kept parallel to the girder height, in order to assess the feasibility of an in-situ repair performed without rotating or otherwise repositioning the member. The campaign was aimed at demonstrating the feasibility of WAAM as an in-situ repair route for conventional steel structures; the assessment of the repair effectiveness from a structural and mechanical standpoint lies beyond the scope of the present study. Likewise, the preparatory milling operations are assumed to have been already performed, the focus being on the subsequent deposition process. Both repairs were performed on a 260 mm deep structural steel I-beam (base grade S355).

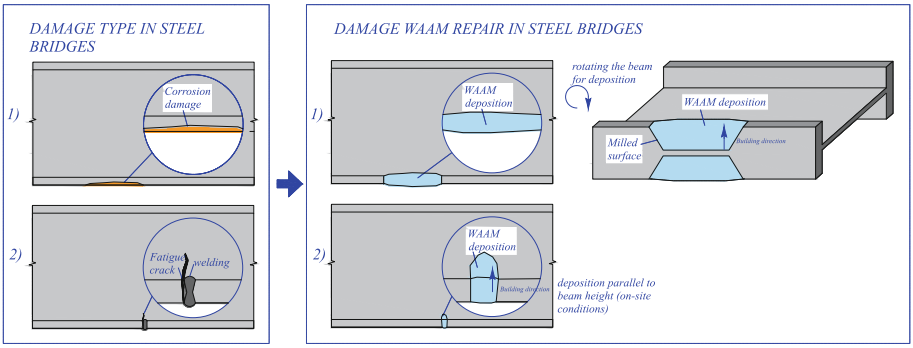


Fig. 5. WAAM repair strategies for the two investigated damage scenarios: diffuse corrosion damage and a local fatigue crack.

The repair geometry was not defined a priori but emerged from the deposition trials, in which two competing requirements had to be reconciled: achieving adequate fusion between the AM70 wire and the groove side walls, and limiting both the deposited volume and the heat input to the thin (4 mm) web. Several considerations arose during printing. Vertical side walls were found to hinder torch access and to promote side-wall lack-of-fusion; inclining them to approximately 70° by milling restored accessibility and consistently produced sound side-wall fusion. In the fatigue-crack repair the same 70° inclination was retained and, to further ease torch access to the root, the beam was chamfered on both sides. A groove width of 12–14 mm proved to be the minimum that still allowed the CMT torch to reach all regions of the notch. The groove geometry

resulting from these trials, with inclined walls extending down to the lower flange and a tapered profile converging on the crack tips, is shown in Fig. 6 and dimensioned in Fig. 7.



Fig. 6. Groove geometry trials on coupon specimens: machined notch profiles with inclined side walls (left); CMT torch positioned at the groove root during initial deposition (right).

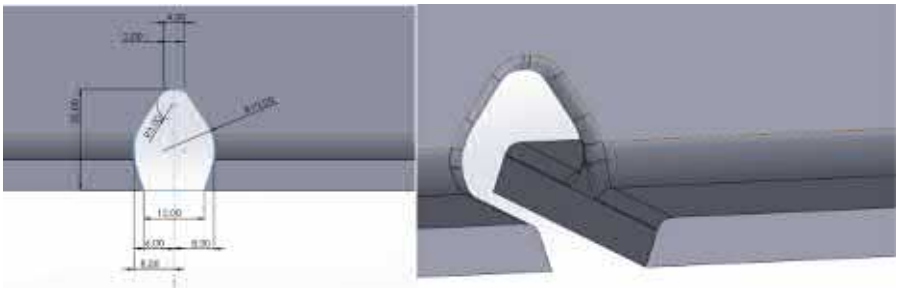


Fig. 7. Proposed (designed) groove geometry for the WAAM repair of the beam web: dimensioned cross-section (left) and rendered profile in the web–flange region (right).

Both repairs were performed with the robotic CMT system described in Sect. 2 (Fig. 8), which fed the high-strength low-alloy wire (Böhler 3Dprint AM70, AWS ER100-G, 1.2 mm in diameter) at a wire feed rate of 4 m/min and a travel speed of 8 mm/s under a C-8 shielding gas. The full set of process parameters is summarised in Table 3. With a deposited yield strength of 429–517 MPa against the 355 MPa of the S355 base, the repair over-matches the parent metal, which is favourable for restoring the local load-bearing capacity. The groove was first machined to the designed geometry (Figs. 6 and 7) and then filled layer by layer along a raster path. To promote a uniform build-up, the deposition direction was reversed by 180° at each successive layer, the deposit progressing from the narrow root towards the wider upper region until the original profile of the damaged region was restored.



Fig. 8. Robotic WAAM repair of the beam: CMT torch in the web groove during deposition, with the first layers already laid (top); first deposit at the web-to-flange junction, with the backing bar clamped beneath the flange (bottom).

Table 3. Process parameters adopted for the WAAM-CMT repair of the steel beam.

Parameter	Value
Welding technology	Cold Metal Transfer (CMT)
Wire material	Böhler 3Dprint AM70 (AWS ER100-G)
Wire diameter	1.2 mm
Wire feed rate	4 m/min
Voltage	13.5 V
Current	146 A
Robot travel speed	8 mm/s
Shielding gas	C-8 (92% Ar – 8% CO_2)
Shielding gas flow rate	16 L/min
Overlapping ratio of adjacent weld beads	26.4%
Path planning strategy	Raster – deposition direction reversed 180° each layer

The procedure produced sound, over-matching deposits that filled the machined grooves and restored the original profile of the beam, confirming the manufacturability of an in-situ WAAM repair on a full-scale steel member; the inclined side walls and tapered profile performed as intended, ensuring side-wall fusion with a contained heat input. The trials nonetheless identified the main process challenges to be addressed for practical deployment: control of the residual stresses arising from the localised thermal cycle, management of the heat-affected zone in the thin web, uniformity of the deposited surface, and accessibility of the torch to the defect within the steel section. A quantitative assessment of the deposit soundness and of the mechanical performance of the repaired member is the object of ongoing work.

5 Conclusions

This paper combined material characterization data with experimental and numerical evidence to demonstrate the repair potential of Wire Arc Additive Manufacturing for damaged steel structural elements. The WAAM-produced low-alloy steel investigated in this study exhibits a homogeneous granular bainitic microstructure yielding moderate strength (YS 429–517 MPa, UTS 770–807 MPa), high ductility (εf 16.4–17.7%), good fatigue resistance (σmax = 590–600 MPa, ≈77% of UTS), and high fracture toughness (JIC = 213–250 kJ/m^2). These properties exceed the minimum requirements of European construction steels and confirm the suitability of WAAM for structural repair applications. A proof-of-concept bridge-scale numerical study illustrated how WAAM enables a step-by-step management of the stress redistribution during repair, progressively reducing the local principal stresses towards the undamaged configuration. A full-scale experimental campaign then demonstrated, as a proof of concept, the manufacturability of over-matching WAAM repairs of two representative damage scenarios on a 260 mm deep structural steel I-beam (base grade S355): diffuse damage on the lower flange and localised damage at the lower-flange toe propagating into the lower web, both repaired with AM70 wire. The repair geometries, defined through the deposition trials with inclined side walls and a tapered profile, ensured adequate side-wall fusion while limiting the heat input to the thin web, and the original profile was restored in both cases. The trials also highlighted the main process challenges to be addressed for practical deployment: control of residual stresses, management of the heat-affected zone, uniformity of the deposited surface, and torch accessibility to the defect within the steel section. Future work should address residual-stress characterisation, non-destructive assessment of deposit soundness, and mechanical testing of repaired members under static and variable-amplitude fatigue loading, leading to full-scale validation on representative bridge components.

Acknowledgments. This work was funded by the European Union through the Research Fund for Coal and Steel (RFCS), under the BriBotic project (Steel Bridge sustainable Repairs with Robotic solutions, Grant Agreement No. 101294240) and the CONSTRUCTADD project (Resource Efficient Construction using Additive Manufacturing), and by Fondazione Ico Falck through the AURELiA project (AUtomated REpair of steeL bridges viA additive manufacturing); the support of the RocWAAM project is also acknowledged. The authors thank Ismail Kurt for carrying out the WAAM repair deposition trials presented in Sect. 4, and gratefully acknowledge Fronius

International GmbH, ABB Robotics and Arroweld Italia for their hardware and technical support, Voestalpine Böhler Welding for supplying the filler material, and all project partners for their contributions.

References

1. Horas CS, Silva JN, Correia JAFO, De Jesus AMP (2023) Fatigue damage assessment on aging riveted metallic railway bridges: a literature review. Structures 58:105664. https://doi.org/10.1016/j.istruc.2023.105664
2. Ayatollahi MR, Razavi SMJ, Chamani HR (2014) Fatigue life extension by crack repair using stop-hole technique under pure mode-I and pure mode-II loading conditions. Procedia Eng. 74:18–21. https://doi.org/10.1016/j.proeng.2014.06.216
3. Al-Emrani M (2002) Fatigue in Riveted Railway Bridges. Chalmers University of Technology, Göteborg
4. Unglaub J, Begemann F, Hensel J, Thiele K (2024) Welding under service conditions – monitoring, repair strategy and rehabilitation. Procedia Struct. Integr. 64:918–924. https://doi.org/10.1016/j.prostr.2024.09.367
5. Gardner L (2023) Metal additive manufacturing in structural engineering – review, advances, opportunities and outlook. Structures 47:2178–2193. https://doi.org/10.1016/j.istruc.2022.12.039
6. Lee JH, Lee CM, Kim DH (2022) Repair of damaged parts using wire arc additive manufacturing in machine tools. J. Mater. Res. Technol. 16:13–24. https://doi.org/10.1016/j.jmrt.2021.11.156
7. Li Y, Han Q, Horváth I, Zhang G (2019) Repairing surface defects of metal parts by groove machining and wire+arc based filling. J. Mater. Process. Technol. 274:116268. https://doi.org/10.1016/j.jmatprotec.2019.116268
8. Zhang S et al (2023) Laser additive manufacturing for infrastructure repair: a case study of a deteriorated steel bridge beam. J. Mater. Sci. Technol. 154:149–158. https://doi.org/10.1016/j.jmst.2023.01.018
9. Ghafoori E et al (2023) Fatigue strengthening of damaged steel members using wire arc additive manufacturing. Eng. Struct. 284:115911. https://doi.org/10.1016/j.engstruct.2023.115911
10. Dahaghin H et al (2024) Wire and arc additive manufacturing for strengthening of metallic components. Thin-Walled Struct. 203:112074. https://doi.org/10.1016/j.tws.2024.112074

Structural Engineering Insights from Darkside-20k: Steel Design for Underground and Cryogenic Environments

Michele Angiolilli[1](✉), Andrea Zani[2], Marco Carlini[3], Roberto Tartaglia[3], Marta Galuppi[3], Filippo Grande[3], Andrea Ianni[4], Mario D'Aniello[5], and Marzio Nessi[6]

[1] Gran Sasso Science Institute, L'Aquila 67100, Italy
michele.angiolilli@gssi.it
[2] INFN-Milano, Milan 20133, Italy
[3] INFN-Laboratori Nazionali del Gran Sasso, L'Aquila 67100, Italy
[4] Princeton University, Princeton, NJ 08544, USA
[5] University of Naples Federico II, Naples 80125, Italy
[6] INFN-Roma, Rome 00186, Italy

Abstract. Steel construction is increasingly extending beyond conventional buildings and industrial plants into advanced facilities where structural systems must satisfy demanding mechanical, thermal and operational requirements. Underground cryogenic research infrastructures represent one of the most challenging examples, requiring structural solutions capable of integrating materials with markedly different mechanical and physical properties while ensuring safety, constructability and long-term performance. The DarkSide-20 k experiment, currently under construction at the INFN Gran Sasso National Laboratory (Italy), provides a representative case study. The facility includes a large cryogenic cryostat approximately 11 m in size, hosting detector systems operating at liquid argon temperature and characterized by a total mass of about 30 t. The project required the development of permanent and temporary steel structures capable of functioning in confined underground spaces, under seismic demand, with strict dimensional tolerances, modular assembly constraints and interaction with precision scientific equipment. Rather than acting solely as the primary load-bearing material, structural steel forms the backbone of a hybrid structural system interacting with cryogenic stainless-steel membranes, multi-layer insulation, polymeric and composite components, elastomeric interfaces and precision mechanical equipment. Achieving the required performance demanded a careful balance between structural stiffness, mechanical resistance, thermal compatibility and construction requirements. This paper presents the principal steel engineering solutions developed for the project, including modular supporting structures, removable temporary works and hybrid interfaces, highlighting design principles that can be transferred to future cryogenic, underground and high-technology industrial facilities.

Keywords: Structural Engineering · Steel Structures · Underground Structures · Cryogenic Structures · Seismic Engineering · Experimental Facilities

© The Author(s), under exclusive license to Springer Nature Switzerland AG 2026
R. Zanon et al. (Eds.): CTA 2026, LNCE 942, pp. 1128–1137, 2026.
https://doi.org/10.1007/978-3-032-39505-4_98

1 Introduction

Structural steel is commonly associated with buildings, bridges and industrial plants, where its role is primarily understood in terms of load-bearing capacity, stiffness, ductility and ease of fabrication. In highly specialized infrastructures, however, these conventional advantages remain necessary but are no longer sufficient. Steel structures must interact with materials and technological components whose functions extend beyond structural resistance to include thermal insulation, cryogenic containment, electrical isolation and precision equipment support.

This condition is particularly evident in underground cryogenic research facilities, where the structural system becomes part of a highly integrated multi-material assembly. The engineering challenge therefore extends beyond the optimization of steel members, requiring a balanced design that simultaneously addresses mechanical performance, thermal compatibility, differential deformation, radiopurity constraints, constructability and long-term serviceability.

The DarkSide-20 k experiment, currently under construction at the INFN Laboratori Nazionali del Gran Sasso (Italy), provides a representative example of these engineering challenges. Although conceived for next-generation dark matter detection, the facility required the development of a large underground cryogenic infrastructure in which structural design was governed not only by the operational configuration, but also by construction, installation and maintenance requirements.

The underground location significantly increased the engineering complexity by imposing severe geometric constraints, restricted access, modular construction strategies, stringent dimensional tolerances and significant seismic demand. Furthermore, several critical design conditions arose during intermediate construction stages, when temporary steel structures, lifting systems and partially assembled configurations became governing components of the structural response. Consequently, the engineering design evolved beyond the conventional verification of the completed structure to encompass the entire construction sequence, from fabrication and underground assembly to final operation.

A comprehensive description of the DS20k infrastructure can be found in [1]. The full-scale experimental system, representing a distinctive engineering feature of the DS-20 k project, is further detailed in [2].

Leaving aside the scientific aspects of the experiment, this paper presents the principal structural steel engineering solutions developed for the facility and discusses their potential applicability to other underground and industrial infrastructures.

2 Facility Overview and Structural Challenges

2.1 Cryostat Outer Structure

The DarkSide-20 k cryostat is a membrane-type cryogenic tank derived from membrane technology originally developed for large liquefied natural gas storage and further adapted for particle-physics applications [3]. It was specifically designed to store approximately 700 m^3 of liquid argon at 87 K (namely about −186 °C) while supporting the detector systems required for dark matter searches. The structural concept relies on a

hybrid system in which the external steel framework provides the primary load-bearing structure, whereas the internal membrane and insulation system (approximately 0.8 m thick) ensures cryogenic containment.

The cryostat has nominal external dimensions of 11.41 m × 11.41 m in plan and 10.76 m in height, enclosing an internal volume of approximately 8.55 m × 8.55 m × 7.90 m. These dimensions are dictated by the required active detector volume together with insulation thickness, service penetrations, installation constraints and the clearances necessary for the suspended detector components.

The cryostat lies on a 280 mm thick C50/60 reinforced concrete sub-foundation with a multilayer interface consisting of G10 electrical insulation, steel plates and elastomeric pads. Besides ensuring electrical insulation, this support system accommodates local contact pressures and contributes to the dynamic behaviour of the structure by partially decoupling the cryostat from its foundation. The structure is intentionally left free from vertical anchorage, while horizontal actions are resisted through dedicated S460 steel brackets acting as unilateral restraints after closure of nominal gaps introduced to preserve the electrical insulation layers.

The structure is designed to resist the hydrostatic pressure exerted by the stored liquid argon, the hydrodynamic pressures induced by the impulsive and convective response of the liquid during seismic excitation, the internal gas overpressure, the permanent load of the suspended detector system (approximately 30 t), and all code-prescribed seismic load combinations. The seismic design explicitly accounted for fluid– structure interaction effects, which govern the distribution of dynamic pressures acting on the membrane containment system and significantly influence the global response of large cryogenic tanks. Owing to the strategic importance of the Gran Sasso National Laboratory, the facility was designed according to the Italian seismic code for Use Class IV structures, adopting a reference seismic life of 100 years and a low-ductility design approach.

The primary supporting structure consists of a three-dimensional lattice assembled from S460ML IPE600V steel members connected through M36 grade 10.9 preloaded HV bolted joints. Externally to the insulation system, a 10 mm thick stiffened steel plate, referred to as the tertiary membrane, provides both a gas-tight enclosure for the nitrogen-filled insulation volume and additional global stiffness to the cryostat.

The original design assumed continuous welded connections between the tertiary membrane and the supporting frame. However, the confined underground construction environment made the execution of hundreds of high-quality welds impractical because of fabrication tolerances, residual stresses, thermal distortions and installation constraints. The welded solution was therefore replaced by dedicated S355NL clamped connections, each secured by two M12 preloaded bolts to the membrane stiffeners and one preloaded M16 bolt to the beam flanges. While considerably improving constructability and installation flexibility, this modification also altered the structural interaction between the tertiary membrane and the steel frame.

A dedicated study was carried out to compare the original welded configuration with the as-built clamped solution, highlighting that the clamped solution produced global displacements about 60% larger than the welded configuration owing to its lower rotational restraint. Nevertheless, the maximum displacement (13.3 mm) remained well

below the H/500 serviceability limit (21.6 mm), with stresses below the design limits, confirming the structural adequacy of the clamped solution. The sensitivity of the clamped connection to realistic installation imperfections was further investigated by accounting for fabrication tolerances and bolt-tightening-induced clamp misalignment, which may cause localized bending of the tertiary membrane stiffeners and secondary stresses in the bolts. Detailed finite element analyses (FEA) enabled the definition of an optimized bolt-tightening procedure to minimize these effects.

2.2 Cryogenic Containment System

The steel outer structure encloses a membrane cryostat specifically designed for long-term storage of liquid argon at approximately 87 K. The cryogenic containment system consists of multiple insulation layers, including plywood, reinforced polyurethane foam, a composite secondary membrane and a 1.2 mm thick corrugated SS primary membrane directly in contact with the liquid argon. The corrugation of the primary membrane accommodates the large thermal contractions occurring during cool-down while maintaining liquid tightness. The entire insulation and containment system is based on the membrane technology originally developed by Gaztransport & Technigaz for liquefied natural gas storage and subsequently adapted for large underground particle-physics experiments. An overall insulation thickness of approximately 800 mm is adopted to satisfy the stringent thermal requirements of the facility.

The integration of the cryogenic containment with the steel supporting structure follows two distinct construction strategies. For the bottom slab and the lateral walls, the insulation system was assembled directly on site by progressively bonding the insulation panels to the previously installed tertiary membrane, itself connected to the steel lattice through dedicated clamping devices. Conversely, the roof adopted a fully modular construction philosophy. Each of the five top-cap modules—comprising one central module, two long modules and two short modules—was completely prefabricated above ground as an integrated unit, combining the steel supporting frame, the tertiary membrane and the complete insulation system. The finished modules were subsequently transported underground and installed as single assemblies, substantially reducing underground fabrication activities, improving quality control and minimizing installation time. Following an initial installation to verify geometric tolerances, four of the five top-cap modules were temporarily removed to allow installation of the suspended detector before final reassembly.

Although the membrane system was primarily designed for cryogenic containment under operating conditions, the detector installation strategy was revised during the project development. Instead of installing a largely pre-assembled detector inside the cryostat, the final approach required in-situ assembly of the detector. This decision reduced the risk of transport-induced damage, ensured the required cleanliness standards, and overcame dimensional constraints associated with underground access and handling (Fig. 1).

The revised installation strategy fundamentally changed the construction loading conditions acting on the cryostat. During detector assembly, the cryogenic containment system had to accommodate personnel, lifting equipment, temporary tooling and the progressive installation of detector components. However, the primary SS membrane and



Fig. 1. (a–g) Installation sequence of the cryostat.

the underlying insulation system were designed exclusively for cryogenic containment under operating conditions and were not intended to sustain concentrated construction loads. To enable in-situ detector assembly while preserving the integrity of the cryogenic containment system, a dedicated removable steel false floor was developed. The structure was designed to completely isolate the primary membrane and the underlying insulation system from temporary construction loads by transferring all installation actions directly to the reinforced concrete sub-foundation through a network of discrete support feet. In addition to providing adequate strength and stiffness for assembly operations, the system had to satisfy stringent constructability requirements, including modular underground installation, compatibility with confined spaces, and complete removability through the DN700 cryostat access opening after completion of detector installation. The installation sequence of the false floor is reported in Fig. 2.

The design of the false floor required a multi-scale numerical investigation. Initial calculations were made to optimize the load-transfer mechanism between the SS walking surface, the supporting steel members and the discrete support feet. These analyses guided the selection of the plate thickness, supporting members, grating system and support footprint to minimize local stress concentrations while ensuring an efficient distribution of concentrated loads.

Subsequently, more detailed calculations were extended to explicitly include the complete multilayer cryogenic insulation system beneath each support foot. Unlike simplified spring-based approaches, the adopted fully coupled model explicitly represented the SS membrane together with each insulation layer, allowing the actual stiffness interaction and contact behaviour between the false floor and the cryogenic containment system to be reproduced. This modelling strategy enabled direct evaluation of stress and deformation fields within the insulation materials, particularly the reinforced polyurethane foam, which represents the most compliant component of the containment system.

The structural response of the insulation was first evaluated under the operational loading condition generated by liquid argon, which represents the design condition of the membrane system. This reference configuration was subsequently compared with

the most demanding installation scenarios, including the temporary support of the fully assembled detector on temporary feet and the movement of heavy components along dedicated rail systems.



Fig. 2. (a–d) Installation sequence of the temporary false floor inside the cryostat.

2.3 Detector

Suspended from the cryostat roof is the DarkSide-20 k detector, a dual-phase liquid argon time projection chamber (LAr-TPC) housed within a low-radioactivity SS vessel (see Fig. 3). The complete suspended system has an overall mass of approximately 30 t and is supported through a dedicated suspension system designed to accommodate thermal contraction while maintaining the strict alignment tolerances required for detector operation. Owing to the interaction between the suspended detector and the surrounding cryostat, dedicated dynamic analyses were also performed to evaluate the seismic response of the suspension system, including detector oscillations and potential impacts between adjacent suspension rods under extreme loading conditions [4]. The detector combines thick PMMA structural components (barrels, anode, and cathode), SS vessels, extraction grids, and optical-plane support structures with arrays of silicon photomultipliers operating at cryogenic temperature. The interaction between materials exhibiting markedly different thermo-mechanical properties, together with stringent radiopurity requirements and sub-millimetric alignment tolerances, imposed engineering constraints extending well beyond conventional strength verification. Differential thermal contraction, frictional interfaces, buoyancy effects under cryogenic conditions, assembly tolerances and construction sequencing became governing design criteria for several detector components.

In the following, some of the key engineering aspects of the main steel components are described.

Regarding the stainless-steel vessel, besides satisfying conventional structural requirements, its design was strongly driven by stringent radiopurity constraints, which

required minimizing the structural mass and the amount of passive material surrounding the active detector volume. The resulting slender shell structure required circumferential and longitudinal stiffening ribs to prevent local buckling while maintaining a limited weight. Dedicated nonlinear stability FE analyses were therefore carried out to optimize the stiffening layout throughout fabrication, transportation and operation. A further engineering challenge concerned the circumferential closure of the vessel. To allow transportation and assembly inside the underground laboratory, the vessel was manufactured in 6 separate segments (two domes and four barrels) joined through specially designed lips sealed by autogenous laser welding performed exclusively from the external side. This solution eliminated internal welding operations, preserving detector cleanliness while minimizing geometric distortions and ensuring the dimensional accuracy required for the subsequent assembly of the internal detector components.

Another critical steel component of the detector is represented by the optical planes, which simultaneously act as the mechanical support for the photodetector units and as the optical interface of the detector. Their design must combine high stiffness with limited structural mass while accommodating thermal contraction, localized support reactions and the stringent alignment requirements of the photodetector arrays. Although the Top and Bottom Optical Planes (TOP and BOP) share essentially the same structural concept, the BOP represents the most demanding configuration, as it supports suspended detector components while operating in close proximity to the cathode under cryogenic conditions. Its structural behaviour is governed by the simultaneous action of self-weight, suspended detector loads, bolt pretension, spring-loaded interfaces and cryogenic thermal contraction. Dedicated three-dimensional thermo-mechanical finite element analyses were therefore developed, explicitly modelling welded joints, bolted connections and the equivalent masses of the PMMA components and photodetector units. The analyses identified the collar regions and corner pillars as the most critical locations, where weld constraints, bolt preload and local load transfer generate the highest stress concentrations. A further engineering challenge arose during detector cooldown. CFD simulations predicted a non-uniform radial temperature distribution and demonstrated that limiting the maximum thermal gradient to approximately 20 K, through an appropriate cooldown rate, was necessary to avoid excessive thermally induced stresses. The final design therefore combined local structural refinements, including optimized weld details and additional reinforcement, with controlled operational procedures.

Finally, the extraction grid consists of more than 1200 SS wires, each 235 μm in diameter, spanning the full detector cross-section and required to remain within an extremely tight planarity tolerance to ensure a uniform extraction electric field. One of the key engineering challenges concerned the supporting frame, whose geometry had to be carefully optimized to limit both in-plane and out-of-plane deformations while simultaneously minimizing structural mass and the amount of passive material surrounding the active volume. The resulting structure is an octagonal SS frame, approximately 1.6 m per side, 70 mm wide and 25.4 mm thick, manufactured as four independent segments joined by countersunk horizontal screws to facilitate fabrication and compliance with the required assembly tolerances. Unlike conventional structural systems, where stiffness is maximized to suppress deformation, the extraction-grid frame was designed according to

a deformation-controlled philosophy. The increased wire pretension required for high-voltage operation would have led to an impractically heavy supporting structure under a conventional design approach. Instead, detailed FEA were used to predict the deformation induced by wire tension, allowing the frame to be manufactured with an initial geometric pre-compensation of approximately 20 mm, recovering its nominal geometry only after the final wire tension was applied. During assembly, temporary pre-tensioning cables were progressively replaced by the final spring-loaded wires to ensure controlled load transfer.

The frame is intentionally left free to slide within the PMMA barrel, accommodating differential thermal contraction during cool-down, while the wire elevation is controlled independently through bridge plates connected by shoulder bolts sliding within vertical slots. Dedicated FEA demonstrated that, even under the governing buoyancy load case at cryogenic temperature, the resulting uplift remained well below the available slot travel, preserving the extraction-gap geometry required for detector operation.

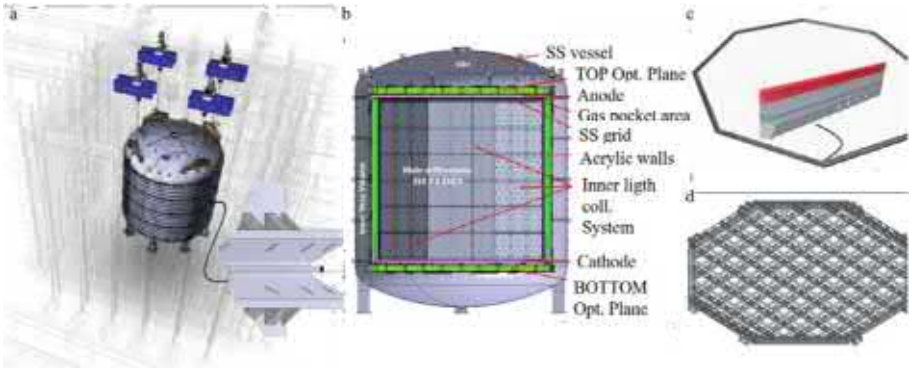


Fig. 3. (a) SS vessel inside the cryostat with detail of the designed lips sealed; (b) TPC enclosed the SS vessel; (c) SS grid frame (detail of the bridge plates in red); (d) SS optical plane.

2.4 Temporary Clean Room Superstructure

The decision to assemble the detector entirely inside the cryostat required the development of a temporary clean-room facility above the cryostat roof. A dedicated steel superstructure was designed to provide an ISO7 environment while supporting the equipment required during detector installation. Besides enclosing the clean-room volume, the structure accommodates a 5 t overhead crane, removable HEPA filter support systems, access platforms, material airlocks and temporary detector support structures, while preserving unobstructed access for handling large detector components.

The design was governed by severe geometric, operational and construction constraints. Support locations were limited to the existing cryostat roof flanges, requiring careful control of local reactions and global deformations. Moreover, the structural layout had to remain compatible with the successive installation stages, including temporary

beam removal, progressive assembly, lifting operations and multiple crane loading configurations. Consequently, several members were positioned according to installation requirements rather than purely structural considerations. The installation sequence of the temporary clean-room superstructure is illustrated in Fig. 4.

A global three-dimensional FE model, including the interaction with the cryostat roof, was developed to assess permanent, operational and seismic load cases. Different construction stages, crane positions and temporary configurations were explicitly analysed. Additional local FE models were subsequently developed for components requiring higher modelling fidelity, including the removable HEPA-filter trusses, crane runway beams, local connections and the temporary Dome Tower supporting the detector during installation.

Beyond structural verification, the numerical analyses directly supported the optimization of member sizing, bracing layouts and connection details, achieving an effective balance between stiffness, constructability and steel weight while limiting load transfer to the cryostat roof. The resulting superstructure became an integral part of the detector assembly infrastructure rather than simply a temporary support frame.



Fig. 4. (a–d) Installation sequence of the temporary clean-room superstructure.

3 Conclusions

The DarkSide-20 k project demonstrates how the design of large underground cryogenic facilities requires structural engineering to extend beyond conventional strength and serviceability verification. Steel structures become integral parts of multi-material systems, where mechanical performance, thermal compatibility, constructability and precision requirements must be addressed simultaneously. The presented engineering solutions illustrate how multidisciplinary challenges can be successfully addressed through an integrated structural design approach, encompassing permanent and temporary steel structures, construction sequencing and interaction with cryogenic and detector systems. The adopted methodologies provide practical guidance for future underground cryogenic and high-technology infrastructures requiring integrated steel engineering solutions.

References

1. Angiolilli M, Carlini M, Ianni A, Nessi M, Tartaglia R, Zani A (2026) Structural engineering solutions for the DarkSide-20k experiment: design, modelling and on-site implementation. Procedia Struct Integrity 78:1807–1814
2. Zani A, DarkSide-20k Collaboration (2024) The DarkSide-20k experiment. J. Instrum. 19(3):C03058
3. Abi B, DUNE Collaboration et al (2020) Volume I: introduction to DUNE. J. Instrum. 15(8):T08008
4. Angiolilli M, DarkSide-20k collaboration (2026) Seismic dynamic interaction between cryostat, suspended detector and support floor during DarkSide-20k installation phases. In: Geotechnical, Geological and Earthquake Engineering. Springer, Cham. (in press)

Author Index

A
Abar, Bahram Mirzaie 208
Abita, Matteo 46, 1075, 1087
Ahmad, Adil 554
Ahmad, Tahir 410, 809
Alibeigibeni, Alireza 576
Aluffi, Giovanni Massimo 901
Amaddeo, Carmen 586
Anagnostou, Nikolaos 527
Andreacola, Francesca Romana 770
Andreotti, Roberto 245
Angiolilli, Michele 1128
Ansalone, Anna Carmela 646
Antonuccio, Erica 925
Ascione, Fabrizio 91, 103, 1012
Asgarkhani, Neda 1012
Auad, Gaspar Andrés 991
Averardi Ripari, Massimo 901

B
Babovic, Neira 14, 1109
Baldassino, Nadia 283, 296, 369
Bandini, Leonardo 723
Barbieri, Bruna 635
Basileo, Giulio 46
Bedon, Chiara 24, 621, 1039
Belleri, A. 1052
Bellicoso, Alessandra 1087
Bello, Micael 554
Bellotti, Valentina 723
Ben, Marco Dal 58
Benvenuti, Edoardo 554, 845
Bernardi, Martina 369
Bernuzzi, Claudio 269, 283, 576
Berruti, Gaia 217
Bertagnoli, Gabriele 681, 878
Berto, Filippo 971
Bezerra, Luciano M. 143
Blasi, Matteo Giuseppe 702
Blogg, Douglas 128
Bogdan, Teodora 554
Bompa, Dan V. 527, 540
Bonelli, Alessio 245
Bonilla, Jorge 143
Boretti, Valentina 878
Bozzacco, Gemma 200
Brancaleoni, Fabio 901
Brando, Giuseppe 770
Brugnolli, Marco 156
Bursi, Oreste S. 156, 245

C
Campiche, Alessia 357
Cantelmi, Daniele 878
Cantisani, G. 1052
Carlini, Marco 1128
Carluccio, Giuseppe 456
Castaldo, Paolo 991, 1001
Castri, Daniele 1075
Catanzano, Alessandro 971
Cerbone, Iolanda 890
Chalarca, Bryan 389
Chioatero, Claudia 936
Chiostrini, Sandro 322
Ciammitti, Laura 1087
Cibelli, Antonio 471, 494
Cicia, Massimo 188
Cii, Stefani 723
Cioni, Paolo 936
Concu, Giovanna 576
Condurso, Salvatore 870
Consales, Marco 217
Corte, G. Della 1052
Cucuzza, Raffaele 681
Cusano, Andrea 217

© The Editor(s) (if applicable) and The Author(s), under exclusive license to Springer Nature Switzerland AG 2026
R. Zanon et al. (Eds.): CTA 2026, LNCE 942, pp. 1139–1142, 2026.
https://doi.org/10.1007/978-3-032-39505-4

D
D'Acunto, Pierluigi 36
D'Addesa, Vito 419, 432
D'Aniello, Mario 188, 208, 712, 1128
D'Anna, Antonio 36
Davino, Antonio 890
De Rosa, Gabriella 512
De Santis, Paola 471
de Silva, Donatella 471, 494, 512
Del Vecchio, Andrea 901
Dell'Oro, Paolo 67
Derkowski, Wit 586
Di Cristofano, Marco 770
Di Donato, Danilo 46, 1075, 1087
Di Filippo, Rocco 245
Di Lorenzo, Gianmaria 890, 1024
Di Sabatino, Umberto 1075
Domaneschi, Marco 758

E
Elia, Vito 858
Epicoco, Rodolfo 878
Esposito, Francesco 103, 1012
Eteme Minkada, M. 1052

F
Fabbrocino, Francesco 444
Faggiano, Beatrice 567
Fagone, Mario 322
Faiella, Diana 103
Fasan, Marco 621, 1039
Fernandes, José 960
Ferraioli, Massimiliano 410, 646, 690, 809
Fieno, Luigi 914
Fiorino, Luigi 419, 432
Folco, Umberto 878
Formisano, Antonio 256, 659, 669, 758, 890

G
Götz, Frank 174
Gabbianelli, Giammaria 389
Galasso, Carmine 91
Galuppi, Marta 1128
Gargiulo, Nunzia 494
Gargiulo, Sabato 24
Gasparini, Giada 14, 36, 1109
Gastaldello, Marco 971
Ghini, Emma 36
Gino, Diego 991, 1001
Giordano, Aldo 858
Giordano, Luca 1001
Giordano, Pier Francesco 1097
Girardi, Stefano 283, 296
Gnazzo, Massimino 712
Grande, Ernesto 79, 115
Grande, Filippo 1128
Gualdi, M. 1052
Gunnarsson, Tina 845

I
Ianni, Andrea 1128
Imbimbo, Maura 79, 115
Imbrenda, Andrea 835
Iovane, Giacomo 567

K
Kanyilmaz, Alper 1116
Kazemi, Farzin 1012
Kovacs, Rebekah 128

L
Laghi, Vittoria 14, 36, 1109
Landolfo, Raffaele 188, 200, 208, 419, 432, 567, 712, 747, 890, 1024
Latour, Massimo 735
Lavacchini, Giovanni 322, 334
Lavino, Angelo 809
Lettieri, Annarosa 690, 735
Liapopoulou, Maria 782
Lima, Jerfson M. 143
Limongelli, Maria Pina 1097
Liuzzo, Riccardo 1097
Longobardi, Giovanna 669
Loss, Cristiano 527, 540
Lucidi, Alice 269, 310
Luisi, Emanuela 217

M
Maccone, Guido 456
Maddaloni, Giuseppe 217, 357
Maglio, Maria 635, 782
Maiorana, Emanuele 165
Mandara, Alberto 809
Marano, Giuseppe Carlo 681
Martelli, Simona 67
Masera, Davide 878
Masiello, Gerardo 24
Matteini, Francesca 334

Mattoccia, Daniele 346
Meglio, Emilia 659, 758, 890
Mei, Alessandro 322, 334
Mele, Elena 3, 91, 103, 1012
Melis, Davide 283
Menardo, Fabio 723
Menghini, Alessandro 1116
Miano, Andrea 471, 512
Miceli, Elena 991, 1001
Micheloni, Michelangelo 925
Milone, Aldo 200
Monte, Francesco 217
Montuori, Rosario 401, 410, 635, 793
Morelli, Francesco 346
Morganti, Renato 46, 1075, 1087
Mottola, Salvatore 646, 690
Moura, Paulo H. R. 143
Mugnos, Giuseppe 502, 598, 947, 1063

N
Naqash, Muhammad T. 256
Nastri, Elide 226, 401, 410, 444, 635, 793
Natali, Agnese 346
Neri, Gabriele 991, 1001
Nessi, Marzio 1128
Nigro, Emidio 471, 494, 512

O
Occhiuzzi, Antonio 357
Odenbreit, Christoph 554
Olivo, Jana 681
Olmez, Hasan N. 156
Orlando, Maurizio 322, 334
Orsi, Goffredo 681

P
Pagnini, L. 1052
Paldino, Domenico 925
Palumbo, Pietro 878
Panepucci, Alessia 1087
Panighel, Federico 870
Parcianello, Enrico 870
Parzanese, Ida Pia 444
Pastore, Marina 401, 410
Pecorari, Osvaldo 646
Petrangeli, Mario Paolo 914
Piluso, Vincenzo 444, 635, 793
Pinna, Francesco 820
Pisani, Marco Andrea 576
Pisapia, Alessandro 444
Pisciottano, Francesco 401, 410, 444, 982
Plaitano, Francesco 226
Polastri, Andrea 914
Polesel, Irene 621
Polidoro, Riccardo Maria 3
Previtali, Barbara 1116
Profico, Francesco 554, 611
Prota, Alessandro 419, 432, 747
Pucinotti, Raffaele 586

R
Rama, Luigi 200
Ranocchiai, Giovanna 322
Rea, Simone 1087
Ricci, A. 1052
Rizzo, Giorgio 870
Ruiz-Oronia, Jorge 389
Runcio, Edoardo 58

S
Sabia, Donato 381
Sabirov, Ilchat 1116
Saccone, Marta 576
Saetta, Anna 971
Safarani, Ward Alarab 381
Saito, Rio 735
Sangiorgio, Valentino 770
Sato, Atsushi 690, 735
Savino, Elisabetta 14, 1109
Scafuri, Chiara 793
Schäfer, Markus 611
Scotta, Roberto 971
Scrivener, Mark 128
Serraiotto, Arianna 296, 369
Serpe, Marina 79, 115
Sesana, Marta Maria 67
Sgarbanti, Marianna 67
Shaghaghi, Arsalan Sadeghi 208
Silva, Ramon 143
Silvestri, Stefano 36
Simoncelli, Marco 269, 283, 310, 576, 820
Soler, Roger 482
Somma, Giuliana 58
Sperandio, Mattia 165
Stizzo, Marco 858
Stochino, Flavio 576, 820
Stratan, Aurel 226
Stroscio, Riccardo 128
Szokalska, Alexandra 936

T
Tartaglia, Roberto 217, 357, 410, 747, 1128
Terracciano, Giusy 1024
Tognaccini, Riccardo 482, 960
Tomei, Valentina 79, 115
Tondolo, Francesco 381
Tosone, Alessandra 46, 1075, 1087
Trentacarlini, Simone 914
Trombetti, Tomaso 1109
Turrini, Nicola 845

U
Ungureanu, Viorel 46
Uwiringiyimana, Godfrey 845

V
Valdes, Monica 576
van Schaijk, Erik 482
Vanin, Mattia 156
Vigoriti, Giuseppe 835

W
Waqar, Saad 1116

Y
Yang, Jie 554
Yousefi, Ali 878

Z
Zandonini, Riccardo 296, 369
Zani, Andrea 1128
Zanon, Gabriele 156, 245
Zanon, Riccardo 554, 611, 845, 982
Zucca, Marco 576, 820
Zulian, Barbara 723
Žužul, J. 1052